

2
AGARD-CP-183

AGARD-CP-183

ADA 028615

AGARD

ADVISORY GROUP FOR AEROSPACE RESEARCH & DEVELOPMENT

7 RUE ANCELLE 92200. NEUILLY SUR SEINE FRANCE

AGARD CONFERENCE PROCEEDINGS No. 183

on

Optical Propagation in the Atmosphere

D D C

RECEIVED
AUG 24 1976
B

NORTH ATLANTIC TREATY ORGANIZATION



DISTRIBUTION AND AVAILABILITY
ON BACK COVER

DISTRIBUTION STATEMENT A

(14)

AGARD-CP-183

NORTH ATLANTIC TREATY ORGANIZATION
ADVISORY GROUP FOR AEROSPACE RESEARCH AND DEVELOPMENT
(ORGANISATION DU TRAITE DE L'ATLANTIQUE NORD)

⑨ Conference Proceedings.

⑥

AGARD Conference Proceedings No. 183

OPTICAL PROPAGATION IN THE ATMOSPHERE

⑪ May 76

⑫ 648p.

DISTRIBUTION STATEMENT A
Approved for public release;
Distribution Unlimited

ACCESSION for		
NTIS	WH/IS Section	<input checked="" type="checkbox"/>
DDC	Diff Section	<input type="checkbox"/>
UNANNOUNCED		<input type="checkbox"/>
JUSTIFICATION		
BY		
DISTRIBUTION/AVAILABILITY CODES		
Dist.	AVAIL.	and/or SPECIAL
A		

4/B

THE MISSION OF AGARD

The mission of AGARD is to bring together the leading personalities of the NATO nations in the fields of science and technology relating to aerospace for the following purposes:

- Exchanging of scientific and technical information;
- Continuously stimulating advances in the aerospace sciences relevant to strengthening the common defence posture;
- Improving the co-operation among member nations in aerospace research and development;
- Providing scientific and technical advice and assistance to the North Atlantic Military Committee in the field of aerospace research and development;
- Rendering scientific and technical assistance, as requested, to other NATO bodies and to member nations in connection with research and development problems in the aerospace field;
- Providing assistance to member nations for the purpose of increasing their scientific and technical potential;
- Recommending effective ways for the member nations to use their research and development capabilities for the common benefit of the NATO community.

The highest authority within AGARD is the National Delegates Board consisting of officially appointed senior representatives from each member nation. The mission of AGARD is carried out through the Panels which are composed of experts appointed by the National Delegates, the Consultant and Exchange Program and the Aerospace Applications Studies Program. The results of AGARD work are reported to the member nations and the NATO Authorities through the AGARD series of publications of which this is one.

Participation in AGARD activities is by invitation only and is normally limited to citizens of the NATO nations.

The content of this publication has been reproduced directly from material supplied by AGARD or the authors.

Published May 1976

Copyright © AGARD 1976
All Rights Reserved

ISBN 92-835-0164-0

681.7.013:551.59



*Printed by Technical Editing and Reproduction Ltd
Harford House, 7-9 Charlotte St, London, W1P 1HD*

PROGRAM AND MEETING OFFICIALS

PROGRAM CHAIRMAN

Dr H.Hodara
Tetra Tech Inc.
Pasadena
USA

PROGRAM COMMITTEE

Mr P.Halley
C.N.E.T.
France

Dr R.Allen
RAE, Farnborough
UK

Dr H.Hohn
University of Tübingen
Germany

Captain J.W.Justice
ARPA Strategic Technology Office
Arlington
USA

Dr G.N.Plass
Texas A & M University
College Station
USA

Dr H.T.Yura
The Aerospace Corporation
Los Angeles
USA

ELECTROMAGNETIC WAVE PROPAGATION PANEL

CHAIRMAN

Prof. I.Ranzi
Istituto Superiore P.T.
Italy

DEPUTY CHAIRMAN

Mr P.Halley
C.N.E.T.
France

PANEL EXECUTIVE

Dr N.R.Ogg
AGARD-NATO
7, rue Ancelle
92200, Neuilly-sur-Seine
France

HOST COORDINATOR

Prof. P.Gudmandsen
Technical University of Lyngby
Denmark

CONTENTS

	Page
PROGRAM AND MEETING OFFICIALS	iii
EDITOR'S INTRODUCTION	viii
	Reference
 <u>SESSION I - ATMOSPHERIC CHARACTERISATION</u>	
OPTICAL MODELLING OF THE ATMOSPHERE by R.A.McClatchey, J.E.A.Selby and J.S.Garing	1
MODELS OF THE ATMOSPHERIC AEROSOLS AND THEIR OPTICAL PROPERTIES by F.P.Shettle and R.W.Fenn	2
A COMPARATIVE STUDY OF ATMOSPHERIC TRANSMISSION AT THREE LASER WAVELENGTHS IN RELATION TO THE METEOROLOGICAL PARAMETERS by P.J.Wright	3
REMOTE AEROSOL SENSING WITH AN ABSOLUTE CALIBRATED DOUBLE FREQUENCY LIDAR by R.Reiter, W.Carnuth, M.Littfass and N.C.Varshneya	4
ATMOSPHERIC EFFECTS RELEVANT TO LASER SPECTROSCOPY by T.Lund and A.G.Kjelaas	5
THE FLUID MECHANICS AND COMPUTER MODELLING OF ATMOSPHERIC TURBULENCE CAUSING OPTICAL PROPAGATION FLUCTUATIONS by W.C.Meecham	6
Paper 7 not available	
QUESTIONS AND COMMENTS ON SESSION I SUMMARY OF SESSION I by D.Höhn	DI
 <u>SESSION II - INCOHERENT PROPAGATION</u>	
CALCULATION OF POLARIZATION AND RADIANCE IN THE ATMOSPHERE by G.N.Plass	8
RADIATIVE TRANSFER IN CLOUDY ATMOSPHERES by K.N.Liou	9
MULTIPLE SCATTERING IN PLANETARY ATMOSPHERES by W.M.Irvine	10
METHODES POUR RESOUDRE L'EQUATION DE TRANSFERT RADIATIF DANS DES COUCHES D'EPAISSEUR FINIE par J.Lenoble	11
REMOTE PROBING OF ATMOSPHERIC PARTICULATES FROM RADIATION EXTINCTION EXPERIMENTS A REVIEW OF METHODS by A.L.Fymat	12
THEORETICAL STUDIES OF THE TRANSFER OF SOLAR RADIATION IN THE ATMOSPHERE by M.J.Kerschgens, E.Raschke and U.Reuter	13
THE MEASUREMENT PROGRAMME OPAQUE OF AC/243 (PANEL IV/RSG.8) ON "SKY AND TERRAIN RADIATION" by T.Bakker	14

**EXPERIMENTAL AND COMPUTATIONAL COMPARISON OF DIFFERENT
METHODS FOR DETERMINATION OF VISUAL RANGE**

by W.Büchtemann, H.Hipp, W.Jessen and R.Neuwirth

15

**TRANSFERT DU RAYONNEMENT DANS UN MILIEU ABSORBANT ET
DIFFUSANT**

par Y.Fouquart et J.C.Buriez

16

FLUORESCENT AND RAMAN SCATTERING IN PARTICLES

by M.Kerker, P.J.McNulty and H.Chew

17

QUESTIONS AND COMMENTS ON SESSION II

SUMMARY OF SESSION II by G.N.Plass

DII

SESSION III - COHERENT PROPAGATION

**PHYSICAL MODEL FOR STRONG OPTICAL WAVE FLUCTUATIONS IN THE
ATMOSPHERE**

by H.T.Yura

18

**LOG-NORMAL PROBABILITY DISTRIBUTION OF STRONG IRRADIANCE
FLUCTUATIONS: AN ASYMPTOTIC ANALYSIS**

by L.R.Bissonnette

19

**TURBULENCE EFFECTS ON TARGET ILLUMINATION BY LASER TRANSMITTER
UNIFIED ANALYSIS AND EXPERIMENTAL VERIFICATION**

by J.R.Kerr

20

**PROPAGATION OF FOCUSED LASER BEAMS IN THE TURBULENT
ATMOSPHERE**

by H.Raidt

21

**PROPAGATION OF FOCUSED TRUNCATED LASER BEAMS IN THE
ATMOSPHERE**

by R.F.Lutomirski

22

MEASUREMENTS OF THE ATMOSPHERIC TRANSFER FUNCTION

by J.C.Dainty and R.J.Scaddan

23

**INTENSITY CORRELATION OF RADIATION SCATTERED ALONG THE PATH
OF A LASER BEAM PROPAGATING IN THE ATMOSPHERE**

by M.Bertolotti, M.Carnevale, B.Crosignani, B.Daino and P.Di Porto

24

MEASUREMENT OF ATMOSPHERIC ATTENUATION AT 6328 Å

by M.Bertolotti, M.Carnevale, B.Daino, M.Galeotti and D.Sette

25

**MEASUREMENTS OF ANGLE OF ARRIVAL FLUCTUATIONS OF A LASER
BEAM DUE TO TURBULENCE**

by A.Consortini

26

A MULTIPLE SCATTERING CORRECTION FOR LIDAR SYSTEMS

by J.V.Winstanley and C.Wigmore

27

**MESURES DE L'ABSORPTION ATMOSPHERIQUE PAR UTILISATION D'UN
RADIOMETRE HETERODYNE INFRA-ROUGE SOLAIRE**

par B.Christophe et M.Camus

28

QUESTIONS AND COMMENTS ON SESSION III

SUMMARY OF SESSION III by H.T.Yura

DIII

SESSION IV - NON-LINEAR PROPAGATION

PROPAGATION OF HIGH POWER LASER BEAMS THROUGH THE ATMOSPHERE: AN OVERVIEW by J.N.Hayes	29
AN OVERVIEW OF THE LIMITATIONS ON THE TRANSMISSION OF HIGH ENERGY LASER BEAMS THROUGH THE ATMOSPHERE BY NONLINEAR EFFECTS by S.Edelberg	30
NUMERICAL METHODS IN HIGH POWER LASER PROPAGATION by P.B.Ulrich	31
THE LIMITATIONS IMPOSED BY ATMOSPHERIC BREAKDOWN ON THE PROPAGATION OF HIGH POWER LASER BEAMS by D.E.Lencioni	32
EXPERIMENTAL DETERMINATION OF SINGLE AND MULTIPLE PULSE PROPAGATION by R.W.O'Neil, H.Kleiman and H.R.Zwicker	33
QUESTIONS AND COMMENTS ON SESSION IV SUMMARY OF SESSION IV by J.N.Hayes	DIV

SESSION V - PROPAGATION LIMITATIONS ON SYSTEMS

COMPENSATED IMAGING by J.W.Justice and R.P.Urtz, Jr	34
DETERMINATION OF SLANT VISUAL RANGE FROM LIDAR SIGNATURES. ANALYSIS OF SIMULATED SIGNATURES by M.Gazzi, V.Vicentini, L.Pantani, B.Radicati, L.Stefanutti and C.Werner	35
COMPUTER SIMULATION OF ATMOSPHERIC TURBULENCE AND COMPENSATED IMAGING SYSTEMS by B.L.McGlamery	36
HOW MANY PICTURES DO YOU HAVE TO TAKE TO GET A GOOD ONE? by D.L.Fried	37
REMOTE PROBING OF WINDS AND REFRACTIVE TURBULENCE USING OPTICAL TECHNIQUES by S.F.Clifford	38
MEASURED VISIBLE SPECTRUM PROPERTIES OF REAL ATMOSPHERES by S.Q.Duntley	39
PASSIVE AND ACTIVE ATMOSPHERIC VISION by D.H.Höhn	40
DECREASE OF CONTRAST IN THE ATMOSPHERE: STATISTICAL PRESENTATION OF THE RESULTS OF DAYTIME AND NIGHTTIME MEASUREMENTS by J.Van Schie and J.Rogge	41
BENDING OF RAYS OF LIGHT ABOVE THE SEA SURFACE by P.A.Stokseth and A.Nordbryhn	42
ATMOSPHERIC LIMITATIONS OF ACTIVE AND PASSIVE NIGHT VISION SYSTEMS by E.G.D.Youngs	43
USING LIDAR FOR MEASURING VISIBILITY by J.F.Ruger	44

Reference

**THE INFLUENCE OF THE ATMOSPHERE BETWEEN HELICOPTERS AND
GROUND-TARGETS ON THE DOWNWARD AND UPWARD VISIBILITY**
by H.E.Hoffmann

45

QUESTIONS AND COMMENTS ON SESSION V
SUMMARY OF SESSION V by R.R.Allan

DV

EDITOR'S INTRODUCTION

A majority of military optical systems operate in the atmosphere and their performance is often degraded by weather. For several decades researchers have studied in-depth the performance limitations imposed by the atmosphere and devised techniques to get around these problems. The purpose of this symposium was to bring together and update our understanding of atmospheric optical propagation, present a comprehensive review of the state-of-the-art, and provide interaction among the key researchers in the NATO community.

I believe the reader will find that the proceedings of this conference fulfill this goal. Some of the papers presented included topics not usually covered in previous unclassified meetings, in particular, nonlinear propagation with high power lasers, and adaptive optics techniques to overcome blurring by turbulence.

The conference was organized in five sessions, in the following logical order. Session 1, "Atmospheric Characterization", dealt with the physics of the atmosphere and the models available to predict optical propagation. Session 2, "Incoherent Propagation", and Session 3, "Coherent Propagation", presented theoretical and experimental results regarding propagation of light from conventional sources and lasers respectively. Session 4, "Non-Linear Propagation", was one of the rare unclassified sessions which dealt with theory and experiments with high power lasers and their nonlinear effects in the atmosphere. Finally, Session 5, "Propagation Limitations on Systems", was intended to illustrate the effects of atmospheric limitations on a few typical unclassified military systems and some of the techniques proposed to overcome these limitations.

A review of each session by its chairman or one of the panel members follows with a summary of salient features and the remaining problems.

OPTICAL MODELLING OF THE ATMOSPHERE

BY

ROBERT A. McCLATCHEY
JOHN E.A. SELBY
JOHN S. GARING
Air Force Cambridge Research Laboratories
Hanscom AFB, Massachusetts
USA

SUMMARY

The optical modelling of the atmosphere requires both a knowledge of the physical properties of the atmosphere as well as the spectroscopic properties of the gases and particulates of which it is composed. In this paper we will first discuss the pertinent atmospheric properties of temperature, pressure and constituent distributions. We will then describe the AFCRL Atmospheric Absorption Line Parameters Compilation, indicating the requirements for such a data compilation and some of the omissions and uncertainties. The Line-by-Line transmittance calculation technique will then be described, indicating the capability of this technique for use in laser propagation studies as well as low spectral resolution applications. The LOWTRAN computer model will be presented together with an indication of its limitations.

1. INTRODUCTION

Optical systems for military applications operate in the ultraviolet visible and infrared parts of the spectrum. In order to understand the propagation characteristics of the atmosphere for radiation in this broad spectral region, it is necessary to understand the details of molecular extinction processes (both absorption and scattering) as well as the details of aerosol absorption and scattering processes.

Beer's law for linear propagation of monochromatic radiation at frequency ν in a homogeneous medium can be expressed as follows:

$$\frac{dI(X, \nu)}{dX} = -\gamma(\nu) I(X, \nu) \quad (1)$$

where $I(X, \nu)$ is the intensity of the radiation at distance X and $\gamma(\nu)$ is the attenuation coefficient.

Transmittance of radiation in the atmosphere is complex owing to the dependence of scattering and absorption coefficients on a number of different physical properties of the atmosphere (Goody, 1964). Solving Equation 1, we have for the monochromatic radiation observed at distance, X , from the source;

$$I(X, \nu) = I(0, \nu) \tau \quad (2)$$

where $I(0, \nu)$ is the intensity of radiation at the source, and τ is the monochromatic transmittance which is given by

$$\tau = \exp(-\gamma X) \quad (3)$$

where γ is an attenuation coefficient and X is the length of the path traversed by the radiation. The attenuation coefficient (γ) is given by

$$\gamma = \sigma + k \quad (4)$$

where σ is the scattering coefficient and k is the absorption coefficient. Equation 3 is only strictly valid when applied to monochromatic radiation.

The scattering and absorption coefficients defined in Equation 4 depend on both the constituent molecules and aerosols in the atmospheric path. If electro-magnetic radiation is incident on a molecule or an aerosol, a portion of the radiation is absorbed and the rest is scattered in all directions. Thus we must make the following definitions:

$$\sigma = \sigma_m + \sigma_a \quad (4a)$$

$$k = k_m + k_a \quad (4b)$$

where the subscripts, m and a , indicate molecule and aerosol respectively. In order to compute the attenuation quantitatively, it is necessary to consider all four of the quantities defined in Equations (4a) and (4b).

The molecular scattering coefficient depends only on the number density of molecules in the radiation path, whereas the molecular absorption coefficient is a function of not only the amount of absorbing gas, but also the local temperature and pressure of the gas. The wavelength dependence of molecular (Rayleigh) scattering is very nearly $\sigma_m \sim \lambda^{-4}$. The variation of the molecular absorption coefficient with wavelength is much more complicated, being a highly oscillatory function of wavelength due to the presence of numerous molecular absorption band complexes as is indicated in Figure 1. These band complexes result for the most part from minor atmospheric constituents. The responsible molecules are (in order of importance): H_2O , CO_2 , O_3 , N_2O , CO , O_2 , CH_4 , N_2 . All of these molecules except for H_2O and O_3 are assumed to

be uniformly mixed by volume in the transmittance calculations we will present.

The quantities g_a and k_a depend on the number density and size distribution of aerosols as well as on their complex index of refraction. A thorough discussion of aerosol effects will be given by Shettle and Fenn elsewhere in this meeting, so we will limit our detailed discussion to molecular absorption effects.

In order to model the optical properties of the atmosphere, it is necessary to study and understand the spectral properties of the appropriate molecules and aerosols and in addition, it is necessary to define the atmosphere in terms of constituent distributions, temperature and pressure. Concerning the problem of molecular absorption, it is required that we know the frequencies, intensities, widths and shapes of all spectral lines in the region of interest. In addition we must be able to model or measure the distributions of water vapor, ozone, and the other absorbing atmospheric gases as well as temperature and pressure along the intended atmospheric path. An uncertainty in the definition of the physical properties of the atmosphere can affect the computed atmospheric transmittance in much the same way as an uncertainty in the parameters defining the absorptive properties of a particular molecule.

In order to provide a base for transmittance modelling, we will discuss the variability and uncertainties in physical models of the atmosphere. We will then describe the AFCRL Atmospheric Absorption Line Parameters Compilation, indicating the requirements for such a data compilation and some of the remaining omissions and uncertainties. The Line-by-Line (LBL) transmittance calculation technique will be briefly described and some results pertinent to laser propagation will be presented. The use of the LBL approach to low spectral resolution transmittance modelling will be discussed as well as other low resolution techniques in which the line parameters compilation can be used directly. A discussion of the LOWTRAN model will be presented with an emphasis on the accuracy and efficiency of the model for system applications.

2. ATMOSPHERIC MODELS

2.1 Standard Atmospheres

A series of six standard atmospheres are described by McClatchey, et al (1972) in terms of height, pressure, temperature, density, water vapor density and ozone density. With the exception of the water vapor and ozone distributions, these models are taken directly from the U.S. Standard Atmosphere Supplements, 1966 and the Handbook of Geophysics and Space Environment, (Valley, 1965). The water densities above 11 km were taken from Sissenwine et al (1968). Three of these model atmospheres are summarized in Figures 2 and 3 and the details for the U.S. Standard Atmosphere are provided in Table 1. More details can be found in the references cited above.

2.2 Composition

Table 2 provides concentrations of a number of additional atmospheric constituents (water and ozone are already covered in the standard atmospheres).

TABLE 2. Concentrations of "Uniformly Mixed Gases" in Dry Air Near Sea Level

Constituent	ppm by volume
CO ₂	322
N ₂ O	0.27
CO	0.19
CH ₄	1.5
O ₂	2.10×10^5

These constituents have been referred to by many as the "uniformly mixed" gases and values provided in Table 2 represent a mean value. Although the major atmospheric constituents N₂ and O₂ can reasonably be assumed to be uniformly mixed, the mixing ratios of many other minor constituents, many of which are important absorbers of infrared radiation, in some cases show temporal and spatial variations. Although, N₂ and O₂ compose the bulk of the atmosphere, they are of minor importance to atmospheric propagation due to their lack of absorption properties in the infrared. The following discussion on the temporal and spatial variability of the gases listed in Table 2 has been largely taken from Cadle (1974).

2.2.1 CO₂ (322 ppmv as a mean value)

The mixing ratio of CO₂ in the atmosphere is increasing by about 0.2 percent per year. Bolin and Bischof (1970) found that the mixing ratio decreased in the stratosphere by about 0.6 ppmv compared with the troposphere. At sea level the mixing ratio is slightly less in the polar regions than in other regions, and higher in urban than rural areas. In the northern hemisphere the CO₂ mixing ratio has seasonal oscillations of 6-9 ppm at the earth's surface.

2.2.2 N₂O (0.27 ppmv in troposphere)

The mixing ratio is relatively constant in the troposphere both with space and time, but decreases in the stratosphere to a value of about 0.1 ppmv at 18 km.

2.2.3 CO (0.19 ppmv as mean sea level value)

The mixing ratio of CO has been found to be variable both with time and space and values ranging between 0.05 and 0.25 ppmv at sea level have been reported. Concentrations are higher in urban areas than in rural areas and CO appears to be present in higher concentrations at night than during the day. A

good mean tropospheric value appears to be 0.13 ppmv decreasing to a value of 0.04 ppmv in the lower stratosphere.

2.2.4 CH₄ (1.5 ppmv near sea level)

The mixing ratio of CH₄ appears to be fairly constant near sea level, and in much of the troposphere (although only a small number of measurements are available). Above the tropopause methane increases rapidly to a value of about 0.25 ppmv at 50 km.

Limited information is available on a number of additional trace gases and is summarized in the report by Cadle (1974). The resulting absorption by these trace gases is expected to be sufficiently small that they will be dominated by the other gases mentioned in the troposphere. For higher altitudes (above 10 km), a good summary of the altitude variation of various gases is given in Figure 4, which is taken from T. Hard (1974).

It can be seen from the discussion provided here that transmittance models will be limited to some extent by the uncertainties in atmospheric models. For accurate predictions of transmittance and for the checking of models against experimental data all of these parameters should be measured in conjunction with optical transmittance measurements.

3. ABSORPTION LINE COMPILATION

In order to accurately compute the monochromatic transmittance of the atmosphere, we must first obtain accurate data describing the frequencies, intensities and line shape of all absorption lines affecting the attenuation at the frequency in question. If our aim is to develop this monochromatic capability throughout the visible, infrared and microwave regions of the spectrum, we must then develop a compilation based on certain constraints dictated by atmospheric abundances.

About 7 years ago an effort was initiated at AFCRL with the aim of providing a complete set of data for all vibration-rotation lines of all naturally occurring molecules of significance in the terrestrial atmosphere. With such data at hand, it would be possible to compute the transmittance appropriate for atmospheric paths by first computing the monochromatic transmittance many times in a finely spaced frequency grid and then degrading the results to any appropriate spectral resolution. The monochromatic results would directly represent the atmospheric transmittance of laser radiation. Up to now the following molecules have been included in this compilation: (1) water vapor; (2) carbon dioxide; (3) ozone; (4) nitrous oxide; (5) carbon monoxide; (6) methane; and (7) oxygen. Plans are currently being implemented to add data on additional species such as NO, NO₂, SO₂, HNO₃, etc. All of these molecules except oxygen are minor constituents of the atmosphere, but nonetheless represent most of the absorption lines in the visible, infrared, and microwave regions.

In order to compute the transmittance due to a given spectral line in the atmosphere it is necessary to describe the absorption coefficient as a function of frequency for each line. The four essential line parameters for each line are the resonant frequency, ν_0 (cm⁻¹), the intensity per absorbing molecule, S (cm⁻¹/molecule cm⁻²), the Lorentz line width parameter, α_0 (cm⁻¹/atm), and the energy of the lower state, E'' (cm⁻¹). The frequency, ν_0 , is independent of both temperature and pressure (except for possibly very small pressure effects of less than 0.01 cm⁻¹/atm, which have been ignored here). The intensity, S , is pressure-independent, and, as discussed below, its temperature dependence can be calculated from E'' and ν_0 .

The line half-width at half maximum, α , is proportional to the pressure, p , and its temperature dependence can be estimated as discussed below.

The precise line shape is a matter of some uncertainty, but in the derivation of line parameters from laboratory measurements, it is customary to start from the Lorentz shape (see Goody, 1964) given in Equation (5).

$$k(\nu) = \frac{S\alpha/\pi}{(\nu - \nu_0)^2 + \alpha^2} \quad (5)$$

$$S = \int k(\nu) d\nu$$

The ability of Equation (5) to describe the true line shape is subject to two limitations. The first, which can be precisely estimated and corrected for by the use of the Voigt shape, occurs when $\alpha_0 p/\alpha_D < 1.0$ where α_D is the Doppler line width. The Doppler line width varies with frequency, temperature and molecular mass as given in Equation (6).

$$\alpha_D = \frac{\nu}{c} \left(\frac{2kT}{m} \right)^{1/2} = 4.298 \times 10^{-7} \nu (T/M)^{1/2} \quad (6)$$

where M = molecular weight and here k = Boltzmann's constant and m = mass of a molecule.

For atmospheric molecules and infrared frequencies, modifications of the Lorentz shape resulting from Doppler effects begin to be required at pressures below 10 mb (above 30 km).

The second limitation concerns possible inadequacies of the Lorentz shape, especially in the distant wings of a line where $|\nu - \nu_0| \gg \alpha$ (see Winters et al, 1964, and Burch et al, 1969) or when the long-range intermolecular forces responsible for collision broadening are dipole-quadrupole, leading to an exponent 1.75 rather than 2.0 for the term $(\nu - \nu_0)$ in Equation 5, (Varanasi and Tejwani, 1972).

Throughout this compilation we assume the validity of the Lorentz exponent.

The line intensity is temperature dependent through the Boltzmann factor and the partition function as indicated in Equation (7).

$$S(T) = \frac{S(T_s) Q_v(T_s) Q_r(T_s)}{Q_v(T) Q_r(T)} \left[\frac{1 - \exp^{-\frac{1.439E''}{T}}}{1 - \exp^{-\frac{1.439E''}{T_s}}} \right] \exp \left[\frac{1.439E'' (T - T_s)}{T T_s} \right] \quad (7)$$

where E'' (in cm^{-1}) is the energy of the lower state of the transition and where Q_v and Q_r are the vibrational and rotational partition functions.

It is also necessary to know the temperature variation of α . In the absence of specific indications to the contrary, the equation $\alpha(T)/\alpha(T_s) = (T/T_s)^{-n}$, with $n = 4$, corresponding to the assumption of temperature-independent collision diameters, may be made. The validity of the assumption is more uncertain, the larger the dependence of the diameter on the particular rotation-vibration transition, (that is, it is most unrealistic for H_2O and low-J transitions of the other molecules). The theory of Tsao and Cornette (1954) when applied to the determination of line width for H_2O lines gives a wide variation of n about the mean value of 0.62 (Benedict and Kaplan, 1959). Measurements made with a CO_2 laser (Ely and McCubbin, 1970) indicate a value of $n=1.0$ for the P20 line of the $10.4 \mu\text{m}$ CO_2 band.

An examination of Equations (5) and (7) indicates that it is necessary to know the ν_0 , $S(T_s)$, $\alpha(P_0, T_s)$ and E'' value for each line in order to compute a spectrum. The data compilation described here contains these four quantities for each of the more than 130,000 lines between $1 \mu\text{m}$ and the far infrared belonging to the seven molecular species listed in Table 3.

Table 3. Intensity Criteria for Lines Included in Compilation

Molecule	Identification No.	Minimum Intensity* Criterion at $T=296\text{K}$	Existing Intensity Minimum at $T=296\text{K}$
H_2O	1	3×10^{-27}	3×10^{-27}
CO_2	2	2.2×10^{-26}	3.7×10^{-27}
O_3	3	3.5×10^{-24}	3.5×10^{-24}
N_2O	4	3.0×10^{-23}	4.0×10^{-23}
CO	5	8.3×10^{-23}	1.9×10^{-23}
CH_4	6	3.3×10^{-24}	3.3×10^{-24}
O_2	7	3.7×10^{-30}	3.7×10^{-30}

* Units are $\text{cm}^{-1}/(\text{molecule-cm}^{-2})$

In order to establish the "Minimum Intensity Criterion" values given in Table 3, an extreme atmospheric path was considered, assuming the gas concentrations specified in Table 1 and maximum concentrations over the path of 3×10^{24} molecules/ cm^2 for water vapor and 1×10^{20} molecules/ cm^2 for ozone. This extreme radiation path was the atmospheric path tangent to the earth's surface, and extending from space to space. Using this criterion, lines yielding less than 10 percent absorption at the line center would normally be omitted.

Although this absolute line intensity cut off was established, it has not always been possible to achieve. In some cases it would have been unrealistic to push calculations to this limit when experimental confirmation fell far short. There are two specific areas in which this absolute cut off has been violated: (1) In regions of very strong absorption, very weak lines above this absolute limit have been neglected; (2) Q-branch lines below this limit have occasionally been included where it is felt that the accumulation of many weak, closely spaced lines would still produce an appreciable absorption under some atmospheric circumstances. In some cases, (for example, CO_2), sufficient laboratory measurements and theoretical work were available so that this limit was exceeded throughout the infrared.

Half-widths of lines have been added where available. In some cases, it is felt that insufficient data exist to warrant the inclusion of a variable half-width. In these cases, a mean, constant value has been inserted for each molecular species and values are given in Table 4. Line widths for H_2O have been calculated based on the Anderson Theory (Anderson, 1949) modified by eliminating the distance of closest approach. This modification gives results comparing favorably with the measurements of Blum et al, 1972 for a number of high-J lines. Line widths for CO_2 have been taken from the theoretical work of Yamamoto et al, 1968 who applied the Anderson Theory to $\text{CO}_2 - \text{N}_2$ collisions.

Table 4. Mean Half-width Values

Molecule	Half-width ($\text{cm}^{-1}/\text{atm}$)	References
O_3	0.11	Lichtenstein et al (1971)
N_2O	0.08	Toth (1971)
CO	0.06	Bouanich and Haeusler (1972)
CH_4	0.055	Varanasi (1971) (see Section 6.3)
O_2	0.060	Burch and Gryvnak (1969)

The accuracy of transmittance calculations due to molecular absorption can be seen to depend on three quantities: (1) The accuracy of the line parameters; (2) The accuracy of the assumed line shape; and (3) The accuracy of the description of the atmosphere in terms of temperature, pressure, and constituent distributions. We can get a feel for the first of these by examining Table 5.

Table 5. Accuracy of Data

Molecule	$\nu(\text{cm}^{-1})$	S	α
H ₂ O	$\pm 0.00001-0.05$	1-10% Rotat. 10%-X2 others	$\pm 10\%-X3$
CO ₂	± 0.01	$\pm 5\%$	$\pm 10\%$
O ₃	$\pm 0.01-1.0$	$\pm 10\%$	Constant Value
N ₂ O	± 0.01	$\pm 5\%$	Constant Value
CO	$\pm 0.001-0.01$	$\pm 2\%-\pm 10\%$	$\pm 10\%$
CH ₄	± 0.01	$\pm 20\%$	Constant Value
O ₂	± 0.01	$\pm 10\%$	Constant Value

As can be seen, it is difficult to specify simply the accuracy of these line parameters because they are different from one band to another for a given molecule and are also a function of the line intensity. This is so because of the increased experimental confirmation available for the stronger lines. In the microwave region absorption line positions can be measured very accurately due to available measurement techniques. This same kind of precision is becoming more highly developed in the infrared.

4. CONTINUUM ABSORPTION

In addition to the spectral absorption lines described above, there are several spectral regions of relatively continuous absorption. Several of these are of interest because they fall in the atmospheric "windows" e.g. in the 1 μm and 4 μm regions ($\sim 10,000 \text{ cm}^{-1}$ and $2,500 \text{ cm}^{-1}$), from 8-14 μm (1250 cm^{-1} to 700 cm^{-1}) and near 22 μm (450 cm^{-1}). In other spectral regions the contribution by nearby absorption lines is much greater than that by the continuum absorption, so that for practical purposes the continuum effect can be neglected, although it may be greater than in the windows.

This continuous absorption is caused by one or more of the following three processes: (1) extreme wings of strong collision-broadened absorption lines centered more than $10-20 \text{ cm}^{-1}$ away; (2) pressure induced absorption resulting from transitions that are forbidden for unperturbed molecules; and (3) the possible existence of the water dimer (H₂O:H₂O) in the case of the 8 to 14 μm region.

The absorption coefficient due to continuum absorption can be expressed as

$$k = C_s P_s + C_b P_b \quad (8)$$

where C_s is the self-broadened coefficient and C_b is the foreign gas broadening coefficient, P_s is the partial pressure of the absorbing gas and P_b is the foreign gas pressure.

Figure 5 gives the spectral dependence of C_b for water vapor absorption in the 8 to 14 μm region for three temperatures (Burch, 1970). The C_b value has been most reliably measured by McCoy et al, 1969, and is found for nitrogen broadening to be $C_b = 0.005 C_s$ at room temperature at 10.6 μm .

Figure 6 gives the spectral dependence of C_b for the water vapor absorption in the region near 4 μm for four different temperatures (Burch et al, 1971). Note that the $T=296^\circ\text{K}$ curve is an extrapolation based on the measurements at higher temperature. These same workers found the ratio C_b/C_s for nitrogen broadening to be 0.12 ± 0.03 in the 4 μm region.

Figure 7 gives the spectral dependence of the absorption coefficient due to the pressure-induced nitrogen absorption centered near 2330 cm^{-1} (Burch et al, 1971). Measurements have also been made by Shapiro and Gush, 1966, and Farmer and Houghton, 1966. Since the foreign gas broadening in this case results mainly from oxygen which has a constant mixing ratio in the atmosphere, Equation (8) reduces to

$$k = \text{Const.} \times P \quad (9)$$

The constant in Equation 9 is directly proportional to total pressure, P , the absorption coefficient depends on P^2 . The nitrogen absorption coefficients given in Figure 7 are expressed in the units $\text{atm}^{-2} \text{ Km}^{-1}$.

Since line wings as given by the Lorentz shape, Equation (5), have been found to be in error in the extreme wings (e.g. overestimating the absorption for CO₂ and underestimating the absorption for H₂O) it is difficult to state an appropriate rule to follow for truncating the Lorentz line profile, since this also depends to a large extent on the problem being considered.

An additional absorption feature of importance to the transmittance of neodymium laser radiation is due to the oxygen dimer, (O₂)₂. Measurements made by Curcio (1966) show that its effect cannot be neglected for long atmospheric paths ($>80 \text{ Km}$) near sea level. Figure 8 shows the transmittance of solar energy as a function of wavelength for several solar positions. Although the absorption is significant for large zenith angles, the attenuation in this region is still dominated by aerosol effects.

5. LINE-BY-LINE COMPUTATION TECHNIQUES

In the case of pure molecular absorption, $\gamma(\nu)$ expressed in Equation 1 is the absorption coefficient. The monochromatic transmittance for a given atmospheric species through a path containing Δm_j absorbing molecules is then given by Equation 10.

$$\tau_j(\nu) = \exp \left[-k_j(\nu) \Delta m_j \right] \quad (10)$$

The quantity, j , refers to the j^{th} molecular species. In general $k_j = \sum_i k_{ji}$, where the k_{ji} is the absorption coefficient for each absorption line (i) of a molecule of type j contributing to the absorption at frequency ν . In addition, to the absorption by many lines of molecular species, j , there may also be absorption at frequency, ν , due to lines of other molecular species, so we must generalize Equation 10 as follows.

$$\tau(\nu) = \exp \left[-\sum_j k_j(\nu) \Delta m_j \right] \quad (11)$$

In general, the atmospheric path over which the transmittance is required is not uniform - i.e. it contains temperature, pressure, and constituent gradients. Therefore, we must replace Δm_j by dm_j and integrate to obtain the proper exponent in Equation 11. Thus, this exponent (the optical depth) is defined in Equation 12.

$$\eta = \int \sum_j k_j(\nu) dm_j \quad (12)$$

Using this technique together with the line parameters described above, we can generate an "infinite resolution" spectrum such as that shown in Figures 9 and 10. For laser applications this type of calculation is a requirement because the laser beam is spectrally very narrow compared with the width of pressure-broadened atmospheric absorption lines. High resolution synthetic spectra of this kind have been computed for much of the infrared and detailed calculations have been made for a large number of specific laser emission frequencies by McClatchey 1971, McClatchey and Selby 1972a, 1972b, 1974, and McClatchey et al 1972. The AFCRL Atmospheric Absorption Line Parameters Compilation on which these calculations are based is described in more detail by McClatchey, et al (1973).

Figures 9 and 10 provide high resolution transmittance spectra using the data and technique described above. The calculations are for a 10 km horizontal path at sea level corresponding to the mid-latitude winter model atmosphere in the 4 and 10 micrometer regions. Similar spectra have been computed covering the entire spectral region from .76 to 31.25 micrometers. Although this work was first undertaken in connection with investigations of the atmospheric propagation of CO₂, CO, HF and DF laser systems, the resulting spectra can be used to roughly estimate the effects of molecular absorption on the propagation of any laser system throughout the specified spectral region. Tables similar to Table 6 have been constructed for a large number of laser emission lines for CO₂, CO, HF, DF and several other laser systems. Table 6 provides the attenuation coefficient for a given laser line as a function of altitude for 6 model atmospheres and two aerosol models. From tables such as these it is possible to quickly estimate the attenuation of a given laser line for a specific atmospheric path.

There is some experimental confirmation of these high resolution transmittance calculations. An example is shown in Figure 11 in which some emission measurements in the 10 micrometer region are compared with calculations. Measurements made by Long et al (1973) on several CO laser lines indicate that the calculations tend to underestimate the absorption, especially when the laser emission line is far from the center of a water vapor line. This underestimate is as much as a factor of 2 in attenuation coefficient for some lines. It has been suggested that a non-Lorentzian line shape can largely explain the observations. An outdoor measurement made by Gilmartin (1973) has indicated satisfactory agreement for the 5-4 P15 line of CO. Disagreements exist between different experimenters on the magnitude of the water vapor continuum absorption in the 10 micrometer region. Since this has a significant impact on the attenuation of the P20 CO₂ laser line, some 20-30% discrepancies in the atmospheric window may be due to that cause. Measurements of DF laser transmittance measurements in the laboratory have been reported by Spencer, (1973) and he obtains satisfactory agreement with calculation.

6. LOW RESOLUTION MODELLING

In many applications, it is impossible to measure radiation at a single frequency (or very narrow spectral interval). Instead one measures the transmittance $\bar{\tau}_{\Delta\nu}(\nu)$ averaged over the spectral interval, $\Delta\nu$, accepted by the receiver, as indicated in Equation 13.

$$\bar{\tau}_{\Delta\nu}(\nu) = \frac{1}{\Delta\nu} \int \tau(\nu) d\nu \quad (13)$$

where ν is the central frequency in the interval, $\Delta\nu$. Consequently for many applications one is interested in knowing the transmittance of the atmosphere averaged over a relatively wide spectral interval, that is, for low resolution.

Thus, the term transmittance is somewhat ambiguous unless it is qualified by some indication of the spectral resolution, $\Delta\nu$, over which it is averaged. This is particularly true in the case of molecular absorption, since the absorption coefficient k_m is a rapidly varying function of frequency. It is because of the rapid variation of k_m with frequency that the averaged transmittance τ does not, in general, obey a simple exponential law. That is

$$\bar{\tau}_{\Delta\nu}(\nu) = \frac{1}{\Delta\nu} \int \exp \left[-k_m(\nu) \Delta m \right] d\nu \neq \exp \left[-\bar{K}(\nu) \Delta m \right] \quad (14)$$

where k represents the net monochromatic molecular absorption coefficient and where \bar{K} is an average absorption coefficient, which cannot in most cases be defined when $\Delta\nu$ is much greater than the half-width of a spectral line.

There are four basic approaches to obtaining low resolution transmittance values for a given path through the atmosphere due to molecular absorption. These are; (1) direct measurements over the required path; (2) measurements in the laboratory under simulated conditions; (3) line-by-line (monochromatic) calculations based on a detailed knowledge of the spectroscopic line parameters which are then averaged over the required spectral interval, and (4) calculations based on band model techniques (which use available laboratory and/or field transmittance measurements or actual line data as a basis).

From the point of view of computations, method 3 involves a considerable amount of work and computer time, and consequently method 4 has been used most frequently. Even with the availability of the necessary line compilation, there is a place for efficient and accurate low spectral resolution models. Because of the inefficiency of low spectral resolution calculations by line-by-line techniques, we may think of the data compilation as a foundation and basis for comparison of other, more efficient low resolution models. However, there is a need for optical modelling at spectral resolution where current low resolution models are not applicable. Our only choice, then is to resort to degraded monochromatic calculations or to devise new models capable of providing the required results.

One such approach that relates easily to the data compilation described above is the direct application of the Goody random model, utilizing appropriate sums of parameters obtained from the AFCRL absorption line compilation. Provided that there are sufficient lines in the spectral interval, $\Delta\nu$, so that the assumption of randomness with respect to the line frequencies can be made, and assuming an exponential distribution of line intensities in the interval, we obtain Equation 15 for the average transmittance in the interval.

$$\bar{\tau} = \exp \left\{ - \frac{m \cdot \sum S_i}{\Delta\nu \left[1 + \frac{m}{4} \left(\frac{\sum S_i}{\sum \sqrt{S_i a_i}} \right)^2 \right]^{\frac{1}{2}}} \right\} \quad (15)$$

It can be seen that this expression requires sums of intensities and sums of square roots of the intensity-half width products. As an example, these are provided for water vapor in Figure 12, in which the parameters were summed over 5 cm^{-1} increments and spaced 1 cm^{-1} apart. Thus, the resulting spectral resolution will be 5 cm^{-1} . Similar sums have also been computed for ozone and carbon dioxide lines. Figures 13-14 show the results of using these parameters in a Goody random model formulation and then comparing these calculations with the degraded monochromatic technique. Table 7 summarizes the results of calculations made for each of these band complexes for a number of different conditions. Such calculation techniques may be required for certain applications in order to provide the required accuracy, but they still require rather large amounts of computation time and they are not readily amenable to quick estimation. As a result, method 4 above still has a wide applicability, especially for systems studies.

A code that has been developed along these lines at AFCRL, the LOWTRAN code, will now be briefly described. The LOWTRAN code was constructed as a moderately accurate, but very efficient computer routine based on a single parameter model of molecular absorption. Transmittance at a given frequency through the atmosphere, in general, depends on three parameters; pressure, number of absorbing molecules, and the temperature. The LOWTRAN technique recognizes the minor importance of temperature dependence and thus, specifies a mean temperature of 273K. The number of absorbing molecules and the pressure are combined in an appropriate way to define a single independent variable so as to minimize errors.

In the report by McClatchey et al (1972) three empirical transmittance functions have been determined from laboratory and synthetic transmittance data based on Equation (16) for (1) H_2O , (2) O_3 , and (3) the combined contributions of the uniformly mixed gases.

$$\bar{\tau}_{\Delta\nu}(\nu) = f \left(C(\nu) \Delta m P^n \right) \quad (16)$$

Synthetic spectra here refers to monochromatic (line-by-line) transmittance calculations degraded in resolution by convolution with an appropriate slit function. It was found that Equation (16) gave the best fit to laboratory and theoretical data over a wide spectral interval when; (1) $n=0.9$ for H_2O , (2) $n=0.4$ for O_3 , and (3) $n=0.75$ for the uniformly mixed gases.

The corresponding empirical transmittance functions were found to give better agreement with laboratory and synthetic transmittance data than the commonly used band models over a wide range of pressures and absorber amounts.

The procedure used for determining the parameter n and function, f , defined in Equation (16) will be briefly outline below. By taking the logarithm of the inverse of Equation (16), it will be seen that

$$n \log P + \log \Delta m = \log f^{-1} \left[\bar{\tau}_{\Delta\nu}(\nu) \right] - \log C(\nu) \quad (17)$$

Thus, for a given frequency, ν , and fixed values of average transmittance, $\bar{\tau}_{\Delta\nu}(\nu)$, the right-hand side of Equation (16) becomes a constant.

A mean value for n was determined from Equation (17) for a wide range of frequencies and several values of $\bar{\tau}$. Then for each frequency, $\bar{\tau}$ was plotted against $\log \Delta m P^n$, and the curves superimposed and the best mean curve determined. The "mean" curve thus obtained constitutes the empirical transmittance function and is displayed as the transmittance scale and associated scaling factor, $\log (\Delta m P^n)$, in the sample prediction chart given in Figure 15. Similar charts have been provided by McClatchey, et al (1972) for six other atmospheric gases of major importance in atmospheric absorption. In addition a computer version of this technique has been constructed (LOWTRAN) and is presented in a report by Selby and McClatchey (1972) with a revised model (LOWTRAN 3) presented in a second report by Selby and McClatchey (1975).

The LOWTRAN 3 Computer Code has been compared with a large number of laboratory and field measurements. Some samples of these comparisons are provided here. Figure 16 shows a laboratory comparison with the measurements of Howard, Burch and Williams (1955) in the 2.7 μm water vapor band. Figure 17 shows a transmittance spectrum measured by Gebbie et al (1951) from a 1 sea-mile path over water, covering the 0.5 to 15 μm region. Figure 8 shows a comparison of LOWTRAN with the results of Yates and Taylor (1960) covering the spectral region from 0.5 to 19 μm . The apparent discrepancy in the 10 μm region is believed to be due to the fact that Yates and Taylor artificially set the transmittance level to be 100% in this window region (since they were unable to estimate the water vapor continuum contribution).

Further studies are proceeding to update and validate both the low resolution and high resolution atmospheric transmittance prediction schemes. Further work is required in order to understand and reliably predict the water vapor continuum absorption in the 10 μm region.

7. REFERENCES

- Anderson, P.W. (1949) Physical Review 76 5:647
- Benedict, W.S. and Kaplan, L.D. (1959) J. Chem. Phys. 30, 2:388
- Blum, F.A., Nill, K.W., Kelley, P.L., Calawa, A.P. and Harman, T.C. (1972) Science 177:694
- Bolin, B. and Bischof, W., Variations in the Carbon Dioxide Content of the Atmosphere in the Northern Hemisphere, Tellus, 22, 431-442, (1970)
- Burch, C.B., Gryvnak, D.A., Patty, R.R. and Bartky, C.F. (1969) J. Op. Soc. Am. 59, 3:267
- Burch, D.E. (1970) Semiannual Technical Report, Investigation of the Absorption of Infrared Radiation by Atmospheric Gases U-4784, January 1970
- Burch, D.E., Gryvnak, D.A. and Pembroke, J.D. (1971) Philco-Ford Corp. Aeronutronic Division, Contract No. F19628-69-C-0263, U-4897, ASTIA AD882876
- Cadle, R.D., (1974) Report to Task Group V, U.S. Committee on Extension to the Standard Atmosphere Trace Constituents, Preprint
- Curcio, J.A., Absorption in the Atmosphere by the Oxygen Dimer (O) Complex at 1.06 Microns, Report of NRL Progress, PBI73468, October 1966
- Ely, R. and McCubbin, T.K. (1970) Ap. Op. 9, 5:1230
- Farmer, C.B. and Houghton, J.T., (1966), Nature 209, 1341 and 5030
- Gebbie, H.A., Harding, W.R., Hilsum, C., Pryce, A.W. and Roberts, V. (1951), Proc. Roy. Soc. 206A:87
- Gilmartin, T.J. (1973) Measurements of the Atmosphere Attenuation of CO and CO₂ Laser Radiation, MIT Lincoln Laboratory, unpublished
- Goody, R.M., Atmospheric Radiation I, Theoretical Basis, (1964), Clarendon Press
- Hard, T., private communication (1974)
- Howard, J.N., Burch, D.L., Williams, D., (1955) Near-Infrared Transmission Through Synthetic Atmospheres, AFCRL-TR-55-213, Geophysical Research Papers No. 40
- Long, R.K., Mills, R.S. and Trusty, G.I. (1973) Experimental Studies of the Partial and Total Pressure Dependence of Water Vapor Absorption Coefficients for Highly Transmitting CO Laser Lines, RADCL-TR-73 Technical Report, February 1973
- McClatchey, R.A., Fenn, R.W., Selby, J.E.A., Volz, F.E. and Garing, J.S., (1972) Optical Properties of the Atmosphere (Third Edition), AFCRL-73-0497, August 1972
- McClatchey, R.A. (1971) Atmospheric Attenuation of CO Laser Radiation, AFCRL-71-0370, ERP 359
- McClatchey, R.A. and Selby, J.E.A. (1972a) Atmospheric Attenuation of HF and DF Laser Radiation, AFCRL-72-0312, ERP 400
- McClatchey, R.A. and Selby, J.E.A. (1972b) Atmospheric Transmittance, 7-30 μm : Attenuation of CO₂ Laser Radiation, AFCRL-72-0611, ERP 419
- McClatchey, R.A., Benedict, W.S., Clough, S.A., Burch, D.E., Colfee, R.F., Fox, K., Rothman, L.S. and Garing, J.S. (1973), AFCRL Atmospheric Absorption Line Parameters Compilation, AFCRL-TR-73-0096, ERP 434
- McClatchey, R.A. and Selby, J.E.A., Atmospheric Attenuation of Laser Radiation from 0.76 to 31.25 Micrometers, AFCRL-TR-74-0003, ERP 460
- McCoy, J.H., Rensch, D.B. and Long, R.K. (1969) Appl. Opt. 8:1471
- Plass, G.N. (1958) J. Opt. Soc. Am. 48:690
- Selby, J.E.A. and McClatchey, R.A., Atmospheric Transmittance from 0.25 to 28.5 μm : Computer Code LOWTRAN 2, AFCRL-72-0745, ERP 427

- Selby, J.E.A. and McClatchey, R.A., Atmospheric Transmittance from 0.25 to 28.5 μm : Computer Code LOWTRAN 3, AFCRL-TR-75-0255, ERP 513
- Shapiro, M.M. and Gush, H.P. (1966) Canad. J. Phys. 44:949
- Sissenwine, N., Grantham, D.D., Salmela, H.A., (1968) Humidity Up to the Mesopause, AFCRL-68-0550
- Spencer, D.J. (1973) Atmospheric Gas Absorption at DF Laser Wavelengths, Proceedings of the Meeting Absorption of Laser Radiation in the Atmosphere, April 4-5, 1973, Mitre Corp., Report M73-86, Vol. II
- Tsao, C.J. and Curnutte, B. (1954), Linewidths of Pressure Broadened Spectral Lines, Scientific Report 1A-8, Contract AF19(122)65. The Ohio State University, June 1954
- Valley, S.L., Ed., (1965) Handbook of Geophysics and Space Environment, AFCRL
- Varanasi, P. and Tejwani, G.D.T., (1972), J.Q.S.R.T., 12:849
- Winters, B.H., Silverman, S. and Benedict, W.S., (1964), J.Q.S.R.T., 4:527

Table 1 - Model Atmosphere Used as a Basis for the Computation of Atmospheric Optical Properties.

U.S. STANDARD ATMOSPHERE, 1962					
Ht. (km)	Pressure (mb)	Temp. (°K)	Density (g/m ³)	Water Vapor (g/m ³)	Ozone (g/m ³)
0	1.013E+03	288.1	1.225E+03	5.9E+00	5.4E-05
1	8.986E+02	281.6	1.111E+03	4.2E+00	5.4E-05
2	7.950E+02	275.1	1.007E+03	2.9E+00	5.4E-05
3	7.012E+02	268.7	9.093E+02	1.8E+00	5.0E-05
4	6.166E+02	262.2	8.193E+02	1.1E+00	4.6E-05
5	5.405E+02	255.7	7.364E+02	6.4E-01	4.5E-05
6	4.722E+02	249.2	6.601E+02	3.8E-01	4.5E-05
7	4.111E+02	242.7	5.900E+02	2.1E-01	4.8E-05
8	3.565E+02	236.2	5.258E+02	1.2E-01	5.2E-05
9	3.080E+02	229.7	4.671E+02	4.6E-02	7.1E-05
10	2.650E+02	223.2	4.135E+02	1.8E-02	9.0E-05
11	2.270E+02	216.8	3.648E+02	8.2E-03	1.3E-04
12	1.940E+02	216.6	3.119E+02	3.7E-03	1.6E-04
13	1.658E+02	216.6	2.666E+02	1.8E-03	1.7E-04
14	1.417E+02	216.6	2.279E+02	8.4E-04	1.9E-04
15	1.211E+02	216.6	1.948E+02	7.2E-04	2.1E-04
16	1.035E+02	216.6	1.665E+02	6.1E-04	2.3E-04
17	8.850E+01	216.6	1.423E+02	5.2E-04	2.8E-04
18	7.565E+01	216.6	1.216E+02	4.4E-04	3.2E-04
19	6.467E+01	216.6	1.040E+02	4.4E-04	3.5E-04
20	5.529E+01	216.6	8.891E+01	4.4E-04	3.8E-04
21	4.729E+01	217.6	7.572E+01	4.8E-04	3.8E-04
22	4.047E+01	218.6	6.451E+01	5.2E-04	3.9E-04
23	3.467E+01	219.6	5.500E+01	5.7E-04	3.8E-04
24	2.972E+01	220.6	4.694E+01	6.1E-04	3.6E-04
25	2.549E+01	221.6	4.008E+01	6.6E-04	3.4E-04
30	1.197E+01	226.5	1.841E+01	3.8E-04	2.0E-04
35	5.746E+00	236.5	8.463E+00	1.6E-04	1.1E-04
40	2.871E+00	250.4	3.996E+00	6.7E-05	4.9E-05
45	1.491E+00	264.2	1.966E+00	3.2E-05	1.7E-05
50	7.978E-01	270.6	1.027E+00	1.2E-05	4.0E-06
70	5.520E-02	219.7	8.754E-02	1.5E-07	8.6E-08
100	3.008E-04	210.0	4.989E-04	1.0E-09	4.3E-11

Table 6 - Values of Attenuation Coefficient/km as a Function of Altitude for the 10.591 μ m Laser Wave-length and 5 Atmospheric Models.

$\lambda = 10.591 \mu\text{m}$														
Altitude	TROPICAL		MIDLATITUDE SUMMER		MIDLATITUDE WINTER		SUBARCTIC SUMMER		SUBARCTIC WINTER		CLEAR		HAZY	
	k_m (km^{-1})	σ_m (km^{-1})	k_m (km^{-1})	σ_m (km^{-1})	k_m (km^{-1})	σ_m (km^{-1})	k_m (km^{-1})	σ_m (km^{-1})	k_m (km^{-1})	σ_m (km^{-1})	k_a (km^{-1})	σ_a (km^{-1})	k_a (km^{-1})	σ_a (km^{-1})
0	5.780E-01	<1.0E-06	3.582E-01	<1.0E-06	7.937E-02	<1.0E-06	2.006E-01	<1.0E-06	4.118E-02	<1.0E-06	5.48E-03	4.65E-03	2.61E-02	2.27E-02
0-1	5.172E-01		3.254E-01		7.312E-02		1.818E-01		4.147E-02		3.64E-03	3.09E-03	1.61E-02	1.37E-02
1-2	2.845E-01		1.877E-01		5.895E-02		1.137E-01		4.002E-02		1.58E-03	1.34E-03	5.90E-03	5.01E-03
2-3	1.807E-01		1.152E-01		4.911E-02		8.152E-02		3.516E-02		6.75E-04	5.73E-04	2.16E-03	1.83E-03
3-4	9.618E-02		7.582E-02		4.043E-02		6.090E-02		3.048E-02		3.18E-04	2.70E-04	7.88E-04	6.68E-04
4-5	6.289E-02		5.544E-02		3.240E-02		4.663E-02		2.453E-02		2.01E-04	1.70E-04	2.88E-04	2.44E-04
5-6	5.019E-02		4.468E-02		2.622E-02		3.737E-02		1.932E-02		1.46E-04	1.24E-04	1.46E-04	1.24E-04
6-7	3.880E-02		3.752E-02		2.147E-02		2.861E-02		1.508E-02		1.18E-04	1.00E-04	1.18E-04	1.00E-04
7-8	3.200E-02		3.018E-02		1.728E-02		2.277E-02		1.171E-02		1.16E-04	9.83E-05	1.16E-04	9.83E-05
8-9	2.834E-02		2.378E-02		1.405E-02		1.788E-02		9.593E-03		1.15E-04	9.77E-05	1.15E-04	9.77E-05
9-10	2.078E-02		1.952E-02		1.083E-02		1.375E-02		8.932E-03		1.11E-04	9.45E-05	1.11E-04	9.45E-05
10-11	1.651E-02		1.574E-02		9.813E-03		1.195E-02		8.921E-03		1.06E-04	9.04E-05	1.06E-04	9.04E-05
11-12	1.207E-02		1.241E-02		9.484E-03		1.229E-02		8.908E-03		1.06E-04	8.96E-05	1.06E-04	8.96E-05
12-13	1.035E-02		9.534E-03		9.358E-03		1.181E-02		8.733E-03		1.04E-04	8.83E-05	1.04E-04	8.83E-05
13-14	7.302E-03		8.377E-03		9.340E-03		1.229E-02		9.109E-03		9.89E-05	8.39E-05	9.89E-05	8.39E-05
14-15	5.850E-03		8.700E-03		9.001E-03		1.222E-02		8.891E-03		9.49E-05	8.06E-05	9.49E-05	8.06E-05
15-16	4.330E-03		8.491E-03		8.749E-03		1.168E-02		8.773E-03		8.97E-05	7.61E-05	8.97E-05	7.61E-05
16-17	3.318E-03		8.364E-03		8.573E-03		1.217E-02		8.559E-03		8.69E-05	7.38E-05	8.69E-05	7.38E-05
17-18	3.556E-03		8.467E-03		8.556E-03		1.203E-02		8.324E-03		8.50E-05	7.21E-05	8.50E-05	7.21E-05
18-19	4.350E-03		8.560E-03		8.249E-03		1.199E-02		8.209E-03		7.68E-05	6.51E-05	7.68E-05	6.51E-05
19-20	5.194E-03		8.929E-03		8.011E-03		1.217E-02		7.884E-03		6.04E-05	5.12E-05	6.04E-05	5.12E-05
20-21	6.273E-03		9.186E-03		8.186E-03		1.186E-02		7.784E-03		4.40E-05	3.74E-05	4.40E-05	3.74E-05
21-22	7.471E-03		9.719E-03		8.194E-03		1.208E-02		7.523E-03		3.25E-05	2.76E-05	3.25E-05	2.76E-05
22-23	8.351E-03		1.010E-02		8.161E-03		1.208E-02		7.208E-03		2.47E-05	2.09E-05	2.47E-05	2.09E-05
23-24	9.041E-03		1.114E-02		8.107E-03		1.199E-02		7.329E-03		1.92E-05	1.63E-05	1.92E-05	1.63E-05
24-25	9.808E-03		1.112E-02		8.378E-03		1.275E-02		6.837E-03		1.57E-05	1.33E-05	1.57E-05	1.33E-05
25-30	1.203E-02		1.327E-02		8.087E-03		1.453E-02		7.238E-03		7.90E-06	6.71E-06	7.90E-06	6.71E-06
30-35	1.180E-02		1.319E-02		6.848E-03		2.007E-02		5.785E-03		2.23E-06	1.89E-06	2.23E-06	1.89E-06
35-40	1.101E-02		1.269E-02		6.714E-03		1.395E-02		5.099E-03		<1.0E-06	<1.0E-06	<1.0E-06	<1.0E-06
40-45	8.845E-03		1.063E-02		6.023E-03		1.189E-02		4.100E-03					
45-50	6.030E-03		7.522E-03		4.405E-03		8.186E-03		3.082E-03					
50-70	9.007E-04		1.077E-03		2.744E-04		1.097E-03		7.761E-04					
70-100	1.535E-05		1.743E-05		1.580E-04		1.762E-05		1.765E-05					

Table 7 - Comparison of Integrated Absorption Results.

H_2O				
P (mb)	W (mol./cm ²)	W (LBL)	W ₅ (RANDOM)	W ₂₀ (RANDOM)
1079.64	3.41×10^{20}	320	273	339
800.00	2.0×10^{22}	665	592	673
400.00	8.0×10^{20}	321	275	334
139.95	1.50×10^{20}	112	102	121

CO_2			
P (mb)	W (mol./cm ²)	W (LBL)	W ₅ (RANDOM)
1024	2.60×10^{21}	164	164
500	7.00×10^{21}	179	178
100	1.40×10^{20}	55.8	60.0
100 (T=250K)	1.40×10^{20}	47.4	51.0
10	1.40×10^{19}	8.45	9.77

O_3			
P (mb)	W (mol./cm ²)	W (LBL)	W ₅ (RANDOM)
399.87	1.83×10^{19}	70.3	70.5
66.65	7.53×10^{19}	91.3	92.4
66.65	1.722×10^{19}	55.2	59.7
19.96	2.69×10^{19}	50.8	53.4
19.96	1.21×10^{19}	35.9	38.2

INFRARED ATMOSPHERIC TRANSMISSION

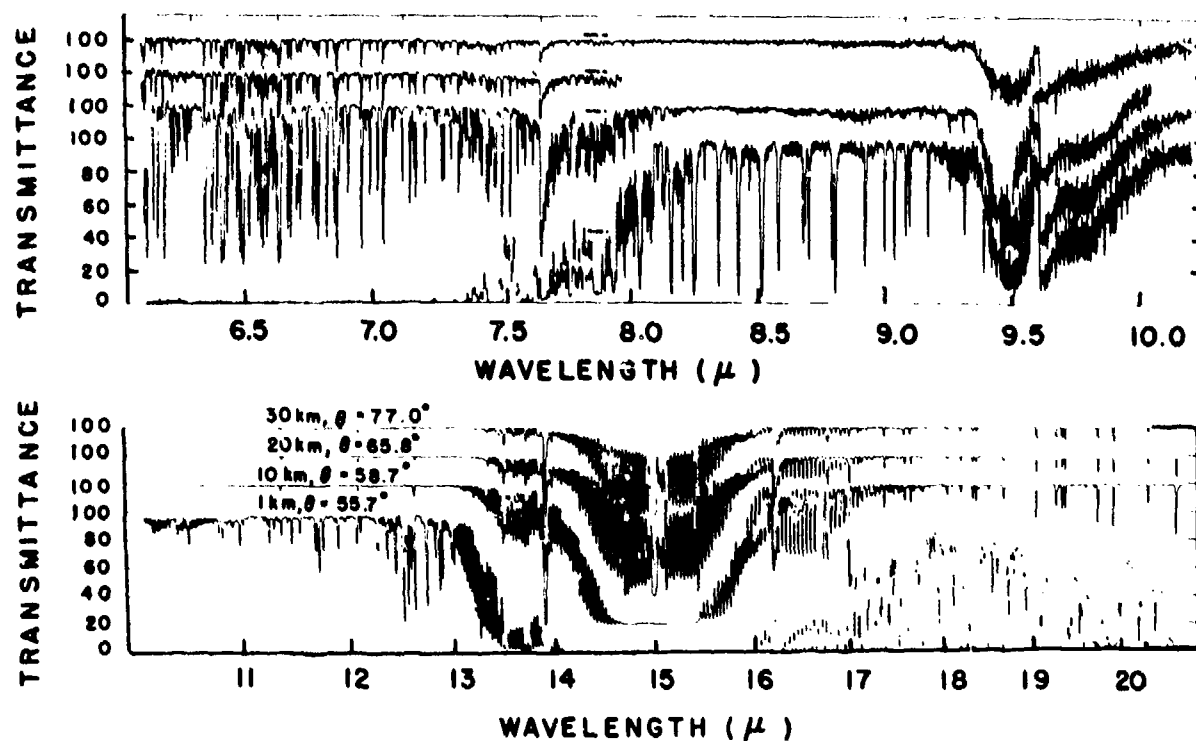


Figure 1 - Solar Spectra Measured from Balloon Platform at the Indicated Altitudes and Zenith Angles.

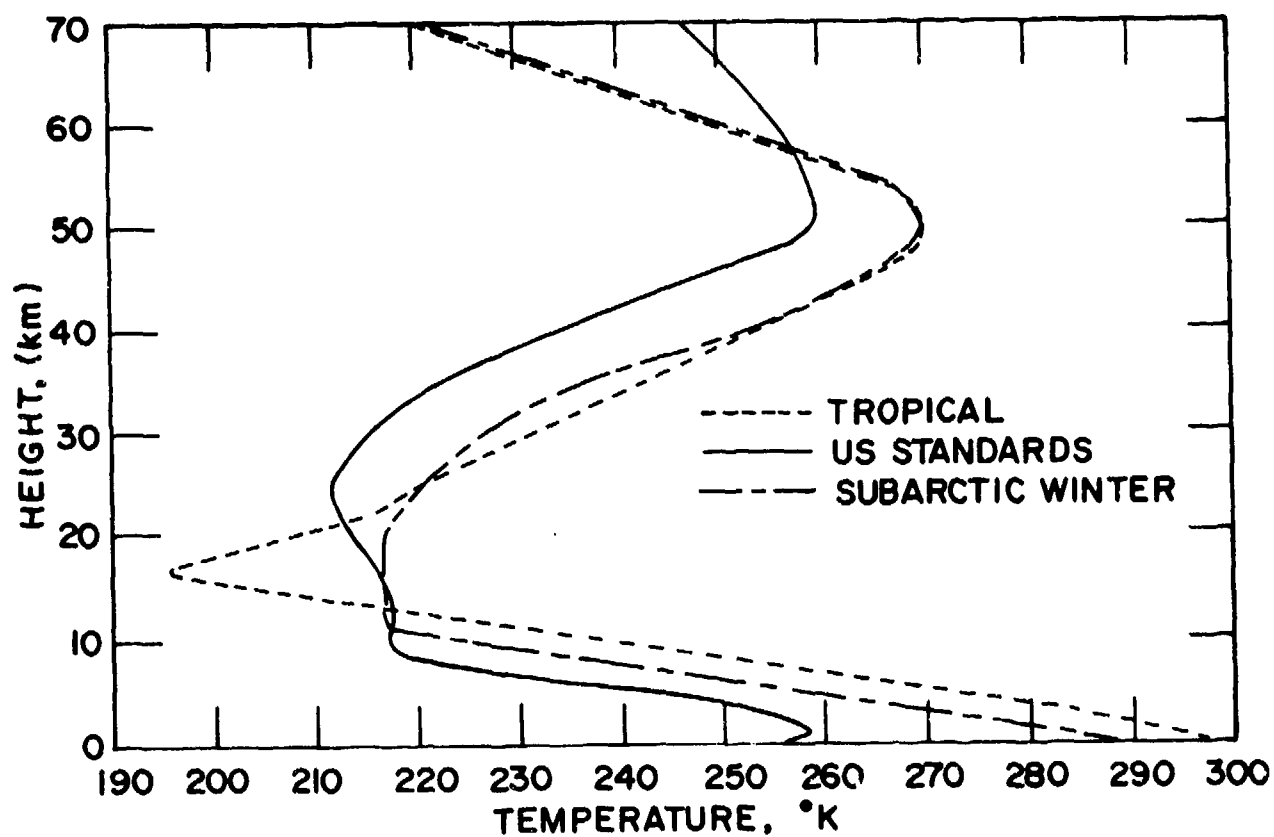


Figure 2 - Temperature Distributions for Three of the Standard Model Atmospheres.

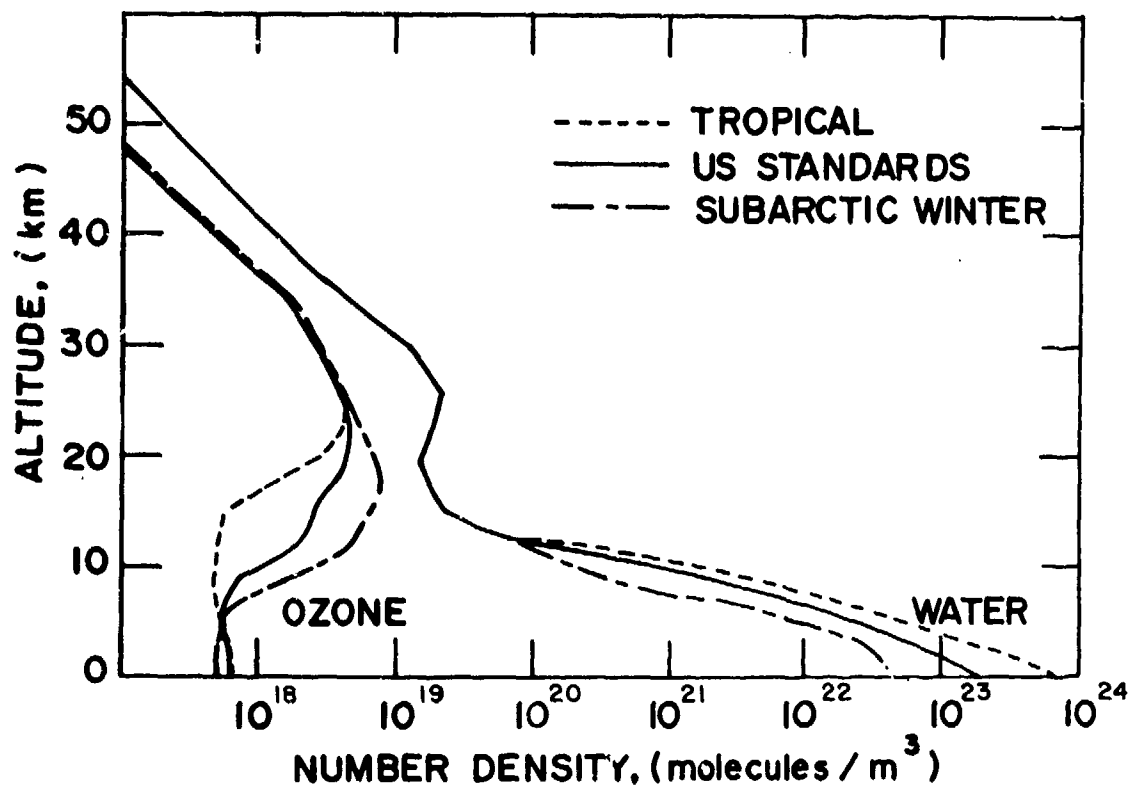


Figure 3 - Water Vapor and Ozone Distributions for Three of the Standard Model Atmospheres.

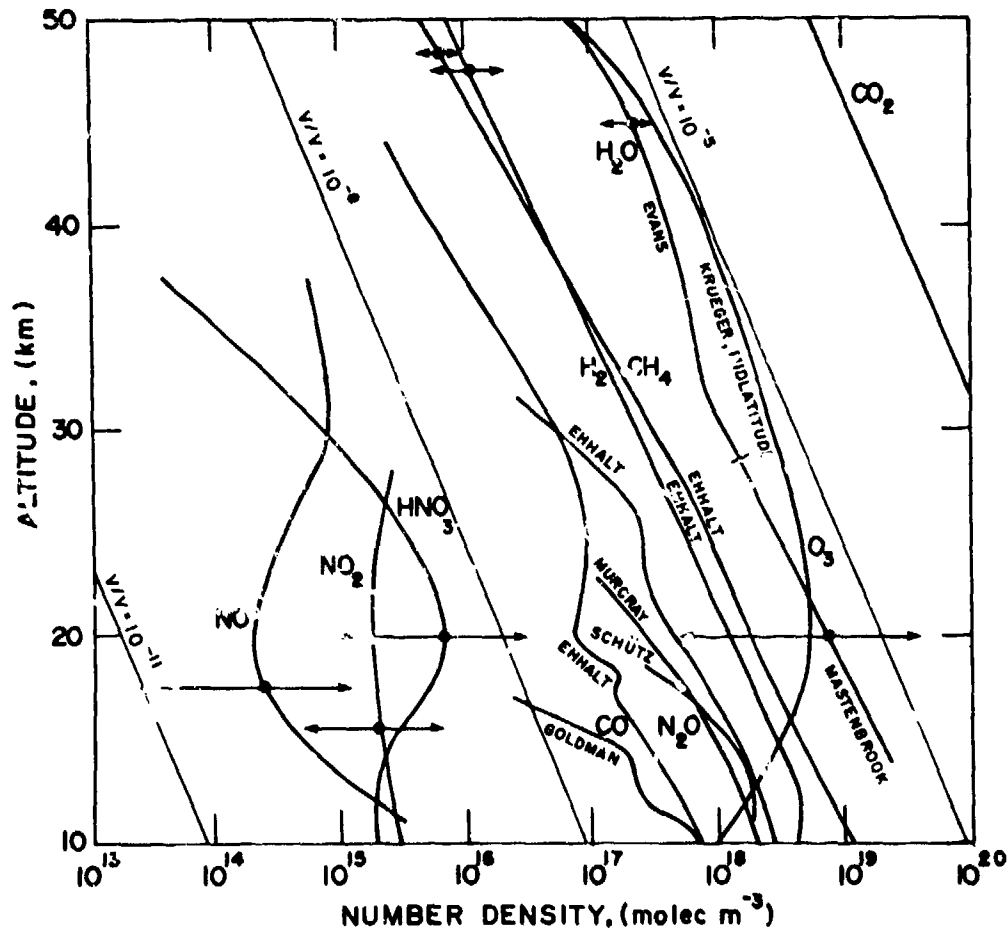


Figure 4 - Atmospheric Constituent Distributions above 10 km.

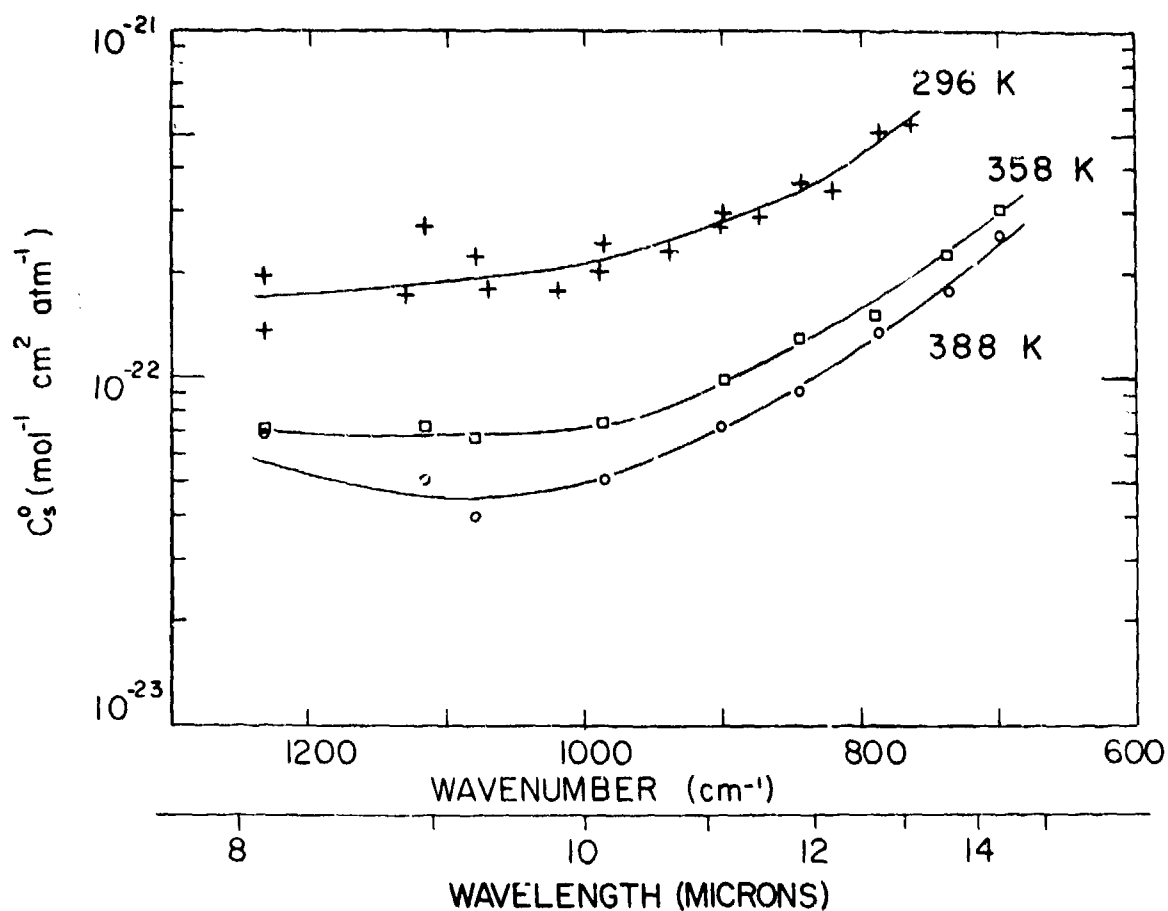


Figure 5 - Normalized Continuum Absorption Coefficient between 700 and 1250 cm^{-1} for Pure Water Vapor at Three Temperatures.

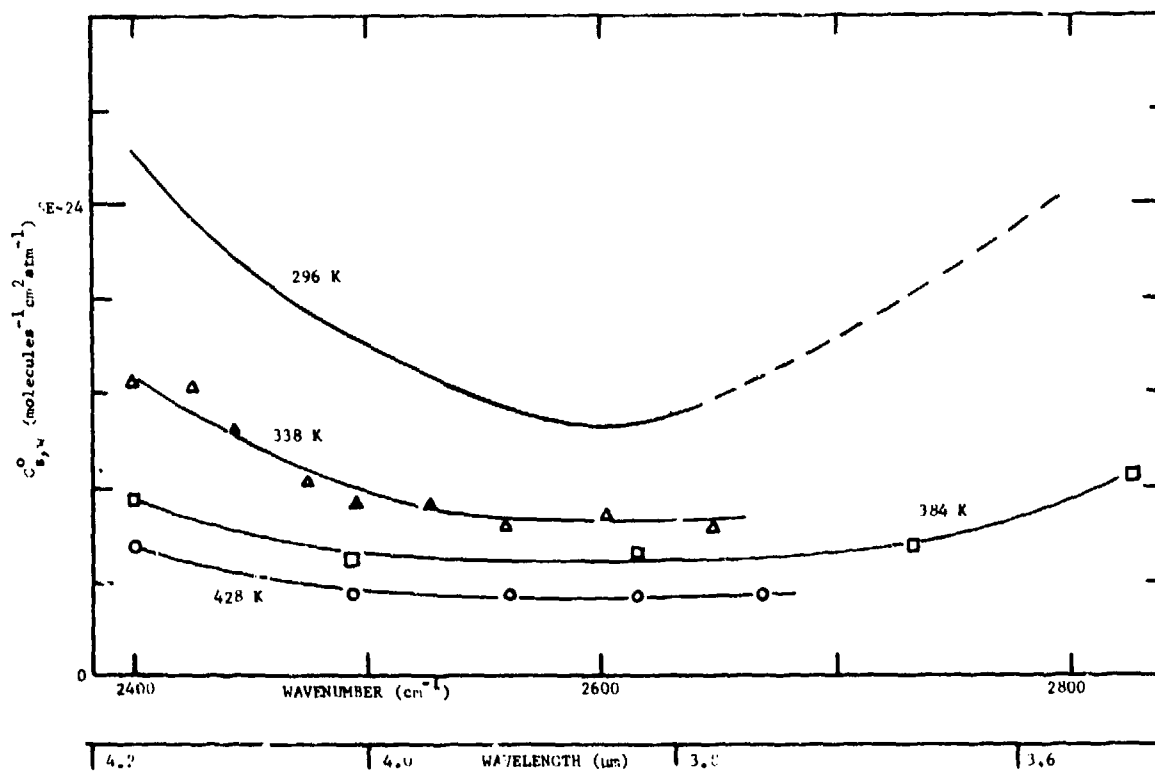


Figure 6 - Normalized Continuum Absorption Coefficient between 2400 and 2820 cm^{-1} for Pure Water Vapor at Four Temperatures.

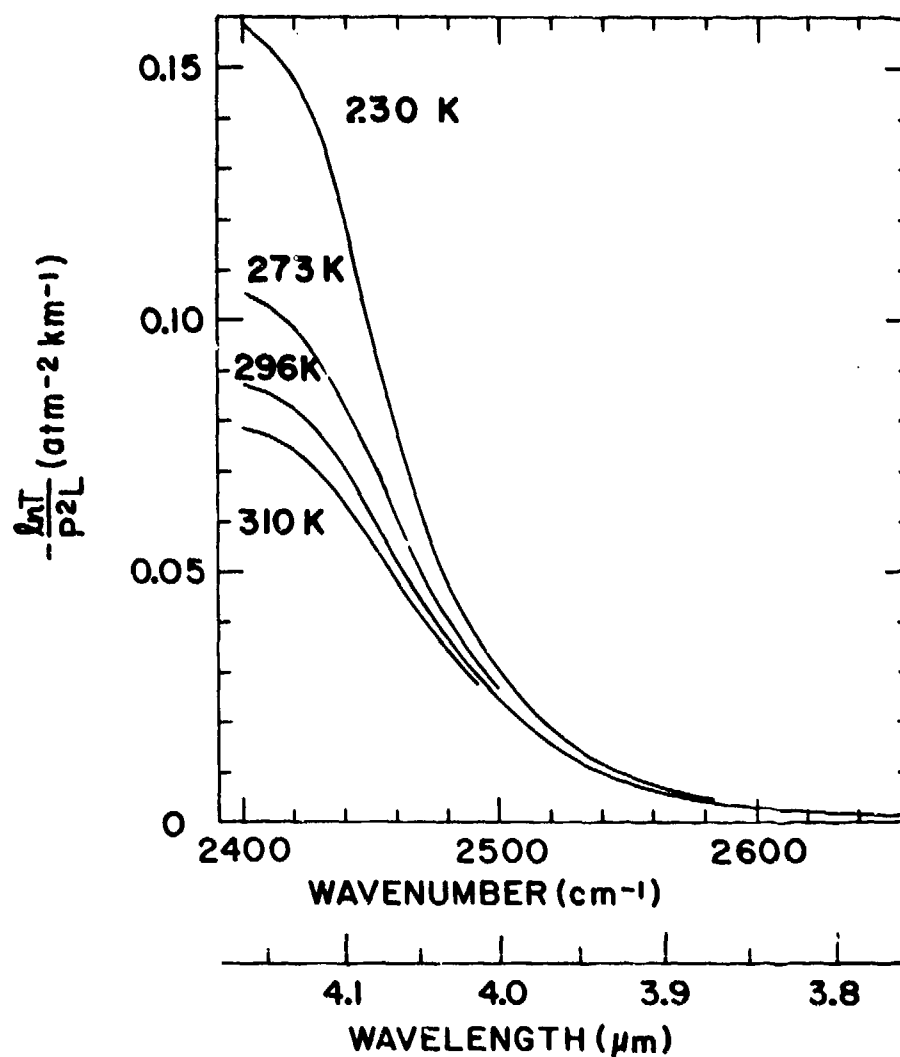


Figure 7 - Spectral Plot of Collision Induced Nitrogen Absorption Coefficient in the 4 μ m Region at Four Temperatures.

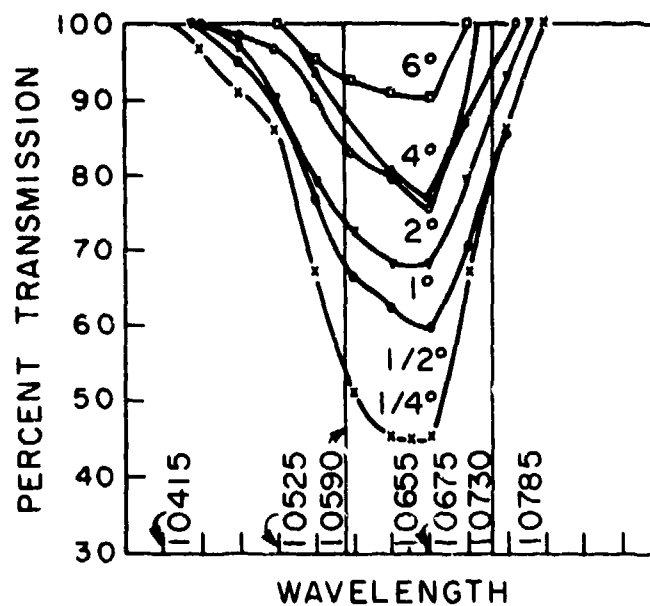


Figure 8 - Profiles of Transmission vs Wavelength Throughout the $(O_2)_2$ Band for Six Solar Positions (from Curcio, 1966).

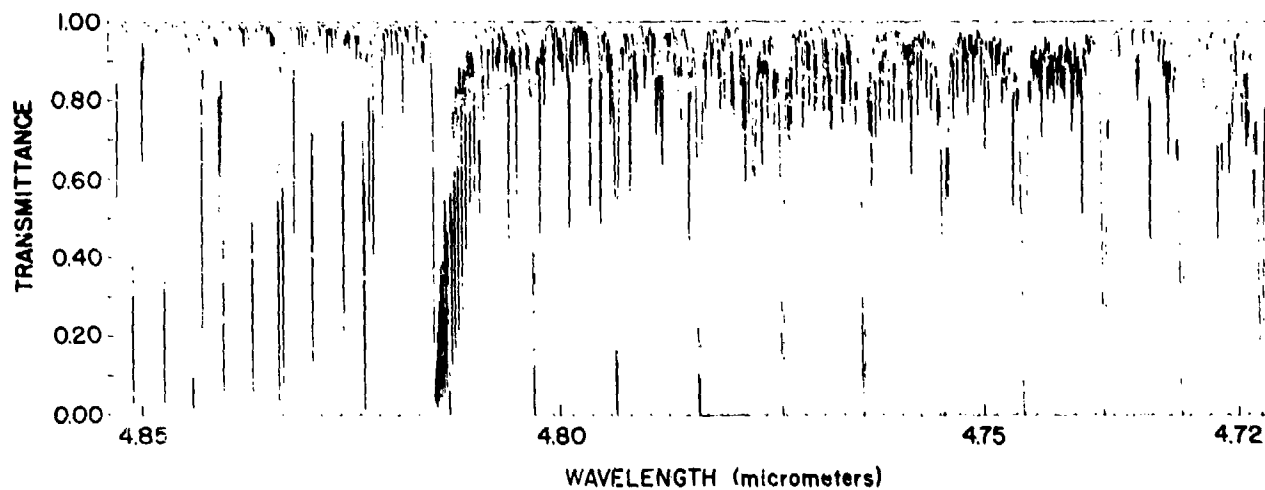


Figure 9 - Atmospheric Transmittance over 16 km Horizontal Path at 12 km Altitude (4.8 μ m region).

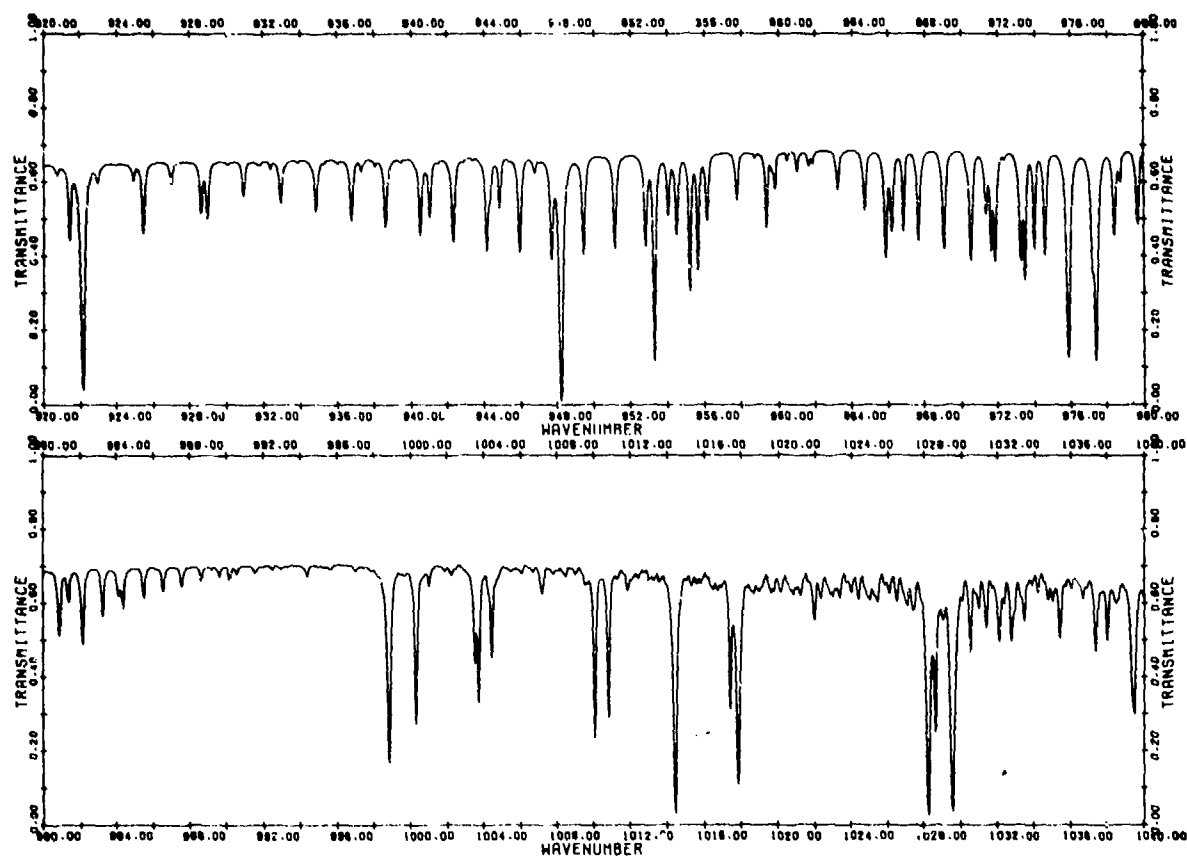


Figure 10- Atmospheric Transmittance over 10 km Horizontal Path at Sea Level (10 μ m region).

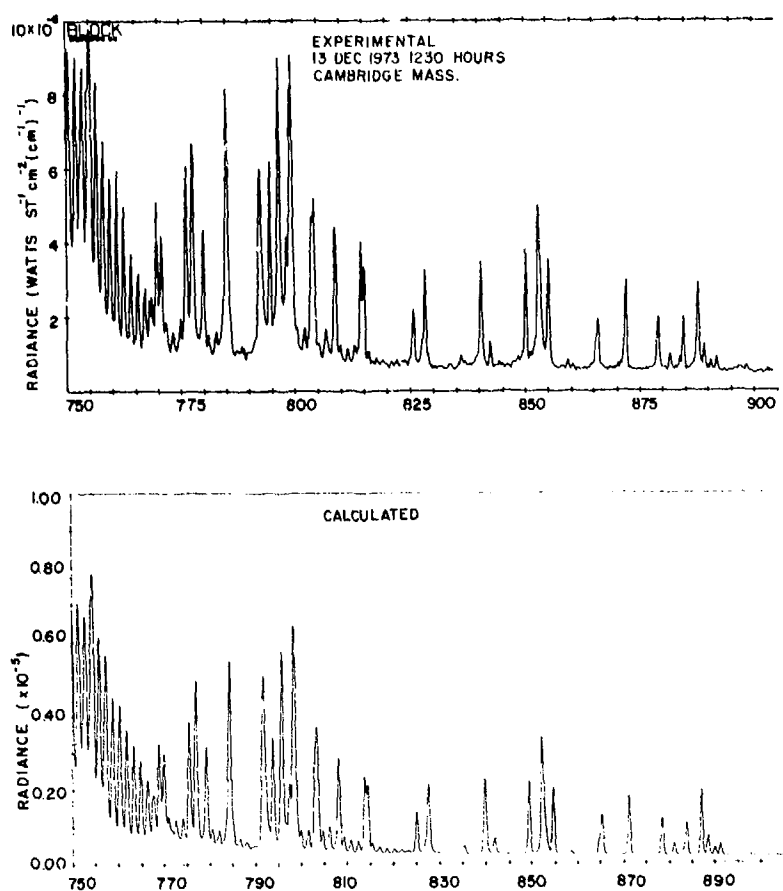


Figure 11- Comparison of Calculated and Measured Emission Spectra in 12 μm Region.

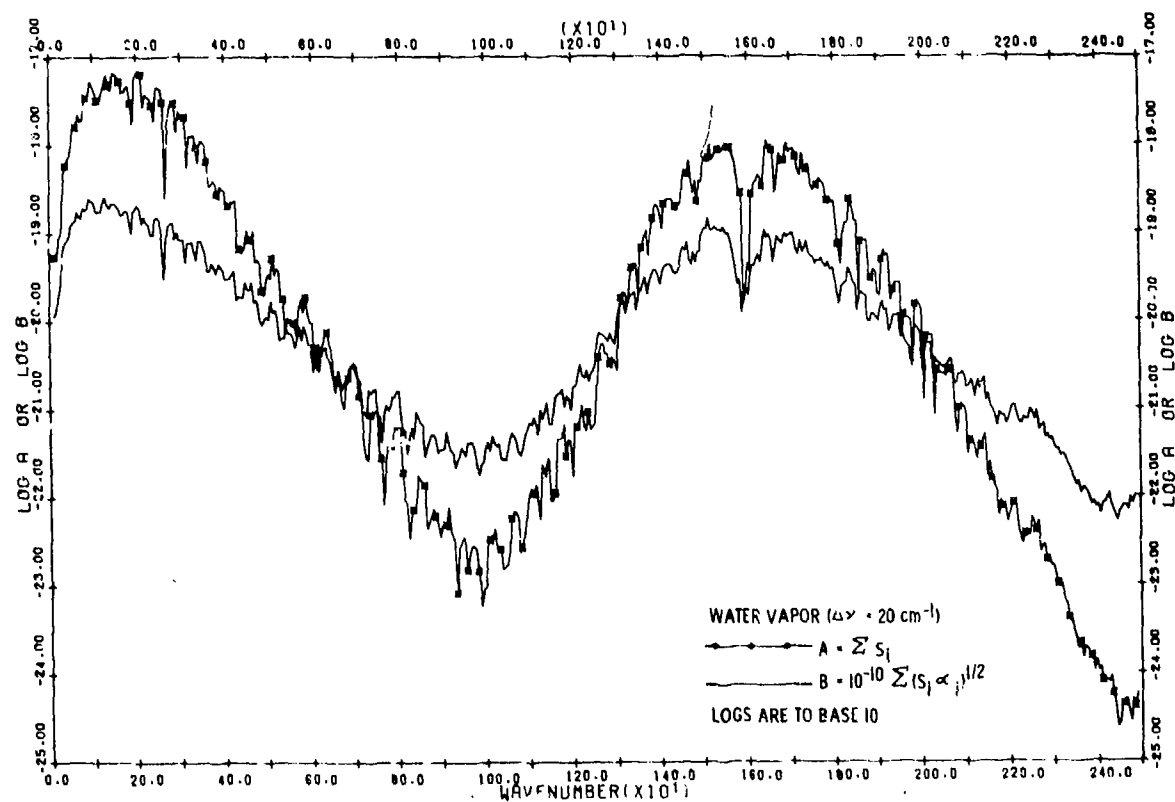


Figure 12- Curves of $\sum S_i$ and $\sum (S_i \alpha_i)^{1/2}$ for 20 cm^{-1} Intervals for the Water Vapor Data Included in AFCL Data Compilation for $T=296\text{K}$.

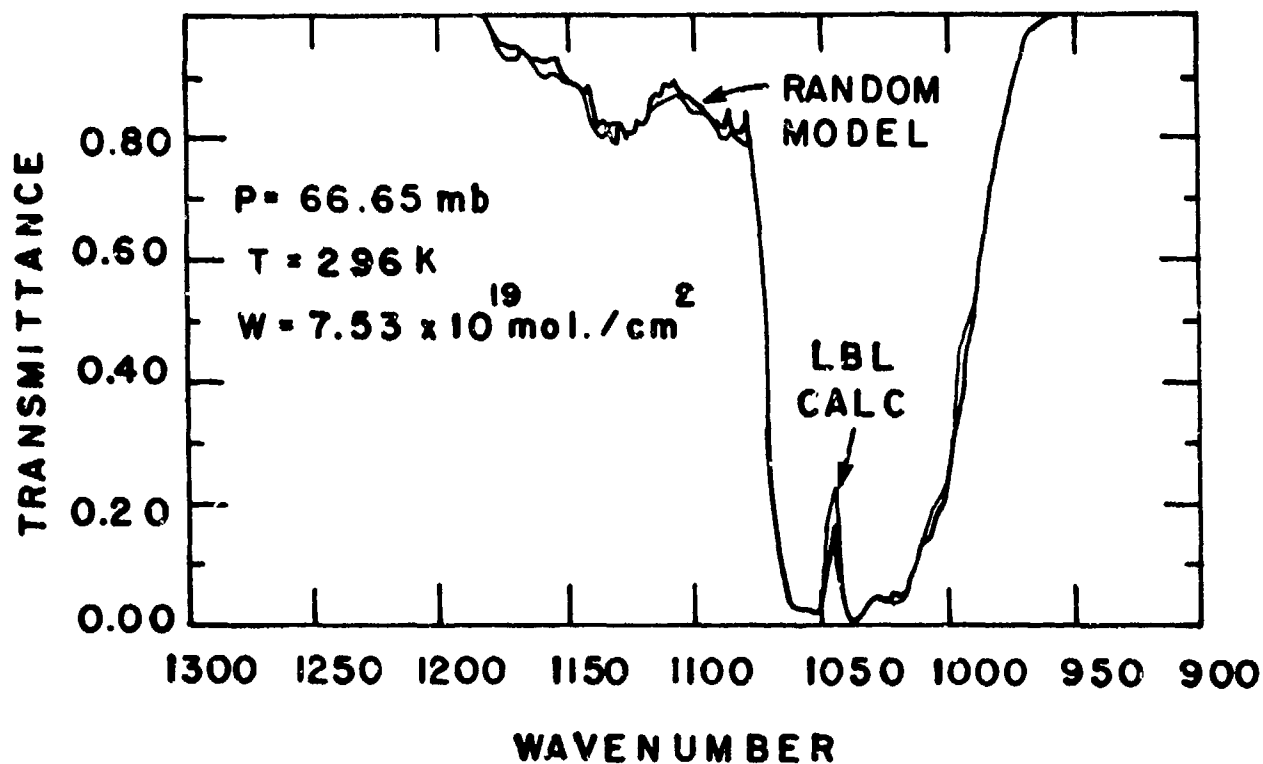


Figure 13- Comparison of LBL Calculations with Random Model for 9.6 μm Ozone Band.

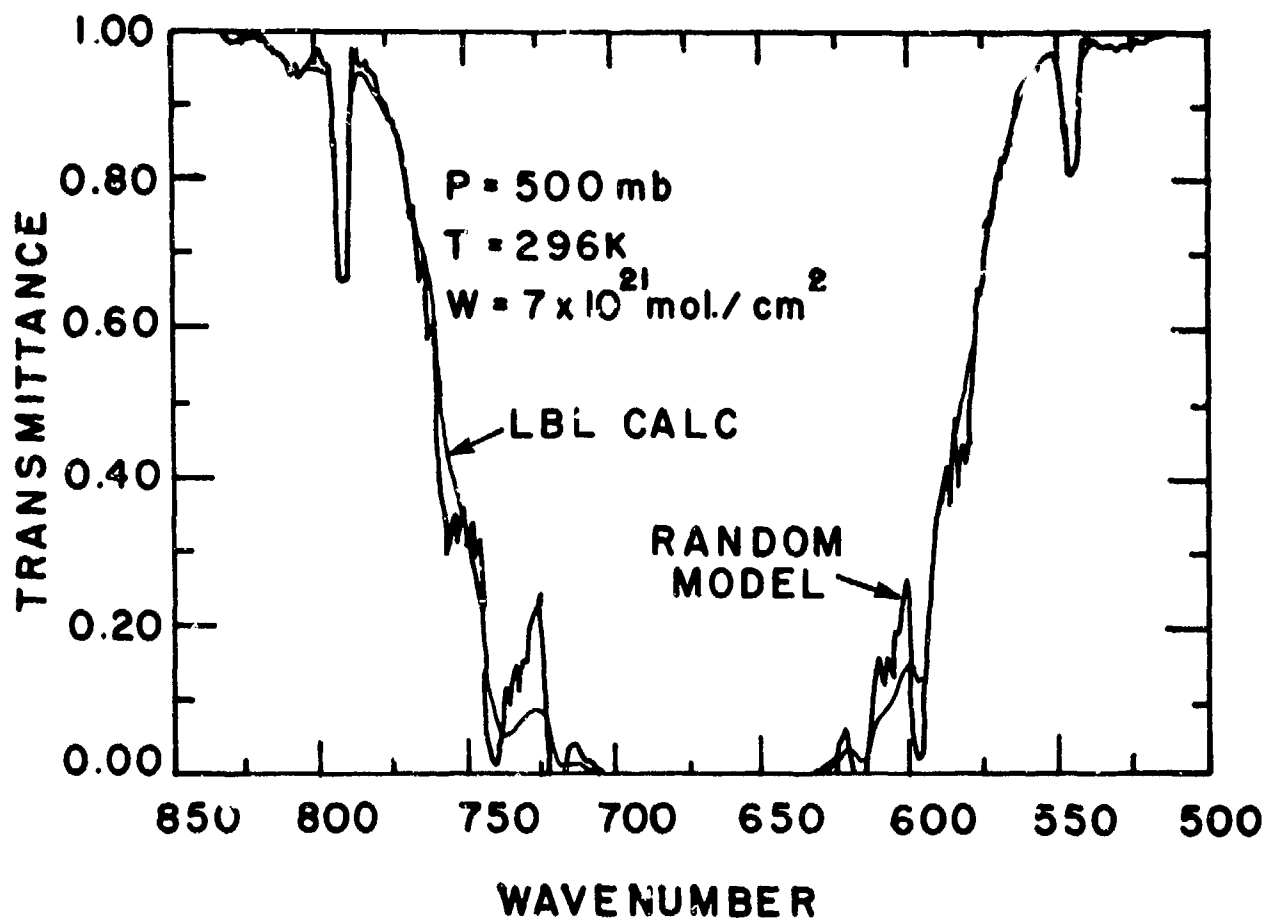


Figure 14- Comparison of LBL Calculations with Random Model for 15 μm Carbon Dioxide Band.

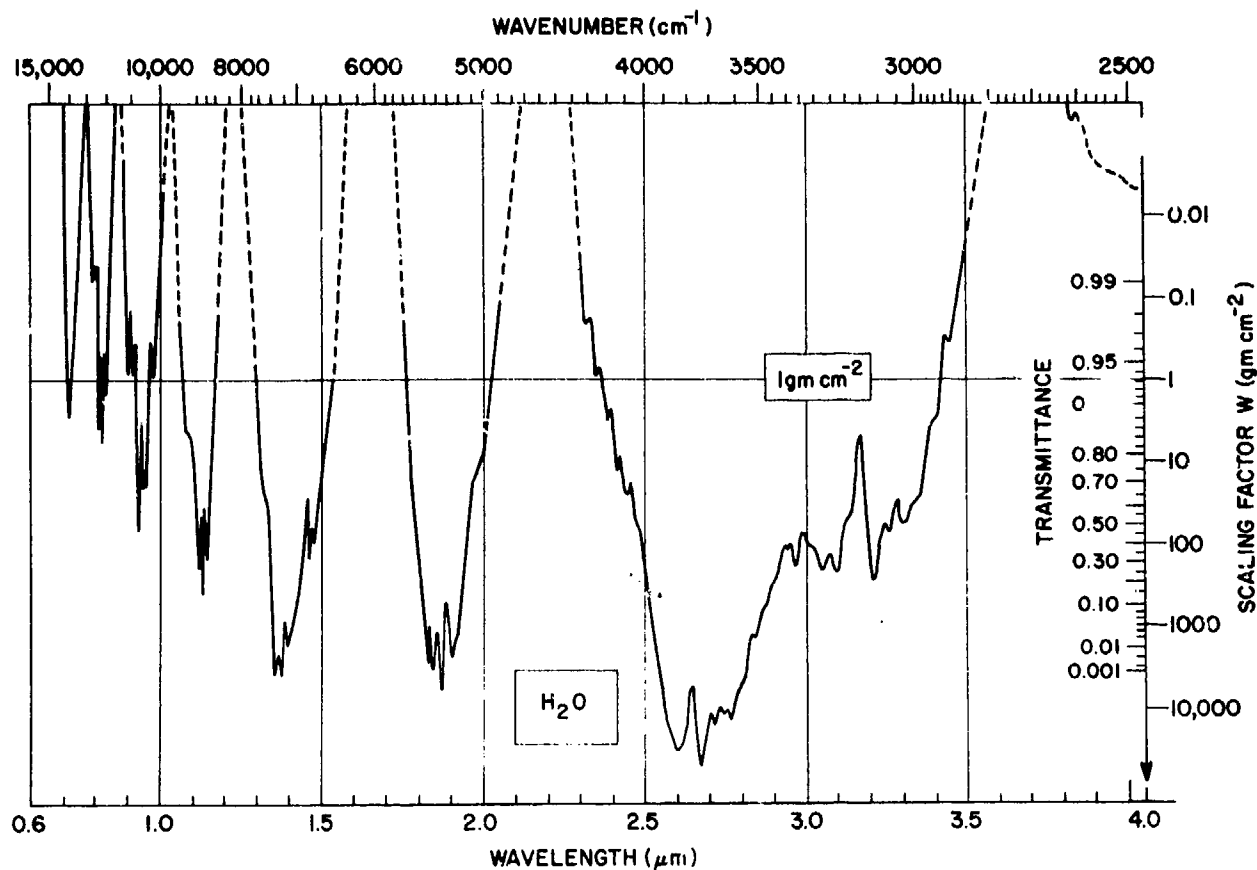


Figure 15- Prediction Chart for Water Vapor Transmittance (0.6 - 4.0 μm).

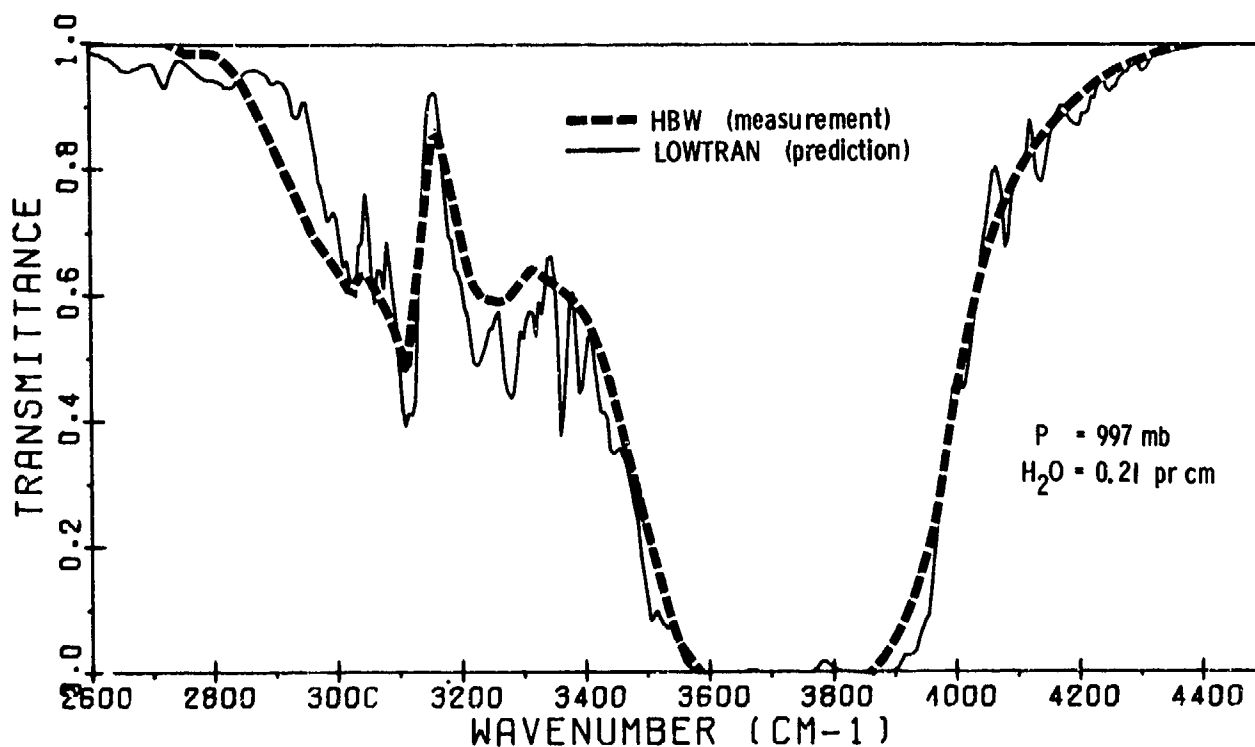


Figure 16- Comparison of LOWTRAN 3 Transmittance with Howard, Burch and Williams.

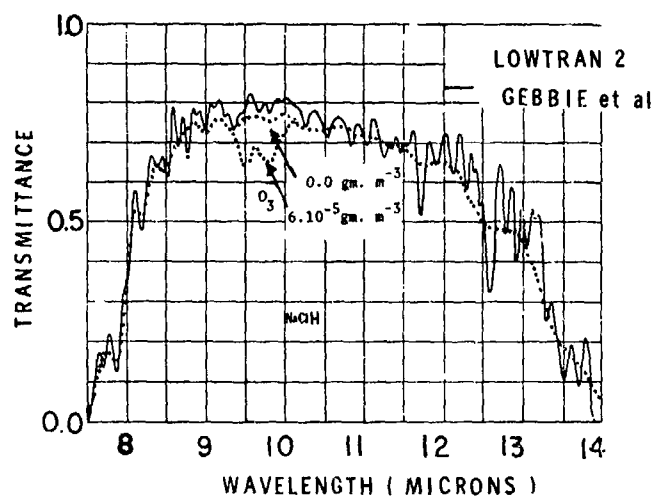
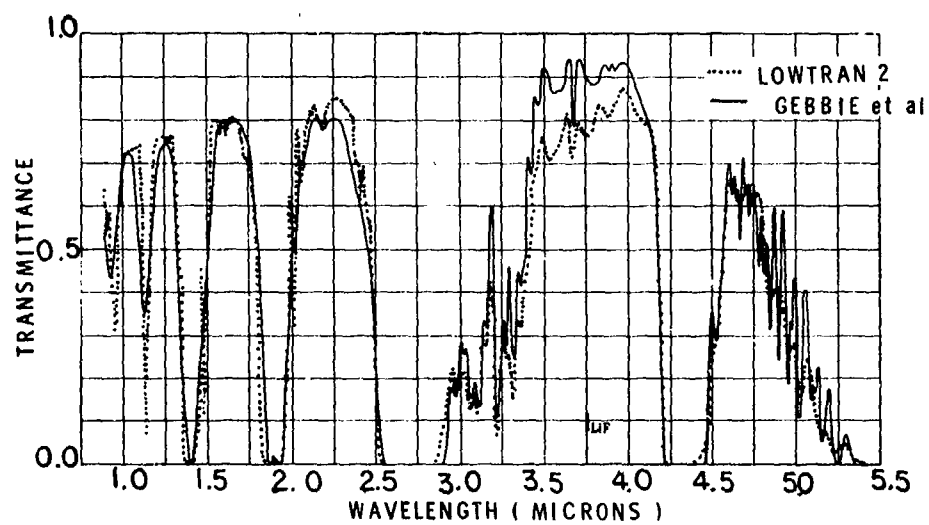


Figure 17- Comparison of LOWTRAN 3 and Measurement of Atmospheric Transmittance for a 1 Nautical Mile Path.

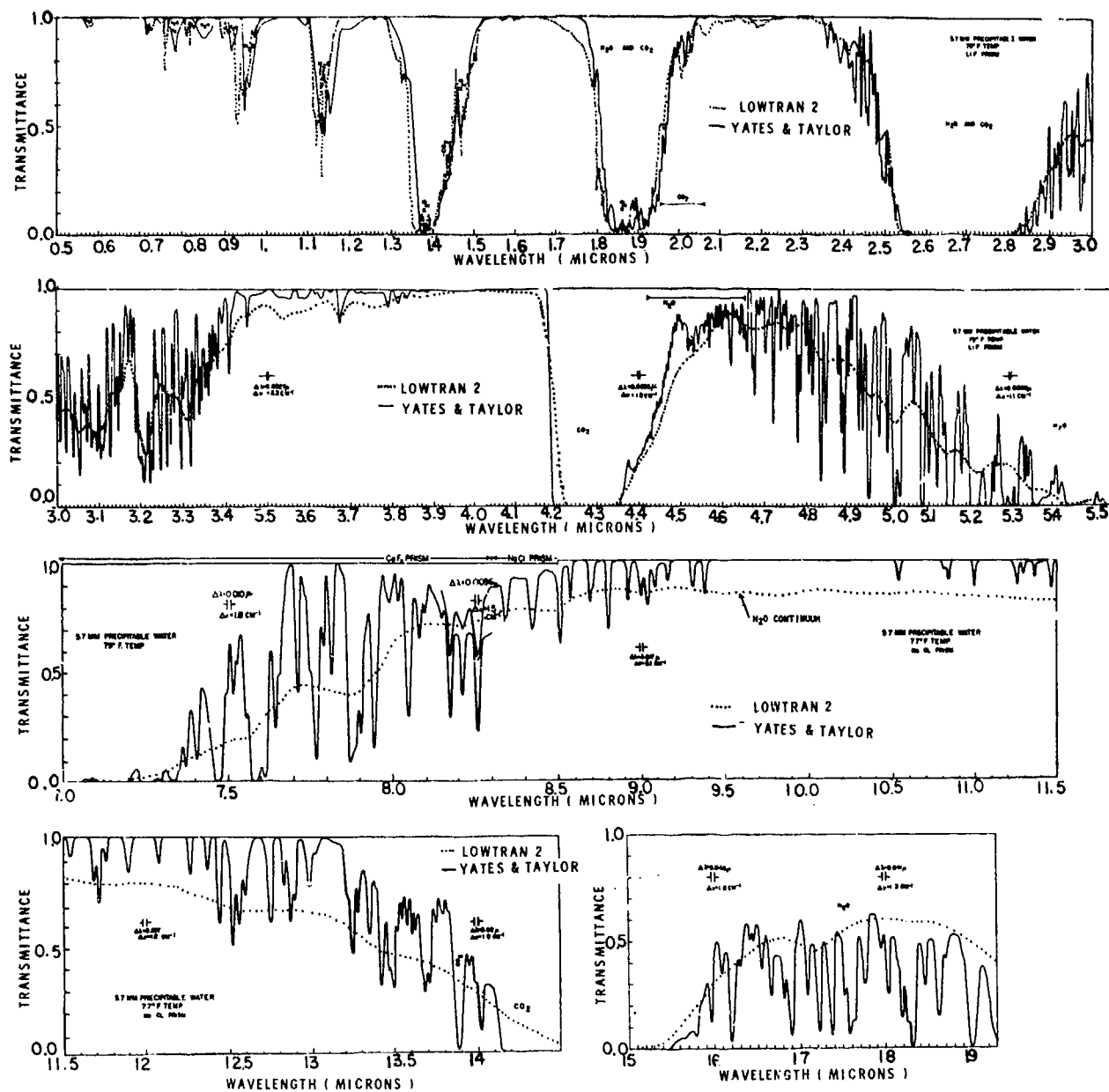


Figure 18- Comparison of LOWTRAN 3 and Measurement of Atmospheric Transmittance over a 0.3 km Path in the Chesapeake Bay Area.

MODELS OF THE ATMOSPHERIC AEROSOLS AND THEIR OPTICAL PROPERTIES

Eric P. Shettle and Robert W. Fenn
AFCRL
Hanscom AFB, Bedford, MA 01731
United States of America

ABSTRACT

Aerosol models have been developed for the boundary layer, the upper troposphere, the stratosphere, and mesosphere. In the boundary layer they describe 3 different environments: rural, urban and maritime. In the upper troposphere and stratosphere two different models represent spring-summer and fall-winter conditions. In the stratosphere they describe several levels of volcanic dust concentrations and the background conditions. For each model the coefficients for extinction, scattering and absorption, angular scattering distribution and other optical parameters have been computed for wavelengths between 0.2 and 40 μ m. The aerosol models are being presented along with a discussion of their experimental basis. The optical properties of these models are being discussed and some examples of their effect on the overall atmospheric transmission properties and atmospheric contrast reduction are presented.

1. INTRODUCTION

The aerosol models described in this paper supplement the aerosol components of atmospheric optical models previously developed at AFCRL (ELTERMAN, 1964, 1968, 1970; MCCLATCHEY et al., 1970). The vertical distribution of aerosol attenuation in the upper troposphere and stratosphere in these models was primarily based on several years of searchlight measurements in a fixed location (ELTERMAN 1966 and 1968). IVLEV (1967 and 1969) has made a review of the available experimental data up through 1967. Based on this review Ivlev presented a model of the vertical distribution of aerosol particles and their extinction of visible light.

The aerosol component in these models was based on experimental measurements which were made during and prior to the mid 1960's. At this time there was sufficient experimental data available to define an average stratospheric and upper tropospheric aerosol profile with some different haze concentrations in the lower troposphere (up to a few km altitude) with exponential vertical decrease in particle concentration.

During the past decade in this country and elsewhere extensive additional measurements from ground as well as airborne and space platforms have been made of aerosol concentrations, their size distribution, and optical properties, to warrant the development of updated aerosol models which also describe some of the temporal and spatial variations in atmospheric aerosol distributions and properties.

The models of the atmospheric aerosol and their optical properties developed below are based on a review of the available data on the nature of the aerosols, their sizes, their distribution and variability. However it must be emphasized that these models only represent a simplified version of typical conditions. Existing experiment data are not sufficient to describe the frequency of occurrence or variance of the different models.

In this study a number of different aerosol models for each of 4 different altitude regimes has been developed. The vertical distribution of the attenuation coefficients for these models is shown in Fig. 1. Also shown for comparison are the Rayleigh profile, and ELTERMAN'S 1968 Model.

(a) For the Boundary Layer (below 2 km) 10 models have been defined which describe the aerosols in rural, urban, and maritime environments for several surface meteorological ranges between 2 and 50 km.

(b) For the upper troposphere there are two models which represent spring and summer conditions versus fall and winter conditions.

(c) In the stratosphere (up to 30 km) models are presented for background, moderate, high, and extreme volcanic conditions for each of the two seasonal models.

(d) For the upper atmosphere (above 30 km) two models are presented. One of these corresponds to the most likely background conditions and the other represents the high aerosol concentrations often observed at these altitudes (in thin layers).

In the following sections, a more detailed description of the models will be presented along with a discussion of their experimental basis, and then some possible applications of the models will be discussed with some examples.

2. AEROSOL MODELS

2.1. Boundary Layer Aerosols

The range of conditions in the boundary layer (up to 2 kilometers) is represented by three different aerosol models (rural, urban, or maritime) for each of five meteorological ranges between 2 and 50 kilometers. Not all of the fifteen possible configurations are included because they do not represent meaningful conditions; for example an urban type aerosol mixture would not be present with visibilities as high as 50 kilometers.

In the boundary layer the shape of the aerosol size distribution and composition for the 3 surface models are assumed to be invariant with altitude. Therefore only the total particle number is being varied. Although the number density of air molecules decreases always more or less exponentially with altitude, there is considerable experimental data which show that the aerosol concentration very often has a rather different vertical profile. One finds that especially under low visibility conditions the aerosols are concentrated in a layer from the surface up to about 1 to 3 kilometers altitude and that this haze layer has a rather sharp top, (e.g. see DUNTLEY et al., 1972).

The vertical distribution for clear and moderately clear conditions, 50 and 23 kilometer meteorological ranges respectively, is taken to be exponential, similar to the profiles used by ELTERMAN (1964, 1968) following the work of PENNDORF (1954). For the hazy conditions (10, 5, and 2 km meteorological ranges) the aerosol extinction is taken to be independent of height up to $1\frac{1}{2}$ km with a pronounced decrease above that height.

2.1.1. Rural Aerosols

The "Rural Model" is intended to represent the aerosol conditions one finds in continental areas which are not directly influenced by urban and/or industrial aerosol sources. This continental, rural aerosol background is partly the product of reactions between various gases in the atmosphere and partly due to dust particles picked up from the surface. The particle concentration is largely dependent on the history of the airmass, carrying the aerosol particles. In stagnating airmasses, e.g. under wintertype temperature inversions, the concentrations may increase to values causing the surface layer visibilities to drop to a few kilometers.

Aerosol samples from all over the globe from rain-out and direct sampling have been analyzed by VOLZ (1972) for their optical/IR refractive index properties. Based primarily on these measurements the rural model is assumed to be composed of a mixture of 70% of water soluble substance (ammonium and calcium sulfate, and also organic compounds) and 30% dustlike aerosols. The resulting refractive index model is supported by other measurements (e.g. FISCHER, 1973; WARD et al., 1973; and GRAMS et al., 1974).

JUNGE (1963) suggested that most measured aerosol size distributions over the range of radius from 0.1 to $10\mu\text{m}$ could be described by an inverse power law. More recent experimental data from various investigators show that the power law model appears to be valid even for large particles out to 70 to $100\mu\text{m}$. If one plots these experimental data as the log volume distribution, $dV/d(\log r)$ versus $\log r$, a bimodal structure becomes apparent, with one broad peak in the 0.1 to $1\mu\text{m}$ diameter range and the second and larger peak between 5 and $100\mu\text{m}$ (e.g. see WHITBY et al., 1972). In order to represent this feature as well as to be approximately consistent with the Junge distribution the size distribution used for the rural model is the sum of two log-normal distributions which can be expressed as:

$$\frac{dN(r)}{dr} = \sum_{i=1}^2 \left(\frac{N_i}{\ln(10) \cdot r \cdot \sigma_i \sqrt{2\pi}} \right) \exp - \left[\frac{(\log r - \log r_i)^2}{2 \sigma_i^2} \right] \quad (1)$$

where $N(r)$ is the cumulative number density. The parameters defining this size distribution are given in Table 1, and it is illustrated in Fig. (2). Over the size range 0.1 to $10\mu\text{m}$ the present model is similar to the modified "haze C" used by MCCLATCHY et al. (1970) which was based on DEIRMENDJIAN'S (1964) "haze C".

2.1.2. Urban Aerosol Model

In urban areas the rural aerosol background gets modified by the addition of aerosols from combustion products and industrial sources. The urban aerosol model therefore was taken to be a mixture of the rural aerosol with carbonaceous aerosols. The sootlike aerosols are assumed to have the same size distribution as both components of the rural model. The proportions of the sootlike aerosols and the rural type of aerosol mixture are assumed to be 35% and 65% respectively. The refractive index of the sootlike aerosols was based on the soot data in TWITTY & WEINMAN'S (1971) survey of the refractive index of carbonaceous materials.

2.1.3. Maritime Aerosol Model

The aerosol compositions and distributions over the oceans are significantly different from continental aerosol types. The maritime aerosol component is due to salt particles which are caused by

the evaporation of seaspray droplets. Together with the continental aerosol background they form a fairly uniform maritime aerosol which is representative for the boundary layer in the lower 1-2 km in the atmosphere. The maritime aerosol model, therefore has been composed of 2 components: the sea spray produced component; and a continental component which was assumed identical to the rural aerosol with the exception that most of the very large particles were eliminated, since they are eventually lost due to fallout as the airmasses move across the oceans. This model is similar to the one suggested by JUNGE (1963 and 1972) and is supported by the measurements of MESZAROS and VISSY (1974). The size distribution is shown in Fig. 3 and the parameters for the size distribution are given in Table 1.

The properties of the seaspray produced component especially in the lower 100m or so above the water depend strongly on relative humidity and also windspeed. The number of seaspray produced aerosols increase with windspeed, especially the larger particles. The size distribution also is a function of relative humidity since the hygroscopic particles begin to grow by absorption of water if the relative humidity reaches values above 70 percent. The dependence of humidity and windspeed has not yet been incorporated into the maritime aerosol model; however these dependences will be added later. The present maritime aerosol model corresponds to moderate windspeeds and a relative humidity of approximately 80%. Above the immediate surface layer the maritime aerosol becomes less variable and for this region the maritime model is quite representative.

The refractive index is based on that for a solution of sea salt in water, using a weighted average of the refractive indices of water and sea salt. The refractive index of the sea salt is primarily taken from the measurements of VOLZ (1972b). For the refractive index of water the survey of HALE and QUERRY (1973) was used.

TABLE 1

SIZE DISTRIBUTIONS

(Normalized to 1 particle/cm³)

LOG NORMAL

Type of Aerosol	N ₁ *	r ₁	σ ₁	N ₂ *	r ₂	σ ₂
Rural	0.9999975	0.005μ	0.475	2.5x10 ⁻⁶	0.5	0.475
Urban	0.9999975	0.005μ	0.475	2.5x10 ⁻⁶	0.5	0.475
Maritime - Continental Origin	1.	0.005μ	0.475	-	-	-
Maritime - Sea Spray Origin	1.	0.3μ	0.4	-	-	-
Tropospheric	1.	0.005μ	0.475	-	-	-
Meteoric Dust	1.	0.03μ	0.5	-	-	-

MODIFIED GAMMA

	A	α	γ	b
Background Stratospheric	324	1	1	18
Fresh Volcanic	341.33	1	$\frac{1}{2}$	8
Aged Volcanic	5,461.33	1	$\frac{1}{2}$	16

$$*N_1 + N_2 = 1$$

2.2 Upper Troposphere

In the troposphere above the boundary layer, the distribution and nature of the atmospheric aerosols becomes less sensitive to geography and the meso or synoptic scale meteorological variations. Accordingly in this region the aerosol properties become more uniform and can be described by a general tropospheric aerosol model. The tropospheric model represents an extremely clear condition and can be described by the rural model without the large particle component. Larger aerosol particles will be depleted due to settling with time. There is some indication from experimental data, that the tropospheric aerosol concentrations are somewhat higher during the spring-summer season than during the fall-winter period, (BLIFFORD and RINGER, 1969; and HOFMANN et al., 1974). Different vertical distributions are given to represent these seasonal changes.

2.3 Stratospheric Aerosol Models

Measurement programs carried out over many years show that in the 10 to 30 km region there exists a background aerosol in the stratosphere which has a rather uniform global distribution. This background aerosol is considered to be mostly composed of sulfate particles formed by photochemical reactions.

These background levels are occasionally increased by factors of 100 or more by the injection of dust from massive volcanic eruptions. Once these particles have been injected into the stratosphere they are spread out over large portions of the globe by the stratospheric circulations, and it requires months to years for them to become slowly removed from the stratosphere.

One conclusion from measurements over the past 15 years is that the stratospheric aerosol concentration during the middle and late 1960's was still above normal background levels (see ELTERMAN et al., 1973; FOX et al., 1973; HOFMANN et al., 1974; and RUSSELL et al., 1974), due to a residual of the aerosols injected into the stratosphere by the eruption of Mt. Agung during the spring of 1963, and other eruptions up through 1968 (VOLZ, 1970). It was measurements made during this time period of elevated aerosol concentration which served as the major input to ELTERMAN'S (1968) and IVLEV'S (1967 & 1969) models.

Recent measurements indicate that volcanic conditions once again exist in the stratosphere due to the October 1974 eruption of the Fuego Volcano in Guatemala (see MCCORMICK & FULLER, 1975; MEINEL & MEINEL, 1975; ELTERMAN, 1975; and VOLZ, 1975a).

From these general concepts it was concluded that it would be meaningful to develop 4 different vertical distribution models for the stratosphere: a background model, and 3 different volcanic aerosol profiles (moderate, high, & extreme) which can represent either different amounts of volcanic material injected into the stratosphere or the decrease over time from the extreme conditions following a major event such as the Krakatoa explosion (SYMONS, 1888).

The experimental data also confirm a seasonal trend in the stratospheric aerosol distributions. Fig. 1 shows these stratospheric models and also for comparison the 1968 Elterman model which was based on data collected during the period several years after the Agung eruption in 1963 and therefore is representative for the moderate volcanic conditions.

The background aerosols are taken to be a 75% solution of sulfuric acid in water following the work of ROSEN (1971) and TOON & POLLACK (1973). The complex refractive index as a function of wavelength is based on the measurements of REMSBERG (1971 and 1973) and PALMER and WILLIAMS (1975). The refractive index for the volcanic models is based on the measurements of VOLZ (1973) on volcanic dust.

There are two volcanic aerosol size models; a "Fresh Volcanic Model" represents the size distribution of aerosols shortly after a volcanic eruption; and a "Volcanic Model" representing the aerosol about a year after an eruption. Both size distributions were chosen mainly on the basis of MOSSOP'S (1964) measurements following the eruption of Mt. Agung. The size distribution was also made consistent with the observed wavelength dependence of extinction due to volcanic aerosols, and in the case of the "Fresh Volcanic" Model consistent with the observation of optical phenomena such as Bishop's rings, and a blue or green sun sometimes observed following major volcanic eruptions (see DEIRMENDJIAN, 1969 and 1973; and VOLZ, 1970, 1975b). These size distributions are represented by a modified gamma distribution:

$$\frac{dN}{dr} = n(r) = Ar^{\alpha} \exp(-br^{\beta})$$

whose parameters are given in Table 1.

Either of the two volcanic size distribution models can be appropriate to use with the "moderate" or "high" volcanic vertical profiles, depending on whether these profiles represent a major eruption after a couple of years or a recent weaker eruption. It should be noted that, the profiles may have a much more layered structure than is shown in the model distributions, particularly shortly after a volcanic injection of dust into the atmosphere.

2.4. Upper Atmosphere

The aerosols above 30 km represent only a very small portion of the total aerosol content of the atmosphere so for many applications they can be neglected. However when the effects of the lower atmosphere are small, such as satellite observations of the limb of the earth's atmosphere or determining the ozone distribution by inverting measurements of backscattered ultraviolet from the atmosphere, the aerosols in the upper atmosphere may not be negligible. For this reason and for completeness, models of the aerosols in the upper atmosphere have been developed.

The major component of the normal upper atmospheric aerosols is considered to be meteoric dust following the conclusions reached by NEWKIRK and EDDY (1964) and later ROSEN (1969) in his review article. Meteoric or cometary dust also form some of the layers occasionally observed in the upper atmosphere. POULTNEY (1972) has related most of the Lidar observations (through 1970) of layers in the upper atmosphere to either cometary sources of micrometeoroid showers or noctilucent cloud observations.

The refractive index of meteoric dust is based on the work of VOLZ and SHETTLE (1975) who determined the complex refractive index for a mixture of chondrite dust which represents the major type of meteorite falling on the earth. The size distribution is similar in shape to the one developed by FARLOW and FERRY (1972) and has been represented by a log-normal distribution whose parameters are given in Table 1.

Fig. 1 shows in addition to the normal upper atmospheric model an extreme model similar to IVLEV'S (1967, 1969) model for the upper atmosphere. Attenuation coefficients this large occur in layers with thicknesses no greater than a few kilometers. At different times these layers can be either micrometeoroid dust or noctilucent clouds.

3. OPTICAL PROPERTIES

Based on the Mie theory for scattering by spherical particles, the coefficients for scattering, absorption and extinction, the angular scattering functions, polarization, and other optical properties for these aerosol models have been determined for a range of wavelength values from 0.2 to 40 μm including 11 laser wavelength values.

Fig. 4 gives a comparison of the wavelength dependence of the extinction coefficient for the various surface models. The extinction coefficients in Fig. 4-9 are all normalized to an extinction coefficient of 0.158 km^{-1} at a wavelength of $0.55 \mu\text{m}$ (corresponding to a surface visibility of about 23 km in order to be comparable with the Elterman and LOWTRAN (SELBY & MCCLATCHEY, 1972) models. Figure 4 shows in addition to the extinction coefficients for the rural, urban, maritime and tropospheric aerosol models also that for the model included in LOWTRAN 3 which will be published soon (the aerosol model in LOWTRAN 3 is based on a preliminary version of the present rural model). One notices that the tropospheric model has a much steeper wavelength dependence because of its lack of large particles and conversely the maritime model because of the large sea aerosol component a much smaller λ -dependence than the remaining three models. There is surprisingly little difference between the rural and urban model extinction coefficients. These similarities do, however, not hold for the coefficients for scattering and absorption as can be seen from Figures 5 and 6. The ratio of scattering to absorption are quite different for the rural and urban models, primarily because of the higher absorption coefficient of the soot component in the urban aerosol. The variations in the absorption and scattering coefficients for the maritime and tropospheric aerosol models are even larger, almost two orders of magnitude (Fig. 7 & 8). The sharp changes which occur in the coefficients near $10 \mu\text{m}$, and which are due to the anomalous refractive index in this region, are in opposite directions for the scattering and absorption and therefore balance each other to some extent in the extinction coefficient.

Fig. 9 gives the extinction coefficients for the background stratospheric and the volcanic aerosol models, and Fig. 10 shows the spectral variation of the single scattering albedo, i.e. the ratio of total scattered light to extinction, which is therefore a measure for the relative contributions of scattering and absorption to the total extinction. One will notice the rapid change in the relative importance of aerosol scattering and absorption in the middle IR spectral region. This is due to two factors, an increase in the absorption because of an increase in the imaginary part of the refractive index in the IR, and a decrease in the contribution from scattering as the wavelength becomes significantly larger than the size of the aerosols.

There are also some noticeable differences between the angular scattering functions of these various aerosol models. Figs. 11 and 12 give examples for 2 wavelengths 1.06 and $10.59 \mu\text{m}$. Both figures give the phase function, which is defined such that the integral from 0° to 180° becomes 1. The angular scattering dependence is shown for the principal components of which the various aerosol models are composed of.

4. APPLICATIONS

Some examples of calculated atmospheric transmittances are shown in Tables 2 and 3 to illustrate the effect of the various aerosol models on the transmission of radiation at 0.55 , 1.06 and $10.59 \mu\text{m}$ wavelength. Table 2 gives total atmospheric transmittances for a 1 km horizontal path at ground level through atmospheres of different optical properties. The transmittances are derived from the coefficients for molecular absorption and scattering as well as aerosol absorption and scattering. Several important conclusions can be drawn from these numbers: Under very good visibility conditions (50 km), the transmittance at $10.59 \mu\text{m}$ is determined by molecular absorption, primarily the water vapor continuum. Only for visibilities below about 10 km the effect of aerosol attenuation becomes significant at that wavelength. At $1.06 \mu\text{m}$ the aerosol attenuation contribution to the total extinction is considerable larger, and therefore also the differences between the different models become more pronounced. For instance in a 2 km visibility atmosphere the transmittance at $1.06 \mu\text{m}$ differs by a factor two between the urban and the maritime model, and even in a 10 km visibility situation there is a 30% difference in transmittance over a 1 km path between a rural and a maritime model. The transmittances at $0.55 \mu\text{m}$ are, by definition, identical if the visibility is the same. One also notices that except for the 2 km visibility models the transmittance at $10.59 \mu\text{m}$ is less than at $1.06 \mu\text{m}$. This is due to the strong influence of molecular attenuation to the total extinction.

Table 3 gives a comparison of transmittances for 3 stratospheric aerosol models. In this case the transmittances have been calculated for a 10 km horizontal path at 20 km altitude. The total aerosol particle densities are in accordance with the summer profile data of Fig. 1. These numbers again reflect the influence of molecular absorption at $10.59 \mu\text{m}$ except for the extreme volcanic case. Note that molecular absorption here is due to the wings of the $9.6 \mu\text{m}$ ozone band. The low transmittance at $1.06 \mu\text{m}$ for the extreme volcanic model is caused by the anomalous wavelength dependence in the extinction coefficient in this spectral region, which is in agreement with experimental observations.

Another application of the aerosol models is in determining the effects of the atmosphere on the observed contrast of an object and its background, C . One measure of these atmospheric effects on contrast is the contrast transmission, T_c , which is the ratio of the apparent contrast of an object to the inherent

contrast, C_0 , of the object and its background (i.e. without the intervening atmosphere):

$$T_c = C/C_0$$

Figure 13 illustrates the results of calculations of the contrast transmission for the rural atmospheric model as seen from a 20 km altitude. As might be expected the reduction in contrast is greatest looking near the horizon (which is near 95° instead of 90° because of the observing altitude); this is because of both increase in the path radiance, or light scattered into the field of view, and a decrease in the radiance directly from the object because of the increase of the viewing path length through the atmosphere. The azimuthal dependence is small except when the sun is near the horizon; it therefore is only shown for the case of zenith angle 80° .

The effect of different atmospheric conditions on the contrast can be studied by examining the ratios of the contrast transmissions for the different atmospheric models as in Figure 14. This figure presents the ratio of T_c , using the urban aerosol model in the boundary layer, to T_c with a rural type model in boundary layer. For both of these cases the surface meteorological range was taken to be 10 km, so the only differences in the optical properties of the model atmospheres are the relative amounts of absorption and scattering, and minor differences in the phase functions. It can be seen that with sun high in the sky the contrast transmission through the urban atmosphere is higher than for the rural model, whereas when the sun is near the horizon T_c is higher for the rural conditions. This is a result of the relative contribution of multiple scattering (which is reduced for the urban atmosphere) to the path radiance and the surface illumination, and its dependence on the sun and viewing geometries. Another significant factor is the relative importance of scattering within the boundary layer versus scattering above the boundary layer (where there is no difference between the rural and urban models), for the different geometries.

Using the Maritime aerosol model, the contrast transmission is comparable to that for the Model Rural atmosphere. Only with the sun within 20° to 30° of the horizon, where T_c for the Maritime Model is 20% higher than for the rural conditions, do the contrast transmissions differ by more than the 5 to 10% error in the calculations.

TABLE 2

Aerosol Model	Visibility	$\lambda = .55\mu m$	$1.06\mu m$	$10.591\mu m$
rural	50 km	0.925	0.970	0.694
	10 km	0.677	0.843	0.673
urban	10 km	0.677	0.822	0.673
	2 km	0.142	0.368	0.578
maritime	10 km	0.677	0.691	0.657
	2 km	0.142	0.181	0.509

TABLE 3

Atmospheric Transmittance for a 10 Km Horizontal Path at 20 Km Altitude

	$\lambda = 0.55\mu m$	$1.06\mu m$	$10.591\mu m$
Background	0.984	0.997	0.908
Mod. Volcanic	0.976	0.992	0.913
Extreme Volcanic	0.364	0.346	0.634

5. SUMMARY

In summary the models which have been described here, allow the prediction of the optical properties of the atmosphere over a wide spectral range, from the UV and visible through the IR. The various models exhibit significant differences in the wavelength dependence of their optical characteristics. These differences must be considered in any attempt to infer the infrared properties of the atmosphere from those in the visible; e.g. relating IR transmission to visibility statistics.

A conclusion which we believe, one must also draw from such model studies is, that because of the sensitivity of the atmospheric optical properties to the different aerosol characteristics, it will be very important for future planning to develop a data base for the variance and the geographical distributions, and frequency of occurrence of the various aerosol types. A program designed to develop such a data base for Europe is OPAQUE, which will be described by Mr. Bakker in paper No. 15 at this meeting.

The complete review of the aerosol properties, a detailed description of the models, and tables of results will be contained in a forthcoming AFGL technical report.

REFERENCES

- BLIFFORD, I.H. and L.D. RINGER, 1969, "The Size and Number Distribution of Aerosols in the Continental Troposphere," J. Atmos. Sci., 26, 716-726.
- DEIRMENDJIAN, D., 1964, "Scattering and Polarization Properties of Water Clouds and Hazes in the Visible and Infrared," Appl. Opt., 3, 187-196.
- DEIRMENDJIAN, D., 1969, Electromagnetic Scattering on Spherical Polydispersions, American Elsevier, New York, pp 290.
- DEIRMENDJIAN, D., 1973, "On Volcanic and Other Turbidity Anomalies", Advances in Geophysics., 16, 267-296.
- DUNTLEY, S.Q., R.W. JOHNSON, and J.I. GORDON, 1972, "Airborne Measurements of Optical Atmospheric Properties, Summary and Review", Univ. of Calif. San Diego, Scripps Institution of Oceanography, Visibility Laboratory, SIO Ref 72-82 and AFCRL-72-0593.
- ELTERMAN, L., 1964, "Atmospheric Attenuation Model, 1964, in the Ultraviolet, Visible, and Infrared Regions for Altitudes to 50 km", Tech. Report AFCRL-64-740 (Sept. 1964).
- ELTERMAN, L., 1966, "An Atlas of Aerosol Attenuation and Extinction Profiles for the Troposphere and Stratosphere", Tech. Report AFCRL-66-828 (Dec. 1966).
- ELTERMAN, L., 1968, "UV, Visible, and IR Attenuation for Altitudes to 50 km, 1968", Tech. Report AFCRL-68-0153 (April 1968).
- ELTERMAN, L., 1970, "Vertical Attenuation Model with Eight Surface Meteorological Ranges 2 to 13 Kilometers," Tech. Report AFCRL-70-0200 (March 1970).
- ELTERMAN, L., 1975, "Stratospheric Aerosol Parameters for the Fuego Volcanic Incursion", Appl. Opt., 14, 1262-1263.
- ELTERMAN, L., R.B. TOOLIN, and J.D. ESSEX, 1973, "Stratospheric Aerosol Measurements with Implications for Global Climate", Appl. Opt., 12, 330-337.
- FARLOW, N.H., and G.V. FERRY, 1972, "Cosmic Dust in the Mesosphere", Space Res., 12, 369-380.
- FISCHER, K., 1973, "Mass Absorption Coefficient of Natural Aerosol Particles in the 0.4-2.4 μ m Wavelength Interval", Beitr. Physik Atmos., 46, 89-100.
- FOX, R.J., G.W. GRAMS, B.G. SCHUSTER, and J.A. WEINMAN, 1973, "Measurements of Stratospheric Aerosols by Airborne Laser Radar", J. Geophys. Res., 78, 7789-7801.
- GRAMS, G.W., I.H. BLIFFORD, JR., D.A. GILLETTE, and P.B. RUSSELL, 1974, "Complex Index of Refraction of Airborne Soil Particles", J. Appl. Meteor., 13, 459-471.
- HALF, G.M. and M.R. QUERRY, 1973, "Optical Constants of Water in the 200-nm to 200- μ m wavelength Region", Appl. Opt., 12, 555-563.
- HOFMANN, D.J., J.M. ROSEN, and T.J. PEPIN, 1974, "Global Measurements of the Time Variations and Morphology of the Stratospheric Aerosol", Proceedings of the Third Conference on the Climatic Impact Assessment Program: Feb. 26-Mar. 1, 1974. Ed. by A.J. Broderick and T.M. Hard (DOT-TJC-OST-74-15).
- IVLEV, L.S., 1967, "Aerosol Model of the Atmosphere", Prob. Fiz. Atmos., No. 7, Leningrad, pp 125-160, translated by Foreign Science and Technology Center, Dept. of the Army, available from U.S. National Technical Information Service (AD 760-393).
- IVLEV, L.S., 1969, "Atmospheric Aerosol", pp 28-42 in Radiation Characteristics of the Atmosphere and the Earth's Surface, Ed. K. Ya Kondratyev, Amerind Publishing Co., New Delhi, available from U.S. National Technical Information Service (No. TT-71-58003).
- JUNGE, C.E., 1961, Air Chemistry and Radioactivity, pp 382, Academic Press, New York.
- JUNGE, C.E., 1972, "Our Knowledge of the Physico-Chemistry of Aerosols in the Undisturbed Marine Environment", J. Geophys. Res., 77, 5183-5200.
- MCCLATCHEY, R., R. FENN, J. SELBY, F. VOLZ, and J. GARING, 1970, "Optical Properties of the Atmosphere", Tech. Report AFCRL-70-0527, (1970). Also revised editions AFCRL-71-0279 and AFCRL-72-0497.
- MCCORMICK, M.P. and W.H. FULLER, JR., 1975, "Lidar Measurements of Two Intense Stratospheric Dust Layers", Appl. Opt., 14, 4-5.

- MEINEL, A.B. and M.P. MEINEL, 1975, "Stratospheric Dust Event of November 1974", Science, 188, 477-478.
- MESZAROS, A. and K. VISSY, 1974, "Concentration, Size Distribution and Chemical Nature of Atmospheric Aerosol Particles in Remote Oceanic Areas", J. Aerosol Sci., 5, 101-109.
- MOSSOP, S.C., 1964, "Volcanic Dust Collected at an Altitude of 20 km", Nature, 203, 824-827.
- NEWKIRK, G., JR., and J.A. EDDY, 1964, "Light Scattering by Particles in the Upper Atmosphere", J. Atmos. Sci., 21, 35-60.
- PALMER, K.F. and D. WILLIAMS, 1975, "Optical Constants of Sulfuric Acid: Application to the Clouds of Venus?", Appl. Opt., 14, 208-219.
- PENDORF, R., 1954, "The Vertical Distribution of Mie Particles in the Troposphere", Geophys. Res. Paper No. 25, AFCRL, Bedford, MA
- POULTNEY, S.K., 1972, "Laser Radar Studies of Upper Atmosphere Dust Layers and the Relation of Temporary Increases in Dust to Cometary Micrometeoroid Streams", Space Res., 12, 403-421.
- REMSBERG, E.E., 1971, Radiative Properties of Several Probable Constituents of Atmospheric Aerosols. PH.D Thesis, Dept. of Meteorology, University of Wisconsin, Madison.
- REMSBERG, E.E., 1973, "Stratospheric Aerosol Properties and Their Effects on Infrared Radiation", J. Geophys. Res., 78, 1401-1408.
- ROSEN, J.M., 1969, "Stratospheric Dust and its Relationship to the Meteoric Influx", Space Sci. Rev., 9, 58-89.
- ROSEN, J.M., 1971, "The Boiling Point of Stratospheric Aerosols", J. Appl. Meteor., 10, 1044-1046.
- RUSSELL, P.B., W. VIEZEE, and R.D. HAKE, 1974, "Lidar Measurements of Stratospheric Aerosols over Menlo Park, California, Oct. 1972-March 1974"; Final Report, June 1974, under Contract NAS2-7261.
- SELBY, J.E.A. and R.M. MCCLATCHEY, 1972, Atmospheric Transmittance From 0.25 to 28.5 μ m: Computer Code LOWTRAN 2, AFCRL-TR-72-0745, ERP 427.
- SYMONS, G.J. (Ed.), 1888, The Eruption of Krakatoa and Subsequent Phenomena, Report of the Krakatoa Committee. Truebner and Co., London, pp 497.
- TOON, O.B. and J.P. POLLACK, 1973, "Physical Properties of the Stratospheric Aerosol", J. Geophys. Res., 78, 7051-7056.
- TWITTY, J.T. and J.A. WEINMAN, 1971, "Radiative Properties of Carbonaceous Aerosols", J. Appl. Meteor., 10, 725-731.
- VOLZ, F.E., 1970a, "On Dust in the Tropical and Midlatitude Stratosphere from Recent Twilight Measurements", J. Geophys. Res., 75, 1641-1646.
- VOLZ, F.E., 1970b, "Atmospheric Turbidity After the Agung Eruption of 1963 and Size Distribution of the Volcanic Aerosol", J. Geophys. Res., 75, 5185-5194.
- VOLZ, F.E., 1972a, "Infrared Absorption by Atmospheric Aerosol Substances", J. Geophys. Res., 77, 1017-1031.
- VOLZ, F.E., 1972b, "Infrared Refractive Index of Atmospheric Aerosol Substances", Appl. Opt., 11, 755-759.
- VOLZ, F.E., 1973, "Infrared Optical Constants of Ammonium Sulfate, Sahara Dust, Volcanic Pumice, and Flyash", Appl. Opt., 12, 564-568.
- VOLZ, F.E., 1975a, "New Volcanic Twilights", Science, 189, 48-50.
- VOLZ, F.E., 1975b, "Distribution of Turbidity After the 1912 Katmai Eruption in Alaska", J. Geophys. Res., 80, 2643-2648.
- VOLZ, F.E. and E.P. SHETTL, 1975, "Optical Constants of Meteoric Dust", under preparation.
- WARD, G., K.M. CUSHING, R.D. MCPETERS and E.S. GREEN, 1973, "Atmospheric Aerosol Index of Refraction and Size Altitude Distribution from Bistatic Laser Scattering and Solar Aureole Measurements", Appl. Opt., 12, 2585-2592.
- WHITBY, K.T., R.B. HUSAR and B.Y.H. LIU, 1972, "The Aerosol Size Distribution of Los Angeles Smog", J. Colloid and Interface Sci., 39, 177-204.

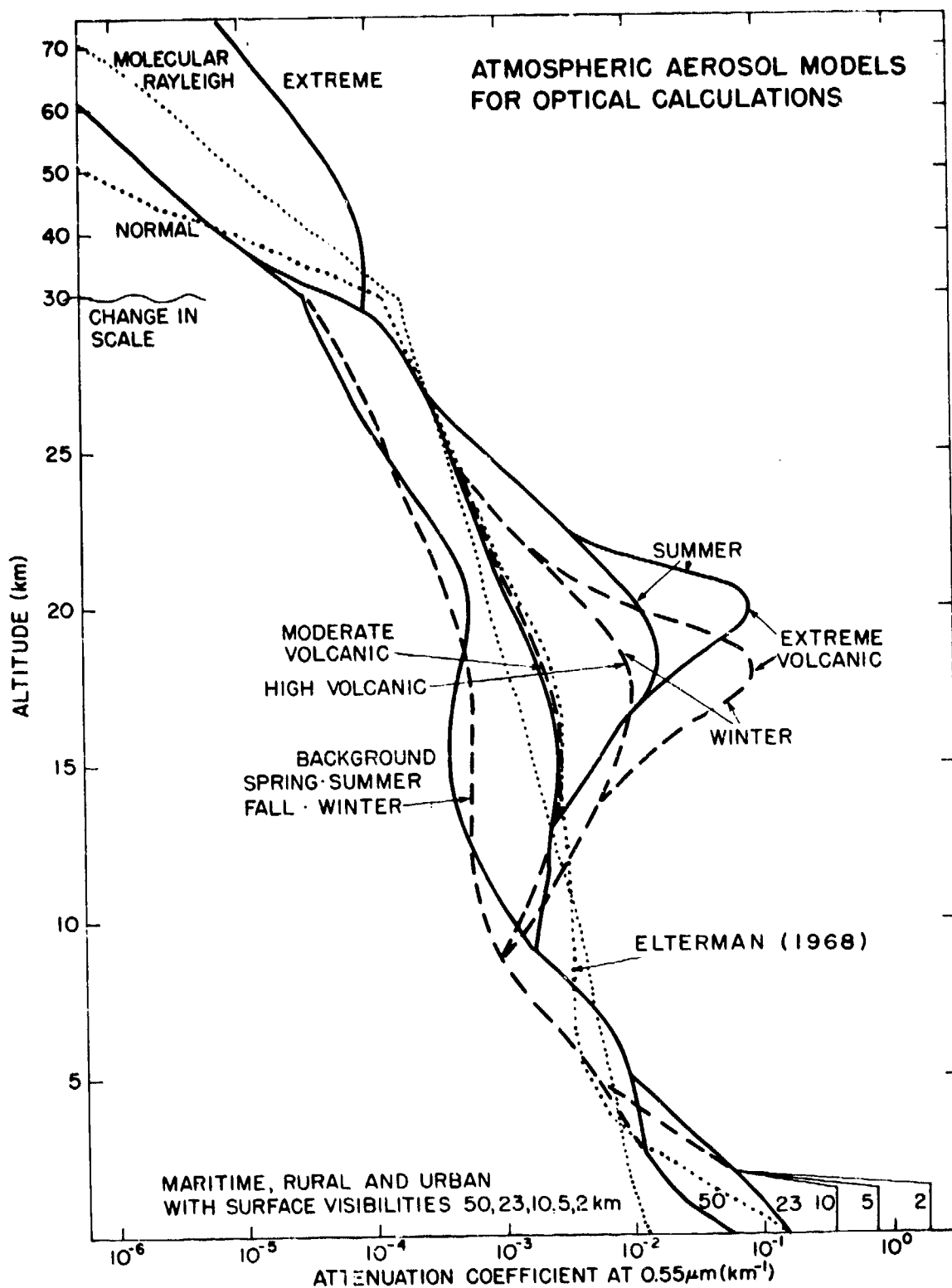


Figure 1. The vertical distribution of the aerosol extinction (at 0.55 microns) for the different models. Also shown for comparison are the Rayleigh profile (dotted line) and Elterman's (1968) Model. Between 2 and 30 Kilometers, where a distinction on a seasonal basis is made, the Spring-Summer conditions are indicated with a solid line and Fall-Winter conditions are indicated by a dashed line.

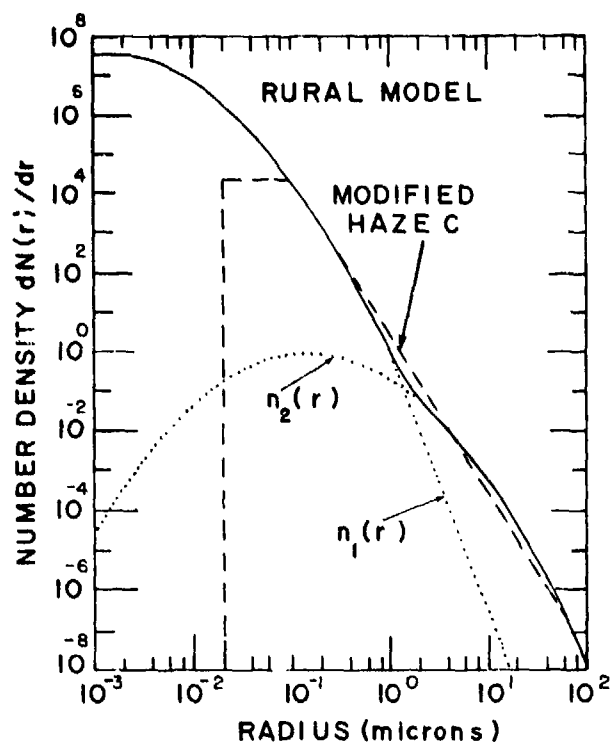


Figure 2. Size distribution for the present rural Aerosol Model (solid line) compared with the modified haze C model (dashed line). Also are the individual log normal distributions (dotted lines) which make up the rural model.

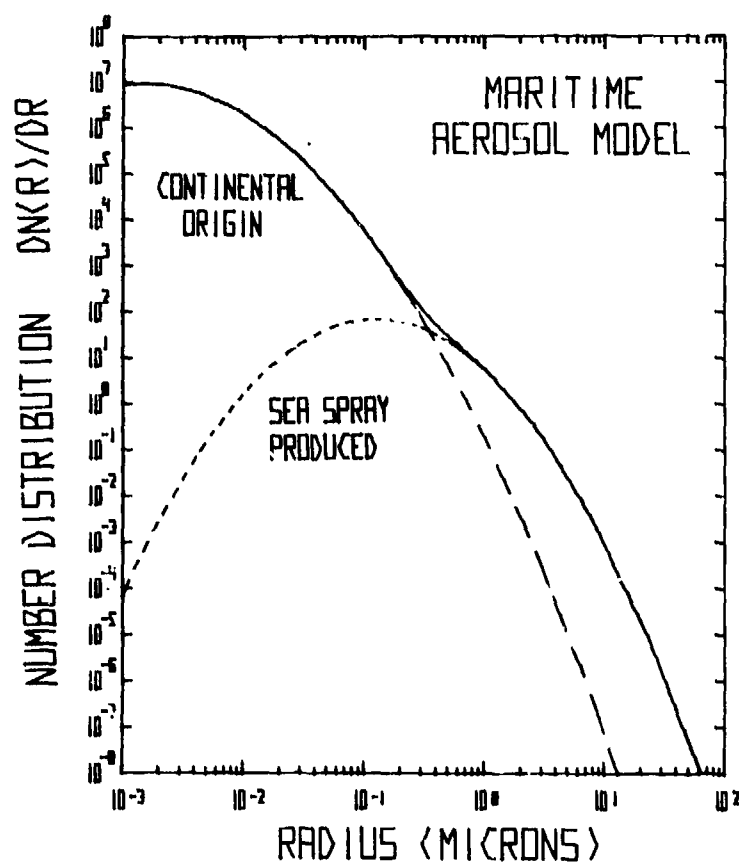


Figure 3. Size distribution for the Maritime Aerosol Model. Also shown are the aerosols of continental origin (long dashes) and the sea spray produced aerosols (short dashes).

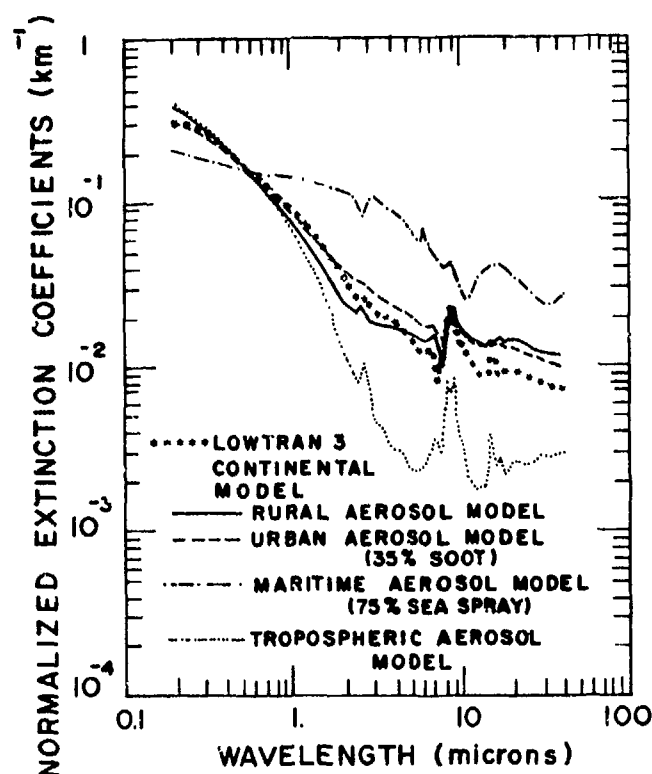


Figure 4. Extinction coefficients for the lower atmospheric aerosol models as a function of wavelength. The particle concentrations have been normalized so the extinction at 0.55 microns corresponds to a 23 km meteorological range, to facilitate a comparison of the wavelength dependence of the extinction for the different models.

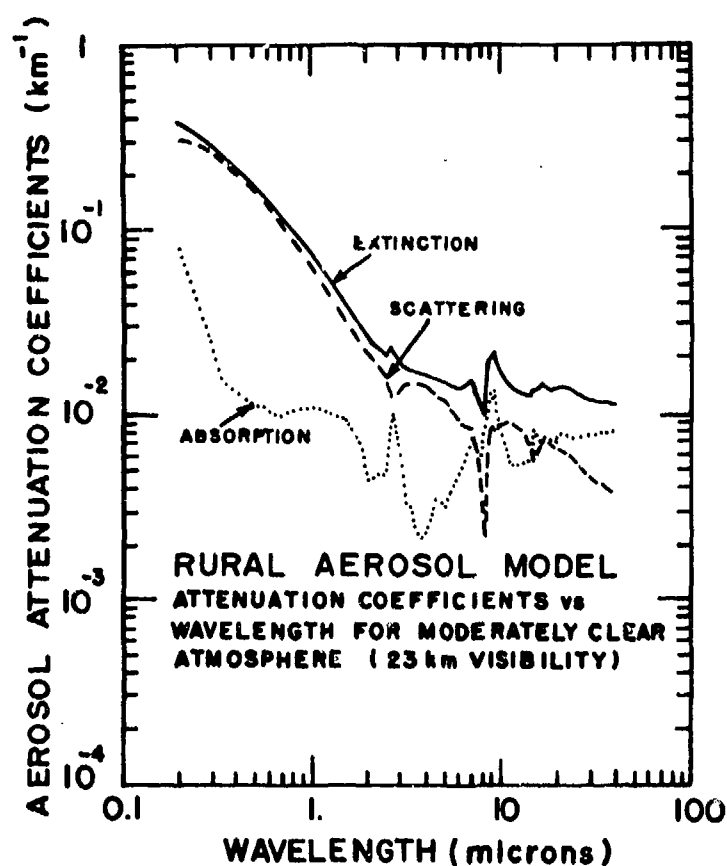


Figure 5. Scattering (dashed line), Absorption (dotted line) and Extinction (solid line) coefficients for the Rural Aerosol Model. As in Figure 4 the extinction coefficient is normalized to give a meteorological range of 23 km at 0.55 microns.

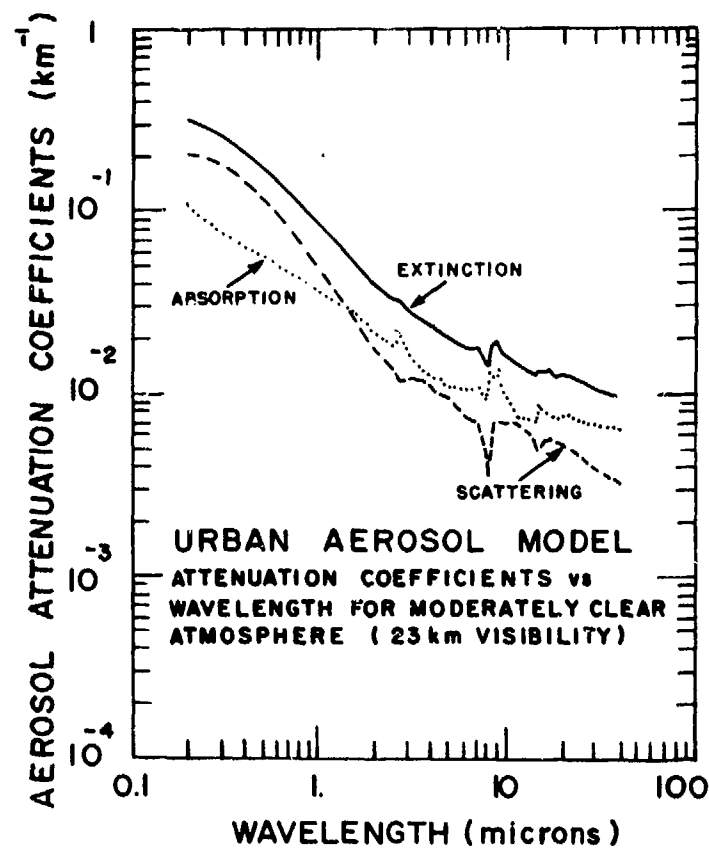


Figure 6. Same as Fig. 5 for the Urban Aerosol Model.

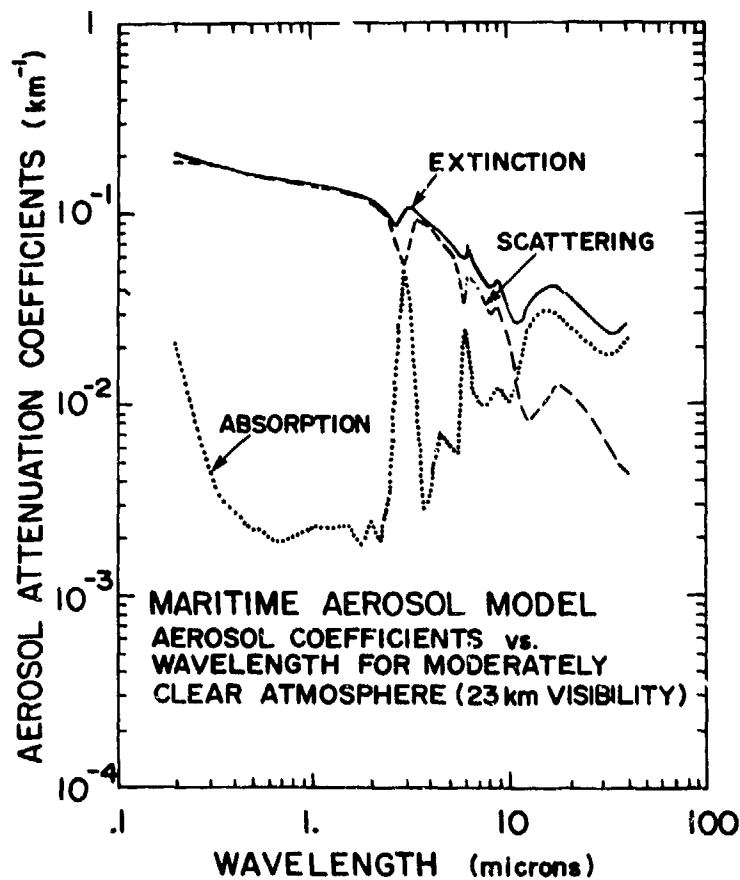


Figure 7. Same as Fig. 5 for the Maritime Aerosol Model.

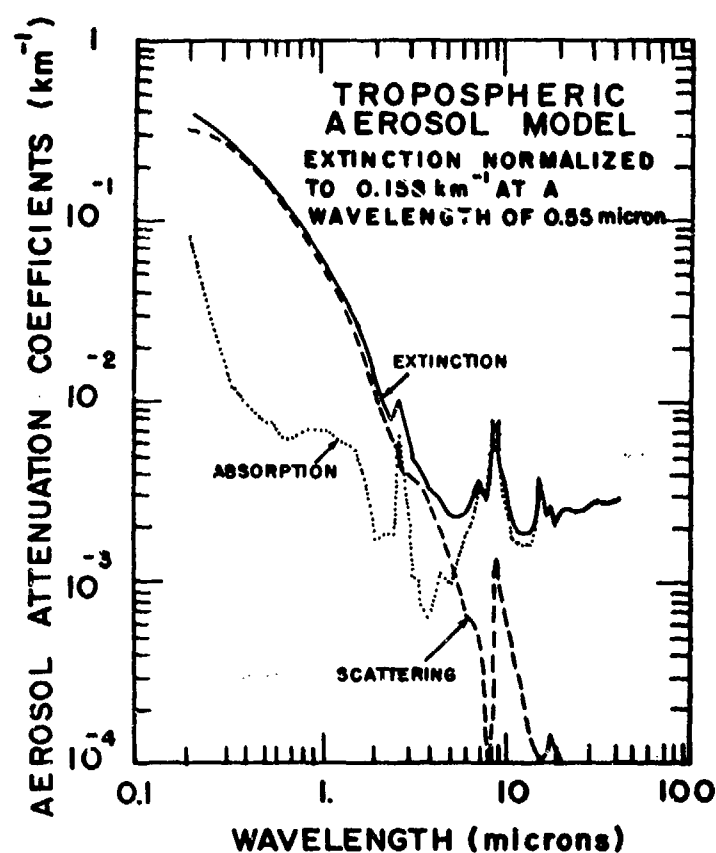


Figure 8. Same as Fig. 5 for the Tropospheric Aerosol Model.

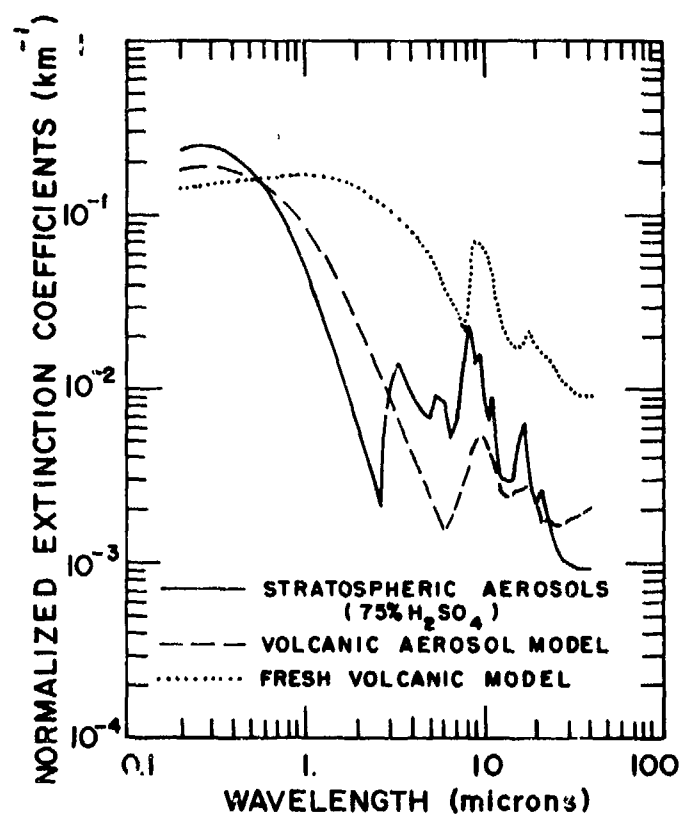


Figure 9. Extinction coefficients for the different stratospheric aerosol models (background stratospheric, volcanic, and fresh volcanic). The particle concentrations have been normalized so the extinction coefficient is 0.158 km^{-1} , at 0.55 microns, to facilitate comparison with the other models.

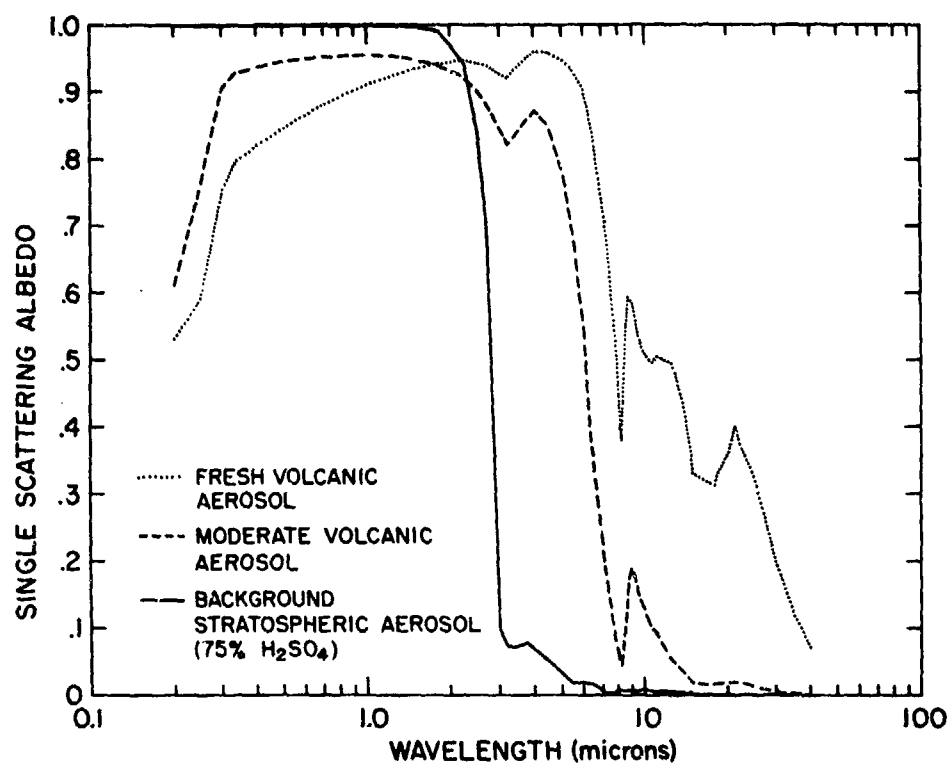


Figure 10. Single Scattering Albedo for the different Stratosphere Aerosol Models, versus wavelength. Single Scattering Albedo is the ratio of scattering to total extinction.

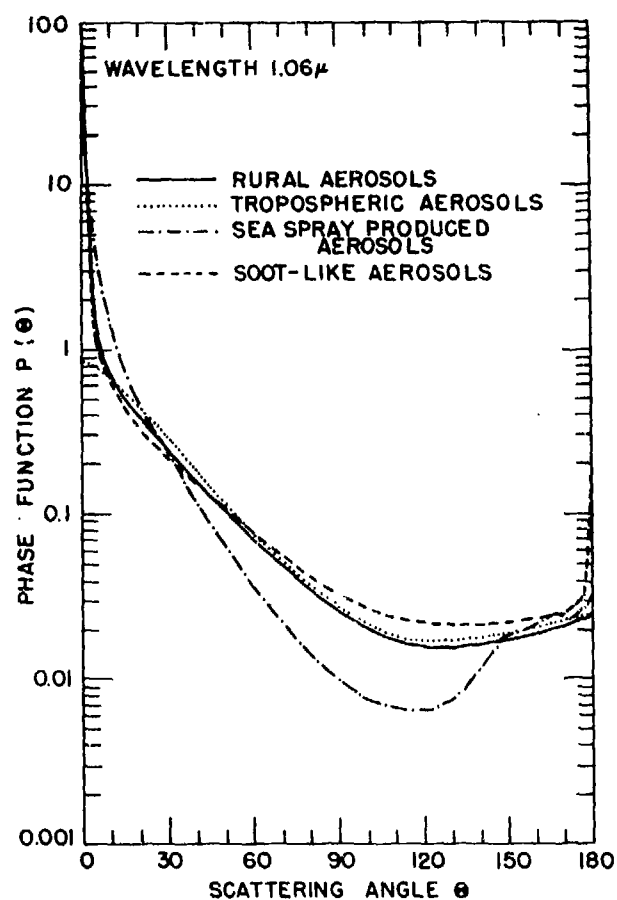


Figure 11. Angular distribution of scattered light for different lower atmospheric aerosol models, at wavelength of 1.06 microns. The phase function, $P(\theta)$, is the differential probability

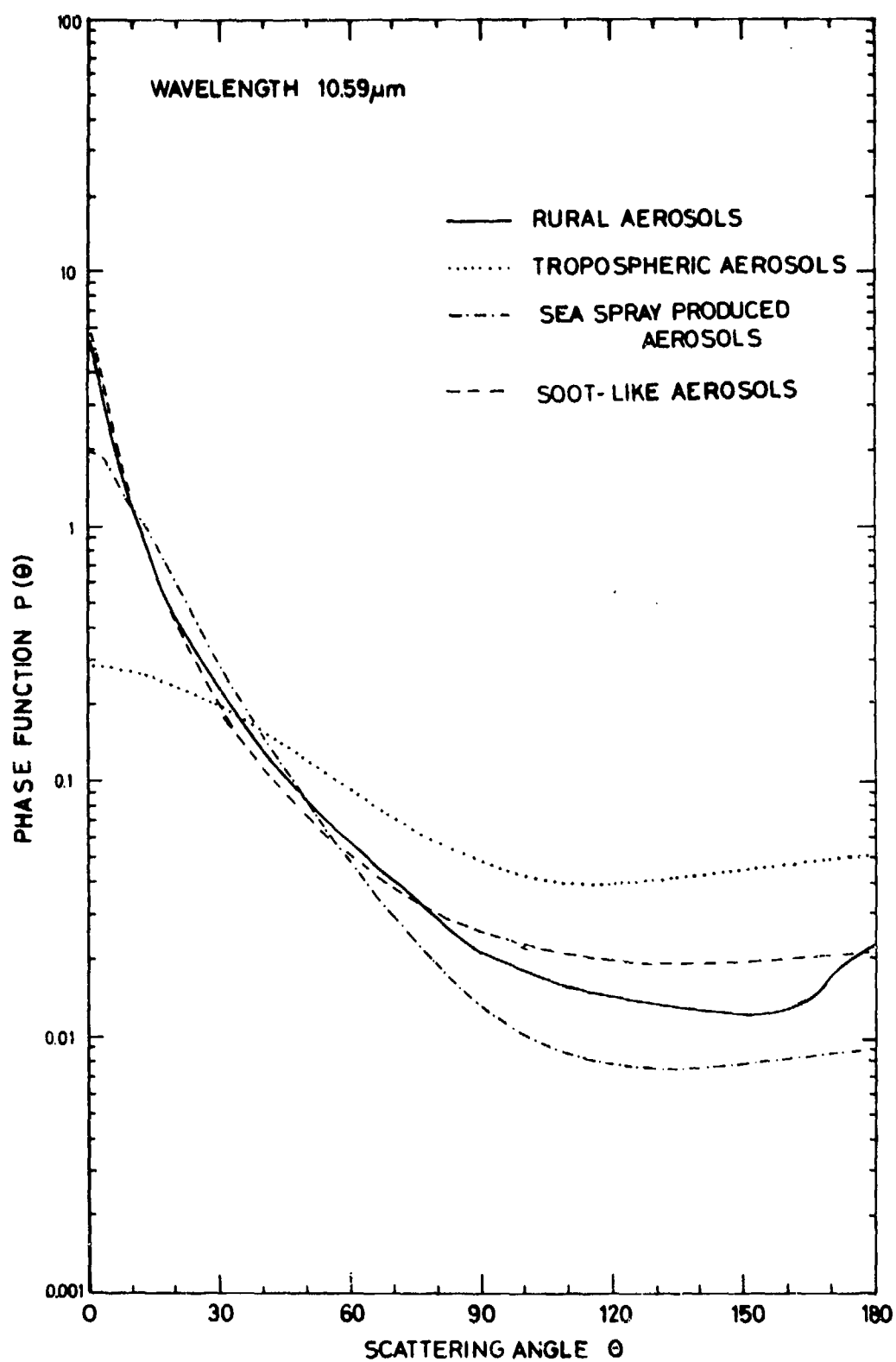


Figure 12. Same as Fig. 11 for a wavelength of 10.591 microns.

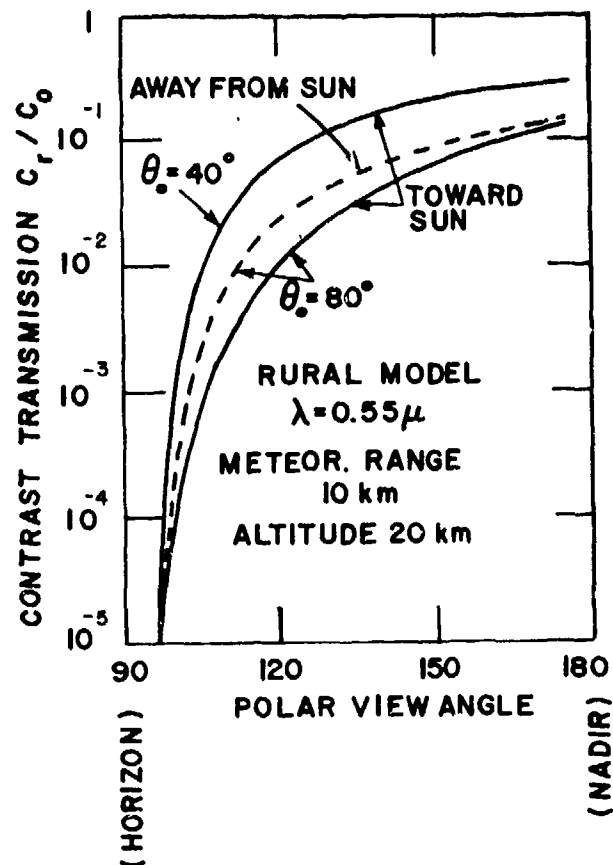


Figure 13. Contrast transmission for the rural model atmosphere, for different viewing directions.

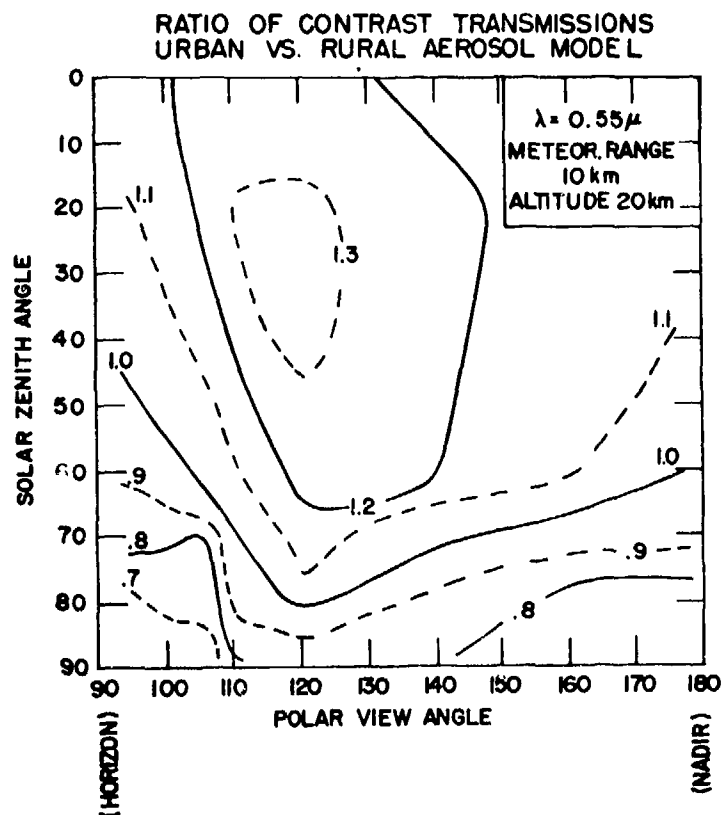


Figure 14. Ratio of Contrast Transmission in the Urban Model Atmosphere to Contrast Transmission in the Rural Model Atmosphere for a 0° azimuth angle (looking towards the sun).

A COMPARATIVE STUDY OF ATMOSPHERIC TRANSMISSION AT THREE LASER WAVELENGTHS IN RELATION TO THE
METEOROLOGICAL PARAMETERS

P. J. Wright
Plessey Radar Ltd.
Newport Road
Coves
Isle of Wight.

SUMMARY

This paper describes work carried out to date under a contract to study experimentally and theoretically the transmission through the atmosphere of laser radiation at $0.63\mu\text{m}$, $1.06\mu\text{m}$ and $10.6\mu\text{m}$. A transmissometer operated continuously measures the attenuation of the three wavelengths simultaneously over a common path length. Results are compared with deductions from the theory of scattering of electromagnetic radiation due to Mie. Meteorological data recorded at the same time will enable correlations of transmission with atmospheric conditions to be made.

1. INTRODUCTION

Future military range finders and target markers will use either Neodymium (Nd^{3+}) or Carbon Dioxide (CO_2) lasers as the primary transmitting source. The operational usefulness of these systems will be determined by the characteristics of the atmosphere through which the radiation must pass. In particular the Nd^{3+} and CO_2 laser radiation at $1.06\mu\text{m}$ and $10.6\mu\text{m}$ respectively, is attenuated in the atmosphere by aerosol scattering as well as by water vapour and carbon dioxide absorption at $10.6\mu\text{m}$.

Published data concerning these propagation losses, particularly due to scattering, are not extensive enough for a decision to be reached as to the most suitable wavelength $1.06\mu\text{m}$ or $10.6\mu\text{m}$, to be adopted for any particular operational requirement.

The prime objective of the present study is therefore the comparative measurement of the atmospheric attenuation of CO_2 and Nd^{3+} laser radiation under a wide variety of meteorological conditions. Objective assessment of the relative usefulness of these laser sources will then be possible. Correlations with the meteorological parameters will enable the performance to be predicted in any locality in which meteorological records are available. Both a practical and a theoretical approach to the problem is being made and it is hoped that a suitable combination of results from these methods will yield an acceptable solution.

Two complete transmissometers have been built, one located at Coves on the Isle of Wight the other at the Royal Aircraft Establishment, Farnborough, Hampshire. Apart from periods of enforced down time for replacement of laser tubes and lamps and equipment breakdown one of these is operated continuously 24 hours a day. Standard meteorological data is recorded simultaneously with the transmissometer readings so that correlations with these parameters may be attempted. The programme is currently in the data-gathering phase and further results during fog and mist are required before theories can be fully tested.

2. ATTENUATION MECHANISMS

Under conditions of single scattering only the monochromatic transmittance along a homogeneous path in the atmosphere is exponentially related to distance by

$$T = \exp(-\alpha l)$$

where α = attenuation coefficient (Km^{-1})
 l = path length (Kms)

It has been found (Zuev et al 1967) that single scattering theory can account for the observed attenuation for optical depths (αl) up to 25 when the radiation is in the form of a narrow collimated beam such as from a laser. In general the attenuation is produced by absorption and scattering of the electromagnetic radiation by both molecules and aerosol particles. Thus the attenuation coefficient may be subdivided into the sum of four components $\alpha = \alpha_m + \alpha_a + \sigma_m + \sigma_a$ where σ is the scattering coefficient, K is the absorption coefficient and the subscripts 'm' and 'a' refer to molecules and aerosols respectively. Whereas the molecular scattering coefficient is a function of the number of molecules in the path only, the molecular absorption coefficient is dependent on the local temperature and pressure also. The wavelength dependence of molecular scattering is λ^{-4} for visible and infra-red radiation, while the variation with wavelength of molecular absorption is complex owing to the large number of discrete absorption lines of the various atmospheric constituents. This study is primarily concerned with extinction coefficients between the limits 0.6 Km^{-1} to 6.0 Km^{-1} and the transmissometer has been optimised to cover this range. Apart from molecular absorption by H_2O and CO_2 at $10.6\mu\text{m}$ the most important attenuation mechanism at these values is aerosol scattering and the paper will therefore be devoted to this aspect.

TRANSMISSOMETER EQUIPMENT

Experimentally the atmospheric transmission is monitored by a total energy double reflecting transmissometer over a total path length of 560 meters. The double reflecting principle, comprising a single transmitter - receiver with two retro-reflectors spaced at distances R1 and R2 from the transmitter is capable of greater accuracy than other designs (Killick and Bateman 1972). The extinction coefficient is calculated from the ratio of the transmissions over the two path lengths thus:-

$$\sigma = \frac{-1}{(R2-R1)} \log \left(\frac{T1}{T2} \right)$$

The great advantage of this technique is that provided the two retro-reflectors are identical the computed extinction coefficient is independent of the efficiency of the optical system.

3.1. Optical Design

The two retro-reflectors are of the focussing type consisting of a small plane secondary mirror at the focus of a paraboloidal primary reflector. The first retro-reflector is at 10 meters from the transmitter and the second at 280 meters. In the absence of atmospheric turbulence the returning radiation is focussed down to a spot size approaching that which leaves the transmitter. The acceptance apertures of both retro-reflectors and receivers are such that the full beam width is collected under all conditions. Each laser beam is chopped and transmitted through a 50% beamsplitter which samples the outgoing beam for driving a phase sensitive detector and for monitoring the laser output power. It also serves to direct the returning beam on to the signal detector. Since 50% of the return also passes into the laser some attenuation is required to prevent optical feedback affecting the operation of the laser. The three wavelengths, 0.63 μ m to 10.6 μ m are combined into a single coaxial beam by means of a 'cold' mirror and a germanium flat. A schematic of the optical layout is shown in figure 1. The returning radiation is separated into the three wavelengths by the same components and focussed by 5 cm diameter lenses on to the appropriate detector element.

3.2. Electrical Design

Plessey Pyroelectric detectors are used to detect the 10.6 μ m radiation while UDT PIN 10 photo-diodes are employed for the other two wavelengths. The chopped signal is amplified and rectified by the phase sensitive detectors. The reference signal level is used to control the gain of the amplifier stage such that the output is independent of laser power fluctuations. This ensures that the output level is directly proportional to transmission. The signal output together with housekeeping data and the readings from the standard meteorological instruments are fed to the data acquisition system. This also controls the sequence of operations for the whole experiment. Readings are normally taken at 15 minute intervals except when the visibility is in the range of interest when the rate is automatically switched to reading every 3 minutes. The whole station is designed for unattended operation except for routine daily checks and replacement of data tapes. Data is punched onto paper tape for subsequent analysis by computer for presentation in a format suitable for comparison with theoretical expectations.

4. ANALYSIS OF RESULTS - COMPARISON WITH THEORY

In order to sensibly interpret the results from the transmissometer it is necessary to conduct a theoretical exercise into the effects of scattering on the propagation of radiation in the atmosphere. This involves the use of the computation of the extinction due to scattering for a range of atmospheric aerosol models.

4.1. Mie Scattering

The complete description of the scattering of electro-magnetic radiation by a single particle is given by the Mie theory (Mie 1908). However, the rigorous theory is inconvenient to use and expensive in computer time and for the purpose of this study an approximation formula has been used (Van de Hulst 1957). This is valid over a restricted range of refractive indices close to unity but is extended in range and accuracy by an empirical correction formula (Diermndjian 1969). For refractive indices in the range 1.0 - 1.50 with an imaginary (absorbing component) part up to 0.25 the corrected approximation is within 4% of the exact formulation. It is therefore perfectly satisfactory for computations on the scattering of visible and infra-red radiation by the atmospheric aerosol.

4.2. Aerosol Size Distribution

In dealing with the real atmosphere it is necessary to make some simplifying assumptions regarding the nature of the atmospheric aerosol. The simplest possible assumption will be used unless it is subsequently shown to be inadequate. The model chosen for this study is therefore an aerosol consisting of a suspension of spherical water droplets with a size distribution described by a gamma function distribution (Zuev 1970)

$$f(a) = \frac{1}{\Gamma(\mu+1)} \left(\frac{a}{r} \right)^\mu e^{-a/r} \quad \dots \dots \dots (1)$$

where a = particle radius
 r = most probable radius
 μ = width parameter

and the expression is normalised to unit particle concentration. At large radii this distribution becomes identical with the familiar Junge power law. It is one of the family of distributions chosen by Diermndjian as a model for haze and cloud. It is also mathematically convenient to use as it may be readily integrated

to give the total liquid water content from

$$q = \frac{4}{3} \pi \int_0^{\infty} a^3 r(a) da \quad \dots\dots\dots(11)$$

$$= \frac{4}{3} \pi \sum_{\mu} \frac{a^3}{\mu^3} (\mu+1) (\mu+2) (\mu+3) \quad \dots\dots\dots(111)$$

in units of volume per unit volume of aerosol per unit particle concentration.

4.3. Computation of Extinction Coefficient

The extinction coefficient for any wavelength in the model atmosphere may be calculated by integrating the loss due to scattering and absorption by a single particle over the size distribution of the atmospheric polydispersion.

$$\sigma_{\text{ext}} = N \int_0^{\infty} \pi a^2 f_{\text{ext}}(a, m) r(a) da \quad \dots\dots\dots(1v)$$

where N = total number of particles per unit volume

and $f_{\text{ext}}(a, m)$ = efficiency factor for extinction for a single particle of radius 'a' and refractive index 'm'.

This expression has been evaluated by numerical integration for a wide range of values of the parameters of the distribution function for all the wavelengths of interest. The results have been presented in the form of a plot of the attenuation coefficient versus modal radius for various values of μ and refractive index. It is found that varying the refractive index or the width parameter has relatively little effect compared to variations in the value of r . Figure 2 shows the theoretical attenuation at 1.06 μm and 10.6 μm normalised to unit liquid water content. From this it may be observed that at 10.6 μm the attenuation is almost directly proportional to the liquid water content being almost independent of the way in which this is distributed. For the present study it is convenient to consider the ratio of attenuations at the two wavelengths and to assume a constant value of 2 for the parameter μ . The ratio of attenuations is then determined only by the modal radius. Using the experimentally determined values of extinction coefficient and with the assumptions made above it is then possible to derive values for r from the ratio of attenuations and hence a value for q the liquid water content from the attenuation of 10.6 μm . A value for N , the particle concentration, may then be calculated. A useful way of presenting the results is to consider a plot of $d10.6$ versus $d1.06$. Figure 3 shows a computed map of $d10.6$ against $d1.06$ indicating the locus of points with constant r and constant N . It may be seen that for small radii ($r < 5 \mu\text{m}$) each point on the plot corresponds to a unique value of N and r . Comparison of figure 3 with a plot of experimental data in the same format therefore gives an immediate insight into trends of particle sizes and numbers.

5. PRELIMINARY EXPERIMENTAL RESULTS

Some results obtained during the month of May from the Farnborough site are presented in the form of a scatter plot of $d10.6$ against $d1.06$ in figure 4. Two distinct trends are immediately apparent from this plot, one indicating modal radii less than $1 \mu\text{m}$ and the other radii greater than $5 \mu\text{m}$ with few points in between. This is typical of all the results obtained to date and the effect may also be seen in a plot of extinction coefficients against time for a fog which occurred in the early hours of 9th May, 1975 shown in figure 5.

It is seen that the attenuation at 1.06 μm and 0.63 μm increased steadily while no change at all was observed at 10.6 μm until a very sharp increase occurred at all three wavelengths taking the extinction coefficients beyond the normal operating range of the transmissometer.

5.1. Interpretation of Results

The interpretation of this in terms of particle sizes is that the aerosol particles apparently grow steadily in size until a critical radius is reached beyond which further growth takes place very rapidly to reach a new equilibrium. These conclusions are substantiated by measurements of drop size distributions made during the progress of a radiation fog (Garland 1973, Roach 1973). During the first phase of the fog the drop size distribution was mono-modal with a predominant drop size below $1 \mu\text{m}$ radius. As the fog developed a second peak around $10 \mu\text{m}$ appeared in the distribution curves. It is these larger droplets that contribute mostly to the liquid water content and to the attenuation at 10.6 μm . It is postulated (Neiburger and Chien 1960) that the small droplets represent hygroscopic particles which have taken up water until they reach equilibrium with the surrounding saturated air and the second peak is made up of particles whose critical supersaturations have been exceeded, resulting in growth limited by the supply of water vapour.

5.2. Correlation of Parameters

One of the aims of the study is to attempt to correlate the attenuations at 1.06 μm and 10.6 μm with standard meteorological parameters. Since the attenuation is largely determined by the nature of the atmospheric aerosol it seems feasible to use the microphysical parameters of the fog as an intermediate step and look for correlations between these and the meteorological data. For particles which are large compared with the wavelength of observation the efficiency factor for scattering oscillates about the value 2.0 and eventually becomes constant for very large radii. Thus provided the droplets are distributed over a reasonably wide range of sizes then we can put $\sigma_{\text{ext}} = 2.0$ in equation (1v) and integrate to obtain $\sigma = 6\pi N r^2 \dots\dots\dots(v)$.

Using the values of N and r derived from the attenuations at $1.06\mu\text{m}$ and $10.6\mu\text{m}$ (after correction for molecular absorption at $10.6\mu\text{m}$), the value of Nr^2 has been plotted against the extinction at $0.63\mu\text{m}$. As may be seen in figure 6 (considering the assumptions made) there is quite good agreement between the experimental points and equation (v). Since it is to be expected that there is a very close correlation between the extinction at $0.63\mu\text{m}$ and the meteorological visibility through the relation $V = 3.0/\delta$ (for 5% contrast limit) this implies that one can derive a value for Nr^2 from a knowledge of the visibility. It then requires one other correlation between N and r or some function of both with for instance relative humidity to enable values of the parameters to be determined separately from the meteorological conditions thus allowing the extinction coefficient at any wavelength in the infra-red to be predicted. Work is currently in progress to attempt to identify such a correlation.

5.3. Statistics of Extinction Coefficients

The other aim of the study is to compare the performance of systems using Nd-YAG laser and a CO_2 laser. With this in mind the data has been presented in the form of a cumulative probability plot. Figure 7 shows the probability of the extinction at the specified wavelength not exceeding a given value. It includes records made from October 1974 to May 1975. One can deduce from this that if it is desired to operate a system over a long path length where extinctions of $< 0.4 \text{ Km}^{-1}$ are significant, then a $1.06\mu\text{m}$ laser would have a greater percentage operating time than a $10.6\mu\text{m}$ system, while for shorter path lengths the $10.6\mu\text{m}$ laser has the advantage. This is due to the residual atmospheric absorption at $10.6\mu\text{m}$ which limits the transmission at this wavelength under clear conditions.

6. CONCLUSIONS

Measurements with a multi-wavelength transmissometer described above and theoretical calculations using an approximation to the Mie scattering formula indicate that there is no unique relation between the attenuation due to scattering at $10.6\mu\text{m}$ and $1.06\mu\text{m}$ or $0.63\mu\text{m}$. The ratio of attenuations at two wavelengths has been used to deduce a value for the modal radius of an assumed drop size distribution and values so obtained are shown to be in good agreement with a theoretical formulation for visibility as a function of the distribution parameters. Over the range of extinction coefficients measured by this transmissometer ($0.6 - 6.0 \text{ Km}^{-1}$) the CO_2 laser had the greatest probability of penetrating a given distance during the winter 74/75.

ACKNOWLEDGEMENT

This work has been carried out under contract to the M.O.D.(P.E.) with R.A.E., acting a technical authority. Special thanks are due to Dr. R. R. Allen and Mr. S. Craig of Space Dept., R.A.E. for technical and practical assistance during the preparation of this paper.

REFERENCES

- DEIRMENDJIAN, D., 1969, "Electromagnetic Scattering on Spherical Polydispersions", Elsevier, p.29-33.
- GARLAND, J.A., BRANSON, J.R. and COX, L.C., 1973, "A Study of the Contribution of Pollution to Visibility in a Radiation Fog". Atmospheric Environment, 7, p.1079-1092.
- KILLICK, D.E. and BATEMAN, D.A., 1972, Proc. Electro-Optics Int. Conf., Brighton, England, p.319.
- MIE, G., 1908, Ann. Phys.(Leips), 25, p.377.
- NEIBURGER, M and CHIEN, C.W., 1960, "Computations of the Growth of Cloud Drops by Condensation using an Electronic Digital Computer", Geophys. Monographs, 5, p.191-209.
- ROACH, W.T., ADAMS, R.J., GARLAND, J.A. and GOLDSMITH, P., 1973, "A Field Study of Radiation Fog", Faraday Symposium of the Chemical Society, No. 7, p.209.
- VAN DE HULST, H.C., 1957, "Light Scattering by Small Particles", Wiley.
- ZUEV, V.E., KABANOV, M.V. and SAVEL'EV, B.A., 1967, Izv. ANad, Nauk, SSSR, Fiz. Atmos.i.Okeana 3, p.724.

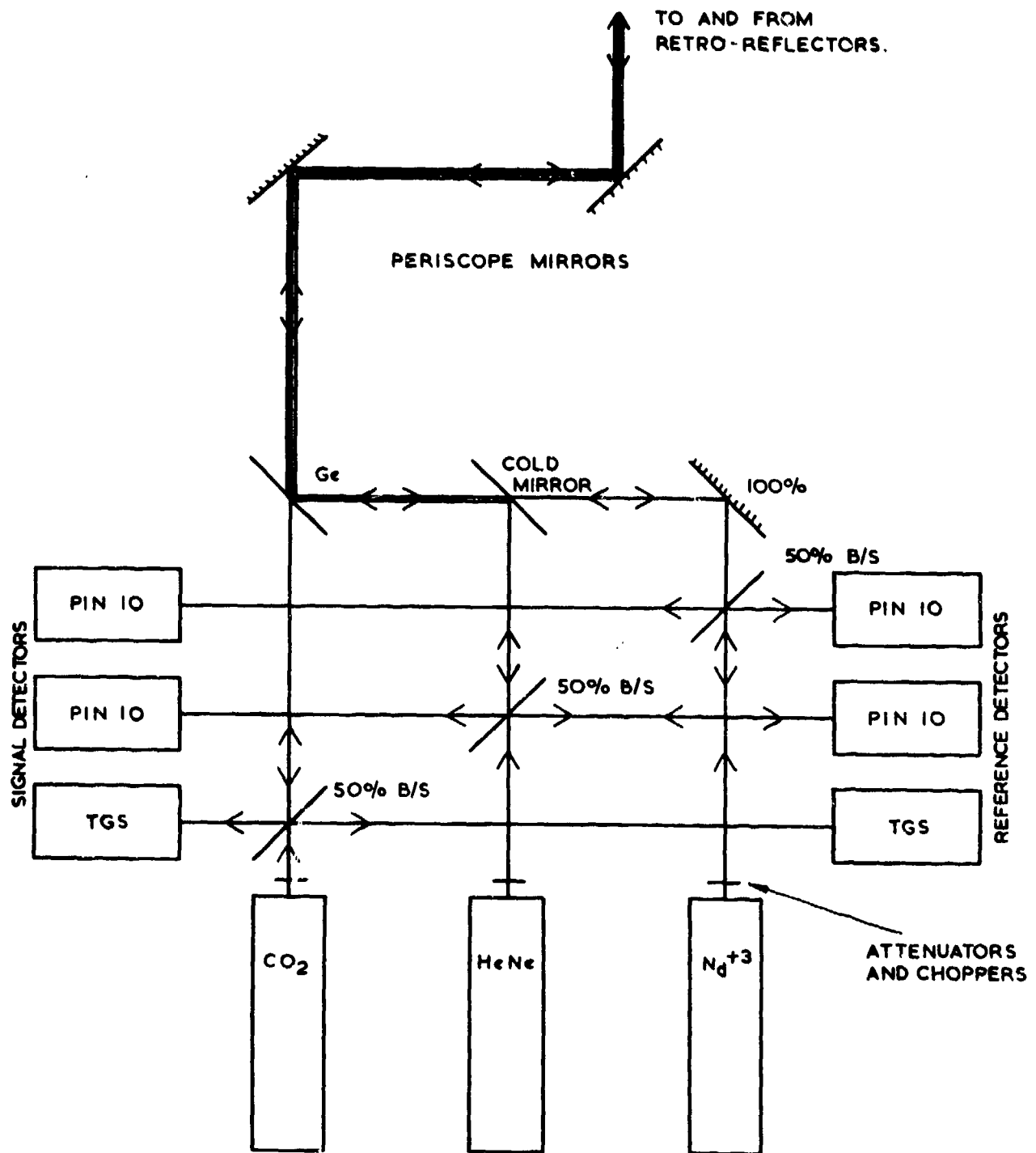


Figure 1. Optical arrangement of transmissometer.

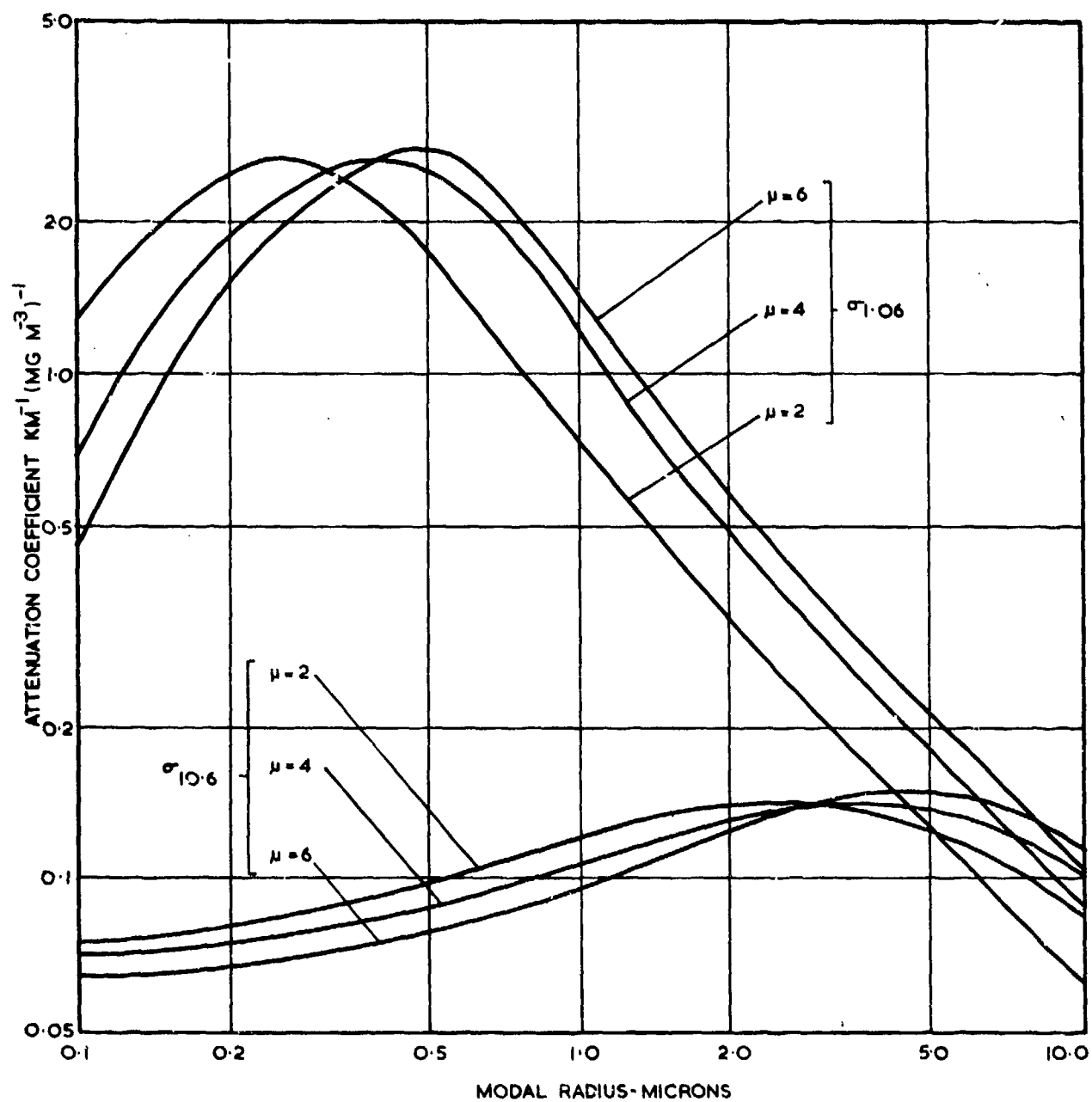


Figure 2. Theoretical attenuation at 1.06 μm and 10.6 μm versus modal radius for unit liquid water content with μ as a parameter.

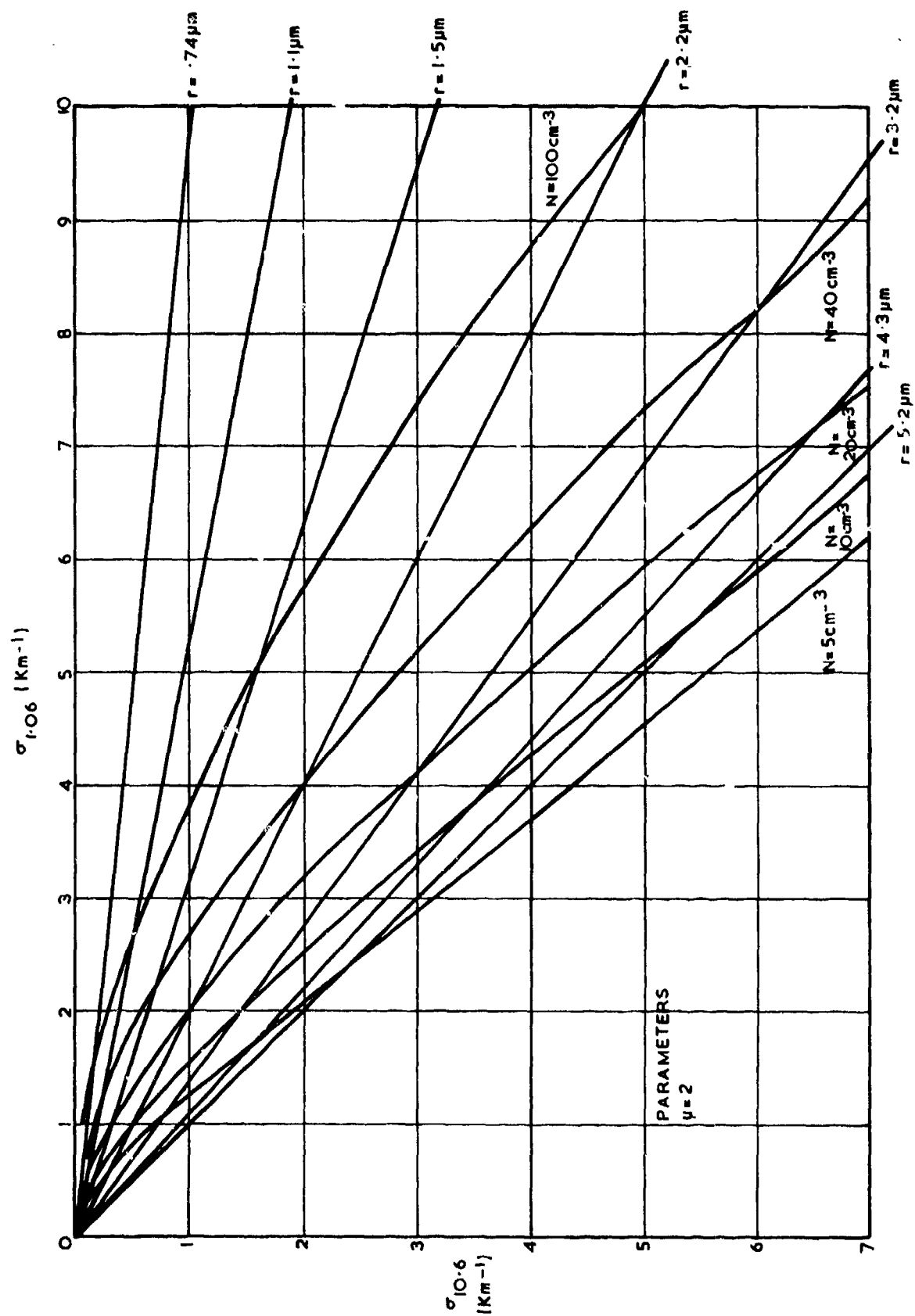


Figure 3. Theoretical attenuation at $10.6 \mu\text{m}$ versus that at $1.06 \mu\text{m}$ for a range of values of N and z .

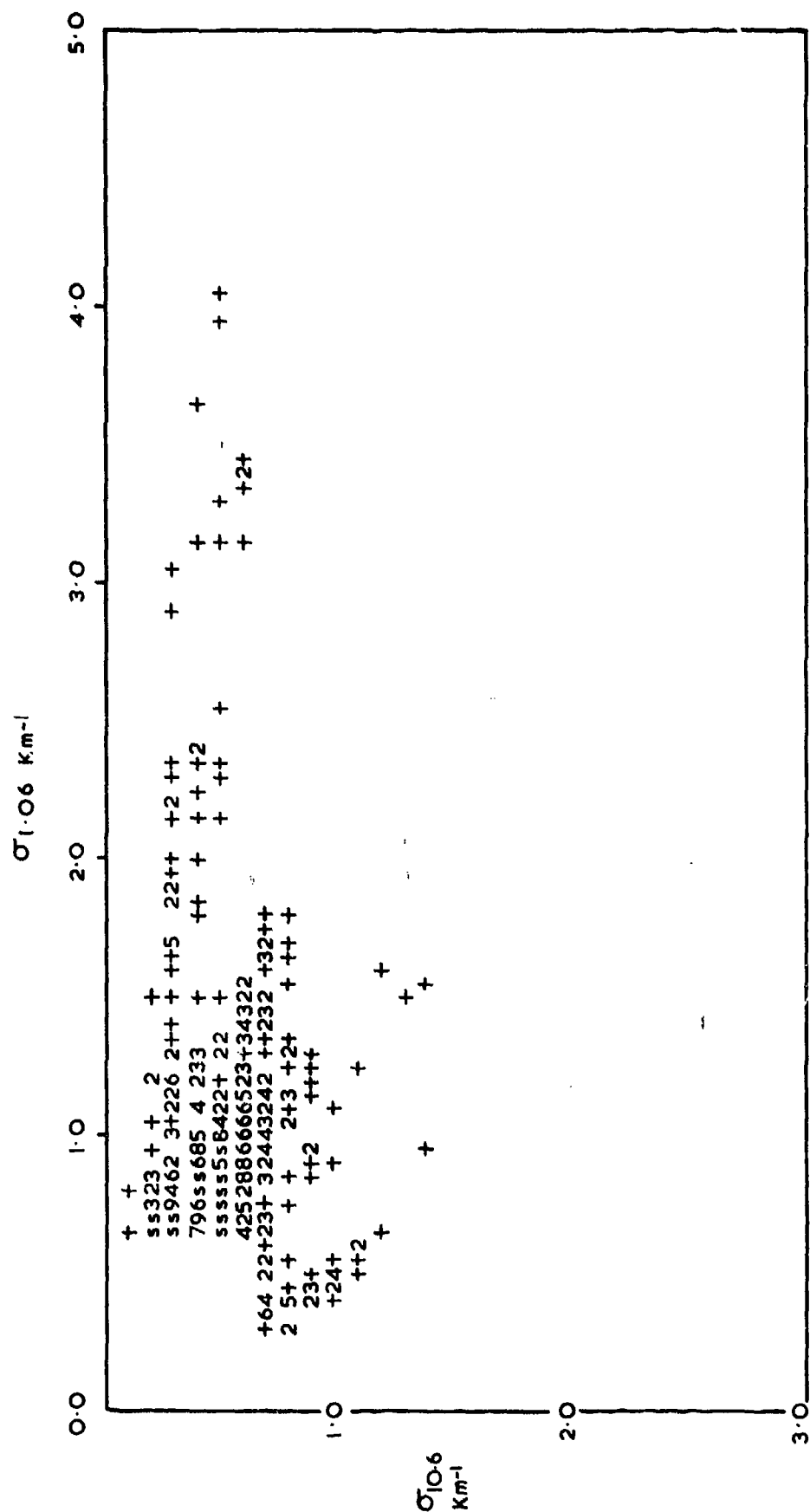


Figure 4. Scatter plot of experimental results for May 1975 of attenuation at 10.6 μm and 1.06 μm .

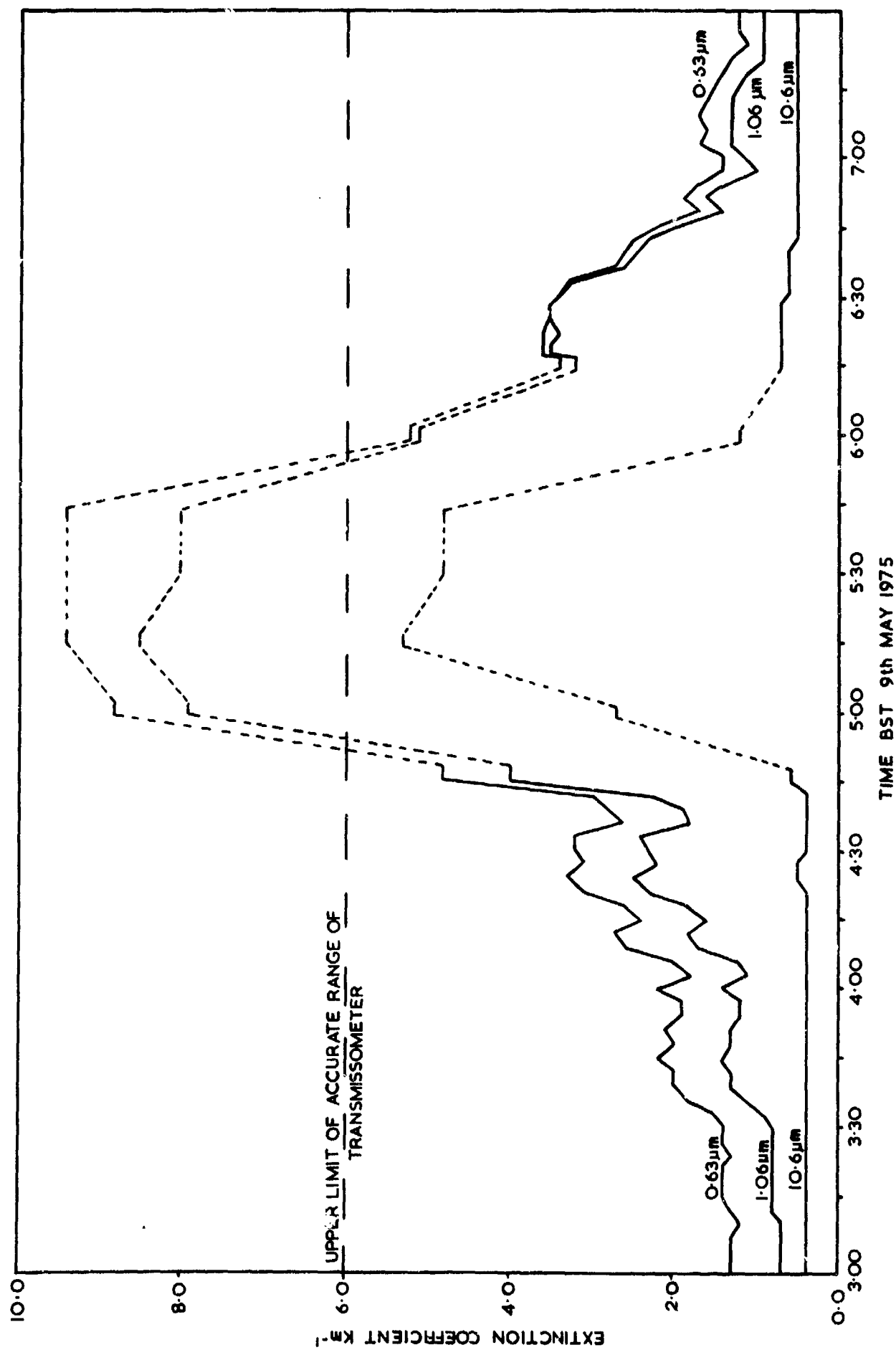


Figure 5. Time plot of attenuations at $0.63 \mu\text{m}$, $1.06 \mu\text{m}$ and $10.6 \mu\text{m}$ for the fog of 9th May, 1975.

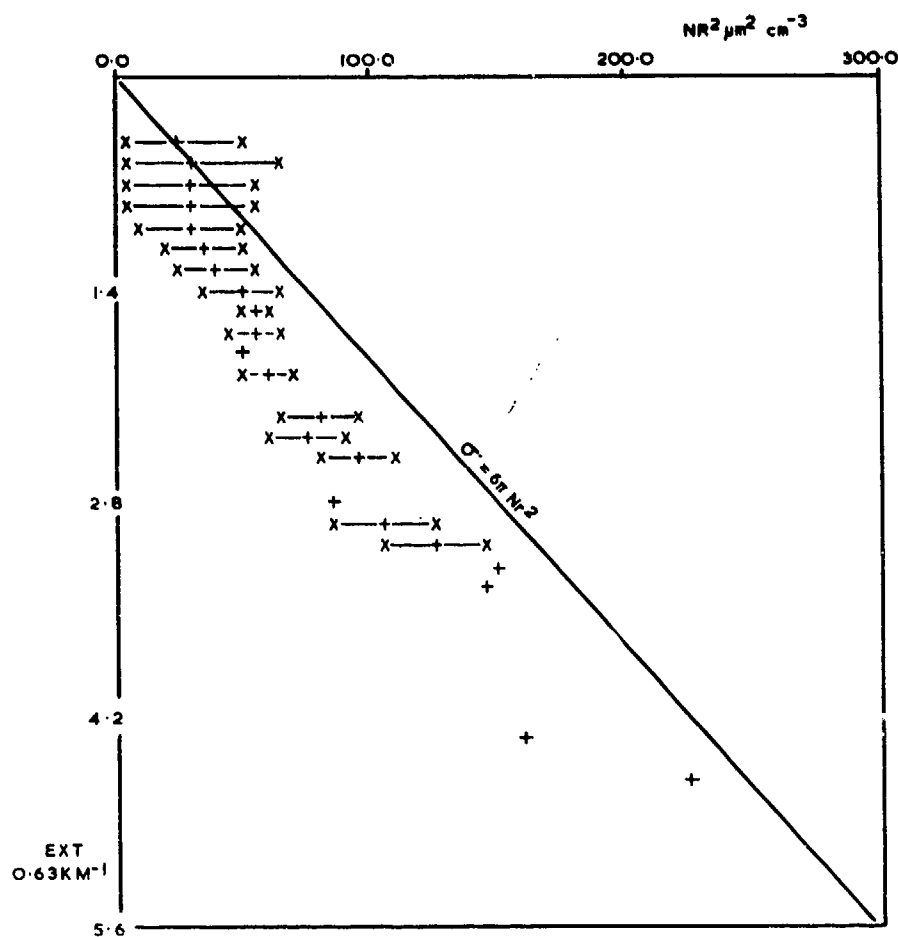


Figure 6. Experimentally determined values of NR^2 plotted against the attenuation at $0.63 \mu\text{m}$.

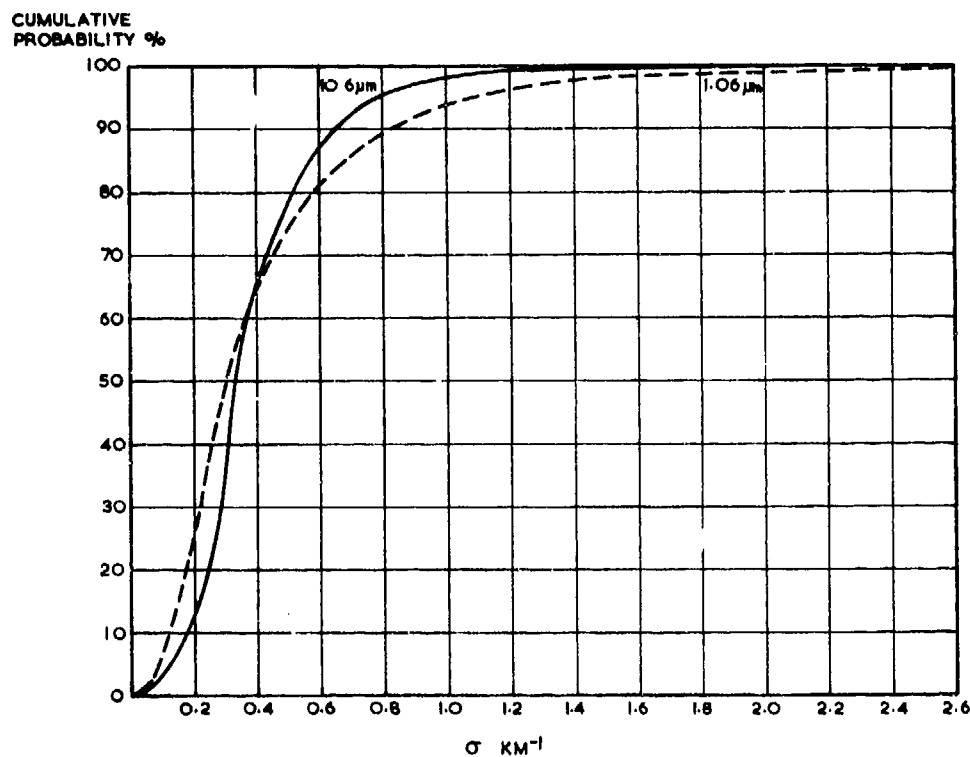


Figure 7. Cumulative probability of the attenuation at $1.06 \mu\text{m}$ and $10.6 \mu\text{m}$ not exceeding a given value for results obtained during October 1974 to May 1975.

REMOTE AEROSOL SENSING WITH AN ABSOLUTE CALIBRATED DOUBLE FREQUENCY LIDAR

R. Reiter, W. Carnuth and M. Littfaß,
Institute for Atmospheric Environmental Research, Garmisch-Partenkirchen, Germany
of the Fraunhofer-Society
and
N.C. Varshneya,
University of Roorkee, India

SUMMARY

A two-frequency (694 and 347 nm wavelength) lidar system, using a Q-switched ruby laser transmitter with frequency doubler and a 52 cm dia. receiving telescope, for remote aerosol sensing up to more than 30 km altitude is described. The system includes electronic data acquisition and processing. Sufficient sensitivity for high altitude stratospheric measurements is provided by ten-channel photon counting combined with range gating of the photomultiplier tube, and a mechanical chopper for rejection of the non-coherent ruby fluorescence. The system is now being absolutely calibrated by comparison between lidar backscatter profiles on the one hand, and theoretical backscatter functions calculated from experimental aerosol and aerological data, using Rayleigh and Mie scattering theories, on the other. The experimental data are acquired at mountain stations at 740, 1800 and 3000 m altitude by means of five-stage impactors and of cable car probes and radiosondes. Examples of tropospheric lidar backscatter profiles, together with aerosol and aerological profiles, as well as stratospheric lidar measurements are presented.

1. INTRODUCTION

For more than 10 years the Institute for Atmospheric Environmental Research of the Fraunhofer Society has been operating a system of 3 geophysical measuring stations in the area of Garmisch-Partenkirchen in the Bavarian Alps. The Institute itself is located at the outskirts of the town at 740 m a.s.l. and serves as valley station. The other 2 stations are located on two neighboring mountain peaks (Wank peak and Zugspitze peak) at 1780 m a.s.l. and 2964 m a.s.l., respectively. The base distance between these two mountain stations is 15 km. The Institute is situated approximately half-way between these mountain stations. Both of the latter are readily accessible by cable car and, during daytime, are manned with one technician, each (REITER, R., 1969a).

At these stations continuous measurements of number concentration and size distribution of aerosol particles are conducted within the scope of several geophysical research programs to study the vertical distribution of atmospheric aerosols. To this end, 5-stage impactors are used for the size range above approximately .2 microns, and Rich type Aitken nuclei counters with diffusion chambers for smaller particles from .01 microns in diameter (CARNUTH, W., 1970, and REITER, R., 1969b). At our Wank peak station we are additionally employing a Royco particle size spectrometer. Furthermore, continuous chemical analyses of aerosol samples have been conducted at Wank peak station, since about 5 years (REITER, R., SLADKOVIC, R., and PÖTZL, K., 1974).

To extend our aerosol measurements to the altitude ranges between the station levels, additional measurements by cable car probes were taken up in 1967. By this means, vertical profiles of aerological (temperature, humidity, wind speed) and atmospheric-electrical parameters (polar electric conductivity and potential gradient) are measured as functions of atmospheric pressure. These data are radioed to the Institute where they are recorded (REITER, R., 1967, 1968).

Electrical conductivity is essentially determined by the concentration of small ions in air. These small ions will diffuse onto aerosol particles and thus lose their mobility. For this reason conductivity is an indirect measure of particle concentration.

Direct acquisition of aerosol data by cable car is limited with regard to weight and power supply of the equipment. For about one year now, a small battery powered General Electric Aitken nucleus counter has been available which may be incorporated into the Zugspitze cable car telemetry system to directly supply profiles of nucleus concentration, but not of size distribution.

Development of the laser-radar (lidar), in recent years, has provided a means of expanding our aerosol measuring program, especially into altitude ranges beyond station levels (Zugspitze peak 3 km). We therefore set ourselves to developing a calibrated lidar system capable of supplying quantitative data on aerosol number concentration and particle size distribution in the stratum extending from a few 100 m up to at least 20 to 30 km.

The mode of operation of the lidar is very similar to the conventional microwave radar: a high-energy laser pulse (usually a Q-switched ruby laser is employed) is emitted

and the light scattered by aerosol particles and air molecules is measured as a function of travel time or distance, and related to output power. Thus a qualitative representation of aerosol distribution along the measured distance is quickly obtained in a simple manner. Determination of quantitative data of aerosol constitution, however, is much more difficult since in an intricate manner the scattering cross section of the particles is a function of a number of parameters, primarily of size or size distribution and refractive index. Theoretically it is entirely impossible to deduce quantitative information on number concentration of the particles from one single frequency lidar return, unless plausible assumptions can be made as to their size distribution, chemical composition, etc.

Additional information on particle size distribution can be obtained by varying either the scattering angle (bistatic lidar, as opposed to monostatic where transmitter and receiver are at the same place, resulting in an invariable scattering angle of 180°) or the transmitter wave length.

The influence of size distribution on angle dependence of scattered-light intensity is a function of the forward scatter as increasing with particle size according to Mie's theory. However, measuring the angle dependence of scattered light by means of bistatic lidar is done quite rarely since it involves considerable experimental difficulties. So, it is altogether impossible, with any justifiable effort to obtain, within a short period, return signals from one and the same volume of air, under varying scattering angles.

Variation of transmitter frequency is much simpler to realize, technologically, either by employing several lasers of different types, or by using frequency doubling. According to Mie's theory of scattering, the scattering cross section is appreciably different from zero only for such particles whose scattering parameter $Q = 2\pi r/\lambda$ (r = particle radius; λ = wave length of laser light used) is at least equal to 1, or whose diameter is greater than or equal to the third part of wave length. Thus the higher the transmitter frequency the smaller the particles that can be identified. This will permit subdividing the size range into several partial intervals, so to speak.

Our lidar system which is described in detail in the following section, works on two wave lengths: (i) that of the ruby laser, 694 nm, and (ii) that obtained by frequency doubling, 347 nm. Early in 1976 a second unit will be available, a mobile one which, in addition to these frequencies, is equipped with a frequency doubled neodymium glass laser with a wave length of 533 nm.

Interpretation of the backscatter profiles measured can theoretically be done by applying Mie's theory. However, because of the intricacy of the Mie scatter functions certain simplifying assumptions must be made, particularly in regard to shape and constitution of the scattering particles. Except for cylinders of infinite length, the functions can be computed strictly only for homogeneous spheres whose refractive index is known, a precondition which in nature is met only in more or less close approximation. The refractive index, aside from physico-chemical composition, is severely dependent upon water contents and thus can likewise be stated only approximately.

In this situation we are able to great advantage to apply our aerosol data, which are available for the lower troposphere up to 3000 m a.s.l., to computing theoretical backscatter profiles, comparing these with the ones measured, and thus experimentally calibrating the unit.

To this end the following individual determinants are available:

- (a) 694 nm and 347 nm lidar returns;
- (b) data on aerosol number concentration and particle size distribution from our 700 m, 1800 m and 3000 m station levels, plus vertical profiles of Aitken nucleus concentration from the entire range between 700 m and 3000 m a.s.l.;
- (c) vertical profiles of temperature and humidity, measured by our own radiosondes.

An essential precondition to these investigations of course is a calibration of the lidar system as such, strictly from a point of view of measuring techniques, i.e. both the laser energy emitted and the incident scattered-light power, must be known, from time to time, at least up to a constant factor. For details in this respect see below.

2. DESCRIPTION OF THE LIDAR SYSTEM

Arrangement of system and working mode are briefly explained by Fig. 1, representing the mechanical layout, and by the block diagram, Fig. 2, showing the electronics in detail, as follows. The Q-switch ruby laser (1) (Q-switch by Kerr cell or Pockels cell (5)) is mounted horizontally on a solid frame in a penthouse structure on our Institute building. Its maximum output is 2 joules corresponding to 100 MW at a pulse duration of 20 ns, its total beam divergence 3 mrad. Power for the flash lamp is taken from a 782 mfd capacitor. The charging voltage is adjustable between 1.0 kV and 3.2 kV and is regulated to exactly 1%. Charging time is just a few tenths of a second, thus a

The receiver unit is mounted vertically in a waterproof case (19) which is rigidly installed in the open on the platform of the building. For reasons of economy and safety, a swivelling arrangement was dispensed with. The signals are received by a Cassegrain telescope (16) of astronomical quality, its primary reflector (17) diameter 52 cm, focal length 380 cm. In the secondary focus we find, in sequence, an iris diaphragm (21), an optical shutter (22), a neutral wedge (23), a filter turret (24) with interference filters for the two wave lengths used, and a collimating lens (28). Shutter, neutral wedge, and filter turret are remote controlled. Below the lens (28) there is the photomultiplier tube (25), type EMI 9816, with S20 cathode, in a commercial cooling box. In front of it a polarization filter (29) may be inserted to measure polarization. Furthermore a coil (31) is installed in the cooling box, by means of which, via a special control unit (33), amplification of the photomultiplier tube is achieved, increasing with the square of transit time.

Above the secondary reflector (18) of the telescope a carriage (14) moved by a servo-motor is installed, upon which a KDP frequency doubler, and one 45 deg. mirror for each of the two transmitter frequencies, are adjustably mounted. Through an aperture in the wall of the building the laser beam, inside the receiver case, will hit either the one mirror directly, or the second one after passing the doubler and will be directed vertically.

The receiver case is thermostated and covered on top by a tilted quartz glass plate, in the center of which a horizontal window (20) is found, also of quartz glass. Through the latter the laser beam will exit upward.

Via a glass fiber cable (35) and appropriate filters, part of the light reflected back from the exit window, will be received by one photodiode (34) for each of the two frequencies. The signals delivered by these diodes are digitized by an AD converter and will provide a measure of transmitter power output. A calorimeter (37) can be installed above the exit window (20) for absolute calibration of the diodes.

The backscatter signals received by the photomultiplier tube are processed analogously if of sufficient intensity. To this end they are fed, via a fast gain-switching amplifier (43) for reducing of count range into a Biomation 8100 transient recorder (39) where they are stored in digitized form.

With an amplitude resolution of 8 bit the recorder has a storage capacity of 2048 words and maximum sampling rate of 100 MHz. For further processing in the computer the stored data are output on punch tape (42).

Due to increasing resolution into single photon pulses very weak signals from high altitudes cannot be analog-recorded. For this situation a ten-channel photon counter with a resolution of 200 MHz and range gating facility is available. The ten channels are gated after an adjustable delay time for time intervals which are presettable, too, and which in turn correspond to defined altitude levels. By changing certain single potentials at the dynode chain the PMT normally blocked is simultaneously triggered. This device termed range gating facility prevents overloading of the PMT by intensive short-range signals and can also be of great advantage with analog measurements.

Accurate recording of weak signals from high altitudes requires additional suppression of the relatively long lasting incoherent ruby fluorescence which, acting as an interference in case of strong backscatter from very short range, could superpose the measuring signal. In addition a mechanical chopper (45) is available blocking the beam path completely after 137 μ sec which corresponds to an altitude of 21 km. An appropriate electronic control with optical sensors ensures exact synchronization of chopper passage and Q-switch triggering.

3. THEORETICAL BASIS

In evaluating lidar signals, i.e. in deducing desired aerosol parameters from measured data, a number of theoretico-mathematical problems are encountered which are outlined as follows.

The light power backscattered from an air volume located at distance R from the receiver, and entering the receiver, is proportional to the intensity of illumination at this point, at the effective receiver surface as well as inversely proportional to the square of distance. Furthermore it is proportional to the backscatter cross section consisting of a molecular component (Rayleigh scattering) and an aerosol component (Mie scattering). The latter is the desired measured value. Finally it must be considered that the emitted laser light as well as the backscattered light are more or less considerably weakened by extinction. And again it is the scattering of air molecules and aerosol particles which predominantly contributes to extinction; the rest can be ascribed to particle absorption and possibly, in the case of wave lengths below 400 nm, to fluorescence excitation. The interrelations outlined can be represented by the so-called lidar equation, as follows:

$$P(\lambda)/E(\lambda) = c \left[\rho_M(\lambda) + \rho_A(\lambda) \right] (2R^2)^{-1} \exp \left[-2 \int_0^R [\alpha_M(r, \lambda) + \alpha_A(r, \lambda)] dr \right]$$

wherein

λ	=	transmitter wavelength (694 or 347 nm)
R	=	distance between receiver and scattering volume considered
E	=	output laser pulse energy (Joules)
P	=	power flux incident on the receiver (Watts/m ²)
c	=	velocity of light
B_M	=	molecular backscatter function
B_A	=	aerosol backscatter function
Q_M	=	molecular volume scattering coefficient
Q_A	=	aerosol volume scattering coefficient

To determine the wanted aerosol backscatter coefficient the relation P/E for both wavelengths must first be known. This calls for calibration of transmitter and receiver in terms of measuring technique. Absolute measuring of transmitter pulse energy by calorimeter and photodiode is relatively simple. By contrast, due to the great number of ingoing parameters (effective transmitter surface, permeability of optical parts, quantum efficiency of photocathode) sufficiently accurate measurement of $P(R, \lambda)$, i.e. determination of the constant K in the proportionality $i(R, \lambda) = K(\lambda, V)$, $P(R, \lambda)$, V = PMT high voltage, existing between P and the PMT output current $i(R, \lambda)$ is possible only by attaining and evaluating returned signals from an atmosphere of known backscattering properties. Air masses with a minimum aerosol number concentration and a correspondingly predominant Rayleigh scattering, are the most suitable for this purpose. Due to the advantageous location of our observing station in an alpine valley far away from large settlements or industrial areas such atmospheric conditions are not infrequent, especially in winter. Since the vertical profiles of temperature and humidity only are required, the Rayleigh scattering can theoretically be computed with considerably greater reliability than the Mie scattering. These vertical profiles can from time to time be determined by our own Rawinsonde. Suitable weather situations can be selected with advantage by using our aerosol data measured at our stations as well as by cable car probes.

Once the system constant is found by calibration measurements, and thus the ratio P/E in the lidar equation is known, the next problem would be the computation of aerosol backscattering function $B_A(R, \lambda)$ from the lidar signals continuously obtained. The problem is complicated by the fact that in the extinction term, aerosol constitution enters into the lidar equation a second time in the form of $Q(r, \lambda)$ and not only with its value at the point of measurement ($r = R$) but with that along the entire distance between point of measurements and receiver.

In order to solve this problem a method of calculation has been developed where the atmosphere is from time to time appropriately subdivided into horizontal layers. In this manner the lidar equation may be evaluated by increments, starting from $R = 0$. Altitude profiles of the variable $B = PR^2/E$ which are calculated and plotted from the measured data by means of computer, are used as a basis particularly for selecting altitude steps. For our computations it was necessary to recalculate and tabulate the very intricate Mie scattering functions for a number of values of the complex refractive index and for several particle size distributions, for which no tables were as yet available in literature.

The refractive index is a function of chemical particle composition, and among other things very sensitive on water content of the particles and hence on air humidity. Hence, relative humidity is to be considered in computing theoretical scattering functions. Comprehensive studies have been conducted by HÄNEL (1968, 1971, 1972) concerning the relationship between relative humidity, on the one hand, and water content and refractive index of the particles, on the other, the results of which were used in our calculations. According to this, particles will absorb practically no water below 70% humidity; above this value, depending on chemical composition, absorption is more or less considerable, especially as saturation is approached.

Since lidar data up to now are available in two wavelengths only, a 2-parameter model must be assumed for size distribution of aerosol particles. As suggested by our impactor data as well as the findings of other authors we chose a so-called bimodal distribution, consisting of two log normal distributions ("coarse" and "fine" particles) of a constant half-band width and position of maxima but variable heights adjusted to respective measured data. A schematic flow chart of the calibration procedure is represented in the block diagram, Fig. 3. Practical evaluation examples are found in Part 4.2.

4. OPERATING EXAMPLES

4.1. Empirical Comparisons of Lidar Backscatter Profiles with Cable Car Sonde Data

A few examples of empiric comparisons between lidar backscatter profiles, on the one hand, and vertical profiles of Aitken

nuclei number concentration, on the other, are presented below, see Figs. 4 through 8.

In detail, the following parameters are measured by cable car sondes:

- (a) Temperature (T),
- (b) Wet-bulb or psychrometer temperature (T'). This is the temperature of a ventilated, wet-tissue covered thermistor. It is the more below air temperature T, the drier the air, thus providing a measure of relative humidity. Both temperature scales rise to the left.
- (c) Polar electric conductivities λ_+ , λ_- . As mentioned above, as a result of aerosol particles capturing small ions, conductivity will decrease with increasing particle number concentration. Thus, the purer the air, the greater the value of conductivity. Consideration must be given to the fact that high particle concentrations are measured with a lesser accuracy than low ones. Conductivity scales also rise to the left.
- (d) Aitken nuclei number concentration, N. A small Aitken nuclei counter provides total number of all particles per cc, above a limiting value of about $.01 \mu\text{m}$ diameter which is determined by the expansion ratio, but otherwise irrespective of size distribution. Again, the scale rises to the left.

These profiles are compared against our lidar data which are represented by the variable $B = PZ^2/E$ (P = incident radiation power; Z = distance or altitude; E = transmitter pulse energy) in relative units, standardized, however, for each wavelength so as to be comparable among each other. As the lidar equation shows, term B or, respectively B_R for 694 nm wavelength, and B_{UV} for 347 nm, is proportional to the backscattering function, excepting extinction losses. Because of the short measuring distance in this case, extinction is not assumed to have any considerable effect, at least in the red. Unlike all other parameters the B-scale in the graphs rises to the right.

In comparing B to N it must be considered that the backscattering function, unlike nuclei concentration, is a function of particle size distribution, roughly speaking in the form of preference to the large particles. Therefore, exact parallelism of the two parameters is not to be expected.

The profiles shown in Figs. 4 - 8 were recorded 11 June 75 during a weather situation which is very typical of a mountain valley opening into a plain: Due to heating of the mountain slopes by insolation in the hours of the forenoon air will ascend there. The resultant suction will cause air from the fore-plain which is more polluted and frequently also more humid, to be carried up the valley more and more. This process will stop toward the evening and be reversed in the course of the night. The flown-in air is replaced by air of a low aerosol content, flowing down from the slopes.

The Fig. 4 diagram, at 1020 CET, still shows an inversion at 2100 m a.s.l., well defined by temperature increase and humidity decrease, which had developed as a result of nocturnal radiation. Underneath we find, demonstrated by increased lidar backscatter and CN concentration plus decreased conductivity, a largely homogeneous well mixed layer of an aerosol content higher than that found above the inversion. The step in lidar backscatter intensity is more distinct in the red (B_R) than in the ultraviolet (B_{UV}). This situation observed quite frequently may be explained by the considerably higher molecular component of the backscattering function in the short wave range. Closely below the inversion a maximum is found in the B_R -curve, which is absent with the Aitken nuclei. However, it turns up again as minimum in the conductivity profile. This is assumed to be the phenomenon of precondensation. Within the range of the highest relative humidity marked by the shortest distance between T and T', the particles have absorbed water to such an extent that increased backscatter and capture of small ions have resulted. This interpretation is corroborated by the Fig. 5 diagram, which shows the conditions 20 minutes later. At the inversion single cumuli have already developed, one of which was temporarily located at the zenith within the field of view of the receiver at time of the 694 nm lidar measurement causing a correspondingly intensive signal. Conductivities here show a very distinct minimum, while again no increased nuclei concentration is observed. With certainty the minimum of conductivity has been caused by the relatively fast capture of small ions on cloud droplets. Speed of capture of Aitken nuclei on cloud droplets is considerably slower, hence a similar effect is not observed.

Some time later, at 1413, the inversion has disintegrated between 2.1 and 2.2 km a.s.l., due to increasing turbulence. No structure whatsoever is found in lieu of it in any of the profiles. However, by the behavior of CN, λ_+ , B_R and B_{UV} air of high aerosol content having flown in from the foreplain can be detected in the lower layers. At its upper boundary, at 1450 m a.s.l., development of a new inversion has commenced. Different fine structures of CN and B_R may be caused by local conditions, inasmuch as we are here dealing with a dynamic process occurring in the horizontal (the distance between lidar and cable car sites is approximately 10 km).

About an hour later (1503 CET, Fig. 7) readily indicated by the behavior of lidar and cable car data, the upper boundary of the air masses flowing up the valley has ascended to 1550 m a.s.l. and, like the temperature inversion at the same altitude, has become more distinct. Again half an hour later the upper aerosol boundary has arrived at 1750 m

a.s.l. Below, the fine structure of B_p and CN has weakened. An interesting observation is the now existing minimum of particle concentration in the zone of inversion, becoming apparent in the CN and conductivity profiles, and judging from the absence of a corresponding minimum in the B_p profile is apparently limited to the small particles.

4.2. A Calibrated Aerosol Density and Size Distribution Profile Obtained from Backscatter Profiles in Two Frequencies

The example is taken from a series of lidar firings made on February 26, 1975 at 0940 CET. It coincides with

- a radiosonde ascent yielding the Rayleigh scattering profiles,
- data transmission from the Zugspitze cable car telemetry system,
- simultaneous measurements of the aerosol size distribution at the three stations.

Although lidar data were recorded up to a maximum height of 6750 m a.s.l. and radiosonde data are available up to 29 km, the evaluation was limited to a maximum height of 3000 m a.s.l. This is the range where detailed comparison with aerological and aerosol measurements is possible.

This comparison is shown in Fig. 9. The density profiles for fine and coarse aerosol fit fairly well to the particle concentrations derived from the impactor measurements at Wank peak (denoted by W_1 and W_2) and at Zugspitze (denoted by Z_1 and Z_2). The concentration values W_1 , W_2 , Z_1 and Z_2 are obtained by integration of the corresponding log-normal size distributions fitted to the measured size spectra (Figs. 10 a-c).

The calibration was carried out by calculating the system constants for both lidar frequencies in an iterative solution of the lidar equation starting with the known aerosol densities W_1 and W_2 at Wank level and stepping down to the level of the lidar installation in order to eliminate the effect of aerosol extinction. It has to be pointed out that the calibration routine is not yet completely straightforward and automatic. This inconvenience is mainly due to some arbitrariness in the choice of the backscatter signal backgrounds, as can be seen from the density profiles. The absence of fine aerosol data above 2100 m a.s.l. means that in the course of the evaluation routine negative particle concentrations occurred probably due to an overestimation of the 347 nm backscatter signal background. Variation of this parameter would lead to an increase in the number of fine particles and to a simultaneous decrease in the number of coarse particles.

4.3. Examples for High Altitude Lidar Measurements Using Photon Counting Technique

The range gating technique allows the application of much higher PMT voltages during nighttime with no sky background present, without overloading of the tube by the strong short-range signal. The resulting high gain factor is necessary for getting single photon pulses of sufficient amplitude. First measurements performed with range gating revealed the return signal to be too intensive for photon counting even at more than 40 km altitude, if maximum receiver sensitivity is applied, i.e. if the gray wedge is set to its minimum attenuation position. Fig. 11 shows a series of analog signals recorded with the Biomation 8100 using range gating of the PMT. The gate delay, i.e. the time lag between Q-switching and the beginning of the gate interval had been set to successively increasing values of 60, 80, ..., 300 microseconds, corresponding to altitudes of 9 to 45 km above station level (9.75 to 45.75 km above sea level). The length of the gate interval itself was 30 μ sec or 4.5 km. This resulted in a set of overlapping partial signals, which are presented as original strip chart plots in the figure. The surprisingly high signal amplitude, which by far exceeds the time resolution limit of the PMT-photon counter system, clearly shows up in the diagram. This circumstance is very favorable for photon counting, since proper positioning of the gray wedge allows optimizing of the receiver sensitivity, i.e. avoiding both insufficient signal resolution due to poor statistics and piling up of photon peaks, resulting from too high photon count rates.

On August 19, 1975, a series of return signals was recorded using photon counting. The gray wedge had been shifted to a 6% transmissivity position. Again the gate delay was set to 60, 80, ... 300 μ sec and additionally to 400 and 500 μ sec (60.75 and 75.75 km above sea level). The length of the gate interval was 30 μ sec again (3 μ sec per channel). The evaluation of the results showed that, with the ten laser firings per range gate setting, the number of photon counts per channel was still too small for sufficient amplitude resolution. For a proper presentation of the data, therefore, the counts of three adjacent channels (channels No. 2 - 4, 5 - 7, and 8 - 10, respectively) were added, and range-corrected by multiplying with the square of distance. This series of lidar shots was performed two times, with and without using the fluorescence suppression device.

The diagrams Fig. 12a and 12b represent the two backscatter profiles in a semi-logarithmic scale, together with the density profile of the standard atmosphere, which had been fitted to the backscatter profiles at 10 km altitude. The signal Fig. 12a was recorded with, the signal Fig. 12b without using the fluorescence suppression. The lidar backscatter profile quite closely follows the atmospheric density profile up to about 20 km altitude. This is to be expected since, due to the low particle number concentrations at higher altitudes, the molecular part of the backscatter cross section should predominate.

Above 20 km, however, an increasing deviation between the backscatter and molecular density profiles is observed, strongly indicating a superimposed background signal. Since this background is only slightly reduced by the fluorescence suppression device,

as a comparison of Figs. 12a and 12b clearly shows, it is very improbably caused by ruby fluorescence stray light bypassing the chopper. In the future, testing measurements are to be performed to find out the origin of this background. In the case it would turn out to be an overload effect of the PMT cathode due to the strong short-range signal (KENT et al., 1971), it should be possible to eliminate or at least reduce this background by further reducing the receiver sensitivity by means of the gray wedge. Otherwise, if the background is unavoidable at all, it must be subtracted from the backscatter profiles. This should be practicable since it actually doesn't affect very much the signals from the ranges of main interest up to 20 km altitude.

5. CONCLUSIONS AND FUTURE PLANS

The hitherto gained experiences proved the lidar method in general and especially our system to be a powerful tool at least for qualitative aerosol sensing and ranging up to more than 20 km altitude. Quantitative aerosol sensing requires a careful calibration of the system and the knowledge of additional parameters, mainly the size distribution of the particles. The two-frequency method, after calibration by comparison with simultaneously acquired aerological and aerosol data, can be considered as an useful first approach. (In 1976, an additional mobile lidar system will be available, allowing three frequency operation using a second, frequency doubled Neodymium glass laser transmitter with 553 nm wavelength).

In the near future, the main efforts are to be made carrying out more simultaneous lidar and aerosol and aerological measurements under different atmospheric conditions, thus improving and completing the calibration procedure. Then, with the present lidar system, and, later on, with the second mobile unit, continuous measurements are to be performed for studying horizontal and vertical variations in aerosol constitution, aerosol transport processes and processes of local cloud formation and disintegration, and, finally, for a general control of atmospheric pollution up to the lower stratosphere.

6. ACKNOWLEDGMENTS

The authors gratefully appreciate and acknowledge the funding of this research by the European Research Office (ERO) of the United States Army, the Commission of the European Communities, the German Defense Ministry and the German Ministry for Research and Technology.

7. REFERENCES

CARNUTH, W., 1970, "Aerosol Size Distribution at 700, 1800, and 3000 m A.S.L.", J. Geophys. Res. 75, 2999.

HAENEL, G., 1968, "The Real Part of the Mean Complex Refractive Index and the Mean Density of Samples of Atmospheric Aerosol Particles", Tellus XX, 3.

HAENEL, G., 1971, "New Results Concerning the Dependence of Visibility on Relative Humidity and their Significance in a Model for Visibility Forecast", Beiträge zur Physik der Atmosphäre 44, 137.

HAENEL, G., 1972, "Computation of the Extinction of Visible Radiation by Atmospheric Aerosol Particles as a Function of the Relative Humidity, Based upon Measured Properties", J. Aerosol Science 3, 377.

KENT, G.S., SANDLAND, P., and WRIGHT, R.W.H., 1971, "A Second-Generation Laser Radar", J. Appl. Met. 10, 443.

REITER, R., 1967, "Eine Fernübertragungsanlage zur Registrierung aerologischer Daten von Seilbahngondeln", Met. Rundschau 20, 38.

REITER, R., 1968, "Die erweiterte Fernübertragungsanlage zur Registrierung aerologischer Daten von Seilbahngondeln - Aerosolstudien an Inversionen", Met. Rundschau 21, 3.

REITER, R., 1969a, "Die alpinen Observatoriumseinrichtungen der Physikalisch-Bioklimatischen Forschungsstelle Garmisch-Partenkirchen", Met. Rundschau 22, 70.

REITER, R., 1969b, "Effects of Vertical Mixing, Precipitation, Clouds, Airmass Characteristics and Atmospheric Ultraviolet Radiation on the Abundance and Size Distribution of Aitken Nuclei, as Evidenced by Several Years of Recordings at 700 and 1800 m A.S.L.", 7th Conf. on Condensation and Ice Nuclei, Prague-Vienna, proceedings page 355.

REITER, R., SLADKOVIC, R., and PÖTZL, K., 1974, "Eine vierjährige Reihe aerosolchemischer Reinluftuntersuchungen in 1780 m Meereshöhe", Wiss. Mitteilungen des Inst. für Atmosphärische Umweltforschung, 9.

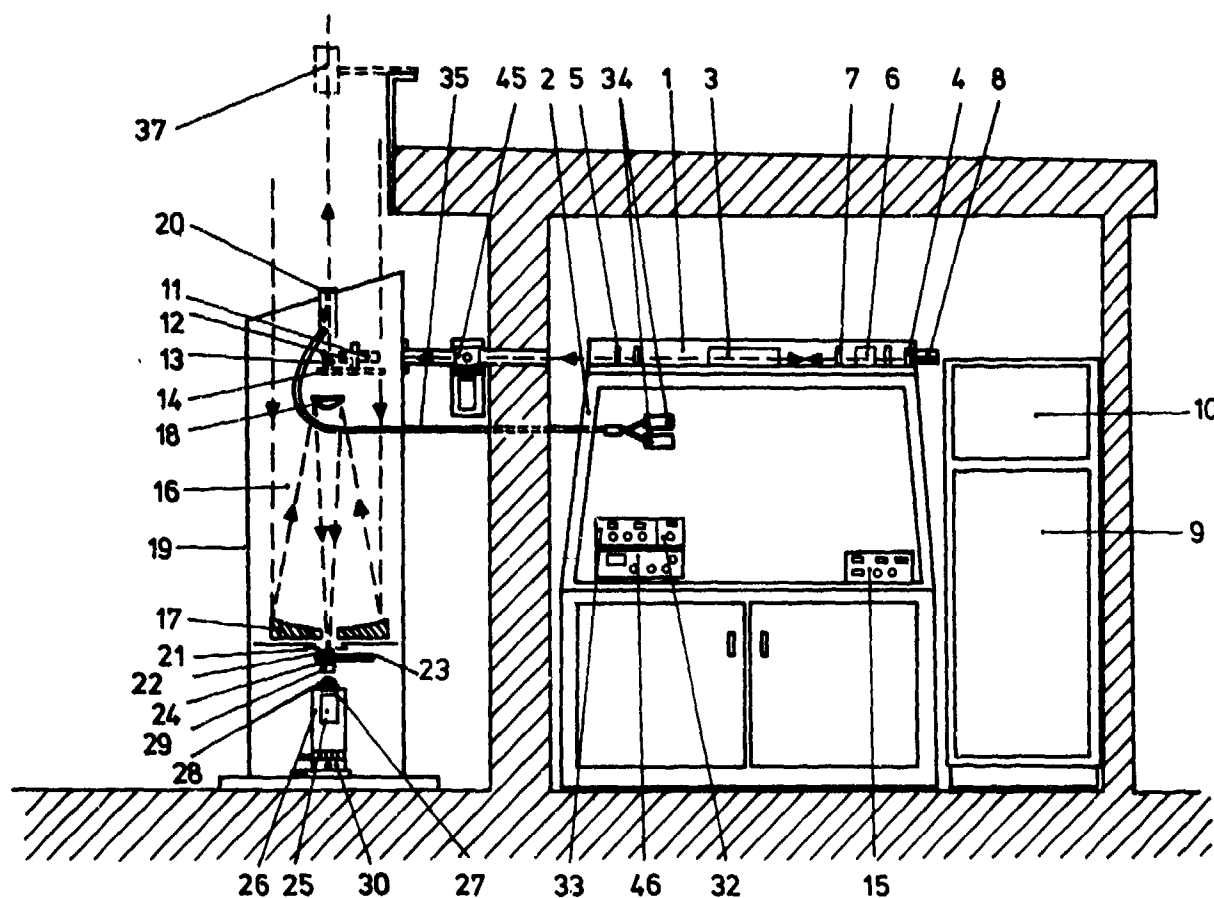


Fig.1 Mechanical layout of the lidar system. Explanations see text

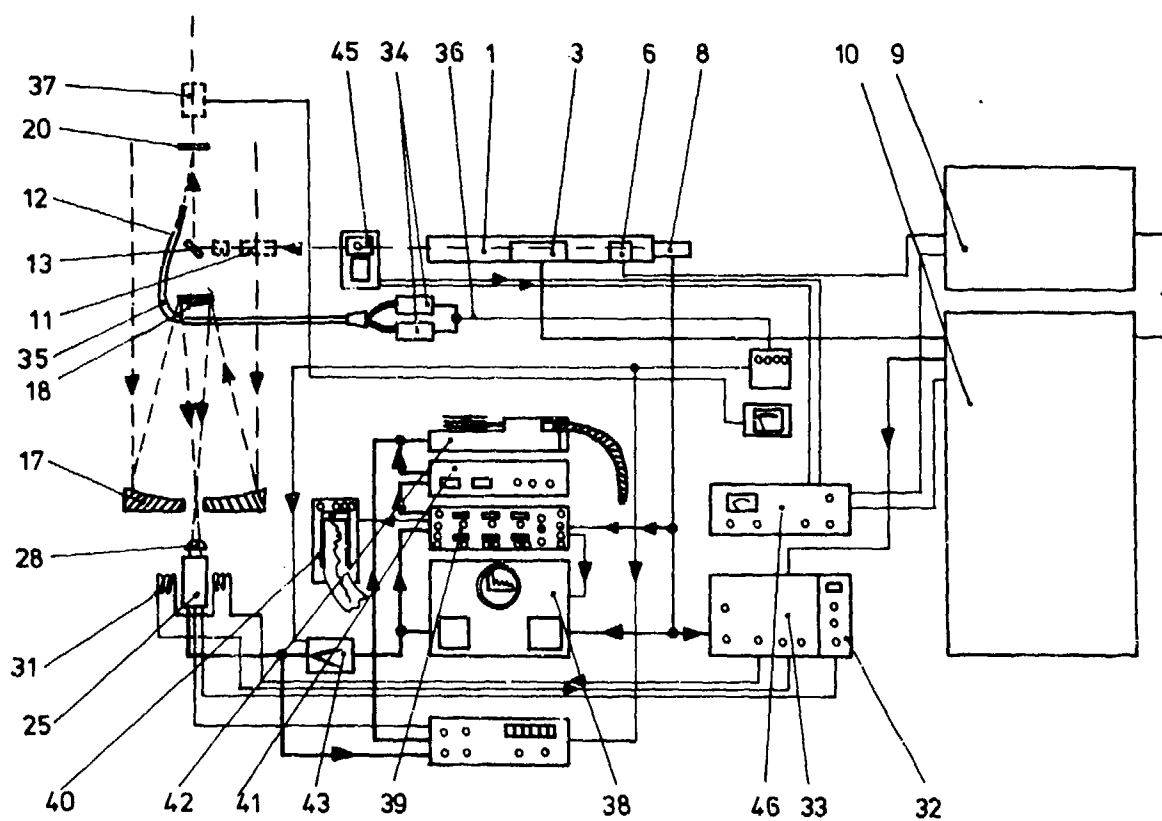


Fig.2 Block diagram of the electronic part of the lidar system

CALIBRATED DOUBLE FREQUENCY LIDAR

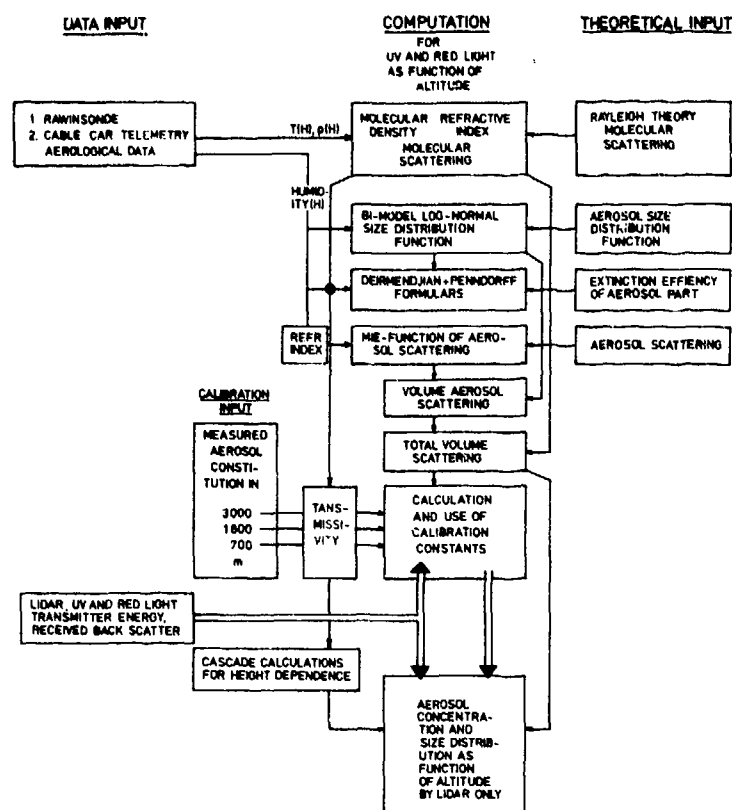


Fig.3 Schematic flow chart of the theoretical calibration procedure

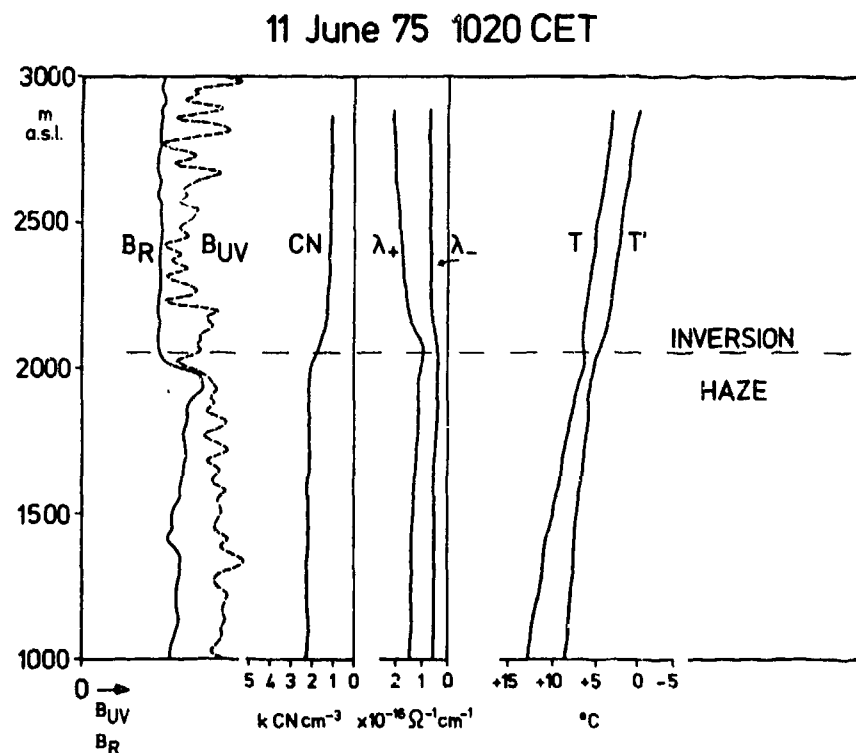


Fig.4 A sequence of 694/347 nm lidar backscatter profiles (B_R , B_{UV}) and simultaneous aerological profiles measured by the cable car sonde. CN = Aitken nuclei number concentration, λ_+ , λ_- = polar electronic conductivities, T = dry temperature, T' = wet temperature

11 June 75 1040 CET

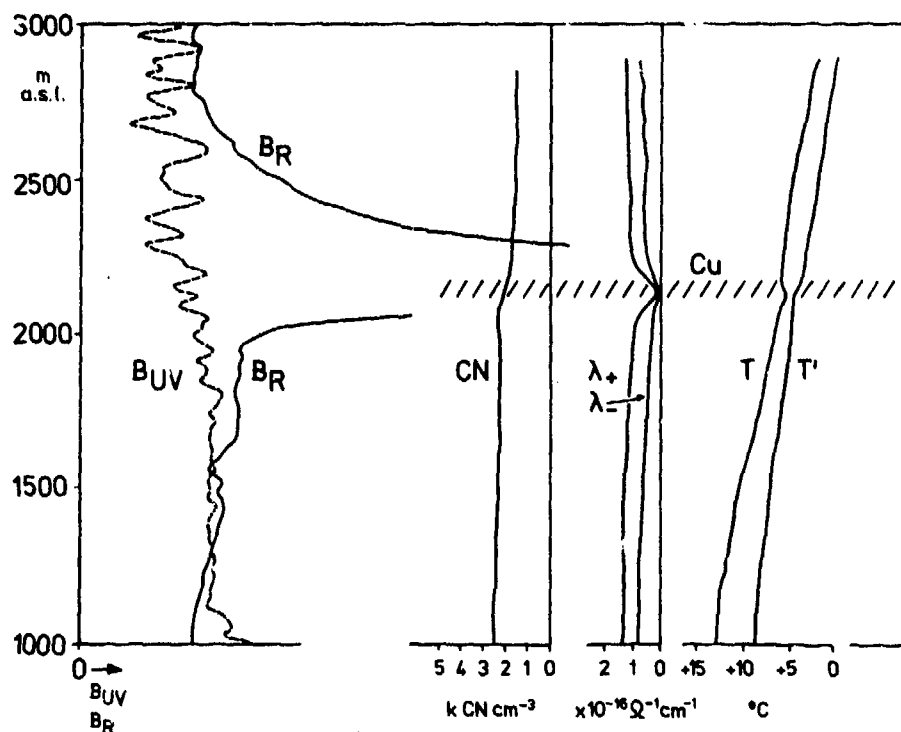


Fig.5 A sequence of 694/347 nm lidar backscatter profiles (B_R , B_{UV}) and simultaneous aerological profiles measured by the cable car sonde. CN = Aitken nuclei number concentration, λ_+ , λ_- = polar electronic conductivities, T = dry temperature, T' = wet temperature

11 June 75 1413 CET

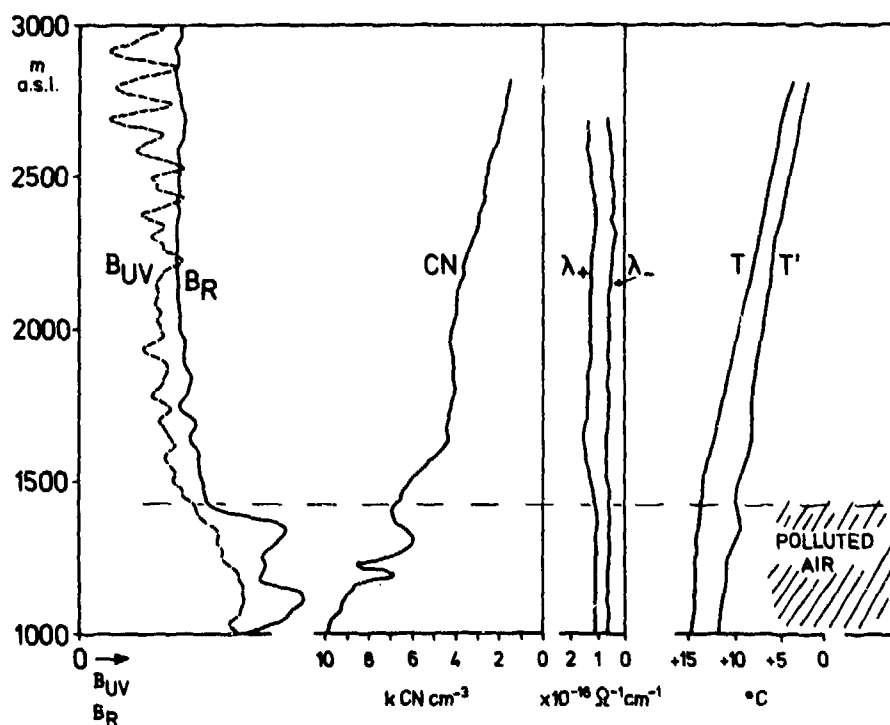


Fig.6 A sequence of 694/347 nm lidar backscatter profiles (B_R , B_{UV}) and simultaneous aerological profiles measured by the cable car sonde. CN = Aitken nuclei number concentration, λ_+ , λ_- = polar electronic conductivities, T = dry temperature, T' = wet temperature

11 June 75 1503 CET

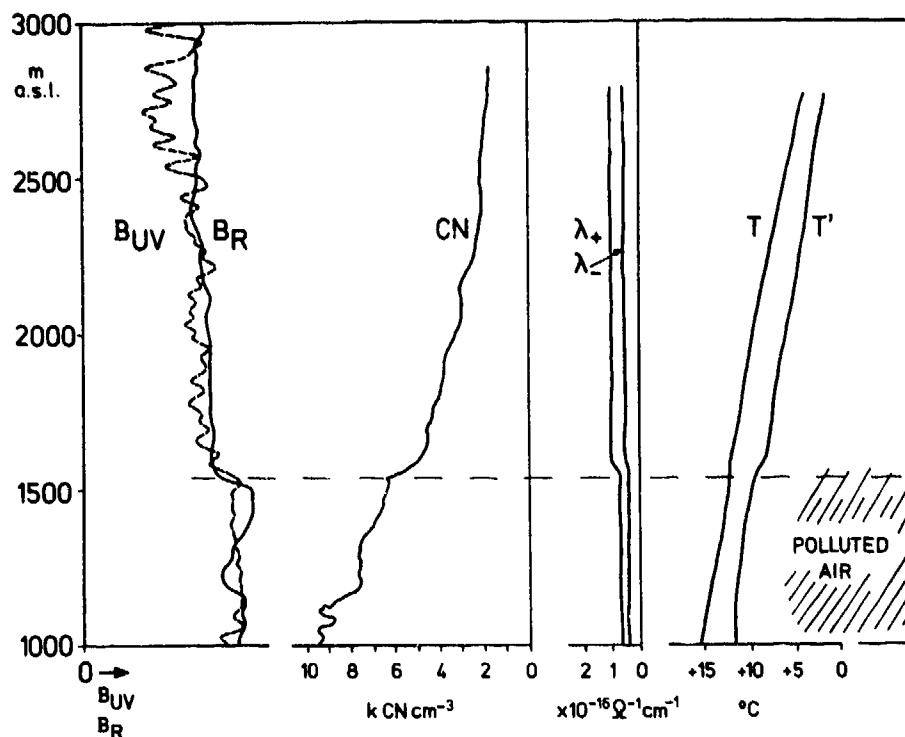


Fig.7 A sequence of 694/347 nm lidar backscatter profiles (B_R , B_{UV}) and simultaneous aerological profiles measured by the cable car sonde. CN = Aitken nuclei number concentration, λ_+ , λ_- = polar electronic conductivities, T = dry temperature, T' = wet temperature

11 June 75 1532 CET

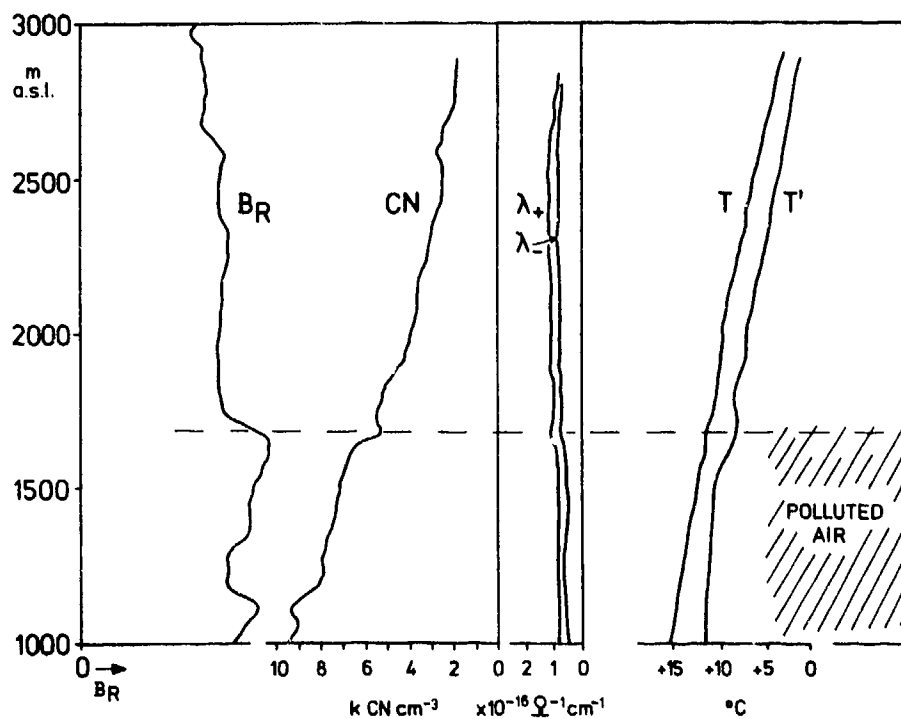


Fig.8 A sequence of 694/347 nm lidar backscatter profiles (B_R , B_{UV}) and simultaneous aerological profiles measured by the cable car sonde. CN = Aitken nuclei number concentration, λ_+ , λ_- = polar electronic conductivities, T = dry temperature, T' = wet temperature

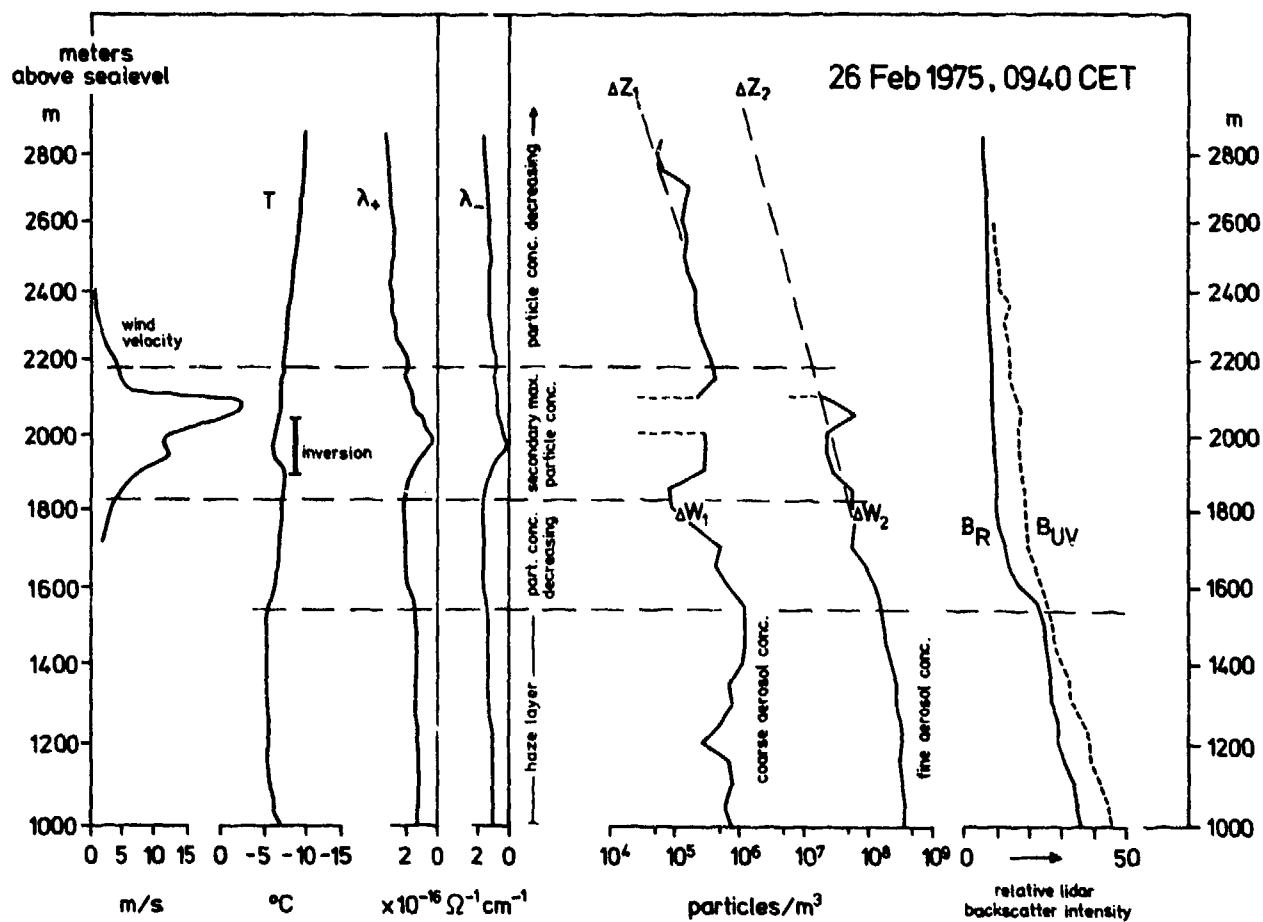


Fig.9 Examples of profiles of coarse and fine aerosol number concentrations, calculated from the red (B_R , 694 nm) and UV (B_{UV} , 347 nm) lidar backscatter profiles. Simultaneous aerological cable car profiles are also presented. W_1, W_2 = impactor measurements of coarse and fine aerosol number concentrations at Wank peak, Z_1, Z_2 = corresponding data from Zugspitze peak

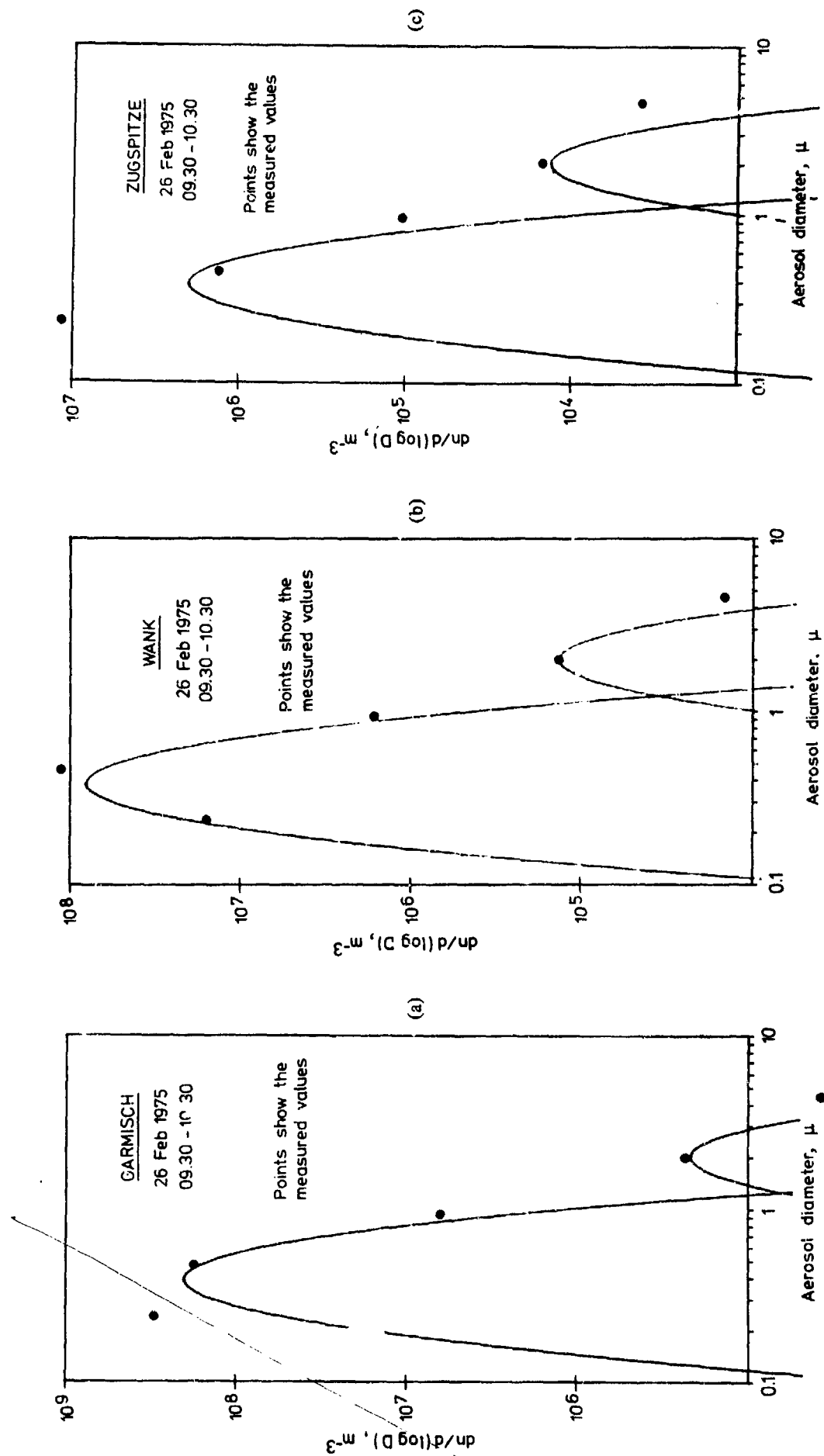


Fig.10 Impactor measurements of aerosol size distribution (points) and fitted bimodal distributions (coarse and fine particles) from the valley station (Garmisch), Wank peak and Zugspitze peak

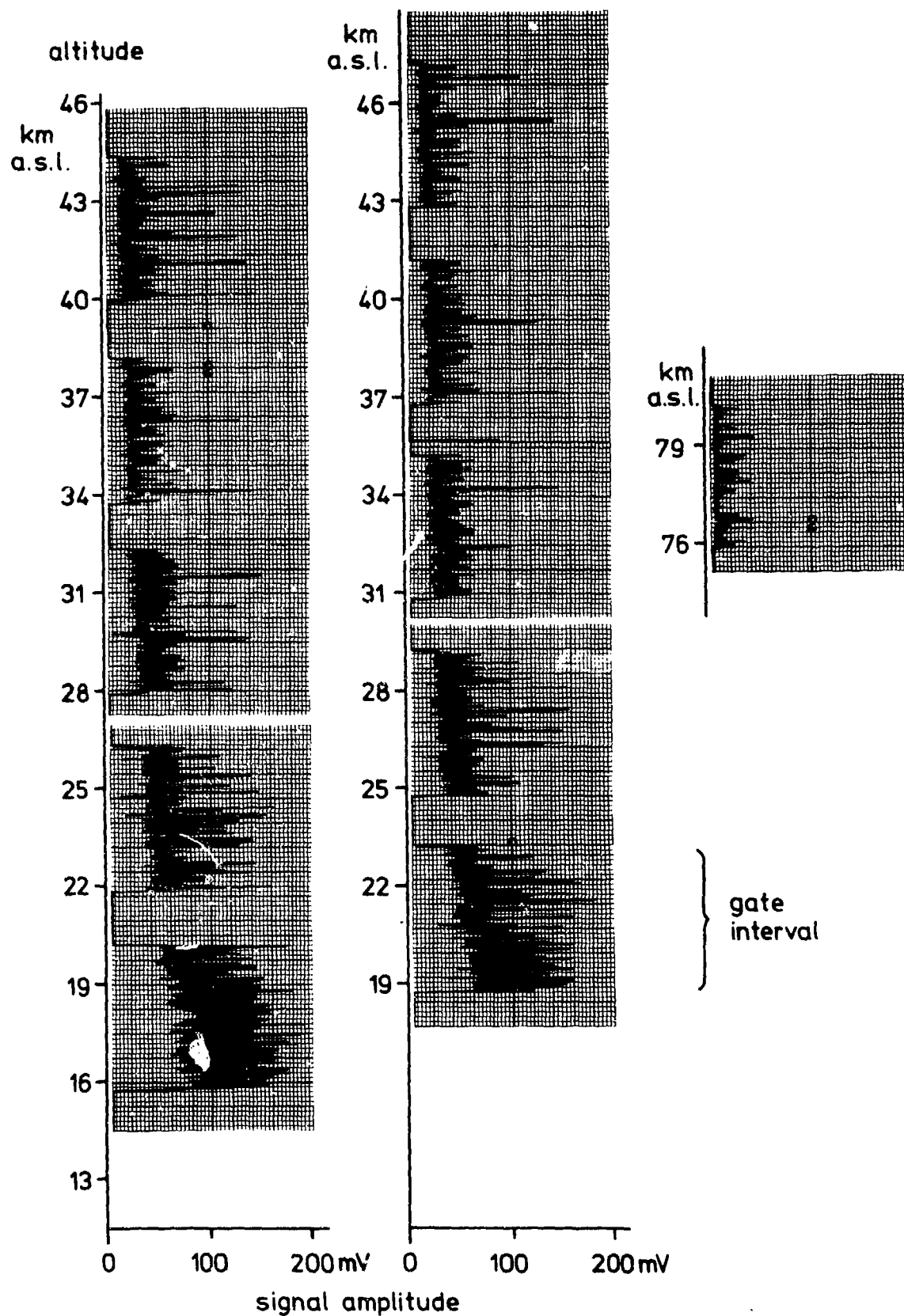


Fig.11 Series of original analog records of night-time high-altitude 694 nm lidar returns

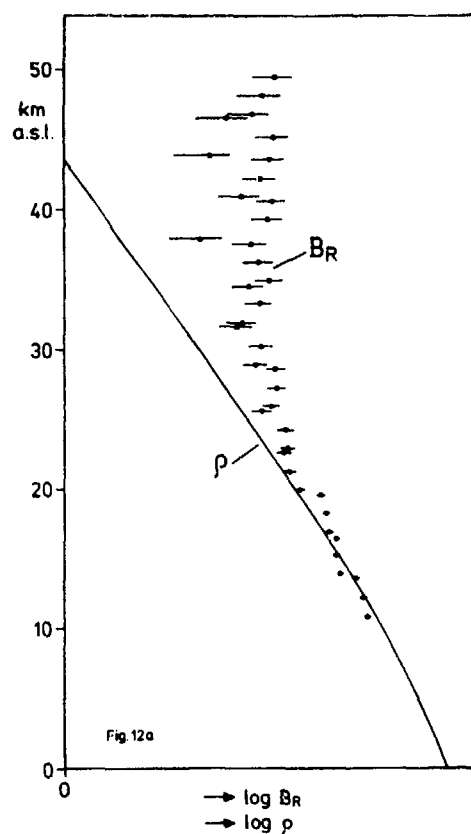


Fig.12(a) B_R = high-altitude 694 nm lidar backscatter profile measured by photon counting, in semi-log scale. Error bars denote standard deviation. Ruby fluorescence rejected. ρ = density of standard atmosphere

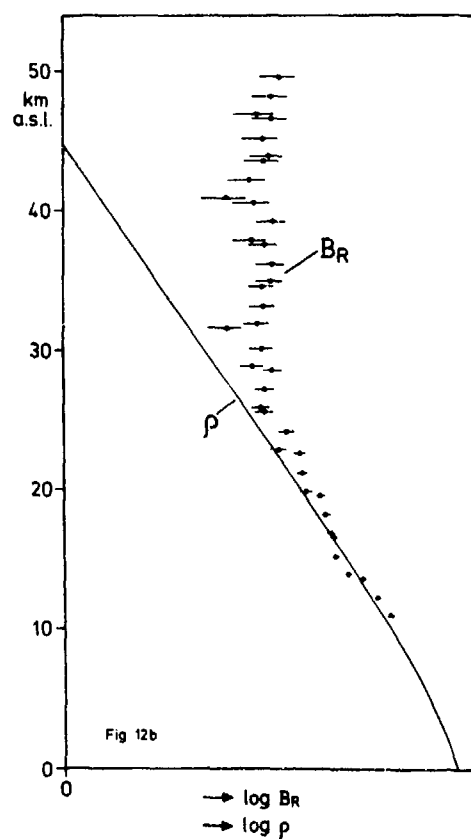


Fig.12(b) Similar measurement as presented in Figure 12(a), ruby fluorescence not rejected

ATMOSPHERIC EFFECTS RELEVANT TO LASER SPECTROSCOPY

T. Lund and A.G. Kjelaas
Norwegian Defence Research Establishment
P.O. Box 25 - N-2007 Kjeller
Norway

SUMMARY

A qualitative discussion pointing out some of the sources of error and fluctuations in a long-path laser differential absorption system measuring the concentration of atmospheric gaseous pollutants, is given. Except for single gas detectors using narrow optical frequency ranges ($<1 \text{ cm}^{-1}$), the unpredictable or unknown spread in the dispersive properties of the extinction caused by continuum absorption and scatter, is of major concern. In addition, the limitations of fast cross-correlation of signals to compensate for turbulence induced fluctuations is discussed.

1. INTRODUCTION

The purpose of this contribution is to discuss the various sources of error and fluctuations limiting the sensitivity of an air pollution monitoring system utilizing differential absorption of laser radiation on a long atmospheric path. In particular we will estimate the effects of a turbulent, humid and scattering atmosphere.

Most common pollutants are simple molecules with a resolved vibration-rotational spectrum even at atmospheric pressures. A system designed for detection of one specific pollutant may take advantage of the well defined narrow ($0.05 - 0.15 \text{ cm}^{-1}$) absorption lines and use a continuously tunable or frequency modulated laser like the semiconductor diode or the high-pressure waveguide molecular laser.

However, in many applications, for instance detection of toxic gases with broad, featureless absorption bands, and in general, in multifrequency approaches to quantitative analysis, one has to deal with comparatively large frequency differences, typically 100 cm^{-1} or more. Moreover, the laser source does not always produce the optimum frequencies or the ones that uniquely matches the peak absorption of the different molecules.

Even if we find a set of laser lines such that line absorption interference may be regarded unimportant, we still have to worry about attenuation caused by particle scatter, turbulence and in some cases, continuum absorption.

These contributions do all have dispersive properties that create interfering signals, and proper compensation requires ability to predict these frequency dependences. This is in general only possible to a certain extent due to lack of complete knowledge of the distribution and the extinction properties of the constituents responsible for the attenuation.

In order to discuss this we choose to consider a particularly simple system with a laser beam propagating one way to a distant receiver. The laser is switched between two preselected optical frequencies, for instance two lines in a CO_2 laser. One of these frequencies is absorbed by the pollutant molecules, the other is not. The magnitude of the selectively absorbed laser power is then used to determine the average concentration of the pollutant. We will not discuss interference caused by line absorption in any other molecule.

The layout is shown in Figure 1. The signal processing incorporates a chopper frequency f and a signal averaging time constant or output filter bandwidth B . The pathlength is l , average pressure P_0 and temperature T_0 . The atmospheric path is further characterized by humidity, aerosol density and size distribution, and by its turbulent state, i.e. the spatial size distribution of temperature eddies and the wind speed.

We will assume that Beer's-law is valid, that is, the laser is always regarded as monochromatic and the partial pressure of the pollutant is low enough to neglect any effect of self-broadening. Since the pollutant concentration is computed from comparative transmission measurements, the primary error contributors are, as stated before, not the amplitude of the extinctions and fluctuations but the differences between contributions at ν_a and ν_b . We will therefore always look for the dispersive properties of the atmospheric effects, and correspondingly, the lack of correlation between fluctuations.

The sensitivity (in such a system) is limited primarily by interference caused by dispersion in the water vapour continuum absorption and the aerosol scatter losses.

Secondarily, false signals may be induced by non-compensated intensity variations caused by turbulence and fluctuations in total amount of water over the path. It may be argued that these can be compensated by fast cross-correlation of the two signals, effectively "freezing" the atmosphere during a single measurement. This is true provided the "frozen" atmosphere is non-dispersive or, in other words, if the amplitudes of the intensity variations are completely correlated at all frequencies.

The final main contributor is detector noise, in particular at low levels of received power. In addition, mechanical stability should be considered when choosing laser beam parameters. The effects of turbulence and detector noise can always be reduced by averaging or decreasing the bandwidth of the output filter, but, thereby reducing the instrument's ability to follow rapid signal changes.

The accuracy of a measurement is also directly related to how precise the specific absorption coefficient of the pollutant is known, and, because of its dependence upon temperature and pressure, a correct estimate of these parameters is necessary.

2. THE SIGNAL EQUATION

The time dependent transmission of a low power laser beam at optical frequencies ν_a and ν_b are,

$$\begin{aligned} T_a &= e^{-(k_a c + \sigma_a)l} \\ T_b &= e^{-\sigma_b l} \end{aligned} \quad (1)$$

k_a - path average molecular absorption coefficient at ν_a ($\text{atm}^{-1} \text{cm}^{-1}$)

c - volume concentration or partial pressure of the gas to be detected (atm)

σ - extinction coefficient due to water vapour continuum absorption and aerosol scatter

The transmission measurements are either done simultaneously or the source is chopped and switched from one frequency to the other. In each case the measured transmission is averaged over a certain time aperture covering some fraction of the chopper period.

The average concentration c is obtained by log-conversion of the ratio of the two transmissions

$$c = \frac{1}{k_a l} (\ln T_b - \ln T_a) - \frac{\Delta\sigma}{k_a} \quad (2)$$

$$\Delta\sigma = \sigma_a - \sigma_b$$

In our system the concentration therefore appears as an a-c signal which may be further processed by a phase-locked amplifier.

3. THE MOLECULAR ABSORPTION COEFFICIENT

The primary source of inaccuracy in concentration is errors in the estimated k_a -value.

Even though significant deviations have been predicted and measured, the absorption lines are, at pressures close to 1 atmosphere, almost exclusively assumed to be Lorentzian in shape.

$$k_a = \frac{S}{\pi\gamma} \cdot \left(\frac{1}{x^2 + 1} \right), \quad x = \frac{\nu_a - \nu_0}{\gamma} \quad (3)$$

where

ν_0 is the center frequency

S is the total line strength, and

γ is the linewidth

The relations for S and γ , valid for certain classes of simple molecules are:

$$S = S_0 \cdot \left(\frac{T}{T_0} \right)^{3/2}, \quad \gamma = \gamma_0 \frac{T}{T_0} \left(\frac{T_0}{T} \right)^{1/2} \quad (4)$$

S_0 and γ_0 are measured at temperature T_0 and pressure P_0 .

k_a may vary along the path due to local pressure and temperature changes

$$\left(\frac{\Delta k_a}{k_a T} \right) = \left(1 + \frac{1}{x^2 + 1} \right) \frac{\Delta T}{T_0} \quad (= \left(\frac{\Delta C}{C} \right)_T) \quad (5)$$

$$\left(\frac{\Delta k_a}{k_a P} \right) = \left(\frac{x^2 - 1}{x^2 + 1} \right) \frac{\Delta P}{P_0} \quad (= \left(\frac{\Delta C}{C} \right)_P) \quad (6)$$

But, since local $\Delta T/T_0$ typically are less than 10^{-3} over short horizontal paths and since the effect of local temperature fluctuations around some average value is to create second order fluctuations in the average k_a -value, no significant error is introduced by replacing k_a with its linear average. Moreover, such local and rapid variations are adiabatic and corresponding pressure changes will partly offset the effect on k_a .

~~Non-adiabatic, however, are deviations from estimated mean values.~~

A system continuously monitoring pollution levels, looking for instance for small daily variations, should therefore have means for accurate temperature and pressure tracking.

In addition, the position of the laser line relative to the peak of the absorption line (x) should be known to a precision comparable to the accuracy of the measurement of mean temperature and pressure.

4. THE WATER VAPOUR CONTINUUM

Uncompensated extinction expressed by $\Delta\sigma/k_a$ (2) adds directly to the concentration. We want to establish quantitative estimates of the various contributions, and we will at this point limit the discussion to the frequency range available with a CO_2 laser. We should keep in mind that the fundamental limitations is not the extinction dispersion itself but the lack of knowledge about or ability to predict the dispersion because of the inherent stochastic nature of its origin.

The water vapour continuum absorption in the 10μ range is at present not completely understood, but some useful experimental data is available. Attempts to fit the measured values in terms of water vapour - and dry air pressure have not been wholly successful. There seems to be a general agreement though that the explanation is one or more of the following:

- 1) extreme wings of strong absorption lines
- 2) pressure induced absorption resulting from transitions that are forbidden in the unperturbed molecule
- 3) possible existence of water dimers

If the continuum results from a combination of completely different and independent mechanisms we are left with a relation that contains more than one coefficient.

The relation found to fit experimental data has the form (McCOY, 1969)

$$\sigma_c = C \cdot p \left(p + \frac{P}{B-1} \right) \quad (7)$$

where C contains the rate of change of water vapour absorption cross section with partial water vapour pressure p . P is the total atmospheric pressure. B can be interpreted as the ratio of the rate of change of absorption cross section with water vapour pressure to the rate of change of absorption cross section with dry air pressure. Experiments have revealed large uncertainties, particularly in B .

This illustrates the need for a new model that may be of the form

$$\sigma = C_s p^2 + C_f p P \quad (8)$$

where C_s and C_f are so far, nonrelated (KELLEY, 1975).

Figure 2 shows a summary of recent outdoor measurements using the 10.6μ P20 line. The solid line is from a better controlled laboratory experiment.

Figure 3 gives the results of some measurements with laser lines selected for minimum line absorption.

From these graphs we obtain an approximate relation for the extinction dispersion in horizontal paths at sea level

$$\frac{\partial \sigma_c}{\partial p} = 9.2 \cdot 10^{-6} p + 2.3 \cdot 10^{-6} p^2 \text{ (km}^{-1}/\text{cm}^{-1}) \quad (9)$$

where p is water vapour pressure in torr.

On hot, humid days the water vapour pressure may be as high as 30 torr.

To keep the signal change less than 1% over a 1 km path the frequency difference $\nu_a - \nu_b$ should be less than 5 cm^{-1} .

The effect of temperature on σ_c has not been established.

5. AEROSOLS

Even a gross estimate of aerosol losses requires extensive knowledge about size and probably also shape distributions. If we include absorption, which seems necessary in the 10μ range, we have to consider composition of the particulate matter as well. Scatter and absorption cross sections, at least for simply shaped particles, can be calculated, given the complex index of refractions, for almost any possible size-distribution; little is known though about the effects of irregular shapes. But, even if we have a complete theoretical apparatus at hand, we are faced with a large volume of real atmosphere, where particle sizes and compositions may vary over a large spectrum, even locally.

We know that equally sized or monodisperse aerosols scatter, according to Mie's theory, as

$$\sigma_s = C \lambda^{-q} \quad (10)$$

where $q = 0$ in the large particle region and $q = 4$ for small particles ($\sim \ll \lambda$).

Various attempts have been made to devise average or expected size distributions and the results are useful in certain wavelength ranges.

Figure 4 shows some theoretical results. Middleton's visibility relation may be extrapolated to $q = 1.3$ for average seeing conditions in the long wavelength range. McClatchey's curve is based on a modified continental haze size distribution model (McCLATCHEY, 1971). Included are also different predictions for mixtures of continental and maritime aerosols. These suggest that the extinction may be described by a λ^{-q} relation and that q at 10μ probably take on values in the 1 to 0.3 range.

The scatter dispersion will determine the amount of interference:

$$\frac{\partial \sigma_s}{\partial \lambda} = -q C \lambda^{-(q+1)} = -q \sigma_s \cdot \frac{1}{\lambda} \quad (11)$$

When the attenuation at 10μ is 20 dB/km typical of average fog density ($\sim 30 \text{ mg/m}^3$), the interference caused by difference in extinction at 9.2 and 10.8μ is

$$0.22 \text{ km}^{-1} \quad \text{for} \quad q = 0.3$$

and

$$0.58 \text{ km}^{-1} \quad \text{for} \quad q = 1$$

If the pollutant gas has a specific absorption of say $10 (\text{atm cm})^{-1}$ the fog creates a signal that could have been due to a concentration of 0.2 to 0.6 ppm. Since the span of possible q 's is wide, it seems that not much can be gained simply by using the average extinction to predict the interference and apply correction measures.

Raindrop size distributions peak at 1 - 3 mm and little dispersion is expected ($r \gg \lambda$) at 10μ even when correction for small angle forward scatter is included.

Figure 5 displays an overview of 10.6μ attenuation due to atmospheric water vapour and aerosols.

6. TURBULENCE

Water interference is range independent. The effects of an uncertainty in the transmission measurements on the derived concentration will in general have a path length dependence (2).

The prime sources of signal current fluctuations are:

- detector noise and
- atmospheric scintillation

Detector noise, which to a large extent determines the choice of an optimum path length, is not directly related to this discussion and will be omitted.

Intensity fluctuations caused by movement of refractive index irregularities in the path can, as argued before, be cancelled by real time correlation provided both laser frequencies experience the same or correlated fluctuations.

Figure 6 taken from a recent paper by MANDICS et al (1974), indicates the effect of frequency separation on the correlation or coherence of the fluctuations.

$k_1 = 2\pi/\lambda_1$, and $k_2 = 2\pi/\lambda_2$ are the wavenumbers of the lower and higher propagating frequencies respectively. The coherence diminishes very rapidly when the normalized frequency Ω exceeds some critical value Ω_c , determined largely by the optical frequency separation.

$$\Omega_c = \frac{2\pi f_c}{V_1} \cdot \sqrt{\frac{L}{k_2}} \quad (12)$$

The critical frequency corresponds to a certain smallest refractive index irregularity in the path. In our case, with a CO_2 laser, ($k_1/k_{2 \text{ min}} = 0.9$) this cut-off size can be of the order of one half of the diameter of the first Fresnel zone, $\sqrt{\lambda L}$. Irregularities smaller than this will produce intensity patterns at the receiver that are non-correlated.

It is generally accepted, however, that the size of the irregularities that most effectively produce scintillation on beam axis at the receiver is, on the major part of the path, just equal to this radius of the Fresnel zone. Smaller irregularities will contribute effectively only if they are close to the receiver or close to the source. Those close to the receiver are responsible for the small scale intensity patterns or the corresponding high frequency components in the fluctuation spectrum. However, these are the components that are most effectively damped by a finite receiver aperture.

If we apply the full frequency range of the CO_2 laser, a major part of the fluctuations will be uncorrelated since the critical size of the irregularity everywhere is larger or equal to the size of the most effective one.

The real implication of this is that signal fluctuations due to turbulence can not be completely compensated by real-time correlation. But we may take advantage of the correlation properties to be able to utilize a lower chopper frequency. This may well be appreciated for instance when thermal and pyro-electric detectors are used.

The coherence is close to unity (but never reaches unity for finite frequency difference) at all frequencies below cut-off while the spectrum of the fluctuations even without any aperture averaging effect drops off by $r^{-8/3}$.

As a rule, one should therefore choose a chopper frequency that comes close to but does not exceed the correlation cut-off frequency. This may present a problem. Since the cut-off frequency f_c scales with the transverse wind speed, ($\Omega_c = V_1/f_c$) measurements up-wind in calm weather favour low chopper frequency or actually long independent averaging time before computation of concentration. If $(k_1/k_2) = 0.9$, f_c is approximately 20 Hz at $V_1 = 1$ m/s. The need for an adjustable chopper speed is of course reduced if beam parameters and receiver aperture size can be chosen such that the remaining uncorrelated part of the fluctuation spectrum is depressed.

An alternative approach is to neglect any possible correlation and apply a high chopper frequency since the temporal power spectrum of the intensity fluctuations diminishes rapidly above a certain frequency determined by the time required for the most effective scatterer to cross the beam axis.

The expected added reduction of the high frequency components by aperture averaging, in particular when the beam is focussed on the receiver, will, except for small optical frequency differences and unique conditions of strong turbulence in clean, dry air, reduce the sensitivity limits well below the level set by the extinction dispersion.

7. CONCLUSION

The sensitivity and accuracy of a long path air pollution monitoring system is limited by a number of factors relating to the physical parameters describing the atmospheric "sample"-path. Most significant in a system utilizing a relatively wide optical frequency range seems to be lack of knowledge about the different contributions to the dispersive properties of the extinction caused by water vapour absorption and aerosol scattering.

A system exclusively detecting a simple molecular specie, thus using a narrow ($\sim 1 \text{ cm}^{-1}$) frequency band, is rather limited by detector noise or scintillation induced by turbulence. A well designed optical system and optimum choice of path length and detector type (cooled or uncooled detector), depends chiefly on the specific requirements to the instrument.

REFERENCES

- GULLBERG, K. et al., "Dämpning av CO_2 -laser strålning i atmosfären, FOA 2 rapport A2542-E3, E4, E6, Sept. 1971.
- KELLEY, P.L. et al., "The molecular contribution to the infrared laser transmittance of the natural atmosphere". Keynote-paper at NATO Expert Conference on laser spectroscopy of the atmosphere, Rjukan, Norway, June 1975 (to be published in Optical and Quantum Electronics, March 1976).
- MANDICS, P.A. et al., "Multifrequency coherences of short term fluctuations of line-of-sight signals - Electromagnetic and acoustic", Radio Science, 9, 8, 723, Aug.-Sept. 1974.
- McCLATCHEY, R.A. et al., "Optical properties of the atmosphere", AFCRL-71-0279, Environmental Research Paper 354, May 1971.
- McCOY, I.H. et al., "Water vapour continuum absorption of carbon dioxide laser radiation near 10μ ", Applied Optics, 8, 7, 1471, July 1969.
- MIDDLETON, W.E.K., "Vision through the atmosphere", University of Toronto Press, Toronto 1952.
- WOODMAN, D.P., "Limitations in using atmospheric models for laser transmission estimates", Applied Optics, 13, 10, 2193, Oct. 1974.

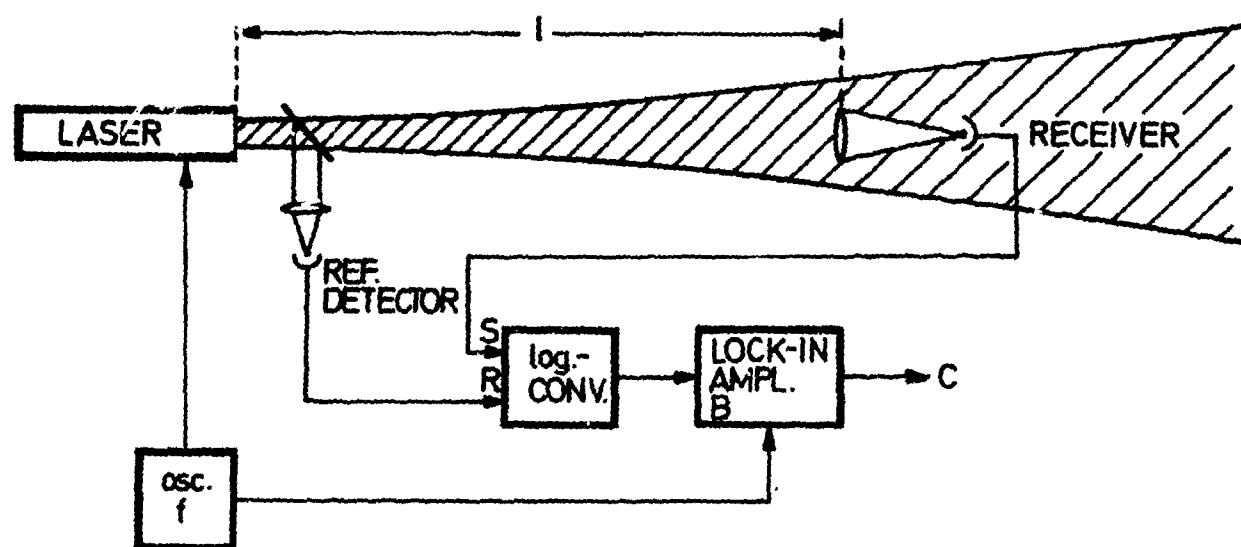
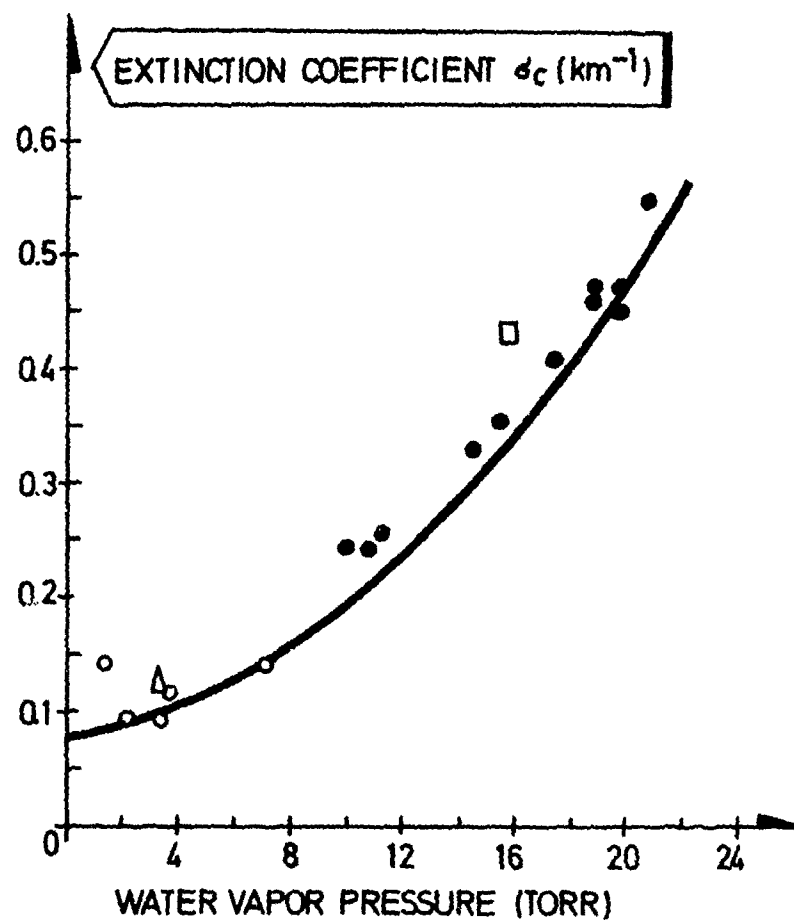


Fig. 1 Conceptual instrument layout.

Fig. 2 Comparison of laboratory and outdoor water vapour extinction data for P(20) CO₂ laser line (from KELLEY, 1975). Solid laboratory curve from McCoy, 1969.

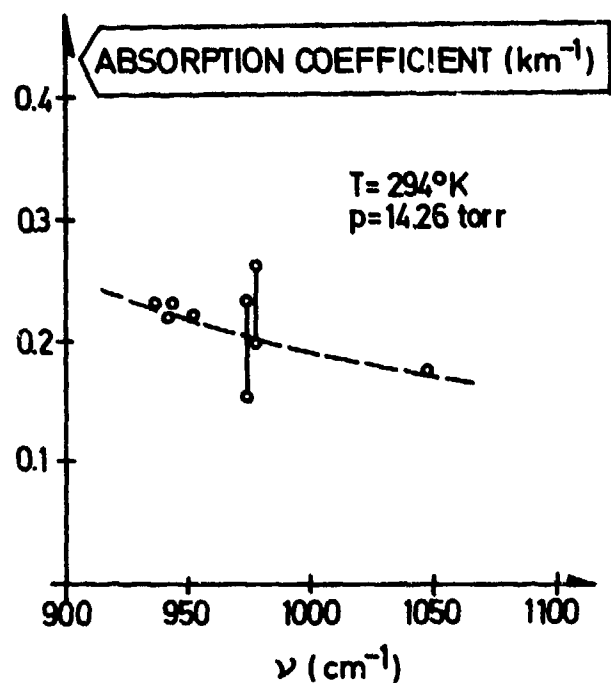


Fig. 3 Water vapour continuum absorption coefficient vs. optical frequency in the 10μ region. (LONG/KELLEY, 1975).

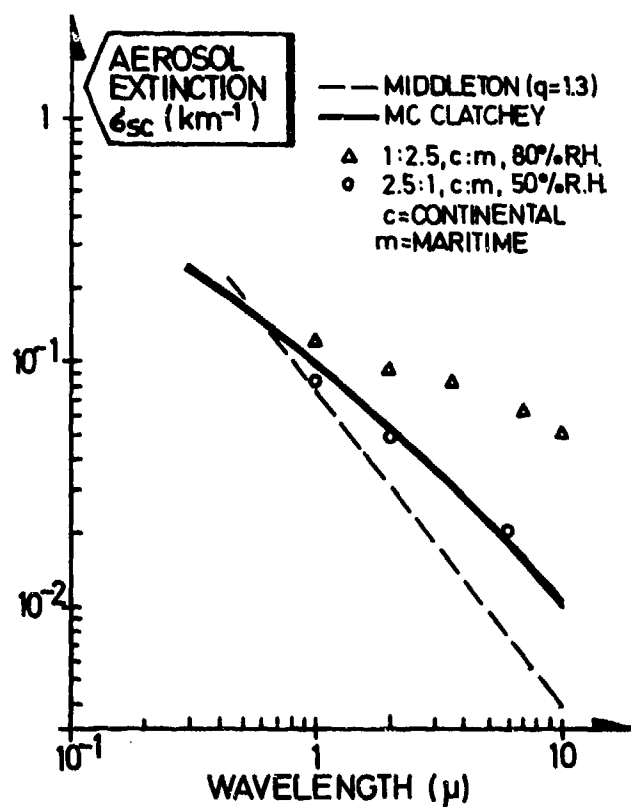


Fig. 4 Aerosol extinction-model comparison (WOODMAN, 1974) for good visibility conditions.

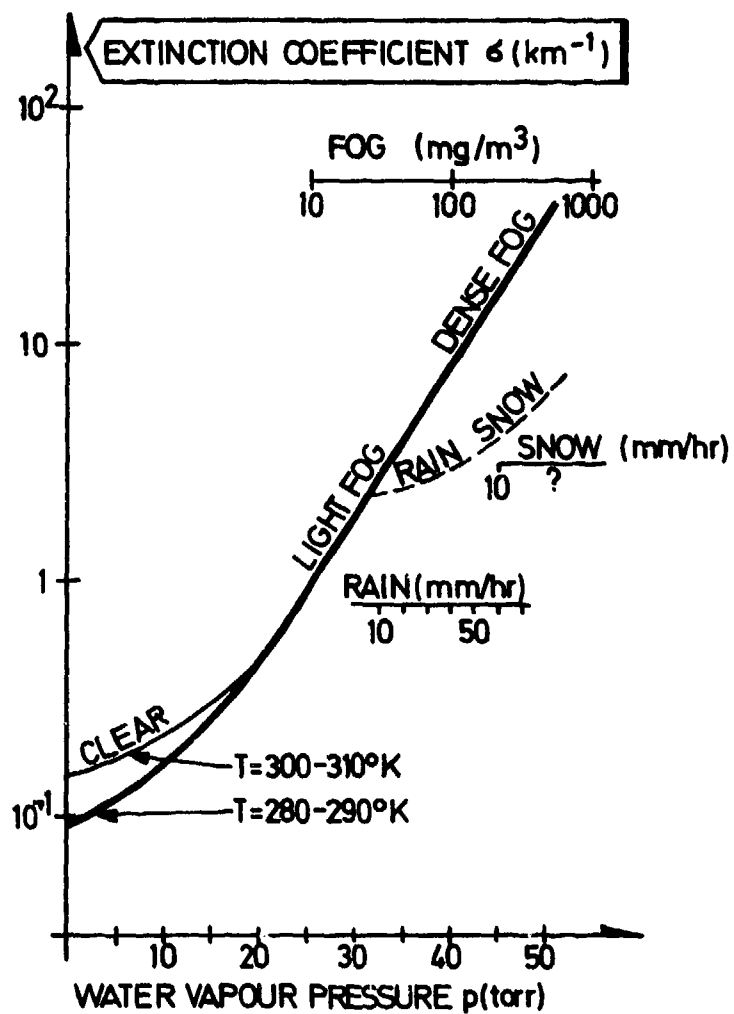
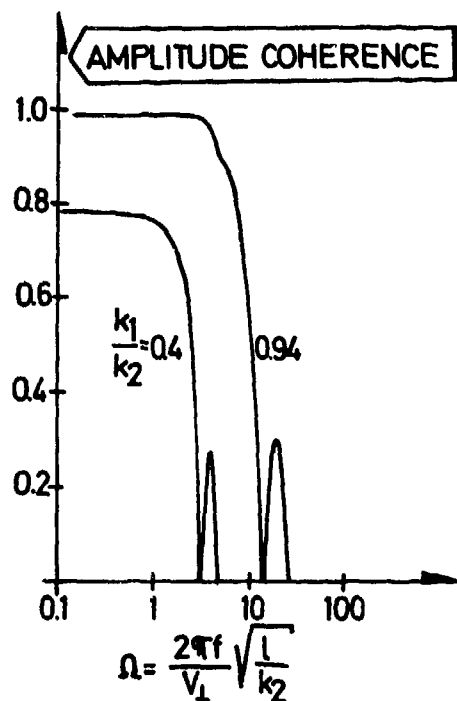


Fig. 5 10μ atmospheric extinction. Overview (GULLBERG, 1971).



THE FLUID MECHANICS AND COMPUTER MODELING OF ATMOSPHERIC TURBULENCE
CAUSING OPTICAL PROPAGATION FLUCTUATIONS

William C. Meecham*
University of California, Los Angeles, California, USA

SUMMARY

First, optical refractive index fluctuations, caused primarily by temperature fluctuations, are examined from the viewpoint of what is known by fluid dynamicists about atmospheric turbulence effects. We write the various field quantities (temperature, velocity and pressure) in terms of their averages and their fluctuations from those averages. The variations of the index of refraction with the fluid variables is discussed. The cross correlations of fluid velocity, of temperature, and of velocity with temperature are presented. We review step-by-step the consequences of statistical stationarity, statistical homogeneity, and statistical isotropy. A new, modified discussion of the Kolmogoroff cascade theory of turbulence is presented and its consequences analyzed for their bearing upon correlation functions and energy spectra. Using this fluid mechanical information we then consider the modeling of propagation-fluctuation problems using computer-generated realizations of index variations, with given statistical properties. As an example we consider geometrical-optics propagation. We know that the log of the fractional change in field amplitude is proportional to $\int_0^L (L-x) [(\partial^2/\partial y^2 + \partial^2/\partial z^2) n_1(x)] dx$ with L the total path length, y and z normal to the direction of propagation and n_1 the index fluctuation. A typical computer modeling problem consists of being given that the square bracket, $[]$, in the amplitude expression above has log normal statistics, i.e. that $[] = \lambda \ln(u/n)$ where $u(x)$ is joint normal (λ and n are parameters) and being given that the spectrum of u is that determined by the Kolmogoroff 5/3 law for the fluid velocity spectrum. We can calculate amplitude fluctuations by substituting realizations for the random process $u(x)$ with the stated statistics. This is done using the (first term of the) Wiener-Hermite expansion:

$$u(x) = \int_{-\infty}^{\infty} K(x-x_1) H(x_1) dx_1$$

with K a non-random function (the square of the Fourier transform of K is the energy spectrum of $u(x)$); H is the random white noise process. Realizations of H are generated by breaking the x_1 -axis into a set of cells of width Δ . The H is generated by choosing values independently in each cell, Δ , from a Gaussian distribution of variance Δ^{-1} . The above equation is constructed in such a way that u is statistically homogeneous (not a necessary restriction). The selection of computer-generated values from a Gaussian distribution is easily accomplished by the use of a familiar transformation and algorithm, which will be presented. Using these methods and substituting statistical realizations of $[]$ into the integral for amplitude fluctuations, one can generate a set of realizations of the fluctuating amplitude, from which one may obtain desired statistical properties, e.g. the standard deviation of the amplitude, etc. Physical optics problems require random integrands as a function of vector (position) arguments; the Wiener-Hermite generalizations will be presented. If the effect of non-Gaussian characteristics of u are desired the appropriate generalization of the representation is easily obtained.

1. INTRODUCTION

We are interested in the effect of atmospheric turbulence on optical propagation. Turbulent phenomena comprise one of the great unsolved areas of science and engineering. We begin with a general review of the fluid mechanics of turbulence. The equations governing fluid motions are well known. One might wonder, in such a circumstance, why turbulent phenomena are not by now completely understood. The reason that this is so, as will be seen in succeeding sections, is that the governing equations are strongly non-linear. As a consequence, the great body of mathematics developed chiefly for linear differential equations is not useful. Fluid dynamicists have dealt with these difficulties chiefly by specializing flows to idealized situations involving boundary layers, wakes, etc., and by approximating turbulent behavior with not always satisfactory empirical laws and rules. If one attempts to solve the equations of motion for turbulent fluids, one finds extremely complicated solutions (functions of position and of time) corresponding to the observed complexities of turbulent flow. Indeed the solutions, either as calculated when this is possible (rarely), or the experimentally observed field variables are so complicated that it is not likely that detailed information concerning them would be useful even if it were available. The approach to these difficulties has been largely one of taking statistical averages of the physical quantities of interest. These averaged quantities have a much simpler dependence upon the position coordinates and upon the time than do the individual fluctuating members from which the averages are constructed. This is the procedure followed in this paper.

To begin we sketch the derivation of the equations governing fluid motion and discuss those equations. After some simplifications suited to the atmospheric turbulence problems at hand we write various field quantities in terms of their averages and their fluctuations from those averages. Some background information on fluid mechanical properties is presented. In particular the variations of the index of refraction with the field variables is discussed (the index is of particular importance for optical propagation in the atmosphere). Then the cross correlations of fluid velocity, of temperature, and of velocity with temperature are presented. The time average for obtaining these correlations is defined. We then discuss step-by-step the consequences of statistical stationarity, statistical homogeneity, and statistical isotropy. The structure functions involving velocity and temperature fluctuations are defined. A new, modified discussion of the cascade theory of turbulence is presented and its consequences analyzed for their bearing upon correlation functions. Experimental data supporting the so called five-thirds law for the velocity energy spectrum are presented.

Following the presentation of this fluid mechanical information, the processes of generating density fields with stated statistical properties is described. It is shown how one can use Wiener-Hermite expansions to produce realizations, which can in turn be used for computer experiments.

*The author is also a consultant to the Oregon Graduate Center, Beaverton, USA, and to Aerospace Corporation, El Segundo, California, USA.

2. GOVERNING EQUATIONS OF FLUID MECHANICS

The equations of fluid mechanics which are relevant to our atmospheric problems are those involving the motion of viscous, compressible, Newtonian fluid (this last referring to a fluid in which the viscous stress is proportional to the rate of shear strain) in a uniform gravitational field and non-rotating system (Coriolis force effects can be treated separately). They are given in standard references (e.g. Landau and Lifshitz, 1959). It should be remarked at the outset that the equations, though initially quite complicated, can usually be considerably simplified for atmospheric turbulence problems. A brief discussion of the derivation of the equations will be helpful. In deriving the equations a useful concept is that of the substantial derivative. Consider a small element of mass within the fluid at some position at a given initial time. The time rate of change of some property of that element of mass, following it as it flows, can be obtained by differentiation. Suppose that the property is given the name F . The rate of change of that property following the flow (the substantial derivative or convected derivative) is found to be¹

$$\frac{D}{Dt} F \equiv \frac{\partial F}{\partial t} + u_i^* F_{,i} \quad (1)$$

Here \underline{u}^* (with components u_i^*) is the local value of the fluid velocity. We adopt the notation which will be convenient here: $F_{,i} = \partial F / \partial x_i$, where x_i are the Cartesian coordinates of position with x_3 vertical; the coordinates will sometimes be designated x, y, z . Further, we adopt the summation convention; that is, we should sum from 1 to 3 over subscripts which are repeated within a single term.²

We can make use of the substantial or convective derivative given in (1) to obtain the governing equations. First of all, consider the equation of continuity. The quantity of mass of a given element of fluid must be conserved as the element flows: its substantial derivative must vanish. Let $F = \rho^* \delta V$, where δV is a small volume of fluid at a given instant and ρ^* is its density. Then, since the mass must be conserved, we know

$$\frac{D}{Dt} (\rho^* \delta V) = 0. \quad (2)$$

By simple manipulation, one can show that,³

$$\frac{\partial \rho^*}{\partial t} + (\rho^* u_i^*)_{,i} = 0. \quad (3)$$

Consider Newton's Law, $\underline{f} = (d/dt)m\underline{V}$. Again using (1) for the time rate of change of a quantity following the flow, where now for F we use the i^{th} component of the momentum given by $\rho^* \delta V u_i^*$, we have the relation

$$\frac{1}{\delta V} \frac{D}{Dt} (\rho^* u_i^* \delta V) = G_i, \quad (4)$$

where G_i represents the force per unit volume exerted upon the element of fluid⁴. For our purposes there are three forces acting within the fluid: the force due to pressure changes within the fluid, the force due to viscous stress within the fluid, and the force of gravity.

The mathematical derivation of expressions for the three forces can be found in, for example, Landau and Lifshitz (1959). The pressure force per unit volume is the negative of the pressure gradient (there is no such pressure force in a constant pressure field). The viscous force per volume, allowing for variable viscosity at this stage, is the divergence of the viscous stress. The Newtonian viscous stress, details aside, is the most general symmetric tensor of second-rank which one can form from first-order derivatives of the velocity. The gravitational force per unit volume is in the negative x_3 -direction and of magnitude $\rho^* g$. We substitute the three forces for the right-hand side of (4). In the left-hand side make use of the continuity equation given in (3). One finds for the Navier-Stokes equations governing fluid flow⁵

$$\rho^* \left(\frac{\partial u_i^*}{\partial t} + u_{i,j}^* u_j^* \right) = \left[- \left(p^* + \frac{2}{3} \mu u_{j,j}^* \right) \delta_{ik} + \mu \left(u_{i,k}^* + u_{k,i}^* \right) \right]_{,k} - \rho^* g \delta_{3i}. \quad (5)$$

Here g is the acceleration due to gravity, assumed constant. The μ is the fluid viscosity and p^* is the fluid pressure. The δ_{ij} is Kronecker's Delta; it is unity if the subscripts are equal, and otherwise zero.

Consider now the entropy of the moving fluid. The entropy changes in general during the fluid motion. One obtains for the equation governing time rate of change of the entropy following the fluid flow (Landau and Lifshitz, 1959)

$$\rho^* T^* (DS/Dt) = u_{i,j}^* \left[- \frac{2}{3} \mu u_{m,m}^* \delta_{ij} + \mu (u_{i,j}^* + u_{j,i}^*) \right] + (k T^*_{,i})_{,i}. \quad (6)$$

Here T^* is the temperature, S is the entropy per mass, and k is the thermal conductivity. The entropy changes for two reasons. The action of the viscous stresses generates heat which can be shown to lead to the first term on the right side. Further there is heat conduction which also changes the entropy; the net conduction is the divergence of the thermal heat flux giving the second term.

The equation of state for the atmosphere is to an excellent approximation that for an ideal gas,

$$p^* = R \rho^* T^* \quad (7)$$

where R is the gas constant per mass, which, for an ideal gas, leads to the relation

$$R = c_p - c_v, \quad (8)$$

where c_p and c_v are the specific heats of air per unit mass at constant pressure and constant volume. (We neglect effects of variable moisture content.)

Consider now the dependence of density changes upon pressure and temperature. There are pressure fluctuations in the atmospheric boundary layer (caused by velocity fluctuations) of order $(10^{-6})\sigma_u^2$ where σ_u is the RMS (gust) velocity fluctuation, say 3 meters per second. Temperature fluctuations there are of order one degree Kelvin. Hence; in cgs, $(\sigma_p/\bar{p}) \sim (\frac{1}{2} \times 10^{-3}) \times (3 \times 10^2)^2 (10^6) \sim \frac{1}{2} \times 10^{-4}$; $(\sigma_T/\bar{T}) \sim \frac{1}{3} \times 10^{-2}$, where the overbars indicate time averages, discussed below. Consequently from (7) for the small relative fluctuations which we have, we can neglect the effect of pressure fluctuations on the density fluctuations.

The difficult nonlinear character of the equations makes simplification essential. This is usually accomplished by asking for less information. Instead of searching for the complicated functions representing the pressure etc., we ask rather for their (much simpler) averages. We are lead to define the following variables:

$$\begin{aligned} p^* &= \bar{p} + p \\ T^* &= \bar{T} + T \\ \rho^* &= \bar{\rho} + \rho \end{aligned} \quad (9)$$

and

$$\underline{u}^* = \underline{\bar{u}} + \underline{u} \quad (10)$$

These quantities can be substituted in the fluid equations and needed averages found.

3. BACKGROUND INFORMATION ON FLUID MECHANICAL AND RELATED PROPERTIES

3.1 Discussion of Index of Refraction

When we are particularly interested in optical frequency propagation, the main effect of the atmosphere comes from changes in the refractive index. The refractive index depends primarily upon the density of the atmosphere. We find in standard references (Allen, 1964) that

$$\Delta n \equiv n - 1 = 82.6 \times 10^{-6} p^* / T^* \quad (11)$$

with n the refractive index, p^* the pressure in milli-bars and T^* the temperature in degrees Kelvin. We represent RMS fluctuations of quantities by σ with a subscript indicating the variable involved and find

$$[\sigma_n / (n - 1)]^2 = (\sigma_p / \bar{p})^2 + (\sigma_T / \bar{T})^2 \quad (12)$$

valid for small relative fluctuations and neglecting any (slight) statistical dependence of the pressure on temperature fluctuations. In the above discussion we found we could neglect the effect of pressure fluctuations so,

$$\sigma_n \approx + \left[82.6 \times 10^{-6} \frac{\bar{p}}{\bar{T}} \right] \frac{\sigma_T}{\bar{T}} \quad (13)$$

3.2 Simplifying Statistical Assumptions

We suppose, as discussed earlier, that the wind velocity is given by

$$\underline{\bar{u}} + \underline{u} \quad (14)$$

where $\underline{\bar{u}}$ is the average wind speed and \underline{u} is the instantaneous departure from that average.

We consider the cross correlation of quantities measured at two different positions. It is convenient in what follows to define the three Cartesian components, u_i , of the velocity fluctuation vector \underline{u} . Consider the cross correlation of the velocity fluctuations measured at two points, \underline{x}' and \underline{x}'' . This correlation is defined by the time average, represented by $\langle \rangle$ (we use this and overbar interchangeably).

$$Q_{ij}(\underline{x}', \underline{x}'', t) \equiv \left\langle u_i(\underline{x}', t') u_j(\underline{x}'', t' + t) \right\rangle = \lim_{T \text{ large}} \frac{1}{T} \int_0^T u_i(\underline{x}', t') u_j(\underline{x}'', t' + t) dt' \quad (15)$$

Our assumption that the process is statistically stationary means that the correlation is approximately independent of which segment, T , of velocity fluctuation we use in the determination of the average (correlation function). Other cross correlations are important to us; the cross correlation of temperature fluctuations is:

$$S(\underline{x}', \underline{x}'', t) \equiv \left\langle T(\underline{x}', t') T(\underline{x}'', t' + t) \right\rangle, \quad (16)$$

with the average defined as the time average in a way analogous to that in (15). The often-important transport of the temperature fluctuations within the turbulent atmosphere is controlled by the cross correlation of the velocity with the temperature, defined by

$$T_i(\underline{x}', \underline{x}'', t) \equiv \left\langle T(\underline{x}', t') u_i(\underline{x}'', t' + t) \right\rangle. \quad (17)$$

The time average is analogous to that of (15). When the two points of measurement, \underline{x}' and \underline{x}'' are separated by a distance considerably greater than some length (outer scale) L_0 , the fluctuations become statistically independent of one another and it follows that the correlations given in (15)-(17) go to zero (this is so because by the definition (14) the average of the fluctuations themselves must vanish). Similarly, if the

time delay, t , between the measurements, even though the two points are closer than L_0 , exceeds a time characteristics of the turbulence T_0 , then again the fluctuating quantities become statistically independent of one another and the cross correlations given in (15)-(17) go to zero. This time, T_0 , is called the correlation time for the turbulent process. It is typically dependent upon the quantities already defined. In most turbulent processes when measurements are made moving with the mean flow,

$$T_0 = \frac{L_0}{\bar{u}} \quad (18)$$

Often, atmosphere turbulence shows little statistical change when we move from one position to another. Such behavior is called *statistical homogeneity*. It is, of course, not rigorously true in any application. In the atmosphere, the situation is complicated by the fact that the large scale characteristics change when we move vertically a distance L_0 , the scale of the turbulence. Nevertheless, for many purposes, the assumption of statistical homogeneity is a useful approximation. For such homogeneous turbulence, the correlations (15)-(17) reduce to functions of time and space functions of the displacement vector

$$\mathbf{r} \equiv \mathbf{r}'' - \mathbf{r}' \quad (19)$$

between the two points at which measurements are made.

Often the average quantities defined here, in particular the smaller-scale characteristics, are approximately independent of the orientation of the displacement factor \mathbf{r} . The idealization that the turbulence has this property is called *statistical isotropy*. This is a further, most useful, simplifying assumption for the discussion of atmospheric turbulence. In conjunction with the previously discussed simplifying assumptions, statistical isotropy leads to the following reductions of complexity in the cross-correlations (15)-(17). The reader is referred to Batchelor (1953) for a more extended discussion of the symmetry characteristics presented here:

$$Q_{ij} = Q_1(r, t) r_i r_j + Q_2(r, t) \delta_{ij}; \quad (20)$$

$$S = S_1(r, t); \quad (21)$$

$$T_i = T_1(r, t) r_i. \quad (22)$$

The coefficient functions Q_1 , Q_2 , S_1 , and T_1 are called "scalar generators" and depend only on the length of the displacement vector \mathbf{r} and on the time delay between the measurements. The simple rule for forming all such statistically isotropic correlations is to make up all relevant combinations of the vector components r_i and of the Kronecker delta symbol δ_{ij} , as seen in the examples here.

These assumptions are often found to be valid for the smaller-scaled structure; but for the large scales, that is, for the large eddies, such simplifying assumptions cannot be justified. Velocity and temperature differences are approximately homogeneous and isotropic if r is small compared with L_0 . Thus, consider "structure functions" for these fluctuating quantities. For example, define a structure function for the velocity fluctuation as in (23). (Structure functions are usually defined for simultaneous measurements. When time is a variable, it will be implicit in what follows.) Thus,

$$D_{ij}(\mathbf{r}', \mathbf{r}'') \equiv \langle [u_i(\mathbf{r}') - u_i(\mathbf{r}'')] [u_j(\mathbf{r}') - u_j(\mathbf{r}'')] \rangle. \quad (23)$$

For $|\mathbf{r}'' - \mathbf{r}'| \equiv |\mathbf{r}| \ll L_0$ this correlation is often assumed to be statistically homogeneous and isotropic, that is, to depend only on r : The smaller scale structure within the turbulence is of more universal form than is the large-scale. For such small scales, we can write D_{ij} in a form similar to (20) (with $t = 0$ for the simultaneous measurements under discussion). The structure function notation follows Tatarskii (1959).

In a way analogous to that for the velocity structure function, one can define a structure function for temperature when small-scale effects are statistically homogeneous and isotropic:

$$D_T(\mathbf{r}) = \langle [T(\mathbf{r}') - T(\mathbf{r}' + \mathbf{r})]^2 \rangle \approx 2S_1(0) - 2S_1(r) \quad (24)$$

with the function S_1 defined in (16) and (21) for simultaneous measurements. When needed, one could similarly define the cross correlation between temperature fluctuations and velocity fluctuations.

3.3 The Cascade Theory of Turbulence

There is a simplifying hypothesis concerning the nature of the energy transfer within turbulence which is useful in connection with atmospheric problems. Some years ago Kolmogorov (1941) proposed the following view of the turbulent energy transfer process (Fig. 1). A quantity of power per mass, ϵ , is supplied to the turbulence, usually being injected in the largest turbulence scale, of order L_0 (through the non-linearity of the fluid flow process). This energy is passed, again because of the non-linearity of the equations of motion, down to those eddies which dissipate the energy. (If the equations were linear, there would be no energy transfer between different size eddies.) The dissipating eddies are very small, with size of order ℓ_0 , the so-called inner scale. These eddies dissipate the energy as heat. Kolmogorov makes an assumption concerning the way in which the non-linearities of the fluid flow pass energy from the very large eddies to the very small ones: One might reasonably suppose that this quantity of energy per second per mass, ϵ , is passed from the largest to the next smaller eddies; and in turn from those to yet smaller eddies and so on, down to the smallest (dissipation) eddies, of size ℓ_0 . This (assumed) transfer is called a cascade. There is, as yet, only indirect experimental evidence that this

is the mode of energy transfer. Nevertheless, if we suppose that this is the process, there is a considerable simplification in the turbulence description. Suppose that we want to find the energy spectrum $E(k)$ the turbulent energy per wave number. The parameters in the problem consist of ϵ , ℓ_0 , L_0 , and σ_u . The quantities ϵ , L_0 , and σ_u are known to be connected by the following empirical relation (Batchelor, 1953)

$$\epsilon \sim A \frac{\sigma_u^3}{L_0} \quad (25)$$

If one believes that the rate of loss of energy from the large eddies is independent of the small-scale viscosity dependent effects then (25) follows by dimensional analysis.⁶ Put another way, we might suppose that the transfer of energy from larger to smaller eddies is accomplished by the nonlinear inertial effects, with viscosity playing a role only in the energy dissipation (into heat) by the smallest eddies. Thus we can eliminate one of the parameters appearing in (25) let that one be σ_u . If we examine the energy spectrum in the intermediate range

$$\ell_0 \ll 2\pi k^{-1} \ll L_0 \quad (26)$$

we may reasonably suppose that the function $E(k)$ is independent of ℓ_0 (the inner scale) and L_0 (the outer scale). Of course, in order that (26) be possible, it is necessary that L_0 be extremely large compared with ℓ_0 . Allowing an order of magnitude for the range of variation of $2\pi k^{-1}$ we see from (26) that we need

$$\frac{L_0}{\ell_0} = Re^{3/4} > 10^3$$

with

$$Re' \equiv \frac{\sigma_u L_0}{\nu} \quad (27)$$

using the size of ℓ_0 given in (29) below. Such large Reynolds's numbers are indeed attained in lower-atmospheric turbulence. Using dimensional analysis, it immediately follows from the above reasoning that the energy spectrum is given by

$$E(k) = a_1 \epsilon^{2/3} k^{-5/3}, \quad \frac{2\pi}{L_0} \ll k \ll \frac{2\pi}{\ell_0} \quad (28)$$

where here and below the a_n are dimensionless constants of order unity.

Before discussing this energy spectrum function, consider the inner scale, ℓ_0 . Kolmogorov suggested (as seems plausible from the nature of the physical process) that the inner scale is independent of the outer scale, L_0 , and thus depends only upon ϵ and upon the kinematic viscosity, ν . In such a case one obtains from the use of dimensional analysis the following result for the inner scale:

$$\ell_0 = a_2 (\nu^3/\epsilon)^{1/4} \quad (29)$$

In the atmosphere, ℓ_0 is typically of order of millimeters (Monson et al., 1969). Similarly the average velocity change associated with the dissipation is found by dimensional analysis,

$$\overline{(\Delta u)^2}^{1/2} \sim (\nu\epsilon)^{1/4} \quad (30)$$

The results of some important measurements of $E(k)$ by Grant et al. (1962), are shown in Fig. 2. These experiments were performed in British Columbia in a tidal channel near Vancouver. The results are plotted log-log, to bring out the proposed algebraic dependence of the energy spectrum function upon the wave number see (28). It is seen that the spectrum in these experiments had the suggested form over eight octaves of k . The quantity, ϵ , was obtained by integration. The energy spectrum, $E(k)$, was measured directly, in effect using its definition. It is noted that these experiments show that the inner scale, the scale at which dissipation occurs, is of order ℓ_0 , as defined in (29). It is approximately at ℓ_0 that the spectrum shows an abrupt reduction, not at the Taylor dissipation length λ_T . The reason that this is so can be seen in the following way (we adopt the view that the cascade description of the turbulent process is valid). The dissipation may be supposed to consist of velocity jumps $\Delta u^{2/3}$ (30) with a volume average of order $(\nu\epsilon)^{1/4}$, where the characteristic distance in which the jump occurs is of order $(\nu^3/\epsilon)^{1/4}$ (29). These dissipation regions are assumed to occupy a fraction α of the volume of the turbulence; of course, α would be near unity if the dissipation regions completely fill the volume.

From the Kolmogorov cascade theory we obtain an estimate for $\overline{(\Delta u)^2}^{1/2}$ which is the characteristic size of the small-scale velocity fluctuations associated with the viscous dissipation process. The dissipation could be spread somewhat uniformly throughout the turbulent flow. Recent work dealing with the intermittency of turbulent flow suggests that in fact the dissipation may occur in slip regions. In such a case the individual velocity changes, when they occur, are larger than the average represented by $(\Delta u^2)^{1/2}$. It is of interest to see how the average quantity is related to the typical velocity jump involved in the dissipation process. Call the typical velocity jump Δu ; then utilizing the definition that the dissipation occurs within a fraction α of the total turbulent volume, we see

$$\Delta u \sim \alpha^{-1} (\nu\epsilon)^{1/4} \quad (31)$$

If one adopts the customary view that the turbulence is quite intermittent, one may expect to find small values of α , and consequently, to find that the typical velocity jump, Δu , involved in the dissipation process is relatively large, but relatively infrequently encountered. Many other experiments, both in the ocean and in the atmosphere, have verified the Kolmogorov dependence of the energy spectrum function.

The behavior of the energy spectrum function reflects in a corresponding simplification of the correlation function for small separations of the measuring points. Using dimensional analysis, one obtains a result

$$Q(r, 0) \sim \epsilon^2 r^{2/3} \quad (32)$$

The velocity structure function defined earlier takes the form

$$D_{rr}(r) = C(\epsilon r)^{2/3}, \quad \ell_0 \ll r \ll L_0. \quad (33)$$

Similarly the temperature-fluctuation structure function within the same range of r is,

$$D_T(r) = C_T \epsilon^2 r^{2/3}, \quad \ell_0 \ll r \ll L_0. \quad (34)$$

We are often concerned with changes in the index of refraction. We define a structure function for such changes,

$$D_n(r) = \langle [n(\mathbf{r}') - n(\mathbf{r}' + \mathbf{r})]^2 \rangle, \quad (35)$$

where we again suppose that small scale effects are homogeneous and isotropic. Then employ the definition, (16), the result in (13), the Kolmogorov form for the temperature structure function to find,

$$D_n(r) = C_n \epsilon^2 r^{2/3}, \quad \ell_0 \ll r \ll L_0. \quad (36)$$

4. OUTLINE OF PROBLEM AND METHOD OF COMPUTER MODELLING.

Under the assumption that the radiation wavelength is small compared with the scale of atmospheric (temperature) fluctuations, we know Tatarskii (1959) that the log of the received amplitude is proportional to

$$\int_0^L (L-x) \nabla_N^2 r(x) dx \quad (37)$$

or

$$\int_0^R \frac{\rho(R-\rho)}{R} \nabla_N^2 r(x) dx$$

for plane and spherical sources respectively. Here the path length is L and R respectively; and

$$\begin{aligned} \nabla_N^2 n &= \frac{\partial^2 n}{\partial y^2} + \frac{\partial^2 n}{\partial z^2} && \text{plane wave} \\ &= \nabla^2 n - \frac{1}{\rho^2} \frac{\partial}{\partial \rho} \left(\rho^2 \frac{\partial n}{\partial \rho} \right) && \text{spherical wave} \end{aligned} \quad (38)$$

Thus $\nabla_N^2 n$ is the Laplacian in the direction normal to that of propagation. The n is the index of refraction, as described, primarily dependent on the temperature for our work.

We are given the statistics of $\nabla_N^2 n$. It is supposed here (Elliott, 1974) that this quantity has a Johnson distribution (Hahn and Shapiro, 1967) defined by the transformation

$$\nabla_N^2 n(x) = \lambda \operatorname{sh} \frac{u(x)}{\eta} \quad (39)$$

where u is (presumed joint-) Gaussian and λ and η are parameters determined from the moments of the process $\nabla_N^2 n$. A log-normal distribution is also of interest; that process is obtained by changing the sh function in (39) to the logarithm.

To calculate individual fluctuating amplitudes [the expressions (37)] we calculate ensemble members $\nabla_N^2 n$, substitute in (37) and integrate numerically. We want, as described, ensemble members with a Johnson distribution. These are obtained by calculating Gaussian ensemble members $u(x)$. Then use the transformation (39) to find ensemble members $\nabla_N^2 n$. The task remaining is to show how to find ensemble members $u(x)$ for substitution in (39).

We shall assume that the atmospheric temperature fluctuation is statistically homogeneous.

GENERATION OF GAUSSIAN ENSEMBLES.

For this purpose we make use of the Wiener-Hermite representation [see e.g. Meecham and Siegel (1964)].

Wiener proposed an expansion useful for Gaussian and nearly Gaussian processes. The expansion is for the random process (the time series) itself and is based on the ideal random function — sometimes called the white noise function. This process can best be described as follows (we need only the one-dimensional scalar form). Suppose that the x -axis is divided up into cells of width Δx . In each cell assume that the process is constant with amplitude chosen from a Gaussian distribution, with variance Δx^{-1} . The process is

statistically independent in neighboring cells. One member of the ensemble for the process is shown in Fig. 3. Every member is such a histogram. The *ideal* random function is found by letting $\Delta x \rightarrow 0$. We designate this process $H(x)$.

For computer work we keep a finite Δx . Each realization of $H(x)$ is found by computing such a histogram. The method of finding the Gaussian amplitudes is described in the Appendix. Evidently any integral over H will be Gaussian (to all orders) for it will be a sum of independent Gaussian processes. Then consider the special integral (a sum in our work)

$$u(x) = \int_{-\infty}^{\infty} K(x - x_1) H(x_1) dx_1 \quad (40)$$

where $K(x)$ is a nonrandom function. Evidently every member of the ensemble of functions $u(x)$ will be continuous and will possess continuous derivatives if the kernel K is sufficiently well behaved. The use of the difference argument in (40) leads to the result that the process u is statistically homogeneous. From the definitions we have for the correlation,

$$\begin{aligned} \langle H(x_1) H(x_2) \rangle &= \Delta x, & x_1 \text{ and } x_2 \text{ in same cell} \\ &= 0, & \text{otherwise.} \end{aligned} \quad (41)$$

Using this property we find

$$\begin{aligned} Q(r) &\equiv \langle u(x) u(x+r) \rangle \\ &= \int_{-\infty}^{\infty} K(x_1) K(x_1+r) dx_1 \end{aligned} \quad (42)$$

which is statistically homogeneous as suggested. Higher moments yield analogous results. The method can be extended to non-Gaussian processes, but such are not needed here.

We can take the Fourier transform of (42) and find the energy spectrum (differing here by a constant from some definitions)

$$\begin{aligned} E(k) &= \int_{-\infty}^{\infty} e^{ikr} Q(r) dr \\ &= |K(k)|^2 \end{aligned} \quad (43)$$

with

$$K(k) \equiv \int_{-\infty}^{\infty} e^{ikx} K(x) dx \quad (44)$$

To find the kernel $K(x)$ to be used in the construction of the ensemble members $u(x)$ given by (40), proceed as follows. Invert the relation (39), using temperature (index of refraction) data:

$$u(x) = \eta \operatorname{sh}^{-1} \left[\lambda^{-1} V_N^2 n(x) \right] \quad (45)$$

Calculate the energy spectrum, $E(k)$, of the process $u(x)$, so obtained. From (43) we see

$$K(k) = E^{1/2}(k) \quad (46)$$

up to a phase factor, which can be set equal to zero without loss of generality. $K(x)$ is then found by inverting (44).

We can sum up the results of this section as follows: The log of the amplitude of optical propagation fluctuations is given, in the high frequency approximation, by (37). We wish to conduct a computer experiment, constructing realizations of the fluctuating amplitude from realizations of the random atmosphere, where the statistics of the index of refraction (temperature) fluctuation are given (Johnson distribution). Such a process can be obtained from (39) where $u(x)$ is Gaussian. We must now construct Gaussian realizations $u(x)$. This is done by means of the Wiener-Hermite representation. First a realization of the white noise process $H(x)$ is constructed according to the rules described in the previous section. (For this we need to choose, on the computer, numbers from a Gaussian distribution with a prescribed variance; the method is outlined in the Appendix.) Then the integral in (40) is carried out numerically, using this realization of $H(x)$; we obtain in this way one realization of $u(x)$. Then as just described, the realization of the derivatives of the index is obtained. We need the kernel function $K(x)$ for the Gaussian process $u(x)$. It is found to be the inverse Fourier transform of the square root of the energy spectrum function of the process $u(x)$; see (46). To construct other realizations, the entire process is repeated. One may determine the statistical characteristics of the fluctuation amplitude from a large number of such realizations.

APPENDIX: GENERATING A GAUSSIAN PROCESS

Suppose we generate random numbers y with a flat distribution $\tilde{P}(y)$ over $(0,1)$, on the computer:

$$\begin{aligned} \tilde{P}(y) &= 1, & 0 \leq y \leq 1 \\ &= 0, & \text{other } y. \end{aligned}$$

Then x has a Gaussian distribution with variance σ^2 where

$$y = (2\pi\sigma^2)^{-1/2} \int_{-\infty}^{\infty} e^{-x^2/2\sigma^2} dx \quad (47)$$

Thus, generate y ; then invert (47) to find the required x . [An efficient algorithm for the inversion of this function is given by Abramowitz (1963).]

To prove the above assertion we must show that

$$\tilde{F}(y)dy = P(x)dx \quad (48)$$

where P is Gaussian with the given variance.

Differentiating (47) we find from (48)

$$\frac{dy}{dx} = (2\pi\sigma^2)^{-1/2} e^{-x^2/2\sigma^2} = P(x)$$

so $P(x)$ is Gaussian with variance σ^2 . [It is clear that y has the right range, i.e. $(0,1)$].

FOOTNOTES

1. In terms of derivatives this is $(\partial F/\partial t) = \partial F/\partial t + u_1^* \partial F/\partial x_1$. It is worth commenting here that we use the equations in their Eulerian form, that is where the derivatives are taken in a fixed frame of reference. The Lagrangian form has derivatives taken in a frame moving locally with the fluid (again "following the flow", i.e., for the time derivative just D/Dt).
2. An alternative discussion is: With $F = F(x,y,z,t)$ then ΔF equals the change in F due to change in time at a fixed point in the fluid plus the change in F which would occur for F not a function of time, but varying with position. This equals $\Delta F = \Delta t(\partial F/\partial t) + \Delta x(\partial F/\partial x) + \Delta y(\partial F/\partial y) + \Delta z(\partial F/\partial z)$, which implies (1).
3. In terms of derivatives this equation is $\partial \rho^* / \partial t + \partial(\rho^* u_1^*) / \partial x_1 = 0$.
4. The forces on a given fluid element give the time rate of change of the momentum of that fluid element: we need the *substantial* derivative of the momentum for a proper statement of Newton's law.
5. In the notation of vector analysis, this is $\rho^* \left(\frac{\partial \underline{u}}{\partial t} + \underline{u} \cdot \nabla \underline{u} \right) = -\nabla p^* - \frac{2}{3} \nabla (\mu \nabla \cdot \underline{u}) + \frac{\partial}{\partial x_k} \mu \frac{\partial u_k^*}{\partial x_k} + \frac{\partial}{\partial x_k} \mu \nabla u_k^* - \rho^* g \underline{k}$ with \underline{k} the unit vector in the x_3 -direction.
6. Dimensional analysis is of particular importance in fluid mechanics. Such analysis is performed as follows: Suppose we have parameters and variables, of importance in a particular problem, called x_1, x_2, \dots, x_n . Form all possible independent dimensionless quantities from them, called $\chi_1, \chi_2, \dots, \chi_m$. Then any physical law for the problem can be written in the form $\Pi(\chi_1, \chi_2, \dots, \chi_m) = 0$ where Π is some function. For example, consider the period of a simple pendulum. We may reasonably suppose that the important parameters are L , the length of the pendulum; M , its mass and g . We have only one possible dimensionless variable gL^2/L . Then solving $\Pi(gL^2/L) = 0$ for τ we have $\tau = a \sqrt{L/g}$ where a is dimensionless. Constants like a are usually of order unity (between 0.1 and 10) for reasons known only to God. For this problem $a = 2\pi$ of course.

REFERENCES

- Abramowitz, A., 1963, *Handbook of Mathematical Functions*, pp. 931-933, McGraw-Hill.
- Allen, C.W., 1964, *Astrophysical Quantities*, University of London, Athlon Press, London.
- Batchelor, G.K., 1953, *Homogeneous Turbulence*, Cambridge University Press, Cambridge, England.
- Elliott, 1974, Private communication.
- Grant, H.L., Stewart, R.W., and Moilliet, A., 1962, "Turbulence Spectra from a Tidal Channel," *Journal of Fluid Mechanics*, 12, 241-268.
- Hahn, G.J., and Shapiro, S.F., 1967, *Statistical Models in Engineering*, Wiley.
- Kolmogorov, A.N., 1941, "The Local Structure of Turbulence in Incompressible Viscous Flow for Very Large Reynolds Numbers," *C.R. Academy of Sciences, URSS*, 30, 301.
- Landau, L.D., and Lifshitz, E.M., 1959, "Course in Theoretical Physics," *Fluid Mechanics*, 6, English ed., Pergamon Press.
- Meecham, W.C. and Siegel, A., 1964, "Physics of Fluids," 7, 1178.
- Monson, K.R., Jones, G.W., and Mielke, R.H., et al. 1969, The Boeing Company, "Low Altitude Atmospheric Turbulence LOW-LOCAT, Phase III Interim Report," Vol. I Data Acquisition and Analysis, Technical Report AFFDL-TR-69-63, 242.
- Tatarskii, V.L., 1959, *The Theory of Fluctuation Effects for Wave Propagation in a Turbulent Atmosphere*, Academy of Science, USSR Press.

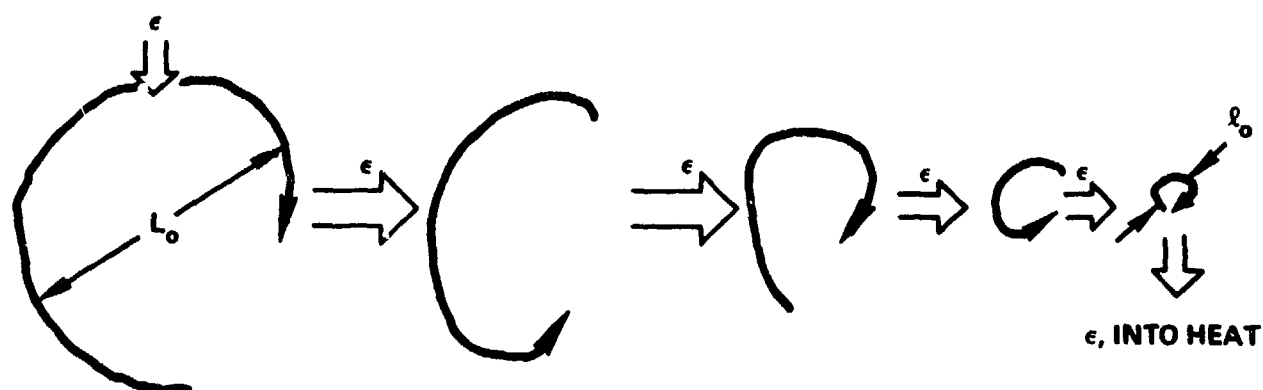


Fig.1 Sketch of the hierarchy of eddies for energy cascade.

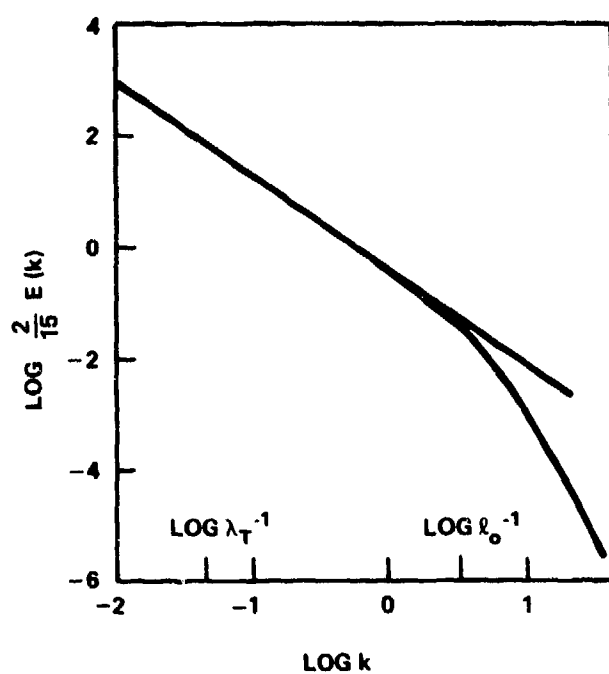


Fig.2 A logarithmic plot of the spectrum for one run. The straight line has a slope of $-5/3$; k is in cm^{-1} (Grant et al., 1962).

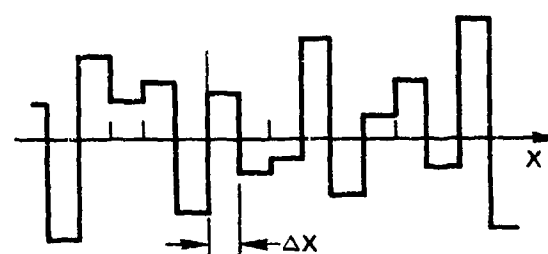


Fig.3 A Realization of the White Noise Process.

QUESTIONS AND COMMENTS
ON SESSION I

OPTICAL MODELING OF THE ATMOSPHERE

Dr. Edel: Could you please indicate shortly the difference between codes LOWTRAN 2 and LOWTRAN 3?

Dr. McClatchey: LOWTRAN 3 has modifications in 2.7 micrometer water vapor absorption coefficients. Secondly, the aerosol model has been modified to reflect the new aerosol model referred to by Dr. Fenn as the "Continental" model. This model contains more recent complex index of refraction results due to the work of Dr. Volzand thus contains a greater amount of spectral detail.

In addition the computer code has been modified to permit more flexibility for introducing meteorological measurements.

ATMOSPHERIC AEROSOLS: MODELS OF THEIR OPTICAL PROPERTIES

Dr. G. N. Plass: There is data that indicates that a spherical layer of water builds up around an aerosol particle as the humidity increases. Has this been taken into account in the models?

Dr. R. W. Fenn: The present maritime aerosol model presents a humidity condition of approximately 80% and moderate windspeed for seaspray generation. We are planning to develop some functional relationships for these dependencies to be incorporated into the LOWTRAN transmission program.

Dr. D. H. Hohn: Around 10 μ m relative minimum and maximum of the extinction coefficients were demonstrated. What is the physical reason for them?

Dr. R. W. Fenn: These features in the extinction coefficient are caused by variations in the complex refractive index, in particular the imaginary part, or absorption coefficient of aerosol material.

A COMPARATIVE STUDY OF ATMOSPHERIC TRANSMISSION AT THREE LASER WAVELENGTHS IN
RELATION TO THE METEOROLOGICAL PARAMETERS

Dr. R. W. Fenn: Some of the discrepancies between the experimental data and theoretical models may be due to the modified Gamma distribution which underestimates the large particles. At longer wavelengths (\approx a few microns) the larger particles are the main contributor to the extinction.

Dr. P. J. Wright: What you say may well be true because although the model I have chosen seems to be self-consistent in that one can fairly successfully predict the attenuation at one wavelength from observations made at two other wavelengths. The actual values of the parameters tend to be slightly different from what one might expect the true values to be (as measured by a particle sizing apparatus). We do plan to investigate other distribution models as part of the future work on this contract.

Note added after the discussion

The apparent discrepancy between the theoretical line of $\sigma_{0.63}$ versus the value of Nr^2 and the experimental points can be explained entirely on the fact that the assumption $m_{ext} = 2.0$ used in computing the theoretical line is not very accurate as the particle sizes involved are not that much greater than the wavelength at 0.63 μ m under the conditions encountered in this experiment. Examination of Figure 6 will reveal that the fit is better at higher values of extinction coefficient when the particles are larger and the assumption that $m_{ext} = 2.0$ is more nearly valid. By making a reasonable assumption about the actual particle sizes involved, I could have drawn a theoretical line that filled the experimental points almost exactly.

Dr. D. H. Hohn: With the 2-Retroreflector transmissometer concept it is necessary to discern between the signals reflected by the retros. With an earlier Plessey instrument this was realized by using active retros chopped with different frequencies. What method is used with the above mentioned instrument, and why active retros are no longer used?

Dr. P. J. Wright: The Transmissometer is built as a total energy system in that the received signal is totally reflected from either the near reflector or the far reflector. The two measurements are separated in time and the near reflector must be moved out of the beam to allow the radiation to reach the far reflector. With this type of arrangement one in principal obtains an absolute value for the extinction coefficient, as the difference (or ratio) between the two signals depends only on the attenuation in the atmospheric path between the two retroreflectors. In practice one must make a small correction for differences between the efficiencies of the two retroreflectors.

Dr. G. N. Plass: I am somewhat surprised when approximate Mie equations are used today, since exact calculations can be made which run quickly on modern computers. Such a code is available by writing to Dr. J. V. Dave of IBM Corp., San Jose, California. Your results shown in Figure 2 go out to very large size parameters. I am not aware of an approximate formula that is valid over the complete size range shown in your figure. What approximate equation did you use?

Dr. P. J. Wright: We do in fact have the code supplied by Dr. J. V. Dave and have used it on our computer when required and as a check on the approximation. The formula which has been used is that given by H. C. Van de Hulst (as referenced in the paper) with a correction factor due to Dier-

mendjian. The accuracy of this formula is more than adequate over the range of particle sizes and refractive indices employed, particularly in view of the fact that we are comparing the results with experimental measurements which are themselves subject to launch larger errors.

Apart from savings in computer time, the approximation formula gives one greater flexibility in the model in that the refractive index may be varied, for instance as a function of relative humidity of particle size.

THE FLUID MECHANICS AND COMPUTER MODELLING OF ATMOSPHERIC TURBULENCE CAUSING OPTICAL PROPAGATION FLUCTUATIONS

Dr. B. L. McGlamery: Once you have constructed an instantaneous realization of a thick atmosphere, how would you calculate the propagation of a plane wave through the atmosphere?

Dr. William C. Meecham: Once the individual realization has been constructed giving an example of index of refraction fluctuation within the atmosphere, the fluctuating index function can be inserted for example in the standard integral giving laser intensity fluctuations as a function of index fluctuations. Of course the same index of refraction function can be used in other more complicated theoretical formulas in order to verify the validity of such theories. Similarly, the fluctuation function could be used to examine through numerical experiment questions involving beam cantillation, beam tilt and alike.

DETERMINATION EXPERIMENTALE DE L'ABSORPTION ATMOSPHERIQUE AU NIVEAU DE LA MER SUR LES RAIES DU LASER CO₂(9-11μ)

Dr. J. H. Blythe: Have you observed anomalous propagation effects, in the maritime evaporation duct?

Mr. B. Contenin: No. We only made relative measurements over the entire spectral band. If the phenomenon to which you alluded affects the entire spectrum is likely that we could not observe it.

Dr. R. A. McClatchey: (1) I feel that discrepancy on P40 line is probably explainable in terms of omitted water vapor line. As our data have now been modified, I will examine this upon returning to my office. I am pleased to see that the agreement in general is so good. (2) What was the measured CO₂ concentration?

Mr. B. Contenin: The present discrepancy on the P40 line between the theoretical predictions of McClatchey and my experimental results has been recognized in a recent paper, September 1975: W. Schnell-Applied Optics, Vol. 14, No. 69 (September 75). It is likely that McClatchey's explanation for the discrepancy is correct, and I would appreciate if he keeps me abreast of his future work on this topic.

The CO₂ concentration was essentially constant during those experiments, of the order of 225 to 250 ppm.

Summary of Session I
ATMOSPHERIC CHARACTERIZATION

by
Dr. D. Höhn, Chairman

A. Session Highlights

Progress in atmospheric modelling with respect to optical and IR propagation were described in papers No. 1 and No. 2 by McClatchey et al and Shettle et al respectively, all of Air Force Cambridge Research Laboratories. Experimental confirmation to a high level of accuracy was given in paper No. 5, Atmospheric Effects Relevant to Laser Spectroscopy by Kjelaas and Lund, for meteorological situations of high visibility.

B. Problem Areas that Remain

Further knowledge on the complex index of refraction of the atmospheric aerosol at wavelengths $\lambda \geq 5\mu\text{m}$ is needed as well as better instrumentation for aerosol diagnostics.

Further aerosol collecting and subsequent analyses as well as further relevant optical/IR propagation experiments are necessary to derive atmospheric models that can be used in the thermal range of the spectrum i. e. thermal imaging and CO₂ - laser applications, and for meteorological conditions of low visibility (strong haze, fog, precipitations).

This is of extreme importance for the evaluation and optimization of future systems and even for present military optronic systems such as thermal imagers, range finders, designators, etc.

Calculations of Polarization and Radiance in the Atmosphere

Gilbert N. Plass
Department of Physics
Texas A&M University
College Station, Texas, U. S. A.

SUMMARY

Two different methods for the solution of radiative transfer problems, matrix operator and Monte Carlo, are discussed. A wide range of problems can currently be solved by the matrix operator method. As an example of the use of the method, results are given for the radiance and polarization of the radiation scattered from haze layers as well as from models of the real atmosphere. The variation of the radiance, polarization, and ellipticity with the aerosol amount in the real atmosphere model is presented. These results are compared with measurements reported in the literature. The Monte Carlo method is applied to the problem of calculation of the radiance and polarization of the photons in the atmosphere when there is an ocean as the lower surface. It is found that the turbidity of the ocean can be deduced from the upwelling radiance measured at some height in the atmosphere. The downwelling radiation just beneath the ocean surface is elliptically polarized at those angles where it is derived from the total internal reflection of the upwelling radiation at the ocean surface.

1. INTRODUCTION

Solar photons follow a complicated path in the earth's atmosphere being scattered and absorbed by the various types of molecules and particulate matter of the atmosphere as well as by the ocean and various solids on the earth's surface. It is only within the last decade that it has been possible to calculate with some assurance the radiation at various levels in the atmosphere under various conditions using realistic models. Techniques for solving the multiple scattering problem were first developed for Rayleigh and isotropic scattering. However, the scattering from aerosols whose size is of the order of and greater than the wavelength of light is important in the real problem; the forward scattered intensity in this case may be many orders of magnitude greater than that at 90° or in the backward direction. Numerical techniques had to be developed to solve the radiative transfer equations for aerosol scattering. The techniques that have been used for this problem include: 1. successive orders of scattering; 2. iteration; 3. doubling; 4. discrete ordinate; 5. spherical harmonics; 6. matrix operator; 7. Monte Carlo. It is not possible to review all of these techniques in this short article. Furthermore many of the other participants in this meeting are presenting results calculated by one or more of these methods and are describing their method. Each method has advantages and disadvantages, so that the best technique for one problem may not be the best for another.

In this article the wide variety of problems that can be solved by the matrix operator and Monte Carlo methods is indicated. All of our calculations have been done by one of these two methods which we naturally believe have advantages for many types of problems. Both of these methods have long histories and many scientists have contributed to their development. The history of the matrix operator method has been given by Plass, G. N., Kattawar, G. W., and Catchings, F. W. (1973), while the Monte Carlo method is discussed by Plass, G. N. and Kattawar, G. W. (1971). The chief disadvantage of the Monte Carlo method is that there is a statistical fluctuation or "experimental error" in the results which depends on the number of photon histories followed. However, this is the only method that has been used to solve such complicated problems as the radiance at twilight (the spherical earth must be taken into account) and the radiance and polarization in the atmosphere-ocean system (taking account of the reflection and refraction of the light at the ocean surface and the effect of waves). Very asymmetric phase functions for aerosols large compared to the wavelength of light can be used with no complications in the Monte Carlo method.

The matrix operator method is an entirely rigorous numerical method for the calculation of the radiance and polarization. The solutions can be obtained accurately for optically thick layers (the statistical fluctuations are likely to be large in this region for the Monte Carlo method). The various types of solutions that can be obtained at present by the matrix operator method are shown in this article. Extension of the method to highly asymmetric phase functions, spherical geometry, and the calculation of the polarization in the atmosphere-ocean system may require computers with greater speed and memory than are now available.

2. RADIATION SCATTERED BY HAZE LAYERS

In this section we present some typical results for the radiation field scattered by a plane parallel haze layer. All components of the Stokes vector were calculated by the matrix operator method so that the radiance, polarization, and ellipticity of the radiation were obtained. Previously Dave, J. V. (1970), Herman, B. M. et al (1971), and Hansen, J. E. (1969) have reported results for the scattering of radiation from haze layers. However, all of their published results were limited in various ways. Dave only gave results for an aerosol size parameter of 10 and up to an optical depth of 10. Hansen showed results for the reflected light only.

Our calculations were made for the haze L model proposed by Deirmendjian, D., (1969). The number of particles with a given radius is proportional to $r^2 \exp(-15.11 r^{1/2})$, where r is the particle radius. The real and imaginary parts of the index of refraction were taken as 1.55 and 0.05 respectively, reasonable values for continental hazes in the visible. The single scattering phase matrix was calculated by the method described by Kattawar, G. W. et al (1973). The calculated single scattering albedo is 0.717. The single scattering function obtained from this phase matrix is shown in Fig. 1. There is a fairly strong maximum in the backward direction and a slight maximum at the rainbow angle.

The upward radiance reflected from haze layers of various optical thicknesses is shown in Fig. 2. The cosine of the solar zenith angle $\mu_0 = 0.188$ ($\theta_0 = 79.15^\circ$). A single curve in the figure shows the

variation of the radiance from the solar horizon on the left of the figure to the nadir (at the center) to the antisolar horizon (at the right) in the principal plane containing the incident direction of the solar rays. For haze layers with small optical thickness (τ) the radiance decreases by four orders of magnitude between the solar horizon and the nadir and increases by two orders of magnitude from the nadir to the antisolar horizon. When $\tau = 16$, the curve has approached its asymptotic limit on the scale of this figure.

The downward radiance is given in Fig. 3 for the photons transmitted through haze layers of various optical thicknesses and observed at the lower boundary. The downward radiance increases until the optical thickness is of the order of unity. The maximum is at the solar horizon (left of figure) when the haze layer has small optical thickness. As the optical thickness further increases, the maximum value for the transmitted radiance moves from the solar horizon to the zenith. When $\tau = 16$, the maximum is at the zenith and the radiance is independent of the azimuthal angle (ϕ) on the scale of the figure.

The polarization of the radiation scattered by aerosol layers exhibits various new features which are not found in scattering from Rayleigh type particles. One major difference is that the polarization of single scattered radiation from aerosols exhibits one or more zeros in between the end points of the curve. The polarization of single scattered photons from haze L is shown in Fig. 4. It should be noted that the polarization is zero for scattering angles of 3.53° and 25.6° and that it is small when the scattering angle is less than 25.6° .

The polarization of the radiation transmitted through haze layers of various optical thicknesses for the same solar zenith angle ($\theta_0 = 79.15^\circ$) is shown in Fig. 5. The behaviour of the neutral points (angle at which the polarization is zero) is entirely different than for Rayleigh scattering. There is a non-Rayleigh neutral point near $\mu = 0.59$ (53.6°) at small optical thicknesses. As the optical thickness of the haze layer increases, it has moved only slightly to 57.6° for $\tau = 2$. Interestingly a second neutral point appears at the horizon when $\tau = 1.4$ and there are two non-Rayleigh neutral points when $1.4 < \tau < 2.3$. When $\tau > 2.3$ there are no neutral points for the transmitted radiation.

The position of the non-Rayleigh neutral points for five solar zenith angles is given in Fig. 6. The curves vary greatly in shape depending on the solar angle. There are zero, one, or two of these neutral points depending on the optical thickness.

The angle which the direction of polarization (maximum intensity component) makes with the direction of the meridian plane containing the final photon direction called χ . The values of χ for the reflected and transmitted photons are shown in Fig. 7. The variation of χ with optical thickness is very small for the reflected photons. On the other hand χ varies appreciably with τ for the transmitted photons.

The light scattered by a haze layer is in general elliptically polarized. The ellipticity of the light is shown in Fig. 8. The variation is obviously complicated, particularly in the case of the transmitted light.

So far all of the results have been for the radiation observed at either the upper or lower boundary of the haze layer. It is also possible to calculate the radiance at interior points within the haze layer. The downward normalized radiance is shown in Fig. 9 at various optical depths within a haze layer of great optical thickness. The normalized radiance is defined as the actual radiance multiplied by π and divided by the downward diffuse flux at the optical depth τ . Thus the variation of the radiance with zenith angle at different depths can conveniently be compared. At small optical depths beneath the upper surface, the radiance has a maximum around the direction of the solar beam. At larger optical depths this maximum moves to the zenith and the interior radiance becomes independent of azimuth. The shape of the radiance distribution no longer changes with τ ; this is called the asymptotic radiance distribution.

The upward normalized radiance for the same case is shown in Fig. 10. Near the upper surface there is a pronounced maximum near the solar horizon. At large optical depths within the medium the normalized radiance becomes independent of τ and approaches the asymptotic radiance distribution. The asymptotic distribution for the upward radiance has a minimum at the nadir, while that for the downward radiance has a maximum at the zenith.

The upward normalized interior radiance near the lower surface of an optical deep medium is shown in Fig. 11. The photon has lost all memory of the incident solar direction by the time it reaches the lower surface of an optically deep medium, so that the radiance is independent of azimuth. The shape of the radiance curves depends solely on the scattering and absorbing properties of the haze layer and of the lower boundary.

3. RADIATION SCATTERED BY ATMOSPHERIC MODELS

The radiation field for a realistic model of the earth's atmosphere has been calculated by the matrix operator method. Early studies by Sekera, Z. (1956) and others compared atmospheric models that considered only Rayleigh scattering to observational data. These results clearly indicate that one must include the scattering and absorption due to aerosols and absorption due to ozone as well as the Rayleigh scattering in performing realistic calculations for the earth's atmosphere. The model is necessarily inhomogeneous since the concentration of aerosols and ozone relative to the molecular or Rayleigh constituent vary with altitude. The matrix operator method easily performs these calculations utilizing the algorithm for combining two arbitrary layers. The results reported in this section were obtained by S. J. Hitzfelder, G. W. Kattawar, and G. N. Plass.

Elterman's model (Elterman, L., 1969) was used for the extinction coefficients of the Rayleigh, aerosol, and ozone constituents as a function of height. Two models were derived from the Elterman model, the unchanged or normal model, and the one-third normal model, in which the aerosol constituent was reduced to one-third the normal amount. These two models were considered to study the effects of varying the aerosol content of the earth's atmosphere. These calculations were performed at $\lambda = 0.55 \mu\text{m}$, in the middle of the visible region. For the normal model, the total optical depth was 0.378; for the one-third normal model, the total optical depth was 0.212. In addition to a different optical depth the one-third normal model has a different effective phase matrix than the normal model. These two differences affect the results considerably.

The haze L distribution was used to calculate the phase matrix for the aerosols. The resulting single scattered intensity is shown in Fig. 1 and the single scattered polarization in Fig. 4. The sign of the polarization produced by the haze phase matrix is, over most of the range, opposite to that produced by Rayleigh scattering. This produces interesting effects in the polarization of the reflected and transmitted radiation.

The surface of the earth has a considerable effect on both the radiance and polarization. Although it is not realistic, a Lambert surface is considered at the bottom of the atmosphere. It is the simplest surface to model, and little is known about the polarization effects of real surfaces. Three values of the surface albedo are considered, $A = 0, 0.15$, and 0.90 . The zero value is considered for two reasons: it is easy to calculate and in comparison with other values it helps to demonstrate the effect of a real surface on the radiation reflected and transmitted. A reasonable average value for the albedo of the various surfaces on the earth is 0.15 . Since a snow covered surface closely approximates a Lambert surface with an albedo of about 0.9 , this value was also included in the calculations.

The transmitted radiance at the earth's surface for both models and all three surface albedos is shown in Fig. 12 for the sun at the zenith ($\mu_0 = 1$). The single scattered radiance is also given for both models. The radiance is greater for the normal than for the one-third normal atmosphere at all angles of observation except near the horizon. There is horizon brightening for the one-third normal atmosphere and horizon darkening for the normal atmosphere. The explanation is connected with the fact that the transmitted radiation through a pure Rayleigh atmosphere shows horizon brightening up to an optical depth of about 0.25 and horizon darkening at greater optical depths.

The polarization of the transmitted photons is shown in Fig. 13 for the same cases. The one-third normal atmosphere has a larger polarization at all angles in each case than the normal model. The cause of this is twofold. The optical depth is smaller for the one-third normal atmosphere and in general, the less multiple scattering that occurs, the less the dilution from the single scattering polarization. The second effect is due to the single scattering polarization. The greater the amount of aerosol in the atmosphere, the greater effect the opposite sign of the aerosol single scattering polarization will have in decreasing the Rayleigh single scattering polarization. This is seen in the two single scattering curves in Fig. 13. The one-third normal atmosphere single scattering has its maximum closer to the horizon, that is closer to a 90° single scattering angle, than is the case for the normal atmosphere curves. As the amount of aerosol increases, this peak moves toward the zenith. The polarization decreases as the surface albedo increases. This effect is expected since the increased radiance due to the surface is randomly polarized and thus decreases the overall polarization.

The reflected radiance at the top of the atmosphere is given in Fig. 14 when the sun is at the zenith. The slight increase in radiance at the antisolar point ($\mu = 1$) for the cases of single scattering and of $A = 0$ is due to the glory in the aerosol phase function. The glory is more evident in the normal atmosphere case because of the larger effect of the aerosol.

When $A = 0.15$ and 0.9 the radiance varies little with the angle of observation. There is an interesting point. When $A = 0$, the radiance is greater at most angles for the normal aerosol model than for the one-third normal model. On the other hand the one-third normal radiance is greater for the non-zero albedo cases. The reason is that the total downward flux including the direct solar beam is greater for the one-third than for the normal aerosol model. When the albedo is non-zero, this extra contribution after reflection from the lower surface makes the reflected radiance at the top of the atmosphere greater for the one-third than for the normal model.

The polarization of the reflected photons is shown in Fig. 15. The polarization as expected decreases rapidly as the surface albedo increases. If the scattering were entirely Rayleigh, the neutral point would be at the nadir ($\mu = 1$). The neutral point for the normal atmosphere model is at about $\mu = 0.92$ (23°) for single scattering and $\mu = 0.94$ (20°) for the normal aerosol amount. It does not vary appreciably with the surface albedo. The aerosols cause the neutral point to move away from the nadir. The large positive peak in the aerosol polarization cancels the negative Rayleigh polarization at an angle determined by the ratio of aerosol to Rayleigh scattering.

As an example of another solar angle, the polarization of the transmitted photons is shown in Fig. 16 when $\mu_0 = 0.171$ (80.18°) in the principal plane. The maximum polarization occurs at $\mu = 0.98$ which is about 90° from the incident beam. This peak is characteristic of Rayleigh scattering. The single scattering peak for Rayleigh scattering would be precisely 90° from the incident direction and the polarization would be 100%. Deviations from this are caused by the finite optical thickness of the atmosphere and by the aerosol scattering. The maximum polarization in Fig. 16 is 0.601 and 0.778 for one-third normal and for normal aerosol amounts respectively. The neutral points are changed by the introduction of the aerosols. The Arago points change appreciably as the aerosol amount changes from one-third to normal, while there is relatively little change in the position of the Babinet points.

The polarization of the transmitted radiation out of the principal plane is shown in Figs. 17 and 18 for the azimuthal angles $\phi = 30^\circ$ and 150° and $\phi = 90^\circ$ respectively. Note that neutral points do not occur out of the principal plane. At most angles the polarization increases as ϕ approaches 90° with

the curves becoming almost flat at $\phi = 90^\circ$. In the $\phi = 90^\circ$ plane, the single scattering angle is almost constant and very close to 90° . At this angle the maximum single scattering polarization occurs for Rayleigh scattering. Thus the polarization in general increases and becomes almost constant as the $\phi = 90^\circ$ plane is approached.

If a and b are proportional to the major and minor axes respectively of the ellipse described by the end point of the electric vector, the ratio $b/a = \tan \beta$ is defined as the measure of the ellipticity of the radiation. It can be computed directly from the Stokes parameters of the radiation. The ellipticity, $\tan \beta$, for the transmitted radiation is shown in Fig. 19 for $\mu_0 = 0.171$ and $\phi = 30^\circ$ and 150° . The ellipticity changes very little with the surface albedo. Thus the only curves shown are for $A = 0$. Our model for the atmosphere assumed spherical aerosol particles. The phase matrix for spherical particles has a zero entry in the fourth row and first column; thus incident unpolarized radiation cannot create a circular component from a single scattering. In addition, in the Rayleigh phase matrix, all entries in the fourth row are zero except for the fourth column. Therefore a Rayleigh scattering atmosphere cannot create a circular component even by multiple scattering. It can only alter an already existing component.

The absolute value of the ellipticity is greater for the normal than for the one-third normal aerosol model, except near the zeros of the function (see Fig. 19). The shape of the curves is very similar for both models. The ellipticity increases in magnitude rapidly as the horizon is approached. Other results not shown here show that this increase near the horizon is not as large in the $\phi = 90^\circ$ plane. A comparison of the results for the polarization and ellipticity shows that in general the ellipticity is large in a region where the polarization is small and visa versa. When the four Stokes components are I, Q, U, V , the polarization P is

$$P = \frac{(Q^2 + U^2 + V^2)^{1/2}}{I}$$

and the ellipticity b/a is

$$b/a = \tan \beta = -\tan\left\{\frac{1}{2} \sin^{-1} \frac{V}{(Q^2 + U^2 + V^2)^{1/2}}\right\} = -\frac{1}{2} V(Q^2 + U^2 + V^2)^{-1/2}.$$

For these equations it is seen that whenever $Q^2 + U^2 + V^2$ is nearly as large as I that the polarization is large and the ellipticity is small. The ellipticity is zero whenever V is zero. It has been claimed that the values of the ellipticity in the region where the polarization is small are uncertain due to truncation errors. We believe that our values are real and are not caused by truncation errors because all of the values of P, χ (the angle of polarization), and b/a are very well behaved in this region.

It was stated earlier that a Rayleigh atmosphere could not produce an elliptically polarized beam. A comparison of the ellipticity values for the real atmosphere model with those for a haze L layer of corresponding depth shows the same features in both. The sharpness of some of the haze L features are smoothed out in the real atmosphere by scattering from the Rayleigh component.

We next consider the radiation observed at the top of the atmosphere as reflected from our real atmosphere models. The reflected radiance for $\mu_0 = 0.171$ in the principal plane is shown in Fig. 20. Curves are shown for all three surface albedos and for both models as well as for the single scattering curves. In the forward scattering half plane ($\phi = 0^\circ$), the normal atmosphere has the larger intensity in general, while in the $\phi = 180^\circ$ half plane, the one-third normal atmosphere has the larger intensity. The forward scattering peak of the aerosols is more pronounced in the normal model, thus making the radiance greater in this case near the solar horizon. The back scattering is more dependent upon the Rayleigh phase function and it is more predominant in the one-third normal model.

The polarization of the reflected radiation in the principal plane is shown in Fig. 21 for $\mu_0 = 0.171$. The Babinet neutral point is seen in the $\phi = 180^\circ$ half plane, but the Brewster or Arago point is not visible. It may be so close to the horizon that the data does not show it or there may not be one in this case. There are two neutral points for the normal aerosol model. The polarization near the nadir is greater for the one-third normal model than for the normal model when the surface albedo is zero. However, when $A = 0.9$, the normal model actually has the larger polarization. This is related to the greater absorption in the normal model and consequent smaller downward flux which reaches the lower surface and is reflected as unpolarized radiation.

The ellipticity of the reflected radiation is shown in Fig. 22 for $\mu_0 = 0.171$ and $\phi = 30^\circ$ and 150° . The ellipticity for the normal and one-third normal models is again similar with the normal model having the larger ellipticity. The ellipticity of the reflected radiation is smaller than that of the transmitted. This effect is to be expected since double and higher order scatterings, with the second or higher order scatterings by the aerosol, cause ellipticity. A photon reaching the surface of the atmosphere has traversed an optical path at least equal to the optical depth of the atmosphere and has traveled through all of the aerosol. A photon escaping from the top of the atmosphere can traverse an optical path less than the total depth of the atmosphere and can miss most of the aerosol which is near the bottom. Thus it is more probable for a photon reaching the surface to be elliptically polarized and thus the transmitted ellipticity is greater.

When the curves for the ellipticity of the reflected radiation from the real atmosphere model are compared with those for a haze L layer, it is found that the Rayleigh scattering changes their shape considerably. As one example, the ellipticity is negative in the entire half plane $\phi = 30^\circ$ for a haze L layer, but has both positive and negative regions for the real atmosphere model (Fig. 22).

Recently some excellent measurements of the polarization of skylight have been reported by Coulson, K. L. *et al* (1974). These measurements were made at Mauna Loa Observatory, Hawaii at an altitude of 3416 m. Only a limited comparison can be made with our calculations, since our results for the transmitted radiation are at sea level and at a wavelength of $0.55 \mu\text{m}$, a wavelength not included in their measurements. The maximum polarization of downwelling radiation at any zenith angle as a function of the sun's elevation is shown in Fig. 23 for the normal, one-third normal, and for two Rayleigh cases. The shapes of the curves are all similar, but the values of the maximum polarization are less for the real than for a Rayleigh atmosphere. Coulson's data shows large fluctuations, presumably due to the day-to-day variations of the content of the atmosphere. Their data suggest a decrease in the maximum polarization with an increase in the solar elevation. Their maximum polarizations were larger than our calculated ones, a fact easily explained by their 3416 m altitude.

The angular distance between the Babinet points or the neutral point above the sun, versus solar elevation is shown in Fig. 24 for the normal and one-third normal models. The position of the neutral points is virtually independent of the surface albedo. An interesting feature is that the Babinet point is closer to the sun for the normal than for the one-third normal atmosphere. The explanation is connected with the polarization from the aerosols which has the opposite sign from Rayleigh scattering and thus keeps the neutral points closer to the sun in spite of the larger optical thickness of the normal model.

Coulson's measurements for the position of the Babinet point at a wavelength of $0.40 \mu\text{m}$ again have considerable scatter, but are qualitatively similar to the curves in Fig. 24. The angular position is as much as twice as large as that given by the calculations, which may be due to the difference in wavelength and a correspondingly larger optical thickness of the atmosphere at the ultraviolet wavelength.

The angular distance between the Brewster point and the solar point is shown in Fig. 25 as a function of solar elevation. Coulson's data again has a great deal of scatter, but seems to follow the linear trend predicted by the calculations.

4. RADIATION IN THE ATMOSPHERE-OCEAN SYSTEM

A determination of the complete radiation field including polarization in a realistic model of the atmosphere with an ocean surface below seems beyond the capabilities of present day computers when a technique similar to the matrix operator method is used. This is an example of a problem that can be profitably solved by a Monte Carlo method. This work was done by Plass, G. N., Kattawar, G. W., and Guinn, J. A., Jr. The solar photons undergo absorption and multiple scattering by aerosols and atmospheric molecules, reflection and refraction at the ocean surface, and further absorption and multiple scattering by hydrosols and water molecules of the ocean. Additional complexity arises from scattering and absorption by the ocean floor and from refraction and reflection (including total internal reflection at some angles) of the upwelling light at the ocean boundary. The resulting radiation field exhibits high polarization in certain directions as a result of these many different kinds of photon interactions.

In a typical Monte Carlo calculation the sequence of events is as follows. The position of the first collision of the solar photon is determined. If it is in the atmosphere, random numbers determine from the cross-section ratios for the appropriate atmospheric layer whether it is a Rayleigh (molecular) or Mie (aerosols) collision. The method of statistical weights is used throughout the program (Plass, G. N., and Kattawar, G. W., 1971) and the absorption is accounted for by simply multiplying the weight by the ratio of the total scattering cross-section to the total cross-section for all processes. A photon history is terminated only when the weight falls below some pre-assigned value (taken as 10^{-6} in all calculations reported here). The scattering angle is chosen from the distribution obtained from the single-scattering matrix for either Rayleigh or aerosol scattering, as appropriate. The Stokes vector is rotated into the scattering plane before each collision and rotated back into the meridian plane afterward by the use of rotation matrices. The process is repeated until the photon reaches the atmosphere-ocean surface.

At the atmosphere-ocean interface a random number is used in the Monte Carlo calculation to determine whether a given photon is reflected or transmitted at the surface; the probability for reflection and transmission at a particular angle of incidence is calculated from the Fresnel equations with a refractive index of 1.338. When the photons are incident from below the surface, the calculations take account of total internal reflection at the appropriate angles. When the photon undergoes a collision within the ocean, random numbers determine from the cross-section ratio whether the photon is scattered from a Rayleigh (molecular) or Mie (hydrosol) center, and the weight is modified appropriately to account for absorption. The new scattering angle is determined from the Rayleigh or the hydrosol single-scattering matrix as appropriate.

A typical computer run on the CDC 7600 takes 3 1/2 minutes, during which time 550,000 photon collisions are processed. The results give the four components of the Stokes vector, the degree and direction of polarization, and the ellipticity of the upward and downward radiance as a function of the zenith and azimuthal angles. All of these results are given for 11 different detectors, which are located at various heights in the atmosphere and ocean.

A small sample of the results that we have calculated is shown in the next few figures. The radiance is given in Fig. 26 for a solar zenith angle of 31.79° . Both the upward and downward radiation are shown on one figure. One finds from left to right: solar horizon, incident sun, zenith, anti-solar horizon, nadir, reflected sun (above ocean surface), solar horizon. The downward radiation is represented on the left half of the graph and the upward on the right half. All photons within 30° in azimuth of the principal plane have been averaged into the results. A wavelength of $0.46 \mu\text{m}$ and a clear ocean model (ratio of total scattering cross-section to total cross-section is 0.514 and ratio of Rayleigh scattering cross-section to total cross-section is 0.218) are assumed. The radiance is shown

at five detector locations: top of atmosphere (triangle with point up); just above ocean surface (cross); just below ocean surface (circle); an optical depth of unity below the ocean surface (square).

The downward radiance just above the ocean surface decreases appreciably just after one passes through the zenith and then slowly increases toward the antisolar horizon. The upward radiance has a minimum near the nadir. The most interesting feature is the variation of the downward radiance just below the ocean surface. The critical angle is at 48.36° ($\mu = -0.6644$); all radiation from the direct sunlight and from the sky enters a calm ocean within the cone bounded by this 48.36° angle from the zenith. Thus the downward radiance is much larger within this cone than outside of it. Outside of the cone the only downward radiation arises from upwelling light (usually very weak compared to the downwelling light) that undergoes total internal reflection at the underside of the ocean surface. The large drop of the radiance outside of the critical angle is evident in Fig. 26.

Other calculations not further reported here show that the upwelling light can be used as a measure of the turbidity of the ocean. The minimum value of the upward radiance just above the ocean surface as a function of the nadir angle of observation increases 640% from a turbid to a clear ocean model. Even at the top of the atmosphere the increase is 40%.

The polarization of the radiation is shown in Fig. 27 for the same solar zenith angle as in the previous figure. The polarization of the downward radiation just above the ocean surface (crosses) decreases from the solar horizon to a small value at the zenith and then increases to a relatively large value near the antisolar horizon. This increase is caused by nearly right angle scattering from Rayleigh scattering centers. The polarization of the upward radiation decreases from the anti-solar horizon to the nadir and increases to a large value (0.72) at the Brewster angle (53.23° ; $\mu = 0.60$) and then decreases somewhat toward the solar horizon. The polarization of the upwelling light observed at the top of the atmosphere (triangle, point up) is appreciable except near the nadir. It is large over a wide range of angles around the Brewster angle.

It is interesting to point out that the downwelling radiation just below the ocean surface is elliptically polarized (Fig. 28). This figure assumes a solar zenith angle of 70.12° . The top half is for the principal plane and the bottom half for a plane at right angles to the principal plane. The ellipticity is appreciable at all viewing angles outside of the critical cone that admits light from the direct sun and sky. The ellipticity arises from the total internal reflection of the water at the underside of the ocean surface.

5. CONCLUSIONS

The solution of a wide variety of problems in multiple scattering can be obtained by the matrix operator and Monte Carlo methods. These include the calculation of the radiance and polarization of the radiation scattered from cloud layers of various types and thicknesses as well as from models of the real atmosphere with varying aerosol amounts over both land and ocean surfaces. The results of such calculation enable us to understand the dependence of the radiation on the many different determining factors in a real atmosphere.

This research was supported in part by grant NGR-44-001-117 from the National Aeronautics and Space Administration.

REFERENCES

- Coulson, K.L., R.L. Walraven, and L.B. Sooho, 1974, "Polarization of Skylight at an Altitude of 3416 m (11200 ft.) on Mauna Loa, Hawaii", Final Report, Grant No. N-22-161-72(N) and NGL 05-003-404, Dept. of Agricultural Engineering, University of California, Davis, Calif.
- Dave, J.V., 1970, "Coefficients of the Legendre and Fourier Series for the Scattering Functions of Spherical Particles", Appl. Opt. 9, 1888 (1970).
- Diermendjian, D., 1969, "Electromagnetic Scattering on Spherical Polydispersions", Elsevier, New York.
- Elterman, L., R. Wexler, and D.T. Chang, 1969, "Features of Tropospheric and Stratospheric Dust", Appl. Opt., 8, 893.
- Hansen, J. E., 1969, "Exact and Approximate Solutions for Multiple Scattering by Cloudy and Hazy Planetary Atmospheres", J. Atmosph. Sci., 26, 478.
- Herman, B.M., S.R. Browning, and R.J. Curran, 1971, "The Effect of Atmospheric Aerosols on Scattered Sunlight", J. Atmosph. Sci., 28, 419.
- Kattawar, G.W., S.J. Hitzfelder, and J. Binstock, 1973, "An Explicit Form of the Mie Phase Matrix for Multiple Scattering Calculations in the I, Q, U, and V Representation", J. Atmosph. Sci., 30, 289.
- Plass, G.N., and G.W. Kattawar, 1971, "Radiance and polarization of the Earth's Atmosphere with Haze and Clouds", J. Atmosph. Sci., 28, 1187.
- Plass, G.N., G.W. Kattawar, and F. E. Catchings, 1973, "Matrix Operator Theory of Radiative Transfer. 1: Rayleigh Scattering; 2: Scattering from Maritime Haze", Appl. Opt., 12, 314 and 1071.
- Sekera, Z., 1956, "Global Radiation Resulting from Multiple Scattering in a Rayleigh Atmosphere", Adv. Geophys., 3, 43.

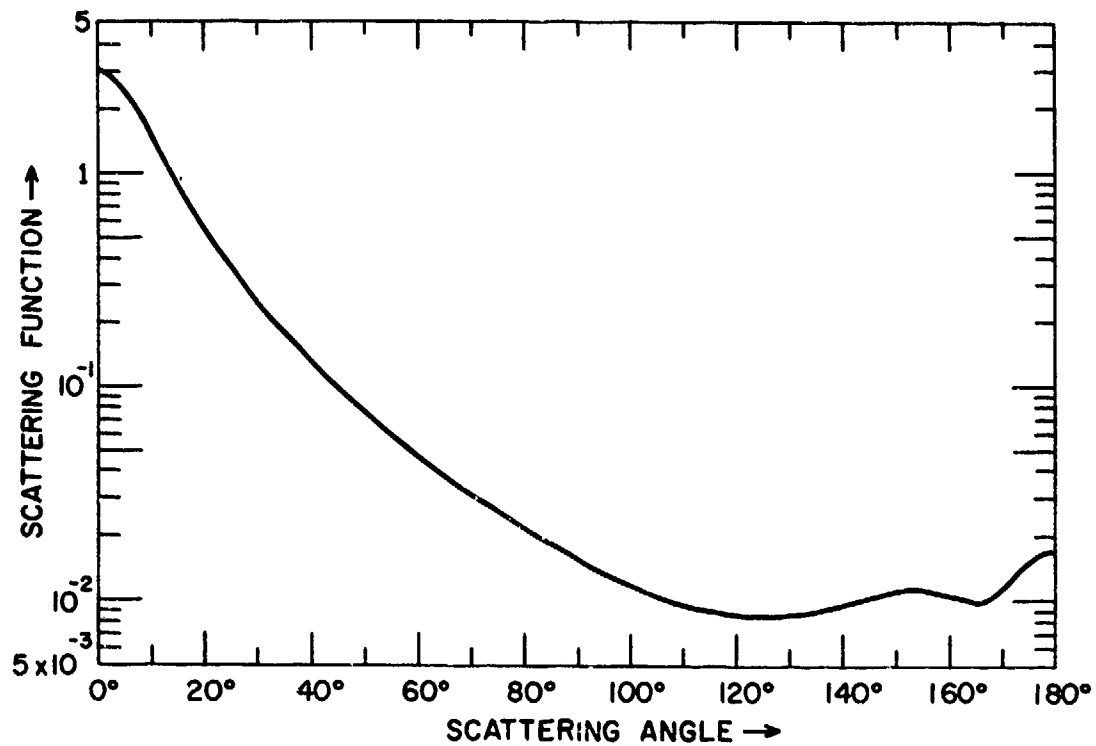


Fig. 1. Intensity of single scattered radiation from haze L phase matrix as a function of the scattering angle.

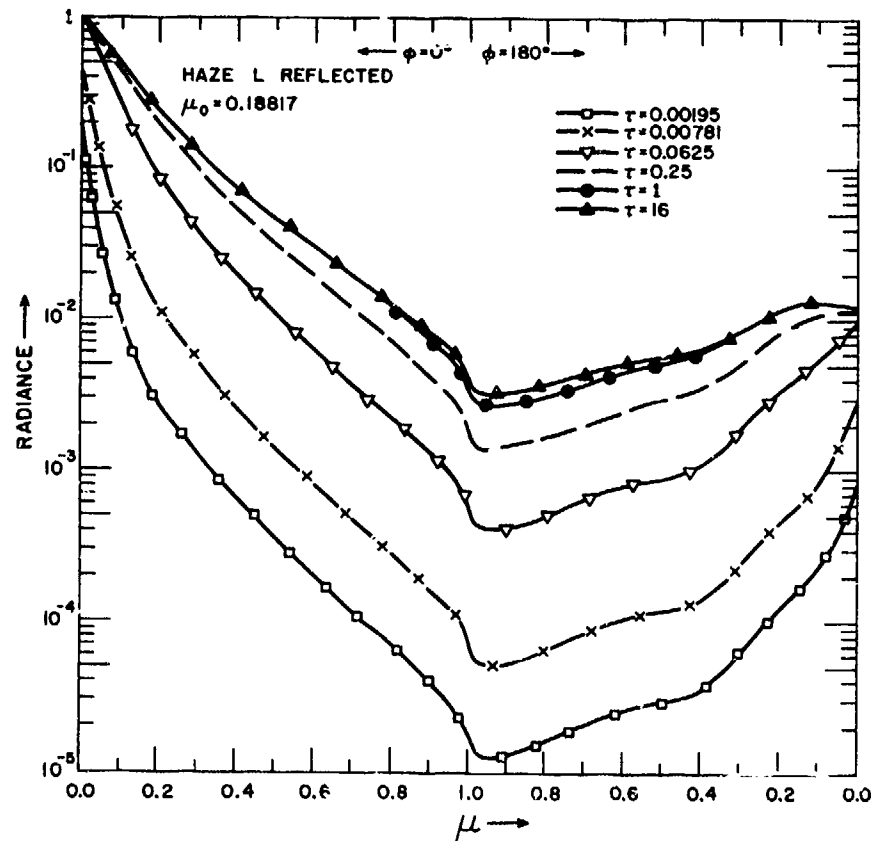


Fig. 2. Upward radiance for haze L, μ_0 (cosine of nadir angle) = 0.18817, A (surface albedo) = 0, and ϕ (azimuthal angle) = 0° and 180° , observed at upper surface of layer. The left hand portion of the graph is for an azimuthal angle $\phi = 0^\circ$ and the right hand portion is for $\phi = 180^\circ$. The solar horizon is at the left of the figure, the nadir is at the center, followed by the antisolar point and the antisolar horizon at the right. Curves are given for layers with various values of the optical thickness τ .

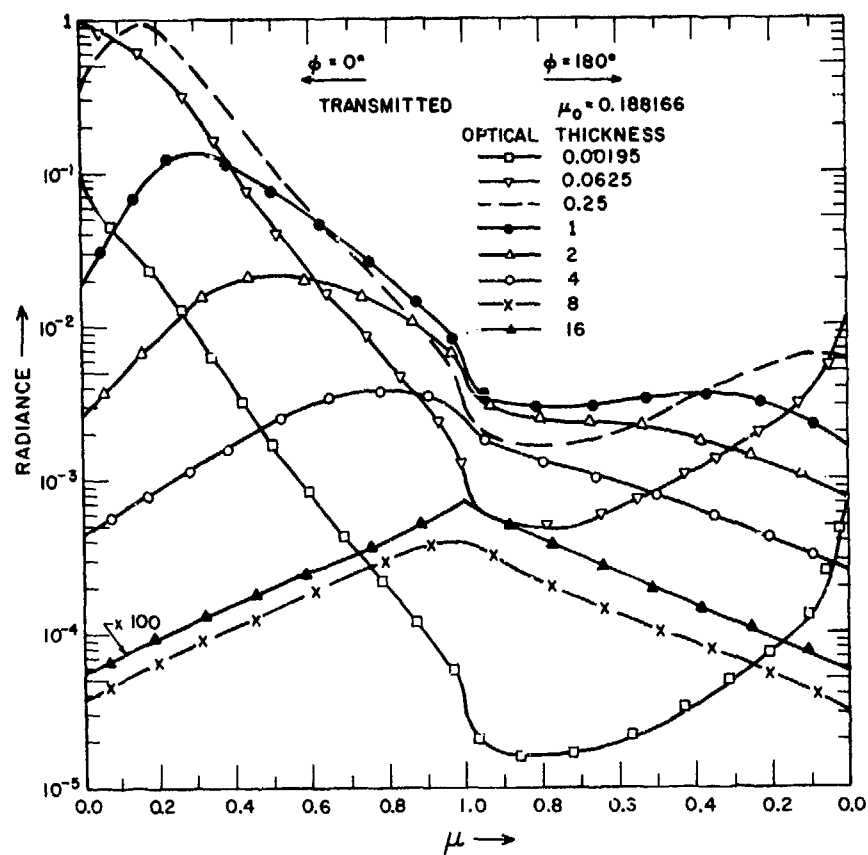


Fig. 3. Downward radiance for haze L, $\mu_0 = 0.18817$, $A = 0$, and $\phi = 0^\circ$ and 180° , observed at lower surface of layer. The azimuthal angle $\phi = 0^\circ$ for the left hand portion of the graph and 180° for the right. The solar horizon is at the left of the figure, followed by the zenith, and the anti-solar horizon on the right.

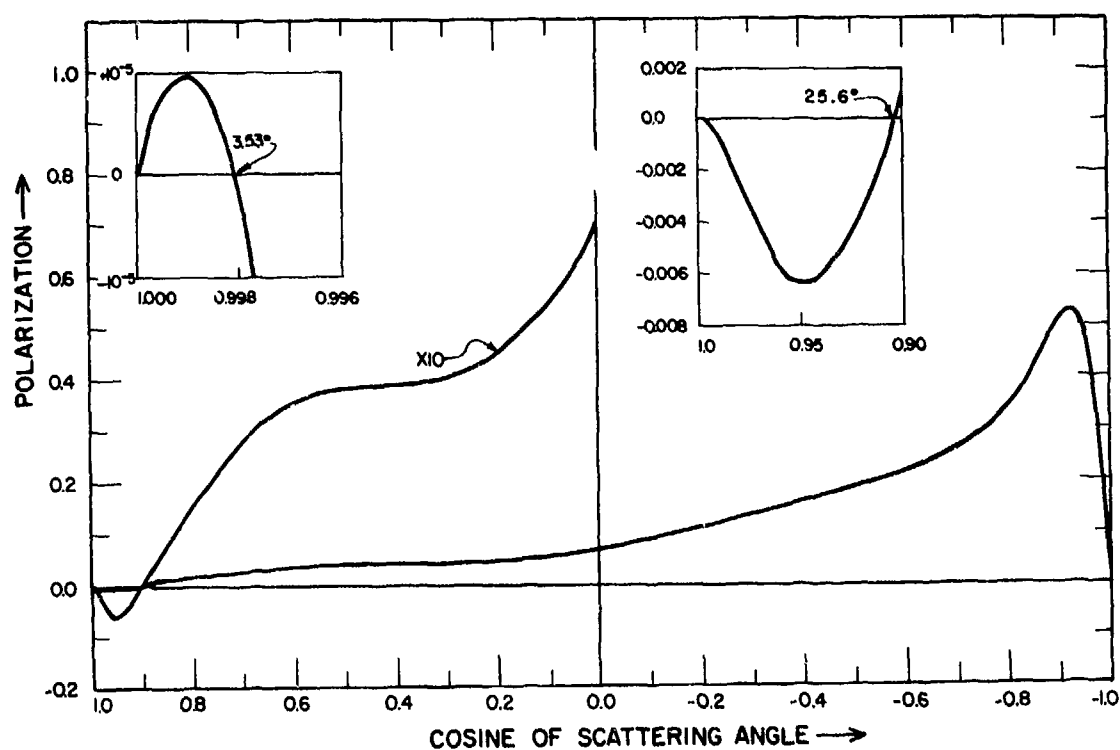


Fig. 4. Polarization of single scattered photons from haze L. The two insets show the polarization for scattering angles near 0° . The abscissa is the cosine of the scattering angle.

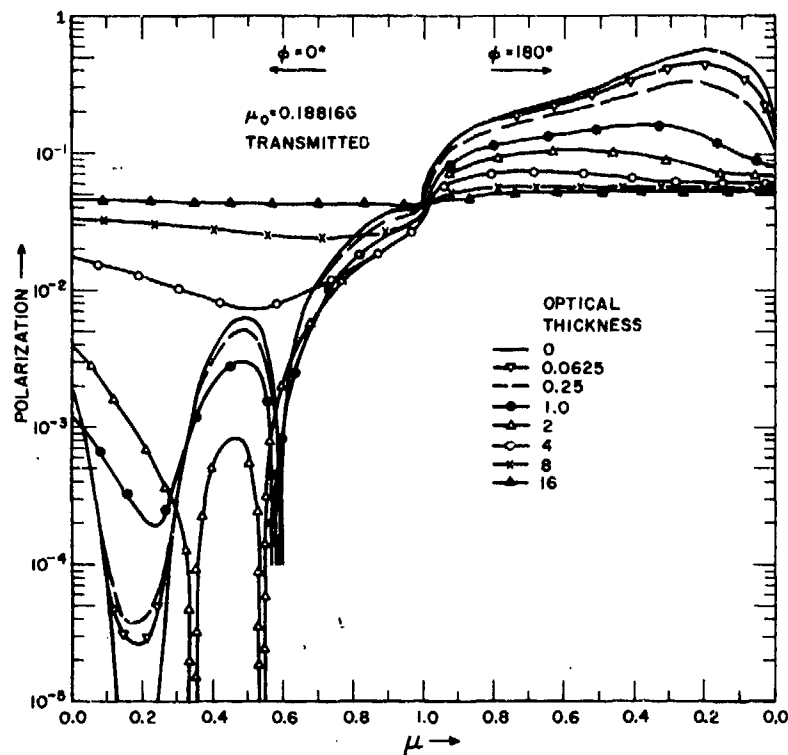


Fig. 5. Polarization of the downward radiation for haze L for $\mu_0 = 0.18817$, $A = 0$, and $\phi = 0^\circ$ and 180° for layers of various optical thicknesses.

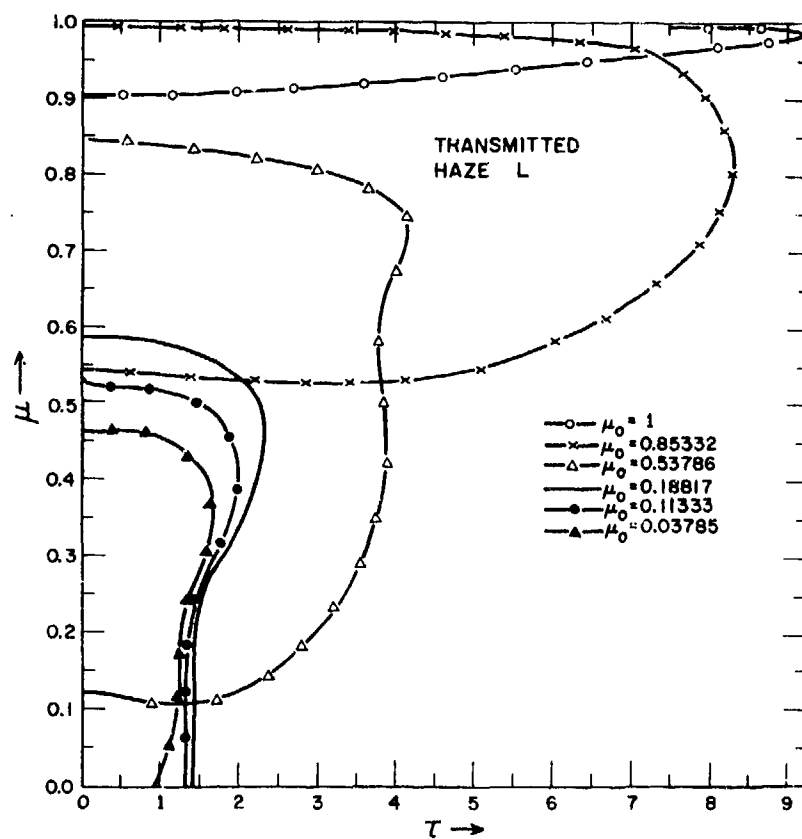


Fig. 6. Position of non-Rayleigh neutral points for photons transmitted through a haze L layer. Curves are given for six different solar zenith angles. The ordinate is the cosine of the zenith angle and the abscissa is the optical thickness of the scattering layer.

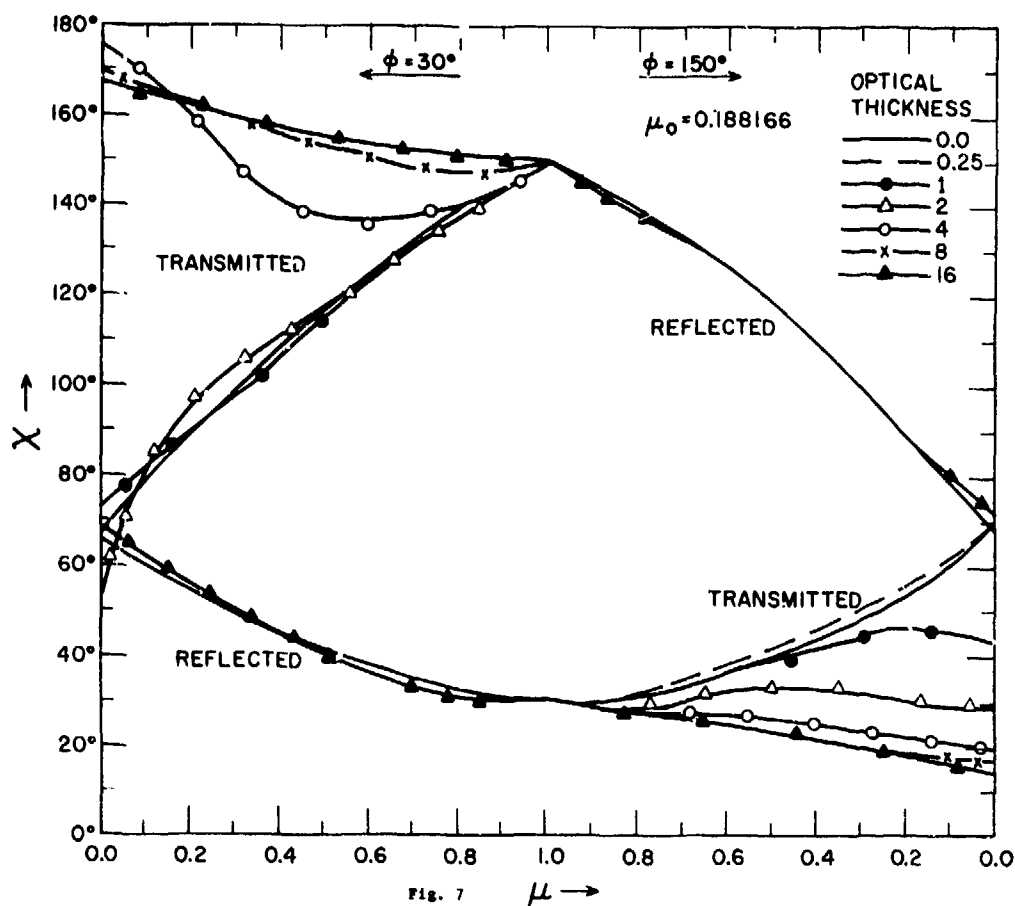


Fig. 7

Fig. 7. The angle χ which the direction of polarization makes with the direction of the meridian plane containing the final photon direction. Curves are given for the photons reflected from and transmitted through a layer of optical thickness τ for $\mu_0 = 0.18817$, $A = 0$, and $\phi = 30^\circ$ and 150° .

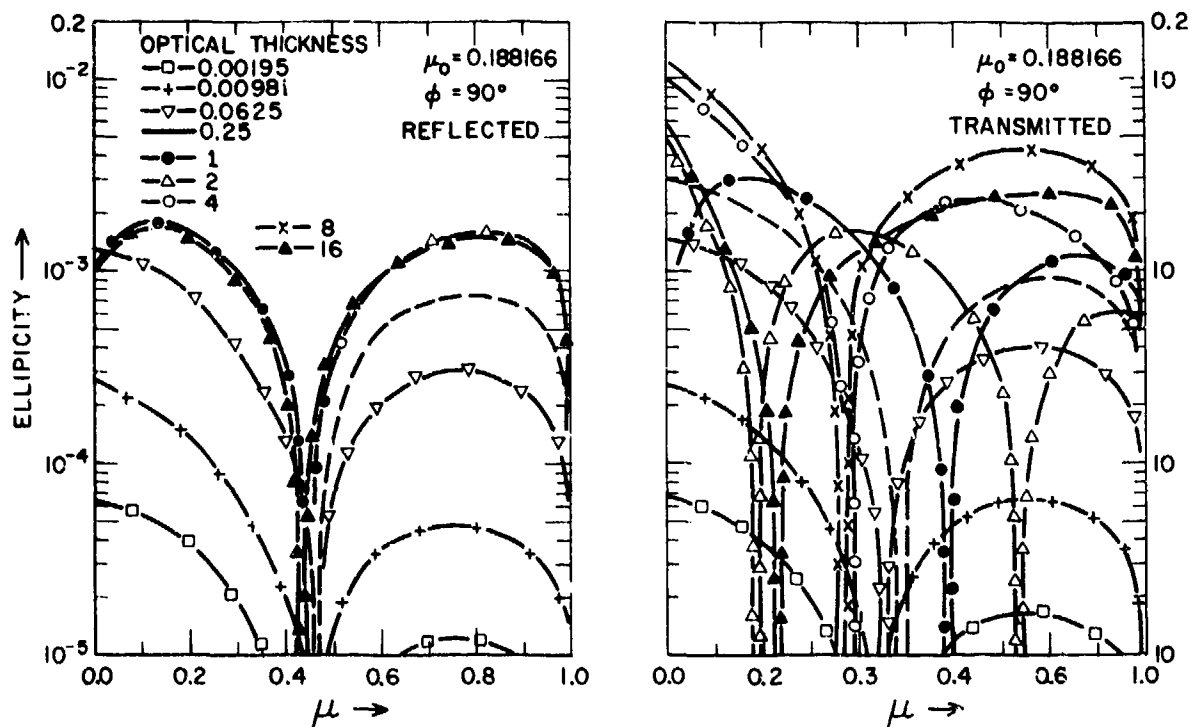


Fig. 8. The ellipticity of the photons reflected from and transmitted through a layer of optical thickness τ . Curves are given for $\mu_0 = 0.18817$, $A = 0$, and $\phi = 90^\circ$.

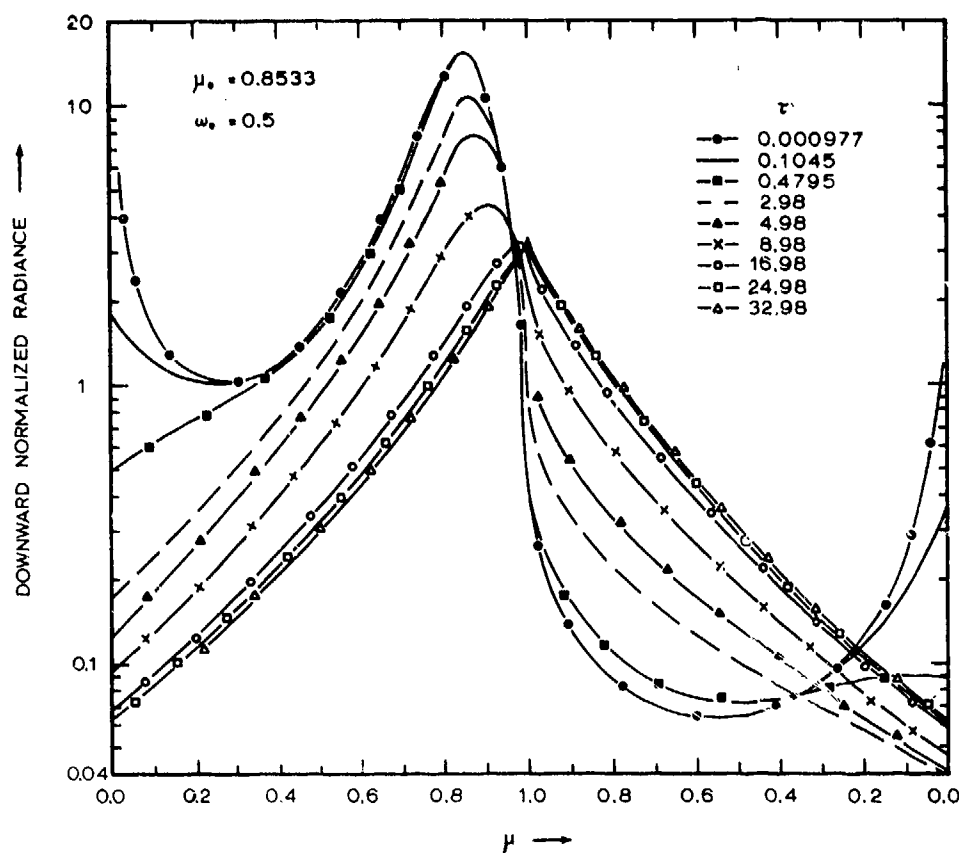


Fig. 9. Downward normalized interior radiance for $\mu_0 = 0.85332$ and ω_0 (single scattering albedo) = 0.5 for various values of τ (optical depth within medium measured from upper surface).

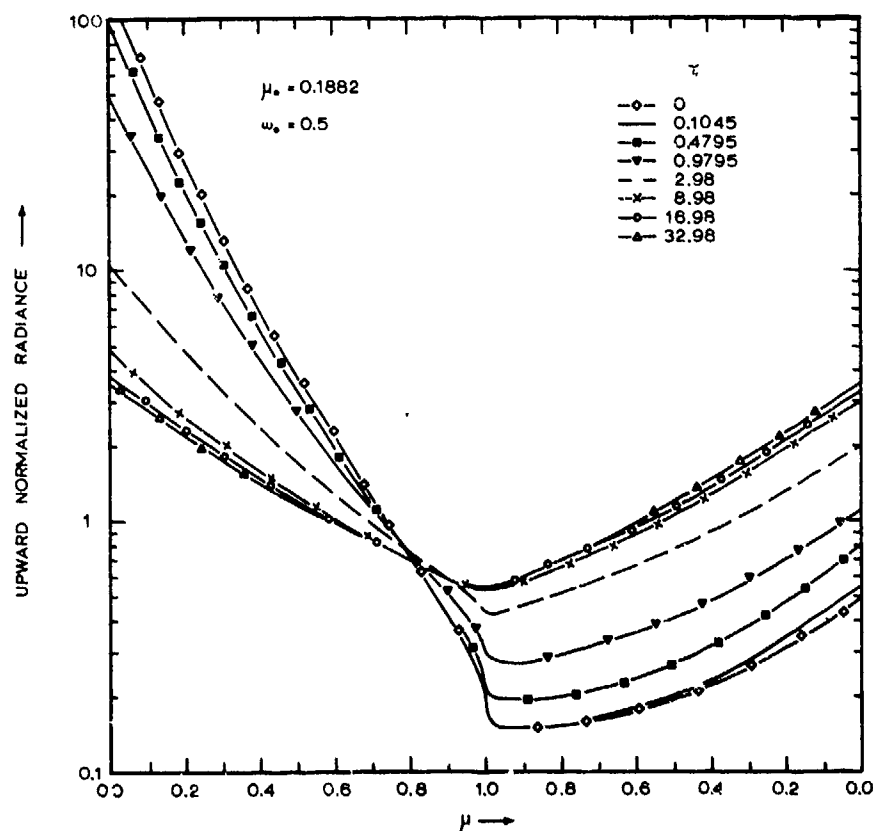


Fig. 10. Upward normalized interior radiance for $\mu_0 = 0.18817$ and $\omega_0 = 0.5$.

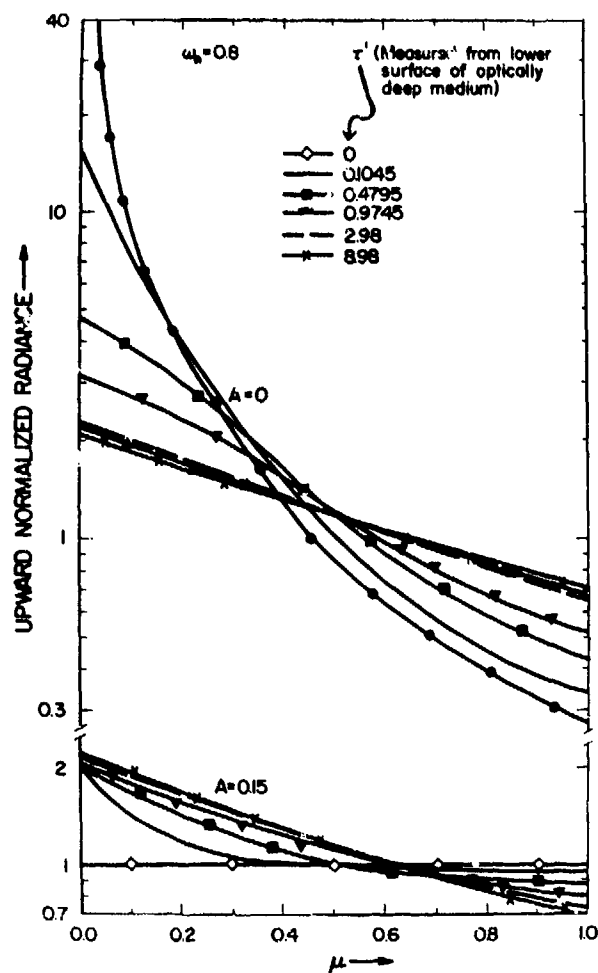


Fig. 11. Upward normalized interior radiance for $\omega_0 = 0.8$ and $A = 0$ (upper curves) and $A = 0.15$ (lower curves). The optical thickness τ' is measured from the lower surface of an optically deep medium.

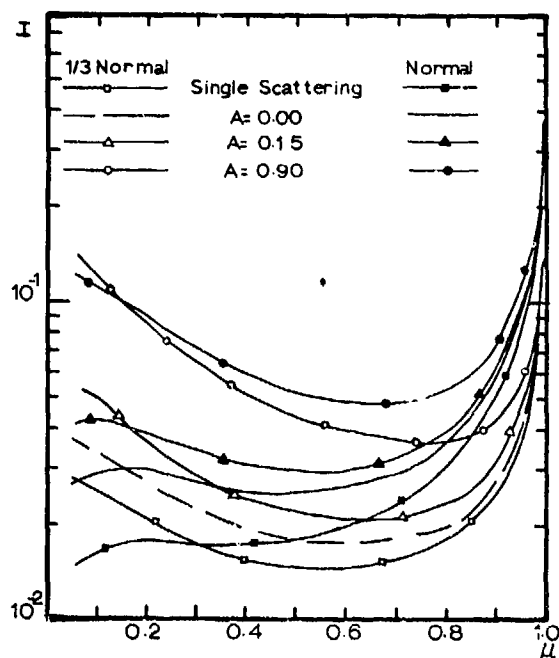


Fig. 12. Transmitted radiance at earth's surface for real atmosphere model, $\mu_0 = 1$ (sun at zenith), $A = 0, 0.15$, and 0.9 , and for the normal aerosol amount. Curves are also shown for the radiance due to single scattering only.

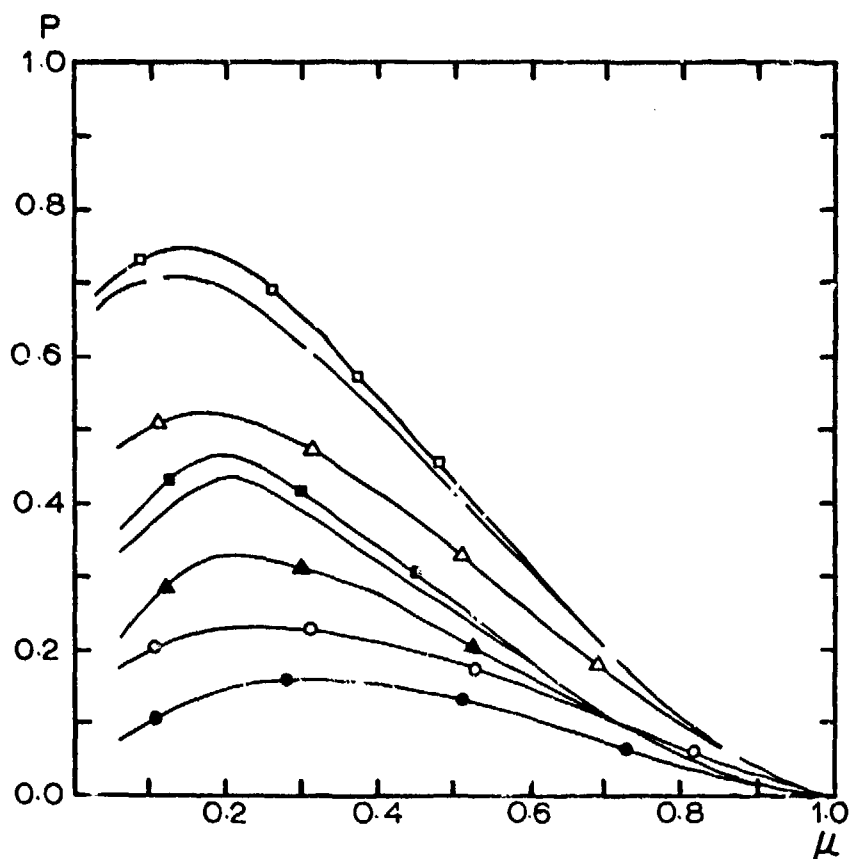


Fig. 13. Polarization of transmitted photons at earth's surface. See Fig. 12 for key.

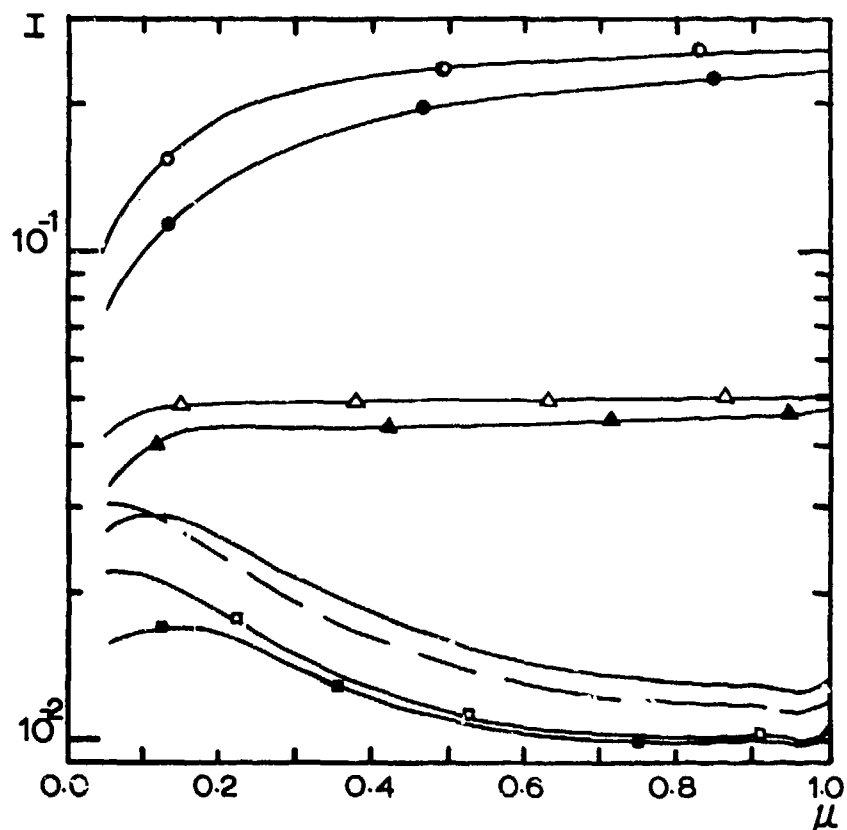


Fig. 14. Reflected radiance at top of earth's atmosphere for real atmosphere model. See Fig. 12 for key.

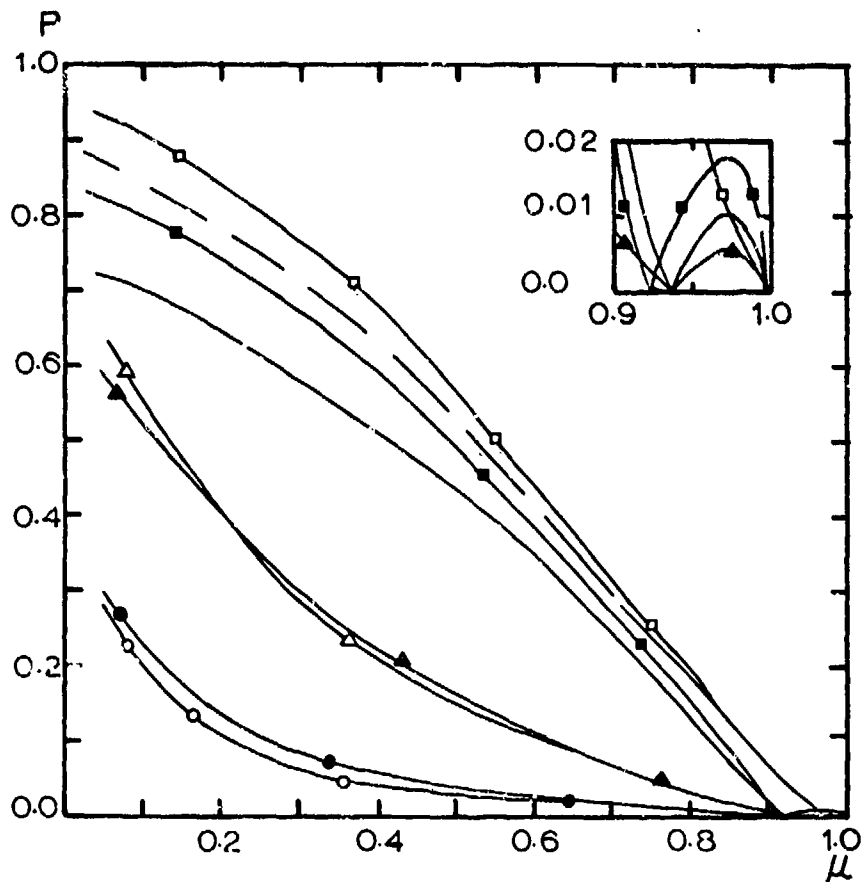


Fig. 15. Polarization of reflected photons at top of earth's atmosphere. See Fig. 12 for key.

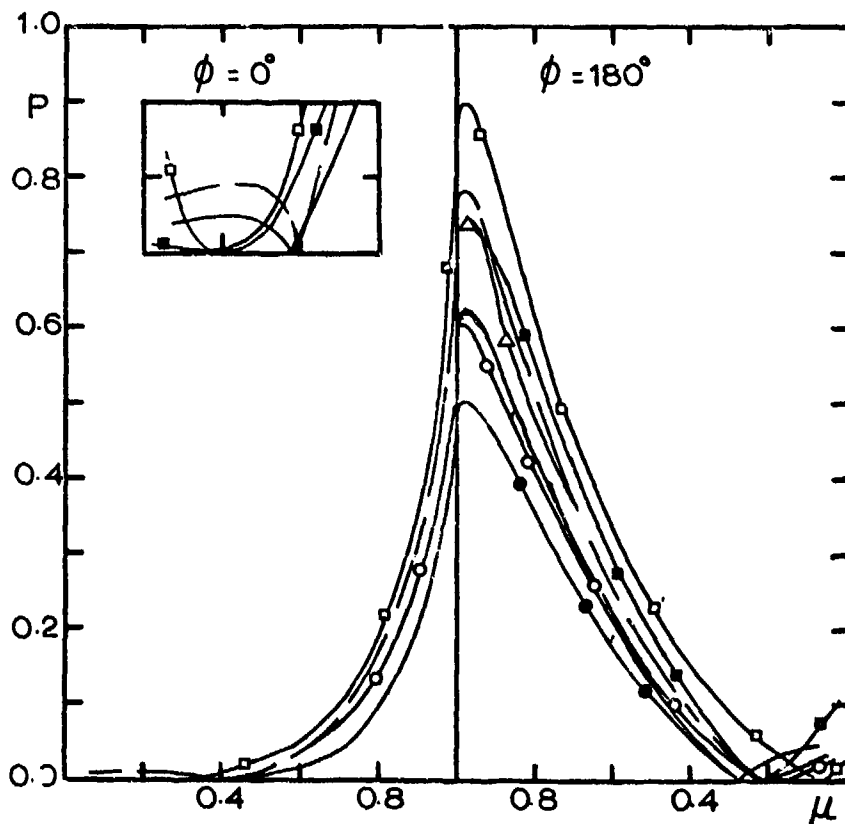


Fig. 16. Polarization of transmitted photons at earth's surface for $\mu_0 = 0.171$ and $\phi = 0^\circ$ and 180° . See Fig. 12 for key.

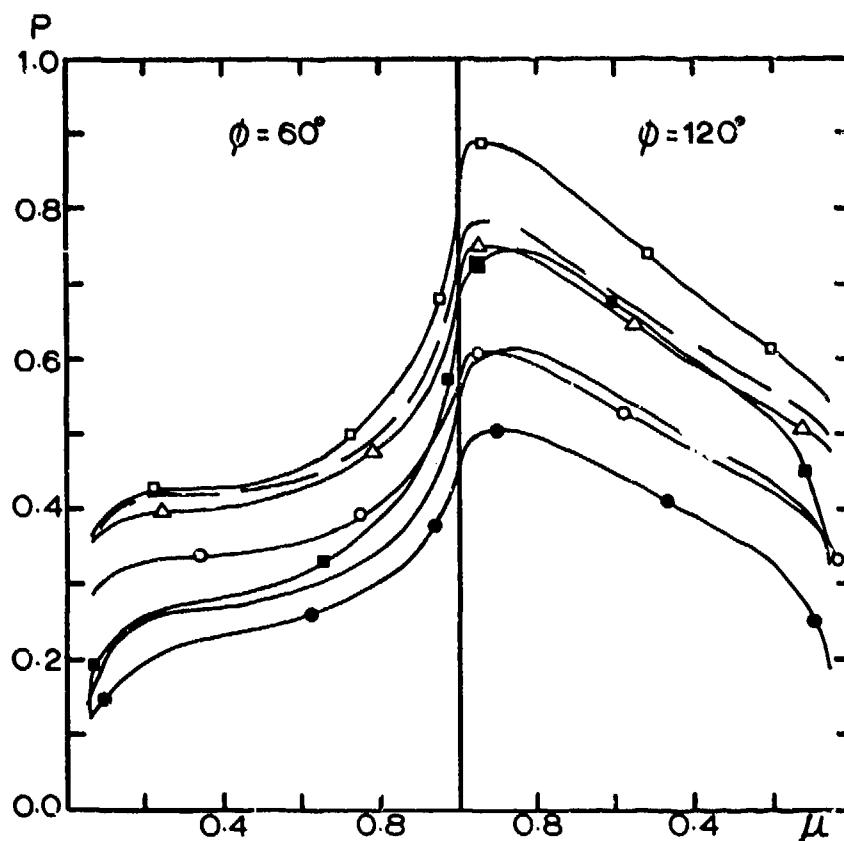


Fig. 17. Polarization of transmitted photons at earth's surface for $\mu_0 = 0.171$ and $\phi = 60^\circ$ and 120° . See Fig. 12 for key.

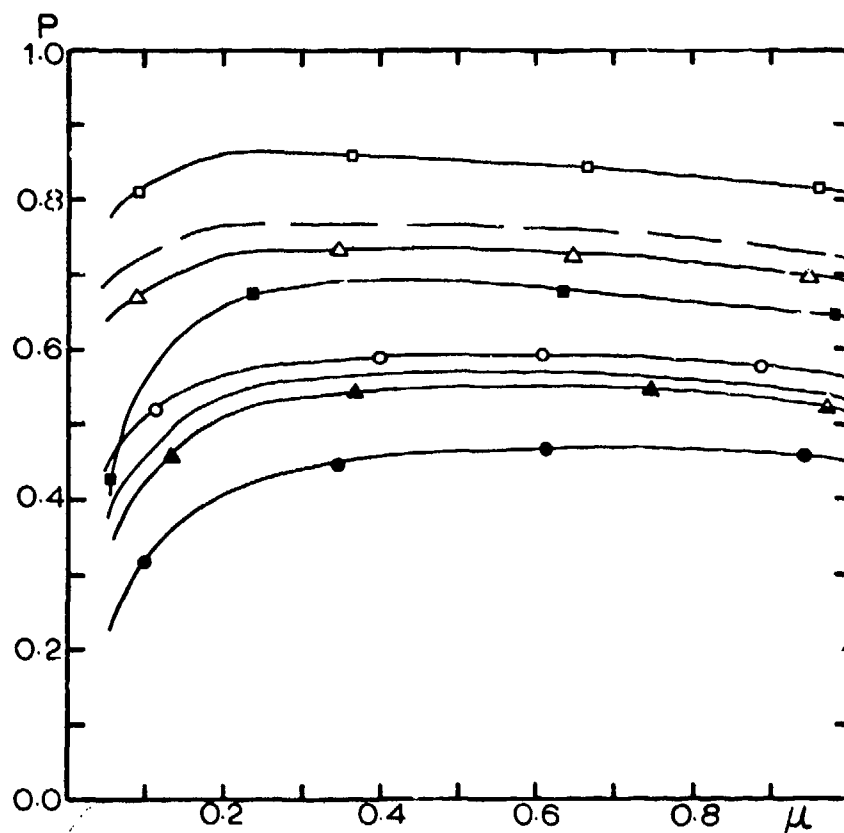


Fig. 18. Polarization of transmitted photons at earth's surface for $\mu_0 = 0.171$ and $\phi = 90^\circ$. See Fig. 12 for key.

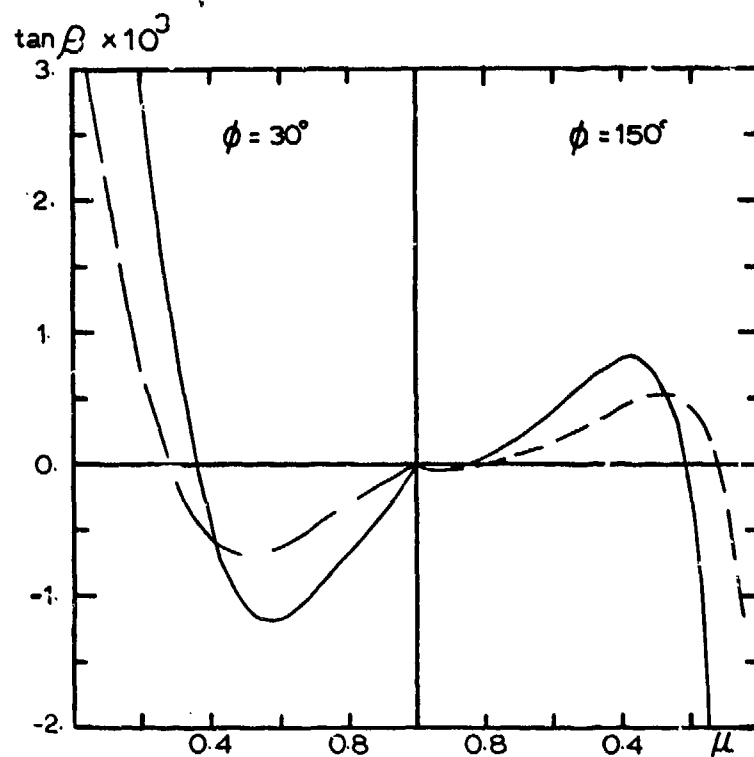


Fig. 19. Ellipticity of transmitted photons at earth's surface for $\mu_0 = 0.171$ and $\phi = 30^\circ$ and 150° . See Fig. 12 for key.

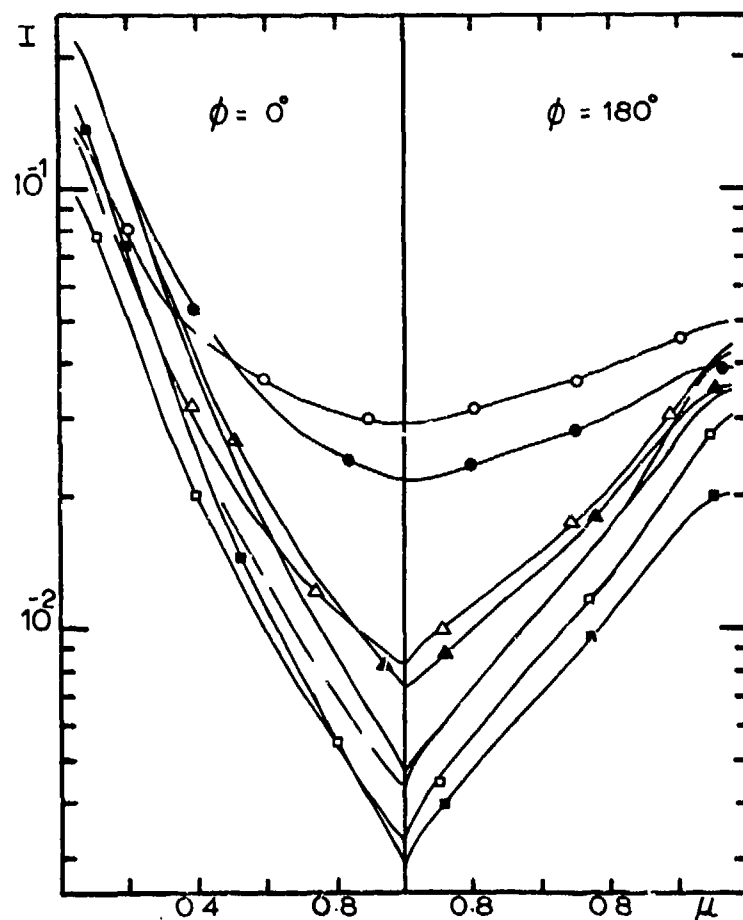


Fig. 20. Radiance of reflected photons at top of earth's atmosphere for $\mu_0 = 0.171$ and $\phi = 0^\circ$ and 180° . See Fig. 12 for key.

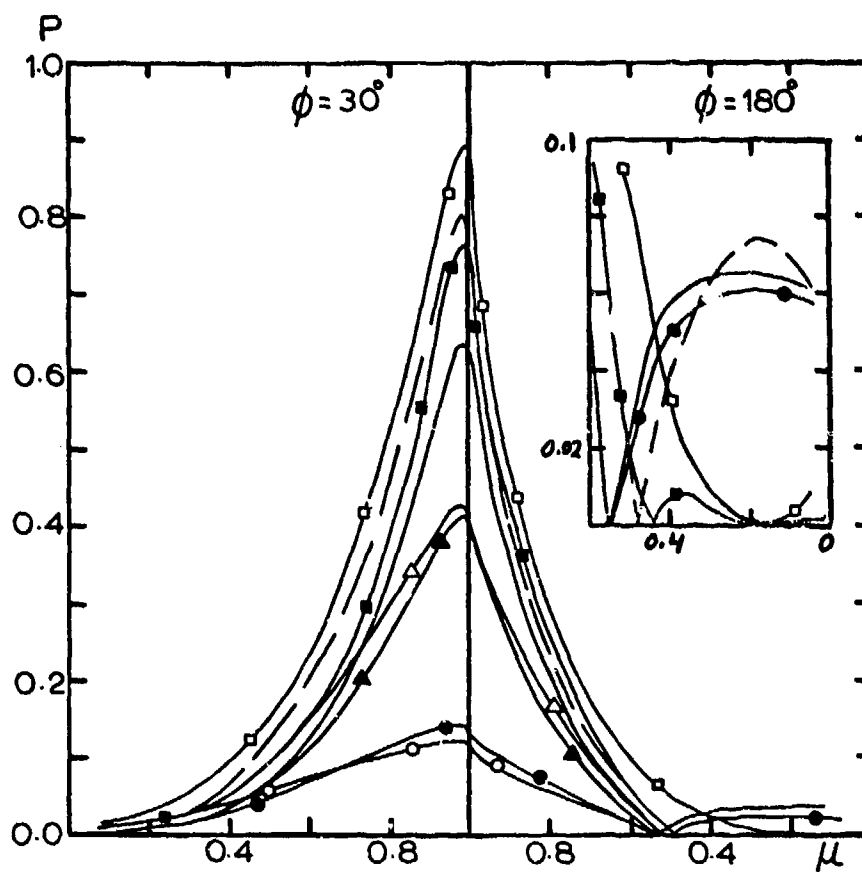


Fig. 21. Polarization of reflected photons at top of earth's atmosphere for $\mu_0 = 0.171$ and $\phi = 0^\circ$ and 180°

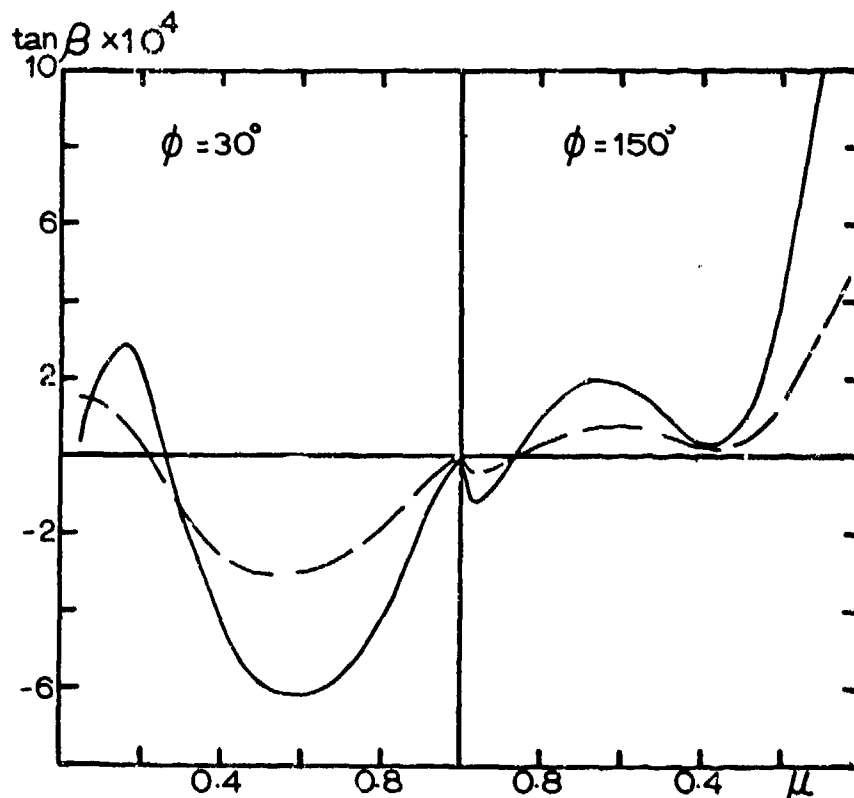


Fig. 22. Ellipticity of reflected photons at top of earth's atmosphere for $\mu_0 = 0.171$ and $\phi = 30^\circ$ and 150° . See Fig. 12 for key.

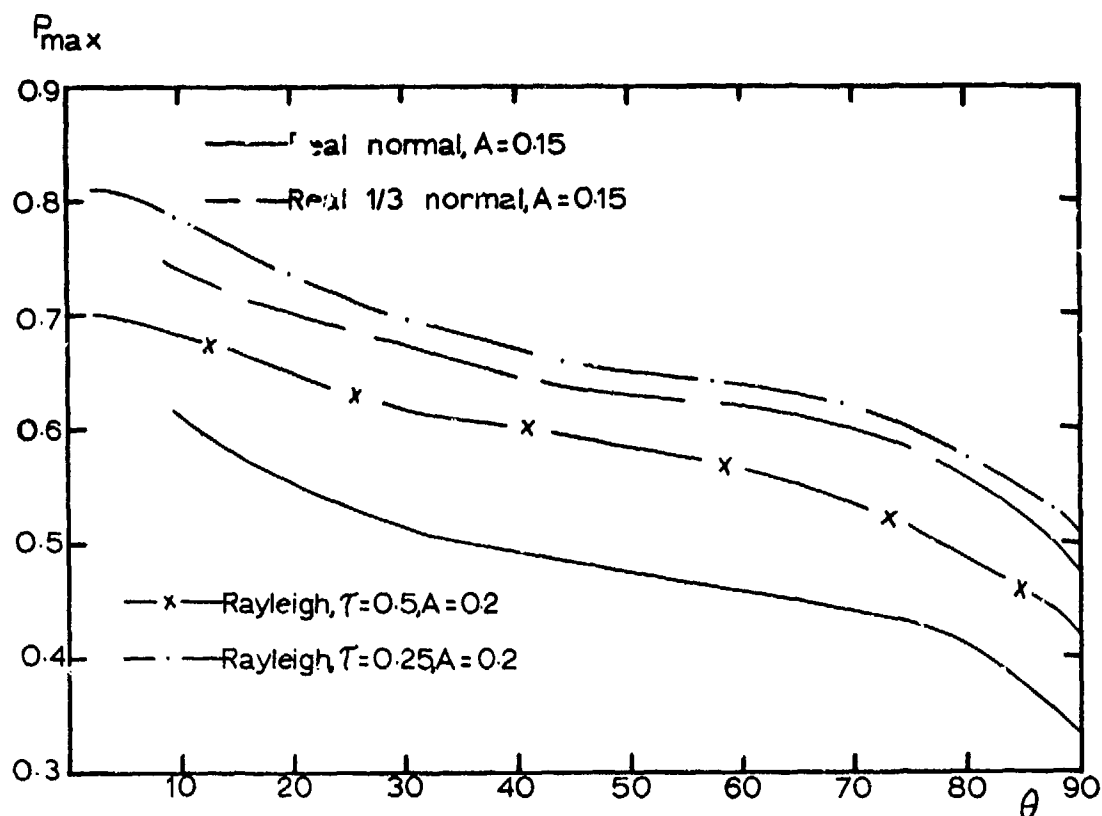


Fig. 23. Maximum polarization of downwelling radiation at any zenith angle as a function of solar elevation. Curves are shown for the real atmosphere model with normal and one-third normal aerosol amounts and $A = 0.15$ as well as for a Rayleigh atmosphere with optical thickness 0.25 and 0.5 and $A = 0.2$.

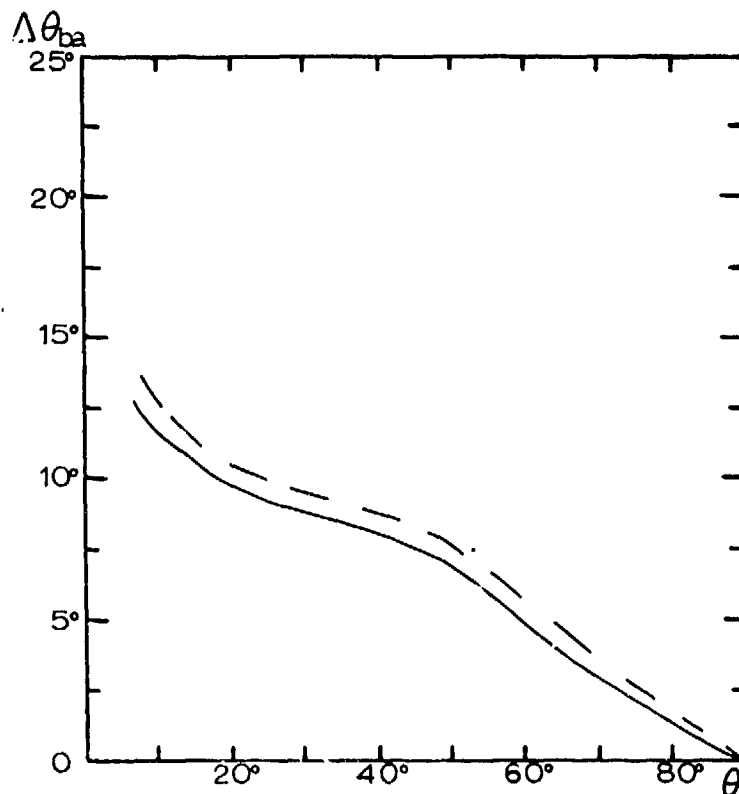


Fig. 24. The angular distance between the Babinet point and the solar point as a function of the solar elevation. The solid and dashed curves are for the normal and one-third normal aerosol amounts in the real atmosphere model.

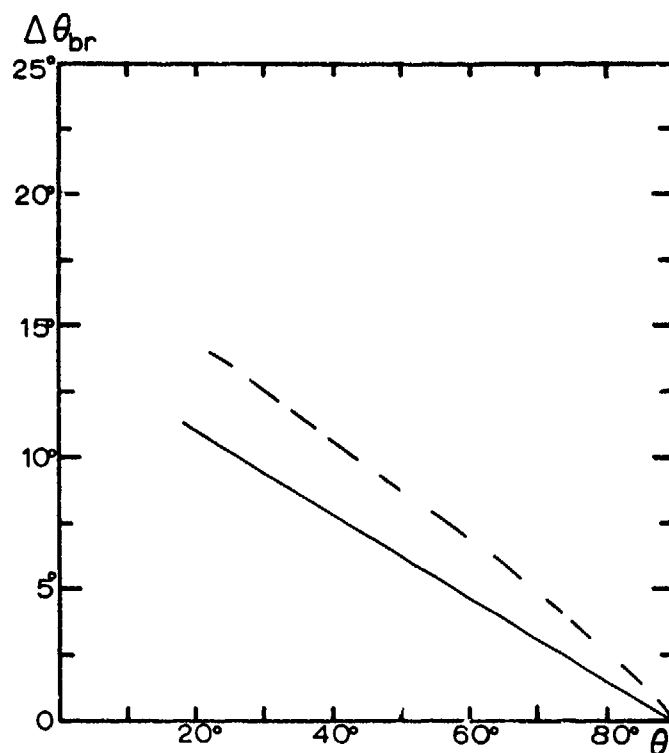


Fig. 25. Angular distance between the Brewster point and the solar point as a function of the solar elevation. The solid and dashed curves are for the normal and one-third normal aerosol amounts in the real atmosphere model.

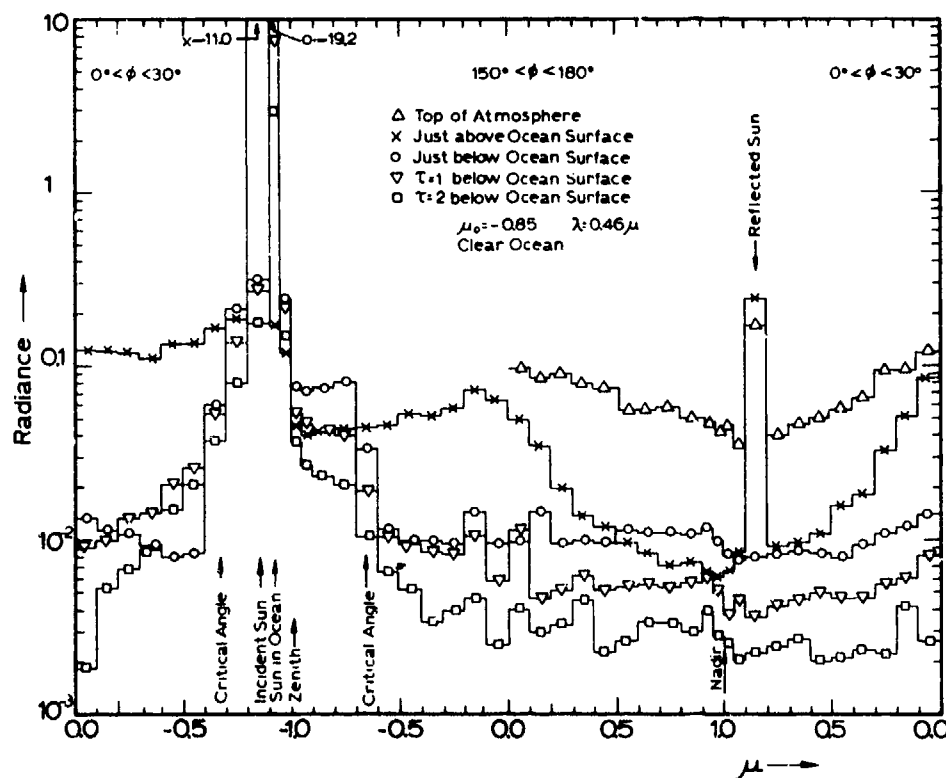


Fig. 26. Radiance as a function of zenith angle of observation for $\mu_0 = 0.85$ (31.79°), $\lambda = 0.46 \mu$, and a clear ocean model. As a particular curve is followed from left to right, one passes the solar horizon (at left side), critical angle, incident sun, sun in ocean, zenith, antisolar horizon, nadir, reflected sun (above ocean surface), solar horizon (at right side). The left half of the figure is for downwelling photons and the right half is for upwelling. The results are averaged over a range of azimuthal angles 30° on each side of the principal plane ($0^\circ < \phi < 30^\circ$ and $150^\circ < \phi < 180^\circ$).

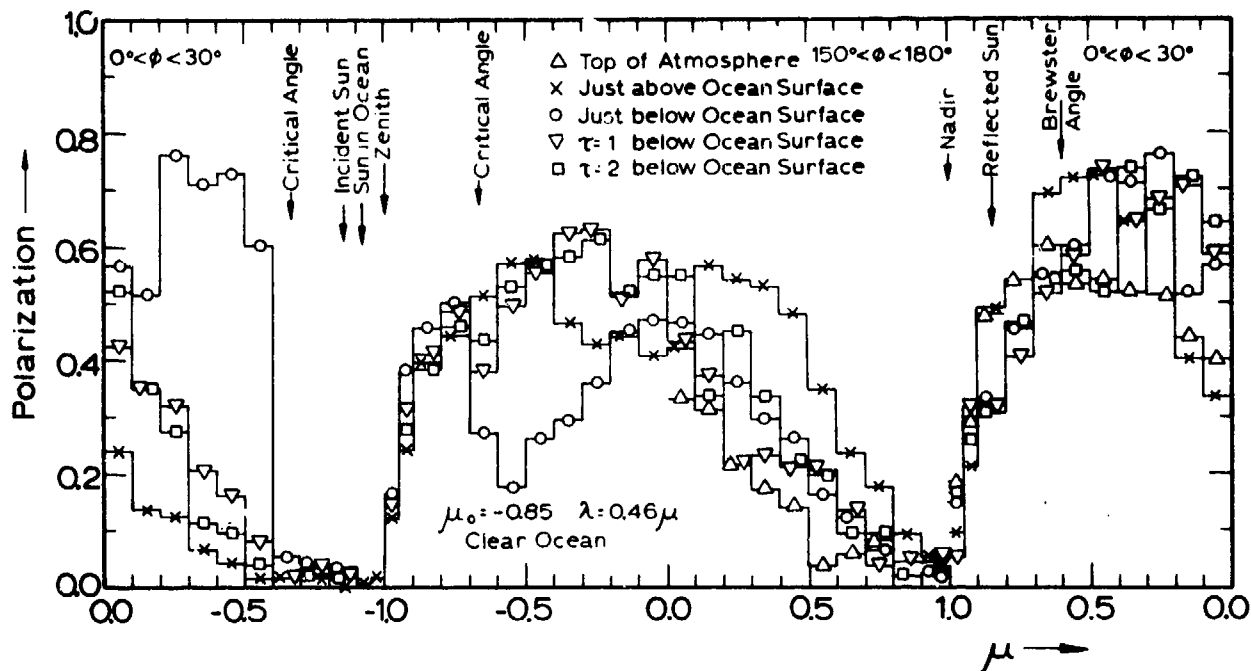


Fig. 27. Polarization as a function of μ for $\mu_0 = 0.85$, $0^\circ < \phi < 30^\circ$ and $150^\circ < \phi < 180^\circ$, $\lambda = 0.46 \mu$, and clear ocean model.

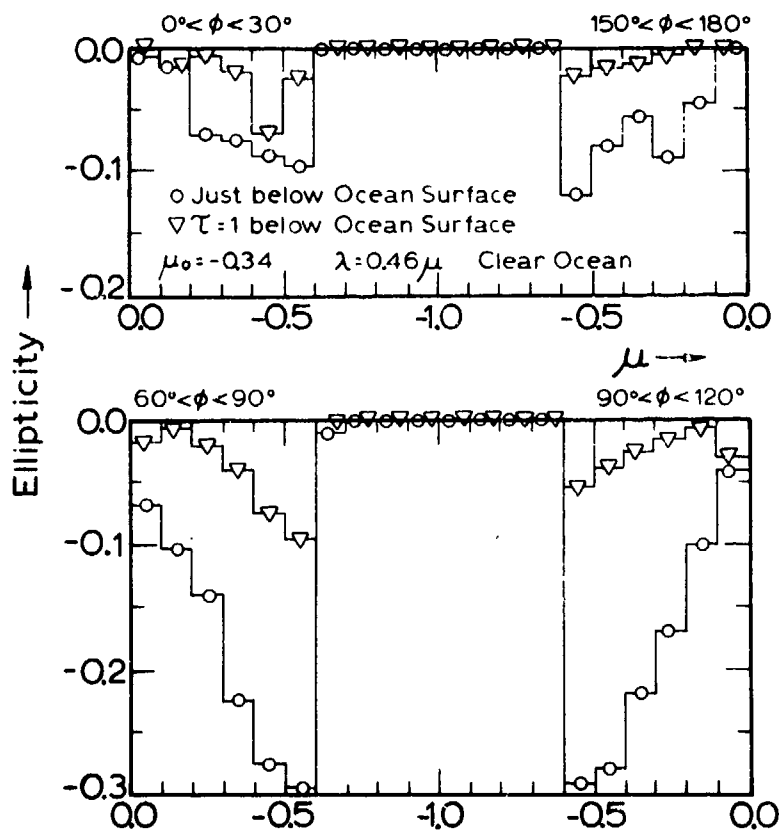


Fig. 28. Ellipticity as a function of μ for $\mu_0 = 0.34$ (70.12°), $0^\circ < \phi < 30^\circ$ and $150^\circ < \phi < 180^\circ$ (upper curves) and $60^\circ < \phi < 90^\circ$ and $90^\circ < \phi < 120^\circ$ (lower curves), $\lambda = 0.46 \mu$, and clear ocean model.

RADIATIVE TRANSFER IN CLOUDY ATMOSPHERES

K. N. Liou
Department of Meteorology, University of Utah
Salt Lake City, Utah 84112

SUMMARY

Band-by-band calculations have been carried out to evaluate the reflection, absorption and transmission of solar radiation by cloud layers and model cloudy atmospheres in the entire solar spectrum. The radiation transfer program is based on the discrete-ordinate method with applications to inhomogeneous atmospheres. The gaseous absorption in scattering atmospheres is taken into account by means of exponential fits to the total band absorption based on laboratory measurements. Thick clouds such as nimbostratus and cumulonimbus reflect 80-90% and absorb 10-20% of the solar radiation incident upon them. The reflection and absorption of a fairweather cumulus with a thickness of 0.45 km are about 68-85% and 4-9%, respectively. A thin stratus, whose thickness is 0.1 km, reflects about 45-72% and absorbs about 1-6% of the solar flux incident on the cloud top. The reflection of a 0.6 km thick altostratus is about 57-77%, with a higher absorption of 8-15%. Comparisons with aircraft observations reveal that within the uncertainties of the thickness and cloud particle characteristics theoretical computations yield higher reflection and lower absorption values for most of the water clouds. These comparisons indicate that clouds in the atmosphere are likely to be consisted of absorbing aerosol particles.

1. INTRODUCTION

Clouds occupy regularly over about 50% of the planet earth. They absorb and scatter the incoming solar radiation, while emitting thermal infrared radiation according to their temperature. The transfer of radiation through cloud layers depends on the particle phase, concentration, size and size distribution, all of which determine the properties of the volume single-scattering albedo and phase function. In addition, the cloud thickness is also a significant parameter whose change strongly influences the absorption, reflection and transmission of radiation. The amount of energy absorbed and/or emitted represents one of the prime sources determining the stability of cloud layers and is further associated with atmospheric motion.

In recent years, the reflection and absorption of the incident solar radiation by clouds have begun to be extensively investigated. Aircraft measurements revealed that clouds may absorb as much as 20-40% of solar radiation incident upon them (see e.g., Drummond and Hickey, 1971; Reynolds, et al., 1975). However, the mechanism responsible for this large absorption and its variability are mainly unknown. It is the purpose of this paper to investigate from a theoretical point of view the absorption, reflection and transmission of solar radiation in model cloudy atmospheres.

A radiation scheme has been developed by which the absorption of water vapor in the near infrared regions of the solar spectrum can be inserted into the transfer program for inhomogeneous cloudy atmospheres. The incorporation of water vapor absorption in scattering atmospheres is accomplished by a series of the exponential fits to the total absorptivity of each H_2O band on the basis of laboratory measured data (Howard, et al., 1956). For the fitting purpose, we have derived a new formula for the total absorption of water vapor with a new parameter representing both the pressure and path length, so that fitting procedures can be performed once and for all.

Three-layer model atmospheres are constructed. They consist of cloudless atmospheres above and below a single cloud layer, and with gaseous absorption in all three layers based upon representative model atmospheres suggested by McClatchey, et al. (1972). Clouds are classified into six types (London, 1957; Sasamori, et al., 1972) whose base heights and thicknesses are obtained from the climatological data. The observed particle-size distribution and number density for each type of clouds are employed to calculate single-scattering properties of cloud particles from the Mie scattering theory.

The basic transfer method is based on the discrete-ordinate method for radiative transfer (Liou, 1973) with further applications to inhomogeneous atmospheres (Liou, 1975). Band-by-band calculations (Liou and Sasamori, 1975) are carried out for the absorption, reflection and transmission of solar radiation in model cloudy atmospheres. The computed reflection and absorption of the incident solar radiation by clouds are compared with those obtained by aircraft measurements published by Drummond and Hickey (1971), and Reynolds, et al. (1975).

2. MODEL CLOUDY ATMOSPHERES

The climatological data for a tropical atmosphere tabulated by McClatchey, et al. (1972) is employed in this study. The parameters include the height, pressure, temperature, molecular density, and water vapor density which were given at 1 km height intervals up to 25 km (Figure 1).

Clouds are divided into six types whose base heights z_b and thicknesses Δz_c are given in Table 1. The mean temperatures of clouds are obtained by averaging the temperatures of the cloud top and base. From the mean cloud temperature \bar{T} , the vapor pressure e may be evaluated based on saturated conditions.

Furthermore, from the equation of state, the water vapor density within a cloud is

$$\rho_w = e/R_w T, \quad (2.1)$$

where $R_w = 4.168 \times 10^6 \text{ erg deg}^{-1} \text{ gm}^{-1}$. And the water vapor path length is given by

$$\Delta u_c = \rho_w \Delta z_c. \quad (2.2)$$

We tabulate all the relevant parameters in Table 1.

The observed particle size distributions for fair weather cumulus (Cu), cumulonimbus (Cb), stratus (St), and nimbostratus (Ns) and altostratus (As) are based on the observations by Battan and Reitan (1957), Weickmann and aufm Kampe (1953), Singleton and Smith (1960), and Diem (1948), respectively. The number densities N for each type of water clouds are listed in the last column of Table 1. The wavelength dependent real and imaginary parts of the refractive indices for water are taken from values tabulated by Irvine and Pollack (1968). On the basis of the above information Mie scattering computations (see e.g., Liou and Hansen, 1971) may be made to obtain the volume scattering and absorption cross-sections and the phase function.

The model cloudy atmosphere is considered to be plane-parallel with variations only in the vertical direction. It is further divided into several sub-layers according to the cloud location. With all this information, analyses and computations for the absorption and scattering processes in model cloudy atmospheres may be carried out.

Table 1. CLOUD PARAMETERS

Cloud Types	z_b (km)	Δz_c (km)	T (°K)	e (mb)	u (gm cm ⁻²)	N (cm ⁻³)
Low cloud (Cu, Sc)	1.7	0.45	288	17.044	0.577	300
Middle cloud (As, Ac)	4.2	0.6	274	6.566	0.311	450
High cloud (Ci, Cs, Cc)	4.6	1.7	234	0.144	0.023	0.1
Nimbostratus (Ns)	1.4	4.0	280	10.013	3.098	330
Cumulonimbus (Cb)	1.7	6.0	270	4.898	2.357	75
Stratus (St)	1.4	0.1	291	20.630	0.154	178

3. ABSORPTION AND SCATTERING PROPERTIES OF GASES AND CLOUD PARTICLES

3.1 Water Vapor Absorption

Laboratory measurements of the total absorption for water vapor bands at 6.3, 3.2, 2.7, 1.87, 1.38, 1.1 and 0.94 μm under simulated atmospheric conditions were performed by Howard, et al. (1956). Two empirical formulas were derived for small and large total absorption, respectively, as follows:

$$A = \int A_\nu d\nu = \begin{cases} c u^{1/2} (P + e)^k & \text{for } A < A_c, \\ C + D \log u + K \log (P + e) & \text{for } A > A_c. \end{cases} \quad (3.1)$$

In the above equation, ν represents wavenumber (cm⁻¹), A the band area in wavenumber (cm⁻¹), A_ν the fractional absorption within band at ν , u the absorbing path (gm cm⁻² for H₂O; cm atm for CO₂), e the partial pressure of absorption gases (mm Hg), P the partial pressure of non-absorbing gas (mm Hg), A_c the critical band area above which the strong band expression becomes applicable and c , k , C , D , and K are empirically determined constants.

For the convenience of incorporating the gaseous absorption into scattering atmospheres, a modified formula is derived from the above absorption formulas such that a smooth absorption curve for every value of water vapor path length can be obtained. This formula is given by

$$\bar{A} = \frac{1}{\Delta \nu} [C + D \log_{10} (x + x_0)], \quad (3.2)$$

where

$$x = u P^{K/D}, \quad (3.3)$$

$$x_0 = 1(C/D). \quad (3.4)$$

We then fit the total absorption for each band by a series of exponential functions as follows:

$$\bar{A} = 1 - \sum_{m=1}^M w_m \exp(-k_m x), \quad (3.5)$$

where w_m and k_m are band parameters independent of atmospheric conditions, and M is the total number of sub-intervals for each band. The determination of equivalent absorption coefficients k_m similar to Equation (3.5) has been previously noted by Yamamoto, et al. (1971), Houghton and Hunt (1971), Liou (1974) and Lacis and Hansen (1974). Values of w_m and k_m by five-term exponential fits were given by Liou and Sasamori (1975).

After w_m and k_m are derived, the optical depths of water vapor for each band and for l atmospheric layer are given by

$$\Delta\tau_m^l = k_m \Delta x_l, \quad m = 1, 2, \dots, M, \quad (3.6)$$

where

$$\Delta x_l = u_{l+1} P_{l+1}^{K/D} - u_l P_l^{K/D}, \quad (3.7)$$

and

$$P_l = \int_0^{u_l} P du / \int_0^{u_l} du, \quad (3.8)$$

where P_l denotes an effective pressure of the atmosphere above the level l . This expression places all the absorption matter along a pressure gradient at one pressure P_l . In the above analyses, the so-called C-G two-parameter approximation (Curtis, 1952; Godson, 1954) is applied to account for the effect of pressure dependence of absorption in an inhomogeneous atmosphere.

3.2 Single Scattering by Molecules

The Rayleigh scattering optical depth $\Delta\tau_l^R$ for a given wavelength λ and a thickness of Δz_l may be obtained from

$$\Delta\tau_l^R(\lambda) = \sigma^R(\lambda) \int_{\Delta z_l} N(z) dz, \quad (3.9)$$

where $\sigma^R(\lambda)$ represents the Rayleigh scattering cross-section, and $N(z)$ is the number of molecules per unit volume at a given height z .

Furthermore, the normalized phase function for Rayleigh scattering is simply

$$P^R(\theta) = \frac{3}{4} (1 + \cos^2 \theta) \quad (3.10)$$

with θ being the scattering angle.

3.3 Single Scattering by Cloud Particles

Clouds are composed of particles which are much larger than the incident wavelength in the solar spectrum. Consequently the dipole mode for scattering is no longer valid. For spherical water drops, single scattering properties may be described by the exact Mie solution. However, knowledge of light scattering by non-spherical ice crystals is extremely limited. No attempt is made here to discuss problems of non-sphericity on the scattered radiation of clouds. Thus, we shall assume that all clouds to be considered are consisted of spherical particles for the convenience of discussions in this work. Information of cloud types, cloud heights and cloud thicknesses based on climatological data have been discussed in the section on model atmospheres. In that section, we also discuss the size distribution and number density for each cloud type, along with the real and imaginary parts of the refractive indices for both ice and water in the solar spectrum. With all this information, we may calculate the phase function and the scattering and absorption cross-sections of cloud particles.

The optical depths due to the scattering and absorption of cloud particles are given by

$$\Delta\tau_{s,a}^M = \Delta z_c \int_{\Delta r} \sigma_{s,a}^M(\lambda, r) n(r) dr, \quad (3.11)$$

where Δz_c is the thickness of a cloud, σ_s^M and σ_a^M represent, respectively, the scattering and absorption cross-sections of a cloud particle with radius of r , the values of which also depend on the refractive index and $n(r)$ dr denotes the numbers of cloud particles per unit volume within the size range of dr . The normalized Mie phase functions $P^M(\theta)$ of a fair weather cumulus for wavelengths in the solar spectrum are shown in Figure 2. Calculations have also been made for other cloud types discussed previously.

Furthermore, the density of water vapor ρ_w within a cloud may be estimated from the mean cloud temperature (based on the temperature of the model atmosphere) assuming saturated conditions. The water vapor path length is given in Equation (2.2).

3.4 Parameters for Single Scattering

With all the above information of the absorption and scattering properties of gases and cloud particle, we may define the single scattering albedo, the phase function and the total optical depth, respectively, for a volume of cloud particles and molecules uniformly mixed at a given layer l as

$$\tilde{\omega}_0 = \frac{\Delta\tau^R + \Delta\tau_s^M}{(\Delta\tau^R + \Delta\tau_s^M) + (\Delta\tau_a^M + k_m \Delta x_l)} , \quad (3.12)$$

$$P(\theta) = \frac{\Delta\tau_s^M P^M(\theta) + \Delta\tau^R P^R(\theta)}{\Delta\tau_s^M + \Delta\tau^R} , \quad (3.13)$$

$$\Delta\tau_l = \Delta\tau^R + \Delta\tau_s^M + \Delta\tau_a^M + k_m \Delta x_l . \quad (3.14)$$

For a layer of no cloud particles, we note that $\Delta\tau_s^M = \Delta\tau_a^M = 0$.

4. RADIATIVE TRANSFER IN INHOMOGENEOUS ATMOSPHERES

The appropriate equation describing the diffuse solar radiation field when the vertical distribution of fluxes is considered may be written as

$$\mu \frac{dI(\tau, \mu)}{d\tau} = I(\tau, \mu) - \tilde{\omega}_0(\tau) J(\tau, \mu) , \quad (4.1)$$

where the source function for solar radiation

$$J(\tau, \mu) = \frac{1}{2} \int_{-1}^{+1} P(\tau; \mu, \mu') I(\tau, \mu') d\mu' + \frac{1}{4} F_0 P(\tau; \mu, \mu_0) \exp(-\tau/\mu_0) . \quad (4.2)$$

In Equation (4.1), $\tilde{\omega}_0(\tau)$ denotes the single scattering albedo either for Rayleigh and/or Mie layer, I the intensity, τ the optical depth, F_0 the solar flux, and μ and μ_0 the cosine of the emergent and solar zenith angles, respectively.

The model atmosphere is divided into several sub-layers within which the phase function and single scattering albedo are constants with respect to the optical depth τ . We may then carry out computations for single scattering properties as discussed in the previous sections. After phase functions for each layer are obtained, they are expanded in Legendre polynomials p_k as

$$P(\tau_l; \mu, \mu') = \sum_{k=0}^N \tilde{\omega}_k p_k(\mu) p_k(\mu') , \quad l = 1, 2, \dots, N . \quad (4.3)$$

where $\tilde{\omega}_k$ can be determined by

$$\tilde{\omega}_k = \frac{2k+1}{2} \int_{-1}^{+1} P(\mu) p_k(\mu) d\mu . \quad (4.4)$$

On the basis of the discrete-ordinate method for radiative transfer for homogeneous layers developed by Liou (1973), the solution of the above transfer equation for l sub-layer may be written as

$$I^{\ell}(\tau, \mu_i) = \sum_{j=-n}^n L_j^{\ell} \phi_j^{\ell}(\mu_i) \exp(-k_j^{\ell} \tau) + Z^{\ell}(\mu_i) \exp(-\tau/\mu_0), \quad i = -n, n, \quad \ell = 0, 1, \dots, N, \quad (4.5)$$

where $\phi_j^{\ell}(\mu_i)$ and k_j^{ℓ} represent the eigenfunction and eigenvalue of the solution, respectively, $Z^{\ell}(\mu_i)$ is associated with the solar flux, the solar zenith angle and the H-function (Chandrasekhar, 1950), and L_j^{ℓ} are constants of proportionality to be determined by the following simultaneous equations.

At the top of the atmosphere ($\tau = 0$) there is no diffuse intensity so that

$$I^1(0, -\mu_i) = 0 \quad \text{for } i = 1, n. \quad (4.6)$$

On the interface of each homogeneous layer, we have

$$I^{\ell}(\tau_{\ell}, \mu_i) = I^{\ell+1}(\tau_{\ell}, \mu_i) \quad \text{for } i = -n, n, \quad 0 < \ell < N, \quad (4.7)$$

where τ_{ℓ} denotes the optical depth from the top of the atmosphere to the bottom of the ℓ layer. At the bottom of the atmosphere, assuming an isotropic ground reflection A_s , we have

$$I^N(\tau_N, \mu_i) = \frac{A_s}{\pi} [F^{\dagger}(\tau_N) + \mu_0 \pi F_0 \exp(-\tau_N/\mu_0)], \quad (4.8)$$

where

$$F^{\dagger}(\tau_N) = 2\pi \sum_{i=1}^n I^N(\tau_N, -\mu_i) a_i \mu_i. \quad (4.9)$$

In Equation (4.8) a_i is the Gaussian weight. Equations (4.6), (4.7) and (4.8) contain $N \times 2n$ equations for the determination of $N \times 2n$ L_j^{ℓ} coefficients simultaneously. After obtaining L_j^{ℓ} , the intensity within each layer may then be computed from Equation (4.5).

Finally, the upward and downward fluxes for any given τ within each layer are

$$F^{\uparrow}(\tau) = 2\pi \sum_{i=1}^n I(\tau, \mu_i) a_i \mu_i, \quad (4.10)$$

$$F^{\downarrow}(\tau) = -2\pi \sum_{i=1}^n I(\tau, -\mu_i) a_i \mu_i - \mu_0 \pi F_0 \exp(-\tau/\mu_0). \quad (4.11)$$

The net flux is therefore

$$F(\tau) = F^{\uparrow}(\tau) + F^{\downarrow}(\tau). \quad (4.12)$$

5. DEFINITIONS OF THE RADIATIVE PROPERTIES OF ATMOSPHERES AND CLOUDS

The radiation scheme described above deals with the transfer of radiation in an absorption band which is divided into several sub-spectral regions. To obtain the reflection (local albedo) and absorption of the atmosphere or the cloud for the entire solar spectrum, proper summation over the fluxes in each sub-spectral region weighed by the appropriate percentage of solar flux is required.

5.1 Entire Atmospheres

The reflection γ may be defined as the ratio of the reflected flux at the top of the atmosphere to the incident solar flux perpendicular to the stratification of the atmosphere. Thus, for each spectral band

$$\gamma_i = \begin{cases} \sum_m F_m^{\uparrow}(0) w_m / \mu_0 f_{\Delta\lambda_i} & \text{for } H_2O \text{ bands,} \\ F_1^{\uparrow}(0) / \mu_0 f_{\Delta\lambda_i} & \text{otherwise,} \end{cases} \quad (5.1)$$

where $f_{\Delta\lambda_i}$ denotes the amount of solar flux in the i 's spectral band, and m is the number of the sub-band

interval according to the exponential fit described in Section 3.1.

The reflection of the earth-atmospheric system for the entire solar spectrum is to be evaluated by summing all the spectral reflection weighed by the appropriate percentage of the solar flux within each band interval as

$$\gamma = \sum_i \gamma_i f_{\Delta\lambda_i} / S_0, \quad (5.2)$$

where S_0 is the solar constant.

In addition to the reflection, it is equally important to study the total absorption within the atmosphere due to both water vapor and cloud particles. Its value may be obtained by the net flux divergence at the top and bottom of the atmosphere. For i's absorption spectral interval we have

$$\alpha_i = \begin{cases} \sum_m [F_m(\tau_N) - F_m(0)] w_m / \mu_0 f_{\Delta\lambda_i} & \text{for H}_2\text{O bands,} \\ [F_i(\tau_N) - F_i(0)] / \mu_0 f_{\Delta\lambda_i} & \text{otherwise.} \end{cases} \quad (5.3)$$

The total absorption within the atmosphere due to solar radiation is, therefore

$$\alpha = \sum_i \alpha_i f_{\Delta\lambda_i} / S_0. \quad (5.4)$$

5.2 Cloud Layers

Similar to the above definitions, the reflection (or local albedo) of a cloud layer may be defined as the ratio of the reflected flux to the incident solar flux normal to the cloud top. Hence, the reflection for each spectral band

$$\gamma_i^c = \begin{cases} \sum_m F_m^\uparrow(\tau_t) w_m / \sum_m F_m^\uparrow(\tau_t) w_m & \text{for H}_2\text{O bands,} \\ F_i^\uparrow(\tau_t) / F_i^\uparrow(\tau_t) & \text{otherwise.} \end{cases} \quad (5.5)$$

where τ_t denotes the optical depth at the cloud top. The reflection of a cloud layer for the entire solar spectrum is given by

$$\gamma^c = \sum_i \gamma_i^c f_{\Delta\lambda_i} / S_0. \quad (5.6)$$

Moreover, the absorption of solar flux within a cloud layer can be evaluated from the net flux divergence at the top and bottom of that cloud. For each spectral band, it is defined as

$$\alpha_i^c = \begin{cases} \sum_m [F_m(\tau_t) - F_m(\tau_b)] w_m / \sum_m F_m^\uparrow(\tau_t) w_m & \text{for H}_2\text{O bands,} \\ [F_i(\tau_t) - F_i(\tau_b)] / F_i^\uparrow(\tau_t) & \text{otherwise.} \end{cases} \quad (5.7)$$

where τ_b denotes the optical depth at the cloud base. The total absorption within a cloud layer for the entire solar spectrum is, therefore

$$\alpha^c = \sum_i \alpha_i^c f_{\Delta\lambda_i} / S_0. \quad (5.8)$$

6. RESULTS

6.1 Theoretical Calculations

The inhomogeneous cloudy atmosphere is divided into three layers consisting of cloudless atmospheres above and below a single cloud layer. Each layer is considered to be homogeneous with respect to the single-scattering albedo and the phase function defined in sub-section 3.4. The spectral solar flux at the top of the atmosphere is taken from the table in *Astrophysical Quantities* (Allen, 1963, p. 272). Band-by-band calculations are carried out for the transfer of solar radiation in inhomogeneous cloudy

atmospheres based on the discrete-ordinate method for radiative transfer. The final resulting absorption, reflection and transmission for the cloud layer and the entire atmosphere are obtained according to the formulas defined in Section 5. We have chosen a surface albedo of 0.1 in the calculations.

Figure 3 shows the absorption and reflection of solar radiation as functions of the cosine of the solar zenith angle for five cloud types. The absorption and reflection are normalized with respect to the downward flux at the cloud top. Owing to the large geometrical thickness and broad particle spectrum, the cloud-particle optical depths of the nimbostratus and cumulonimbus at a visible wavelength of 0.5 μ m are about 500 and 700, respectively. In order to carry out the transfer calculations including water vapor absorption, a reduction of the cloud-particle optical depth to a value of 250 was made. Because the optical depths of Ns and Cb are modified to a similar value, and because their geometrical locations in the atmosphere are approximately the same, the differences in the resulting radiation parameters are found negligibly small. We have performed two additional calculations employing optical depths of 200 and 150 to check the possible errors in reducing the optical depth. We have found that the changes in the values of reflection and absorption for the three cases considered (i.e., optical depths of 250, 200 and 150) are within about 1% and 3%, respectively. Thus, the reflection and absorption presented in Figure 3 for Ns and Cb are believed to be reliable to within about 5%. Values of the cloud reflection illustrate that Ns and Cb reflect about 80 to 90% of the solar flux incident upon them. The scattering of cloud particles obviously is responsible for the large reflection. The corresponding absorption within these clouds indicates a value of about 20% when the sun is overhead. Absorption of solar radiation by both water vapor and cloud particles in the near infrared is responsible for the cloud absorption.

Although the geometrical thickness of the cumulus used in this study is only about 0.5 km, large reflection values ranging from 68 to 85% are obtained. About 9% of the solar flux incident upon it is absorbed when the sun is overhead. The reflection and absorption values for a stratus, whose geometrical thickness is 0.1 km, are from 45 to 72% and from 1 to 6%, respectively. Altostratus reflects about 57 to 77% of the solar flux. These values are somewhere in between those of Cu and St. On the other hand, however, the absorption of solar flux by As is greater than that by Cu and St with values ranging from 8 to 15%. The larger absorption, which takes place in the middle cloud, is primarily due to its higher appearance in the atmosphere. In this case, since the concentration of water vapor above the cloud is relatively small, a large portion of solar flux penetrates the atmosphere and is absorbed by the cloud. This evidence indicates that the cloud location in the atmosphere is important as to the absorption of solar radiation energy in the cloud layer.

The total absorption and reflection for the entire cloudy atmospheres are shown in Figure 4. For the Cu case, the total atmospheric absorption is about 24% when the sun is overhead, and 35% when the sun is close to the horizon. As for the As case, it is interesting to note that as compared with the Cu case larger absorption occurs when the sun is near the zenith, while smaller absorption takes place when the sun is close to the horizon. Values of the reflection at the top of the atmosphere containing Cu, St and As clouds are smaller as compared to those of the clouds alone, because more solar flux is absorbed in the atmosphere above and below the cloud layer. As for the Ns and Cb cases, since clouds dominate the radiation processes, values of the reflection and absorption for cloudy atmospheres are about the same with and without considering the atmosphere above and below the cloud layer.

Figure 5 presents the total transmission, which includes the direct as well as diffuse components, at the bottom of the atmosphere. Only about 1 to 3% of the solar flux can penetrate the atmosphere containing Ns and Cb clouds. When the sun is overhead, values of the transmission for Cu, St and As atmospheres are about 20, 27 and 45%, respectively. The transmission values decrease when the sun moves toward the horizon. The transmitted solar flux represents one of the important energy sources available to the earth's surface.

6.2 Comparison with Observations

Aircraft measurements of the reflection and absorption of solar radiation by cloud layers were reported by Reynolds et al. (1975) and Drummond and Hickey (1971). These observations were made when solar elevation angles were greater than 60° (i.e., $\mu_0 > 0.856$). We tabulate in Table 2 the observed reflection and absorption for various cloud types, along with the present theoretical values.

Table 2. OBSERVED AND COMPUTED REFLECTION (γ^C) AND ABSORPTION (α^C) OF SOLAR RADIATION FOR VARIOUS CLOUD TYPES

		Drummond and Hickey	Reynolds, Vonder Haar and Cox	Liou ($\mu_0=1$)
St, Cu	γ^C	47-56%	37-42%	45-67%
	α^C	---	12-36%	6-9%
As, Ac	γ^C	40%	---	56%
	α^C	15%	---	15%
Cb, Ns	γ^C	---	66%	78%
	α^C	---	31%	19%
Ci, Cs	γ^C	20%	47-59%	---
	α^C	---	13-14%	---

Before examining the values presented in Table 2, it should be emphasized that the theoretical calculations employ the cloud thicknesses and locations presented in Figure 1, while the observed data provides no information on them. We have not been able to carry out the transfer calculations for cirrus clouds because the information on the single-scattering properties of non-spherical ice crystals in the solar spectrum are still lacking. Qualitatively we find that the computed reflection and absorption values are generally higher and smaller, respectively, than those obtained from aircraft measurement. The reasons for these discrepancies may be caused by (1) the uncertainties in the observations and definitions on the fluxes at the top and bottom of cloud layers, (2) the differences in the geometrical depth, particle size and concentration between calculations and observations, and (3) the possible existence of absorbing aerosol particles in the cloud layer (Twomey, 1972). Points (1) and (2) may be solved if a careful and comprehensive field experiment including cloud physics measurements is undertaken. However, point (3) requires the knowledge of the refractive indices for aerosols in the entire solar spectrum and the concentration and sizes of aerosols that may exist in the cloud layer.

7. CONCLUSIONS

A radiation scheme has been developed by which the absorption of water vapor and carbon dioxide in the near infrared regions of the solar spectrum can be incorporated into the transfer program for inhomogeneous cloudy atmospheres. The incorporation of gaseous absorption in scattering atmospheres is accomplished by a series of exponential fits to the total absorption based on laboratory measurements. A new empirical formula for the total absorption of water vapor has been derived with a new parameter representing both the pressure and path length, so that fitting procedures can be performed once and for all.

Band-by-band calculations have been carried out to evaluate the reflection, absorption and transmission of the cloud layer and the model cloudy atmosphere in the entire solar spectrum. The reflected solar fluxes at the top of the atmospheres containing cumulus, stratus and altostratus are found to be smaller than those of the clouds alone, owing to the additional absorption by the gases above and below the cloud layer.

Thick clouds such as nimbostratus and cumulonimbus reflect 80-90% and absorb 10-20% of the solar flux incident upon them. Effects of the atmospheres above and below them are shown to be fairly small. The reflection of a fair weather cumulus with a thickness 0.45 km is found to be about 68-85%, but its absorption is only about 4-9%. A thin stratus whose thickness is 0.1 km reflects about 45-72% and absorbs about 1-6% of the solar flux incident on the cloud top. Reflection of a 0.6 km thick middle cloud is about 57 to 77%. Because its higher location in the atmosphere, higher absorption of about 8 to 15% is obtained. On the basis of these calculations, it is evident that the location of the cloud in the atmosphere is important as to the cloud absorption. Comparisons with aircraft observations reveal that within the uncertainties of the thickness and cloud particle characteristics theoretical calculations yield higher reflection and lower absorption values for most of the water clouds.

Acknowledgments. This research was supported by the Atmospheric Sciences Section of the National Science Foundation under Grant DES75-05216. This research was also partially supported by the Air Force Cambridge Research Laboratory under Contract F19628-75-C-0107.

REFERENCES

- Allen, C. W., 1963, Astrophysical Quantities, University of London, The Athlone Press, 291 pp.
- Battan, L. J. and Reitan, C. H., 1957, Droplet size measurement in convective clouds, Artificial Stimulation of Rain, London, Pergamon Press, 184 pp.
- Chandrasekhar, S., 1950, Radiative Transfer, New York, Dover Publ., 393 pp.
- Curtis, A. R., 1952, Discussion of a paper by Goody, Quart. J. Roy. Meteor. Soc., **78**, 638-640.
- Diem, M., 1948, Messungen der Frosse von Wolkenelementen II, Meteor. Rundschau, **9**, 261-273.
- Drummond, A. J. and Hickey, J. R., 1971, Large-scale reflection and absorption of solar radiation by clouds as influencing earth radiation budget: New aircraft measurement, Preprints of papers, Intern. Conf. Weather Modification, Canberra, Australia Acad. Sci. and Amer. Meteor. Soc., 267-276.
- Godson, W. L., 1955, The computation of infrared transmission by atmospheric water vapor, J. Meteor., **12**, 272-284.
- Houghton, J. T. and Hunt, G. E., 1971, The detection of ice clouds from remote measurements of their emission in the far infrared. Quart. J. Roy. Meteor. Soc., **96**, 1-17.
- Howard, J. N., Burch, D. L. and Williams, D., 1956, Near infrared transmission through synthetic atmospheres, J. Opt. Soc. Am., **46**, 186-190.
- Irvine, W. M. and Pollack, J. B., 1968, Infrared optical properties of water and ice spheres, Icarus, **8**, 324-366.

- Lacis, A. A. and Hansen, J. E., 1974, A parameterization for the absorption of solar radiation in the earth's atmosphere, J. Atmos. Sci., 31, 118-123.
- Liou, K. N., 1973, A numerical experiment on Chandrasekhar's discrete-ordinate method for radiative transfer: Applications to cloudy and hazy atmospheres, J. Atmos. Sci., 30, 1303-1326.
- , 1974, On the radiative properties of cirrus in the window region and their influence on remote sensing of the atmosphere, J. Atmos. Sci., 31, 522-532.
- , 1975, Applications of the discrete-ordinate method for radiative transfer to inhomogeneous aerosol atmospheres, J. Geophys. Res., 80, 3434-3440.
- and Hansen, J. E., 1971, Intensity and polarization for single scattering by polydisperse spheres: A comparison of ray optics and Mie theory, J. Atmos. Sci., 28, 995-1004.
- and Sasamori, T., 1975, On the transfer of solar radiation in aerosol atmospheres, J. Atmos. Sci., 32, (in press).
- London, J., 1957, A study of the atmospheric heat balance, Final Rept., Contract No. AF19(122)-165, Dept. of Meteorology, New York University.
- McClatchey, R. A., et al., 1972, Optical properties of the atmosphere, Environmental Res. Pap., 354, AFCRL.
- Reynolds, D. W., Vonder Haar, T. H. and Cox, S. K., 1975, The effect of solar radiation absorption in the tropical troposphere, J. Appl. Meteor., 14, 433-444.
- Sasamori, T., London, J. and Hoyt, D. V., 1972, Radiation budget of the southern hemisphere, Meteor. Monographs, 13, 9-23.
- Singleton, F. and Smith, D. F., 1960, Some observations of drop size distributions in low layer clouds, Quart. J. Roy. Meteor. Soc., 86, 454-467.
- Twomey, S., 1972, The effect of cloud scattering on the absorption of solar radiation by atmospheric dust, J. Atmos. Sci., 29, 1156-1159.
- Weickmann, H. K. and aufm Kampe, H. J., 1953, Physical properties of cumulus clouds, J. Meteor., 10, 204-211.
- Weinman, J. A. and Guetter, P. J., 1972, Penetration of solar irradiances through the atmosphere and plant canopies, J. Appl. Meteor., 11, 136-140.
- Yamamoto, G., Tanaka, M. and Asano, S., 1970, Radiative transfer in the infrared region, J. Atmos. Sci., 27, 282-292.

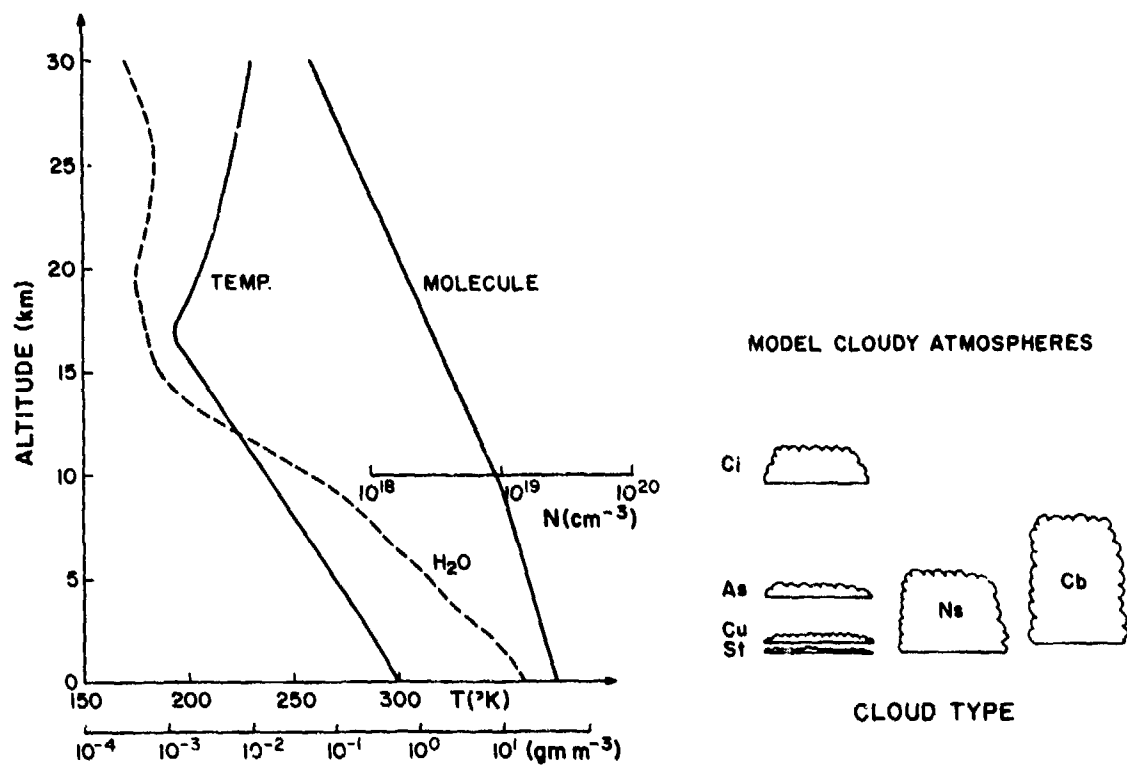


Figure 1. Model cloudy atmospheres employed in this study. The temperature, water vapor density and molecular concentration profiles are for a mean tropical atmosphere. The climatological base heights and thicknesses of six cloud types are shown in the right-hand side.

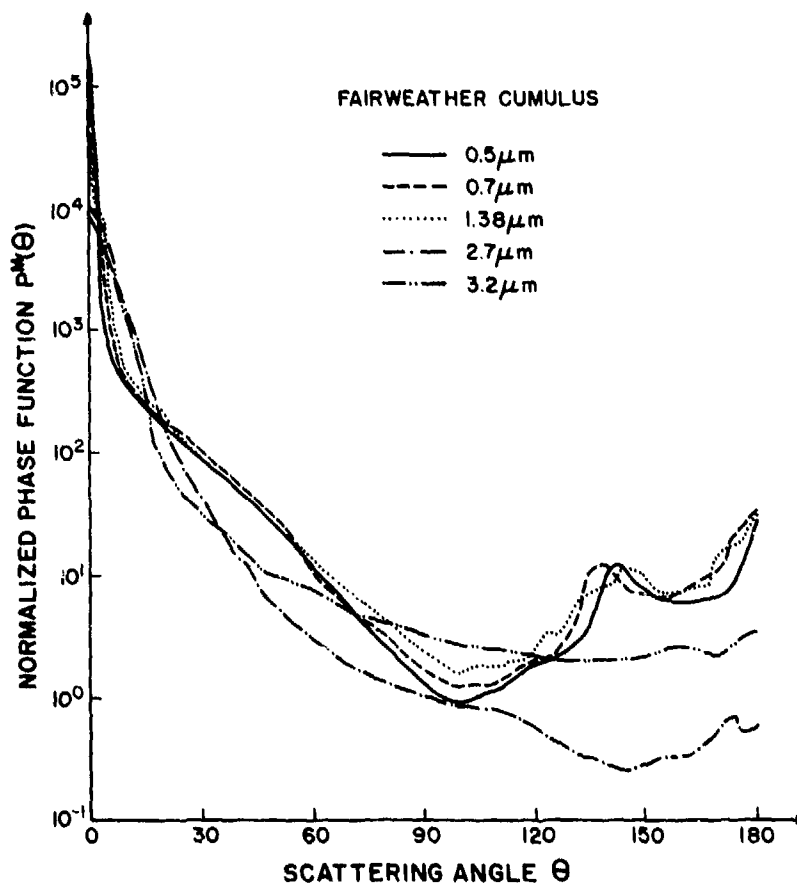


Figure 2. Normalized phase functions of a fair weather cumulus as functions of the scattering angle for various wavelengths in the solar spectrum.

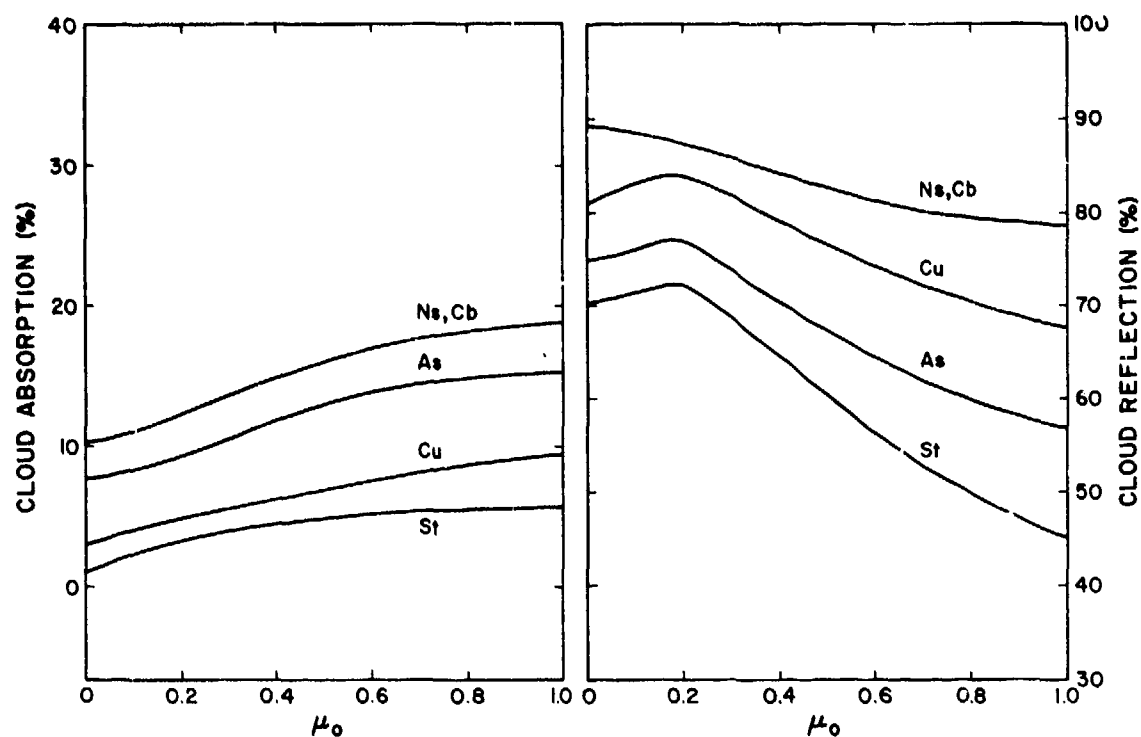


Figure 3. The absorption and reflection of solar radiation by five cloud layers as functions of the cosine of the solar zenith angle.

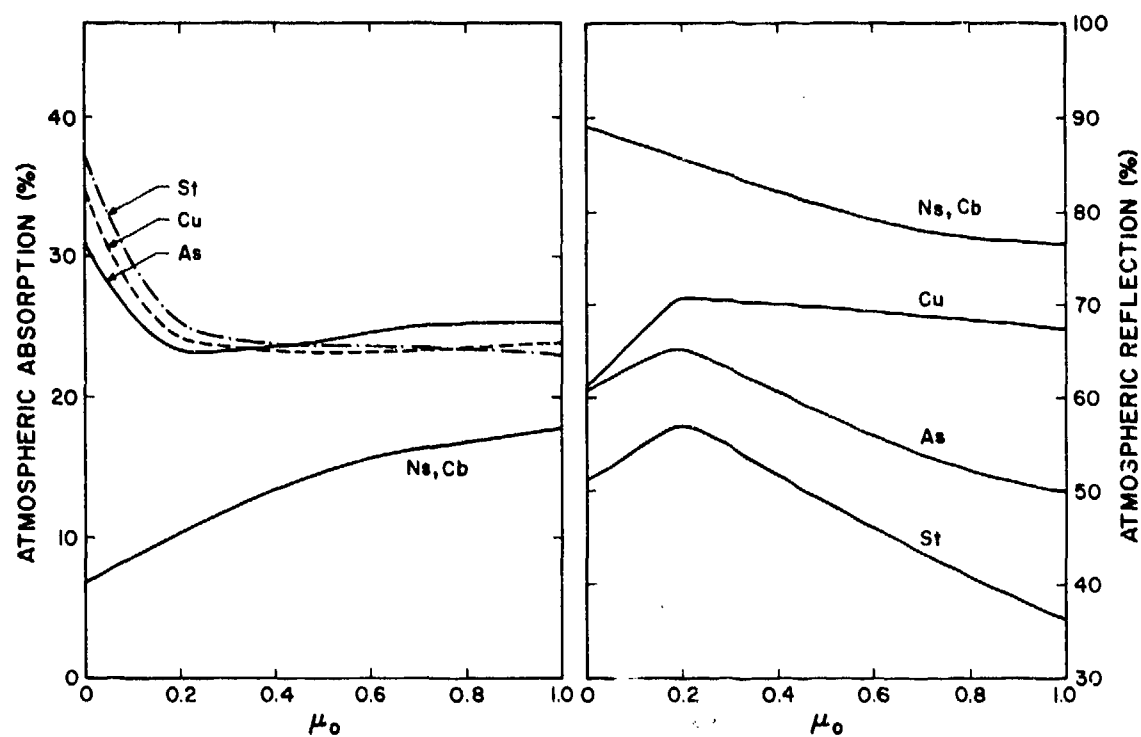


Figure 4. The absorption and reflection of solar radiation by five cloudy atmospheres as functions of the cosine of the solar zenith angle.

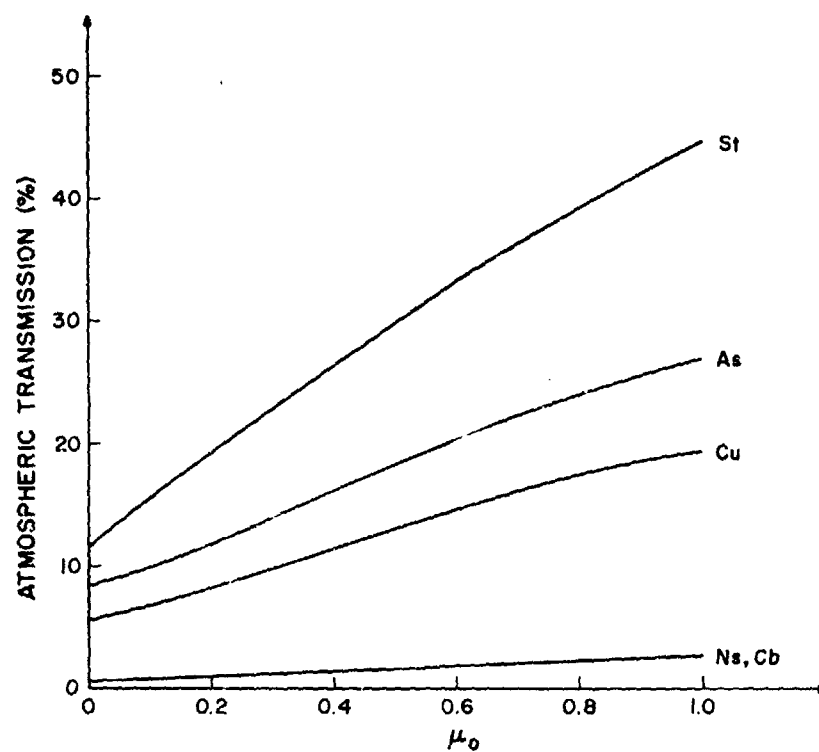


Figure 5 The transmission (including direct and diffuse components) of solar radiation at the bottom of five cloudy atmospheres. The transmitted solar flux in cloudy atmospheres represents an important energy source available to the earth's surface.

MULTIPLE SCATTERING IN PLANETARY ATMOSPHERES

William M. Irvine
Department of Physics and Astronomy
University of Massachusetts
Amherst, Massachusetts 01002
USA

SUMMARY

Certain simple procedures for solving radiative transfer problems in planetary atmospheres are reviewed: the similarity relations relating isotropic to anisotropic scattering, asymptotic results relating known solutions for semi-infinite layers to desired solutions for optical depths $\tau \gg 1$, and expansions relating known solutions for conservative scattering to desired solutions for the nearly conservative case. The complications introduced by atmospheric inhomogeneity, surface reflection, and spectral features are also discussed.

1. INTRODUCTION

Radiative transfer problems in planetary atmospheres may conveniently be referred to as multiple scattering problems, provided that the wavelength being considered is short enough that thermal emission by the atmosphere is not important, or that the thermal emission profile of the atmosphere is taken as known. The sources of radiation then have known properties, and the atmospheric radiation field results from multiple scattering and absorption of photons emitted by these sources.

The principal difficulties in solving such problems arise first, from the frequently highly anisotropic nature of the individual scattering processes and the resultant mathematical complexity of multiple scattering, and second, from the possible presence of atmospheric and surface inhomogeneities. There have been several recent reviews discussing the solution of multiple scattering problems in planetary atmospheres (Hunt, 1971; van de Hulst, 1971; Sobolev, 1972; Irvine and Lenoble, 1974; Lenoble, 1974; Hansen and Travis, 1974; Irvine, 1975), so that I shall assume a knowledge of the relevant terminology and the basic theory. It appears in addition that other speakers at this conference will cover most of the present state of knowledge concerning numerical solution of multiple scattering problems in typical cloudy or hazy atmospheres that are plane-parallel and (somewhat) homogeneous, as well as the inverse problem of deducing the properties of an atmosphere from observations of the radiation field. I shall therefore concentrate on certain approximate procedures which are fast and convenient, on methods for extrapolating from known results, and on deviations from the "standard" homogeneous, plane-parallel problem. For convenience, the discussion will be mostly restricted to the scalar transfer problem, so that polarization may be neglected. The resultant intensities will normally be accurate to a few percent, which is generally sufficient, given our imprecise knowledge of actual atmospheric properties in most circumstances.

I shall use astrophysical terminology, and thus refer to intensity (I) rather than radiance and to flux rather than irradiance. Initially attention will be restricted to homogeneous, plane-parallel atmospheres.

2. SIMILARITY RELATIONS

The equation of radiative transfer which determines the radiation field is for a plane-parallel atmosphere

$$\mu \frac{dI}{d\tau} = -I(\tau, \Omega) + B(\tau, \Omega), \quad (1)$$

where τ is the vertical optical depth, $\Omega = (\arccos \mu, \phi)$ symbolizes the dependence on a polar and an azimuthal angle, and the function B describes the sources of radiation in an elemental volume of the atmosphere. Thus, if atmospheric thermal emission may be neglected relative to solar radiation and if the latter is approximated as a parallel beam (almost always appropriate; cf., however, Irvine, 1975), the source function takes the form

$$B(\tau, \Omega) = \frac{\tilde{\omega}_0}{4\pi} \int_{4\pi} d\Omega' p(\Omega, \Omega') I(\tau, \Omega') + \frac{\tilde{\omega}_0}{4} F e^{-\tau/\mu_0} p(\Omega, \Omega_0), \quad (2)$$

where $\tilde{\omega}_0$ is the single scattering albedo (ratio of scattering to scattering plus absorption coefficients), $p(\Omega, \Omega')$ is the phase function (scattering diagram), solar radiation is incident in a direction $\Omega_0 \equiv (\arccos \mu_0, \phi = 0)$ with flux πF through a surface normal to that direction, and $\int_{4\pi} d\Omega'$ denotes integration over all directions. All of the quantities I , B , τ , $\tilde{\omega}_0$, F , and p are functions of wavelength, so that equations (1) and (2) refer to monochromatic radiation.

When $p \equiv 1$, the single scattering is isotropic, and the solution to equation (1) has been tabulated in terms of the so-called H functions (for semi-infinite atmospheres) or X and Y functions (for atmospheres with finite optical thickness τ_0). A listing of such tables is contained in Irvine and Lenoble (1974), Lenoble (1974), and Irvine (1975). It would obviously be a great simplification in planetary scattering if the solution for a given anisotropic phase function could be reduced to the known solution for isotropic scattering. We would expect that such a transformation might exist provided that the radiation field has been "smoothed" by a large percentage of multiple scattering and/or by integration over angle. Such "smoothing" is necessary to remove the sharp maxima and minima which are present

in the primary scattered radiation if the phase function is highly anisotropic. Obviously no information concerning the azimuthal dependence of the radiation field can be obtained from such a comparison, since for isotropic scattering the intensity is independent of azimuth.

Such similarity relations have been used for some time in neutron transport theory (cf. Davison, 1958). It may be shown that the solution to a given transport problem for a single scattering albedo $\tilde{\omega}_0$ and optical thickness τ_0 will be "similar" (may be approximated by) the solution to the same problem for isotropic scattering and an albedo $\tilde{\omega}_0^*$ and optical thickness τ_0^* , where

$$\tilde{\omega}_0^* = \frac{(1-g)\tilde{\omega}_0}{1-g\tilde{\omega}_0}, \quad (3)$$

$$\tau_0^* = (1-g\tilde{\omega}_0)\tau_0, \quad (4)$$

and g is the asymmetry factor

$$g = \frac{1}{2} \int_{-1}^1 d\mu \mu p(\mu), \quad (5)$$

which characterizes the anisotropy of the phase function. The normalization of p requires that $-1 \leq g \leq 1$, with isotropic scattering corresponding to $g = 0$. Van de Hulst has expressed the similarity relations in the form

$$k^*\tau^* = k\tau_0 \quad (6)$$

$$\frac{1 - \omega_0^*}{k^*} = \frac{1 - \tilde{\omega}_0}{k}, \quad (7)$$

where k is the inverse diffusion length, which is determined by solving the "characteristic equation" for a given phase function. It is the smallest discrete eigenvalue of the transfer equation, so that deep within a homogeneous medium illuminated from outside the radiation field decays as $e^{-k\tau}$. For isotropic scattering

$$\frac{\tilde{\omega}_0}{2k} \ln\left(\frac{1+k}{1-k}\right) = 1, \quad (8)$$

while Figure 1 presents curves relating $\tilde{\omega}_0$, k , and g for the case of the Henyey-Greenstein phase function

$$p(\cos\gamma) = (1-g^2)/(1+g^2-2g\cos\gamma)^{3/2}. \quad (9)$$

Equation (9) is a convenient phase function for modeling purposes, since it may be varied from purely forward scattering ($g = 1$) to purely backward scattering ($g = -1$) by changing just the one parameter g . The similarity relations suggest that the curves in Figure 1 will apply quite closely to any phase function with the same $g = \langle \cos\gamma \rangle$. For the most interesting case of $(1 - \tilde{\omega}_0) \ll 1$, equations (6) and (7) reduce to equations (3) and (4) (cf. Sobolev, 1972, Ch. VIII).

The validity of the relations (6) and (7) for determining the profile of absorption lines formed in a scattering and absorbing atmosphere has been studied by Hansen (1969), who finds good agreement for thick atmospheres with the exact theoretical results except for large angles of incidence of the solar radiation. The validity for integrated quantities such as the albedo is even more striking (van de Hulst and Grossman, 1968). Let us consider the details of such computations.

2.1. Albedos of Semi-Infinite Atmospheres

In this case the properties of any underlying surface can be ignored. It is important to point out, however, under what conditions an actual atmosphere may be considered to be semi-infinite. If the atmosphere is weakly absorbing, in the sense that $[3(1 - \tilde{\omega}_0)(1 - g)]^{1/2} \tau_0 \ll 1$, the atmospheric reflection will be identical to that of a semi-infinite atmosphere to $O([3(1 - g)\tau_0]^{-1})$. In contrast, when $k\tau \gg 1$, the departure from the semi-infinite condition is $O(e^{-2k\tau_0})$.

The ratio of reflected to incident flux on a plane-parallel atmosphere is the plane albedo $A(\mu_0)$ of the atmosphere, and is a function of the angle of incidence $\arccos \mu_0$. For a spherical planet the ratio of total reflected to incident flux is called the Bond or spherical albedo,

$$A_B = 2 \int_0^1 d\mu_0 \mu_0 A(\mu_0). \quad (10)$$

The plane and spherical albedos are given for isotropic scattering by

$$A(\mu_0) = 1 - H(\mu_0)(1 - \tilde{\omega}_0)^{1/2}, \quad (11)$$

$$A_B = 1 - (1 - \tilde{\omega}_0)^{1/2} h_1, \quad (12)$$

where $H(\mu)$ is the familiar Chandrasekhar H-function and h_1 is its first moment $\int d\mu \mu H(\mu)$. Note that h_1 and H are functions of $\tilde{\omega}_0$, although this is often not explicitly indicated.

2.2. Albedos and Surface Illumination for Finite Atmospheres

If the atmospheric optical thickness is not semi-infinite, we must in general take account of the reflecting properties of the planetary surface. Detailed results have been obtained only for isotropic (Lambert Law) surface reflection and specular reflection. We shall confine ourselves to the former case, referring the reader to Sobolev (1972, Ch. IV. §5), and Casti, Kalaba, and Ueno (1969) for a discussion of the latter.

For a finite atmosphere both the albedo and the flux $V(\mu_0, \tau_0)$ illuminating the planetary surface (expressed as a fraction of the incident solar flux at the top of the atmosphere) are important.

Let a be the surface albedo. We may then express the albedo and the surface illumination in the case $a \neq 0$ in terms of quantities characterizing the atmosphere in the absence of such a surface (i.e., for $a = 0$). Designating the former quantities with a superposed bar, we have (e.g., Sobolev, 1972, Ch. IV)

$$\bar{A}(\mu_0, \tau_0) = A(\mu_0, \tau_0) + \frac{a V_s(\tau_0)}{1 - a A_s(\tau_0)} V(\mu_0, \tau_0) \quad (13)$$

and

$$\bar{V}(\mu_0, \tau_0) = \frac{V(\mu_0, \tau_0)}{1 - a A_s(\tau_0)}, \quad (14)$$

where, in analogy to the definition of A_s ,

$$V_s(\tau_0) = 2 \int_0^1 d\mu_0 \mu_0 V(\mu_0, \tau_0). \quad (15)$$

The problem is thus reduced to finding the reflected and transmitted flux in the absence of an underlying surface.

These latter quantities may be written in terms of the auxiliary functions ϕ and ψ as

$$A(\mu_0, \tau_0) = 1 - \phi(\mu_0, \tau_0)/\mu_0 \quad (16)$$

and

$$V(\mu_0, \tau_0) = \psi(\mu_0, \tau_0)/\mu_0. \quad (17)$$

The corresponding spherical albedo and surface illumination are given in terms of the moments of ϕ and ψ as

$$A_s(\tau_0) = 1 - 2 \int_0^1 d\mu_0 \phi(\mu_0, \tau_0) \quad (18)$$

and

$$V_s(\tau_0) = 2 \int_0^1 d\mu_0 \psi(\mu_0, \tau_0). \quad (19)$$

The auxiliary functions are in turn expressed in terms of the more familiar X and Y function by (suppressing the dependence upon τ_0)

$$\phi(\mu) = \frac{2\mu(1 - \tilde{\omega}_0)[(2 - \tilde{\omega}_0 \alpha_0) X(\mu) + \tilde{\omega}_0 \beta_0 Y(\mu)]}{(2 - \tilde{\omega}_0 \alpha_0)^2 - (\tilde{\omega}_0 \beta_0)^2} \quad (20)$$

$$\psi(\mu) = \frac{2\mu(1 - \tilde{\omega}_0)[\tilde{\omega}_0 \beta_0 X(\mu) + (2 - \tilde{\omega}_0 \alpha_0) Y(\mu)]}{(2 - \tilde{\omega}_0 \alpha_0)^2 - (\tilde{\omega}_0 \beta_0)^2} \quad (21)$$

where

$$\alpha_0 = \int_0^1 d\mu X(\mu), \quad \beta_0 = \int_0^1 d\mu Y(\mu).$$

Since as $\tau_0 \rightarrow \infty$, $X(\mu) \rightarrow H(\mu)$, $Y(\mu) \rightarrow 0$, and $\alpha_0 \rightarrow h_0 = 2\tilde{\omega}_0^{-1} [1 - (1 - \tilde{\omega}_0)^{1/2}]$, equations (16) and (20) reduce to equation (11) in the limit of a semi-infinite atmosphere. Tables of X and Y are referenced by Lenoble (1974) and Irvine (1975). We emphasize again that ϕ , ψ , X , Y , and their moments are functions

of $\tilde{\omega}_0$ and hence (normally) of wavelength. The steps in the similarity procedure are thus: (1) relate the known values of $\tilde{\omega}_0$, g , and τ_0 to the "similar" values for isotropic scattering; (2) solve the appropriate isotropic problem for A , A_s , V , and V_s for the case of no surface reflection ($a = 0$) by using tables of X and Y functions; (3) find the desired albedo or surface illumination for $a \neq 0$ from equations (13) and (14).

Approximate values for the flux at any level in an atmosphere may be obtained without using tabulated values (such as H , X , and Y) by procedures such as the Eddington and the Two Stream approximations. These methods are often useful, but in view of existing reviews and other papers at this conference we shall not discuss them further.

2.3. Intensity

Perhaps the most convenient and rapid approximation to use if the angular dependence of the radiation field is desired is a combination of exact first order scattering plus higher order scattering computed for the appropriate isotropic case from the similarity principles. We find

$$R(\Omega, \Omega_0, \tau_0) = \frac{\tilde{\omega}_0 F}{4} \left[\frac{X(\mu) X(\mu_0) - Y(\mu) Y(\mu_0) + [p(\Omega, \Omega_0) - 1][1 - \exp(-\tau_0(\mu^{-1} + \mu_0^{-1}))]}{\mu + \mu_0} \right] \quad (22a)$$

for the reflected intensity, and

$$T(\Omega, \Omega_0, \tau_0) = \frac{\tilde{\omega}_0 F}{4} \left[\frac{X(\mu_0) Y(\mu) - X(\mu) Y(\mu_0) + (p(\Omega, \Omega_0) - 1)(e^{-\tau_0/\mu} - e^{-\tau_0/\mu_0})}{\mu - \mu_0} \right] \quad (22b)$$

for the transmitted intensity, where (as previously) $X(\mu) \equiv X(\mu, \tau_0^*, \tilde{\omega}_0^*)$ and $Y(\mu) \equiv Y(\mu, \tau_0^*, \tilde{\omega}_0^*)$ are given for isotropic scattering in appropriate tables and τ_0^* and $\tilde{\omega}_0^*$ are related to τ_0 and $\tilde{\omega}_0$ by equations (3) - (4) or (6) - (7).

3. ASYMPTOTIC RELATIONS AND EXPANSIONS FOR SMALL ABSORPTION

The specific intensity of radiation may be approximated with the aid of the similarity relations described in the previous section and appropriate tables of H or X and Y functions. There is, however, an annoying tendency for tables to exclude those particular values that are needed for the application at hand. In this connection asymptotic expressions or expansions in terms of a small parameter are often very helpful. Such expressions may be found to relate solutions for semi-infinite atmospheres ($\tau_0 = \infty$) to desired solutions for $\tau_0 \gg 1$, and also to relate solutions for conservative atmospheres ($\tilde{\omega}_0 = 1$) to solutions for the weakly absorbing case ($1 - \tilde{\omega}_0 \ll 1$). Van de Hulst (e.g., 1968) and Sobolev (e.g., 1972) have emphasized this approach, which may of course be used with numerically computed values for arbitrary phase functions, as well as when tabular values are available. Van de Hulst has emphasized that by an appropriate choice of abscissa it is often possible to interpolate accurately between $\tau_0 = \infty$ and values as small as $\tau_0 \approx 3$.

The asymptotic relations for $\tau_0 \gg 1$ make use of quantities which describe the radiation field deep within a homogeneous, semi-infinite medium illuminated from without. If the illuminating flux is πF , as in equation (2), the intensity and source function in this "deep regime" take the azimuth-independent form (Sobolev, 1972)

$$I(\tau, \mu) = F u(\mu_0) \mu_0 i(\mu) e^{-k\tau} \quad (\tau \gg 1), \quad (23)$$

$$B(\tau, \mu) = F u(\mu_0) \mu_0 b(\mu) e^{-k\tau} \quad (\tau \gg 1), \quad (24)$$

where $u(\mu)$ is the "escape function" which describes the relative angular distribution of radiation emerging from a very thick atmosphere with radiation sources at great depths, $i(\mu)$ and $b(\mu)$ describe the angular dependence of the intensity and of the source function in the deep regime, and k is the inverse diffusion length defined previously. It may be shown that

$$i(\mu) = b(\mu)(1 - k\mu)^{-1}, \quad (25)$$

while $b(\mu)$ satisfies the integral equation

$$b(\mu) = \frac{\tilde{\omega}_0}{2} \int_{-1}^1 d\mu' p^0(\mu, \mu') \frac{b(\mu')}{(1 - k\mu')}, \quad (26)$$

where $p^0(\mu, \mu')$ is the azimuthal average of the phase function.

The functions $i(\mu)$, $b(\mu)$, and $u(\mu)$ thus depend in general on the phase function p and the single scattering albedo $\tilde{\omega}_0$. Asymptotic expressions exist, however, in certain cases. Thus, for nearly conservative scattering we obtain

$$i(\mu) = 1 + 3 \left(\frac{1 - \tilde{\omega}_0}{3 - X_1} \right)^{1/2} \mu + (1 - \tilde{\omega}_0) \left(1 + \frac{10}{(5 - X_2)} P_2(\mu_0) \right) \quad (1 - \tilde{\omega}_0) \ll 1 \quad (27)$$

plus terms $O((1 - \tilde{\omega}_0)^{3/2})$, with a similar expression for $b(\mu)$. In equation (27) X_1 are the coefficients of the expansion of the phase function in Legendre polynomials $P_1(\mu)$:

$$P(\mu) = \sum_{i=0}^n X_i P_i(\mu) . \quad (28)$$

Since the asymmetry factor $g = X_1/3$, we see from (27) that $i(\mu)$ depends only on g (not on higher moments of p) through order $(1 - \tilde{\omega}_0)^{1/2}$. The function $u(\mu)$ also depends only weakly on the form of the phase function. In the present case of weak absorption

$$u(\mu) = u_0(\mu)(1 - kD) + O(k^2) , \quad (29)$$

where (cf. eq. (43))

$$D = \frac{6}{3 - X_1} \int_0^1 d\mu \mu^2 u_0(\mu)$$

and u_0 is the function u for $\tilde{\omega}_0 = 1$. The latter function may be approximately represented in linear form as

$$u_0(\mu) = (1 + \beta\mu)(1 + 2\beta/3)^{-1} , \quad (30)$$

where

$$\beta^{-1} = \frac{1}{\pi} \int_0^\pi d\theta \sin^2\theta p(\cos\theta) .$$

The above quantities may now be used to write asymptotic expressions for, e.g., the azimuth independent portion of the reflection R and transmission T functions, which are related to the reflection in the semi-infinite case by

$$R(\mu, \mu_0, \tau_0) = R_\infty(\mu, \mu_0) - \frac{M N e^{-2k\tau_0}}{1 - N^2 e^{-2k\tau_0}} u(\mu) u(\mu_0) \quad (\tau_0 \gg 1) , \quad (31)$$

$$T(\mu, \mu_0, \tau_0) = \frac{M e^{-k\tau_0}}{1 - N^2 e^{-k\tau_0}} u(\mu) u(\mu_0) \quad (\tau_0 \gg 1) , \quad (32)$$

and M and N are constants defined by

$$N = 2 \int_0^1 d\mu_0 \mu_0 u(\mu_0) i(-\mu_0) , \quad (33)$$

$$M = 2 \int_{-1}^1 d\mu \mu i^2(\mu) .$$

In practice, $u(\mu)$ may be found from the tabular or computed values of transmitted intensity for sufficiently large τ_0 (if equation (29) is not applicable), while the constants M and N may be obtained by solving equation (31) or (32) at two values of τ_0 in the asymptotic regime (given that R or T is known at those τ_0).

Various simplifications are possible in equations (31) - (32) in certain cases. If absorption is small ($1 - \tilde{\omega}_0 \ll 1$, so that $k \ll 1$)

$$R(\mu, \mu_0, \tau_0) = R_\infty^0(\mu, \mu_0) - h(\tau_0) u_0(\mu) u_0(\mu_0) , \quad (34)$$

$$T(\mu, \mu_0, \tau_0) = e^{k\tau_0} f(\tau_0) u_0(\mu) u_0(\mu_0) , \quad (35)$$

where

$$h(\tau_0) = \frac{4k}{3(1 - g)} + f(\tau_0) ,$$

$$f(\tau_0) = \frac{8k}{3(1 - g)(e^{2k\tau_0} - 1) + 6\delta k} ,$$

$$\delta = 4 \int_0^1 d\mu \mu^2 u_0(\mu) ,$$

and $u_0(\mu)$ and $R_\infty^0(\mu, \mu_0)$ refer to the case $\tilde{\omega}_0 = 1$.

In the conservative case ($\tilde{\omega}_0 = 1$) or more generally if $k\tau_0 \ll 1$, equations (34) and (35) take the particularly simple form

$$R(\mu, \mu_0, \tau_0) = R_\infty^0(\mu, \mu_0) - 4 \frac{u_0(\mu) u_0(\mu_0)}{3(1-g)\tau_0 + 36} \quad (36)$$

$$\tau(\mu, \mu_0, \tau_0) = \frac{4 u_0(\mu) u_0(\mu_0)}{3(1-g)\tau_0 + 36} \quad (37)$$

Other particular cases, such as $k\tau_0 \gg 1$, may be easily deduced from (31) and (32).

Returning to the case of small true absorption ($1 - \tilde{\omega}_0 \ll 1$), we may write limiting expressions for the plane and spherical albedos of a semi-infinite atmosphere as

$$A(\mu_0) = 1 - 4 \left(\frac{1 - \tilde{\omega}_0}{3 - X_1} \right)^{1/2} u_0(\mu) + \left[\frac{15}{(5 - X_2)} v_0(\mu_0) + \frac{D}{(3 - X_1)} u_0(\mu_0) \right] (1 - \tilde{\omega}_0), \quad (38)$$

($\tau_0 = \infty$)

$$A_s = 1 - 4 \left(\frac{1 - \tilde{\omega}_0}{3 - X_1} \right)^{1/2} + D \left(\frac{1 - \tilde{\omega}_0}{3 - X_1} \right), \quad (39)$$

where the constant

$$D = 24 \int_0^1 d\mu \mu^2 u_0(\mu), \quad (40)$$

the function

$$v_0(\mu_0) = \mu_0^2 - 2 \int_0^1 d\mu \mu^3 R_\infty^0(\mu, \mu_0) \quad (41)$$

is normalized such that $\int_0^1 d\mu \mu v_0(\mu) = 1$, and R_∞^0 is the reflection function (reflection coefficient) for the case $\tilde{\omega}_0 = 1$. The constant D depends only weakly on the form of the phase function, and may in practice be approximated by the value $D = 8.5$ for isotropic scattering.

If the reflected intensity is desired, we note that its average over azimuth is given by

$$R_\infty(\mu, \mu_0) = R_\infty^0(\mu, \mu_0) - \frac{4k}{(3 - X_1)} u_0(\mu_0) u_0(\mu) + O(k^2) \quad (\tau_0 = \infty). \quad (42)$$

Since

$$k = [(1 - \tilde{\omega}_0)(3 - X_1)]^{1/2} + O(1 - \tilde{\omega}_0), \quad (43)$$

equation (42) is correct to $O(1 - \tilde{\omega}_0)$.

Similar expressions may be written for the albedo and surface illumination in the presence of an underlying surface (Sobolev, 1972, Ch. 4).

4. MORE REALISTIC MODELS

The homogeneous, plane-parallel models which form the basis for the results described in previous sections are sometimes too simplified to elucidate actual physical situations. We shall now comment briefly on more complex situations.

4.1 Horizontal Inhomogeneity

Anyone who has flown above a cloud deck must have observed the striking departures from the idealized plane-parallel state which frequently occur. The only approach for planetary atmospheres used heretofore in this situation seems to be the Monte Carlo method. The results suggest that the presence of deep towers and troughs, such as might be expected for cumulus clouds on Earth and perhaps on a planet with violent convective regions such as Jupiter (cf. Squires, 1957), can profoundly influence the form of the radiation field emerging from the atmosphere. The difference from the plane-parallel case is particularly marked when absorption is present ($\tilde{\omega}_0 < 1$; cf. Van Blerkom, 1971). In addition, the presence of horizontal striations will of course introduce an azimuthal dependence in the radiation field, even if the phase function is isotropic.

Appleby and Van Blerkom (1974) have studied the center to limb variation and the variation with phase angle of the equivalent width of absorption lines in planetary spectra. A simple square line shape was used, and a square wave cloud profile with maxima (and minima) running normal to the scan direction was assumed. The resulting curves are qualitatively similar to those obtained by Hunt (1973) for vertically inhomogeneous atmospheres, and show the possible pitfalls of interpreting observational data with an oversimplified model (even though Hunt's models are themselves the most sophisticated yet applied

to the Jovian atmosphere).

Investigation of this problem should have a top priority within present multiple scattering theory.

4.2. Shadowing and Surface Reflection

Usual multiple scattering theory assumes that the scattering centers in the atmosphere are far enough apart so that each particle is in the far field of the scattered radiation from any other particle. According to van de Hulst (1957), this requires that the interparticle distance be greater than about 3ρ , where ρ is the particle radius. This condition would seem to apply to all conceivable atmospheric situations including multiple scattering by large rain drops.

If, on the other hand, the constituent scatterers making up a particulate medium are sufficiently close together that the wavelength $\lambda \ll \rho^2/\Delta$, where Δ is the mean free photon path (or the slant thickness of the layer, if that is smaller), they will cast shadows on each other. If such a medium is viewed from the direction of incident radiation (scattering angle $\gamma = \pi$), no shadows can be seen. This phenomenon produces the bright region observed around an airplane shadow when flying over a rough ground or around one's own shadow cast upon dewy grass, and apparently also the "opposition effect" or anomalous brightening at small phase angles observed for a number of astronomical objects (including the Moon, Mars, Saturn's rings, and certain asteroids, and also for powdered surfaces in the laboratory (Oetking, 1966; Hapke, 1968; Lumme, 1971)). Analysis of the effect may be viewed as part of another largely untouched theoretical problem, the nature of the reflection from natural surfaces.

If the "surface particles" may be taken to be randomly distributed in three dimensions, the problem may be reduced to the computation of a correction to the usual multiple scattering theory used in atmospheric calculations, at least in so far as diffraction of light into the shadow behind each particle may be neglected (Irvine, 1966). The environment within Saturn's rings may approximate such random conditions, but the necessity for particle support in the vertical direction means that it cannot strictly apply to a surface. Nonetheless, Veverka (1974) has obtained good agreement with the observed reflectivity of the Moon and of powdered surfaces using the Irvine (1966) procedure.

Further comparison of theory and experiment is clearly needed. The case of partially transparent particles ($1 - \omega_0 \ll 1$) is particularly important. In this case multiple scattering will predominate, and it is important to determine if the opposition peak will be washed out. There is as yet insufficient laboratory data available for comparison with theory. It is interesting that even small objects in the solar system seem to have a low density regolith (e.g., Phobos and Deimos, cf. Pollack, 1975), so that their surfaces may approximate dense "atmospheres".

4.3. Computation of Spectra

Absorption spectra formed by diffuse reflection or transmission of solar radiation through a partially absorbing planetary atmosphere call for special attention. Both the line shape

$$r_v = \frac{I_v}{I_c}$$

and the equivalent width

$$W = \int dv (1 - r_v)$$

are of interest, where I_c is the intensity in the continuous spectrum adjacent to the line and I_v is the intensity in the line.

To obtain a precision comparable with that obtainable by modern observational procedures, a theoretician must evaluate I_v at a large number of frequencies within the absorption band. At any given frequency, if the assumptions referred to in Section II in this connection are valid, any of the usual methods (cf. Irvine, 1975) may be used. The requirement of multiple calculations may, however, change the computing economics involved in choosing the optimum procedure.

It is possible, provided $p(\cos\gamma)$ is independent of frequency within the limited frequency range of the absorption feature and that the atmosphere is homogeneous, to reduce the problem to the solution of a single transfer problem in the continuum plus the performance of a quadrature or sum. This procedure requires a knowledge of either the probability distribution of photon path lengths travelled by the reflected light (Appleby and Irvine, 1973; Kargin, Krasnokutskaya, and Feigel'son, 1972; Fouquart and Lenoble, 1973) or the intensity corresponding to successive orders of scattering (Uesugi, Irvine, and Kawata, 1971; van de Hulst, 1970a). Determination of the former quantity also provides additional physical insight into the nature of the line formation process. Results at present are limited to homogeneous atmospheres, but with this restriction both methods look promising. Because of the smoothing character of the integration process which specifies the intensity, it would seem that great accuracy is not needed in the determination of the probability distribution, and approximate or numerical results have been obtained by van de Hulst (1974), Romanova (1965), and Fouquart (1974), as well as by the authors cited previously.

An approximate procedure based on use of a variational principle whose extremum gives the reflectivity has been proposed by Stokes and DeMarcus (1971). The method is strictly applicable only for isotropic scattering and for $\mu = \mu_0$, but it is very rapid and has proved quite useful in applications to the outer planets, for which the phase angle is always small (e.g., Michalsky et al., 1974). The method is directly applicable to vertically inhomogeneous atmospheres, but it is not obvious in this case how to

interpret the similarity relations for transformation of the results to more realistic phase functions.

The perturbation procedure proposed by Fymat and Abhyankar (1970, and earlier references therein) may also be used to reduce the problem of determining a spectral line profile to the solution of a single transfer problem. This procedure works for any continuum albedo.

This research has been supported in part by the National Aeronautics and Space Administration under grant NGL 22-010-023.

REFERENCES

1. J. F. Appleby and W. M. Irvine, 1973, "Path Length Distributions of Photons Diffusely Reflected from a Semi-Infinite Atmosphere", Ap. J. **183**, 337.
2. J. F. Appleby and D. J. Van Blerkom, 1974, "Absorption Line Studies of Reflection from Horizontally Inhomogeneous Layers", Icarus, **24**, 51.
3. J. L. Casti, R. Kalaba, and S. Ueno, 1969, "Reflection and Transmission Functions for Finite Isotropically Scattering Atmospheres with Specular Reflectors", J. Quant. Spect. Rad. Trans. **2**, 537.
4. B. Davison, 1958, Neutron Transport Theory, Oxford University Press.
5. D. Deirmendjian, 1969, Electromagnetic Scattering on Spherical Polydispersions, American Elsevier Pub. Co., New York.
6. Y. Fouquart, 1974, "Utilisation des Approximants de Pade pour l'étude des Largeurs Equivalentes des Raies Formees en Atmosphere Diffusante", J. Quant. Spec. Rad. Trans. **14**, 497.
7. Y. Fouquart and J. Lenoble, 1973, "Formation des Raies Spectrales et Etude des Courbes de Croissance dans une Atmosphere Diffusante Semi-Infinite", J. Quant. Spec. Rad. Trans. **13**, 447.
8. J. E. Hansen, 1969, "Absorption Line Formation in a Scattering Planetary Atmosphere: A Test of van de Hulst's Similarity Relations", Ap. J. **158**, 337.
9. J. E. Hansen and J. W. Hovenier, 1971, "The Doubling Method Applied to Multiple Scattering of Polarized Light", J. Quant. Spec. Rad. Trans. **11**, 809.
10. J. E. Hansen and L. D. Travis, 1974, "Light Scattering in Planetary Atmospheres", Space Sci. Revs. **16**, 527.
11. B. W. Hapke, 1968, "On the Particle Size Distribution of Lunar Soil", Planet Space Sci. **16**, 1.
12. G. E. Hunt, 1971, "A Review of Computational Techniques for Analyzing the Transfer of Radiation through a Model Cloudy Atmosphere", J. Quant. Spec. Rad. Trans. **11**, 655.
13. G. E. Hunt, 1973, "Formation of Spectral Lines in Planetary Atmospheres IV. Theoretical Evidence for Structure of the Jovian Clouds from Spectroscopic Observations of Methane and Hydrogen Quadrupole Lines", Icarus **18**, 637.
14. W. M. Irvine, 1966, "The Shadowing Effects in Diffuse Reflection", J. Geophys. Res. **71**, 2931.
15. W. M. Irvine and J. Lenoble, 1974, "Solving Multiple Scattering Problems in Planetary Atmospheres", in UCLA Internation. Conf. Radiat. Remote Probing Atmos. ed. J. G. Kuriyan, Western Periodicals Co., North Hollywood, Calif., 1-57.
16. W. M. Irvine, 1975, "Multiple Scattering in Planetary Atmospheres", Icarus, in press.
17. B. A. Kargin, L. D. Krasnokutskaya, and E. M. Feigel'son, 1972, "Reflection and Absorption of Solar Energy in Cloud Layers", Fiz. Atmosfer. Okean. **8**, 505.
18. G. P. Kuiper, 1947, The Atmospheres of the Earth and Planets, University of Chicago Press.
19. J. Lenoble, 1974, Standard Procedures to Compute Atmospheric Radiative Transfer in a Scattering Atmosphere, Vol. I, Lab. Optique Atmospherique, Univ. Sciences Tech. Lille, France.
20. K. Lumme, 1971, "Interpretations of the Light Curves of Some Non-Atmospheric Bodies in the Solar System", Astrophys. Space Sci. **13**, 219.
21. J. J. Michalsky, R. A. Stokes, R. W. Avery, and W. C. DeMarcus, 1974, "Molecular Band Variations as a Probe of the Vertical Structure of the Jovian Atmosphere", Icarus **21**, 55.
22. P. Oetking, 1966, "Photometric Studies of Diffusely Reflecting Surfaces with Applications to the Brightness of the Moon", J. Geophys. Res. **71**, 2505.
23. G. O. Olaofe and S. Levine, 1967, "Electromagnetic Scattering by a Spherically Symmetric Inhomogeneous Particle", in Electromagnetic Scattering, ed. R. L. Rowell and R. F. Stein, Gordon and Breach Pub. Co.
24. J. B. Pollack, 1975, "Phobos and Deimos, a Review", Space Science Revs., in press.

25. L. M. Romanova, 1965, "Limiting Cases of the Distribution of Paths for Photons Emerging from a Thick Light-Scattering Layer", Fiz. Atmos. Okean. 1, 599.
26. V. V. Sobolev, 1972, Rasseyanie Sveta v Atmosferakh Planet, Izd. "Nauka", Moscow. [Light Scattering in Planetary Atmospheres, Pergamon Press, 1975].
27. P. Squires, 1957, "The Equatorial Clouds of Jupiter", Ap. J. 126, 185.
28. R. A. Stokes and W. C. DeMarcus, 1971, "A Simple Technique for Calculating Line Profiles of Inhomogeneous Planetary Atmospheres", Icarus 14, 307.
29. A. Uesugi, W. M. Irvine and Y. Kawata, 1971, "Formation of Absorption Spectra by Diffuse Reflection from a Semi-Infinite Planetary Atmosphere", J. Quant. Spec. Rad. Trans. 11, 797.
30. D. Van Blerkom, 1971, "Diffuse Reflection from Clouds with Horizontal Inhomogeneities", Ap. J. 166, 235.
31. H. C. van de Hulst, 1957, Light Scattering by Small Particles, John Wiley & Sons, New York.
32. H. C. van de Hulst, 1968, "Asymptotic Fitting, A Method for Solving Anisotropic Transfer Problems in Thick Layers", J. Comp. Phys. 3, 291.
33. H. C. van de Hulst, 1970, "High Order Scattering in Diffuse Reflection from a Semi-Infinite Atmosphere", Astron. and Astrophys. 2, 374.
34. H. C. van de Hulst, 1971, "Multiple Scattering in Planetary Atmospheres", J. Quant. Spect. Rad. Trans. 11, 785.
35. H. C. van de Hulst, 1974, "Multiple Scattering in Cloud Layers: Some Results", UCLA International Conf. Radiat. Remote Probing Atmos., ed. J. G. Kuriyan, Western Periodicals Co., North Hollywood, Calif., pp. 162-195.
36. H. C. van de Hulst and K. Grossman, 1968, "Multiple Light Scattering in Planetary Atmospheres", in The Atmospheres of Venus and Mars, ed. J. C. Brandt and M. B. McElroy, Gordon and Breach Science Pub.
37. J. Veverka, 1974, "Photometry and Polarimetry of Satellite Surfaces", IAU Colloq. 28, in press.

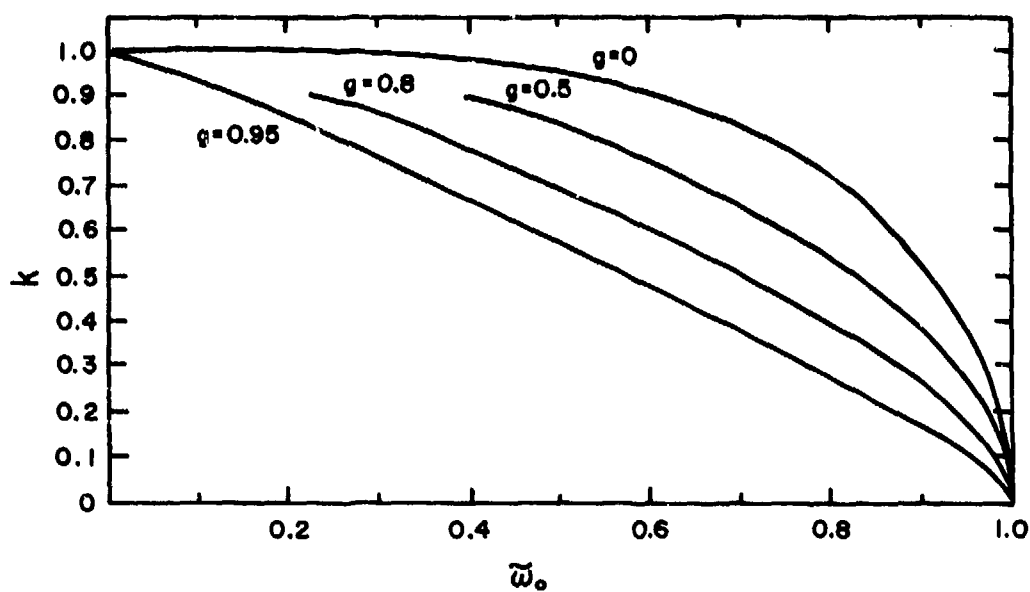


FIGURE 1: Inverse diffusion length k as a function of single scattering albedo $\tilde{\omega}_0$ for a Henyey-Greenstein phase function (9) with four choices of the asymmetry factor $g = \langle \cos \gamma \rangle$.

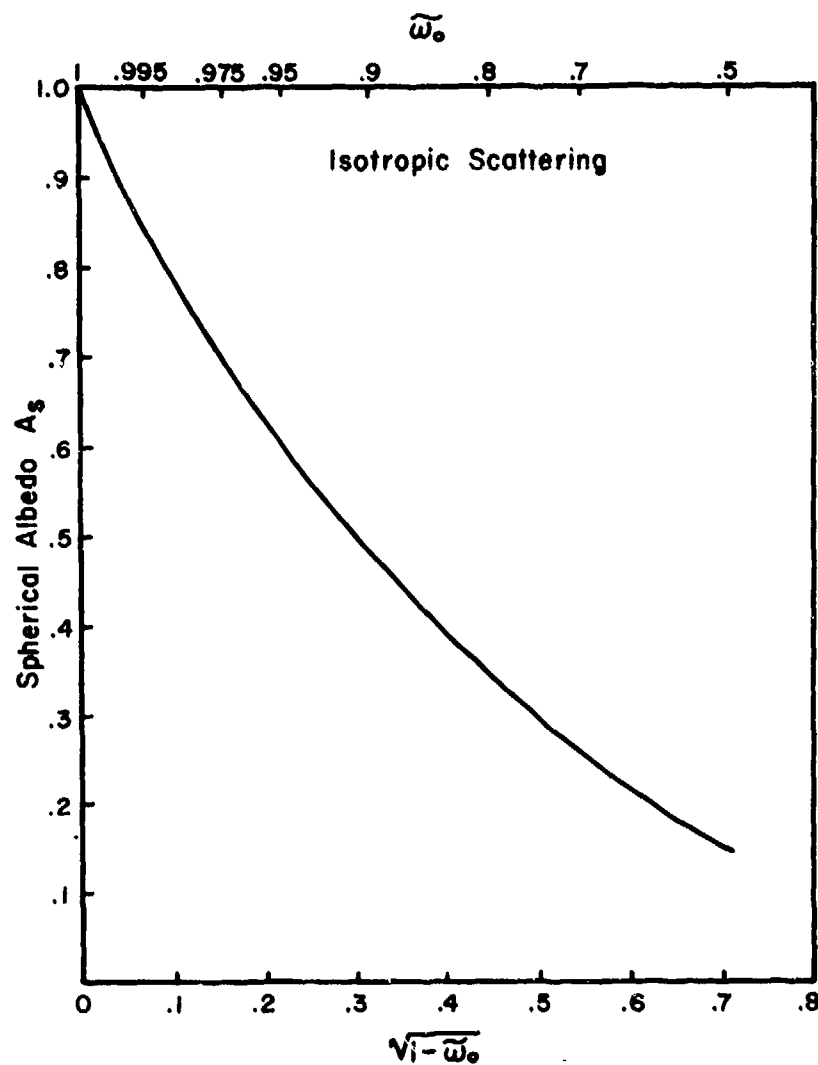


FIGURE 2: Spherical albedo A_s of an isotropically scattering semi-infinite atmosphere as a function of single scattering albedo $\tilde{\omega}_0$.

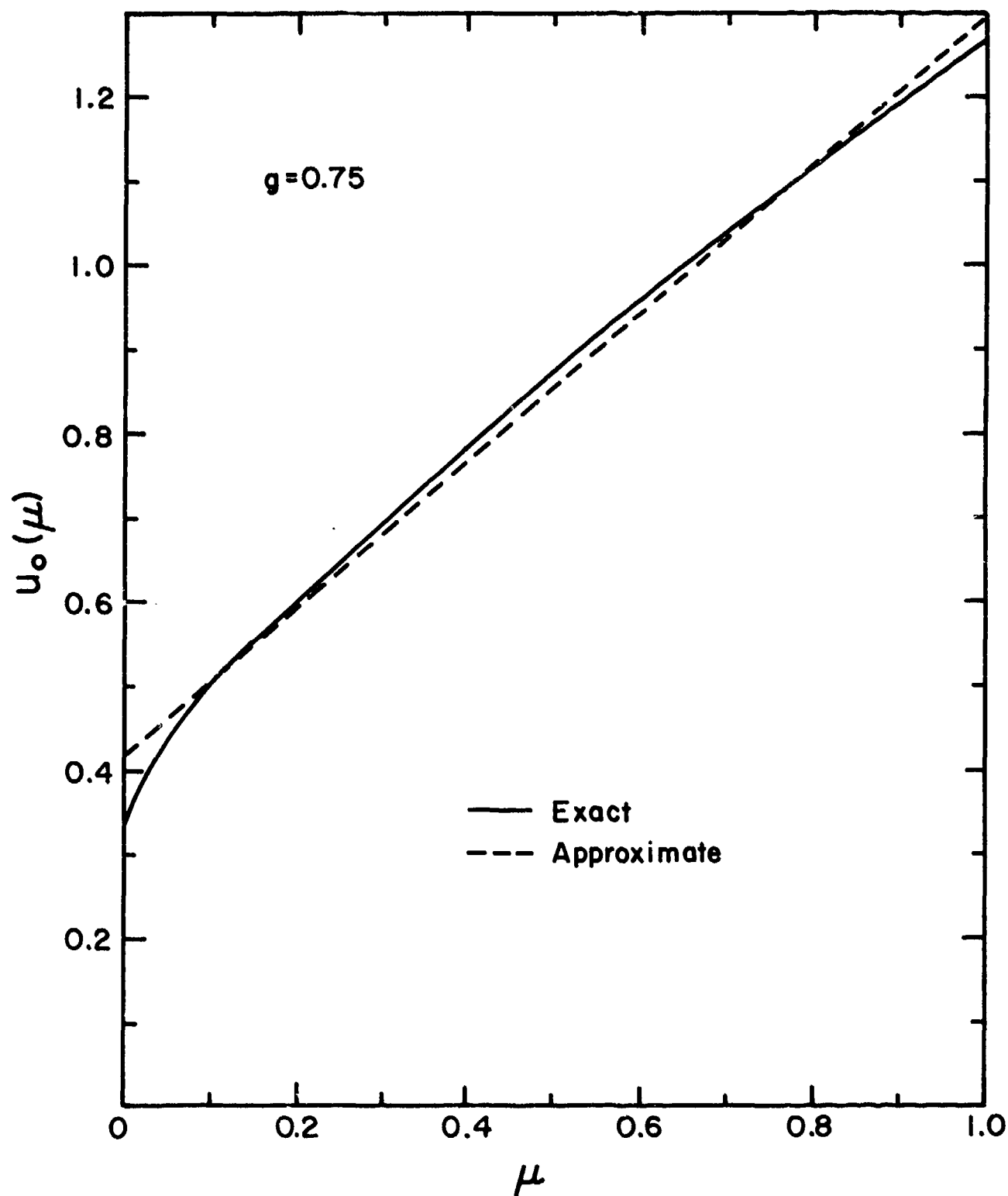


FIGURE 3: Escape function $u_0(\mu)$ for conservative scattering ($\tilde{\omega}_0 = 1$) with a Henyey-Greenstein phase function (equation 9) and an asymmetry factor $g = 0.75$. Straight line is the approximation given by equation (30).

METHODES POUR RESOUDRE L'EQUATION DE TRANSFERT RADIATIF
DANS DES COUCHES D'EPAISSEUR FINIE

J. LENOBLE

LABORATOIRE D'OPTIQUE ATMOSPHERIQUE - ERA n° 466 du C.N.R.S.
UNIVERSITE DES SCIENCES ET TECHNIQUES DE LILLE
B.P. 36 --59650 VILLENEUVE D'ASCQ - FRANCE

RESUME

Après avoir rappelé les caractéristiques générales du problème de transfert radiatif, on passe brièvement en revue les méthodes de solution pour une atmosphère plan-parallèle homogène horizontalement et on donne quelques comparaisons numériques. Ensuite les problèmes plus difficiles d'inhomogénéités horizontales et de sphéricité sont considérés.

SUMMARY

METHODS FOR SOLVING THE EQUATION OF RADIATIVE TRANSFER
THROUGH FINITE THICKNESS LAYERS

After recalling the general problem of radiative transfer, the methods of solution for a plane-parallel horizontally homogeneous atmosphere are briefly reviewed, a few numerical comparisons are shown. Then the more difficult problems of horizontal inhomogeneities and of sphericity are considered.

1 - INTRODUCTION

La propagation de la lumière même dans une atmosphère claire dépend des diffusions multiples par les molécules d'air et les aérosols ; à fortiori le phénomène de diffusion devient prépondérant dans les nuages ou le brouillard.

Après avoir rappelé les principales définitions et l'équation de transfert qui régit le rayonnement dans une atmosphère diffuseuse, nous envisagerons successivement, par ordre de complexité croissante, le cas des atmosphères plan-parallèles homogènes, présentant des inhomogénéités verticales, puis présentant des inhomogénéités horizontales et enfin le cas des atmosphères sphériques.

2 - DEFINITIONS - EQUATION DE TRANSFERT

2-1 - Caractéristiques de l'atmosphère

L'atmosphère sera caractérisée, en chaque point, et pour chaque fréquence, par le coefficient d'extinction $K = k + \sigma$, somme du coefficient d'absorption k et du coefficient de diffusion σ , par l'albédo pour une diffusion $\omega_0 = \sigma/K$, et par la fonction de phase $p(\theta)$ qui définit la répartition du rayonnement diffusé en fonction de l'angle θ entre la direction d'incidence et la direction de diffusion ; $p(\theta)$ est normalisée avec la condition

$$\iint p(\theta) d\omega = 4\pi$$

(1)

Enfin on définira l'épaisseur optique correspondant à un trajet géométrique S par

$$\tau = \int_0^S K(s) ds \quad (2)$$

2-2- Caractéristiques du champ radiatif

Le champ radiatif sera défini par sa luminance énergétique monochromatique $I(\vec{r}, \vec{\Omega})$, où ν est la fréquence, \vec{r} le rayon vecteur caractérisant chaque point à partir d'une origine O et $\vec{\Omega}$ la direction de propagation.

Dans la suite nous nous placerons toujours en rayonnement monochromatique et nous omettrons l'indice ν . Il sera en général commode de réserver I pour le champ de rayonnement diffus, auquel on ajoutera le rayonnement directement transmis des sources.

Le flux net en un point (\vec{r}) à travers un plan perpendiculaire à la direction $\vec{\Omega}$ sera

$$F_{\vec{\Omega}}(\vec{r}) = \iint I(\vec{r}, \vec{\Omega}') \cos(\vec{\Omega}, \vec{\Omega}') d\omega \quad (3)$$

$$= F_{\vec{\Omega}}^+(\vec{r}) - F_{\vec{\Omega}}^-(\vec{r}) \quad (4)$$

où F^+ et F^- sont respectivement les éclairagements énergétiques monochromatiques sur les deux faces du plan considéré.

Notons enfin que l'utilisation d'un formalisme matriciel permet de tenir compte de l'état de polarisation du rayonnement par des équations analogues à celles que nous développerons ici sans polarisation.

2-3 - Equation de transfert

L'équation de transfert s'obtient sans peine, en faisant le bilan d'énergie dans un élément de volume, sous la forme

$$\vec{\Omega} \cdot \vec{\nabla} I(\vec{r}, \vec{\Omega}) = K(\vec{r}) \{ I(\vec{r}, \vec{\Omega}) - J(\vec{r}, \vec{\Omega}) \}, \quad (5)$$

où la fonction source J s'écrit

$$J(\vec{r}, \vec{\Omega}) = \frac{\bar{\omega}_0(\vec{r})}{4\pi} \iint p(\vec{r}; \vec{\Omega}, \vec{\Omega}') I(\vec{r}, \vec{\Omega}') d\omega' + \mathcal{J}(\vec{r}, \vec{\Omega}) + (1 - \bar{\omega}_0(\vec{r})) B(\vec{r}) \quad (6)$$

le premier terme correspond aux diffusions multiples, le deuxième aux sources intérieures ou extérieures et le troisième à l'émission thermique, $B(\vec{r})$ étant la luminance du corps noir à la température qui règne au point (\vec{r}).

Dans la suite, nous nous intéresserons à la diffusion dans l'atmosphère du rayonnement solaire, qui constituera la seule source, et l'émission thermique pourra être négligée.

Des conditions aux limites de l'atmosphère doivent être associées à l'équation (6).

3 - ATMOSPHERE PLAN-PARALLELE HOMOGENE

Nous considérerons ici une atmosphère limitée par deux plans parallèles infinis et éclairée uniformément sur sa face supérieure par le faisceau parallèle du soleil (Fig. 1).

La seule variable de position sera alors l'altitude z et une direction $\vec{\Omega}$ sera repérée par l'angle θ avec la verticale ascendante (ou $\mu = \cos\theta$), et un azimuth ϕ .

Remarquons immédiatement qu'une atmosphère où le coefficient d'extinction K varie avec l'altitude z se ramène au cas d'une atmosphère homogène en utilisant comme variable d'altitude, l'épaisseur optique τ au dessus de l'altitude considérée,

$$\tau = \int_z^Z K(z) dz \quad (7)$$

l'épaisseur optique totale sera

$$\tau_1 = \int_0^Z K(z) dz \quad (8)$$

L'équation de transfert s'écrit alors

$$\mu \frac{\partial I(\tau; \mu, \phi)}{\partial \tau} = I(\tau; \mu, \phi) - J(\tau; \mu, \phi) \quad (9)$$

avec

$$J(\tau; \mu, \phi) = \frac{\bar{\omega}_0}{4\pi} \int_0^{2\pi} \int_{-1}^{+1} p(\mu, \phi; \mu', \phi') I(\tau; \mu', \phi) d\mu' d\phi' + \frac{\bar{\omega}_0}{4} p(\mu, \phi; \mu_0, \phi_0) \pi F e^{\tau/\mu_0}, \quad (10)$$

où πF est l'éclairement produit par le faisceau incident sur un plan normal à sa direction (μ_0, ϕ_0) .
Les conditions aux limites seront alors

$$\begin{aligned} I(0; \mu < 0, \phi) &= 0, \\ I(\tau_1; \mu > 0, \phi) &\text{ donné par la loi de réflexion du sol.} \end{aligned} \quad (11)$$

En intégrant (9) avec les conditions aux limites, on peut exprimer I en fonction de J ; cette expression combinée avec (10) donne une forme intégrale de l'équation de transfert portant sur I ou sur J .

Il est parfois commode d'introduire les fonctions de réflexion et de transmission d'une couche d'épaisseur τ_1 , définies par

$$\begin{aligned} I^+(0; +\mu, \phi) &= \frac{1}{4\pi\mu} S(\tau_1; \mu, \phi; \mu_0, \phi_0) \pi F, \\ I^-(\tau_1; -\mu, \phi) &= \frac{1}{4\pi\mu} T(\tau_1; \mu, \phi; \mu_0, \phi_0) \pi F. \end{aligned} \quad (12)$$

A partir de principes d'invariance et de l'équation de transfert on peut obtenir des équations intégrales non linéaires portant sur S et T .

D'autre part en utilisant des principes d'interaction, on peut exprimer les fonctions S et T pour une couche d'épaisseur $\tau_1 = \tau'_1 + \tau''_1$, à partir de ces mêmes fonctions connues pour les couches τ'_1 et τ''_1 .

Si on utilise comme représentation mathématique de la fonction de phase un développement en polynômes de Legendre

$$p(\theta) = \sum_{\ell=0}^L \beta_\ell P_\ell(\cos\theta), \quad (13)$$

on peut introduire un développement en série de Fourier de la luminance

$$I(\tau; \mu, \phi) = \sum_{S=0}^L (2-\delta_S^0) I^S(\tau; \mu) \cos S(\phi - \phi_0), \quad (14)$$

et séparer l'équation de transfert en $(L+1)$ équations portant sur les $I^S(\tau; \mu)$.

3-1 - Méthodes analytiques exactes

Les méthodes analytiques exactes ont surtout l'intérêt d'éclairer la structure mathématique et le comportement général des solutions de l'équation de transfert, mais elles n'ont pu en général être développées et en tout cas appliquées que pour des lois de diffusion très simples (isotrope ou Rayleigh).

La méthode des fonctions propres singulières (Case et Zweifel - 1967) utilise directement l'équation de transfert (9) et la méthode de Wiener-Hopf (Hopf - 1934) la forme intégrale de cette équation.

La méthode des principes d'invariances (Chandrasekhar - 1950) permet d'exprimer le rayonnement sortant des deux faces de la couche à partir de fonctions $X(\mu)$ et $Y(\mu)$ dont de nombreuses tables numériques existent pour les cas simples mentionnés ci-dessus. Pour cette raison elle sert souvent de test de comparaisons aux méthodes numériques.

3-2 - Méthodes pour ordinateurs

Nous regrouperons sous ce titre l'ensemble des méthodes qui sont actuellement couramment utilisées pour calculer le champ radiatif dans les atmosphères planétaires.

Certaines peuvent être considérées comme purement numériques, comme la Méthode de Monté-Carlo (Plaza et Kattawar 1971), ou la "DART Method" (Gray et al. 1973); elles demandent des temps de calcul longs pour une précision moyenne et ne sont pas compétitives dans le cas simple d'une atmosphère plan parallèle homogène. Elles prennent par contre tout leur intérêt dans les cas plus complexes, comme nous le verrons plus loin.

Les autres méthodes utilisent un traitement analytique plus ou moins long avant le calcul numérique sur ordinateur.

La méthode des ordres successifs consiste comme son nom l'indique à résoudre l'équation de transfert (9) pour le rayonnement diffusé n fois à partir de la fonction source (10) due au rayonnement diffusé $(n-1)$ fois (Lenoble 1954); elle suit donc de près la réalité du processus physique, mais le temps de calcul croît rapidement avec τ_1 , surtout quand $\bar{\omega}_0$ est voisin de 1. Notons que pour les couches très minces, le premier terme qui correspond à la diffusion primaire et peut s'exprimer analytiquement constitue une approximation suffisante de la luminance totale. La méthode d'itération de Gauss-Seidel (Herman 1963) est également lente pour τ_1 grand.

La méthode des harmoniques sphériques (Deuzé et al. 1973, et celle des ordonnées discrètes (Liou 1973) consistent toutes les deux à résoudre approximativement (9), la première en représentant $I^s(\tau, \mu)$ en série de fonctions associées de Legendre, et la deuxième en approchant l'intégrale par une somme finie de termes. Les deux méthodes sont voisines et semblent avantageuses au point de vue temps de calcul.

Plusieurs méthodes travaillent sur les fonctions de réflexion et transmission : "Matrix Operator Method" (Grant et Hunt 1969, Plass et al. 1973), "Adding Method" sous la forme très avantageuse de "Doubling" pour les couches homogènes (Hansen 1969), "Invariant Imbedding Method" (Bellman et al. 1963). Ces méthodes semblent avoir des efficacités du même ordre et ont été très largement employées.

Les tableaux I et II donnent quelques exemples de comparaisons de méthodes.

3-3 - Méthodes approximatives

Les méthodes décrites ci-dessus ont en commun l'inconvénient de nécessiter un travail important de programmation et l'emploi d'ordinateurs relativement puissants ; dans le cas, où les calculs doivent être répétés pour de nombreuses valeurs des paramètres, les temps machine risquent de devenir prohibitifs ; d'où la recherche de méthodes approximatives permettant de réduire largement le temps calcul ou même d'éviter l'emploi de l'ordinateur.

Ces méthodes impliquent en général une approximation assez grossières du problème de transfert et des propriétés de l'atmosphère et elles ne permettent pas d'obtenir correctement la représentation détaillée du champ radiatif ; elles sont donc en général employées essentiellement pour les calculs des flux.

Nous citerons comme méthodes approchées les relations de similarité (Van de Hulst et Grossman 1968), la méthode d'Eddington (Kawata et Irvine 1970), la méthode à deux flux qui comprend diverses variantes (Lyzena, 1973) et la méthode du noyau exponentiel (Wang, 1972). Suivant l'épaisseur optique de la couche, sa fonction de phase et son albédo pour une diffusion, l'une ou l'autre de ces méthodes se révélera préférable. Des comparaisons de flux sont données dans le tableau III.

4 - ATMOSPHERE PLAN-PARALLELE INHOMOGENE VERTICALEMENT

Nous avons déjà noté que le cas où seul le coefficient d'extinction K varie avec l'altitude, peut se ramener rigoureusement au cas d'une atmosphère homogène ; c'est le cas où l'absorption est due aux particules diffusantes elles-mêmes ou bien le cas où centres absorbants et diffusants restent uniformément mélangés et où seule leur densité varie (Ex : atmosphère moléculaire pure, hors des bandes d'absorption de l'ozone).

Si les particules diffusantes restent partout les mêmes mais que leur rapport de mélange avec l'absorbant varie avec l'altitude, la fonction de phase $p(\theta)$ reste constante, mais l'albédo pour une diffusion ω devient fonction de z (Ex : atmosphère moléculaire dans les bandes de l'onde atmosphère contenant des aérosols non répartis proportionnellement à la pression du gaz absorbant si la diffusion moléculaire est négligeable).

Enfin si la nature ou les dimensions des particules diffusantes varient avec l'altitude, la fonction de phase devient également fonction de z (Ex : atmosphère où aérosols et molécules contribuent à la diffusion, avec un rapport de mélange fonction de z).

La plupart des méthodes développées au § 3-2 s'adoptent sans difficultés à ce cas. Néanmoins les plus rapides, qui tiraient leur avantage de l'homogénéité de l'atmosphère ne s'appliquent plus directement. Le meilleur exemple en est la "Doubling Method" qui a partir des fonctions S et T pour une couche mince d'épaisseur τ , calculait ces mêmes fonctions pour les couches $2\tau, 4\tau, 8\tau, \dots$ etc, et qui doit dans le cas inhomogène être remplacée par la "Adding Method" qui consiste à superposer des couches fines de même épaisseur et est beaucoup plus lente. De même les harmoniques sphériques ne peuvent plus être développées analytiquement aussi loin (Canosa et Penafielu, 1973).

Dans le cas où seul ω est fonction de z , il est peut-être avantageux de déduire les résultats pour l'atmosphère inhomogène, à partir de ceux de l'atmosphère homogène par une méthode de perturbation (Deuzé et al., 1973, Fymat et Abhyankar, 1969).

5 - ATMOSPHERE PLAN-PARALLELE INHOMOGENE HORIZONTALEMENT

Nous classerons dans cette catégorie le cas d'une atmosphère elle-même homogène au-dessus d'un sol inhomogène ; l'inhomogénéité horizontale du champ radiatif est alors introduite à travers les conditions aux limites.

Mais le problème le plus difficile et sans doute le plus important est celui des nuages dispersés de dimensions finies.

Dans l'atmosphère inhomogène horizontalement un point doit être repéré par ses trois coordonnées (x, y, z) et l'équation de transfert s'écrit

$$\begin{aligned} (1-\mu^2)^{1/2} \cos\phi \frac{\partial I(x, y, z; \mu, \phi)}{\partial x} + (1-\mu^2)^{1/2} \sin\phi \frac{\partial I(x, y, z; \mu, \phi)}{\partial y} \\ + \mu \frac{\partial I(x, y, z; \mu, \phi)}{\partial z} = -K(x, y, z) \{I(x, y, z; \mu, \phi) - J(x, y, z; \mu, \phi)\} \end{aligned} \quad (5)$$

avec

$$J(x, y, z; \mu, \phi) = \frac{\bar{\omega}_0(x, y, z)}{4\pi} \int_0^{2\pi} \int_0^{\pi} p(x, y, z; \mu, \phi; \mu', \phi') I(x, y, z; \mu', \phi') d\mu' d\phi' \\ + \frac{\bar{\omega}_0(x, y, z)}{4} p(x, y, z; \mu, \phi; \mu_0, \phi_0) F \exp \left(\frac{1}{\mu_0} \int_z^\infty K(x', y', z') dz' \right) . \quad (16)$$

Même en utilisant des représentations mathématiques très simplifiées de l'inhomogénéité, le traitement analytique ou semi-analytique de ces équations se révèle difficile et assez peu de tentatives dans ce sens ont été faites.

La méthode de Monté Carlo au contraire permet de traiter ce type de problèmes sans difficultés de principe, bien qu'au prix de temps calcul élevés (Kee et Cox, 1974 - Van Blerkom 1971).

Une solution approximative consiste à calculer le rayonnement pour une couverture nuageuse partielle à partir des résultats pour une couverture uniforme et en l'absence de nuages. Elle ne permet sans doute d'obtenir que les flux et ne tient évidemment pas compte des diffusions latérales par les nuages qui sont importantes (Kee et Cox, 1974).

5 - ATMOSPHERE SPHERIQUE

Le modèle d'une atmosphère plan-parallèle constitue une bonne approximation de l'atmosphère terrestre, tant que ni la direction d'incidence, ni la direction d'observation ne sont trop proches de l'horizon. Par contre dans les problèmes de crépuscule ou de visées à l'horizon, qui interviennent fréquemment dans les méthodes de télédétection, il faut tenir compte de la sphéricité de la terre.

Si on utilise toujours un système de coordonnées sphériques avec l'axe des z coïncidant avec la verticale locale oM , une direction \vec{n} sera repérée par $\theta = \arccos \mu$ et ϕ , et un point M par $oM = r$ et indirectement par la direction (μ_0, ϕ_0) du soleil. En supposant de plus que l'atmosphère a la symétrie sphérique, c'est-à-dire que ses propriétés en un point ne dépendent que de r (cas analogue à l'homogénéité horizontale dans l'hypothèse plan-parallèle), l'équation de transfert s'écrit

$$\left[\mu \frac{\partial}{\partial r} + \frac{1-\mu^2}{r} \frac{\partial}{\partial \mu} + \frac{(1-\mu^2)^{1/2} (1-\mu_0^2)^{1/2}}{r} \left\{ \cos(\phi-\phi_0) \frac{\partial}{\partial \mu_0} \right. \right. \\ \left. \left. + \frac{\mu_0}{1-\mu_0^2} \sin(\phi-\phi_0) \frac{\partial}{\partial (\phi-\phi_0)} \right\} \right] I(r, \mu_0, \phi_0; \mu, \phi) = -K(r) \left(I(r; \mu_0, \phi_0; \mu, \phi) - J(r; \mu_0, \phi_0; \mu, \phi) \right) , \quad (17)$$

avec

$$J(r; \mu_0, \phi_0; \mu, \phi) = \frac{\bar{\omega}_0(r)}{4\pi} \int_0^{2\pi} \int_{-1}^{+1} p(r; \mu, \phi; \mu', \phi') I(r; \mu_0, \phi_0; \mu', \phi') d\mu' d\phi' \\ + \frac{\bar{\omega}_0(r)}{4} p(r; \mu, \phi; \mu_0, \phi_0) F \exp \{-\tau(r, \mu_0)\} \quad (18)$$

Là encore la méthode de Monté Carlo s'applique et la DART Method (Gray et al., 1973) a été spécialement conçue pour ce type de problème. Néanmoins d'assez nombreux travaux ont été consacrés à la recherche de méthodes analytiques et ont donné des résultats au moins dans les cas simples (Minin et Sobolev, 1963, Smokty, 1969, Bellman et al., 1969).

6 - CONCLUSION

Quand l'atmosphère peut-être assimilée à une couche plan-parallèle horizontalement homogène, de nombreuses méthodes permettent de résoudre l'équation de transfert et le choix entre ces méthodes sera dictée par le type de problème envisagé, la précision désirée et enfin les moyens de calcul disponibles.

Par contre dans les cas plus complexes, où il est nécessaire de tenir compte des inhomogénéités horizontales ou de la sphéricité, un gros travail reste à faire pour améliorer les méthodes existantes et en rechercher de nouvelles.

REFERENCES

Une description détaillée des méthodes, ainsi qu'une bibliographie étendue est donnée dans la monographie suivante :

I.A.M.A.P. Radiation Commission (1974) "Standard Procedures to Compute Atmospheric Radiative Transfer in a Scattering Atmosphere".

- BELLMAN R.E., KAGIWADA H.H., KALABA R.E., UENO S., 1969 - "Diffuse Reflection of Solar Rays by a Spherical Shell Atmosphere". - *Icarus* 11, 417.
- BELLMAN R., KALABA R., PRESTRUD M.C., 1963 - "Invariant Imbedding and Radiative Transfer in Slabs of Finite Thickness". - American Elsevier Publ. Co. New York.
- CASE K.M., ZWEIFEL P.F., 1967 - "Linear Transport Theory". - Addison - Wesley Publ.
- CANOSA J., PENAFIELD H.R., 1973 - "A Direct Solution of the Radiative Transfer Equation : Application to Rayleigh and Mie Atmospheres". - *Jl. Quant. Spect. Rad. Transfer*, 13, 21.
- CHANDRASEKHAR S., 1950 - "Radiative Transfer" - Oxford Univ. Press - Dover Publ. (1960).
- DEUZE J.L., DEVAUX C., HERMAN M., 1973 - "Utilisation de la Méthode des Harmoniques Sphériques dans les calculs de transfert radiatif. - Extension au cas de couches diffusantes d'absorption variable" *Nouv. Rev. Opt.*, 4, 307.
- DEVAUX C., FOUQUART Y., HERMAN M., LENOBLE J., 1973 - "Comparaison de diverses méthodes de résolution de l'équation de transfert du rayonnement dans un milieu diffusant". - *Jl. Quant. Spect. Rad. Transfer*, 13, 1421.
- FYMAT A.L., ABHYANKAR K.D., 1969 - "Theory of Radiative Transfer in Inhomogeneous Atmospheres - I". - *Astroph. Jl.*, 158, 315.
- GRANT I.P., HUNT G.E., 1969 - "Discrete Space Theory of Radiative Transfer - I - Fundamentals". - *Proc. Roy. Soc. A* 313, 183.
- GRAY C.R., MALCHOW M.L., MERRIT D.C., VAR R.E., WHITNEY C.K., 1973 - "Aerosol Physical Properties from Satellite Horizon Inversion Profile". - Report NASA CR. 112311.
- HANSEN J.E., 1969 - "Radiative Transfer by Doubling very Thin Layers". - *Astroph. Jl.*, 155, 565.
- HERMAN B.M., 1963 - "A Numerical Solution to the Equation of Radiative Transfer for Particles in the Mie Region". - Ph. D. Dissertation University of Arizona - Tucson.
- HOPF E., 1934 - "Mathematical Problems of Radiative Equilibrium". - Cambridge Univ. Press.
- KAWATA Y., IRVINE W.M., 1970 - "The Eddington Approximation for Planetary Atmospheres". - *Astroph. Jl.*, 160, 787.
- LENOBLE J., 1954 - "Contribution à l'étude du rayonnement ultraviolet solaire, de sa diffusion dans l'atmosphère, et de sa pénétration dans la mer". - *Ann. Geophys.*, 10, 187.
- LIU K.N., 1973 - "A Numerical Experiment on Chandrasekhar's Discrete Ordinate Method for Radiative Transfer. Applications to Cloudy and Hazy Atmospheres". - *Jl. Atm. Sc.*, 30, 1303.
- LYZENGA D.R., 1973 - "Note on the Modified Two-Stream Approximation of Sagan and Pollack". - *Icarus*, 19, 240.
- Mc KEE T.B., COX S.K., 1974 - "Scattering of Visible Radiation by Finite Clouds". - *Jl. Atm. Sc.*, 31, 1885.
- MININ I.N., SOBOLEV V.V. 1963 - "On the Theory of Light Scattering in Planetary Atmospheres". - *Sov. Astron. Jl.*, 7, 379.
- PLASS G.N., KATTAWAR G.W., CATCHINGS F.G., 1973 - "Matrix Operator Theory of Radiative Transfer. - I - Rayleigh Scattering". - *App. Optics*, 12, 314.
- PLASS G.N., KATTAWAR G.W., 1971 - "Radiance and Polarization of the Earth's Atmosphere with Haze and Clouds". - *Jl. Atm. Sc.*, 28, 1187.
- SMOKTY O.I., 1969 - "Multiple Light Scattering in the Spherical Planetary Atmosphere". - *Pure Appl. Geoph.*, 72, 214.
- VAN BLERKOM D.J., 1971 - "Diffuse Reflection from Clouds with Horizontal Inhomogeneities". - *Astroph. Jl.*, 166, 235.
- VAN DE HULST H.C., GROSSMAN K., 1968 - "Multiple Scattering in Planetary Atmospheres" in "The Atmospheres of Mars and Venus". - ed. by Brandt and Mc Elroy - Gordon and Breach - New York.
- WANG L., 1972 - "Anisotropic Non Conservative Scattering in a Semi-Infinite Medium". - *Astr. Jl.*, 174, 671.

Tableau I - Luminance rétrodiffusée par une couche d'épaisseur optique $\tau_1 = 8$ éclairée en incidence normale ($\pi F = \pi$) pour des particules $\alpha = 5, m = 1,33$, avec $\omega_0 = 0,95$ et $0,99$, calculée par les harmoniques sphériques (HS) le doubling (D) et les ordres successifs (OS) (Devaux et al, 1974)

μ	$\omega_0 = 0,95$			$\omega_0 = 0,99$		
	HS	D	OS	HS	D	OS
0,01305	0,10219	0,10145	0,098445	0,16208	0,16092	0,15496
0,06747	0,12618	0,12669	0,012338	0,20121	0,20211	0,19542
0,16030	0,15406	0,15450	0,015255	0,25004	0,25082	0,24610
0,28330	0,17140	0,17162	0,017077	0,28804	0,28844	0,28539
0,42556	0,17627	0,17636	0,017613	0,30824	0,30841	0,30650
0,50000	0,17748	/	/	0,31434	/	/
0,57444	0,17944	0,17948	0,017941	0,31933	0,31941	0,31817
0,71670	0,18323	0,18325	0,018309	0,32422	0,32428	0,32341
0,83970	0,17821	0,17823	0,017790	0,31553	0,31558	0,31496
0,93253	0,16763	0,16765	0,016718	0,29963	0,29967	0,29922
0,98695	0,16359	0,16371	0,016306	0,29175	0,29180	0,29143
1,00000	0,16369	0,16371	/	0,29090	0,29094	/

Tableau II - Luminance diffusée à diverses profondeurs τ par une couche de brume de type L, d'épaisseur optique $\tau_1 = 1$ avec $\omega_0 = 0,9$ éclairée en incidence normale ($\pi F = \pi$), calculée par les harmoniques sphériques (HS), la "Matrix Operator Method" (MO) et la Méthode de Monte-Carlo (MC).
 Pour les deux dernières méthodes, les résultats nous ont été aimablement communiqués, respectivement par G.N. Plass et G.W. Kattawar et par G. Mikhailov et S. Kiznetsov dans le cadre d'un programme de comparaisons numériques de la commission du Rayonnement de l'I.A.M.A.P.

μ	$\tau = 0$			$\tau = 0,05$			$\tau = 0,1$		
	HS	MO	MC	HS	MO	MC	HS	MO	MC
1	0,0279	0,0279	0,0147	0,0266	0,0265	0,0141	0,0251	0,0251	0,0134
0,8	0,0314	0,0314	0,0292	0,0301	0,0300	0,0276	0,0286	0,0286	0,0265
0,6	0,0391	0,0391	0,0376	0,0379	0,0379	0,0366	0,0365	0,0365	0,0359
0,4	0,0535	0,0533	0,0515	0,0529	0,0528	0,0523	0,0521	0,0520	0,0525
0,2	0,0669	0,0666	0,0637	0,0690	0,0690	0,0696	0,0705	0,0703	0,0730
- 0,2				0,0131	0,0132	0,0116	0,0253	0,0254	0,0228
- 0,4				0,00952	0,00952	0,00945	0,0191	0,0190	0,0186
- 0,6				0,0125	0,0125	0,0129	0,0249	0,0249	0,0253
- 0,8				0,0286	0,0292	0,0312	0,0560	0,0573	0,0605
- 1				0,327	0,327	0,323	0,626	0,628	0,612

Tableau II suite

μ	$\tau = 0,2$			$\tau = 0,5$			$\tau = 1$		
	HS	MO	MC	HS	MO	MC	HS	MO	MC
1	0,0223	0,0223	0,0122	0,0137	0,0137	0,0080			
0,8	0,0257	0,0256	0,0242	0,0161	0,0160	0,0151			
0,6	0,0334	0,0334	0,0357	0,0221	0,0221	0,0210			
0,4	0,0497	0,0495	0,0493	0,0368	0,0368	0,0361			
0,2	0,0720	0,0719	0,0727	0,0667	0,0668	0,0674			
- 0,2	0,0467	0,0471	0,0480	0,0916	0,0916	0,0862	0,124	0,124	0,122
- 0,4	0,0378	0,0378	0,0381	0,0883	0,0884	0,0870	0,148	0,148	0,148
- 0,6	0,0490	0,0491	0,0495	0,115	0,115	0,118	0,201	0,201	0,203
- 0,8	0,108	0,110	0,115	0,239	0,240	0,257	0,387	0,393	0,405
- 1	1,152	1,154	1,11	2,240	2,244	2,18	2,967	2,972	2,86

Tableau III - Flux net $|F(\tau) + \mu \pi F e^{\tau/\mu_0}|$ calculé exactement et par diverses méthodes approchées, méthode à deux flux standard (TS St) méthode à deux flux modifiée (TS Mod), méthode d'Eddington (Edd) pour un flux incident $\pi F = \pi$

Cas 1 - Brume L $\tau_1 = 1$ $\tau_0 = 1$ $\mu_0 = -1$
 Cas 2 - Brume L $\tau_1 = 1$ $\tau_0 = 0,9$ $\mu_0 = -1$
 Cas 3 - Brume L $\tau_1 = 1$ $\tau_0 = 0,9$ $\mu_0 = -0,5$
 Cas 4 - Nuage Cl $\tau_1 = 64$ $\tau_0 = 1$ $\mu_0 = -1$
 Cas 5 - Nuage Cl $\tau_1 = 64$ $\tau_0 = 0,9$ $\mu_0 = -1$

Les résultats des méthodes approchées nous ont été aimablement communiquées par W.M. Irvine dans le cadre d'un programme de comparaisons numériques de la Commission du Rayonnement de l'I.A.M.A.P.

τ	Cas 1				Cas 2				Cas 3			
	Exact	TS St	TS Mod	Edd	Exact	TS St	TS Mod	Edd	Exact	TS St	TS Mod	Edd
0	2,97	3,02	2,86	3,11	3,02	3,05	2,92	2,20	1,35	1,48	1,38	1,20
0,05	2,97	2,99	2,86	3,02	3,00	3,02	2,86	2,14	1,33	1,45	1,36	1,14
0,1	2,97	2,86	2,84	2,91	2,98	3,00	2,84	2,18	1,31	1,44	1,25	1,10
0,2	2,97	3,01	2,86	3,14	2,95	2,98	2,60	1,95	1,27	1,43	1,30	1,05
0,5	2,97	3,04	2,85	3,16	2,84	2,88	2,79	1,94	1,16	1,33	1,21	0,99
0,75	2,97	3,02	2,83	3,18	2,75	2,80	2,68	2,05	1,08	1,26	1,14	0,98
1	2,97	2,85	3,17	3,00	2,67	2,73	2,60	1,97	1,02	1,19	1,09	0,90

REMOTE PROBING OF ATMOSPHERIC PARTICULATES FROM RADIATION EXTINCTION EXPERIMENTS: A REVIEW OF METHODS

Alain L. Fymat

Jet Propulsion Laboratory, California Institute of Technology
4800 Oak Grove Drive, Pasadena, California 91103, USA

SUMMARY

The existing methodology for reconstructing the particle size distribution and inferring the refractive index of absorbing and scattering atmospheric particulates is critically reviewed. Emphasis is placed on method capabilities and shortcomings and, whenever possible, on achievable accuracy. The nature of the associated remote probing problem is analyzed with regard to the effects (not the properties) of the particulates on EM wave propagation in the atmosphere. The parameterization of size distribution is studied within the unifying framework of Pearson's distribution curves. The inversions of extinction measurements and their ratios are considered separately, and the potentialities of each type of measurement are identified. Work lacking in each of the methods reviewed is indicated. Inverse methods for determining effective size distribution model parameters from extinction data include Junge's and the author's methods. The methods determining the effective size distribution are those of Phillips-Twomey; an essential modification of this method by the author; Hanson; Backus-Gilbert; and Shifrin-Perelman. The author's method of determining both the effective complex refractive index and size distribution model parameters from the same data is also presented. Lastly, the author's determination from extinction ratio data of the complex refractive index independent of size distribution is discussed and error analyzed.

1. INTRODUCTION

Propagation in the atmosphere of arbitrarily coherent light beams is known to be limited by the presence of particulates (clouds, fog, haze). The magnitude of this effect depends on the geometrical, compositional and structural properties of these particles (i.e., respectively, shape; inhomogeneity of material and complex refractive index; size distribution and concentration). For homogeneous particles of simple shape (e.g., spheres), the effect can in principle be approximately evaluated in all its detailed spectral and angular variations applying radiative transfer theory to somewhat idealized atmospheric models (Bahethi, O. M., and Fraser, R. S., 1975; Fymat, A. L., Devaux, C., Herman, M., and Lenoble, J., 1975; Hansen, J. E., and Travis, L. D., 1974; Irvine, W. M., 1975; Kerschgens, M., Raschke, M. E., and Reuter, U., 1975; Lenoble, J., 1974, 1975; Liou, K. N., 1975; and Plass, G. N., 1975). In the absence of specific information regarding the particles properties, such radiative transfer studies are extremely valuable for bracketing the extent of propagation disturbance under arbitrary operating conditions. The resulting information, unfortunately, is usually not sufficiently precise in terms of engineering parameters for optical systems designs. It also rarely applies, if at all, to actual atmospheric conditions. The situation could be considerably improved, however, if the particles properties could be reconstructed from experiment, and subsequently inserted in the available radiative transfer codes. In this manner the above bracketing would be extremely narrowed, the only limiting factors being the instrumental noise, the numerical noises inherent both in the data inversion techniques used for retrieving the particles parameters and in the transfer codes, and the degrees of idealizations of these and the inverse codes. But, more importantly, it would become possible to evaluate in (or near) real-time the particles effects on light propagation for any atmospheric and operating conditions.

The aim of this article is to review critically the existing methodology for inferring the optical parameters of atmospheric particulates with particular emphasis on method capabilities and limitations and, whenever possible, achievable accuracy under favorable and adverse conditions. Active and passive remote sensing from the ground and from an airborne or orbiting platform will be considered. The methods reviewed are those utilizing measurements of light extinction by absorption and scattering from both host gases and embedded particles, the so-called direct radiation case. The diffuse radiation case resulting from primary and multiple scattering by the same gases and particles, including the consequent induced polarization and the combination of both cases, have been reviewed elsewhere (Fymat, A. L., 1975).

2. NATURE OF THE REMOTE PROBING PROBLEM

In studies of atmospheric effects on light propagation, as opposed to environmental and micrometeorological studies, we are not necessarily interested in the true particles properties but rather in the simplest equivalent (or effective) properties that would produce the identical effects. This is a fortunate situation for question regarding the model-dependence, or even the uniqueness of results yielded by a given model, loose because much of their significance providing these results explain the observations and have physical meaning.

Indeed, under certain circumstances, it is possible to simulate the effects of nonspherical particles of arbitrary orientation by spherical ones (Holland, A. C., and Gagne, G., 1970; Burch, D. E., Pembrook, J. D., and Reisman, E., 1970), those of anisotropic scattering by appropriately scaled isotropic scattering (van de Hulst, H. C., and Grossman, K., 1968), and those of a vertically inhomogeneous atmosphere by a vertically homogeneous one on which a variable perturbation has been superimposed (Fymat, A. L., and Abhyankar, K. D., 1969a, b; 1970a, b). From there on it becomes both convenient and reasonable to investigate simple atmospheric and scattering models providing these models are physical and able to reproduce the observed effects. This is certainly compatible with the very nature of the inverse mathematical problem. Thus, we may conceive that for a given light input, a set of atmospheric and scattering models could exist that match the detected light output. And, within any element of this set, the

medium physical parameters reconstructed from these data may not even be unique, although the various determinations may be physically meaningful. If we were only interested in the physical parameters characterizing the particulates, the non-uniqueness situations described would, if they occur, totally prevent us from determining the true values of these parameters. However, the situation may not be so tragic if we are only concerned with the effects which these particles have on light propagation. There we would only be interested in that set of physical effective parameters that can mimic the measurements. These effective parameters could be provided by idealized models.

3. PARAMETERIZATION OF PARTICLE SIZE DISTRIBUTION

In most of the methods to be discussed below for remotely sensing the effects of atmospheric particulates, an analytic representation is used for the size distribution of the assembly of particulates. A number of such representations can be found; for example:

Power distribution:

$$n(r) = cr^{-\alpha}; \quad (1a)$$

Exponential distribution:

$$n(r) = ce^{-\beta/r}; \quad (1b)$$

Normal distribution:

$$n(r) = ce^{-\beta r^2}; \quad (1c)$$

Gamma distribution (1):

$$n(r) = cr^{\alpha} e^{-\beta r}, \quad (1d)$$

where the constants c can be determined from the relation:

$$\int_0^{\infty} n(r) dr = N, \quad (2)$$

N = particle number density, and both these constants and the parameters α and β are expressible in terms of the moments of the corresponding distribution:

$$m_n = \int_0^{\infty} r^n n(r) dr, \quad n = 0, 1, 2, \dots \quad (3)$$

We should like to indicate (this does not appear to be recognized in the atmospheric literature) that the distributions in Eqs. (1), and many others not listed, are all solutions of the celebrated differential equation¹ of K. Pearson (1914, 1931):

$$\frac{d}{dr} n(r) = \frac{a_0 + a_1 r}{F(r)} n(r), \quad (4a)$$

where $F(r)$, a general function of r , is used to encompass the case $dn(r)/dr \neq 0$ even if $n(r) = 0$, i.e., the distribution curve is not tangential to the r -axis at the origin. Expanding $F(r)$ by Maclaurin's theorem in ascending powers of r , we get:

$$\frac{d}{dr} n(r) = \frac{a_0 + a_1 r}{b_0 + b_1 r + b_2 r^2 + \dots} n(r), \quad (4b)$$

where the coefficients (hereafter called Pearson's coefficients) are expressible in terms of m_n . This could be seen by rewriting Eq. (4b) as:

$$(a_0 + a_1 r) n(r) = (b_0 + b_1 r + b_2 r^2 + \dots) \frac{dn(r)}{dr},$$

¹This is a slight modification of the original equation given by Pearson. In the latter equation, the numerator on the right-side read $(a + r)$. Although our equation can easily be reduced to Pearson's, we have

multiplying both sides of this expression by r^n , integrating them over r , and integrating by parts the right-side of the equation thus obtained. These operations yield a moment relation which for $n = 0, 1, 2, \dots$ gives a system of equations in the Pearson's coefficients. In this manner, it is found that

$$\frac{a_0}{a_1} = \frac{v_{32}}{D} \left(\frac{v_{42}}{v_2} + 3 \right) = \frac{b_1}{a_1}, \quad (5a)$$

$$\frac{b_0}{a_1} = \frac{1}{D} \left(4v_{42} - 3v_{32}^2 \right), \quad \frac{b_2}{a_1} = \frac{1}{D} \left(\frac{2v_{42}}{v_2} - \frac{3v_{32}^2}{v_2} - 6 \right), \quad (5b)$$

where

$$D = 2 \left(\frac{v_{42}}{v_2} - \frac{6v_{32}^2}{v_2} - 9 \right)$$

and v_{ij} are the ratios:

$$v_{ij} = \frac{v_i}{v_j} = v_{ji}^{-1}, \quad \frac{v_{ij}}{v_{kj}} = v_{ik}. \quad (5d)$$

The moments v are computed about the mean of the distribution while the moments m are about the origin. Simple formulae exist in the literature for converting either moments into the other ones. It may be noted that all coefficients in Eqs. (5) involve moments up to the fourth-order. In other words, on the basis of Pearson's theory, we conclude that the distributions (1a)-(1d) require at least up to fourth-order moments for their characterization. It is clear that using only smaller order moments would result in inaccurate descriptions of the size distribution effects on light propagation. Next, it is known in statistical distribution theory that additional constants b_3, b_4, \dots in Eq. (4b) would involve higher-order moments than the fourth which in statistical work are generally considered as untrustworthy. Pearson's classical Main Types I, IV and VI and Transition Types II, III, V, and VII to XII of systems of curves are obtained from a consideration of the roots of the equation $b_0 + b_1r + b_2r^2 = 0$. As illustrations, the normal curve of error is obtained when $b_1 = b_2 = 0$. (This is a particular case of Type II), and the Power law and the Gamma distributions are all of Type III. Table 1 lists for convenience the values of Pearson's coefficients for the distributions in Eqs. (1a)-(1d). These coefficients could be expressed in terms of moments using the relations in Eqs. (5).

Since, as shown, the distributions listed and many others form a family of solutions of Eq. (4), it is clear that there is actually much less disparity than is suggested by the partial list of distributions in Eqs. (1a) - (1d). These points, viz. the reconciliation of the various distributions and the need to consider at least fourth-order moments, were not recognized previously, at least not from the viewpoint of Pearson's differential equation. It must be noted however that the latter conclusion was reached earlier by Hansen, J. E. (1971) from physical considerations and later verified numerically (Hansen, J. E., and Travis, L. D., 1974).

Hansen suggested to use the following:

Gamma distribution (II)

$$n(r) = c r^{(1-3b)/b} e^{-r/ab}, \quad c = \frac{N}{(ab)^{1/b-2} \left[\frac{1}{b} - 3 \right]!}, \quad (1e)$$

because it has the property that the parameters a and b are respectively identical to an effective radius and an effective variance defined as:

$$\left. \begin{aligned} a &= r_{\text{eff}} = m_{32}, \\ b &= v_{\text{eff}} = \frac{1}{m_2^2} (m_{42} - m_{32}^2) = \frac{m_{43}}{m_{32}} - 1. \end{aligned} \right\} \quad (6)$$

The corresponding Pearson's coefficients are also listed in Table 1. Note that again fourth-order moments are involved. Interestingly, the above authors also showed (see their Fig. 14) that if the distribution in Eq. 1(e) is used as a standard the corresponding effects on the scattered radiation, specifically on the phase-function and the degree of linear polarization (resulting from single scattering of

unpolarized incident light) are substantially the same at all scattering angles as those resulting from the distribution in Eq. (1a), the

Bimodal Gamma distribution:

$$n(r) = \sum_i c_i n_i(r), \quad i = 1, 2, \quad (1f)$$

where n_i are obtained from Eq. (1e) using different parameters a and/or b , and the

Lognormal distribution:

$$n(r) = \alpha r^{-1} e^{-\frac{1}{2} \left(\ln(r/r_0) / \sqrt{\pi} \alpha \right)^2} \quad (1g)$$

In this comparison, r_{eff} and v_{eff} were chosen to be identical for all distributions studied. Notable discrepancies between the effects of these distributions were observed (see their Fig. 15) when only the mean radius, \bar{r} , and the variance, σ^2 , usually defined by

$$\bar{r} = m_{10}, \quad \sigma^2 = m_{20} - m_{10}^2 \quad (7)$$

were likewise considered showing that second and lower order moments are insufficient for a proper characterization of the size distribution effects.² If correct, these results would show that within the context of analytical modelling of particle size distribution for light scattering studies, it is only necessary to use a distribution whose parameters are expressed in terms of at least fourth-order moments, such as for example the Gamma distribution (II). Conversely, within the same context, the results also show that scattered light measurements can only yield expressions in these moments, such as the effective mean radius, a , and the effective variance, b ; they will not provide the actual distribution. It is not known whether the same conclusions hold true for the case of light extinction which is of particular interest here.

4. PHYSICAL MODEL AND UNKNOWN PARAMETERS

The following model will be considered: a mixture of i different species of gases and j different species of particulates constitutes the atmosphere. Effects due to ground surface reflection can be disregarded. Each gas will be characterized by an absorption cross-section, K_g , a scattering cross-section, σ_g , and a number density, N_g . These three characteristics will exhibit spatial variations while the former two possess additionally frequency variations. From these parameters all gaseous effects could be evaluated in detail when the geometry of the atmosphere is specified. On using Rayleigh-Cabannes formula applicable to anisotropic molecules (see, e.g., Chandrasekhar, S., 1950):

$$\sigma_g = \frac{8\pi^3}{3} \frac{(m_g^2 - 1)^2}{\lambda^4 N_g^2} \cdot \frac{3(2 + \delta)}{6 - 7\delta} \quad (8)$$

² To encompass the lognormal distribution, our form, Eq. (4b), of Pearson's equation must further be modified to read:

$$\frac{d}{dr} n(r) = \frac{a_0 + a_1 \ln r}{b_0 + b_1 r + b_2 r^2 + \dots} \quad (4c)$$

indicating that a generalized Pearson's type differential equation could have the form:

$$\frac{d}{dr} n(r) = \frac{a_0 + a_1 f(r)}{b_0 + b_1 r + b_2 r^2 + \dots} \quad (4d)$$

And, for multimodal distributions, the form to use should be:

$$\frac{d}{dr} n(r) = \sum_i \frac{a_{0,i} + a_{1,i} f(r)}{b_{0,i} + b_{1,i} r + b_{2,i} r^2 + \dots}, \quad i = 1, 2, 3, \dots \quad (4e)$$

it is seen that, aside from N_g , the parameter $\bar{\sigma}_g$ involves in fact two additional parameters: the (real) refractive index, m_g , and the depolarization factor, δ , of the particular gaseous species. In summary, each gas would be characterized by four parameters: \bar{K}_g , m_g , δ and N_g , and their spatial and frequency variations, as appropriate. On the other hand, each particulate species would be characterized by a complex refractive index, $m_p = m_r - im_i$, a characteristic size and distribution, $n(a)$, and a number density, N_p . These various parameters exhibit spatial variations while the refractive index may additionally present frequency variations. Thus, each particulate species would be characterized by the three parameters: m_r , m_i , N_p and the distribution $n(a)$, and their frequency and spatial variations as appropriate. It may be noted that with the parameters listed the scattering, absorption and extinction optical thicknesses of the model atmosphere considered can be evaluated straightforwardly.

The several methods now to be discussed will consider that only a few of the above atmospheric parameters are unknown. The limitations and capabilities of these methods will thus be more easily gauged against the reference model just set forth.

The methods could be classified either mathematically according to the type of mathematical expressions to be "inverted", or physically according to the nature of the observables of the light field. The physical classification will here be adopted. It turns out that inferring atmospheric physical parameters from direct radiation measurements involves the inversion of first kind integral equations. Ratios of such measurements and therefore also ratios of such equations will also be studied. It is thus evident that the successful solution of the inverse problem is critically dependent on our ability to "invert" these particular equations. Fortunately, the corresponding methodology is a rich one, and this fact coupled with our understanding of the effects of each atmospheric parameter variations on the observed light field enables us, at least in some cases, to carry out the inversion successfully.

5. INVERSION OF DIRECT RADIATION MEASUREMENTS

The observable is the radiation beam propagating linearly from source to detector and its frequency variations. It has two components (i) the light transmitted directly with attenuation (i.e., absorption and scattering) along the line-of-sight, and (ii) the diffuse light that consists of both primary scattering in, and higher-order of scattering into, the forward direction. The diffuse component is comparatively negligible, and this reduces to a statement of Bouguer-Beer-Lambert law;

$$\underline{I} = \underline{I}_0 \exp [-\tau_{\text{ext}} M(\mu)] , \quad (9)$$

where \underline{I}_0 and \underline{I} denote respectively the incident and transmitted Stokes' 4-vectors whose components are the usual Stokes' parameters (or any other equivalent representation of light polarization state). Note that \underline{I} and \underline{I}_0 are in the same arbitrary state of polarization since the exponential attenuation does not introduce any polarization. When the Sun is used as the source, the corresponding radiation being unpolarized, \underline{I} and \underline{I}_0 reduce to scalars (specific intensities), and Eq. (9) simplifies to:

$$I = I_0 \exp [-\tau_{\text{ext}} M(\mu)] . \quad (9a)$$

Also, in Eq. (9) or (9a), τ_{ext} is the extinction (= absorption + scattering) or total optical thickness of the atmosphere, and $M(\mu)$ is the relative air mass in the line-of-sight which makes an angle $\theta = \cos^{-1} \mu$ with the local normal to the plane of stratification of the atmosphere (parallel to the surface); θ is counted positive for upward directions and conversely. The detailed expression of $M(\mu)$, not given here, includes both curvature and refraction effects (see Fessenkov, V. G., 1955). For example neglecting refraction, and away from the limb, $M = \mu^{-1}$. This is the usual expression most frequently used in atmospheric optics. Equation (9) or (9a) applies across the spectrum, and can be made the basis of ground-based, airborne or space measurements for the experimental determination of τ_{ext} . It is the unraveling of the physical information contained in τ_{ext} that is the primary interest of this section.

5.1 Statement of Problem

For simplicity consider Eq. (9a). [This expression also applies to each component of Eq. (9).] Inverting this equation yields the measurable quantity:

$$M^{-1}(\mu) \ln \left(\frac{I}{I_0} \right) = -\tau_{\text{ext}} . \quad (10)$$

Experiment should provide reliable measurements of this quantity since absolute calibration is not required. All the physical information on the atmospheric particulates is contained in τ_{ext} . For the model described in section 4, this information could be retrieved by "inverting" the double integral expression

$$\begin{aligned} E[\lambda; m^j, n^j(a)] &= M^{-1}(\mu) \ln \left(\frac{I}{I_0} \right) - \int_{z_1}^{z_2} \epsilon_g^j(z) dz \\ &= \int_{z_1}^{z_2} dz \left\{ \int_0^\infty G[a(z)] Q_{\text{ext}}[a(z), m(z; \lambda)] n[z, a(z)] da \right\}^j , \end{aligned} \quad (11)$$

where λ is the wavelength, a is a characteristic dimension, z is altitude, $\epsilon_g = N_g \bar{\epsilon}_g$, $\bar{\epsilon}_g = K_g + \sigma_g$, G is the geometrical cross-section, Q is an efficiency factor (the subscript referring to a specific physical process: absorption, scattering or their combination which is the extinction), $Q_{\text{ext}} = Q_{\text{abs}} + Q_{\text{sca}}$, and the superscripts follow Einstein's summation convention:

$$(\dots)^l \equiv \sum_i (\dots)_i, \quad l = i, j.$$

For example, for spheres, a is the particle radius, r , and $G(r) = \pi r^2$. Likewise for circular cylinders: $G(r) = 2lr^2$ where l is the ratio of the length to the radius. For these two types of particles, the required expressions for Q are well-known and available in the literature (see, e.g., Hulst, H. C. van de, 1957). In Eq. (11) it may be noted that, because of the gradient of relative humidity in the atmosphere which may cause the particles to change size by condensation, G was made to depend explicitly on z . Likewise, Q and n may also vary within the atmosphere. Thus, the measurement in Eq. (10) immediately provides one atmospheric parameter; i.e., τ_{ext} ; further information on the microstructure and chemical composition of the particles, i.e., respectively $n(a)$ and m , could be obtained only through "inversion" of the right-side of Eq. (11) utilizing several measurements $E(\lambda)$. At this time, this task has been carried out only under the following restrictive assumptions:

- $\epsilon_g^i(z)$, or simply its altitude-integrated value, is known.
- The z -dependence of the product $(G Q_{\text{ext}} n)$ can be factored out and the integrated value of this factor is known. Note that this is less restrictive than considering that $a(z)$, $m(z)$ and $n(z)$ are all z -independent.

Further assumptions will be made within each of the methods of inversion. There are two general classes of such methods, those assuming the knowledge of the refractive index but not postulating any size distribution model and, conversely, those postulating a distribution model but leaving the refractive index unknown. All methods have concentrated on spherical particles for which Mie's theory is available. However, any other shape of particles could be handled if the corresponding Q_{ext} were known. This is a primary limitation in present radiation theory. Before reviewing these methods, we shall first analyze Eq. (11) in a simple case.

5.2 Analysis of Direct Problem

Assume as said earlier that $\epsilon_g^i(z)$ is known or determined so that $E(\lambda)$ becomes a measurable quantity for a set of λ -values. Assume further that there is only one type of particles, and that $a(z)$, $n(z)$ and $m(z)$ are independent of the altitude z . (The case of slowly varying functions of z could in principle be handled.) Under these assumptions, Eq. (11) reduces to

$$E[\lambda, m, n(a)] = \int_0^\infty G(a) Q_{\text{ext}}[a, m(\lambda)] n(a) da. \quad (11a)$$

For spheres, $G(a = r) = \pi r^2$, and further introducing the (dimensionless) size parameter $x = kr$, $k = 2\pi/\lambda$, this equation can be rewritten

$$E[\lambda; m, n(x)] = \pi k^{-3} \int_0^\infty x^2 Q_{\text{ext}}[x, m(\lambda)] n(x) dx. \quad (11b)$$

Few results have been published on the "weighting functions" $\pi k^{-3} x^2 Q_{\text{ext}}$, or even Q_{ext} , for various size distributions and parametric values of x and λ . For $m(\lambda) \equiv 1.50$, H. Quenzel (1970) has provided $Q_{\text{ext}}(r)$ for different λ 's (see his Fig. 1; see also Fig. 4.12 of Burch et al., loc. cit.; Fig. 2 of Wright, P. J., 1975; and Figs. 4 to 9 of Shettle, E. P., 1975). All curves start from the origin and after a series of oscillations converge to the theoretically predicted value of 2. For small r values, they exhibit separate although strongly overlapping peaks while at larger values, say $r \geq 2 \mu\text{m}$, the oscillations diminish strongly in amplitude and at still larger r values they hardly differ from each other. The locations of the peaks indicate those radius values that are efficiently sampled by the wavelengths corresponding to the curves. Thus, the wavelengths 0.4, 0.9, 1.3 and 1.9 μm are the most efficient in sampling the approximate radius values 0.5, 1.0, 1.6 and 2.3 μm , respectively, under the conditions studied by Quenzel. Larger sizes could be sampled by longer wavelengths. However, there is an upper bound of approximately 2-2.5 μm since, as clearly indicated by the Figure, the efficiency of larger particles is relatively the same at all longer wavelengths. Sampling of sizes smaller than approximately 0.1 μm is also bounded by O_2 and O_3 absorption bands. Numerous similar curves for single particle scattering can be found in van de Hulst, H. C. (1957) and Deirmendjian, D., (1969). Plots of the modified kernel

$$K(\lambda, \alpha) = \pi n 10 \times 10^{-\alpha} Q_{\text{ext}} \left[\frac{2\pi \times 10^\alpha}{\lambda}, m(\lambda) \right],$$

where $\alpha = \log_{10} r$ and $m(\lambda) \approx 1.50$, have also been published for $0.350 \leq \lambda \leq 2.270 \mu\text{m}$ (Yamamoto, G., and Tanaka, M., 1969).

The reason for this change of variable is the following: if the Junge distribution is assumed to be a good model for atmospheric aerosols, then $f(\alpha) = 10^{4\alpha} n(\alpha)$ will not change much with α . This property will indeed make the determination of $f(\alpha)$ easier than that of the original $n(r)$.

These latter curves have essentially single well-defined maxima. However, the maxima strongly overlap which will cause some concern in the resolution in α achievable in the inverse problem. For the Gamma distribution (I) with $m = 1.34$, $c = 1$, $\alpha = 2$ and $\beta = 15$ (this corresponds to a haze model), curves of $Q_{\text{ext}}(\lambda)$ for various λ 's are provided in Fig. 1. The particle radii vary between 0.005 and $6.0 \mu\text{m}$. (For each wavelength, only seven values of Q_{ext} were computed and smooth curves, which necessarily may not reproduce the exact curves, were drawn.)

In the particular case of a monodispersion: $n(x) = N\delta(x - x_0)$, where δ is Dirac's function and x_0 is the common size parameter, it may be noted that Eq. (11b) reduces to

$$E[\lambda; m, x_0] = N\pi k^{-3} x_0^2 Q_{\text{ext}}[x_0, m(\lambda)] . \quad (11c)$$

This expression has been used for experimentally determining the quantity $Nx_0^2 Q_{\text{ext}}[x_0, m(\lambda)]$ by Pepin, T. J. (1969) at $\lambda = 0.367, 0.43, 0.595$ and $0.91 \mu\text{m}$. It forms the basis of the Stratospheric Aerosol Measurement (SAM-II) Experiment on Nimbus G (McCormick, N. P., 1975).

5.3 Inverse Methods: Determination of Effective Size Distribution Model Parameters

Within a range of wavelengths of interest, and assuming that $m(\lambda)$ is known within this range, the following methods have been developed for extracting, from measurements of $E(\lambda)$, effective parameters for model size distributions.

5.3.1 Junge's Method

Inserting Eq. (1a) converted to the variable x into Eq. (11b), this latter equation becomes:

$$E(\lambda; \alpha) = \pi c k^{\alpha-3} \int_0^\infty Q_{\text{ext}}(\lambda; x) x^{2-\alpha} dx . \quad (12)$$

Figure 2 displays the variations of Q_{ext} with λ for the same conditions as Fig. 1. Curves are given for three different refractive index values covering approximately the range of possible index values for aerosols; sets of curves are provided for radius values $r = 0.16 \mu\text{m}$. The curves for water-type aerosols are seen not to exhibit any systematic feature. However, for the other two refractive indices, especially for $r \geq 2 \mu\text{m}$, the curves are almost the same to the accuracy of the graph. They also show a slow, slightly and monotonously increasing variation with increasing λ . These results suggest that beyond a certain refractive index and particle radius, the aerosol extinction is virtually independent of refractive index at all radii and a slowly varying function of λ , at least in the visible region. A more detailed study is however needed in order to determine the index and radius cut-off values beyond which these preliminary conclusions would generally hold. Under these conditions, the knowledge of the refractive index, postulated at the beginning of this section, is not even necessary. Furthermore, the variation of Q_{ext} with λ could be parameterized in a very simple fashion so that the integral in the right-side of Eq. (12) becomes a known function of α , say $q(\alpha)$. And we can write:

$$E(\lambda; \alpha) \sim q(\alpha) \lambda^{3-\alpha} . \quad (13)$$

The problem is now an extremely simple one. It consists in fitting the experimental curve $E(\lambda)$ with the function $q(\alpha) \lambda^{3-\alpha}$ by trying successively several α values until a satisfactory agreement has been reached. The value of α providing such a match will then be used in Eq. (1a) to yield $n(r)$. This method was proposed earlier by C. Junge (1963) for more restrictive conditions than those considered here. It agrees with the well-known empirical formula of A. K. Angstrom (1970) for atmospheric aerosols:

$$E(\lambda; \lambda) \sim \lambda^{-\gamma} , \quad \gamma = \alpha - 3 . \quad (14)$$

This technique has been widely used in investigations of atmospheric aerosols (see, for example, Pepin, T. J., 1970; Shaw, G. E., Reagan, J. A., and Herman, B., 1973). The main disadvantages of the method are: (i) The efficiency factor for aerosol extinction is assumed to be a slowly varying function of the wavelength. As shown by Fig. 2 this is true only beyond certain particle radius and refractive index values. Nevertheless, the method appears to lack sensitivity relatively to the refractive index. Thus, for values of this parameter in the range $m = 1.33$ (pure water) and $m = 1.55 - 0.1$ to $1.55 - 0.05$ (transparent to highly absorbing dry sea-salt particles), it has been claimed that the recovered size distributions are not substantially different from one another (Quenzel, H., 1970). (ii) The method is model-dependent. Note, however, that the power distribution with $2.5 \leq \alpha \leq 3.5$ has experimentally been found to describe world-wide pollution for a large variety of continental conditions (Junge, C., 1963)

with a wide range of aerosol concentrations corresponding to a 1-100-km visibility range. (iii) It does not use the available data advantageously for arriving at the solution. The data play only the role of a reference against which computational results are contrasted. At no step, however, are they used for improving on the approximate solution derived at each step of the comparison.

No study of the uniqueness of the derived size distributions is available. However, authors who have used the method (e.g., Quenzel, H., 1970) report that grossly different size distributions cannot be derived from the same extinction curve. An advantage of the method is its sensitivity to the location of the mode radius and the slope of the distribution.

5.3.2 Fymat's Method

This is a modification of Phillips-Twomey Method described in the following Section in the case where a model distribution is assumed. The minimization of the relevant quadratic function is carried out using a minimization search procedure instead of the partial derivative concept and matrix inversions used by Phillips and Twomey. For details refer to Section 5.4.2.

5.4 Inverse Methods: Determination of Effective Size Distribution

The following methods rest on the same general assumption as that described in Section 5.3. However, the effective size distribution is left completely undetermined.

5.4.1 Phillips-Twomey Method

Return to Eq. (11b), which can be written in the general form

$$g(x) = \int_a^b K(x, y)f(y)dy, \quad (15)$$

where the known functions $g(x) = E(\lambda)$ and $K(x, y) = \pi k^{-3} x^2 Q[m(\lambda), x]$ are bounded and continuous. Because $n(x)$ vanishes at both ends $x = x_{\min}$ and $x = x_{\max}$ (generally $x_{\min} \approx 0$ and x_{\max} approaches the noise level asymptotically), the original integration limits $(0, \infty)$ have been replaced by (a, b) , so that Eq. (15) is truly non-singular. There is a basic mathematical difficulty with the solution $f(y)$ of this equation, namely, the solution fails to be either unique or a continuous function of the observable $g(x)$, or both. It is first noted (Phillips, D. L., 1962) that Eq. (15) is unstable³ in the sense that large (high-frequency) changes in $f(y)$, i.e., $\delta f = \sin \omega t$, $\omega \gg 0$, would result in small changes in $g(x)$, and that none of previously proposed methods has been successful for arbitrary $K(x, y)$ when $g(x)$ is known with some inaccuracy. As a result, inversion techniques based on the replacement of Eq. (15) by an algebraic linear system tend to give unrealistic, oscillatory solutions, even though the residual errors in the fit to the observable function may be small. Thus, in order to obtain a solution of Eq. (15), one must take into account both the accuracy of $g(x)$ and the shape of $K(x, y)$; these two factors dictate to a large extent the success of the method of solution. This remark is the basis of the method of Phillips-Twomey.

First, rewrite Eq. (15) in the matrix form

$$Af = g + \epsilon, \quad (16)$$

where ϵ is the error vector attached to the experimental vector g , and A includes the weight factors in reducing Eq. (15) to the linear system, Eq. (16), by a quadrature. The method of solution is apperanted to the classical methods of linear programming in that a certain quadratic function, say $Q(f)$, must be minimized subject to the following constraints: (i) Eq. (16), and (ii) ϵ varies within permissible limits, e.g.,

$$\sum_i \epsilon_i^2 \leq e^2 \text{ (constant) }.$$

The introduction of the latter constraint represents the error criterion which will enable us to select a stable unique solution from the infinite manifold of possible solutions. The manifold comprises all solutions whose integral transforms lie within a prescribed neighborhood of g . This constraint has the effect of smoothing f .

The problem becomes that of finding f such that $Q(f)$ is a minimum and $\epsilon^T \epsilon$ is a constant. (The superscript T denotes matrix transposition.) If γ is a Lagrangian multiplier (this is the smoothing factor such that the larger γ the smoother the solution), then the required solution is provided by the differential equation

$$\frac{\partial}{\partial f} \left\{ \epsilon^T \epsilon + \gamma Q(f) \right\} = 0, \quad (17)$$

³This is a result of Riemann's lemma, as pointed out by Franklin, J. N. (1970).

i. e., using Eq. (16),

$$\frac{\partial}{\partial \underline{f}} \left\{ (\underline{A}\underline{f} - \underline{g})^T (\underline{A}\underline{f} - \underline{g}) + \gamma Q(\underline{f}) \right\} = \underline{0},$$

or, writing out the term within curly braces,

$$\underline{f}^T \underline{A}^T \underline{A} - \underline{g}^T \underline{A} + \gamma \frac{\partial Q}{\partial \underline{f}} = \underline{0}.$$

The last relation will still be satisfied if one takes the transpose:

$$\underline{A}^T \underline{A} \underline{f} + \gamma \left(\frac{\partial Q}{\partial \underline{f}} \right)^T = \underline{A}^T \underline{g}. \quad (18)$$

Equation (18) will provide the required solution \underline{f} . It is clear, however, that the explicit form of this solution will depend on the functional form of the quadratic $Q(\underline{f})$ being minimized. When minimizing the Nth-difference (Twomey, S., 1965) $Q(\underline{f})$ can be written

$$Q = \underline{f}^T \underline{H} \underline{f}, \quad (19)$$

where \underline{H} represents the symmetrical matrix of Nth-difference coefficients. Differentiating Eq. (19) with respect to \underline{f} and substituting into Eq. (18), we get the solution

$$\underline{f} = (\underline{A}^T \underline{A} + \gamma \underline{H})^{-1} \underline{A}^T \underline{g}. \quad (20)$$

This expression derived by Twomey, S., (1963) can be shown to be entirely equivalent to that provided earlier by Phillips. Equation (20) can be rewritten

$$[(\underline{A}^T)^{-1} \underline{A}^T \underline{A} + \gamma (\underline{A}^T)^{-1} \underline{H}] \underline{f} = \underline{g}.$$

From the identity $(\underline{A}^T)^{-1} \underline{A}^T = (\underline{A} \underline{A}^{-1})^T = \underline{I}^T = \underline{I}$ (\underline{I} = identity matrix), it follows that

$$\underline{f} = (\underline{A} + \gamma \underline{B})^{-1} \underline{g}, \quad \underline{B} = (\underline{A}^{-1})^T \underline{H}, \quad (21)$$

which is identical to Phillips's result. Twomey's expression is preferable to that of Phillips because it requires the inversion of only one matrix, i. e., $\underline{A}^T \underline{A} + \gamma \underline{H}$, instead of two inversions, i. e., \underline{A}^{-1} and $(\underline{A} + \gamma \underline{B})^{-1}$, and because it can be applied to both square and rectangular (overdetermined systems) matrices rather than square matrices alone.

Alternatively, one could minimize the Squares of the Absolute Departures from a Trial Solution. The quadratic is here written

$$Q = (\underline{f}^T - \underline{p}^T) \underline{f}, \quad (22)$$

where \underline{p} is the vector trial solution. As earlier, differentiating Eq. (22) and substituting into Eq. (16), we obtain

$$\underline{f} = (\underline{A}^T \underline{A} + \gamma \underline{I})^{-1} (\underline{A}^T \underline{g} + \gamma \underline{p}). \quad (23)$$

One could also minimize the Squares of the Relative Departures from a Trial Solution. The former solution, Eq. (23), is still valid, but the Lagrangian multiplier matrix $\gamma \underline{I}$ should be replaced by the matrix $\gamma \underline{p}^{-2}$, and we have⁴

$$\underline{f} = (\underline{A}^T \underline{A} + \gamma \underline{p}^{-2})^{-1} (\underline{A}^T \underline{g} + \gamma \underline{p}^{-1}). \quad (24)$$

where \underline{p} is the diagonal matrix of elements p_i .

⁴ A typographical error is present in Twomey's (1963) expression; one should read $\gamma \underline{p}^{-1}$ in the second bracket and not $\gamma \underline{p}$.

Lastly, one could also minimize the variance by simply redefining \underline{H} in the above expressions. Generally, we can write:⁵

$$\underline{f} = (\underline{A}^T \underline{A} + \gamma \underline{L})^{-1} (\underline{A}^T \underline{g} + \gamma \underline{p}_L), \quad (25)$$

where for $\underline{L} = \underline{H}$, $\underline{L} = \underline{p}^{-2}$, we have $\underline{p}_L = 0$, \underline{p} , \underline{p}^{-1} , respectively.

The determination of γ has not yet been discussed. This quantity is implicitly determined once the error bound ϵ^2 has been assigned a value. In practice several values of γ are tried for which \underline{f} is computed and then $\underline{A}\underline{f}$ compared with \underline{g} . The first value for which $\underline{A}\underline{f} - \underline{g}$ is less than or equal to ϵ (where ϵ includes all sources of error: measurement, truncation, quadrature, approximation) can usually be retained as the final solution. A more refined value of γ can of course be obtained by studying the curve $\epsilon(\gamma)$. In practical experience, it has been found that γ varies quite slowly, so that its selection poses no problems.

An application of this method to both synthetic and experimental data is available, (Yamamoto, G., and Tanaka, M., 1963). Equation (11b) is first rewritten in the form

$$k(\lambda) + \epsilon(\lambda) = \int_{x_g}^{x_f} K(\lambda, \alpha) f(\alpha) d\alpha, \quad (26)$$

where all quantities have been defined in Section 5.2. Yamamoto and Tanaka used both solutions, Eqs. (20) and (23). The solution in Eq. (20) was first obtained by approximating f with a step-function and then subsequently using this result as a trial solution in Eq. (23). For $\lambda \in (0.350-2.270 \mu\text{m})$ good reconstructions of the size distribution $n(r)$ were obtained for particle radii $r \in (0.1-5 \text{ to } 10 \mu\text{m})$. Outside of this range, the distribution is systematically overestimated (see their Fig. 2).

A two-dimensional version of the method described in this subsection has been developed (Tingey, D. L., 1972). This extension is of interest when the aerosol under study is a mixture of two types of aerosols having different size distributions. A further generalization to a higher dimension is completely feasible.

It may lastly be noted that the smoothing operators $\gamma \underline{L}$ and $\gamma \underline{p}_L$ may introduce long-period departures from the true solution. A realistic solution to the inversion problem is then a compromise between oversmoothing and noise rejection. In other words, optimum smoothing operators are sought such that all errors in the solution (random and systematic errors) will be minimized, that is to say, the operators are determined by both the mathematical method and the input data. This is just the principle of the "optimum Wiener filter" (Brault, J. W., and White, O. R., 1971) which the inversion method will try to determine in every case.

An important advantage of the method just described is that no assumption is made regarding the analytical form of the solution. No size-distribution model is assumed, which is an attractive feature for aerosols. The method has been successful in solving a number of inverse atmospheric problems (e.g., determination of particle size distribution from measurements of either direct or scattered radiation and from diffusional decay measurements; determination of vertical ozone distribution from light scattering measurements; determination of the physical conditions inside the solar atmosphere from the observed limb darkening (Kunasz, C. V., Jefferies, J. T., and White, O. R., 1973). However, some disadvantages may attach to the method, as we shall attempt to describe. The key element of the method is the minimization of the quantity [see Eq. (17)]

$$T = \epsilon^T \epsilon + \gamma Q(\underline{f}). \quad (27)$$

The minimization is performed using the classical partial derivative concept $\partial/\partial \underline{f}$ which can be carried out analytically only in part. The evaluation of $\partial Q/\partial \underline{f}$ remains to be accomplished [see Eq. (18)]. Depending on the form selected for the quadratic, the derivative may or may not result in numerical difficulties. In any event, for those forms of Q studied earlier, this derivative could be obtained simply. Nevertheless, this is the case only for these assumed forms of Q . One may conceive of other expressions of Q that may be more appropriate to any given problem but that do not lend themselves to straightforward differentiation. On the other hand, matrices must always be inverted [see Eqs. (21), (23), (24), and (25)] in this method. Depending on the quadrature matrix \underline{A} and on the smoothing matrix \underline{L} , such inversions may conceivably result in difficulties, particularly when the matrix to be inverted is nearly singular (this happens frequently in practice). Lastly, there is an inefficiency (admittedly not crucial) in the procedure, since it is required to repeat the complete numerical treatment for several values of γ in order to select the appropriate γ .

The method to be described next is a proposal for overcoming these difficulties whenever they are present. It requires neither derivatives nor matrix inversions.

⁵This is a more general expression than that derived by Twomey, S., (1963).

5.4.2 Fymat's Method

Let $\tilde{E}_i = \tilde{E}(\lambda_i)$, $i = 1, 2, \dots, N$, denote the data points, and $E_j = E(\lambda_j)$, $j = 1, 2, \dots, M$, $M \geq N$, the corresponding computations from Eq. (11b). In vector notation these two vectors can be written as \tilde{E} and E , respectively. Equation (27) becomes

$$T' = (E - \tilde{E})^T (E - \tilde{E}) + \gamma Q(f), \quad (28)$$

where the quadratic Q is of order j , so that T' is also of order j . Instead of considering the squares of the absolute residuals (first term on the right-hand side of the last equation), we may alternatively consider the relative residuals, so that

$$T'' = [\alpha \tilde{E}^{-1} (E - \tilde{E})]^T [\alpha \tilde{E}^{-1} (E - \tilde{E})] + \gamma Q(f), \quad (29)$$

where α is a diagonal matrix of elements $\{\alpha_i\}$ accounting for the spectral resolution of the data or their relative accuracy or both. The function $T \equiv T'$, T'' is to be minimized. For example, in the case where Q is a difference expression of arbitrary order, Eq. (28) can be written explicitly:

$$T' = \sum_{i=1}^N \left\{ E_i - \sum_{j=1}^M D_{ij} n_j \right\}^2 + \gamma \sum_{k=1}^M \sum_{j=1}^M H_{kj} n_k n_j, \quad (28a)$$

where the integration on the right-hand side of Eq. (11b) has been replaced by an appropriate quadrature with matrix elements D_{ij} , and n_l , $l = k, j$, is the size distribution at the l th quadrature point. The function $T = T'$, T'' represents the equation of a hypersurface, and it is required to find the minimum, say T_{\min} , of this surface. Various methods are available in the literature for finding the minimum of a function without computing derivatives; see more particularly the minimization search method (MSM) utilized for inverse radiative-transfer problems (Fymat, A. L., 1972; Fymat, A. L., and Kalaba, R. E., 1974). If indeed T presents a unique minimum, then with some experience in the use of optimization methods, this could be a highly successful method. There are two different ways in which the method could be used.

(i) Model of $n(r)$ postulated. Assume that the Gamma distribution (II) is an appropriate model. Then, with Eq. (1e), Eq. (11b) becomes

$$E(\lambda; a, b) = \int_0^\infty Q[m(\lambda), x] x^{(1-b)/b} e^{-x/kab} dx, \quad (30)$$

where the constant

$$C = \frac{\pi N k^{-2}}{(kab)^{1/b-2} \left[\left(\frac{1}{b} - 3 \right)! \right]}$$

will be assumed to be known, for simplicity. The function T therefore contains the two dependent variables a , and b , and the problem reduces to that of the determination of that doublet (a, b) that minimizes T .

(ii) Model of $n(r)$ Not Postulated. A discrete version of Eq. (11b) is obtained by replacing the integral by a finite sum using an accurate quadrature formula of order M . Since $n(x)$ is usually bounded at both ends, smooth and monotonic, a very high-order quadrature may not be required. We obtain:

$$E(\lambda) = A \sum_{j=1}^M Q_j x_j^2 n(x_j) w_j, \quad (31)$$

where w_j are the weights of the corresponding quadrature points, $Q_j = Q[m(\lambda), x_j]$, and $A = \pi k^{-3}$.

Now, it is possible to generate $n(x_j)$ by the translation process

$$n(x_j) = \delta_j n^{(0)}(x_j), \quad (32)$$

where $n^{(0)}$ is some arbitrary initial distribution and δ_j are unknown coefficients. (Note that the translation may operate on any point, whether of the quadrature or not.) On substituting Eq. (32) into Eq. (31), we get

$$E(\lambda; \delta_j) = A \sum_{j=1}^M Q_j x_j^2 n^{(0)}(x_j) \delta_j w_j. \quad (33)$$

The problem is now that of the determination of the minimizing multiplet $(\delta_1, \delta_2, \dots, \delta_M)$. The minimization of the corresponding T function by the MSM is of course possible. The smaller M is, the easier it will be.

The application of the MSM just described to the reconstruction of the particle size distribution, whether a model of the distribution has been assumed or not, has not yet been tested numerically for the direct radiation.

5.4.3 Hanson's Method

Although we shall limit ourselves to Hanson's (1971) inversion technique based on a singular value decomposition, let us also note the works in Smithies, F., 1958; Golub, G., and Kahan, W., 1965; Baker, C. T. H., Fox, L., Mayers, O. F., and Wright, K., 1964. The technique begins with the finite-sum approximation of the infinite integral in Eq. (11b):

$$Af = g. \quad (34)$$

However, rather than considering ξ as in Eq. (16), a weighted least-squares version of Eq. (34) is used, in which the weighting diagonal matrix $W = \text{diag}(\sigma_1^{-1}, \sigma_2^{-1}, \dots, \sigma_N^{-1})$, where σ_i is the standard deviation of the i th element of ξ , is introduced, so that Eq. (34) becomes

$$W Af = W g. \quad (35)$$

Recall that W is an $N \times N$ matrix, A is an $N \times M$ (quadrature) matrix, f is an M -vector, and g is an N -vector, $M \leq N$. Hanson suggests using for the elements of f and g , the following:

$$f(y_j) \equiv f_j = f[y_0 + (j-1)\Delta y], \quad j = 1, 2, \dots, M, \quad (36)$$

i. e., the y_j appearing in the kernel in A are equally spaced, and the x_i , $i = 1, 2, \dots, N$, consist of all $P \geq N$ solutions to equations of the form

$$g(x_i) \equiv g_i = g_0 + i\Delta g, \quad i = 1, 2, \dots, N, \quad (37)$$

where

$$\Delta g = \frac{g_{N+1} - g_0}{N+1}. \quad (38)$$

In so doing, the x_i are chosen in a manner that takes into account the variations of g (they are chosen most densely in regions of rapid changes), and that uses only the observed subdomain of g . This approach, although not compulsory, has the drawbacks that it requires an initial fitting and smoothing of the experimental data, and the numerical solution of the N equations in Eq. (37).

The problem is now to solve Eq. (35). For this purpose, a singular-value decomposition of the $N \times M$ product matrix WA is first performed, i. e.,

$$WA = U \begin{bmatrix} X_M \\ 0 \end{bmatrix} V^T = U X_{M,0} V^T, \quad (39)$$

where U is an $N \times N$ orthonormal matrix, V^T is an $M \times M$ orthonormal matrix, and $X_M = \text{diag}(x_1, x_2, \dots, x_M)$, where $\{x_i\}$ is the non-increasing sequence $x_1 \geq x_2 \geq \dots \geq x_M \geq 0$ of singular values of A (i. e., the positive square roots of eigenvalues of $A^T A$). Equation (35) then becomes

$$(X_{M,0} V^T) f = U^T W g. \quad (40)$$

The vector $\underline{V}^T \underline{f}$ in this last equation is simply the solution \underline{f} projected on the increasingly oscillatory columns of \underline{V}^T . As earlier, the direct solution of Eq. (40) would be ill-conditioned. As a solution-stabilizing process, one can resort to the smoothing constraint of Phillips and Twomey. Instead, Hanson suggests neglecting the contribution of the highly oscillatory eigenvectors which correspond to small eigenvalues. In other words, in place of Eq. (40), one solves

$$\begin{bmatrix} X_i \\ 0 \end{bmatrix} \underline{V}^T \underline{f} \equiv \underline{X}_{i,0} \underline{V}^T \underline{f} = \underline{U}^T \underline{W} \underline{g}, \quad (41)$$

with $\underline{X}_i = \text{diag}(x_1, x_2, \dots, x_i < x_M)$, where i is the largest integer such that the contribution from eigenvectors of order $j > i$ is commensurate with the uncertainty in the data. The solution is then

$$\underline{f} = \underline{V}(\underline{X}_{i,0})^{-1} \underline{W} \underline{g},$$

where

$$(\underline{X}_{i,0})^{-1} = \text{diag}(x_1^{-1}, x_2^{-1}, \dots, x_i^{-1}). \quad (42)$$

Important advantages of this technique, which resembles a Fourier filter, are: (i) it involves minimal a priori constraints on the solution; (ii) it reduces to a minimum the introduction of error due to arbitrary constraint or data redundancy; (iii) it involves no derivatives; and (iv) it computes no inverse matrices. $[(\underline{X}_{i,0})^{-1}]$ is constructed straightforwardly from the elements of \underline{X}_i . Unfortunately, no numerical study of this method in the context of aerosol size distribution is available.

5.4.4 Backus-Gilbert Method

Return to Eqs. (15) and (16) and assume that the errors in the measurements are distributed with mean zero and a known covariance matrix \underline{S} given by

$$\underline{S}_\epsilon = E \left\{ \underline{\epsilon} \underline{\epsilon}^T \right\}, \quad (43)$$

where E is the operator of the expected value over the joint probability density of errors $\underline{\epsilon} = (\epsilon_1, \epsilon_2, \dots, \epsilon_n)^T$. Other distributions of the errors can be selected if desired.

The method (Backus, G., and Gilbert, F., 1970) constructs averaging kernels that are suitable for an inversion of Eq. (15). These kernels are formed by linear combinations of the original kernels as

$$\underline{A}(y) = \underline{a}(y) \underline{K}(y), \quad (44)$$

where $\underline{a} = (a_1, a_2, \dots, a_n)$ and $\underline{K} = (K_1, K_2, \dots, K_n)^T$ with K_i , $i = 1, 2, \dots, n$ being the kernels corresponding to the n physical measurements. The averaging kernels are unimodular:

$$\int_a^b \underline{A}(y) dy = 1; \quad (45)$$

they can be used to form weighted linear averages of the solution $f(y)$ over the range (a, b) :

$$\bar{f}_A = \int_a^b \underline{A}(y) f(y) dy. \quad (46)$$

The coefficient vector \underline{a} in Eq. (44) is determined as follows. The average in Eq. (46) can be considered as representative of the value of f at some y , say $y = y_0$, if \underline{A} is large around y_0 and negligible outside of this value, i.e., if $\underline{A}(y) \sim \delta(y - y_0)$, where δ is Dirac's delta function. Thus, we can choose \underline{a} so that $\underline{A}(y)$ best approximates $\delta(y - y_0)$ in a least-squares sense. The condition

$$\int_a^b [\underline{A}(y) - \delta(y - y_0)]^2 dy = \int_a^b (\underline{a} \underline{K} - \delta)^2 dy = \text{minimum} \quad (47)$$

therefore provides $\bar{a}_0 = \bar{a}(y = y_0)$, from which the local average of f is determined:

$$\begin{aligned}\bar{f}_A(y = y_0) &= \int_a^b A(y_0, y) f(y) dy \\ &= \bar{a}_0 \int_a^b K(y_0, y) \underline{f}(y) dy,\end{aligned}\quad (48)$$

where

$$\underline{f} = (f_1, f_2, \dots, f_n)^T;$$

i. e., if $\underline{g} = (g_1, g_2, \dots, g_n)^T$,

$$\bar{f}_A(y = y_0) = \bar{a}_0 \underline{g}. \quad (49)$$

The algorithm starts, therefore, by the determination of \bar{a}_0 by the condition in Eq. (47); the quantity thus obtained is then used with the data vector \underline{g} to form the local average value of the solution in Eq. (49). The procedure is then repeated at as many values of y , say y_j , $j = 0, 1, 2, \dots, m$, as desired. The complete procedure can be summarized in a compact form as follows:

$$\int_a^b (\bar{a}_j K - \delta_j)^2 dy = \text{minimum} \Rightarrow \bar{a}_j, \quad (50)$$

$$\bar{f}_A^{(j)} = \bar{a}_j \underline{g}, \quad j = 0, 1, 2, \dots, m, \quad (51)$$

where

$$\bar{a}_j = \bar{a}(y = y_j), \quad \delta_j = (y - y_j), \quad \text{and} \quad \bar{f}_A^{(j)} = \bar{f}_A(y = y_j).$$

Now, instead of the minimizing condition in Eq. (50), it may be more useful to minimize the spread

$$\begin{aligned}S(y_j) &= 12 \int_a^b (y - y_j)^2 A^2(y) dy \\ &= 12 \int_a^b (y - y_j)^2 \{ [\bar{a}_j K_u(y)] \times [\bar{a}_j K_v(y)] \} dy, \quad u, v = 1, 2, \dots, n,\end{aligned}\quad (52)$$

where \times is the Kronecker product. And, since

$$\begin{aligned}[\bar{a}_j K_u(y)] \times [\bar{a}_j K_v(y)] &= \bar{a}_j [K_u(y)] \times K_v^T(y) \bar{a}_j^T \\ &= \bar{a}_j \underline{S}' \bar{a}_j^T, \quad \{ \underline{S}' \} = \{ K_u K_v \},\end{aligned}\quad (53)$$

we have

$$S(y_j) = \bar{a}_j \underline{S} \bar{a}_j^T, \quad (54)$$

where

$$\underline{S} = 12 \int_a^b (y - y_j)^2 \underline{S}^1 dy \quad (55)$$

with elements

$$S_{uv} = 12 \int_a^b (y - y_j)^2 K_u(y) K_v(y) dy, \quad u, v = 1, 2, \dots, n. \quad (56)$$

The spread is normalized so that $s(y_j) = w$ for a rectangular averaging kernel centered at $y = y_j$ with width equal to w and height equal to w^{-1} . The values of a_j are here obtained by the minimization of Eq. (54). The algorithm described by Eq. (50) and (51) remains formally the same, except that Eq. (50) is now replaced by

$$s(y_j) = \underline{a}_j \underline{S} \underline{a}_j^T = \text{minimum} \Rightarrow \underline{a}_j. \quad (57)$$

In addition to determining \underline{a}_j , the spread $s(y_j)$ can also be used to express the size resolution inherent in $K(y)$. Furthermore, besides resolution, it is necessary to consider the effect of inaccuracies in the given data vector \underline{g} on the error in the solution $\underline{F}^{(j)}$. The variance of this latter quantity, say $V^{(j)}$, is given by

$$V^{(j)} = \underline{a}_j \underline{S}_\epsilon \underline{a}_j^T. \quad (58)$$

As shown by Backus and Gilbert, improving the resolution (i.e., decreasing the spread) can be achieved only by degrading the accuracy (i.e., increasing the variance), and for any physical problem some trade-off between these two quantities is necessary. A trade-off curve (error vs. resolution) is usually computed for effecting the appropriate compromise.

The real advantage of the method is not its claim to successful inversion of experimental data, but rather the uniqueness of the answer it provides within the error bars determined by the trade-off (accuracy vs. resolution). No application of this method to direct radiation data has been made, so that it is difficult to predict how well it will perform in practice.

5.4.5 Shifrin-Perelman Method

For spheres with refractive index near unity, $|m - 1| \ll 1$, H. C. van de Hulst (1957; Sec. 11.2) has shown that

$$Q = 4 \operatorname{Re}\{K(ip)\}, \quad (59)$$

where the phase-shift parameter $\rho = 2x |m - 1|$ and the function

$$K(w) = \frac{1}{2} + \frac{e^{-w}}{w} + \frac{e^{-w} - 1}{w^2}. \quad (60)$$

In the case of non-absorbing spheres (m real), Eq. (59) becomes

$$Q = 2 - 4 \frac{\sin \rho}{\rho} + 4 \frac{(1 - \cos \rho)}{\rho^2}. \quad (61)$$

van de Hulst qualifies this result in the following manner: "This is one of the most useful formulae in the whole domain of the Mie theory, because it describes the salient features of the extinction curve not only for m close to 1 but even for values of m as large as 2" (Ref. loc. cit., pp. 176-77). On the other hand, for an absorbing particle, the corresponding expression is

$$\begin{aligned}
Q &= 4\operatorname{Re}\{K(i\rho + \rho \tan \beta)\} \\
&= 2 - 4 e^{-\rho \tan \beta} \left(\frac{\cos \beta}{\rho} \right) \left[\sin(\rho - \beta) + \left(\frac{\cos \beta}{\rho} \right) \cos(\rho - 2\beta) \right] \\
&\quad + 4 \left(\frac{\cos \beta}{\rho} \right)^2 \cos 2\beta,
\end{aligned} \tag{62}$$

where $\tan \beta = n'/(n - 1)$. For $\beta = 0$ (i. e., $n' = 0$), Eq. (62) reduces to Eq. (61).

Thereupon Shifrin and Perelman (1963) introduce the dimensionless variables

$$a = \frac{r}{r_0}, \quad \zeta = \frac{r_0}{\lambda}, \quad n(a) = n(r)r_0^4, \quad g(v\beta) = A^{-1}E(\lambda)r_0, \tag{63}$$

where r_0 is the unit of length and $\beta = 2\pi(m - 1)$. Then, with Eq. (63), Eq. (11b) with the variable r becomes:

$$g(\zeta\beta) = \int_0^\infty K(\beta\zeta a)m(a)da, \tag{64}$$

where

$$K(\beta\zeta a) = Q[m(\lambda), r], \quad m(a) = a^2 n(a). \tag{65}$$

[Note how the dimensionless quantities $m(a)$ and $g(v\beta)$ are connected to the dimensional quantities $n(r)$ and $E(\lambda)$ by the expressions in Eqs. (64) and (65).] Next, apply the Mellin transformation to both sides of Eq. (64). We obtain formally

$$\begin{aligned}
\int_0^\infty \zeta^{s-1} g(\zeta\beta) d\zeta &= \int_0^\infty \zeta^{s-1} \left\{ \int_0^\infty K(\beta\zeta a)m(a)da \right\} d\zeta \\
&= \int_0^\infty m(a)a^{-s} \left\{ \int_0^\infty K(\beta\zeta a)(\zeta a)^{s-1} d(\zeta a) \right\} da \\
&= \int_0^\infty K(\beta z)z^{s-1} dz \int_0^\infty m(a)a^{-s} da, \quad z = \zeta a,
\end{aligned} \tag{66}$$

that is,

$$G(s) = L(s)M(1 - s), \tag{67}$$

where G , L , and M denote the Mellin transforms

$$G(s) = \int_0^\infty \zeta^{s-1} g(\zeta\beta) d\zeta,$$

$$L(s) = \int_0^\infty z^{s-1} K(\beta z) dz,$$

$$M(s) = \int_0^{\infty} a^{s-1} m(a) da. \quad (68)$$

Hence

$$m(a) = \frac{1}{2\pi i} \int_{c-i\infty}^{c+i\infty} \left\{ \frac{G(1-s)}{L(1-s)} \right\} a^{-s} ds, \quad (69)$$

where the integration can be carried out for any $c = \text{Re}(s)$ for which Mellin transformation conditions are fulfilled. The problem is now that of evaluating $G(s)$ and $L(s)$. It has been considered only for the case of non-absorbing spheres. Shifrin and Perel'man have shown that the Mellin transform of Eq. (61) is

$$L(s) = - \frac{2^{1-s} \cos(\pi s/2) \Gamma(s)}{\beta^s (2-s)} \neq 0 \quad (-2 < \text{Re } s < 0); \quad (70)$$

and using the recursion formula for Γ -functions,

$$\Gamma(s) \cos \frac{\pi s}{2} = \frac{\pi}{2\Gamma(1-s) \cos[\pi(1-s)/2]}, \quad (71)$$

we get

$$L^{-1}(1-s) = - \frac{1}{\pi} (2\beta)^{1-s} (1-s) \Gamma(s) \cos \frac{\pi s}{2}, \quad (1 < \text{Re } s < 3). \quad (72)$$

They have also shown that the functions $G(1-s)$ and $G(1-s)/L(1-s)$ are both analytic within the range $1 < \text{Re } s < 3$. Equation (69), where G and L are respectively given by Eqs. (68) and (72), is the analytical inverse expression providing the size distribution. The main advantages of this approach are the following: (i) An analytical inversion formula, rather than a completely numerical inversion, is provided. (ii) The formula is strictly applicable for non-absorbing particles with m near unity. However, since the Mellin transform G can be evaluated numerically [without necessarily effecting the corresponding integration analytically as in Eq. (72)] the case of absorbing particles raises no serious difficulties. In addition, as stated earlier, it is expected that the formula will hold approximately true for refractive index values up to 2. (iii) No assumption is made regarding the shape of the size distribution.

The method has been used extensively by Shifrin and his collaborators. The work of these authors indicates that one main drawback of the method is the necessity, for inversion purposes, of knowing the entire spectrum of $E(\lambda)$ [or $g(\zeta\beta)$] for $\lambda \in (0, \infty)$.

5.5 Inverse Methods: Determination of Effective Complex Refractive Index and Size Distribution Model Parameters

The basic assumption here is only that the refractive index, which may be complex, is constant throughout the wavelength range of interest. The problem is therefore the determination of both the real and imaginary parts of the index and the distribution parameters. Only the following method has been developed.

5.5.1 Fymat's Method

Consider again the Gamma distribution (I) for example. As in Section 5.4.2 denote by $E(\lambda; m_r, m_i; \alpha, \beta)$ the model computations of Eq. (11b) and by $\tilde{E}(\lambda; m_r, m_i; \alpha, \beta)$ the corresponding measurements. The dependence of both these quantities on the refractive index and the size distribution has been explicitly written. Now, using the euclidean norm, we define the objective (or performance) function:

$$S(m_r, m_i; \alpha, \beta) = \sum_{\lambda} [E(\lambda) - \tilde{E}(\lambda)]^2. \quad (73)$$

This is the equation of a four-surface. Its minimum, that is that quadruplet $(m_r, m_i; \alpha, \beta)$ that minimizes the sum of squares of absolute deviations figuring in the right side, provides the solution. The number of unknown parameters can be increased such as may be required by multimodal distributions. Also, a norm different from the euclidean norm could be used in the definition of the objective function S . (We have already introduced the relative deviations in Section 5.4.2.)

As an example, Table 2 illustrates a sample result for the Gamma (I) distribution with $\alpha = 2$ (fixed). In the above example, the measurements were simulated by using Eq. (11b) for the set of nine wavelengths; $\lambda = 0.40, 0.45, 0.49, 0.525, 0.575, 0.61, 0.64, 0.67$, and $0.70 \mu\text{m}$. As for Figures 1 and 2, the size distribution extended from 0.005 to $6.0 \mu\text{m}$. Although this result has not been optimized, it is seen that the highest accuracy is obtained in recovery of the distribution parameter. Excellent accuracy is also the case for the real part of the refractive index; the imaginary part of the index, however, is not as sensitive to direct radiation and can be determined only to within few percent. With the inverse solution thus determined the transmission was recomputed. It is contrasted with the "measured" transmission at all wavelength channels in Table 3. The table shows that the corresponding relative errors are only fractions of one percent at all but the two wavelengths 0.61 and $0.64 \mu\text{m}$.

The results presented in Tables 2 and 3 are preliminary. An extension to include a larger number of distribution parameters, as well as the determination of the minimal number of required wavelength channels and an error analysis are needed. Nevertheless, they show the following advantages of the method: (i) Extremely high sensitivity to the size distribution, (at least to the modal radius). (ii) Very high sensitivity to the real part of the refractive index. (iii) Smaller sensitivity to the imaginary part of the index which remains, however, very adequate. For very little absorbing aerosols, the expected accuracy in retrieving the imaginary part is expected to degrade with decreasing values of this parameter. (iv) It does not appear necessary to assume that the refractive index is known as in the methods of Section 5.4; it is only assumed that it remains constant over the spectral range considered. An extension of the method to the translation procedure described earlier in Section 5.4.2 (ii) although in principle feasible, remains to be investigated.

6. INVERSION OF RATIOS OF DIRECT RADIATION MEASUREMENTS

Returning to the general equation, Eq. (11), it is seen that if the z -dependence of the integrand in the right-side could be factored out as a common factor, say $F(z)$, i.e., the z -variations of particle characteristic length, refractive index and size distribution are identical for all j -species of particles, then, we could write:⁶

$$E[\lambda; m^j, n^j(a)] = \int_{z_1}^{z_2} F(z) dz \times \left\{ \int_0^\infty G(a) Q_{\text{ext}}[a, m(\lambda)] n(a) da \right\}^j. \quad (11c)$$

Now, for a single aerosol species, denoting by (u, v) any pair of wavelengths, it is seen that the ratio⁷

$$R_{u,v}[\lambda; m, n(a)] = \frac{E[u; m, n(a)]}{E[v; m, n(a)]} = \frac{\int_0^\infty G(a) Q_{\text{ext}}[a, m(u)] n(a) da}{\int_0^\infty G(a) Q_{\text{ext}}[a, m(v)] n(a) da} \quad (74)$$

is z -independent and free of any systematic error. In particular in the case of spherical particles, this ratio becomes:

$$R_{uv}[\lambda; m, n(r)] = \left(\frac{u}{v} \right)^3 \frac{\int_0^\infty x^2 Q_{\text{ext}}[x, m(u)] n(x) dx}{\int_0^\infty x^2 Q_{\text{ext}}[x, m(v)] n(x) dx}. \quad (75)$$

The problem remains the determination of m and $n(x)$.

⁶In order not to unduly complicate the notation, we keep the same notation G , Q_{ext} and n before and after factorization.

⁷The use of extinction ratios appears to have first been proposed by Burch et al. (loc. cit.).

6.1 Analysis of Direct Problem

A convenient analysis is provided by contour maps of the objective function now defined as:

$$S(m_r, m_i; n(x)) = \sum [R_{uv} - \tilde{R}_{uv}]^2, \quad (76)$$

where the summation is carried out over all ratios. Although in principle one could characterize $n(x)$ by the δ_j translation parameters of Eq. (32), a better visualization of the contour maps would be achieved by limiting the number of such parameters. For convenience, therefore, we shall use the Gamma (I) distribution with $\alpha = 2$ (fixed) so that S reduces to $S(m_r, m_i; \beta)$. The measurements \tilde{R}_{uv} were as before simulated by computing Eq. (75) for the case $m_r = 1.44$, $m_i = -0.03$ and $\beta = 15.0$. The computed ratios R_{uv} were then obtained for $m_r = 1.34$ (0.01) 1.54, $-m_i = 0$ (0.01) 0.10 and $\beta = 8(1) 31$, i.e., for 5,544 cases.

Figures 3 to 5 are contour plots of the latter surface in the (m_r, m_i) -parameter space for the three values $\beta = 8, 15$ and 25 corresponding to modal radii $0.25, 0.133$ and $0.08 \mu m$, respectively. For these widely different β 's, it is seen that the contour plots are virtually identical indicating, in conflict with a recent claim (Kuriyan, J. G., Phillips, D. L., and Chahine, M. T., 1974), that the extinction ratio is insensitive to the distribution parameter β . The above Figures also show that the surface S has a single unique minimum which is located at the exact values of m_r and m_i . A finer (m_r, m_i) grid about this minimum should provide the precise location. However, this grid approach, which may otherwise be visually convenient when the number of unknown parameters is small, is nevertheless time-consuming and inefficient when the number of parameters increases. The minimization search method is considerably more systematic and efficient; its use will later be illustrated.

Table 4 further illustrates the insensitivity of the extinction ratio data to β . For the case $m_r = 1.44$ and $m_i = -0.03$, the figures in the table represent the relative errors

$$\Delta\beta = 100 \frac{R_{uv}(\beta) - R_{uv}(15.0)}{R_{uv}(15.0)}. \quad (77)$$

Various areas have been delimited within this table; these correspond to the level of insensitivity to β according to the measurement accuracy following the code indicated below the Table. For example, for a measurement accuracy of 0.1%, the area bounded by the dotted lines represents the domain of uncertainty in β ; it is seen to extend between approximately $\beta = 8$ to $\beta = 23$. Even for the extremely high (unrealistic) accuracy of 0.001% the continuous lines in the table indicate an insensitivity to β from approximately 11 or 12 to 18 or 19.

The contour curves for $\beta = 15$ and $\alpha = 1.0$ (0.2) 3.0 are indistinguishable from Figures 3 to 5 further showing that the extinction ratios are insensitive to this other distribution parameter.

6.2 Inverse Methods: Determination of Effective Complex Refractive Index Independent of Size Distribution

As just demonstrated, the extinction ratios have the important property of being completely insensitive to the size distribution. They are however extremely sensitive to the complex refractive index. One may therefore first determine this parameter, and from the data on extinction subsequently reconstruct the size distribution. It appears preferable therefore to record the extinction data and to perform their ratios rather than to register ratios only. In this manner the same data could be used for determining both the refractive index and the distribution. However, if only the index is of interest, or if the distribution is to be reconstructed from different data, then, of course, recording the ratios only should prove sufficient.

6.2.1 Fymat's Method

Our minimization search method has been applied to the minimization of the S -function in Eq. (76) in an extensive set of experiments. The results of these experiments will be published elsewhere. Some are illustrated in Tables 5 and 6. The nine wavelengths indicated in the first column of Table 3, denoted sequentially by 0, 1, ..., 9, define the nine ratios R_{uv} . The "true" values of the complex refractive index and the size distribution parameter are listed in the second row of Table 5. The MSM was then initiated with various initial guesses for m_r , m_i and β . The results in this last Table show that (i) As expected the ratios R_{uv} are insensitive to β as already demonstrated using the contour analysis of the direct problem. In the 3-dimensional parameter space (m_r, m_i, β) , the inversion proceeds almost parallel to the β -axis. This is so because the final recovered value of β is essentially the same as the corresponding initial guess; (ii) Both components of the complex refractive index can be retrieved extremely accurately (see the relative errors in columns 4 and 6). (iii) When the ratios are recomputed with the inverse solution, they do not depart from the true ratios by more than few units in the 4th or 5th decimal place. This is shown in the last column of Table 5, only for the non-identical ratios.

The sensitivity of the inverse solution to the number and accuracy of the measured ratios is illustrated in Table 6. It is seen that (i) the parameter β is completely insensitive to both the number and the accuracy of the ratios; (ii) The accuracy in the real part of the refractive index is always extremely

high and, although it degrades with noisier data, it is never larger than fractions of a percent for two-significant figures; (iii) The accuracy in the index imaginary part is also high but it degrades more quickly with increasing noise; (iv) There is no substantial improvement in the inverse solution when increasing the number of ratios from six to nine for comparable accuracy; and it is preferable to have six accurate ratios than nine less accurate ratios; (v) Three ratios can also provide accurate inverse solutions. However, tests not illustrated here show that the choice of these ratios influences this accuracy, particularly that on m_1 .

7. SUMMARY AND CONCLUSIONS

In investigating the effects of absorbing and scattering particulates on electromagnetic wave propagation in the atmosphere, we have seen that it is only sufficient to consider an "effective" working model that is however capable of mimicking the true effects. It is then reasonable to utilize a model particle size distribution whose parameters consist of expressions involving up to fourth-order moments of the distribution; these parameters may be determined experimentally. Most such distributions have been shown to belong to Pearson's family of distribution curves. The basic equation in the inverse problem of reconstructing the distribution and retrieving the complex refractive index is provided by Eq. (11) for a mixture of an arbitrary number of gaseous and particulate species. Under certain restrictive assumptions, this inversion can be carried out in a variety of different ways. The merits of these methods have been set forth. In applying Junge's method for inferring the power distribution parameter, more work is needed in determining the ranges of particle radius and refractive index values within which the atmospheric extinction factor is truly a slowly varying function of wavelength. Certain shortcomings of the Phillips-Twomey method, particularly the a priori knowledge of the refractive index, can be overcome by an application of the author's Minimization Search Method (MSM) to either a model or an actual distribution. Numerical work is however needed in this area. Applications of Hanson's and Backus-Gilbert methods are still lacking, while an extension of Shifrin-Perel'man analytical method to absorbing particles remains needed. In those wavelength regions where the refractive index is essentially constant, the MSM is able to retrieve with high accuracy both the complex refractive index and size distribution parameter(s). Contrary to previous assertions it was shown that extinction ratios are completely insensitive to the size distribution. In this case, a determination of the complex refractive index independent of size distribution effects is possible. This was demonstrated with highly accurate results by the MSM.

In the various methods listed more work is needed with the following objectives: (i) domain of sizes than can be effectively sampled, particularly the upper bound; (ii) minimal number of wavelength channels; and (iii) tolerable experimental noise. Although some results are already available in these three areas, their optimization and the consideration of several distributions by the same method are essentially lacking.

ACKNOWLEDGEMENTS

I should like to thank Dr. R. E. Kalaba for bringing to my attention Pearson's differential equation in connection with size distribution parameterization. I also thank Drs. P. J. Wright and E. P. Shuttle for communicating their results prior to publication. This paper presents the results of one phase of research carried out at the Jet Propulsion Laboratory under Contract No. NAS7-100 with the National Aeronautics and Space Administration.

REFERENCES

- Angström, A. K., 1970, in Advances in Geophysics, Vol. 14, 269, Eds. Landsberg, H. E., and Van Mieghem, J.
- Backus, G., and Gilbert, F., 1970, *Philos. Trans. Roy. Soc. Lond.* 266, 123.
- Bahethi, O. P., and Fraser, R. S., 1975, NASA-GSFC Report X-910-75-52.
- Baker, C. T. H., Fox, L., Mayers, O. F., and Wright, K., 1964, *Comput. J.*, 7, 141.
- Brault, J. M., and White, O. R., 1971, *Astron. Astrophys.* 13, 169.
- Burch, D. E., Pembroke, J. D., and Reisman, E., 1970, Philco-Ford Corporation Report No. U-4789, NASA-CR-86343.
- Chandrasekhar, S., 1950, Radiative Transfer, Clarendon, Oxford (reprinted by Dover, New York, 1960), 49.
- Deirmendjian, D., 1969, Electromagnetic Scattering on Spherical Polydispersions, Elsevier, New York.
- Fessenkov, V. G., 1955, *Astron. Zh.*, 32, 265.
- Franklin, J. N., 1970, *J. Math. Anal.*, 31, 682.
- Fymat, A. L., 1972, in *Proc. Intern. Radiat. Symp.* 243 (Sendai, Japan).
- Fymat, A. L., 1975, *Appl. Math. Comp.*, 1, 131.
- Fymat, A. L., and Abhyankar, K. D., 1969a,b, *Astrophys. J.*, 158, 315, 325; 1970a,b, 159, 1009, 1019.
- Fymat, A. L., and Kalaba, R. E., 1974, *J. Quant. Spectros. Radiat. Transf.*, 14, 919.
- Fymat, A. L., DeVaux, C., Herman, M., and Lenoble, J., 1975 (to be submitted).
- Golub, G., and Kahan, W., *SIAM J. Numer. Anal.* 2, 205.
- Hansen, J. E., 1971, *J. Atmos. Sci.*, 28, 1400.
- Hansen, J. E. and Travis, L. D., 1974 *Space Sci. Rev.*, 16, 527.
- Hanson, R. J., 1971, *SIAM J. Numer. Anal.*, 8, 616.
- Holland, A. C., and Gagne, G., 1970, *Appl. Opt.*, 9, 1113.
- Hulst, H. C. van de, 1959, Light Scattering by Small Particles, Wiley, New York.
- Hulst, H. C. van de, and Grossman, K., 1968, in The Atmospheres of Venus and Mars, Eds. Brandt, J. C., and Mc Elroy, M. B.
- Irvine, W. M., 1975, these Proceedings.
- Junge, C., 1963, Air Chemistry and Radioactivity, Academic, New York, 1975.
- Kerschgens, M., Raschke, M. E., and Reuter, U., 1975, these Proceedings.
- Kunasz, C. V., Jefferies, J. T., and White, O. R., 1973, *Astron. Astrophys.*, 28, 15.
- Kuriyan, J. G., Phillips, D. H., and Chahine, M. T., 1974, *J. Atmos. Sci.*, 31, 2233.
- Lenoble, J., 1974, Ed. Standard Procedures to Compute Radiative Transfer in a Scattering Atmosphere, Tech. Rep. World Meteor. Org. (to be published).
- Lenoble, J., 1975, these Proceedings.
- Liou, K. N., 1975, these Proceedings.
- Pearson, K., 1914, 1931 Ed. Tables for Statisticians and Biometricians: I, II, Cambridge, England.
- Pepin, T. J., 1969, 1970, U. of Wyoming Rep. No. AP-31, AP-34.
- Phillips, D. L., 1962, *J. Assoc. Comp. Mach.*, 9, 84.
- Plass, G. N., 1975, these Proceedings.
- Quenzel, H., 1970, *J. Geophys. Res.*, 75, 2915.
- Shaw, G. E., Reagan, J. A., and Herman, B. M., 1973, *J. Appl. Meteor.*, 12, 374.
- Shettle, E. P., and Fenn, R. W., 1975, these Proceedings.

Shifrin, K. S., and Perel'man, A. Ya, 1963, Opt. Spectros. 15, 285.

Smithies, F., 1958, Integral Equations, Cambridge, England.

Tinger, D. L., 1972, in Proc. 1970 Conf. Atmos. Radiat., 9. (Fort Collins, Colorado).

Twomey, S., 1963, J. Assoc. Comput. Mach., 10, 97.

Twomey, S., 1965, J. Franklin Inst., 279, 95.

Yamamoto, G., and Tanaka, M., 1969, Appl. Optics, 8, 447.

Wright, P. J., 1975, these Proceedings.

Table 1: Pearson's coefficients for some parameterizations of atmospheric particle size distributions

Distribution	a_0	a_1	b_0	b_1	b_2
Power	$-\alpha$	0	0	1	0
Exponential	β	0	0	0	1
Normal	0	-2β	1	0	0
Gamma (I)	α	$-\beta$	0	1	0
Gamma (II)	$a(1 - 3b)$	-1	0	ab	0

Table 2: Illustrating the Application of the Minimization Search Method to the Inverse Determination of the Complex Refractive Index and Size Distribution Effective Mode Radius

Real Part of Refractive Index, m_r			Imaginary Part of Refractive Index, m_i			2/Effective Mode Radius, β			Objective Function, S
True	Inverse	$\Delta(\%)$	True	Inverse	$\Delta(\%)$	True	Inverse	$\Delta(\%)$	
1.440	1.441	0.069	-0.030	-0.031	3.848	15.000	15.001	0.009	4.22 - 7

Table 3: Contrasting the Transmitted Direct Radiation Computed from the Inverse Solution with the Simulated Corresponding Data

$\lambda(\mu\text{m})$	Direct Radiation Transmission		
	Computed	Simulated	Relative Error %
0.400	0.828179-2	0.827608-2	0.069
0.450	0.907967-2	0.911478-2	0.387
0.490	0.977180-2	0.981614-2	0.454
0.525	0.993856-2	0.997020-2	0.318
0.575	0.958635-2	0.959207-2	0.060
0.610	0.891428-2	0.843517-2	5.375
0.640	0.846704-2	0.889876-2	5.099
0.670	0.820403-2	0.818091-2	0.282
0.700	0.783714-2	0.780071-2	0.465

Table 5: Illustrating the Application of the Minimization Search Method to Recovering the Complex Refractive Index and Size Distribution Parameter

Wavelength Ratios		m_r	$ \Delta m_r $ (%)	$-m_i$	$ \Delta m_i $ (%)	β	$ R - \bar{R} $
$R_{00}, R_{01},$ $R_{02}, R_{03},$ $R_{04}, R_{05},$ $R_{06}, R_{07},$ R_{08}	True values	1.44		0.03		15	
	Guess	1.40		0.01		12.0	$\Delta R_{05} = 0.00006$
	MSM*	1.43997	0.002	0.02999	0.033	11.8804	$\Delta R_{06} = 0.0001$
	Guess	1.40		0.01		18.0	$\Delta R_{02} = 0.00005$
	MSM	1.43999	0.0007%	0.02999	0.033	17.8802	$\Delta R_{05} = 0.00006$ $\Delta R_{06} = 0.0001$
	Guess	1.38		0.025		13.5	$\Delta R_{02} = 0.00006$
	MSM	1.43998	0.001%	0.02999	0.033	13.1909	$\Delta R_{05} = 0.00006$ $\Delta R_{06} = 0.0001$

* Minimization Search Method.

Table 6: Illustrating the Sensitivity of the Inverse Solution for the Complex Refractive Index and Size Distribution Parameter to the Number of Extinction Ratios and Their Accuracy

Wavelength Ratios	Number of Significant Figures		m_r	$ \Delta m_r $ (%)	$-m_i$	$ \Delta m_i $ (%)	β
$R_{00}, R_{01},$ $R_{02}, R_{03},$ $R_{04}, R_{05},$ $R_{06}, R_{07},$ R_{08}		True values	1.44		0.03		15.0
		Guess	1.38		0.025		13.5
	4	MSM	1.43998	0.001	0.02999	0.033	13.1909
	3	MSM	1.44015	0.010	0.03007	0.233	13.1874
	2	MSM	1.43840	0.111	0.02776	7.467	13.3377
$R_{00}, R_{01},$ $R_{03}, R_{04},$ R_{06}, R_{08}	3	MSM	1.44009	0.006	0.03009	0.285	13.2460
	2	MSM	1.43716	0.197	0.02686	10.483	13.3280
$R_{11}, R_{15},$ R_{17}	3	MSM	1.44093	0.065	0.03009	0.303	13.3913
	2	MSM	1.44570	0.396	0.02656	11.455	13.5131

Table 4: Illustrating the Insensitivity of the Extinction Ratio as a Function of Wavelength to the Particle Size Distribution Parameter

$\beta \backslash \lambda$	0.45	0.49	0.525	0.575	0.61	0.64	0.67	0.70
8	0.0264	0.0298	0.0445	0.0832	0.1264	0.1696	0.1908	0.1989
9	0.0097	0.0110	0.0164	0.0306	0.0466	0.0625	0.0702	0.0735
10	0.0035	0.0040	0.0060	0.0112	0.0171	0.0229	0.0257	0.0273
11	0.0013	0.0015	0.0022	0.0042	0.0062	0.0084	0.0089	0.0094
12	0.0004	0.0006	0.0008	0.0015	0.0023	0.0030	0.0030	0.0038
13	0.0001	0.0002	0.0002	0.0006	0.0008	0.0010	0.0010	0.0009
14	0.0000	0.0001	0.0001	0.0002	0.0002	0.0003	0.0000	0.0000
15	0.0000	0.0000	0.0000	0.0000	0.0000	0.0000	0.0000	0.0000
16	0.0001	0.0001	0.0001	0.0001	0.0001	0.0002	0.0000	0.0000
17	0.0002	0.0002	0.0004	0.0003	0.0003	0.0004	0.0010	0.0000
18	0.0004	0.0007	0.0008	0.0009	0.0010	0.0010	0.0010	0.0009
19	0.0012	0.0019	0.0023	0.0024	0.0025	0.0025	0.0030	0.0028
20	0.0033	0.0052	0.0061	0.0067	0.0066	0.0066	0.0069	0.0066
21	0.0088	0.0141	0.0167	0.0182	0.0177	0.0177	0.0188	0.0179
22	0.0238	0.0384	0.0453	0.0493	0.0482	0.0478	0.0494	0.0490
23	0.0645	0.1041	0.1229	0.1336	0.1305	0.1304	0.1325	0.1320
24	0.1742	0.2817	0.3325	0.3617	0.3532	0.3503	0.3588	0.3563
25	0.4675	0.7570	0.8943	0.9733	0.9502	0.9432	0.9658	0.9595
26	3.1770	2.9293	1.8157	0.3927	0.0210	0.7765	0.9262	0.6098
27	1.7884	0.0926	0.8605	1.7033	0.1176	0.5073	2.7075	3.5535
28	3.3692	1.5580	4.0406	6.0713	2.9787	4.6707	2.3339	2.4582
29	6.9479	5.2720	4.1998	2.9636	5.7156	4.0361	10.8785	10.9422
30	16.3302	4.0105	11.6555	10.8407	6.6112	7.8650	1.3394	2.5600
31	16.7168	4.6318	11.0039	10.1242	5.8426	7.0861	2.2034	1.7098

error upper bounds:

————— 0.001%
 - - - - - 0.005%
 - . - . - 0.01%
 - - x - - x 0.05%
 0.1%

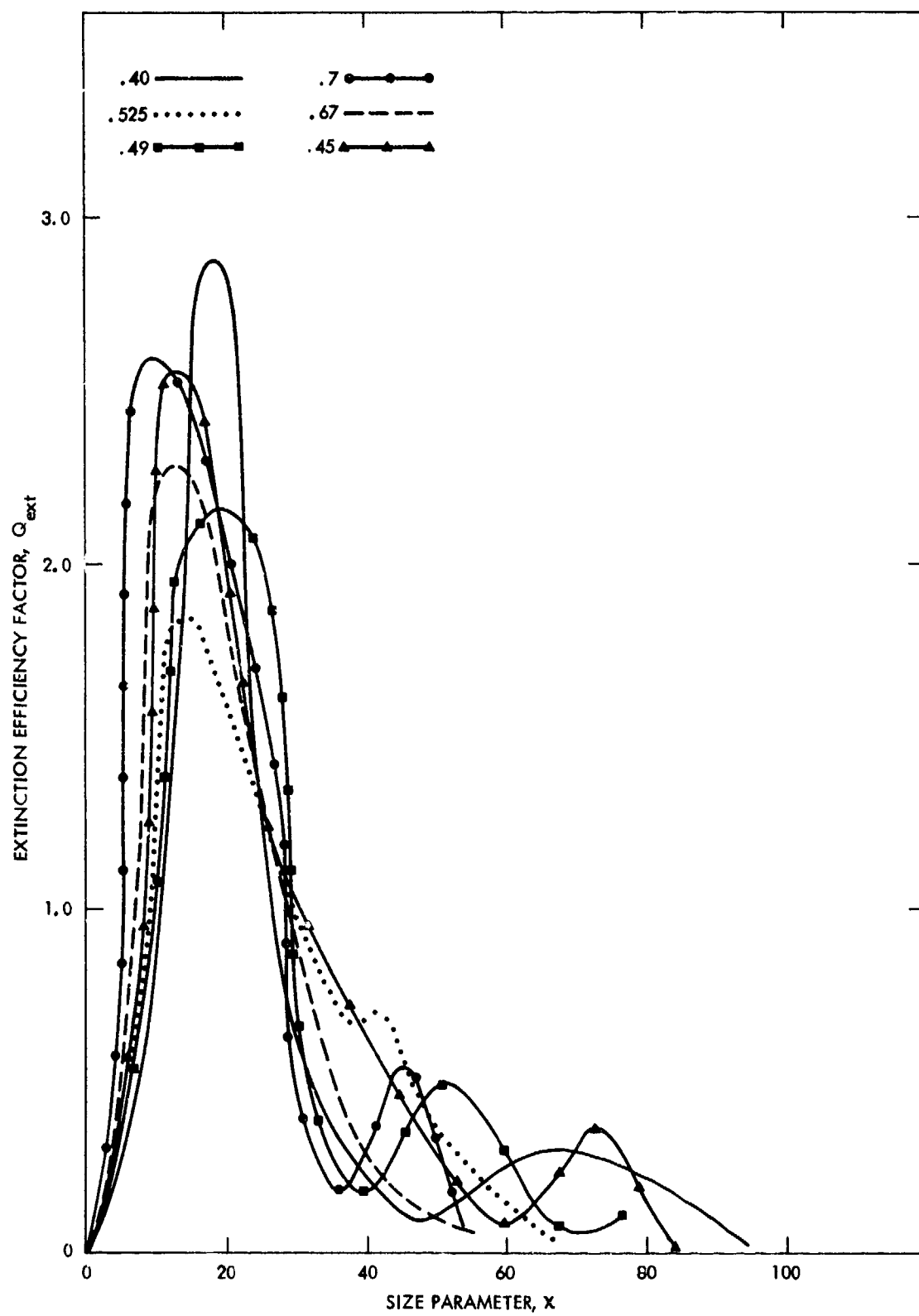


Fig.1 Extinction efficiency factor of a polydispersion of particles as a function of size parameter for several wavelengths

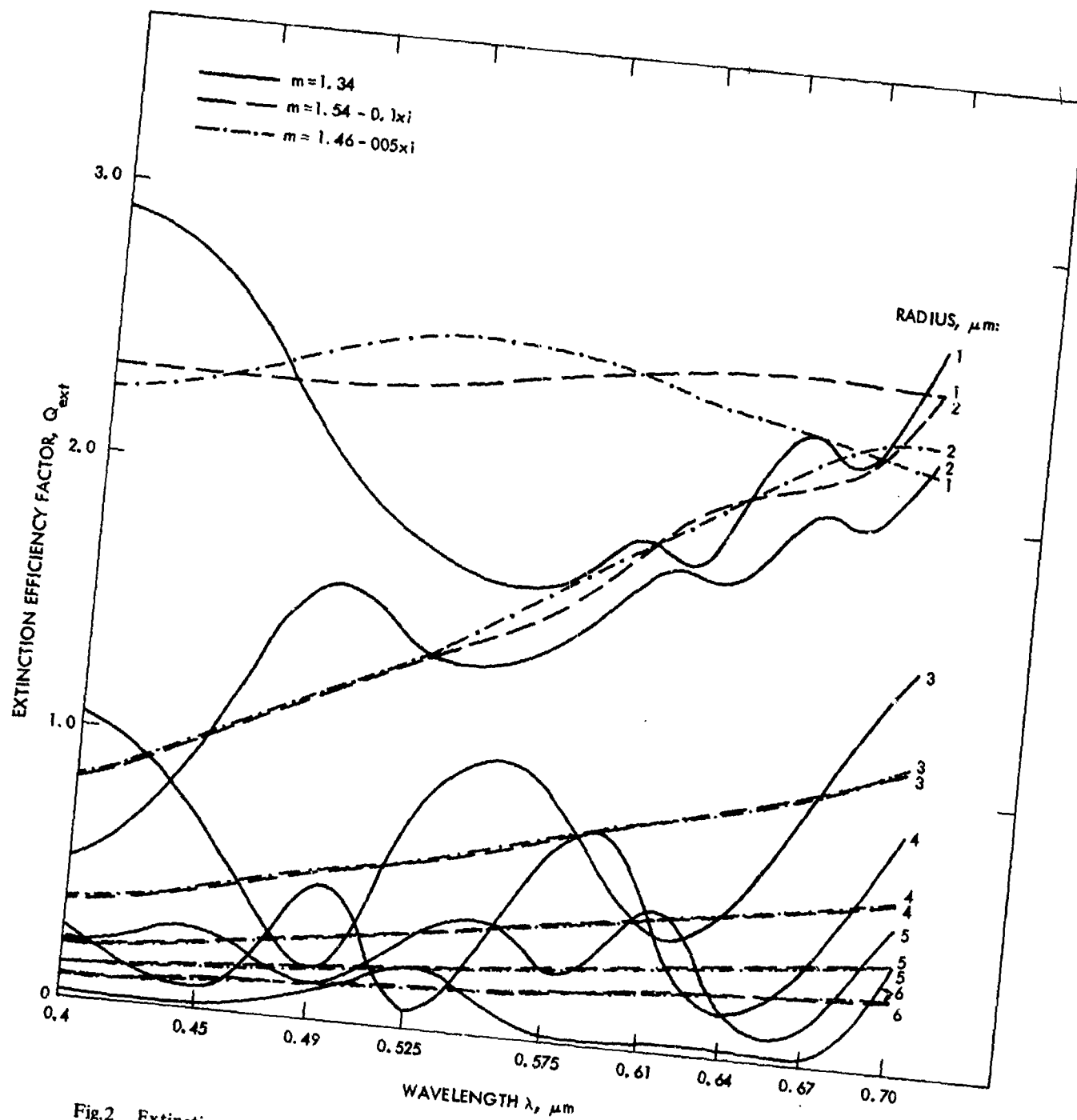


Fig.2 Extinction efficiency factor of a polydispersion of particles as a function of wavelength for several particle radii

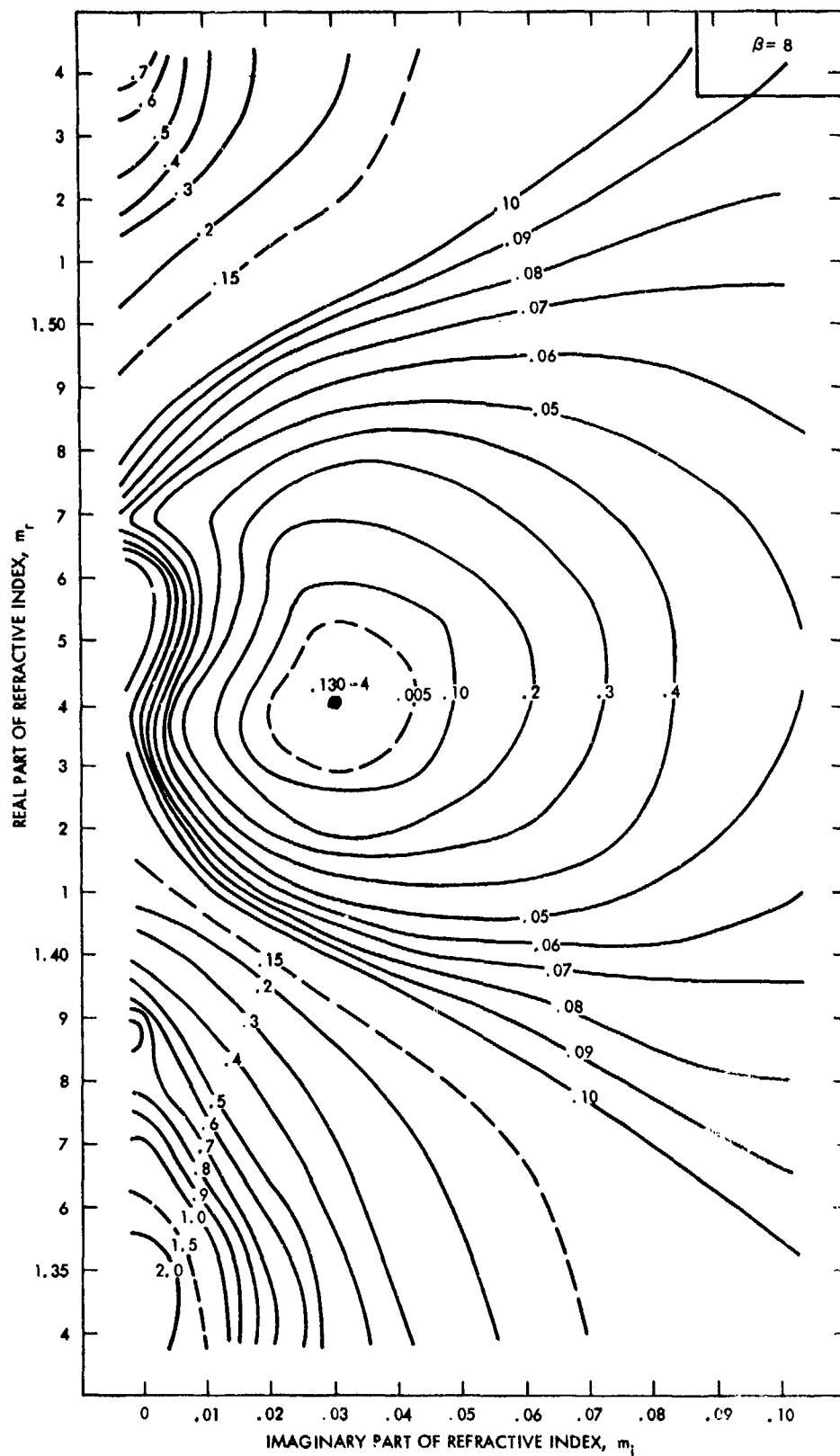


Fig.3 Contour curves of the surface $S(m_r, m_i)$ for distribution modal radius at $0.25 \mu\text{m}$ ($\beta = 8$)

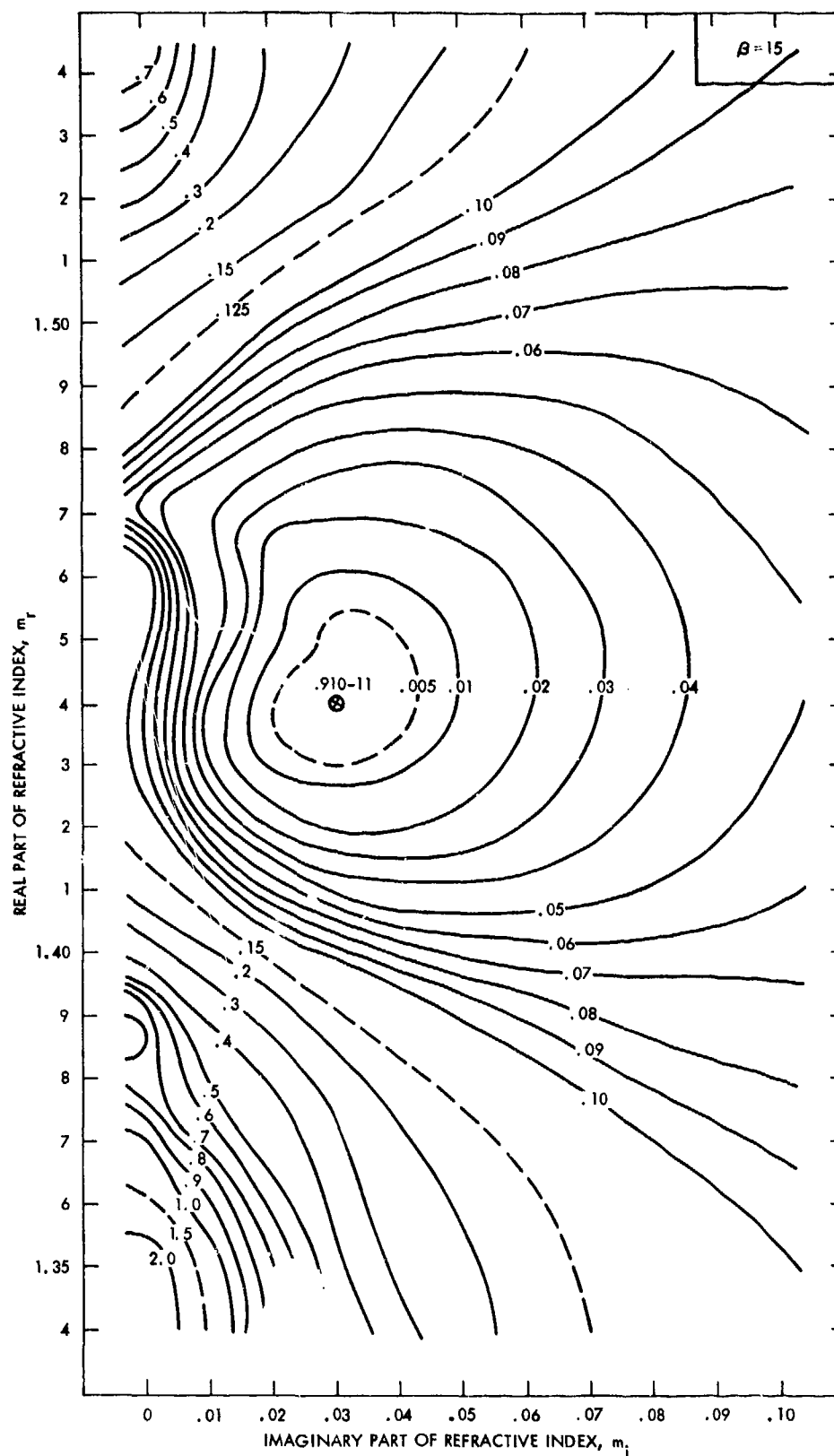


Fig.4 Contour curves of the surface $S(m_r, m_i)$ for distribution modal radius at $0.133 \mu\text{m}$ ($\beta = 15$)

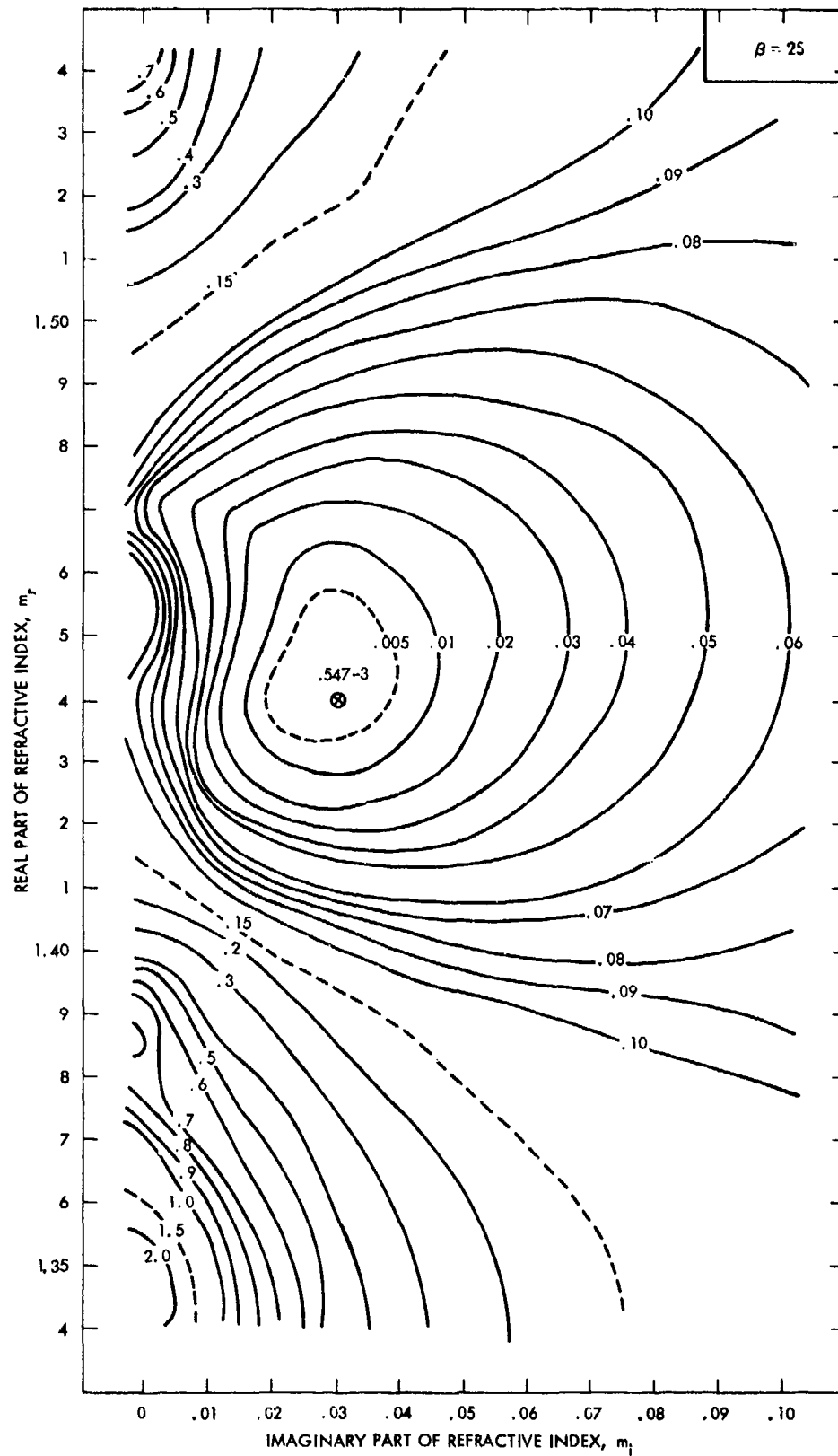


Fig.5 Contour curves of the surface $S(m_r, m_i)$ for distribution modal radius at $0.08 \mu\text{m}$ ($\beta = 25$)

THEORETICAL STUDIES OF THE TRANSFER OF SOLAR RADIATION IN THE ATMOSPHERE

M.J. Kerschgens, E. Raschke, U. Reuter
Institut für Geophysik und Meteorologie
Universität zu Köln, Fed. Rep. of Germany

Abstract:

The transfer of solar radiation in one-dimensional model atmospheres has been computed for the wavelength range from 0.2 to 3.58 μm with an iterative solution of the radiative transfer equation. This method allows detailed considerations of the absorption, heating and albedo with respect to multiple anisotropic scattering in the atmosphere and reflection at ground.

Absorption by O_3 , H_2O , CO_2 , O_2 and aerosols has been taken into account. The transmission in near infrared bands of CO_2 and H_2O is approximated by exponential series derived from spectral measurements by MOSKALENKO. Various vertical distributions of H_2O and aerosols are considered and also two different boundaries are used: a rough ocean surface and a bright sandy desert.

It is shown, for instance that as a result of the higher albedo of the sand surface, the absorption increases by 5 to 7 % depending on the solar height. Aerosol layers in the lower troposphere are much more effective respective to absorption. They may alter by almost 40 % the radiative heating.

1. Introduction

It is the aim of the research reported here to determine accurately with computations the diabatic heating of the atmosphere and of the ground by absorption of solar radiative energy. The computational method consists in an iterative solution of the radiative transfer equation which adequately accounts for multiple scattering processes. Polarization effects are neglected, due to their very small contributions to the energy fluxes (Hansen, 1971). Further the atmosphere is assumed inhomogeneous only in its vertical extension. The solar spectrum is taken from 200 to 3580 nm according to LABS and NECKEL (1968) and divided into 37 subintervals. The lower boundary is chosen to be a wind-roughened ocean surface, or a desert sand (after DIRMHIRN, 1968). Phase functions for molecular and particulate scattering have been mixed in each spectral interval according to the ratio of coefficients of total to molecular scattering; where four different layers are considered.

These calculations may repeat to some extent many others reported at present in the literature, but it is tried here to consider rather realistic atmospheric models up to 70 km altitude and to check the influence of all radiative transfer parameters (e.g. scattering and transmission functions) on the derived radiative flux divergences.

2. Atmospheric models

Most of the results shown here pertain to a subtropical summer model (STS) of the troposphere with a mean (after Mc CLATCHEY et.al., 1971) and also a realistic (from the APEX expedition of the vessel Meteor in 1969) water vapour profile in the troposphere and with a constant mixing ratio of 2.10^{-6} g/g in the stratosphere (Fig. 1). The abundance of CO_2 and O_2 is assumed with constant mixing ratios and ozone profiles are taken from published data (Mc CLATCHEY et.al., 1971, Fig. 2). Vertical profiles of aerosol and molecular scattering coefficients are taken from ELTERMANN (1968); the former ones are altered

to demonstrate the effects of the stratospheric (volcanic) and tropospheric (e.g.: Saharian dust) particle layers upon the radiative heating of the atmosphere. Throughout all calculations a single scattering albedo of all aerosols of $\bar{\omega}_s = 0.85$ is assumed.

3. Transmissions functions for all gases

Absorption of solar radiation by ozone in the near UV and visible part of the spectrum has been computed with transmission functions determined for fine spectral intervals by ELTERMANN (1968) and DÜTSCH (1970). For oxygen (760 nm-band) and all bands of watervapor and carbon dioxide mean band transmission functions have been derived from spectral data published by Mc CLATCHEY et.al. (1971) and MOSKALENKO (1968, 1969), respectively.

3.1: Approximations with finite series of exponentials

Since these band transmissions functions are non - exponential as required, they have been approximated by finite series of exponentials as defined in Equ. (1)

$$(1) \quad \tau_\lambda = \sum_{i=1}^n a_i \cdot e^{b_i x \cdot \left(\frac{p}{p_0}\right)^m}$$

where τ_λ = band transmission, where λ may be the wavelength of the band center,

n = number of terms

p = pressure of air; $p_0 = 1013.5$ mb

m = exponent of pressure correction, taken from data sources mentioned above,

x = absorber path length

The coefficients a_i , where $\sum_{i=1}^n a_i = 1$, and the exponents b_i (≤ 0) are determined with a least square fit method with a precision of about 1 % for $n < 8$ even for extreme long path - lengths. An example is shown in Fig. 3. The oscillations of the fit, although they appear to be very weak, are responsible for errors in the vertical profiles of heating rates, since they cause drastic changes in the sign and magnitude of the first derivative of τ_λ , which is proportional to the flux divergence profile. We have compared such profiles obtained from different accurate (1 % and 0.5 % as largest deviations) fits. They show differences in various levels of up to 9 %, but the total absorption in an atmospheric column remains unaltered.

The transmission functions available now in various publications deviate, unfortunately, very considerably as it is shown here in an example in Fig. 4. There, mean band transmissions for two water vapour bands (ν_2 and ν_3) have been determined from data by MOSKALENKO (1968, 1969), HOWARD et.al. (1956, hereafter called HBW) and CLATCHEY et.al. (1971).

Using MOSKALENKO's data and those by HBW entirely different profiles of radiative flux divergence in the troposphere are obtained, as shown in Fig. 5. There the notations HBW 1 and HBW 2 refer to different exact approximations by RASCHKE and STUCKE (1973). In almost all layers below 11 km except at about 8 km, the heating calculated with data by MOSKALENKO is lower than the others, which show different extremes due to oscillations of their fits. In all three calculations almost no differences are found in the upper stratosphere and lower mesosphere due to negligibly small absorption by water vapour and carbon dioxide.

4. Contribution of various radiative transport parameter to the absorption

An impression on the dependence of heating in various layers on the solar zenith angle can be obtained from Fig. 6. There curves shift not only due to

changes of the incoming amount of radiation but also relatively in their shape. The slight maximum found for high sun at about 8 km moves up to about 10 km with sinking sun, while also in lowest kilometers the absorption increases relatively. In this particular model the absorption in the troposphere (0-17 km) increases from 20 % ($\lambda_0 = 7.5^\circ$) to 22 % (37.5°) and 28 % (65.5°). The contribution of different gaseous components to the tropospheric heating is shown in Fig. 7. The curves 1, 2 and 3 confirm other findings, that CO_2 contributes to solar heating only in lower stratospheric and upper tropospheric layers. The absorption in layers below 2 km is to 25 % due to absorption in aerosols, while the increase of path length by multiple scattering contributes up to 30 % to the heating in all layers below 20 - 25 km. The absorption in all stratospheric layers is dominated by ozone and reacts very sensitive to changes in the near ultraviolet components of the extraterrestrial solar spectrum. Integration over an entire day of insolation yields curves shown in Fig. 8, which still show a maximum of radiative temperature change at an altitude of 8 - 9 km and even higher values near ground and near the stratosphere. These curves, and also others in Fig. 7, show a drastic increase of the absorption in all atmospheric layers up to 25 km altitude, if the boundary condition is changed from an ocean surface (with mean albedoes between 5 - 15 %) to desert sand (~ 30%). The planetary boundary layer then receives up to 50 % more energy and even stratospheric layers experience a larger heating. In other calculations, not shown here, it has been shown, that for high cloud surfaces the radiative heating of the lower and middle stratosphere increases more than shown here. These boundary effects need to be parametrized in dependence on the cloud top albedo and altitude and ground albedo, respectively. It should be mentioned here, that computed values of the radiative temperature change are almost independent on the shape of phase functions, which however alter considerably the albedo of the model and the radiation budget at ground.

5. Dust layers

Special attention has been paid to atmospheric dust layers. Sahara dust cloud occur very often over the Atlantic ocean in the layer atop of the trade inversion and below 5 km. Their radiative heating effect is shown in Fig. 9 (right hand side). There an increase of absorption is found by almost 22 % - 66 % in the entire troposphere, while on the other side the albedo raises from 7.8 to 20 %. Thus, a Saharian dust cloud increases the direct solar heating of the atmosphere, in particular below 5 km, but the ocean itself receives less energy. Such effects obtained much attention during the GATE field experiments.

Similarly a stratospheric dust layer, as shown in Fig. 10, increases the local heating and may cause actual increases of temperature. Its effect on the albedo and radiation budget at ground has been found much less pronounced than in the case studied before.

6. Conclusive remarks

The results described briefly in this paper demonstrate the importance of the various atmospheric constituents, of the surface albedo and of transmission functions on computations of solar radiative heating in cloudfree atmospheric models with realistic vertical stratifications up to 70 km altitude. They are only a small selection of calculations done so far. Further studies are intended to obtain a basis for proper parametrisation of solar radiative heating based on atmospheric state parameters which are obtained observationally and

also in circulation models. They need more realistic data on extinction by particles and the inclusion of clouds. It must be concluded, however, that the success of this work depends strongly on the accuracy of transmission functions for water vapour and perhaps also for the other gases and aerosols. This conclusion should stimulate further experimental and theoretical work in this respect.

References

- Dirmhirn, I., 1968, "Das Strahlungsfeld im Lebensraum", Akad.Ver.Ges., Frankfurt am Main.
- Eltermann, L., 1968, "UV, visible & infrared attenuation to 50 km", AFCRL - 68 - 0153.
- Hansen, J.E., 1971, "Multiple Scattering of Polarized Light in Planetary Atmospheres. Part I. The Doubling Method", J. Atmos. Sci., 28, 120 - 125.
- Howard, J.N. Burch, D.E., Williams, D., 1956, "Near infrared transmission through synthetic atmospheres", J. Opt. Soc. Am., 46, 186, 237, 242, 334, 452.
- Labs, D., Neckel, H., 1968, "The Radiation of the Solar Photosphere from 2000 Å to 100 μm", Zeitschrift für Astrophysik, 69, S. 1 - 73.
- Linke, F., Baur, F., 1970, "Meteorologisches Taschenbuch", Band II, Leipzig, Akad. Verl. Ges., 514 - 572.
- Mc Clatchey, R.A. Fenn, R.W., Selby, Z.E.A., Volz, F.E., Garing, J.S., 1971, "Optical Properties of the Atmosphere", AFCRL - 71 - 0279.
- Moskalenko, N.I., Golubitskiy, B.M., 1968, "Spectral Transmission Function in the H₂O and CO₂ Bands", IZV., Atm. and Oce. Phys., Vol. 4, pp 346 - 359.
- Moskalenko, N.I., 1969, "The Spectral Transmission Function in the Bands of the Water-Vapor, O₃, N₂O, and N₂ Atmospheric Components", IZV., Atm. and Oce. Phys., Vol. 5, pp 1179 - 1190.
- Raschke, E., Stucke, U., 1973, "Approximations of Band Transmission Functions by Finite Sums of Exponentials", Beiträge zur Physik der Atmosphäre, Band 46, S. 203 - 212.

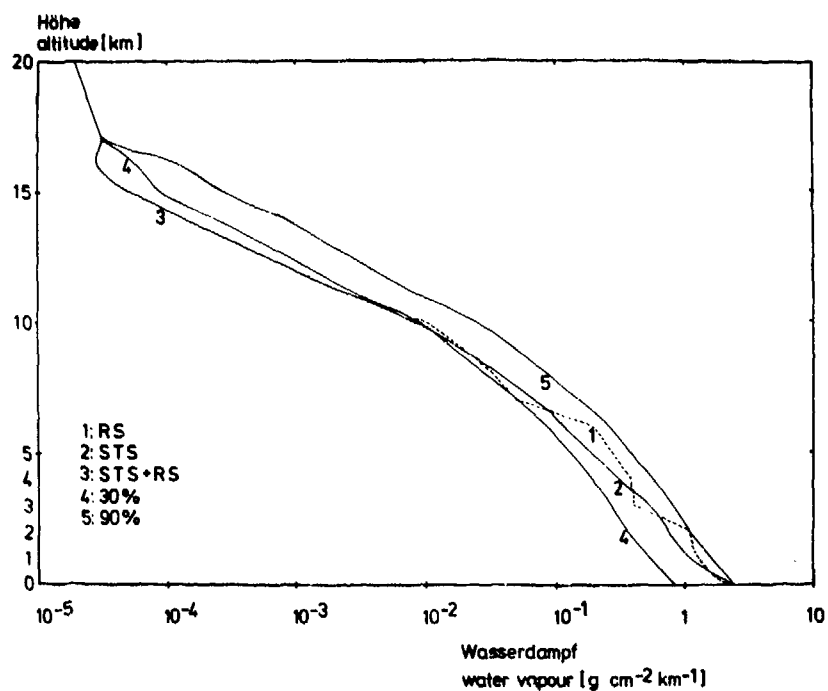


Fig. 1 : Water vapour profiles

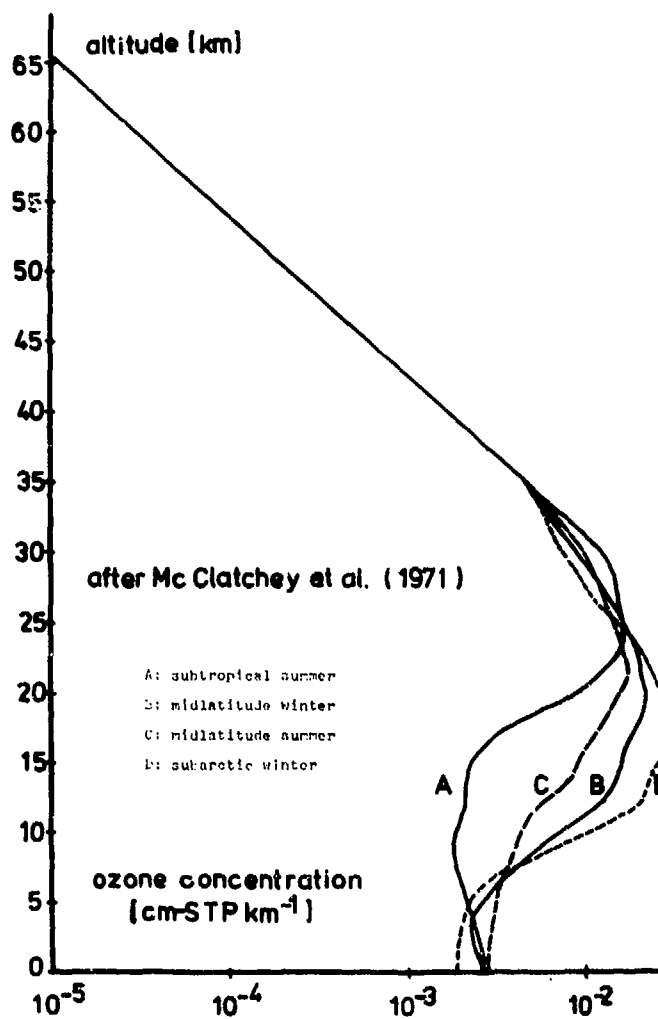


Fig. 2 : Ozone profiles

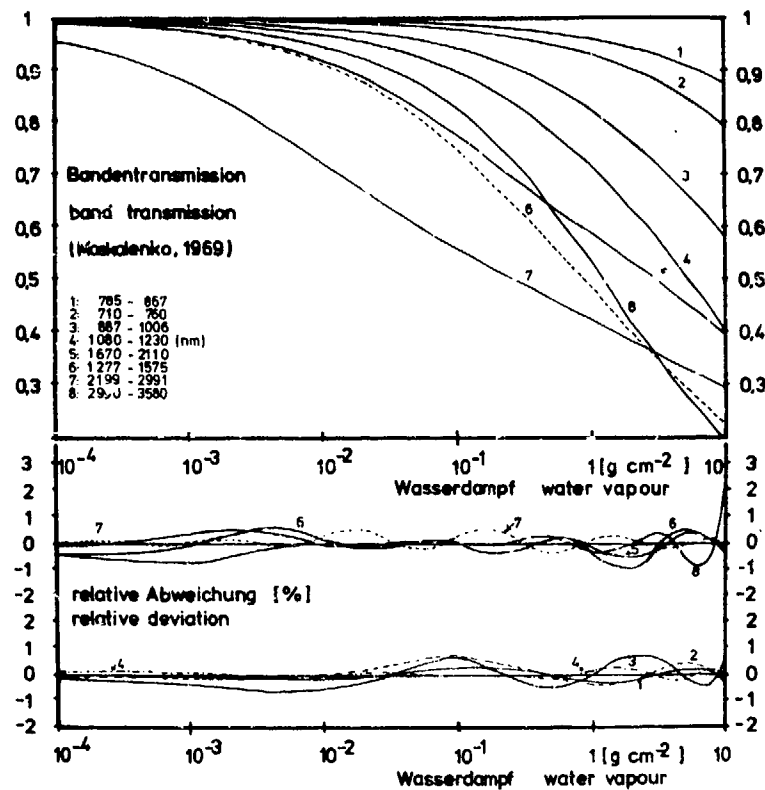


Fig. 3 : Transmission functions water vapour bands (after MOSKALENKO, 1968) and the relative deviations of their fits with a finite series of exponentials.

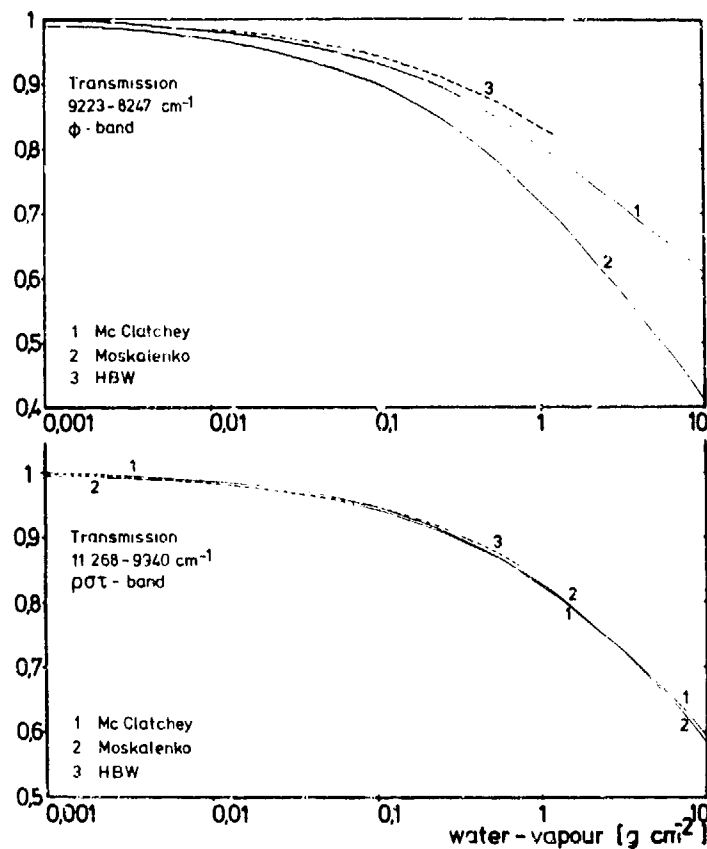


Fig. 4 : Comparison of band transmission functions obtained from spectral data of different authors.

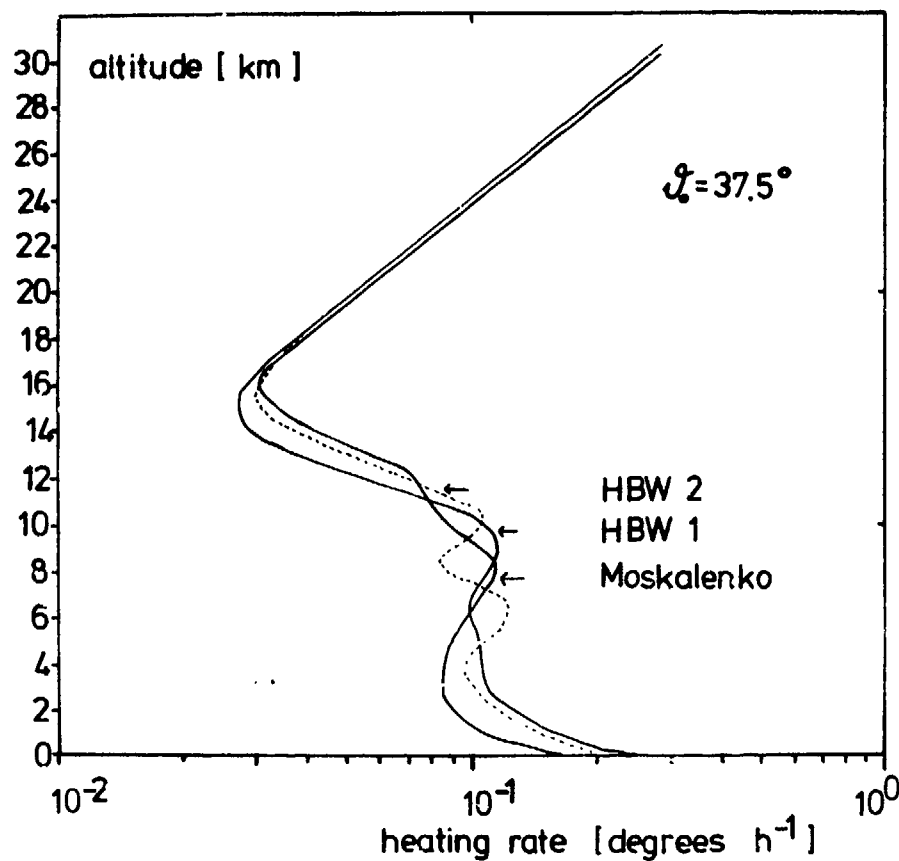


Fig. 5 : Vertical heating rate profiles computed for the STS model over ocean with absorption data after MOSKALENKO (1968, 69) and HOWARD et.al. (1956). The latter are taken with two different accurate fits.

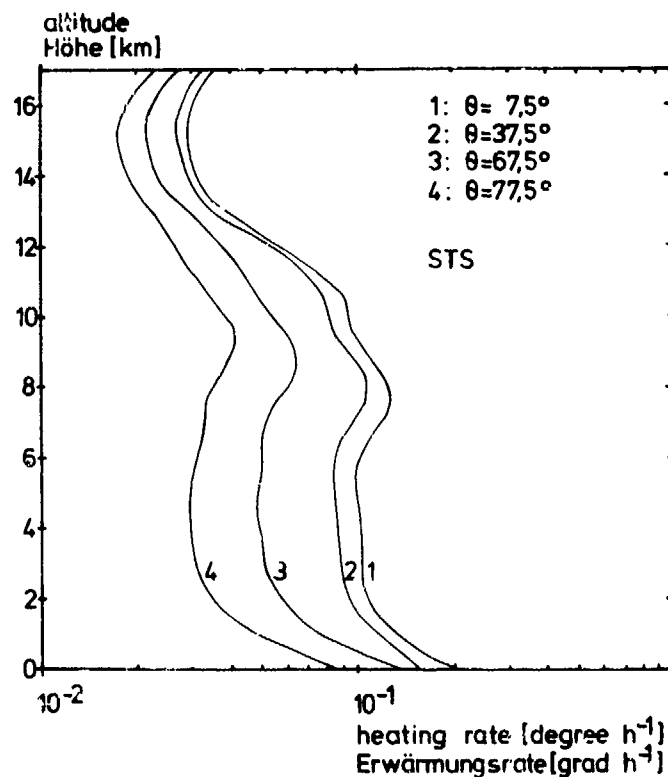


Fig. 6 : Vertical heating rate profiles computed for different solar zenith angles (model STS over ocean).

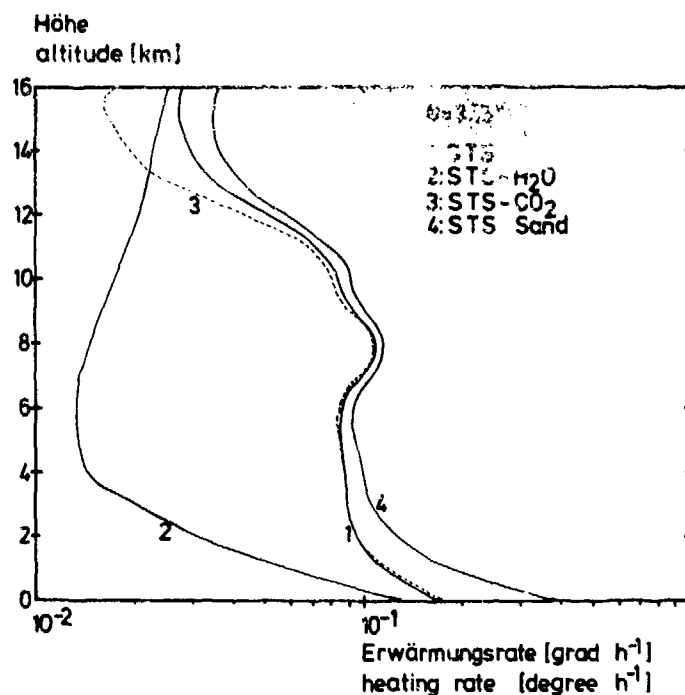


Fig. 7 : Vertical heating rate profiles computed for the STS model over ocean (1) neglecting alternatively the absorption H₂O (2), CO₂ (3); and over a sand surface (4) with all absorbers, respectively.

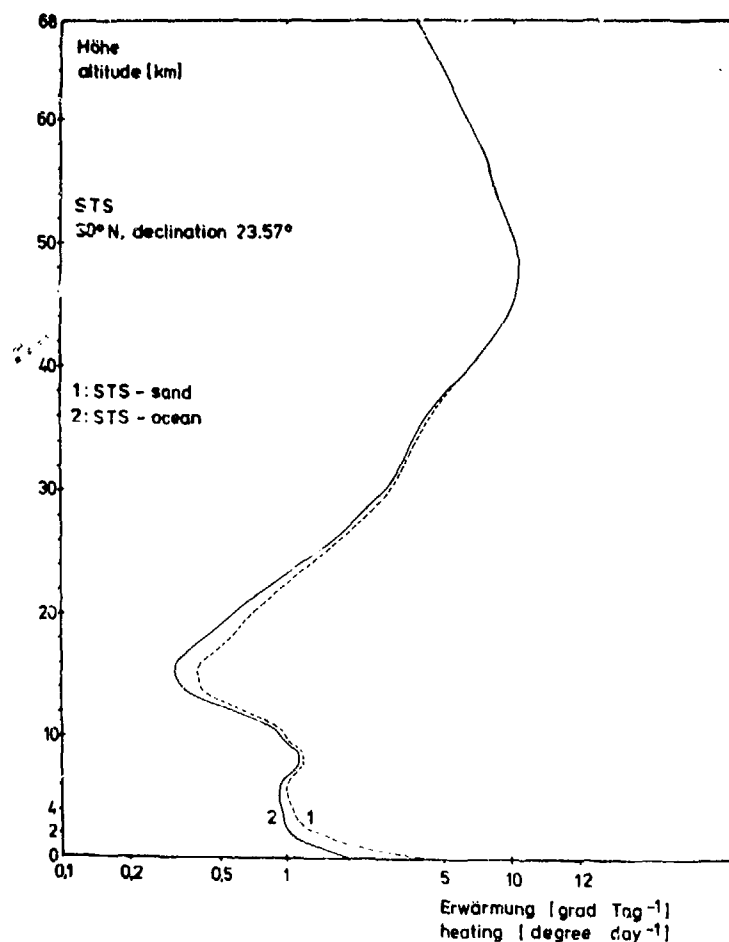


Fig. 8 : Daily solar heating of the entire atmosphere above ocean (1) and desert sand (2) at 30°N and a solar declination of + 23°57'.

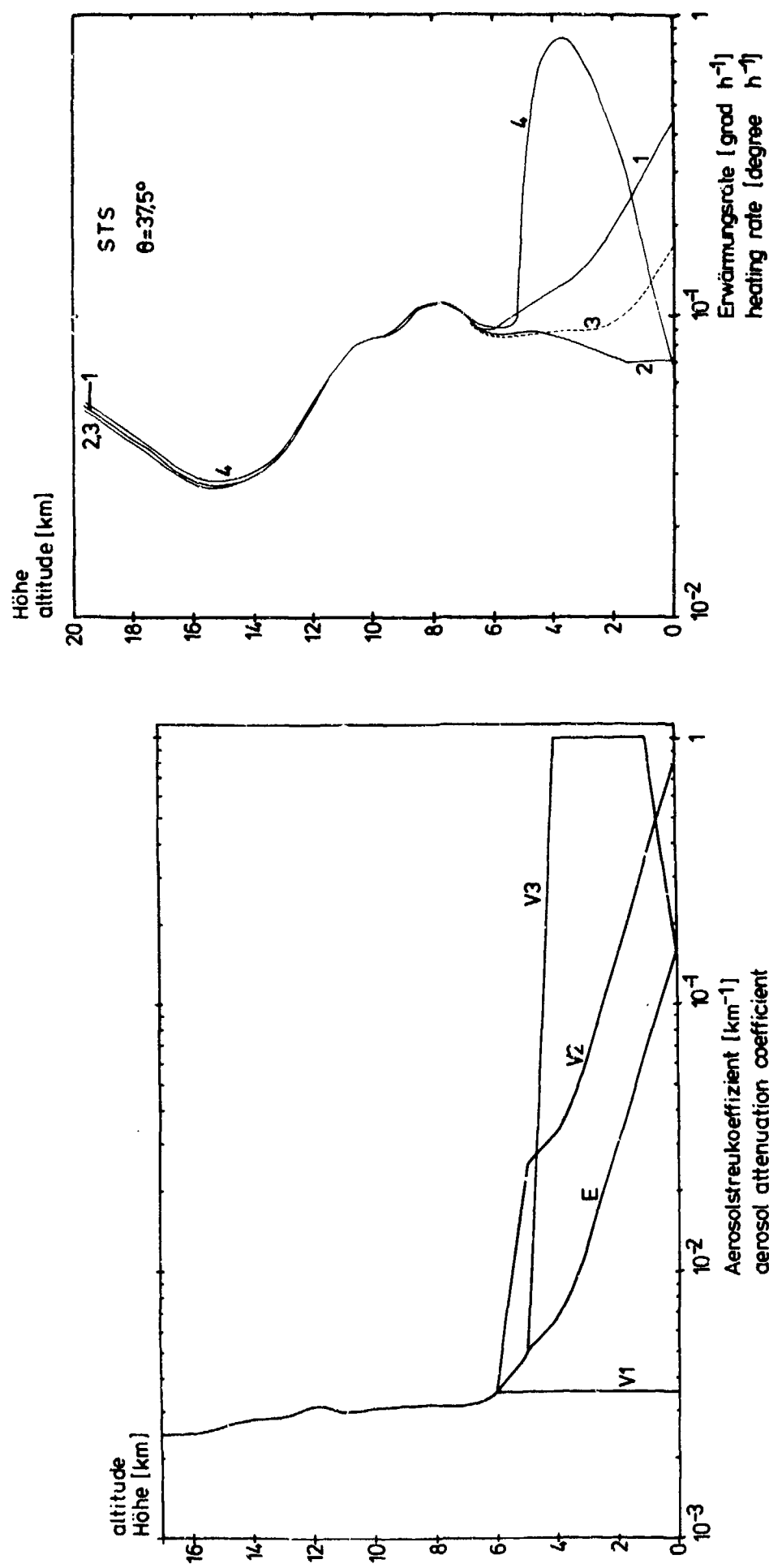


Fig. 9 : The effect of lower tropospheric dust on the heating.

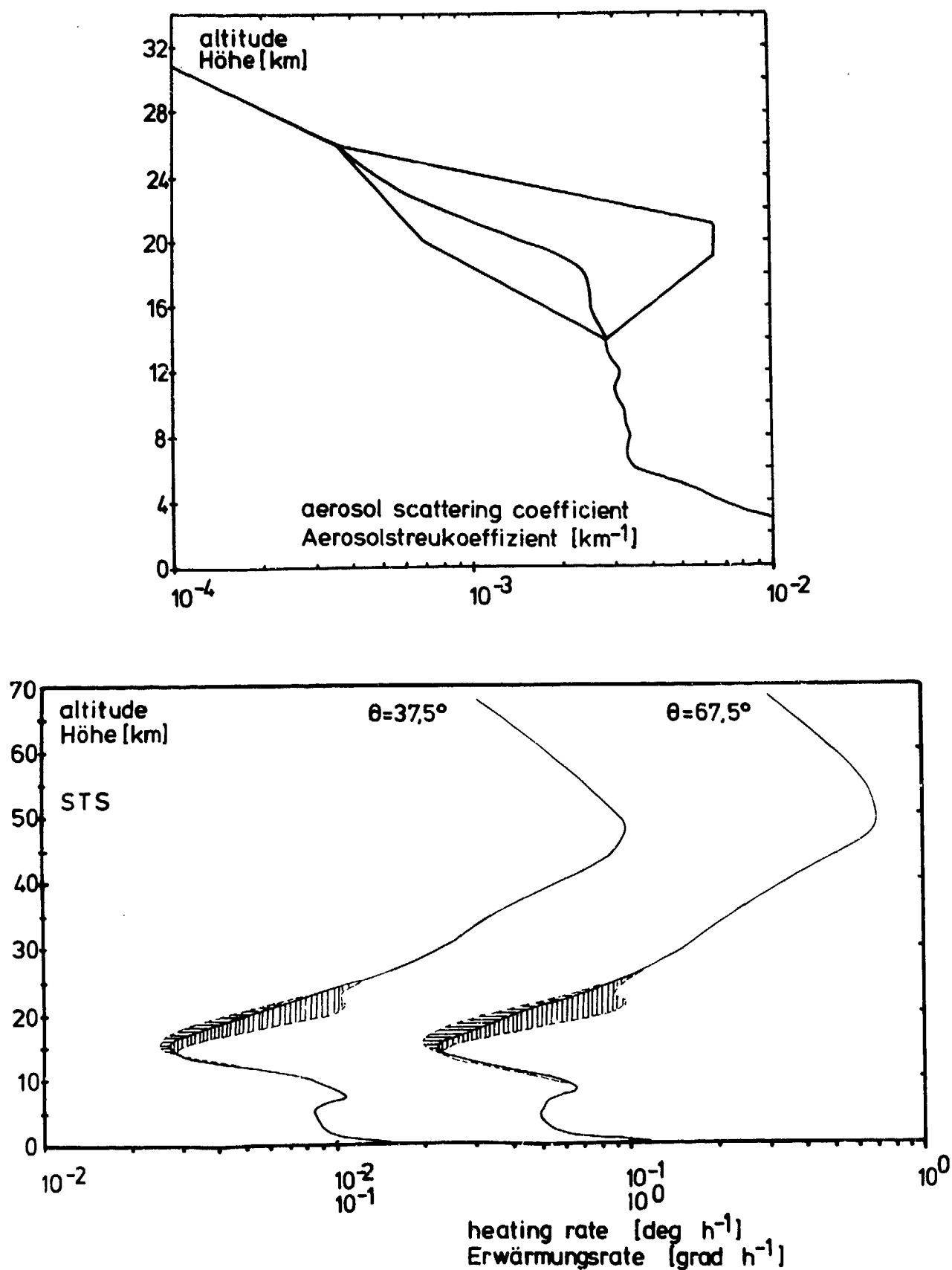


Fig.10 : The effect of lower stratospheric dust on the heating.

The Measurement Programme OPAQUE of AC/243,
(Panel IV/RSG.8) on "Sky and Terrain Radiation"

T. Bakker

Physics Laboratory NDRO-TNO
P.O. Box 2864
The Hague
Netherlands

SUMMARY

Within the framework of the Nato Study Group AC/243(Panel IV/RSG.8) {formerly AC/243(Panel III/RSG.3)} a measurement programme will be carried out regarding optical parameters of the atmosphere and environmental characteristics. These measurements will be carried out in a synoptical timescale at various locations in Western Europe.

The aim of the project is to develop a data-base of those parameters of the atmosphere and the environment that affect or may affect the performance of optical and electro-optical sensors during military operations. From the correlation with the meteorological data the possibilities of forecasting the performance of the above-mentioned sensors will be studied.

The programme consists of a minimum required set of parameters, to be measured at fixed times (every hour on the hour, local mean time) on all sites during a period of at least two years. Besides at some of the sites a programme of recommended additional measurements will be carried out during limited time periods.

1. INTRODUCTION

Within the framework of the Nato Research Study Group AC/243(Panel IV/RSG.8) a measurement programme will be carried out regarding optical parameters of the atmosphere and characteristics of the environment. In particular those parameters will be measured, that effect or may affect the performance of optical and/or electro-optical equipment during military operations and missions.

The measurements will be carried out in a synoptic timescale at various measuring sites, whose geographical positions are scattered over Western-Europe. The measuring period will be at least two years. The meteorological parameters will be measured at the same time.

The types of missions in mind, for which the measurement results are relevant, are:

- Observation, surveillance and reconnaissance
- Target identification, acquisition and tracking
- Weapon-guidance (e.g. homing-systems)
- Weapon delivery
- Countermeasures

The types of sensors, involved, are:

- Image-intensifiers
- Low-light level television
- Gated-viewing equipment
- Far-infrared Equipment
- Lasers

2. AIMS

The aims of the project are the following:

- a. To develop a data base of the relevant parameters of the atmosphere and environment, allowing an evaluation of the above-mentioned sensors during military missions. For this reason the collected data must have statistical meaning. That means a sufficiently large number of data must be available. It must be possible to study the diurnal and seasonal variations of the parameters from the data.
In order to determine the dependence on geographical and climatological conditions the parameters must be measured on corresponding times at various locations.
- b. To study correlations between the measured parameters. In particular the dependence of these parameters on meteorological and climatological conditions will be determined.
- c. To develop models for the atmospheric and environmental characteristics which can be used for the simulation of the performance of optical and electro-optical equipment on a computer.
- d. To develop forecasting techniques in order to estimate the performance of the above-mentioned sensors during military operations under given or expected meteorological conditions.

3. ORGANIZATION

In order to realize the programme a large number of measurements must be carried out at various places in Western-Europe. Preferably the geographical locations should cover the areas of Scandinavia, Central and Southern Europe (including the Mediterranean Sea). The only real solution to carry out the programme would be on a multi-national basis. The responsibility for the procurement, installation, operation and maintenance of the measuring equipment must be taken by the cooperating nations.

The existing Research Study Group AC/243(Panel IV/RSG.8) {formerly AC/243(Panel III/RSG.3) on "Sky and Terrain Radiation"} is a very suitable group to handle this project, because the proposed measurements and studies fit well into its Terms of Reference. As a matter of fact until now these kind of measurements were carried out in an un-coordinated way by the various member countries of this group. The project OPAQUE extends and streamlines the programmes of the individual member countries in such a way, that they merge into one common programme of measurements, performed at a synoptical time basis at various locations

In Europe.

4. GENERAL PHYSICAL BACKGROUND

The performance of every optical or electro-optical sensor, receiving information through the atmosphere is affected by absorption, by the atmospheric scattering properties, by turbulences and atmospheric refraction.

So the important parameters to be measured are:

- The atmospheric transmission
- The luminance (or radiance) of the atmosphere
- The degradation of contrast
- the turbulences

These quantities are functions of the luminance distribution, the microscopic properties of the atmosphere (aerosols), the solar irradiation, the reflection of the terrain background, cloud cover etc. These parameters should be measured in the wavelength region extending from the visible into the far-infrared region (up to 14 μm).

In the far-infrared region the apparent radiation temperature of the terrain and its variation in space (clutter) are not only determined by the momentary irradiation conditions due to the sun, but they depend strongly on the conditions during the past hours too.

In general the factors mentioned have a strong influence on the amount of energy received from a target, on the reduction of the observed contrast between a target and its surroundings, on the amount of clutter present in the terrain, in which the targets, to be observed are located and on the distribution (in space and time) of energy in a transmitted beam of radiation.

5. DESCRIPTION OF THE PROGRAMME

The OPAQUE measurement programme consists of:

The minimum required programme

This part of the programme must be carried out at every measuring station, at prescribed times (every hour on the hour, local mean time).

A programme of recommended additional measurements

These measurements will be carried out at some of the measuring sites only and mostly during limited time periods.

The measurement period is two years

5.1 The minimum OPAQUE programme:

The following parameters will be measured at all sites every hour on the hour (local mean time).¹⁾

5.1.1 The extinction coefficient σ

This parameter is measured in the photopic spectral wavelength region. This coefficient may be determined either by measuring the beam transmission over a given distance (σ_t) or by measuring the scattering of the atmosphere (σ_s) with the help of a point visibility meter or nephelometer.

The meteorological visual range V_N is connected with the extinction coefficient by the relation:

$$V_N = \frac{3,91}{\sigma}$$

corresponding to a transmission of 0,02.

The measuring range of the instrument should be at least from $V_N = 500$ m to $V_N = 10$ km, preferably it should extend to $V_N = 20$ km.

5.1.2 The horizontal illuminance E_h

The instrument should measure the illuminance on a horizontal plane during day and night. The dependence of the sensitivity on the wavelength corresponds to a photopic response curve (according to the definition of illuminance).

5.1.3 The vertical illuminance at four azimuths: E_v (N, E, S, W)

The instrument should measure the illuminance on vertical planes. The normal on these planes should be oriented in the directions: North, East, South and West within 2° . The measurements will be carried out during day and night. The dependence of the sensitivity on wavelength corresponds to a photopic response curve.

5.1.4 The path luminance towards the East at night: L_p

The path luminance is the amount of light scattered in a direction opposite to the direction of observation by a column of the atmosphere. This parameter is directly related to the loss of contrast through the atmosphere (see appendix).

The parameter is measured by a teluminance meter looking to an ideally black target, located at a distance of 100 m towards the East of the teluminance meter. (See fig. 1) The spectral sensitivity of the measurement system is photopic.

5.1.5 The path luminance at four azimuths during day: F_p

The same parameter mentioned under 5.1.4 should be measured during day in the directions N,E,S,W ($\pm 2^\circ$). The sensitivity of night and day path luminance meters should be such, that there is a range of luminances, over which both instruments can operate simultaneously. The spectral sensitivity of the measurement system is photopic again.

5.1.6 The spectral solar transmission: T_{Sj}

The measurements will be carried out with a pyrhellometer. This instrument remains pointed in the direction of the sun and measures essentially the amount of sun radiation received. It has a field of view of approximately $50^\circ 30'$. From this measurement the total atmospheric transmission T_{Sj} can be deduced. Besides it gives information about the irradiation of the earth surface. This is important for correlation with the fluctuations in the apparent radiation temperature of the terrain (clutter) in the far-infrared region. (See 5.2.3). Moreover the sun radiation has a strong influence on the amount of turbulences in the atmosphere. (See 5.1.8).

This parameter will be measured in the following spectral bands:

1. $0,94 \pm 0,03 \mu m$
2. $0,40 \pm 0,03 \mu m$
3. $1,60 \pm 0,05 \mu m$
4. $1,06 \pm 0,03 \mu m$
5. $0,75 \pm 0,03 \mu m$
6. $0,55 \pm 0,03 \mu m$
7. Photopic
8. Open ($0,35 - 3,5 \mu m$)

5.1.7 The transmission coefficient in the far-infrared wavelength region: T_j

This parameter will be measured over a distance of 500 m, preferably along a track close to and parallel with the one where the extinction (See 5.1.1) in the visible region is measured. The source should have a temperature of $1000^\circ C$. The measurements will be carried out in four different wavelength regions: i.e.

- | | | |
|------------|------|---------------------|
| 1-1 : | 3,4 | - 5,0 μm band |
| 2 : | 8 | - 12 μm band |
| 3 : | 8,25 | - 13,2 μm band |
| 4 : either | 2 | - 14 μm band |
| or | 3,4 | - 5,5 μm band |

5.1.8 Temperature fluctuation parameter $(D_T)^{\frac{1}{2}} = \{ < (\Delta T)^2 > \}^{\frac{1}{2}}$

This parameter gives an indication of the turbulences present in the atmosphere. It is an important parameter, because it is related to the ultimate resolution capabilities of observation systems over long distances. Besides beam wandering and beam spread of laser systems (laser-designators, laser-range-finders, laser-trackers) depend on these turbulences in the atmosphere.

Due to the delicate nature of the measuring equipment it is not certain at the moment whether this measurement can be performed automatically every hour on the hour. It might turn out, that manual operation is required. In that case this parameter will only be measured during limited periods of time.

5.1.9 Meteorological parameters

Besides the information available from nearby official meteorological stations the following parameters will be measured at the measurement sites:

1. temperature : TT
2. dew point (or relative humidity): $T_d T_d$ (or $H_r H_r$)
3. pressure : $P.P.P.$
4. wind direction dd
5. wind speed ff_2 at a height of 2 m
(if possible ff_{10} at a height of 10 m too)
6. precipitation: RR
7. rain rate : rr

For correlation purposes with the transmission in the far-infrared region the equipment to measure the rain rate rr should have a short time constant. ("instantaneous" rain-rate).

5.2 ADDITIONAL RECOMMENDED MEASUREMENTS

From the large number of possible additional measurements the following will be carried out or are under consideration.

- 5.2.1 Measurement of some of the parameters mentioned under 5.1 more frequently than once every hour and/or in other wavelength regions (e.g. in the near infrared region ($0,6 - 1,2 \mu m$) or at specific important laser wavelengths ($0,9, 1,06, \text{ and } 10,6 \mu m$)).
- 5.2.2 Measurements carried out from airplanes equipped with measuring apparatus. In this way the parameters measured at various heights can be correlated with those measured at the station on the ground. Measurements from airplanes also give the possibility to correlate parameters measured at one location with those measured at other places within a relatively short time.
- 5.2.3 Measurement of the apparent radiation temperature of the terrain and of characteristic objects in the far-infrared region. For these measurements a special Sky- and Terrain Scanner, scanning along a vertical 360° track has been developed by the United States and is planned to be installed at some of the measuring sites.
- 5.2.4 Measurement of aerosol distributions. These measurements will be very useful in the interpretation of the measured parameters, in particu-

lar the transmission in the far-infrared region. It will give a better understanding of the correlation between the measured parameters and the microscopic constituents of the atmosphere. It will certainly be of much help in forecasting the atmospheric transmission properties in the far-infrared regions at places where it is almost impossible to measure them directly (e.g. at the high-seas). At many sites these measurements will be carried out. Besides the U.S. Army Atmospheric Laboratories offered to install at all measuring sites equipment to analyze aerosol substances.

- 5.2.5 Direct contrast loss measurements both in the visible and far-infrared regions.
- 5.2.6 Laser scatter measurements.
These measurements are important in connection with detection and localization of laser sources in the field and in connection with the security of laser-communication links.
- 5.2.7 Optical turbulence measurements.
At some sites optical turbulence measurements will be carried out in order to correlate them with the measured values of the temperature fluctuation parameter D_T^{-1} (See 5.1.8).
- 5.2.8 Measurements with observation equipment.
Occasionally trials with observation systems will be carried out in order to correlate the performance of these apparatus with the measured parameters.
- 5.2.9 Cloud cover measurement.
At several sites the possibilities for installation of equipment to measure automatically the cloud cover during day and night are looked for.

5.3 RELIABILITY, CALIBRATION AND INTERCOMPARISON

During one measurement cycle many parameters are checked and cross-checked in order to determine the reproducibility of the measurements. For correlation purposes it is important that the conditions during the measurement cycle time (some minutes) remain constant. For that reason some of the parameters will be either measured at the beginning and at the end of the measurement cycle or will be monitored during the measurement cycle. In the latter case the maximum and minimum values of the parameter will be specified.

In order to ensure that the measured parameters are reliable and intercomparable a transportable calibration and intercomparison set of equipment will make trips along the sites.

5.4 DATA BANK

All measured data after having proved to be reliable will be sent to the Databank. The United Kingdom will take care of this bank. Periodically an output of all the received data will be sent to the participating nations.

Formats and codes in which the measured data must be sent to the bank have been prepared.

6. MEASUREMENT STATIONS:

At this moment commitments have been made for the following stations:

1. A station at Lolland in Denmark.
This station is installed by Canada and Denmark. It will be operated and maintained by Danish personnel. It is located close to the sea.
2. A station at Meppen in Germany.
This station is installed by the United States. It will be operated by German personnel.
3. A station at the Airbase Ypenburg (near the Hague) in the Netherlands.
This station will be more or less representative of an urban environment.
4. A station at Christchurch in the United Kingdom. Besides the United Kingdom has mobile equipment to perform measurements at other locations.
5. A station near Tübingen at the Schwäbische Alb in Germany.
Germany too has transportable equipment under development to perform measurements at other locations.
6. A station at Bruz (near Rennes, Bretagne) in France.
7. A station at Trapani (Sicily) in Italy.
The Italian station will be close to the sea. This location is representative for the Mediterranean environment.

7. TIME SCHEDULE

The first station (2) is expected to be in operation in november 1975. Stations (1), (3), (4) and (5) are expected to be in operation in early 1976. Station (6) and (7) will be in operation in summer 1976.

The measurements will be performed for at least 2 years. It is expected and hoped that some of the stations will be in operation for a longer time period than 2 years, in order to get more reliable statistics.

8. POINTS OF CONTACT

Additional information regarding the above-mentioned stations can be given by the representatives of the participating countries in the OPAQUE project.

Canada : Mr. G.A. Morley
Canadian Defence Research Establishment Valcartier
P.O.Box 880
Courcellette P.Q. G0A 1 R0

Denmark : Mr. N.C. Nielsen
Danish Defence Research Establishment
Osterbrogades Kaserne
DK 2100 Copenhagen Ø

France : Mr. C. Germont
SEFT/ST - OPT
Fort d'Issy
92 Issy les Moulineaux

Germany : Dr. D.H. Höhn
Forschungsinstitut für Optik
74 Tübingen 1
Schloss Kressbach
Kressbacherstrasse

Italy : col. F. Pelligrini
Consiglio Tecnico Scientifico della Difesa
Ufficio Elettronica
Via C. Pascal 6
Roma

Netherlands : Mr. J. v. Schie
Physics Laboratory TNO
Oude Waalsdorperweg 63
P.O. Box 2864
The Hague

United Kingdom : Dr. W.A. Shand
Ministry of Defence (Procurement Executive)
Signals Research and Development Establishment
Christchurch, Hants

United States : Mr. J.R. Moulton
Nightvision Laboratory
Amesl-NV-VI
Fort Belvoir
Virginia 22060

Dr. R.W. Fenn
Air Force Cambridge Research Laboratories
L.G. Hanscom Base
Bedford
Massachusetts 01730

9. ACKNOWLEDGEMENT

It is a pleasure for me, as Chairman of the Group to mention the good atmosphere and working spirit within the Research Study Group.

All the members, mentioned under 8 and their collaborators have contributed substantially to the programme and to this paper.

APPENDIX

Looking to a target with a luminance L_0 [cd m⁻²] against a background with luminance L_0^1 the contrast at very short distances is given by:

$$C_0 = \frac{L_0 - L_0^1}{L_0 + L_0^1} \quad (1)$$

(The defined parameter C_0 frequently is called 'modulation' in the literature.)

At a distance R the luminance of the target L_R is different from L_0 due to two effects:

1st Scattering of incoming radiation due to the column of atmosphere between observer and observed object.

2nd Extinction in the atmosphere. For a homogeneous atmosphere the transmission:

$$T = e^{-\sigma R} \quad (2)$$

Under homogeneous conditions the apparent luminances of target and background at a range R are given by:

$$L_R = L_0 T + L_H (1 - T) \quad (3)$$

$$\text{and } L_R^1 = L_0^1 T + L_H (1 - T) \quad (4)$$

L_H is the luminance of the horizon ($R \rightarrow \infty$)

So the apparent contrast at a distance R is:

$$C_R = \frac{L_R - L_R^1}{L_R + L_R^1} \quad (5)$$

It can be shown from 1,2,3,4 and 5, that

$$C_R = C_0 \left[1 + \frac{2 (1 - T) L_H}{T (L_0 + L_0^1)} \right]^{-1} \quad (6)$$

The measured parameter L_p can be referred to L_H by means of equations (3) and (2). For an ideally black target, $L_0 = P_0$, and formula (3) reads:

$$L_p = L_H \{ 1 - T (R = 100 \text{ m}) \}$$

The parameter T ($R = 100 \text{ m}$) follows from (2) after substitution of the measured value of σ .

Instead of luminances the illumination levels and diffuse reflectances of targets and backgrounds can be used in order to calculate the contrast degradation.

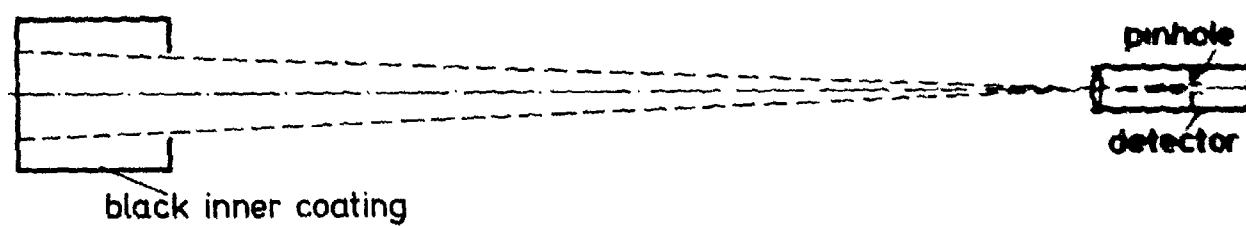


fig 1 : Principle of a path luminance meter (ref 5.1.4)

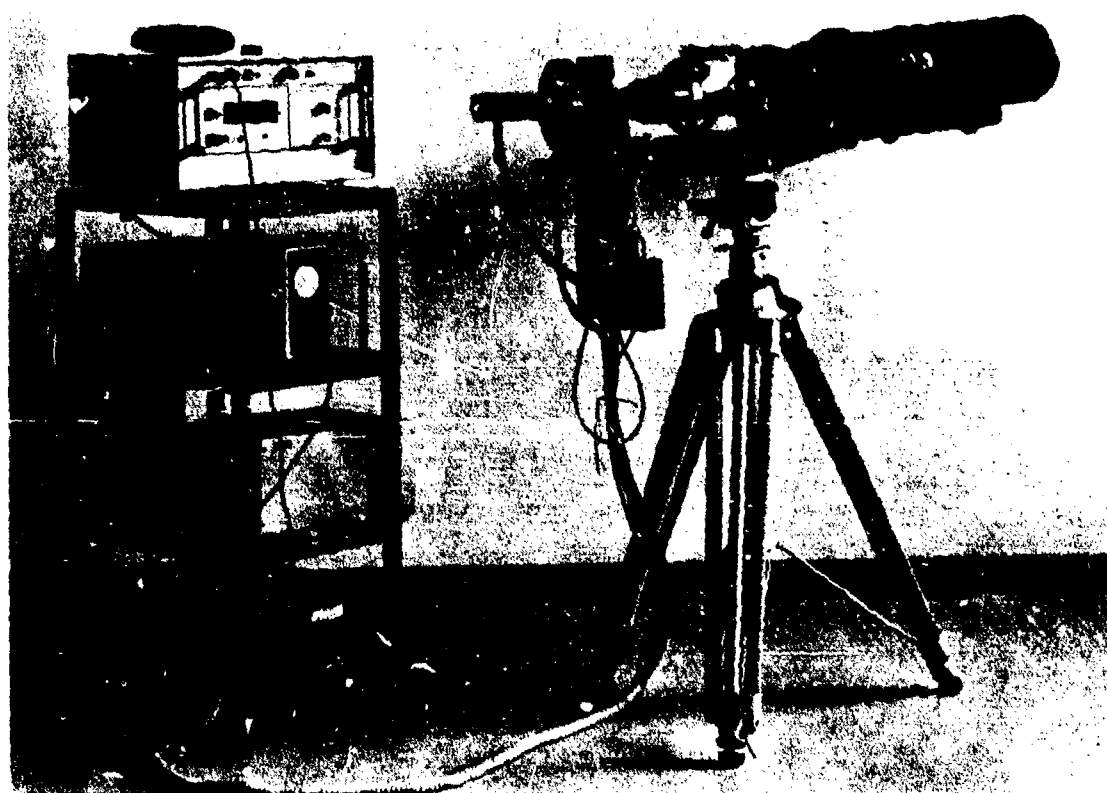


fig 2 : Example of a teleluminance meter (ref. 5.1.4)



fig 3 : Construction of the horizontal (E_h) and vertical (E_v) illuminance meters
(ref. 5.1.2 and 5.1.3)
(courtesy: Air Force Cambridge Research Laboratories).



fig 4 : Top view of the horizontal (E_h) and vertical (E_v) illuminance meters
(ref. 5.1.2 and 5.1.3)
(courtesy: Air Force Cambridge Research Laboratories)

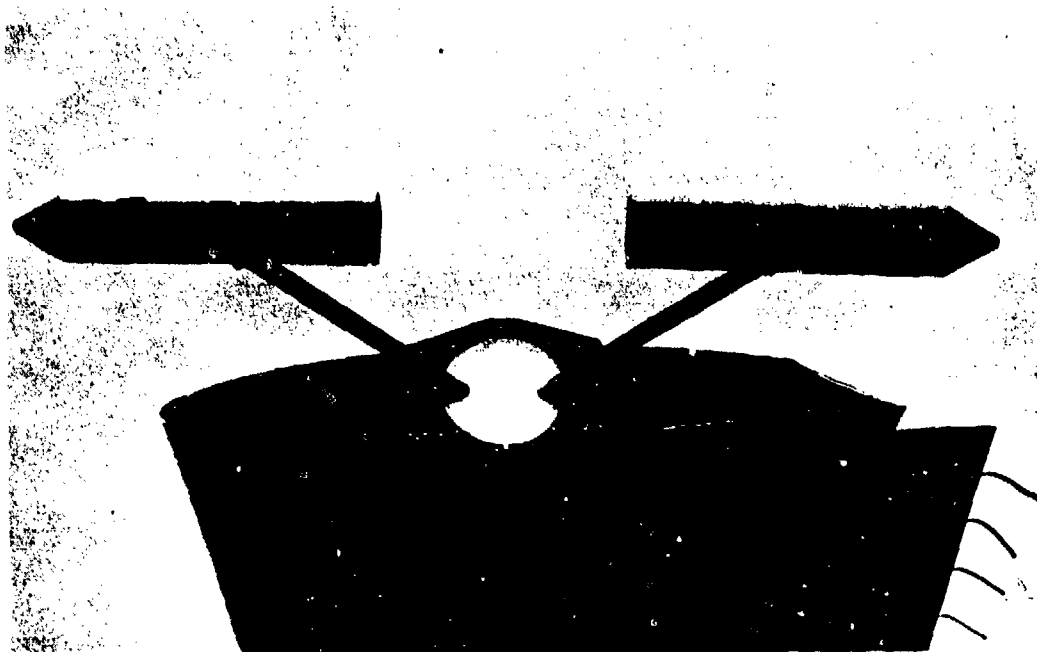


fig 5 : Path luminance measurements from an airplane (courtesy: Air Force Cambridge Research Laboratories)(ref. 5.2.2)

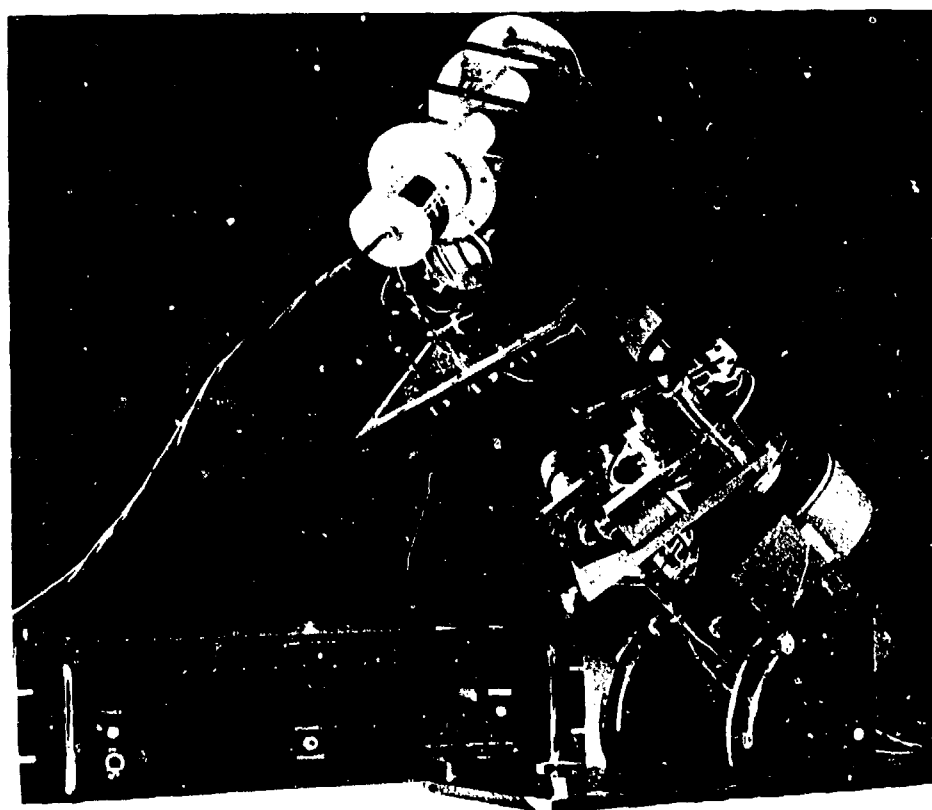


fig 6 : Pyrheliometer with reversing mechanism (courtesy Forschungsinstitut für Optik, Tübingen) (ref. 5.1.6)

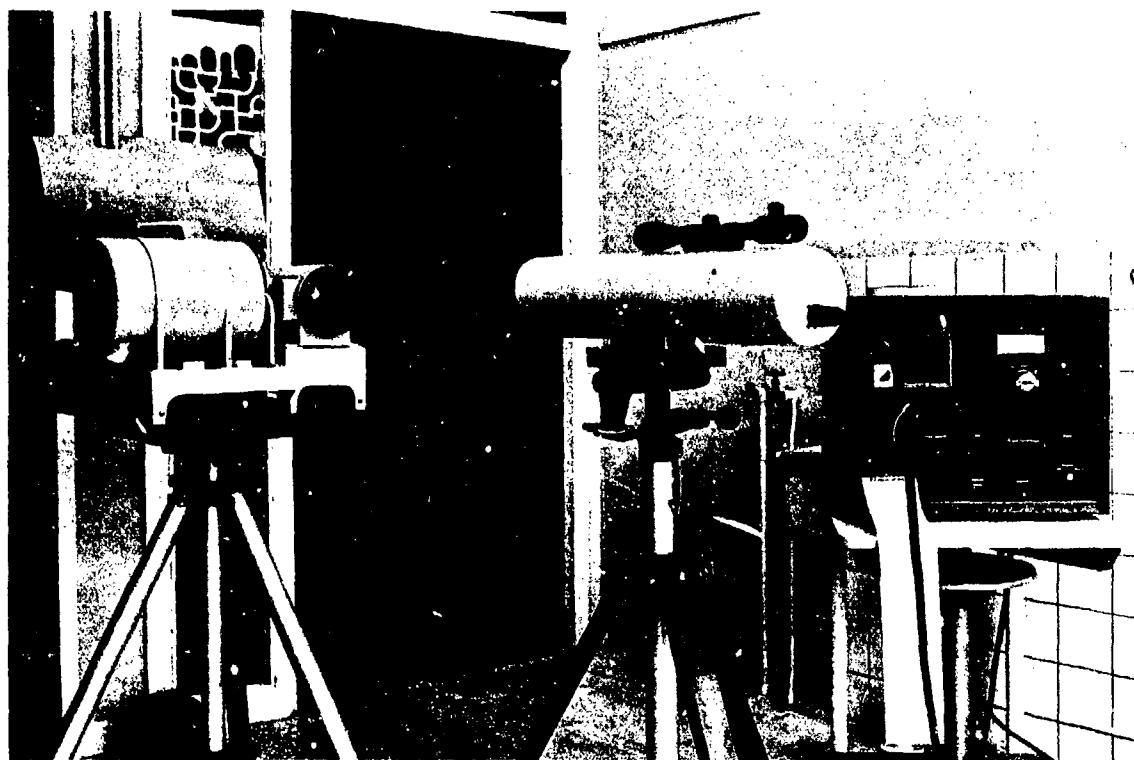


fig 7 : Infrared Transmissometer (ref. 5.1.7)

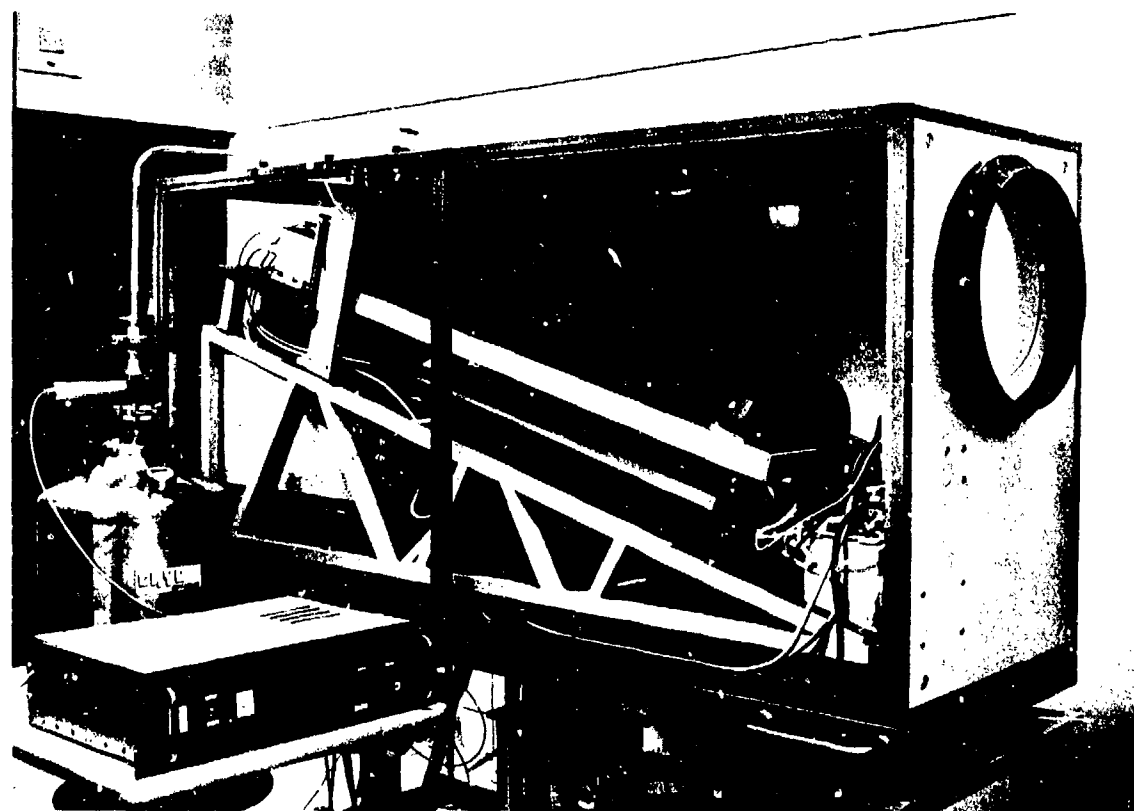


fig 8 : Equipment to measure the loss of contrast in the far-infrared regions.
(ref. 5.2.5)

EXPERIMENTAL AND COMPUTATIONAL COMPARISON OF DIFFERENT METHODS FOR DETERMINATION OF VISUAL RANGE

W. Büchtemann, H. Hipp, W. Jessen, R. Neuwirth,

Forschungsinstitut für Optik

74 Tübingen 1, Schl. Kresbach

F.R. Germany

SUMMARY

Three visibility meters of different type have been run simultaneously over several weeks. At the same time aerosol spectra were collected using an optical counter.

The visibility readings are compared under several meteorological conditions.

A Junge distribution or a modified T-distribution has been fitted to the experimental aerosol size distribution. Using Mie's theory and the data recorded, the readings of the instruments have been compared with the computed total extinction and the values computed based on the actual instrument parameters, i.e. especially the angular response in the case of two scattering type instruments. A good agreement between the observational visibilities is obtained, except under particular meteorological conditions. Computed visibilities give a generally correct prediction of the measured extinction.

1. INTRODUCTION AND GENERAL REMARKS

Progress in electronics has considerably improved the development of automatically operating visibility meters, applicable to routine meteorological work and thus complementing or replacing the former direct eye observation. Instruments of different types are operating in several meteorological services, military services, air-ports, aboard ships or on remote measuring sites, e.g. light-houses, which become more and more equipped by automatic instrumentation.

There are essentially three types of visibility measuring devices with measuring principles based on three different physical effects:

1. Transmissometers, determining total extinction,
2. Instruments, using scattered light,
3. Instruments, based on indirect methods, e.g. measuring aerosol distribution.

It is the aim of this paper to report on simultaneous registrations from three different instruments - one transmissometer and two scattering instruments- and to compare the observational results with theoretical calculations on atmospheric aerosol scattering, according to Mie's theory under different operational and actual meteorological conditions. The calculations were based on aerosol spectra measured with an optical counter. Assuming spherical particles, a known refractive index, and a known aerosol size distribution, the scattering and extinction properties of the particle ensemble can be computed according to this theory, which in the past has been extensively applied to scattering computations with varying success, depending on the aim of the investigation (Kerker, M., 1969). Discrepancies could mostly be attributed to the non-sphericity of the particle or to an uncertainty of the refractive index. Recently, a thorough theoretical investigation has been carried out, examining the accuracy of various visibility meters using different operating principles (Quenzel, H., et al., 1975).

Using comparatively simple methods to determine the aerosol spectrum, the following computational investigations have been performed in addition to the observational comparison of visibility meters:

1. Computations of the absolute magnitude of the total extinction using the measured aerosol size distribution and comparison with the measured extinction.
2. Computation of the scattered energy as seen by the two scatter devices and comparison with the measured signal.
3. Comparison of differences in the measured values with computed differences, i.e.:
To which extent can these differences be explained by a straight-forward assumption of spherical particles with a constant refractive index and an idealized size distribution?

2. MEASURING PROGRAM AND INSTRUMENTAL SET

Three visibility meters of different types, as described below, were run simultaneously for several weeks during February/March 1975. At the same time meteorological data on temperature, humidity, and precipitation were collected with a standard instrumental set. Furthermore an aerosol counter was simultaneously operating to measure the aerosol spectra.

The visibility meter set was as follows:

2.1 Transmissometer (ELTRO)

Transmissometers form the oldest category and belong to the "double-ended" devices. A schematic diagram of the ELTRO is given in Fig.1. The instrument can operate on two base lengths $L_1 = 2 \times 15$ m and $L_2 = 2 \times 150$ m, and measures transmittance τ due to total atmospheric extinction along the optical path. Standard visual range is then related to total extinction via Koschmieder's relation (Koschmieder, H., 1925), apart from effects of spectral weighting (see Chapter 3.).

The source consists of a tungsten filament lamp, the receiver has a photopic response. To obtain optimal accuracy an automatic switching between the two base lengths is installed and guarantees an accuracy of $\leq 5\%$ for all ranges from 20 m to 10 km.

2.2 Backscatter (IMPULSPHYSIK)

This device belonging to the category of backscatter instruments does as a single-ended instrument not have the disadvantage to require an extended base length. Backscatter devices like the VIDEOGRAPH used with these experiments consist of a projector and receiver, both mounted in the same casing (Fig.2). The receiver measures only the light scattered back from a certain volume of the atmosphere illuminated by the outgoing beam. So only scattering from angles between 177° and 179° is recorded. As a light source serves a high-powered xenon spark lamp (72 pulses/min., 1 μ sec pulse length) inside the projector, which produces a parallel beam with a peak intensity of 10^9 cd. The spectrum of the lamp contains practically no IR and lies in the blue-white region. The modulated light source allows to distinguish the backscatter signal from daylight when detected by the receiver.

Extended test series (Vogt, H., 1968) in routine meteorological service have demonstrated that in most cases it gives results in satisfactory agreement with visibility estimates from experienced observers.

2.3 Point Visibility Meter (AEG)

This type measures scattering like the VIDEOGRAPH, but integrates over a certain solid angle interval. The instrument is schematically presented in Fig.3. A flash lamp generates light pulses at a rate of about 0.1 sec^{-1} and illuminates a small atmospheric volume ($\approx 790 \text{ cm}^3$). The light scattered from this volume into the angle interval

(here $10^\circ - 120^\circ$) serves as a measure for the instantaneous visibility at the point of measurement.

2.4 Aerosol Counter (ROYCO)

Aerosol spectra were measured by a ROYCO particle counter, Model 225. This instrument counts optically the aerosol particles of $0.5 \mu\text{m}$ diameter and larger in concentrations up to $3 \times 10^3 \text{ cm}^{-3}$. Readout is given in five channels for the following diameter ranges:

0.5 - $0.7 \mu\text{m}$,

0.7 - $1.4 \mu\text{m}$,

1.4 - $3.0 \mu\text{m}$,

3.0 - $5.0 \mu\text{m}$,

> $5.0 \mu\text{m}$.

The flow rate is selectable between 600 and 60 cm^3 per second. Sizing accuracy is $\pm 5\%$, based on pulse height measurement.

3. PHYSICAL MEASURING PRINCIPLES OF VISIBILITY METERS

Following Koschmieder, H., (1925) standard visual range V_N is related to the extinction coefficient via

$$V_N = \frac{3.91}{\beta_{\text{ext}}} \quad (3.1)$$

β_{ext} being the extinction coefficient, which in turn is composed of the volume scattering coefficient β_{sca} and the absorption coefficient β_{abs} :

$$\beta_{\text{ext}} = \beta_{\text{sca}} + \beta_{\text{abs}} \quad (3.2)$$

It is advantageous and widely accepted to define V_N with the monochromatic extinction coefficient β_{ext} at $\lambda = 550 \text{ nm}$, $\beta_{\text{ext}}(550 \text{ nm})$. Extinctions obtained e.g. with a receiver with photopic response and sources of different colour temperatures usually differ only slightly from the monochromatic values (Ruppensberg, G.H., et al., 1971). Measured visibilities are denoted with V , the transmissometer values are approximately equal to the standard visual range, i.e. $V \approx V_N$, hence denoted with V_N .

Scattering visibility meters often determine visibility with the relation

$$V = \frac{C_{\text{Dev}}}{\beta_{\text{Dev}}} \quad (3.3)$$

where index "Dev" refers to "Device", β_{Dev} is the scattering coefficient for a certain solid angle, and C_{Dev} a calibration constant. In the computations the angle has been taken symmetrical around the incident light beam, so the scattering coefficient can be represented by

$$\beta_{\text{Dev}} = \beta(\theta_l, \theta_u) = \int_{\theta_l}^{\theta_u} \beta'(\theta) \sin \theta \, d\theta \quad (3.4)$$

θ_l and θ_u are the lower and upper limits, $\beta'(\theta)$ is the differential volume scattering coefficient, θ the scattering angle between incident and scattered light. θ_{Dev} defined in this way gives no ambiguity connected with the polarization of the scattered light, unpolarized incident light assumed.

Relation (3.2) is used for the AEG point visibility meter. Some scattering instruments- especially backscattering-

use an empirical relation (Curcio, J.A., et al., 1958):

$$V_B = \frac{C_B}{A_B^\delta}, \quad (3.5)$$

where C_B is the calibration constant and $\delta \geq 1$. A formula similar to Equ. (3.5) has been used to evaluate the VIDEOGRAPH records, however, for the computation relations (3.3) and (3.4) had to be applied.

4. MIE COMPUTATIONS

Mie's theory gives for the differential cross section $\sigma(\theta, \alpha)$ (Kerker, M., 1969) for unpolarized monochromatic radiation of wavelength λ and a particle size parameter $\alpha = 2\pi r/\lambda$ (r = radius):

$$\sigma(\theta, \alpha) = \frac{\lambda^2}{8\pi} (I_1(\alpha) + I_2(\alpha)). \quad (4.1)$$

Here I_1 and I_2 are the intensity functions, θ the scattering angle. The monochromatic differential volume scattering coefficient $\beta'(\lambda, \theta)$ is obtained by integration over a certain particle size range with a size density $n(\alpha)$:

$$\beta'(\lambda, \theta) = \frac{\lambda}{2\pi} \int_{\alpha_l}^{\alpha_u} n(\alpha) \sigma(\theta, \alpha) d\alpha. \quad (4.2)$$

The lower and upper bound α_l and α_u have to be chosen in such a way, that no appreciable contribution from outside these bounds occurs. With (4.1) and (4.2) the scattering coefficient $\beta(\lambda; \theta_l, \theta_u)$ becomes:

$$\beta(\lambda; \theta_l, \theta_u) = \frac{\lambda}{2\pi} \int_{\alpha_l}^{\alpha_u} n(\alpha) \int_{\theta_l}^{\theta_u} \sigma(\theta, \alpha) \sin \theta d\theta d\alpha. \quad (4.3)$$

Having a transmitter-receiver combination with non-monochromatic response, an additional wavelength integration is necessary.

However, the results for the size distributions and solid angles used were not very sensitive against λ -variations. So, throughout the calculations a wavelength of $\lambda = 550$ nm was used, resulting in the assumption $\beta(\theta_l, \theta_u) = \beta(550 \text{ nm}, \theta_l, \theta_u)$. A refractive index $n = 1.5 - 0.02i$ was chosen (Quenzel, H., et al., 1975).

This integration (4.3) was carried out using a modified algorithm obtained from Giese, R.H., (1971), over a size interval from $r = 0.04$ to $20 \mu\text{m}$ with sufficiently small size and angle increments. The integral was evaluated for the AEG ($\theta_u = 120^\circ$, $\theta_l = 10^\circ$) and for the VIDEOGRAPH ($\theta_u = 179^\circ$, $\theta_l = 177^\circ$). Integration between $\theta_u = 180^\circ$ and $\theta_l = 0^\circ$ gives the total scattering coefficient β_{sca} . In addition the total extinction coefficient $\beta_{\text{ext}} = \beta_{\text{sca}} + \beta_{\text{abs}}$ was calculated with respect to the transmissometer results.

The particle size distribution $n(\alpha)$ could not directly be taken from the aerosol counts. Experimentally particle counts in the size range $r = 0.5$ to $5 \mu\text{m}$ were obtained, the last channel counting particles with radii $\geq 5 \mu\text{m}$. For the computations particle sizes outside these ranges or with higher resolution were needed. Therefore a numerical fit to analytical distributions was performed.

Frequently a Junge distribution (Junge, C. E., 1963)

$$n(r) = Cr^{-\nu} \quad (4.4)$$

is used for higher visibilities and a modified Γ -distribution (Deirmendjian, D., 1969)

$$n(r) = a r^\beta \exp(-br^\gamma) \text{ with } 0 \leq r < \infty \quad (4.5)$$

for haze and fog.

a , β , b and γ are positive constants with β being an integer.

Some experimental distributions are adequately described by a Foltzik distribution (Foltzik, L., 1964) which consists of a sum of logarithmic Gaussian distributions

$$n(r) = \sum_i N_i \exp \left(-a_i \left(\ln \frac{r}{r_{oi}} \right)^2 \right) \quad (4.6)$$

where N_i , a_i , and r_{oi} are constants. Such a distribution can have several relative maxima. The actual ROYCO measurements revealed no such fine structure. So, the Foltzik distributions were disregarded.

A Junge distribution was fitted to each spectrum by a least square fit yielding ν -exponents ranging from 3.4 to 5.2 using discrete ν -values with an increment of 0.2.

Concurrently a fit with the Γ -distribution was made, varying the independent variables β , b , and γ over reasonable ranges, resulting in 96 different spectra.

The measuring range of the ROYCO did usually not allow a proper decision between Junge and Γ -distribution, especially never a maximum was found. However, the optical differences of these two types of distributions were quite distinct, even when fitted to the same set of measured aerosol data. This is illustrated in Fig.4. Here the quantity (Equ.(3.4))

$$\beta_N(\theta) := \frac{\beta(0, \theta_u)}{\beta_{\text{ext}}} \quad (4.7)$$

is plotted versus θ for Junge exponents $\nu = 3.6, 4.0, 4.6$, and for the Γ -distribution with $b = 17.5$, $\gamma = 1.0$ and $\beta = 2$.

$\beta_N(\theta)$ represents the energy scattered into a cone with subtending angle θ in comparison to the totally extincted energy.

The variations for different Junge distributions are not so pronounced in comparison to that for the Γ -distribution. With the Junge distribution the energy scattered into a 10° - cone is over 40% compared to approximately 10% in the case of a Γ -distribution. This is due to the fact that beyond $5 \mu\text{m}$ the Γ -distribution becomes much steeper than the Junge distribution and that the pronounced forward scattering and absorption of the larger particles is less dominant.

The influence on an instrument, which detects only part of the scattered energy is quite obvious. For our computation it meant, that for the general form of the distribution some a-priori-information had to be inferred. This implied that for lower visibilities (in the case of haze), where a Γ -distribution could be assumed, the ROYCO-compatible distribution yielded a less pronounced forward scattering compared to a fair visibility condition, which in turn implies, that the AEG-V -value should be too low. This seems to be corroborated by the experiment (see section 5). In fog, where the maximum of the distribution is displaced to larger radii, the situation is reversed.

5. OBSERVATIONAL AND COMPUTATIONAL RESULTS

5.1 Visibility Data

Visibility registrations were evaluated on an hourly base. For all valid data a statistical analysis was performed. Correlations of our visibility data are plotted in Figs. 5, 6, and 7. Fig. 5 and 6 show all ELTRO-values versus VIDEOGRAPH and AEG readings resp., as obtained during the whole measuring period. In Fig. 7 the VIDEOGRAPH is plotted versus the AEG point visibility meter. All data are plotted in logarithmic scales. A regression line $Y = Ax+B$ has further been added. Fig. 5 and 6 contain only 223 points, the latter 620. This arises from the following reason:

The ELTRO data from 18.00 to 8.00 h proved to be unreliable, because it had turned out, that a bird used to stay over night inside the heated housing of the ELTRO optic sensor, thus causing a systematic reduction of transmittance.

Mean correlation coefficients R and regression parameters A and B are compiled in Table 1:

	R	A	B
ELTRO-VIDEOGR.	0.81	0.986	-0.942
ELTRO-AEG	0.80	1.080	-0.532
VIDEOGR.-AEG	0.82	0.804	1.655

Table 1: Correlation coefficient R and regression parameters A,B for different visibility meter combinations.

Consequently a good mean correlation near 0.8 in all three cases comes out. A systematic deviation from an ideal regression line (45°) is obtained as indicated by parameters A and B. It is most pronounced in the case of the comparison VIDEOGRAPH-AEG, i.e. backscatter - point visibility meter.

Striking deviations in visibility agreement are in most cases due to ambiguities in the instrumental records caused by special meteorological events like rain showers and patchy fog. Under such conditions rapid changes in visibility readings are possible and cannot properly be resolved. Part of the strong discrepancies can, however, be attributed to fog or snow cases which are demonstrated in some more detail in the next section.

5.2 Special Meteorological Conditions

Generally the data set examined here covered relatively high visibilities above 10 km. So, only a few cases with special events were obtained:

5 days with fog,

1 day with several hours of rainfall and snow.

An example for fog during the morning hours is given in Fig. 8 (24. Febr. 1975). Here the courses of the visibility meter readings are plotted on a logarithmic scale versus time. During the morning hours there is a pronounced discrepancy between the AEG and VIDEOGRAPH by a factor of 3 to 5. The observers from the nearby meteorological station reported dense fog with visibilities below 200 m between 0.00 and 10.00 h, as added in Fig. 8.

It is obvious that the AEG is in better agreement with these estimates, even if one considers that eye observations tend to underestimate actual ranges due to the observer's instructions to report the lowest values.

Absolutely wrong is the VIDEOGRAPH with values between 1 km and 10 km. This was also true for all other fog

cases.

After 10.00 h fog began to dissolve and the relatively good agreement between all instruments returned.

The inverse behaviour was observed during a day with rain and snowfall (Fig.9). Here the VIDEOGRAPH (and ELTRO) recorded remarkable lower visibilities than the AEG scattering device. Hereafter the extreme deviations between two instruments can reach more than one order of magnitude. On the other hand a severe discrepancy during rain could not be detected.

5.3 Comparison between Observation and Calculation

In Fig.10 the calculated standard visual range V_N^C based on computed extinction is plotted against the experimental ELTRO readings V_N^E . For all computed values a Junge distribution was assumed. The concentration factor C and the exponent ν are taken from the ROYCO fit calculations. In Fig.10 - 12, the five classes of the ν -exponent are coded by different symbols as explained in the legends. The general agreement is obvious, some striking deviations can be explained by particular meteorological conditions - especially snow with rain or fog.

The absolute values of the measured visibilities however, are on the average only approximately one third of the calculated ones. This fact is supposedly mainly due to maladjusted flow rate in the ROYCO, which is proportional to the absolute value of the particle density.

In Fig.11 and 12 the corresponding values have been plotted for the VIDEOGRAPH and AEG, i.e. experimental values are compared with visibilities computed from the scattered energies, as seen by the instruments (on an arbitrary scale). For the experimental values factory calibration curves were used, which implies the use of Equ.3.1, 3.3, and 3.5 for the ELTRO, AEG, and VIDEOGRAPH respectively.

The general relative agreement is fairly good. So it can be concluded, that the assumption of a Junge distribution and Mie scatterers in connection with an optical ROYCO-type aerosol counter is suitable for theoretical visibility calculations with some restrictions:

The general accuracy is reduced compared to straight visibility meters. Under conditions, where visibility is determined by large particles (esp. rain, snow), the computed values can be erroneous by an order of magnitude.

The applicability can further be checked by analyzing if the theory yields a correct prediction of the differences between the transmissometer and the scattering instrument readings:

If one assumes a Junge distribution, the reading of the AEG (integrating from $\theta_1 = 10^\circ$ to $\theta_u = 120^\circ$) and the VIDEOGRAPH (backscatter, $\theta_1 = 177^\circ$, $\theta_u = 179^\circ$) should decrease -following computation-compared with a transmissometer (ELTRO), if the Junge exponent is increased. In the case of the computed AEG-visual range V_{AEG}^C this can be shown as follows: Using Equ. (3.1), (3.3), and (3.4) one finds the relation:

$$\frac{V_{AEG}^C}{V_N^C} = k \frac{\beta_{ext}}{\beta(10^\circ, 120^\circ)} \quad (5.1)$$

where k is a constant only dependent on geometry, not on size distribution. Dividing the right side of (5.1) by β_{ext} one gets (see Equ.4.7):

$$\frac{V_{AEG}^C}{V_N^C} = \frac{k \beta_{ext}}{\beta(0^\circ, 120^\circ) - \beta(0^\circ, 10^\circ)} = \frac{k}{\beta_N(120^\circ) - \beta_N(10^\circ)} \quad (5.2)$$

With the aid of Fig.4 one verifies that the denominator of (5.2) actually increases with increasing ν , hence V_{AEG}^C decreases in comparison to V_N^C . The calculation reveals the same dependence for the VIDEOGRAPH, however, due to the empirical calibration (Equ.3.5), the analysis is not so straight forward. Using only experimental visi-

bility values $V_N^E \geq 5$ km, where Junge distributions usually are assumed and performing the comparison, one finds no obvious correlation between the measured and the computed quotient V_{AEG}/V_N . Furthermore, the actual deviations are much more pronounced than the computed ones. Bearing in mind that the results were gained for a particular geographical location it can be concluded that the differential volume scattering coefficient $\beta'(\theta)$ as influencing the AEG (integrating) and the VIDEOGRAPH (backscatter) cannot accurately be computed by assuming Mie-scatterers with constant refractive index and a size distribution following a power law.

Going to visibilities $V_N^E < 5$ km without fog cases, it can be expected that a Junge distribution is replaced by a haze-distribution (T -distribution). In such a case the AEG should show distinct lower readings. This can be deduced from Fig.4 and Equ.(5.2): Fig.4 shows an integrated scattering coefficient $\beta_N(\theta)$ based on actually measured particle counts assuming a T -distribution. Such a distribution yields relatively more received energy and hence a lower AEG-visibility value. This seems to be corroborated by the measurements (see Fig.6).

The regression line depicted there nearly coincides with the ideal 45° regression. At lower visual ranges V_N^E (without fog or snow) the AEG readings show the expected tendency to lower values. The situation is reversed during fog cases, where the maximum of the aerosol spectrum is shifted to larger particles and the instrument receives relatively less scattered energy. More fog cases should be examined to investigate this behaviour more thoroughly.

The VIDEOGRAPH proves to be less sensitive against changes in the size distribution type (transition from Junge to T -distribution) and shows the effects less pronounced.

6. CONCLUSIONS

The following conclusions can be drawn from this study:

- 1) Under most meteorological conditions transmissometers and scattering visibility meters provide very similar results. However, under particular meteorological conditions - like fog and snow - severe discrepancies can occur.
- 2) Computations using Mie's theory and experimentally determined particle size distributions give a generally correct prediction of the measured extinction (apart from instrumental shortcomings).

Regarding the prediction of the discrepancies in the different operation principles the situation is more complex:

- 1) At large visual ranges the differences could not be predicted by assuming a simple Junge distribution and Mie scatterers.
- 2) At medium ranges (haze) computations are in accordance with observation.

REFERENCES

- Curcio, J.A., and G.L.Knestrik, (1958): Correlation between atmospheric transmission and backscattering, J.Opt.Soc.Am., Vol.48, 686.
- Deirmendijan, D., (1969): Electromagnetic scattering on spherical polydispersions, Am.Elsevier Publ.Comp., New York.
- Foitzik, L., (1964): The spectral extinction of the atmospheric aerosol by Mie particles with different Gaussian distributions, Symp.on Atm.Radiation, Leningrad.
- Giese, R.H., (1971): Tabellen von Mie-Streufunktionen, BMBW Forschungsbericht W 71 - 23.
- Junge, C.E., (1963): Air chemistry and radioactivity, Int.Geophys.Ser., Vol.4, Acad.Press, New York, London.
- Kerker, M., (1969): The scattering of light and other electromagnetic radiation, Acad.Press, New York, London.

Koschmieder, H., (1925): Theorie der horizontalen Sichtweite, Beitr. Phys. fr. Atm., Vol. 12, 33.

Quenzel, H., G.H. Ruppensberg, and R. Schellhase, (1975): Calculations about the systematic error of visibility meters measuring scattered light, Atm. Environment, to be published.

Ruppensberg, G.H., H.v. Redwitz, and R. Schellhase, (1971): Atmosphärische Lichtdurchlässigkeit und Streuung im sichtbaren Spektralbereich und in den Fenstern des IR-Bereiches bis zu 5 μm . BMVg - FBWT 71-16.

Vogt, H., (1968): Visibility measurements using backscattered light, J. Atm. Sci., Vol. 25, 912.

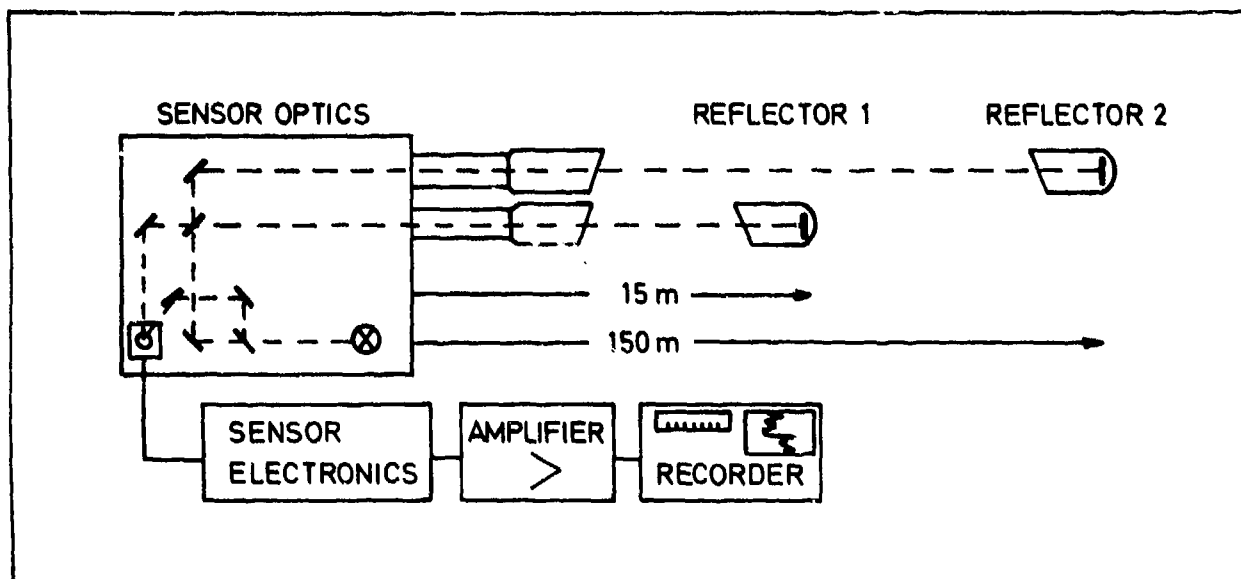


Fig. 1 Block diagram of the ELTRO-transmissometer

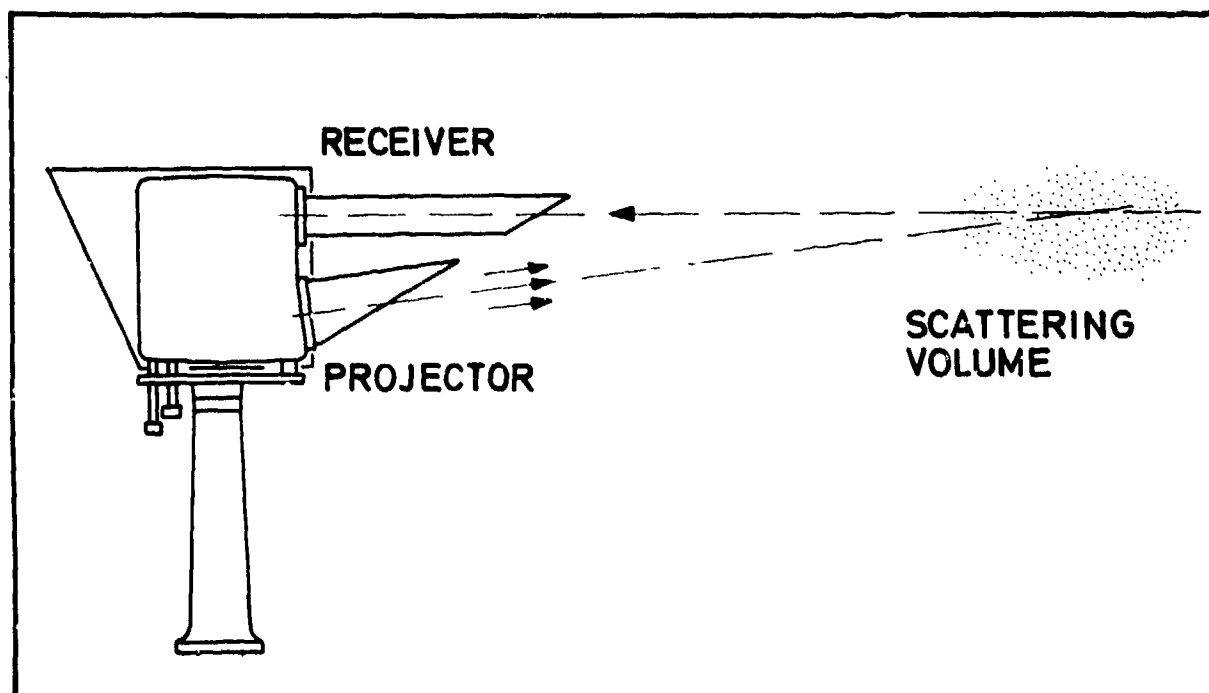


Fig. 2 Schematic diagram of the backscatter visibility meter (VIDEOGRAPH)

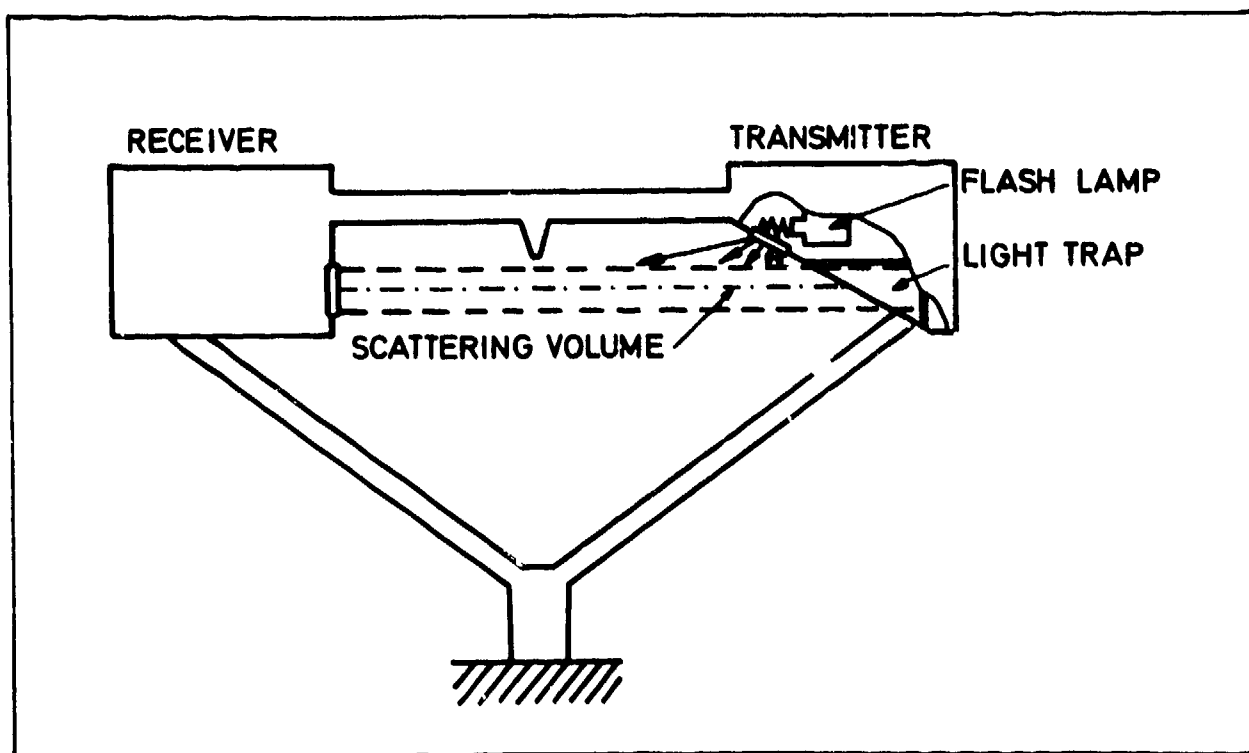


Fig. 3 AEG-point-visibility meter (schematic).

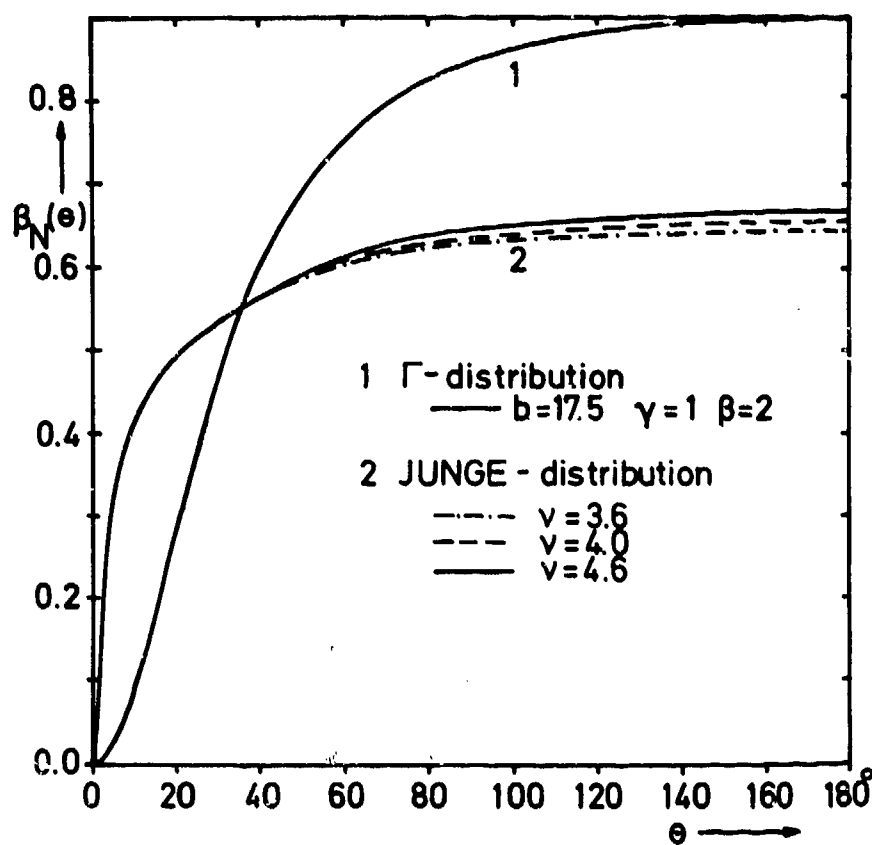


Fig. 4 Normalized integral scattering coefficient $\beta_N(\theta)$ versus scattering angle θ .

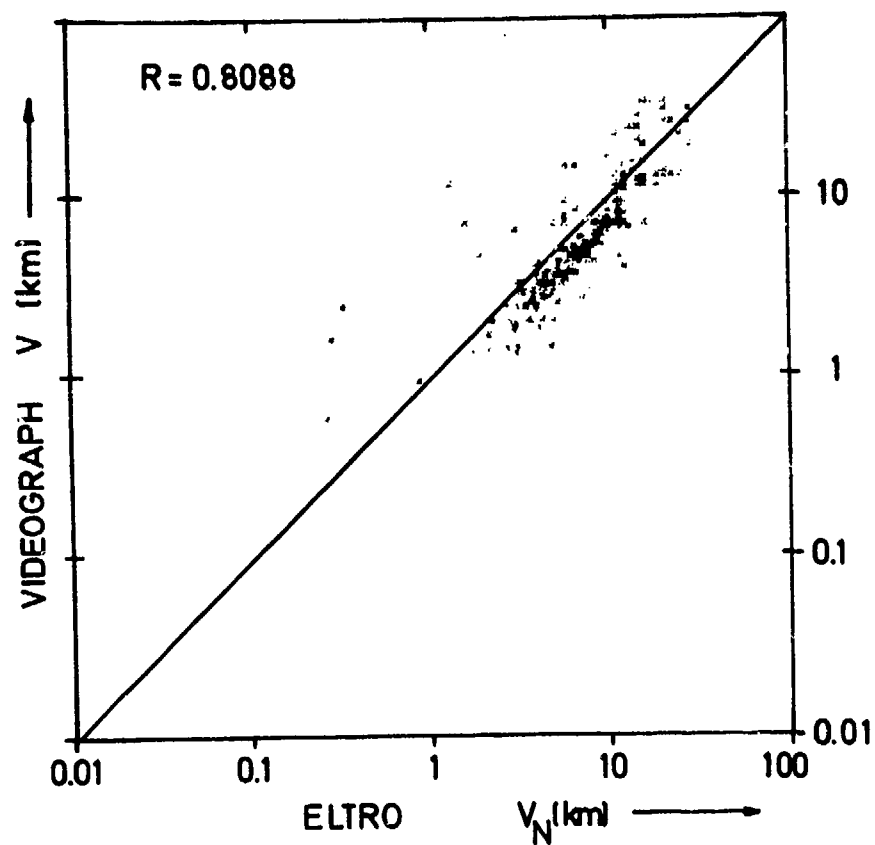


Fig. 5 Correlation between transmissometer (ELTRO) and backscatter instrument (VIDEOGRAPH) with regression line (Correlation coefficient R).

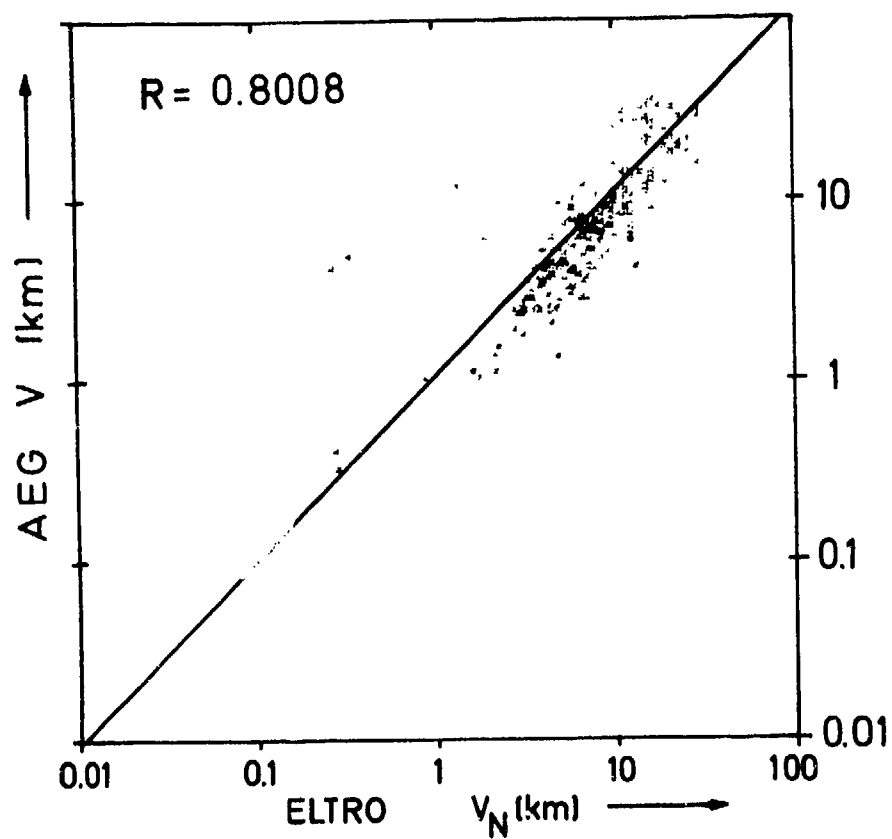


Fig. 6 Correlation between transmissometer (ELTRO) and point visibility meter (AEG) with regression line (Correlation coefficient R).

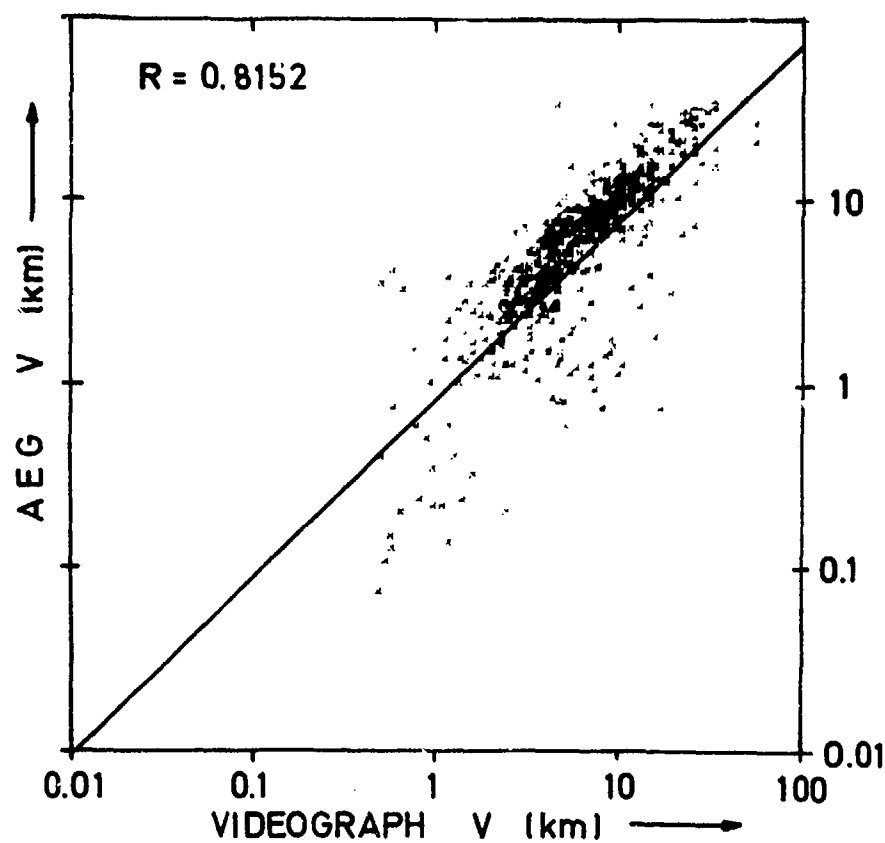


Fig. 7 Correlation between backscatter instrument (VIDEOGRAPH) and point visibility meter (AEG) with regression line (Correlation coefficient R).

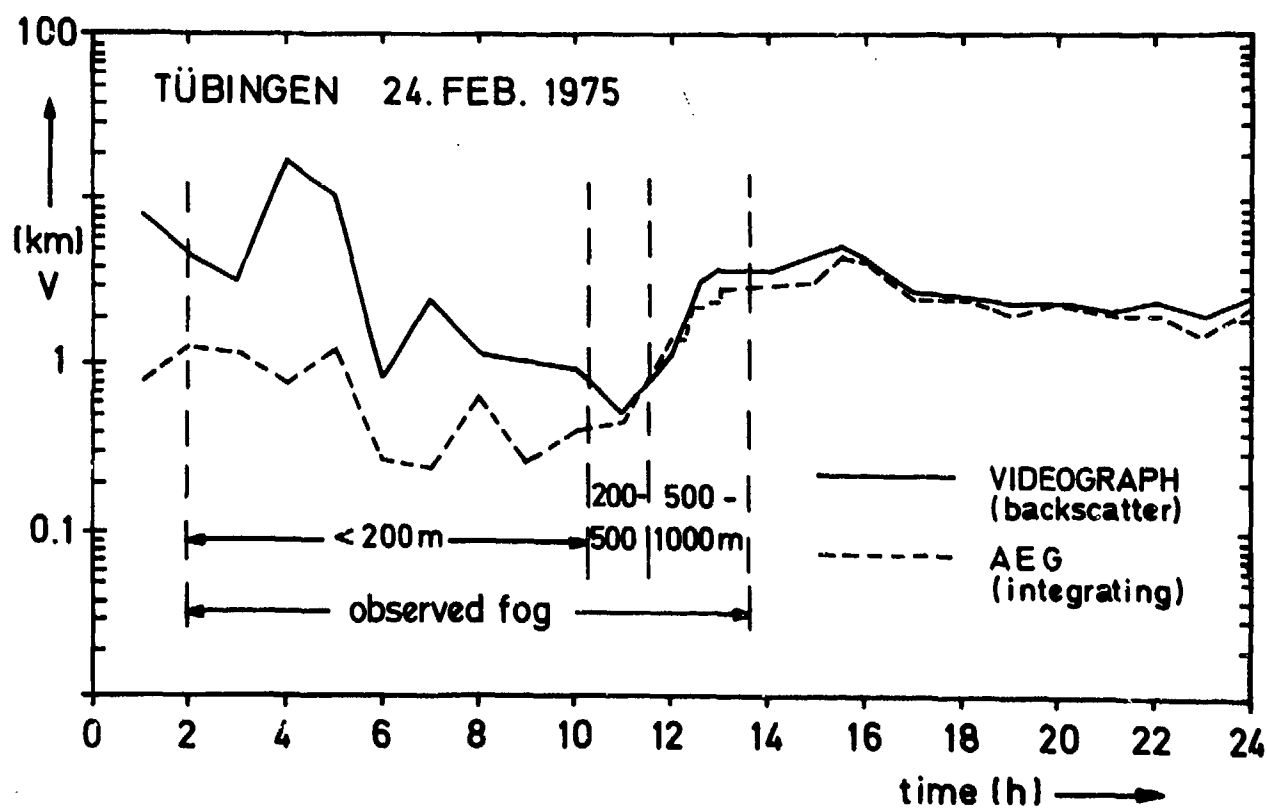


Fig. 8 Visibility records of two instruments for 24. Febr. 1975 in Tübingen with observed visibilities from Weather Service during a fog situation.

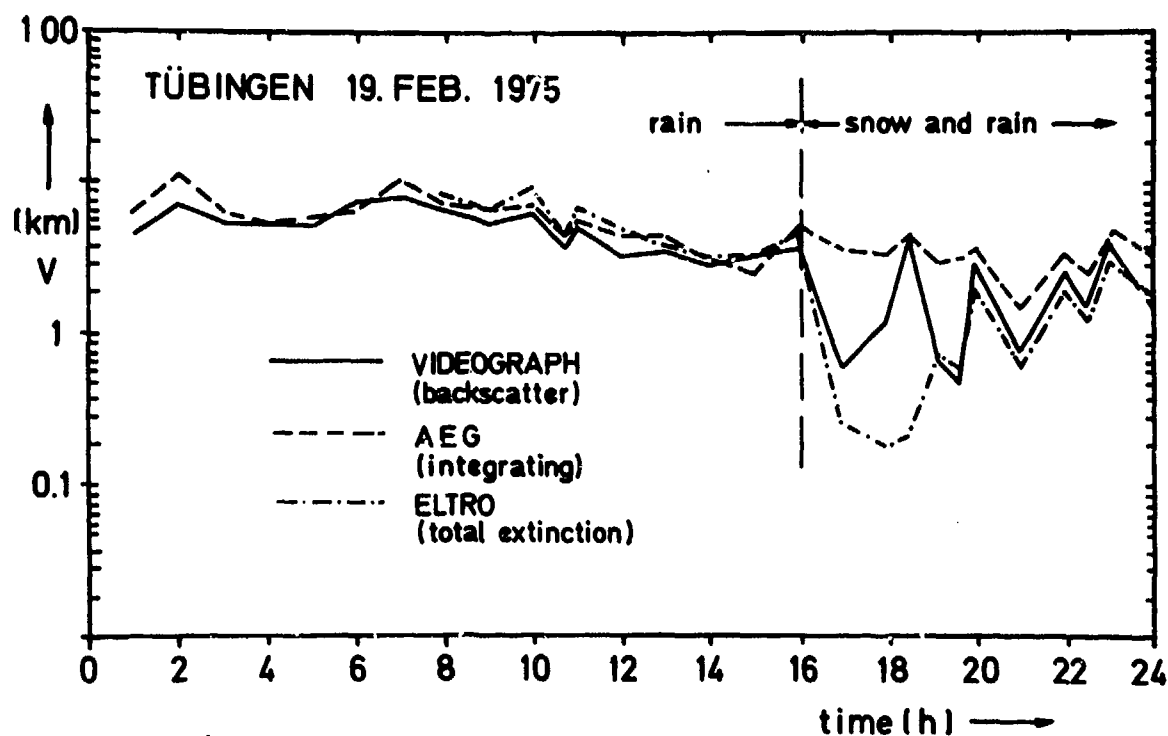


Fig. 9 Visibility records of three instruments for 18. Febr. 1975 in Tübingen during a rain and snow situation.

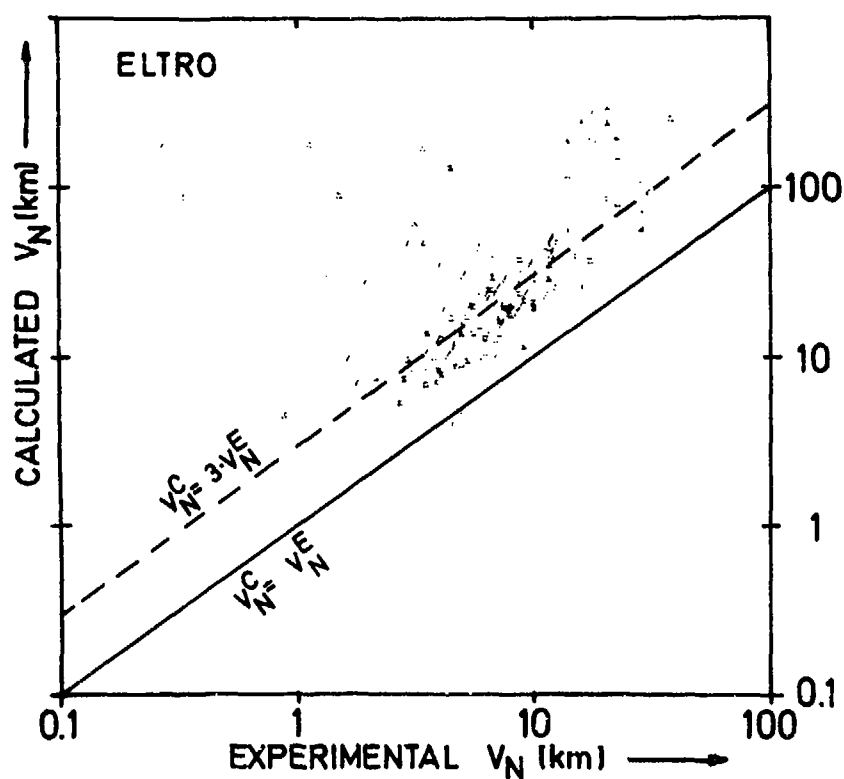


Fig. 10 Comparison between calculated and experimental visibilities for the transmitter (ELTRO).

V_N^C = calculated V_N , V_N^E = experimental V_N .

Symbols as follows (JUNGÉ-exponent):

○ $\nu = 3.0$ and 3.2

□ $\nu = 4.2$ and 4.4

△ $\nu = 3.4$ and 3.6

◇ $\nu = 4.6$ and 4.8

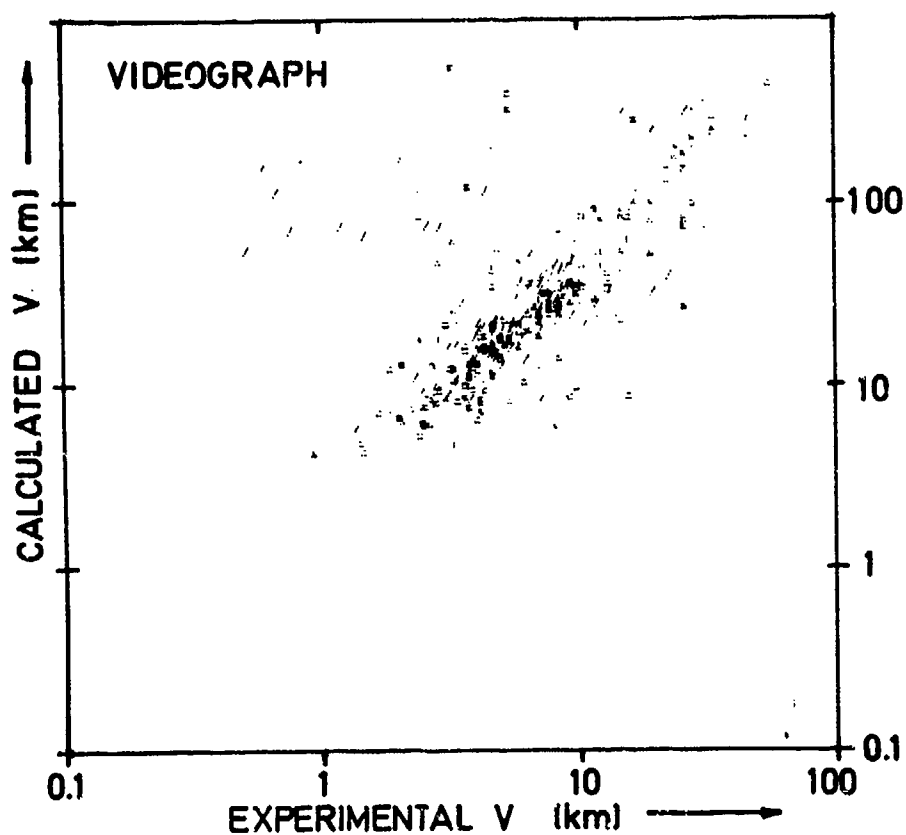


Fig. 11 Comparison between calculated and experimental visibilities for the backscatter instrument (VIDEOGRAPH). Symbols same as in Fig. 10.

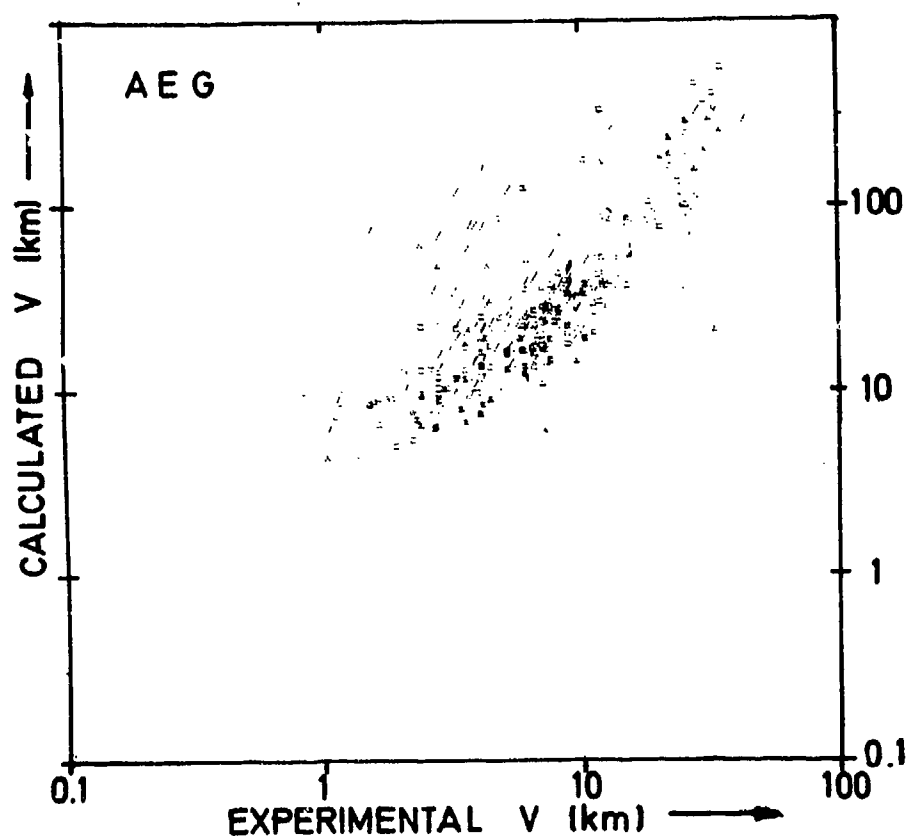


Fig. 12 Comparison between calculated and experimental visibilities for the point visibility meter (AEG). Symbols same as in Fig. 10.

TRANSFERT DU RAYONNEMENT DANS UN MILIEU ABSORBANT ET DIFFUSANT

PAR

Y. FOUQUART ET J.C. BURIEZ

LABORATOIRE D'OPTIQUE ATMOSPHERIQUE

UNIVERSITE DES SCIENCES ET TECHNIQUES DE LILLE

B.P. 36 - 59650 VILLENEUVE D'ASCQ - FRANCE

RESUME

Le calcul du transfert du rayonnement dans une atmosphère diffusante et absorbante est particulièrement compliqué du fait que les processus d'absorption par le gaz et de diffusion par les particules ont lieu simultanément. Les techniques les plus généralement utilisées sont coûteuses et mal adaptées à l'interprétation physique des observations.

La méthode la plus efficace consiste à employer la distribution du chemin optique des photons diffusés $p(\lambda)$ qui permet de séparer l'absorption de la diffusion. La distribution $p(\lambda)$ est calculée pour une atmosphère diffusante donnée au moyen des Approximants de Padé. La résolution de l'équation de transfert en milieu diffusant peut être effectuée au moyen de n'importe quelle méthode approximative ou précise, l'absorption par les gaz peut être calculée au moyen des modèles de bandes.

De nombreuses applications de cette méthode sont possibles : interprétation des spectres formés dans des atmosphères nuageuses, calcul des flux et des échauffements radiatifs, étude des milieux diffusants inhomogènes.

Dans ce papier la méthode est exposée et appliquée au calcul de l'intensité réfléchie par un nuage inhomogène.

SUMMARY

RADIATIVE TRANSFERT IN A SCATTERING ABSORBING MEDIUM

The computation of Radiative Transfert in a scattering and absorbing atmosphere is particularly complicated because absorption by the gases and scattering by the particles occur simultaneously. The technics which are generally used are time consuming and inadequate for physical interpretations of data.

The most suitable method is to use the "distribution of photon optical path" $p(\lambda)$ which makes it possible to disjoin absorption and scattering. The distribution $p(\lambda)$ is computed for a given scattering medium by means of Pade Approximants. The solution of the Transfert Equation may be computed by means of any approximate or accurate method and absorption by gases may be computed by means of band models.

Numerous applications of this method are possible : interpretation of the spectra formed in cloudy atmospheres, computation of fluxes and heating rates, study of inhomogeneous scattering medium.

In this paper the method is presented and applied to the calculation of the intensity reflected by an inhomogeneous cloud.

I - INTRODUCTION

La détermination des bilans radiatifs des atmosphères, l'étude des spectres réfléchis par les planètes, les méthodes de sondage optique nécessitent une connaissance approfondie du transfert de rayonnement dans les atmosphères planétaires. Le cas des milieux diffusants est particulièrement compliqué du fait que les processus de diffusion par les particules et d'absorption par les gaz ont lieu simultanément.

L'utilisation de la distribution du chemin optique des photons diffusés apporte une simplification considérable en déconnectant les deux processus ; il est alors possible d'employer n'importe quelle méthode de résolution de l'équation de transfert et les problèmes qui concernent l'absorption par les gaz peuvent être résolus au moyen des mêmes méthodes que dans le cas des atmosphères claires.

La détermination des quantités moyennes sur la fréquence (intensité, flux ou échauffement radiatif) est ainsi grandement facilitée ; l'utilisation de la fonction de distribution permet de ramener le calcul de ces quantités à celui d'une fonction de transmission moyenne du gaz absorbant, qui peut être effectué facilement à l'aide d'un modèle de bande. Cette méthode a été souvent utilisée (KARGIN et al, 1972), (FOUQUART et PRUVOST, 1974), car elle seule permet un calcul rapide.

De même, on peut obtenir une expression simple des largeurs équivalentes des raies spectrales observées dans le rayonnement réfléchi par les planètes (FOUQUART et LENOBLE, 1973).

Enfin, il est possible de calculer approximativement l'intensité réfléchie par une couche diffusante dans laquelle l'absorption augmente avec la profondeur optique, et de déduire, de l'analyse du rayonnement réfléchi, certaines caractéristiques physiques de l'atmosphère ambiante ou de la couche elle-même. Mais il est alors nécessaire de déterminer la profondeur de pénétration du rayonnement. C'est cette

notion que nous allons développer après avoir rappelé brièvement les principales méthodes de calcul de la fonction de distribution.

II - LA DISTRIBUTION DU CHEMIN OPTIQUE DES PHOTONS DIFFUSES

Considérons une couche diffusante, plane-parallèle, d'épaisseur optique τ ; nous repèrerons une direction donnée par l'azimut ϕ et le cosinus de la colatitude $\mu = \cos\theta$; soient σ et k_c les coefficients de diffusion et d'absorption des particules, et k_v le coefficient d'absorption du gaz à la fréquence ν .

Définissons l'albédo de diffusion du continu

$$\omega_c = \sigma / (\sigma + k_c) \quad (1)$$

et l'albédo de diffusion à la fréquence ν

$$\omega_\nu = \sigma / (\sigma + k_c + k_\nu) \quad (2)$$

Soit $I(\omega_\nu, t, \tau) \equiv I(\omega_\nu, \tau, \mu, \phi; \mu_0, \phi_0, t)$ l'intensité diffusée dans la direction (μ, ϕ) pour une incidence (μ_0, ϕ_0) par la couche considérée, à la profondeur optique t .

Dans ces conditions, la distribution du chemin optique $p(\lambda)$ des photons observés à la profondeur optique t , après avoir parcouru dans le nuage un trajet de longueur totale L , c'est-à-dire un chemin optique total dans le continu $\lambda = (\sigma + k_c) L$, est définie par (VAN DE HULST et IRVINE, 1962)

$$I(\omega_\nu, t, \tau) = I(\omega_c, t, \tau) \int_0^\infty p(\lambda) \exp\left(-\frac{k_\nu \lambda}{\sigma + k_c}\right) d\lambda \quad (3)$$

avec la condition de normalisation

$$\int_0^\infty p(\lambda) d\lambda = 1. \quad (4)$$

Posons

$$r = k_\nu / (\sigma + k_c) = \omega_c / \omega_\nu - 1 \quad (5)$$

Nous pouvons écrire

$$I(\omega_\nu, t, \tau) / I(\omega_c, t, \tau) = L_{r, \lambda} \{p(\lambda)\} \quad (6)$$

où $L_{r, \lambda} \{p(\lambda)\}$ est la transformée de Laplace de $p(\lambda)$; le chemin optique moyen, parcouru par les photons observés à la profondeur t , peut alors se mettre sous la forme

$$\langle \lambda \rangle = \int_0^\infty \lambda p(\lambda) d\lambda = \frac{1}{I(\omega_c, t, \tau)} \left[\frac{d}{dr} I(\omega_\nu, t, \tau) \right]_{r=0} \quad (7)$$

Nous employons ici une écriture simplifiée, mais il faut se rappeler que la fonction de distribution dépend des directions (μ, ϕ) et (μ_0, ϕ_0) , de la profondeur optique considérée, et des caractéristiques du nuage (albédo continu, épaisseur optique, indice et granulométrie des gouttes).

III - METHODES DE CALCUL DE LA FONCTION DE DISTRIBUTION

Dans le cas des couches diffusantes semi-infinies, l'expression de la fonction de distribution des photons sortant du nuage après y avoir subi n diffusions, a été donnée par IRVINE (1964)

$$p_n(\lambda) = e^{-\lambda} \lambda^{n-1} / (n-1)! \quad (8)$$

Lorsque l'intensité réfléchie est connue pour chaque ordre de diffusion, la fonction de distribution s'obtient par simple sommation

$$p(\lambda) = \sum_{n=1}^{\infty} p_n(\lambda) I_n(\omega_c, 0, \infty) / I(\omega_c, 0, \infty) \quad (9)$$

UESUGI et IRVINE (1970 a et b), VAN DE HULST (1970) ont proposé des développements asymptotiques de $I_n(\omega_c, 0, \infty)$ qui permettent de réduire le temps de calcul correspondant.

La fonction de distribution peut être obtenue plus directement en utilisant une méthode de Monte-Carlo (KARGIN et al, 1972), (APPLEBY et IRVINE, 1973) ; cette méthode n'est pas limitative et peut être utilisée de façon tout à fait générale ; son inconvénient majeur réside dans la longueur des calculs et leur relative imprécision.

Les autres méthodes de calcul de $p(\lambda)$ consistent à inverser la transformée de Laplace de la relation (6), les intensités $I(\omega_\nu, t, \tau)$ étant obtenues au moyen de n'importe quelle méthode de résolution de l'équation de transfert (LENÔBLE, 1975).

HEINRICH (1973) a utilisé une méthode d'inversion proposée par BELLMAN et al (1966) ; elle consiste à remplacer l'intégrale qui figure dans l'expression (3) par une quadrature de Gauss ; on obtient alors un système linéaire qu'il suffit d'inverser pour obtenir des valeurs discrètes de $p(\lambda)$. Cependant cette méthode est instable car la matrice du système est très mal conditionnée.

La méthode que nous avons employée (FOUQUART, 1974) consiste à rechercher une interpolation de la fonction à inverser sous forme d'une fraction rationnelle (ou approximant de Padé de type II)

$$I(\omega_v, t, \tau) / I(\omega_c, t, \tau) = P_{N-1}(r) / Q_N(r) \quad (10)$$

où $P_{N-1}(r)$ et $Q_N(r)$ sont des polynômes de degré respectifs $N-1$ et N . Après décomposition en éléments simples, l'inversion est immédiate et la fonction de distribution s'écrit

$$p(\lambda) = \sum_{m=1}^N A_m \exp(\gamma_m \lambda) \quad (11)$$

où γ_m est la m^e racine de $Q_N(r)$ et A_m le résidu correspondant.

IV - LA PROFONDEUR DE PENETRATION DU RAYONNEMENT DANS UNE ATMOSPHERE DIFFUSANTE

Si N photons sont réfléchis au total par un nuage d'épaisseur optique infinie, le nombre total de photons réfléchis par un nuage similaire d'épaisseur optique τ est $N I(\omega_c, 0, \tau) / I(\omega_c, 0, \infty)$. Le nombre de photons qui ont suivi un chemin optique λ dans le nuage d'épaisseur optique τ est donc

$$N p_\tau(\lambda) I(\omega_c, 0, \tau) / I(\omega_c, 0, \infty) = N f_\tau(\lambda) \quad (12)$$

où $p_\tau(\lambda)$ est la distribution correspondant au nuage d'épaisseur optique τ .

Nous introduisons donc la nouvelle fonction de distribution $f_\tau(\lambda)$ normalisée de la façon suivante :

$$\int_0^\infty f_\tau(\lambda) d\lambda = I(\omega_c, 0, \tau) / I(\omega_c, 0, \infty) \quad (13)$$

Si un photon a , durant le processus de diffusion, suivi un chemin optique total λ , il est clair qu'il n'a pas pu atteindre une profondeur optique supérieure à $t = \lambda/2$ et, les couches situées en dessous de $t = \lambda/2$ n'influencent donc pas le processus de diffusion d'un tel photon. Autrement dit, le nombre de photons sortant d'un nuage d'épaisseur optique τ et ayant suivi un chemin total $\lambda < 2\tau$ est rigoureusement égal au nombre de photons sortant d'un nuage similaire d'épaisseur optique quelconque $\tau' > \tau$ et ayant suivi au total un chemin optique $\lambda < 2\tau$. Il s'en suit que

$$f_\tau(\lambda) \equiv p_\infty(\lambda), \text{ si } \lambda < 2\tau \quad (14)$$

Les fonctions de distribution $f_\tau(\lambda)$, calculées d'après (11) et (12) correspondant au cas $\mu = \nu_0 = 1$, sont présentées (figure 1) pour différentes épaisseurs optiques τ , pour un nuage de particules monodispersées, de paramètre de MIE $\alpha = 2$, d'indice $n = 1,33$, avec un albédo continu $\omega_c = 0,999$. On pourra noter que la différence entre $p_\infty(\lambda)$ et $f_\tau(\lambda)$ n'est notable que pour des valeurs de λ nettement supérieures à 2τ .

Lorsque les fonctions de distribution $f_\tau(\lambda)$ correspondant aux diverses épaisseurs optiques sont connues, il est possible d'en déduire la contribution relative des différents niveaux du nuage au processus de diffusion. Le tableau (1) présente, pour le cas du nuage décrit précédemment, le rapport $f_\tau(\lambda) / p_\infty(\lambda)$ qui correspond à la proportion des photons réfléchis dans des couches de différentes épaisseurs optiques τ , parmi le nombre total de photons réfléchis par le nuage infini après avoir parcouru le même chemin optique λ . Deux valeurs de λ ont été choisies : $\lambda = 87$ et $\lambda = 50$; le cas $\lambda = 87$ correspond au chemin optique moyen $\langle \lambda \rangle$ du nuage infini. Sur la figure (2), on a représenté la quantité $g_\lambda(\tau) = (f_\tau(\lambda) - f_{\tau-1}(\lambda)) / p_\infty(\lambda)$ qui représente, parmi les photons qui ont parcouru le chemin optique λ , la proportion de ceux qui ont pénétré jusqu'à la couche comprise entre τ et $\tau - 1$.

Il est intéressant de noter que, d'après le tableau (1), près de 45 % des photons qui ont suivi un chemin optique $\lambda = 50$ ont pénétré jusqu'à une profondeur optique comprise entre 7 et 10 et plus de 80 % entre 6 et 12 ; dans le cas où $\lambda = 87$, 45 % des photons ont pénétré jusqu'à une profondeur comprise entre 10 et 14 et 80 % entre 9 et 18. La pénétration du rayonnement dans une couche diffusante avant sa réflexion est donc fortement localisée particulièrement pour les faibles chemins optiques.

Tableau 1

Nombre de photons réfléchis par une couche nuageuse en fonction de son épaisseur optique τ , pour 100 photons dans le cas semi-infini.

$$100 f_{\tau}(\lambda)/p_{\infty}(\lambda)$$

τ	$\lambda = 87$	$\lambda = 50$
1	0	0
2	0	0
3	0	0
4	0	0,5
5	0,1	3,14
6	0,4	9,7
7	1,8	21,4
8	5,3	36,5
9	11,7	52,0
10	20,5	66,6
11	31,2	78,8
12	42,8	87,9
13	54,3	93,7
14	64,8	97,3
15	73,8	99,3
16	80,7	100
17	87,4	100
18	91,6	100
19	94,0	100
20	96,4	100
∞	100	100

Nous définirons donc la fonction de distribution des photons qui ont suivi un chemin optique λ et pénétré jusqu'à une profondeur optique t par

$$p(\lambda, t) = \frac{d}{dt} (f_t(\lambda)). \quad (15)$$

Cette fonction de distribution possède les propriétés suivantes :

$$\int_0^{\infty} p(\lambda, t) dt = p_{\infty}(\lambda). \quad (16)$$

$$\int_0^{\infty} p(\lambda, t) d\lambda = \frac{d}{dt} \int_0^{\infty} f_t(\lambda) d\lambda = \frac{d}{dt} \left[\frac{I(\omega_c, 0, t)}{I(\omega_c, 0, \infty)} \right]. \quad (17)$$

$$\int_0^{\infty} \int_0^{\infty} p(\lambda, t) dt d\lambda = \int_0^{\infty} p_{\infty}(\lambda) d\lambda = 1, \quad (18)$$

$$\text{et } p(\lambda, t) = 0, \text{ si } \lambda < 2t. \quad (19)$$

Avec ces notations, nous pouvons écrire

$$g_{\lambda}(\tau) = \left(\int_{\tau-1}^{\tau} p(\lambda, t) dt \right) / p_{\infty}(\lambda);$$

la figure (2) présente donc une approximation de $p(\lambda, t)/p_{\infty}(\lambda)$ pour deux valeurs de λ .

Il est maintenant possible de définir la pénétration moyenne correspondant à un chemin optique λ donné, pour un nuage d'épaisseur optique totale τ par

$$\bar{t}(\lambda) = \left(\int_0^{\tau} t p(\lambda, t) dt \right) \left(\int_0^{\tau} p(\lambda, t) dt \right)^{-1}. \quad (20)$$

Dans le cas présenté figure (2), les pénétrations moyennes calculées d'après la relation (20), sont approximativement $\bar{t}(50) = 9,0$ et $\bar{t}(87) = 12,7$.

La pénétration moyenne est évidemment dépendante de l'épaisseur optique totale de la couche diffusante et devrait s'écrire $\bar{t}(\lambda, \tau)$; cependant, si le fond du nuage est adjacent à un corps noir, deux cas peuvent être considérés :

(i) si l'épaisseur optique τ est plus grande que la pénétration moyenne correspondant au nuage semi-infini $\bar{t}(\lambda, \infty)$, le résultat est approximativement le même que pour le nuage semi-infini, surtout si l'on considère des chemins optiques assez faibles.

(ii) si l'épaisseur optique du nuage est inférieure à $\bar{t}(\lambda, \infty)$, on trouve évidemment que la majorité des photons a pénétré jusqu'à un niveau proche du fond de la couche diffusante (ces résultats peuvent être vérifiés à partir du tableau (1)). Donc, pour une couche d'épaisseur optique τ , nous pouvons écrire approximativement

$$\bar{t}(\lambda, \tau) \sim \bar{t}(\lambda, \infty) \quad \text{si } \tau > \bar{t}(\lambda, \infty)$$

et

$$\bar{t}(\lambda, \tau) \sim \tau \quad \text{si } \tau < \bar{t}(\lambda, \infty).$$

(21)

V - METHODES DE CALCUL DE LA PROFONDEUR DE PENETRATION

La figure (3) présente les fonctions $p(\lambda, t)/p(\lambda)$ pour un nuage correspondant à une granulométrie de type C_1 de DEIRMENDJANN (1969), pour un rayon critique de $0,8 \mu$, à une longueur d'onde de $0,8 \mu$; l'indice des particules est $n = 1,44$; l'albédo continu est $\omega_c = 0,9997$; les directions d'incidence et d'observation correspondent à $\mu = \mu_0 = 0,866$ ($\phi = \phi_0 = 0$). Les pénétrations $\bar{t}(\lambda)$ qui s'en déduisent sont présentées figure (4). Pour les obtenir à partir de l'équation (20), il a fallu calculer les fonctions $p(\lambda, t)$ et donc les distributions $f_t(\lambda)$ pour un assez grand nombre de valeurs de τ . Cette méthode de calcul de la pénétration moyenne est donc longue et pénible ; de plus, les risques de propagation d'erreur sont assez grands dans la mesure où $p(\lambda, t)$ représente la différence de deux fonctions obtenues par inversion de la transformée de Laplace.

Dans la pratique, nous calculons le chemin optique moyen associé à une pénétration jusqu'à une profondeur optique donnée :

$$\bar{\lambda}(t) = \frac{\int_0^\infty \lambda p(\lambda, t) d\lambda}{\int_0^\infty p(\lambda, t) d\lambda} \quad (22)$$

De la définition (15) de $p(\lambda, t)$ avec (17), il suit immédiatement que

$$\bar{\lambda}(t) = \frac{d}{dt} \left[\int_0^\infty \lambda f_t(\lambda) d\lambda \right] \left[\frac{dI(\omega_c, 0, t)}{dt} \right]^{-1} I(\omega_c),$$

soit, compte tenu de (12) et (7)

$$\bar{\lambda}(t) = \frac{d}{dt} \left[\langle \lambda_t \rangle I(\omega_c, 0, t) \right] \left[\frac{dI(\omega_c, 0, t)}{dt} \right]^{-1}, \quad (23)$$

ou encore

$$\bar{\lambda}(t) = - \frac{d}{dt} \left[\frac{d}{dr} I(r, t) \right]_{r=0} \left[\frac{dI(\omega_c, 0, t)}{dt} \right]^{-1} \quad (24)$$

Les chemins optiques moyens $\langle \lambda_t \rangle$ étant des quantités intégrées peuvent être obtenus avec précision même si $f_t(\lambda)$ est connu de manière très approximative ; le calcul de $\bar{\lambda}(t)$ est donc beaucoup plus précis que celui de $\bar{t}(\lambda)$.

Les fonctions de distribution normalisées $f_t(\lambda)$ n'étant connues que pour des valeurs discrètes de t , on utilise pour calculer $\bar{\lambda}(t)$ l'expression approximative équivalente

$$\bar{\lambda}(\tau, \tau') = \frac{I(\omega_c, 0, \tau') \langle \lambda_{\tau'} \rangle - I(\omega_c, 0, \tau) \langle \lambda_{\tau} \rangle}{I(\omega_c, 0, \tau') - I(\omega_c, 0, \tau)} \quad (25)$$

immédiatement déduite de (23) et qui exprime alors le chemin optique moyen associé à la pénétration dans une couche diffusante finie et localisée entre les profondeurs optiques τ et τ' . Une telle approximation est en général suffisante lorsque $\tau' - \tau$ est de l'ordre de 1 ou 2.

Il y a une très bonne corrélation entre la pénétration moyenne $\bar{t}(\lambda)$ et le chemin moyen associé à une pénétration donnée $\bar{\lambda}(t)$. Dans le cas du nuage de particules monodispersées ($\alpha=2$), nous avons déjà trouvé $\bar{t}(50) \sim 9,0$ et $\bar{t}(87) \sim 12,7$ alors que la relation (25) permet d'obtenir $\bar{\lambda}(9) \sim 49$ et $\bar{\lambda}(12,7) \sim 86$.

L'examen de la figure (4) permet aussi de vérifier cette corrélation puisque nous y avons tracé la fonction inverse $\bar{\lambda}(t)$, où $\lambda(t)$ est calculé d'après (25).

Nous pourrions donc raisonnablement supposer que $\bar{t}(\lambda)$ est la fonction inverse $\bar{\lambda}^{-1}(t)$, soit

$$\begin{aligned}\bar{t}(\bar{\lambda}(t)) &= t \\ \bar{\lambda}(\bar{t}(\lambda)) &= \lambda\end{aligned}\quad (26)$$

La profondeur de pénétration sera donc implicitement déterminée par l'intermédiaire des relations (26) et, (25) ou (24).

Le trajet réel suivi par les photons à l'intérieur d'un nuage ne dépend que du nombre de particules diffusantes et de leurs caractéristiques, il est donc indépendant de l'absorption. Il semble raisonnable d'admettre qu'en l'absence d'absorption, les photons qui ont au total parcouru le chemin moyen associé à une pénétration jusqu'à la profondeur optique t ont effectivement pénétré jusqu'à une profondeur voisine de t . En présence d'absorption, le trajet réellement suivi par les photons n'est nullement modifié, la profondeur de pénétration $\bar{t}(\lambda)$ est donc indépendante de l'absorption, mais puisque la distribution des photons qui ont parcouru le chemin optique λ dans un nuage homogène est atténuée du facteur $\exp(-r\lambda)$, le chemin moyen $\bar{\lambda}(t)$ associé à une pénétration jusqu'en t dépend de la fréquence ; les photons qui ont suivi le chemin le plus long étant les plus atténués. L'approximation (26) sera donc utilisée en calculant $\bar{\lambda}(t)$ pour une absorption très faible.

Pratiquement, le calcul de $\bar{\lambda}(t)$ au moyen de l'expression (25) reste assez long puisqu'il nécessite le calcul du chemin optique moyen pour des couches d'épaisseur optique croissante. Pour obtenir ces quantités, il faut auparavant calculer l'intensité réfléchie pour des directions (μ, ϕ) et (μ_0, ϕ_0) considérées, pour plusieurs valeurs de l'albédo de diffusion ω_0 et ceci pour chaque épaisseur optique. Il serait donc intéressant d'obtenir une expression approximative plus simple de $\bar{\lambda}(t)$, ce qui serait possible à partir de l'expression exacte (24) à la condition de connaître l'intensité sous la forme d'une fonction dépendant explicitement de l'épaisseur optique t de la couche considérée et de la variable r , c'est-à-dire de l'albédo de diffusion simple ω . Seules les méthodes approximatives de résolution de l'équation de transfert ont pour résultat des formules analytiques simples bien adaptées à ce genre de problème.

En utilisant la méthode du noyau exponentiel (WANG, 1972) étendu au cas des couches finies (HERMAN, 1973) une expression approximative simple de $\bar{\lambda}(t)$ peut être obtenue (FOUQUART, 1975). Dans le cas des grandes profondeurs optiques et lorsque $1 - \omega_c \ll 1$ cette expression se simplifie et l'on obtient

$$\bar{\lambda}(t) = \{(b^2 - a\beta_1) / 3a\} t^2 \quad (27)$$

avec les conditions $t \gg 1$ et $t \ll (1 - \omega_c)^{-1/2}$ où $b = 3/2$, $a = 3/4$ et β_1 est le premier coefficient du développement de la fonction de diffusion en polynômes de Legendre.

VI - APPLICATION A L'INTENSITE REFLECHIE PAR UN NUAGE INHOMOGENE

A partir des notions définies dans les paragraphes précédents, il est possible de calculer approximativement l'intensité réfléchie par une couche diffusante dans laquelle l'absorption augmente avec la profondeur optique.

A chaque chemin optique λ , est associée une couche (comprise entre 0 et $\bar{t}(\lambda)$) dans laquelle les photons correspondants ont été réfléchis. Ainsi que nous l'avons remarqué au paragraphe V, l'épaisseur de cette couche ($\bar{t}(\lambda)$) est indépendante de l'absorption par les gaz, mais le nombre des photons réfléchis est atténué par un facteur $\exp(-k_v \lambda / (\sigma + k_v))$ où k_v est le coefficient d'absorption du gaz. Dans le cas où k_v est fonction de la profondeur optique, les photons qui ont parcouru un chemin optique λ , ayant en moyenne pénétré jusqu'en $\bar{t}(\lambda)$ ont subi une absorption caractéristique de la couche comprise entre 0 et $\bar{t}(\lambda)$. On peut alors écrire que leur probabilité de sortie est atténuée du facteur $\exp(-k_v(\bar{t}(\lambda))\lambda / (\sigma + k_v))$ où \bar{t}_λ représente la profondeur optique efficace, comprise entre 0 et $\bar{t}(\lambda)$ et évidemment fonction de λ .

Le chemin optique réellement suivi par les photons entre deux niveaux consécutifs t et $t + dt$ n'étant pas connu, nous ne pouvons obtenir qu'une valeur très approximative de \bar{t}_λ . Cependant pour les photons qui pénétrèrent modérément à l'intérieur du nuage, le chemin moyen de pénétration $\lambda(t)$ est proportionnelle à t^2 (équ. 27) ; il en résulte que $(d\bar{\lambda}(t)/dt) dt \approx 2t dt$ représente le chemin moyen parcouru dans la couche comprise entre t et $t + dt$. Ce chemin est maximum autour de la profondeur de pénétration (t maximum) ; de plus nous considérons le cas où l'absorption croît avec la profondeur optique ; les photons les plus absorbés sont donc les plus pénétrants et la profondeur optique efficace \bar{t}_λ doit être assez voisine de $\bar{t}(\lambda)$.

Si, dans tout le nuage, l'absorption étant constante et égale, à celle qui règne au sommet ($k_v(t) \equiv k_v(t=0) = k_0$) les photons parcoureraient en moyenne le chemin optique $\langle \lambda_0 \rangle$, soit

$$\langle \lambda_0 \rangle = \int_0^\infty p(\lambda) \exp(-r_0 \lambda) d\lambda / \int_0^\infty p(\lambda) \exp(-r_0 \lambda) d\lambda, \quad (28)$$

où $p(\lambda)$ a été calculé pour le continu ω_c , et $r_0 = k_0 / (\sigma + k_0)$.

Ces photons pénétreraient jusqu'à une profondeur optique voisine de $\bar{t}(\langle \lambda_0 \rangle)$. Si, dans tout le nuage, l'absorption était celle qui règne à cette profondeur ($k_v(t) \equiv k_v(\bar{t}(\langle \lambda_0 \rangle)) = k_1$) les photons parcoureraient en moyenne $\langle \lambda_1 \rangle$ calculé pour $r_1 = r(k_1)$ et pénétreraient jusqu'à $\bar{t}(\langle \lambda_1 \rangle)$. Intuitivement,

l'absorption a essentiellement affecté les photons dont la profondeur de pénétration est comprise entre $t(<\lambda_0>)$ et $t(<\lambda_1>)$, c'est donc dans cette zone que se trouve la profondeur efficace que nous recherchons. Compte-tenu du rôle prépondérant joué par les couches les plus profondes, nous pouvons raisonnablement identifier la profondeur optique efficace à la profondeur de pénétration d'un nuage homogène équivalent pour lequel la distribution $p(\lambda)$ ainsi que la profondeur $t(\lambda)$ peuvent être connues

$$t_v^* = t(<\lambda(\tau_v^*)>). \quad (29)$$

Cette relation définit implicitement la profondeur optique efficace qui s'obtient par un calcul itératif simple : initialement $t = 0$ et donc $\omega = \omega(t=0)$, la première itération donne $t_1 = t(<\lambda_0>)$ et $\omega(t_1)$; la deuxième itération donne $t_2 = t(<\lambda_1>)$, etc... La convergence est rapide.

L'intensité réfléchie est donc, à la fréquence ν

$$I(\omega_v, 0, \tau) = I(\omega_c, 0, \tau) \int_0^\infty p(\lambda) \exp(-\tau(t_v^*)\lambda) d\lambda. \quad (30)$$

La méthode que nous proposons est arbitraire et si elle ne semble pas déraisonnable, nous n'en avons pas pour autant trouvé de véritable justification ; cependant elle donne, dans l'ensemble, de très bons résultats.

Tests et comparaisons

En diffusion isotrope, pour un milieu semi-infini et lorsque l'albédo décroît avec la profondeur optique suivant la loi $\omega(t) = \omega_0 e^{-st}$, CHAMBERLAIN et Mc ELROY (1966) ont calculé la profondeur optique efficace au moyen d'une méthode fort différente qui utilise l'expression approximative des fonctions H (VAN DE HULST, 1952), (CHANDRASEKHAR, 1950) lorsque $1 - \omega < 1$. Leur solution, lorsque t^* est faible, $(1-\omega)^{1/2} \ll 1$ et $s \ll 1-\omega$ s'écrit

$$t_c^* = 2^{-1} \{3(1-\omega(t_c^*))\}^{-1/2} \quad (31)$$

Il est d'autre part, possible de calculer exactement l'intensité réfléchie par un nuage inhomogène par la méthode des Ordres Successifs de Diffusion (FOUQUART, 1971), (DUMME, 1974), cependant ceci n'est possible que pour un milieu d'épaisseur optique finie. Lors des tests effectués, l'albédo maximum étudié étant de 0,999, nous avons fixé l'épaisseur optique totale $\tau_1 = 40$. Dans le cas homogène et si $\omega = 0,999$, cette épaisseur optique permet d'obtenir l'intensité réfléchie par une couche semi-infinie à moins de 1 % près. Les tableaux (2), (3) et (4) permettent de comparer les intensités obtenues à partir de la méthode que nous proposons aux résultats de CHAMBERLAIN et aux résultats exacts pour diverses valeurs de ω_0 et s .

D'une façon générale, notre méthode s'avère plus précise que celle de CHAMBERLAIN bien que toutes deux donnent de bons résultats. L'erreur maximum atteint 11 % dans le cas de l'incidence la plus faible ($\mu = 0,125$) et pour $s = 0,1$ pour la méthode de CHAMBERLAIN et reste inférieure à 7 % pour notre méthode ($\omega_0 = 0,999$) ; dans le cas où l'inhomogénéité est faible ($s = 0,001$) l'erreur reste inférieure à 1,5 % pour CHAMBERLAIN et à 0,5 % dans notre cas.

Il faut remarquer, à ce sujet, que la méthode de CHAMBERLAIN est essentiellement valable dans les cas de faible inhomogénéité ce qui explique l'erreur enregistrée pour $s = 0,1$. D'autre part, cette méthode ne s'applique, théoriquement, qu'aux milieux d'épaisseur optique infinie, ceci peut expliquer le fait que dans le cas où $s = 0,001$, l'erreur augmente lorsque ω_0 croît, l'épaisseur optique utilisée dans les Ordres Successifs pour approximer un milieu semi-infini est sans doute trop faible et l'erreur de 1,5 % pour $\omega_0 = 0,999$ est de l'ordre de grandeur de la précision des Ordres Successifs.

Nous avons effectué un test dans le cas d'un nuage composé de particules de paramètre de MIE $\alpha = 2\pi r/\lambda = 2$ et d'épaisseur optique $\tau = 20$. La variation de ω en fonction de la profondeur optique est $\omega(t) = \omega_0 e^{-st}$ où $s = 0,001$. Les résultats sont présentés au tableau (5) ; l'erreur maximum (1,7 %) est atteinte pour $\mu = 0,368$, $\omega = 0,999$, mais il faut remarquer que l'expression approximative (27) de la profondeur de pénétration que nous avons utilisée dans ce calcul ne tient pas compte des directions d'incidence et de réflexion μ_0 et μ dont l'effet n'est pas entièrement négligeable pour les faibles valeurs de λ ; la méthode étant très empirique et très approximative, on peut considérer que la précision obtenue reste bonne.

Tableau 2

Intensité réfléchie par un nuage isotrope inhomogène $\omega(t) = \omega_0 e^{-st}$ $\mu_0 = -1$
 Epaisseur optique totale $\tau = 40$ $s = 0,001$

ω_0	$\mu = 0,982$			$\mu = 0,587$			$\mu = 0,125$		
	Exact	C(*)	Formule (29)	Exact	C(*)	Formule (29)	Exact	C(*)	Formule (29)
0,999	0,797	0,784	0,797	0,792	0,779	0,794	0,710	0,700	0,714
0,998	0,784	0,774	0,784	0,781	0,771	0,783	0,703	0,694	0,707
0,997	0,771	0,764	0,772	0,771	0,762	0,773	0,696	0,689	0,700
0,996	0,759	0,754	0,761	0,761	0,754	0,763	0,690	0,683	0,693
0,995	0,749	0,744	0,750	0,752	0,746	0,754	0,684	0,678	0,686
0,994	0,738	0,735	0,740	0,743	0,738	0,745	0,678	0,672	0,680
0,993	0,728	0,726	0,730	0,734	0,731	0,736	0,672	0,666	0,674
0,992		0,717	0,720		0,723	0,728		0,663	0,669
0,991		0,709	0,711		0,716	0,721		0,658	0,663
0,99	0,708	0,700	0,703	0,717	0,709	0,713	0,660	0,653	0,658
0,97	0,581	0,579	0,578	0,605	0,602	0,603	0,581	0,579	0,580
0,95	0,502	0,501	0,500	0,533	0,532	0,532	0,514	0,527	0,527
0,93	0,445	0,444	0,443	0,480	0,479	0,479	0,487	0,486	0,486
0,91	0,400	0,400	0,400	0,437	0,436	0,436	0,453	0,452	0,452
0,89	0,364	0,364	0,364	0,401	0,401	0,401	0,423	0,423	0,423

(*) C = Résultats de CHAMBERLAIN

Tableau 3

Intensité réfléchie par un nuage isotrope inhomogène $\omega(t) = \omega_0 e^{-st}$ $\mu_0 = -1$
 Epaisseur optique totale $\tau = 40$ $s = 0,01$

ω_0	$\mu = 0,982$			$\mu = 0,587$			$\mu = 0,125$		
	Exact	C(*)	Formule (29)	Exact	C(*)	Formule (29)	Exact	C(*)	Formule (29)
0,999	0,645	0,638	0,642	0,672	0,655	0,668	0,639	0,616	0,637
0,998	0,639	0,634	0,637	0,667	0,651	0,664	0,635	0,614	0,634
0,997	0,634	0,630	0,632	0,662	0,648	0,659	0,632	0,611	0,631
0,996	0,629	0,625	0,628	0,657	0,644	0,655	0,628	0,608	0,627
0,995	0,624	0,621	0,623	0,653	0,640	0,651	0,625	0,606	0,624
0,994	0,619	0,617	0,619	0,648	0,637	0,647	0,622	0,603	0,621
0,993	0,615	0,613	0,614	0,644	0,633	0,642	0,618	0,601	0,618
0,992	0,609	0,609	0,610	0,639	0,629	0,638	0,615	0,598	0,615
0,991	0,605	0,605	0,606	0,635	0,626	0,634	0,612	0,596	0,612
0,99	0,601	0,601	0,601	0,631	0,622	0,630	0,609	0,593	0,609
0,97	0,523	0,524	0,527	0,559	0,557	0,561	0,554	0,546	0,554
0,95	0,466	0,470	0,470	0,504	0,504	0,506	0,511	0,505	0,511
0,93	0,420	0,424	0,424	0,459	0,459	0,461	0,475	0,471	0,475
0,91	0,382	0,386	0,385	0,421	0,422	0,423	0,444	0,441	0,444

(*) C = Résultats de CHAMBERLAIN

Tableau 4

Intensité réfléchie par un nuage isotrope inhomogène $\omega(t) = \omega_0 e^{-st}$ $\mu_0 = -1$
 Epaisseur optique totale $\tau = 40$ $s = 0,1$

ω_0	$\mu = 0,982$			$\mu = 0,587$			$\mu = 0,125$		
	Exact	$(*)_C$	Formule (29)	Exact	$(*)_C$	Formule (29)	Exact	$(*)_C$	Formule (29)
0,999	0,394	0,398	0,396	0,454		0,442	0,505	0,451	0,476
0,998	0,393	0,397	0,394	0,453		0,441	0,504	0,450	0,475
0,997	0,392	0,396	0,393	0,451		0,440	0,502	0,449	0,474
0,996	0,390	0,395	0,392	0,449		0,439	0,501	0,448	0,473
0,995	0,389	0,393	0,391	0,448		0,438	0,499	0,447	0,472
0,994	0,387	0,392	0,390	0,446		0,436	0,498	0,446	0,471
0,993	0,386	0,391	0,389	0,445		0,435	0,497	0,445	0,469
0,992	0,384	0,390	0,388	0,443		0,434	0,495	0,444	0,468
0,991	0,383	0,388	0,386	0,442		0,433	0,494	0,443	0,467
0,99	0,382	0,387	0,385	0,440		0,432	0,492	0,442	0,466
0,97	0,356	0,364	0,363	0,412		0,409	0,466	0,423	0,444
0,95	0,332	0,342	0,343	0,386		0,387	0,441	0,405	0,424
0,93	0,311	0,322	0,323	0,363		0,366	0,418	0,387	0,404
0,91	0,292	0,303	0,305	0,342		0,346	0,397	0,370	0,386

$(*)_C$ = Résultats de CHAMBERLAIN

Tableau 5

Intensité réfléchie par un nuage inhomogène de particules monodispersées ($\alpha=2$)

$\omega(t) = \omega_0 e^{-st}$ $s = 0,001$ $\mu_0 = -1$
 Epaisseur optique totale $\tau = 20$

ω_0	$\mu = 0,987$		$\mu = 0,368$	
	Exact	Formule (29)	Exact	Formule (29)
0,999	0,695	0,690	0,580	0,571
0,998	0,677	0,673	0,568	0,559
0,997	0,659	0,658	0,556	0,548
0,996	0,643	0,643	0,545	0,538
0,995	0,628	0,628	0,534	0,528
0,994	0,614	0,614	0,524	0,519
0,993	0,599	0,601	0,514	0,510
0,992	0,586	0,588	0,505	0,501
0,991	0,573	0,576	0,496	0,492
0,99	0,561	0,564	0,488	0,484
0,98	0,463	0,468	0,418	0,417
0,97	0,394	0,398	0,367	0,366

REFERENCES

- APPLEBY J.F. and IRVINE W.M., 1973, "Path Length Distributions of Photons Diffusely Reflected from a Semi-Infinite Atmosphere", *Astroph. J.*, 183, p 337.
- BELLMAN R., KALABA R.E. and LOCKETT J.A., 1966, "Numerical Inversion of the Laplace Transform", New-York.
- CHAMBERLAIN J.W. and Mc ELROY M.B., 1966, "Diffuse Reflection by an Inhomogeneous Planetary Atmosphere", *Astroph. J.*, 144, p 1148.
- CHANDRASEKHAR S., 1950, "Radiative Transfer", Clarendon Press, Oxford.
- DEIRMENDJANN D., 1969, "The Electromagnetic Scattering of Spherical Polydispersions", Elsevier, New-York.
- DEUZE J.L., 1974, "Etude de la polarisation du rayonnement par les milieux diffusants ; Application à la polarisation localisée de Vénus", Thèse de Spécialité, Université des Sciences et Techniques de Lille.
- FOUQUART Y., 1971, "Effet de la diffusion sur l'échauffement radiatif dû au rayonnement solaire", *Jl. Quant. Spectros. Radiat. Transfer*, 11, p 709.
- FOUQUART Y., 1974, "Utilisation des Approximants de Padé pour l'étude des largeurs équivalentes des raies formées en atmosphère diffusante", *Jl. Quant. Spectros. Radiat. Transfer*, 14, p 497.
- FOUQUART Y., 1975, "Contribution à l'étude des spectres réfléchis par les atmosphères planétaires diffusantes ; Application à Vénus", Thèse, Université des Sciences et Techniques de Lille.
- FOUQUART Y. et LENOBLE J., 1973, "Formation des raies spectrales et étude des courbes de croissance dans une atmosphère diffusante semi-infinie", *Jl. Quant. Spectros. Radiat. Transfer*, 13, p 447.
- FOUQUART Y. and PRUVOST P., 1974, "Accurate Computations of Fluxes and Heating Rates in Case of Cloudy Atmospheres", First I.A.M.A.P. - I.A.P.S.O. Conjugued Assembly, Melbourne.
- HEINRICH M., 1973, "Transmission, Reflection by Clouds Under Consideration of Droplet and Band absorption", Proceedings of the International Radiation Symposium, Sendai, Japon, p 88.
- HERMAN M., DEVAUX C. et BIGOURD C., 1973, "Albedos plan et sphérique - Extension de la méthode de Wang", Rapport Interne, Laboratoire d'Optique Atmosphérique, Université des Sciences et Techniques de Lille.
- IRVINE W.M., 1964, "The Formation of Absorption Bands and the Distribution of Photon Optical Paths in a Scattering Atmosphere", *B.A.N.*, 17, p 266.
- KARGIN B.A., KRASNOKUTSKAYA L.D. and FEYGEL'SON YE.M., 1972, "Reflection and Absorption of Solar Radiant Energy by Cloud Layers", *Bull. (Izv.) Acad. Sc. USSR*, 8, p 287.
- LENOBLE J., 1975, "Méthodes pour résoudre l'équation de transfert radiatif dans des couches d'épaisseur finie", AGARD Conference Proceedings on Optical Propagation in the Atmosphere, p 12-1.
- UESUGI A. and IRVINE W.M., 1970 a, "Multiple Scattering in a Plane-Parallel Atmosphere : I - Successive Scattering in a Semi-Infinite Medium", *Astroph. J.*, 159, p 127.
- UESUGI A. and IRVINE W.M., 1970 b, "Multiple Scattering in a Plane-Parallel Atmosphere : II - Curves of Growth for Reflection Spectra", *Astroph. J.*, 161, p 243.
- VAN DE HULST H.C., 1952, "The Atmosphere of the Earth and Planets", ed. G. KUIPER, Chicago University Press, Chap. III.
- VAN DE HULST H.C., 1970, "High-Order Scattering in Diffuse Reflection From a Semi-Infinite Atmosphere", *Astronomy and Astrophysics*, 9, p 374.
- VAN DE HULST H.C. and IRVINE W.M., 1962, "General Report on Radiation Transfert in Planets : Scattering in Model Planetary Atmospheres", *La Physique des Planètes, Congrès et Colloques de l'Université de Liège*, 24, p 78.
- WANG L., 1972, "Anisotropic Nonconservative Scattering in a Semi-Infinite Medium", *Astrophys. J.*, 174, p 671.

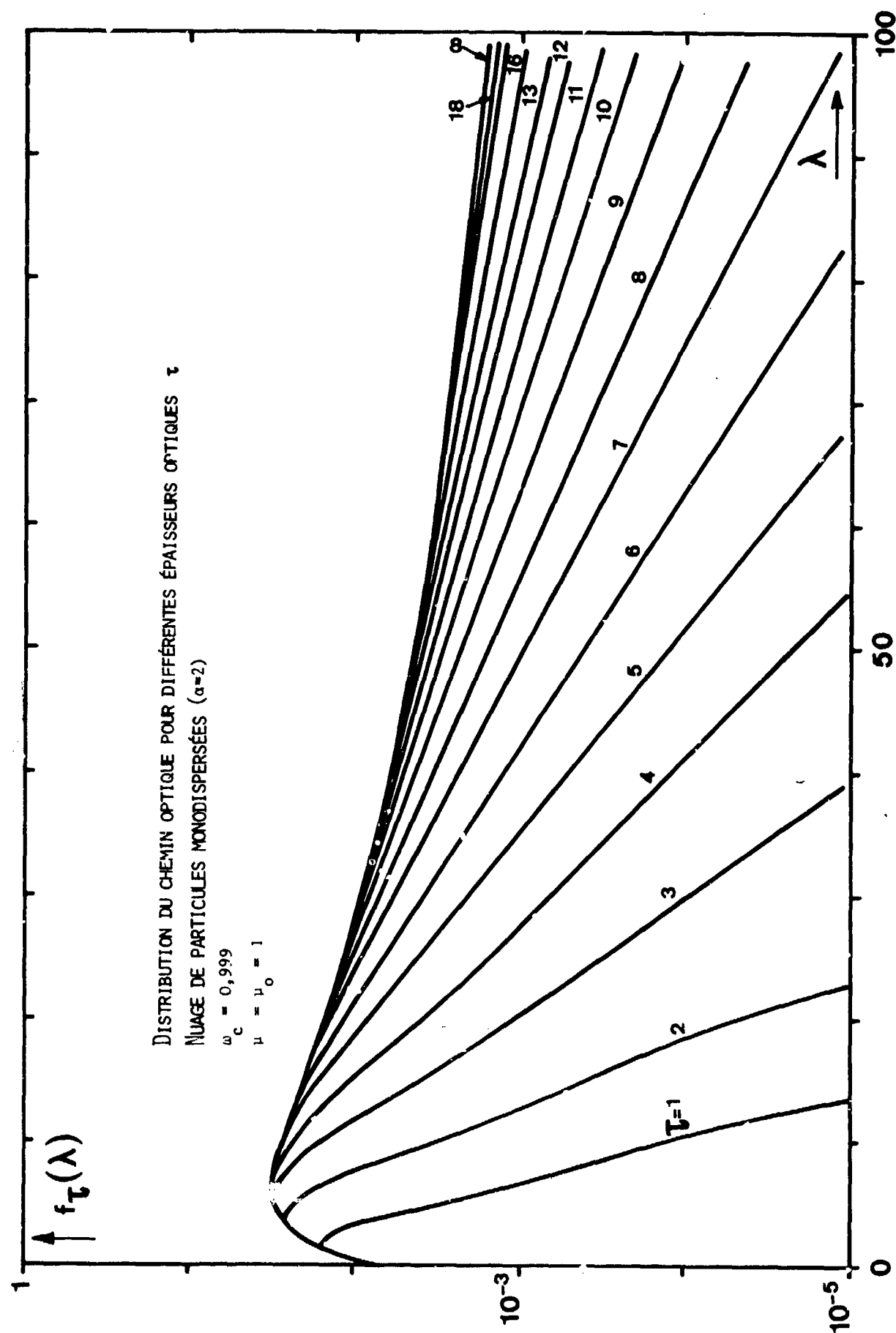


Figure 1

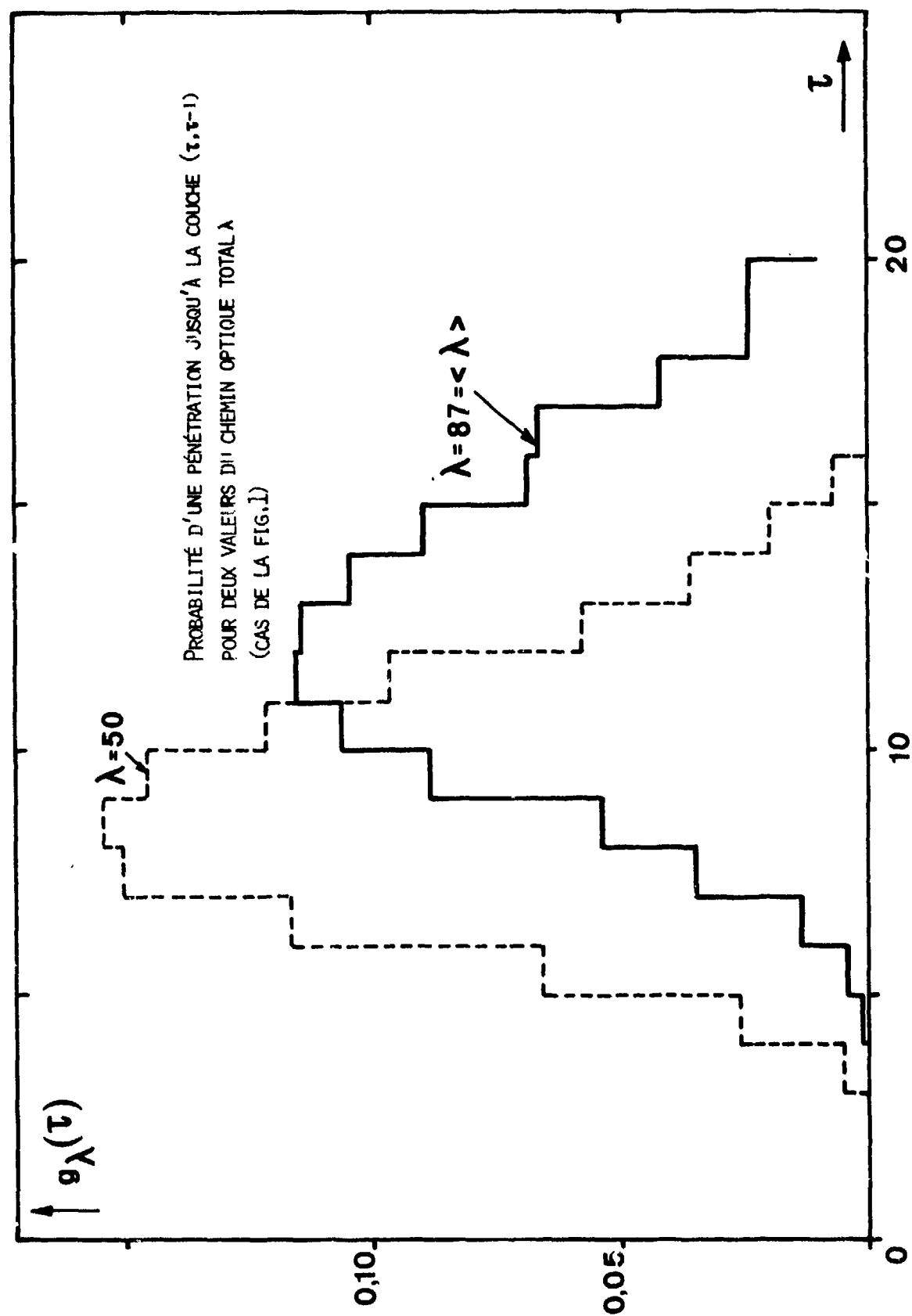


Figure 2

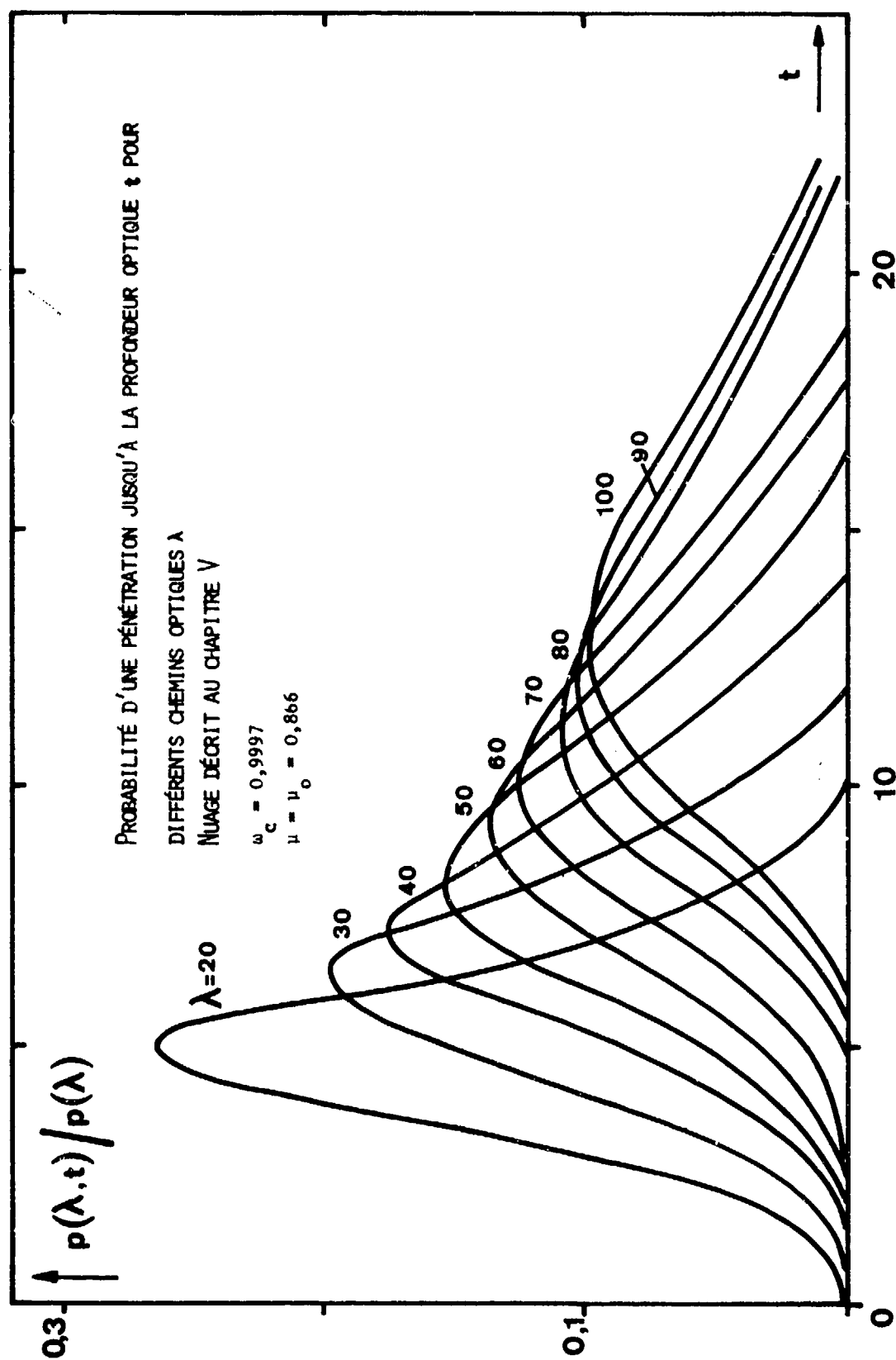


Figure 3

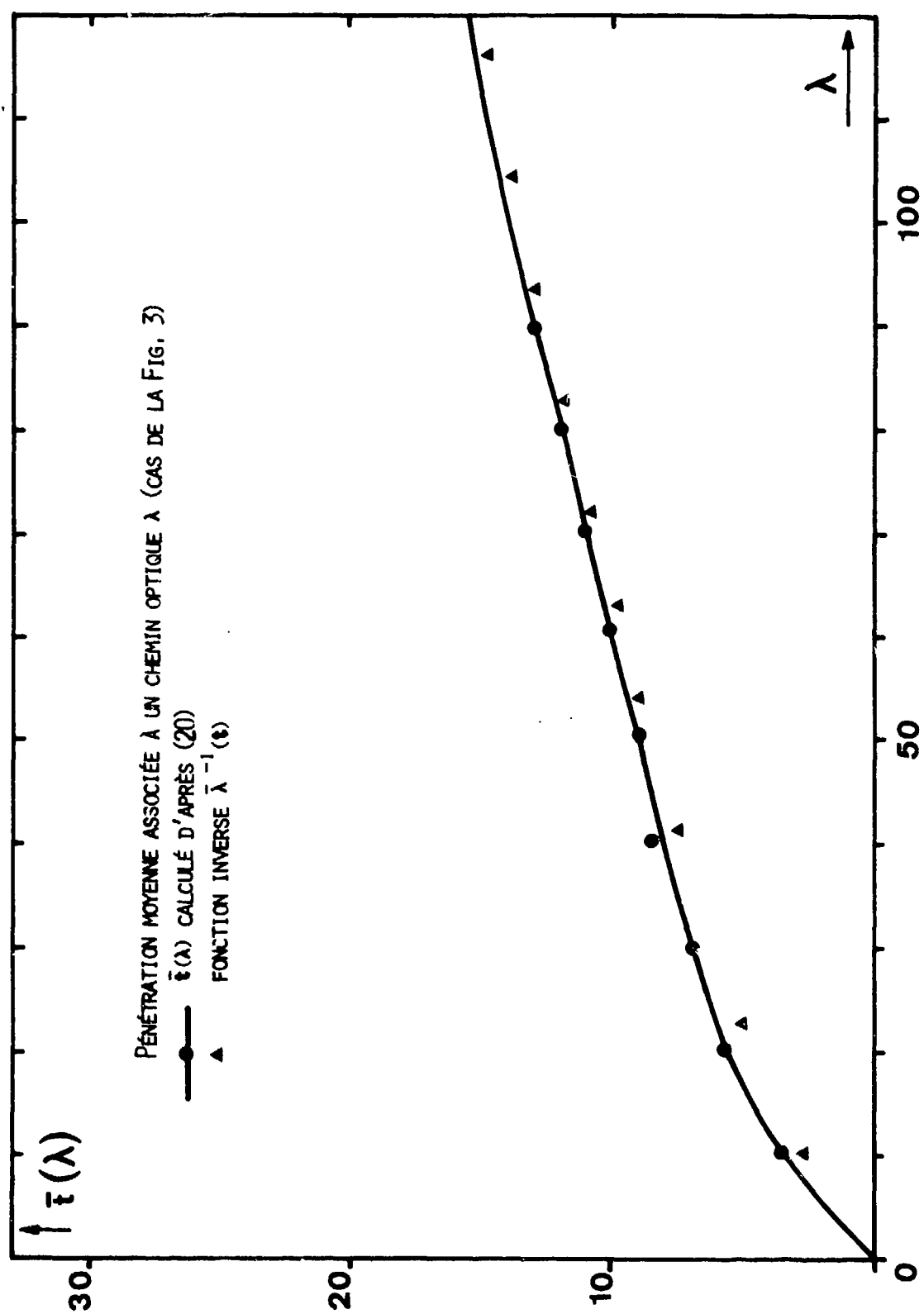


Figure 4

FLUORESCENT AND RAMAN SCATTERING IN PARTICLES

M. Kerker, P.J. McNulty and H. Chew
Clarkson College of Technology
Potsdam, N.Y. 13676, U.S.A.

SUMMARY

When inelastically scattering molecules are distributed within a small particle, they respond to the local nonuniform electromagnetic field within the particle. The outgoing inelastic field is obtained by matching at the boundary the dipole field of the emitting molecules plus an internal field with the outgoing field. In this way, it is possible to express the inelastic radiances in terms of the geometry and optical properties of the particle, of the distribution of inelastically scattering molecules within the particle, and of the molecular polarizability, for both coherent and incoherent scattering.

1. INTRODUCTION

Radiant energy absorbed by small particles is often degraded to heat and in the atmosphere this will affect the transport of solar radiation and ultimately the climate. In addition, the particle itself may be impelled to move. The origin of such motion lies in the nonuniform electromagnetic field within the particle which in turn results in nonuniform generation of heat and in a steady state nonuniform temperature distribution at the surface (KERKER and COOKE, 1973). In space, this will give rise to a contribution to the radiation pressure which has heretofore been overlooked, and in the atmosphere there will be a radiometric force which will move the particle, a motion termed photophoresis (KERKER, 1974).

The same nonuniform electromagnetic field within the particle may excite molecular transitions if appropriate species are present. This will result in emission at frequencies other than that of the incident radiation. Fluorescent and Raman scattering are examples of such transitions. In this paper, we pose the following questions: How does such inelastic scattering depend upon the particle geometry and refractive index? How does it depend upon the distributions of inelastically scattering molecules within the particle?

There are a number of areas where these questions arise. For example, the particle may be a biological cell which has been tagged with fluorescent molecules that attach to the DNA, the cytoplasm, or the cell membrane. The fluorescence can then be used to monitor specific cell functions or in cell identification and sorting systems. (BONNER *et al.*, 1972; YATANGAS and CLARKSON, 1974).

As another example, atmospheric aerosols may fluoresce (GELBWACHS and BIRNBAUM, 1973) and this might be used to provide a means for chemical identification of ambient aerosols and to measure aerosol content in the atmosphere. Also, Raman and fluorescent backscattering are used for remote sensing of molecular species in the atmosphere. If the broadband fluorescence signals of the aerosol constituent should fall in the detection band for the Raman scattering or fluorescence of the free molecules, this will interfere with LIDAR determinations based upon these interactions.

2. MODEL FOR FLUORESCENT AND RAMAN SCATTERING BY MOLECULES EMBEDDED IN PARTICLES

The point of view here is classical. The local exciting field within the particle and the angular distribution of the emitted radiation depend strongly upon the particle geometry and refractive index. The molecular transitions depend only on the local field.

The model is depicted in Fig. 1. If an electromagnetic wave of angular frequency ω_0 is incident on a particle, the scattered radiation will consist of an elastic part (at angular frequency ω_0) and an inelastic part at other frequencies. We consider here only inelastic scattering which arises from molecular transitions and omit consideration of quasielastic Brillouin scattering. The electromagnetic field inside the particle likewise consists of a transmitted field (at frequency ω_0) and secondary fields at other frequencies.

The solution for the elastically scattered field is obtained by matching the transmitted field with the external field (sum of incident and scattered field) at the boundary. The scattering cross section is obtained by summing over the scattered radiances and the absorption cross section is obtained from an energy balance or from the "extinction theorem". (See KERKER, 1969, where earlier references to the work of Lorenz, Love, Mie, Debye, et al. are cited.)

We now turn to the matter of inelastic scattering by molecules within the particle. These may be distributed as an admixture or as a solid solution or they may comprise the particle completely. The molecular transitions are excited by the local electromagnetic field just as if the molecules were in the bulk material; the quantum mechanical processes are not affected by the particle boundary. Accordingly, the emission at a particular frequency (ω) will be proportional to the localized absorption at the exciting frequency (ω_0).

This leads directly to a comparison between the inelastic scattering by a particulate system and that for the same volume of substance in the bulk. Of course, now we restrict the system to a uniform distribution of inelastically scattering molecules. The ratio for inelastic scattering will be the same as the ratio of absorption of electromagnetic radiation at the exciting frequency in the particulate system relative to the absorption in the bulk and is given by (KERKER, 1973)

$$\eta = C_{\text{abs}}/kl \quad (1)$$

where C_{abs} is the absorption cross section of the particle, k is the bulk absorption coefficient of the substance and l is the thickness if the particle were to be smeared out as a thin layer of unit cross sectional area.

The effect can be illustrated by consideration of a spherical particle that is small compared with the wavelength; then Rayleigh's law holds and

$$\eta = (-1.5/nk) \text{Im} [(m^2 - 1) (m^2 + 2)] \quad (2)$$

where nk is the imaginary part of the complex refractive index m and Im denotes the imaginary part of the expression which follows it. The magnitude of the effect is illustrated in the following table:

Table 1*

m	η
1.29 - 0.01i	.87
1.50 - 0.01i	.75
2.00 - 0.01i	.50
2.20 - 0.01i	.42
3.00 - 0.01i	.22

* The values of η tabulated in M. Kerker (1973) are each in error by the factor $1/n$.

Obviously there would be gross errors if the volume of fluorescent material were to be estimated without taking into account the effect of the particulate nature of the sample.

This model can be articulated in more detail to answer the questions raised at the beginning of this paper. The inelastically scattered field will be expressed in terms of the geometrical and optical properties of the particle, of the distribution of inelastically scattering molecules within the particle and of the polarizability of these molecules. The emission at any location within the particle is characterized by the field of an induced dipole at this location whose moment is given by the effective polarizability (a tensor in general) multiplying the transmitted electric field. The polarizability must be known from studies of the substance in the bulk and from the distribution of the active molecules within the particles. The transmitted field is known from the elastic scattering problem (KERKER and COOKE, 1973) so that the induced dipole and its field can be expressed in terms of known parameters. In addition, there will be an internal field due to the particle boundary and outside of the particle there is the outgoing field at this frequency. The outgoing field can be determined in terms of the dipole field by the standard boundary conditions which state that a frequency ω , the tangential components of the field vectors within the particle (dipole plus internal field) and outside must be continuous at the boundary.

For an arbitrary distribution of inelastically scattering species within the particle, the result can be obtained by superposition. For coherent scattering the fields arising from different locations within the particle must be added; for incoherent scattering the radiances must be added.

3. RESULTS

The detailed analysis has been presented elsewhere (KERKER et al., 1976). Here we write down the principle results. The notation is that of Jackson (1962), except for the vector spherical harmonics $\vec{Y}_{j\ell m}$ which are written in the notation of Edmonds (1957).

Consider an induced dipole \vec{p} oscillating at the shifted frequency ω at some arbitrary coordinate \vec{r}' inside a dielectric particle (medium 1). The strength of the dipole is assumed to be a linear function of the components of the transmitted field $\vec{E}_1^0(\vec{r}', \omega_0)$. The vector potential at the coordinate \vec{r} due to this dipole may be written, after suppressing the factor $e^{-i\omega t}$,

$$\begin{aligned}\vec{A}_d &= -ik_1 \vec{p} e^{ik_1 |\vec{r}-\vec{r}'|} / |\vec{r}-\vec{r}'| \\ &= 4\pi k_1^2 \vec{p} \sum_{\ell, m} j_\ell(k_1 r) h_\ell^{(1)}(k_1 r') Y_{\ell m}^*(\hat{r}') Y_{\ell m}(\hat{r}), \quad (3)\end{aligned}$$

where we have used the standard expansion of $e^{ik|\vec{r}-\vec{r}'|} / |\vec{r}-\vec{r}'|$ in terms of spherical harmonics and Bessel functions. The magnetic induction due to this dipole is

$$\begin{aligned}\vec{B}_d &= \nabla \times \vec{A}_d = 4\pi k_1^3 \sum_{\ell, m} j_\ell(k_1 r') h_\ell^{(1)}(k_1 r) \hat{r} \times \vec{p} Y_{\ell m}^*(\hat{r}') Y_{\ell m}(\hat{r}) \\ &\quad + (4\pi i k_1^2 / r) \sum_{\ell, m} j_\ell(k_1 r') h_\ell^{(1)}(k_1 r) \hat{r} \times \vec{p} [\hat{r} \times \vec{Y}_{\ell m}(\hat{r})] \quad (4)\end{aligned}$$

where j_ℓ , $h_\ell^{(1)}$ denote spherical Bessel functions, and $h_\ell^{(1)'}(x) = (d/dx)h_\ell^{(1)}(x)$. We expand this and the corresponding electric field in series of vector spherical harmonics

$$\begin{aligned}\vec{B}_d(\vec{r}) &= \sum_{\ell, m} \{ a_E(\ell, m) h_\ell^{(1)}(k_1 r) \vec{Y}_{\ell \ell m}(\hat{r}) \\ &\quad - (ic/\omega) a_M(\ell, m) \nabla \times [h_\ell^{(1)}(k_1 r) \vec{Y}_{\ell \ell m}(\hat{r})] \} \\ \vec{E}_d(\vec{r}) &= \sum_{\ell, m} \{ (ic/n_1^2 \omega) a_E(\ell, m) \nabla \times [h_\ell^{(1)}(k_1 r) \vec{Y}_{\ell \ell m}(\hat{r})] \\ &\quad + a_M(\ell, m) h_\ell^{(1)}(k_1 r) \vec{Y}_{\ell \ell m}(\hat{r}) \}. \end{aligned} \quad (5)$$

The internal fields due to the particle can be expanded similarly if we replace $h_\ell^{(1)}$ by j_ℓ

$$\begin{aligned}\vec{B}_p(\vec{r}) &= \sum_{\ell, m} \{ b_E(\ell, m) j_\ell(k_1 r) \vec{Y}_{\ell \ell m}(\hat{r}) \\ &\quad - (ic/\omega) b_M(\ell, m) \nabla \times [j_\ell(k_1 r) \vec{Y}_{\ell \ell m}(\hat{r})] \} \\ \vec{E}_p(\vec{r}) &= \sum_{\ell, m} \{ (ic/n_1^2 \omega) b_E(\ell, m) \nabla \times [j_\ell(k_1 r) \vec{Y}_{\ell \ell m}(\hat{r})] \\ &\quad + b_M(\ell, m) j_\ell(k_1 r) \vec{Y}_{\ell \ell m}(\hat{r}) \} \end{aligned} \quad (6)$$

Here and below, n_1 and n_2 denote the indices of refraction of media 1 and 2, respectively. The magnetic induction and electric field inside are given by, respectively,

$$\vec{E}_1(\vec{r}) = \vec{E}_d(\vec{r}) + \vec{E}_p(\vec{r}), \quad \vec{B}_1(\vec{r}) = \vec{B}_d(\vec{r}) + \vec{B}_p(\vec{r}). \quad (7)$$

The scattered fields outside the particle (medium 2) have similar expansions

$$\begin{aligned}\vec{B}_2(\vec{r}) &= \sum_{\ell, m} \{ c_E(\ell, m) h_\ell^{(1)}(k_2 r) \vec{Y}_{\ell \ell m}(\hat{r}) \\ &\quad - (ic/\omega) c_M(\ell, m) \nabla \times [h_\ell^{(1)}(k_2 r) \vec{Y}_{\ell \ell m}(\hat{r})] \} \\ \vec{E}_2(\vec{r}) &= \sum_{\ell, m} \{ (ic/n_2^2 \omega) c_E(\ell, m) \nabla \times [h_\ell^{(1)}(k_2 r) \vec{Y}_{\ell \ell m}(\hat{r})] \\ &\quad + c_M(\ell, m) h_\ell^{(1)}(k_2 r) \vec{Y}_{\ell \ell m}(\hat{r}) \}. \end{aligned} \quad (8)$$

The coefficients $a_E(l, m)$ and $a_M(l, m)$ in Eq. (5) may be obtained from Eq. (4) by using the orthogonal properties of the vector spherical harmonics. The details of this quite lengthy calculation have been given elsewhere. The results may be written

$$\begin{aligned}
 a_E(l, m) &= 2\pi i k_1^3 [l(l+1)(2l+1)]^{-1/2} j_l(k_1 r') \vec{p} \\
 &\quad \cdot [(l+1)(2l-1)]^{-1/2} j_{l-1}(k_1 r') \vec{e}^- \\
 &\quad + l(2l+3)^{-1/2} j_{l+1}(k_1 r') \vec{e}^+ \\
 a_M(l, m) &= -2\pi i k^2 (\omega/c) [l(l+1)]^{-1/2} j_l(k_1 r') \vec{p} \cdot \vec{M}
 \end{aligned} \quad (9)$$

where

$$\begin{aligned}
 \epsilon_x^- &= [(l+m)(l+m-1)]^{-1/2} Y_{l-1, m-1}^*(\hat{r}') \\
 &\quad - [(l-m)(l-m-1)]^{1/2} Y_{l-1, m+1}^*(\hat{r}') \\
 \epsilon_y^- &= -i \{ [(l+m)(l+m-1)]^{1/2} Y_{l-1, m-1}^*(\hat{r}') \\
 &\quad + [(l-m)(l-m-1)]^{1/2} Y_{l-1, m+1}^*(\hat{r}') \} \\
 \epsilon_z^- &= -2 [(l+m)(l-m)]^{1/2} Y_{l-1, m}^*(\hat{r}') \\
 \epsilon_x^+ &= [(l+m+1)(l+m+2)]^{1/2} Y_{l+1, m+1}^*(\hat{r}') \\
 &\quad - [(l-m+1)(l-m+2)]^{1/2} Y_{l+1, m-1}^*(\hat{r}') \\
 \epsilon_y^+ &= i \{ [(l+m+1)(l+m+2)]^{1/2} Y_{l+1, m+1}^*(\hat{r}') \\
 &\quad + [(l-m+1)(l-m+2)]^{1/2} Y_{l+1, m-1}^*(\hat{r}') \} \\
 \epsilon_z^+ &= -2 [(l+m+1)(l-m+1)]^{1/2} Y_{l+1, m}^*(\hat{r}')
 \end{aligned} \quad (10)$$

and

$$\begin{aligned}
M_x &= [(\ell-m)(\ell+m+1)]^{1/2} Y_{\ell,m+1}^*(\hat{r}') \\
&\quad + [(\ell+m)(\ell-m+1)]^{1/2} Y_{\ell,m-1}^*(\hat{r}') \\
M_y &= i\{[(\ell-m)(\ell+m+1)]^{1/2} Y_{\ell,m+1}^*(\hat{r}') \\
&\quad - [(\ell+m)(\ell-m+1)]^{1/2} Y_{\ell,m-1}^*(\hat{r}')\} \\
M_z &= 2m Y_{\ell m}^*(\hat{r}').
\end{aligned} \tag{11}$$

The expansion coefficients $c_E(\ell, m)$ and $c_M(\ell, m)$ for the scattered fields are determined in terms of the coefficients $a_E(\ell, m)$ and $a_M(\ell, m)$ given above by the boundary conditions that the tangential components of $\vec{E}_2(\vec{r})$ and $\vec{H}_2(\vec{r}) = \vec{B}_2(\vec{r})/\mu_2$ be equal to those of $\vec{E}_1(\vec{r})$ and $\vec{H}_1(\vec{r}) = \vec{B}_1(\vec{r})/\mu_1$, respectively, at the surface of the particle. For the important special case when the particle is a sphere of radius a , these boundary conditions give

$$c_E(\ell, m) = \frac{(i\mu_2 n_2^2/k_1 a) a_E(\ell, m)}{\mu_2 n_1^2 j_\ell(k_1 a) [k_2 a h_\ell^{(1)}(k_2 a)]' - \mu_1 n_2^2 h_\ell^{(1)}(k_2 a) [k_1 a j_\ell(k_1 a)]'} \tag{12}$$

$$c_M(\ell, m) = \frac{(i\mu_2/k_1 a) a_M(\ell, m)}{\mu_2 h_\ell^{(1)}(k_2 a) [k_1 a j_\ell(k_1 a)]' - \mu_1 j_\ell(k_1 a) [k_2 a h_\ell^{(1)}(k_2 a)]'} \tag{13}$$

where $[xf(x)]'$ denotes $(d/dx)[xf(x)]$. We have used the properties of the Wronskians of the spherical Bessel functions to simplify the numerators. The scattered fields at large distances are given by replacing $h_\ell^{(1)}(k_2 r)$ by its asymptotic form $(-i)^{\ell+1} e^{ik_2 r}/k_2 r$ in Eq. (8).

4. DISCUSSION

Detailed calculations of the differential scattering cross sections for spherical particles based on this model are in progress. They require extensive computer calculations of the type needed for Mie scattering. These calculations will determine the extent of the deviation between fluorescence and Raman scattering by molecules embedded in small particles and the corresponding cross sections for inelastic scattering by the same molecules in bulk. Only when these corrections can be made can LIDAR techniques be used for quantitative determination of the presence of specific molecules in the atmospheric aerosol.

REFERENCES

- BONNER, W.A., HULETT, H.R., SWEET, R.G., AND HERZENBERG, L.A., 1972, "Fluorescence Activated Cell Sorting", Rev. Sci. Inst. 43, 404.
- EDMONDS, A.R., 1957, Angular Momentum in Quantum Mechanics, Princeton, Princeton, N.J.
- GELBWACHS, J., and BIRNBAUM, M., 1973, "Fluorescence of Atmospheric Aerosols and Lidar Implications", Appl. Opt. 12, 2442.
- JACKSON, J.D., 1962, Classical Electrodynamics, John Wiley and Son, New York.
- KERKER, M., 1974, "Movement of Small Particles by Light", American Sci. 62, 92.
- KERKER, M., 1969, The Scattering of Light and Other Electromagnetic Radiation, Academic Press, New York.
- KERKER, M., and COOKE, D.D., 1973, "Radiation Pressure on Absorbing Spheres and Photophoresis", Appl. Opt. 12, 1378.
- KERKER, M., 1973, "Fluorescence of Aerosols", Appl. Opt. 12, 2787.
- KERKER, M., CHEW, H., and MCNULTY, P.J., 1975, "Fluorescent and Raman Scattering by Molecules Embedded in a Particle", to be published.
- YATANGAS, X., and CLARKSON, B.D., 1974, "Flow Microfluorometric Analysis of Cell Killing with Cytotoxic Drugs", J. Histochem. and Cytochem. 22, 651.

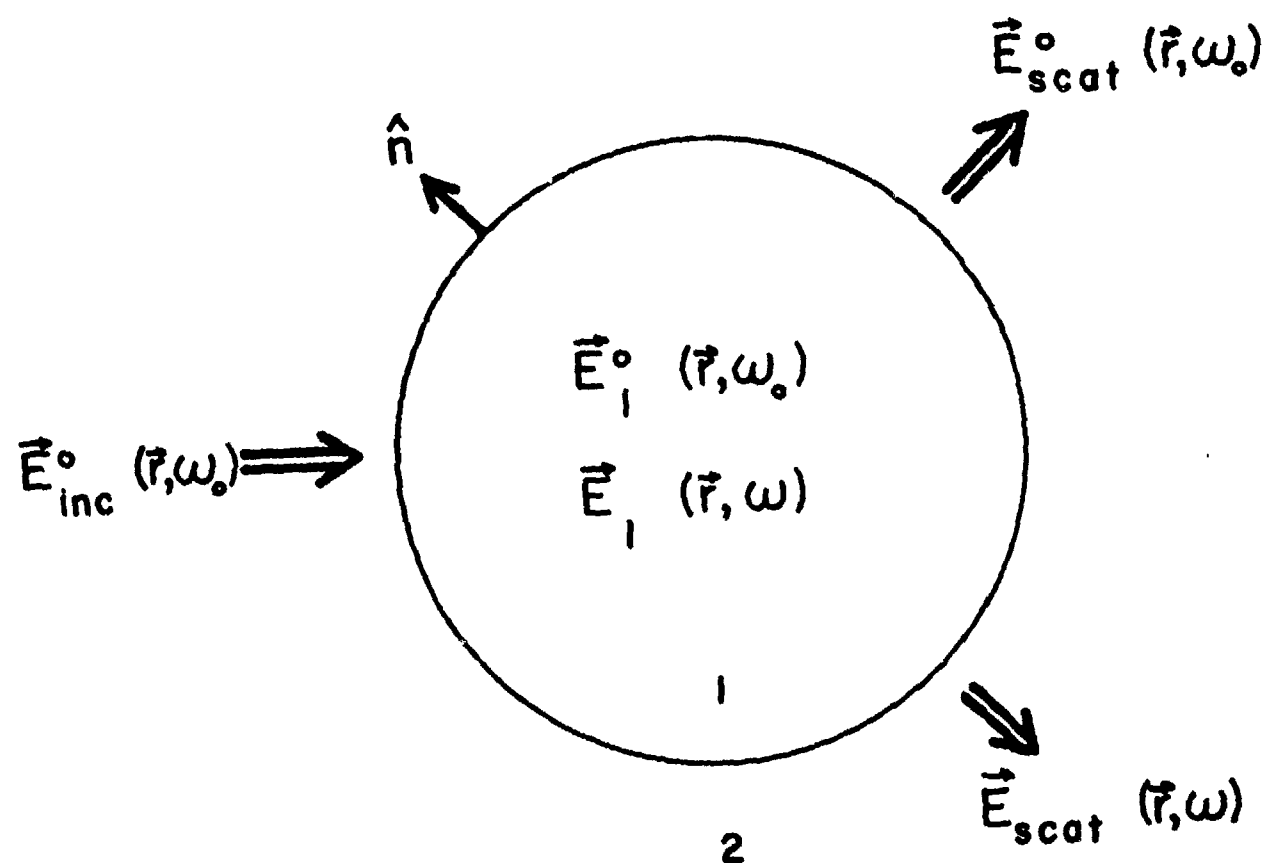


Fig. 1. Electric fields inside and outside the particle. The angular frequencies of the incident and inelastically scattered waves are denoted by ω_0 and ω , respectively.

QUESTIONS AND COMMENTS
ON SESSION II

CALCULATIONS OF POLARIZATION AND RADIANCE IN THE ATMOSPHERE

Mr W.H.Irvine: What form of ocean-atmosphere interface did you consider?

Dr G.N.Plass: We have done calculations for both smooth ocean surface and an ocean with waves. In the latter case we used the Cox-Munk distribution of wave slopes. Each time that a photon struck the ocean-atmosphere interface, a particular slope for the ocean surface was chosen from the Cox-Munk distribution of wave slopes.

Mr R.W.Fenn: There might be some considerable practical use in looking at the wavelength dependence of the polarization of radiation. Have you made any calculation for that?

Dr G.N.Plass: Yes, we have made calculations at several different wave lengths in the visible and near infrared.

METHODS POUR RESOUDRE L'EQUATION DE TRANSFERT RADIATIF DANS DES COUCHES D'EPAISSEUR FINIE

Dr. W. M. Irvine: How does the accuracy of the DART method compare in general to the other methods?

Dr. J. Lenoble: We have comparisons for two or three cases of haze and clouds with albedo for single scattering equal to one and 0.9 and the accuracy seems to remain always of the order of 10%; that means it is less accurate than methods like spherical harmonics and about of the same accuracy as Monte Carlo method.

THEORETICAL STUDIES OF THE TRANSFER OF SOLAR RADIATION IN THE ATMOSPHERE

Dr. W. Edil: Did you make calculations also for atmospheres which are realistic for the European Scenario, as most of the model atmospheres of McClatchey don't seem to fit very well with i. e. German atmospheric conditions?

Dr. M. J. Kerschgens: No we didn't. The only realistic profile we have used so far is the sounding of the vessel Meteor.

Dr. W. M. Irvine: What angular reflectivity did you use for Saharan sand? What maximum optical depths did you treat using the method of successive scattering?

The pronounced effect of the heating rate which you find for Saharan sand in the atmosphere is similar to the effects observed on the planet Mars during Martian dust storms.

Dr. M. J. Kerschgens: We supposed the surface to be a Lambert surface. I think the maximum optical depth that can be computed with this method is about 10.

Dr. P. J. Wright: Have you taken into account the effect of self-pressure broadening of water vapor, which I have seen reported as being responsible for errors of several °C/Hr in the atmospheric heating rates near sea level if neglected?

Dr. M. J. Kerschgens: We took into account the pressure broadening by using the reduction form $(P/P_0)^n$, the exponent depending on the gases which absorb and on the bands where these gases absorb. Thermal broadening can be neglected as shown by Russian authors in connection with the work of Moskalenko.

THE MEASUREMENT PROGRAMME OPAQUE OF AC/243 (PANEL IV/RSG8) ON "EKY AND TERRAIN RADIATION"

Dr. D. H. Watson: Are you able to give any information on the format of data from the data bank? Will it be computer compatible? Written record or tape?

Dr. T. Bakker: All the measured data will be sent to a central Data Bank, located in the United Kingdom. They will be sent every month in an agreed format from all sites to the U.K. Certainly the agreed format is computer compatible.

The total information content of the data bank will be stored on magnetic tapes. These tapes are available to participants in the project only.

Every three months there will be an output of the data bank in the form of histograms.

Dr. David L. Fried: Will the cloud cover measurements include cloud altitude data? Information on cloud ceiling height in the first several km is of direct significance in certain military applications.

Dr. T. Bakker: The exact measurement method of the cloud cover has not yet been determined. In particular at night the measurements cannot be easily performed in an automatic way.

Besides the information on cloud ceilings from nearby meteorological stations, measurements of cloud heights are under consideration at some of the OPAQUE Sites.

Dr. P. J. Wright: Can you please say why, when it is anticipated that future military systems will increasingly use the infrared regions of the spectrum, that the emphasis appears to be placed on photopic measurements, particularly in the Minimum required program.

Dr. T. Bakker: I agree, we would have liked more infrared measurements in the Minimum program. However, reliable far-infrared measuring equipment is still rare and as all far-infrared equipment is rather expensive. Including the additional measurement program, the following parameters will be measured:

- the transmission in four bands of the far-infrared atmospheric windows.
- the variations in the radiation temperature along a vertical track (Sky- and Terrain Scanner)
- direct measurements of contrast loss in various bands of the far-infrared wavelength region.

As has been mentioned in the paper, the aerosol measurements will be carried out at most of the sites, and they are of much use for the interpretation and forecasting of infrared transmission properties. Besides the measurement results of the pyrhellometer give information that can be used for correlation purposes with the apparent variations in radiation temperature in the terrain. Also, the meteorological data (relative humidity, rain rate) will give useful information for the interpretation of infrared data.

EXPERIMENTAL AND COMPUTATIONAL COMPARISON OF DIFFERENT METHODS FOR DETERMINATION OF VISUAL RANGE

- Dr. J. Van Schie: The AEG instrument has a thick bar above the scattering volume, therefore it cannot measure correctly during rain and snow. Did you also try out the instrument turned over 390°?
- Dr. W. Buchtemann: The instrument is equipped in its present form with an electronic limiting circuitry preventing large pulses from being processed in order to eliminate false signals produced by small flying animals, and preventing also signals produced by rain or snow from being recorded.

FLUORESCENT AND RAMAN SCATTERING IN PARTICLES

- Dr. R. A. McClatchey: I don't fully understand the applications of this theoretical study. Can this method be used to determine the physical and chemical properties of particulates? Can you give us some examples?
- Dr. P. McNulty: The model determines how the induced fluorescence and/or Raman scattering change for molecules in particles or droplets from what is observed when the molecules lie in a bulk medium. This correction is necessary for remote sensing applications that involve aerosols or particles. The angular distribution and polarization of the emitted radiation may be used to obtain information on the size of the particles or droplets. When this data is combined with elastic light-scattering data measured simultaneously, they can be used to provide information on the distribution of scattering molecules within the particle.
- Dr. W. M. Irvine: I am surprised that in treating what is basically a quantum phenomenon such as the Raman effect you can use a purely classical treatment. Aren't the perturbations of the molecules of interest by the surrounding molecules of the aerosol of great importance? How in practice do you know how to distribute the fluorescing molecules within an aerosol particle, or does it make much difference?
- Dr. P. McNulty: A classical treatment of the type outlined here provides what in our opinion is the best method of calculating the portion of the incident field that reaches each molecule of interest within the particle. It is also used to determine how the fluorescence is altered as it leaves the particle because of the geometrical and optical properties of the particle. The actual molecular transitions are of course quantum phenomena and are influenced by the molecules interactions with its neighbors. We assume here that these perturbations are the same in a particle of a given composition as they would be in the same material in bulk form.
- M. Kerber and J. Krathavil at Clarkson are preparing spherical polystyrene particles that contain uniform distributions of fluorescing dye molecules for experimental comparison with the model. Until we have computer calculations and experimental data to test the model, it is not possible to state with certainty how great the effect of changing the distribution of fluorescing molecules within the particle will be on the observed emission.

Summary of Session II
INCOHERENT PROPAGATION

by
Dr. G. N. Plass, Chairman

The session on incoherent propagation included both theoretical and experimental papers.

On the theoretical side it is evident that one can now calculate the intensity distribution of the multiple scattered sunlight in the atmosphere from realistic models. This could not have been done a decade ago. The rapid progress is due to: (1) the development of several powerful new computation methods such as matrix operator, successive orders, iteration, and Monte Carlo; (2) the availability of high speed computers with large memories.

There are still some theoretical problems on which additional development work needs to be done including: (1) spherical coordinates where the spherical shape of the earth really makes a difference compared to a plane-parallel atmosphere; (2) integration over frequency (when the absorption varies rapidly with frequency as in an absorption band); (3) horizontal inhomogeneities, (as broken cloud cover or variations in ground surface with coordinates).

Necessary input data to theoretical models include the variation of temperature and density with height, the nature of the ground or ocean surface, and the aerosol properties (size distribution of radii, number distribution with height; index of refraction). Additional experimental work is badly needed on the reflection of light by the ground and on the aerosol properties.

Various extensive measurement programs of atmospheric radiation such as program "Opaque" are starting. There is need for much more experimental information of this type and all serious programs of this type are welcome. It is essential that the various parameters needed for the theoretical models be measured at the same time as the radiative measures are made. This will enable comparisons between the theory and experiment. There has been reasonable agreement in the past, but a lack of knowledge of one or more of the model parameters has made exact comparison difficult.

PHYSICAL MODEL FOR STRONG OPTICAL
WAVE FLUCTUATIONS IN THE ATMOSPHERE

H. T. Yura
Electronics Research Laboratory
The Aerospace Corporation
P.O. Box 92957
Los Angeles, California 90009

ABSTRACT

This paper presents elementary derivations of the basic phase and amplitude statistics of an optical wave propagating in a turbulent medium (e.g., the atmosphere). Both plane and spherical waves are discussed. We present results that are valid in the regime of strong amplitude fluctuations (i.e., the regime where the variance of irradiance saturates). We first give an elementary derivation of phase fluctuations, obtaining all of the well known results of Tatarskii. With regard to amplitude fluctuations, Tatarskii's geometrical-optics model of scintillation has been generalized to include both diffraction and the loss of spatial coherence of the optical wave as it propagates through the turbulent medium. An estimate is obtained of the amplitude fluctuations that agrees with the results of perturbation theory for $\sigma_T^2 \ll 1$ and saturates to a constant value of the order unity for $\sigma_T^2 \gg 1$ (σ_T^2 is the amplitude variance calculated on the basis of perturbation theory). In the saturation regime we show that both the plane- and spherical wave variance of irradiance saturates to the same constant (non-zero value). In addition, we have calculated the amplitude correlation function. For $\sigma_T^2 \ll 1$, the amplitude correlation function agrees with the results of perturbation theory and for the Kolmogorov spectrum is characterized by a correlation length of the order $(L/k)^{1/2}$, where L is the propagation distance and k is the optical wave number. Conversely, for $\sigma_T^2 \gg 1$ the amplitude correlation length decreases with increasing propagation distance and is shown to be equal to the lateral coherence length of the waves $\rho_0(L)$. In this regime, a residual correlation tail is obtained in agreement with recent experiments. The temporal power spectrum of the irradiance fluctuations in saturation regime are derived and compared to experiment. It is found that the agreement is good.

1. INTRODUCTION

The study of the statistics of optical wave propagation in turbulent media has received increased interest in recent years. This interest is due primarily to the advent of laser systems operating in the atmosphere and ocean. For instance, the design and development of laser communication and radar systems operating in the atmosphere should be based on the results of the analysis of an optical wave field propagating in turbulent media. Other areas of interest where the interaction of an optical beam with random media is important include astronomy, optical reconnaissance and remote sensing. Therefore it is important to have a theory for predicting the nature of the propagation of a beam of light in a random medium. During the last fifteen years a great deal of progress was made on this problem [1-5]. In particular, useful expressions were obtained for essentially all optical wave quantities of interest. In particular, results have been obtained for beam irradiance, scintillation, coherence, etc., as a function of propagation distance L , optical wave number k (equal to 2π divided by the optical wavelength λ), and the parameters that describe the turbulent medium. These results were shown to be in fairly good agreement with experiment. The agreement between experiment agrees very well with theory in the regime of weak fluctuations. In the regime of strong fluctuations, that is, in the regime where the variance of irradiance saturates, experiment and the results of recent theoretical efforts [6, 7, 8] appear to agree well qualitatively, and quantitatively [9].

Although a great body of literature exists on this subject (see for example Refs. 4 and 5 for excellent reviews that list several hundred references), much of the analysis is mathematically complex, inhibiting an understanding of the underlying physical optic effects. In this paper we will derive the basic amplitude and phase statistics which play a central role in propagation theory using a minimum of mathematics. Rather, we will employ physically intuitive arguments that will enable us to obtain all of the plane and spherical wave statistics (to within a numerical multiplicative factor of the order unity). We believe that a physical approach is useful for a complete understanding of wave propagation in turbulent media and should be used in a complimentary fashion along with the rigorous derivations given in the literature.

First we will outline the model assumed for the index of refraction fluctuations in the atmosphere and then give a physical derivation of phase and amplitude statistics. Random fluctuations of temperature in the earth's atmosphere result in fluctuations in the index of refraction. These fluctuations are in general functions of the position \underline{r} and time t so that the index of refraction n can be written as

$$n(\underline{r}, t) = 1 + n_1(\underline{r}, t), \quad (1)$$

where n_1 is the fluctuation in the index of refraction. For clear-air atmospheric turbulence, we have that $|n_1| \ll 1$, and $\langle n_1 \rangle = 0$, where angular brackets denote the ensemble average. It is also possible to assume that the temporal dependence of n_1 is mainly due to a net transport of the inhomogeneities of the medium as a whole past the line of site (e.g., due to atmospheric winds) so that $n_1(\underline{r}, t) = n_1(\underline{r} - \underline{v}(\underline{r})t)$, where $\underline{v}(\underline{r})$ is the local "wind" velocity. This assumption is known as Taylor's frozen-flow hypothesis and appears to hold in most practical cases of interest. Here we are primarily interested in obtaining spatial statistics and so for the moment we ignore the temporal behavior of n_1 , returning to temporal effects later.

For simplicity, we assume that the turbulence condition are both homogeneous and isotropic. For atmospheric turbulence we employ the much used Kolmogorov model according to which within a particular range of separations between \underline{r}_1 and \underline{r}_2 that

$$\langle [n(\underline{r}_1) - n(\underline{r}_2)]^2 \rangle = C_n^2 |\underline{r}_1 - \underline{r}_2|^{2/3}, \quad l_0 \ll |\underline{r}_1 - \underline{r}_2| \ll L_0 \quad (2)$$

where l_0 and L_0 are called the inner and outer scales of turbulence, respectively, and C_n is called the index structure constant. In the atmosphere, l_0 is of the order a few millimeters to a centimeter and, for horizontal propagation in the lower atmosphere, L_0 is of the order the height above ground.

For turbulent eddy sizes, of characteristic length r , within the inertial subrange (i.e., $l_0 \ll r \ll L_0$), the Kolmogorov "2/3" law implies that to a numerical multiplicative factor of the order unity the mean square index fluctuation associated with the scale size r increases as the two-thirds power of that scale size. That is,

$$\langle n_1^2(r) \rangle \sim C_n^2 r^{2/3}, \quad l_0 \ll r \ll L_0. \quad (3)$$

For separations larger than L_0 , the mean square index fluctuation does not increase with increasing separation, rather it levels off to a value of the order $C_n^2 L_0^{2/3}$. Conversely, for separations small compared with l_0 , friction effects due to viscosity result in a very rapid decrease in the index fluctuations and for many applications can be taken as being equal to zero (l_0 is frequently smaller than any length of interest in a propagation problem resulting in negligible contributions due to the smallest scale sizes).

In summary, the present analysis is restricted to a weakly inhomogeneous medium with characteristic scale lengths much greater than the optical wavelength. Furthermore, it is assumed that the characteristics of the medium do not change appreciably during an oscillation of the optical field, for otherwise frequency spreading (Doppler effects) becomes important. At ir and visible wavelengths this condition is satisfied in the atmosphere. The electromagnetic field considered has a time dependence given by $\exp(i\omega t)$. The time dependent wave equation is replaced by the Helmholtz equation for a random inhomogeneous medium. The electrical conductivity and magnetic permeability of the medium are taken to be 0 and 1, respectively. Finally, only the case of a scalar (plane and spherical) wave propagating in a spatially homogeneous and isotropic turbulent medium is discussed.

2. PHASE STATISTICS

Consider a plane wave impinging on a random medium that occupies the half-space $z \geq 0$. Normalizing the amplitude of the wave to unity in the absence of turbulence and suppressing the time dependence we have that the optical wave at propagation distance L can be expressed as e^{ikL} . In the presence of the random medium we express the optical wave function as $U(\underline{r}) = A \exp(ikL + i\phi)$, where, in general, both the amplitude perturbation A and phase perturbation ϕ are random functions of position \underline{r} in the medium. In this section we assume that A is constant and consider phase fluctuations only.

The mutual coherence function (MCF), which is defined as the cross-correlation function, i.e., second statistical moment, of the complex field in a plane perpendicular to the mean direction of propagation, is important for a number of reasons (e.g.; it describes the loss of coherence of an initially coherent wave propagating in the medium). Neglecting amplitude effects the MCF is given by

$$M = \langle U(\underline{r}_1) U^*(\underline{r}_2) \rangle = \langle \exp\{i[\phi(\underline{r}_1) - \phi(\underline{r}_2)]\} \rangle \quad (4)$$

where $\underline{r}_{1,2} = (\underline{p}_{1,2}, L)$, and $\underline{p}_{1,2}$ is a two-dimensional vector in a plane transverse to the optic axis at propagation distance L (see Figure 1).

In order to calculate the ensemble average indicated in Eq. (4), it is convenient to first obtain an expression for $\phi(\underline{r})$. To this end, we note that since $\lambda \ll$ turbulent scale sizes of the medium, geometrical optics should yield a reasonable estimate for $\phi(\underline{r})$ [1,2]. We will show that geometrical optics is entirely adequate to obtain the second order phase statistics, first obtained by Tatarskii [1,2] and Chernov [3].

According to geometrical optics, the phase perturbation ϕ resulting from the fluctuation in the index of refraction n_1 is given by

$$\phi = k \int_{\text{path}} n_1(s) ds \quad (5)$$

where s is position along the ray path. For plane waves the paths are approximately straight lines parallel to the z -axis, as indicated in Fig. 1. As long as the propagation distance L is much larger than the integral correlation scale of n_1 (as it will be for essentially all cases of practical interest), Eq. (5) indicates that we add together a large number of uncorrelated terms to obtain ϕ . Hence because of the central limit theorem, we conclude that ϕ will be normally distributed, independent of the distribution of n_1 . A normal distribution is completely characterized by two parameters, its mean and variance. Since $\langle n_1 \rangle = 0$, it follows directly from Eq. (5) that $\langle \phi \rangle = 0$. The cross-correlation function of the phase is obtained from Eq. (5) as

$$\begin{aligned}
B_\phi(|\underline{r}_1 - \underline{r}_2|) &= \langle \phi(\underline{r}_1) \phi(\underline{r}_2) \rangle = k^2 \langle (\int n_1(s_1) ds_1) (\int n_1(s_2) ds_2) \rangle \\
&= k^2 \iint ds_1 ds_2 \langle n_1(s_1) n_1(s_2) \rangle = k^2 \iint ds_1 ds_2 B_n(|s_1 - s_2|)
\end{aligned} \quad (6)$$

where we have introduced the index autocorrelation function B_n . Since the medium is assumed statistically stationary and isotropic, it follows that B_n is a function of the magnitude of the difference of the two points s_1 and s_2 .

From Fig. 1 we find that

$$|s_1 - s_2| = (z_{12}^2 + \rho^2)^{1/2} \quad (7)$$

where

$$\rho = |\underline{r}_1 - \underline{r}_2|$$

and

$$z_{12} = z_1 - z_2 \quad (8)$$

Note that the mean square phase, $\phi_0^2 = \langle \phi^2 \rangle$, is obtained from Eq. (6) as $B_\phi(0)$. Thus, in general, the phase is normally distributed with a zero mean value and with a second moment given formally by Eq. (6).

Returning now to the evaluation of the ensemble average indicated in Eq. (4). It can be shown that if the random function f is normally distributed,

$$\langle e^f \rangle = \exp \left[\langle f \rangle + \frac{1}{2} \langle [f - \langle f \rangle]^2 \rangle \right] \quad (9)$$

Applying Eq. (9) to Eq. (4) with $f = i[\phi(r_1) - \phi(r_2)]$ yields

$$M = \exp \left[-\frac{1}{2} D_\phi(\rho) \right] \quad (10)$$

where

$$D_\phi(\rho) = \langle [\phi(\underline{r}_1) - \phi(\underline{r}_2)]^2 \rangle \quad (11)$$

is called the phase structure function in the literature [1, 2], and $\rho = \underline{r}_1 - \underline{r}_2$. Expanding the square in Eq. (11) and invoking stationarity yields that

$$M = \exp \left[-\frac{1}{2} D_\phi(\rho) \right] = \exp \left\{ -\phi_0^2 [1 - b_\phi(\rho)] \right\} \quad (12)$$

where ϕ_0^2 is the mean square phase fluctuation at a point and $b_\phi(\rho)$ is the normalized phase correlation function defined as

$$b_\phi(\rho) = \frac{\langle \phi(\underline{r}_1) \phi(\underline{r}_2) \rangle}{\langle \phi^2 \rangle} = \frac{B_\phi(\rho)}{\phi_0^2} \quad (13)$$

From its definition it is seen that $b_\phi(0) = 1$. Furthermore, for sufficiently large separations ρ (i.e., large compared to the outer scale of turbulence) the ray that arrives at \underline{r}_1 is statistically independent of the ray arriving at \underline{r}_2 from which it follows that $b_\phi \rightarrow 0$. That is, for large ρ , $\langle U(\underline{r}_1) U^*(\underline{r}_2) \rangle \rightarrow \langle U(\underline{r}_1) \rangle \times \langle U^*(\underline{r}_2) \rangle = \langle U \rangle^2 = \exp(-\phi_0^2)$. The MCF decreases monotonically from $M(0) = 1$ to $M(\infty) = \exp(-\phi_0^2)$.

While it is a straightforward numerical procedure to compute M directly for a given functional form of the index correlation function, it is useful, indeed preferable, to have approximate formulas for the mutual coherence function for estimating the coherence at various ranges.

We assume that the medium is composed of a continuum of independent turbulent eddies from a minimum scale size l_0 to a maximum scale size L_0 . Consider for a moment an eddy of scale size a . We now calculate the contribution to M from this eddy size. Since the eddies are independent the resulting MCF due to all eddies will be the product of the MCF due to a single scale size over all scale sizes. A physically adequate and mathematically convenient form for B_n is a gaussian. As we shall show, the gaussian form is sufficient for a complete determination of second order phase statistics. Indeed, any physically correct form for B_n will suffice; however the gaussian is particularly convenient mathematically. Thus, consider that

$$B_n(\rho) = \langle n_1^2 \rangle \exp(-\rho^2/a^2), \quad (14)$$

where $\langle n_1^2 \rangle$ is the mean square fluctuation in the index of refraction and a is the eddy scale size of interest. Substituting Eq. (14) into Eq. (6), making use of Eq. (7) and (8) yields, for plane waves,

$$B_\phi(\rho) = k^2 \langle n_1^2 \rangle e^{-\rho^2/a^2} \int_0^L dz_1 \int_0^L dz_2 e^{-(z_1 - z_2)^2/a^2} \quad (15)$$

Changing variables from z_1, z_2 to $\eta = z_1 - z_2$ and $\xi = (z_1 + z_2)/2$, and noting that $L \gg a$ allows one to express B_ϕ as

$$B_\phi(\rho) \approx k^2 \langle n_1^2 \rangle L e^{-\rho^2/a^2} \int_0^\infty d\eta e^{-\eta^2/a^2} = \phi_0^2 e^{-\rho^2/a^2} \quad (16)$$

where

$$\phi_0^2 = \frac{\sqrt{\pi}}{2} k^2 \langle n_1^2 \rangle a L. \quad (17)$$

Indeed, the phase variance ϕ_0^2 for a single scale size a can be shown on physical grounds to always be of the order $k^2 \langle n_1^2 \rangle a L$. Consider an eddy of size a . The phase change of a ray passing through this eddy is of the order $k n_1 a$. The mean square phase change per eddy is of the order $k^2 \langle n_1^2 \rangle a^2$. For a total path length L , there are of the order L/a eddies traversed by the ray. Thus, for independent eddies, the mean square phase change is equal to the mean square phase change per eddy multiplied by the number of eddies traversed by the ray. That is,

$$\phi_0^2 \sim (k^2 \langle n_1^2 \rangle a^2) (L/a) = k^2 \langle n_1^2 \rangle a L.$$

From Eqs. (13) and (16) we deduce that the normalized correlation coefficient for plane waves is

$$b_\phi(\rho) = \frac{B_\phi(\rho)}{\phi_0^2} = e^{-\rho^2/a^2} \quad (18)$$

Thus from Eqs. (10), (12), and (16) we find that

$$M_a(\rho) = \exp[-\phi_0^2(a) (1 - e^{-\rho^2/a^2})] \quad (19)$$

where, in general,

$$\phi_0^2(a) \sim k^2 \langle n_1^2(a) \rangle a L, \quad (20)$$

and is given explicitly for a gaussian index autocorrelation function by Eq. (17). Note that ϕ_0^2 can be written as $2z/z_c$ where the extinction length $z_c \sim [k^2 \langle n_1^2 \rangle a]^{-1}$ is the distance where the coherent part of the optical field is reduced by $1/e$ from its value at $z = 0$.

Now for a continuum of eddy sizes-distributed according to the Kolmogorov "2/3" law, we obtain from Eqs. (3) and (20) that

$$\phi_0^2(a) \sim k^2 C_n^2 L a^{5/3} \quad (21)$$

Examination of Eq. (21) reveals that the largest eddies are most effective in contributing to the total phase variance at a point. In fact, for a distribution of independent eddies we have

$$\phi_0^2 \sim \sum_{l_0}^{L_0} (k^2 C_n^2 L) a^{5/3} \sim k^2 C_n^2 L L_0^{5/3}, \quad (22)$$

in agreement in order of magnitude with the results of the rigorous calculation of Tatarskii and others (the numerical multiplicative constant is approximately 0.39). Furthermore, the resulting MCF of a distribution of independent eddies is

$$M(\rho) = \prod_{l_0}^{L_0} M_a(\rho) = \exp \left\{ - \sum_{l_0}^{L_0} \phi_0^2(a) [1 - e^{-\rho^2/a^2}] \right\} \quad (23)$$

where, for the Kolmogorov "2/3" law, $\phi_0^2(a)$ is given by Eq. (21). Examination of Eq. (23) reveals that there are three distinct range values for ρ .

Range 1: $\rho \gg L_0$. Over this range $b_\phi(\rho) = 0$ since ρ is larger than the outer scale of turbulence. It follows from Eq. (23) that for $\rho \gg L_0$

$$M = \exp \left\{ - \sum_{l_0}^{L_0} \phi_0^2(a) \right\} \sim \exp \left[- \phi_0^2(L_0) \right] = \exp \left[- k^2 C_n^2 L L_0^{5/3} \right]. \quad (24)$$

Thus, in this regime the MCF is a constant independent of ρ [and equal to $\langle U \rangle^2 = \exp(-\langle \phi^2 \rangle)$].

Range 2: $l_0 \ll \rho \ll L_0$. This range of ρ values is called the inertial subrange and is the most interesting case in practice. In the inertial subrange an examination of Eqs. (21) and (23) reveals that the argument of the outer exponential in Eq. (23) increases proportional to $a^{5/3}$ for $a < \rho$, reaches a maximum for $a \sim \rho$, and decreases proportional to $a^{-1/6}$ for $a > \rho$. Thus the most effective eddy scales in the inertial subrange are those of scale lengths of the order the separation of interest. As a result we obtain that for $l_0 \ll \rho \ll L_0$

$$M(\rho) = \exp[-(\rho/\rho_0)^{5/3}], \quad (24)$$

where, the "coherence length" ρ_0 is given by

$$\rho_0 \sim (k^2 C_n^2 L)^{-3/5}, \quad (25)$$

This result agrees, to within a numerical multiplicative factor of the order unity, with the results of Tatarskii [1, 2]. In the inertial subrange the phase structure function is proportional to $\rho^{5/3}$ and for almost all cases of practical concern is the regime of separations of interest.

Range 3: $\rho \ll l_0$. In this regime ρ is much smaller than all eddy scale sizes from which it follows that the inner exponent in Eq. (23) may be expanded for each a as $\exp(-\rho^2/a^2) \cong 1 - \rho^2/a^2$. (In general it can be shown [2] that the underlying structure function has the property for $\rho \rightarrow 0$ that $D(\rho) \sim O(\rho^2)$. For the case of homogeneous and isotropic turbulence this implies that $B \sim 1 - O(\rho^2)$.) As a result, we obtain from Eqs. (21) and (23) that the argument of the outer exponent in Eq. (23) is proportional to $a^{-1/6}$. Thus for $\rho \ll l_0$, the main contribution to the sum indicated in Eq. (23) are for eddies of the order l_0 , the inner scale of turbulence. Thus, for $\rho \ll l_0$, we obtain the estimate that

$$M(\rho) = \exp[-(k^2 C_n^2 L/l_0^{1/3}) \rho^2] \quad (26)$$

In this regime of separations the phase structure function is a quadratic function of ρ . The results obtained in Eq. (26) are in agreement, to within a numerical multiplicative factor of the order unity, with the results of Tatarskii.

As alluded to previously, the inertial subrange is the regime of interest in practice. We note from Eq. (25) that the restriction $l_0 \ll \rho \ll L_0$ is equivalent to the propagation distance condition that $z_c \ll L \ll z_1$, where the $z_c \sim (k^2 C_n^2 L_0^{5/3})^{-1}$ is the distance at which the coherent part of the field is reduced by $1/e$ from its value at $L = 0$, and $z_1 \sim (k^2 C_n^2 l_0^{5/3})^{-1}$ is the propagation distance at which the coherence length, ρ_0 , is equal to the inner scale of turbulence. For example, for $l_0 = 1$ mm, $L_0 = 1$ m, $\lambda = 1$ μ , and $C_n^2 = 10^{-14}$ m^{-2/3} (fairly strong turbulence conditions), we obtain that $z_c \sim 2.5$ m, and $z_1 \sim 2.5$ km, while for $C_n^2 = 10^{-16}$ (fairly weak turbulence conditions) and the same value for the other parameters we obtain that $z_c \sim 250$ m, and $z_1 \sim 250$ km. In many applications of interest the distance z_1 is frequently much larger than the propagation distance of interest. For L less than z_1 , the inner scale does not enter into the analysis (i.e., $\rho_0 > l_0$ and we can approximate the plane wave MCF by the convenient form ($L < z_1$))

$$\left. \begin{aligned} M(\rho) &\cong \exp \left\{ -\phi_0^2 \left[1 - \exp \left[-\frac{1}{2} \left(\frac{\rho}{\rho_0} \right)^{5/3} \right] \right] \right\} = \exp \left\{ -\phi_0^2 \left[1 - \exp \left[-(\rho/L_0)^{5/3} \right] \right] \right\} \\ &\quad - \exp \left[-(\rho/\rho_0)^{5/3} \right], \quad \rho \ll L_0 \\ &\quad - \exp \left[-\phi_0^2 \right], \quad \rho \gtrsim L_0. \end{aligned} \right\} \quad (27)$$

Next we indicate for spherical waves the modification to the plane wave results. Consider a monochromatic point source located at the origin and we seek to determine the resulting MCF for separation ρ at propagation distance L . With reference to Fig. 2, the derivation that led to Eqs. (6) - (8), and noting that the correlation scales of the medium are much less than the propagation distance L we find for spherical waves that

$$B_\phi \cong k^2 \int_0^L dz_1 \int_0^L dz_2 B_n(|s_1 - s_2|) \quad (28)$$

where

$$|s_1 - s_2| = [z_1^2 + (t\rho)^2]^{1/2}$$

and

$$t = \frac{z_1 + z_2}{2L} \quad (29)$$

The modification for spherical wave propagation is geometrical in nature. The dependence on the quantity t in Eq. (29) reflects the spherical expansion of the wave as it propagates through the medium. We note from Eqs. (28) - (29) that the phase variance for spherical waves is identical to that obtained for plane waves, as it should. The resulting MCF for spherical waves is

$$M_s(\rho) = \exp \left\{ - \phi_0^2 \left[1 - \int_0^1 b_p(\rho t) dt \right] \right\} \quad (30)$$

where b_p is the plane wave normalized phase correlation coefficient. Thus, the spherical wave coherence function is obtained directly from the plane wave results, as indicated above. For uniform turbulence conditions, it is seen that the estimates of M obtained for the three range values for ρ discussed above apply to spherical waves. The only difference being, for ranges 2 and 3, a numerical multiplicative factor (the additional factor multiplying $\rho^{5/3}$ and ρ^2 being $3/8$ and $1/3$, respectively).

The spherical wave coherence length is in general, greater than the corresponding plane wave coherence length, as expected intuitively from geometrical expansion. Note that, in contrast to plane waves, for inhomogeneous turbulence conditions the spherical wave coherence length is dependent on source location (e.g., spherical wave distortions for propagating up and down through the atmosphere are quite different implying corresponding differences in the ultimate achievable resolution).

The spherical wave mutual coherence function plays an important role in propagation theory. For example, it describes the reduction in lateral coherence between different elements of a transmitting or receiving aperture, effectively transforming them into partially coherent apertures, with the degree of coherence decreasing with increasing propagation distance through the medium. In general, the resulting mean irradiance distribution (in space for a transmitting system, or in the image plane for receiving system) is characteristics of a coherent aperture of dimension ρ_0 . If ρ_0 is smaller than the diameter of the physical aperture D , the resulting radiation pattern is characteristic of that of an aperture of diameter ρ_0 rather than D . Hence, in the far field, the scattering half angle is given by the reciprocal of the product of the wave-number and the radius of the "effective" coherent aperture (which is approximately given by the smaller of $\rho_0/2$ or $D/2$).

By physically intuitive arguments we have obtained the basic phase statistics results obtained by Tatarskii using perturbation theory and the method of spectral expansions [1,2]. Note from Eq. (6) that the phase statistics are directly proportional to the index of refraction correlation function. The incremental contribution to B_p from random inhomogeneities in a slab of thickness Δz located at a distance L is proportional to the product of the index fluctuations located in the slab, which is (assumed) independent of the properties of the optical wave. This suggests that the results derived above [which agree with the second order (in n_1) perturbation theory results] should be valid for arbitrary propagation distance L . In particular, they should be valid in the regime where the normalized variance of irradiance saturates. In the so-called saturation regime, the method of smooth perturbation applied to amplitude fluctuations is not valid. As we shall see, the incremental contribution to amplitude fluctuations from eddies in a slab of thickness Δz , in contrast to phase fluctuations, are dependent on the coherence properties of the wave in the medium at the slab.

3. AMPLITUDE STATISTICS

Of all the optical field quantities discussed in the literature, the irradiance fluctuations or scintillation (i.e., irregular changes in brightness) have been the most frequently measured and the least well understood. If a small photodetector is placed in the path of an optical beam propagating under suitable turbulent conditions, several dB rms fluctuations in light intensity are observed with a "scintillation bandwidth" of a few tenths to a few hundred Hertz [1]. In the general case of beam wave propagation, irradiance fluctuations can be generated by intensity variations within the beam which vary temporally (beam breakup) or by the beam as a whole wandering past the detector. Here, attention is confined to the propagation of waves of infinite lateral extent (plane waves), hence, scintillation is only produced by beam breakup. Tatarskii [1,2] has derived expressions based on perturbation theory, for the amplitude statistics of a plane wave propagating through a turbulent medium. These theoretical results predict that the amplitude fluctuations at a point increase without bound with increasing propagation distance. A measure of the theoretical value of "amplitude variance based on perturbation theory and the Kolmogorov spectrum is the quantity

$$\sigma_T^2 = C_n^2 k^{7/6} L^{11/6} = (L/z_A)^{11/6}, \quad (31)$$

where

$$z_A = \frac{1}{C_n^{12/11} k^{7/11}} \quad (32)$$

k is the optical wave number, L is the propagation distance and C_n is the index structure constant. However, experimental measurements [3-6] indicate that the amplitude variance agrees with the perturbation theory results only when the fluctuations are small ($\sigma_T^2 \ll 1$). For $\sigma_T^2 \gtrsim 1$ (i.e., $L \gtrsim z_A$), it has been found experimentally that the amplitude fluctuations do not increase with either increasing path length or turbulence strength, rather, they saturate to a value of the order unity.

Based on perturbation theory, Tatarskii predicts an amplitude correlation function characterized by a correlation length $\sim (L/k)^{1/2}$ with no appreciable correlation beyond this value. Experimentally,

Tatarskii's $(L/k)^{1/2}$ prediction for the amplitude correlation length is found to be obtained for $L \ll z_A$ (i.e., $\sigma_T^2 \ll 1$) only. For strong fluctuations, the recent experiments of Kerr show a decrease in correlation length with increasing σ_T^2 . In addition Kerr finds a large residual correlation tail for large detector separations, a result which is in marked contrast to the perturbation theory result.

Many attempts have been made to calculate amplitude statistics for $\sigma_T^2 \gtrsim 1$. For example, a number of workers have tried using the renormalization [2, 10-13] techniques of field theory [2, 10, 13], a mathematically complex approach which involves the selective summing and neglecting of very complicated terms in a series representation. Such an approach leads a few physical insights and, to keep the problem mathematically tractable, it is necessary to delete or approximate a very large number of terms. Furthermore, it is extremely difficult in most cases to even estimate the size of the neglected terms. In general, it appears that the renormalization technique has led to few new results. Brown [14] has made numerical calculations for a two-dimensional plane wave and has obtained numerical results in good agreement with observations, although he has made no attempt to interpret his results physically in the saturation regime.

Here, we generalize Tatarskii's [15] physical model for amplitude fluctuations to include both diffraction and the loss of lateral spatial coherence of the wave as it penetrates further into the medium. In all cases results are obtained which are in qualitative agreement with experiment. The results of the present analysis agree with perturbation theory for $\sigma_T^2 \ll 1$. For $\sigma_T^2 \gtrsim 1$ we obtain a saturation of amplitude variance, a decrease in the amplitude correlation length, and a residual correlation tail. In particular, we conclude for $\sigma_T^2 \gg 1$ that the amplitude correlation length is of the order of the lateral coherence length of the wave $\rho_0(L)$ (which is a decreasing function of propagation distance). That is, in the saturation regime the amplitude and phase correlation lengths are equal.

The physical mechanisms through which turbulence induces beam break up is the random focusing of light by refractive inhomogeneities in the path of the optical wave. The simplest physical model of this effect which retains the essential physics is a plane wave, of wave number k , incident upon a series of closely packed isotropic refractive eddies of "radius" a and refractive index n_1 relative to the surrounding medium (where the refractive index is assumed to be equal to unity). The scattering for the range of parameters of interest, $|n_1| \lesssim 10^{-6}$, $ka \gg 1$, is primarily in the forward direction. In the geometric optics approximation, the condition $|n_1| \ll 1$ implies negligible reflection at the surface of the eddy and that each ray traverses the eddy virtually unperturbed in direction (the refraction angle at each surface is $\sim n_1$).

First, a single eddy size will be considered before generalizing the discussion to include a distribution of eddy sizes. In the paraxial approximation, it is well known that an eddy of radius a can act as a lens with a focal length $f \sim a/n_1$. For $n_1 > 0$, the lens is convergent, while for $n_1 < 0$, there is a virtual focal point behind the lens at $f \sim a/n_1$, and the lens is divergent. In the atmosphere, typical values for a and n_1 , are a few centimeters and $|n_1| < 10^{-6}$ which implies that $f \gtrsim 10$ km. For most practical applications, the propagation distance L can be assumed to be much less than the focal distance f . (The saturation phenomenon has been observed, under strong turbulence conditions, for $L \lesssim 1$ km). Therefore, we assume in this paper that $L/f \ll 1$.

A plane wave is incident along the positive z -axis on a random medium that occupies the half space $z \geq 0$ and we seek to determine the amplitude statistics in the plane $z = L$. With reference to Fig. 3, consider the situation with regard to those eddies located within a slab bounded by the planes $z = z$ and $z = z + \Delta z$, where the thickness of the slab Δz is assumed small compared to L . Now the wave impinging on this slab is not, in general, a coherent plane wave. As the initial plane wave penetrates the medium it becomes partially coherent due to the loss of transverse spatial coherence with increasing penetration distance. The degree of transverse spatial coherence is a monotonically decreasing function of penetration distance.

The mutual coherence function (MCF), defined as the cross-correlation function of the complex fields in a direction transverse to the direction of propagation is the quantity that describes the loss of coherence of an initially coherent wave propagating in the random medium. For example, the MCF, for a Kolmogorov spectrum, for transverse separation ρ within the inertial subrange is given by [see Eqs. (24)-(27)]

$$M(\rho, z) = \exp \left[- \left(\frac{\rho}{\rho_0} \right)^{5/3} \right], \quad L_0 \ll \rho \ll L_0 \quad (33)$$

where

$$\rho_0 \approx \left[1.45 k^2 C_n^2 z \right]^{-3/5} \quad (34)$$

The quantity ρ_0 can be taken as a measure of the transverse coherence length of the wave. That is, the oscillations of the wave at points separated by a large (small) distance compared to ρ_0 are mutually incoherent (coherent). The expression given above for M , the first order perturbation result, has been found experimentally to adequately describe the loss of transverse coherence [16, 17]. In our model the perturbation results for the loss of transverse coherence for the amplitude fluctuations are used. Thus, the impinging wave on the slab is partially coherent, its coherence properties being described by its MCF. The ability of a (turbulent) lens to focus a partially coherent field can be considerably less than for a coherent field, implying reduced amplitude fluctuations. In addition, after the wave interacts with

the focusing eddies in the slab it propagates a further distance ($L-z$) through the medium and continues to lose transverse spatial coherence. It is necessary to include the loss of transverse coherence of the wave into the analysis to obtain the saturation of amplitude fluctuations. Its neglect, as we shall see, leads one to obtain the results of perturbation theory (that is, the amplitude fluctuations increase with increasing propagation distance).

To obtain an estimate of the amplitude fluctuations we generalize Tatarskii's [15] geometric optics analysis to automatically include both diffraction and multiple scattering (loss of transverse coherence). We can obtain an estimate of the amplitude fluctuations induced by the eddies being swept (or blown by the wind) past the line of sight between the source and observer in the following way. The instantaneous field distribution at a point \underline{r} in the observation plane, due to the medium in the slab can be obtained via the Huygens-Fresnel principle. This principle, applied to the case at hand, states that every point of the wavefront in the slab may be considered as a center of a secondary disturbance which gives rise to spherical wavelets, and the wavefront at a later instant may be regarded as the envelope of these wavelets. It has been shown [18], that the Huygens-Fresnel principle is that the secondary wavefront will again be determined by the envelope of spherical wavelets from the primary wavefront, but each wavelet will now be determined by the propagation of a spherical wave propagating through the turbulent medium.

First, we neglect the effect of the intervening medium, apart from the slab, and obtain an estimate of the relative amplitude change at the observation point \underline{r} , compared with the amplitude change in the absence of the slab. We then generalize to include the effect of the intervening medium. Considering the slab as the effective source for radiation of the secondary wavelets, the field at the observation point \underline{r} due to the slab at z can be written as

$$A_s(\underline{r}, z) = \sum_i A_l(\underline{p}_i) + A_{\text{rest}} \quad (35)$$

where $A_l(\underline{p}_i)$ is the contribution to the amplitude from the turbulent "lens" located in the slab at coordinate \underline{p}_i , the summation over i indicates a summation over all eddies within the slab, and A_{rest} is the contribution to the amplitude from the intervening space between the eddies in the slab. The quantity A_{rest} can be obtained from Babinet's principle by imagining that we remove the turbulent "lenses" from the slab, leaving "holes" in their place. For this case we must have that

$$\sum_i A_h(\underline{p}_i) + A_{\text{rest}} = A_0 \quad (36)$$

where the first term on the left hand side of Eq. (36) represents the contribution from the holes and A_0 is the field that impinges on the slab. Eliminating A_{rest} from Eq. (35), we obtain

$$A_s(\underline{r}, z) = \sum_i [A_l(\underline{p}_i) - A_h(\underline{p}_i)] + A_0$$

The quantity A_h can be obtained from A_l by setting the focal length of the lens f equal to infinity. Hence, the relative amplitude change at the observation point due to the slab is

$$\begin{aligned} \delta A_s &= A_s(\underline{r}, z) - A_0 = \sum_i [A_l(\underline{p}_i) - A_h(\underline{p}_i)] \\ &= \sum_i \delta A_s(\underline{p}_i) \end{aligned} \quad (37)$$

In order to obtain a quantitative expression for A_l and A_h we model the turbulent eddies by a gaussian refractive index distribution centered at \underline{p}_i . Of course, turbulent eddies do not have a gaussian shape nor are they perfectly spherical. However, the choice of a gaussian shape permits simple analytic expressions for A_l and A_h to be obtained. In any event, it is expected that, to a factor of the order unity, the gaussian model for the turbulent eddies is a valid approximation.

Let the transmittance distribution of the field, due to a turbulent eddy located in the slab at coordinate \underline{p}_i equal $\exp[-p_i^2(a^{-2} + ikf^{-1})/2]$, where a is the "radius" and $f \sim a/n_1$ is the focal length of the eddy. For simplicity let the observation point be located on the optic axis at propagation distance L from the source (i.e., propagation distance $L - z$ from the slab). A direct application of the vacuum Huygens-Fresnel principle yields the field at the observation point, $A_l(\underline{p}_i)$, due to the turbulent lens gives

$$A_l(\underline{p}_i) = \frac{ie^{ikL} A_0 \exp[ikp_i^2/2z']}{\left[\frac{z'}{ka} + i \left(1 - \frac{z'}{f} \right) a \right]} \exp \left\{ - \frac{p_i^2 \left[1 - \frac{ika^2}{z'} \left(1 - \frac{z'}{f} \right) \right]}{2 \left[\left(\frac{z'}{ka} \right)^2 + a^2 \left(1 - \frac{z'}{f} \right)^2 \right]} \right\} \quad (38)$$

where $z' = L - z$, and A_0 is the unperturbed field amplitude. The quantity $A_h(\underline{p}_i)$ is obtained from the expression for $A_l(\underline{p}_i)$ by setting $|f| = \infty$.

We are interested in the case $L/f \ll 1$ and from Eq. (38) we obtain, to lowest order in L/f

$$\delta A_s(p_i) = A_f(p_i) - A_h(p_i) \sim ia A_0 \left(\frac{z'}{f} \right) e^{i\phi} \left[1 - \frac{p_i^2}{2[(z'/ka)^2 + a^2]} \right] \times \left[\frac{1}{\frac{z'}{ka} + ia} \right] \exp \left[- \frac{p_i^2}{2[(z'/ka)^2 + a^2]} \right], \quad (39)$$

where

$$\phi = kL + \frac{kp_i^2}{2f}.$$

Note that δA_s is proportional to $n_1(p_i)$, the relative index of refraction of the eddy centered at p_i , hence, it follows that $\langle \delta A_s \rangle = 0$ since $\langle n_1 \rangle = 0$. Furthermore, terms of the form $\langle \delta A_s(p_i) \delta A_s(p_j) \rangle = 0$ for $i \neq j$, since the eddies are assumed independent. Therefore, it follows that

$$\sigma_{slab}^2 \sim \langle |\delta A_s|^2 \rangle = \langle \left| \sum_i \delta A_s(p_i) \right|^2 \rangle \quad (40)$$

$$= \sum_i \langle |\delta A_s(p_i)|^2 \rangle. \quad (41)$$

Passing to the continuum limit (i.e., the number of eddies in an area S being given by $S/\pi a^2$), Eq. (41) reduces to

$$\sigma_{slab}^2 \sim \int \frac{d^2 p}{(\pi a^2)} \langle |\delta A_s(p)|^2 \rangle. \quad (42)$$

After substituting Eq. (39) into Eq. (42), the integration over p yields

$$\sigma_{slab}^2 \sim \frac{a^2}{\left[\left(\frac{z'}{ka} \right)^2 + a^2 \right]} \langle (z'/f)^2 \rangle = \frac{\langle n_1^2 \rangle (z')^2}{\left[\left(\frac{z'}{ka} \right)^2 + a^2 \right]}. \quad (43)$$

In the geometrical optics limit, $L \ll ka^2$, Eq. (43) reduces to $\sigma_{slab}^2 \sim \langle (z'/f)^2 \rangle$, in agreement with Tatarskii's result [15]. In general, Eq. (43) gives the contribution to the amplitude fluctuations, including the effects of diffraction, due to the slab located at z .

The total contributions to the amplitude fluctuations are obtained by summing over all (independent) slabs;

$$\sigma_a^2(L) = \sum_{slabs} \sigma_{slab}^2 \sim \int_0^L \sigma_{slab}(z) \frac{dz}{a}, \quad (44)$$

where the subscript a on σ refers to a single scale size. Substituting Eq. (43) into Eq. (44) yields

$$\sigma_a^2(L) \sim \langle n_1^2 \rangle \int_0^L \left(\frac{dz}{a} \right) \frac{(z')^2}{\left[\left(\frac{z'}{ka} \right)^2 + a^2 \right]} \quad (45)$$

where $z' = L - z$. As can be easily seen, estimates of amplitude fluctuations based on Eq. (45) indicate that σ^2 increases without limit as $L \rightarrow \infty$. That is, Eq. (45) does not give saturation. To obtain bounded amplitude fluctuations it is necessary to include the degrading effects of the intervening medium.

Equation (45) was derived by assuming no intervening medium between the slab and the observation plane. We take into account the degrading effects of the intervening medium by the following physical argument. In vacuum, the diffraction angle from a coherent radiator of size a is of the order $1/ka$. If we consider diffraction in the presence of turbulence, the corresponding diffraction angle is increased due to multiple scatterings in the medium. On the basis of the extended Huygens-Fresnel principle it has been shown that the angular spread θ^2 at a propagation distance x is given by

$$\theta^2 \approx \frac{1}{k^2 a^2} + \frac{1}{k^2 \rho_0^2(x)}, \quad (46)$$

where $\rho_0(x)$ is the lateral coherence length of a point source [18, 19]. The quantity ρ_0 is defined as that value of transverse separation such that $M(\rho_0, x) = 1/e$, where M is the mutual coherence function (MCF) of a spherical wave [20]. Physically, the MCF describes the reduction in lateral coherence between different elements of the transmitting aperture, effectively transforming it into a partially coherent radiator with the degree of coherence decreasing with increasing distance from the aperture. For sufficiently large x , $\rho_0(x) \ll D$, the radiation is characterized by an effective coherent aperture of size $\rho_0(x)$, i.e.,

$\theta \sim 1/k\rho_0(x)$. In addition, it follows directly from reciprocity that the above considerations apply equally as well to an imaging situation [2]. Indeed, the effective coherent aperture for the imaging (reciprocal) case is given by $a^{-2} + \rho_0^{-2}(y)$, where a is the physical radius of the aperture, $\rho_0^2(y)$ is the lateral coherence length of the wave that is impinging on the "imaging" lens, and y is the propagation distance from the source to the lens.

Application of these considerations to the case of the turbulent lens in the slab at a distance z from the source yields a diffraction spot size at the observation plane of the order $(z'/k\bar{a})^2$ where \bar{a} , the effective coherent aperture, is given by

$$\frac{1}{\bar{a}^2} = \frac{1}{a^2} + \frac{1}{\rho_{op}^2(z)} + \frac{1}{\rho_{os}^2(L-z)}, \quad (47)$$

where the subscripts p and s refer to plane and spherical waves, respectively. The second and third terms on the right hand side of Eq. (47) represent the effects of the intervening medium. The second term arises from propagation from the source to the slab; the third term represents the effect of the medium on the wave subsequent to the interaction with a turbulent lens in the slab at z .

Therefore Eq. (45) is modified to include the effects of multiple scattering by replacing $(z'/ka)^2$ by $(z'/k\bar{a})^2$, where \bar{a} is given by Eq. (47). We have

$$\sigma_a^2(L) \sim \frac{\langle n_1^2 \rangle}{a^3} \int_0^L \frac{dz(L-z)^2}{\left[\left(\frac{z'}{k\bar{a}} \right)^2 + 1 \right]}, \quad (48)$$

a result that applies to a single turbulent scale size a . The result for a distribution of scale sizes (which are statistically independent) can be obtained by summing Eq. (48) over all scale sizes. Thus, the generalization of Eq. (48) to include a distribution of scale sizes is

$$\sigma^2 = \sum_{a_{\min} \leq a \leq a_{\max}} \sigma_a^2 \quad (49)$$

$$\rightarrow \int_{a_{\max}}^{a_{\min}} \sigma_a^2 \frac{da}{a}, \quad (50)$$

where Eq. (50) applies to the continuum limit.

From Eqs. (48) and (50) we obtain

$$\sigma^2 \sim \int_{a_{\min}}^{a_{\max}} \frac{da}{a^4} \langle n_1^2(a) \rangle \int_0^L \frac{dz(L-z)^2}{\left[\left(\frac{z'}{k\bar{a}} \right)^2 + 1 \right]} \quad (51)$$

where $z' = L - z$ and we permit that, in the general case, the index fluctuations is a function of eddy size (e.g., the Kolmogorov continuum model).

Single Scale Model

The case of a single scale size a and a gaussian shaped MCF will now be considered. In this case we have for plane waves [22]

$$M(\rho, z) = \exp \left[- \frac{2\pi\rho^2}{z_c a^2} \right]. \quad (52)$$

The quantity

$$z_c \approx \frac{1}{k^2 \langle n_1^2 \rangle a}$$

is the propagation distance where the average field is reduced by the factor $1/e$ compared to its value at the origin. Thus $(M(\rho_0) = 1/e)$

$$\rho_0(z) \sim a \left(\frac{z_c}{z} \right)^{1/2} \quad (53)$$

where here, and in the following, we omit factors of the order unity. In particular, no distinction will be made between the lateral coherence length for plane and spherical waves, their ratio being a numerical factor of the order unity. Hence, from Eqs. (47) and (53) we obtain

$$\frac{1}{a^2} = \frac{1}{a^2} + \frac{L-z}{z_c a^2} + -\frac{z}{z_c a^2} = \frac{1}{a^2} + \frac{L}{z_c a^2} \quad (54)$$

Thus, from Eqs. (48) and (54) we find that

$$\sigma_a^2(L) \sim \frac{\langle n_1^2 \rangle L^3}{a^3} \int_0^1 dt \frac{t^2}{1+t^2 \left\{ \left(\frac{L}{ka^2} \right)^2 \left(1 + \frac{L}{z_c} \right) \right\}} = \frac{L/z_c}{1 + \frac{L}{z_c}} \left\{ 1 - \frac{\tan^{-1} \left[\frac{L}{ka^2} \left(1 + \frac{L}{z_c} \right)^{1/2} \right]}{\frac{L}{ka^2} \left(1 + \frac{L}{z_c} \right)^{1/2}} \right\} \quad (55)$$

Examination of Eq. (55) reveals that σ_a^2 remains bounded as $L \rightarrow \infty$. In particular, $\lim_{L \rightarrow \infty} \sigma_a^2(L) = 1$; the amplitude fluctuations saturate to a value of the order unity, a value that is a constant, independent of wavelength and the parameters that describe the medium. Furthermore, for values of L small compared to z_c , Eq. (55) reduces to Tatarskii's perturbation results [22]. For instance, for $L \ll z_c$ we obtain

$$\begin{aligned} \sigma_a^2 &\sim \frac{L}{z_c} \left[1 - \frac{\tan^{-1} (L/ka^2)}{L/ka^2} \right] \rightarrow \langle n_1^2 \rangle \frac{L^3}{a^3}, \quad \text{for } L \ll ka^2 \\ &\rightarrow \langle n_1^2 \rangle k^2 a L, \quad \text{for } L \gg ka^2 \end{aligned} \quad (56)$$

In Fig. 4, σ_a^2 is plotted as a function of L/z_c for various values $\alpha = z_c/ka^2$. In general, σ_a^2 is given by the perturbation results for $L \lesssim z_c$ only. For $L \gtrsim z_c$, σ_a^2 tends asymptotically to a constant as $L \rightarrow \infty$.

Kolmogorov Continuum

To relate the case of a continuous distribution of scale sizes to the Kolmogorov continuum model, we note from Eq. (2) that, in the Kolmogorov inertial subrange

$$\langle [n_1(r_1) - n_1(r_2)]^2 \rangle = C_n^2 |r_1 - r_2|^{2/3}, \quad \ell_0 \ll |r_1 - r_2| \ll L_0 \quad (57)$$

where C_n is the structure constant, and ℓ_0 and L_0 are the inner and outer scale of turbulence, respectively. Equation (57) implies that the refractive index associated with a given scale size increases as the one-third power of that scale size, and we obtain the estimate

$$\langle n_1^2(a) \rangle \sim C_n^2 a^{2/3} \quad (58)$$

Furthermore, for this case the lateral coherence length for plane and spherical waves is known to be

$$\rho_0(z) \sim \frac{1}{[k^2 C_n^2 z]^{3/5}} \quad (59)$$

Substituting Eqs. (58) and (59) into Eq. (51) yields

$$\sigma^2 \sim C_n^2 L^3 \int_0^1 dt t^2 \int_{\ell_0}^{L_0} \frac{da}{a^4} \left\{ \frac{a^{2/3}}{1+t^2 \left(\frac{L}{ka^2} \right) \left[\frac{L}{ka^2} + \frac{L}{k\rho_0^2(L)} \left(t^{6/5} + (1-t)^{6/5} \right) \right]} \right\} \quad (60)$$

where $\rho_0(L)$ is given by Eq. (59) and

$$t = 1 - \frac{z}{L}$$

It is customary to express these results in terms of spatial wave number K , rather than scale size a . Therefore, let

$$a = \frac{1}{K}. \quad (61)$$

From Eqs. (60) and (61) we obtain

$$\sigma^2 \sim Q_0^{5/3} \int_{Q_1}^{Q_2} dQ Q^{4/3} \int_0^1 \frac{dt t^2}{1+t^2 Q^2 [Q^2 + Q_0^2(t)]}, \quad (62)$$

where the normalized spatial wave number Q is introduced

$$Q = \left(\sqrt{\frac{L}{k}} \right) K \quad (63)$$

and the various parameters are defined by

$$Q_o^2(t) = Q_o^2 \left[t^{6/5} + (1-t)^{6/5} \right], \quad (64)$$

$$Q_o^2 = \frac{L}{k \rho_o^2(L)} \quad (65)$$

$$Q_1 = \sqrt{\frac{L}{k L_o^2}} \quad (66)$$

and

$$Q_2 = \sqrt{\frac{L}{k L_o^2}} \quad (67)$$

To relate these results to Tatarskii's we note that Eq. (60) can be written as [note: $Q_o^{5/3} = [L/k \rho_o^2(L)]^{5/6} = C_n^2 k^{7/6} L^{11/6}$]

$$\sigma^2 \sim Q_o^{5/3} \int_{Q_1}^{Q_2} \Phi_n(Q) f_A(Q) Q dQ, \quad (68)$$

where the normalized spectral density is

$$\Phi_n(Q) = \frac{1}{Q^{11/3}} \quad (69)$$

and the "effective" amplitude filter function is

$$f_A(Q) = Q^4 \int_0^1 \frac{dt t^2}{1 + t^2 Q^2 [Q^2 + Q_o^2(t)]}. \quad (70)$$

The amplitude filter function $f_A(Q)$ gives a measure of the relative efficiency of an irregularity of a given size, located at a given position along the transmission path, in producing fluctuations at the observation plane. We note that Eq. (68) can be generalized immediately to the case of a modified von Karman spectrum by integrating over all Q and setting

$$\Phi_n(Q) = \frac{\exp(-k L_o^2 Q^2 / L)}{\left[Q^2 + \frac{L}{k L_o^2} \right]^{11/6}}.$$

In addition, examination of Eq. (68) reveals that the quantity $\Phi_n(Q) f_A(Q)$ can be interpreted as being proportional to the amplitude spectral coefficient in a two-dimensional Fourier expansion of the fluctuations. Indeed, Eq. (58) can be written in the general form

$$\sigma^2 \sim \int_0^\infty F_A(K) K dK \quad (68a)$$

where

$$F_A(K) = \pi k^2 L f_A(K) \Phi_n(K)$$

is the two-dimensional spectral density of the amplitude fluctuations in the L -plane and $\Phi_n(K)$ is, now, the arbitrary spectral density of the index of refraction fluctuations. For example, the amplitude covariance function $B_A(\rho)$ can be obtained from Eq. (68) by inserting the factor $J_0(Q\bar{\rho})$, where ρ is the lateral separation and $\bar{\rho} = \rho/(L/k)^{1/2}$ in the integral.

Examination of Eq. (70) reveals that the main contribution to the t -integral occurs for $t \approx 1$, i.e., $z \ll L$. This is obvious from a geometrical optics viewpoint in that the furthest eddies from the observation plane are primarily responsible for inducing amplitude fluctuations. Therefore, we may approximate $t^{6/5} + (1-t)^{6/5}$ by unity, from which it follows that

$$f_A(Q) \approx \int_0^1 \frac{dt t^2}{1 + t^2 (Q^2 + Q_o^2)} = \left(\frac{Q^2}{Q^2 + Q_o^2} \right) \left[1 - \frac{\tan^{-1} \left(Q \sqrt{Q^2 + Q_o^2} \right)}{Q \sqrt{Q^2 + Q_o^2}} \right] \quad (71)$$

From Eq. (65), the quantity Q_0 can be written as

$$Q_0^{5/3} = C_n^2 k^{7/6} L^{11/6} = (L/z_A)^{11/6} \quad (72)$$

where

$$z_A = \frac{1}{C_n^{12/11} k^{7/11}} \quad (73)$$

is the distance where $\sigma_T^2 \sim 1$. We note that saturation is observed experimentally for $L \gtrsim z_A$. In this regard we consider the limit of Eq. (71) for small Q_0 , i.e., $L \ll z_A$:

$$f_A(Q) = 1 - \frac{\tan^{-1} Q^2}{Q^2}, \quad Q_0 \ll 1. \quad (74)$$

Thus, in this limit we obtain from Eqs. (74), (68), and (69) that ($l_0 \ll (L/k)^{1/2} \ll L_0$)

$$\sigma^2 \sim Q_0^{5/3} \int_{Q_1}^{Q_2} Q^{-11/3} \left[1 - \frac{\tan^{-1} Q^2}{Q^2} \right] Q dQ \approx 0.92 C_n^2 k^{7/6} L^{11/6}, \quad l_0 \ll (L/k)^{1/2} \ll L_0 \quad (75)$$

On the other hand, Tatarskii's perturbation results are given by [22]

$$\sigma_T^2 \sim 0.65 Q_0^{5/3} \int_{Q_1}^{Q_2} Q^{-11/3} \left[1 - \frac{\sin Q^2}{Q^2} \right] Q dQ \approx 0.31 C_n^2 k^{7/6} L^{11/6}, \quad l_0 \ll (L/k)^{1/2} \ll L_0 \quad (76)$$

Thus, to a numerical factor of the order unity, the results of the present analysis, in the limit $L \ll z_A$, agree with Tatarskii's perturbation result.

Next consider the limit of $Q_0 \gg 1$, i.e., $L \gg z_A$. Equation (68) can be written as

$$\sigma^2 \sim Q_0^{5/3} \int_{Q_1}^{Q_2} dQ Q^{4/3} \frac{\left\{ 1 - \frac{\tan^{-1} Q \sqrt{Q^2 + Q_0^2}}{Q \sqrt{Q^2 + Q_0^2}} \right\}}{Q^2 (Q^2 + Q_0^2)} = \int_a^b \frac{dy y^{4/3}}{y^2 (y^2 + 1)} \left\{ 1 - \frac{\tan^{-1} [y \sqrt{y^2 + 1} Q_0]}{y \sqrt{y^2 + 1} Q_0} \right\}, \quad (77)$$

where

$$a = \frac{Q_1}{Q_0} = \frac{\rho_0(L)}{L_0} \quad (78)$$

and

$$b = \frac{Q_2}{Q_0} = \frac{\rho_0(L)}{l_0}. \quad (79)$$

Consider the case of the inertial subrange ($l_0 \ll \rho_0(L) \ll L_0$) and $L \gg z_A$ ($Q_0 \gg 1$). These conditions are not severe and are representative of the practical situation. In this case, Eq. (77) can be written as ($a \ll 1$, $b \gg 1$)

$$\sigma^2 \approx \int_0^\infty \frac{dy y^{-2/3}}{y^2 + 1} = \frac{\pi}{2 \cos(\pi/3)} = \pi. \quad (80)$$

Thus, for $L \gg z_A$ the amplitude fluctuations saturate to a constant value of the order unity, independent of wavelength and parameters which describe the turbulent medium.

We note that the condition $l_0 \ll \rho_0(L) \ll L_0$ is equivalent to the condition $z_c \ll L \ll z_i$, where

$$z_c \sim \frac{1}{k^2 C_n^2 L_0^{5/3}} \quad (81)$$

is the propagation distance at which the average field is reduced by the factor $1/e$ compared to its value at the origin and

$$z_i \sim \frac{1}{k^2 C_n^2 l_0^{5/3}} \quad (82)$$

is the propagation distance where the lateral coherence length of the field is of the order the inner scale. We have shown for $\rho_0(L)$ in the inertial subrange but $L \gg z_A$ (i.e., $z_c \ll z_A \ll L \ll z_i$) that the amplitude fluctuations saturate to a constant value of the order of unity. This is also the case for $L \gg z_i$, z_A . This assertion can be easily proved in a manner identical to the derivation of Eq. (80) from Eq. (77). The only difference being that, for $L \gg z_i$, the lateral coherence length ρ_0 is given by [see Eq. (26)]

$$\rho_0^2(L) \sim \frac{l_0^{1/3}}{C_n^2 k^2 L}, \quad L \gg z_i. \quad (83)$$

Thus, to the extent of the validity of the present physical mode, the amplitude fluctuations tend asymptotically to a constant value of the order as $L \rightarrow \infty$. The results of the present analysis are in agreement with the perturbation theory results for $L \ll z_A = 1/C_n^{12/11} k^{7/11}$ only.

Next, we present an estimate of the amplitude correlation function in the saturation regime. As previously noted, the amplitude correlation function can be obtained from Eq. (68) by inserting the factor $J_0(Q\bar{\rho})$ in the integral. Normalizing the amplitude correlation function to unity at $\rho = 0$, we have

$$B_A(\rho) = \frac{\int_0^\infty f_n(Q) f_A(Q) J_0(Q\bar{\rho}) Q dQ}{\int_0^\infty f_n(Q) f_A(Q) Q dQ}, \quad (84)$$

where $\bar{\rho} = \rho/(L/k)^{1/2}$ and the limits on the integral are now understood to be contained implicitly in $f_n(Q)$.

Consider the Kolmogorov spectrum, where $f_A(Q)$ is given by Eq. (71) or Eq. (70). Examination of the ensuing integrals in Eq. (84) reveals the following general features. For $Q_0(L) \ll 1$ (i.e., $L \ll z_A$), the main contribution to the Q integral occurs for $Q \sim 1$, from which it can be shown that the characteristic correlation length ρ_A , defined as $B_A(\rho_A) \approx 1/e$, is given by $\bar{\rho}_A \approx 1$, i.e., $\rho_A \approx (L/k)^{1/2}$. Thus, in this limit we obtain the perturbation theory result. Conversely, for the case of $Q_0(L) \gg 1$ (i.e., $L \gg z_A$), the main contribution to the Q integral occurs for $Q \approx Q_0$. As a result, it can be shown for $L \gg z_A$ that the amplitude correlation length is now

$$\left. \begin{aligned} \rho_A &\approx Q_0(L) \sqrt{\frac{L}{k}}, \\ &= \rho_0(L) \sim \frac{1}{(C_n^2 k^2 L)^{3/5}}, \quad l_0 \ll \rho_0(L) \ll L_0 \end{aligned} \right\} L \gg z_A. \quad (85)$$

That is, for $L \gg z_A$ the amplitude correlation length is of order the lateral coherence length which, in general, is a decreasing function of propagation distance. For $L \ll z_A$, ρ_A initially increases as \sqrt{L} [$\rho_0(L) > (L/k)^{1/2}$], reaches a maximum value for $L \sim z_A$ [$\rho_0(z_A) \approx (z_A/k)^{1/2}$], and finally, decreases as $\rho_0(L)$ for $L \gg z_A$ [$\rho_0(L) < (L/k)^{1/2}$]. This feature is illustrated in Fig. 5, where $B_A(\rho)$ is plotted as a function of normalized lateral separation $\bar{\rho}$ for various values of $\sigma_T^2 = C_n^2 k^{7/6} L^{11/6}$. Examination of Fig. 5 reveals, in addition to the characteristics of $B_A(\rho)$ discussed above, a long positive correlation tail is obtained for $\sigma_T^2 \gg 1$. These characteristics have been seen experimentally by J. R. Dunphy and J. R. Kerr [23] and by Gracheva et al. [24]. Figure 5 is a plot of $B_A(\rho)$ for the case of a finite inner scale l_0 . For L much less than both kl_0^2 and z_A , ρ_A is approximately equal to l_0 in agreement with the perturbation theory result. Conversely, for $L \gg z_A$ one finds $\rho_A \sim \rho_0(L)$; that is, ρ_A is a decreasing function of propagation distance L . In the saturation regime, the amplitude and phase correlation length are both equal to $\rho_0(L)$. In all cases we obtain a long positive tail whenever $L \gg z_A$. This residual correlation over large separations implies a reduced receiver aperture averaging effect as compared to the case of $L \ll z_A$.

Amplitude Temporal Frequency Spectrum

Next, we derive an expression for the optical amplitude temporal-frequency spectrum of a plane wave which is valid under strong scintillation conditions (i.e., in the saturation regime). Previous treatments [1, 2] have been based on a perturbative analysis of the log-amplitude covariance and do not apply in the saturation regime.

Following Tatarskii [1], the amplitude temporal frequency spectrum is given by

$$W(\nu) = 4 \int_0^\infty d\tau \cos(2\pi \nu \tau) R_A(\tau), \quad (86)$$

where ν is the frequency and $R_A(\tau)$ is the log-amplitude time auto-correlation function. Tatarskii has shown, by assuming Taylor's hypothesis, that statistical homogeneity allows the determination of the power spectrum as [1]

$$R_A(\tau) = B_A(\nu_n \tau)$$

where $B_A(\rho)$ is the log-amplitude covariance function, ρ is the separation in a plane transverse to the optic axis at propagation distance L , and ν_n is the component of the wind velocity normal to the optic axis.

Now, the log-amplitude correlation function is given, for plane waves and isotropic turbulence conditions by [1]

$$B_A(\rho) = 2\pi \int_0^\infty F_A(K) J_0(K\rho) K dK, \quad (87)$$

where K is the spatial wave number, J_0 is the Bessel function of the first kind of order zero, and

$$F_A(K) = \pi k^2 L f_A(K) \Phi_n(K). \quad (88)$$

Previous treatments have been based on the perturbation result:

$$f_A(K) = 1 - \frac{k}{K^2 L} \sin\left(\frac{K^2 L}{k}\right), \quad (89)$$

a result which is valid for $\sigma_T^2 \lesssim 1$ only. Here we base our calculation of the temporal spectrum on the amplitude filter factor derived above:

$$f_A(K) = \left(\frac{K^2}{K^2 + K_0^2} \right) \left(1 - \frac{\tan^{-1} \left\{ (L/k) K \sqrt{K^2 + K_0^2} \right\}}{(L/k) K \sqrt{K^2 + K_0^2}} \right), \quad (90)$$

where $K_0 = 1/\rho_0$ and ρ_0 is the lateral coherence length of the wave at propagation distance L .

We now present numerical results for $W(\nu)$, which are based on the Kolmogorov spectrum. For comparing theory with experiment, it is customary to introduce the dimensionless quantity [1]

$$U(\nu) \equiv \frac{\nu W(\nu)}{\int_0^\infty W(\nu) d\nu}, \quad (91)$$

which satisfies the condition of being normalized in logarithmic units, i.e., $\int_0^\infty U(\nu) d \log \nu = 1$. Consider the Kolmogorov spectrum

$$\Phi_n(K) = \frac{0.033 C_n^2}{K^{11/3}}, \quad (92)$$

where C_n^2 is the index structure constant. The normalized functions $\nu W(\nu) / \int_0^\infty W(\nu) d\nu$ and $\nu_0 W(\nu) / \int_0^\infty W(\nu) d\nu$, obtained by numerical integration, are shown in Figs. 6 and 7, respectively for various values of σ_T^2 , where here $\sigma_T^2 = 0.31 C_n^2 k^{7/6} L^{11/6}$.

Examination of Figs. 6 and 7 reveals that the normalized log-amplitude temporal spectrum is a universal function of ν/ν_0 only for $\sigma_T^2 \lesssim 1$, where $\nu_0 = \nu_n (2\pi \lambda L)^{-1/2}$. For $\sigma_T^2 > 1$, the normalized spectrum is both a function of σ_T^2 and ν_0 .

For $\sigma_T^2 \lesssim 1$, the peak in the spectrum occurs for $\nu_{\text{peak}} = \nu_0$, in agreement with the results of perturbation theory [1,2]. On the other hand, for $\sigma_T^2 \gtrsim 1$, the peak in the spectrum shifts to higher frequencies and the spectrum broadens. The peak in the temporal spectrum for $\sigma_T^2 \gtrsim 1$ is given by $\nu_{\text{peak}} \approx \nu_0 \sigma_T^{6/5} = \nu_n / \rho_0$. This is because the amplitude correlation length in the saturation regime is given by ρ_0 , rather than $\sqrt{L/k}$ (note, $\rho_0 < \sqrt{L/k}$ for $\sigma_T^2 > 1$). The broadening of the spectrum results from the residual positive correlation tail in $B_A(\rho)$ for $\sigma_T^2 \gtrsim 1$. It follows that, since both the spectrum broadens and $\int_0^\infty W(\nu) d\nu = \text{log-amplitude variance} = \text{constant}$ in the saturation regime, the maximum value of the spectrum decreases for increasing values of $\sigma_T^2 \gg 1$, $U(\nu) \propto \nu^{-1/3}$ and $\nu^{-5/3}$ as ν tends to zero and infinity, respectively. These features are displayed in Figs. 6 and 7. Gracheva et al. [24] has experimentally measured the normalized power spectrum $U(\nu)$ in the saturation regime. These experimental results, presented in Fig. 13 of Ref. 24, are in good qualitative agreement with the theoretical results discussed above and displayed in Fig. 6.

It is concluded that in order to obtain all of the scintillation temporal spectral components in the saturation regime, it is necessary to use an electronic bandwidth based on a peak frequency $\sim \nu_0(\sigma_T)^{6/5}$ rather than ν_0 in experimental investigations of strong amplitude fluctuations. The result of using too small an electronic bandwidth would be an apparent decrease of the log-amplitude variance for increasing values of σ_T^2 .

Physically, the qualitative features of the temporal power spectrum in the saturation regime discussed above can be expected to be very insensitive to beam geometry. Indeed, the recent data of Garcheva et al. [24] indicate that the geometry of the initial laser beam (e.g., collimated, divergent) has practically no influence on the statistical characteristics of strong irradiance fluctuations.

Spherical Waves

We conclude by a brief discussion of spherical wave amplitude statistics. The modification of the plane wave results for spherical wave propagation are, as for phase effects, purely geometrical. For the case of a point source at the origin, the transmittance factor for the turbulent lens centered at \underline{p} in the slab located at propagation distance z from the origin (i.e., a propagation distance $z' = L - z$ from the observer) contains the additional multiplicative factor $\exp[+ik(\underline{r} - \underline{p})^2/2z]$ as compared to the propagation of a plane wave. In a manner similar to that which led from Eq. (38) to Eq. (51), it can be shown that the modification to Eq. (51) for the spherical-wave amplitude variance is obtained by inserting in the integrand the additional multiplicative factor $(z/L)^2$. That is, the spherical wave amplitude filter function, valid for arbitrary values of σ_T^2 , is obtained as

$$f_A^s(K) = Q^4 \int_0^1 \frac{dt t^2 (1-t)^2}{1 + t^2 (1-t)^2 Q^2 [Q^2 + Q_0^2(t)]} \quad (93)$$

where

$$Q^2 = \frac{LK^2}{k} \quad (94)$$

and

$$Q_0^2(t) = \frac{L}{k} \left[\frac{1}{\rho_0^2(Lt)} + \frac{1}{\rho_0^2[L(1-t)]} \right] \quad (95)$$

Next, we calculate the ratio of the plane-wave to the spherical-wave log-amplitude variance for the Kolmogorov spectrum. Let

$$R = \frac{\langle x_p^2 \rangle}{\langle x_s^2 \rangle} \quad (96)$$

where the subscripts p and s refer to plane and spherical waves, respectively. From Eq. (93) and the corresponding expression for plane waves, we obtain \dagger . (The limits on the integrals appearing in Eq. (19) are understood to be contained implicitly in $\dagger_n(Q)$.)

$$R = \frac{\int_{Q_1}^{Q_2} f_A^p(Q) \dagger_n(Q) Q dQ}{\int_{Q_1}^{Q_2} f_A^s(Q) \dagger_n(Q) Q dQ} \quad (97)$$

which, for the Kolmogorov spectrum, yields

$$R = \frac{\int_{Q_1}^{Q_2} f_A^p(Q) Q^{-8/3} dQ}{\int_{Q_1}^{Q_2} f_A^s(Q) Q^{-8/3} dQ} \quad (98)$$

where Q_1 and Q_2 are given by Eqs. (66) and (67), respectively.

First, consider the geometrical-optics limit $L \ll kL_0^2$, i.e., $Q^2 \ll 1$. We find that

$$R = \frac{\int_0^1 dt (1-t)^2}{\int_0^1 dt t^2 (1-t)^2} = 10,$$

in agreement with the result of Tatarskii [1].

Next, consider the case $L \gg k \rho_0^2$, but $\sigma_T^2 \ll 1$, i.e., wave optics in the regime of weak irradiance fluctuations. In this regime, Q_0^2 in Eqs. (93) and (70) can be neglected with respect to Q^2 . We find that

$$R \approx \frac{\int_0^\infty dQ Q^{4/3} \int_0^1 dt t^2 [1 + t^2 Q^4]^{-1}}{\int_0^\infty dQ Q^{4/3} \int_0^1 dt t^2 (1-t)^2 [1 + t^2 (1-t)^2 Q^4]^{-1}} \quad (99)$$

Numerical integration yields $R \approx 2.47$, in agreement with the results of Tartarskii [1]. Finally, consider the saturation regime. In this regime, $Q_0^2 \gg 1$, and we obtain, from Eqs. (93) and (70),

$$f_A^s(Q) = f_A^p(Q) = \frac{Q^2}{Q^2 + Q_0^2} \quad (100)$$

Thus, from Eq. (98) we conclude that in the saturation regime

$$R = \frac{\langle x_p^2 \rangle}{\langle x_s^2 \rangle} = 1$$

That is, in the saturation regime, the variances of irradiance fluctuations of a plane and spherical wave are equal (i.e., both saturate to the same constant value). Indeed, Eq. (24) suggests that the amplitude filter function in the saturation regime is independent of the initial beam geometry and is equal to $Q^2(Q^2 + Q_0^2)^{-1}$. This implies that the log-amplitude variance for an arbitrary beam wave saturates to the same constant, independent of the initial beam geometry. (See Ref. 24.) These results are in agreement with the experimental result [24] that the beam geometry has practically no influence on the statistical characteristics of strong irradiance fluctuations (e.g., see Figs. 5b and 5c of Ref. 25). The plane-to-spherical-wave log-amplitude variance ratio in the wave-optics regime (i.e., $L \gg k \rho_0^2$) is plotted in Fig. 8 as a function of σ_T^2 .

In the saturation regime, the normalized log-amplitude covariance function $b_A(\rho)$ for both plane and spherical waves and the Kolmogorov spectrum can be written as

$$b_A(\rho) \equiv \frac{B_A(\rho)}{B_A(0)} = \frac{1}{\pi} \int_0^1 dt \int_0^\infty \frac{J_0\left(x \frac{\rho_t}{\rho_0}\right)}{1+x^2} x^{-2/3} dx \quad (\sigma_T^2 \gg 1) \quad (101)$$

where $\rho_t = \rho$ and $t\rho$ for plane and spherical waves, respectively. From Eq. (101) it follows that, in the saturation regime, the log-amplitude covariance function is a universal function of ρ/ρ_0 , in contrast to the regime of weak fluctuations ($\sigma_T^2 \ll 1$) where the log-amplitude covariance is a universal function of $\rho/(L/k)^{1/2}$. Figure 9 is a plot of Eq. (101) as a function of ρ/ρ_0 . The asymptotic limits of $b_A(\rho)$ are obtained directly from Eq. (101). We find that ($\sigma_T^2 \gg 1$)

$$\lim_{\rho \rightarrow 0} b_A(\rho) \approx \begin{cases} 1 - \frac{3}{4\pi} \left(\frac{\rho}{\rho_0}\right)^{5/3} + \dots & \text{(plane wave)} \\ 1 - \frac{9}{32\pi} \left(\frac{\rho}{\rho_0}\right)^{5/3} + \dots & \text{(spherical wave)} \end{cases}$$

and

$$\lim_{\rho \rightarrow \infty} b_A(\rho) \approx \begin{cases} \frac{3}{\pi} \left(\frac{\rho_0}{\rho}\right)^{1/3} + \dots & \text{(plane wave)} \\ \frac{9}{2\pi} \left(\frac{\rho_0}{\rho}\right)^{1/3} + \dots & \text{(spherical wave)} \end{cases} \quad (102)$$

The asymptotic limits in the saturation regime are in contrast to the results of perturbation theory (valid for $\sigma_T^2 \ll 1$) where [2]

$$\lim_{\rho \rightarrow 0} b_A(\rho) \approx 1 - O\left(\frac{k\rho^2}{L}\right)^{5/6} + \dots$$

and

where the numerical coefficients of the (kp^2/K) term in Eqs. (103) differ for plane and spherical waves, and are of the order unity. Thus, in the saturation regime, the covariance function scales with ρ_0 (rather than with the Fresnel length) and, for large ρ decays rather slowly ($\sim \rho^{-1/3}$), as compared to the regime of weak fluctuations, where, for large ρ , $b_A(\rho) \sim \rho^{-7/3}$. Furthermore, it can be shown that, in the saturation regime, the aperture averaging factor, as defined by Fried [25] of a circular receiving aperture of diameter D varies as $(\rho_0/D)^{1/3}$ for $D \gg \rho_0$, in contrast to the regime of weak fluctuations where the aperture averaging factor varies as $[(L/k)^{1/2}/D]^{7/3}$ for $D \gg (L/k)^{1/2}$.

4. CONCLUSIONS

By elementary physical arguments we have deduced the qualitative functional dependence of amplitude and phase statistics on the optical wave number, propagation distance and the parameters that describe the turbulent medium. We have attempted to delineate the underlying physical mechanisms which produce such fluctuations and as such the derivations presented here should complement the more rigorous analysis presented elsewhere (see, for example, Refs. 4 and 5). Although we have limited our discussion to the case of plane and spherical-wave amplitude and phase statistics for constant turbulence conditions, the extension to the case of inhomogeneous turbulence conditions is straightforward.

Finally, the propagation of beam waves in a turbulent medium is determined from a knowledge of the propagation characteristics of spherical waves via the extended Huygens-Fresnel principle [20]. As a result, the qualitative dependence of the characteristics of beam waves (e.g., beam spreading, on-axis irradiance) can be obtained directly from the spherical wave coherence length discussed above [19].

5. REFERENCES

1. TATARSKII, V. I., 1971, "Wave Propagation in a Turbulent Medium," McGraw-Hill.
2. TATARSKII, V. I., 1971, "The Effects of the Turbulent Atmosphere on Wave Propagation," National Technical Information Service, U.S. Department of Commerce, Springfield, Va.
3. CHERNOV, L. A., "Wave Propagation in a Random Medium," 1960, McGraw-Hill.
4. BARABANENKOV, Y. N., Y. A. KRAVSTOV, S. M. RYTOV, AND V. I. TATARSKII, *Sov. Phys.-Usp* **13**, 551 (1971).
5. PROKHOROV, A. M., F. V. BUNKIN, K. S. GOCHELASVILY, AND V. I. SHISHOV, *Proc. IEEE* **63**, 790 (1975).
6. YURA, H. T., *J. Opt. Soc. Am.* **64**, 59 (1974).
7. CLIFFORD, S. F., G. R. OCHS, AND R. S. LAURENCE, *J. Opt. Soc. Am.* **64**, 148 (1974).
8. FANTE, R. L., *Radio Sci. (New Series)* **10**, 77 (1975).
9. FANTE, R. L., *J. Opt. Soc. Am.* **64**, 608 (1975).
10. TATARSKII, V. I., and M. E. GERTSENSHTEIN, *JETP* **17**, 458 (1963).
11. TATARSKII, V. I., *JETP* **22**, 1083 (1964).
12. DeWOLF, D. A., *Radio Sci.* **2**, 1379 (1967).
13. DeWOLF, D. A., *J. Opt. Soc. Am.* **51**, 1029 (1968).
14. BROWN, W. R., *J. Opt. Soc. Am.* **62**, 966 (1972).
15. Ref. 2, Chap. 3.
16. BOURICUS, G. M. B., and S. F. CLIFFORD, *J. Opt. Soc. Am.* **60**, 1484 (1970).
17. HUFNAGEL, R. E., and N. R. STANLEY, *J. Opt. Soc. Am.* **54**, 52 (1964).
18. LUTOMIRSKI, R. F., and H. T. YURA, *Appl. Opt.* **10**, 1652 (1971).
19. YURA, H. T., *Appl. Opt.* **10**, 2771 (1971).
20. LUTOMIRSKI, R. F., and H. T. YURA, *J. Opt. Soc. Am.* **61**, 482 (1971).
21. FRIED, D. L., and H. T. YURA, *J. Opt. Soc. Am.* **62**, 600 (1972).
22. Ref. 1, Chap. 7.
23. DUNPHY, J. R., and J. R. KERR, *J. Opt. Soc. Am.* **63**, 981 (1973).
24. GRACHEVA, M. E., A. S. GURVICH, S. S. KASHKAROV, AND V. V. POKASOV, *Similarity Correlations and Their Experimental Verifications in the Case of Strong Intensity Fluctuations of Laser Radiation* [Akademia Nauk. SSSR, Otdelenie Oceanologii, Fiziki, Atmosfery i. Geografii (Russian Preprint)], pp. 1-39, report of work prior to publication, Moscow (1973). English translation available from The Aerospace Corp. Library Services, Literature Research Group, P. O. Box 92957, Los Angeles, Calif. 90009. Translation No. LRG-73-T-28.
25. FRIED, D. L., *J. Opt. Soc. Am.* **55**, 169 (1967).

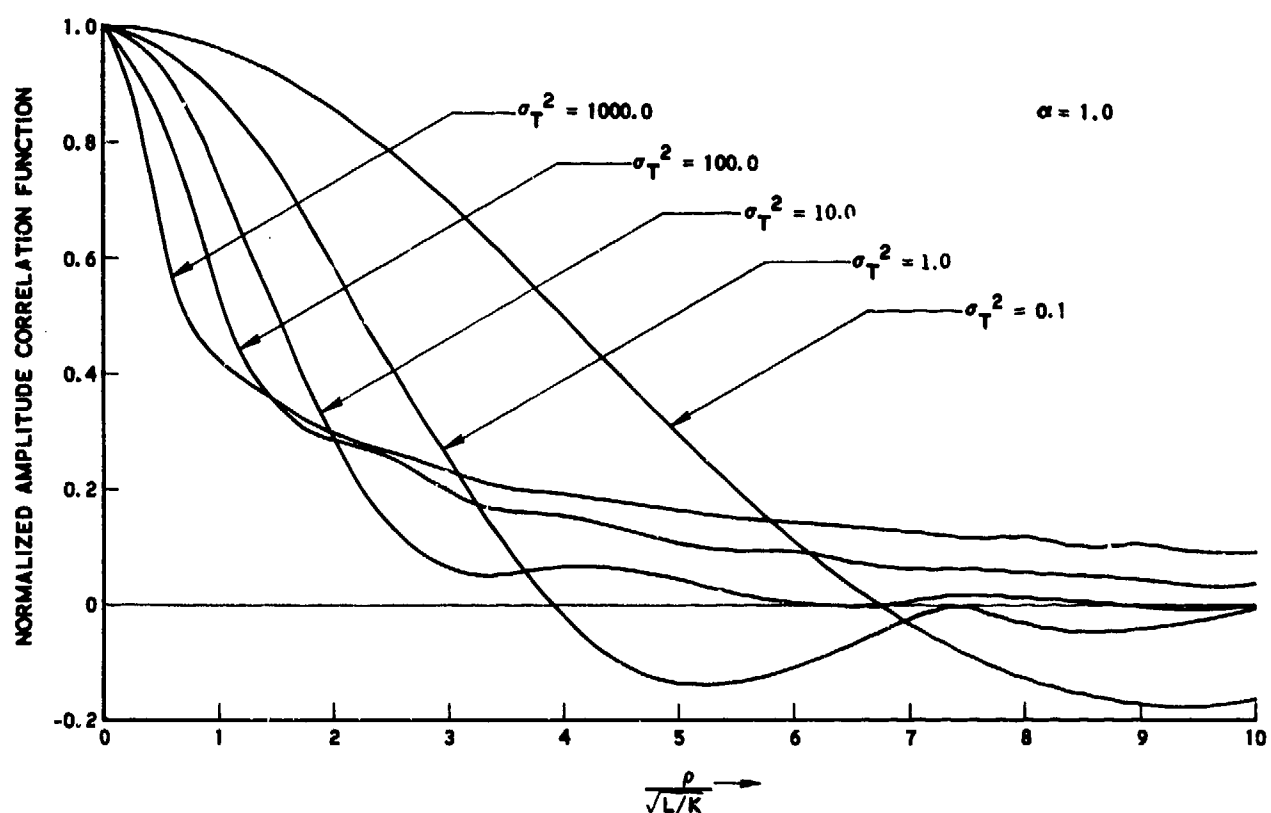
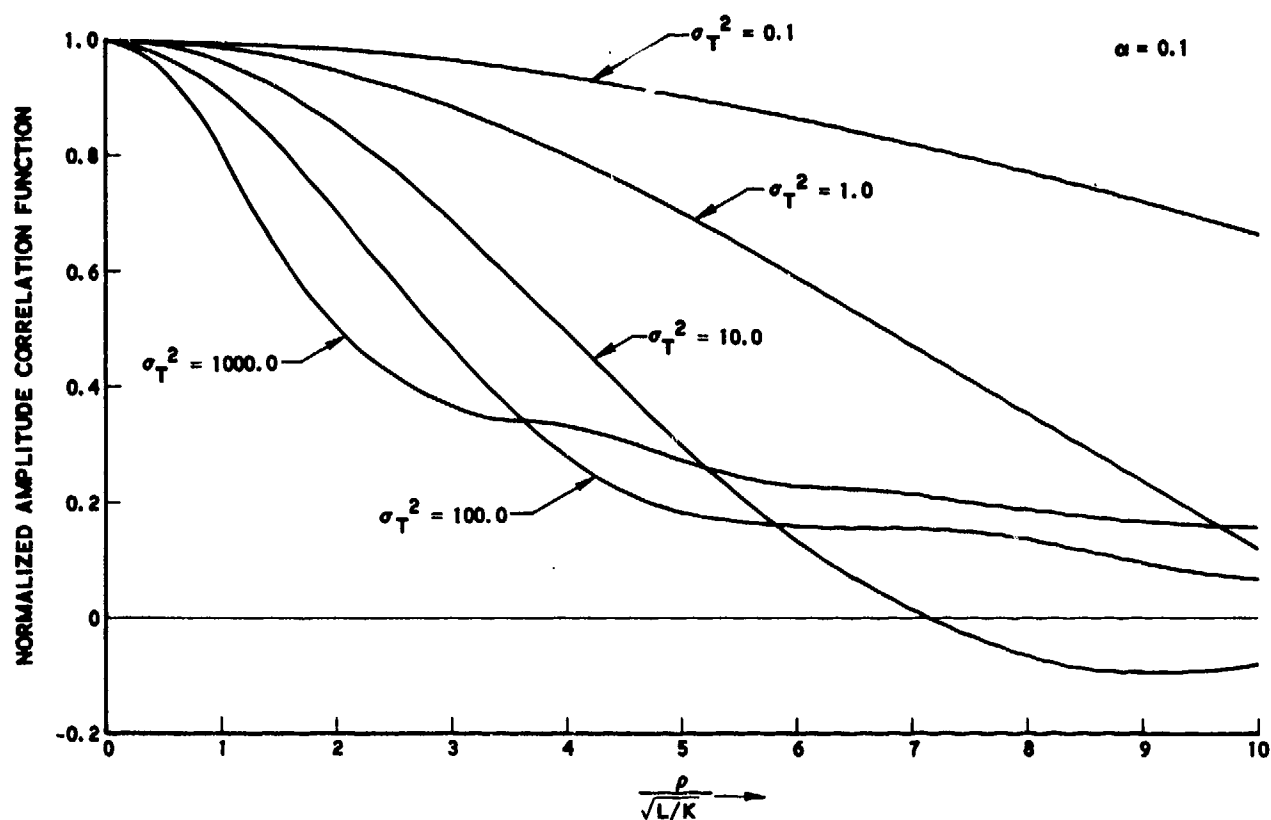


Fig.5 Normalized amplitude-correlation function, for the Kolmogorov spectrum, as a function of normalized transverse separation $\rho / (L/k)^{1/2}$ for various values of $\alpha (= z_A / k l_0^2)$ and σ_T^2 . Values of σ_T^2 much greater (less) than unity correspond to the saturation (perturbation-theory) regime.

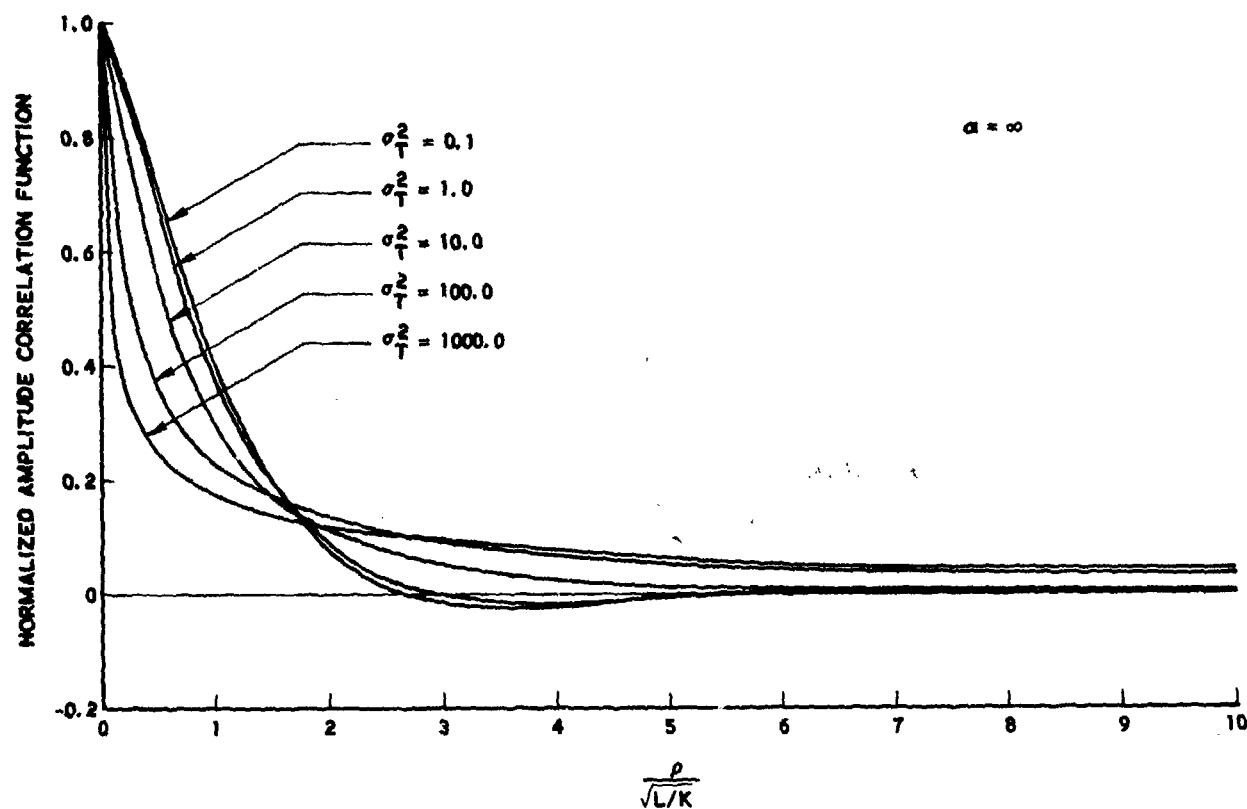


Fig.5 (Concluded)

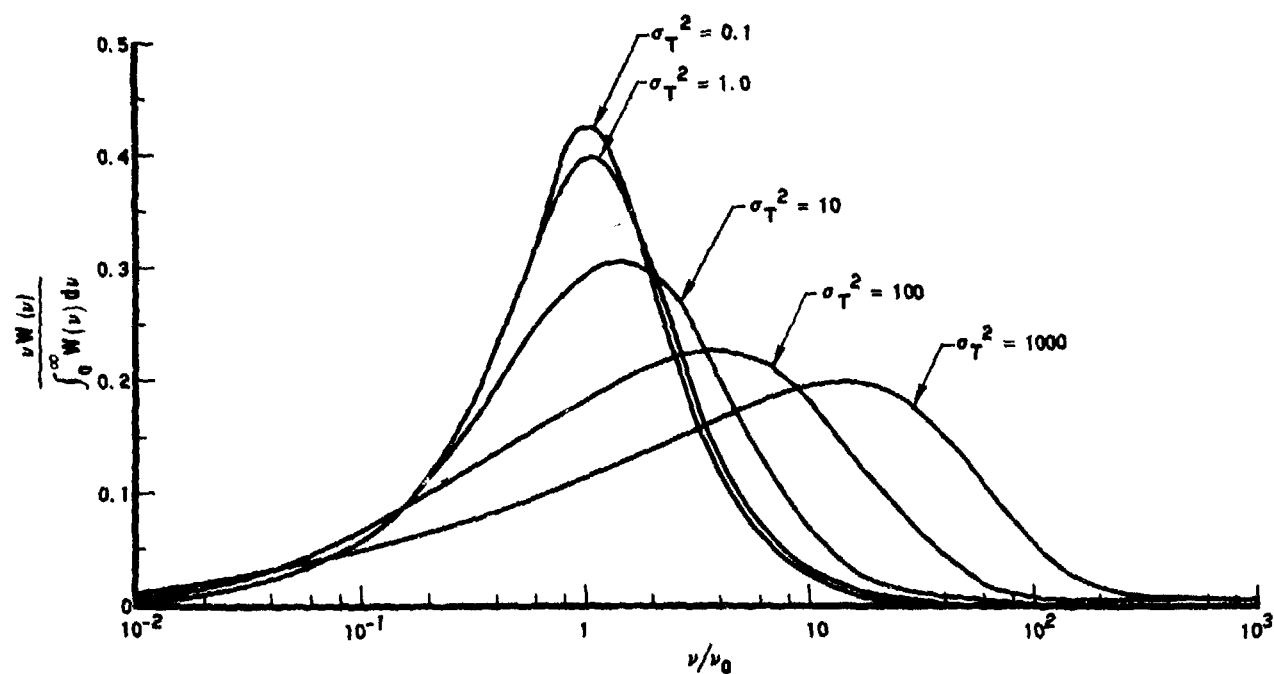


Fig.6 Normalized temporal-frequency spectrum for plane wave log-amplitude fluctuations as a function of $\nu_0 = v_n(2\pi\lambda L)^{1/2}$, for various values of σ_T^2 .

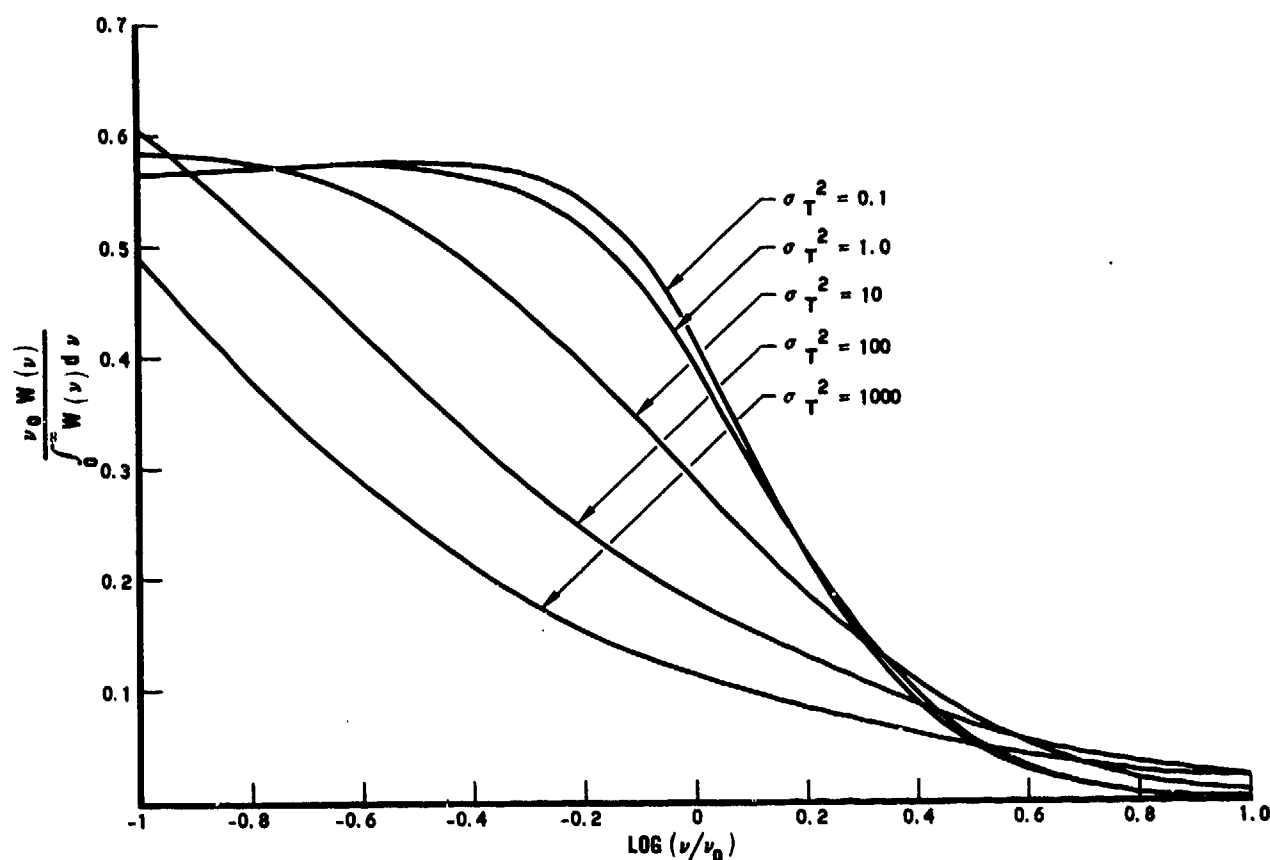


Fig.7 Temporal power spectrum of plane wave log-amplitude fluctuations vs $\log \Omega$, where $\Omega = \nu/\nu_0$, for various values of σ_T^2 .

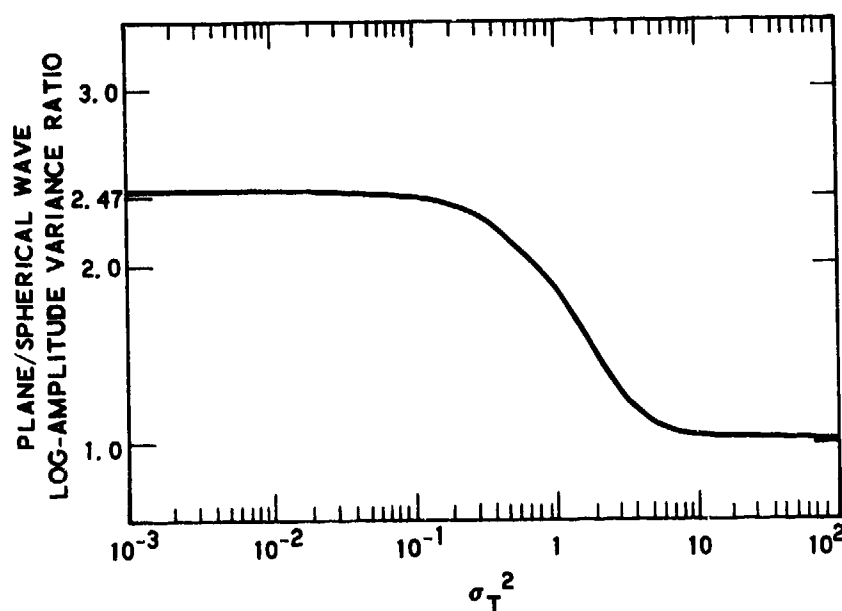


Fig.8 Plane - to spherical-wave log-amplitude variance ratio as a function of σ_T^2 for the Kolmogorov spectrum in the wave optics regime (i.e., $L \gg k l_0^2$).

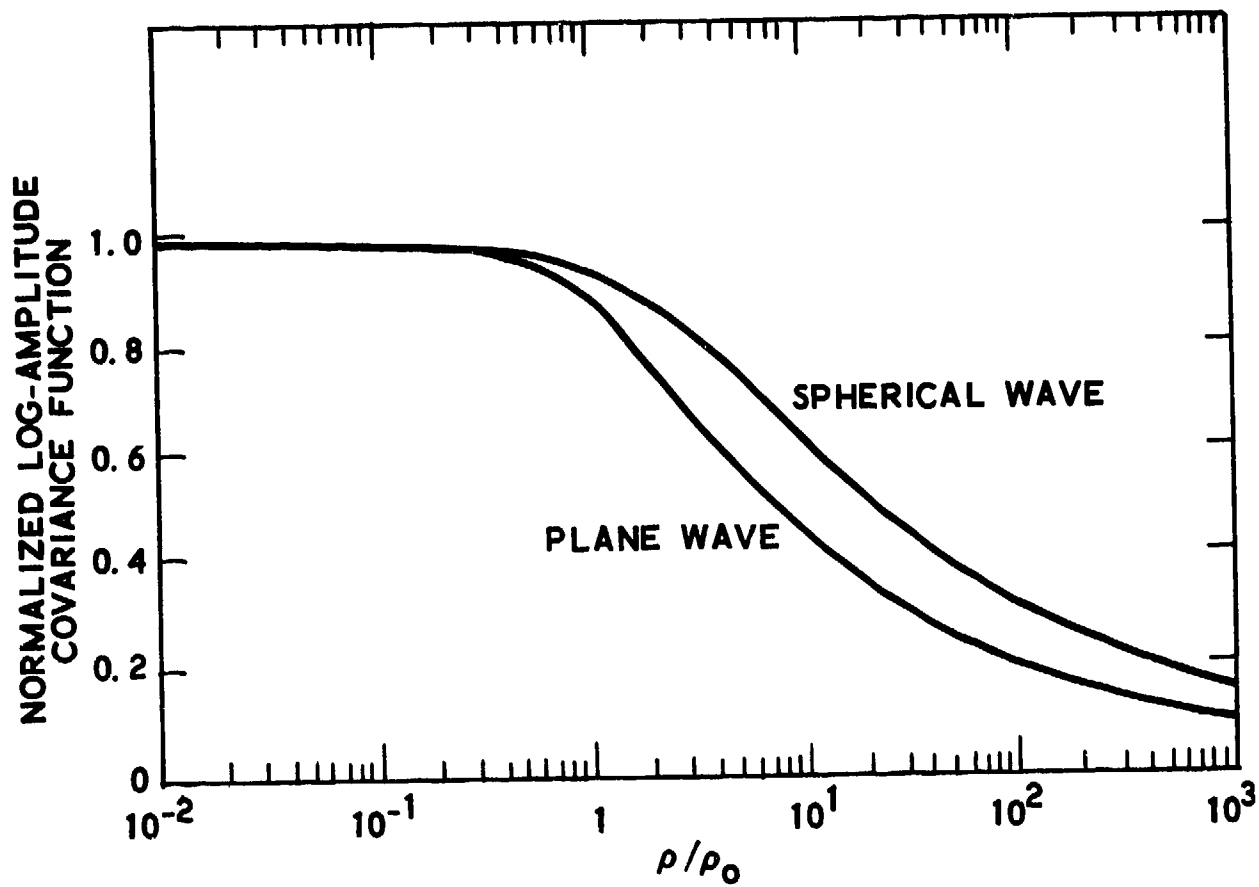


Fig.9 Normalized log-amplitude covariance function of plane and spherical waves as a function of ρ/ρ_0 for the Kolmogorov spectrum in the saturation regime (i.e., $\sigma_T^2 \gg 1$).

LOG-NORMAL PROBABILITY DISTRIBUTION OF STRONG IRRADIANCE FLUCTUATIONS:

AN ASYMPTOTIC ANALYSIS

Luc R. Bissonnette
 Defence Research Establishment Valcartier
 P.O. Box 880
 Courcellette, P.Q.
 CANADA GOA 1R0

SUMMARY

The asymptotic solutions for the first- and second-order statistical moments of the amplitude of a plane optical wave propagating in a turbulent atmosphere are derived from Maxwell's equations. These solutions show that the irradiance variance diverges to infinity if the irradiance probability distribution is everywhere log-normal. Therefore, the widely used log-normal hypothesis is incompatible with the observation of the saturation of the irradiance variance. Using the same asymptotic solutions, it is shown that the irradiance variance tends to unity if, alternately, the wave amplitude has a normal distribution in the saturation region. The latter result is much more consistent with the measured saturation levels. Finally, direct probability measurements in a simulated atmosphere tend to confirm that the actual distribution is close to normal at saturation distances.

1. INTRODUCTION

One important and still unsettled problem connected with the study of the propagation of optical waves in turbulent media is the form of the probability distribution of the irradiance fluctuations. Well-established governing equations exist for the statistical moments of the electric field but no formal model equation has been discovered for its probability distribution. However, approximations or hypotheses concerning the latter have always been sought to relate the higher order statistical moments to the lower order moments. These simplifications are very often necessary to work out solutions. Most, if not all, theoretical approaches to this problem use explicitly or implicitly some form of probability distribution hypothesis. In regions where Rytov's method is valid, application of the central limit theorem strongly supports the log-normal probability distribution of the irradiance fluctuations. However, in regions where saturation of the irradiance variance is observed, the results are theoretically more controversial: equally convincing arguments have been presented in support of either a log-normal or a Rice-Nakagami distribution of the turbulent irradiance! Experimentally, many direct measurements seem to support the log-normal hypothesis throughout the propagation range but recent Russian data show relatively significant deviations from log-normal in the saturation region.

The situation depicted in the preceding paragraph is described and referenced by WANG and STROHBEHN (1974a, 1974b). They present numerical results which show that the irradiance probability distribution cannot be exactly log-normal in the saturation region. We arrive at the same conclusion in this report. Using straightforward mathematical and statistical arguments, we deduce the asymptotic solutions for the first- and second-order moments of the wave amplitude in the case of a plane wave. From these asymptotic solutions, we demonstrate that the log-normal formula for the relative irradiance variance, β^2 , grows indefinitely with propagation distance. Obviously, this divergence is unacceptable in view of the numerous experimental observations of a saturation regime where β^2 is bounded. On the other hand, if the wave amplitude is assumed to obey a normal distribution in the saturation region, we find from the same solutions that β^2 tends to unity. This value is much more consistent with published data on the saturated irradiance variance. Interestingly, this normal probability distribution hypothesis is reasonably well corroborated by direct probability measurements in a laboratory simulation of the turbulent atmosphere.

The merit of the present method is that it does not require extensive analytical or numerical manipulations. Our results are based on simple asymptotic solutions which are independent of closure approximations and which are valid for an unspecified refractive index covariance function.

2. PROPAGATION MODEL

We consider a source pulsating at a single and constant angular frequency ω . The resulting electromagnetic field is allowed to propagate in a medium having a constant relative magnetic permeability μ and a randomly distributed relative dielectric constant ϵ . As is commonly done in most studies regarding the effects of turbulence on optical propagation in the earth's atmosphere, it is assumed that $\epsilon\mu$ is real and that the random fluctuations in ϵ are much smaller than its average value. Consistent with the latter hypothesis, we neglect polarization. Under these conditions, the electric field E can be considered a scalar E and it is conveniently written as follows:

$$E = A \exp [jk(z+\phi) - j\omega t], \quad (1)$$

where $j = \sqrt{-1}$, $k = \frac{n_0 \omega}{c}$ is the wave number, n_0 is the unperturbed index of refraction, c is the speed of light in free space, z is the distance along the propagation axis, ϕ is a phase function to be specified later and A is the wave amplitude. Upon substituting relation (1) for E in the equation for the electric field in a medium with a randomly distributed dielectric constant, we have, after separation:

$$[\nabla(z+\phi)]^2 = \left(\frac{n}{n_0}\right)^2, \quad (2)$$

$$\nabla(z+\phi) \cdot \nabla A + \frac{1}{2k} \nabla^2(z+\phi) = \frac{j}{2k} \nabla^2 A, \quad (3)$$

where $n = \sqrt{\mu\epsilon}$ is the instantaneous refractive index.

The representation of the electric field defined by relation (1) where ϕ and A satisfy equations (2) and (3) is not unique but, except for the explicit approximations given above, equations (1-3) are an exact form of Maxwell's equations. The reader will note that equation (2) is the eikonal equation. Hence, function ϕ is real and represents the geometrical optics fluctuations of the phase front. Mathematically, the subdivision of the equation for the electric field into equations (2) and (3) constitutes the system which contains the least number of terms of disparate orders of magnitude since the wave number k , which is very large at optical frequencies, appears only once in equations (2) and (3).

Consistent with the hypothesis of small fluctuations of the index of refraction, i.e. $(n-n_0)/n_0 \ll 1$, we make the paraxial approximation. More explicitly, we assume:

$$\frac{\partial \phi}{\partial z} \ll 1, \quad (4)$$

$$\frac{\partial^2 Q}{\partial z^2} \ll \nabla_t^2 Q, \quad (5)$$

where Q represents either A or ϕ and where ∇_t is the gradient operator in the plane transverse to the optical axis of propagation. Using relations (4) and (5), equations (2) and (3) become:

$$\frac{\partial \phi}{\partial z} + \frac{1}{2} (\nabla_t \phi)^2 = \frac{n-n_0}{n_0}, \quad (6)$$

$$\frac{\partial A}{\partial z} + \nabla_t \phi \cdot \nabla_t A + \frac{1}{2k} \nabla_t^2 \phi = \frac{j}{2k} \nabla_t^2 A. \quad (7)$$

We prefer, in the following treatment, to use the notation:

$$\underline{V} = \nabla_t \phi, \quad (8)$$

where, in the paraxial approximation, \underline{V} denotes the vector angle subtended locally by the instantaneous geometrical ray passing through this point. Using equation (8) and noting that $\nabla_t \times \underline{V} \equiv 0$, equations (6) and (7) may be rewritten as follows:

$$\left(\frac{\partial}{\partial z} + \underline{V} \cdot \nabla_t \right) \underline{V} = \nabla_t \frac{(n-n_0)}{n_0}, \quad (9)$$

$$\left(\frac{\partial}{\partial z} + \underline{V} \cdot \nabla_t \right) A = -\frac{1}{2} A \nabla_t \cdot \underline{V} + \frac{j}{2k} \nabla_t^2 A. \quad (10)$$

Equations (9) and (10) constitute our basic model for the instantaneous geometrical angle-of-arrival \underline{V} and wave amplitude A . They are used here to obtain the asymptotic behaviours of the first- and second-order statistical moments of A . Some general features are worth noting. The operator $\left(\frac{\partial}{\partial z} + \underline{V} \cdot \nabla_t \right)$

indicates derivation along a geometrical ray. The term $\frac{1}{2} A \nabla_t \cdot \underline{V}$ represents the geometrical effects, upon A , of the converging and diverging rays and $\frac{j}{2k} \nabla_t^2 A$ is the diffractive contribution. Neglecting the latter term on the grounds that k is large constitutes the geometrical optics approximation.

3. LOG-NORMAL DISTRIBUTION OF THE WAVE AMPLITUDE

The log-normal probability distribution hypothesis implies that the logarithm of the electric field $E = A \exp[jk\phi + jkz - j\omega t]$ has a normal distribution (TATARSKII, 1967; LAWRENCE and STROHBEHN, 1970). Using the notation $A = A_0 \exp[\chi + jk\psi]$, with χ and ψ real and $A_0 = \text{cst.}$, and noting that kz , ωt and A_0 are deterministic variables, it follows that $[\chi + jk(\psi + \phi)]$ is normally distributed. The quantities $k\psi$ and $k\phi$ represent respectively the diffractive and the geometrical phase perturbations. A theorem of the probability theory states that all marginal densities of a normal multi-dimensional density are also normal (FELLER, 1966). Therefore, the functions χ and $(\chi + jk\psi)$, in particular, are normally distributed. We use this result to relate the normalized irradiance variance $\beta^2 = \langle (AA^*)^2 \rangle - \langle AA^* \rangle^2 / \langle AA^* \rangle^2$, where $AA^* = EE^*$ is the instantaneous irradiance, to the first- and second-order statistical moments of the wave amplitude A . The upper asterisk designates a complex conjugate and the angular brackets indicate ensemble averages. From the normality of χ and $(\chi + jk\psi)$, it is trivial to demonstrate that:

$$\beta^2 = \langle (X - \langle X \rangle)^2 \rangle - 1, \quad (11)$$

$$\langle AA^* \rangle = A_0^2 \langle e^{2\chi} \rangle = e^{2\langle \chi - \langle \chi \rangle \rangle^2}, \quad (12)$$

$$\langle (AA^*)^2 \rangle = A_0^4 \langle e^{4\chi} \rangle = e^{4\langle \chi - \langle \chi \rangle \rangle^2} + 2jk\langle \chi - \langle \chi \rangle \rangle (\psi - \langle \psi \rangle) \rangle \quad (13)$$

$$\langle A \rangle \langle A^* \rangle = \langle AA^* \rangle e^{-\langle (X - \langle X \rangle)^2 \rangle} e^{-k^2 \langle (\psi - \langle \psi \rangle)^2 \rangle}. \quad (14)$$

Combining equations (11), (13) and (14), we obtain:

$$\beta^2 = \frac{\langle AA^* \rangle^2}{[\langle A \rangle \langle A^* \rangle]^2} - 1, \quad (15)$$

where $|\langle A^2 \rangle|$ denotes the magnitude of the complex quantity $\langle A^2 \rangle$. In the remainder of the text, equation (15) is often referred to as the log-normal expression of the normalized irradiance variance.

The approach followed here consists of deriving from equations (9) and (10) the asymptotic limits of the statistical moments $\langle A \rangle$, $\langle AA^* \rangle$ and $|\langle A^2 \rangle|$. These asymptotic functions are substituted in expression (15) and the result compared with experimental data to determine the consequences or implications of the log-normal hypothesis.

As is commonly done in this field, we postulate that the refractive index fluctuations are statistically homogeneous. Without loss of generality, we consider plane waves only. Indeed, it is sufficient to demonstrate that a constitutive hypothesis fails in a given application to prove its inconsistency. From the latter assumption, we deduce that $\langle \nabla \rangle = 0$ and that the derivatives, in the transverse plane, of any average quantity vanish exactly.

From equations (9) and (10), we easily obtain:

$$\frac{\partial}{\partial z} AA^* + \nabla_t \cdot (\nabla AA^*) = \frac{j}{2k} \nabla_t \cdot [A^* \nabla_t A - A \nabla_t A^*].$$

Hence, for plane waves, we have:

$$\frac{d}{dz} \langle AA^* \rangle = 0 \Rightarrow \langle AA^* \rangle = A_0^2 = \text{cst}. \quad (16)$$

Equation (16) expresses the principle of irradiance conservation, a predictable result which confirms the validity of the method of deriving the equations for the statistical moments.

If we denote by lower-case letter the fluctuating part of the amplitude A , i.e. $a = A - \langle A \rangle$, we have:

$$\langle AA^* \rangle = \langle A \rangle \langle A^* \rangle + \langle aa^* \rangle. \quad (17)$$

Inspection of equations (16) and (17) reveals that the turbulent irradiance $\langle aa^* \rangle$ is extracted from the mean field irradiance $[\langle A \rangle \langle A^* \rangle]$. Statistically, it appears extremely doubtful that this mechanism could spontaneously reverse itself with increasing propagation distance z . In other words, it is very improbable that non-turbulent irradiance could spontaneously be produced out of turbulent irradiance. Therefore, asymptotic oscillations of $\langle aa^* \rangle$ and $[\langle A \rangle \langle A^* \rangle]$ are ruled out as very unlikely. Since both expressions are positive definite, we conclude from equations (16) and (17) that $\langle aa^* \rangle$ and $[\langle A \rangle \langle A^* \rangle]$ must tend toward constant values as $z \rightarrow \infty$, or, equivalently, that the z -derivatives of these quantities must vanish asymptotically.

The hypothesis of non-oscillation of $\langle aa^* \rangle$ and $[\langle A \rangle \langle A^* \rangle]$ forms the basis of the proposed asymptotic solutions. Essentially, this postulate is derived from the more general observation that stochastic processes naturally tend to assume the most probable or the most random statistical state, i.e. the state which contains the largest number of degrees of freedom. In our application of a plane optical wave propagating in a homogeneous turbulent atmosphere, a decrease in the turbulent irradiance $\langle aa^* \rangle$ corresponds to a decrease in the number of permissible degrees of freedom since, by conservation, it necessarily implies an increase in the non-random fraction of the total irradiance. Consequently, it is indeed improbable that $\langle aa^* \rangle$ could spontaneously begin to decrease or oscillate with increasing values of z .

Averaging equation (10), we obtain for plane waves:

$$\frac{d}{dz} \langle A \rangle = \frac{j}{2k} \langle \nabla_t \cdot \nabla \rangle, \quad (18)$$

from which we derive the following equation for $\langle A \rangle \langle A^* \rangle$:

$$\frac{d}{dz} \langle A \rangle \langle A^* \rangle = \frac{j}{2k} \langle A^* \rangle \langle \nabla_t \cdot \nabla \rangle + \frac{j}{2k} \langle A \rangle \langle \nabla_t \cdot \nabla \rangle. \quad (19)$$

Since $[\langle A \rangle \langle A^* \rangle]$ asymptotically tends toward a constant, the right-hand side of equation (19) must vanish monotonically as $z \rightarrow \infty$. Therefore, either, or both, $\langle A \rangle$ and $\langle \nabla_t \cdot \nabla \rangle$ must go to zero as $z \rightarrow \infty$. We will show that $\langle \nabla_t \cdot \nabla \rangle$ cannot tend to zero if the asymptotic limit of $\langle A \rangle$ is non-zero.

From equations (9) and (10), we derive the following equation for $\langle \nabla_t \cdot \nabla \rangle$:

$$\frac{d}{dz} \langle \nabla_t \cdot \nabla \rangle = \langle A \rangle \left\{ -\frac{1}{2} \langle (\nabla_t \cdot \nabla)^2 \rangle + \frac{\text{c.c.m.}}{\langle A \rangle} \right\}, \quad (20)$$

where c.c.m. stands for cross correlation moments involving the fluctuating amplitude a , the vector angle V or the index of refraction n . The latter terms depend on both equations (9) and (10). In other words, they are functions of both the geometrical and the diffractive effects. By comparison, $\langle (\nabla_t \cdot \nabla)^2 \rangle$ is governed by equation (9) only; in particular, $\langle (\nabla_t \cdot \nabla)^2 \rangle$ is wave number independent. Hence, because they are functions of different processes, the terms within brackets in the right-hand side of equation (20) cannot cancel each other exactly and reproducibly under general conditions, except perhaps at some discrete points. Moreover,

$\langle \nabla_{\perp} V \rangle^2$ is positive definite and, according to the very definition of V , it remains non-zero as long as turbulence persists, i.e. for all values of $z > 0$. Hence, in general, the right-hand side of equation (20) cannot monotonically vanish if $\langle A \rangle$ tends to a non-zero limit. Therefore, it is impossible for $\langle \nabla_{\perp} V \rangle$ to remain constant and in particular zero if $\langle A \rangle$ is non-zero. Applying this result to equation (19) and recalling that the z -derivative of $\langle A \rangle \langle A \rangle^*$ must vanish asymptotically, it follows that the average amplitude $\langle A \rangle$ must go to zero with increasing z , i.e.:

$$\langle A \rangle \rightarrow 0 \text{ as } z \rightarrow \infty, \quad (21)$$

from which it follows that:

$$\langle A \rangle \langle A \rangle^* \rightarrow 0 \text{ as } z \rightarrow \infty. \quad (22)$$

It is worth noting that the latter result was heuristically predictable from our starting postulate that a stochastic process naturally tends toward a state of maximum randomness. Given equations (16) and (17), equation (22) expresses the fact that all available irradiance has been transformed into turbulent irradiance or, equivalently, that the original wave has been completely and totally scattered. This situation should indeed correspond to the most random state of irradiance distribution. Therefore, the analysis of the preceding paragraphs demonstrates that the postulate of maximum randomness and Maxwell's equations are mutually consistent.

To obtain the asymptotic value of the log-normal formula (15) for the irradiance variance, there remains to determine the behaviour of $\langle A^2 \rangle$ as $z \rightarrow \infty$. Denoting by R and I the real and imaginary parts of A and by r and i the real and imaginary parts of $a = A - \langle A \rangle$, we have:

$$\begin{aligned} \langle A^2 \rangle^2 &= [\langle A \rangle \langle A \rangle^*]^2 + [\langle r^2 \rangle - \langle i^2 \rangle]^2 + 4 \langle ri \rangle^2 \\ &\quad + 2[\langle R \rangle^2 - \langle I \rangle^2] [\langle r^2 \rangle - \langle i^2 \rangle] + 8 \langle R \rangle \langle I \rangle \langle ri \rangle. \end{aligned} \quad (23)$$

From equation (10), we derive the following equation for $\langle A^2 \rangle$ which is valid for plane waves:

$$\frac{d}{dz} \langle A^2 \rangle = \frac{j}{k} \langle \nabla_{\perp}^2 A \rangle. \quad (24)$$

Consistent with the hypotheses of plane wave and of statistical homogeneity of the index of refraction, we deduce that A is statistically homogeneous in planes transverse to the optical axis. Thus, we can rewrite the latter equation as follows:

$$\frac{d}{dz} \langle A^2 \rangle = \frac{j}{k} \lim_{\xi \rightarrow 0} \nabla_{\xi}^2 \langle a(z, \rho) a(z, \rho + \xi) \rangle,$$

where ρ and ξ are position vectors in the transverse plane. Equating the real and imaginary parts, we have:

$$\frac{d}{dz} [\langle R^2 \rangle - \langle I^2 \rangle] = -\frac{1}{k} \lim_{\xi \rightarrow 0} \nabla_{\xi}^2 [\langle i(z, \rho) r(z, \rho + \xi) \rangle + \langle r(z, \rho) i(z, \rho + \xi) \rangle], \quad (25)$$

$$\frac{d}{dz} \langle RI \rangle = \frac{1}{2k} \lim_{\xi \rightarrow 0} \nabla_{\xi}^2 [\langle r(z, \rho) r(z, \rho + \xi) \rangle - \langle i(z, \rho) i(z, \rho + \xi) \rangle]. \quad (26)$$

It is trivial to demonstrate that:

$$\begin{aligned} |\langle R^2 \rangle - \langle I^2 \rangle| &\leq \langle R^2 \rangle + \langle I^2 \rangle = \langle AA^* \rangle, \\ |\langle RI \rangle| &\leq \frac{1}{2} [\langle R^2 \rangle + \langle I^2 \rangle] = \frac{1}{2} \langle AA^* \rangle. \end{aligned}$$

Therefore, from equation (16) we deduce that the expressions $[\langle R^2 \rangle - \langle I^2 \rangle]$ and $\langle RI \rangle$ are bounded. If oscillations are ruled out, this implies that the right-hand side expressions of equations (25) and (26) must vanish asymptotically (we will consider the possibility of oscillations later on). The second derivatives at $\xi=0$ of the individual covariance functions which appear in equations (25) and (26) are not likely to vanish independently of the functions themselves. On the contrary, experimental (DUNPHY and KERR, 1973) and theoretical (BROWN, 1972; YURA, 1974a) investigations indicate that the decrease of the amplitude correlation as $\xi \rightarrow 0$ becomes more rapid with increasing propagation distance or turbulence strength. In other words, the second order derivatives, at zero separation, of the amplitude and phase covariances generally grow with z . Therefore, we conclude that the complex covariance $\langle a(z, \rho) a(z, \rho + \xi) \rangle$ must vanish as $z \rightarrow \infty$ and $\xi \rightarrow 0$. In particular, at $\xi=0$ we must have:

$$\langle r^2 \rangle - \langle i^2 \rangle \rightarrow 0 \text{ as } z \rightarrow \infty, \quad (27)$$

$$\langle ri \rangle \rightarrow 0 \text{ as } z \rightarrow \infty, \quad (28)$$

and:

$$\frac{d}{dz} [\langle R^2 \rangle - \langle I^2 \rangle] = O(\langle ri \rangle) \text{ as } z \rightarrow \infty, \quad (29)$$

$$\frac{d}{dz} \langle RI \rangle = O(\langle r^2 \rangle - \langle i^2 \rangle) \text{ as } z \rightarrow \infty, \quad (30)$$

where $S(u) = O(T(u))$ as $u \rightarrow u_0$ signifies that the ratio S/T remains bounded in some neighbourhood of u_0 .

Therefore, it follows from equations (22), (23), (27) and (28) that:

$$|\langle A^2 \rangle| \rightarrow 0 \text{ as } z \rightarrow \infty. \quad (31)$$

Substitution of equations (22) and (31) for $\langle A \rangle \langle A^* \rangle$ and $\langle A^2 \rangle$ into formula (15) leads to an indetermination $0/0$. Therefore, to compute the asymptotic value of the log-normal expression for β^2 , we must compare the rates at which $\langle A \rangle \langle A^* \rangle$ and $\langle A^2 \rangle$ respectively tend to zero.

From standard theorems, we have:

$$|\langle R \rangle^2 - \langle I \rangle^2| \leq \langle A \rangle \langle A^* \rangle, \quad (32)$$

$$|\langle R \rangle \langle I \rangle| \leq \frac{1}{2} \langle A \rangle \langle A^* \rangle. \quad (33)$$

Inspection of equation (23) together with the inequalities (32) and (33) reveals that $\langle A^2 \rangle$ cannot tend to zero faster than $\langle A \rangle \langle A^* \rangle$ unless $\langle r^2 \rangle - \langle i^2 \rangle$ and/or $\langle ri \rangle$ tend to zero at the same rate as $\langle A \rangle \langle A^* \rangle$ does; if only one of the expressions $\langle r^2 \rangle - \langle i^2 \rangle$ and $\langle ri \rangle$ satisfies the latter condition, the remaining one must evidently vanish more rapidly than $\langle A \rangle \langle A^* \rangle$. Only then is it conceivable that the fourth and/or the fifth term in formula (23) could combine with $\langle A \rangle \langle A^* \rangle^2$ and the other positive definite terms to form a result vanishing at a rate faster than the individual terms. This constitutes the only case where the log-normal expression (15) for the irradiance variance could possibly tend to a bounded value as $z \rightarrow \infty$. Since the magnitude of $\langle A^2 \rangle$ goes to zero at the same rate as the largest of its real and imaginary parts, we would have in this situation, from equations (29) and (30), that:

$$\frac{d}{dz} \langle A^2 \rangle = 0 \langle A \rangle \langle A^* \rangle \text{ as } z \rightarrow \infty. \quad (34)$$

Applying the rule of l'Hospital and utilizing equations (16) and (34), the asymptotic value of the log-normal formula (15) would behave as follows:

$$\beta^2 \rightarrow \text{cst.} \left\{ \lim_{z \rightarrow \infty} \left[2 \frac{d}{dz} \langle A \rangle \langle A^* \rangle \right]^{-1} \right\}^2 - 1 \quad \text{as } z \rightarrow \infty.$$

But we have already established that $\frac{d}{dz} \langle A \rangle \langle A^* \rangle \rightarrow 0$ as $z \rightarrow \infty$. Hence, even the most favourable conditions yield a diverging log-normal irradiance variance. Therefore, we conclude that the hypothesis of log-normal probability distribution necessarily leads to

$$\beta^2 \rightarrow \infty \quad \text{as } z \rightarrow \infty, \quad (35)$$

at least in the case of plane waves.

There remains to consider the possibility of asymptotic oscillations of $\langle A^2 \rangle$. In principle, the irradiance could alternate between the components $\langle R^2 \rangle$ and $\langle I^2 \rangle$ without inducing oscillations of the quantities $\langle A \rangle \langle A^* \rangle$ and $\langle A^2 \rangle$. However, in the present situation of plane waves propagating in homogeneous turbulence, it is very difficult to imagine a mechanism which could give rise to such oscillations. In any case, should $\langle A^2 \rangle$ oscillate asymptotically, it is evident from equations (15) and (22) that β^2 would still strongly diverge or alternate unrealistically between $+\infty$ and $-\infty$.

In summary, the asymptotic limits of the first- and second-order statistical moments of the electric field amplitude, which are solutions to Maxwell's equations in the case of a plane wave propagating in a homogeneous turbulent medium, imply that the irradiance variance, as obtained from the log-normal probability distribution hypothesis, grows indefinitely. This result is in obvious conflict with all experimental observations. Therefore, we conclude that the probability distribution of the electric field of an optical wave propagating in turbulence cannot, in general, remain log-normal as the propagation range increases.

For the preceding asymptotic results to be practical, it is important to specify where infinity ($z \rightarrow \infty$) actually begins. An order of magnitude estimate of the characteristic propagation length ℓ , on which the decay of the average amplitude $\langle A \rangle$ scales, is derived in appendix. Making the 2/3-power law hypothesis for the index covariance function and assuming $\ell_0 < L_0$, it is found that:

$$\ell_c = 1.1 \ell_0^{7/9} C_n^{-2/3} n_0^{2/3}, \quad (A8)$$

where C_n , ℓ_0 and L_0 are respectively the index structure parameter, the inner scale of turbulence and the outer scale of turbulence. Taking $\ell_0 = 5$ mm, we have:

- for strong turbulence, $C_n = 5 \times 10^{-7} \text{ m}^{-1/3}$,
 $\ell_c \approx 300 \text{ m}$;
- for intermediate turbulence, $C_n = 4 \times 10^{-8} \text{ m}^{-1/3}$,
 $\ell_c \approx 1.5 \text{ km}$; and
- for weak turbulence, $C_n = 8 \times 10^{-9} \text{ m}^{-1/3}$,
 $\ell_c \approx 5 \text{ km}$.

Despite the roughness of the approximations leading to (A8) and the uncertainty regarding the inner scale ℓ and its possible variation with C_n , the estimates of the characteristic propagation length ℓ_c given above indicate quite convincingly that the asymptotic solutions derived in this section become applicable at distances corresponding to the experimentally observed saturation regime.

4. NORMAL DISTRIBUTION OF THE WAVE AMPLITUDE

The asymptotic solutions derived in the previous section can also give information concerning the plausibility of other distributions. In particular, we consider in this section the possibility that the wave amplitude is normally distributed at large propagation distances.

Using the notation defined earlier, the variance of the irradiance is given by:

$$\begin{aligned}
\langle (AA^*)^2 \rangle - \langle AA^* \rangle^2 &= \langle (aa^*)^2 \rangle + 2[\langle A \rangle \langle aa^*a^* \rangle + \langle A \rangle^* \langle aaa^* \rangle] \\
&\quad - \langle aa^* \rangle^2 + 2\langle A \rangle \langle A \rangle^* \langle aa^* \rangle \\
&\quad + \langle A \rangle \langle A \rangle \langle a^*a^* \rangle + \langle A \rangle^* \langle A \rangle^* \langle aa \rangle.
\end{aligned}
\tag{36}$$

If the turbulent amplitude a is normally distributed, the following simplifying equations are applicable:

$$\langle aa^*a^* \rangle = \langle aaa^* \rangle = 0, \tag{37}$$

$$\langle (aa^*)^2 \rangle = 2\langle aa^* \rangle^2 + \langle aa \rangle \langle a^*a^* \rangle. \tag{38}$$

Hence, the normal probability formula for the normalized irradiance variance is:

$$\begin{aligned}
\beta^2 &= \langle AA^* \rangle^{-2} \{ \langle aa^* \rangle^2 + \langle aa \rangle \langle a^*a^* \rangle + 2\langle A \rangle \langle A \rangle^* \langle aa^* \rangle \\
&\quad + \langle A \rangle \langle A \rangle \langle a^*a^* \rangle + \langle A \rangle^* \langle A \rangle^* \langle aa \rangle \}.
\end{aligned}
\tag{39}$$

Therefore, from equations (16) and (17) and the asymptotic expressions (21), (22), (27) and (28), it follows, for a plane wave, that:

$$\beta^2 \rightarrow 1.0 \text{ as } z \rightarrow \infty, \tag{40}$$

if the wave amplitude has a normal probability distribution.

The experimental saturation values for the normalized irradiance standard deviation vary substantially according to various sources. For example, we find that: $\beta \rightarrow 1.0$ (LIVINGSTON et al., 1970); $\beta \rightarrow 1.1$ (TATARSKI, 1971); $\beta \rightarrow 1.1$ (KHMELEVTSOV, 1973); $\beta \rightarrow 1.23$ (CLIFFORD et al., 1974); and $\beta \rightarrow 1.3$ (DABBERDT et al., 1973). These numbers are representative of the data spread. They were generally obtained using a point source but recent theoretical results (YURA, 1974b) suggest that the saturation level is the same for plane and spherical waves. Hence, the hypothesis of normal probability distribution of the wave amplitude applied to our asymptotic solutions yields a saturation value of the normalized irradiance standard deviation which seems to be smaller, by 0 to 30% depending on the data source, than the measured values. The differences are well within the experimental scatter affecting each set of data so that our theoretical prediction can be considered well corroborated. Consequently, the normal probability distribution hypothesis appears very plausible in the saturation region, at least in so far as the irradiance variance is concerned.

In view of the relatively important data spread, a laboratory experiment was designed to simulate the turbulent atmosphere. A full description of the apparatus will be given in subsequent publications. In short, the thermal turbulences are created by electrically heating the bottom of a 1.5-m long, 50-cm deep and 50-cm wide water tank. The average water temperature is maintained constant by circulating cold water in a heat exchanger located just below the water surface. Typically, homogeneous temperature fluctuations, of the order of 0.5°C in standard deviation, are routinely produced with excellent reproducibility. This corresponds to an index structure parameter $C_n = 1.55 \times 10^{-4} \text{ m}^{-1/3}$, which is 300 times greater than what is normally referred to as strong atmospheric turbulence. Hence, the characteristic propagation distances are considerably reduced and saturation phenomena are easily observed in the laboratory. The 2/3-power law, or the Obukhov-Kolmogorov model, of the refractive index structure function is approximately verified over separations ranging from 1 to 7 or 8 mm. The light source is a 50-mW He-Ne laser. All data reported here are recorded on the axis of the beam which is collimated and expanded to a 50-mm diameter. Folding mirrors are used to increase the propagation path.

The instantaneous irradiance is detected by a pinhole-optical filter-photomultiplier assembly. The photomultiplier signal is digitized and transferred to the central computer where all data analyses are performed digitally.

The measured normalized standard deviation β of the irradiance fluctuations on the beam axis is plotted as a function of z in figure 1. Saturation is clearly shown to occur at distances $z > 2 \text{ m}$. This is in excellent agreement with formula (A8) if ℓ is assumed to be of the order of 1 mm. The saturation level is very close to unity. Hence, the value derived from our asymptotic solutions and the hypothesis of normal probability distribution of the wave amplitude is very well corroborated in this simulation experiment.

Making use of the asymptotic solutions (21), (27) and (28), it is easy to demonstrate that the irradiance ($H=AA^*$) probability distribution, corresponding to the normal probability distribution of the wave amplitude, is given by:

$$P(H/\beta\langle H \rangle) = 1 - \exp(-H/\beta\langle H \rangle). \tag{41}$$

In figure 2, equation (41) is compared to the distribution calculated from a 2500-point, 1.5 min irradiance sample recorded on the beam axis at a saturation distance $z=3.3 \text{ m}$. The agreement is not excellent but nevertheless satisfactory considering the simplicity of the normal approximation. Deviations are less than 10% in terms of the logarithm of $(1-P)$ over the three decades available, and they are typical, both in magnitude and trend. It is emphasized that the parameters $\langle H \rangle$ and β , which are used to plot the experimental points, are the true average value and the true normalized standard deviation of the irradiance data; they were not determined by a best fit to equation (41).

Figure 2 is a comparison between irradiance probability measurements and the probability function inferred from the hypothesis of normal distribution of the wave amplitude using the asymptotic solutions (21), (27) and (28) which were deduced directly from Maxwell's equations. Hence, the experiment shows that the normal probability distribution and Maxwell's equations are mutually consistent in the saturation region.

Pursuing further the analysis, it was found, as in many atmospheric experiments, that a log-normal function also fits the data with reasonable accuracy, i.e. of the same order as that shown in figure 2. But, not surprisingly, the fitted log-normal function yields a finite value of β (generally different from the true normalized standard deviation), in complete disagreement with solution (35). Since the latter result was obtained directly from Maxwell's equations with no closure approximation other than the log-normal hypothesis, it follows that the seemingly valid log-normal distribution in the saturation region is either not self-consistent, or not consistent with Maxwell's equations. In other words, a log-normal function can apparently be fitted to the probability data at various locations z , but solution (35) and the observation of a saturation regime show that the variation along z of the parameter β which would characterize this empirical function cannot satisfy Maxwell's equations in a manner self-consistent with the log-normal distribution. Therefore, the often publicized experimental support for the log-normal distribution in the saturation region has no theoretical foundation, it appears to have a local empirical value only. By comparison, the normal distribution hypothesis was shown to give results which, at least, are theoretically and experimentally compatible throughout the propagation range.

5. CONCLUSIONS

Two principal conclusions can be formulated from the theoretical and experimental results of this study.

Firstly, it is concluded that the hypothesis of exact log-normal probability distribution of the irradiance fluctuations is incompatible with the experimental observation of a saturation regime of the irradiance variance. It was demonstrated directly from Maxwell's equation and without closure approximations nor hypotheses concerning the refractive index structure function, that the normalized irradiance variance of a monochromatic optical plane wave propagating in homogeneous turbulence diverges to infinity if the irradiance remains log-normally distributed in the saturation region. Therefore, any theoretical model making use of the exact log-normal distribution is liable to produce inconsistent answers.

Secondly, it is concluded that a normal probability distribution of the wave amplitude is a very plausible approximation in the saturation regime. On the one hand, this is reasonably well confirmed by the atmospherically measured saturation values of the normalized irradiance standard deviation β . Although the predicted value of β is on the average 15% smaller than the reported data, the differences are well within the experimental scatter which limits most atmospheric measurements. On the other hand, it is found that both the irradiance standard deviation and the irradiance probability measurements in a laboratory controlled turbulent atmosphere agree very satisfactorily with the normal probability distribution in the saturation region.

These results have obvious implications with regard to the modelling of the effects of turbulence on long range atmospheric propagation of visible and infrared laser beams. For example, many leading theoretical models dealing with saturation (e.g. YURA, 1974a; CLIFFORD, OCHS and LAWRENCE, 1974; and DeWOLF, 1973a, 1973b, 1974) agree in some implicit or explicit fashion with the log-normal probability distribution. Consequently, some of the constitutive hypotheses of these theories would need further clarification in the light of the conclusions summarized above.

APPENDIX: PROPAGATION LENGTH SCALE

We derive here an estimate of the characteristic propagation distance ℓ_c on which the decay of the average amplitude $\langle A \rangle$ scales. The reader is reminded that the method of this appendix leads to order of magnitude estimates only and that the resulting value of the characteristic propagation length ℓ_c should be used accordingly.

Replacing the variables in equation (18) by their representative values, we have:

$$\frac{A_0}{\ell_c} \approx \frac{1}{2} 0(\langle A \nabla_t \cdot \nabla \rangle). \quad (A1)$$

Performing the same type of operation on equation (20), we obtain:

$$\frac{0(\langle A \nabla_t \cdot \nabla \rangle)}{\ell_c} \approx \frac{1}{2} A_0 0(\langle (\nabla_t \cdot \nabla)^2 \rangle). \quad (A2)$$

We have dropped the cross-correlation moments in the resulting equation (A2) not because they are negligible, which is generally not the case, but because the first term is representative of the magnitude of the right-hand side expression of equation (20) and, thus, sufficient for an order of magnitude analysis. The first term is purely geometric. Therefore, the resulting ℓ_c should be strictly applicable in the geometrical optics limit only. Combining equations (A1) and (A2), we find:

$$\ell_c^2 \approx \frac{4}{0(\langle (\nabla_t \cdot \nabla)^2 \rangle)}. \quad (A3)$$

Neglecting the nonlinear contributions to $\langle (\nabla_t \cdot \nabla)^2 \rangle$ since the variance of the angle-of-arrival,

$\langle V_t \cdot V \rangle$, is much smaller than unity, we derive from equation (9) that:

$$\langle (V_t \cdot V)^2 \rangle \approx \lim_{\rho_2 \rightarrow \rho_1} \int_0^z \int_0^z dz_1 dz_2 \left\langle v_{\rho_1}^2 \frac{(n_1 - n_0)}{n_0} v_{\rho_2}^2 \frac{(n_2 - n_0)}{n_0} \right\rangle \quad (A4)$$

where subscripts 1 and 2 refer to different transverse planes. Since the correlation length of the index of refraction fluctuations is generally much smaller than the propagation distances of interest, we approximate equation (A4) as follows:

$$\langle (V_t \cdot V)^2 \rangle \approx \lim_{\rho_2 \rightarrow \rho_1} \int_0^z dz_1 \int_{-\infty}^{\infty} ds \left\langle v_{\rho_1}^2 \frac{[n(z_1, \rho_1) - n_0]}{n_0} v_{\rho_2}^2 \frac{[n(z_1 + s, \rho_2) - n_0]}{n_0} \right\rangle \quad (A5)$$

Assuming that the index n is statistically homogeneous and isotropic and using the 2/3-power law or the Obukhov-Kolmogorov model (Tatarskii, 1967), equation (A5) becomes:

$$\langle (V_t \cdot V)^2 \rangle \approx -z \int_{\ell_0}^{L_0} ds \lim_{\rho \rightarrow 0} v_{\rho}^2 v_{\rho}^2 [n_0^{-2} C_n^2 (s^2 + \rho^2)^{1/3}], \quad (A6)$$

where C_n^2 , ℓ_0 and L_0 are respectively the index structure parameter, the inner scale of turbulence and the outer scale of turbulence. To simplify equation (A6), we have postulated that the contributions to the integral for values of s outside the range (ℓ_0, L_0) are negligible; this approximation should be sufficient for an order of magnitude estimate. Finally, taking $\ell_0 \ll L_0$, we get:

$$\langle (V_t \cdot V)^2 \rangle \approx \frac{64}{21} z C_n^2 \ell_0^{-7/3} n_0^{-2}. \quad (A7)$$

Substituting relation (A7) for $\langle (V_t \cdot V)^2 \rangle$ in equation (A3) with C_n and ℓ_0 assumed constant, and taking $O(z) = \ell_c$, we obtain the formula:

$$\ell_c \approx 1.1 \ell_0^{7/9} C_n^{-2/3} n_0^{2/3}. \quad (A8)$$

This expression is representative of the geometrical effects only. It is worth noting that this ℓ_c corresponds, within a numerical factor of the order of unity, to a characteristic length which could be derived from Tatarskii's geometrical optics solution for the log-amplitude variance (Tatarskii, 1967, eq. 6.68).

REFERENCES

1. BORN, M. and WOLF, E., 1959, "Principles of Optics" (Pergamon Press Inc., New York).
2. BROWN, W.P., Jr., 1972, "Fourth Moment of a Wave Propagating in a Random Medium", J. Opt. Soc. Am., Vol. 62, No. 8, p. 966.
3. CLIFFORD, S.P., OCHS, G.R. and LAWRENCE, R.S., 1974, "Saturation of optical scintillation by strong turbulence", J. Opt. Soc. Am., Vol. 64, No. 2, p. 148.
4. DABBERDT, Walter F. and JOHNSON, Warren B., 1973, "Analysis of Multiwavelength Observations of Optical Scintillation", Appl. Opt., Vol. 12, No. 7, p. 1544.
5. DeWOLF, D.A., 1973a, "Strong irradiance fluctuations in turbulent air: plane waves", J. Opt. Soc. Am., Vol. 63, No. 2, p. 171.
6. DeWOLF, D.A., 1973b, "Strong irradiance fluctuations in turbulent air, II. Spherical waves", J. Opt. Soc. Am., Vol. 63, No. 10, p. 1249.
7. DeWOLF, D.A., 1974, "Strong irradiance fluctuations in turbulent air, III. Diffraction cutoff", J. Opt. Soc. Am., Vol. 64, No. 3, p. 360.
8. DUNPHY, James R. and KERR, Richard J., 1973, "Scintillation measurements for large integrated-path turbulence", J. Opt. Soc. Am., Vol. 63, No. 8, p. 981.
9. FELLER, William, 1966, "An Introduction to Probability Theory and its Applications" (John Wiley and Sons, Inc., New York), Vol. II, Chap. III, Sec. 6.
10. KHELEVTSOV, 1973, "Propagation of Laser Radiation in a Turbulent Atmosphere", Appl. Opt., Vol. 12, No. 10, p. 2421.
11. LAWRENCE, Robert S. and STROHBEHN, John W., 1970, "A Survey of Clear-Air Propagation Effects Relevant to Optical Communications", Proceedings of the IEEE, Vol. 58, No. 10, p. 1523.
12. LIVINGSTON, Peter M., DEITZ, Paul H. and ALCARAZ, Ernest C., 1970, "Light Propagation through a Turbulent Atmosphere: Measurements of the Optical-Filter Function", J. Opt. Soc. Am., Vol. 60, No. 7, p. 925.
13. Tatarskii, V.I., 1967, "Wave Propagation in a Turbulent Medium", (Dover Publications, New York).

14. TATARSKII, V.I., 1971, "The Effects of the Turbulent Atmosphere on Wave Propagation", National Technical Information Service, U.S. Dept. of Commerce, Springfield, Va.
15. WANG, Ting-i and STROHBEHN, John W., 1974a, "Log-normal paradox in atmospheric scintillations", J. Opt. Soc. Am., Vol. 64, No. 5, p. 583.
16. WANG, Ting-i and STROHBEHN, John W., 1974b, "Perturbed log-normal distribution of irradiance fluctuations", J. Opt. Soc. Am., Vol. 64, No. 7, p. 994.
17. YURA, H.T., 1974a, "Physical model for strong optical-amplitude fluctuations in a turbulent medium", J. Opt. Soc. Am., Vol. 64, No. 1, p. 59.
18. YURA, H.T., 1974b, "Irradiance fluctuations of a spherical wave propagating under saturation conditions", J. Opt. Soc. Am., Vol. 64, No. 11, p. 1526.

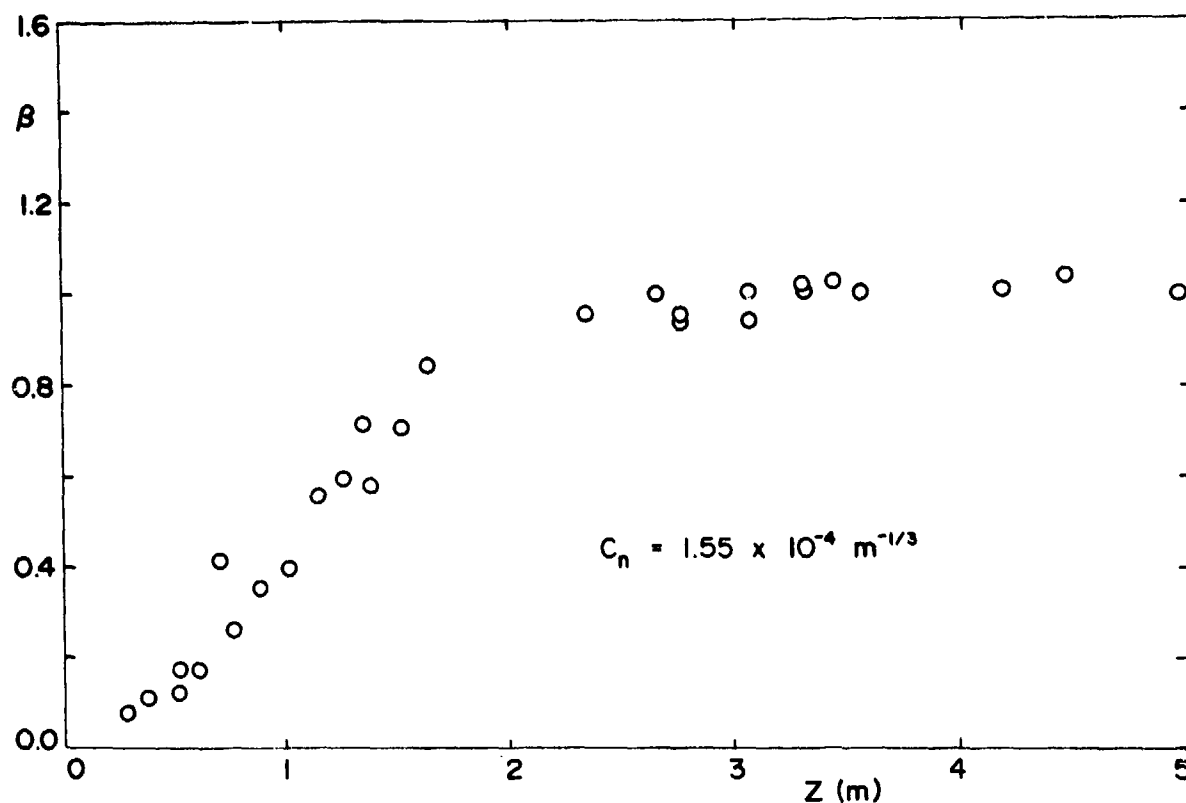


FIGURE 1: Normalized standard deviation of irradiance fluctuations as a function of propagation distance. O : data recorded on the axis of a 50-mm He-Ne laser beam propagating in turbulent water, $C_n = 1.55 \times 10^{-4} \text{ m}^{-1/3}$.

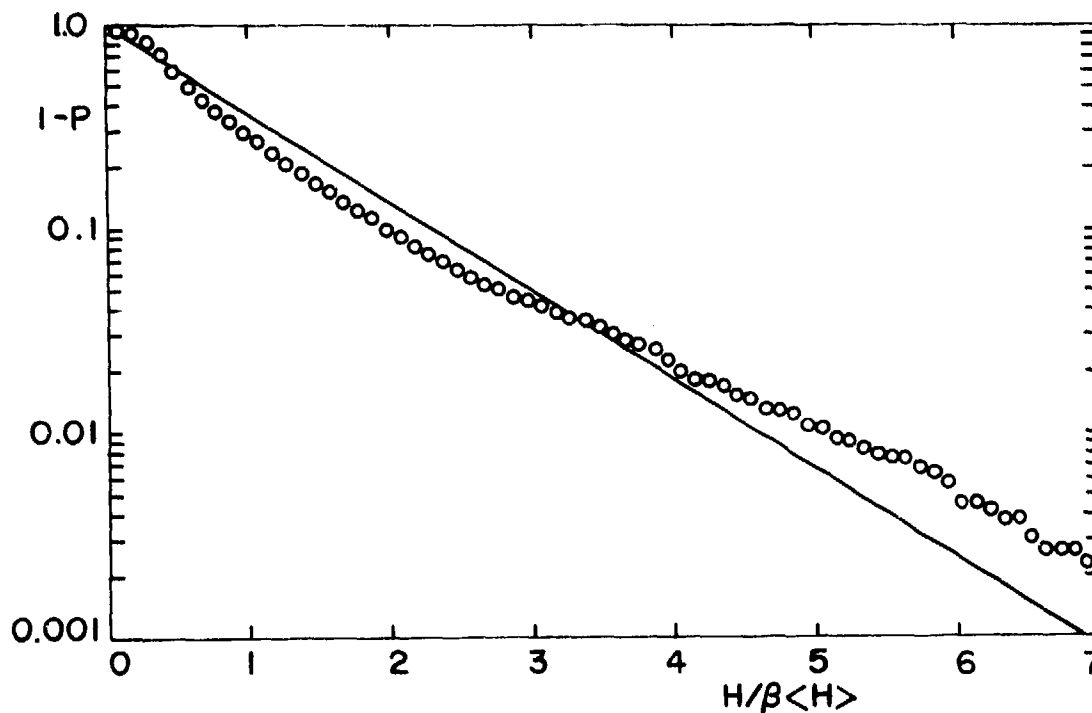


FIGURE 2: Irradiance probability distribution. O : distribution measured at a saturation distance $z=3.3\text{m}$ on the axis of a 50-mm He-Ne laser beam propagating in turbulent water, $C_n = 1.55 \times 10^{-4} \text{ m}^{-1/3}$. —: theoretical prediction based on the normal probability distribution of the wave amplitude and the asymptotic solutions for the first- and second-order statistical moments of the wave amplitude.

TURBULENCE EFFECTS ON TARGET ILLUMINATION BY LASER TRANSMITTER:
UNIFIED ANALYSIS AND EXPERIMENTAL VERIFICATION*

J. Richard Kerr
 Oregon Graduate Center for Study and Research
 Beaverton, Oregon 97005, U.S.A.

SUMMARY

A phenomenological and analytical description is given of atmospheric turbulence effects on laser beam waves, including the improved target irradiance characteristics resulting from cancellation of turbulence-induced beam wander through reciprocity tracking. The mechanisms related to the mean irradiance include diffraction, wander, and wavefront distortion (beamspread), while irradiance-fading is caused by wander, first-order scintillation, and coherent fading. The phenomenological description unifies the often fragmentary and inconsistent treatment of beam wave phenomena found in the literature, and is sufficiently accurate for engineering purposes. It will be shown that wander-cancellation and control of the transmitter beam diameter can result in substantial improvements in target illumination. The analyses are compared with experimental data for the detailed statistical and spectral characteristics of on-axis target irradiance.

1. INTRODUCTION

Target-illumination systems for laser radar, designation, communications, and other applications may be severely affected by turbulence effects which include beam spreading, wander, and scintillation. The theoretical descriptions of these phenomena for a finite beam wave have been fragmentary and inconsistent. In particular, the relative advantages to be achieved through the use of optical transmitter techniques with various degrees of sophistication have not been readily evaluated.

In this paper a unified phenomenological analysis of these effects will be given and shown to agree with the available results of a rigorous application of the Huygens-Fresnel principle as extended to a random medium. The mean and variance of target irradiance will be described as a function of transmitter size and focus, wavelength, pathlength, and turbulence strength, including the case of saturation or multiple scattering with a large-Fresnel-number system. In particular, the effects of wander-cancellation through reciprocity tracking and illumination improvement through aperture size and focus control will be evaluated.

For a given integrated-path turbulence level, the optimum beam diameter (D) is of the order of the coherence radius (ρ_0) for a point source propagating over the reciprocal path; a larger beam will result in less mean irradiance and greater fluctuations on target, with a normalized variance which approaches unity for large values of (D/ρ_0). It will also be shown that this parameter (D/ρ_0) is largely but not completely sufficient to determine the performance of a focused illuminator for an arbitrary case.

The analyses will be compared with experimental data for the detailed statistical and spectral characteristics of on-axis target irradiance.

2. ANALYTICAL AND PHENOMENOLOGICAL DESCRIPTION

2.1 First Moment or Mean Irradiance

The analytical approach represents an extension of recent Huygens-Fresnel and reciprocity formalisms (Lutomirski, R.F. and Yura, H. T., 1971; Yura, H. T., 1971; Fried, D. L. and Yura, H.T., 1972). The general expression for the mean irradiance on target is given by (Yura, H. T., 1973)

$$\bar{I}(\bar{p}) = \left(\frac{k}{2\pi z}\right)^2 \int d^2 \bar{\rho} M(\bar{\rho}) e^{-\frac{ik}{z} \bar{p} \cdot \bar{\rho}} \int d^2 \bar{R} U\left(\bar{R} + \frac{\bar{\rho}}{2}\right) U^*\left(\bar{R} - \frac{\bar{\rho}}{2}\right) e^{\frac{ik}{z} \bar{\rho} \cdot \bar{R}} \quad (1)$$

where

\bar{p} = transverse position vector for target point under consideration
 k = optical wavenumber
 z = path length
 $\bar{R}, \bar{\rho}$ = sum and difference coordinates in the transmitter aperture, respectively
 M = atmospheric modulation transfer function
 and U = complex transmitter amplitude distribution.

*This work sponsored by the Defense Advanced Research Projects Agency and the Air Force System Command's Rome Air Development Center, Griffiss Air Force Base, New York.

We immediately specialize the transmitter to the case of a gaussian beam with nominal radius (a) and output radius of curvature (f), to write the second integral as

$$I' = e^{-\frac{\rho^2}{4a^2}} |U_0|^2 \int d^2 \bar{R} e^{-\frac{R^2}{a^2}} 1k \bar{R} \cdot \bar{\rho} \left(\frac{1}{z} - \frac{1}{f} \right) e^{-\frac{k^2 a^2 \rho^2}{4} \left(\frac{1}{z} - \frac{1}{f} \right)^2} \quad (2)$$

We put this back into Eq. (1), and integrate over the polar coordinate ϕ , resulting in

$$\bar{I}(\bar{\rho}) = \frac{k^2 a^2}{2z^2} |U_0|^2 \int_0^\infty d\rho \rho M(\rho) J_0\left(\frac{k}{z} \rho \bar{\rho}\right) e^{-\frac{\rho^2}{4} \left[\frac{1}{a^2} + k^2 a^2 \left(\frac{1}{z} - \frac{1}{f} \right)^2 \right]} \quad (3)$$

Finally, we specialize to an on-axis point ($\rho = 0$), with the transmitter focused on the target ($f = z$):

$$\bar{I} = \frac{k^2 a^2}{2z^2} |U_0|^2 \int_0^\infty d\rho \rho M(\rho) e^{-\rho^2/4a^2} \quad (4)$$

This includes the special case of a collimated beam ($f = z = \infty$), and the expression may be immediately compared to that for a reciprocal case of a heterodyne receiver, in which a plane wave (or infinite focus) has generally been assumed (Fried, D. L., 1967).

We denote the transmitter diameter as $D = 2a$, and define $x = \rho/D$. The MTF is that for a point source over a reciprocal path (Fried, D.L. and Yura, H. T., 1972):

$$M(Dx) = e^{-(Dx/\rho_0)^{5/3}} \quad (5)$$

In this expression, the coherence parameter (ρ_0) is obtainable as an integral over the reciprocal path (S) from the target to the transmitter:

$$\rho_0 = \left[1.45 k^2 \int_0^z C_n^2(s) \left(\frac{s}{z} \right)^{5/3} ds \right]^{-\frac{3}{5}} \quad (6)$$

where C_n^2 is the refractive index structure constant (Lawrence, R.S. and Strohbehn, J. W., 1970).

We thus have

$$\bar{I} = \frac{k^2 D^4 |U_0|^2}{8z^2} \int_0^\infty dx x e^{-x^2} e^{-(Dx/\rho_0)^{5/3}} \quad (7)$$

We point out that the dependence on the Fresnel number $(ka^2/z)^{1/2}$ has disappeared from the integral, and the pertinent independent variable is simply (D/ρ_0) . This means that basic conclusions drawn from earlier analyses (Fried, D.L., 1967) of the reciprocal, heterodyne receiver case will be valid for a focused or collimated transmitter with $f = z$, over an arbitrary (nonuniform) path; it is only necessary to know $M(\rho)$ or ρ_0 for the path.

It is useful to normalize Eq. (7) in two alternative ways. If we let the turbulence strength go to zero ($\rho_0 \rightarrow \infty$), we have

$$\bar{I} \left(\frac{D}{\rho_0} = 0 \right) \equiv \bar{I}_0 = \frac{k^2 D^4 |U_0|^2}{16z^2} \quad (8a)$$

and (7) can be written as

$$\bar{I} = 2 \bar{I}_0 \int_0^\infty dx x e^{-x^2} e^{-(Dx/\rho_0)^{5/3}} \quad (9a)$$

Since $\bar{I}_0 \sim |U_0|^2 D^2 \times k^2 D^2 / z^2 = \text{Transmitter Power} \times k^2 D^2 / z^2$, this normalization is convenient for constant D and variable ρ_0 or turbulence strength. The opposite extreme is that of strong turbulence and/or a large transmitter:

$$\bar{I} \left(\frac{D}{\rho_0} \rightarrow \infty \right) \equiv \bar{I}_\infty = \frac{0.551 \rho_0^2 k^2 D^2 |U_0|^2}{8z^2} \quad (8b)$$

which is obtained from a series expansion of (e^{-x^2}) in Eq. (7). We then write (7) as

$$\bar{I} = \left(\frac{D^2}{0.551 \rho_0^2} \right) \bar{I}_\infty \int_0^\infty x e^{-x^2} e^{-(Dx/\rho_0)^{5/3}} \quad (9b)$$

We note that $\bar{I}_\infty \sim |U_0|^2 D^2 \times k^2 \rho_0^2 / z^2 \sim \text{Transmitter Power} \times k^2 \rho_0^2 / z^2$, so that this normalization is convenient for turbulence strength constant and variable D . From Eqs. (8a, 8b), we note that

$$\frac{\bar{I}_\infty}{\bar{I}_0} = 1.1 \frac{\rho_0^2}{D^2} \quad (10a)$$

It will be useful later to introduce a further parameter r_0 (Fried, D.L., 1967; Fried, D.L., 1966):

$$r_0 = 2.0986 \rho_0$$

in terms of which Eq. (10a) may be rewritten

$$\frac{\bar{I}_\infty}{\bar{I}_0} = \frac{r_0^2}{4D^2} \quad (10b)$$

Also, in order to compare the present results for a gaussian beam taper with the reciprocal, heterodyne or imaging case in the literature (Fried, D.L., 1967; Fried, D.L., 1966), it is useful to define an "effective aperture" (D_{eff}) which can be compared with the uniform circular case treated in these references. At the same time, the effects of truncation can be introduced. We have shown (Kerr, J. R., 1974) that the effective diameter of a truncated gaussian beam is given by

$$D_{\text{eff}} = 4a \left(\frac{1 - e^{-\eta/2}}{\sqrt{1 - e^{-\eta}}} \right) \quad (11)$$

where $\eta = (\text{truncation diameter})^2 / 4a^2$. In particular, if the truncation is negligible ($\eta \rightarrow \infty$), then $D_{\text{eff}} = 4a = 2D$ and Eq. (10b) becomes

$$\frac{\bar{I}_w}{\bar{I}_0} = \frac{r_o^2}{D_{\text{eff}}^2} \quad (10c)$$

This in fact is the significance or basic definition of r_o , and through the reasonings of reciprocity (Fried, D.L. and Yura, H.T., 1972), the above ratio is also applicable to the resolution of imaging systems (Fried, D.L., 1966) and signal-to-noise ratio of heterodyne receivers (Fried, D.L., 1967).

The mean irradiance as given in Eqs. (9a, 9b) is shown in Fig. 1. Also shown is the result from Ref. 5 for the resolution of an imaging system with uniform (rather than gaussian) aperture weighting, with the abscissa appropriately adjusted ($D = D_{\text{eff}}/2$). The curve is seen to differ only in minor detail from that for the gaussian (transmitter) aperture.

The above discussion was limited to a fixed aperture, which corresponds in the reciprocal imaging case to the "long-term" resolution. We are also interested in the performance of a system which tracks a point on the target in order to cancel atmospherically induced wander; this corresponds in the reciprocal case to the "short-term" image resolution (Fried, D.L., 1966) or a "wavefront-tilt-tracking" heterodyne receiver (Fried, D.L., 1967). This problem has been addressed by Fried in terms of the "short-term MTF" for a uniformly weighted aperture (Fried, D.L., 1967; Fried, D.L., 1966). This is not a true MTF, however, in that it is dependent upon the aperture weighting, and it has been misapplied to the gaussian case (Yura, H.T., 1973). The problem has also been treated by Kon (Kon, A. I., 1970) who uses an expression for mean irradiance which is essentially identical to that of the Huygens-Fresnel formulation, and a straightforward definition of the beam centroid. However, his results appear to contain a serious error in the numerical evaluation.

In the absence of an analytical solution for the gaussian-beam, wander-tracked case, we will assume that the uniform-aperture case treated by Fried does not differ materially, providing a correction is made for the effective aperture diameter. This is supported below in the discussions of the phenomenological model and the experimental data. The result, shown in terms of the ratio of mean irradiance with wander-tracking (\bar{I}_T) to that with a static aperture, is shown in Figure 2. The maximum improvement with proper aperture size control is predicted to be 6.2 dB.

The first moment may also be written in terms of a phenomenological model, wherein we represent the total mean-square solid-angular beamspread as consisting of terms owing to free-space diffraction [$\sim 1/k^2 D^2$], turbulence-induced wander [$\sim D(D)/k^2 D^2 \sim (D/3\rho_0^{5/3} k^2)^{-1}$], and turbulence-induced (Yura, H.T., 1973) beamspread [$\sim 1/k^2 \rho_0^2$]. By defining these mean-square spreads in terms of their effects on mean irradiance, we avoid questions of alternative angular definitions. Note that the wander as here defined is a totally geometric-optics or refractive mechanism.

We now write the mean irradiance (Eq. 7) as

$$\bar{I} = \frac{|U_o|^2 D^2}{16z^2} \frac{1}{\frac{C_1'}{k^2 D^2} + \left[C_2' \left(\frac{D}{\rho_0} \right)^{-1/3} + C_3' \right] \frac{1}{k^2 \rho_0^2}} \quad (12a)$$

where the constants $C_{1,2,3}'$ remain to be determined. These constants will be simplified if we cast this equation in terms of $D_{\text{eff}} (=2D)$ and r_o :

$$\bar{I} = \frac{|U_o|^2 D_{\text{eff}}^2}{256z^2} \frac{1}{\frac{C_1}{k^2 D_{\text{eff}}^2} + \left[C_2 \left(\frac{D}{r_o} \right)^{-1/3} + C_3 \right] \frac{1}{k^2 r_o^2}} \quad (12b)$$

From free-space beamwave optics, or Eq. (7) with $\rho_0 \rightarrow \infty$, we know that $C_1 = C_1' = 1$. From Eq. (8b), with $\rho_0 = 0$, we have $C_3' = 0.907$, $C_3 = 1$.

The determination of C_2' or C_2 is less straightforward. For the case of the static aperture, we find that the curve of Eq. (12a) with $C_2' = C_2 = 0$ is practically indistinguishable from that of Eq. (7) or Figure 1. This suggests that the wander effect is essentially contained in the $1/k^2 \rho_0^2$ term of Eq. (12a). It follows that for the wander-tracked case, the appropriate value of C_2 will be negative, in order to subtract out the wander effect. Although we do not yet have a reliable Huygens-Fresnel result for the gaussian-beam case, as indicated above we believe that the uniform aperture results will be substantially similar (Fried, D.L., 1966).

In Figure 3, we plot the analytical results of Ref. 5 for a uniform aperture, and Eq. (12a) with $C_2' = -1.08$. (The corresponding value of C_2 in Eq. (12b) is -1.18 .) This value was chosen so that the maximum irradiance gain over that for a very large aperture would agree with the analytical result; the predicted improvement factor for target irradiance using tracking and aperture size control over that of a large, static aperture is 3.4, or 10.6 dB in receiver photocurrent. This peak occurs at $D/\rho_0 \approx 4$, and as will be seen below, the tracking improvement in irradiance fading is also optimized for $3 \lesssim C_2 \lesssim D/\rho_0 \lesssim 5$.

To summarize this section, an engineering expression for the mean irradiance as a function of transmitter aperture and turbulence-induced coherence scale can be written from Eq. (12b) as

$$\bar{I} = \frac{|U_0|^2 D_{\text{eff}}^2}{256\pi^2} \frac{1}{\frac{1}{k^2 D_{\text{eff}}^2} + \left[C \left(\frac{D_{\text{eff}}}{r_0} \right)^{-1/3} + 1 \right] \frac{1}{k^2 r_0^2}} \quad (13)$$

where $C = 0$ for a static aperture and -1.18 for a wander-tracking aperture. The asymptotic breakpoint between free-space diffraction and turbulence-induced beamspread occurs at $D_{\text{eff}} = r_0$ and wander predominates for D_{eff}/r_0 somewhat greater than unity. The parameter D_{eff} is the physical aperture diameter in the case of uniform illumination, and is equal to $4a$ for a gaussian beam profile.

2.2 Second Moment or Irradiance Fluctuations (Fading)

The problem of the second moment of irradiance is considerably more difficult. In the Huygens Fresnel formulation, this involves an eight-fold integral (Fried, D.L., 1967; Yura, H.T., 1972). Fried's earlier analysis (Fried, D.L. 1967) of "atmospheric modulation noise" in a heterodyne receiver which by reciprocity represents the same problem as considered here, contains serious inaccuracies owing to approximations used. Interesting work on this problem was recently reported by Banakh, et al (Banakh, V. A., 1974). Using the assumptions that the atmospheric perturbation of the propagation Green's function is essentially a phase effect, and that the phase distribution is gaussian, they reduced the problem to a six-fold integral which they then evaluated using Monte Carlo techniques. The result appears qualitatively correct, and will be seen below to agree in general with our phenomenological description. It does however predict that (D/ρ_0) is the only pertinent independent variable, while we believe the Fresnel number to be pertinent in certain parameter realms; this latter dependence is lost through the phase-only assumption in the Green's function. As a further consequence of the approximations used, the expression (17) in that paper for the mean irradiance is incorrect.

We show now that a phenomenological approach can yield very useful results. To accomplish this, we separate the fading mechanisms into (1) wander, (2) first-order scintillation, and (3) coherent fading.

Using a development from Titterton (Titterton, P.J., 1973), we write the normalized irradiance variance due to wander as

$$\sigma_{I_{\text{wander}}}^2 = \frac{4\gamma^2}{4\gamma+1} \quad (14)$$

where γ is defined as the ratio of the mean-square wander angle to the short-term beamspread angle. Using the earlier C_2 term (Eq. 12a) for wander angle, this becomes

$$\gamma = \frac{|C_2'| \left(\frac{D}{\rho_0} \right)^{-1/3} \frac{1}{k^2 \rho_0^2}}{\frac{1}{k^2 D^2} + \left[-|C_2'| \left(\frac{D}{\rho_0} \right)^{-1/3} + 0.907 \right] \frac{1}{k^2 \rho_0^2}} \quad (15)$$

$$= \frac{|C_2'| \left(\frac{D}{\rho_0} \right)^{5/3}}{1 + \left[-|C_2'| \left(\frac{D}{\rho_0} \right)^{-1/3} + 0.907 \right] \frac{D^2}{\rho_0^2}}$$

We insert this expression into Eq. (14) and obtain a result for wander-induced variance as a function of (D/ρ_0) . The general behavior can be seen by approximating the function in terms of four log-linear realms as shown in Figure 4. The breakpoints occur at values of D/ρ_0 on the order of $1/2$, 1 , and 100 , with a maximum value of $\sigma_{I_{\text{wander}}}^2$ somewhat greater than unity.

By "first-order scintillation", we mean that which would be predicted for a focused transmitter by the Rytov Approach (Ishimaru, A., 1969; Fried, D.L. and Schmelzter, R.A., 1967; Kerr, J. R. and Eiss, R., 1972; Kerr, J. R. and Dunphy, J. R., 1973). This includes the "transmitter-smoothing of scintillations". For this to occur, the target (or at least the turbulence (Kerr, J. R. and Dunphy, J.R., 1973)) must be in the transmitter near field, and D must be smaller than ρ_0 . Hence the applicable inequality is

$$\rho_0 > D > \sqrt{z/k}$$

The requirement that ρ_0 be greater than $\sqrt{z/k}$ is dimensionally equivalent to requiring that scintillations from a point source be "unsaturated" (Lawrence, R.S. and Strohbehn, J.W., 1970).

The customary way to write this fading term (Fried, D.L., 1967) is

$$\sigma_{I \text{ scintillation}}^2 = e^{4\beta\sigma_X^2} - 1 \quad (16)$$

where it is assumed that these fluctuations are log normal, and σ_X^2 is the log amplitude variance for a point source (Lawrence, R. S. and Strohbehn, J.W., 1970):

$$\begin{aligned} \sigma_X^2 &= 0.124 C_n^2 k^{7/6} z^{11/6} \\ &= 0.228 \left[\frac{\sqrt{z/k}}{\rho_0} \right]^{5/3} \end{aligned} \quad (17)$$

The smoothing factor β is a function of the Fresnel number, so that this fading mechanism is not a universal function of D/ρ_0 . For large Fresnel numbers, β is proportional (Kerr, J.R. and Eiss, R., 1972) to $D^{-7/3}$. Also, if we assume significant smoothing such that $\beta\sigma_X^2 \ll 1$, we can write Eq. (16) as

$$\sigma_{I \text{ scintillation}}^2 \approx 0.912 \beta \left[\frac{\sqrt{z/k}}{\rho_0} \right]^{5/3} \quad (16a)$$

Coherent fading or beam-breakup scintillation corresponds in a reciprocal heterodyne receiver to "atmospheric modulation noise" (Fried, D.L., 1967), and predominates for $D > \rho_0$, i.e., the realm of turbulence-induced beamspread. The correct form for this fading term is not known, but we expect it to be an increasing and nearly universal function of D/ρ_0 . However, contrary to an earlier approximate analysis (Fried, D.L., 1967) it does not increase without limit (Banakh, V. A., 1974).

Brown has shown that, for $N = D^2/\rho_0^2 \gg 1$ oscillators having identical frequencies but independent mutual phases, the normalized variance is

$$\sigma_{I \text{ coherent fading}}^2 \approx 1 - \frac{1 - (e^{4\sigma_X^2} - 1)}{D^2/\rho_0^2} \quad (18a)$$

$\left(\frac{D}{\rho_0} \gg 1 \right)$

where σ_X^2 represents the fading of an individual oscillator. This model describes the present case of $D^2/\rho_0^2 \gg 1$ independent coherence areas effectively making up the transmitter aperture, and the variance approaches unity for large (D/ρ_0) . The function is again not universally dependent on D/ρ_0 , and for $\sigma_X^2 \ll 1$, may be written

$$\sigma_{I \text{ coherent fading}}^2 \approx 1 - \frac{1 + 4\sigma_X^2}{\frac{D^2}{\rho_0^2}} \quad (18b)$$

$\left(\frac{D}{\rho_0} \gg 1 \right)$

The general behavior is shown in Figure 5. Also, an analytical proof of the unity asymptote for large (D/ρ_0) is given in Appendix A.

We may combine the three fading mechanisms as shown in Figure 6, where it is assumed that σ_X^2 and $\rho_0/\sqrt{z/k}$ have been specified. Alternatively, we may specify the Fresnel number and vary the turbulence strength, resulting in the curve shown in Figure 7. The latter curve, including wander effects is in general agreement with the recent Russian result (Banakh, V.A., 1974).

The predicted behavior with wander tracking is readily determined by dropping the contribution from that mechanism. It is apparent that a significant reduction in fading can be achieved through the cancellation of wander and the control of aperture size; the optimum aperture is essentially that which max-

minizes the mean irradiance in the presence of tracking, and too large an aperture can have significantly deleterious effects on fading performance.

Finally, we point out that the predicted reduction in scintillations as compared to those from a point source (Figure 6), i.e. with wander tracking, may be difficult to realize in practice. This realm will only clearly exist when $\rho_0 \gg \sqrt{z}/k$ (or $\sigma_x^2 \ll 1$), so that scintillations are weak in general. More importantly, the requirements on accuracy of focus and high-quality optics are quite severe (Kerr, J.R. and Dunphy, J. R., 1973); a very small wavefront distortion will destroy the predicted smoothing.

2.3 Other Considerations

The preceding discussion has been explicitly concerned with the case of a focused beam over a horizontal path. For the case of a general turbulence profile over the path, the coherence parameter is given as an integration over the reciprocal path by Eq. (6). All phenomenological expressions above which are universal functions of D/ρ_0 are thus immediately applicable to the general path. First-order scintillations and coherent fading depend also on σ_x^2 for a point source, likewise determined over the reciprocal path. The degrading effect of a given level of turbulence on transmitter coherence is most heavily weighted towards the transmitter end, so that an uplinkbeam tends to be incoherent or broken up while a downlink beam remains intact. The transmitter smoothing of scintillations for a collimated uplinkbeam has been considered in Ref. 13.

For the non-focused case, we return to Eq. (3) and define a generalized beam parameter:

$$a' = \left[\frac{1}{a^2} + \left(\frac{1}{z} - \frac{1}{f} \right)^2 k^2 a^2 \right]^{-1/2} \quad (19)$$

The defocusing term will reduce and wholly determine a' unless a precise focus adjustment ($z \approx f$) is used. In any event, if $\rho_0 \gg a'$, the beam term predominates in Eq. (3); this will apply to a downlink in particular. If $\rho_0 \ll a'$, the atmospheric term predominates regardless of (reasonable) beam adjustment; this applies to a large-aperture uplink. In general, once a' is determined from Eq. (19) and ρ_0 is known, the mean irradiance is determined from the same curve as in the horizontal, focused case.

For the wander-tracked case, there will appear an optical-system-dependent correction to the atmospheric term in Eq. (3). This will be significant only for a' on the order of ρ_0 , which can apply for an uplinkbeam having a limited aperture size.

We have so far in this discussion neglected effects relating to the limitation on the extent of the inertial subrange of turbulence (Lawrence, R.S. and Strohbehn, J.W., 1970). Lutomirski and Yura have considered the effects of the outer scale (Lutomirski, R. F. and Yura, H.T. 1971; Yura, H.T., 1973) and in part of it they derived first-order corrections to such quantities as turbulence-induced beamspread and coherence scale ρ_0 , where "corrections" refer to the use of the modified von Karman in place of the (nontruncated) Kolmogorov spectrum (Lutomirski, R.F. and Yura, H.T., 1971). The corrections are such as to increase ρ_0 , since the von Karman spectrum has less energy at low wavenumbers than does the Kolmogorov. As discussed below, our data (and those of others) indicate a larger component of wander than predicted by our expressions, especially at large values of D/ρ_0 , and this is thought to be related to large scale bending of the (broken-up) beam. This suggests that there is more energy in certain (anisotropic) turbulence scales than any of the spectral models predict. There is clearly a need for further analytical experimentation on the problem of outer-scale effects, which will be important for infrared systems operating over reasonable pathlengths.

Inner-scale effects can be incorporated through appropriate modifications of the atmospheric MTF or structure function (Lawrence, R.S., and Strohbehn, J.W., 1970). Unfortunately, with the use of such expressions, there has been a tendency in the literature to physically confuse angular beamspread phenomena. We emphasize that wander is the wavelength-independent, geometrical-optics phenomenon, and we suggest that there is little practical significance to inner-scale effects in most situations involving well-developed turbulence.

3. EXPERIMENTAL RESULTS

In this section we present results of systematic experiments with a large, focused, wander-tracking transmitter over a homogeneous, horizontal path. A preliminary report of this work has been previously published (Dunphy, J. R. and Kerr, J. R., 1974). The tracker locks onto a point-source beacon on the target which is coincident with a small detector for irradiance measurements. Although the tracker utilizes a two-dimensional sign x function rather than a true centroid, the experimental discrepancy is not expected to be significant.

The experimental parameters and data collected are summarized in Table I. Current efforts are underway at other pathlengths and wavelengths, including the realm of small D/ρ_0 .

TABLE I

Experimental Parameters and Data Collected

Transmitter and beacon wavelengths: 6328 Å
 Transmitter Power: 75 mW
 Pathlength and Height: 1.6 km, 1.8 m
 Tracker Servo Resonance: 300 Hz (galvanometer-scanners servoed to quadrant photodetector)
 Transmitter Diameter: 15 cm (spatially-filtered, diffraction-limited, truncated gaussian)
 Determination of ρ_0 : microthermal measurement of C^2
 Mean-irradiance averaging time: 100 sec

Variance averaging time: 10 sec on 300 sec data records
 Target receiver bandwidth: 1 kHz

Data from tracker (transmitter): real-time wander signals (servo inputs)
 Data from target (receiver) end: real-time linear and log irradiance signals, mean irradiance

Computation of variances, probability distributions, spectra: digital from FM tape recordings of real-time signals

3.1 Irradiance Signals

The on-axis target irradiance vs. time, with and without wander-tracking, is shown for the weak turbulence case ($D/\rho_0 \approx 1$) in Figure 8a, and the corresponding log irradiance in Figure 8b. The low-frequency nature of the wander-component of the fluctuations is evident. A longer-term record with some smoothing is shown in Figure 9a for ($D/\rho_0 \approx 1$) and Figure 9b for ($D/\rho_0 \gg 1$). It is apparent that, in the latter or high-turbulence case, the advantage of tracking is primarily limited to the longer-term refractive wander.

3.2 Mean Irradiance

The mean-on-axis irradiance for the non-tracked and tracked cases is shown in Figure 10, along with the theoretical predictions given above. These values were corrected for transmitter output-power variations, and the abscissa has been corrected for truncation effects. Since the aperture D was fixed, the appropriate theoretical curves for comparison are those normalized by \bar{I}_0 . Since small values of D/ρ_0 could not be achieved over this path with reasonable turbulence, \bar{I}_0 is not accurately known. However, from Figure 3, we may expect that the largest \bar{I}_T at small (D/ρ_0) is approximately equal to \bar{I}_0 , and this normalization is used in fitting the ordinate to the data. A portion of the non-tracking data points may be depressed somewhat owing to longer-term refractive effects showing up during a single averaging period.

The ρ_0^{-2} dependence of \bar{I} for increasing (D/ρ_0) is generally borne out. For lower strengths of turbulence, the dependence of instantaneous beam spread ($\sim \bar{I}_T^{-1}$) has been empirically stated (Dowling, J.A. and Livingston, P.M., 1973) to be $\sim C \cdot 0.85 \pm 0.62 k^{0.65}$; we find a correlation coefficient of 0.89 for $\gamma < 10$, thus corroborating that observation. For $\gamma > 10$, the correlation coefficient is 6.8×10^{-4} , but we expect an approach to (ρ_0^{-2}) dependence in that regime. The correlation coefficient for $\bar{I} \sim \rho_0^{-2}$ is 0.59 for $D/\rho_0 > 10$.

In Figure 11, we show the ratio (\bar{I}_T/\bar{I}) vs. (D/ρ_0). The theoretical curve is from Figure 2 for a uniform aperture.

3.3 Fluctuations in Irradiance

The normalized variance of irradiance, with and without tracking, is shown vs. (D/ρ_0) in Figure 12. These results compare well with the curves of Figure 7, which are shown again, for comparison with the non-tracked case, we also show the curve from Ref. 1. For the tracked case, the asymptote is seen to be unity as expected; this would also be true for the non-tracked case at sufficiently large D/ρ_0 .

The ratios of the corresponding tracked and non-tracked variances of Figure 12 are shown in Figure 13. The advantage remains substantial for $D/\rho_0 \gg 1$, which suggests large-scale wander effects greater than are included in the theory. It may be pointed out that the reduction in variance for the tracking case is much more substantial if the target signal is low-pass filtered (Dunphy, J.R. and Kerr, J.R., 1974), or if a larger target-receiver aperture is used.

If we process the fading signal directly for the log amplitude, rather than the linear irradiance, and then replot the abscissa in terms of the Rytov log-amplitude variance (σ^2) for a point source, we obtain the data of Figure 14. In this graph, $D/\rho_0 = 1$ corresponds to $\sigma^2 = \chi_R^2 \cdot 3.7 \times 10^{-3}$, and for values substantially larger than this we expect log normality and a simple χ_R^2 relationship between the ordinates of Figures 12 and 14 (i.e., Eq. 16 with $\beta = 1$). In particular, the asymptote $\sigma^2 = 1$ corresponds to $\sigma^2 = 0.17$. It is interesting to note that for the non-tracked case, which is not log-normal at small χ_E values of the abscissa where wander predominates, the value of σ^2 is more or less constant regardless of the turbulence level. In such a case, the statistics vary with χ_E turbulence strength but the degree of (log) fading does not. This is probably a better indication of dynamic range than is σ^2 , since the latter parameter is insensitive to deep fades for log-normal-like fluctuations.

Typical probability distributions for log irradiance are shown in Figure 15a for the tracking and non-tracking cases in weak turbulence ($D/\rho_0 \approx 1$). The residual non-log-normality in the tracking case is related to the details of fading for an approximately-diffraction-limited focal spot. The curve for the non-tracking case remains to be interpreted in terms of the statistics of wander-fading (Titterton, P.J., 1973). For strong turbulence ($D/\rho_0 > 100$), nearly-log-normal distributions are observed, especially with wander-tracking (Figure 15b).

The spectra of the log fading signal for weak turbulence ($D/\rho_0 \approx 1$) are shown in Figure 16a, for the tracking and non-tracking cases. The significant spectral components are below e.g., 10 Hz, and are sharply reduced by tracking, indicating the influence of wander. It is interesting to note that at some low (fractional-Hz) frequency, there is an apparent peak in the non-tracked spectrum, coincident with a dip in the tracked spectrum. This feature was often noted, and is related to a peak in the spectrum relating to wander alone. The log fading spectra for strong turbulence ($D/\rho_0 \approx 100$) is shown in Figure 16b; as beam breakup becomes more severe, so that scintillations predominate over wander, there is a tendency for the spectra of the tracked and non-tracked cases to cross-over at higher frequencies; this may result from tracker response to beam-break-up scintillations and lack of good correspondence between the beacon image at the tracker and the actual distribution of energy at the target.

3.4 Wander Characteristics

The control signal in the wander-tracking system is an analog of the beam wander. An example of a real-time horizontal wander signal is shown in Figure 17a. In some cases, the wander is strongly anisotropic, which can be a manifestation of both slow vertical refractive effects, and of large-scale (larger than outer scale) turbulence anisotropies. An extreme example of the former is shown in Figure 17b, which is from the same data run as Figure 17a. This extreme is typical of night-time operation, but was observed to a much lesser extent in some of the daytime runs which comprise most of the data of this paper. More typically, the rms vertical wander over a short period of time was less than the horizontal value, which is probably related to the anisotropy of turbulence at larger scales.

A quantitative distinction between the two vertical beam-bending mechanisms, i.e., turbulence and slow refraction, can be made using the probability distributions of the wander signal. In Figure 18a we show the distribution for the horizontal signal of Figure 17a, with equivalent high-pass filtering at four different cut-off frequencies. The distributions are gaussian, with coefficients of skewness and kurtosis for the 100 sec⁻¹ case of 3.6×10^{-4} and 3.1 respectively. In Figure 18b, we show the distributions for the vertical signal of Figure 17b, where the non-gaussian nature is quite apparent.

A summary of the characteristics of the wander signals, averaged over a number of runs, is shown in Table II. The ratio of average horizontal/vertical (rms) wander angles is 1.6. The correlation coefficient refers to the basic theoretical prediction (wander term of Eq. 12), namely that the mean-square wander angle is proportional to C_n^2 . In spite of the influence of slow refractive effects, the vertical wander exhibits much less bias than does the horizontal. This may be due to variable-wind effects, which influence the horizontal case only.

The average two-dimensional mean-square wander angle, for the runs included in this paper, implies a value of $|C_2'|$ of 1.16, which is nearly equal to that deduced in the phenomenological discussion above.

TABLE II

Average Characteristics of Beam Wander Signals

	Skewness	Kurtosis	Correlation Coefficient (Experiment vs. Theory)
Vertical	2.0×10^{-2}	2.76	0.90
Horizontal	2.3×10^{-2}	2.89	0.36
Total			0.97

The power spectrum and frequency-weighted spectrum of the wander signal of Figure 17a are shown in Figure 19a. The theoretical phase-difference spectrum, which is closely related, is predicted to fall off with an exponent of $(-2/3, -8/3)$ for frequencies above breakpoints (f_1, f_2) respectively:

$$f_1 \approx v_{\perp} / \text{outerscale}$$

$$f_2 \approx v_{\perp} / D$$

(20)

where v_{\perp} is the perpendicular component of wind velocity. For frequencies below f_1 , the behavior is very sensitive to the detailed behavior of the wind. Since this was a low wind case, we expect a log-log slope of $-8/3$; the actual slope was -2.78 with a correlation coefficient of 0.98. In Figure 19b, horizontal and vertical spectra are shown for a higher (horizontal) wind. The horizontal f_2 is 4 Hz, and the $-2/3$ slope is well supported. The vertical case shows a greater slope, and we note that f_2 for the vertical wind is approximately zero near the ground. In other cases, such as shown in Figure 19c, both the horizontal and vertical spectra fall between the two theoretical slopes.

3.5 Transmitter Focus Effects

As discussed in a preceding section, the first-order theory predicts that a focused, near-field transmitter with wander cancellation will result in the smoothing of scintillations. It is now understood that this effect, if it occurs, can only be realized for the condition $D/\rho_0 < 1$. As a follow-up to our work as reported in Ref. 13, where qualitative evidence of such smoothing was seen, we are conducting experiments on the (wander-tracked) signal fading vs. transmitter focus adjustment. As discussed in that reference, the smoothing effect is expected to be very critically dependent upon focus adjustment.

Attempts to observe this effect are shown in Figures 20 a,b,c. The parameter α_{2z} is simply z/R , where R is the radius of curvature of the transmitter wavefront. As D/ρ_0 approaches unity, the predicted effect is observed, including the large increase in scintillations with slight misadjustments.

Current work involves much lower values of D/ρ_0 , where we hope to observe values σ^2 substantially under those for a point source on the same path. The point source scintillations are necessarily quite low under these conditions, and any residual fading due to e.g. tracker error or jitter will be quite important. However, the tracker resolution is $0.02 \times$ the diffraction limit, and we hope to see substantial smoothing. This effect has important practical implications for uplinkbeams, especially at longer wavelengths (Ishimari, A., 1969; Fried, D.L. and Schmelzter, R.A., 1967; Kerr, J. R. and Eisa, R., 1972; Kerr, J.R. and Dunphy, J.R., 1973).

APPENDIX A. LIMIT OF IRRADIANCE AT LARGE VALUES OF D/ρ_0

It was pointed out above that both the phenomenological model and experimental data suggest that the normalized irradiance variance with a transmitter aperture much larger than the coherence scale must approach unity. Through reciprocity, this would also be true of a large heterodyne receiver. Although this seems to be clearly necessary physically, it disagrees with earlier approximate analyses of heterodyne systems (Fried, D.L., 1967). The purpose of this Appendix is to derive this limit directly from the Huygens-Fresnel expression for the second moment of irradiance (fourth moment of amplitude).

The relevant Huygens-Fresnel expression is given in Ref. 22. For a nontruncated gaussian beam, this may be readily reduced to the eight-fold integral:

$$\begin{aligned} \langle I^2 \rangle = & \left(\frac{k}{2\pi L} \right)^4 \iiint \int d\vec{\rho}_1 d\vec{\rho}_2 d\vec{\rho}_3 d\vec{\rho}_4 \exp \left\{ - \frac{\rho_1^2 + \rho_2^2 + \rho_3^2 + \rho_4^2}{D_g} \right\} \\ & \cdot \exp \left\{ - \left(\frac{D_g}{\rho_0} \right)^{5/3} \frac{1}{D_g^{5/3}} \left[|\vec{\rho}_1 - \vec{\rho}_2|^{5/3} + |\vec{\rho}_3 - \vec{\rho}_4|^{5/3} + |\vec{\rho}_1 - \vec{\rho}_4|^{5/3} \right. \right. \\ & \left. \left. + |\vec{\rho}_2 - \vec{\rho}_3|^{5/3} - |\vec{\rho}_2 - \vec{\rho}_4|^{5/3} - |\vec{\rho}_1 - \vec{\rho}_3|^{5/3} \right] \right\} \exp \left\{ C_\ell(|\vec{\rho}_1 - \vec{\rho}_3|) + C_\ell(|\vec{\rho}_2 - \vec{\rho}_4|) \right\} \quad (A.1) \end{aligned}$$

where D_g is the $\frac{1}{2}$ irradiance diameter, $\vec{\rho}$ is the i^{th} difference-vector in the transmitter plane, and C_ℓ is the log² amplitude covariance function. It may be shown from physical reasoning, or from tedious but straightforward analytical calculations, that the covariance functions may be dropped* when we consider the limit $D_g/\rho_0 \rightarrow \infty$.

We let $x = \rho/D_g$, $\alpha = \frac{D_g}{\rho_0}$, and write (A.1) as

$$\begin{aligned} \langle I^2 \rangle = & \left(\frac{k D_g}{2\pi L} \right)^4 \iiint \int d\vec{x}_1 d\vec{x}_2 d\vec{x}_3 d\vec{x}_4 \exp \left\{ - (x_1^2 + x_2^2 + x_3^2 + x_4^2) \right\} \exp \left\{ - (\alpha)^{5/3} \left[|\vec{x}_1 - \vec{x}_2|^{5/3} \right. \right. \\ & \left. \left. + |\vec{x}_3 - \vec{x}_4|^{5/3} + |\vec{x}_1 - \vec{x}_4|^{5/3} + |\vec{x}_2 - \vec{x}_3|^{5/3} - |\vec{x}_2 - \vec{x}_4|^{5/3} - |\vec{x}_1 - \vec{x}_3|^{5/3} \right] \right\} \quad (A.2) \end{aligned}$$

We now write

$$\begin{aligned} \lim_{\alpha \rightarrow \infty} \exp \left\{ - (\alpha)^{5/3} \left[|\vec{x}_1 - \vec{x}_2|^{5/3} + |\vec{x}_1 - \vec{x}_4|^{5/3} \right] \right\} = & 6/5 \pi \Gamma(6/5) (\alpha)^{-2} \exp \left\{ - (\alpha)^{5/3} |\vec{x}_1 - \vec{x}_4|^{5/3} \right\} \delta(|\vec{x}_1 - \vec{x}_2|) \\ & + 6/5 \pi \Gamma(6/5) (\alpha)^{-2} \exp \left\{ - (\alpha)^{5/3} |\vec{x}_1 - \vec{x}_2|^{5/3} \right\} \delta(|\vec{x}_1 - \vec{x}_4|) \quad (A.3) \end{aligned}$$

i.e.

$$\delta(|\vec{x}_1 - \vec{x}_2|) = \lim_{\alpha \rightarrow \infty} 5/6 \frac{\alpha^2}{\pi \Gamma(6/5)} \exp \left\{ - (\alpha)^{5/3} |\vec{x}_1 - \vec{x}_2|^{5/3} \right\} \quad (A.4)$$

where we note that this satisfies the properties of a delta function:

$$\int_{-\infty}^{\infty} \delta(|\vec{x}_1 - \vec{x}_2|) d\vec{x}_1 = 1 ; \quad \lim_{\vec{x}_1 \rightarrow \vec{x}_2} \delta(|\vec{x}_1 - \vec{x}_2|) = \lim_{\alpha \rightarrow \infty} 5/6 \frac{\alpha^2}{\pi \Gamma(6/5)} \rightarrow \infty$$

*It may also be shown that this is equivalent to dropping the amplitude term in the perturbation Green's function, as done in Ref. 1. In the latter effort, the phase perturbation was assumed to be gaussian, and the problem under discussion here was reduced to a six-fold integral for numerical evaluation. Although the results in the limit of large D_g/ρ_0 agree with those presented here, it may be demonstrated that the dropping of the amplitude term results in inaccuracies at smaller values of D_g/ρ_0 .

$$\delta(|\vec{x}_1 - \vec{x}_2|) \Big|_{\vec{x}_1 \leftrightarrow \vec{x}_2} = \lim_{\alpha \rightarrow \infty} \frac{1}{\alpha} \frac{5}{6} \frac{\alpha^2}{\pi \Gamma(6/5)} \exp \left\{ -(\alpha)^{5/3} |\vec{x}_1 - \vec{x}_2|^{5/3} \right\} = 0$$

Using (A.3) with (A.2), we have

$$\lim_{\alpha \rightarrow \infty} \langle I^2 \rangle = \left(\frac{kD}{2\pi L} \right)^4 (6/5) \frac{\pi \Gamma(5/6)}{\alpha^2} \left\{ \iiint d\vec{x}_2 d\vec{x}_3 d\vec{x}_4 \exp \left[-(2x_2^2 + x_3^2 + x_4^2) \right] \exp \left[-(\alpha)^{5/3} |\vec{x}_3 - \vec{x}_4|^{5/3} \right] \right. \\ \left. + \iiint d\vec{x}_2 d\vec{x}_3 d\vec{x}_4 \exp \left[-(x_2^2 + x_3^2 + 2x_4^2) \right] \exp \left[-(\alpha)^{5/3} |\vec{x}_2 - \vec{x}_3|^{5/3} \right] \right\} \quad (A.5)$$

Iterating this procedure for the term in each of the integrands of the form $\exp \left\{ -(\alpha)^{5/3} |\vec{x}_1 - \vec{x}_j|^{5/3} \right\} \rightarrow 6/5 \pi \Gamma(6/5) \alpha^{-2} \delta(|\vec{x}_1 - \vec{x}_j|)$ results in

$$\lim_{\alpha \rightarrow \infty} \langle I^2 \rangle = \left(\frac{kD}{2\pi L} \right)^4 \left[(6/5) \frac{\pi \Gamma(5/6)}{\alpha^2} \right]^2 \left\{ \iint d\vec{x}_2 d\vec{x}_4 \exp \left[-2(x_2^2 + x_4^2) \right] + \iint d\vec{x}_3 d\vec{x}_4 \exp \left[-2(x_3^2 + x_4^2) \right] \right\} \quad (A.6)$$

$$\lim_{\alpha \rightarrow \infty} \langle I^2 \rangle = \left(\frac{kD}{2\pi L} \right)^4 (3/5)^2 \frac{(2\pi)^2 \Gamma^2(6/5)}{\alpha^4} (\pi/2)^2 (2) = \left(\frac{kD}{2L} \right)^4 (3/5)^2 \frac{\Gamma^2(6/5)}{8} = .0379 \left(\frac{kD}{2L} \right)^4 \quad (A.7)$$

Similarly, we may write

$$\lim_{\alpha \rightarrow \infty} \langle I \rangle = \left(\frac{kD}{2\pi L} \right)^2 \iint d\vec{x}_1 d\vec{x}_2 \exp \left\{ -\frac{x_1^2 + x_2^2}{2} \right\} \exp \left\{ -\alpha^{5/3} |\vec{x}_1 - \vec{x}_2|^{5/3} \right\} \quad (A.8)$$

Using the delta function, this becomes

$$\lim_{\alpha \rightarrow \infty} \langle I \rangle = \left(\frac{kD}{2\pi L} \right)^2 (3/5) \frac{2\pi \Gamma(6/5)}{\alpha^2} \int d\vec{x}_2 e^{-x_2^2/2} = \left(\frac{kD}{L\alpha} \right)^2 (3/5) \frac{\Gamma(6/5)}{4} = .1377 \left(\frac{kD}{L\alpha} \right)^2 \quad (A.9)$$

Finally, we write from (A.7) and (A.9)

$$\lim_{\alpha \rightarrow \infty} \sigma_I^2 = \frac{\langle I_\infty^2 \rangle - \langle I_\infty \rangle^2}{\langle I_\infty \rangle^2} = 1$$

This is the desired result.

References

1. Banakh, V.A., et al, 1974, J. Opt. Soc. Am. 64, 516.
2. Brown, W.P., Jr., 1972, Hughes Research Laboratories, Malibu, California Unpublished Report.
3. Dowling, J.A. and Livingston, P.M., 1973, J. Opt. Soc. Am. 63, 846.
4. Dunphy, J.R. and Kerr, J.R., 1974, J. Opt. Soc. Am. 64, 1015.
5. Fried, D.L., 1966, J. Opt. Soc. Am. 56, 1372.
6. Fried, D.L., 1967, J. Quantum Electr. QE-3, 213.
7. Fried, D.L., 1967, Proc. IEEE 55, 57.
8. Fried, D.L. and Schmeltzer, R.A., 1967, Appl. Opt. 6, 1729.
9. Fried, D.L. and Yura, H.T., 1972, J. Opt. Soc. Am. 62, 600.
10. Gochelashvili, K.S., 1973, Optica Acta 20, 193.
11. Huber, A.J., 1973, Rome Air Development Center, Griffiss AFB Unpublished Report.
12. Ishimaru, A., 1969, Radio Science 4, 295.
13. Kerr, J.R. and Dunphy, J.R., 1973, J. Opt. Soc. Am. 63, 1.
14. Kerr, J.R. and Eiss, R., 1972, J. Opt. Soc. Am. 62, 682.
15. Kerr, J.R., et al, November 1974, Report No. RADG-TR-74-320, Rome Air Development Center, Griffiss AFB.
16. Kon, A.I., 1970, Izv. VUZ Radiofizika 13, 61.
17. Lawrence, R.S., and Strohbehn, J.W., 1970, Proc. IEEE 58, 1523.
18. Lutomirski, R.F. and Yura, H.T., 1971, Appl. Opt. 10, 1652.
19. Lutomirski, R.F. and Yura, H.T., 1971, J. Opt. Soc. Am. 61, 482.
20. Titterton, P.J., 1973, Appl. Opt. 12, 423.
21. Yura, H.T., 1971, Appl. Opt. 10, 2771.
22. Yura, H.T., 1972, Appl. Opt. 11, 1399.
23. Yura, H.T., 1973, J. Opt. Soc. Am. 63, 107.
24. Yura, H.T., 1973, J. Opt. Soc. Am. 63, 567.

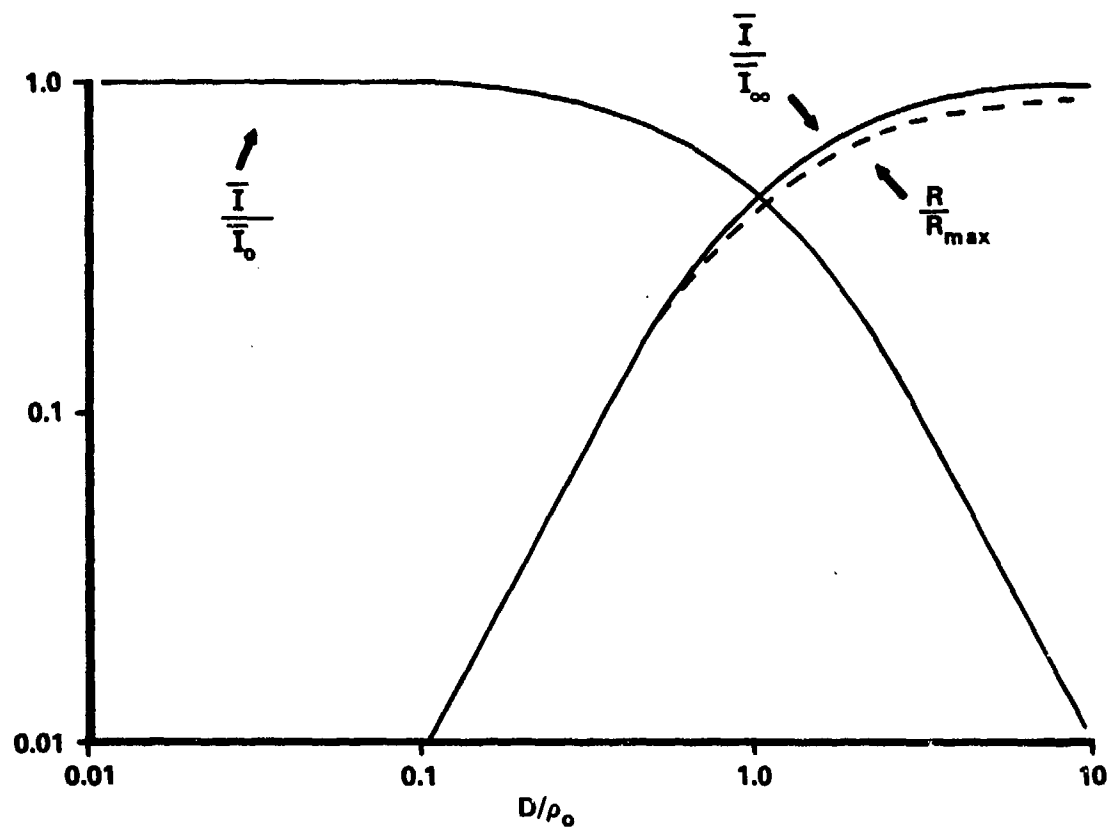


Fig.1 Theoretical non-tracking mean irradiance from Eqs. (9a,b) and long-term image resolution from Ref. 5.

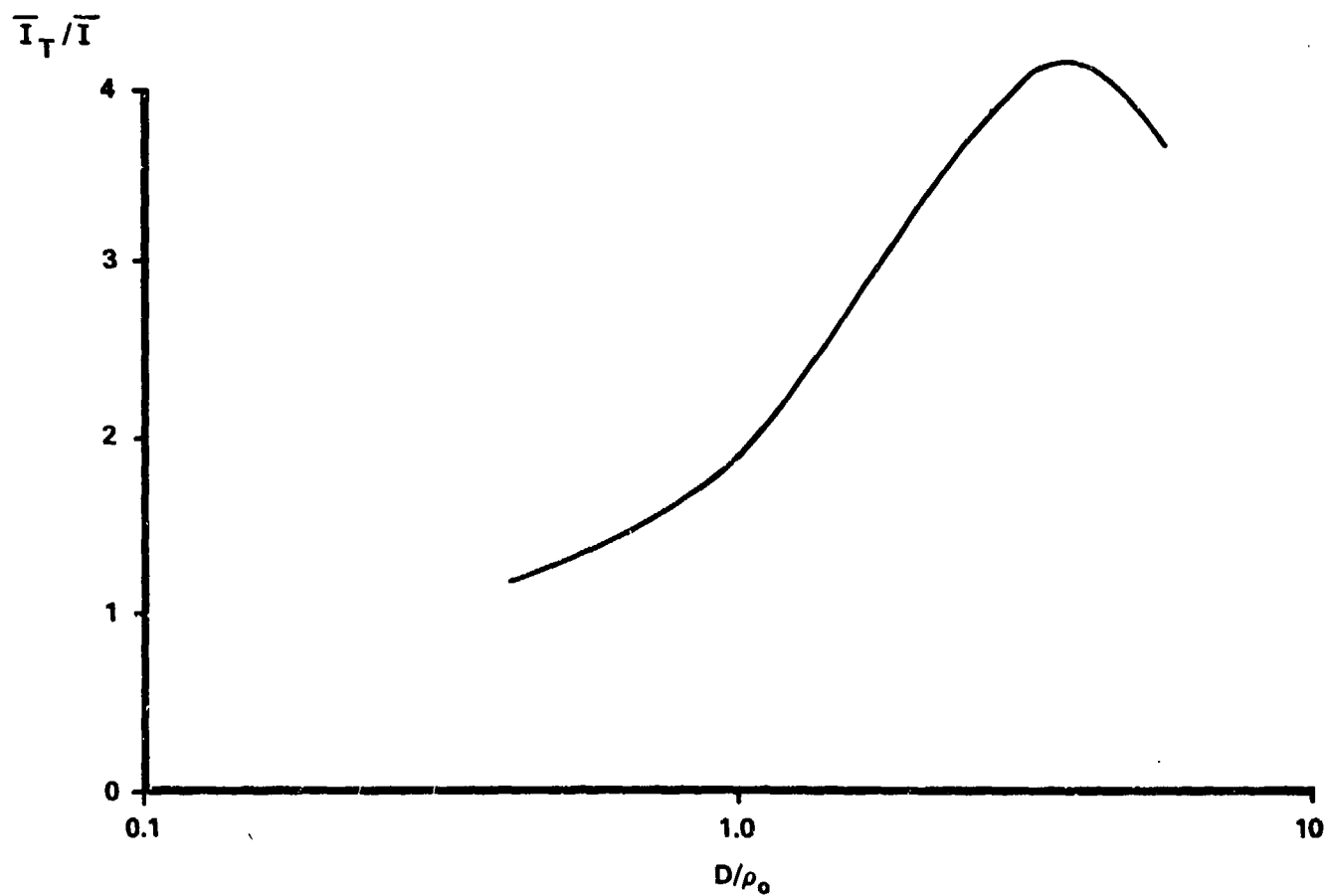


Fig.2 Theoretical $\frac{\bar{I}_T}{\bar{I}}$ from Ref. 5.

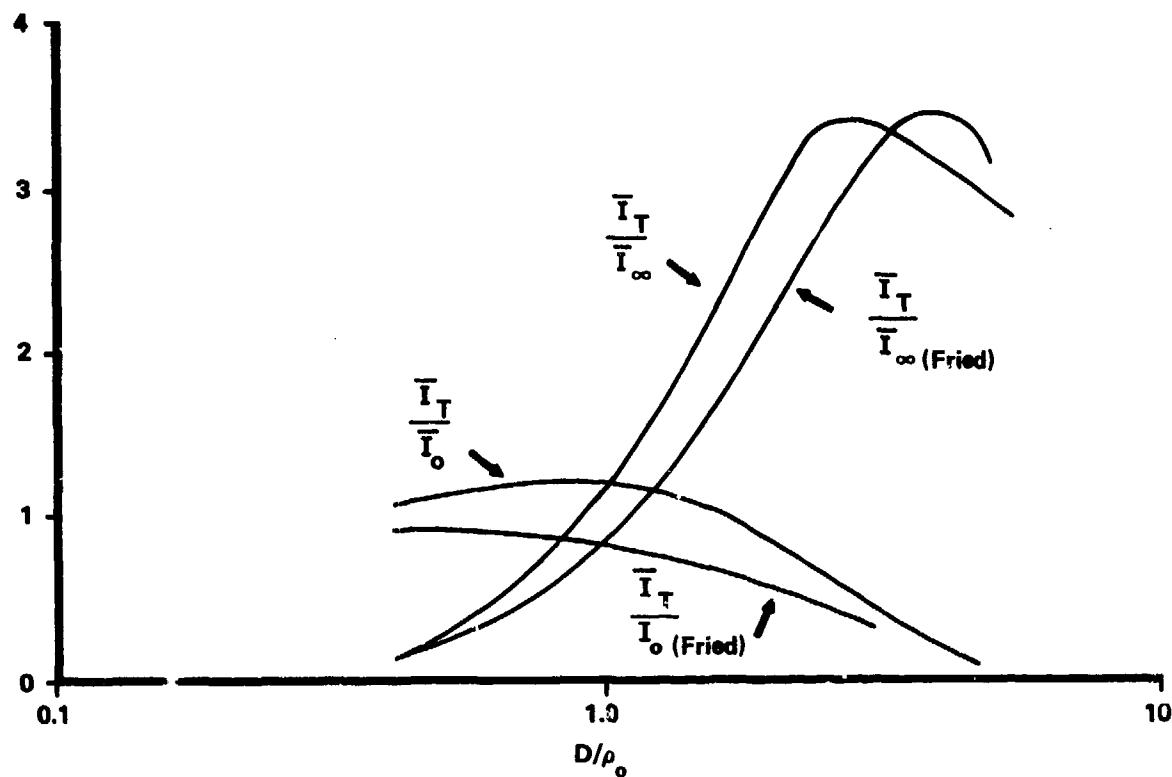


Fig.3 Theoretical mean irradiance with wander-tracking. The upper curve in each pair is from Eq. (12a) and the curve is from Ref. 5.

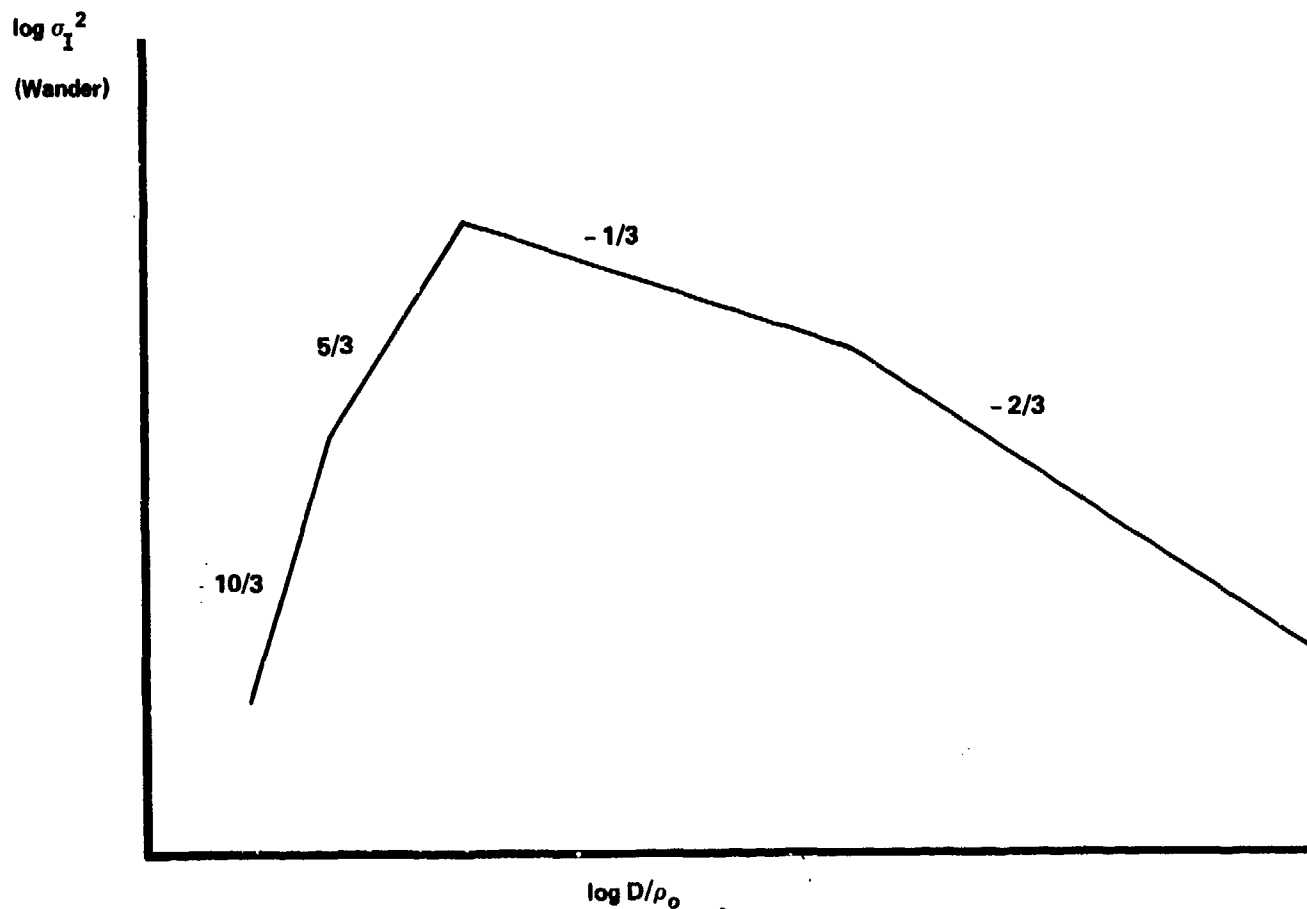


Fig.4 General behavior of Eq. (14) for fading due to beam wander.

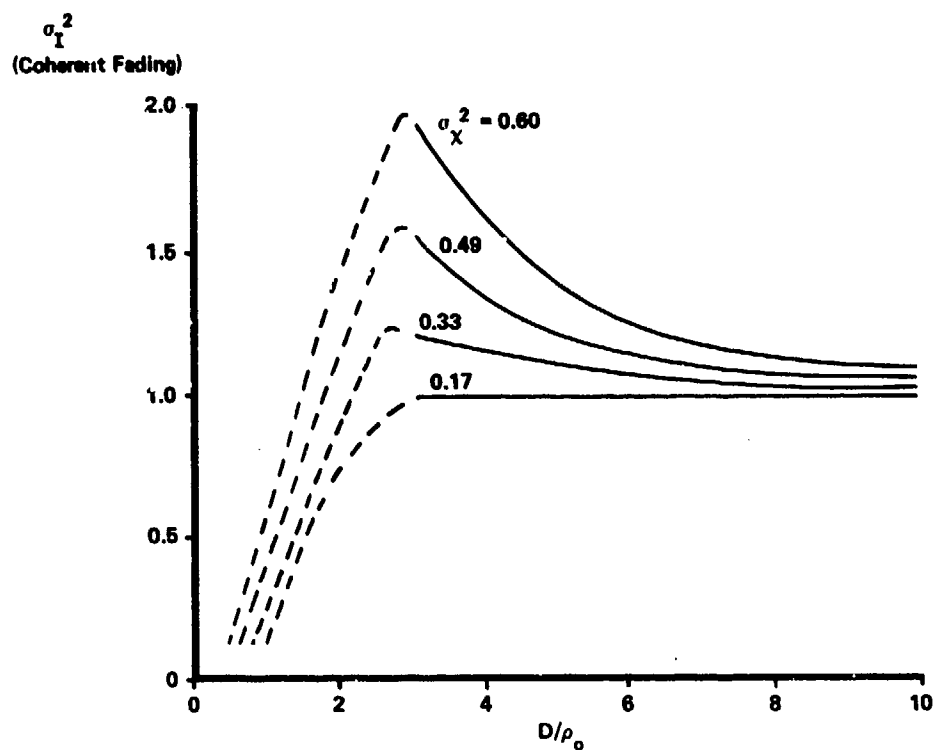


Fig.5 Normalized irradiance variance due to coherent fading (Eq. 17).

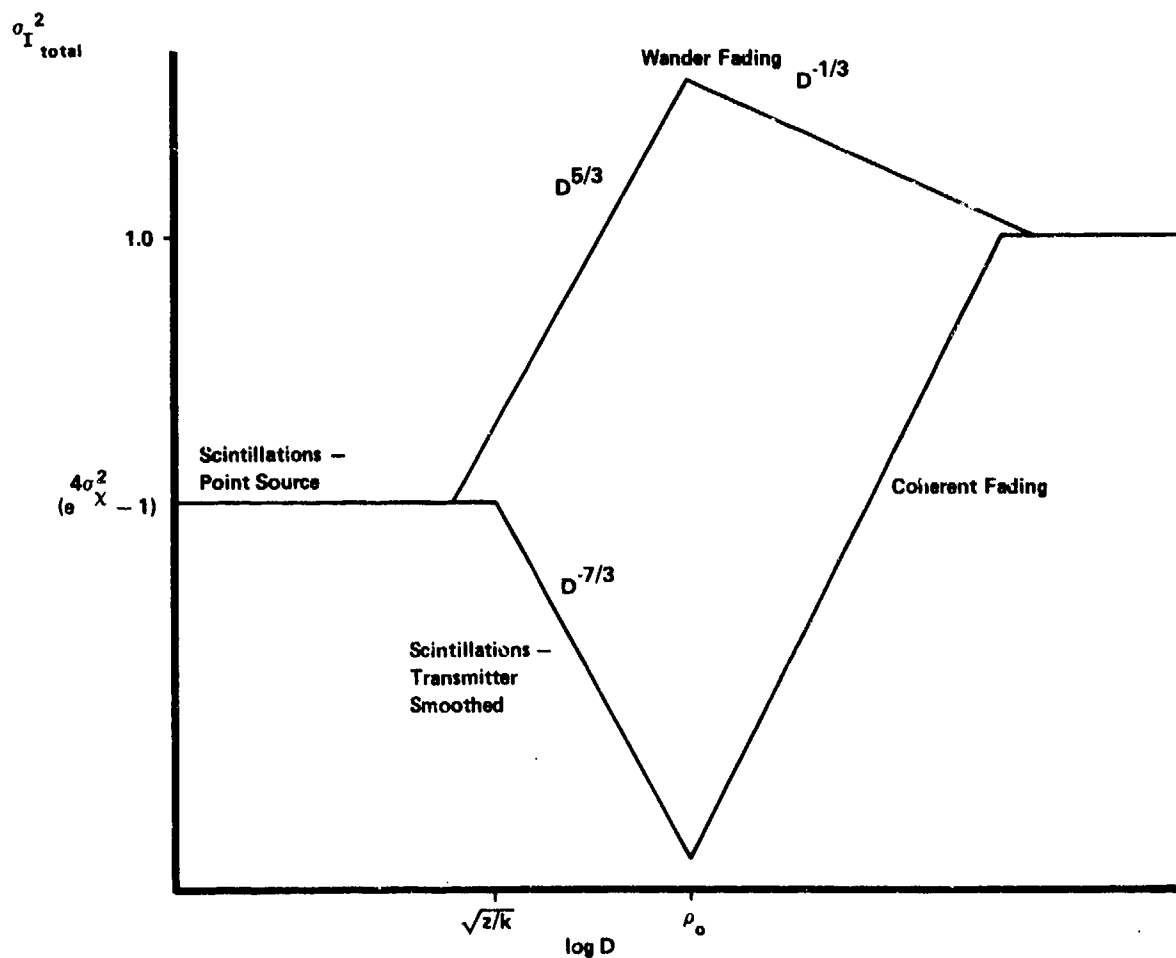


Fig.6 Normalized variance of irradiance vs. transmitter diameter, with and without wander-cancellation.

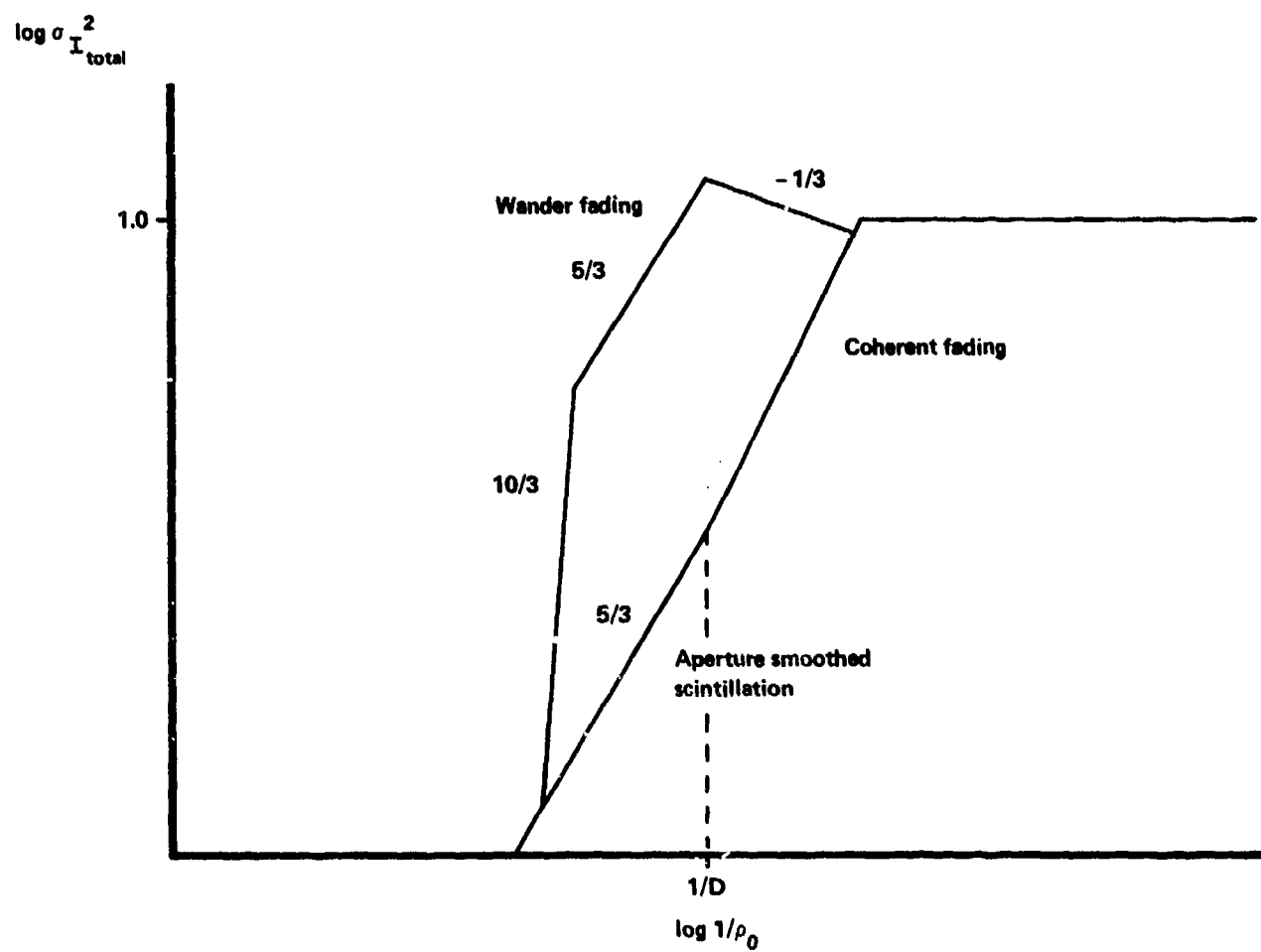
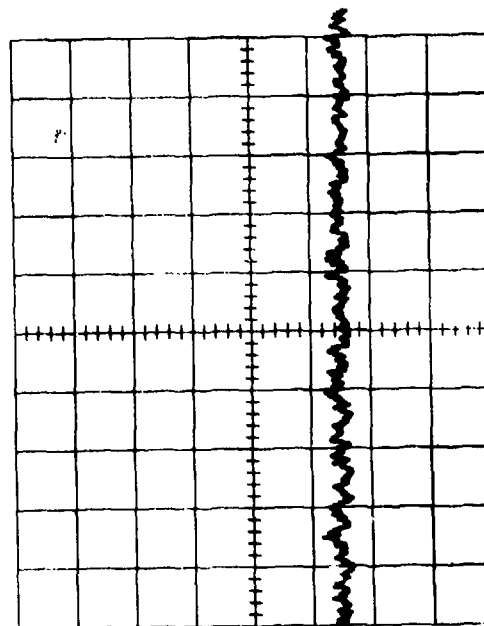
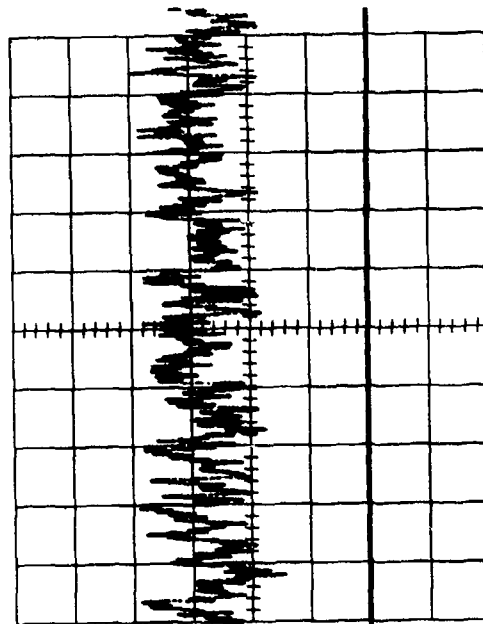
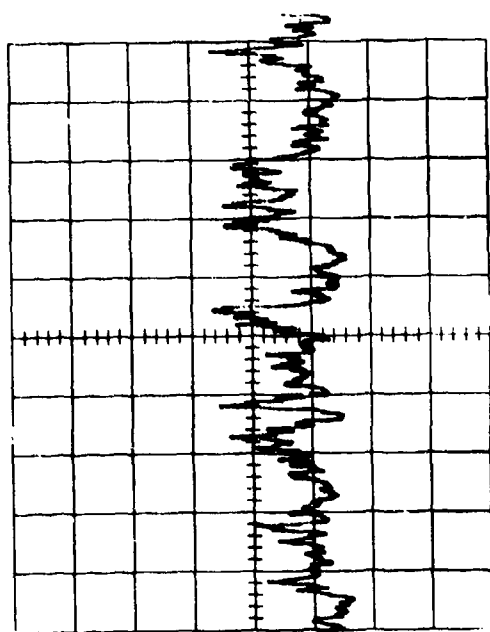
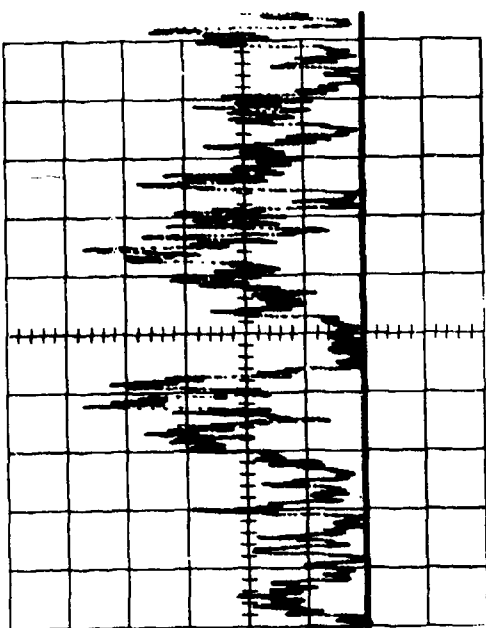


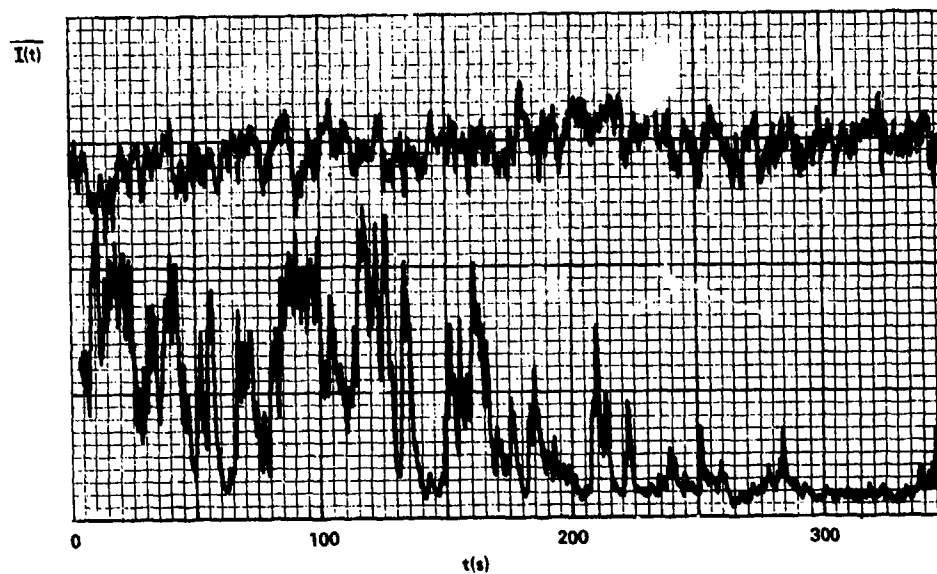
Fig.7 Normalized variance of irradiance vs. coherence scale, with and without wander-cancellation.



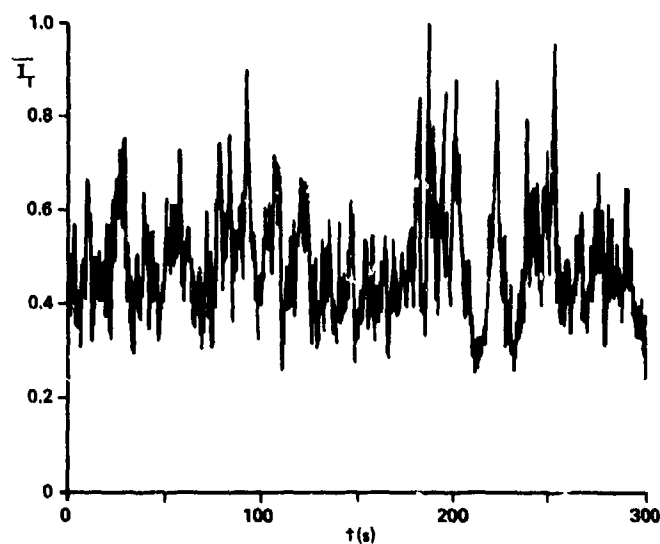
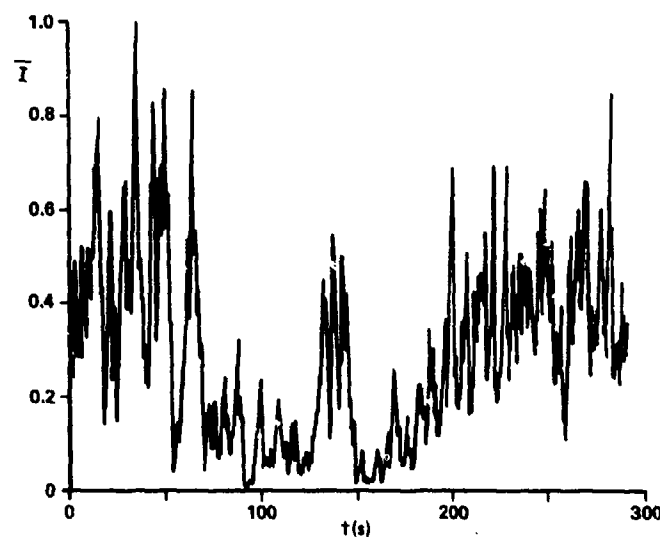
B. Log irradiance (ordinate: one decade/div).

A. Linear irradiance.

Fig. 8 Target irradiance vs. time, with and without wander tracking (lower and upper curves respectively), for weak turbulence ($D/\rho_0 \approx 1$). Abscissa: 0.5 sec/div.



A. Weak turbulence ($D/\rho_0 \approx 1$). The upper trace is for wander tracking.



B. Strong turbulence ($D/\rho_0 = 63$). The lower trace is for wander tracking.

Fig.9 Target irradiance vs. time, with and without wander tracking. The irradiance is smoothed with a 1-sec time constant.

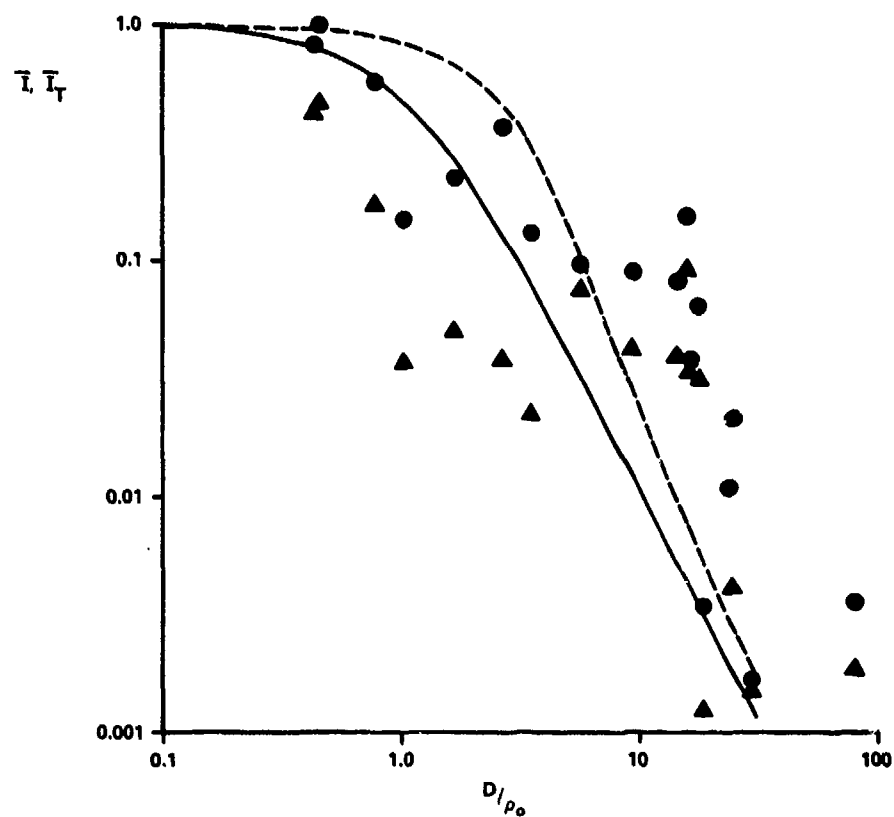


Fig.10 Experimental values of \bar{I}/\bar{I}_0 (Δ) and \bar{I}_T/\bar{I}_0 (\bullet) vs. D/ρ_0 . The theoretical curves are from Figure 1 (—) and Figure 3 (----) respectively.

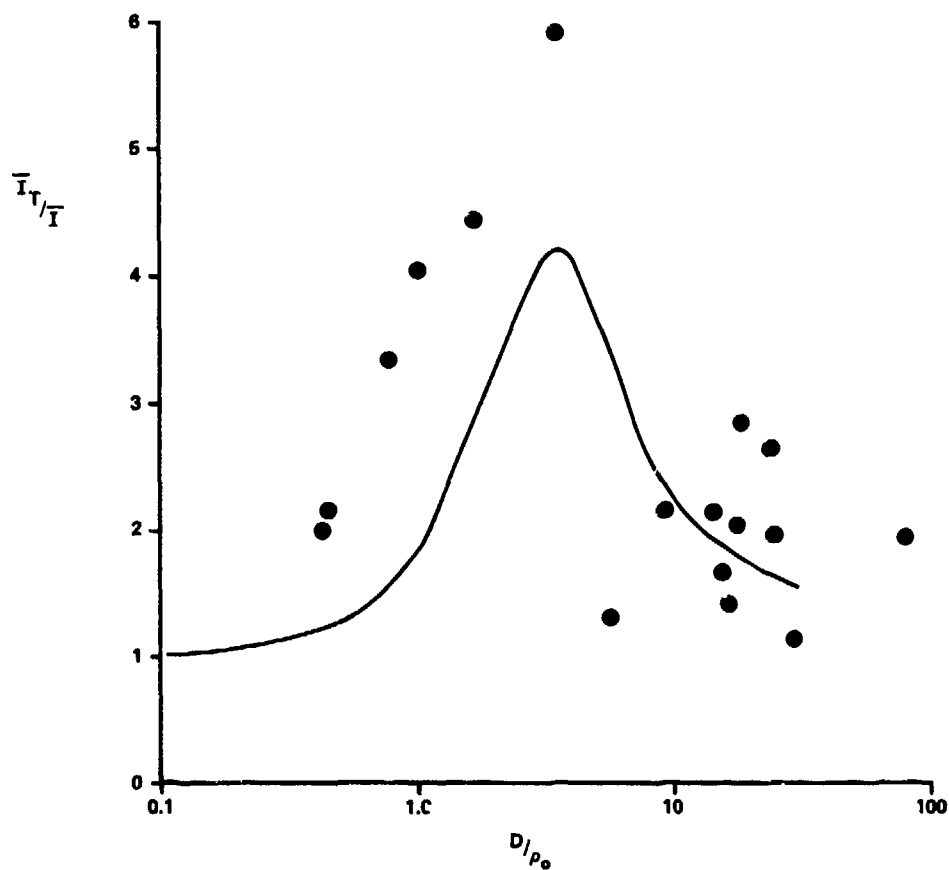


Fig.11 Experimental values of \bar{I}_T/\bar{I} vs. D/ρ_0 . The theoretical curve is from Figure 2.

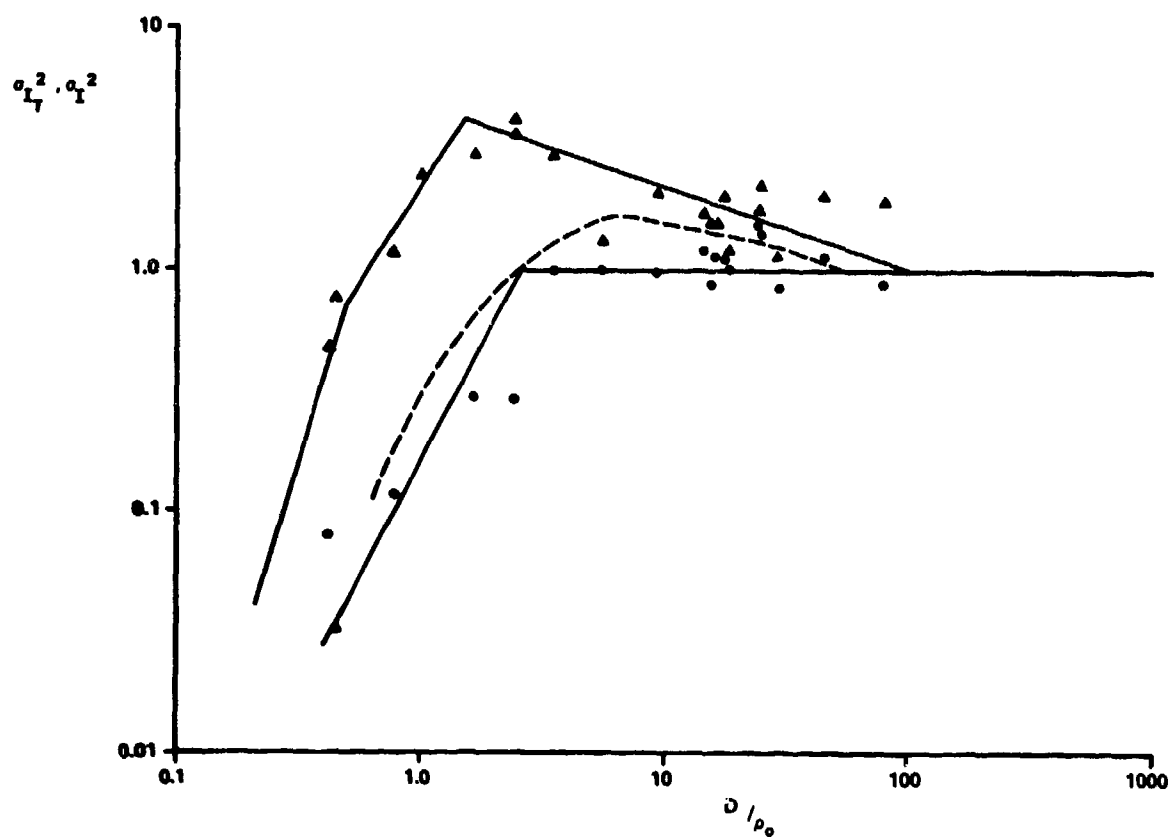


Fig.12 Normalized irradiance variance with (○) and without (Δ) tracking, vs. D/ρ_0 . The theoretical curves are from Figure 7 (—) and Ref. 1 (---).

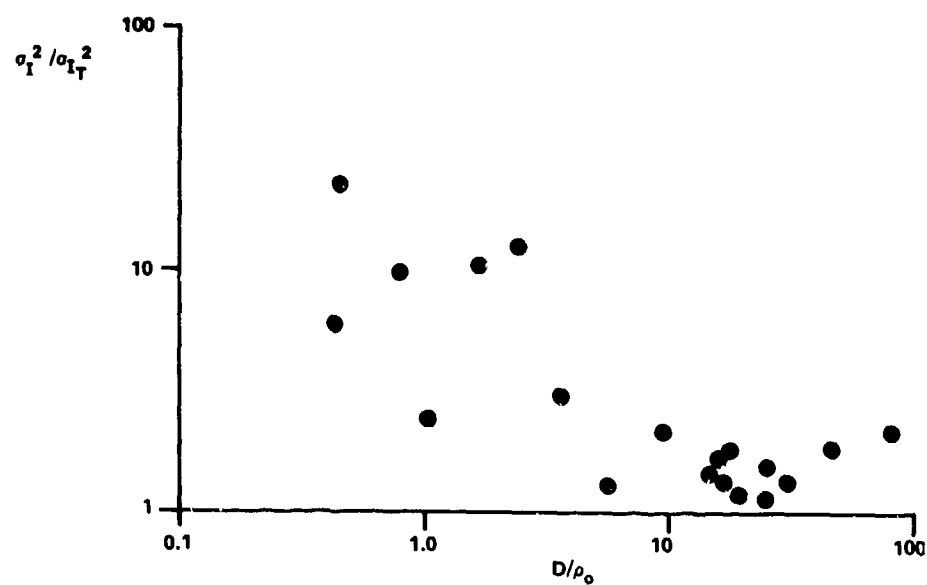


Fig.13 Values of σ_I^2/σ_T^2 vs. D/ρ_0 corresponding to Figure 12.

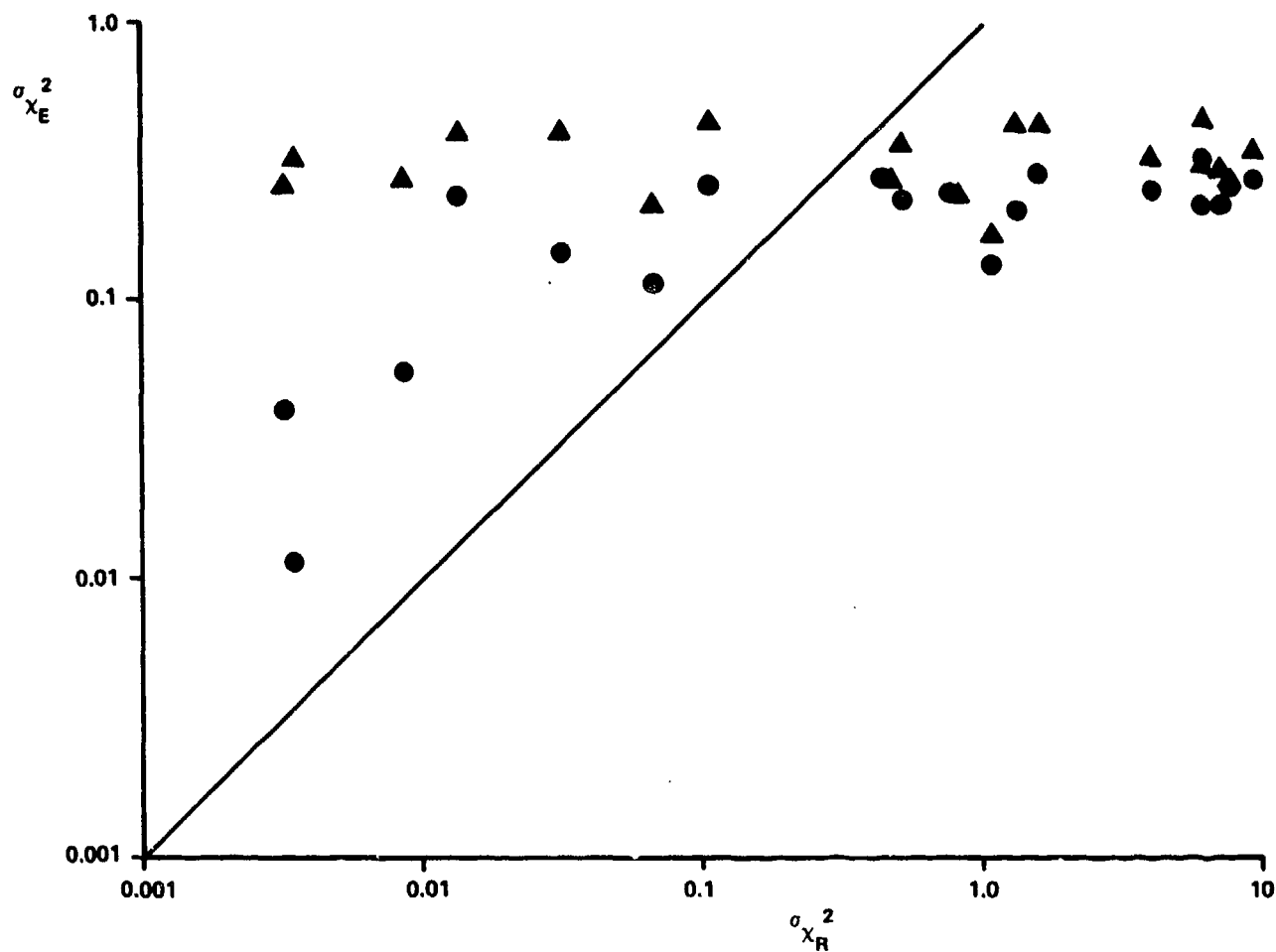
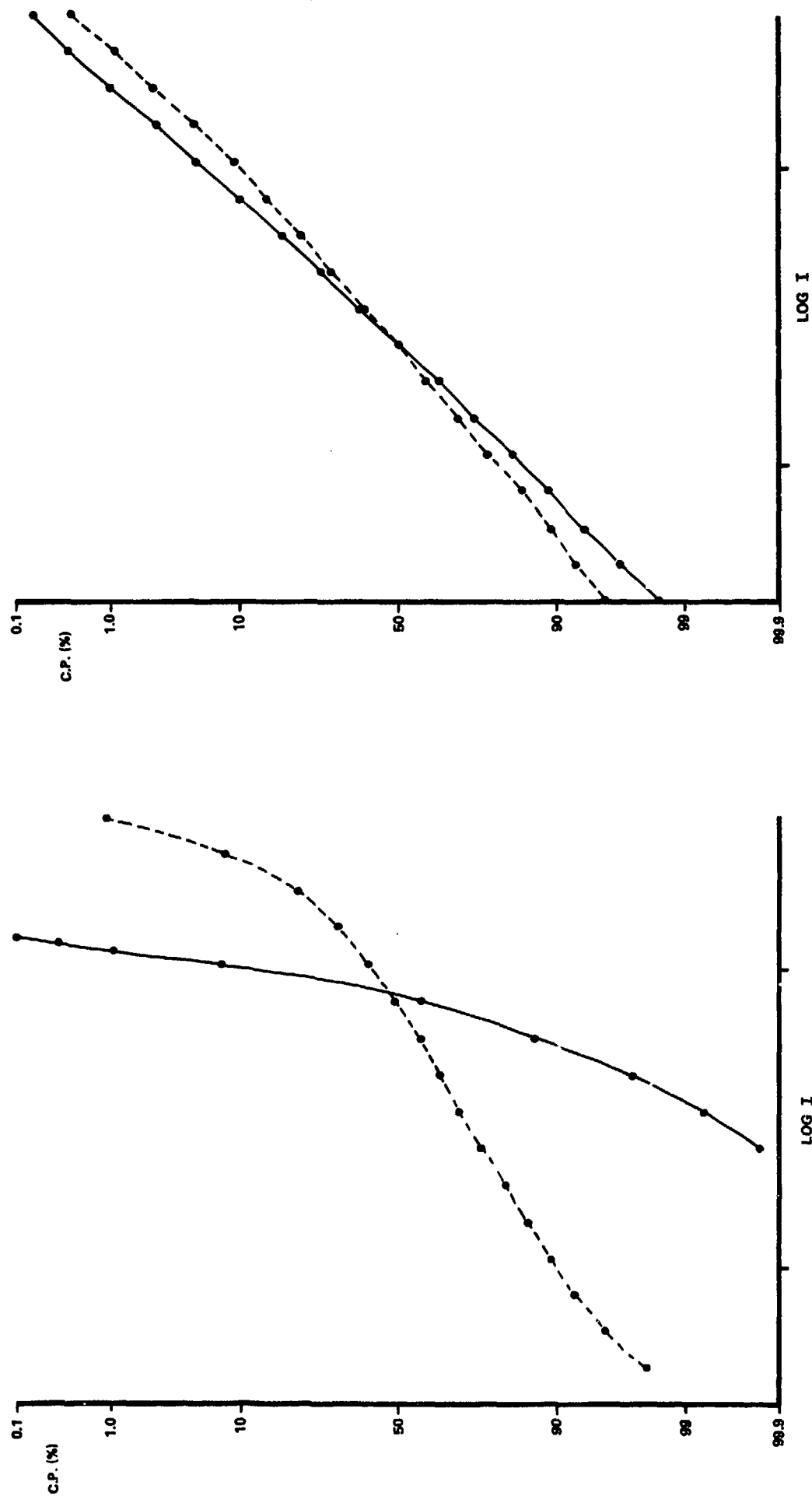
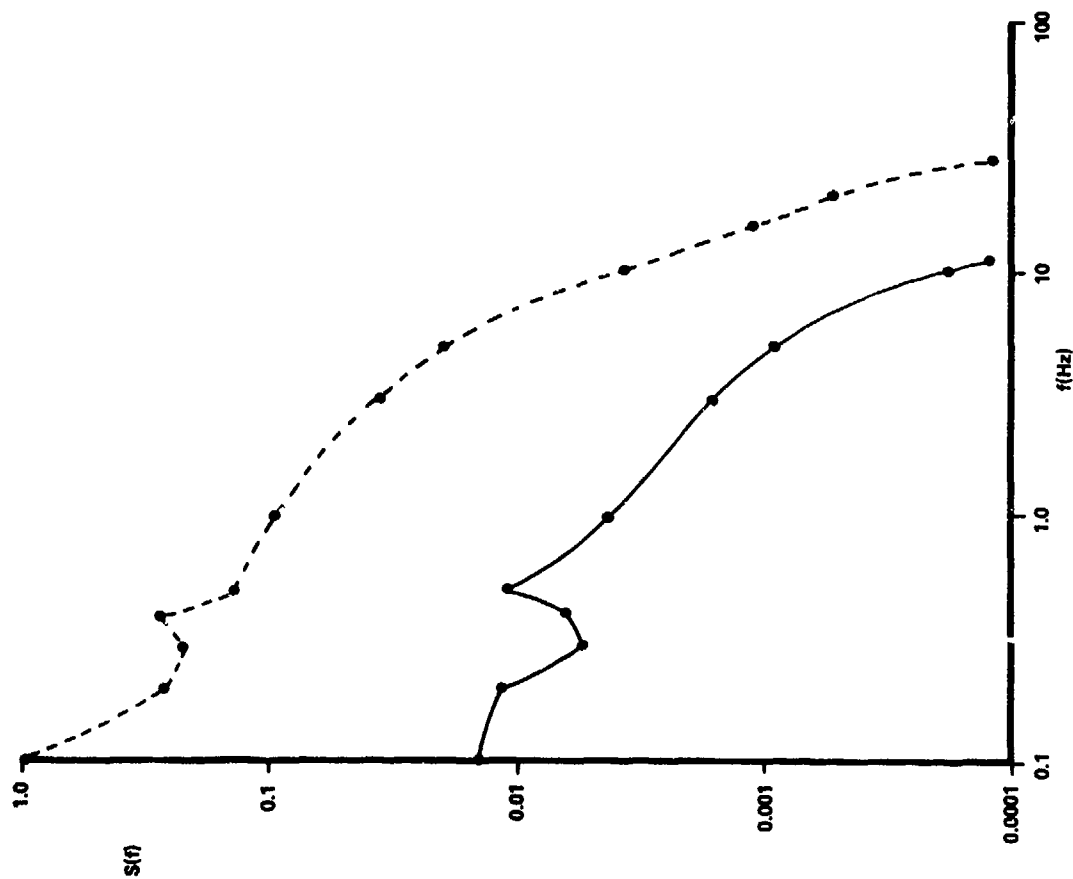
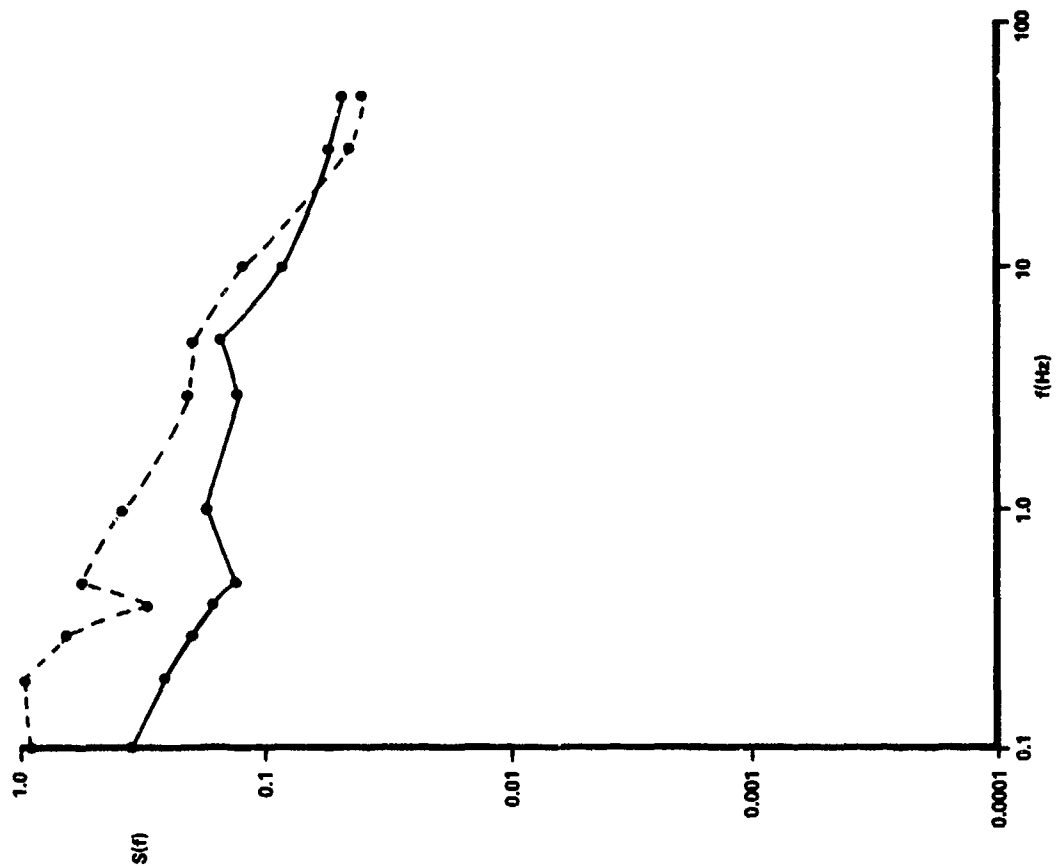
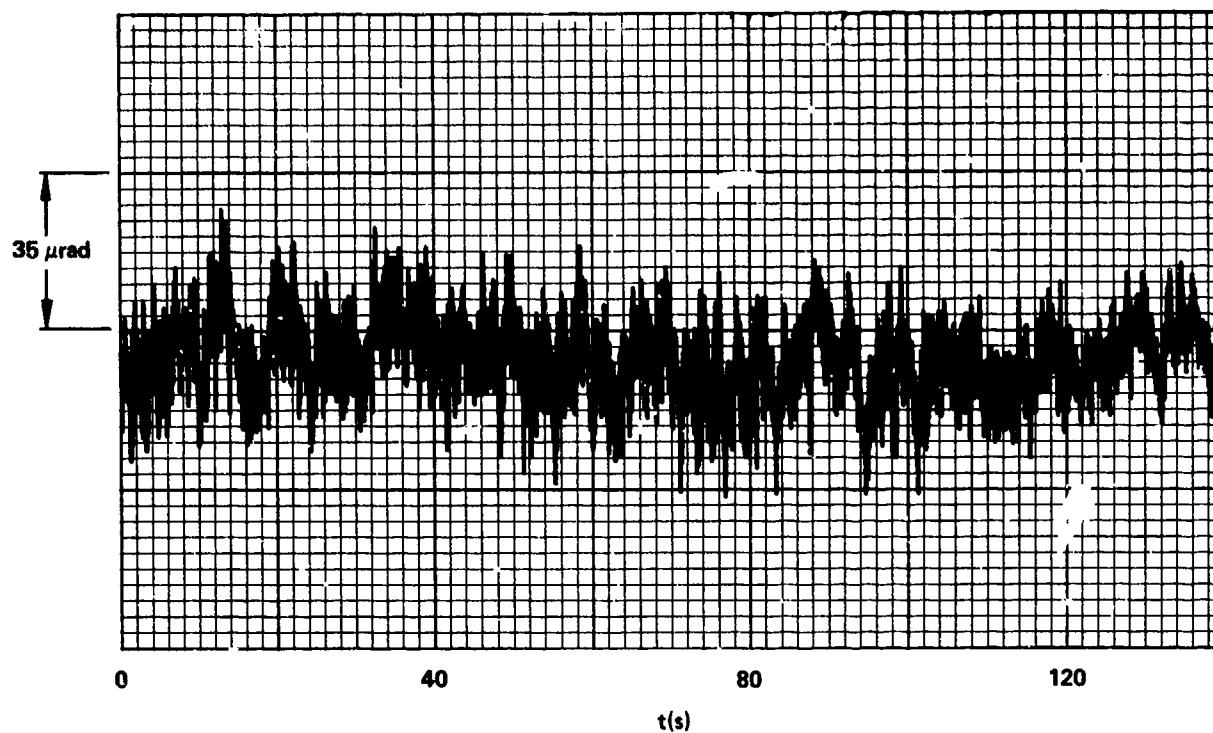


Fig.14 Experimental log amplitude variance ($\sigma^2 \chi_E$ vs. theoretical Rytov value for a point source ($\sigma^2 \chi_R$), with (●) and without (▲) wander tracking. (—) indicates the condition $\sigma^2 \chi_E = \sigma^2 \chi_R$.

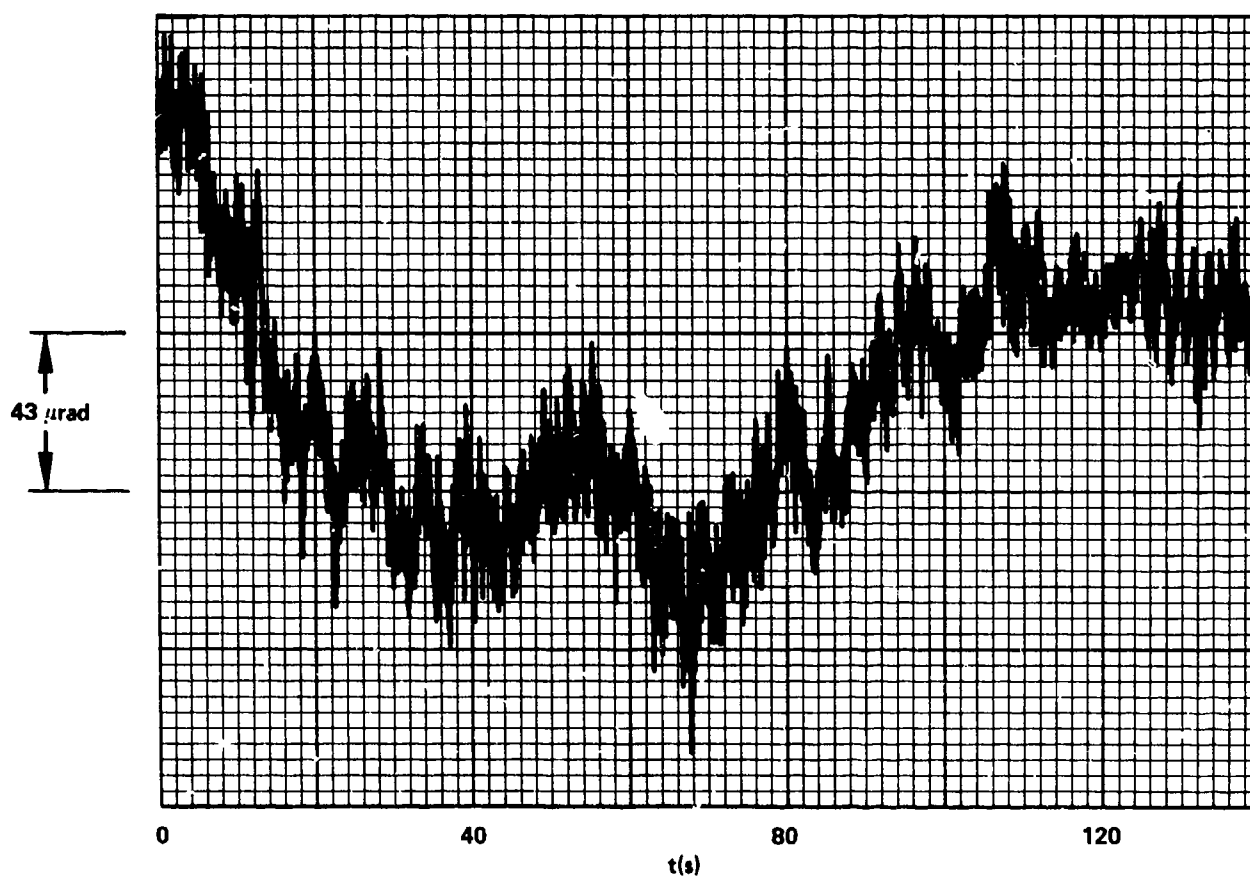


A. Weak turbulence ($D/\rho_0 \approx 1$).
 B. Strong turbulence ($D/\rho_0 > 100$).
 Fig. 15 Cumulative probability for the log irradiance for the vander-tracked (—) and non-tracked (---) cases.

A. Weak turbulence ($D/\rho_0 \approx 1$).B. Strong turbulence ($D/\rho_0 \approx 100$).Fig. 16 Power spectra $S(f)$ for total fading of log irradiance for the wander tracked (—) and non-tracked (---) cases.



A. Horizontal wander.



B. Vertical wander.

Fig.17 Wander signals vs. time for a nighttime run in low wind.

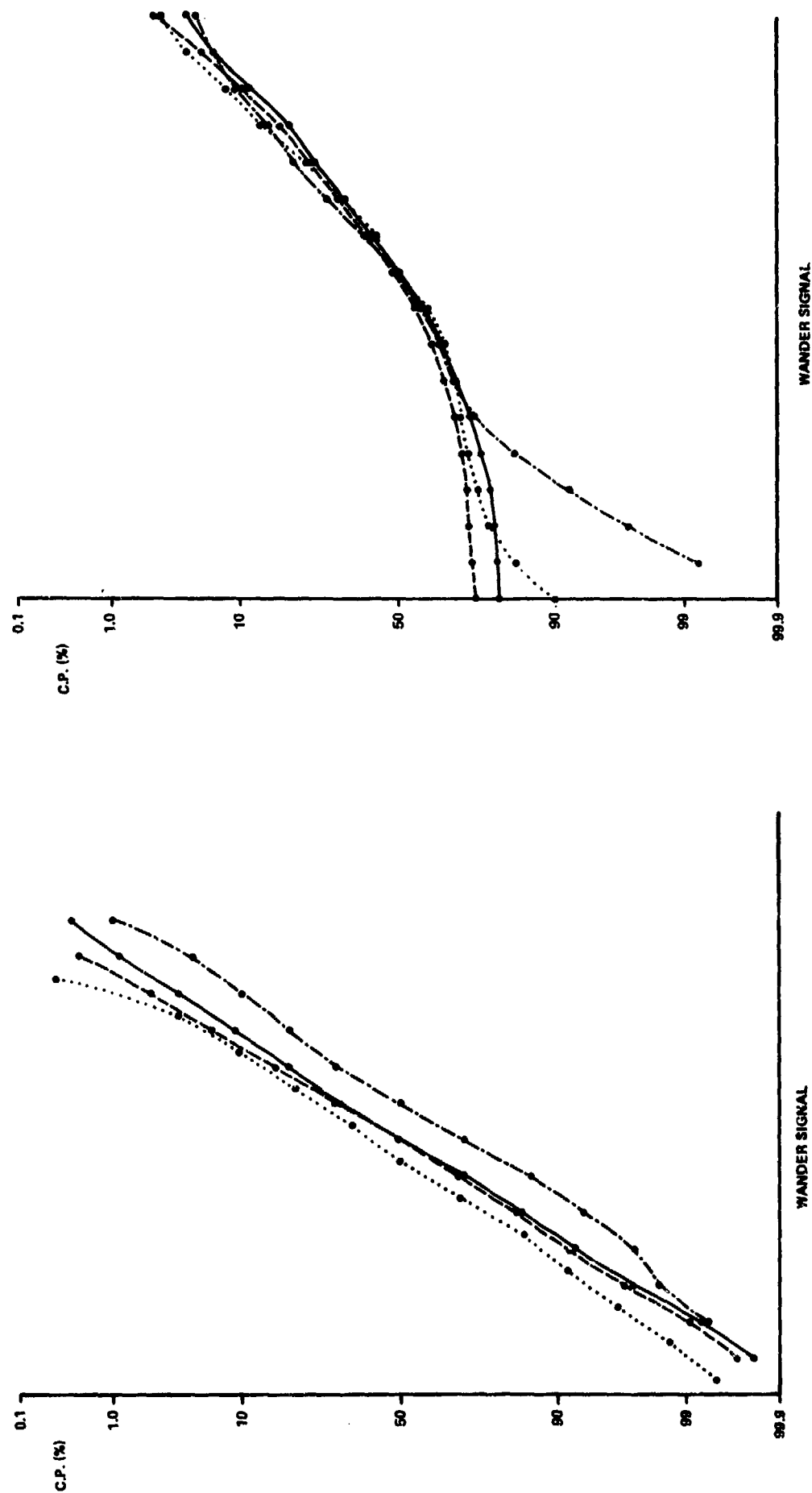


Fig. 18 Cumulative probability for wander signals for Fig. 17, for various high-pass cutoff frequencies. The inverse cutoff frequencies in seconds are 0.01 (—), 0.017 (·····), 0.05 (---), and 0.1 (-·-·-).

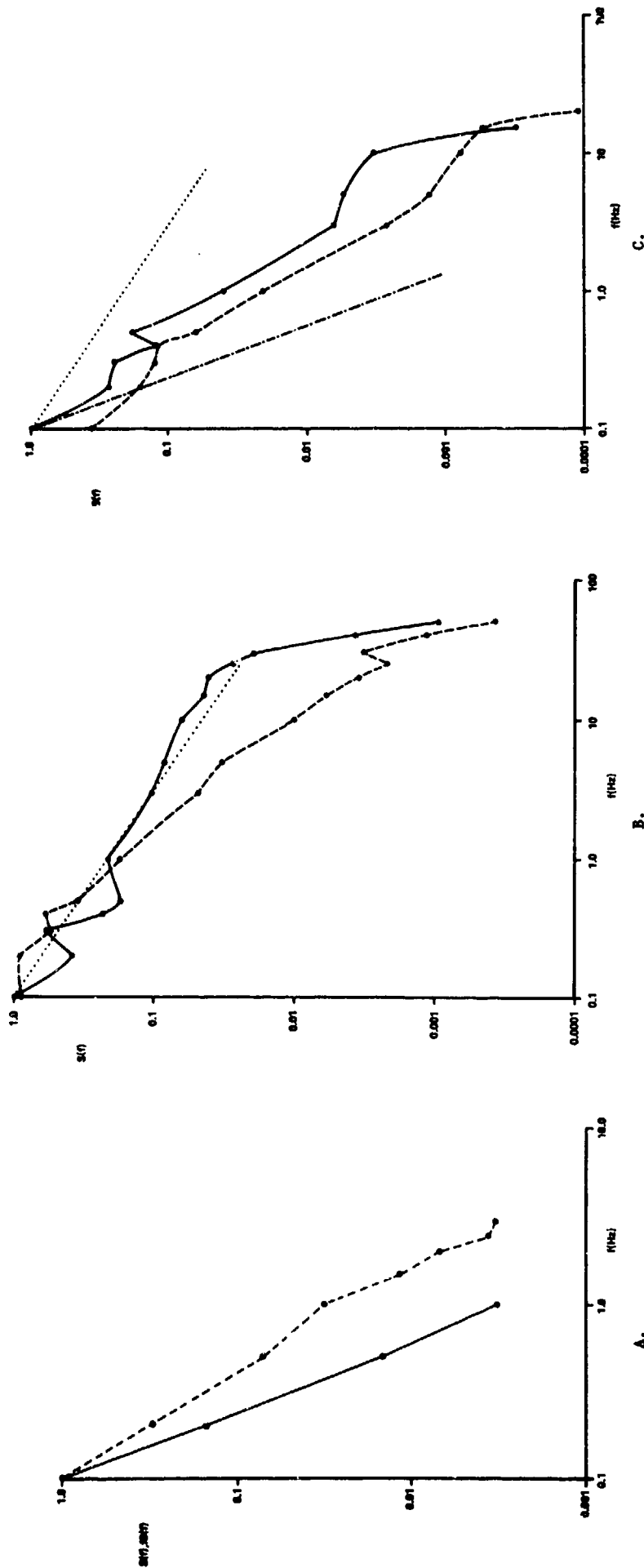
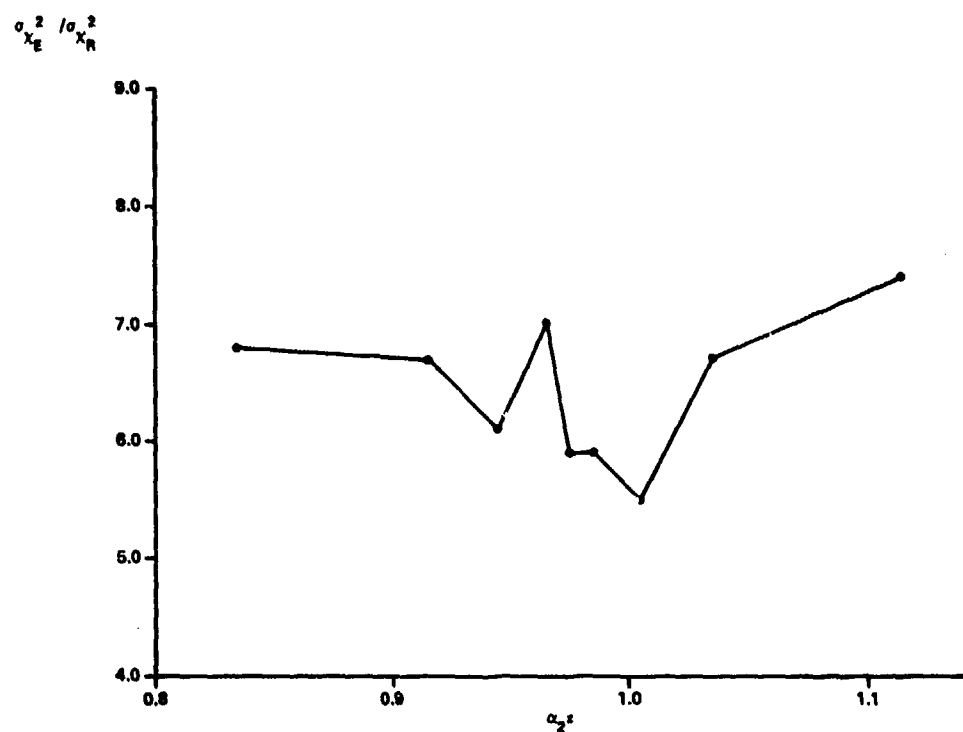
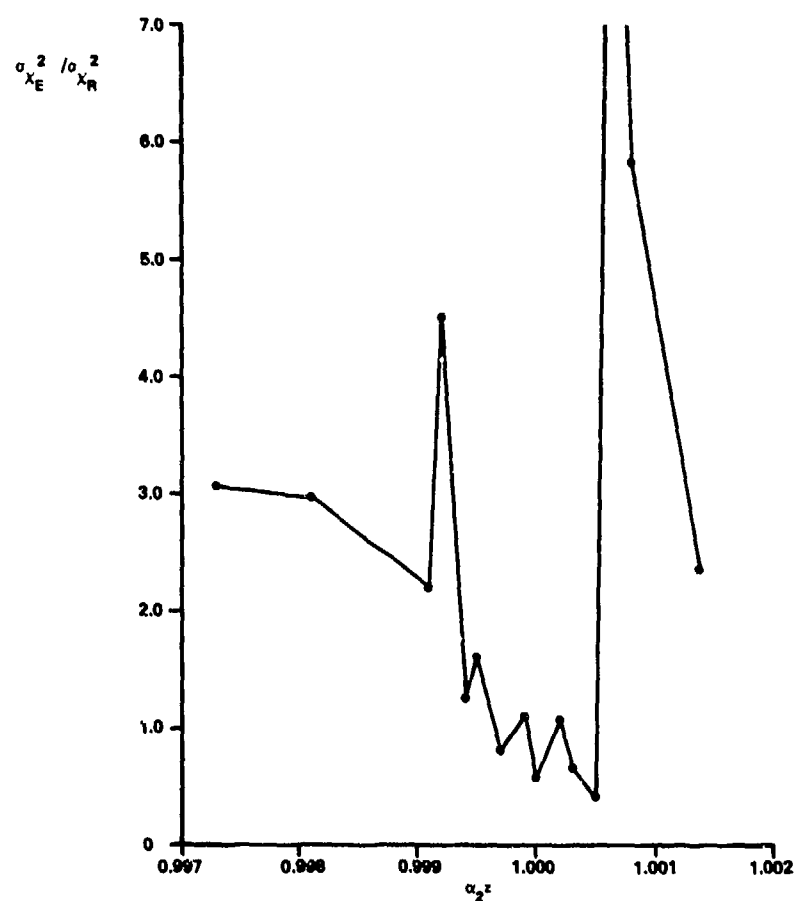


Fig.19 Power spectra $S(f)$ for vander signals.
 A. Spectrum (—) and frequency-weighted spectrum (---) for horizontal signal of Figure 17a.
 B. Spectrum of horizontal (—) and vertical (---) vander signals for significant horizontal wind. (....) indicates an $f^{-2/3}$ dependency.
 C. Spectrum of horizontal (—) and vertical (---) vander signals for low wind speed, exhibiting slopes intermediate to the values $-2/3$ (.....) and $-8/3$ (---).

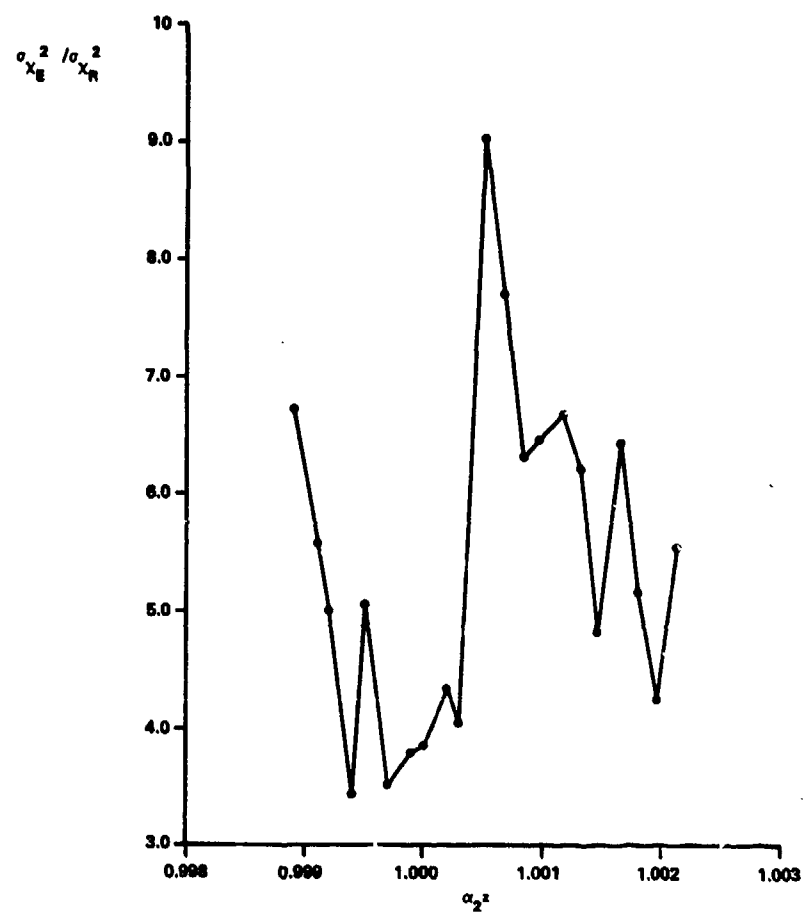


A. $D/\rho_0 = 3.5$.



B. $D/\rho_0 = 2.6$.

Fig.20 Experimental log amplitude variances ($\sigma_{X_E}^2$) normalized by the first-order theoretical values for a point source ($\sigma_{X_R}^2$), vs. focus condition $\alpha_2 z = z/R$ (Ref. 8).



C. $D/\rho_0 = 0.80$.

Fig.20 (Concluded)

PROPAGATION OF FOCUSED LASER BEAMS IN THE TURBULENT ATMOSPHERE

M. Raidt
Forschungsinstitut für Optik
74 Tübingen 1, Schl. Kressbach
F.R. Germany

SUMMARY

Experimental results from investigations of instantaneous intensity distributions in focused laser beams at $0.63 \mu\text{m}$ and $10.6 \mu\text{m}$ at distances of approximately 1.3 km, 5 km and 8.6 km are presented and discussed. At $0.63 \mu\text{m}$ the beam pattern is broken up into several diffraction-scale spots because focusing is saturated, except for weak turbulence and short propagation distance. At $10.6 \mu\text{m}$ the beam pattern is almost uniform, as long as the beam dimensions are smaller than the correlation length of the amplitude.

1. INTRODUCTION

With many military applications of lasers focused beams are used. In this context the laser beam intensity distribution on the focal plane is of great importance, especially the instantaneous one in the case of pulse lasers, which is mainly affected by atmospheric turbulence. When the laser beam interacts with the atmospheric refractive inhomogeneities, this results in coherence degradation, intensity fluctuations, beam wander, beam breathing and consequently beam spread (Höhn, D.H., H. Raidt, and K.W. Gruner, 1973; Yura, H.T., 1973). The irradiance distribution in the focal plane is characteristic of a coherent aperture given by the smaller of the diameters of the transmitter aperture $2a$ or the lateral coherence length of a spherical wave, p_c . Another parameter contributing to the irradiance distribution at large distances might be the lateral correlation length L_c of the amplitude (Yura, H.T., 1973, 1971; Lutomirski, R.F., 1971).

Experiments on an instantaneous intensity distribution at $L = 1.3 \text{ km}$, 5.05 km and 8.6 km will be described for $\lambda = 0.63 \mu\text{m}$ (HeNe) and $10.6 \mu\text{m}$ (CO_2). The results are presented and discussed with respect to some theoretical relations. Basically the findings are in accordance with similar observations of others (Yura, H.T., 1973; Kerr, J.R., and J.R. Dunphy, 1973).

2. EXPERIMENTAL SETUP

The experimental setup is schematically shown in Fig. 1. The transmitter system already described elsewhere (Raidt, H., and D.H. Höhn, 1975), consists of two lasers and an inverted cassegrainian presenting collinear diffraction-limited focused TEM_{00} laser beams at 6328 Å and $10.6 \mu\text{m}$. They are focused onto the receiver planes at $L = 3 \text{ km}$, 5.05 km , and 8.6 km .

The parameters of this system are summarized in Table 1.

At the receiver stations the laser beam patterns were registered using TV-techniques. The HeNe-pattern was observed by means of a TV-camera with Si-vidicon, the CO_2 -pattern by means of one with a pyroelectric vidicon (Heimann, Wiesbaden) and - at $L = 1.3 \text{ km}$ - a sandblasted Al-plate as reflector for $\lambda = 10.6 \mu\text{m}$. In default of

HeNe - Laser Inverted telescope	6328 Å; 15 mW; TEM ₀₀ ; 1.1 mm Ø $f_2/f_1 = 6.64$; 7.3 mm Ø		
CO ₂ - Laser	10.6 μm; 50 W; TEM ₀₀ ; 6.9 mm Ø		
Cassegrainian	20 mm Ø; $f_1 = 35$ mm, 50 mm, or 150 mm 500 mm Ø; $f_2 = 2500$ mm 20 mm Ø bore $f_2/f_1 = 71.4, 50, \text{ and } 16.6$ resp.		
beam diameter at the output mirror	6328 Å: 521 mm, 365 mm, and 121 mm resp. 10.6 μm: 493 mm, 345 mm, and 115 mm resp.		
distance L	1.3 km, 5.05 km, and 8.6 km		
diffraction - limited focused beam diameters at the distances L using the above mentioned output beam diameters	L	$\lambda = 6328 \text{ Å}$	$\lambda = 10.6 \text{ μm}$
	1.3 km	2 mm	35 mm
		3 mm	51 mm
		9 mm	153 mm
	5.05 km	8 mm	140 mm
		11 mm	198 mm
		34 mm	593 mm
	8.6 km	13 mm	235 mm
		19 mm	336 mm
		57 mm	1010 mm

Table 1: Parameters of the transmitter system.

sufficient intensity, at L = 5.05 km and 8.6 km the CO₂ - pattern was imaged from a spherical mirror onto the vidicon by the camera lens, acting as a field lens.

An exposure time of 4 ms proved to be suitable to record "instantaneous" intensity patterns, regarding the effects of atmospheric turbulence (Hahn, D.H., H.Raidt, and K.W.Grüner, 1973; Yura, H.T., 1973; Raidt, H., and D.H.Hahn, 1975).

Along the 5.05 km propagation range the intensity fluctuations in another, collimated HeNe-laser beam were measured. From their variance characteristic, mean structure constant values \overline{C}_n of the atmospheric refractive index fluctuations were calculated. In this way \overline{C}_n values indicating median turbulence were obtained (Hahn, D.H., 1969).

The measurements at L = 1.3 km and 8.6 km were also performed at median turbulence. This fact could be concluded from the observation of the general weather situations and the focused laser beams themselves.

3. RESULTS

3.1 Theoretical Relations

Atmospheric turbulence is producing beam spreading that may result in a saturation of focusing under certain conditions (Hahn, D.H., H.Raidt, and K.W.Grüner, 1973; Yura, H.T., 1971, 1973; Lutomirski, R.F., 1971; Raidt, H., and D.H.Hahn, 1975). One has to distinguish between short-term average (equivalent to "instantaneous" in this context) and long-term average turbulence-induced optical-beam spread (Yura, H.T., 1973). The focused beam diameter $2\rho_{Af}(L, \overline{C}_n)$ can be described by the relation

$$\rho_{Af}^2(L, \overline{C}_n) = \rho_{of}^2(L) + \rho_{Tf}^2(L, \overline{C}_n). \quad (1)$$

Herein $\rho_{of}(L) = \lambda L / \pi a_o$ is the free space diffraction-limited focused beam radius (exp-2 transmitter aperture radius a_o with TEM_{00}), and $\rho_{Tf}(L, \overline{C}_n) \approx 2L/k\rho_c$ is the turbulence induced beam spread, which is only weakly wavelength dependent (Hahn, D.H. et al., 1973; Yura, H.T., 1973; Varvatsis, A.D. et al., 1971).

$\rho_c(L, \overline{C}_n)$ being either the short-term or the long-term lateral coherence length of a spherical wave can be used to describe this spreading. The short-term lateral coherence length $\rho_c^{ST}(L, \overline{C}_n)$ is always greater than the corresponding long-term lateral coherence length $\rho_c^{LT}(L, \overline{C}_n)$, but they become approximately equal in the far field of the effective coherent transmitter aperture (Yura, H.T., 1973). Therefore the long-term values ρ_c^{LT} calculated by (Lutomirski, R.F., 1971) for median turbulence can be used at least for the interpretation of the experiments presented in this context.

Focusing is saturated if

$$W = \frac{\rho_{of}(L)}{\rho_{Tf}(L, \overline{C}_n)} \sim \frac{\rho_c(L, \overline{C}_n)}{a_o} \ll 1. \quad (2)$$

distance L [km]	beam diam. $2a_o$ at output mirror, approx. [m]	$W = \frac{\rho_{of}(L)}{\rho_{Tf}(L, \overline{C}_n)} \sim \frac{\rho_c(L, \overline{C}_n)}{a_o}$	
		$\lambda = 0.63 \mu m$	$\lambda = 10.6 \mu m$
1.3	0.5	0.03	1
	0.3	0.05	1.6
	0.1	0.15	4.8
5.05	0.5	0.01	0.4
	0.3	0.02	0.7
	0.1	0.06	2
8.6	0.5	< 0.01	0.1
	0.3	< 0.02	0.5
	0.1	0.04	1.5

Table 2: Values $W \sim \rho_c(L, \overline{C}_n)/a_o$ for the experiments described above, s. Table 1, at $\lambda = 0.63 \mu m$ and $\lambda = 10.6 \mu m$, for median turbulence, using characteristic values $2a_o$.

In Table 2 this relation is calculated for the experiments described above (s. Table 1). The figures presented there show that at $\lambda = 0.63 \mu\text{m}$ focusing saturation can be expected for all distances L and transmitter apertures $2a_0$ used, except for $L = 1.3 \text{ km}$ and $2a_0 = 10 \text{ cm}$. At $\lambda = 10.6 \mu\text{m}$, focusing will not at all be saturated. If the beam pattern diameter exceeds the corresponding correlation length $L_c \approx \sqrt{\lambda L}$ of turbulence induced intensity fluctuations without focusing, there will exist intensity variations in the pattern due to L_c .

3.2 $\lambda = 0.63 \mu\text{m}$

In Figures 2, 3, and 4 examples for instantaneous intensity distributions for $0.63 \mu\text{m}$ at the distances $L = 1.3 \text{ km}$, 5.05 km , and 8.6 km with three transmitter apertures $2a_0 \approx 50 \text{ cm}$, 30 cm , and 10 cm are shown (actual values see Table 1).

At the shortest distance $L = 1.3 \text{ km}$ and the transmitter apertures $2a_0 = 50 \text{ cm}$ and 30 cm (Figures 2a,b), the beam pattern is broken up into several patches. The beam spreading is considerable, i.e. $\rho_{Af} \gg \rho_{of}$; focusing is saturated. This effect diminishes with decreasing transmitter aperture $2a_0$ and already for $2a_0 = 10 \text{ cm}$ (Fig. 2c) there appears an almost diffraction-limited, i.e. $\rho_{Af} \approx 1.5 \rho_{of}$, and smooth beam pattern. As predicted in Table 2 focusing is not saturated. This observation for $2a_0 = 10 \text{ cm}$ concurs with the suggestion of (Yura, H.T., 1973), that in the near field of the effective coherent transmitter aperture the beam does not break up into multiple blobs as in the far field. The distance $L = 1.3 \text{ km}$ lies in the transition region between near and far field, i.e. $L \sim k \rho_c^2$, with $k = 2\pi/\lambda$. In addition also the aperture diameter $2a_0$ influences the focusing behaviour of the laser beam in the near field as demonstrated in Figures 2a, b. In accordance with Table 2, focusing saturation becomes more pronounced with the longer distances $L = 5.05 \text{ km}$ and 8.6 km for all transmitter apertures $2a_0$ (Figures 3,4). This can be explained by the decrease of the lateral coherence length $\rho_c(L, \bar{C}_n)$ with increasing distance L . The values $W = \rho_c(L, \bar{C}_n)/a_0$ become smaller, the focal plane then also being in the far field of the effective coherent transmitter aperture. As demonstrated for $L = 5.05 \text{ km}$ in (Raidt, H., and D.H. Hahn, 1975) the characteristic size of the patches in the focusing saturated beam is approximately equal to the transmitter diffraction-limited spot size $2\rho_{of}$.

3.3 $\lambda = 10.6 \mu\text{m}$

For $10.6 \mu\text{m}$ at $L = 1.3 \text{ km}$, in contradiction to $0.63 \mu\text{m}$, for all transmitter apertures $2a_0 \approx 50 \text{ cm}$, 30 cm , and 10 cm (actual values see Table 1) the beam pattern is almost uniform as can be seen in Fig. 5. Beam spreading is small, i.e. $\rho_{Af} \approx \rho_{of}$; focusing is not saturated as indicated in Table 2 and also the focal plane is in the near field of the effective coherent transmitter aperture. This proves true also for the longer distances $L = 5.05 \text{ km}$ and 8.6 km . In spite of a focusing - unsaturated CO_2 -laser beam at these distances, which should provide smooth intensity distribution, intensity fluctuations in the beam pattern can be observed for $2a_0 = 10 \text{ cm}$. This fact is demonstrated in Figures 6 and 7. At $L = 8.6 \text{ km}$ the beam pattern seems already to break up for $2a_0 = 30 \text{ cm}$. These intensity fluctuations in the unsaturated focused laser beam are due to the correlation length $L_c \approx \sqrt{\lambda L}$ of the amplitude. Whereas for $2a_0 = 50 \text{ cm}$ and 30 cm the beam diameter is smaller than the correlation length, i.e. $2\rho_{Af} \approx 2\rho_{of} < L_c$, it exceeds the correlation length for $2a_0 = 10 \text{ cm}$, i.e. $2\rho_{Af} \approx 2\rho_{of} > L_c$.

As can be seen from Table 2 and (Lutomirski, R.F., 1971) focusing saturation will occur at larger distances also for the CO_2 - laser beam.

4. CONCLUSIONS

1) Focusing saturation increases with increasing propagation distance L . In the near field of the effective coherent transmitter aperture, $L < k \rho_c^2$, focusing is not saturated for transmitter aperture diameters $2a_0$ even if they are larger than the lateral coherence length, $2a_0 > \rho_c(L, \overline{C}_n)$, but focusing is saturated in the near field too if $2a_0 \gg \rho_c(L, \overline{C}_n)$.

2) If focusing is unsaturated by turbulence, i.e. $\rho_{Af} \sim \rho_{of}$, smooth instantaneous intensity patterns will occur as long as the correlation length L_c is greater than the beam diameter, i.e. $2\rho_{Af} \sim 2\rho_{of} < L_c$. For $2\rho_{Af} > L_c$ the beam will be splitted due to L_c .

If focusing is saturated, i.e. $\rho_{Af} > \rho_{of}$, the beam breaks up into approximately transmitter ($2a_0$) diffraction-limited spots.

3) These effects can plastically be explained by the interaction of beams with atmospheric refractive index inhomogeneities. Turbulent eddies having dimensions greater than the beam diameter lead to refractive effects. The entire beam is quivering around its unperturbed position. This occurs with unsaturated focused laser beams. In the case of focusing saturation, the beam interacts with eddies smaller than the beam diameter and therefore it is splitted into several independently quivering elements, leading to considerable beam spreading.

ACKNOWLEDGMENTS

The author would like to express his gratitude to D.H.Höhn for valuable discussions and to A.Jetter for his technical assistance in the field experiments.

REFERENCES

- Höhn, D.H.; H.Raidt, and K.W.Grüner, 1973, Atmospheric Transmission of Focused Laser Beams (at 6328 Å and 10.6 μm), Report FfO 1973/62, Tübingen, and NATO Laser Seminar Report, Ottawa, Sept.1973.
- Höhn, D.H., 1969, Zur Ausbreitung eines Laserstrahls in der Atmosphäre, Optik, Vol.30, 161 and 239.
- Kerr, J.R., and J.R.Dunphy, 1973, Experimental Effects of Finite Transmitter Apertures on Scintillations, J.Opt.Soc.Am., Vol.63, 1.
- Lutomirski, R.F., 1971, Propagation of a Focused Laser Beam in a Turbulent Atmosphere, US-Report to ARPA, Order No. 189-1 (1971).
- Raidt, H., and D.H.Höhn, 1975, Instantaneous Intensity Distribution in a Focused Laser Beam at 0.63 μm and 10.6 μm Propagating Through the Atmosphere, to be published in Applied Optics 1975 or 1976.
- Varvatsis, A.D., and M.I.Sancer, 1971, Expansion of a Focused Laser Beam in the Turbulent Atmosphere, Can.J.Phys., Vol.49, 1233.
- Yura, H.R., 1971, Atmospheric Turbulence Induced Laser Beam Spread, Appl.Opt., Vol.10, 2771.
- Yura, H.T., 1973, Short-Term Average Optical-Beam Spread in a Turbulent Medium, J.Opt.Soc.Am., Vol.63, 567.

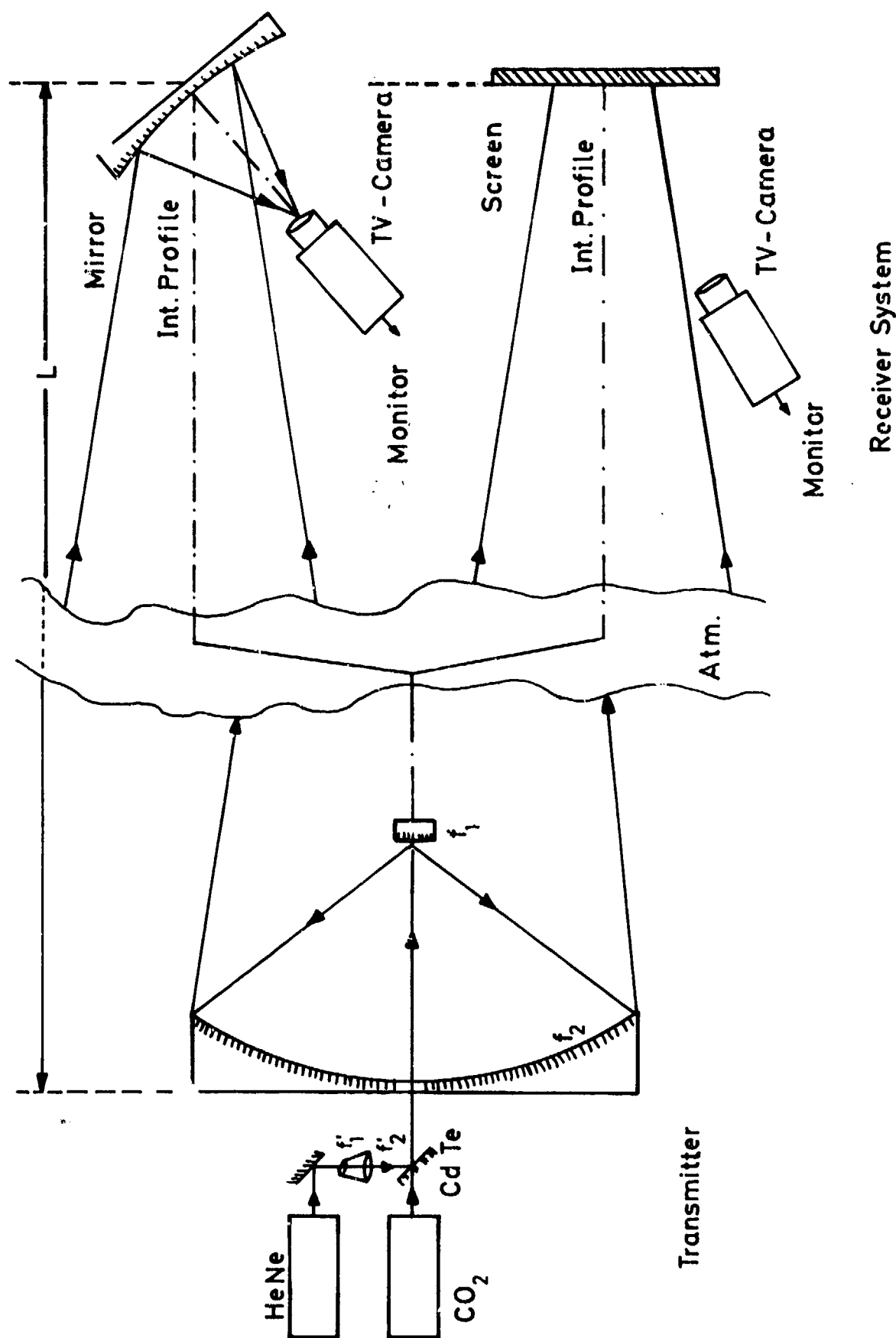


Fig.1 : Schematic experimental setup for investigation of atmospheric propagation of focused laser beams at 0.63 μm and 10.6 μm .

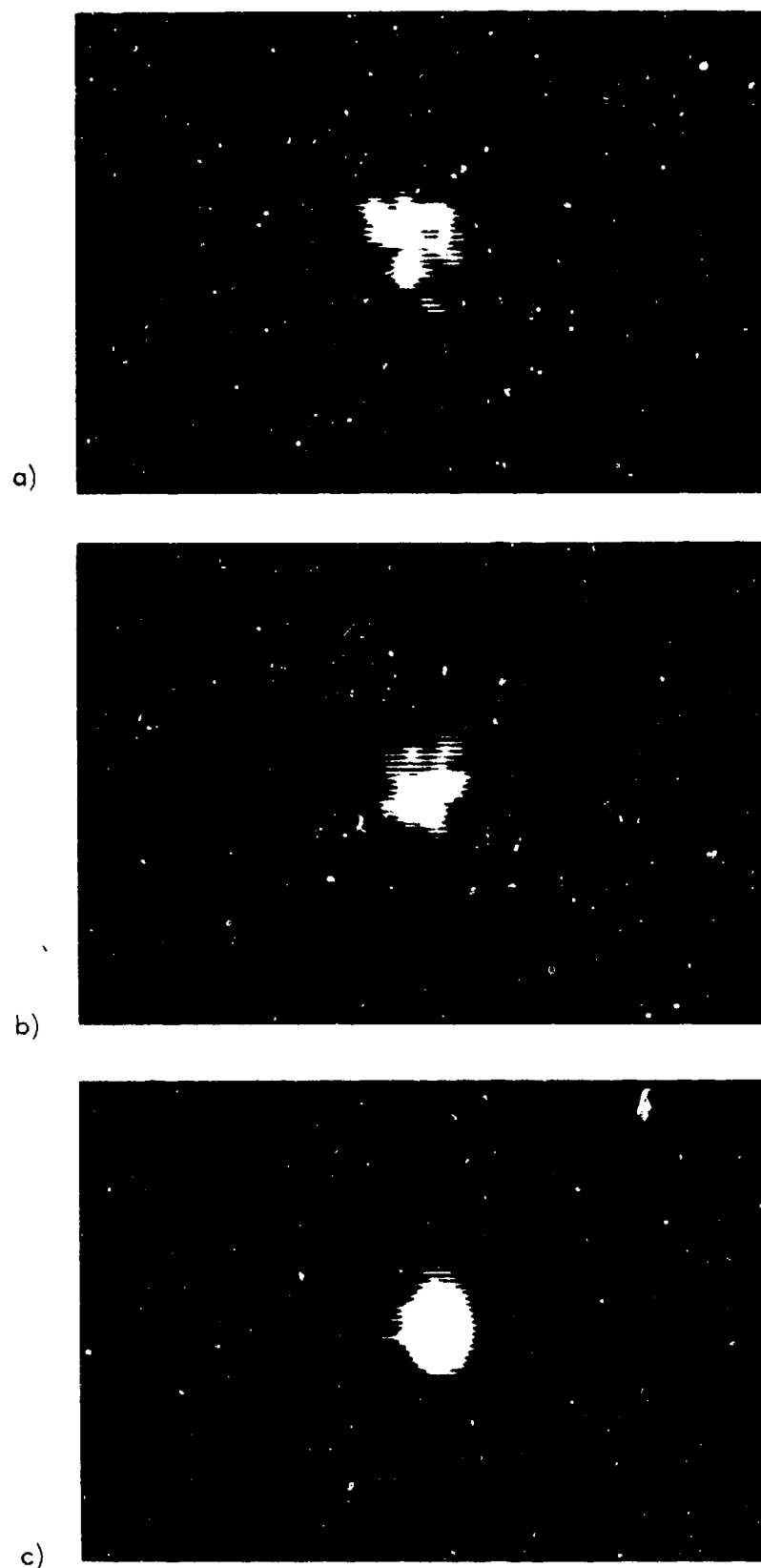


Fig.2: Instantaneous intensity distribution of focused laser beams at $0.63 \mu\text{m}$.
 Measuring conditions: $L = 1.3 \text{ km}$; $\Delta t = 4 \text{ ms}$; median turbulence.
 a) $2a_0 \approx 50 \text{ cm}$; $2a_0 \approx 30 \text{ cm}$; c) $2a_0 \approx 10 \text{ cm}$;
 scale: dash $\cong 5 \text{ cm}$.

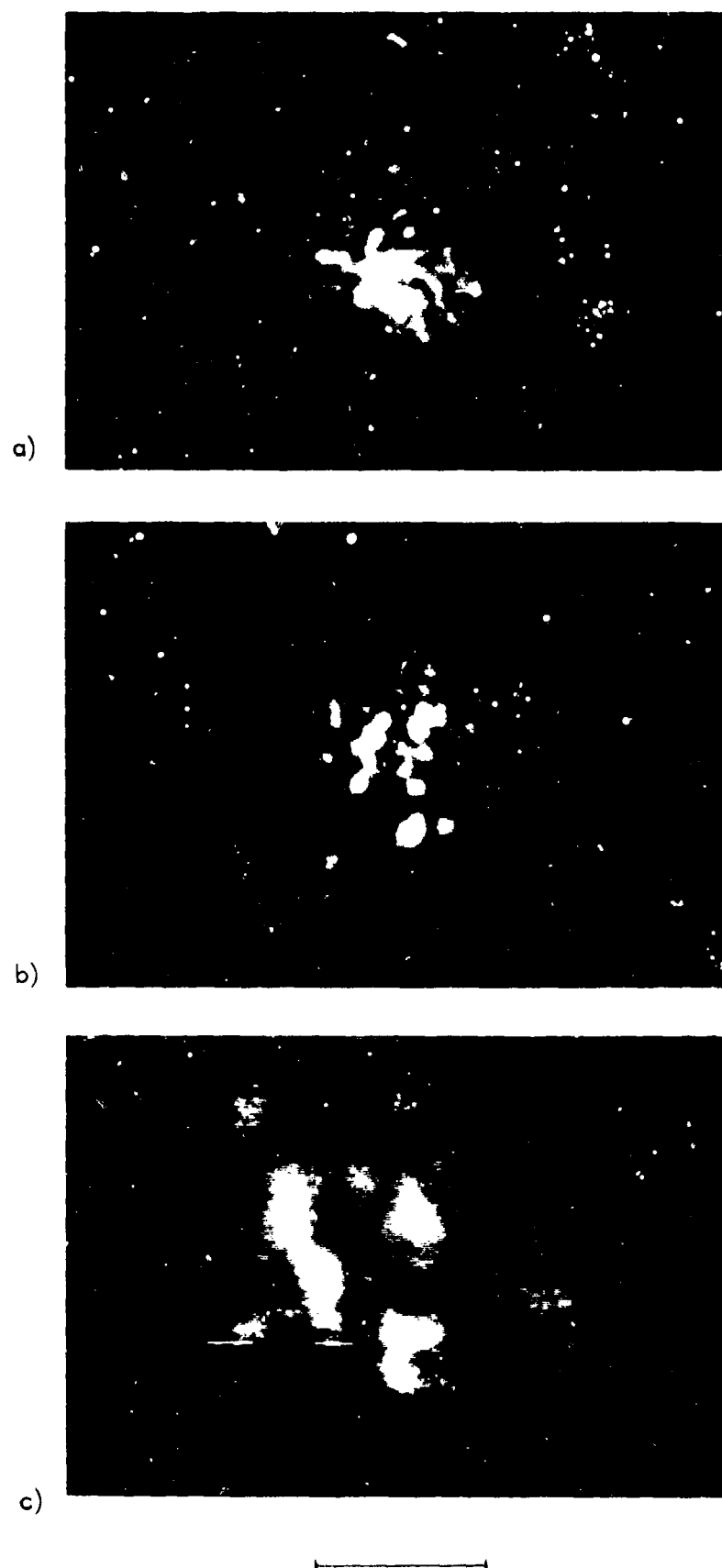


Fig.3: Instantaneous intensity distribution of focused laser beams at $0.63 \mu\text{m}$.
 Measuring conditions: $L = 5.05 \text{ km}$; $\Delta t = 4 \text{ ms}$; median turbulence.
 a) $2a_0 \approx 50 \text{ cm}$; b) $2a_0 \approx 30 \text{ cm}$; c) $2a_0 \approx 10 \text{ cm}$;
 scale: dash $\approx 20 \text{ cm}$.

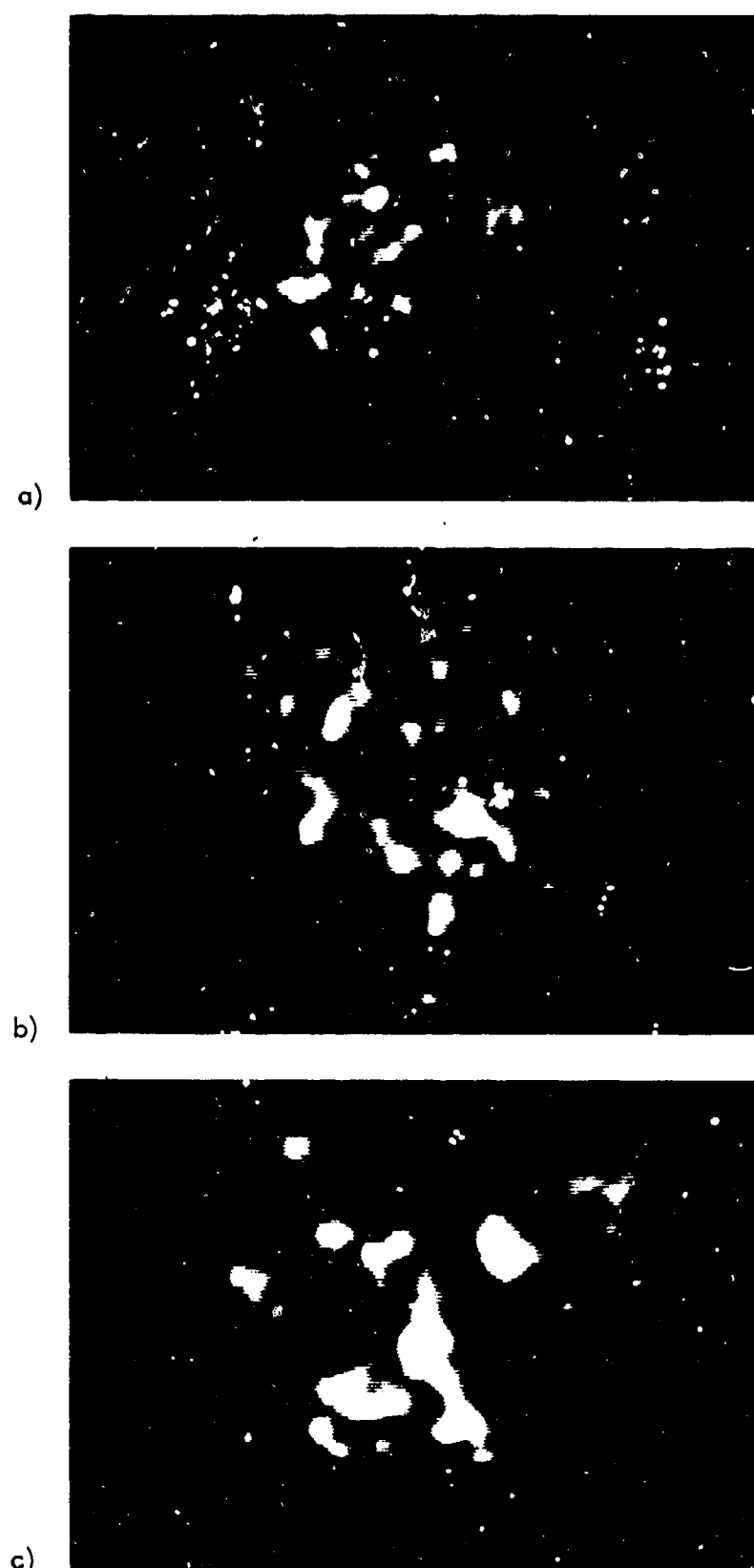


Fig.4: Instantaneous intensity distribution of focused laser beams at $0.63 \mu\text{m}$.
 Measuring conditions: $L = 8.6 \text{ km}$; $\Delta t = 4 \text{ ms}$; median turbulence.
 a) $2a_0 \approx 50 \text{ cm}$; b) $2a_0 \approx 30 \text{ cm}$; c) $2a_0 \approx 10 \text{ cm}$;
 scale: dash $\cong 20 \text{ cm}$.

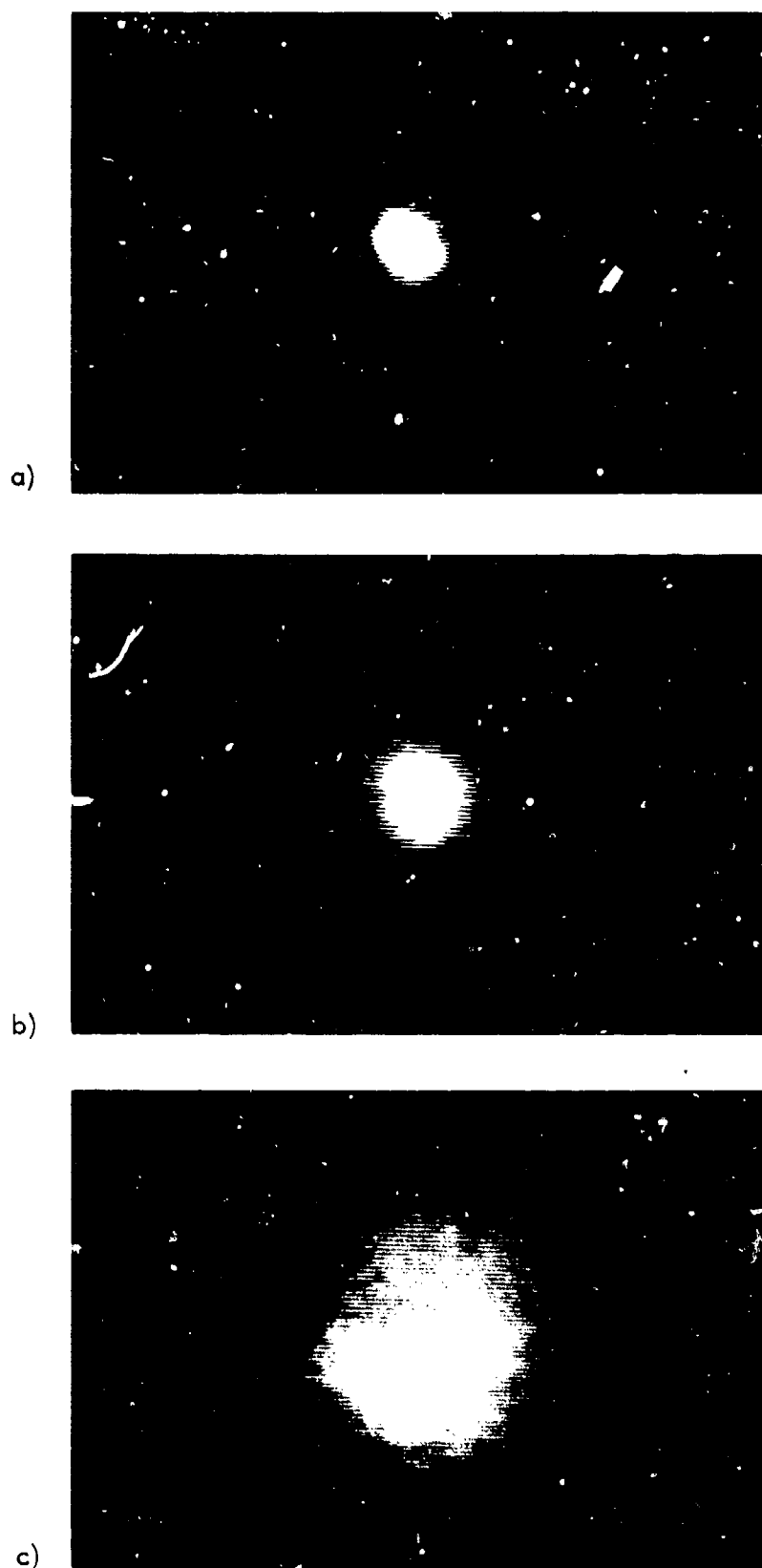


Fig.5: Instantaneous intensity distribution of focused laser beams at $10.6\ \mu\text{m}$.
 Measuring conditions: $L = 1.3\ \text{km}$; $\Delta t = 4\ \text{ms}$; median turbulence.
 a) $2a_0 \approx 50\ \text{cm}$; b) $2a_0 \approx 30\ \text{cm}$; c) $2a_0 \approx 10\ \text{cm}$;
 scale: dash $\triangleq 10\ \text{cm}$.

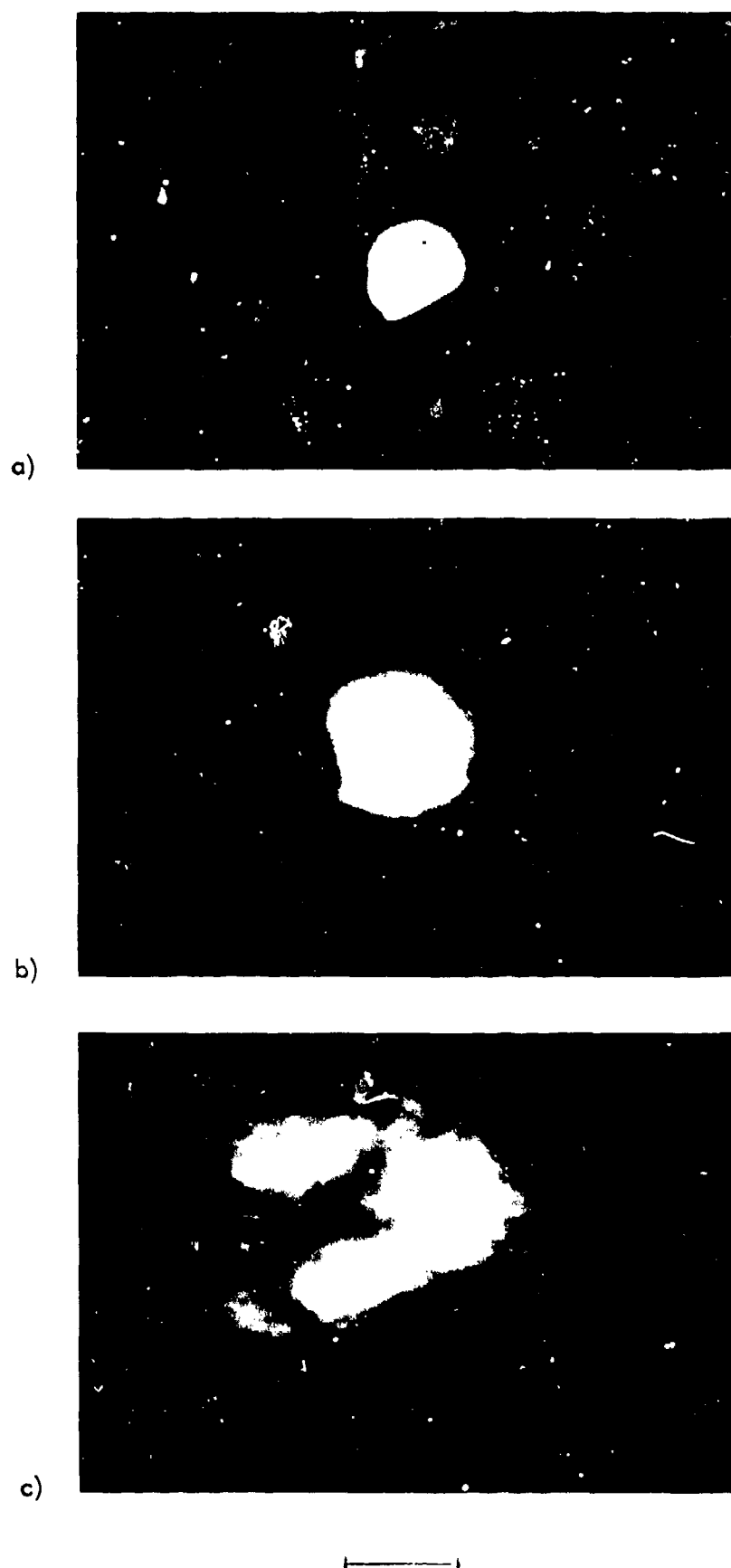


Fig. 6: Instantaneous intensity distribution of focused laser beams at $10.6 \mu\text{m}$.
 Measuring conditions: $L = 5.05 \text{ km}$; $\Delta t = 4 \text{ ms}$; median turbulence.
 a) $2a_0 \approx 50 \text{ cm}$; b) $2a_0 \approx 30 \text{ cm}$; c) $2a_0 \approx 10 \text{ cm}$;
 scale: dash $\approx 20 \text{ cm}$.

a) the small shadow in the spot is caused by the TV-monitor.

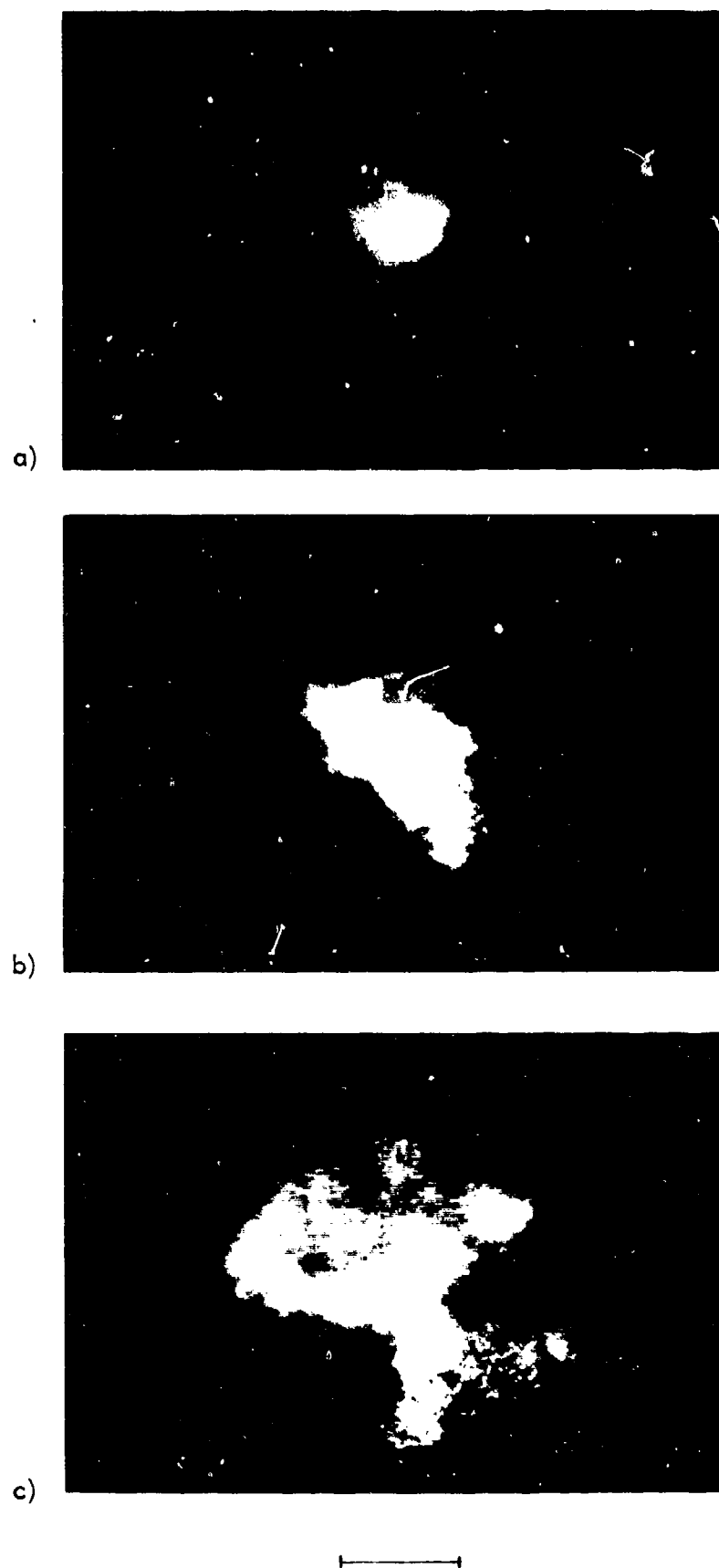


Fig.7: Instantaneous intensity distribution of focused laser beams at $10.6 \mu\text{m}$.
 Measuring conditions: $L = 8.6 \text{ km}$; $\Delta t = 4 \text{ ms}$; median turbulence.
 a) $2a_0 \approx 50 \text{ cm}$; b) $2a_0 \approx 30 \text{ cm}$; c) $2a_0 \approx 10 \text{ cm}$;
 scale: dash $\cong 20 \text{ cm}$.

PROPAGATION OF FOCUSED TRUNCATED LASER BEAMS IN THE ATMOSPHERE

R. F. Lutomirski
Pacific-Sierra Research Corporation
Santa Monica, California

SUMMARY

In this paper, a formula is derived for the mean intensity distribution from a finite beam in terms of the complex disturbance in the aperture and the mutual coherence function (MCF) for a spherical wave in the medium. The formula is used to examine the effects of turbulence on the long-term average intensity produced by a focused, truncated gaussian aperture distribution. In particular, it is shown that (a) while the vacuum focal point intensity will increase as the degree of truncation decreases for a given laser output power, the effect of turbulence limits this increase, and (b) the turbulence can virtually eliminate the vacuum advantage of visible over infrared wavelengths in focusing the beam at practical ranges. Transverse beam patterns and the on-axis intensity are shown for CO₂ wavelength, and a criterion is established for the condition under which the turbulence prevents effective focusing.

1. INTRODUCTION

The output of a laser, with a mirror system designed to keep diffraction losses small, can usually be approximated by a gaussian amplitude and uniform phase distribution (Risken, 1964) across a circular transmitting aperture.[†] Generally, to deliver maximum intensity to a specified receiver, the output beam will be focused onto the target, with the focusing optics truncating the gaussian. The complex field at the exit pupil of the transmitter for this configuration may be approximated by a truncated-gaussian amplitude distribution and quadratic phase distribution. In this paper, we calculate the mean intensity distribution in space, resulting from the above complex field in a transmitting aperture in the presence of a turbulent atmosphere.

Previous analyses for truncated distributions have been limited to vacuum calculations (Campbell and De Shazer, 1969; Kauffman, 1965). The atmospheric calculations have been treated (Schmeltzer, 1967; Ishimaru, 1969; Ho, 1970) by introducing the fluctuation in refractive index as a small parameter in the wave equation, and expanding the fields in powers of this same parameter. This procedure results in the field being expressed as a hierarchy of Born-type integrals over the vacuum fields existing at each point in space. Because of the extreme complexity of these integrals, the atmospheric calculations have been limited to non-truncated (possibly focused) gaussians, for which a closed-form solution exists for the vacuum fields. Even in this special case, because of the approximations necessary to manipulate the expressions, it is not difficult to show that none of the expressions contained in Schmeltzer (1967), Ishimaru (1969), or Ho (1970) conserve the long-term average irradiance over a plane normal to the direction of propagation, implying that even those solutions must be incorrect.

The present analysis is based on a proof developed in an earlier study (Lutomirski, 1970), which states that the Huygens-Fresnel principle^{††} can be extended to a medium exhibiting a spatial variation in refractive index. From this principle, the field due to a disturbance specified over an aperture can be computed by superimposing spherical wavelets radiating from all elements of the aperture. The mean intensity distribution is then found by first computing the intensity at a point from an arbitrary pair of elements in the aperture. Applying a reciprocity theorem (also proven in Lutomirski, 1970), and averaging, reveals that the above quantity is essentially the mutual coherence function (or MCF) for a spherical wave in the medium. The integration over the aperture is performed as a final step, resulting in a simple formula for the mean intensity pattern valid in both the Fresnel and Fraunhofer regions of the aperture. The development is outlined in Sec. 2.

In contrast with previous work, the properties of the medium (e.g., the turbulence parameters) appear only in the MCF of a spherical wave. The present calculation separates the geometry of the problem (i.e., the complex aperture distribution) from the propagation problem, which is determined by the manner in which a spherical wave propagates in the medium. The MCF describes the reduction in lateral coherence between different elements of the aperture, effectively transforming it into a partially coherent radiator, with the degree of coherence decreasing as the distance from the aperture increases. In Sec. 3, the general formula relating the MCF to the spectrum of index of refraction fluctuations for homogeneous isotropic turbulence is presented, and approximate formulas are given for the MCF at various propagation ranges for a modified Kolmogorov spectrum. A curve of normalized coherence length, ρ_0 , defined as the transverse separation at which the coherence is reduced to e^{-1} , versus normalized range, is also presented.

In Sec. 4, the case of a focused, truncated-gaussian field distribution is examined in detail. The general features of the vacuum pattern, with particular emphasis on the effect of truncation, are discussed first. For a fixed laser output power, a curve is presented showing the vacuum variation in focal-point intensity as a function of the degree of truncation. The curve shows, for example, that when the intensity at the circumference of the transmitting aperture is reduced to e^{-3} from the intensity at the center, the intensity at the focus is reduced to ≈ 85 percent of that corresponding to a uniform distribution (this latter distribution maximizes the vacuum gain). The effect of turbulence is shown to reduce this difference in all cases and, in fact, the distribution that maximizes the gain is no longer a uniform one. A criterion is also given for which no further increase in the on-axis intensity at a given range can be realized through focusing because of the turbulence. In a further example it is shown that for a 30-cm beam focused at 0.5 km, the effect of the turbulence is virtually to eliminate the vacuum advantage of visible over infrared wavelengths in focusing the beam.

[†]With confocal mirrors, the lowest-order mode is exactly gaussian.

^{††}See p. 370 of Born and Wolf, 1965.

In addition, beam patterns and the on-axis intensity are shown for CO₂ wavelength, for both a 30-cm and 1-m aperture, using turbulence parameters that are characteristic of paths of the order of a few meters above the ground.

The results are briefly summarized in Sec. 5, where it is argued that the spherical-wave MCF is the basic quantity to be measured for computing the degradation of an intensity pattern.

2. THE HUYGENS FORMULATION

It has been shown (Lutomirski, 1970) that for optical propagation in a weakly inhomogeneous, non-absorbing medium, the field at the observation point \underline{P} from a complex aperture disturbance $U_A(\underline{r}_1)$ can be written as

$$U(\underline{P}) = \frac{-ik}{2\pi} \int G(\underline{P}, \underline{r}_1) U_A(\underline{r}_1) d^2 \underline{r}_1 \quad (1)$$

where $k = 2\pi/\lambda$ is the wave number, \underline{r}_1 is a coordinate in the plane of the aperture, and the integration is carried out over the aperture. The term $G(\underline{P}, \underline{r}_1)$ is the field at point \underline{P} due to the spherical wave propagating in the medium from a delta function source at \underline{r}_1 . Equation (1) is valid for atmospheric optical propagation where the scattered field can be shown to vary slowly over a wavelength for all propagation distances of interest (e.g., $\sim 10^6$ km over horizontal paths), and for sufficiently small scattering angles where the obliquity factor (Born and Wolf, 1965) can be taken as $-1/\lambda$.

The intensity at the point \underline{P} is then given by

$$I(\underline{P}) = U(\underline{P})U^*(\underline{P}) = \left(\frac{k}{2\pi}\right)^2 \iint G(\underline{P}, \underline{r}_1) G^*(\underline{P}, \underline{r}_2) U_A(\underline{r}_1) U_A^*(\underline{r}_2) d^2 \underline{r}_1 d^2 \underline{r}_2 \quad (2)$$

It is shown in Lutomirski (1970) that in a refractive medium,[†] the complex field at \underline{P} due to a point source at \underline{r}_1 is identically equal to the field at \underline{r}_1 due to a point source at \underline{P} —i.e., reciprocity exists in the form $G(\underline{P}, \underline{r}_1) = G(\underline{r}_1, \underline{P})$. Hence, $G(\underline{P}, \underline{r}_1) G^*(\underline{P}, \underline{r}_2) = G(\underline{r}_1, \underline{P}) G^*(\underline{r}_2, \underline{P})$ is the field at \underline{r}_1 , multiplied by the complex conjugates of the field at \underline{r}_2 , due to a spherical-wave source at \underline{P} . The ensemble average (denoted by angular brackets)

$$\langle G(\underline{r}_1, \underline{P}) G^*(\underline{r}_2, \underline{P}) \rangle = \frac{ik \left[|\underline{r}_1 - \underline{P}| - |\underline{r}_2 - \underline{P}| \right]}{|\underline{r}_1 - \underline{P}| |\underline{r}_2 - \underline{P}|} M_S(\underline{r}_1, \underline{r}_2, \underline{P}) \quad (3)$$

is the cross correlation of the complex fields at the points $\underline{r}_1, \underline{r}_2$ due to a unit point source at \underline{P} . When the scattering angles are sufficiently small so that the aperture points $\underline{r}_1, \underline{r}_2$ can be considered as lying on the surface on a sphere centered at \underline{P} , then the function $M_S(\underline{r}_1, \underline{r}_2, \underline{P})$, defined by factoring out the vacuum fields in Eq. (3), is the MCF for a spherical wave.

If the vector \underline{p} is defined as the normal from the z-axis of symmetry to the observation point \underline{P} , then in the small-angle approximation

$$\frac{ik|\underline{r}_1 - \underline{P}|}{|\underline{r}_1 - \underline{P}|} = \frac{\exp \left\{ ik \left[z + \frac{(\underline{r}_1 - \underline{P})^2}{2z} \right] \right\}}{z} \quad (4)$$

Hence, we obtain from Eq. (2)

$$\langle I \rangle(\underline{p}, z) = \left(\frac{k}{2\pi z}\right)^2 \iint \exp \left\{ -\frac{ik}{2z} [2\underline{p} \cdot (\underline{r}_1 - \underline{r}_2) + r_1^2 - r_2^2] \right\} M_S(\underline{r}_1, \underline{r}_2, \underline{P}) U_A(\underline{r}_1) U_A^*(\underline{r}_2) d^2 \underline{r}_1 d^2 \underline{r}_2 \quad (5)$$

Changing variables in Eq. (5) to $\underline{p} = (\underline{r}_1 - \underline{r}_2)/2$, $\underline{r} = (\underline{r}_1 + \underline{r}_2)/2$, and restricting the analysis to the case of homogeneous isotropic turbulence where $M_S(\underline{r}_1, \underline{r}_2, z) = M_S(\underline{p}, z)$ (with $\underline{p} = |\underline{p}|$), yields

$$\langle I \rangle(\underline{p}, z) = \left(\frac{k}{2\pi z}\right)^2 \int d^2 \underline{p} M_S(\underline{p}, z) e^{-(ik/z) \underline{p} \cdot \underline{p}} \int U_A(\underline{r} + \frac{1}{2} \underline{p}) U_A^*(\underline{r} - \frac{1}{2} \underline{p}) e^{(ik/z) \underline{p} \cdot \underline{r}} d^2 \underline{r} \quad (6)$$

Equation (6) gives the mean spatial intensity distribution in both the Fresnel and Fraunhofer regions from an arbitrary complex disturbance in a finite aperture in the presence of a homogeneous, isotropic, turbulent medium. It should be noted that integration of Eq. (6) over the \underline{p} plane yields

$$\int \langle I \rangle d^2 \underline{p} = \int |U_A(\underline{r})|^2 d^2 \underline{r}$$

Hence, this development implies energy conservation for arbitrary aperture functions.

3. THE SPHERICAL-WAVE MCF

The long-term effect of the turbulence on the beam pattern enters through the spherical-wave MCF. Over a uniformly turbulent path, M_S is related to the spectrum of index of refraction fluctuations by the formula (Lutomirski and Yura, 1971)

[†]A more general theorem is proven by Rayleigh (1945)—see p. 380.

$$M_S(\rho, z) = \exp \left\{ -\frac{2z}{z_c} \left[1 - \frac{\int_0^\infty dK \Phi_n(K) \int_0^1 J_0(K\rho u) du}{\int_0^\infty \Phi_n(K) K dK} \right] \right\}, \quad (7)$$

where

$$z_c = \left[2\pi^2 k^2 \int_0^\infty \Phi_n(K) K dK \right]^{-1} \quad (8)$$

is the propagation distance at which the mean spherical-wave field is reduced to e^{-1} of the vacuum field.

A modified Kolmogorov spectrum has been used (Lutomirski and Yura, 1971) for the turbulence

$$\Phi_n(K) = \frac{0.033 C_n^2 e^{-(Kl_0)^2}}{(K^2 + L_0^{-2})^{11/6}} \quad (9)$$

where C_n is the index structure constant, and l_0 and L_0 are the inner and outer scales of turbulence, respectively.

In Fig. 1, a plot of z_c versus C_n^2 is shown for three values of C_n^2 roughly corresponding to weak ($3 \times 10^{-16} \text{ cm}^{-2/3}$), medium ($3 \times 10^{-15} \text{ cm}^{-2/3}$), and strong ($3 \times 10^{-14} \text{ cm}^{-2/3}$) turbulence. For horizontal propagation near the ground, we have used the nominal values $l_0 = 0.1 \text{ cm}$ and $L_0 = 100 \text{ cm}$. In the usual atmospheric case, $l_0 \ll L_0$, and the integral in Eq. (8) can be approximated to yield

$$z_c = (0.39 k^2 C_n^2 L_0^{5/3})^{-1} \quad (10)$$

The mean field-decay length, z_c , and hence the MCF, will depend strongly on the outer scale of turbulence.

Lutomirski and Yura (1971) show that there are three distinct propagation ranges for which approximate expressions exist for the MCF. The first is found by observing that for any z , M_S is a monotonically decreasing function of ρ with $M_S(0, z) = 1$ and $M_S(\infty, z) = \exp[-2z/z_c]$. Substituting Eq. (9) into Eq. (7), it can be seen that this asymptotic value is reached when $\rho \gg L_0$. Physically, when the separation is large compared with the distance over which the refractive index fluctuations (or temperature fluctuations) are correlated, L_0 , then

$$M_S(\rho, z) = \langle U(x_1, z) U(x_1 + \rho, z) \rangle = \langle U(x_1, z) \rangle \langle U(x_1 + \rho, z) \rangle = e^{-2z/z_c} \quad \rho \gg L_0$$

because the light reaching the points (x_1, z) , $(x_1 + \rho, z)$ has propagated through essentially statistically independent media. Hence we define

$$M_S^{(1)} \equiv M_S(\rho, z \ll z_c) = 1$$

To describe the remaining two regions, it is convenient to first characterize the MCF at a given range by the separation ρ_0 , for which $M_S(\rho_0, z) = e^{-1}$. Then the second region is found by observing that for $l_0 \ll \rho_0 \ll L_0$, the integrand in Eq. (7) can be expanded in powers of (ρ/L_0) to yield

$$M_S^{(2)}(\rho, z) = \exp \left\{ -0.55 k^2 C_n^2 z \rho^{5/3} \left[1 - 0.71 \left(\frac{\rho}{L_0} \right)^{1/3} \right] \right\} = \exp \left\{ -1.4 \left(\frac{z}{z_c} \right) \left(\frac{\rho}{L_0} \right)^{5/3} \left[1 - 0.71 \left(\frac{\rho}{L_0} \right)^{1/3} \right] \right\} \quad (11)$$

The expansion proves valid only when $M_S(l_0, z) = 1$ and $M_S(L_0, z) \ll 1$, which implies the range limitation

$$z_c \ll z \ll z_1$$

where

$$z_1 \equiv (0.39 k^2 C_n^2 L_0^{5/3})^{-1} = \left(\frac{L_0}{l_0} \right)^{5/3} z_c$$

For ranges greater than z_1 , $M_S(l_0, z) \ll 1$, and all of the ρ 's of interest are small compared with the inner scale. Then, for $\rho_0 \ll l_0$, the Bessel function in Eq. (7) can be expanded in powers of (ρ/l_0) to yield

$$M_S^{(3)}(\rho, z) = \exp[-k^2 \rho z \rho^2] = \exp \left[-0.80 \left(\frac{z}{z_1} \right) \left(\frac{\rho}{l_0} \right)^2 \right] \quad z \gg z_1 \quad (12)$$

where

$$q = (\pi^2/3) \int_0^{\infty} \Phi_n(K) K^3 dK = 0.56 C_n^2 k_0^{-1/3}.$$

Hence, for propagation paths that are short compared with z_1 , the MCF does not depend on the inner scale, and can be written as

$$M_S(\rho, z) = \exp \left\{ -\frac{2z}{z_c} \left[1 - \frac{5}{3} \left(\frac{\rho}{L_0} \right)^{5/3} \int_0^{\infty} du u J_0(u) \int_0^1 \frac{s^{5/3} ds}{\left[u^2 + \left(\frac{u\rho}{L_0} \right)^2 \right]^{11/6}} \right] \right\} \\ \equiv F\left(\frac{\rho}{L_0}, \frac{z}{z_c}\right) \quad 0 < z < z_1 \quad (13)$$

For the range $0 < z < z_1$ (for $L_0/k_0 = 10^3$, $z_1 = 10^5 z$), ρ_0/L_0 versus z/z_c , obtained by inverting the equation $F(\rho_0/L_0, z/z_c) = e^{-1}$, is plotted in Fig. 2. For ranges $z < z_c/2$, $M_S(\infty, z) > e^{-1}$, and the coherence length as defined here is infinite.

It is apparent that for ρ_0 much greater than the aperture diameter D , M_S in Eq. (6) can be replaced by unity, and the mean intensity is given by its vacuum value. When $\rho_0 \leq D$, the turbulence reduces the average irradiance on a target.

4. THE FOCUSED, TRUNCATED-GAUSSIAN DISTURBANCE

4.1 The Mean Intensity

The complex field in the aperture corresponding to a gaussian amplitude distribution with standard deviation a , focused at range f , and normalized to unit amplitude at the center of the aperture is

$$U_A(|\underline{x}_1|) = U_0 \exp \left[-\frac{1}{2} r_1^2 (a^{-2} + f^{-1}) \right] \quad |\underline{x}_1| \leq D/2 \\ = 0 \quad |\underline{x}_1| > D/2 \quad (14)$$

With U_A given by Eq. (14), the inner integral in Eq. (6) is the integration of the function

$$\exp \left[-a^{-2} \left(r^2 + \frac{1}{4} \rho^2 \right) + ik(z^{-1} - f^{-1}) \underline{\rho} \cdot \underline{x} \right]$$

over the area of overlap of two circles, each of diameter D , with centers relatively displaced at opposite ends of the vector $\underline{\rho}$. The integration is straightforward and yields for the inner integral $D^2 \Gamma_{\delta, \beta}(x)$, where

$$M_{\delta, \beta}(x) = \frac{4}{\pi} \frac{\delta^2}{1 - e^{-\delta^2}} e^{-2\delta^2 x^2} \int_0^{\cos^{-1}(x)} d\phi \int_{x/\cos\phi}^1 e^{-\delta^2(u^2 - 2ux \cos\phi)} \cos[2\beta x(u \cos\phi - x)] u du \quad x \leq 1 \\ = 0 \quad x > 1 \quad (15)$$

where $x = \rho/D$, $\delta = D/2a$, and $\beta = 1/4[kD^2(z^{-1} - f^{-1})]$. Then, using polar coordinates for the $\underline{\rho}$ integration, performing the angular integral, and changing variables from ρ to $x = \rho/D$, yields

$$\langle I \rangle(\alpha, z) = \frac{8W(kD^2)^2}{\pi D^2 (4z)} \int_0^1 x J_0(2\alpha x) M_S(Dx, z) M_{\delta, \beta}(x) dx \quad (16)$$

where J_0 is the zero-order Bessel function, and $\alpha = kDp/2z = kD/2 \tan \theta$, where θ is the angle that the direction to \underline{p} makes with the central direction.

4.2 The Vacuum Pattern and Effect of Truncation

In the limit of zero turbulence, $M_S = 1$, and Eq. (16) reproduces the vacuum intensity pattern. In this limit, it follows from the definition of β that the angular pattern in the focal plane ($z=f$) is identical with the Fraunhofer pattern for the unfocused case ($f=\infty, z=\infty$). Furthermore, because $M_{\delta, \beta}(x)$ is an even function of β , the angular vacuum patterns are identical in planes for which $|z^{-1} - f^{-1}|$ is constant.

For the limit $D \ll a$ ($\delta \rightarrow 0$), the problem reduces to the focusing of a plane wave diffracted by a circular aperture. No simple expression exists for the transverse vacuum intensity except in the focal plane, where the distribution is given by the Airy pattern

$$I_p(p, f) = \frac{1}{4} \left(\frac{kD^2}{4f} \right)^2 \left[\frac{2J_1(\alpha)}{\alpha} \right]^2 \quad \alpha = \frac{kDp}{2f} \quad (17)$$

The on-axis intensity is given by

$$I_p(0, z) = \frac{1}{4} \left(\frac{kD^2}{4z} \right)^2 \left(\frac{\sin \frac{\beta}{4}}{\frac{\beta}{4}} \right)^2, \quad (18)$$

which has an absolute maximum at the focal point. The on-axis nulls are located at

$$z = \frac{z}{1 \pm \frac{16\pi f}{kD^2}} \quad u = 1, 2, \dots$$

When $16\pi f/kD^2 > 1$, the only on-axis nulls lie between the transmitter and the focal plane; when $16\pi f/kD^2 < 1$, there are on-axis nulls beyond the focal plane. In the limit $16\pi f/kD^2 \ll 1$, the nulls--indeed the whole pattern--are symmetric about the focal plane for ranges $|(z-f)/f| \ll 1$.

In the limit $D \gg a$ (or $\delta \rightarrow \infty$), when the aperture does not effectively truncate the gaussian, the vacuum pattern propagates as a gaussian in all transverse planes according to the equation

$$I_s(p, z) = \frac{1}{w^2} e^{-p^2/a^2 w^2} \quad (19)$$

where

$$w^2 = \left(1 - \frac{z}{f}\right)^2 + \left(\frac{z}{ka^2}\right)^2$$

The maximum intensity in this case does not occur at the focal point, but rather on the axis at the shorter range $z = f/[1+(f/ka^2)]$, where the intensity is $1 + (ka^2/f)^2$. Generally, in order to focus the laser beam effectively, the focal length should be much less than the smaller of ka^2 , kD^2 , in which case the intensity at the focal point is approximately the smaller of $(ka^2/f)^2$, $1/4(kD^2/f)^2$.

For the case of arbitrary truncation, the on-axis intensity can be shown to be

$$I(0, z) = \frac{4W}{\pi D^2} \frac{\delta^2}{1-e^{-\delta^2}} \left(\frac{kD^2}{4z} \right)^2 \frac{(1-e^{-\delta^2/2})^2 + 4e^{-\delta^2/2} \sin^2 \frac{\beta}{4}}{\delta^4 + \beta^2} \quad (20)$$

with no simple formula for the transverse pattern, even in the focal plane. The average aperture intensity, defined as the total laser output power, W , divided by the area of the aperture, can be computed by integrating $|U_A|^2$ over the aperture, and is

$$\bar{I} \equiv \frac{4W}{\pi D^2} = \frac{1 - e^{-\delta^2}}{\delta^2} \quad (21)$$

The effect of truncation on the intensity at the focal point for a given output power can then be computed from the gain

$$G = \frac{I(0, f)}{\bar{I}} = \left(\frac{kD^2}{4f} \right)^2 \frac{(1-e^{-\delta^2/2})^2}{\delta^2(1-e^{-\delta^2})} \quad (22)$$

It has been shown (Silver, 1963) that of all possible aperture distributions, the focal-point intensity for a given W is maximized by a uniform disturbance, corresponding in our case to $\delta = 0$, and yielding

$$G_u = \frac{1}{4} \left(\frac{kD^2}{4f} \right)^2$$

In Fig. 3, the normalized gain

$$G_N = \frac{G}{G_u} = \frac{4(1-e^{-\delta^2/2})^2}{\delta^2(1-e^{-\delta^2})} \quad (23)$$

is plotted versus δ^2 , the power of e by which the intensity at the circumference is reduced from the intensity at the center. For example, a ratio of e^{-3} yields a vacuum reduction of *15 percent. The effect of turbulence will be shown to reduce this difference.

4.3 The Effects of Turbulence

The long-term effect of the turbulence, as discussed in Sec. 3, is to reduce the lateral coherence between the fields radiating from different elements of the aperture for separations $\geq \rho_0$. For $\rho_0 < a, D$, the beam will be confined to a circularly symmetric area of dimension $\sim a/k\rho_0$ at a distance z . The ratio of the field intensity to aperture intensity is then $\sim (k\rho_0/z)^2$, and the on-axis intensity can be increased by focusing the beam only if this quantity is considerably greater than unity at the range of interest. In general, this partially coherent aperture will produce an intensity pattern with less detailed structure than the vacuum distribution, and with the maxima and minima tending to be averaged out. Further, because $z_c \sim \lambda^2$, there will be less degradation of longer wavelength patterns. In Figs. 4a-4c, the focal-plane atmospheric patterns, normalized to the vacuum focal-point intensity $(1/4)(kD^2/4f)^2$, are shown for a uniform aperture disturbance with $D/L_0 = 0.01, 0.1$, and 1 , respectively. With z_c determined from Eq. (10) (or Fig. 1) these curves can be used for arbitrary wavelengths. The dashed curve in each figure is the vacuum Airy pattern, Eq. (17), similarly normalized. For a given ratio of z/z_c , the greater the diameter (D/L_0), the less the effective coherence over the aperture, and hence the greater the degradation from the vacuum pattern.

In the remaining examples, the normalized intensities $\langle I \rangle_N$, defined as the ratio of the mean intensities $\langle I \rangle$ to the mean aperture intensity $\bar{I} = 4W/\pi D^2$, are plotted. Turbulence parameters have been chosen that are characteristic of the strengths and scales found from zero to several meters above the ground: $C_n^2 \sim 3 \times 10^{-5} \text{ cm}^{-2/3}$, $L_0 = 0.1 \text{ cm}$, and $L_0 = 100 \text{ cm}$.

Figures 5a and 5b display the effects of truncation on the focal-plane intensity of a $10.6\text{-}\mu$ beam from a 1-m aperture focused at 0.5 km . The vacuum and atmospheric patterns are shown in Fig. 5a for a uniform distribution, whereas in Fig. 5b the gaussian intensity distribution is reduced to e^{-4} at the circumference from its value at the center. In vacuum the truncated distribution has a focal-point intensity of ~ 25 percent less than the uniform case; however, the effect of turbulence is to reduce both intensities such that the difference is only ~ 10 percent. Because the MCF reduces the effective average coherence between different radiating elements of the aperture in a manner that depends only on the distance between them, elements near the edge of the aperture weigh less than those near the center in contributing to the average intensity. Hence, the relative intensity gain of a uniform distribution over a truncated-gaussian distribution will always be less than in the vacuum case. In fact, it can be shown from Eqs. (6) and (21) that in the presence of turbulence, the aperture distribution which maximizes the gain, $G = I(0, f)/\bar{I}$, is, in general, not uniform but somewhat peaked at the center of the aperture.

In Figs. 6a-6c, the focal-plane vacuum and atmospheric patterns are compared for $D = 30 \text{ cm}$, $\delta = 0$, and $z = f = 0.5 \text{ km}$, using the wavelengths 0.6328μ (He-Ne), 1.06μ (Nd), and 10.6μ (CO_2). Although the vacuum intensities at the focal point for the shorter wavelengths are greater (the "antenna gain" is proportional to λ^{-2}), the effect of the atmosphere for the chosen geometry essentially eliminates the shorter wavelength advantage in focusing the beam. For larger apertures, the advantage of CO_2 in producing an intense focal intensity will be greater.

In Figs. 7a-7c, for $\lambda = 10.6 \mu$, the vacuum and atmospheric focal-plane patterns are shown for $D = 1 \text{ m}$ and $\delta = 0$ (uniform distribution) at focal lengths of 0.5 km , 5 km , and 10 km . The long-term effect of the turbulence at the larger ranges is to reduce the on-axis intensity, and to spread out the beam. Hence, the positioning accuracy required to illuminate a target can be considerably less than a vacuum calculation would indicate. As discussed above, the solid curves (with turbulence present) are relatively insensitive to the degree of truncation.

Finally, in Figs. 8a and 8b, the vacuum and atmospheric on-axis intensities are compared for a $10.6\text{-}\mu$ beam focused at 0.5 km with $\delta = 0$, and $D = 30 \text{ cm}$ and 1 m , respectively. The intensities are shown for a range of 50 m on either side of the focal plane. The on-axis intensity for the 30-cm aperture case remains reasonably constant over the 100-m range, with a maximum at $\sim 30 \text{ m}$ on the aperture side of the focal plane. The axial distribution for the 1-m aperture is almost symmetric with respect to the focal plane and obviously requires greater focusing accuracy to produce the available gain of 10^4 at a specified target. At ranges of 5 and 10 km , the on-axis intensities are essentially constant within 50 m of the focal plane and are equal to the focal-point values of Figs. 7b and 7c, respectively.

5. DISCUSSION AND CONCLUSIONS

Based on the results of Secs. 3 and 4, the following procedure can be used to estimate the focal-point intensity.

First, from a knowledge of 1) the index structure constant C_n , 2) the (outer) scale over which the temperature fluctuations are reasonably correlated, L_0 and 3) the wave-number of the radiation, k , the mean-field decay length can be constructed according to Eq. (10) as

$$z_c = \left(0.4 k^2 C_n^2 L_0^{5/3} \right)^{-1}.$$

Then the equivalent coherent aperture size, ρ_0 , at range z , can be computed from Fig. 2. If the smaller of the two quantities $(k\rho_0/z)^2$, $(ka\rho_0/z)^2$ is considerably greater than unity, then the intensity at the range z can be increased by focusing the beam at that range. If this inequality is not satisfied, no intensity amplification can be realized by focusing the beam.

These estimates are also correct for the case of inhomogeneous turbulence when ρ_0 , corresponding to the a^{-1} point of the MCF for the inhomogeneous medium, is used. The formula for the spherical-wave MCF in an inhomogeneous medium is given in Lutomiński and Yura (1971). In either case, if a more precise estimate of the degradation due to the turbulence is required, the integral of Eq. (16) can be evaluated. This will usually be necessary when $\rho_0 \sim a$ or D . When $\rho_0 \ll a, D$, then the approximate formulas of Lutomiński (1970) are applicable.

While the expressions for ρ_0 depend on particular models for the turbulence spectrum for homogeneous turbulence, and model profiles for the inhomogeneous case, the intensity distribution can always be determined from Eq. (6) if the MCF is known. Hence, to predict the beam pattern from an arbitrary wave-front in an aperture, it is the MCF that should be measured rather than specific beam patterns. The measurement of turbulence parameters that rely on specific models for the spectrum are also of limited utility.

This point can be clarified by first observing that Eq. (16) is the Fourier-Bessel transform of the quantity

$$\frac{8W}{\pi D^2} \left(\frac{kD^2}{4z} \right)^2 M_S(Dx, z) M_{\delta, \beta}(x)$$

which can be inverted to yield

$$M_{\delta, \beta} \left(\frac{\rho}{D} \right) M_S(\rho, z) = 2\pi \int_0^\infty J_0 \left(\frac{k\rho p}{z} \right) \langle I \rangle(p, z) p \, dp \quad (24)$$

where $\langle I \rangle(p, z)$ is the mean intensity at a distance p from the axis at range z .

For an arbitrary disturbance in the aperture, the function $M_{\delta, \beta}(x)$ given by Eq. (15) would be replaced by the appropriate overlap integral of Eq. (6). Equation (24) thus provides a possible method for determining part of the MCF from measurements of the beam pattern.

However, because $M_{\delta, \beta}(\rho/D) = 0$ for $\rho \geq D$, inverting the intensity distribution can give no information regarding $M_S(\rho, z)$ for spatial separations larger than the diameter of the transmitting aperture. In particular, to determine the distance z_0 from a beam pattern measurement, it would be necessary to have an aperture diameter greater than the largest scale of turbulence, L_0 , which might be of the order of meters. Hence, if one can determine the spherical-wave MCF for all spatial separations at a given range (e.g., by using an interferometer), one can infer the intensity distribution from an arbitrary aperture distribution at that range, while the reverse is not true unless apertures greater than the coherence length at that range can be constructed. Even if the beam pattern were measured, $M_S(\rho, z)$ would first have to be constructed from Eq. (24) from the given measurement to determine the general response. Therefore, for design purposes, direct measurements of the MCF, which are notably lacking, are required.

REFERENCES

- Born, M., and E. Wolf, 1965, *Principles of Optics*, 3rd ed., Pergamon Press, Oxford.
- Campbell, J. P., and L. G. De Shazer, 1969, "Near Fields of Truncated-Gaussian Apertures," *J. Opt. Soc. Am.*, Vol. 59, No. 11, pp. 1427-29.
- Ho, T. L., 1970, "Coherence Degradation of Gaussian Beams in a Turbulent Atmosphere," *J. Opt. Soc. Am.*, Vol. 60, No. 5, pp. 667-73.
- Ishimaru, A., 1969, "Fluctuations of a Beam Wave Propagating Through a Locally Homogeneous Medium," *Radio Sci.*, Vol. 4, No. 4, pp. 295-305.
- Kauffman, J. F., 1965, "Calculated Radiation Patterns of Truncated Gaussian Aperture Distribution," *IEEE Trans. Ant. and Prop.*, p. 473.
- Lutomirski, R. F., 1970, *Propagation of a Finite Optical Beam in an Inhomogeneous Medium*, The Rand Corporation, RM-6055-ARPA.
- Lutomirski, R. F., and H. T. Yura, 1971, "The Phase Structure and Mutual Coherence Function of an Optical Wave in a Turbulent Atmosphere," *J. Opt. Soc. Am.*, Vol. 61, No. 4, p. 482.
- Rayleigh, J. W. S., 1945, *The Theory of Sound*, Vol. 1, 2d ed., Dover Publications, New York, p. 152.
- Risken, H., 1964, "Calculation of Laser Modes in an Active Perot-Fabry-Interferometer," *Zeitschrift für Physik*, Vol. 180, No. 2, pp. 150-169.
- Schmeltzer, R. A., 1967, "Means, Variances, and Covariances for Laser Beam Propagation Through a Random Medium," *Q. Appl. Math.*, Vol. 24, No. 4, pp. 339-54.
- Silver, S. (ed.), 1963, *Microwave Antenna Theory and Design*, Boston Technical Lithographers, Inc., Lexington, Ma., p. 177.

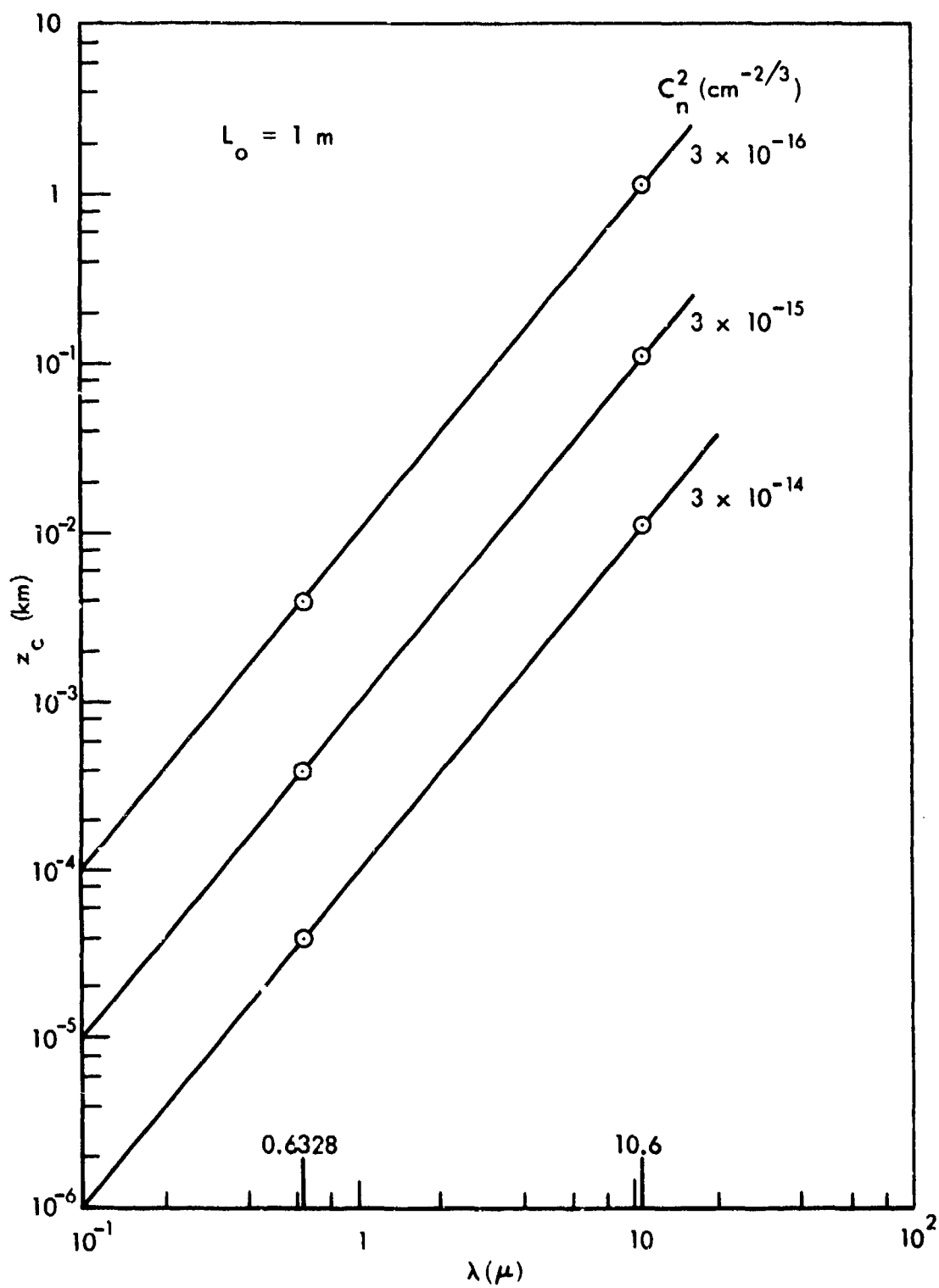


Fig. 1 Propagation distance z_c as a function of wavelength

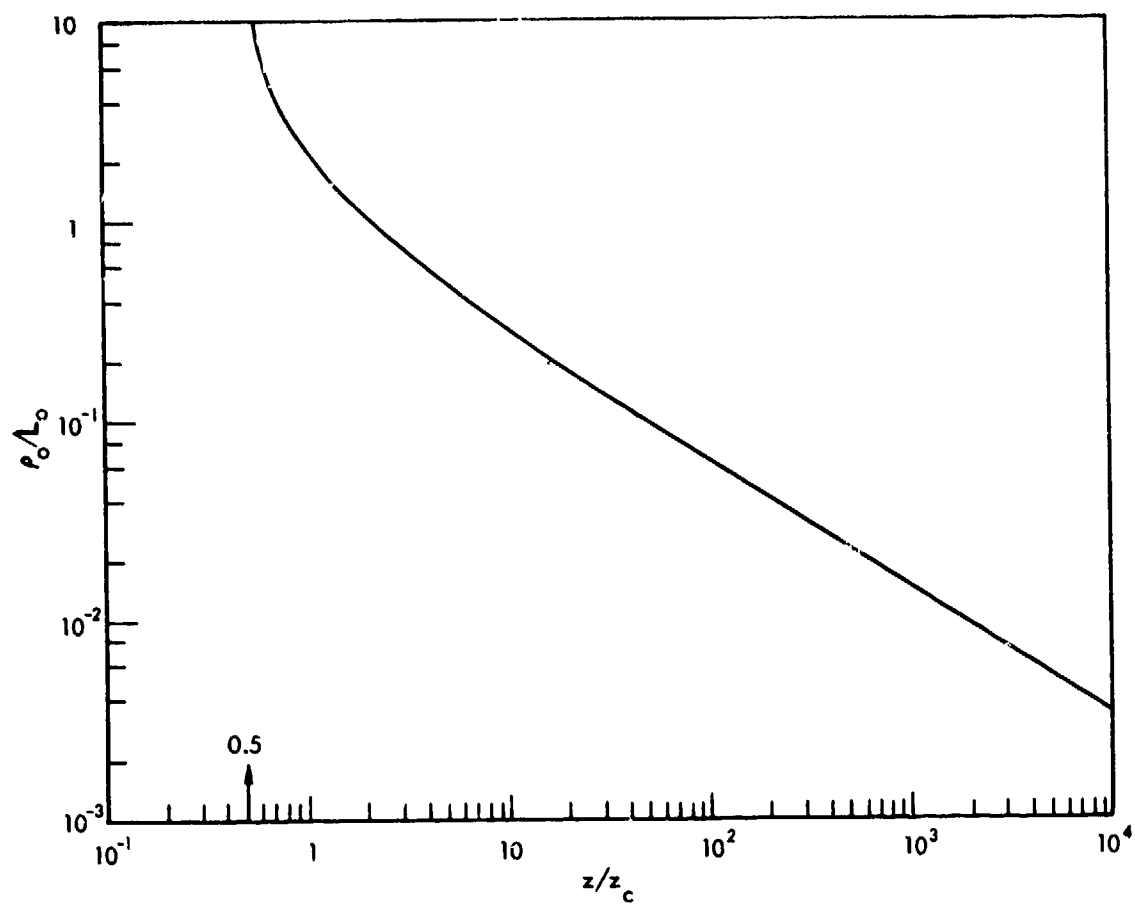


Fig. 2 The normalized coherence length, ρ_0/L_0 , as a function of z/z_c for a spherical wave

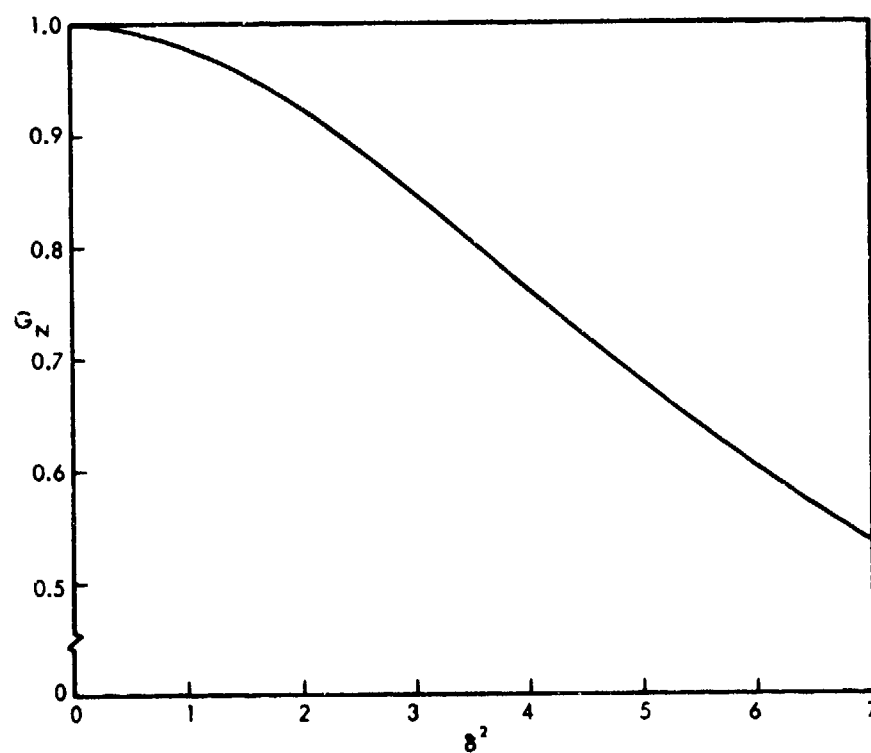


Fig. 3 The normalized gain as a function of δ^2

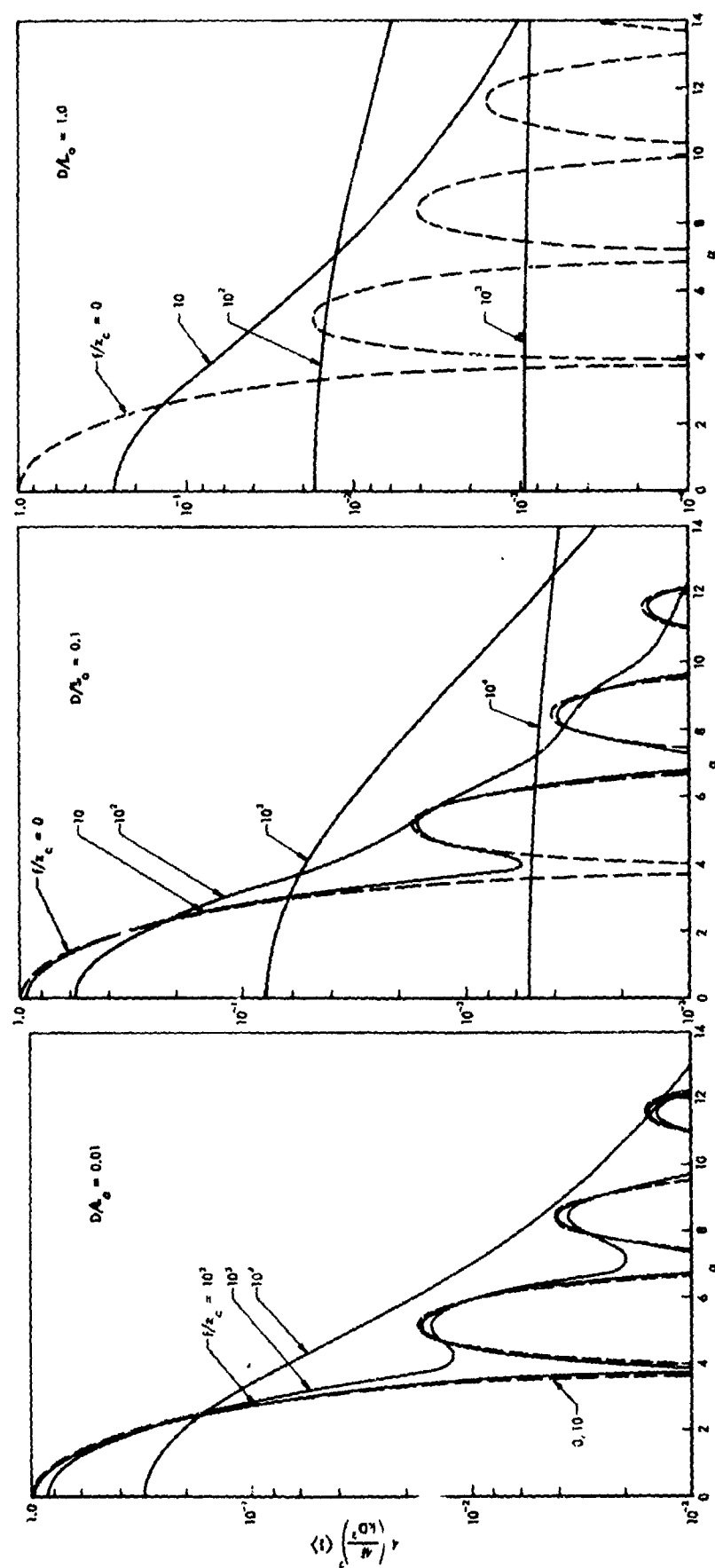


Fig. 4 Normalized focal plane intensity patterns for various values of D/L_0

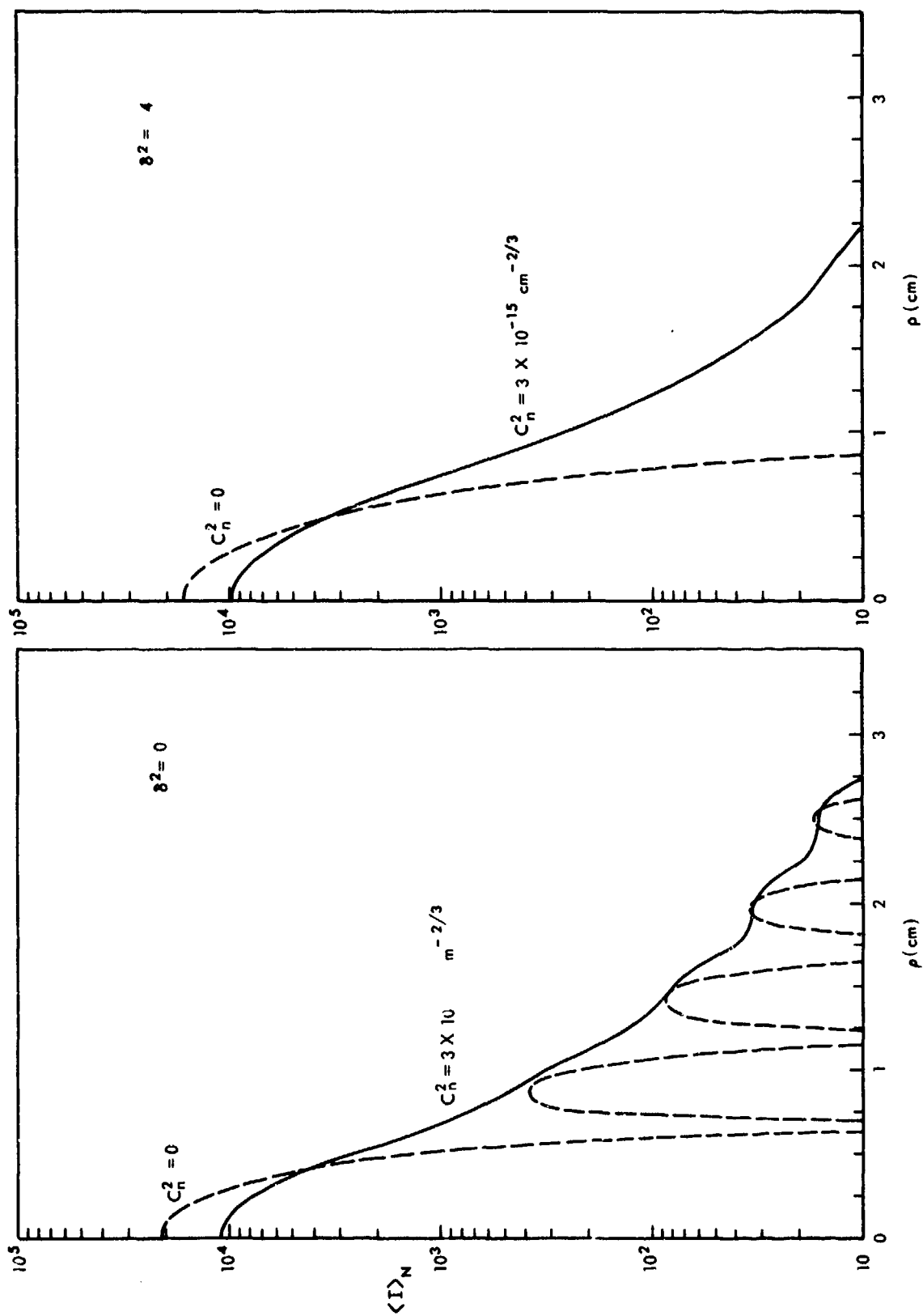


Fig. 5 Comparison of focal plane patterns at $\lambda = 10.6 \mu$ for $D = 1 \text{ m}$ focused at 0.5 km , for (a) uniform and (b) truncated gaussian aperture distribution

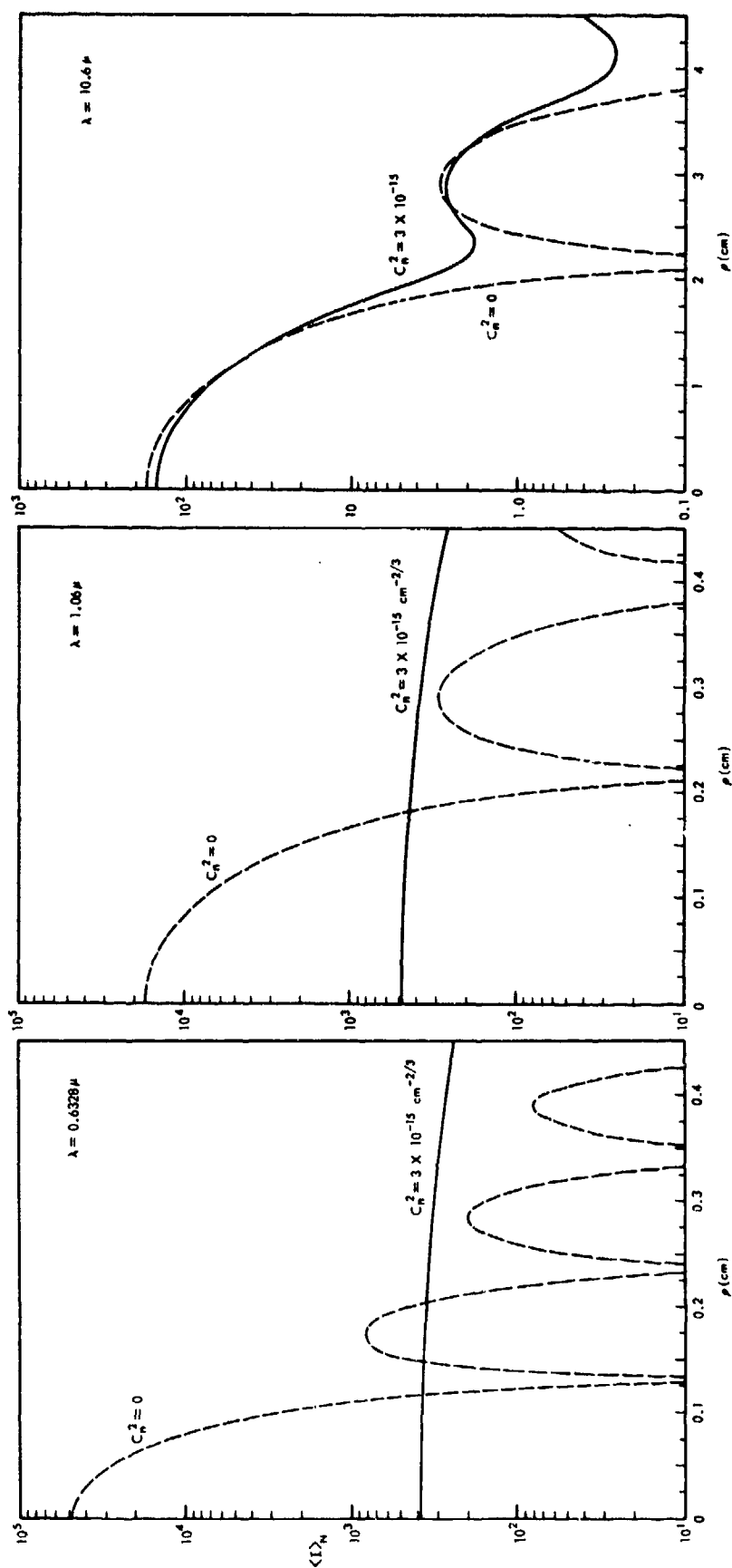


Fig. 6 Comparison of focal plane patterns, for several wavelengths, with a uniform distribution in a 30-cm aperture focused at 0.5 km

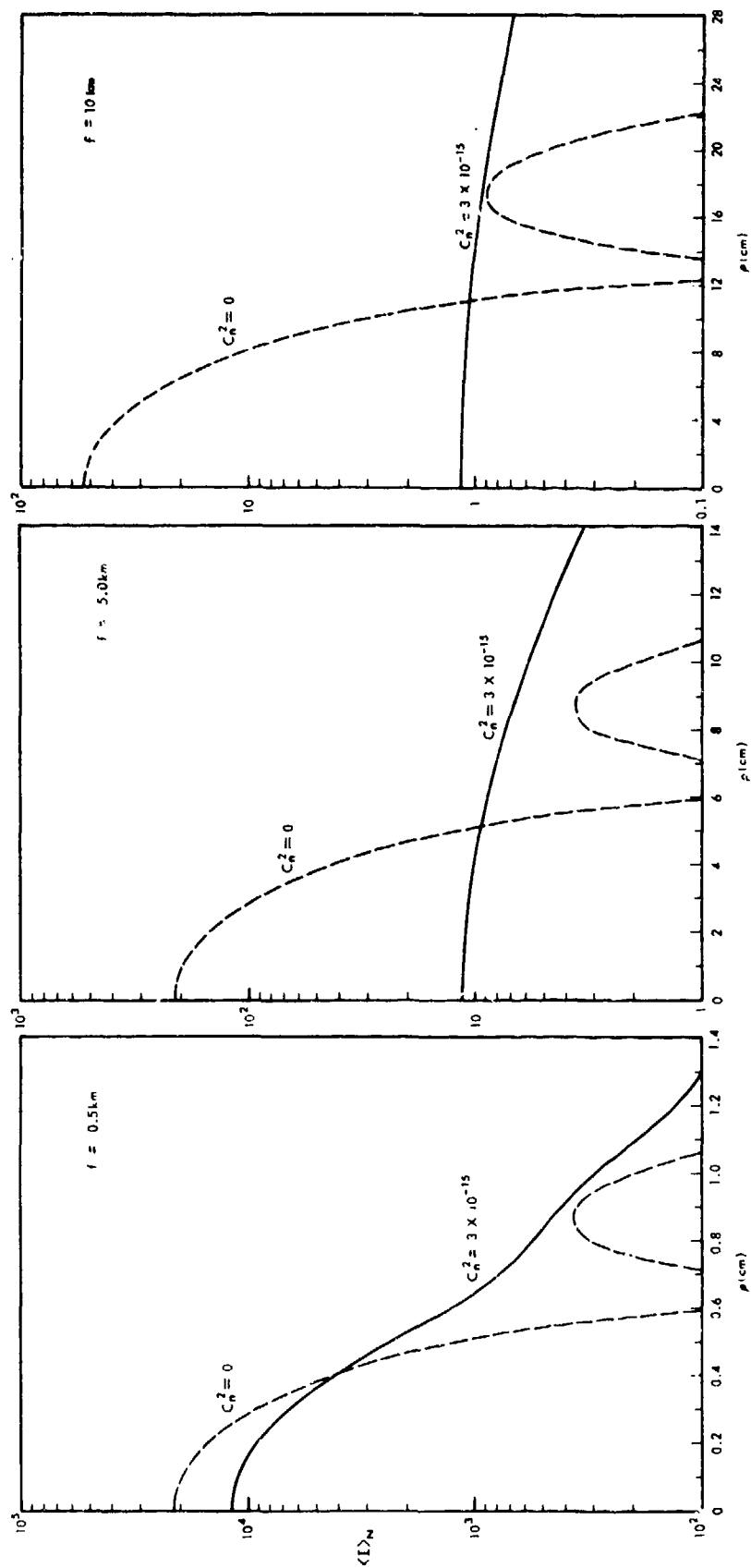


Fig. 7 Focal plane patterns at $\lambda = 10.6\ \mu$ for a uniform distribution in a
l-m aperture

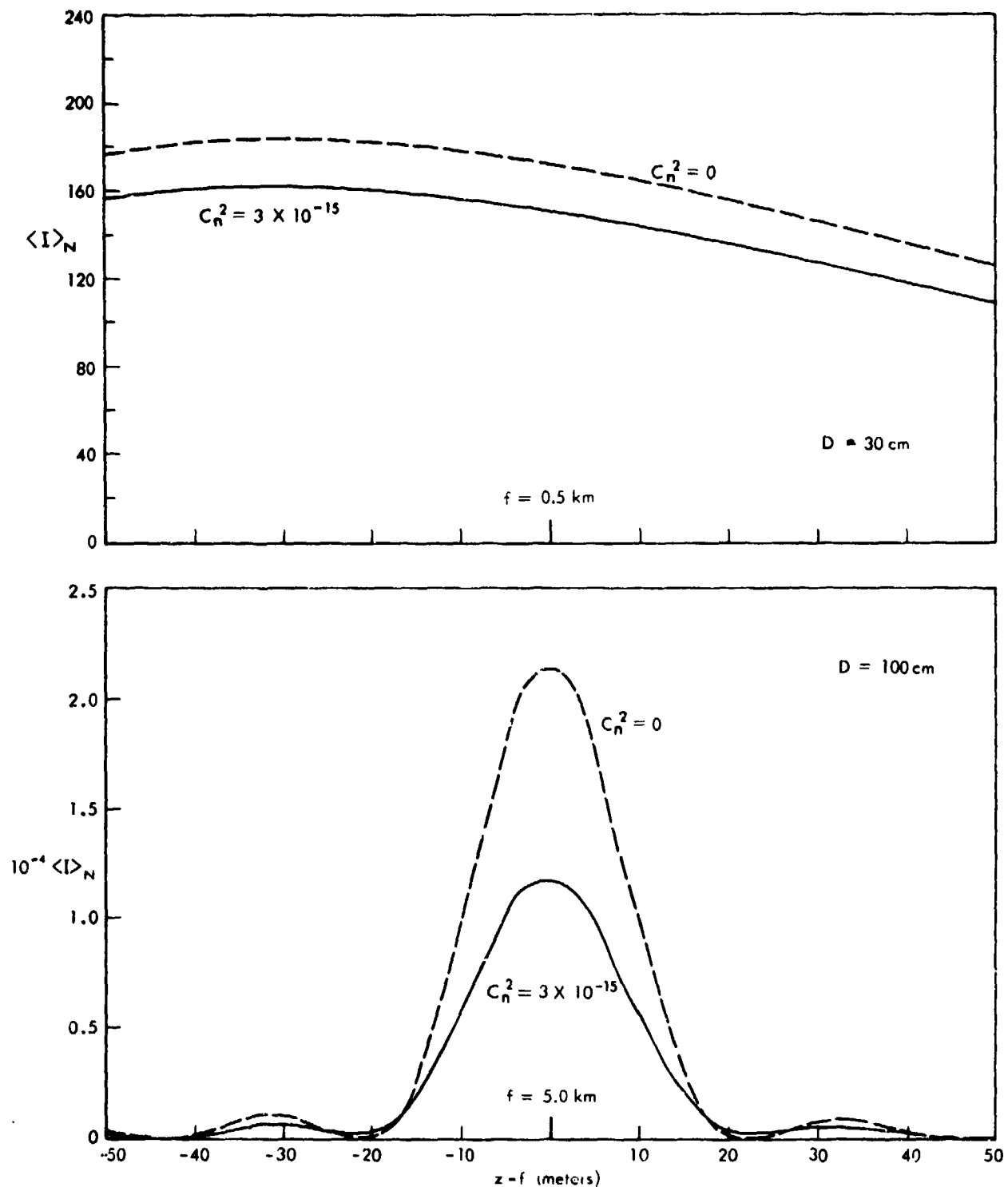


Fig. 8 Comparison of on-axis intensities at $\lambda = 10.6 \mu$ for a uniform distribution focused at 0.5 km

MEASUREMENTS OF THE ATMOSPHERIC TRANSFER FUNCTION

J.C. Dainty

Physics Department, Queen Elizabeth College,
Campden Hill Road, London W8 7AH

R.J. Scaddan

Physics Department (Astronomy), Imperial College,
Prince Consort Road, London SW7

SUMMARY

A wavefront folding interferometer has been constructed with which the long time-averaged modulation transfer function, MTF, of the atmosphere (ie, the long time-averaged mutual coherence function) may be measured. The instrument was used to determine the MTF over 10 nights in June 1974 at Mauna Kea Observatory, Hawaii, using bright stars as sources. The form of the MTF at separations of a few centimetres in the pupil agreed with that predicted on the basis of a Kolmogorov spectrum of turbulence, but there was a departure at larger separations. The MTFs were highly variable both from hour-to-hour and night-to-night; the wavefront correlation region, r_0 , varying from approximately 4 to 20 cm. Increasing the zenith angle generally decreased the correlation region, but no exact relationship was observed.

It is hoped to construct a new interferometer with direct output of the MTF. The design of this instrument will be outlined.

1. INTRODUCTION

Turbulence in the atmosphere causes refractive index fluctuations along the optical path from a light source to an observer. These result in the phenomena of scintillation, increased image size and image motion. The modulation transfer function, MTF, of the atmosphere may be used to completely describe the degrading effects of atmospheric turbulence on an imaging system.

In most astronomical applications the long-exposure MTF is more appropriate than the short-exposure MTF which does not take account of image motion. The long-exposure mutual coherence function also influences the form of the instrumental transfer function for unconventional imaging techniques in astronomy, such as speckle interferometry (Dainty J.C., 1973, Korff D., 1973). Thus the atmospheric MTF is an important parameter, particularly in the selection of a site for an astronomical observatory or the specification of the quality of an astronomical telescope (Brown D.S., 1975).

A wavefront folding interferometer has been constructed (Dainty J.C. and Scaddan R.J., 1974) that measures the long time-averaged mutual coherence function of the wavefront arriving at a telescope pupil; it can be shown that this function is proportional to the atmospheric MTF if the light source is effectively a point source. The instrument was used at Mauna Kea Observatory, Hawaii, for a series of MTF measurements over a period of ten nights in June 1974 (Dainty J.C. and Scaddan R.J., 1975). Hawaii is one of the proposed sites for the Northern Hemisphere Observatory. The form of the MTFs and their variation with time and zenith angle were briefly investigated.

A similar interferometer has been used by Breckinridge (Breckinridge J.B., 1974) to display the real part of the two dimensional Fourier transform of a stellar source.

2. THEORY

For quasi-monochromatic, spatially incoherent light, the image and object in any imaging system are related in the spatial frequency domain by

$$i(u,v) = o(u,v) \cdot T(u,v) \quad (1)$$

where $i(u,v)$ and $o(u,v)$ are the Fourier transforms of the image and object intensities respectively, $T(u,v)$ is the modulation transfer function and (u,v) are spatial frequency variables.

It can be shown (Hufnagel R.E. and Stanley N.R., 1964, Fried D.L., 1966 and Dainty J.C., 1973) that the atmospheric transfer function, $T(u,v)$, is equal to the normalised time-averaged autocorrelation, $\Gamma(x,y)$, of the complex amplitude, $U(x,y)$, at the telescope pupil due to an unresolved star:

$$T_s(u,v) = \frac{\Gamma(x,y)}{\langle I \rangle} = \frac{\langle U^*(x',y') U(x'+x,y'+y) \rangle}{\langle I \rangle} \quad (2)$$

where $\langle I \rangle$ is the long time-averaged intensity and spatial frequencies in the image and distances in the pupil are related by

$$u = \frac{x}{\lambda f}, \quad v = \frac{y}{\lambda f} \quad (3)$$

where λ is the wavelength of light and f is the focal length.

Thus the atmospheric transfer function can be measured by an instrument designed to measure spatial coherence. The essential features of the present instrument are shown in Figure 1. The design is based on an interferometer (Wessely H.W. and Bolstad J.O., 1970) in which the transfer function is determined simultaneously at all spatial frequencies. It is basically a Michelson interferometer in which a roof-prism in one arm reverses the wavefront about the y axis so that the time-averaged output intensity is given by

$$\begin{aligned} \langle I_{out} \rangle &= \langle |U(x,y) + U(-x,y)|^2 \rangle \\ &= 2\{\langle I \rangle + \operatorname{Re} \Gamma(2x,0)\} \end{aligned} \quad (4)$$

Tilt fringes may be introduced parallel to the y axis so that

$$\langle I_{out} \rangle = 2\{\langle I \rangle + \operatorname{Re} \Gamma(2x,0) \cos(2k \sin \beta \cdot x + \Delta \phi(x))\} \quad (5)$$

where β is the tilt angle, $k = 2\pi/\lambda$ and $\Delta \phi(x) = \phi(x,y) - \phi(-x,y)$ is a difference term for the phase aberrations of the telescope and interferometer.

The spatial coherence, Γ , is real and has rotational symmetry for isotropic seeing and therefore the atmospheric MTF can be found from the envelope of a set of cosine fringes.

It should be noted that any aberrations only affect the spacing of the fringes and not their envelope so that the measurement is independent of aberrations provided that $\Delta \phi(x)$ is much less than the coherence length of the light, ie,

$$\Delta \phi(x) \ll \frac{\lambda^2}{\Delta \lambda} \quad (6)$$

where $\Delta \lambda$ is the optical bandwidth. This condition is easily met in practice.

3. INSTRUMENT

The general arrangement of the components mounted on the 12.5 mm thick aluminium alloy base is shown in Figure 2. The instrument is attached to the Cassegrain focus of a telescope so that light enters the interferometer via a hole in the base and a beam bending mirror. This mirror transmits a few percent of the light to a guiding eyepiece.

The collimating lenses not only provide a parallel beam of light in the interferometer, but also image the telescope pupil onto the roof prism. Ghost images in the interferometer are prevented by arranging the beam-splitter, compensator and prism face to be at Brewster angle incidence to minimise reflection of the 'p' polarisation which is subsequently selected in the exit beam with a polarising filter. The beam-splitter is coated with a dielectric multilayer which reflects 40 percent of the 'p' polarisation. The image of the fringes superimposed on the telescope pupil is recorded through an interference filter using a Spectracon image tube (McGee J.D., et al, 1972). The reflecting faces of the roof prism meet at an angle of $90^\circ \pm 1$ arc.sec. and the edge has a radius of curvature of less than 0.1 mm. The plane mirror is mounted in an 'Aero-Tech' interferometric mount which allows precise positioning of the fringes. All of the optical components are figured to give individual wavefront aberrations of less than $\lambda/4$ over a 25 mm aperture.

The interferometer may be adjusted to have zero path difference between its arms by successive use of local mercury and tungsten filament lamps which can be viewed via a moveable mirror. The star image may then be correctly positioned and focussed using an eyepiece arrangement and the Foucault knife-edge test. If the star image is not co-axial with the local source, the orientation and spacing of the fringes will be different. Another eyepiece and moveable mirror are provided for examining the image falling on the Spectracon photocathode.

The image of the telescope pupil is recorded at a scale of approximately $1/50$ and an image of the star may be recorded at a scale of 0.22 mm/arc.sec by exchanging the output lens. This allows comparison of the star image and the point spread function computed from the atmospheric MTF.

4. ANALYSIS

Due to the large number of fringe images that were recorded, it was necessary to select approximately 25 by visual inspection that were representative of particular nights or effects. These were scanned with a Joyce-Loebl microdensitometer with a slit size of 40 μm by 3.0 mm, ie, equivalent to 2mm by 150mm on the telescope pupil. This density distribution is directly proportional to the image intensity distribution due to the linear relationship between density and exposure for the Spectracon image tube. The fringe envelope for each pattern was drawn in by hand and re-plotted on a normalised scale.

The fringe envelope was then corrected for the effect of the bandwidth of the interference filter used in the measurement by dividing by the temporal coherence function of the filter. This was determined by Fourier transformation of the spectral transmittance function of the filter. It was assumed that both the energy distribution of the star and the spectral sensitivity distribution of the Spectracon were constant over the passband of the filter (halfwidth approximately 30nm centred at 520nm).

The star images were scanned along a diameter with a 30 μm square aperture in the microdensitometer to give the point spread function due to the atmosphere and the instrument.

5. RESULTS

Measurements of the atmospheric MTF were made with a 61 cm telescope at Mauna Kea Observatory, Hawaii, from 21 to 30 June, 1974, inclusive. Table 1 lists some of the meteorological data for that period and a visual estimate of the seeing on each night made with the 61 cm telescope.

Date	Night	Temp. at 24.00 hrs, °C	Average wind speed, MPH	Obscuration	Visual Seeing*
June 21	1	-3.3	30	-	Poor
22	2	-2.2	40	-	Average
23	3	-1.3	22	-	Good
24	4	-1.1	7	-	Good
25	5	-2.0	5	-	Average
26	6	0.3	18	Thick cirrus	Average
27	7	-0.5	40	Thin "	Average
28	8	-1.5	25	Thin "	Good
29	9	1.0	17	Thick "	Good
30	10	3.3	4	Thin "	Good

* Poor: image 'diameter' >3 arc.sec.
Average: image 'diameter' 1.5 - 3 arc.sec.
Good: image 'diameter' <1.5 arc.sec.

Table 1

The stars used as sources were mainly α -Lyrae and α -Bootis which may be considered as unresolvable over apertures relevant to the present measurements. Exposure times for fringe pictures through a 30 nm halfwidth filter were approximately 60 s when a 40 kV potential was applied across the Spectracon and G5 emulsion was used (developed for 5 min. in D19). Exposure times for star images were approximately 8 s through an 8 nm halfwidth filter.

Typical atmospheric MTFs for each night are shown in Figures 3 and 4. The abscissa is given both in cycles/arc.sec. and in centimetres in the pupil. The curves are considered to be accurate to approximately 5 percent at modulations greater than 0.2, but reliable values for modulations less than 0.1 cannot in general be given because of measurement noise and the effect of correcting for temporal coherence. All of these measurements were taken within 20° of the zenith.

A comparison is made in Figure 5 between a section through a point spread function (PSF) computed by Hankel transformation of a measured atmospheric MTF and a measured PSF. The measured PSF is wider due to imaging aberrations in the instrument and microdensitometer. This result indicates the advantage to be gained by measuring the mutual coherence function of the wavefront in the pupil rather than the intensity distribution in the image plane.

Figures 6 and 7 give the computed atmospheric PSFs corresponding to the atmospheric MTFs shown in Figures 3 and 4. The shapes of the PSFs are somewhat uncertain due to the relatively large effect of the tails of the MTFs (the region where the accuracy is lowest). However, it can be seen that on a few nights, most of the image energy was encompassed within a circle of 1 arc.sec. diameter.

Throughout some nights there was a large variation of the MTF. This is typified by Figure 8 showing the variation on the third night. On this occasion the seeing improved throughout the night, but as the reverse was sometimes observed, it cannot be said whether this trend was characteristic of the site.

The variation of MTF with zenith angle was briefly investigated. It can be shown (Hufnagel R.E. and Stanley N.R., 1964, Fried D.L., 1966) that the long-exposure atmospheric MTF, $M(\rho)$, can be expressed as

$$M(\rho) = \exp\{-\frac{1}{2}D(\rho)\} \quad (7)$$

where $D(\rho)$ is the wave structure function and ρ is the correlation distance in the pupil. For locally isotropic, homogeneous turbulence with a Kolmogorov turbulence spectrum and a stellar object

$$D(\rho) = 2.91 k^2 \sec \theta \rho^{5/3} \int_{h_1}^{\infty} C_n^2(h) dh \quad (8)$$

where k is the wave number, θ is the zenith angle, $C_n(h)$ is the refractive index structure constant and a function of height h and h_1 is the height of the observatory above the ground.

From equations (7) and (8) we may write

$$\ln(-\ln M(\rho)) = \frac{5}{3} \ln \rho + \ln \sec \theta + \ln(1.45 k^2 \int_{h_1}^{\infty} C_n^2(h) dh) \quad (9)$$

so that for two zenith angles, θ_1 and θ_2 , graphs of $\ln(-\ln M(\rho))$ versus $\ln \rho$ should be straight lines of slope equal to $5/3$ and vertically separated by $\ln(\sec \theta_1 / \sec \theta_2)$. Figure 9 shows the atmospheric MTFs measured at zenith angles of 10° and 47° a short time apart on the fifth night. The value of $(\sec \theta_1 / \sec \theta_2)$ for these angles is 1.44, while that measured from the figure is 1.68 at distances of up to 5 cm in the pupil. It was not possible to obtain much quantitative data in the time available, but it was generally found that the seeing was better at the zenith than at large angles from the zenith. In addition to the time variation of seeing through many nights, there was also an apparently random angular variation that may have been caused by local turbulence, wind or cloud cover.

It should be noted that the results presented here are typical values for only 10 nights. A summary is given in Table 2 which lists the widths of the MTFs and PSFs at the 25 percent level. Also listed are values of r_0 as defined by Fried (Fried DL, 1966).

$$M(\rho) = \exp \left(-3.44 \left(\frac{\rho}{r_0} \right)^{5/3} \right) \quad (10)$$

Observation	25 percent level width			r_0 cm
	MTF		PSF	
	cycle/arc.sec.	cm	arc.sec.	
1a	0.38	4.1	1.1	7.1
1b	0.22	2.4	1.3	4.1
2	0.41	4.3	1.8	7.4
3	0.87	9.4	0.8	16.2
4	0.80	8.6	1.0	14.8
5	0.49	5.3	1.4	9.1
6	0.57	6.1	1.1	10.5
7	0.71	7.6	0.9	13.1
8	1.04	11.2	0.7	19.3
9a	0.87	9.4	1.0	16.2
9b	1.02	11.0	0.8	19.0
10	0.84	9.0	1.0	15.5

Table 2

6. DISCUSSION

A feature of the results of this study is the highly variable nature of the atmospheric MTF. There appeared to be three time scales of variation: a rapid fluctuation (greater than a few Hz) observed by eye when setting up the fringes, an hour-to-hour variation and a night-to-night variation. This suggests that the statistics of the time variation of the MTF should be studied and that any model of the atmosphere should include a time varying factor.

From equation (9) it can be seen that for turbulence with a Kolmogorov spectrum the atmospheric MTF should be a straight line of slope equal to 5/3 when plotted on logarithmic scales. Such graphs are given in figures 10 and 11 for the MTFs measured on nights 1 to 5 and 6 to 10, respectively. It appears that the Kolmogorov two-thirds law is approximately obeyed only for small distances in the pupil. For the case of a modified von Karman spectrum, the form of the MTF is given by

$$M(\rho) = \exp \left\{ -1.45 k^2 \sec \theta \rho^{5/3} \int_{h_1}^{\infty} \left[1 - 0.8 \left(\frac{\rho}{L_0(h)} \right)^{1/3} \right] C_n^2(h) dh \right\} \quad l_0 \ll \rho \ll L_0 \quad (11)$$

where $L_0 = l_0/2\pi$ and L_0 and l_0 are the outer and inner scales of turbulence, respectively. To evaluate this expression the distributions of L_0 and C_n^2 with height must be known; values of the former are rare, especially under the temperature inversion conditions usually found at night.

For the simple case of constant values of L_0 and C_n^2 , the form of the MTF is as shown in Figure 12 for six values of L_0 . Different values of $C_n^2(h)$, k or $\sec \theta$ will merely shift the curves up or down the $\ln\{-\ln M(\rho)\}$ axis. It can be seen that the shape of the curves is similar to that measured, but the overall slope is lower.

7. FUTURE WORK

It is planned to construct a new interferometer in which the fringe modulation at one separation in the pupil is determined in real time. The basic layout of the instrument will be retained except for the polarising components and double photomultiplier system shown in Figure 13. The beams are shown sheared in the interferometer, although several alternative arrangements are possible. In this technique the input beam is plane polarised at 45° to the horizontal and a quarter-wave plate, placed in one arm, has an optical thickness a quarter of a wavelength different for the vertical component of polarisation with respect to that for the horizontal component. A polarising beam-splitter in the output beam separates the two polarisations which are measured by two identical photomultipliers and scanning slits aligned to the fringes at the same separation in the pupil.

For one polarisation, the output intensity distribution may be taken as equation (5). For the other polarisation:

$$\begin{aligned} \langle I_{out} \rangle &= \langle |U(x,y) + U(-x,y)e^{-i\pi/2}|^2 \rangle \\ &= 2\langle I \rangle + \text{Re} \{ \Gamma(2x,0)e^{-i\pi/2} \} \end{aligned} \quad (12)$$

When the tilt fringes are introduced:

$$\langle I_{out} \rangle = 2\langle I \rangle + \text{Re} \{ \Gamma(2x,0) \sin(2k \sin \theta x + \Delta\phi(x)) \} \quad (13)$$

By subtracting a voltage proportional to the average intensity, $\langle I \rangle$, (measured by a third photomultiplier, say, in the other exit beam of the interferometer) from both of the photomultiplier signals and taking the square root of the sum of the squares of the signals, it is possible to obtain a voltage proportional to $\Gamma(2x,0)$. This voltage may be recorded by a magnetic tape or chart recorder. The exposure time is determined by the time constant of the amplifiers or the integration time of the photon counting channels.

The principal advantage of this system is that the fringe modulation is directly available so that, say, the statistics of the time variation of the atmospheric MTF at one separation in the pupil may be easily measured. As this separation in the pupil need not coincide with a fringe maximum, less fringes are required across the image of the telescope pupil so that the temporal coherence function of the filter is a less critical factor.

The main disadvantage of the readout system is that the MTF is not measured simultaneously at all separations in the pupil.

8. ACKNOWLEDGMENTS

We are grateful to the Director and staff of the Institute for Astronomy, University of Hawaii, for the provision of observing time and facilities and to the NHO Site Testing group in Hawaii for supplying some meteorological data. We also wish to thank Professor J. Ring for his encouragement of this work. The project was supported by the Science Research Council, who also provided a studentship for one of us (RJS).

9. REFERENCES

- Breckinridge J.B., 1974 "Two-Dimensional White Light Coherence Interferometer", Appl. Opt., 13, 2760.
- Brown D.S., 1975, "Optical Performance Specification for Astronomical Telescopes", Topical Meeting, Imaging in Astronomy, Cambridge, Mass.
- Dainty J.C., 1973, "Diffraction-Limited Imaging of Stellar Objects using Telescopes of Low Optical Quality", Opt.Comm., 7, 129.
- Dainty J.C. and Scaddan R.J., 1974, "A Coherence Interferometer for Direct Measurement of the Atmospheric Transfer Function", Mon.Not.R.Astr.Soc., 167, 69P.
- Dainty J.C., and Scaddan R.J., 1975, "Measurements of the Atmospheric Transfer Function at Mauna Kea, Hawaii", Mon.Not.R.Astr.Soc., 170, 519.
- Fried D.L., 1966, "Optical Resolution through a Randomly Inhomogeneous Medium for very Long and Very Short Exposures", J.Opt.Soc.Am., 56, 1372.
- Hufnagel R.E., and Stanley N.R., 1964, "Modulation Transfer Function Associated with Image Transmission Through Turbulent Media", J.Opt.Soc.Am., 54, 52.
- Korff D., 1973, "Analysis of a Method for Obtaining Near-Diffraction-Limited Information in the Presence of Atmospheric Turbulence", J.Opt.Soc.Am., 63, 971.
- McGee J.D., et al, 1972, "Extended field Spectracon", Advances in Electronics and Electron Physics, eds. J.D. McGee, B.L. Morgan and E.Kahan, 33, 13, Academic Press, London.
- Wessely H.W., and Bolstad J.O., 1970, "Interferometric Technique for Measuring the Spatial-Correlation Function of Optical Radiation Fields", J.Opt.Soc.Am., 60, 678.

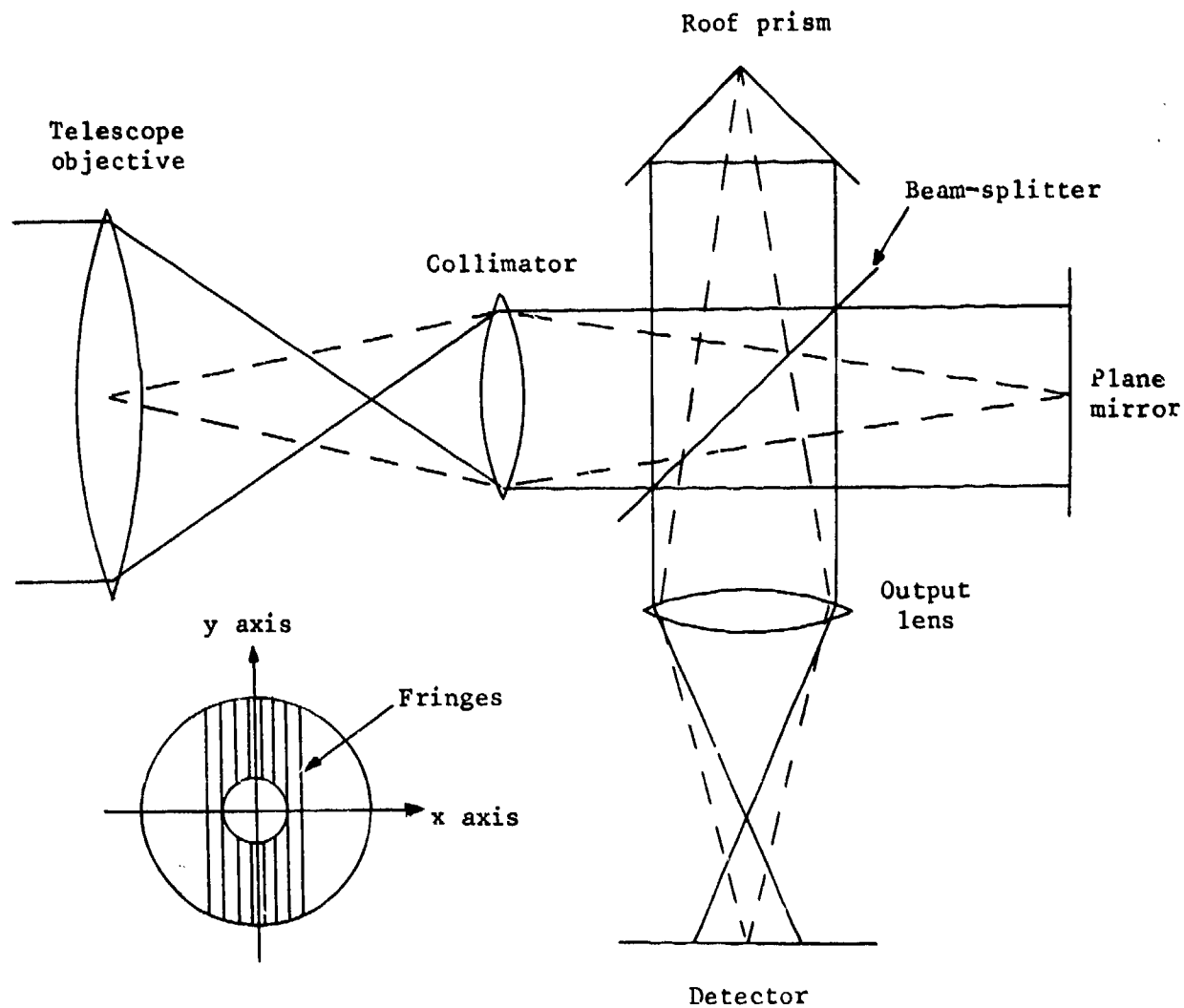


Figure 1 Essential features of the instrument and view of the fringes over a limited region in the x direction.

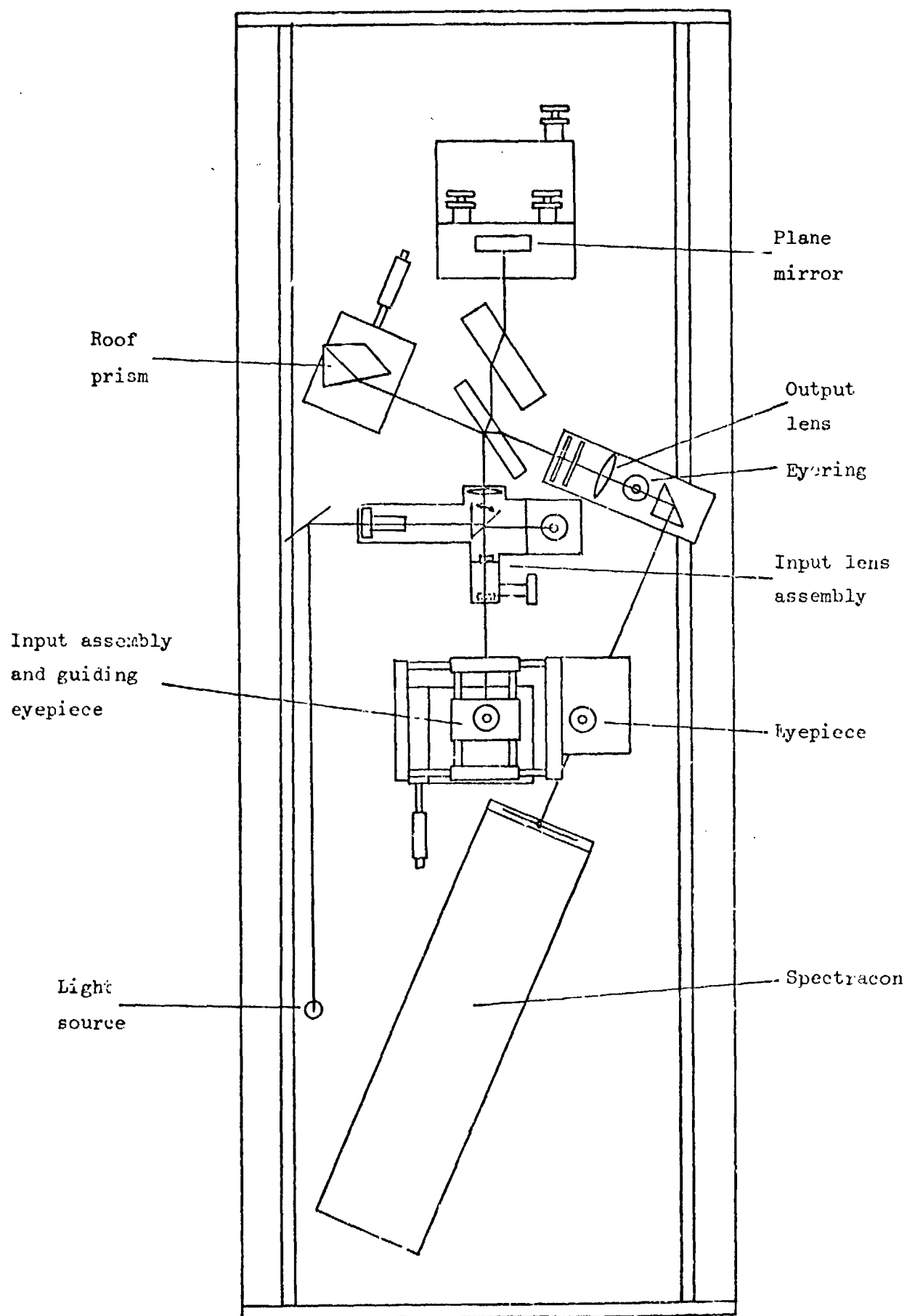


Figure 2 General arrangement of the instrument.

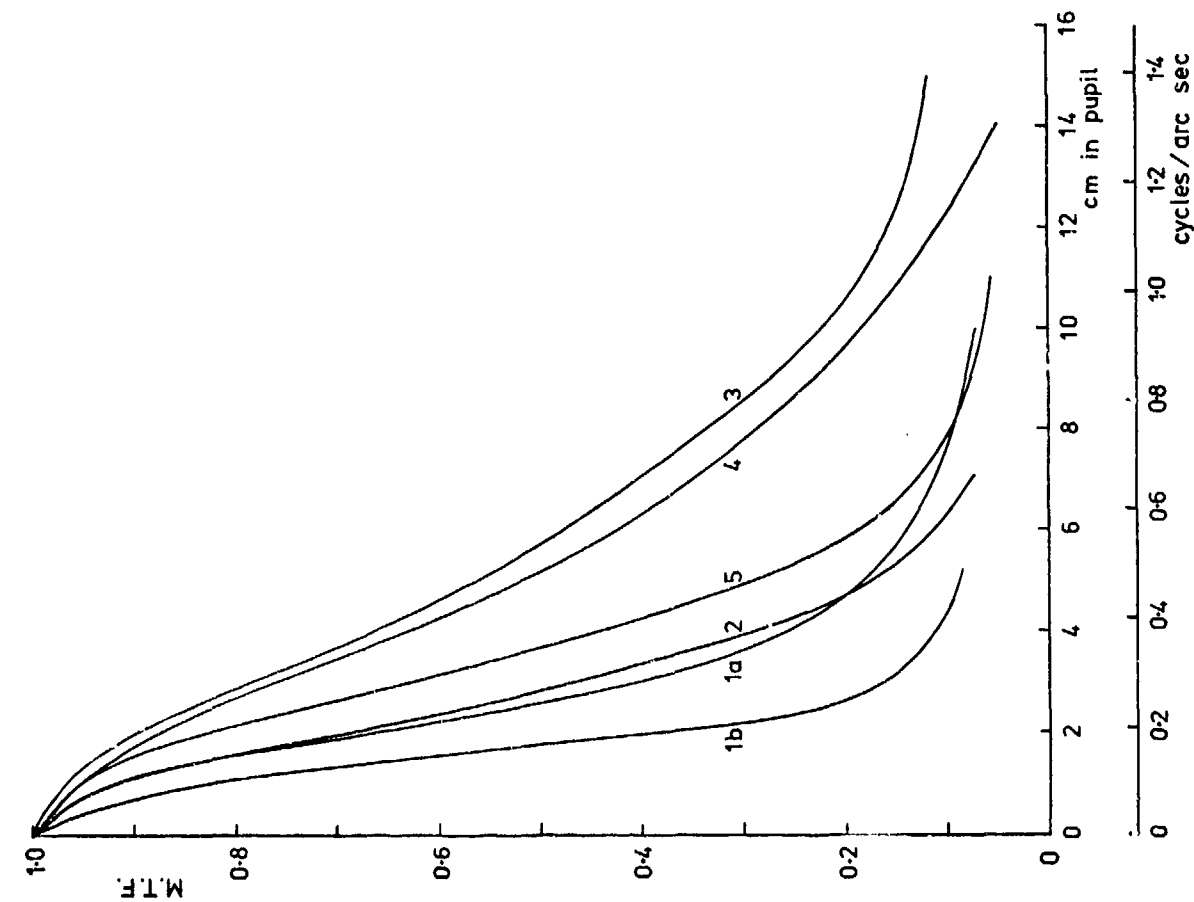


Figure 3 Typical MTF curves for nights 1 to 5. Two curves are given for night 1.

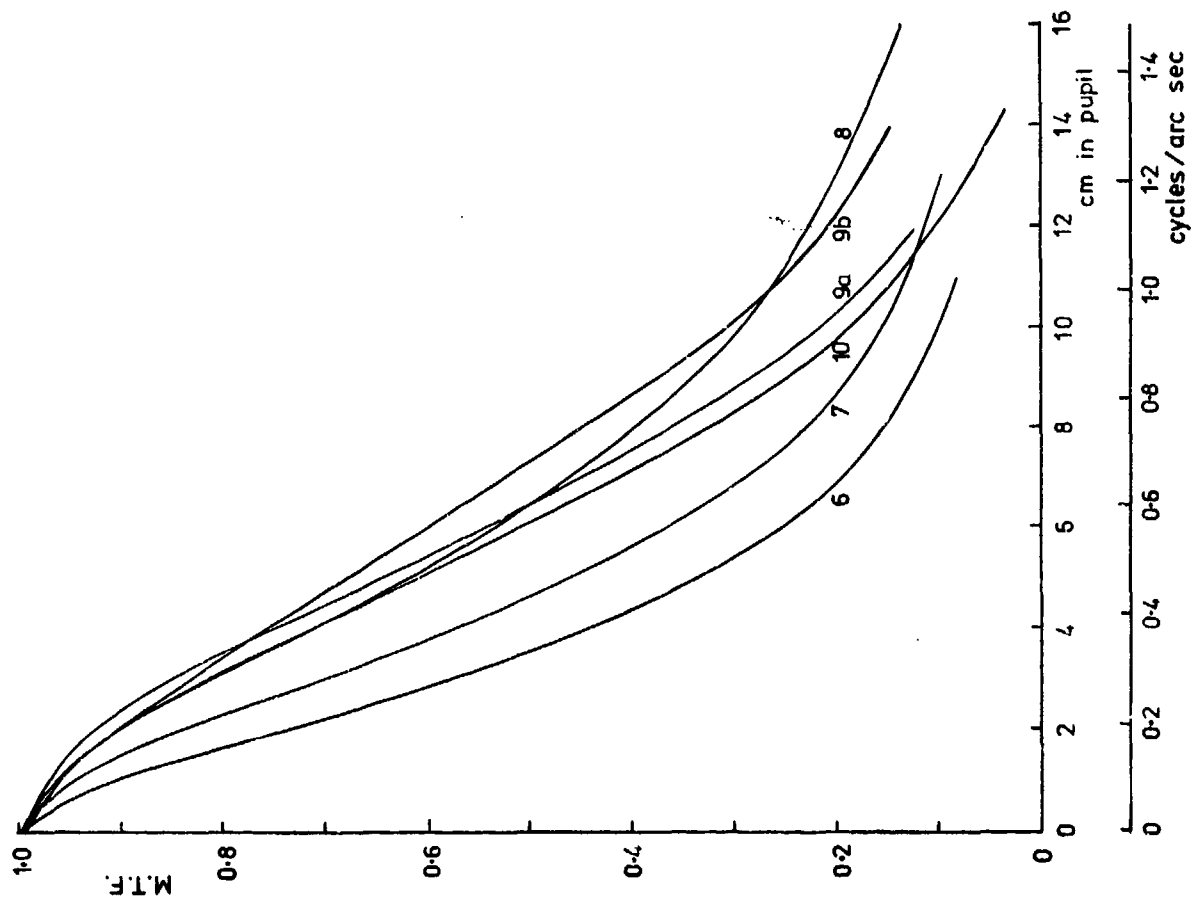


Figure 4 Typical MTF curves for nights 6 to 10. Two curves are given for night 9.

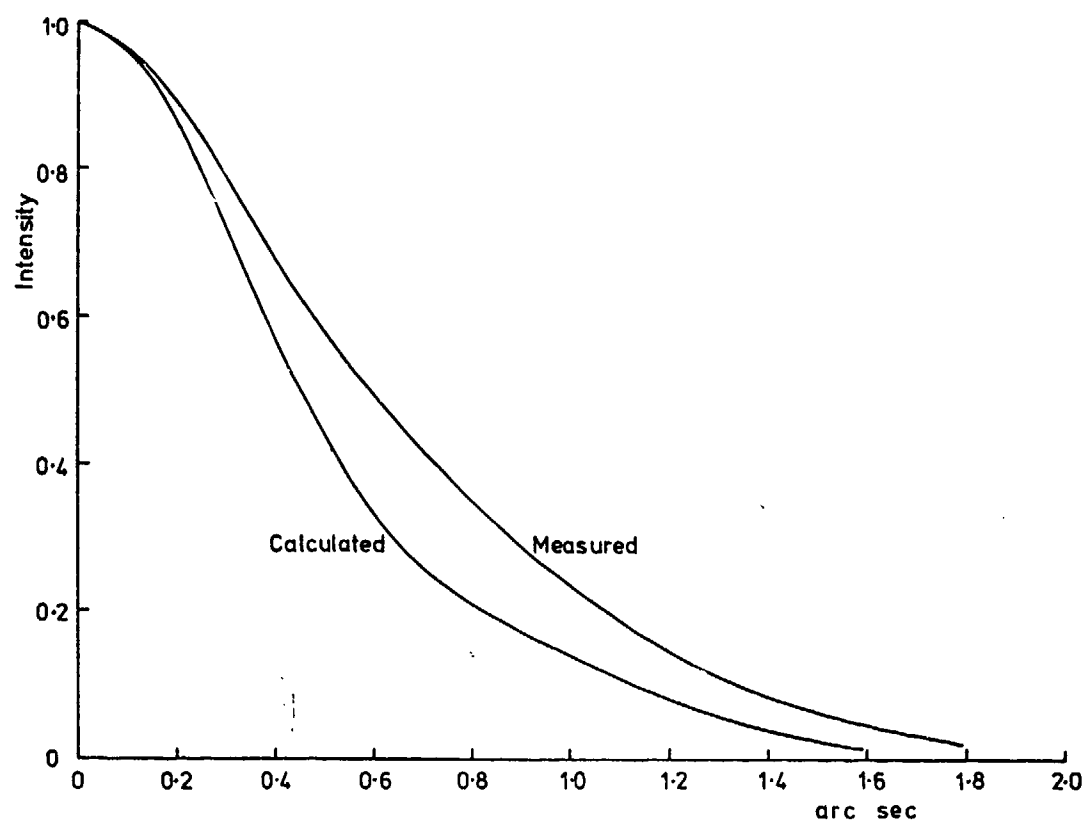


Figure 5 Comparison of point spread functions obtained by direct measurement (contains aberrations of imaging optics) and by computation from the MTF (independent of aberrations).

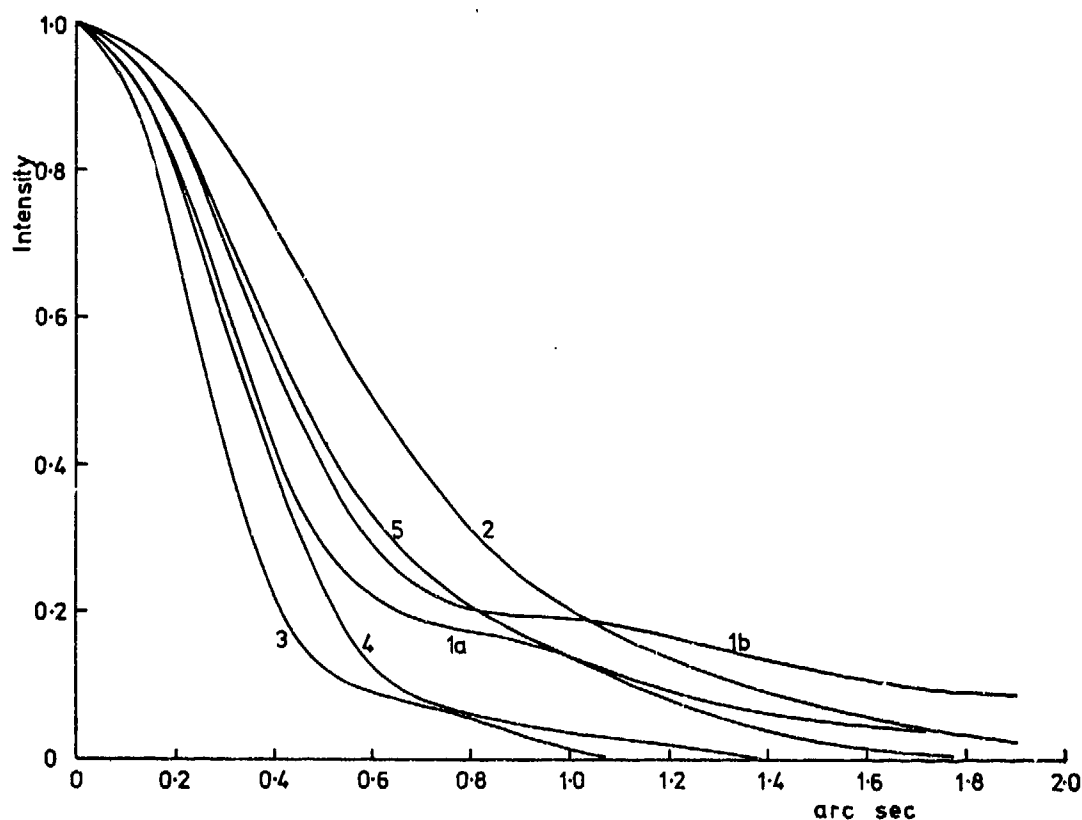


Figure 6 Point spread functions due to seeing computed from typical MTFs for nights 1 to 5.

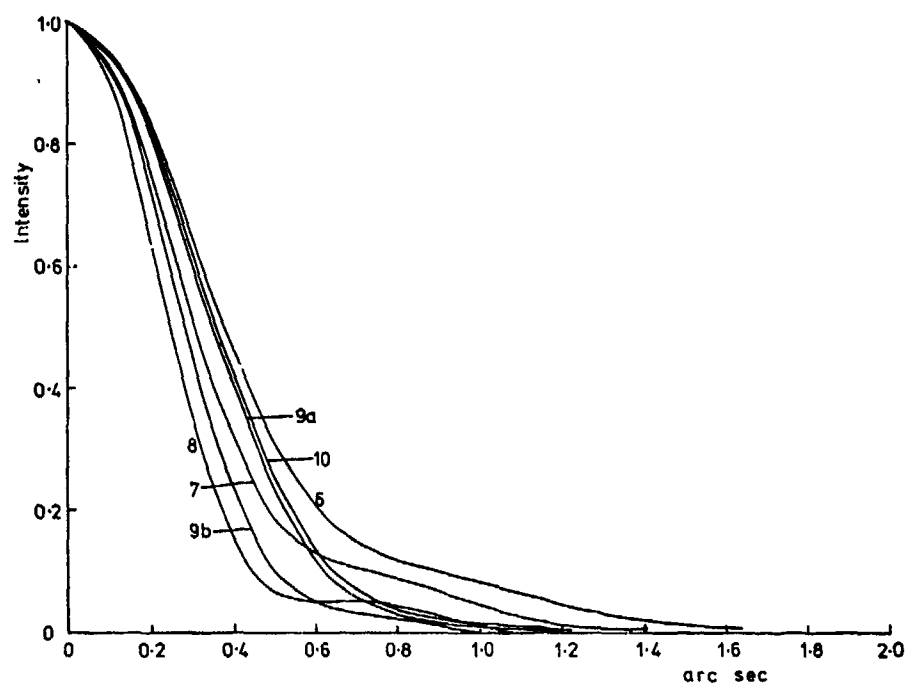


Figure 7 Point spread functions due to seeing computed from typical MTFs for nights 6 to 10.

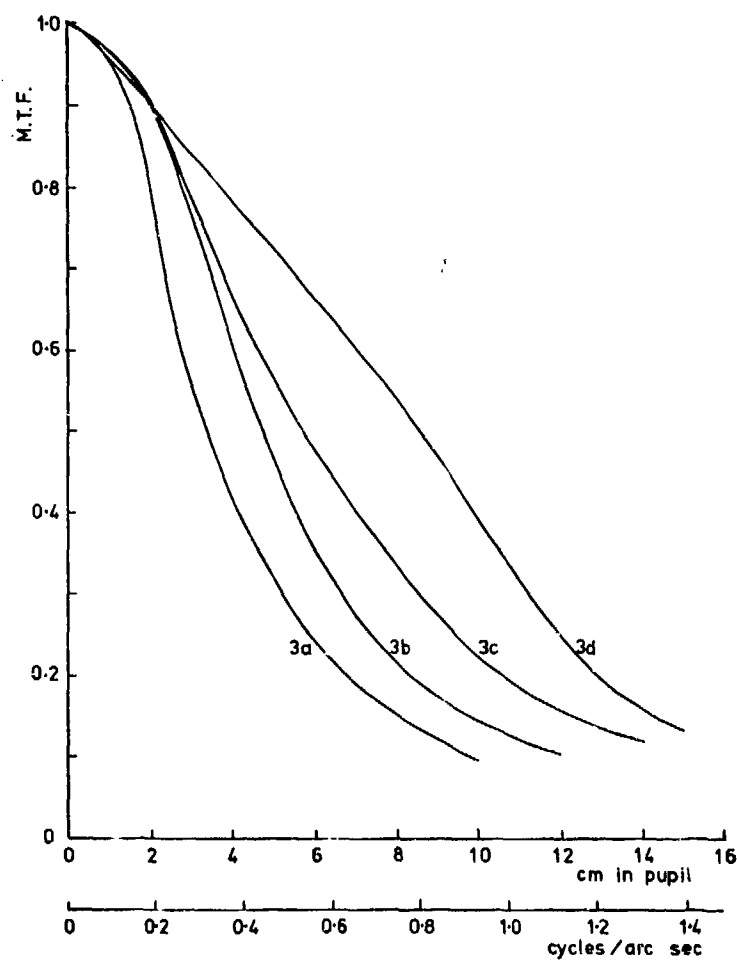


Figure 8 Variation of MTF throughout the third night;
(a) local time (LT) = 21.40, (b) LT = 23.50,
(c) LT = 01.00 and (d) LT = 03.25

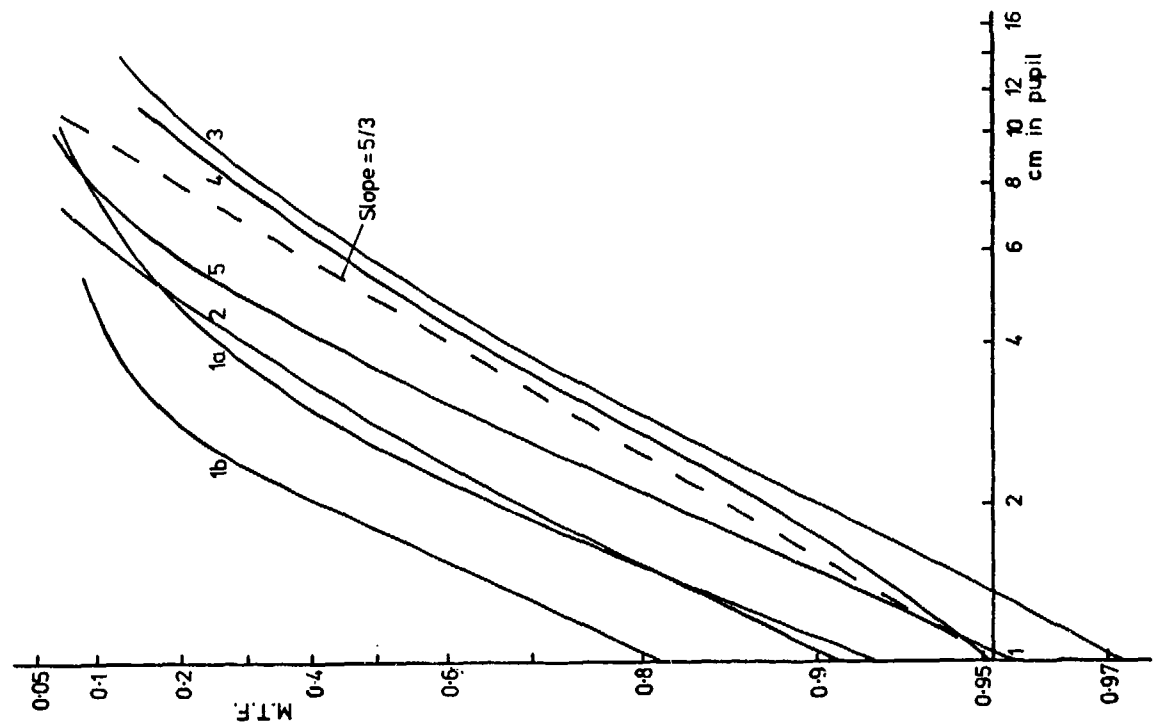


Figure 9 MTFs measured at zenith angles of 10° and 47° .

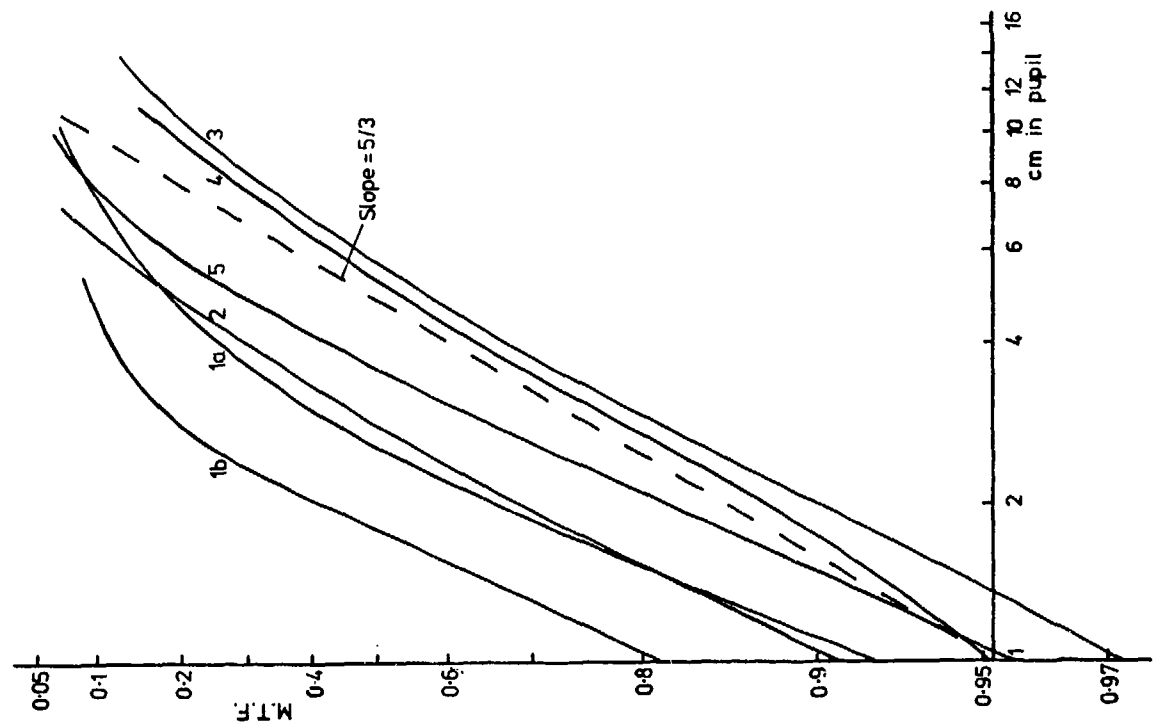


Figure 10 MTF curves of Figure 3 for nights 1 to 5 re-plotted on logarithmic scales. For a Kolmogorov spectrum the slopes should equal $5/3$.

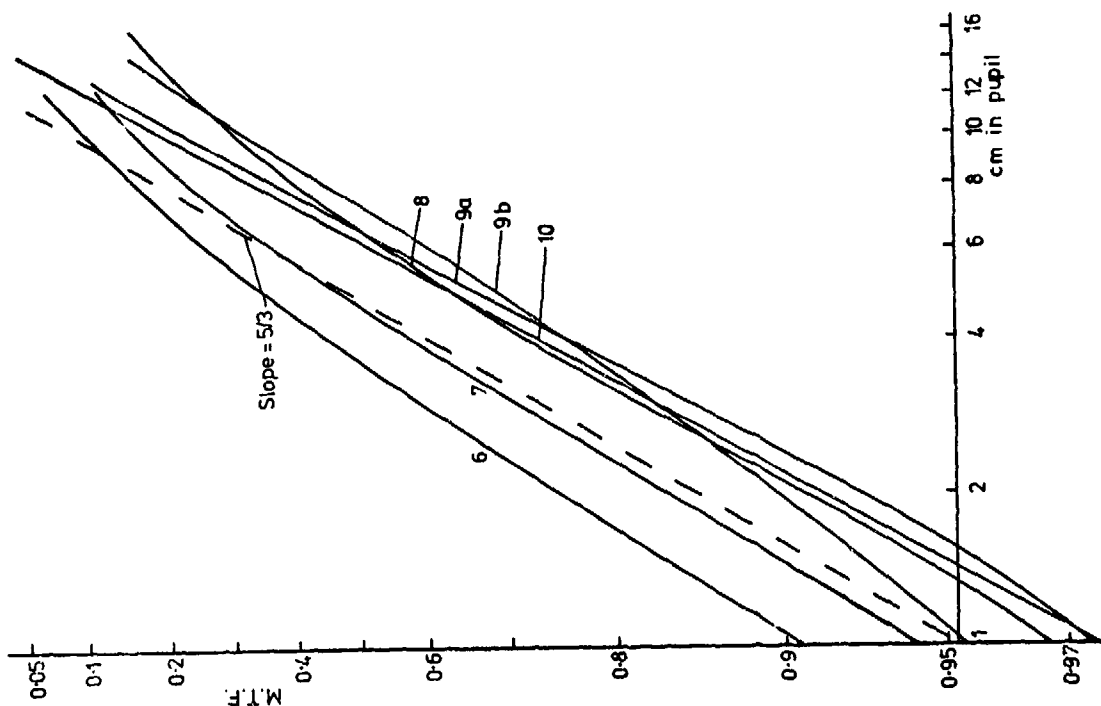


Figure 11 MTF curves of Figure 4 for nights 6 to 10 re-plotted on logarithmic scales.

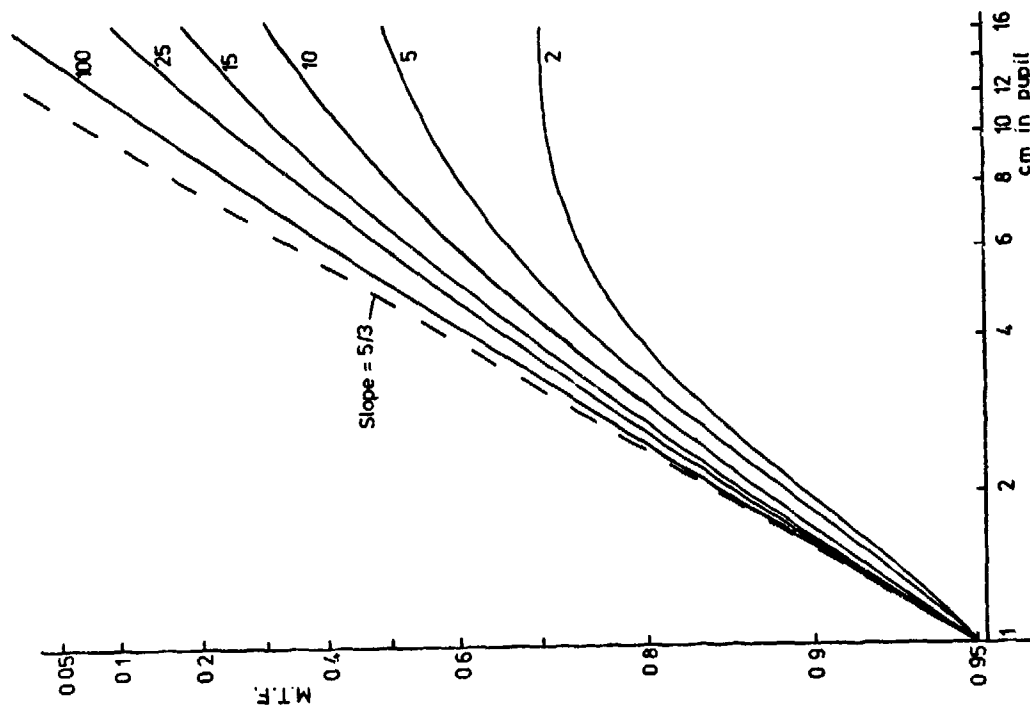


Figure 12 Effect of turbulence on theoretical MTF curves plotted on logarithmic scales for λ_0 values of 2, 5, 10, 15, 25 and 100 cm. Curves are arbitrarily normalised to $M(\rho) = 0.95$ at $\rho = 1$ cm.

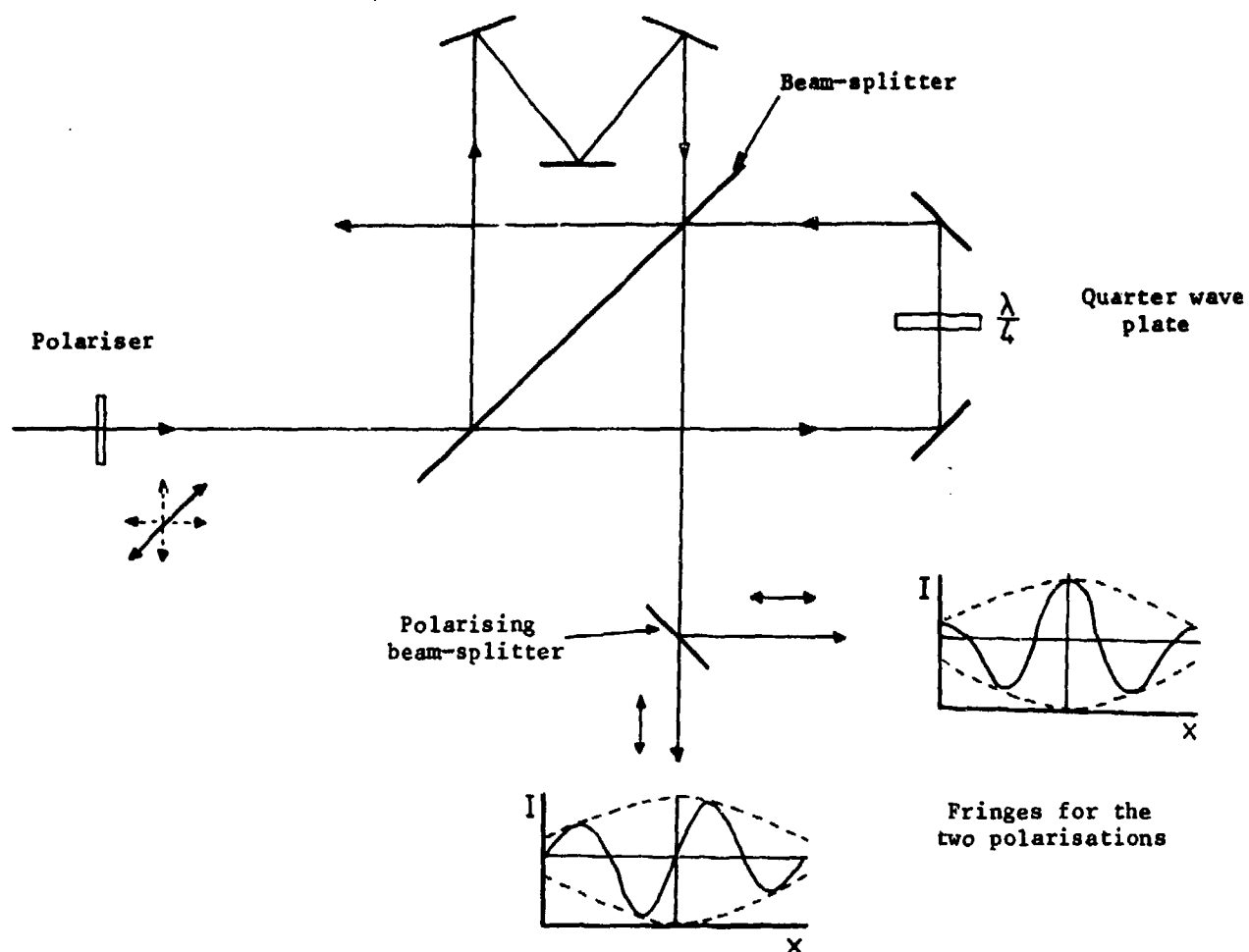


Figure 13 Diagram of proposed interferometer showing polarising components and the fringes obtained in the two output beams.

INTENSITY CORRELATION OF RADIATION SCATTERED ALONG THE PATH OF A LASER BEAM
PROPAGATING IN THE ATMOSPHERE.

M. Bertolotti, Istituto di Fisica Ingegneria, Università di Roma, Roma, Italy

M. Carnevale, B. Crosignani, B. Daino, P. Di Porto, Fondazione U. Bordoni, Viale Trastevere,
108, Roma, Italy

SUMMARY

Correlation properties of the electromagnetic field scattered away from the direction of propagating of a laser beam are studied. The correlation could be used for whenever a direct measurement of the scattered intensity is difficult due to background radiation.

Resides, correlation measurements can be connected with the scale of atmospheric turbulence.

1. INTRODUCTION

The purpose of this communication is to study the characteristic features of light scattered away from a laser beam travelling in the turbulent atmosphere.

It will be demonstrated that this scattered light has coherence properties different from the background and this fact can be used in principle to discriminate in a detector the contribution of scattered laser light from the surrounding sun light.

Let us consider a laser beam travelling in the turbulent atmosphere and a photomultiplier which sees a segment ℓ of the beam through a solid angle $\delta\Omega$ (S. Fig. 1). The electric field of the light impinging on the photomultiplier can be written as

$$\vec{E}_t = \vec{E}_L + \vec{E}_B \quad (1)$$

where \vec{E}_L is the electric field due to the scattered laser light and \vec{E}_B is the electric field due to the background produced essentially by sun light scattered by the atmosphere on the photomultiplier.

If we look at the second order correlation function of the field we have

$$\langle |\vec{E}_t(t)|^2 |\vec{E}_t(0)|^2 \rangle = \langle |\vec{E}_L(t) + \vec{E}_B(t)|^2 |\vec{E}_L(0) + \vec{E}_B(0)|^2 \rangle \quad (2)$$

which due to the statistical independence of the fields \vec{E}_L and \vec{E}_B is simply

$$\begin{aligned} \langle |\vec{E}_t(t)|^2 |\vec{E}_t(0)|^2 \rangle &= \langle |\vec{E}_L(t)|^2 |\vec{E}_L(0)|^2 \rangle + \langle |\vec{E}_B(t)|^2 |\vec{E}_B(0)|^2 \rangle + \\ &+ 2 \langle |\vec{E}_L(0)|^2 \rangle \langle |\vec{E}_B(0)|^2 \rangle + [\langle \vec{E}_B(t) \cdot \vec{E}_B^*(0) \rangle \langle \vec{E}_L^*(t) \cdot \vec{E}_L(0) \rangle + c.c.] \end{aligned} \quad (3)$$

Now let us put attention to the temporal behavior of our correlation function. The correlation time of the background field \vec{E}_B is very short so that, on the time scale of the measurement,

$$\langle |\vec{E}_B(t)|^2 |\vec{E}_B(0)|^2 \rangle = \langle |\vec{E}_B(0)|^2 \rangle^2$$

and

$$\langle \vec{E}_B(t) \cdot \vec{E}_B^*(0) \rangle = 0$$

Finally, we have

$$\langle |\vec{E}_t(t)|^2 |\vec{E}_t(0)|^2 \rangle = \langle |\vec{E}_L(t)|^2 |\vec{E}_L(0)|^2 \rangle + \langle |\vec{E}_B(0)|^2 \rangle^2 \left[1 + \frac{2 \langle |\vec{E}_L(0)|^2 \rangle}{\langle |\vec{E}_B(0)|^2 \rangle} \right] \quad (4)$$

The second order correlation function of the total field on the photomultiplier is therefore just equal, besides a constant term, to the second-order correlation function of the scattered laser field.

2. CALCULATION OF THE SECOND-ORDER CORRELATION FUNCTION OF SCATTERED LASER LIGHT.

Let us, now, consider the first and second-order correlation function of the electric field scattered by an ensemble of identical Mie particles embedded in the atmosphere, under single scattering approximation. This will allow us to have an insight into the statistical properties of the scattered radiation, which will be shown to differ from those of a chaotic field.

We suppose scatterers undergoing turbulent and Brownian motions, stochastic in nature, as well as a deterministic motion due to a drift velocity \vec{U}_0 of the atmosphere, and an incident field, with fixed polarization and with amplitude and phase-fluctuations, which are essentially due to the influence of the atmosphere.

The incident field is given by

$$\vec{E}_I(\vec{r}, t) = \vec{E}_I(t) e^{i[\vec{K}_I \cdot \vec{r} - \omega_I t - \beta(\vec{r}, t)]} \quad (5)$$

where $\vec{E}_I(t)$ is a stochastic real vector with a fixed direction and $\beta(\vec{r}, t)$ a random phase, ω_I and \vec{K}_I representing respectively the average angular frequency and wave number ($K_I = \omega_I/c$) of the quasi-monochromatic incident field. Both quantities $\vec{E}_I(t)$ and $\beta(\vec{r}, t)$ are supposed to suffer temporal fluctuations over time scale much larger than the characteristic period of light. The spatial coordinate does not appear in $\vec{E}_I(t)$ while the phase β is allowed to fluctuate over a generical distance ℓ_p .

The scattered field $\vec{E}_L(\vec{R}, t)$ is of the form

$$\vec{E}_L(\vec{R}, t) = \sum_{i=1}^N \vec{A}(t) e^{i\phi} e^{i\vec{K} \cdot \vec{r}_i(t-R/c) - i\omega_I t - i\beta[\vec{r}_i(t-R/c), t-R/c]} \quad (6)$$

where $\vec{A}(t)$ is a real vector depending on \vec{R} with a fixed direction and a magnitude following the fluctuations of $\vec{E}_I(t)$, $\vec{K} = \vec{K}_I - \vec{K}_S$, ϕ depends on $R \gg \ell_s$ (having chosen the origin of coordinates in a point inside V_S), and the index i ranges over the scatterers, whose number N is supposed to undergo negligible fluctuations. In writing Eq.(6), we have made the realistic assumptions that $\vec{E}_I(t)$ does not vary appreciably in the time interval ℓ_s/c spent by light in crossing V_S , that $v \ell_s / \lambda c \ll 1$ and that

$$|\beta(v \ell_s / c, \ell_s / c) - \beta(0, 0)| \ll 2\pi$$

where v labels an average scatterer velocity, since this entails the possibility of neglecting retardation effects between the microfields scattered by each particle and to use a unique time $t - R/c$. We have also used the relation $\vec{A}(t) \approx \vec{A}(t - R/c)$ due to the slowness of amplitude fluctuations.

We have

$$\vec{r}_i(t) = \int_0^t \vec{U}[\vec{r}_i(t'), t'] dt' + \vec{r}_{B,i}(t) + \vec{r}_{i,0} \quad (7)$$

where $\vec{U} = \vec{U}_0 + \vec{U}'$, \vec{U}' being the fluctuating turbulent atmospheric velocity, $\vec{r}_{B,i}(t)$ represents the displacement of the i -th particle in the time interval $(0, t)$ associated with Brownian motion, and $\vec{r}_{i,0} \equiv \vec{r}_i(0)$.

Introducing Eq.(7) into Eq.(6) we obtain

$$\begin{aligned} \langle \vec{E}_L(t) \cdot \vec{E}_L^*(0) \rangle &= N \langle \vec{A}(t) \cdot \vec{A}(0) \rangle e^{i(\vec{K} \cdot \vec{U}_0 - \omega_I t)} \langle e^{i\vec{K} \cdot \vec{r}_B(t)} \rangle \\ &\times \langle e^{i\vec{K} \cdot \int_0^t \vec{U}'[\vec{r}(t', \vec{r}_0), t'] dt'} \rangle e^{-i[\beta(\vec{U}_0 t, t) - \beta(0, 0)]} \end{aligned} \quad (8)$$

where the symbol $\langle \dots \rangle$ indicates ensemble-averaging operation, $\vec{r}(t, \vec{r}_0)$ labels the position at time t of the scattering element started at position \vec{r}_0 at time t_0 , $\vec{r}_B(t)$ is the Brownian displacement undergone by an arbitrarily chosen particle in a time interval t , and use has been made of the statistical independence between the quantities enclosed in different brackets and of the vanishing of the terms with $i \neq j$ due to the relation $\langle \exp(i\vec{K} \cdot \vec{r}_{ij}) \rangle = 0$ (\vec{r}_i and \vec{r}_j are not correlated for $i \neq j$). The small turbulent and Brownian displacements have been neglected with respect to the spatial scale of the fluctuations of β . The incident field has been assumed to be stationary and the scattering system homogeneous and stationary.

Let us consider the four averages appearing in Eq.(8). Assuming a log-normal probability distribution for the amplitude

$$P(A) = \frac{1}{\sigma A \sqrt{2\pi}} e^{-\frac{[\ln(A/A_0) + \frac{1}{2}\sigma^2]^2}{2\sigma^2}} \quad (9)$$

one has

$$\begin{aligned} \langle A \rangle &= A_0 \\ \langle A^2 \rangle &= A_0^2 e^{\sigma^2} \end{aligned} \quad (10)$$

which is consistent with

$$\langle A(t) A(0) \rangle = A_0^2 (e^{\sigma^2} - 1) h(t) + A_0^2 \quad (11)$$

where $h(t)$ plays the role of temporal normalized amplitude correlation function and ranges from $h(0) = 1$ to $h(t_I) \approx 0$, t_I representing the "correlation time" of amplitude fluctuations.

The second average, involving the turbulent velocities, is given by

$$\langle e^{i\vec{K} \cdot \int_0^t \vec{U}'[\vec{r}(t', \vec{r}_0), t'] dt'} \rangle = e^{-\kappa^2 \langle U_i^2 \rangle t^2 / 2} \quad (12)$$

with $U_i = \vec{U} \cdot \vec{k} / k$, where we have used the fact that U_i does not vary appreciably in the small time necessary for the vanishing of $\langle \vec{E}(t) \cdot \vec{E}^*(0) \rangle$ (see Eq.17), and the property

$$\langle e^{i\psi} \rangle = e^{-\langle \psi^2 \rangle / 2} \quad (13)$$

valid for a normally distribute variable ψ .

The Brownian factor is

$$\langle e^{i\vec{K} \cdot \vec{r}_B(t)} \rangle = e^{-\kappa^2 \frac{KT}{m\alpha} t} \quad (14)$$

where K is the Boltzmann's constant, T the absolute temperature, m the particle mass and $\alpha = 6\pi a \eta / m$, with a and η representing respectively the radius of the particle and the coefficient of viscosity (Chandrasekhar, S., 1943).

The fourth average can be written as

$$\langle e^{-i[\beta(\vec{v}_0, t) - \beta(0,0)]} \rangle = e^{-\langle \beta^2 \rangle [1 - \phi(\vec{v}_0 t) G(t)]} \quad (15)$$

where we have used Eq.(13) and the assumption

$$\langle \beta(\vec{r}, t) \beta(0,0) \rangle = \langle \beta^2 \rangle \phi(\vec{r}) G(t) \quad (16)$$

with $\phi(\vec{r})$ and $G(t)$ ranging from unity to zero respectively over the intervals $(0, \ell)$ and $(0, t)$, ℓ and t representing the correlation length and the correlation of the phase fluctuations.

By using Eqs.(11), (12), (14) and (15) one can write the expression of the first order correlation function given by Eq.(8) as

$$\begin{aligned} \langle \vec{E}_L(t) \cdot \vec{E}_L^*(0) \rangle &= N A_0^2 [(e^{\sigma^2} - 1) h(t) + 1] e^{i(\vec{K} \cdot \vec{v}_0 - \omega_L) t} \\ &\times e^{-\kappa^2 \langle U_i^2 \rangle t^2 / 2} e^{-\kappa^2 \frac{KT}{m\alpha} t} e^{-\langle \beta^2 \rangle [1 - \phi(\vec{v}_0 t) G(t)]} \end{aligned} \quad (17)$$

Let us now evaluate the second order correlation function. From Eq.(6) we have

$$\begin{aligned} \langle |\vec{E}_L(t)|^2 |\vec{E}_L(0)|^2 \rangle &= \langle A^2(t) A^2(0) \rangle \sum_{i,j,\ell,m}^{1/N} \langle e^{i\vec{K} \cdot (\vec{r}_{i0} - \vec{r}_{j0} + \vec{r}_{\ell 0} - \vec{r}_{m0})} \\ &\times e^{i\vec{K} \cdot \int_0^t \vec{U}[\vec{r}(t', \vec{r}_{i0}), t'] dt'} e^{-i\vec{K} \cdot \int_0^t \vec{U}[\vec{r}(t', \vec{r}_{j0}), t'] dt'} e^{i\vec{K} \cdot [\vec{r}_{\ell i}(t) - \vec{r}_{\ell j}(t)]} \\ &\times e^{-i[\beta(\vec{r}_{i0} + \vec{v}_0 t, t) - \beta(\vec{r}_{j0} + \vec{v}_0 t, t) + \beta(\vec{r}_{\ell 0}, 0) - \beta(\vec{r}_{m0}, 0)]} \\ &= N^2 \langle A^2(t) A^2(0) \rangle + N(N-1) \langle A^2(t) A^2(0) \rangle \langle e^{i\vec{K} \cdot \int_0^t \vec{U}[\vec{r}(t', \vec{r}_{i0}), t'] dt'} \\ &\times e^{-i\vec{K} \cdot \int_0^t \vec{U}[\vec{r}(t', \vec{r}_{j0}), t'] dt'} e^{i\vec{K} \cdot \vec{r}_B(t)} \rangle^2 \langle e^{-i[\beta(\vec{r}_{i0} + \vec{v}_0 t, t) \\ &\times e^{-\beta(\vec{r}_{j0} + \vec{v}_0 t, t)}] \rangle \end{aligned} \quad (18)$$

The first term on the R.H.S. of Eq.(18) corresponds to $i=j$ and $\ell=m$, the second term corresponds to $i=m, j=\ell$, while all the other terms vanish due to the presence of rapidly oscillating factors of the kind $\exp(i\vec{k} \cdot \vec{r}_{\ell 0})$.

We now observe that Eq.(9) implies

$$\langle A^4 \rangle = A_0^4 e^{6\sigma^2} \quad (19)$$

which is consistent with

$$\langle A^2(t) A^2(0) \rangle = A_0^4 e^{2\sigma^2} (e^{4\sigma^2} - 1) g(t) + A_0^4 e^{2\sigma^2} \quad (20)$$

where $g(t)$ behaves as $h(t)$.

The use of Eqs.(20),(14),(16) and of Eq.(13), applied to the Gaussian fluctuations of phases and turbulent velocities, allows to write Eq.(18) in the form

$$\begin{aligned} \langle |\vec{E}_L(t)|^2 |\vec{E}_L(0)|^2 \rangle &= N^2 A_0^4 e^{2\sigma^2} [(e^{4\sigma^2} - 1) h^2(t) + 1] \\ &+ N^2 A_0^4 e^{2\sigma^2} [(e^{4\sigma^2} - 1) h^2(t) + 1] \frac{1}{V_s^2} \\ &\times \iint_{V_s} e^{-\kappa^2 \langle \vec{V}_i^2 \rangle} [1 - f(\vec{r}_L - \vec{r}'')] t^2 d\vec{r}' d\vec{r}'' \quad (21) \\ &\times e^{-2\kappa^2 \frac{\kappa T}{m\omega}} e^{-2\langle \beta^2 \rangle} [1 - \phi(\vec{V}_0 t) G(t)] e^{-\frac{2\beta^2}{V_s^2} \left[-\iint \phi(\vec{r}_L - \vec{r}') d\vec{r}' d\vec{r}'' + \iint \phi(\vec{r}_L - \vec{r}' + \vec{V}_0 t) G(t) d\vec{r}' d\vec{r}'' \right]} \end{aligned}$$

where f is the normalized correlation function of velocity fluctuations defined as

$$f(\vec{r}_L - \vec{r}'') = \frac{\langle \vec{V}_L(\vec{r}_L) \vec{V}_L(\vec{r}'') \rangle}{\langle \vec{V}_L^2 \rangle} \quad (22)$$

and $N(N-1) \approx N^2$.

The two Eqs.(17) and (21) furnish

$$\begin{aligned} \langle |\vec{E}_L(t)|^2 |\vec{E}_L(0)|^2 \rangle &= [(e^{4\sigma^2} - 1) h(t) + 1] \langle |\vec{E}_L(0)|^2 \rangle \\ &+ \frac{e^{2\sigma^2} [(e^{4\sigma^2} - 1) h^2(t) + 1]}{[(e^{4\sigma^2} - 1) h(t) + 1]^2} |\langle \vec{E}_L(t) \cdot \vec{E}_L^*(0) \rangle|^2 \\ &\times \frac{1}{V_s^2} \iint e^{\kappa^2 \langle \vec{V}_i^2 \rangle} f(\vec{r}_L - \vec{r}'') t^2 d\vec{r}' d\vec{r}'' e^{2\langle \beta^2 \rangle} \frac{1}{V_s^2} \iint [\phi(\vec{r}_L - \vec{r}') - \phi(\vec{r}_L - \vec{r}' + \vec{V}_0 t) G(t)] d\vec{r}' d\vec{r}'' \quad (23) \end{aligned}$$

We observe that Eq.(23) shows the departure of the scattered field from a chaotic Gaussian radiation, which would behave as (Glauber, R.J., 1963)

$$\langle |\vec{E}_L(t)|^2 |\vec{E}_L(0)|^2 \rangle = \langle |\vec{E}_L(0)|^2 \rangle + |\langle \vec{E}_L(t) \cdot \vec{E}_L^*(0) \rangle|^2 \quad (24)$$

is connected with the intensity and phase fluctuations of the incident field, as well as with the ones of the turbulent velocities.

Equation (21) indicates that the asymptotic value

$$\langle |\vec{E}_L(\infty)|^2 |\vec{E}_L(0)|^2 \rangle = \langle |\vec{E}_L(t)|^2 \rangle^2 = N^2 A_0^4 e^{2\sigma^2} \quad (25)$$

is reached with the characteristic time scale t_I , and with the smallest between the two times $t_B = m \propto 1/k^2 K T$, $t_I = 1/k \langle u_1^2 \rangle$ in the case $V_S/V_T \gg 1$, V_T representing the correlation volume of turbulent velocities. For $V_S/V_T \ll 1$, t_I tends to infinity.

Let us now consider the situation of spatial fluctuation of the incident amplitude taking place over a correlation length ℓ_I such that $\ell_I^3 \ll V_S$. The starting Eq.(7) has to be modified by means of the substitution

$$\vec{A}(t) \rightarrow \vec{A}[\vec{r}_i(t), t]$$

which implies

$$\begin{aligned} \langle \vec{E}_L(t) \cdot \vec{E}_L^*(0) \rangle &= N A_0^2 [(e^{\sigma^2} - 1) h(t) s(\vec{v}_0 t) + 1] e^{i(\vec{k} \cdot \vec{v}_0 - \omega_I)t} \\ &\times e^{-\kappa^2 \langle v_1^2 \rangle t^2/2} e^{-\kappa^2 \frac{KT}{m\alpha} t} e^{-\langle \beta^2 \rangle [1 - \phi(\vec{v}_0 t) G(t)]} \end{aligned} \quad (26)$$

having assumed

$$\langle A(\vec{r}_{i_0} + \vec{v}_0 t, t) A(\vec{r}_{i_0}, 0) \rangle = A_0^2 [(e^{\sigma^2} - 1) h(t) s(\vec{v}_0 t) + 1] \quad (27)$$

with $s(\vec{r})$ ranging from unity to zero over the interval $(0, \ell_I)$, and turbulent and Brownian displacements negligible with respect to ℓ_I in the times of interest.

The second order correlation function can be obtained by observing that the assumption $\ell_I^3 \ll V_S$ implies, in practice, statistical independence between amplitude relative to positions of different particles, so that

$$\langle A^2(\vec{r}_{i_0} + \vec{v}_0 t, t) A^2(\vec{r}_{e_0}, 0) \rangle = \langle A^2 \rangle^2 = A_0^4 e^{2\sigma^2} \quad (i \neq e) \quad (28)$$

(we can correctly neglect the N terms with $i=j = \ell = m$) and (see Eq.(27))

$$\begin{aligned} \langle A(\vec{r}_{i_0} + \vec{v}_0 t, t) A(\vec{r}_{j_0} + \vec{v}_0 t, t) A(\vec{r}_{j_0}, 0) A(\vec{r}_{i_0}, 0) \rangle &= \\ = \langle A(\vec{r}_{i_0} + \vec{v}_0 t, t) A(\vec{r}_{i_0}, 0) \rangle^2 &= \left\{ A_0^2 [(e^{\sigma^2} - 1) h(t) s(\vec{v}_0 t) + 1] \right\}^2, \quad i \neq j \end{aligned} \quad (29)$$

We must now substitute the factor $\langle A^2(t)A^2(0) \rangle$ in the first and second terms in the R.H.S. of Eq.(18) respectively with the R.H.S. of Eqs.(28) and (29), thus obtaining with the help of Eq.(21)

$$\begin{aligned} \langle |\vec{E}_L(t)|^2 |\vec{E}_L(0)|^2 \rangle &= N^2 A_0^4 e^{2\sigma^2} + N^2 \left\{ A_0^2 \left[(e^{\sigma^2} - 1) h(t) s(\vec{v}_0 t) + 1 \right] \right\}^2 \\ &\times \frac{1}{V_s^2} \iint e^{-\kappa^2 \langle U_i^2 \rangle} [1 - f(\vec{r}_i - \vec{r}_{ii})] t^2 d\vec{r}_i d\vec{r}_{ii} e^{2\kappa^2 \frac{KT}{m\alpha} t - 2\beta^2 [1 - \phi(\vec{v}_0 t) G(t)]} \end{aligned} \quad (30)$$

where we have assumed a small phase-correlation length satisfying the relation $\ell_p^3 \ll V_s$. A comparison between Eqs.(26) and (30) gives

$$\begin{aligned} \langle |\vec{E}_L(t)|^2 |\vec{E}_L(0)|^2 \rangle &= \langle |\vec{E}_L(0)|^2 \rangle^2 + |\langle \vec{E}_L(t) \cdot \vec{E}_L^*(0) \rangle|^2 \\ &\times \frac{1}{V_s^2} \iint e^{-\kappa^2 \langle U_i^2 \rangle} f(\vec{r}_i - \vec{r}_{ii}) t^2 d\vec{r}_i d\vec{r}_{ii} \end{aligned} \quad (31)$$

which shows that the departure from a Gaussian statistical behavior of the scattered field is only due to correlations of turbulent velocities. This was to be expected on the basis of the Central Limit Theorem, since the smallness of ℓ_i and ℓ_p implies that the statistical dependence between the microfields scattered by each particle is only connected with turbulence as in the case of an ideal incident monochromatic plane wave (Di Porto et al., 1969, Crosignani et al. 1975).

From Eqs.(4), (23) and (31) it appears that it is possible to distinguish between the light scattered by a laser beam travelling in the turbulent atmosphere and the background sun light.

The experimental scheme is the one shown in Fig.1. The second-order correlation function of the laser field is given by Eqs.(23) or (31) provided that the scattered light is seen in a coherence area.

By varying the solid angle $\delta\Omega$ at the receiver from $\delta\Omega_1 > (\ell/R)^2$ to $\delta\Omega_2 < (\ell/R)^2$, ℓ being the length over which the fluctuations of the different quantities are correlated, a change in the temporal behavior of the correlation function must be seen, according to a graphic similar to Fig.2. The solar light contributes only with a background.

Finally, if we look with an angle $\delta\Omega_1$, the second order correlation function of the field at the receiver is the sum of a constant background plus a time dependent part fluctuating with the shortest of the different times t_B, t_T , and eventually having a tail of length t_I . If, on the contrary, $\delta\Omega$ is changed in such a way that $\delta\Omega < (\ell/R)^2$, the time t_T increases and the temporal behavior of the correlation function is now associated with the shortest of the times t_B and t_I . If the intensity fluctuations are practically not correlated in space, the time scale is given only by t_B .

We have therefore two distinct ways to detect the scattered laser light, that is or by looking for a time behavior in the region around 1 sec (and also for a time behavior in the region around 1 msec, if Eq.(23) can be applied in the case $\delta\Omega_1 > (\ell/R)^2$), or by looking for a change in the temporal behavior of the correlation function by decreasing the solid angle at the receiver.

This last measurement can be also made by performing intensity correlation measurements from two different small volumes at different positions along the direction of propagation of the laser beam (Bertolotti et al., 1971). If the distance between the two volumes is smaller than ℓ_t or ℓ_i , the signal has a time correlated part which is much slower than that associated with a large scattering volume.

3. EXPERIMENTAL RESULTS OBTAINED IN THE LABORATORY

A first measurement has been performed in the laboratory by using smoke particles as scatterers. The intensity correlation of light scattered by a volume of varying dimension ℓ was measured as a function of ℓ . The results are shown in Fig. 3, in which the normalized conditional probability

$$p_c(\tau) = \frac{\langle |\vec{E}(t+\tau)|^2 |\vec{E}(t)|^2 \rangle}{\langle |\vec{E}(t)|^2 \rangle} \quad (32)$$

is plotted as a function of τ with ℓ as a parameter. It is clearly seen a time behavior of $p_c(\tau)$, with a decay time of the order of $t_T \approx 2.5 \times 10^{-4}$ sec, due to the turbulent motion of small particles, which is present for large values of ℓ . When ℓ is decreased to about 3 cm, the temporal behavior of $p_c(\tau)$ exhibits a definite change, becoming slower and slower. This fact can have interesting applications:

- 1) if one knows the distance at which the beam is passing, we can calculate the value of ℓ at which $p_c(\tau)$ changes its time behavior and, accordingly, the correlation length of the turbulence fluctuations ℓ_T can be measured;
- 2) if the distance at which the beam is passing is not known, the knowledge of ℓ_T can furnish a rough idea of its value.

Finally, we can make some considerations on the signal to noise ratio. The physical measured quantity is

$$p_c(\tau) = \frac{\langle |\vec{E}_L(\tau)|^2 |\vec{E}_L(0)|^2 \rangle + \langle |\vec{E}_B(0)|^2 \rangle [1 + 2 \langle |\vec{E}_L(0)|^2 \rangle / \langle |\vec{E}_B(0)|^2 \rangle]}{\langle |\vec{E}_L(0)|^2 \rangle + \langle |\vec{E}_B(0)|^2 \rangle^2 [1 + 2 \langle |\vec{E}_L(0)|^2 \rangle / \langle |\vec{E}_B(0)|^2 \rangle]} \quad (33)$$

If we put

$$\frac{\langle |\vec{E}_L(0)|^2 \rangle}{\langle |\vec{E}_B(0)|^2 \rangle} = \gamma, \quad \langle |\vec{E}_L(\tau)|^2 |\vec{E}_L(0)|^2 \rangle = G^{(2)}(\tau), \quad \langle |\vec{E}_B(0)|^2 \rangle = I_B \quad (34)$$

we have

$$p_c(\tau) = \frac{G^{(2)}(\tau) + I_B(1 + 2\gamma)}{2 I_B^2 \gamma^2 + I_B^2(1 + 2\gamma)} \quad (35)$$

so that

$$\delta = \frac{p_c(0)}{p_c(\infty)} = 1 + \frac{\gamma^2}{\gamma^2 + 2\gamma + 1} \quad (36)$$

This allows to give an order of magnitude of the smallest laser signal which can be detected. For example, in order to have $\delta = 1.01$, must be $\gamma = 0.09$.

BIBLIOGRAPHY

- S. Chandrasekhar, Rev. Mod. Phys. 15, 1 (1943)
 R.J. Glauber, Phys. Rev. 131, 2766 (1963)
 P. Di Porto, B. Crosignani, and M. Bertolotti, J. Appl. Phys. 40, 5083 (1969)
 B. Crosignani, P. Di Porto, and M. Bertolotti, "Statistical properties of scattered light", Academic Press, New York, 1975
 M. Bertolotti, B. Crosignani, B. Daino, and P. Di Porto, J. Phys. A (Gen. Phys.) 4, L47 (1971)

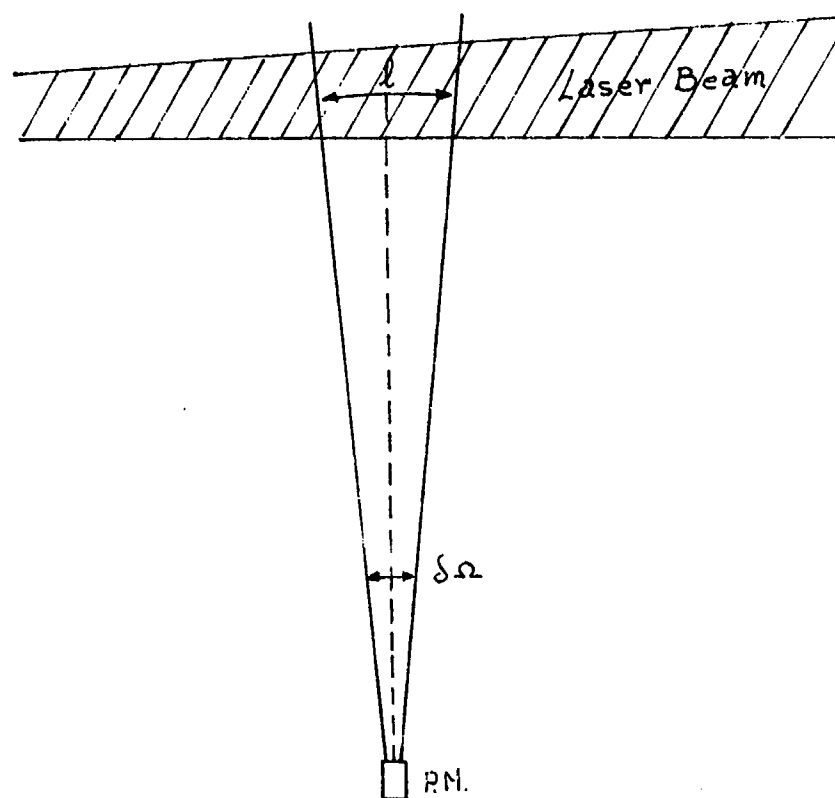


Fig. 1 - Experimental scheme.

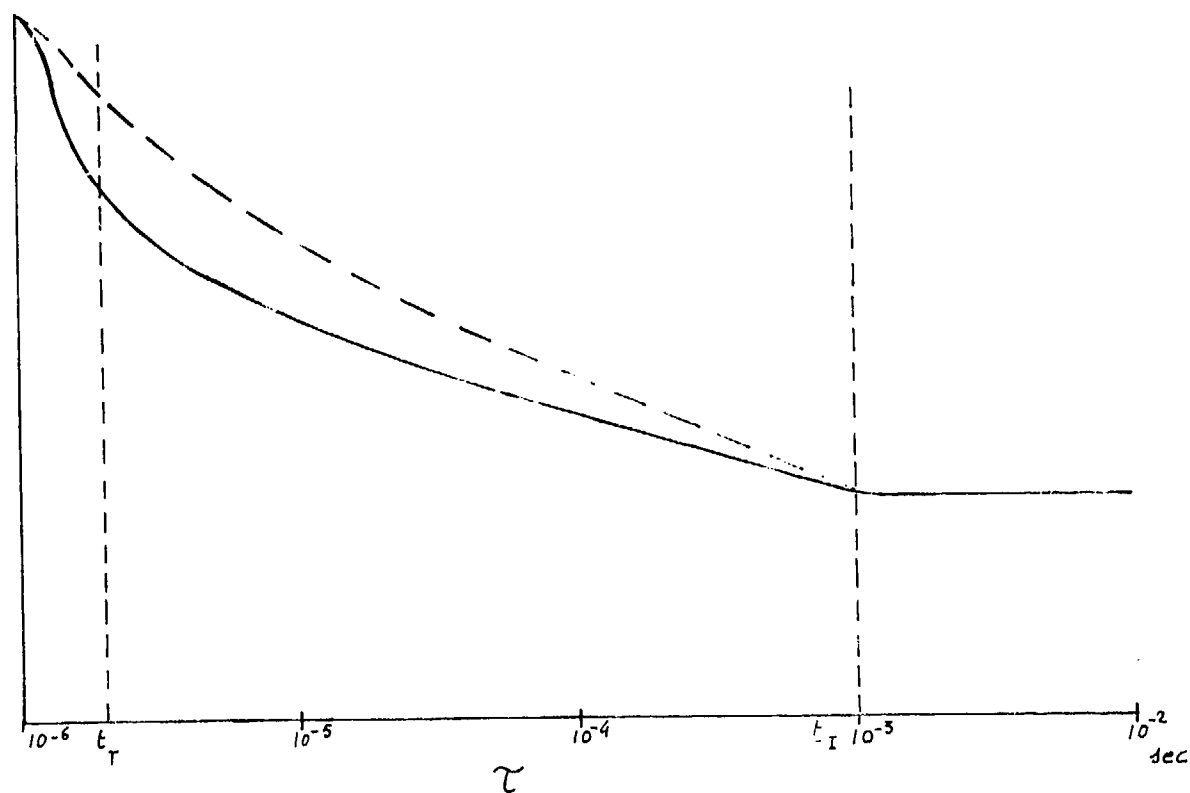


Fig. 2 - Temporal behaviour of the correlation function.

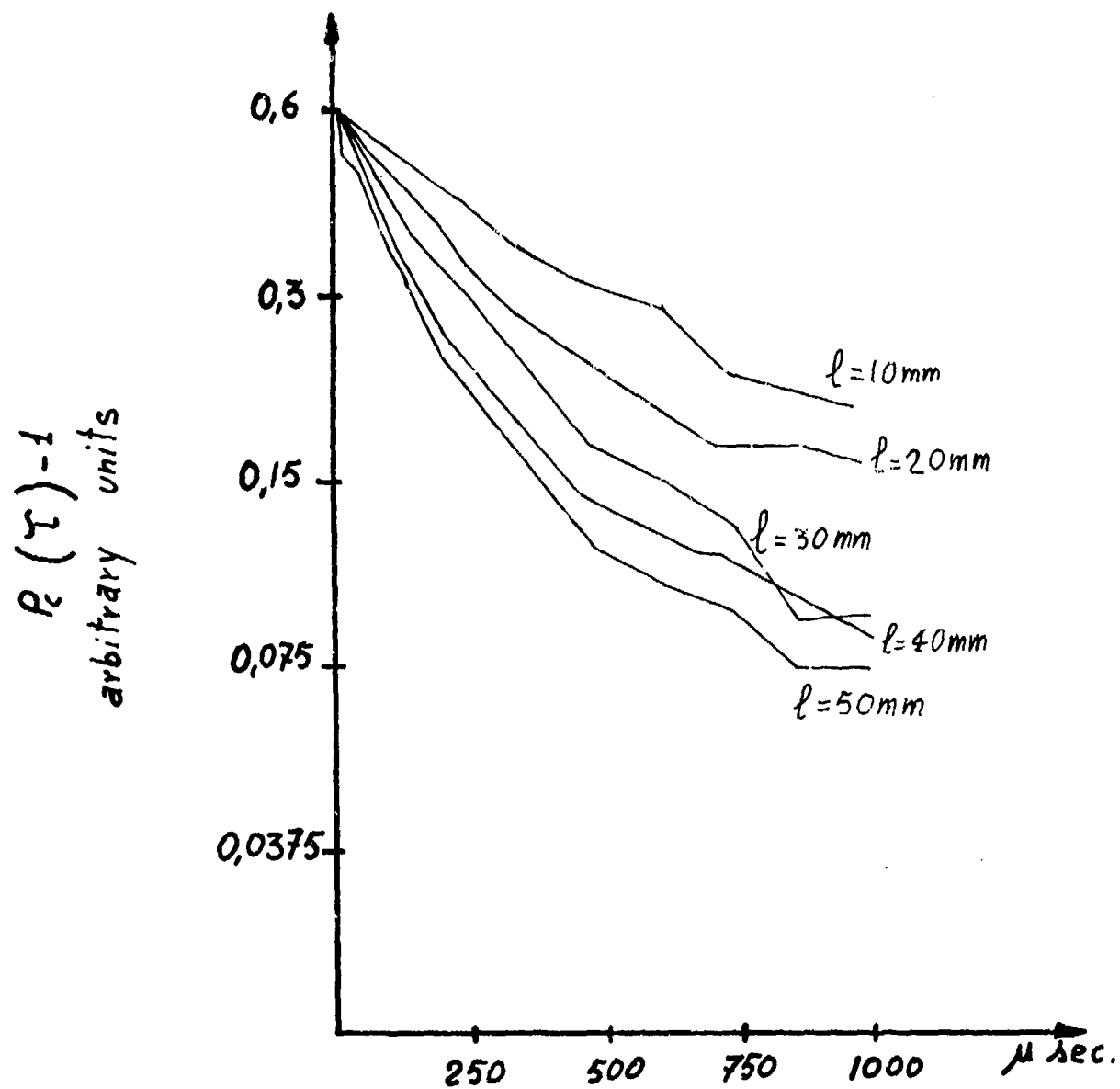


Fig. 3 - Normalized conditional probability as a function of τ

MEASUREMENT OF ATMOSPHERIC ATTENUATION AT 6328 Å

M. Bertolotti, Istituto di Fisica Ingegneria, Università di Roma, Roma, Italy

M. Carnevale, B. Daino, M. Galeotti, Fondazione Ugo Bordoni, Viale Trastevere, 108 Roma, Italy

D. Sette, Istituto di Fisica Ingegneria, Università di Roma, Italy

SUMMARY

The influence of the free atmosphere on the propagation properties of laser beams has been studied at Fondazione U. Bordoni in two different researches.

In the first one, that is now ended, the performances of a communication link are studied through the determination of atmospheric attenuation statistics.

In the second one, now in progress, more direct attention to the effects of turbulence and atmospheric conditions on the propagation of laser beams is paid.

1. STATISTICAL MEASUREMENTS OF 6328 Å ATMOSPHERIC ATTENUATION (*)

The statistics of the atmospheric attenuation plays a determinant role in the evaluation of the confidence level of a laser optical link.

Once the transmitted power and the received power required for a given performance of the system are known, it is the atmospheric attenuation statistics that determines the percentage of time of correct operation of the link.

An extensive study of such a statistics has been performed in Rome, using a sequential laser transmissometer. The scheme of the system is shown in fig. 1. A metallised beam splitter *S* splits the beam of a stabilised 6328 Å He-Ne laser *M*, linearly polarised. One of the two resulting beams is transmitted through the telescope *T*, and is back reflected after a 45 m. path by the reflecting prism *P* towards a photodetector *D*, placed near the transmitter. The output of *D* is sent to a recorder *R*. The other beam is sent through a polarisation analyzer *A* to *D*. A segmented disk operated by an AC motor chops alternately the two beams. Some diaphragms are inserted on the paths to avoid errors due to spurious rays. The transmitted beam diameter is about 1 cm after the transmitting telescope and is slightly larger at the detecting section. The disk chopper is such that in a cycle (lasting 2 min.) the background, the background plus the reference beam, the background plus the received beam are measured respectively for 20, 50 and 50 s. Filtering to reject the background has not been found necessary.

In known atmospheric attenuation conditions the system is calibrated adjusting the power of the reference beam by rotating the analyser until the recorder records a reference to received beam power ratio equal to the atmospheric attenuation. After this calibration the system is operated. The evaluation of the atmospheric attenuation for the calibration is made by measuring the transmitted beam power at the exit of the telescope and at the arrival at the input of the detector *D*, and taking into account the attenuation of the reflecting prism *P*.

Obviously, this calibration is made in quiet weather conditions, in order to have stable attenuation. With this technique an accuracy of about 2% on the ratio of the two beam powers has been obtained. The attenuation is deduced by reading the powers of the reference and of the transmitted beam at the instant corresponding to the exchange of the beams on the detector. The time of the commutation from a beam to the other is short enough to insure that no drift effects have taken place in the apparatus. The instrument

has been operated in our measurements for about $2 \cdot 10^3$ hours, from september 1973 to september 1974. It was operated by an automatic switch set to collect data from 7 a.m. to 2,30 p.m. in every weather condition. Particularly important for the aim of telecommunications, is the cumulative probability distribution of the attenuation, in the range of probability and attenuations that one can expect to be interesting. For this reason our elaboration of the data has been focussed to give this kind of information. A cumulative distribution of the statistical frequency of occurrence of attenuation is reported in fig.2. These data refer to the period 20 september 1973 - 30 june 1974, for a time of measurement of 1446 hours. They evidence the relatively low frequency with which appreciable attenuations (greater than 10 dB/Km) occur in our town. Attenuations greater than 6 dB/Km only have been considered in this elaboration. The continuous line gives the statistical frequency with which attenuations greater than the value reported on the abscissas occur, the dotted one the frequency with which attenuations comprised between the values corresponding to the extremes of the horizontal segments occur. Another interesting information can be the values of the greatest attenuation that has been found in the period. It was 31 dB/Km and occurred on may 6th in heavy rain and hail. During that storm, the attenuation has been greater than 15 dB/Km for about 8 minutes. In fig.3 another cumulative attenuation distribution is reported. It is relative to the three months april, may and june 1974. Here the attenuations considered in the elaboration of data start from 3 dB/Km.

2. MEASUREMENTS OF ATMOSPHERIC ATTENUATION OF HE-NE LASER (**)

The attenuation of a He-Ne laser beam propagated through the free atmosphere has been measured, as a function of time.

We can distinguish two characteristic times in the variations of the attenuation: one referring to the slow fluctuations and one referring to the fast ones.

Fast fluctuations are due to the turbulence and the spectrum is centered around 40-50 Hz with a tail towards some tenth of hertz (scintillation). Slow fluctuations occur in times of the order of some minute or hours, when one must consider molecular absorption or scattering, varying with the instantaneous composition of the atmosphere and the meteorological situation (wind velocity, humidity, temperature, etc.). We are interested in these slow fluctuations, not only from the point of view of statistical collection of data referring to our link, but also by searching for correlations with meteorological parameters. The parameters taken under consideration are temperature, relative humidity, visibility and wind velocity. Another parameter can be added: the rainfall rate.

The propagation is in an urban zone and is 300 m long.

The beam of a 6 mW laser is enlarged by means of a telescope; the diameter of the spot on the receiver is about 30 cm. This arrangement avoids fluctuations of the intensity caused by beam dancing. (The dancing is never strong in our path).

A photocell is used as a receiver with a high response at 6328 Å. A continuous measurement of the attenuation is made.

Fig. 4, as an example, shows a recording of the received signal and of the behaviour of the temperature. Fig. 5 shows the mean received power over samples lasting about 30 minutes each for a period of 24 hours. The behaviour of relative humidity and temperature is also shown.

In order to search for correlation time of slow fluctuations of the attenuation, the autocorrelation function has been calculated. Fig.6 shows, as an example, the autocorrelation function of the beam attenuation of a sample lasting more than 24 hours; in the considered day, which was a quiet sunny day, the attenuation varied with a correlation time of the order of several hours.

Calculations of the cross-correlation with meteorological parameters are in progress.

3. ACKNOWLEDGEMENT

We thank dr L. Muzil for his collaboration to the research exposed in the second paragraph of this paper.

*) This research has been performed by M. Galeotti, B. Dalno and D. Sette.

**) This research has been performed by M. Bertolotti, M. Carnevale and D. Sette.

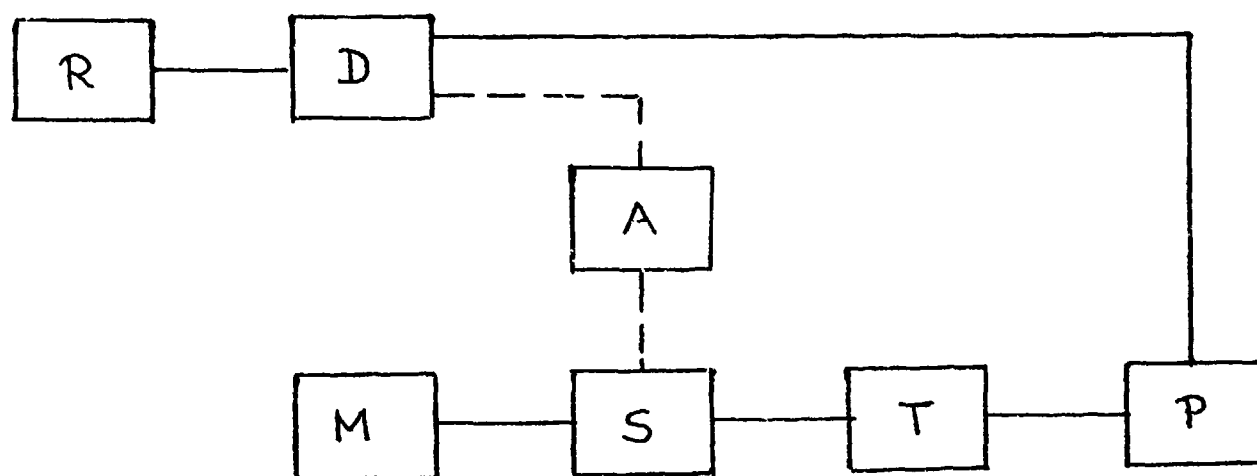


Fig. 1 - Scheme of the system

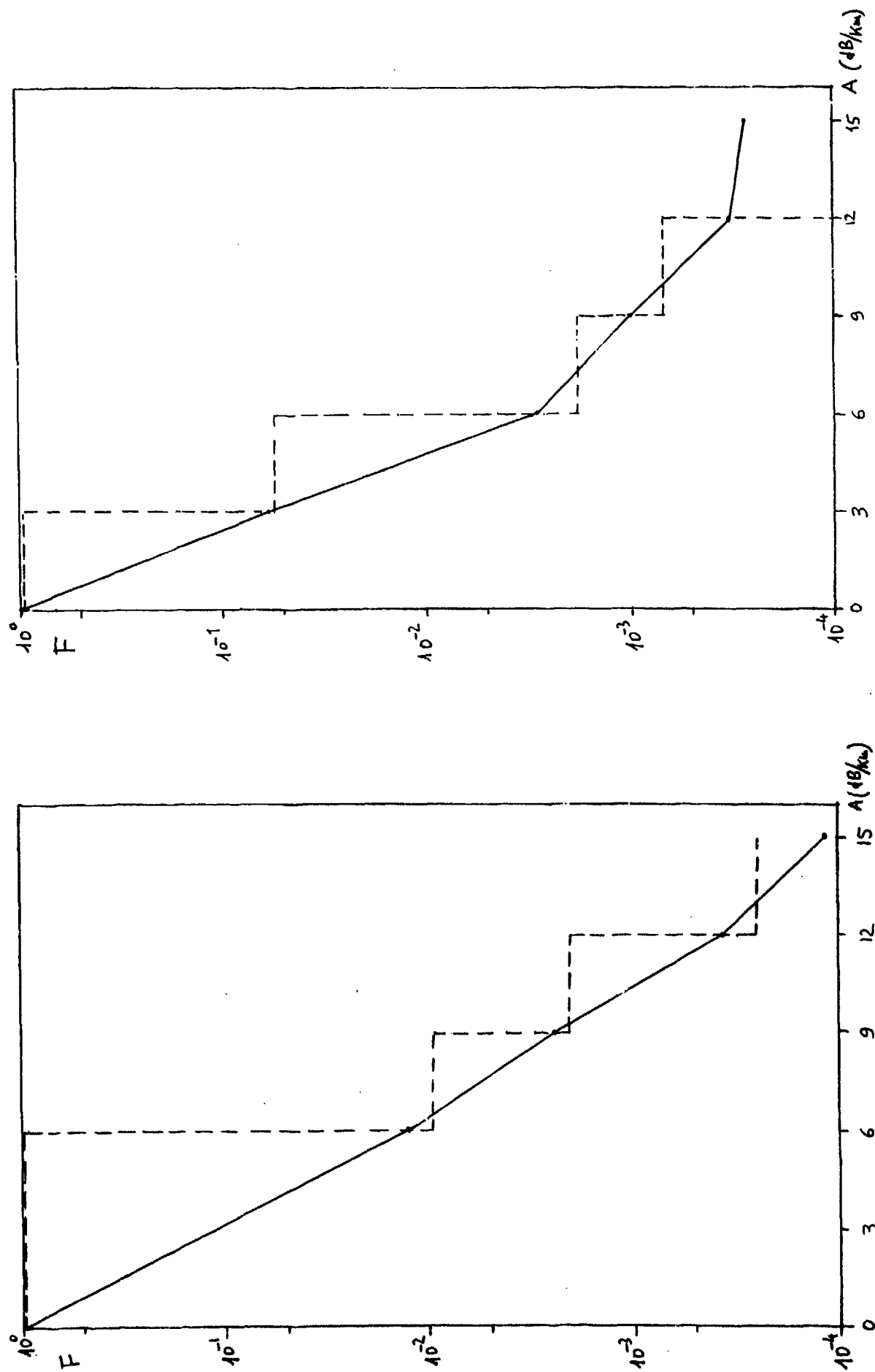


Fig. 2 - Statistical frequency of the attenuations (20 sept. 1973 - 30 june 1974)

Fig. 3 - Statistical frequency of the attenuations (april - june 1974)

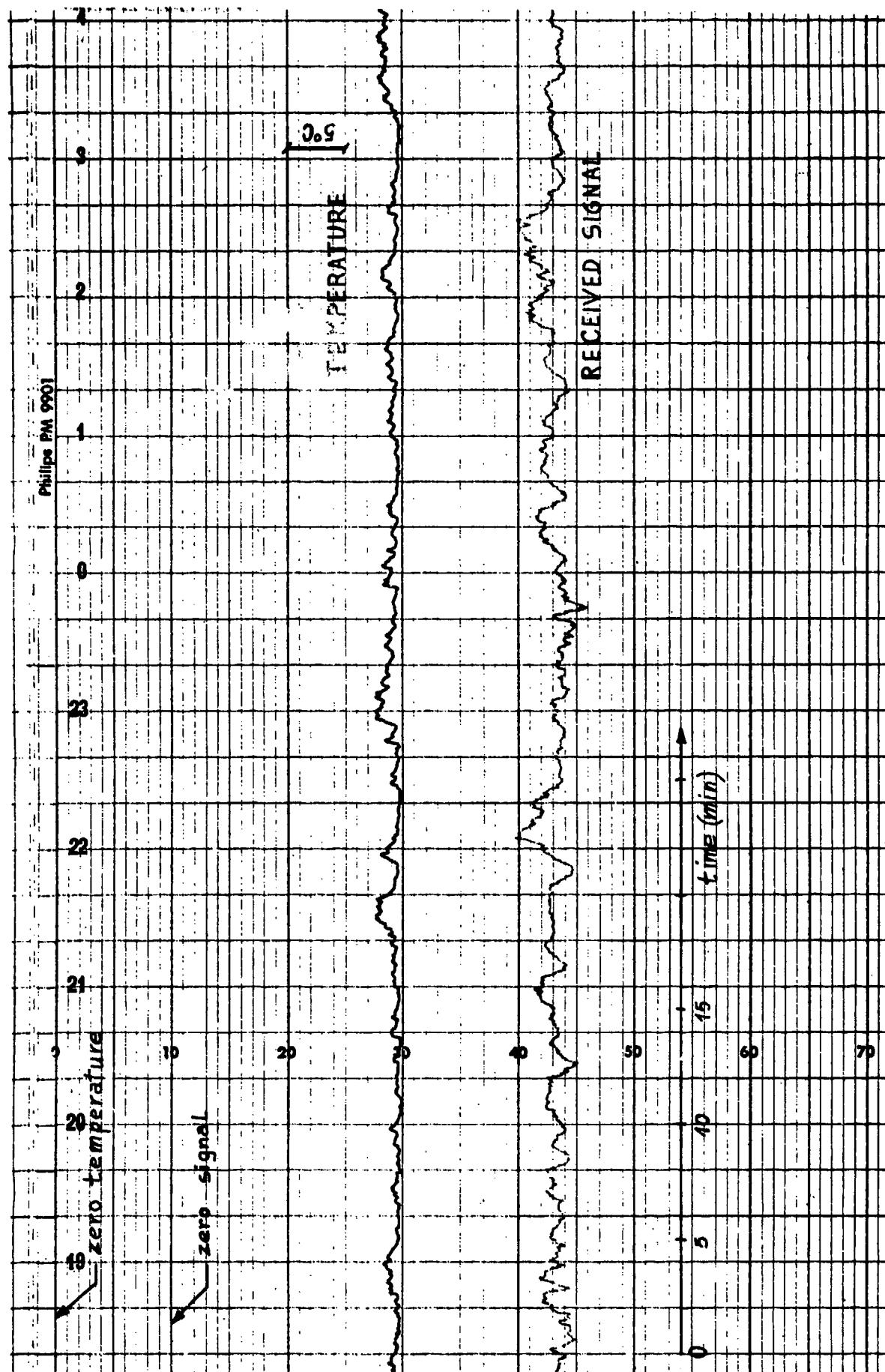


Fig. 4 - The received signal and the temperature as a function of the time.

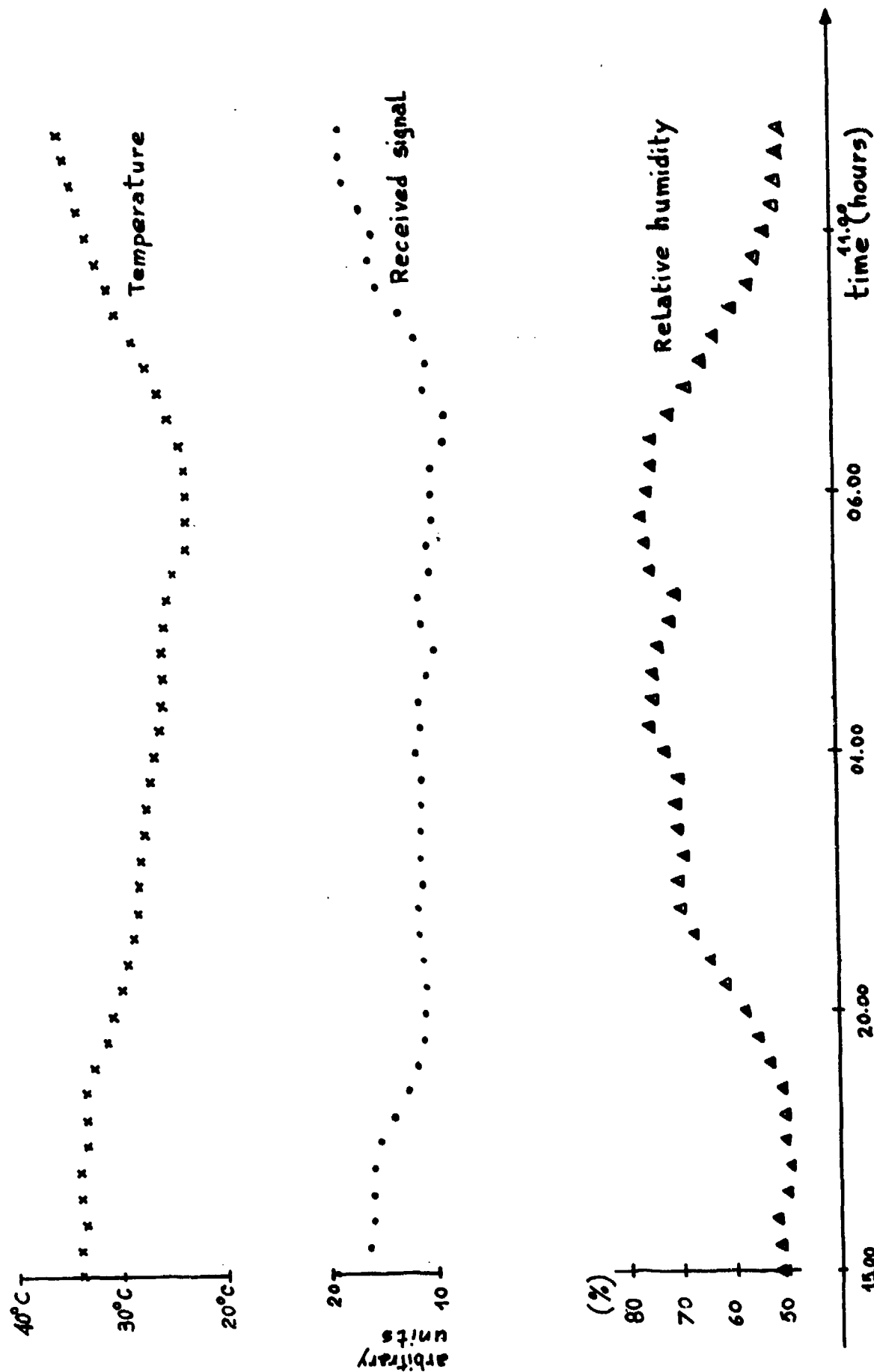


Fig. 5 - Behaviour of the received signal, of the temperature and of the relative humidity in a 24 hours period.

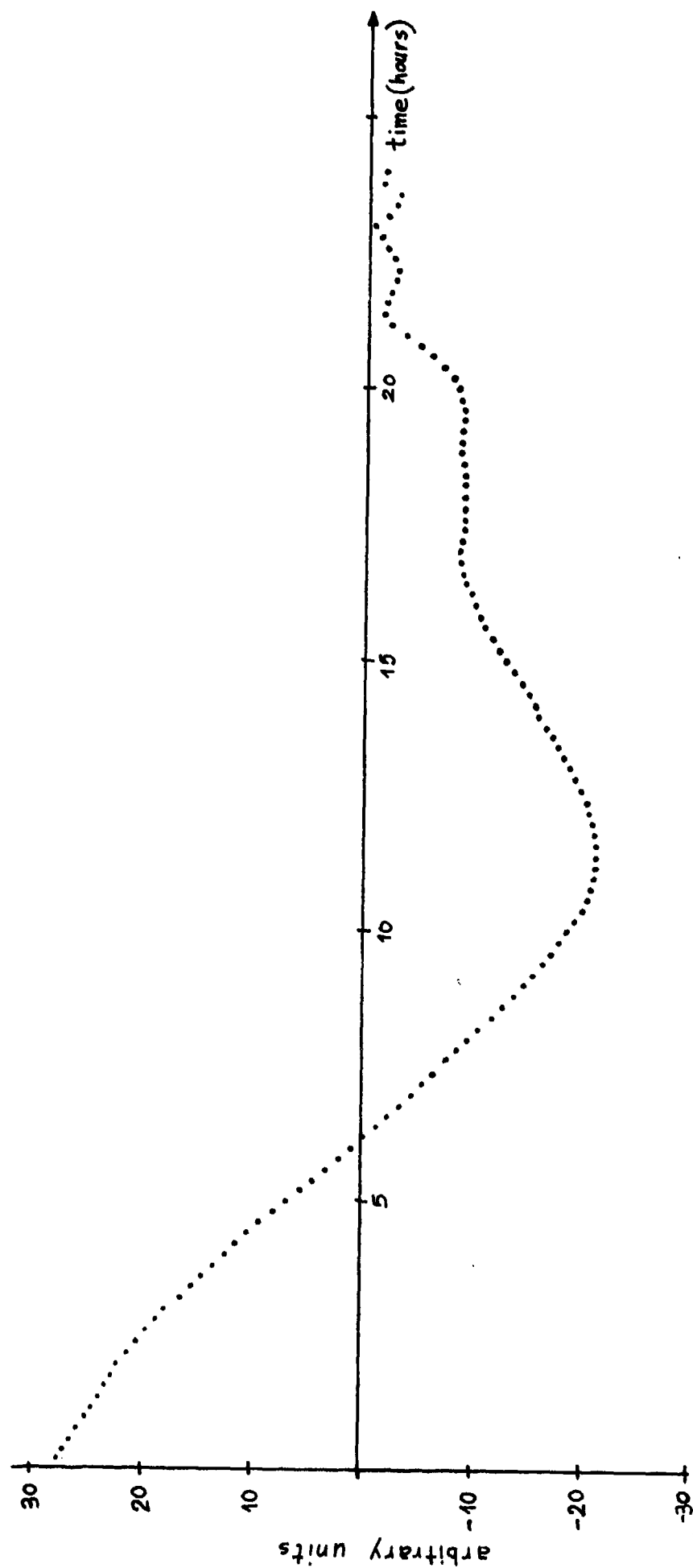


Fig. 6 - Autocorrelation function of the received signal.

MEASUREMENTS OF ANGLE OF ARRIVAL FLUCTUATIONS OF A LASER BEAM DUE TO TURBULENCE

Anna Consortini
Istituto di Ricerca sulle Onde Elettromagnetiche of C.N.R.
Via Panciatichi, 64
50127 Firenze (Italy)

SUMMARY

Measurements are reported of angle of arrival fluctuations of a diverging laser beam after propagation through turbulence, firstly through a thin layer of artificial turbulence, then through the atmosphere at near ground levels. In the first case the influence of the position of the layer is put in evidence. In the case of the atmosphere approximate values of the inner scale of turbulence λ_0 and the structure constant C_n^2 are derived by a comparison with the theory of Tatarski.

1. INTRODUCTION

In recent years we developed a procedure for measuring the fluctuations of angle of arrival at points over a front of an electromagnetic wave, at optical frequency, after propagation through a turbulent medium (ARRIGUCCI A., et alii, 1971; CONSORTINI A., et alii, 1972).

It has been pointed out by several Authors (e.g. Tatarski V.I., 1967; Strohbehn G.W., 1970) that such a kind of measurements are of great importance for the investigation of the turbulence, because they are extremely sensitive to the shape of the spectrum of the turbulence in the inertial subrange and consequently allow a determination of the inner scale λ_0 of the turbulence. Moreover the knowledge of the wavefront distortion by atmospheric turbulence is of importance also for fast detection processing of blurred images as well as for the adaptive techniques for the elimination of image degradation.

In the present paper the results are reported of measurements of angle of arrival fluctuations for a diverging laser beam after a path firstly through a thin layer of artificial turbulence (CONSORTINI A., et alii, 1974), then through the atmosphere at near ground levels. From these measurements the structure functions of the angles of arrival are derived. In the case of atmospheric turbulence propagation the inner scale λ_0 and the structure constant C_n^2 are derived by a comparison with Tatarski's theory.

2. PROPAGATION THROUGH A THIN LAYER OF TURBULENCE

At the emergence of a wave from a turbulent medium the normal to the corrugated wavefront at a point P can be specified by two angles α and β describing its deviation from the unperturbed direction in two orthogonal planes normal to the wavefront. As usual α and β are taken in the horizontal and vertical plane respectively. Fig. 1 refers to our case of spherical wave; α_1, β_1 and α_2, β_2 denote the angles at the two points P_1 and P_2 .

The method for measuring the angle fluctuations is sketched in Fig. 2 and consists essentially in a particular use of the Hartman text. A beam from a laser traverses a layer of turbulent medium, produced by a heater, and then impinges on a mask where small holes, equispaced by ρ , have been made along two perpendicular rows. At a suitable distance, S, from the holed mask a diffusing screen is placed, which intersects the rays emerging from the mask. An analysis of the position of the spots on the screen allows the measurement of the angles at the emergence from the mask. We will call these angles α' and β' in order to distinguish them from those (α and β) at the emergence from the turbulent layer. With reference to Fig. 3 it can be easily shown that, in a first approximation, α and β are related to α' and β' by

$$\begin{aligned}\alpha &= \alpha' \frac{R+L}{R} \\ \beta &= \beta' \frac{R+L}{R}\end{aligned}\tag{1}$$

where R and L denote the distances of the heater from source and holed mask respectively

(Fig.1). Therefore the measurement of σ' , π' allows one to obtain also σ and π . Measurements were made for different locations of the heater; series of measurements were also made in the absence of heater in order to reveal the effect of the turbulence of the room. We will indicate this effect as environmental effect.

The distance $R + L$ source - mask (Fig.1) was kept constant, $R + L = 14$ m - The holes on the mask are 2.5 mm in diameter at a distance $\rho_0 = 1$ cm from one another. Pictures were taken every second with an exposure time $\tau = 1/500$ sec. We used a Hasselblad 500 EL photographic camera with central iris shutter in order to freeze in simultaneously the whole event on the whole photogram. Fig. 4 shows an example of the spots.

The position of each spot is determined manually by measuring the coordinates of the center of the circle which best fits the spot.

A statistical analysis of the fluctuations of the coordinates of the centers of the spots and consequently of σ' and π' is performed by an electronic computer. The quantities obtained are: the structure functions $D_{\sigma'}$, and $D_{\pi'}$, of σ' and π' respectively, both for horizontal and vertical points. Recall that $D_{\sigma'}$ is defined as:

$$D_{\sigma'} = \langle [\sigma'(P_1) - \sigma'(P_2)]^2 \rangle \quad (2)$$

Where the brackets denote averages. An analogous relation holds for $D_{\pi'}$.

The cross correlation function $C_{\sigma', \pi'}$, defined as

$$C_{\sigma', \pi'} = \langle \sigma'(P_1) \pi'(P_2) \rangle \quad (3)$$

is also derived both for points in the horizontal and in the vertical row.

Fig.5 shows the structure function of the angle π' at the mask, plotted versus the distance ρ , in the case of horizontal points for a particular position of the heater along the path, $L = 10$ m. Dots represent the total effect (heater + environment) while crosses, which are obtained by subtracting from the total effect the structure function of the environment, represent the effect of heater only. This subtraction is possible owing to the fact that the two effects are uncorrelated.

It is interesting to note that while the total effect increases when ρ increases the effect due only to the heater tends to saturate for small values of ρ as expected. The different behaviour of the two curves can be explained, at least qualitatively, as an effect of the environment arising in the portion of thickness S (~ 10 m) between the holed mask and the diffusing screen. In this portion one has to deal with the propagation of thin beams, which are very sensitive to the turbulence, and whose structure function seems more affected by the outer than by the inner scale of turbulence, as it can be argued by a comparison between measurements (CONSORTINI A., et alii, 1970) of thin beams propagation and measurements of phase structure function (BURLAMACCHI P., et alii, 1969 and 1970). Typical values of the saturation distance for thin beams in practical cases are generally larger than 10 cm.

Fig.6 shows the correlation functions $C_{\sigma'}(\rho)$, $C_{\pi'}(\rho)$, $C_{\sigma', \pi'}(\rho)$ in a particular case ($L = 5$ m, vertical points, totale effect). As expected $C_{\sigma'}(\rho)$ and $C_{\pi'}(\rho)$ rapidly decrease when ρ increases. From Fig.6 it appears also that the value of the cross correlation function $C_{\sigma', \pi'}(\rho)$ can be considered vanishingly small, in agreement with the theory of Tatarsky. The values of $C_{\sigma', \pi'}$ can give us an idea of the order of magnitude of the systematic errors in the measurements. Analogous results are also obtained for the environmental effect, which indicate that also the "cross correlation" of the thin beams in the zone between mask and screen practically vanishes.

Fig. 7 shows $D_{\sigma'}(\text{sat})$, that is the "saturation" value of $D_{\sigma'}$, due to the heater, plotted versus the heater-mask distance. When L increases the fluctuations of σ' at the mask decrease, as expected. The dashed line is derived from Eq.(1).

3. ATMOSPHERIC PROPAGATION

Measurements have been made through the atmospheric turbulence at near ground levels, over paths of length $Z = 130$ m and $Z = 200$ m, at a height of 1 m and 1.5 m over ground. The beam from a He-Ne laser travels a folded path (not superimposed) in the

atmosphere, and is reflected back by one or more mirrors. Its diameter is of 1 mm at the output from the laser and about 15 cm after the 130 m path.

A picture was taken every second, so that the events in every picture can be considered uncorrelated with those in the previous one. Moreover a sufficiently high number of pictures can be taken in a sufficiently short time (5 to 10 minutes) to consider the turbulence unchanged.

Different persons separately read the coordinates of the centers of the spots in order to reduce the operator's error. In fact the measured values of the fluctuations are very small and not far from the errors of measurements, as will be seen from Fig.8.

Fig.8 shows the structure functions of α and β for points in the horizontal plane as obtained by the measurements of two different operators (crosses and circles) in the case of a path length $Z = 130$ m at an height $h \approx 1$ m above ground. The cross correlation function $C_{\alpha\beta}(\rho)$ as obtained by the two different operators (dots and triangles) is also shown. As foreseen by Tatarski theory, $C_{\alpha\beta}$ practically vanishes.

From a comparison of $C_{\alpha\beta}$ with D_α or D_β it appears also that the measured fluctuations are not far from the limit of measurement accuracy.

In this kind of measurements it was not possible to distinguish the contribution due to thin beams lying in the zone mask-diffusing screen. (This portion of the apparatus was located in a room). However the results of the preceding section can help in a qualitative interpretation of the present results. First of all it seems that the tendency of D_α and D_β to increase for high values of ρ can be due to the thin beams, so that it seems reasonable to neglect this increasing and to surmise that the structure functions for α and β "saturate" at small values of ρ , as expected from Tatarski theory. In order to have an idea of the values of the atmospheric quantities λ_0 and C_n^2 the data are compared with the theoretical ones foreseen by Tatarski theory for isotropic turbulence (Tatarski V.I., 1967, sec.42). The dashed line of Fig. 8 has been obtained from geometrical optics theory in the hypothesis that the structure function, $D_{\alpha,sp}$, of a spherical wave is related to that, $D_{\alpha,pl}$, of a plane wave by

$$D_{\alpha,sp} = \frac{1}{3} D_{\alpha,pl}$$

This is strictly true only when $\rho \ll \lambda_0$ while when $\rho \gg \lambda_0$ the factor $1/3$ is to be replaced by a factor $8/3$. The values of the parameters λ_0 and C_n^2 corresponding to the dashed line are $\lambda_0 = 9$ mm and $C_n^2 = 2.4 \cdot 10^{-14} \text{ cm}^{-2/3}$. Note that they are higher than generally surmised. The value of C_n^2 is consistent with values obtained by us at the same location in analogous conditions with completely different kinds of measurements (BURLAMACCHI P. and CONSORTINI A., 1966, BURLAMACCHI P. et alii, 1969 and 1970, CONSORTINI A. et alii, 1970). The dashed line of D_β in Fig. 8 was obtained from the theory by using the parameters C_n^2 and λ_0 derived from the fitting of D_α . The agreement between theoretical and experimental results is quite satisfactory, an account also of the fact that it was not possible to separate the contribution of thin beams and of their possible anisotropy.

Fig.9 shows the structure function D_α of a subsequent series of measurements. In ascissa also the quantity $\kappa_m \rho$ ($\kappa_m = 5.92/\lambda_0$) is represented. The dashed line refers to the theory as above. The high value of λ_0 is confirmed.

4. CONCLUSIONS

In this paper we described results of measurements of angle of arrival fluctuations of a diverging laser beam after propagation through turbulence. Structure and correlation functions were obtained.

The first part of the paper refers to the propagation through a thin layer of artificial turbulence, produced by a heater. The role played by the layer has been put in evidence.

The second part refers to laser propagation through the atmosphere at near ground levels over path of the order of hundred meters. Some results of the first part where useful for the interpretation of the atmospheric measurements.

As expected from Tatarski theory, the cross correlation between fluctuations in horizontal and vertical plane resulted practically vanishing, for both cases. A comparison with theory allowed also to know approximate values of the inner scale and of the structure constant of the atmospheric turbulence. The present results appears to be promising and encourage us to proceed further and to improve the method of measurement.

5. REFERENCES

- ARRIGUCCI A., CONSORTINI A., RONCHI L., STEFANUTTI L., 1971, "Measurements of Angle of Arrival Fluctuations for an Optical Wave Propagated through the Atmosphere" (URSI Symp. Tbilisi, September 1971) in: 'Electromagnetic Wave Theory', Nayka, Moscow, p.240
- BURLAMACCHI P., CONSORTINI A., RONCHI L., TORALDO DI FRANCIA G., 1969, Alta Frequenza Special Issue on URSI Symposium on Electromagnetic Waves (Stresa, Italy 1968), 38, p.149
- BURLAMACCHI P., CONSORTINI A., RONCHI L., TORALDO DI FRANCIA G., 1970, "Phase Correlation Measurements of a Laser Beam Propagated through a Turbulent Atmosphere" in: Proceedings of EPC/EGARD 13th Symposium on 'Phase and Frequency Instability in Electromagnetic Wave Propagation' (Ankara, Turkey, October 1967), Technivision Services Slough, England, p.665
- BURLAMACCHI P., CONSORTINI A., 1967, Optica Acta, 14, p.17
- CONSORTINI A., RONCHI L., STEFANUTTI L., 1970, Applied Optics, 11, p.2543
- CONSORTINI A., ARRIGUCCI A., RONCHI L., STEFANUTTI L., 1972, "Measurements of Angle of Arrival Fluctuations of an Optical Wave Propagated through the Atmosphere at Near Ground Level" OSA 1972, Annual Meeting - San Francisco 17-20 October, JOSA, 62, p.1354
- CONSORTINI A., PANDOLFINI P., VANNI R., 1974, "Measurements of Angle of Arrival Structure Functions through a Simulated Turbulence" Meeting on Optical Propagation through Turbulence, Boulder, Colo., July 9-11.
- STROHBEHN J.W., 1970, "The Feasibility of Laser Experiments for Measuring the Permittivity Spectrum of the Turbulent Atmosphere", J.Geophys.Res., 75, p.1067
- TATARSKI W.I., 1967, "Wave Propagation in a Turbulent Atmosphere", Nayka, Moscow, (in russian)

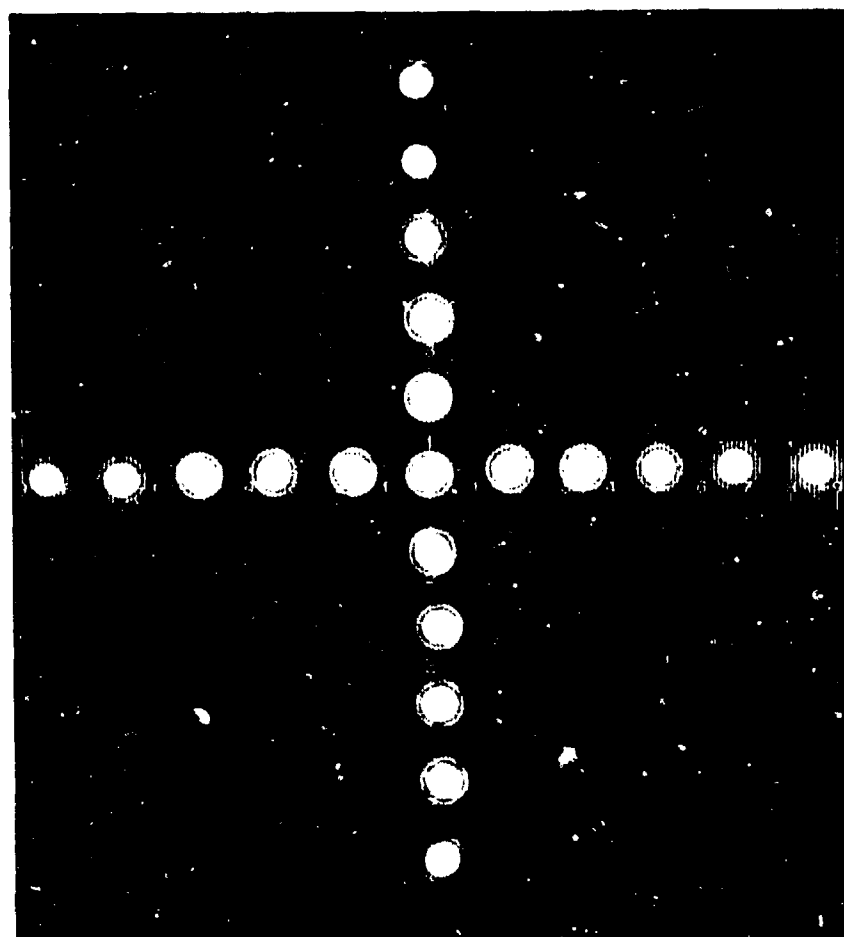


Figure 4

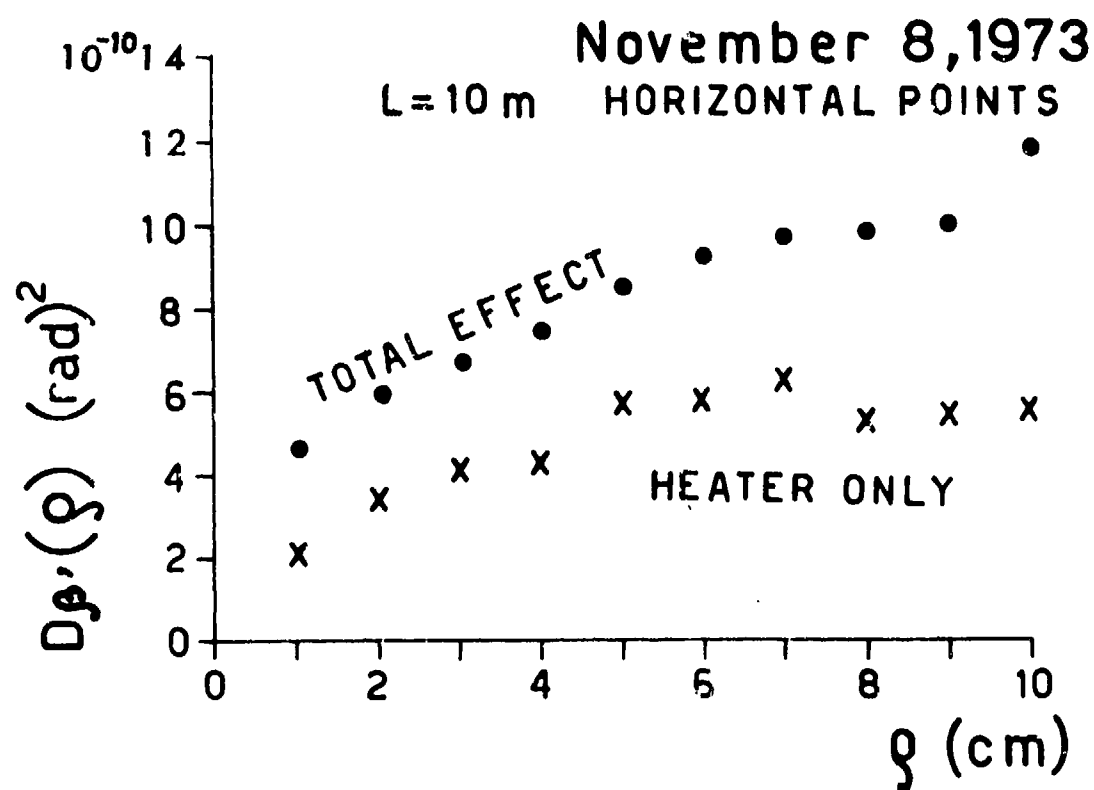


Figure 5

NOVEMBER 8, 1973

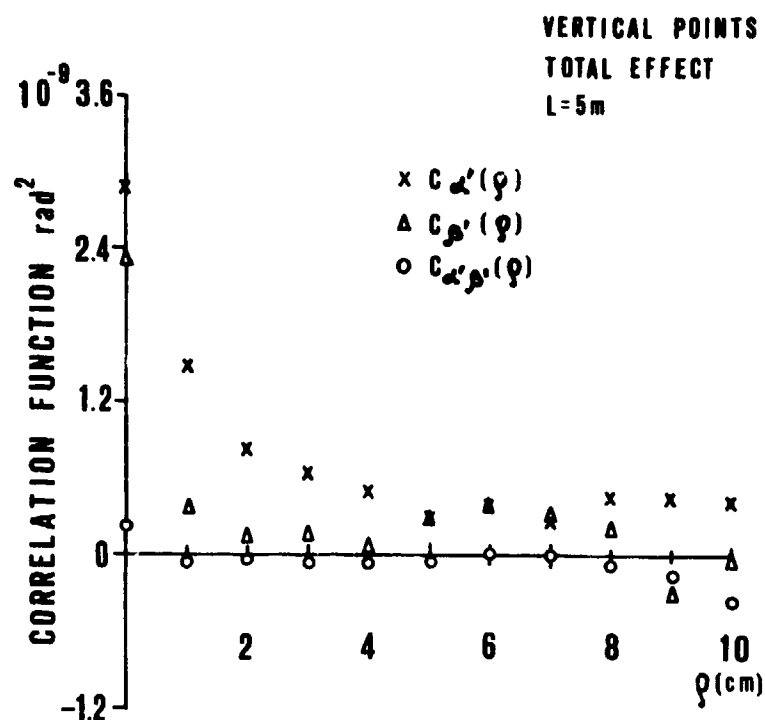


Figure 6

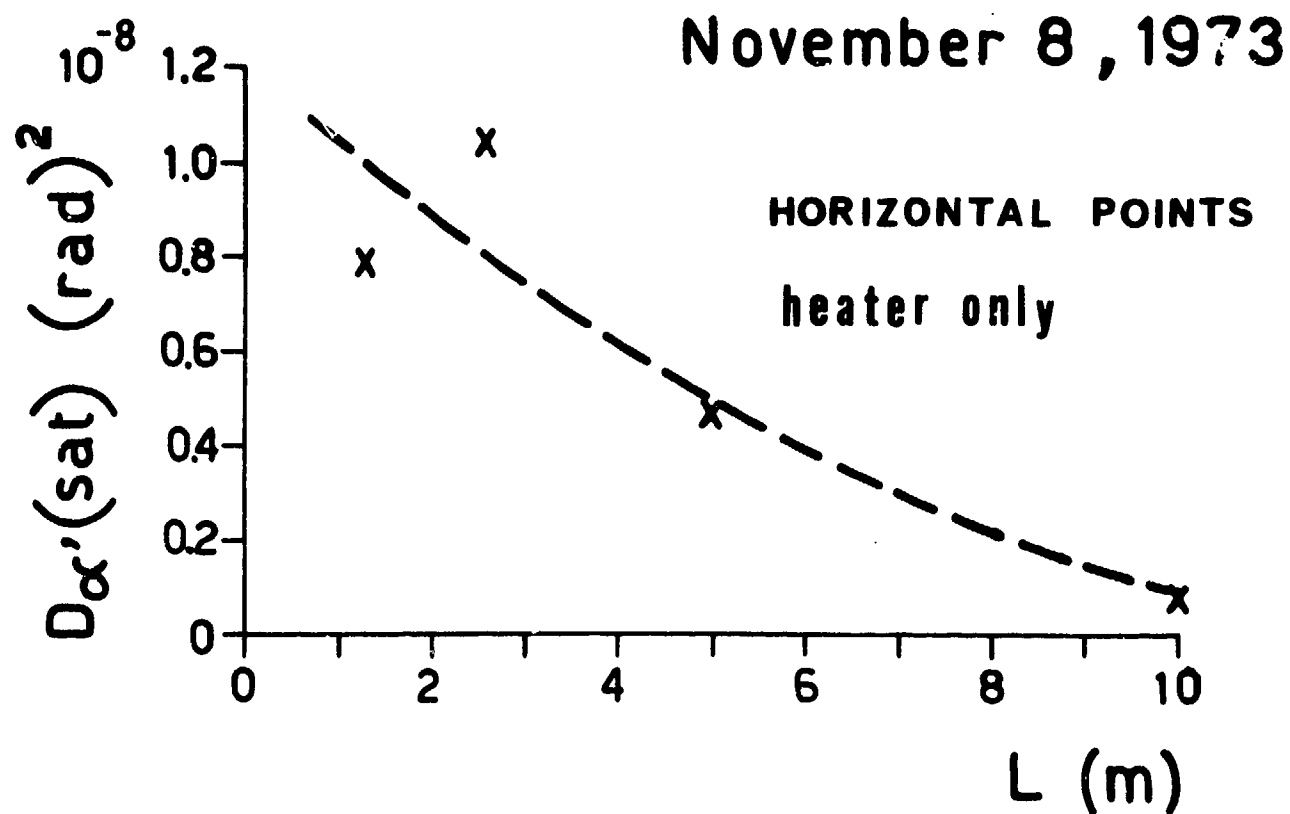


Figure 7

NOVEMBER 8, 1971

HORIZ. POINTS

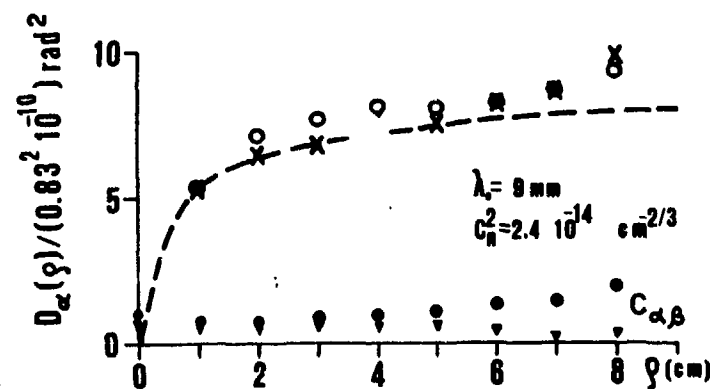
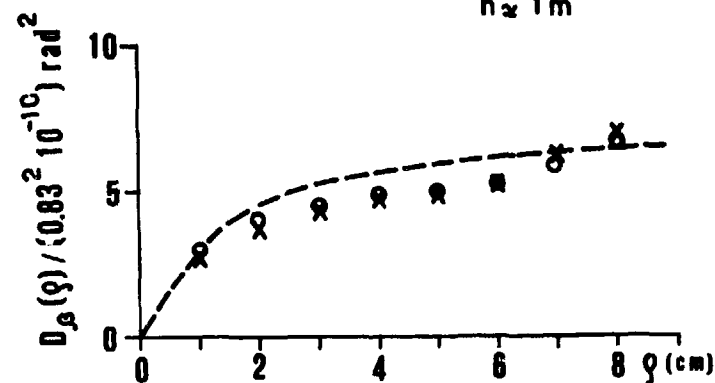
 $Z = 130 \text{ m}$ $h \approx 1 \text{ m}$ 

Figure 8

SEPTEMBER 22, 1972

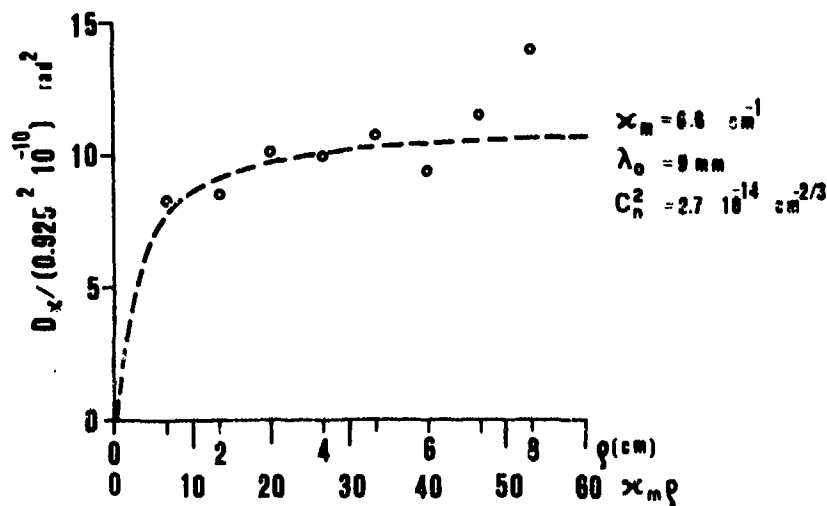
 $Z = 200 \text{ m}$ $h = 1.5 \text{ m}$ 

Figure 9

A MULTIPLE SCATTERING CORRECTION FOR LIDAR SYSTEMS

J. V. Winstanley, C. Wigmore
Plessey Radar
Cowes
Isle of Wight
England

SUMMARY

The approach adopted to multiple scattering phenomena was to treat it as an effective beam-broadening mechanism. At any given range the amount of beam overlap is greater in the cases of fog and smoke than in clear air. In addition, the amount of beam overlap increases as the optical density increases. A beam broadening correction factor may therefore be defined as the ratio of the beam overlap in poor visibility conditions to that in clear air, measured at the same range.

Experimental measurements were made of the beam-broadening factors, using a GaAs lidar system. The results obtained were expressed as a graph of correction factor versus extinction coefficient for each range element, and were in fair agreement with the theoretical models of Chu and Hogg and Kunkel.

1. INTRODUCTION

The approach adopted to multiple scattering phenomena for the lidar is to treat them as an effective beam-broadening mechanism. The concepts involved are illustrated by Fig. 1 which shows schematically the transmitter and receiver fields of view and their amount of overlap in the cases of (a) clear air, (b) thin fog, and (c) thick fog. It is clear that if we consider a fixed range, as represented for example by the line AB in Fig. 1 then the amount of beam overlap is greater in the cases of fog than in clear air. In addition, the amount of beam overlap increases as the fog gets thicker. A beam-broadening correction factor may therefore be defined as the ratio of the beam overlap in fog to that in clear air, measured at the same range. As regards the range-dependence of this factor, it is clear from Fig. 1 that as the range increases the effect may first become more significant, and then decrease in importance as the situation approaches that of complete beam overlap in clear air.

Experiments to measure the extent of beam-broadening due to multiple scattering in all relevant range bins of our lidar were carried out over the period mid-July to mid-October 1974. In this period 11 fogs were used for these measurements, representing a total of 33 hours recording time and 1941 lidar firings. With the aid of the measurements, empirical correction factors for the lidar returns at each range bin have been deduced. The magnitudes and extinction dependences of these correction factors are in agreement with theoretical predictions of small-angle second-order scattering processes. Results obtained using these corrections show much more realistic backscatter parameters and correspondingly improved atmospheric profiles.

2. MULTIPLE SCATTERING THEORY

The assumption of single scattering, i.e. that each particle in an aerosol is exposed only to the radiation of the original beam is only the case if the optical depth (product of extinction coefficient and distance) of the aerosol is less than 0.1 (VAN DE HULST, H.C., 1957). It is worth noting that for the first and last range bins of our lidar, this value corresponds to extinction coefficients of about 2.5km^{-1} and 0.5km^{-1} respectively. This means that the majority of lidar measurements will be affected by multiple scattering phenomena, i.e. each particle of fog is exposed to radiation scattered by other particles, and the original beam has suffered extinction due to other particles. In an effort to make allowance for these effects, the contribution from multiple scattering must be estimated and the lidar analysis amended accordingly.

Some possible approaches to multiple scattering may be summarised as follows:

- (a) Solution of the full equation of radiative transfer, including a source function, (CHANDRASEKHAR, S., 1960). This is in general a still unsolved problem, although under certain restrictive conditions solutions have been obtained, (CHANDRASEKHAR, S., 1960) (MUDGETT, P.S., et. al. 1971).
- (b) Use of mathematical techniques employed for analogous problems in other fields e.g. neutron diffusion, nuclear scattering (ELORANTA, E.W., 1973).
- (c) Monte Carlo techniques for computer simulation of multiple scattering, (PLASS, G.N., et. al. 1968).
- (d) Treatment of multiple scattering as a beam-broadening effect, implying an earlier intersection of the transmitter and receiver cones than would otherwise be the case, (BROWN, R.T. Jr., 1967) (CHU, T.A. et. al. 1968).
- (e) Calculations of second, third, and higher-order corrections as necessary, on the assumption that (i) multiple scattering is the sum of contributions due to the various orders of scattering, and (ii) Nth order scattering is the result of N single scatterings, (DEPAK, A. et. al. 1970).

Of the above list, (a) and (b) were discarded immediately as requiring rather lengthy mathematical analyses with possibly little returns of significance for the current project. Approach (c) is suitable but could only permit a theoretical estimate of multiple scattering contributions and would not be applicable to the problem of amending the experimental lidar analysis procedures. Method (d) is an attractive simplification of the problem but there is a danger that this approach may be rather too crude and may omit important details of the phenomena. This leaves (e), which has the merit of being applicable to the lidar analysis problem and of having been already applied successfully to analyses of other effects, (DEEPAK, A., et. al. 1970) (DOWLING J. Jr., et. al. 1966). Although the assumptions involved in this approach may be open to question, it nevertheless seemed the most promising method. In practice it appears that the second-order correction is the most important so this will be the only one considered for the present, although the technique can be extended to third and higher-order corrections if required.

We summarise below the three theoretical approaches (c, d, e) and highlight the applicability of the results to the specific lidar data analysis problem and the agreement between experimental measurements and the theoretical model.

2.1. Correction for Second-Order Scattering

The geometry for second-order scattering is shown in Fig. 2. The discs shown represent sections through the transmitter and receiver cones at distances r_T and r_R from the Tx, Rx, respectively, with centres O and O'. The first scattering element is at $(r_1 \sin \phi_1, r_1 \cos \phi_1, 0)$ relative to O, and is of thickness δr_1 and area $r_1^2 \delta r_1 \delta \phi_1$. The second scattering element is at $(r_2 \sin \phi_2, r_2 \cos \phi_2 + x \sin \theta)$ relative to O, and is of area $r_2^2 \delta r_2$ and thickness δr_2 . The beam under consideration follows the path shown, such that the distance ℓ between the two scattering elements is given by:

$$\ell^2 = (r_1 \sin \phi_1 - r_2 \sin \phi_2)^2 + (r_1 \cos \phi_1 - r_2 \cos \phi_2 - x \sin \theta)^2 + x^2 \cos^2 \theta \quad (1)$$

The distance x between O and O' and the angle θ on Fig. 2 may be calculated from the receiver and transmitter geometry. Two possibilities for θ arise since signals arriving at time T may have taken one of two paths with $r_R = \frac{ct}{2}$ or $r_T = \frac{ct}{2}$.

The first scattering angle θ' on Fig. 2 is given by $\cos \theta' = \frac{x \cos \theta}{\ell}$

and the second $\theta'' = \pi - \theta'$

Consider a pulse of energy $F(t_0) \delta t_0$ transmitted in time $(t_0, t_0 + \delta t_0)$. Of this a fraction $\exp(-\int_0^{r_T} \sigma(r) dr)$ arrives at O, a fraction $\frac{AS_1}{4\pi r_1^2} \beta(\theta', r_T)$ is scattered by the first scattering element, a fraction $\exp(-\int_0^{r_2} \sigma(r) dr)$ arrives at the second scattering element, a fraction $\frac{AS_2}{4\pi r_2^2} \beta(\theta'', r_R)$ is scattered by the second scattering element and a fraction $\exp(-\int_0^{r_R} \sigma(r) dr)$ arrives at the receiver. In order to arrive at the total return at the receiver we must sum over all angles ϕ_1 and ϕ_2 and all radii r_1 and r_2 . This energy arrives at the receiver in the time interval starting at $\frac{t_0 + r_R + \ell + r_T}{c}$ and of duration $\delta t_0 + \frac{\delta r_T + \delta r_R}{c}$.

Hence we can arrive at an expression of the mean received power

$$P = \frac{cE}{2} \int_0^\infty G(t_0 - r_T - \ell, r_T) dr_T$$

where W is the total transmitted energy and $G(r_R, r_T) = \frac{A}{16 \pi^3 r_R^2 (r_T^2 + r_1^2)^2} \int_0^{2\pi} d\phi_1 \int_c^{2\pi} d\phi_2$

$$\int_c^{r_T \theta_1 + R_1} dr_1 \int_0^{r_R \theta_2 + R_2} dr_2 \times \frac{E_1 E_2}{4} \beta(\theta', r_T) \beta(\pi - \theta', r_R) \times \exp\left(-\int_{\text{total path}} \sigma(u) du\right) \quad \dots \dots \dots (2)$$

AS_1 is the first scattering area AS_2 is the second and A is the cross section of the transmitted cone at r_T .

In fact, the integral splits into two parts when it is recalled that a given pulse may have followed two possible paths to return after time t , i.e. the received instantaneous power is:

$$\frac{c}{2} E \int_0^{\frac{ct}{2}} G\left(\frac{t_0}{2}, r_T\right) dr_T + \int_c^{\frac{ct}{2}} G\left(r_R, \frac{t_0}{2}\right) dr_R$$

Note that the term r_R^{-2} in equation (2) is only appropriate when $r_R \gg r_0$ (the hyperfocal distance);

for $r < r_0$, this term is replaced by r_0^{-2} . Note also that to good approximation the exponential term in (4) may be replaced by the conventional expression

$$\exp\left(-2 \int_0^{\frac{ct}{2}} \sigma(u) du\right)$$

The total instantaneous power received, as given by the expression above is somewhat unwieldy expression involving a five-fold integral. In addition, there is the possibility of an apparent singularity in the presence of the $1/r^2$ term. These factors combine to make the expression totally unsuitable for numerical computation as it stands. Current work is therefore, directed towards finding suitable approximations to reduce equation (2) to a more useful form. In particular we may note that the characteristic peak of the scatter functions in the forward direction may imply that the only angles θ' of importance in equation (2) are those near zero. To illustrate this property Fig. 3 shows the product $\beta(\theta, r)\beta(\pi - \theta, r)$ as a function of θ for the same size distribution function, i.e. effectively independent of position as in a uniform aerosol. These curves are calculated from the tabulated functions in Deirmendjian's book (DEIRMENDJIAN, D., 1969) for three important aerosol size distributions (C1, C2 and C3) at a wavelength of $0.7\mu\text{m}$. They serve to illustrate the importance of the contribution in the region of $\theta = 0$, a feature which is not markedly affected by taking cross-products of scatter functions with different size distributions, corresponding to a non-uniform aerosol. It appears therefore, that only a small range of scattering angles near forward scattering is of importance in second-order scattering corrections to the lidar equation, and this approximation forms the basis of current work on this problem.

A simple and somewhat crude approximation to the second-order correction factor would be to consider only the forward scattering contribution $\beta(0)$. In order to estimate the dependence on σ given by this model, Fig. 4 shows the calculated variation of $\beta(0)/\sigma$. From this it is clear that $\beta(0) \propto \sigma^2$, so that our simple approximation to the second order correction factor is of the form

$$(1 + f(r)\sigma^2)$$

where $f(r)$ is some function of range. This dependence on σ is roughly in agreement with that found experimentally (see section 3).

2.2. Theory of Beam-Broadening Effects

The calculation of the range-dependent function $f(r)$ involves the area of overlap of two circles corresponding to the cross-sections of the two beams. In order to simplify the calculations it has been decided to utilise the beam-broadening model of Chu and Hogg, (CHU, T.S., et. al. 1968). This model assumes a Gaussian form for the initial beam power distribution and a second Gaussian distribution for the scattering pattern of each aerosol particle.

This saves computer time and storage which would otherwise be needed for calculating and storing the accurate Mie scattering functions for each particle. Calculations were then made of the scattering pattern at a given range for a fog of given particle size distribution. In order to minimise computer time we have adopted the model to use only one size distribution - the gamma distribution (ZUEV, V.E., 1970) with an index of 2 and a 'modal' particle radius of $0.8\mu\text{m}$. Variations of fog density in the model are achieved by increasing the density of particles rather than changing the distribution. The other parameters used in the calculation were those appropriate to our lidar, viz. a wavelength of $0.9\mu\text{m}$ and an initial beam radius of 15cm for the transmitted beam. The increase of beam radius with extinction coefficient σ was then calculated as in Fig. 5 at a range of 14m, corresponding roughly to the first lidar range bin. From this it is a relatively simple matter to calculate the broadening factor by considering the amount of overlap of the transmitter and receiver beams at this range; this result is given in Fig. 6.

The results indicate that the larger particles of the distribution have the greatest effect. If we take the beam radius as given by the $1/e^2$ level of the distribution, then it is clear that the effective radius may be increased by as much as 100% as a result of beam-broadening effects.

It should be noted that we have neglected here the corresponding factor for broadening of the receiver acceptance cone; this would have the effect of further increasing the broadening correction factor.

2.3. Monte Carlo Techniques

A recent unpublished M.Sc thesis by Kunkel, (KUNKEL, K.E., 1974) gives another approach to multiple scattering based on a Monte Carlo technique using tabulated scattering phase functions obtained from Mie theory (DEIRMENDJIAN, D., 1969). Kunkel computes the effect of multiple scattering on lidar returns from hazes, clouds, fog and rain for various receiver fields of view, including cases of relevance to our present lidar. The effects are expressed in terms of a correction factor $F(r)$ in the lidar equation, defined by

$$\frac{P(r)}{C(r)} = \beta(\pi, r) \exp \left(-2 \int_0^r \sigma(r) (1 - F(r)) dr \right) \quad (2)$$

$P(r)$ is the power returned to the lidar receiver, $C(r)$ is the calibration, and the other symbols have their conventional meaning. Since it is difficult to calculate the exact structure of $F(r)$, Kunkel works instead with the mean value $\bar{F}(r)$ defined as

$$\bar{F}(r) = \frac{1}{r} \int_0^r F(r) dr \quad (3)$$

In order to compare our experimental results (described in section 3) with Kunkel's theory we have used our exponential correction factors to evaluate F as a function of range r . The results are shown in Fig. 7. The r -dependence and order-of-magnitude of the results are in agreement with Kunkel's theory for a receiver angle of 5mrad (see p.45 of ref. 14) and with his quoted values from Eloranta's unpublished double scattering model.

3. MEASUREMENTS OF BEAM-BROADENING EFFECTS

It has already been remarked above that multiple scattering from aerosol particles can be viewed as a beam-broadening effect of both the transmitter and receiver fields of view. In order to show that this beam-broadening is a real effect, measurements have been made of some summer fogs with a calibration screen placed at the nominal centres of the range bins. It was found that the lidar returns obtained in this way were substantially greater than those using the calibration screen in clear air. Having thus proved the existence of beam-broadening effects and their relevance to lidar analysis we may now interpret the results in terms of 'correction factors' for each range bin. These factors may be obtained by correcting the returns from the screen by the attenuation between lidar and screen. An example is shown in Fig. 8 where $\frac{\text{lidar return in fog from screen} \times \exp(2\sigma r)}{\text{lidar return in clear air from screen}}$

is plotted versus σ for the first range bin. This result, obtained for an early-morning radiation fog, indicates a linear relationship between the 'correction factor' and σ , with values as high as 7 being obtained for the beam-broadening correction.

4. DATA ANALYSIS

In contrast to Kunkel's approach outlined above in which the correction factor for multiple scattering is included in the extinction term, our technique associates the correction with the backscatter coefficient. Thus the new form of the lidar equation, using a linear dependence of correction factor on extinction (see section 2.1. above) may be written:

$$\frac{P(r)}{C(r)} = \beta(r, r) (1 + g(r)\sigma(r)) \exp \left(-2 \int_0^r \sigma(r) dr \right) \quad 5.1$$

where $g(r)$ is a continuous functions of range deduced from the experimental results given in Tables 1(a) - 3(a) for the appropriate receiver configuration. The inclusion of this extra factor in the lidar equation has meant a great deal of alteration to the methods of analysis used for interpreting lidar returns. In the first place, it is no longer possible to solve equation 5.1 by the direct integration method used for the conventional lidar equation. Instead it is necessary to adopt some iterative procedure for finding a solution to equation 5.1 at a given range r .

The increased computer time implied by the methods necessary to solve equation 5.1 has led to the need for a new and simpler technique. Using the well-known backscatter relationship (WINSTANLEY, J.V., et. al. 1974):

$$\beta(r) = A\sigma^n \quad 5.2$$

equation 5.1 may be rewritten in for form:

$$\ln \frac{P(r)}{C(r)} - \frac{1}{(1 + g(r)\sigma(r))} \exp \left(2 \int_0^r \sigma(r) dr \right) = \ln A + n \ln \sigma \quad 5.3$$

Equation 5.3 contains $P(r)/C(r)$ which is known from the lidar returns, and functions of $\sigma(r)$ which may be obtained from independent instruments. Hence it is possible to use a linear regression process in logarithmic space in order to determine A and n . This regression process has a further advantage: it may be used either (a) on the returns from all the range bins for all lidar firings during an entire fog or (b) on the returns from all range bins for one lidar firing. Method (a) has been chosen for the statistically larger number of data points available leading to more reliable values for A and n . Having determined the values of A and n by the method outlined, these values are then used in equation 5.3 to solve the lidar σ -profiles by an iterative process.

5. RESULTS

The beam broadening measurements were made using a calibration screen at the centre of each range bin during shallow summer fogs. Each correction factor was derived from

$$\text{correction factor} = \frac{\text{lidar return}}{\text{calibration factor}} \times \exp(2\sigma r)$$

The mean extinction coefficient σ was found from the Multi Base Line Transmissometer. The results were plotted against σ and appropriate fits were obtained from linear, quadratic and exponential curves.

Table 1 shows the beam broadening data from the first 7 range bins of the Silicon Diode Receiver. Parts (a), (b) and (c) show the equations obtained for linear quadratic and exponential fits respectively and the RMS deviations of the fit.

Beyond range bin 7 the effect falls to zero because the beam overlap further up range is total. The slightly better RMS errors of the quadratic and exponential fits over the linear fit was felt to be insufficient to justify the extra complication of incorporating items in the Lidar analysis and it was therefore decided to use the simplest case, the linear fit.

Table 2 shows the corresponding results for the Photo Multiplier tube receiver. Here the effect of the correction disappears after range bin 3 because the full beam overlap occurs at a shorter range. Once again the linear fit was used in the data analysis.

ACKNOWLEDGEMENTS

The authors wish to acknowledge the invaluable contribution made in this work by Dr. M. J. Adams (now at Southampton University) and Dr. R. Allan (R.A.E., Farnborough). This work has been carried out with the support of the Procurement Executive Branch of the Ministry of Defence. The authors wish to thank the Civil Aviation Authority and the Directors of the Plessey Company for permission to publish this paper.

(c) The Plessey Company Limited 1975.

REFERENCES

1. VAN DE HULST, H.C., 1957, "Light Scattering by Small Particles", New York, John Wiley.
2. CHANDRASEKHAR, S., 1960, "Radiative Transfer", New York, Dover.
3. MUDGETT, P.S., RICHARDS, L.W., 1971, "Multiple Scattering Calculations for Technology", App. Optics 10 1485.
4. ELORANTA, E.V., 1973, "An Approximate Equation for the Multiply Scattered Contribution to a Lidar Return", paper presented at the Fifth Conference on Laser Radar Studies of the Atmosphere, Williamsburg, Virginia.
5. PLASS, G.N., KATTAWAR, G.W., 1968, "Monte Carlo Calculations of Light Scattering from Clouds", App. Optics 7 415.
6. DONATI, S., SONA, A., 1969, "Evaluations of Visibility Improvement in Fog by the Range Gating Technique", Opto. Electronics 1 89.
7. BROWN, R.T., Jr., 1967, "Backscatter Signature Studies for Horizontal and Slant Range Visibility", Final Report on Contract FA65MA-1315, Sperry Rand Research Centre.
8. CHU, T.S., HOGG, D.C., 1968, "Effect of Precipitation of Propagation at 0.63, 3.5 and 10.6 microns", B.S.T.J. 47 723.
9. DEEPAK, A., GREEN, A.W.S., 1970, "Second and Higher Order Scattering of Light in a Setting Polydisperse Aerosol", App. Optics 9 2362.
10. DOWLING, J., Jr., GREEN, A.W.S., 1966, "Second-Order Scattering contributions to the earth's radiance in the middle ultra-violet", The Middle Ultra-Violet: Its Science and Technology, A.W.S. Green, Ed., New York, Wiley.
11. WINSTANLEY, J.V., 1973, "The Use of Lidar for Remotely Measuring Visibility", paper presented at the Fifth Conference on Laser Radar Studies of the Atmosphere, Williamsburg, Virginia.
12. DEIRENDJIAN, D., 1969, "Electromagnetic Scattering on Spherical Polydispersions", New York, Elsevier.
13. ZUEV, V.M., 1970, "Atmospheric Transparency in the Visible and Infra-Red", Israel Program for Scientific Translations.
14. KUNKEL, K.E., 1974, "Monte Carlo Analysis of Multiple Scattered Lidar Returns", M.Sc. Thesis, Univ. Wisconsin.
15. WINSTANLEY, J.V., BURRELL, G.J., 1974, "Evaluation of a GaAs Lidar for the Measurement of Visibility", paper presented at the Fifth Conference on Laser Radar Studies of the Atmosphere, Sendai, Japan.

Table 1 Beam-broadening correction factors for Si detector

(a) Linear fit

R.B.	Range (m)	Factor	R.M.S. deviation
1	14.7	$1 + 0.13\sigma$	15%
2	21.3	$1 + 0.16\sigma$	25%
3	27.8	$1 + 0.14\sigma$	35%
4	32.9	$1 + 0.10\sigma$	27%
5	39.4	$1 + 0.062\sigma$	25%
6	44.8	$1 + 0.035\sigma$	10%
7	55.8	$1 + 0.015\sigma$	22%

(b) Quadratic fit

R.B.	Range (m)	Factor	R.M.S. deviation
1	14.7	$1 + 0.13\sigma + 0.00027\sigma^2$	15%
2	21.3	$1 + 0.091\sigma + 0.0025\sigma^2$	15%
3	27.8	$1 + 0.016\sigma + 0.0053\sigma^2$	14%
4	32.9	$1 - 0.012\sigma + 0.0045\sigma^2$	13%
5 *	39.4	$1 + 0.020\sigma + 0.0018\sigma^2$	21%
6	44.8	$1 + 0.032\sigma + 0.00013\sigma^2$	10%
7	55.8	$1 + 0.046\sigma - 0.0012\sigma^2$	22%

(c) Exponential fit

R.B.	Range (m)	Factor	\bar{F}	R.M.S. deviation
1	14.7	$\exp(0.032\sigma)$	1.1	22%
2	21.3	$\exp(0.031\sigma)$	0.73	21%
3	27.8	$\exp(0.030\sigma)$	0.53	14%
4	32.9	$\exp(0.024\sigma)$	0.37	13%
5*	39.4	$\exp(0.019\sigma)$	0.25	21%
6	44.8	$\exp(0.013\sigma)$	0.14	10%
7	55.8	$\exp(0.0061\sigma)$	0.055	21%

* The results for range bin 5 were in fact obtained with the calibration screen displaced by 2.5m from the centre of the bin, as part of an investigation into the effects of range bin shapes; the result indicates that minimal errors are introduced by these effects.

Table 2

Beam-broadening correction factors for P.M. tube.

(a)

Linear fit

R.B.	Range (m)	Factor	R.M.S. deviation
1	13.7	$1 + 0.29 \sigma$	24%
2	19.8	$1 + 0.35 \sigma$	22%
3	26.7	$1 + 0.037 \sigma$	19%

(b)

Quadratic fit

R.B.	Range (m)	Factor	R.M.S. deviation
1	13.7	$1 + 0.069\sigma + 0.0062\sigma^2$	17%
2	19.8	$1 + 0.12\sigma + 0.0064\sigma^2$	11%
3	26.7	$1 + 0.031\sigma + 0.00019\sigma^2$	18%

(c)

Exponential fit

R.B.	Range (m)	Factor	\bar{F}	R.M.S. deviation
1	13.7	$\exp(0.034\sigma)$	1.2	23%
2	19.8	$\exp(0.037\sigma)$	0.94	24%
3	26.7	$\exp(0.012\sigma)$	0.23	17%

Table 3

Beam Broadening correction factors for P.M. tube in the new position
(5 cm nearer to the mirror)

(a)

Linear fit

R.B.	Range (m)	Factor	R.M.S. deviation
1	13.7	$1 + 0.15\sigma$	11%
2	19.8	$1 + 0.048\sigma$	20%

(b)

Quadratic fit

R.B.	Range (m)	Factor	R.M.S. deviation
1	13.7	$1 + 0.18\sigma - 0.093\sigma^2$	10%
2	19.8	$1 + 0.017\sigma + 0.00096\sigma^2$	16%

(c)

Exponential fit

R.B.	Range (m)	Factor	\bar{F}	R.M.S. deviation
1	13.7	$\exp(0.034\sigma)$	1.2	26%
2	19.8	$\exp(0.014\sigma)$	0.35	16%

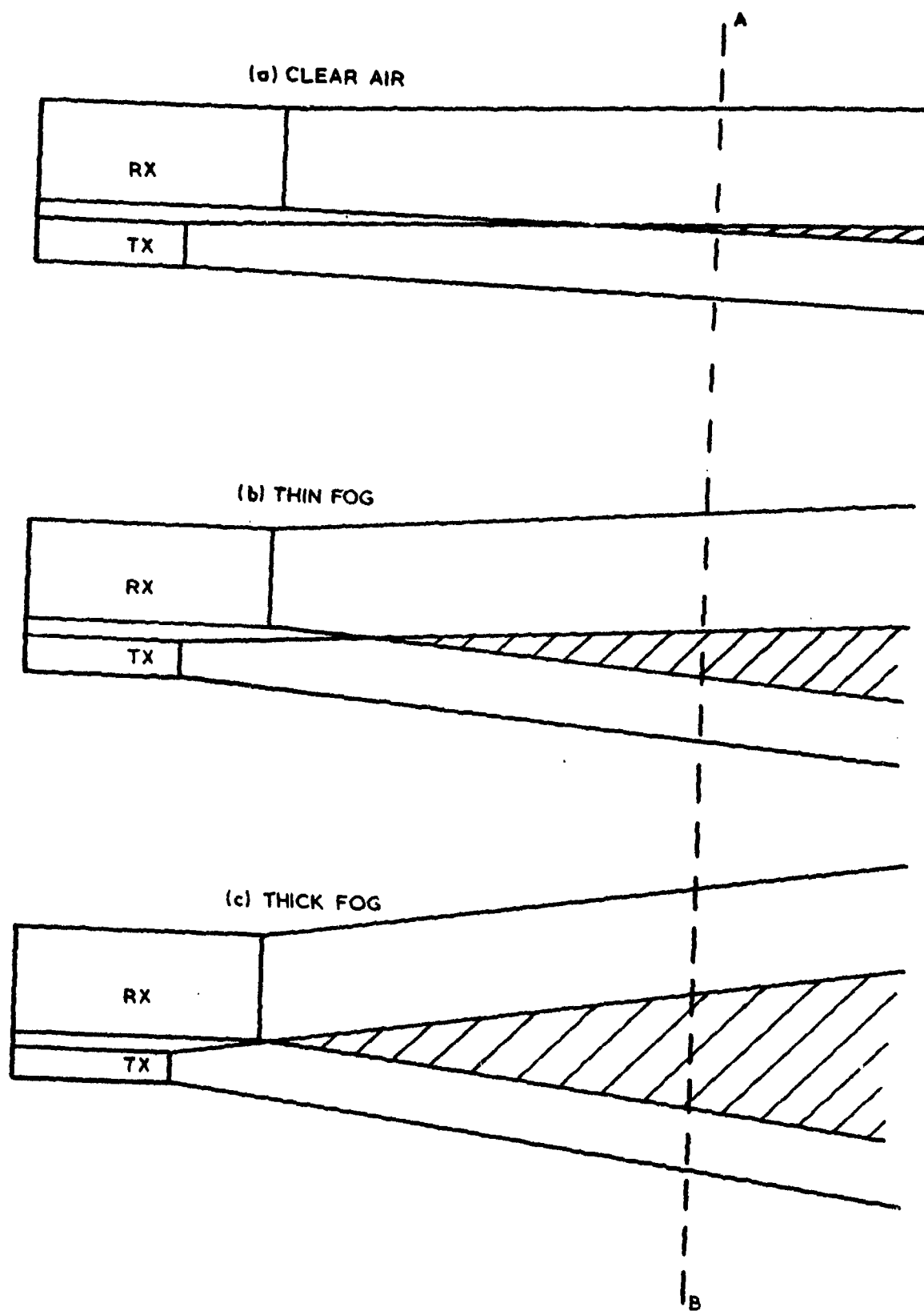


Fig.1 Schematic illustration of beam-broadening.

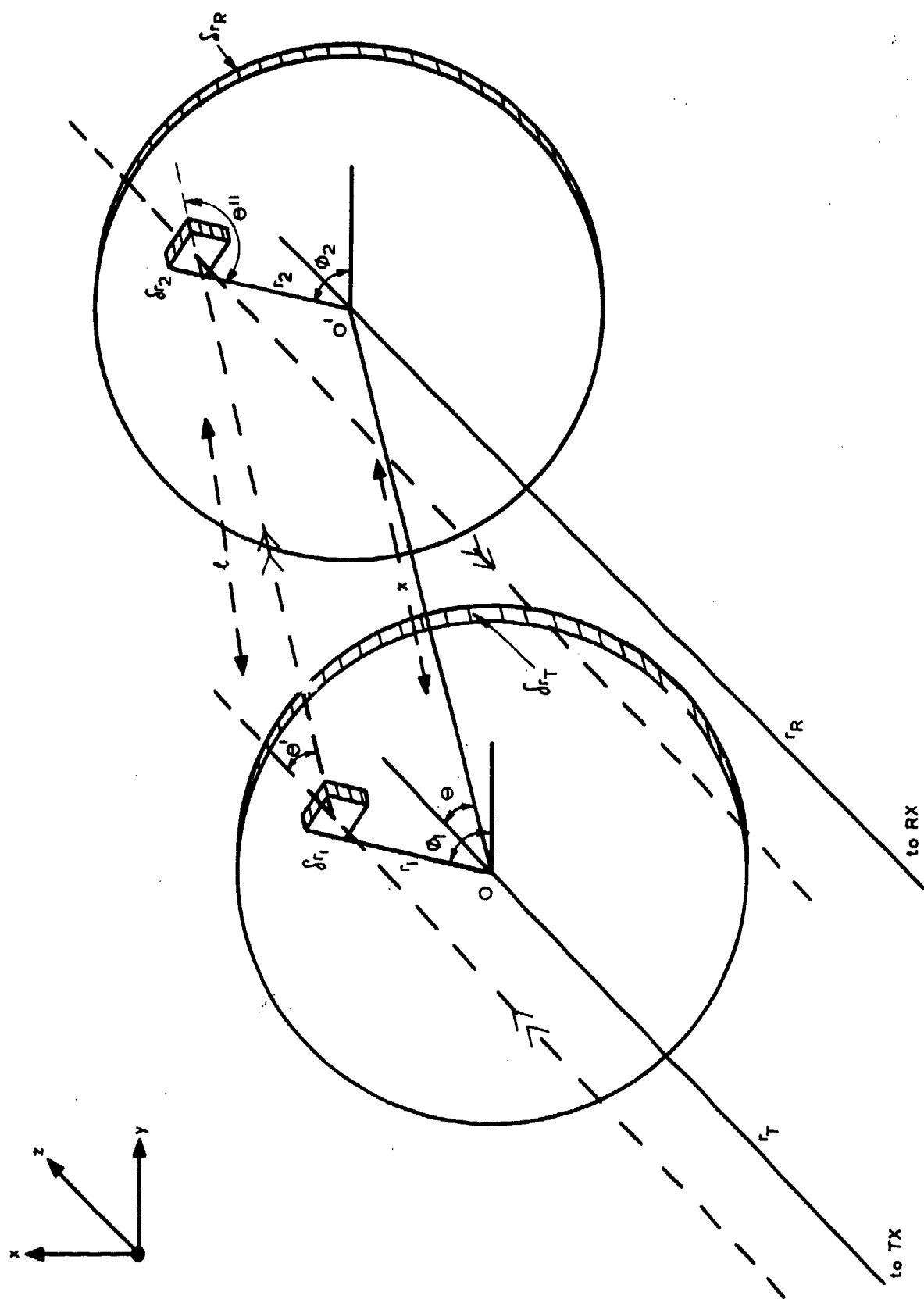


Fig.2 Geometry for second-order scattering

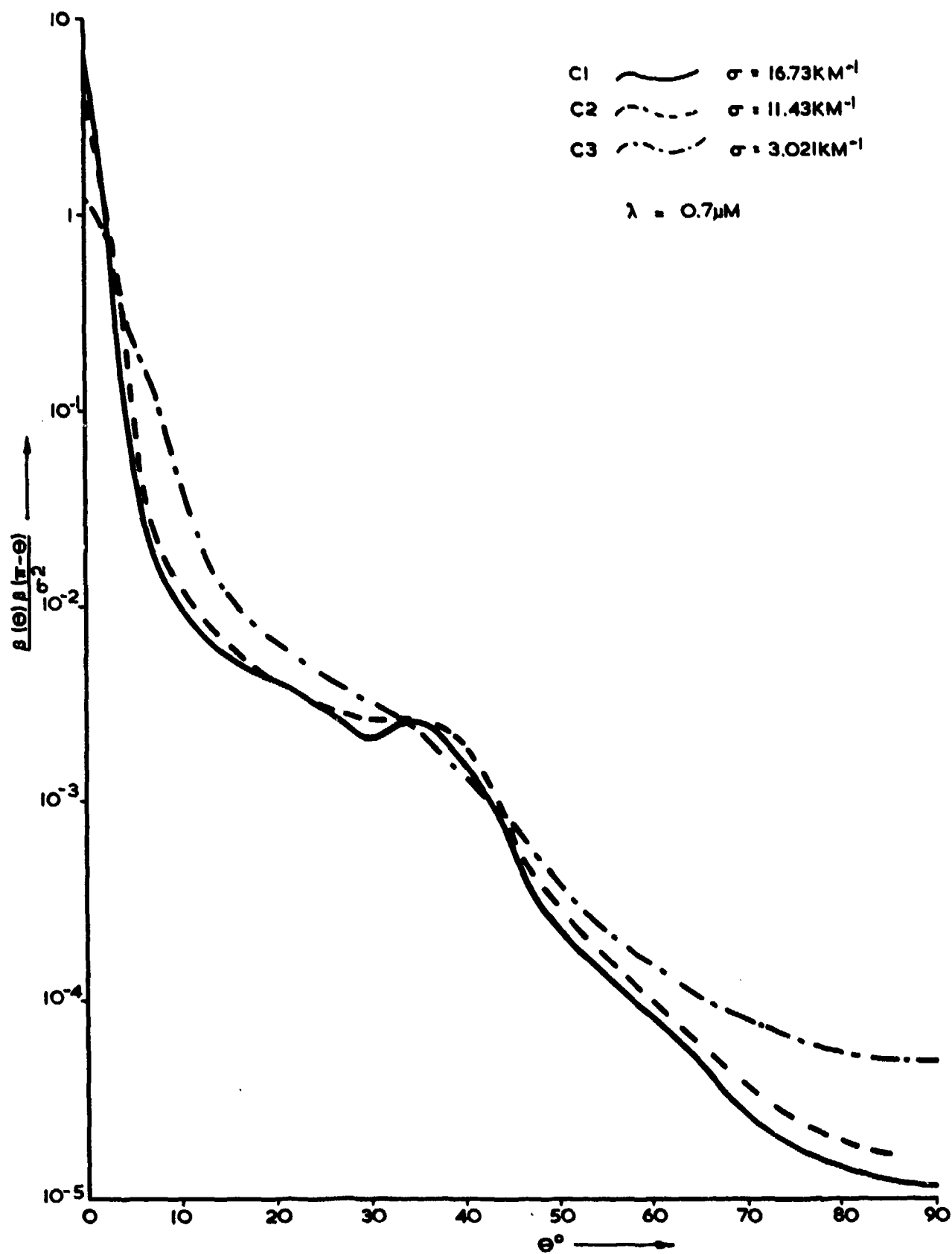


Fig.3 Product of scattering functions at angles θ and $\pi - \theta$, for 3 aerosol size distributions (after Deirmendjian, Ref.12)

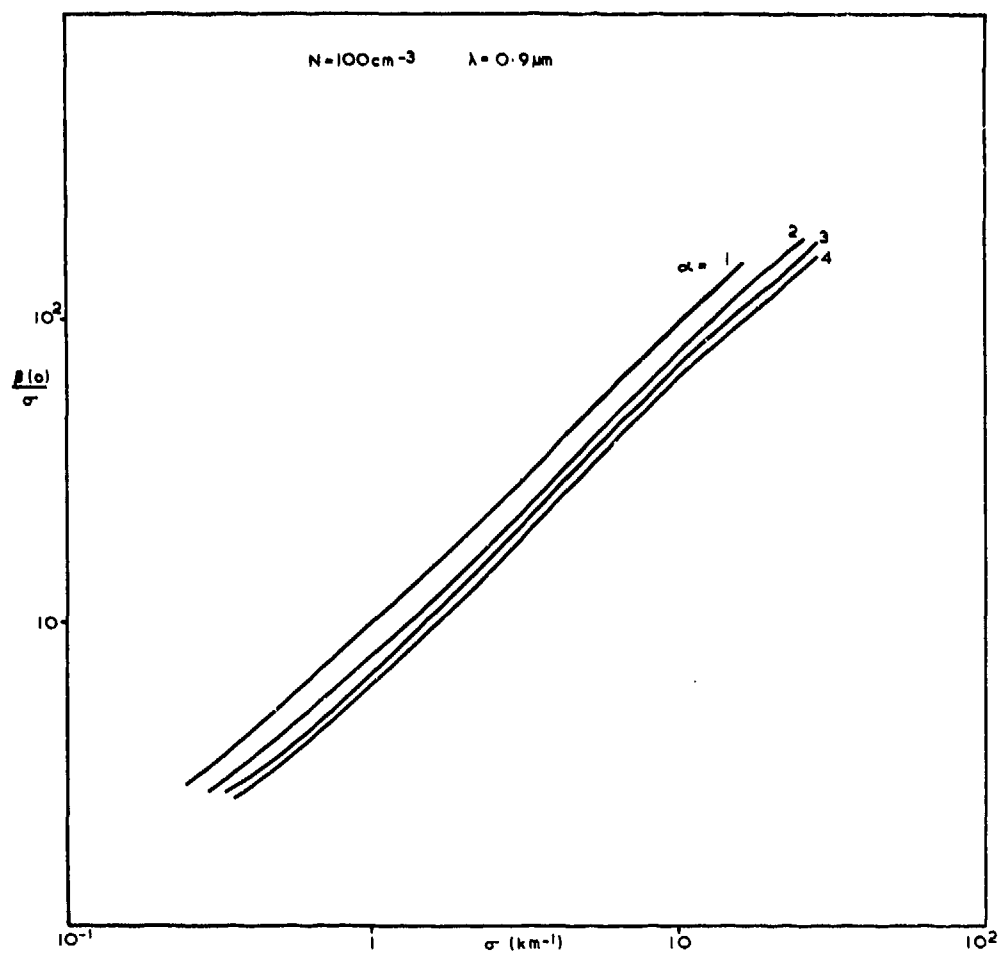
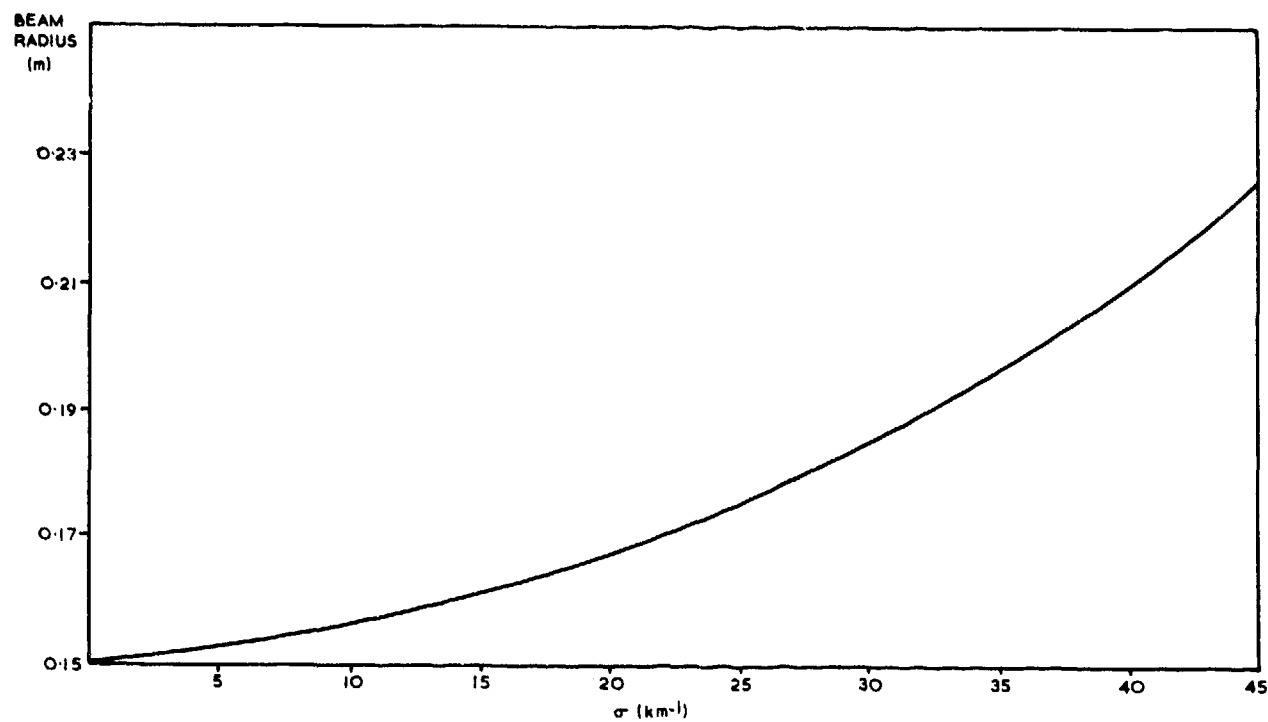
Fig.4 Forward scatter vs σ (calculated)

Fig.5 Theoretical beam radius versus extinction coefficient at range 14m .

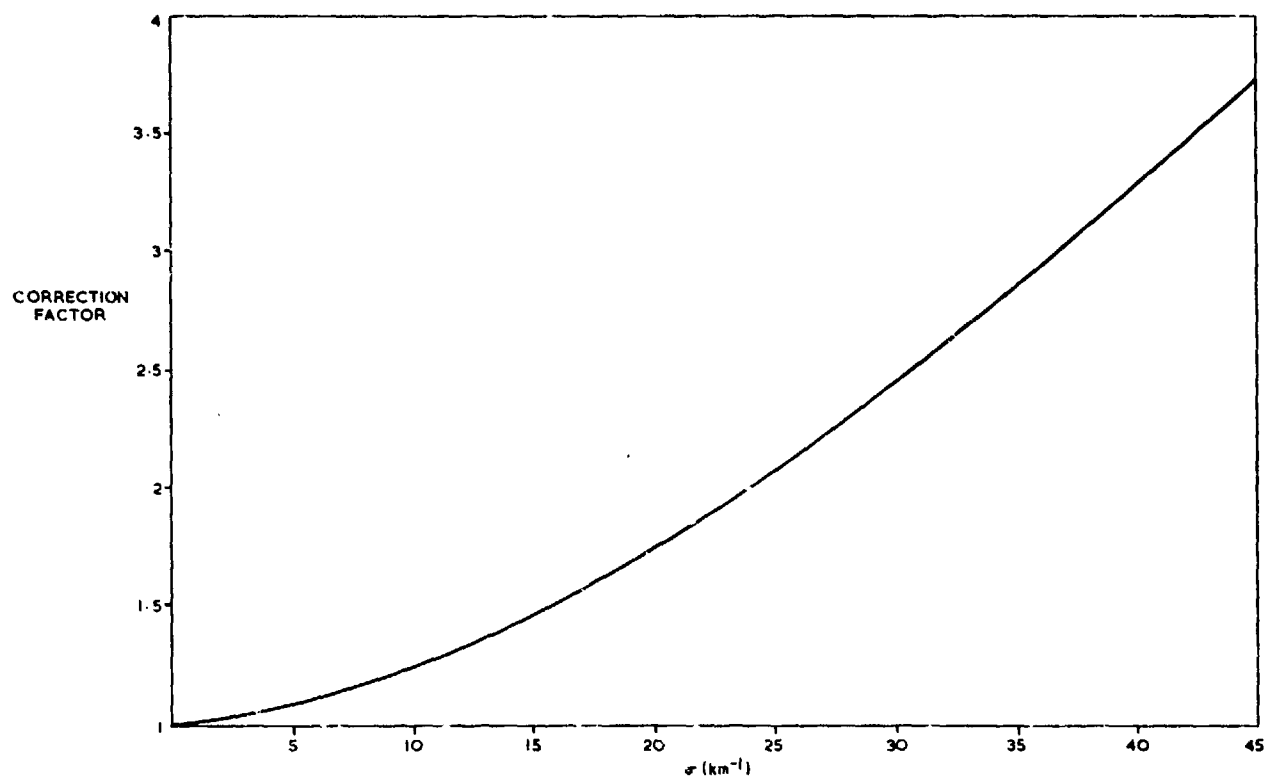


Fig.6 Theoretical beam broadening correction factor versus extinction coefficient σ at range 14m .

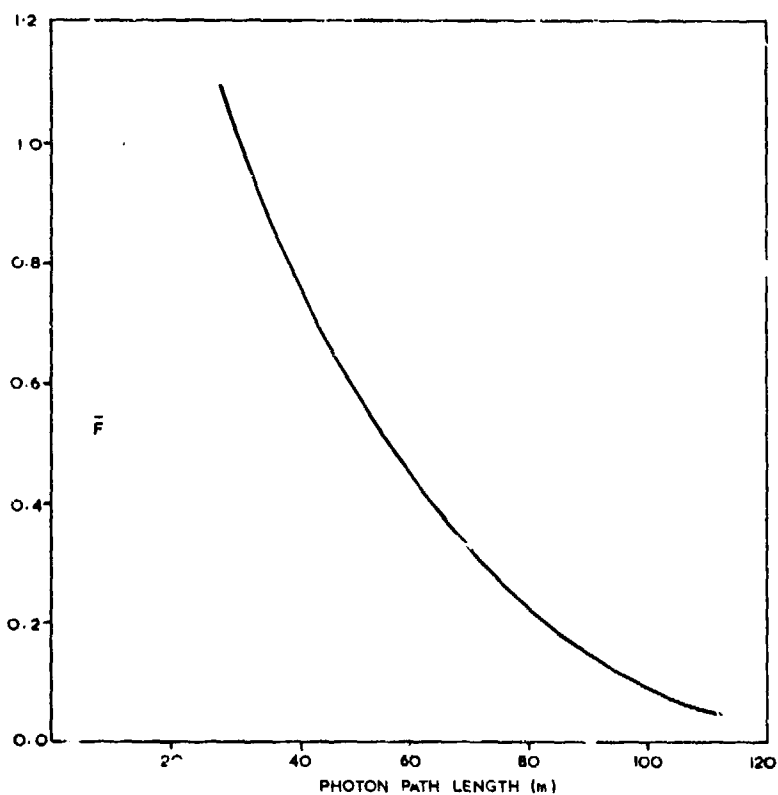


Fig.7 Broadening factor \bar{F} versus photon path length for the SI detector (cf. Reference 14)

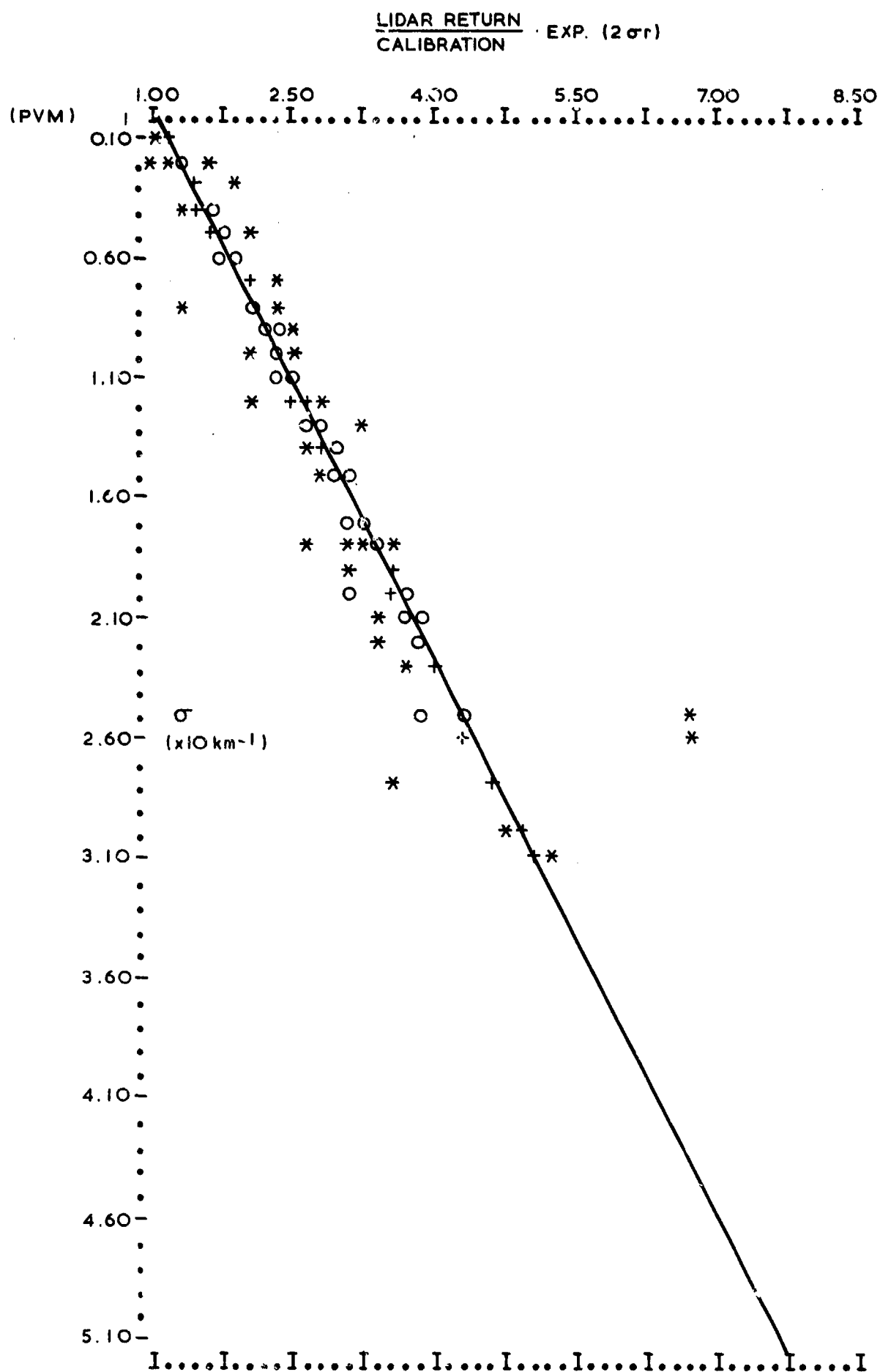


Fig.8 Experimental results of Lidar multiple scattering correction

MESURES DE L'ABSORPTION ATMOSPHERIQUE PAR UTILISATION D'UN RADIOMETRE HETERODYNE INFR-ROUGE SOLAIRE

B.Christophe et M.Cenus
Société Anonyme de Télécommunications
41, Rue Cantagrel
75624 Paris Cedex 13

RESUME

Après avoir décrit le principe de la détection hétérodyne cohérente et incohérente dans l'infr-rouge moyen nous démontrons l'intérêt de cette technique pour la mesure de la transparence de l'atmosphère et nous donnons les premiers résultats obtenus.

I - INTRODUCTION

Le développement de l'optique cohérente et son application pratique en particulier : en télémétrie, télécommunication, désignation d'objectif radar, nécessite une connaissance approfondie du milieu traversé.

C'est ainsi que l'atmosphère terrestre a fait l'objet de diverses études. Une synthèse rapide des principaux résultats conduit à considérer le milieu atmosphérique comme étant anisotrope pour les rayonnements lasers. En effet, les inhomogénéités de composition et les gradients des paramètres physiques, agissent sur la propagation des faisceaux et altèrent leur cohérence.

L'absorption atmosphérique ainsi que les phénomènes de turbulences semblent être des facteurs fondamentaux qui conditionnent le cheminement des faisceaux lasers. Chacun de ces deux facteurs dépend d'un grand nombre de paramètres eux-mêmes variables temporellement et spatialement.

- L'absorption est surtout due à celles des molécules de H₂O, CO₂, O₃, N₂O, CO, O₂, CH₄, N₂ à différentes concentrations, mais les conditions climatiques et la présence d'aérosols en modifient le caractère.

- Les turbulences sont des phénomènes liés aux gradients thermiques, à la vitesse et à la direction des vents, ils sont de caractère aléatoire.

Pour toutes ces raisons, il est très difficile d'élaborer une étude théorique visant à mieux connaître l'absorption atmosphérique sans le support expérimental.

L'expérimentation utilise un récepteur hétérodyne et permet de mesurer l'absorption verticale totale de l'atmosphère sur des longueurs d'ondes intéressantes comme celles d'émission du laser CO₂.

La méthode est très sélective et permet, au moyen de calculs, et d'hypothèses atmosphériques, de déterminer la présence de différents constituants de l'atmosphère.

Cette technique est envisagée pour les mesures de concentration de polluants dans l'atmosphère.

II - PRINCIPE DE LA DETECTION HETERODYNE

Cette technique de battements d'ondes lumineuses analogues à celles utilisées en radio dans un récepteur superhétérodyne a été réalisée par Forrester et Al en 1955 pour la mesure spectroscopique de l'effet Zeeman sur une raie du mercure. Les applications sont restées au stade du Laboratoire pour les mesures de largeur de raie jusqu'à l'apparition du Laser. Le Laser est en effet indispensable comme oscillateur local car seul il possède à la fois la cohérence spatiale et temporelle ainsi que la puissance suffisante.

Le schéma de principe est rappelé fig.1. Un détecteur reçoit deux ondes planes parallèles l'une issue de la source l'autre de l'oscillateur local. Le mélange est réalisé grâce à une lame semi-réfléchissante.

La réponse du détecteur est proportionnelle à la valeur quadratique moyenne du champ électrique total U_T prise sur le temps d'intégration du détecteur T .

$$i(t) = \frac{ne}{h\nu} \frac{1}{T} \int_t^{t+T} [u_o \cos \omega_o t + u_s \cos(\omega_s t + \varphi)]^2 dt$$

Un signal sera donc détecté à la fréquence $\frac{\omega_s - \omega_0}{2\pi}$ si celle-ci est inférieure à la fréquence de coupure du détecteur.

$$\frac{\eta e}{h\nu} \left\{ P_s + P_0 + 2\sqrt{P_0 P_s} \left[\cos.(\omega_s - \omega) t + \psi \right] \right\}$$

Ce résultat montre que le courant généré dans le détecteur est la somme de deux courants $i_0(t)$ et $i_s(t)$

$$i(t) = i_0(t) + i_s(t) \quad i_0(t) = \frac{\eta e}{h\nu} P_0 \quad P_0 \gg P_s$$

$$i_s(t) = \frac{2\eta e}{h\nu} \sqrt{P_0 P_s} \left[\cos.(\omega_s - \omega_0) t + \psi \right]$$

Le courant $i_s(t)$ contient l'information de fréquence $\omega_s/2\pi$ et de phase ψ de l'onde incidente c'est la conservation de cette dernière qui permet de réaliser les expériences d'interférence par transposition de fréquence.

Le courant continu $i_0(t)$ est la source d'un bruit shot qui limite la sensibilité théorique.

La puissance de bruit est donnée par :

$$N = 2 e i_0 \Delta f = \frac{2 e^2 \eta P_0 \Delta f}{h\nu}$$

et le rapport signal sur bruit :

$$\frac{S}{N} = \frac{\eta P_s}{h\nu \Delta f}$$

d'où la puissance minimum détectable est :

$$N.E.P. = \frac{h\nu \Delta f}{\eta}$$

Cette puissance minimum détectable peut être rattachée dans le cas d'une émission corps noir à la température de la source.

Détection hétérodyne d'un signal incohérent

Si nous considérons une source thermique à la température T située à une distance R d'un récepteur hétérodyne, la brillance ΔP émise par une surface élémentaire ΔA de la source dans une bande de fréquence $\Delta \nu$ est donnée par la formule de Planck :

$$\Delta P = \frac{2 h \nu \Delta \nu \Delta A}{\lambda^2 \left[\exp. \frac{h\nu}{kT} - 1 \right]}$$

ou ν = fréquence de la radiation émise

$$\lambda = \text{longueur d'onde} = \frac{c}{\nu}$$

h = constante de Planck

La puissance reçue par le récepteur d'ouverture A_R dans un angle de vue α_R est :

$$P_s = \frac{1}{2} \frac{2 h \nu \Delta \nu}{\left[\exp. \frac{h\nu}{kT} - 1 \right]} \times \frac{A_R A_s}{R^2 \lambda^2} \times F$$

A_s = surface de la source

F = facteur de mixage des ondes

Le facteur $\frac{1}{2}$ est une conséquence de la détection hétérodyne qui ne reçoit qu'une polarisation.

SILVERMAN a montré que le champ de vue d'un tel récepteur vérifie :

$$\Omega_R A_R \sim \lambda^2 \text{ où } \lambda \text{ est la longueur d'onde}$$

Après mixage avec l'oscillateur local la puissance du signal de sortie est proportionnelle à la somme des puissances de la source contenue dans le spectre :

$$f_{LO} + B \text{ et } f_{LO} - B \text{ ou}$$

f_{LO} est la fréquence de l'oscillateur local et

B est la bande passante du système détecteur + préamplificateur.

Le bruit "shot" du détecteur hétérodyne est :

$$NEP = \frac{h \nu B}{\eta}$$

et le rapport signal sur bruit

$$(SNR) = \frac{2 \eta}{\exp \frac{h \nu}{k T} - 1}$$

et après détection et intégration :

$$SNR = \frac{\eta (B \tau)^{1/2}}{2 \exp \frac{h \nu}{k T} - 1}$$

ou τ est la constante de temps d'intégration

L'efficacité d'un tel système dépend donc de deux paramètres caractéristiques du détecteur : le rendement quantique et la bande passante.

Les rendements quantiques habituellement mesurés sont compris entre 20 % et 60 % donc sont proches de la limite théorique de 1 et les bandes passantes de l'ordre de 1 GHz.

III - DETERMINATION DE L'ABSORPTION (Réf. 5.6)

III.1 - Généralités

Si l'on considère que le soleil n'a pas d'action sur le coefficient d'absorption atmosphérique (hypothèse à vérifier en utilisant par exemple la lune ou une planète comme source extra-terrestres), on peut calculer l'absorption globale $K(z)$ de l'atmosphère pour un angle d'observation donné (figure 2).

$$k(z) = \int_0^{\infty} \frac{k(h) dh}{\sqrt{1 - \left(\frac{R}{R+h}\right)^2 \sin^2 z}}$$

ou $K(h)$ représente le coefficient d'absorption d'une couche atmosphérique distincte à l'altitude h , R le rayon de la terre et Z l'inclinaison du soleil par rapport à la verticale. La connaissance de $K(z)$ permet théoriquement de remonter à $K(h)$. Ce calcul n'est valable qu'à une longueur d'onde donnée et de ce fait nécessite une résolution spectrale infinie.

III.2 - Absorption verticale

Dans le cas d'une visée proche de la verticale ($\sin Z$ petit) on a $k(z) \rightarrow k_0$ l'absorption verticale et le signal transmis à travers l'atmosphère est de la forme :

$$S = S_0 \exp. - k_0 h \sec. z \quad \text{avec} \quad \sec. z = \frac{1}{\cos. z}$$

Il vient :

$$\text{Log.} \frac{S}{S_0} = -k_0 h \sec.z$$

Dans le plan $\text{Log.} \frac{S}{S_0}$, $\sec.z$ cette dernière expression se traduit par une droite pour $\sec.z < 10$; la valeur de l'absorption verticale k_0 est déduite de la pente de la droite.

III.3 - Echelle de hauteur de l'absorption

Dans le cas où l'on suppose une absorption uniforme sur une épaisseur h et compte tenu du fait que l'épaisseur traversée en fonction de $\sec.z$ est donnée par :

$$e = \frac{R}{\sec.z} \left[\left(1 + \frac{2h}{R} \sec^2 z \right)^{1/2} - 1 \right]$$

nous pouvons représenter graphiquement la relation qui donne :

$$\text{Log.} \frac{S}{S_0}$$

Dans le cas particulier où l'absorption verticale est de 40 % c'est-à-dire que la transmission est telle que :

$$\tau = \exp. -k_0 h = 0,6 \quad \longrightarrow \quad k_0 h = 0,51$$

on peut écrire :

$$\text{Log.} \frac{S}{S_0} = - (k_0 h) \frac{R}{h \sec.z} \left[\left(1 + \frac{2h}{R} \sec^2 z \right)^{1/2} - 1 \right]$$

Nous obtenons ainsi une échelle de hauteur de l'absorption pour des valeurs de $\sec.z$ variables (figure 3).

Si l'on considère que les mesures sont faites avec un rapport signal sur bruit de 37 dB, on voit que pour une couche absorbante de 10 km, on ne pourra pas prétendre explorer des zones pour lesquelles l'incidence du soleil est supérieure à $\sec.z = 20$ c'est-à-dire $z = 2,85^\circ$. On voit donc apparaître l'un des principaux intérêts suscités par des rapports signaux sur bruits élevés.

IV - CONSTITUTION DE LA CHAÎNE DE MESURES

L'expérience est menée en collaboration avec le Centre d'Etudes et de Recherches Géodésiques et Astrométriques (CERGA) de Grasse. Elle est installée dans un de ses Observatoires situé sur le plateau de Calern.

IV.1 - Optique de réception

Elle est constituée d'un miroir de réception mobile pointant continuellement le soleil et d'un miroir secondaire permettant le renvoi du rayonnement dans la direction de la chaîne de mesures. Un télescope de type Cassegrain est en cours de réalisation; monté sur un "équatorial" il permettra la poursuite de la source solaire et l'analyse de l'espace environnant dans de meilleures conditions.

IV.2 - Oscillateur local

Les premières séries de mesures sont effectuées à l'aide d'un laser à gaz carbonique ($C^{12} O_2$) utilisé comme oscillateur local. Il est constitué d'un tube de pyrex à cathode centrale obstruée aux deux extrémités par des fenêtres en Zn Se maintenues à l'incidence brewsterienne par des supports en alumine. La cavité interférométrique est constituée du côté sortie par un multicouche de Zn Se, de l'autre par un réseau orientable; ce dernier permet l'accord de la cavité sur l'une des raies des branches R et P des transitions $001 \longrightarrow 100$ et $001 \longrightarrow 020$.

Une régulation de fréquence, basée sur le maintien de la raie d'émission au sommet de la courbe de gain, est associée au miroir de sortie par l'intermédiaire d'un élément piézoélectrique.

La détection des fluctuations de puissance est assurée par un détecteur Hg Cd Te; le contrôle des raies d'émission est rendu possible par un spectrographe I.R à lecture directe.

L'oscillateur local ainsi constitué permet une bonne stabilité en fréquence ($< 10^{-7}$) et une dérive en puissance négligeable pour une même raie d'émission.

Il est aussi prévu d'utiliser comme oscillateurs locaux un laser N_2O et un laser CO .

IV.3 - Chaîne de détection

Les premières séries de mesures sont effectuées avec un détecteur Hg Cd Te à large bande (9-11 μ) associé à son circuit de polarisation. Un préamplificateur à large bande et faible bruit rend possible l'observation du bruit blanc qui résulte du battement entre l'oscillateur local et la source solaire très étendue. Une détection synchrone termine la chaîne d'analyse. Sa référence est constituée d'un modulateur à miroir escamotable intercalé sur le trajet incident du faisceau source. Un enregistreur X, t inscrit la variation de l'absorption atmosphérique globale en fonction de la hauteur de l'astre.

Comme nous l'avons indiqué précédemment pour obtenir le maximum d'information sur la structure de l'atmosphère il est nécessaire que le rapport S/N soit aussi proche de la théorie que possible. Nous avons vu que S/N dépendait principalement des caractéristiques du détecteur Hg Cd Te. Nous avons donc entrepris une étude systématique de la sensibilité de ces détecteurs.

V - GENERALITES SUR LES CARACTERISTIQUES DES DETECTEURS Hg Cd Te

La figure 7 rappelle le circuit électrique équivalent d'un détecteur ainsi que les différentes sources de bruit.

A l'aide d'un banc de mesures schématisé sur la figure 6 nous avons étudié très précisément les bruits de la chaîne détectrice.

Nous ne présentons ici que la conclusion de cette étude en insistant toutefois sur les caractéristiques du détecteur PV 1216 (figure 7).

Ces réseaux de courbes font apparaître des phénomènes thermiques et d'avalanche contraires à une bonne détection hétérodyne. Un compromis doit être trouvé quant aux valeurs de la polarisation (nécessaire pour obtenir une grande bande passante) et du courant I_0 provenant de l'oscillateur local laser (afin de rendre le bruit photonique prépondérant).

C'est ainsi que nous avons pu déterminer, pour le détecteur PV 1216 polarisé entre 0,5 et 1 V et éclairé par un courant photonique d'environ 1 mA, une efficacité à la détection de l'ordre de 0,8 dans une bande passante supérieure à 600 MHz. Un minimum détectable de 7.10^{-20} W/Hz pourra alors être envisageable avec un rendement quantique de 30 %.

Cette approche sur les détecteurs photovoltaïques Hg Cd Te doit permettre leur emploi dans de meilleures conditions et ainsi augmenter les possibilités de détection de la chaîne de mesures.

VI - RESULTATS EXPERIMENTAUX

A l'aide du matériel précédemment décrit nous avons entrepris une étude systématique de l'absorption atmosphérique verticale sur différentes raies du laser CO_2 . Les figures 9-10-11 représentent les résultats obtenus sur 3 raies.

L'absorption atmosphérique totale est représentée par la pente de ces différentes courbes pour des sec.z faibles :

$$|K_{oh}| = \frac{\text{Log } \frac{S}{S_0}}{\text{sec.z}}$$

On en déduit immédiatement la transmission verticale :

$$\tau = \exp. - |K_{oh}|$$

Les valeurs de transmission verticale sont comprises entre 0,75 et 0,88 pour les raies mesurées.

Ces 3 résultats ne permettent pas de conclure avec certitude à une absorption plus ou moins importante d'une raie par rapport à une autre. Toutefois une réponse pourra être apportée à cette question en procédant à de nombreuses mesures d'une manière répétée sur les mêmes raies d'émission.

Néanmoins il semble que les mesures faites au coucher du soleil entraînent des absorptions plus grandes que celles effectuées le matin. Il paraît logique d'attribuer ces différences à la présence dans l'atmosphère d'une plus forte concentration de vapeur d'eau dans la soirée.

D'autre part, l'altitude à laquelle sont effectuées les mesures, la très faible humidité de la région ainsi que la bande électronique large, sont autant de facteurs qui expliquent en partie les faibles valeurs de l'absorption atmosphérique dans les domaines spectraux considérés.

VII - CONCLUSION

Le radiomètre infrarouge associé à la technique de détection hétérodyne présente un énorme intérêt de par sa très grande sensibilité et sa haute résolution. Cette méthode nouvelle constitue un excellent moyen de mesure de l'absorption atmosphérique et peut contribuer à la mise en évidence de plages spectrales transparentes.

Nous avons pour principal objectif la réalisation d'un tel appareillage ainsi que son expérimentation sur quelques raies d'émission du laser oscillateur local. La fabrication des divers sous-ensembles ainsi que leur assemblage n'ont posé aucun problème majeur. Il en a été de même des mesures réalisées sur 3 raies d'émission du laser CO_2 : en effet, la transmission verticale a été déterminée avec un excellent rapport signal sur bruit.

Par ailleurs, les travaux réalisés sur le laser N_2O permettent d'envisager son utilisation en tant qu'oscillateur local au sein du radiomètre hétérodyne.

D'autre part, l'étude préliminaire des détecteurs Hg Cd Te doit permettre leur utilisation dans les meilleures conditions et ainsi d'accroître les possibilités futures de la chaîne de mesures.

L'analyse des travaux effectués nous amène à envisager certaines modifications de l'appareillage pour permettre la poursuite éventuelle de l'expérience. En effet, la dispersion des résultats lors des mesures de la transmission verticale est liée pour une grande part aux variations des conditions météorologiques (pourcentage d' H_2O , température, vitesse du vent...); aussi, si l'on veut entreprendre une étude comparative de l'absorption dans le but de déterminer les fenêtres atmosphériques possibles dans la région des $10\ \mu\text{m}$, on est contraint à s'affranchir des phénomènes atmosphériques fluctuants. De ce fait, il nous semble nécessaire de joindre à l'appareillage expérimental actuel, une voie servant de référence. Alors que le canal "mesures" explorerait les régions comprises entre 9 et $11\ \mu\text{m}$, le canal de référence serait maintenu sur la même voie d'émission du second oscillateur local (par exemple $10,59\ \mu\text{m}$) pendant toute la durée des essais. En plus de son caractère référentiel, cette amélioration préciserait l'influence des différents paramètres météorologiques sur la valeur de l'absorption atmosphérique.

BIBLIOGRAPHIE

- I - Infrared Heterodyne Solar Radiometry
JH. MC ELROY - Applied Optics, July 72 vol 11 N° 7 p. 1619
- II - High - Resolution Atmospheric Transmission Measurements Using a Laser Heterodyne Radiometer S.R. King, D.T. Hodges, T.S Hartwick and D.H Barker - Applied Optics, vol 12 N° 6, June 1973 p. 1106
- III - Optical Heterodyne Signal Power obtained from Finite Sized Source of Radiation
H.T YURA Applied Optics, vol 13 - N° 1, January 74 p.150
- IV - The Antenna Properties of Optical Heterodyne Receivers A.E SIEGMAN
Proceedings of the I.E.E.E. vol 54 N° 10, October 66 p. 1350
- V - Heterodyne Detection of blackbody Radiation J.GAY, A. JOURNET, B. CHRISTOPHE, and A. ROBERT Applied Physics letters 22 448 (1973)
- VI - Remote Detection of SO₂ and CO₂ with a Heterodyne Radiometer R.T MENZIES
Applied Physics letters, vol 22 N° 11
- VII - Air Pollution : Remote Detection of Several Pollutant Gases with a Laser Heterodyne Radiometer
R.T MENZIES, M.S SHUMATE, Science, May 1974 p. 570
- VIII - Atmospheric transmittance, 7-30 M μ m :
Attenuation of CO₂ Laser Radiation R.A MC CLATCHEY, and al Air Force Cambridge Research Laboratories
L.G Hanscom Field Massachussetts
12 October 1972
- IX - AFCRL Atmospheric Absorption line Parameters Compilation
R.A MC CLATCHEY et al Air Force Cambridge Research Laboratories
L.G Hanscom Field, Massachussetts
26 - January 1973
- X - Atmospheric Absorption at the Line Center of P (20) CO₂ Laser Radiation
PKL. YIN and R.K Long - Applied Optics
Vol 7 N° 8 August 68 p. 1551
- XI - An Infrared Heterodyne Radiometer for
High Resolution Measurements of Solar Radiation and
Atmospheric transmission B. Peyton and al
I.E.E.E. Vol QE 11 N° 8 p. 975 p. 569

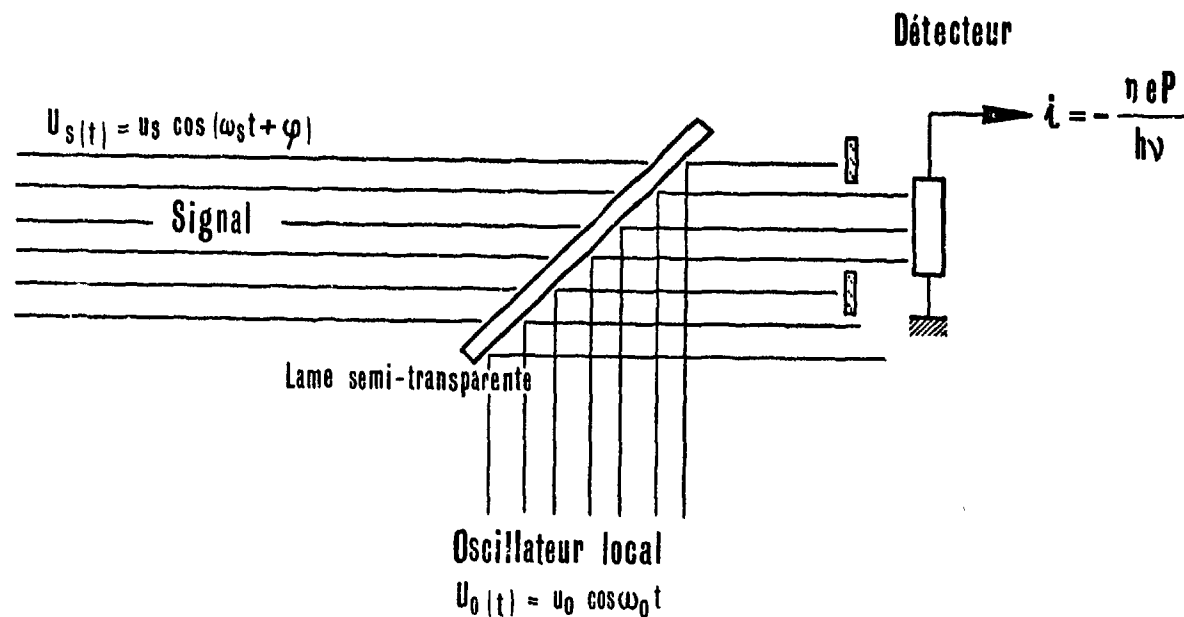
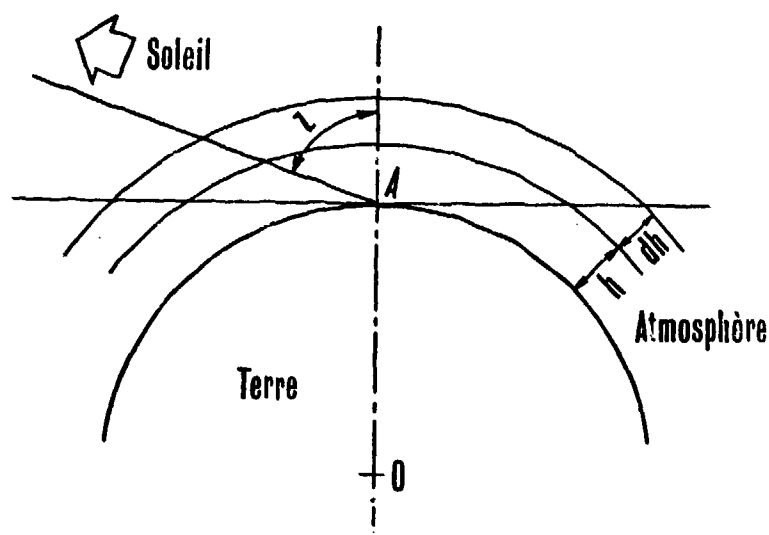


Fig.1 Principe de la détection hétérodyne

Coefficient d'absorption atmosphérique $k(z)$

$$k(z) = \int_0^{\infty} \frac{k(h) dh}{\sqrt{1 - \left(\frac{R}{R+h}\right)^2 \sin^2 z}}$$

avec $k(h) = \text{Cte}$ et $\sin z$ petit
le signal est donné par :

$$S = a e^{-k \cdot h \sec z}$$

Fig.2 Principe de la mesure de l'absorption atmosphérique

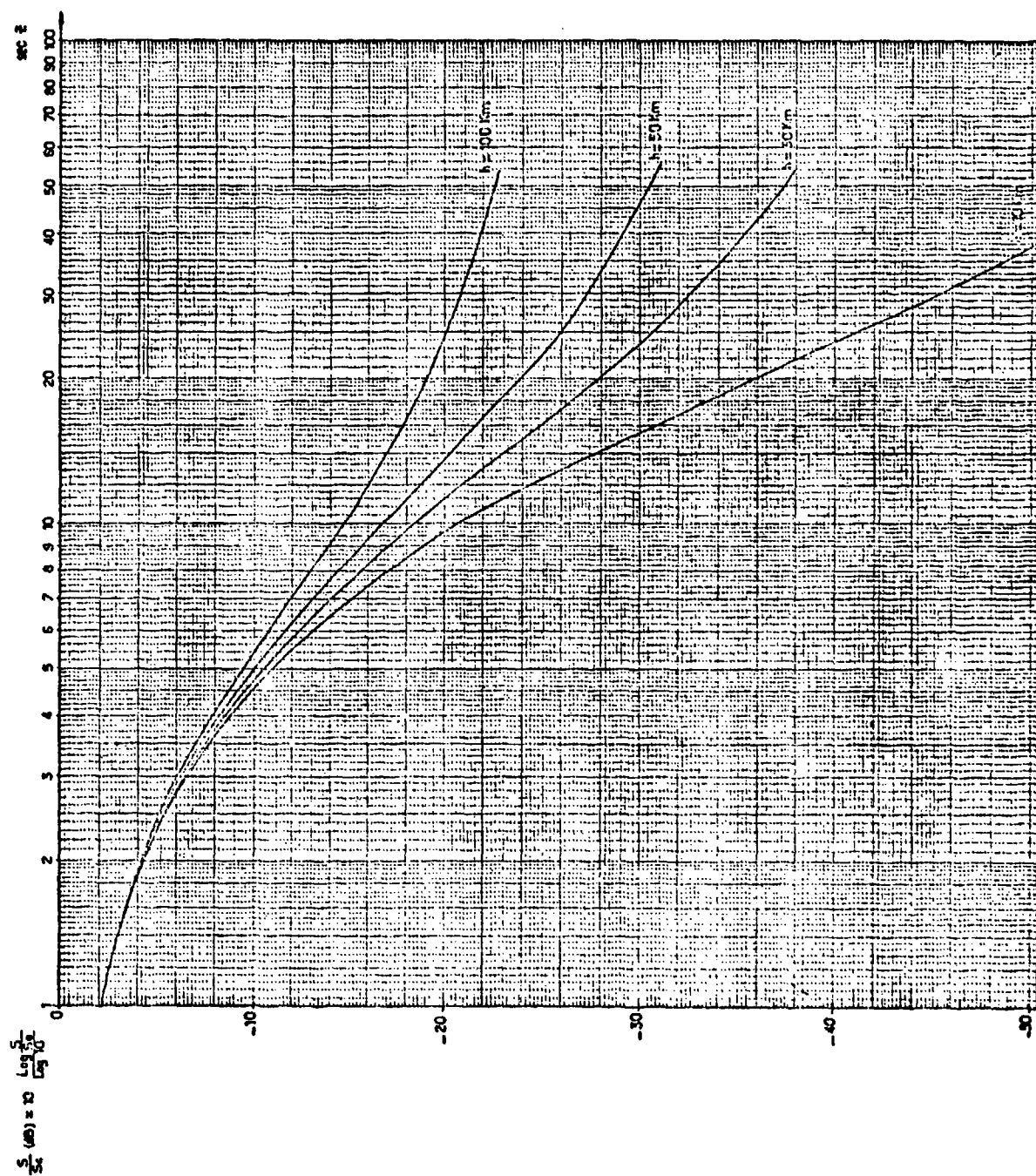


Fig.3 Signal transmis en fonction de l'inclinaison du soleil pour différentes épaisseurs d'atmosphère

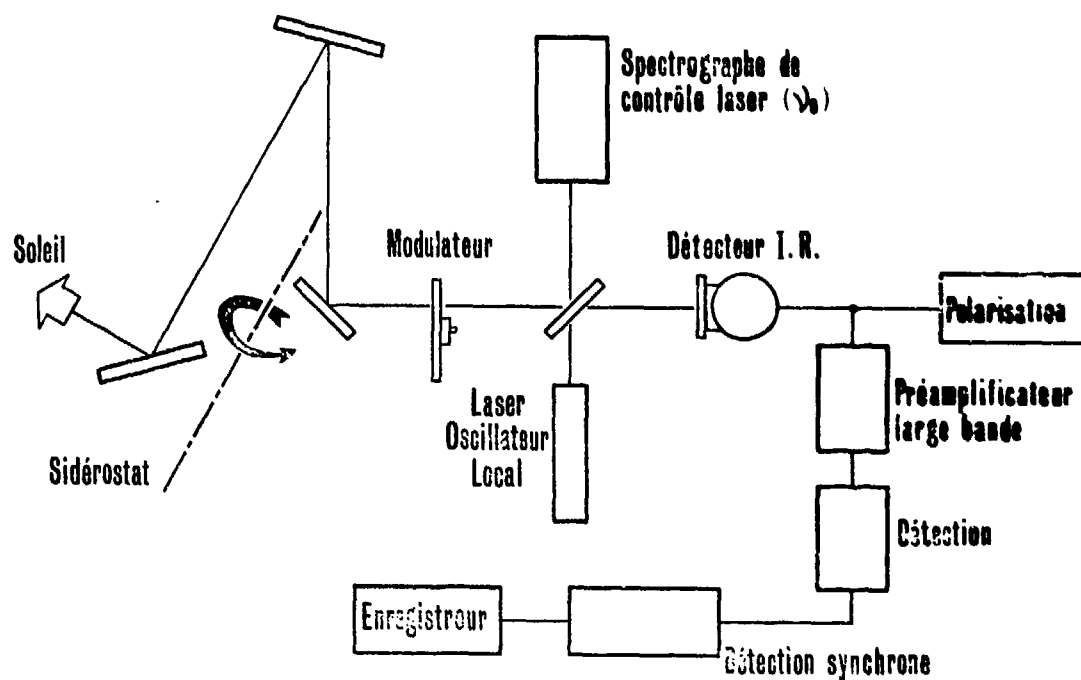
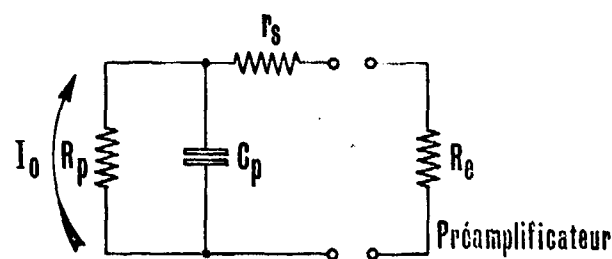


Fig.4 Principe de l'IHR pour des mesures atmosphériques

Circuit équivalent du détecteur



Puissance de bruit à l'entrée : $P_N = (F_0 - 1) k T_e \Delta f$

$$+ \frac{4 k T_d \Delta f R_p R_e}{(r_s + R_p + R_e)^2 + C_p^2 R_p^2 \omega^2 (r_s + R_e)}$$

$$+ \frac{4 k T_d \Delta f r_s R_e (1 + R_p^2 C_p^2 \omega^2)}{(r_s + R_p + R_e)^2 + C_p^2 R_p^2 \omega^2 (r_s + R_e)}$$

$$+ \frac{2 q I_0 \Delta f R_p^2 R_e}{(r_s + R_p + R_e)^2 + C_p^2 R_p^2 \omega^2 (r_s + R_e)}$$

$$I_0 = \frac{\eta q P_{LO}}{h \nu}$$

Puissance signal à l'entrée :

$$2 P_{LO} P_s \left(\frac{\eta q}{h \nu} \right)^2 \frac{R_p^2 R_e}{(r_s + R_p + R_e)^2 + C_p^2 R_p^2 \omega^2 (r_s + R_e)}$$

Figure 5

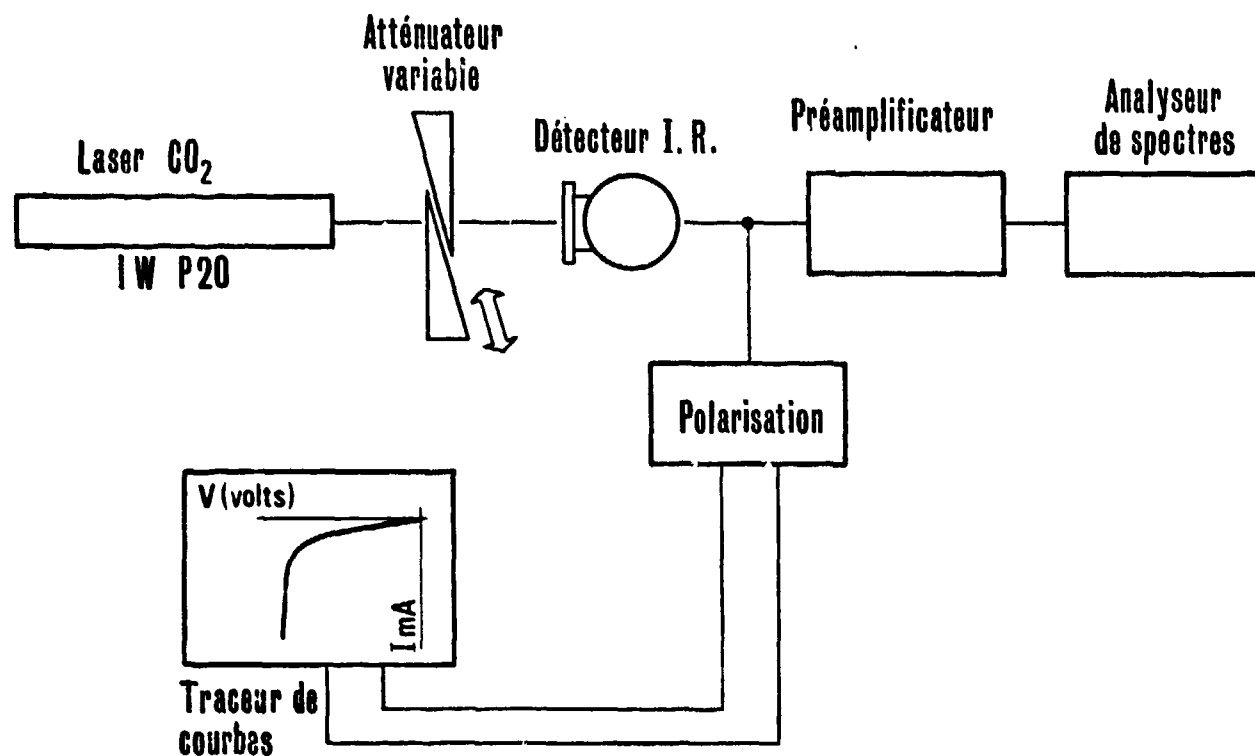


Fig.6 Banc de test des détecteurs

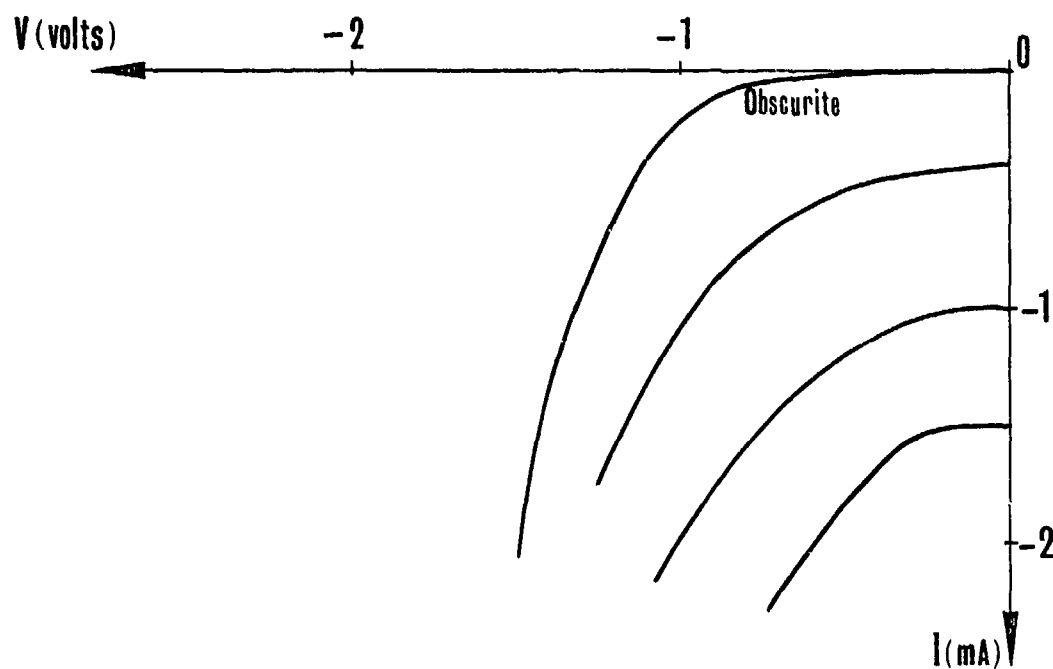
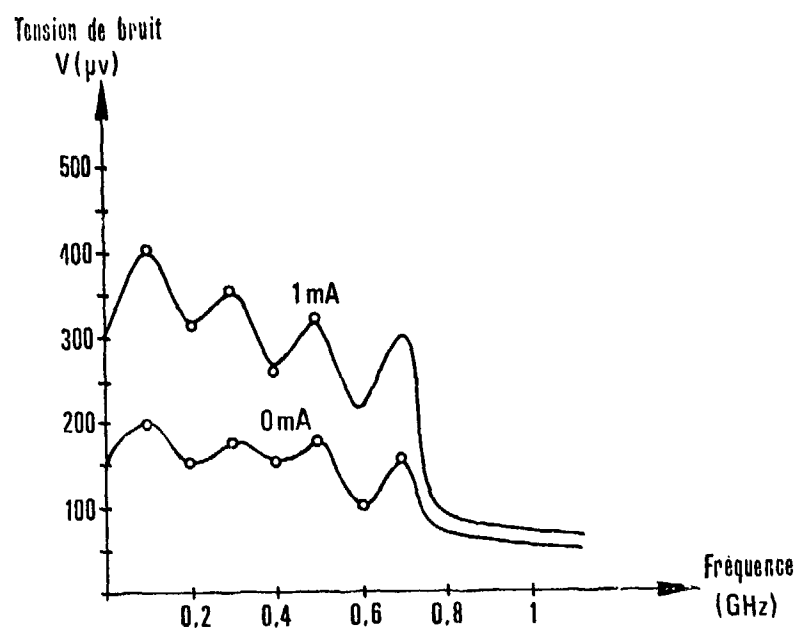
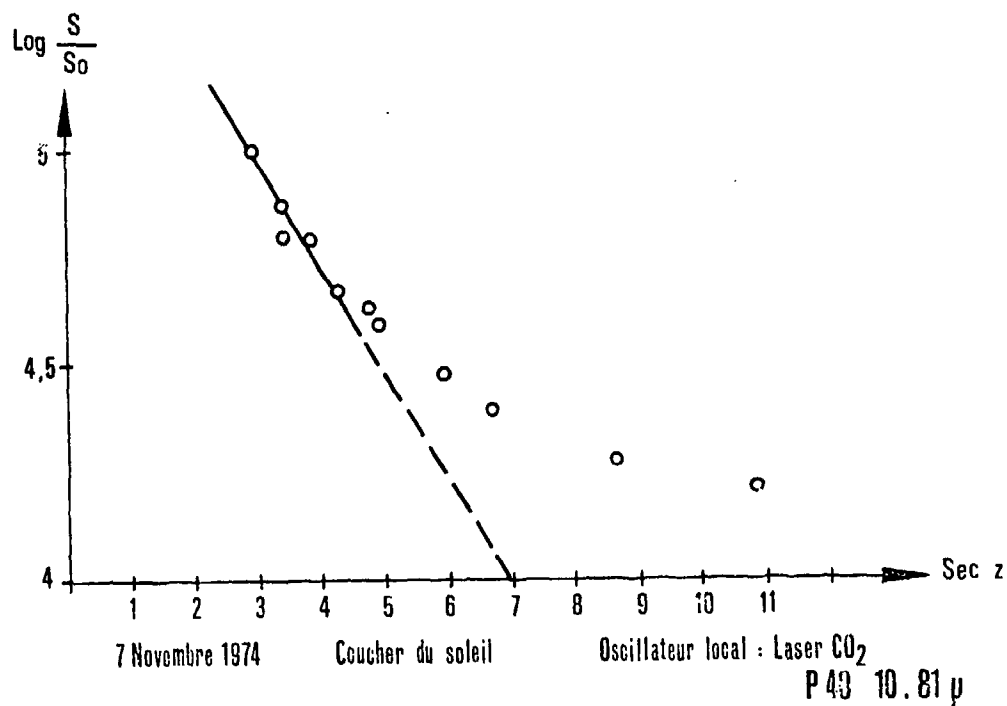


Fig.7 Caractéristiques I.V. du détecteur PV 1216 pour différents éclairagements laser



Bande passante ~ 600 MHz
 Calcul à 200 MHz BW 310^9 Hz
 Courant photovoltaïque 1mA
 Gain du préampli. 55,2 dB
 Bruit théorique $2q I_0 R_{eq} = 1,38 \cdot 10^{-20}$ W
 Bruit mesuré $1,4 \cdot 10^{-20}$ W
 Efficacité = $\frac{\text{Bruit théorique}}{\text{Bruit total}} = 0,8$

Fig.8 Bande passante et efficacité à la détection hétérodyne I.R. du PV 1216



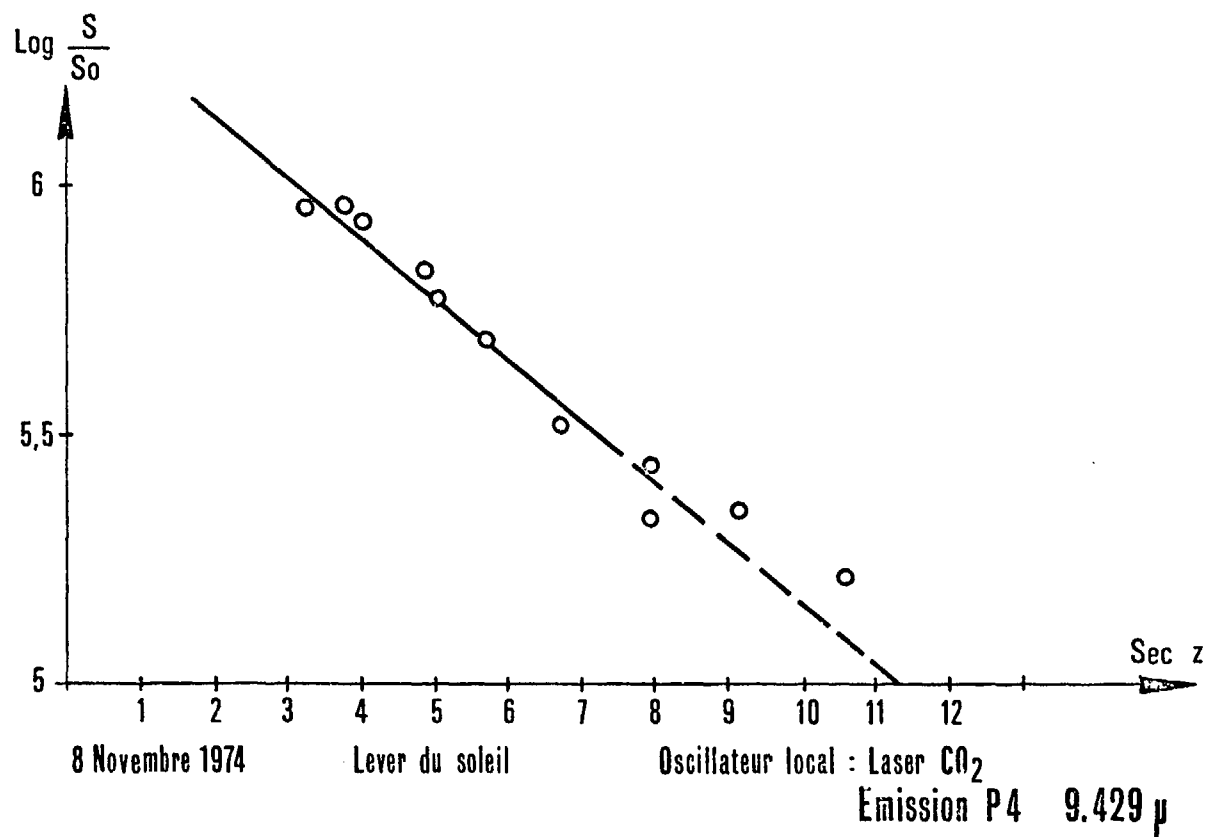


Fig.10 Transmission verticale 0,88

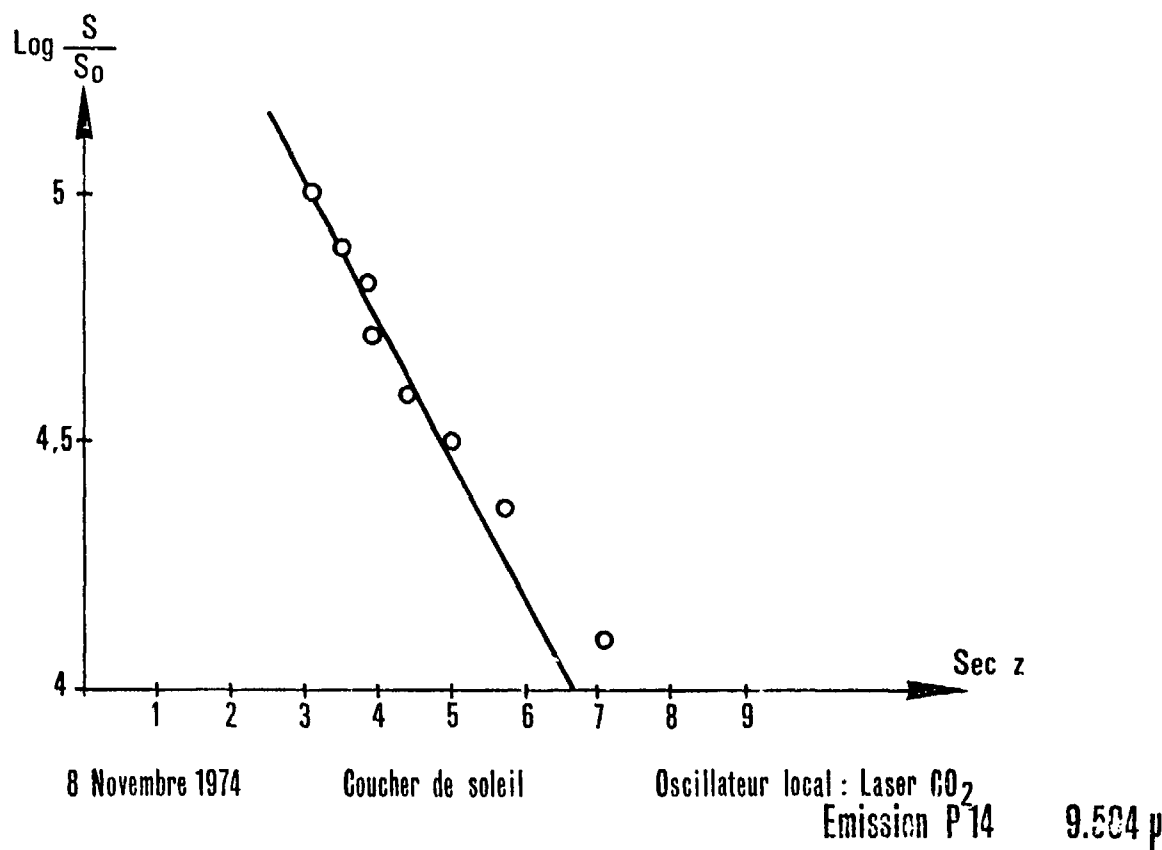


Fig.11 Transmission verticale 0,75

QUESTIONS AND COMMENTS ON SESSION III

LOG-NORMAL PROBABILITY DISTRIBUTION OF STRONG IRRADIANCE FLUCTUATIONS: AN ASYMPTOTIC ANALYSIS

Dr. D. H. Hohn: Regarding the comment of Dr. Fried to this paper, within the context of earlier laser beam propagation measurements* aside from log-normal, even normal intensity distributions were found, as well as distributions in between. The detecting areas used were small, the bandwidths were around some hundred Hz to 1 kHz. The analyzing method (probability paper) could not be verified for a normal distribution, but definitely could for a non log-normal, that can be approximated by a normal.

* D. H. Hohn, Optik 30, 161 and 239 (1969) (D. H. Hohn, Appl. Optics, about 1964, cited in the above mentioned paper)

Dr. L. R. Bissonnette: No reply - no comments.

Dr. Consortini: The starting point of your analysis is the hypothesis that the logarithm of the electric field has a normal distribution which implies that the phase fluctuations be normally distributed. Have you considered the possibility that the phase be not normally distributed? Our group has some unpublished data from which doubt arises about the distribution of phase fluctuations which in some cases do not look as a normal one.

Dr. L. R. Bissonnette: No, the starting point of my analysis is not the hypothesis that the logarithm of the electric field has a normal distribution. I simply use this hypothesis to obtain the log-normal formula for the normalized irradiance variance, equation 15. Then, I derive, independently of any probability distribution and without closure approximations, the asymptotic solutions for the amplitude moments $\langle A \rangle$, $\langle AA^* \rangle$ and $\langle A^2 \rangle$. These solutions are substituted in the log-normal formula and it is found that the resulting expression diverges to infinity, which demonstrates that the log-normal probability distribution for the electric field is an inconsistent approximation. Therefore, your findings that the phase fluctuations do not appear to be normally distributed are actually in complete agreement with my analysis.

Dr. D. L. Fried: In a series of measurements I was involved in about seven years ago, measurements of the probability distribution of intensity scintillation were made under saturation of scintillation condition. We found that over more than ± 2 standard deviations the intensity variation was log-normally distributed. Doesn't this contradict your results?

Dr. L. R. Bissonnette: Yes, I am well aware of this paradox which has already been recognized by Wang and Strohbehn (1974a). I have demonstrated in this paper that the log-normal distribution is either not self-consistent, or not consistent with Maxwell's equations. Therefore, what I can say regarding this paradox is that the apparent experimental support for the log-normal distribution in the saturation region has a local empirical value at best. Incidentally, Prof. Kerr has just told us that his recent measurements (characterized by a small detector, .25 x .25 mm, and a large frequency bandwidth of the receiving electronic equipment) show significant discrepancies with the log-normal formula in the saturation region. Therefore, this question of experimental support is certainly not settled. However, based on the theoretical asymptotic result of this paper, I conclude that the log-normal hypothesis cannot safely be used in constructing propagation models in turbulent media. The reader may find it useful to read the last three paragraphs of Section 4 of this paper which deals with this problem.

MEASUREMENTS OF THE ATMOSPHERIC TRANSFER FUNCTION

Dr. Buchtemann: What is the specific advantage of this interferometric MTF measurement method compared with recording the point image and doing the transfer numerically?

Dr. R. J. Scaddan: The main advantage of the interferometric method is that the measured MTF is independent of the aberrations of the telescope, interferometer, Spectracon and Microdensitometer, whereas the MTF measured by Fourier transforming a recorded point image must be corrected for the MTF of the receiving and analyzing optics. This MTF of the system must be accurately known for the particular conditions of recording and analysis.

INTENSITY CORRELATION OF RADIATION SCATTERED ALONG THE PATH OF A LASER BEAM PROPAGATING IN THE ATMOSPHERE

Dr. R. Reiter: You have taken into account the influence of the relative humidity. However, this influence seems to be rather complex. In the range of about 60 ... 100% relative humidity, the diameter of the aerosol particles varies strongly. So it seems to be necessary to record the aerosol particle size distribution in addition to the other atmospheric parameters.

Dr. M. Bertolotti: No comment.

PROPAGATION OPTIQUE DANS L'ATMOSPHERE

Dr. H. T. Yura: First, heterodyne absorption measurements were made by S. King and T. Hartwick (in the US) at 10.6μ . Their resolution was 10 MHz. They also had to account for the finite diameter of the sum of their signal-to-noise ratio calculations. They also have made heterodyne means at other wavelength (e.g., 3.8μ).

Dr. B. Christophe: It's correct that the signal-to-noise ratio is reduced but this is not a significant drawback in our measurements which are only relative. We hope to undertake measurements in the 5μ band in the future.

Dr. B. Kock: Is it possible to calibrate in absolute numbers the sensitivity of photovoltaic cells in order to be able to measure solar radiation?

Dr. B. Christophe: Not available.

Summary of Session III
COHERENT PROPAGATION

by

Dr. H. T. Yura, Chairman

The topic of coherent propagation can be conveniently divided into two sections, the first having to do with discussions relating to the first and second statistical moments of the optical field (e.g. phase effects, beam spread, while the second relates to discussions of higher order statistical moments (e.g. irradiance statistics or scintillation effects). With regard to the status of affairs concerning the first and second statistical moments it was clear from the papers (Dainty and Scaddan, Kerr, Lutomirski, Raidt, and Yura) that experiment and theory are well in hand. For instance, available theory regarding beam spread (Lutomirski) permits calculating the long term beam spread from an arbitrary laser transmitting aperture. Available experiments (Raidt) on focussed laser beams seem to be in good agreement with theory both qualitatively and quantitatively. From an engineering point of view, a phenomenological description of turbulence effects on laser beams was given (Kerr) including improvements resulting from the cancellation of beam wander through reciprocity tracking. The phenomenological description is analytic and physically based and is sufficiently accurate for many engineering purposes. Measurements of the atmospheric modulation transfer function (Dainty and Scaddan) have been carried out using bright stars as sources. The form of the modulation transfer function agrees with that predicted on the basis of the Kolmogorov spectrum at small separation, but there was a departure at larger separation. This is presumably due to finite outer scale effects, as discussed by Yura. A simple, physically intuitive discussion of phase effects was presented that obtains all of the results of Tatarskii and others using more rigorous mathematical methods. It is felt, with regard to phase and beam spread effects, that this aspect of optical wave propagation is well understood.

The situation regarding irradiance statistics (i.e., the fourth optical moment) has improved greatly during the past two years. Historically, irradiance statistics (or scintillation phenomena) were the most frequently measured and the least well understood. In particular, the saturation of the variance of irradiance has been seen experimentally for over a decade while the theoretical explanation of this phenomena has just recently appeared in the literature. A physical model of irradiance statistics was presented (Yura) which is in accord with much of the experimental observations (as well as other more mathematical theories). In particular, the calculated variance of irradiance, shape of the covariance of irradiance in the saturation regime, and shape of the temporal power spectrum in the saturation regime all seem to be in good agreement with observations. The physical-optic effects leading to saturation phenomena are well understood in that the physical model presented seems to account for most of the observations. However, there still appears to be a question regarding the probability distribution of irradiance (or equivalently, amplitude) in the saturation regime.

A paper by L. Bissonnette purports that the optical wave amplitude has a normal distribution in the saturation regime. Bissonnette first demonstrates that the widely used log-normal hypothesis for the amplitude is inconsistent with the observation of saturation of the variance of irradiance. This point has been discussed previously by various authors in the open literature. Bissonnette then goes on to show that the irradiance variance tends to unity if alternatively, the wave amplitude has a normal distribution. However, he does not prove that other probability distributions (e.g. Rayleigh) are consistent with a saturated irradiance variance. During the ensuing question period several people took issue with the normal distribution for the amplitude. On intuitive grounds, one is led to conclude that the cartesian components of the complex field should be normally distributed in the saturation (or multiply scattered) regime. This implies that the amplitude is Rayleigh distributed (and phase is uniformly distributed between zero and 2π). Indeed, Professor Kerr indicated that a preliminary analysis of his long pathlength scintillation experiments performed this summer tend to support a Rayleigh probability distribution for the wave amplitude. However, this should not be taken as conclusive evidence as more data reduction needs to be carried out. Also, D. Fried noted that strong scintillation experiments carried out a number of years ago in California tended to support a log-normal distribution for the wave amplitude. However, it was noted that a limited electronic bandwidth may have been used in these experiments leading to biased results. Finally, I wish to point out that other authors have concluded that the wave amplitude should be Rayleigh distributed in the asymptotic limit of the saturation regime (e.g. De Wolf, Furutsu and Dyson).

During the round table discussion no major issues evolved, although a number of technical points were discussed. For example, a rather lengthy discussion of an operational definition of the outer scale of turbulence took place, with no definite conclusions being reached. Everyone agrees that physically there must be an outer scale (e.g. the energy in the spectrum must be finite) but how does one account for it in optical measurements in the most general way is still an open issue with some authors.

In summary, I feel that phase effects are very well understood, notwithstanding operational definitions of the outer scale of turbulence. For example, one is able to compute near and far field beam patterns, with and without tilt removal, for an arbitrary laser output field distribution. The physical-optic effects leading to saturation phenomena appear to be well understood. Only the question of the wave amplitude probability distribution in the saturation regime remains. It is felt that this matter will be resolved only after conclusive experiments are performed (e.g. those of J. R. Dunphy and J. R. Kerr).

PROPAGATION OF HIGH POWER LASER BEAMS THROUGH THE ATMOSPHERE; AN OVERVIEW

John N. Hayes
U.S. Naval Research Laboratory
Washington, D. C., U.S.A.

SUMMARY

The major categories of the thermal blooming phenomena encountered in the propagation of high power laser beams in the open atmosphere are developed. The basic physical ideas behind each type of blooming phenomenon are discussed; experimental data and theoretical formulation are briefly presented that show the present state of knowledge of these areas and to introduce the reader to the more detailed subject treatment that will follow in this section of the conference report.

1. INTRODUCTION

High power laser beams propagating through the earth's atmosphere suffer all the effects that low power beams encounter, while, at the same time, creating some of their own—the so-called thermal blooming phenomenon. The new effect here is simple to describe. Absorption of laser radiation by the atmosphere alters the temperature of the ambient air and, in turn, its refractive index. The altered index thereupon changes the characteristics of the propagation of the laser beam. Generally, the temperature change is positive causing the air to act like a thick, weak diverging lens and thereby enlarging the beam size in the focal plane—hence the name “thermal blooming.”

Thermal blooming is a non-linear phenomenon; analytic treatments of the effect are therefore difficult to obtain. The greater amount of the theoretical work on the problem has thus been confined to numerical integration of the basic differential equations of propagation, although some notable analytic successes do exist. On the observational side, we are better off. Laboratory experiments using doped absorption cells and low power beams first demonstrated the reality of the thermal blooming phenomenon (GORDON, J.P., et al., 1965; RIECKHOFF, K.L., 1966; CALLEN, W.R., et al., 1967; MCLEAN, E.A., et al., 1968) and have subsequently been done to provide qualitative features and quantitative data. Although a number of propagation issues remain, in the last five to seven years the basic problems of thermal blooming have been identified; the qualitative character of many aspects of blooming are clearly discernible and, in many instances, quantitative results are available. Moreover theory and experiment are in suspiciously excellent agreement.

Thermal blooming manifests itself in a variety of ways. It has proved useful to categorize the phenomena in accordance with the kind of laser beam under consideration. Hence, we shall speak of CW, pulsed, and multiple pulsed thermal blooming. In the paragraphs to follow, each of these areas will be further developed. Phenomena that tend to complicate the problems will be briefly addressed. The subsequent papers in these proceedings will treat some of these topics more specifically and in greater detail than can be done in a brief resumé.

2. CW THERMAL BLOOMING

For simplicity, the atmosphere is taken to be homogeneous and isotropic in all characteristics except for a constant uniform wind. A CW laser beam, focussed at range f , is turned on at a specified time while slewing through the air; the beam is assumed to be steady after turn-on at very early times, the abrupt switching-on of the heat source in the air creates sound waves which propagate through and out of the beam—these sound waves continuing as long as the beam fluctuates in time. The beam begins the blooming first and most rapidly in the focal volume (we are not interested in the beam beyond focus); the beam spreading travels backward towards the laser source; this “motion” continues until the combined wind and slewing have succeeded in sweeping the heated air out of the beam (HAYES, J.N., 1971; 1972). At that time, a steady state has developed for the beam in the vicinity of the aperture; with the passage of time, the beam reaches the steady state condition at longer and longer ranges until the entire region between aperture and focal plane becomes time independent (cf. WALLACE, J., JR. and CAMAC, M., 1970; AITKEN, A.H., et al., 1971). This will *not* occur, however, if wind and slewing combine algebraically to be zero somewhere along the beam; then the beam will be steady for all ranges short of the zero wind point, the so-called stagnation point, and time-dependent at longer ranges (HAYES, J.N., 1972). This kind of thermal blooming has come to be called “stagnation zone blooming.” (If slew rate and/or wind speed change with time, the stagnation point moves, increasing the complexity of a description of the effect.) For beams slewed at a sufficiently high angular rate, the relative motion between the beam and the air can be Mach 1 at some point between aperture and focus; or the natural (relative) wind speed may be that large. The sound waves generated by the unheated air passing into the beam will then remain in the beam, accumulating, with time, density changes which may distort the beam. In this case, the beam is said to suffer “trans-sonic blooming” (HOGGE, C.B., and BRAU, J.E., 1974; HAYES, J.N., 1974).

Thus, the prime thermal blooming problems associated with steady CW lasers are: (1) transient CW thermal blooming, (2) steady state CW thermal blooming (CWSS), (3) stagnation zone CW thermal blooming (CWSZ), and (4) transonic blooming. By altering the basic simplifying initial premises, one can complicate the details of any one of these topics, but nothing fundamentally new is added.

Steady state CW blooming has received the most attention. Transient thermal blooming is of tertiary interest except as a check on computer codes designed to handle time-dependent problems. Stagnation zone blooming is as important as CWSS and is being actively studied at present, and the transonic case has proved to be an exciting but short-lived topic.

2.1. Steady State CW Thermal Blooming

Qualitative studies by a number of investigators, some previously cited, showed the reality of the CW steady state blooming effect. Quantitative work followed a few years later (cf. GEBHARDT, F.G. and SMITH, D.C., 1971; KLEIMAN, H. and O'NEILL, R.W., 1971). Simple considerations were immediately confirmed; for example, the time for the onset of the steady state is of the order of the wind transit time d/v at the aperture (d = aperture diameter of beam, v = transverse component of wind); the deflection of the beam into the wind, i.e., of light rays into regions of higher refractive index, was observed as expected, and also, for the same physical reason, the pronounced elongation of the beam in the direction orthogonal to the wind vector. The more accurate quantitative data provided a test bed for the refined theoretical analyses that were taking place. Several theoretical groups in the US developed a variety of numerical algorithms to solve the wave equation (BRADLEY, L. and HERRMANN, J., LL; WALLACE, J., AVCO-EVERETT; AITKEN, A., HAYES, J.N., ULRICH, P.B., NRL; HOGGE, C.B., and BUTTS, R.R., AFWL; BREAU, H. and ALCARAZ, E., BRL; later, FLECK, J., JK., LLL; BROWN, W.P., JR., HUGHES; LYNCH, P.J. and BULLOCK, D., TRW; GEBHARDT, F.G., UTRC; and LUTOMIRSKI, R., PACIFIC-SIERRA). The different methods were compared with one another and found to agree, and, finally, were shown to agree with laboratory experiment (HAYES, J.N., et al., 1971). Figure 1 shows a photograph of a cross-section of a steady state CW bloomed beam taken during a UTRC (United Technology Research Center, formerly UARL) experiment; alongside is an iso-irradiance contour plot, generated by the Lincoln Laboratory (LL) theory group, of a closely related case. The qualitative comparison is clearly excellent. An extensive quantitative comparison between the UTRC experimental results and theory, made by the NRL group, is shown in Figure 2. Plotted here is the peak irradiance of the bloomed beam to the peak irradiance of the attenuated but undistorted beam against a dimensionless parameter N , as defined by the UTRC group. The computer simulation of the laboratory experiment is clearly quite good.

The basic physical parameters that must be specified for a complete description of the CW steady state thermal blooming problem are: (1) the beam shape at the aperture, along with a characteristic radial length a , and power P ; (2) the aperture phase, including the focal length f ; (3) the beam wavelength λ , or wave-number $k = 2\pi/\lambda$; (4) the atmospheric absorption coefficient $\alpha_a(\lambda)$ and scattering coefficient $\alpha_s(\lambda)$; (5) the component v of natural wind speed transverse to the beam propagation axis; and (6) the slewing rate Ω . If all discussions are restricted to a fixed beam shape and phase distribution at aperture, there are eight physical numbers to be specified; if range R at which observations are made is distinct from the focal length f , one more parameter is adjoined to the set. The propagation equation (the paraxial approximation to the Kirchhoff equation) may be cast, in several ways, into dimensionless form, wherein the above physical parameters appear in several dimensionless parameter combinations. Current favorites are: (1) the distortion parameter $N_D = (\alpha P / P_c) (v e) (\partial e / \partial t) (k f / a)$, (2) the Fresnel number $N_F = k a^2 / f$, (3) the slewing number $N_w = \Omega f / v$, and (4) the absorption number $N_a = \alpha f$ (BRADLEY, L. and HERRMANN, J., 1974). If range R and focal length are not identical, replace f by R above and introduced (5) the defocussing parameter $N_R = f / R$. The distortion parameter N_D is a measure of the energy deposited in a volume of air that has crossed the aperture and is therefore proportional to $\alpha P / a v$.

A basic characteristic of CW steady state thermal blooming is schematically illustrated in Figure 3, which is a variant of Figure 2. Here we have plotted absolute focal plane peak irradiance against the distortion parameter N_D . Fixing all parameters except power, the abscissa may be read as power. The lower curve is representative of a case with no slewing and the higher, of a non-zero slewing number. The dashed line represents the plot in the presence of attenuation but no blooming, while the solid lines are the curves with blooming present and have been generated theoretically and observed experimentally. A very important feature is noted by the small vertical strokes. For all physical parameters held fixed except power, we see that peak focal plane irradiance achieves a maximum value, called the optimum irradiance, I_{op} , at a finite value of power, the so-called optimum power P_{op} (also called the critical power). The corresponding value of N_D is called the critical distortion parameter. Further increase of laser power creates so much blooming that the peak flux drops. The value of P_{op} will depend upon all the remaining physical variables, which implies that the maximum deliverable peak irradiance and the power levels to accomplish that depends upon the wavelength, absorption, wind speed, slewing and range. The curves also schematically demonstrate the shift to higher values of I_{op} and P_{op} with increased slewing rates; this shift occurs because the higher wind speeds downrange diminish the focal volume contribution to the overall result.

Such curves have come to be called power optimization curves. Curve fits to computer generated data, and to experimental data, have been generated at Lincoln Laboratory, Naval Research Laboratory, United Technology Research Center and elsewhere. There are no unique functional forms and the choice of form may be affected by the degree of accuracy of curve fit that is sought. The virtue of these "scaling laws," as the formula fits have come to be called, is that they enable one to make rapid estimates of thermal blooming effects in application studies, and to determine the values of I_{op} and P_{op} .

The power optimization curves are unique to each beam shape and phase front selection. Nevertheless, all cases studied show the same general characteristics. A family of optimization curves for defocused beams is schematically illustrated in Figure 4, where we see that the optimum power increases with increasing values of the defocussing parameter $N_R = f / R$, while the optimum peak irradiance appears to decrease by about a factor of 2/3 to 1/2. The dashed curve represents the envelope of the optimum irradiance points.

The detailed structure of the power optimization curves may be modified purposefully by a judicious choice of the aperture phase distribution in a preprogrammed or in an active manner. While it is true that CW steady state blooming contributions are approximately equally distributed along the beam, the cumulative phase changes acquired by various light rays along their paths may, in some approximation, be ascribed to an equivalent phase distortion located at the exit aperture of the laser. To the extent that these phases can be calculated in terms of the meteorological and laser parameters, a phase distortion can be deliberately induced in an element of the optical train to compensate for this distortion and thereby partially compensate the blooming. Bradley and Herrmann (BRADLEY, L. and HERRMANN, J., 1974) have shown the feasibility of the idea; Figure 5, taken from their work demonstrates, the dramatic reduction in the blooming that can be achieved in a single case, while Figure 6) shows their alteration of the power optimization curves for truncated Gaussian beams for two slewing numbers. It is seen that the critical distortion parameter is raised and the peak irradiance is increased. Because the thermal effects of the focal volume are reduced by high slewing rates, their method works better for high slew numbers. Coherent optical adaptive techniques (BRIDGES, W.B., et al., 1974) possess the potential to compensate actively both turbulence and thermal blooming.

2.2. CW Stagnation Zone Blooming

CW stagnation zone blooming is as frequent a phenomenon as the CW steady state case, but is considerably more complicated by the introduction of a new variable—time. The physics of CWSZ blooming is not different from that of CWSS blooming, but the numerical work becomes more tedious and lengthy, requiring more "bookkeeping," computer storage space, and computational time. Experiments likewise increase in engineering complexity, particularly for the case of moving stagnation zones.

Early work done on stagnation zone blooming (HAYES, J.N., 1972) set the geometric conditions for the existence and motions of stagnation zones, and semiquantitative arguments showed that zone locations near the focal volume caused the most rapid and most severe deterioration of the beam in the focal plane. A variety of secondary atmospheric phenomena such as laser induced convection, or natural turbulence do not appear to have the necessary short time scales to ameliorate stagnation zone blooming. Within the past year, propagation codes have been developed that can handle these problems (FLECK, J.A., JR., et al., 1975; ULRICH, P.B., 1974). Laboratory simulations performed at UTRC have provided a set of quantitative data against which the computer code predictions can be compared (BERGER, P.J., et al., 1975). Berger has developed a tentative formulation of a stagnation zone scaling law (BERGER, P.J., 1975).

The conditions under which stagnation zone blooming occurs are illustrated in Figure 7. The source is taken to be in motion, relative to the atmosphere, with speed v and the beam is in angular motion with slew rate Ω . If Ω or v varies with time, the location of the stagnation point will move relative to the beam, as indicated in the figure by the dashed arrow. While the combined winds, $v + \Omega Z$, add to zero at one point only, there is a general volume in the beam in which the air is being continuously heated in spite of the beam/air motions. This region is more easily perceived by depicting the total motion relative to the stagnation point at $Z_S = -\Omega/v$, as in Figure 8. The shaded region of the figure depicts the stagnation zone at time t seconds after the beam has been switched on; for a beam focussed at range f , the length of this region is approximately proportional to $a_0(1 - Z_S/f)/\Omega t$, where a_0 is the beam radius at aperture. The absorbed energy, within the stagnation volume, is proportional to $\alpha P/a_0^2(1 - Z_S/f)^2$. Thus, the strength of the lens, after initial transients have decayed, is roughly proportional to $\alpha P/a_0(1 - Z_S/f)$. This simple picture, due to the UTRC group (BERGER, P.J., et al., 1974), shows that the strength of the lens for a stationary stagnation zone, becomes constant after a sufficient passage of time and is stronger closer to the focus. The effect of the "lever arm" must be adjoined to evaluate the amount of blooming as a function of location.

Figure 9 is taken from a forthcoming paper of Berger, et al., and shows the decline in peak irradiance with time at a given observation plane due to blooming in the presence of a stagnation zone. The laboratory simulation was achieved by rotating a horizontal absorption cell, through which a 10.6 μ laser beam passed, about a pivot point whose location could be selected as desired. The black circles are the predictions made with the NRL 4-D code in a computer simulation of the experiment; it was necessary to include natural convection in the theory to obtain agreement with the data. The agreement between theory and experiment is quite good both in the magnitude of the effect and the time scales for the onset of the quasi-steady state. The work of these authors confirms the qualitative ideas about the strength of the effect and its dependence on the important physical parameters and has provided a quantitative basis for further study in this area of thermal blooming.

2.3. CW Transonic Thermal Blooming

If any portion of a laser beam moves, due to slewing or wind speeds, at a speed equal to that of sound, then the sound waves generated by the beam/air interaction will tend to remain stationary in the beam so that the resultant density and index changes increase with time. Beam quality may thus be subsequently affected; the question is the strength of the effect. Exact solutions of the nonlinear hydrodynamic equations for a steady one-dimensional flow in the presence of a fixed one-dimensional heat source have been derived (HAYES, J.N., 1974); the solution show that, at Mach 1, very large density changes develop. These results, however, suffer from the obvious geometrical (and related boundary condition) problems and their implications for the two-dimensional cases are suggestive but unclear. Hodge (HOGGE, C.B. and BRAU, J.E., 1974) independently studied the time development of the density changes in the two dimensional problem by numerical methods and concluded that large density changes could develop. Subsequently, an exact solution of the two-dimensional linearized hydrodynamic problem for an arbitrary moving heat source was derived, independently, by Ellinwood and Mireis (ELLINWOOD, J.C., et al., 1975), Wallace and Pasciak (WALLACE, J., et al., 1975), and by the author (HAYES, J.N., 1974). These solutions approach the steady state solution of Tsien and Bielock (TSIEN, H.S., et al., 1949) as $t \rightarrow \infty$; at Mach 1, this density change becomes infinite (violating the linearization hypothesis, of course). For a slewed beam, Mach 1 will occur at one point only; Bradley (BRADLEY, L., 1974) showed that, when calculating the focal plane phase changes, this singularity was integrable and that the resultant phase distortions were too weak to represent significant alteration of the beam. However if the Mach 1 condition prevails everywhere in the beam, Bradley concludes the effect may then be strong. This result has been confirmed subsequently by propagation calculations by Wallace. Because strong density changes in the linearized hydrodynamic theories are suspect, Wallace (WALLACE, J., JR., 1975), and subsequently Ellinwood and Mireis (ELLINWOOD, J.C., et al., 1975) investigated the nonlinear effects and concluded that nonlinearities greatly suppress the density changes, enhancing Bradley's argument. It appears now that transonic effects will not cause serious perturbations on the quality of a high energy laser beam except under very special circumstances.

3.0. PULSED THERMAL BLOOMING

Short, high power, high energy, single pulse beams suffer a variety of thermal blooming different from the CW steady state kind. Multiple pulse beams will undergo blooming of each kind, but a careful selection of parameters will allow for improved propagation.

3.1. Single Pulse Blooming

The air may be regarded as stationary for short pulses of lengths of the order of tens of microseconds; therefore, the long-term isobaric CW blooming effects discussed in section 2 will not take place. Instead, there are density changes associated with the generation of strong sound waves; these are given by (LONGAKER, P.R. and LITVAK, M.K., 1969)

$$\delta\rho(r, z, t) \approx \frac{\gamma - 1}{5} t^3 \nabla^2 \alpha I(r, z, t)$$

where $I(r, z, t)$ is the local instantaneous beam irradiance. Axial symmetry is assumed here. The peak irradiance distribution in any plane downrange can be shown to be approximately (AITKEN, A.H., et al., 1973)

$$I(0, z, t) = I(0, z, 0)(1 - t^3/t_c^3)$$

where t_c is a characteristic time proportional to the pulse power and depends upon the remaining atmospheric and laser parameters. Beam behavior as a function of time is illustrated in Figure 10. According to the above expression, the on-axis irradiance vanishes at

$t = t_c$; this is not true in reality but the constant t_c is, indeed, an appropriate time scale characterizing the decay of the on-axis intensity. Ulrich (ULRICH, P.B., 1971) has shown, with a wave-optics pulse propagation code, that the above expression for on-axis intensity represents the behavior of a Gaussian beam with very good accuracy.

Two important characteristics of single pulse blooming to be emphasized are: (1) most of the blooming contributions arise from the focal volume, unless the power is extremely high, and (2) the detailed characteristic of the blooming are very strongly shape dependent through the presence of the factor $\nabla^2 I$. The second point is somewhat mitigated by the first since, in the focal region, all beams, through diffraction, tend to look similar to one another. The importance of beam shape increases as power increases because the near-field contributions to blooming increase.

For any conceivable application, when the on-axis intensity drops to zero, the pulse should be terminated thereafter; this leads, from the condition $1 - t_p^2/t_c^2 = 0$, to a relationship between pulse energy E_p and pulse length t_p which is $E_p t_p^2 = \text{constant}$. Thus, every pulsed laser, characterized by a point (E_p, t_p) in an E - t plane, with values of (E, t) "above" the line $E_p t_p^2 = \text{constant}$ will be dominated by thermal blooming in the focal plane.

However, not every laser corresponding to a point below the blooming line will be capable of delivering energy to the focal plane; when the pulse lengths are made very short, air breakdown sets in to limit the fluence delivery (see the paper by Lencioni in these proceedings; for a comprehensive review of laser induced air breakdown, see Smith, D.C., and Meyerand, R.G., 1976 and also SMITH, D.C., 1974). Assuming a unique breakdown threshold intensity I_B , pulse energies and pulse lengths at threshold are related by $E_p \approx I_B t_p \pi a_f^2$, where a_f is beam radius in the focal volume. Thus, a pulse laser will need to have its characteristic point (E_p, t_p) in the E - t plane lying below the curve $E_p t_p^2 = \text{constant}$ and to the right of the curve $E_p = I_B t_p \pi a_f^2$ in order to deliver fluence at the focal plane without hindrance from blooming and breakdown. These restrictions are illustrated in Figure 10. Finally, if a minimum fluence delivery is the objective of a high power single pulse laser, then the pulse energy E_p must exceed a minimum value E_m whatever the pulse length. This lower bound is also indicated in the figure. Thus the combination of pulse energy and pulse length of the desired pulsed high power laser must lie within the unshaded triangle of Figure 10; if E_m exceed the value of E where the breakdown and blooming lines intersect, then no useful single pulse laser exists.

The borders of the triangle of Figure 11 depend upon wavelength, focal length, initial beam size and beam quality. The breakdown border is vague because there is no unique breakdown threshold for a mixture of aerosol sizes and because transmission will also be a function of pulse length. This latter ambiguity arises because the transmission will be limited by the size of the air breakdown plasmas, and for short pulses, this growth may remain small enough to permit some propagation through the beam. Work in this area is in progress.

Experimental confirmation of the theory for single pulse t^3 blooming is discussed in a separate contribution to these proceedings (see O'NEILL, R., JR. and KLEIMAN, H., 1975). We shall see that the verification is quite good.

In the event that t^3 blooming is so weak that no significant beam distortion occurs, then the density changes accumulated in the beam from simple isobaric heating will cause blooming (HAYES, J.N., 1971, and A. KEN, A.H., et al., 1973). This kind of blooming has received quantitative confirmation (CARMEN, R.L., et al., 1968, KENEMUTH, J.R., et al., 1971, and BUSER, R., et al., 1975).

3.2. Multiple Pulse Propagation

Multiple pulse high power beams are potentially affected by the t^3 blooming of single pulse beams and the isobaric heating effect experienced by CW beams. However, a new effect, called enhancement, occurs, which makes it possible, through a judicious choice of parameters, to reduce or eliminate each kind of blooming.

A reduction in the strength of single pulse blooming and, concomitantly, of the density of self-induced air breakdown plasmas may be achieved by defocussing the beam; the decrease influence levels is then to be compensated by repetitive pulsing. At high single pulse energies and low repetition rates with a sufficiently strong wind, one expects to see repeated single pulse beams propagating independently of one another. At high repetition rates and for all pulse energies, one would expect to see behavior similar to that of a CW beam. The intermediate cases therefore become of interest. Wallace proposed, (WALLACE, J., JR., 1973) and was among the first to show (WALLACE, J., JR., and LILLY, J., 1975) that, in the absence of single pulse blooming, intermediate repetition rates could be chosen which would improve the average peak irradiance over that of the *attenuated but undistorted* beam—i.e., instead of *blooming* one could achieve an *enhancement*. The reality of enhancement has been confirmed experimentally (BUSER, R., et al., 1974; also see the presentation of EDELBERG, S., these proceedings). One version of this result is depicted in the graph of Figure 11, computed by Ulrich. The abscissa is the pulse repetition frequency; its relation to the overlap number is indicated on the graph. The ordinate is average peak irradiance, normalized to unity at $N_0 = 1$. Each point of the curve represents the result of a computer calculation for a beam of the same fixed average power as any other point; pulse energy therefore decreases as the repetition frequency increases. The dashed line indicates the peak irradiance level of a CW high power beam under the same conditions. It is seen that as N_0 increases the performance of the MP device approaches that of the CW and it is also true, but not indicated here, that the beams begin to look alike. At zero overlap, the beam propagates without any blooming. For values of N_0 between 1 and 5, the relative peak irradiance increases above unity—hence the term *enhancement*. The optimum value of overlap number will depend upon the wind, aperture size, pulse energy, absorption coefficient and range, among other things. The magnitude of the enhancement at optimum overlap number, for a wide variety of cases studied, is small—i.e., the beam propagates mostly like a vacuum beam. The significant point is that there is no significant degradation of the peak irradiance even though atmospheric heating is taking place.

These calculations were done assuming no single pulse blooming. When t^3 effects cannot be ignored, beam quality is adversely affected. The degree of defocussing chosen to avoid single pulse effects is generally determined by the t^3 blooming theory discussed earlier; when these effects cannot be avoided, then corrections to the multiple pulse code computer results can be made with the same theory.

The multiple pulse computer programs, developed at a number of US laboratories, have the assumption of no single pulse blooming in common, with the exception of the Lawrence Livermore code (FLECK, J.A., JR., et al., 1975) which includes a quasi-self-consistent single pulse blooming correction. As with CW computer codes, the MP programs come in a "steady state" version, and a full time-dependent transient form. The latter is required for the study of multiple pulse stagnation zone blooming.

In addition to the confirmation of the enhancement cited above, extensive multiple pulse propagation experiments are underway at Lincoln Laboratory. Dr. Seymour Edelberg of Lincoln Laboratory discusses these in a special detailed discussion of multiple pulse propagation in the next paper.

3. SPECIAL PROBLEMS

The discussion of the previous sections was based on enormous simplifications of the propagation issues. The real world phenomena will be considerably more complicated. Some of these complications are not essential to the understanding of the thermal blooming effect, although they may be very important. To mention a few topics we have in mind, these include the effect of beam shape, temporal dependence of power and of beam shape, winds variable both in space and time, variable absorption and extinction coefficients, etc. These special topics are very hard to categorize and therefore not amenable to systematic study. It is therefore more suitable to let the specialized devices and atmospheric conditions determine when they should be addressed.

Other categories of special problems that are under active investigation but will only be touched upon here are: (1) aerosols, (2) turbulence, (3) jitter and thermal blooming, (4) kinetic effects, (5) multiline propagation, and (6) adaptive aperture techniques.

3.1. Aerosols

As in the case of low power propagation aerosol extinction must be taken into account in the total extinction coefficient; while aerosols are not necessarily spherical, and refractive indices are not generally known, Mie scattering theory can provide rough estimates of the size of the scattering coefficients. However experimental work on aerosol distributions, compositions and types as well as real attenuation measurements that separate out the molecular and aerosol effects are needed.

Specific questions peculiar to high power propagation arise however. As mentioned, air breakdown occurs creating plasmas that will tend to obstruct propagation. While breakdown thresholds are fairly well in hand, more propagation data are needed. For aerosols that do not cause breakdown, there remains the matter of aerosol heating. Whether or not the aerosols evaporate, all aerosols will heat, some of the absorbed energy being stored internally, the remainder being conducted to the ambient air. For vaporizing aerosols, such as liquid droplets in particular, evaporation constitutes a large heat sink. Thus, not all the aerosol absorption leads to atmospheric heating. The part of the beam energy ultimately transmitted to the air, moreover, results in the formation of regions of hot air, with the aerosol at the center, and temperatures decreasing, roughly, with the inverse of distance from the aerosol. This strong but localized variation is therefore expected to lead to phase distortions of the near field beam that will manifest itself in irradiance fluctuations and beam spreading in the far field patterns in a manner akin to the effects of turbulence. An important difference between the two phenomena is that the average index variation along a light ray is not zero for aerosol heating as it is with turbulence. Several groups of authors (CALEDONIA, G. and TEARE, D., 1974; AVILES, J.B., 1974; LENCIONI, D.E. and KLEIMAN, H., 1974; COOK, and BUTTS, 1974) have shown in different and independent ways, that the average effective index change due to aerosol heating is modeled correctly by an equivalent molecular (i.e., uniform) absorption coefficient, the averaging effect being achieved by the beam itself on propagation through many independent realizations of the random distribution of aerosols both in space and in sizes. These authors show that an equilibrium temperature is reached depending upon particle size and generally increasing with particle size. Caledonia and Teare, and Aviles take into account evaporation and find in addition that particle temperature drops as evaporation reduces the particle radius. Since equilibrium temperature and particle distribution (and hence the amount of heat not transferred to the air) all intensity dependent, averaged aerosol absorption coefficients will in general be dependent upon location within the beam. This fact necessitates computer program changes for computer determination of the effects of aerosol heating.

For the case of multiple pulse beams in the presence of liquid droplets, droplet vaporization and shattering has been seen to occur (see, for example, KAFALAS, P. and HERRMANN, J., 1973 and also GLICKLER, S.L., 1971), causing significant improvement in transmission for successive pulses provided the initial pulse energy is sufficient to vaporize the droplets.

3.2. Turbulence

Because this topic has been addressed quite thoroughly for low power propagation in session 3 of this conference and Dr. W.P. Brown will discuss in detail the case of high power beams in this session, the description here will be brief. Turbulent index fluctuations cause phase variations in the near field of the beam that lead to intensity fluctuations at longer ranges. The beam is, on the average, spread over a larger area in the focal plane than it would otherwise be. The average spread consists, roughly speaking, of two components: A spread due to centroid wander (beam wander) which requires "long" time averages to define and a short term beam spreading. For CW high power beams, the turbulent spreading and the thermal blooming are, in principal, coupled because turbulence-induced wander induces an added small velocity of wind across the beam and because the higher frequency intensity fluctuations alter the character of the beam irradiance patterns that must be used to compute the heating term in the propagation equation. Bradley of Lincoln Laboratory (BRADLEY, L., 1973) has used a method calculating the propagation of the beam with the nonlinear CW equation through fixed phase screens simulating the index fluctuations and averaging the results of many realization of phases; the heating integral is thus calculated in a quasi-self-consistent manner. Brown (BROWN, W.P., JR., 1975) of Hughes Research Laboratory has introduced phase screens that move with the wind and has done time averaging. The methods compare favorably in their results and the reader is referred to the Brown's paper in this conference report for details.

3.3. Jitter and Thermal Blooming

Pointing and tracking laser beams through the atmosphere require the use of real, rather than ideal, optics and servo mechanisms. The result is that pointing will always be in error and efforts to correct the pointing create "jitter." Jitter will cause the focal spot to move and introduce a short and long time average increase in spot size, each of which will also depend upon the amplitude of the jitter signal. For high power beams, this can also introduce slewing winds into the beam which will affect the character of the thermal blooming. High frequency large amplitude jitter will be most likely to cause a jitter/thermal blooming interaction. At high slewing rates, since the contribution to thermal blooming from the focal volume portions of the beam are reduced, any such jitter/blooming interactions are expected to be reduced. Scaled laboratory experiments at UTRC (GEBHARDT, F., 1975) have fully confirmed this expectation and the

effects of jitter and thermal blooming can be combined by root sum square of area spreads, using the appropriate (long or short) time jitter averaging.

3.4. Kinetic Effects

Most propagation calculations assume that the energy absorbed from the laser beam is instantly translated into kinetic energy of the atmospheric molecules. Absorbed energy is, in reality, stored for a finite time in an excited state of the absorbing molecular species; if these times are comparable to or longer than wind transit times across the beam, then these kinetic effects can become important. The so-called "kinetic cooling effect" associated with the absorption of $10.6\ \mu$ radiation by atmospheric CO_2 is a case in point. (WOOD, A.O., CAMAC, M., and GERRY, E., 1971; also see BREIG, E.L., 1972) While the phenomenon has been shown to be considerably less important at sea level than originally thought, it can, (SICA, L., 1973) at altitude reduce the blooming or wind reverse the sign of the effect causing self-focussing leading to improved propagation. However, if or where transonic effects are important, then absorption ordinarily leading to heating ($\delta\rho < a$) at transonic speeds causes compression and positive density changes; when absorption normally leads to kinetic cooling, the signs of the density changes are now reversed.

3.5. Multiline Propagation

Almost all high power lasers will amplify more than one laser line simultaneously, giving rise to two or more beams emanating from the laser aperture. These will not necessarily have the same amplitude and phase characteristics, and will most certainly not have the same atmospheric absorption and extinction coefficients. Each wave will satisfy its own propagation equation, but they are coupled through the index of refraction which is determined by the heating due to all beams. It appears that for truly collinear beams whose wave-lengths are close, each blooms along with the others. This has been demonstrated by Ulrich (ULRICH, P.B., et al., 1974) who first developed a two line code. It follows that a line of high absorption coefficient and low power can seriously bloom a beam of lower absorption and higher power. Thus multiline codes that can propagate the different lines with independent phase and amplitude initial data will become increasingly important for a quantitative characterization of the propagation of realistic high power beams.

3.6. Adaptive Aperture Methods

For multiple pulse blooming where self-blooming effects are minimal and for CW steady state thermal blooming with high slew rates, the phase distortions that affect the far-field beam pattern reside, in the absence of turbulence, in the near field. To the extent that these phase aberrations can be modeled as being localized at the aperture itself, then deliberately induced phase distortions in the laser optics can be created that undo these aberrations and thereby rectify the beam in the far-field. Such a program has proved to be successful in principle; Lincoln Laboratory researchers (BRADLEY, L. and HERRMAN, J., 1974) have shown that the CW power optimization curves can be altered with the result of driving the optimum power upward and increasing the associated optimum peak irradiance by factors of two to three. Active phase adaptation methods for compensation of turbulent deformation of the beam have also been successful demonstrated, (BRIDGES, W.B., et al., 1974) and some compensation of thermal blooming is probably possible as well. These methods may yet prove to be dramatically successful in reducing or eliminating thermal blooming at some power levels, but it is probable that they will reach a power level, appropriate to each atmospheric condition, beyond which improvement cannot be made because of physical limitations to the amount and detail of mirror distortion that can be done and because of the fact that the thermal lensing effect at the higher powers cannot be consigned to the near field.

In the case of multiple pulse beams, Bradley (BRADLEY, L.C., 1974) has shown that phase compensation methods work even better than for CW beams in correcting turbulence and thermal blooming distortions. Wallace (WALLACE, J. JR., 1975) has independently demonstrated the dramatic improvement for the case of thermal blooming. These efforts are still in progress.

4. CONCLUSION

The basic features of the propagation of high energy laser beams through the atmosphere are well understood. The important problems appear to have been identified and, though most have remained intractable analytically, they have been or are being successfully described using numerical methods. Theory has been confirmed by experiment in all cases where tests have been made. Difficult technical problems remain and many detailed quantitative experiments and calculations must still be done for specialized propagation problems; the prospect for a resolution of these remaining kinds of problems within the next year appears very bright.

It has not been possible to prepare a complete reference list and it is very likely that some of the many energetic researchers in the field have been ignored; this is clearly true of my European colleagues. I beg the indulgence of those whose work may have been slighted. A more thorough review (with complete references) of the area of high power propagation will be appearing in the forthcoming article of Walsh and Ulrich. (WALSH, J.L., and ULRICH, P.B., 1976)

REFERENCES

- AITKEN, A.H., HAYES, J.N., and ULRICH, P.B., 1971, "Propagation of $10.6\ \mu$ Laser Beams in a Non-Turbulent Atmosphere," *J. Opt. Soc. Am.*, 61, 679; also see *Appl. Opt.* 11, p. 257, and NRL Report 7293.
- AITKEN, A.H., HAYES, J.N., and ULRICH, P.B., 1973 "Thermal Blooming of Pulsed Focussed Gaussian Laser Beams," *Appl. Opt.*, 12, p. 193.
- AVILES, J.B., 1974, "Thermal Effects of a Vaporizing Water Droplet Aerosol on High Energy Laser Propagation," 1975, (to be published).
- AVIZONIS, P.V., HOGGE, C.B., BUTTS, R.R., and KENEMUTH, J.R., 1972, "Geometric Optics of Thermal Blooming in Gases, Part 1," *Appl. Opt.*, 12, p. 554.

- BERGER, P.J., GEBHARDT, F.G., and SMITH, D.C., 1974, "Thermal Blooming Due to a Stagnation Zone in a Slew Beam," UARL Tech. Reports N921724-7, and N921724-12.
- BERGER, P.J., GEBHARDT, F.G., ULRICH, P.B., and ULRICH, J.J., 1975, "Transient Blooming of a Slew Beam Containing a Stagnation Zone," (to be published).
- BERGER, P.J., 1975, (private communication).
- BRADLEY, L.C., 1973 "Laser Propagation Through a Turbulent Medium," Optics Research (Lincoln Laboratory Report, #1) 1972.
- BRADLEY, L.C., 1974a, "Thermal Blooming in the Transonic Regime," Lincoln Laboratory Technical Report LTP-24, 30 January 1974.
- BRADLEY, L.C., 1974b, (private communication).
- BRADLEY, L.C., and HERRMANN, J., 1974, "Phase Compensation for Thermal Blooming," *Appl. Opt.*, 13, p. 331.
- BROWN, W.P., JR., 1975, "High Energy Laser Propagation," Hughes Research Laboratory Technical Report (Cont. No. N00014-73-C-0460).
- BREIG, E. L., 1972, "Limitations on the Atmospheric Thermal Effects for High Power CO₂ Laser Beams," *J. Opt. Soc. Am.*, 62, p. 518.
- BRIDGES, W.B., BRENNER, P.T., LAZZARA, S.P., NUSSMEIER, T.A., O'MEARA, T.R., SANGUINET, J.A., and BROWN, W.P., JR., 1974, "Coherent Optical Adaptive Techniques," *Appl. Opt.*, 13, p. 291.
- BUSER, R.G., and ROHDE, R.S., 1975, "Transient Thermal Blooming of Long Laser Pulses," *Appl. Opt.*, 14, p. 50.
- BUSER, R.G., ROHDE, R.S., GEBHARDT, F.G., BERGER, P.J., and SMITH, D.G., 1975, "A Study of Thermal Blooming of Repetitively Pulsed Laser Beams," (to be published).
- CALEDONIA, G., and TEARE, D., 1975, "Laser Beam--Atmosphere Aerosol Interactions," PROC. WINTER MEETING OF A.S.M.E., 1975.
- CALLEN, W.R., HUTH, B.G., and PANTELL, R.H., 1967, "Optical Patterns of Thermally Self-Defocussed Light," *App. Phys. Lett.*, 11, p. 103.
- CARMAN, R.L., and KELLEY, P.L., 1968, "Time Dependence in the Thermal Blooming of Laser Beams," *App. Phys. Lett.*, 12, p. 241.
- COOK, R., and BUTTS, R.R., 1974.
- ELLINWOOD, J.C., and MIRELS, H., 1975, "Density Perturbations in Transonic Slew Laser Beams," (to be published).
- FLECK, J.A., JR., MORRIS, J.R., and FEIT, M.J., 1975, "Time Dependent Propagation of High Energy Laser Beams Through the Atmosphere," UCRL Report 51826.
- GEBHARDT, F.G., and SMITH, D.C., 1971, "Self-Induced Thermal Distortion in the Near Field for a Laser Beam in a Moving Medium," *I.E.E.E. J.Q.E.*, 7, p. 63.
- GEBHARDT, F.G., and SMITH, D.C., 1972, "Effects of Diffraction of the Self-Induced Thermal Distortion of a Laser Beam in a Crosswind," *Appl. Opt.*, 11, p. 244.
- GEBHARDT, F.G., 1975, "Jitter and Thermal Blooming," (to be published).
- GORDON, J.P., LEITE, R.C.C., MOORE, R.S., PORTO, S.P.S., and WHINNERY, J.R., 1965, "Long-Transient Effects in Lasers with Inserted Liquid Samplers," *J. Appl. Phys.*, 36, p. 3.
- GLICKLER, S.L., 1971, "Propagation of a 10.6 μ Laser Beam Through a Cloud Including Droplet Vaporization," *Appl. Opt.*, 10, p. 644.
- HAYES, J.N., 1971, "Thermal Blooming of Laser Beams in Gases," NRL Report 7213: See also, *Appl. Opt.*, 11, p. 455.
- HAYES, J.N., 1972, unpublished.
- HAYES, J.N., 1974a, "Thermal Blooming of Rapidly Slued Laser Beams," *Appl. Opt.*, 13, p. 2072.
- HAYES, J.N., 1974b, unpublished.
- HAYES, J.N., ULRICH, P.B., and AITKE, A.H., 1972, "Effects of the Atmosphere on the Propagation of 10.6 μ Laser Beams," *Appl. Opt.*, 11, p. 257.
- HOGGE, C.B., and BRAU, J.E., 1974, "Propagation of High Energy Laser Beams in the Atmosphere," AFWL-TR-74-74.
- KAFALAS, P. and HERRMANN, J., 1973 "Dynamics and Energetics of the Explosive Vaporization of Fog Droplets by a 10.6 μ Laser Pulse," *Appl. Opt.*, 12, p. 772.
- KENEMUTH, J.R., HOGGE, C.B., and AVIZONIS, P.V., 1970, "Thermal Blooming of a 10.6 μ Laser Beam in CO₂," *Appl. Phys. Lett.*, 17, p. 220.
- KLEIMAN, H., and O'NEILL, R.W., 1971, "Deflection of a CO₂ Laser Beam in an Absorbing Gas," *J. Opt. Soc. Am.*, 61, p. 12.
- LEITE, R.C.C., MOORE, R.S., and WHINNERY, J.R., 1964, "Low Absorption Measurements by Means of the Thermal Lens Effect Using a He-Ne Laser," *Appl. Phys. Lett.*, 5, p. 141.
- LONGAKER, P.R., and LITVAK, M.M., 1969, "Perturbation of the Refractive Index of Absorbing Media by a Pulsed Laser Beam," *Appl. Phys.*, 40, p. 4033.
- LENCIONI, D.E., and KLEIMAN, H., 1974, "Effects of Aerosol Particle Heating on Laser Beam Propagation," Lincoln Laboratory Tech. Report LTP-27 (22 July 1974).
- McLEAN, E.A., SICA, L., and GLASS, A.J., 1968, "Interferometric Observation of Absorption Induced Index Change Associated with Thermal Blooming," *Appl. Phys. Lett.*, 13, p. 369.
- O'NEILL, R.W., and KLEIMAN, H., 1975, (these proceedings).
- RIECKHOFF, K.E., 1966, "Self-Induced Divergence of CW Laser Beams in Liquids--A New Nonlinear Effect in the Propagation of Light," *Appl. Phys. Lett.*, 9, p. 87.
- SICA, L., 1973, "Three Beam Interferometer for the Observation of Kinetic Cooling in Air," *Appl. Phys. Lett.*, 12, p. 2848.

- SMITH, D.C., 1974, "Overview of Laser Radiation-Induced Gas Breakdown," UARL-N178.
- SMITH, D.C., and MEYERAND, R.G., 1975, "Laser Induced Gas Breakdown," UTRC75-31.
- TSIEN, H.S., and BEILLOCK, M., 1949, (Title unknown to this author), *J. Aero. Sci.*, 16, p. 756.
- ULRICH, P.B., 1971, "A Numerical Calculation of Thermal Blooming of Pulsed Focussed Laser Beams," Naval Research Laboratory Report 7382 (30 Dec. 1971).
- ULRICH, P.B., 1974, (private communication).
- ULRICH, P.B., HANCOCK, J.H., and HAYES, J.N., 1974, "Simultaneous Two-Wavelength CW Laser Propagation," *J. Opt. Soc. Am.*, 64, p. 549.
- WALLACE, J., JR., and CAMAC, M., 1970, "Effects of Absorption at 10.6 μ on Laser Beam Transmission," *J. Opt. Soc. Am.*, 60, p. 1587.
- WALLACE, J., JR., 1973, (private communication).
- WALLACE, J., JR., and LILLY, J.Q., 1975, "Thermal Blooming of Repetitively Pulsed Laser Beams," *J. Opt. Soc. Am.*, 64, p. 1651.
- WALLACE, J., JR., and PASCIAK, J., 1975a, "Thermal Blooming of Rapidly Slew Laser Beams," (to be published).
- WALLACE, J., JR., 1975, "Compensating for Thermal Blooming of Repetitively Pulsed Lasers," (to be published).
- WALSH, J., and ULRICH, P.B., 1976, "Nonlinear Effects in Atmospheric Propagation," a chapter in "Laser Beam Propagation Through the Atmosphere," in Topics in Applied Physics, Springer-Verlag; (to be published).
- WOOD, A.D., CAMAC, M., and GERRY, E.T., 1971, "Effects of 10.6 μ Laser Induced Air Chemistry on the Atmospheric Refractive Index," *Appl. Opt.*, 10, p. 1877.

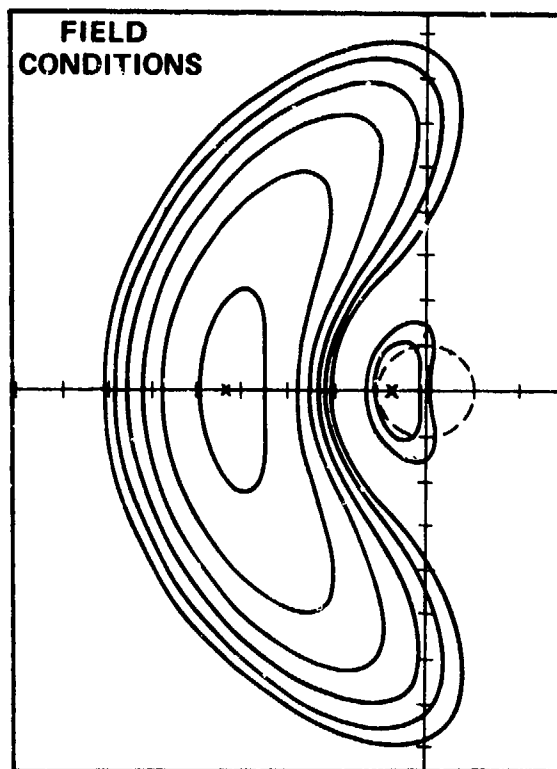
EXPERIMENT



1.2 mm

$N = 13$
 $F = 2.6$
 $N_a = 0.41$

THEORY



3.6 cm/div

$N = 16$
 $F = 2.8$
 $N_a = 0.134$

Fig. 1—CW Steady State Thermal Blooming, one point comparison between experiment and theory. The left hand portion of the figure is a photograph showing the structure of a bloomed beam under the laboratory conditions indicated on the figure, while the right hand figure is an isoirradiance contour plot derived from theory. The comparison is not precise as can be seen by the difference in the corresponding dimensionless parameters, but close enough to show that quantitative prediction of CW steady state thermal blooming is reliable. (This figure is by courtesy of Dr. Fred Gebhardt, United Technology Research Laboratory and Dr. L.C. Bradley and Dr. J. Herrmann of Lincoln Laboratory.)

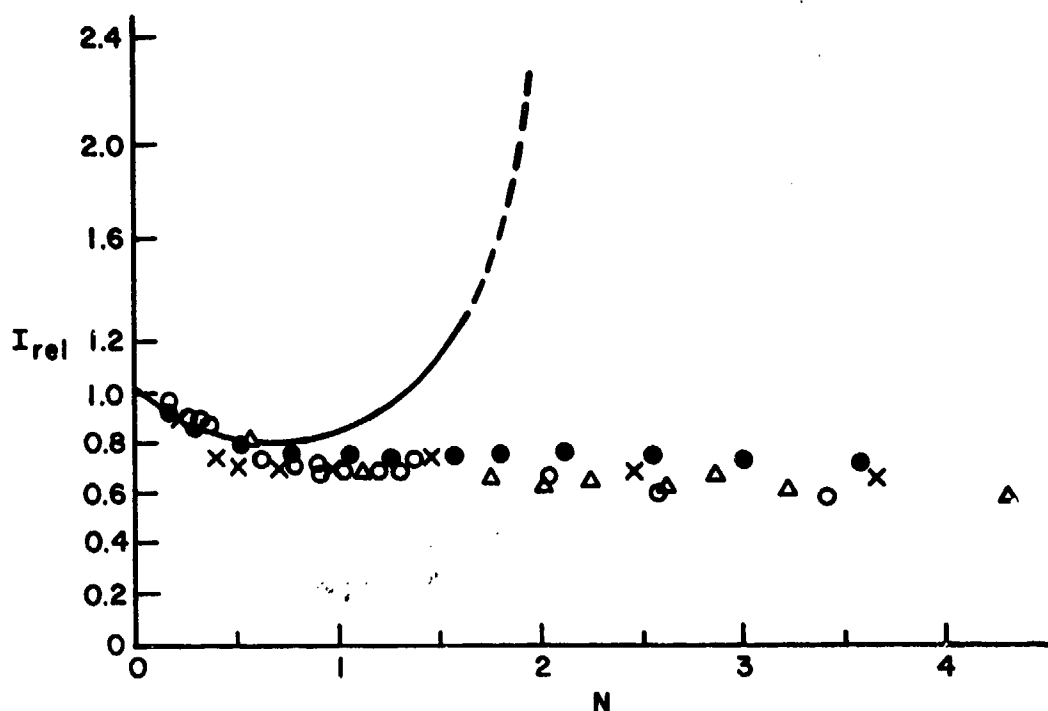


Fig. 2—Plotted here is the observed intensity divided by the unbloomed intensity as a function of the dimensionless parameter N as defined by Gebhardt, et al. 1971; the crosses X, circle O, and triangles Δ represent data obtained by Gebhardt et al. of UTRC in a laboratory simulation of thermal blooming. The solid circles are taken from the calculations of the NRL group (Hayes, et al., 1971) in a wave optics computer simulation of the experiments. The solid-dashed curve represents a geometrical optics theory of the experiment.

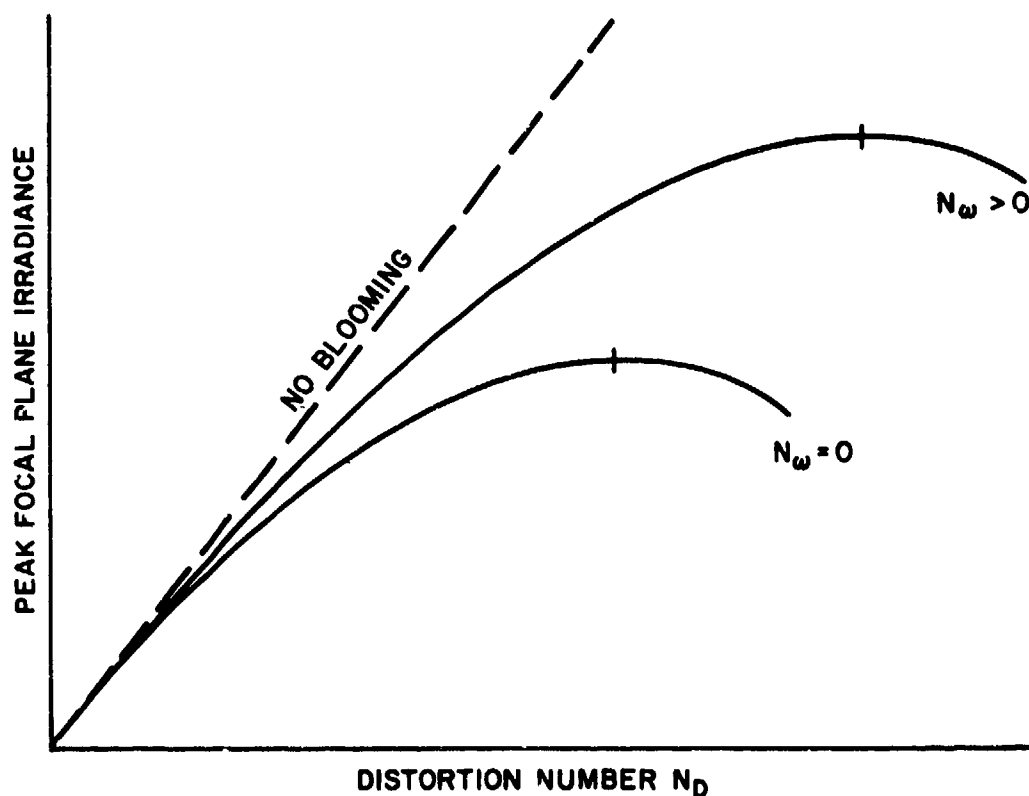


Fig. 3—Schematic Representation of Power Optimization Curve. The ordinate here represents an absolute quantity, the peak irradiance of the beam in the focal plane while the abscissa is the distortion number defined in the text, and is proportional to power. The lower curve represents the no slewing case while the upper curve is for positive slewing. The optimum power points, indicated by vertical bars moves to higher

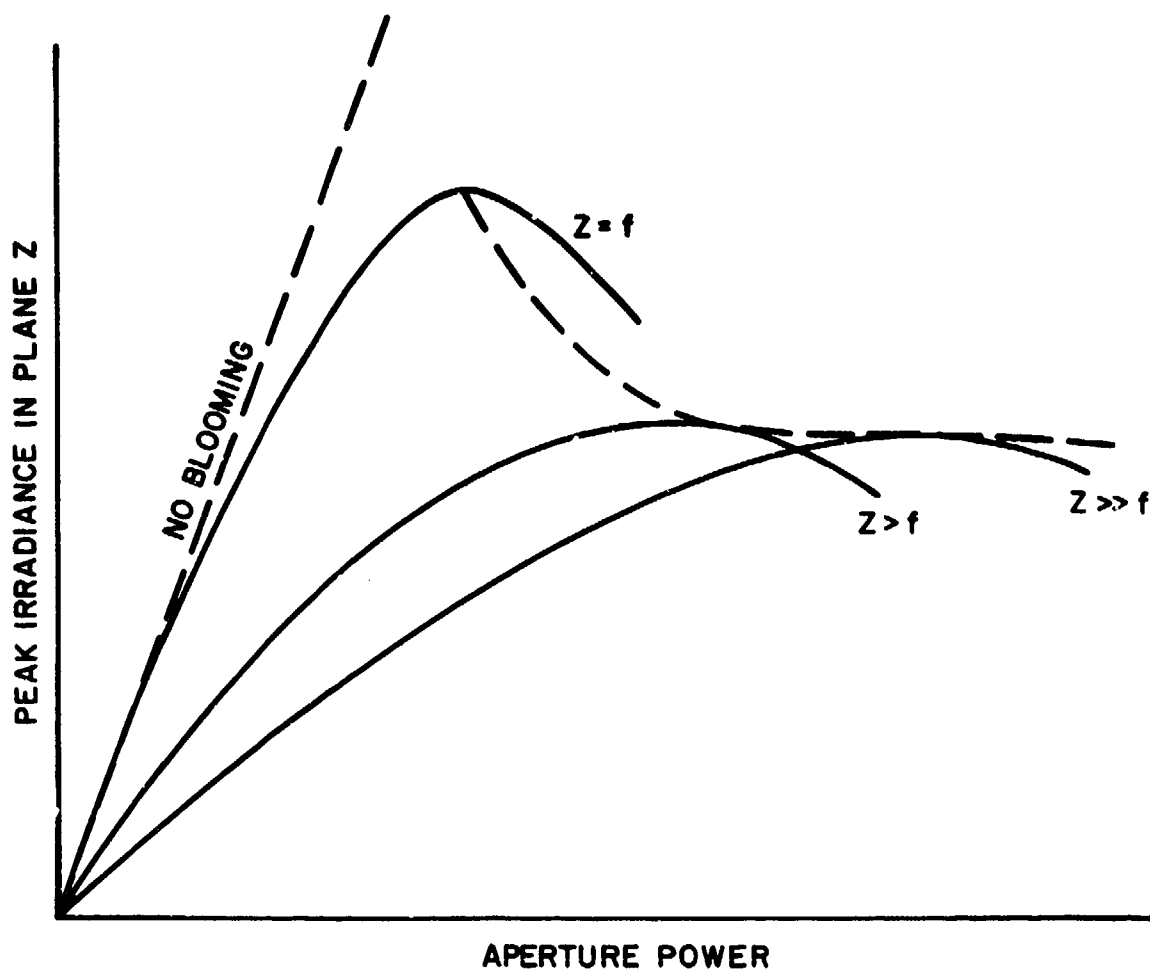


Fig. 4—Schematic Representation of Power Optimization Curves with Defocussing. Here I_{peak} represents peak irradiances in the plane Z with the beam focussed at plane f . The curves show that optimum power increases as defocussing increases; however, peak irradiances drops from the focussed beam values with their envelope illustrated schematically by the dashed curve.

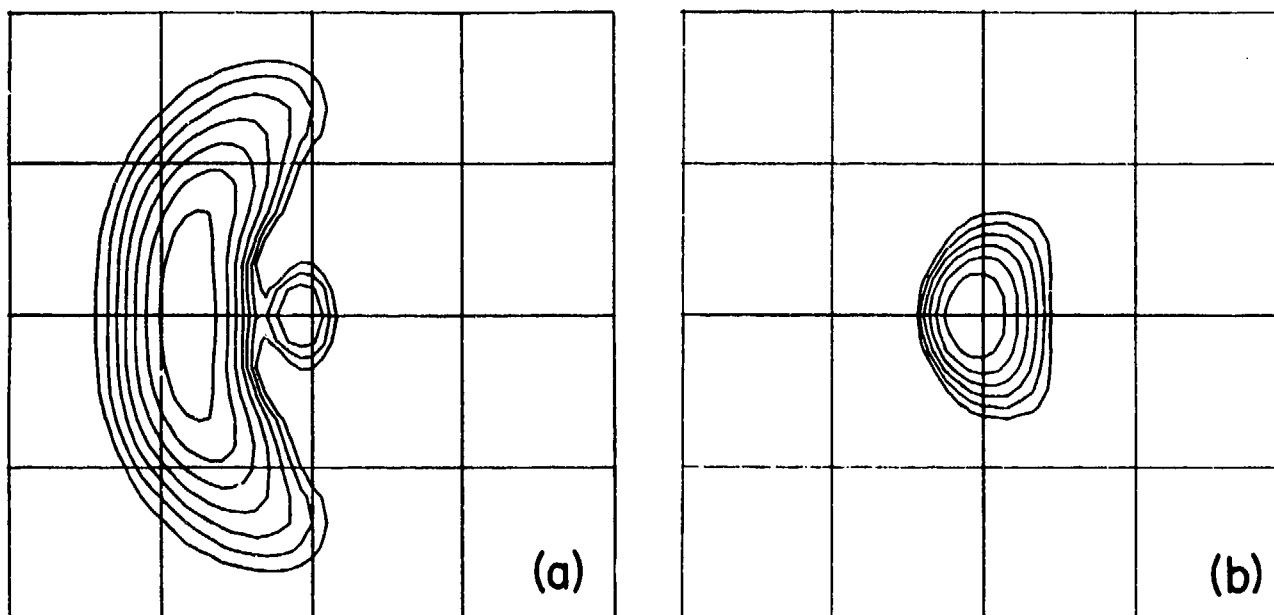


Fig. 5—Iso-irradiance contour plots in the focal plane of a truncated Gaussian beam (a) without correction, (b) with correction. Contours are separated by 2 dB; the highest contour in (b) is 6 dB higher than the one in (a). (Courtesy of Dr. L.C. Bradley and Dr. Jan Herrmann, Lincoln Laboratory; see Bradley and Herrmann, 1974)

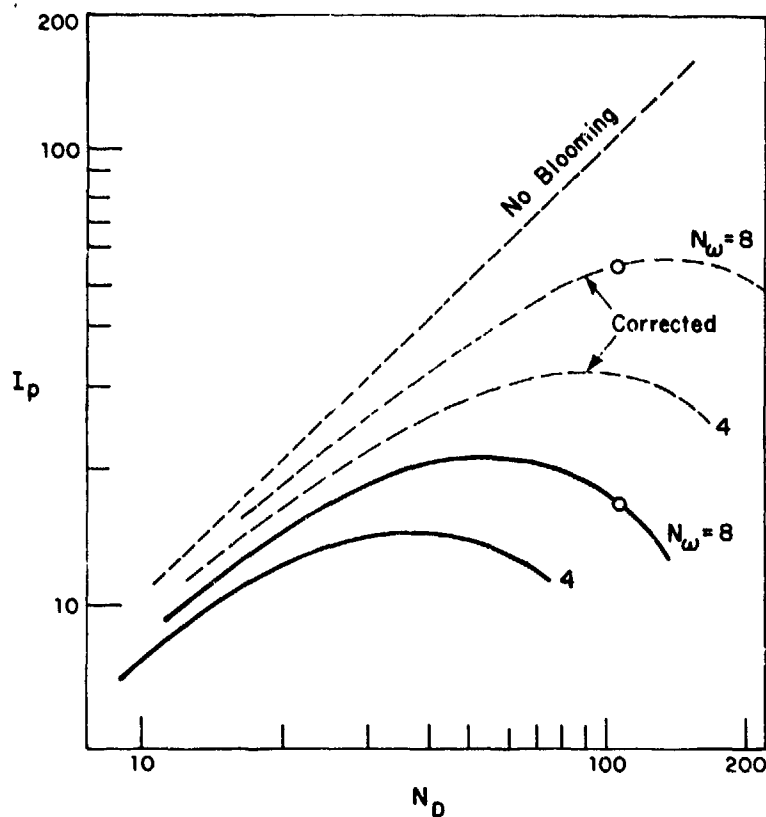


Fig. 6—Normalized peak irradiance $I_p = N_D A_0 / A$, where A_0 is the diffraction limited focal area and A the focal area of the bloomed beam, is a function of the distortion number N_D . The circled points correspond to the condition of the previous figure. The dashed curves, for slewing numbers 4 and 8, show the kinds of improvements that deformable mirrors can make on the power optimization curves.

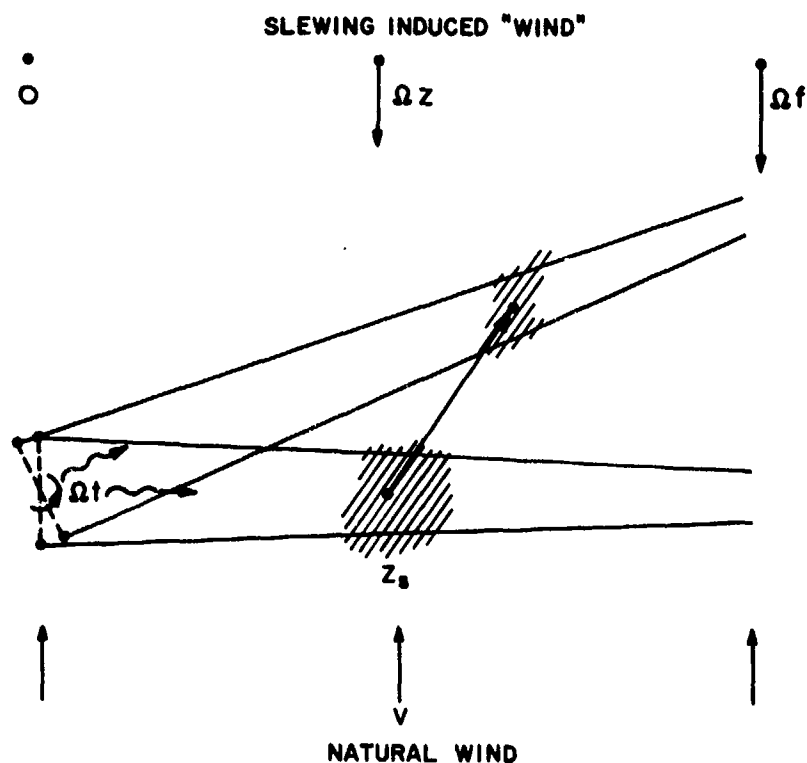


Fig. 7—Stagnation Zone Geometry. The geometric arrangement of natural wind vector v and the wind induced by slewing that gives rise to stagnation zones is shown above. The stagnation point is marked Z_s and the shaded region about it is the stagnation zone. The motion of the stagnation zone when Ω or v

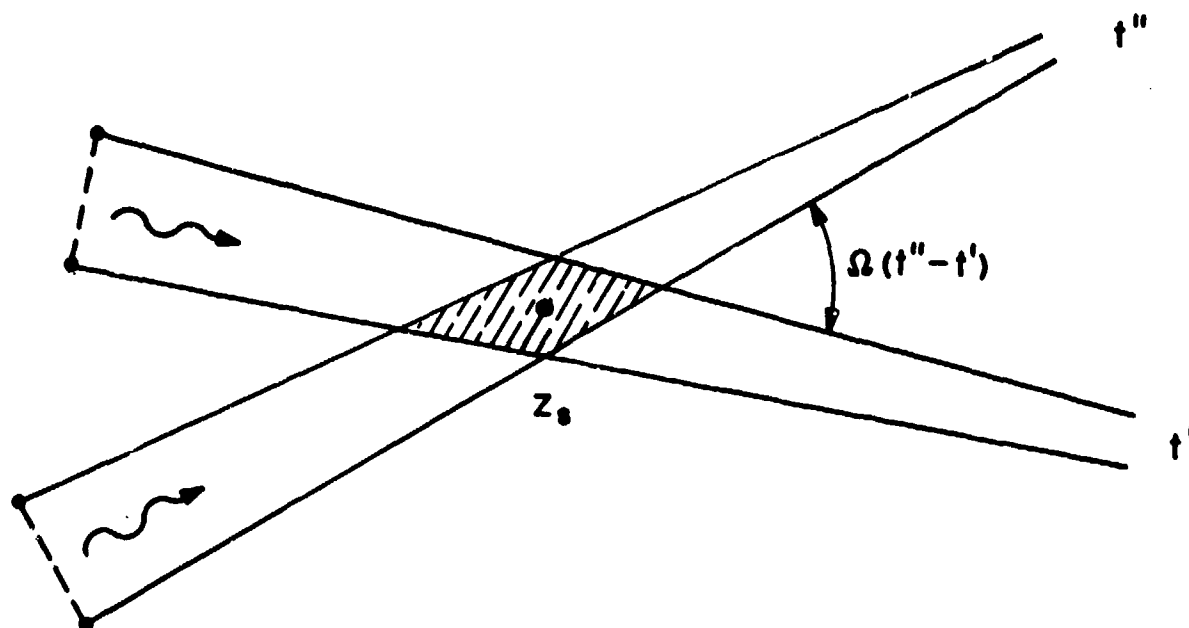


Fig. 8—Stagnation Zone Geometry from a different vantage point. By choosing a coordinate system fixed with respect to the stagnation point Z_s , the beam is seen to revolve about the stagnation point. The stagnation zone is the shaded region of overlap of the beam at two different times; as $t_2 - t_1$ increases, the length of the stagnation zone decreases leading to the quasi-steady state model of Berger, et al.

STAGNATION ZONE STUDY

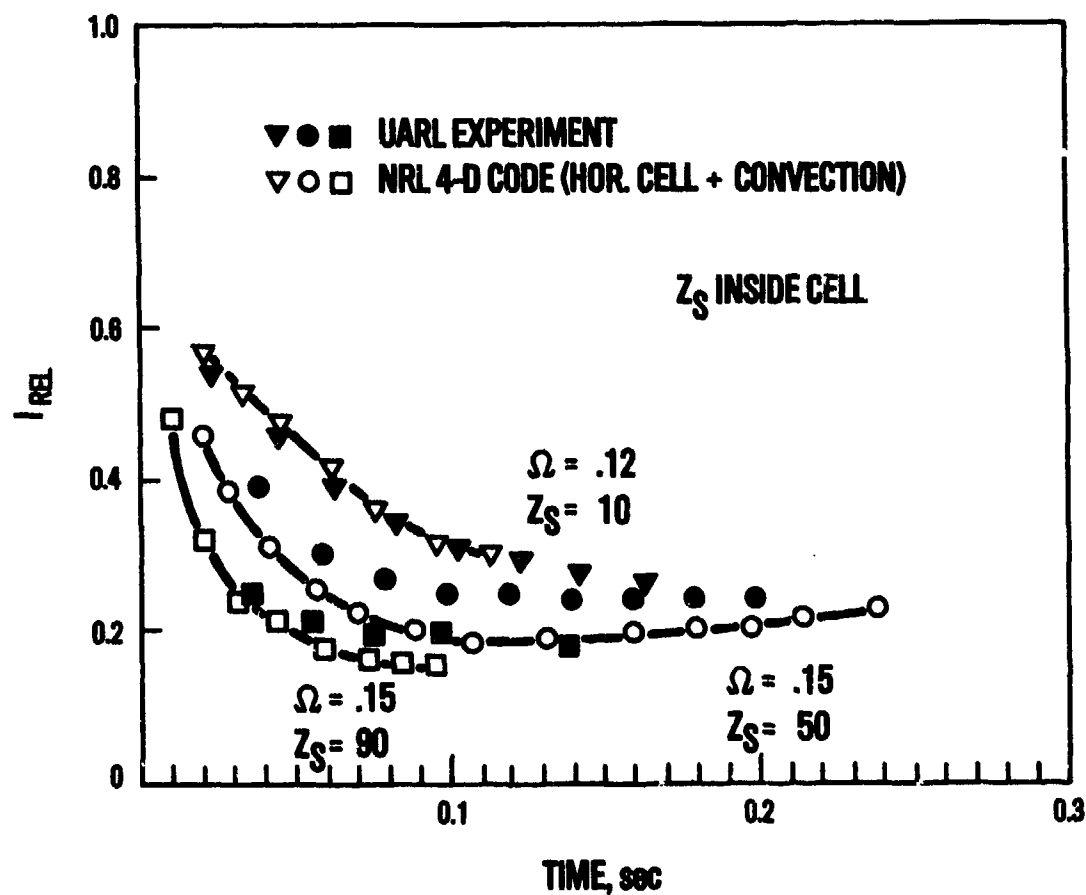


Fig. 9—Stagnation Zone Blooming, comparison of experiment and theory. The decay of peak irradiance in the observation plane is plotted against time. The solid points represent the experimental data obtained in a

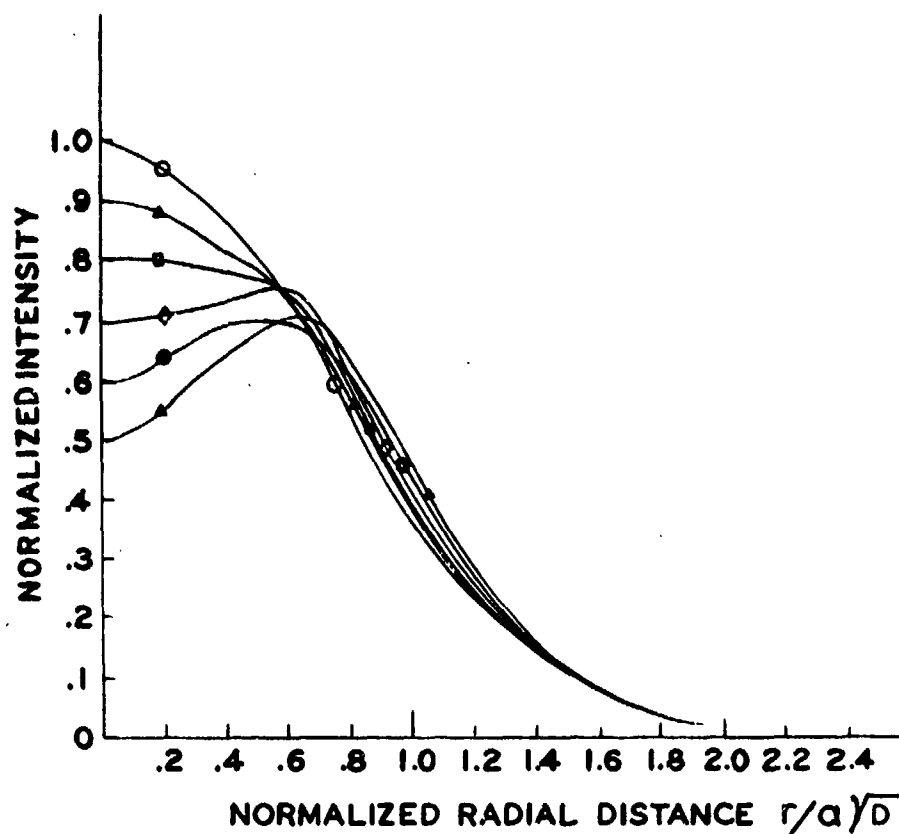


Fig. 10—Focal plane irradiance levels as a function of time for single pulse r^3 blooming, taken from (Aitken, et al., 1973)

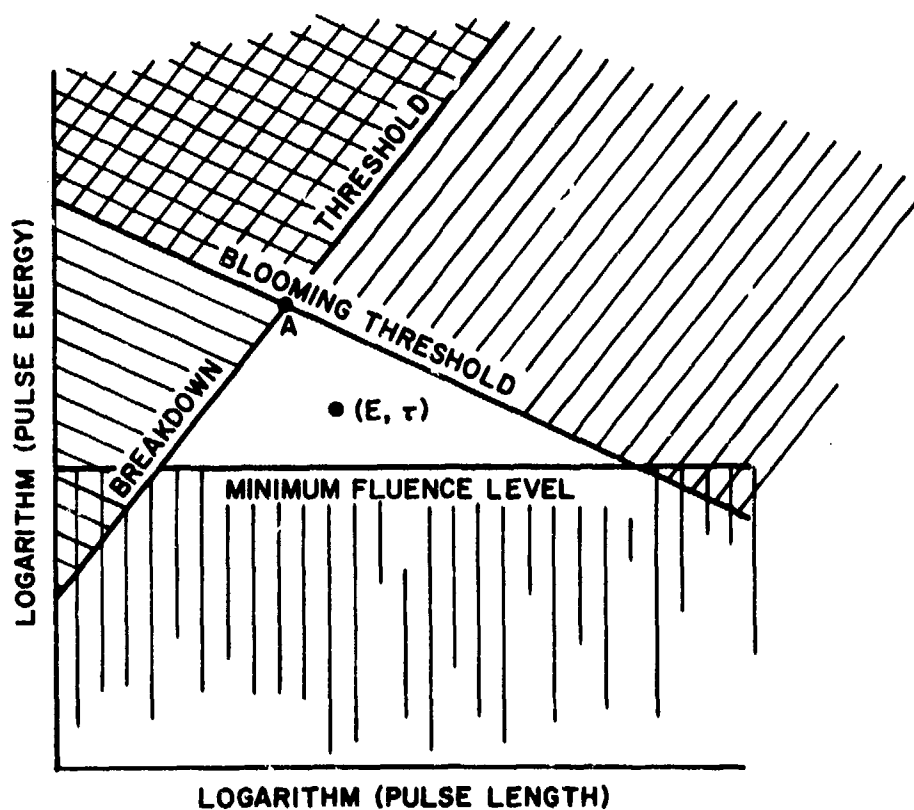


Fig. 11— (E_p, t_p) diagram for single pulsed lasers. Practical single pulse lasers must have their representative points (E_p, t_p) for pulse energy and pulse length lie within the open triangle. If the threshold level lies above point A, the triangle does not exist.

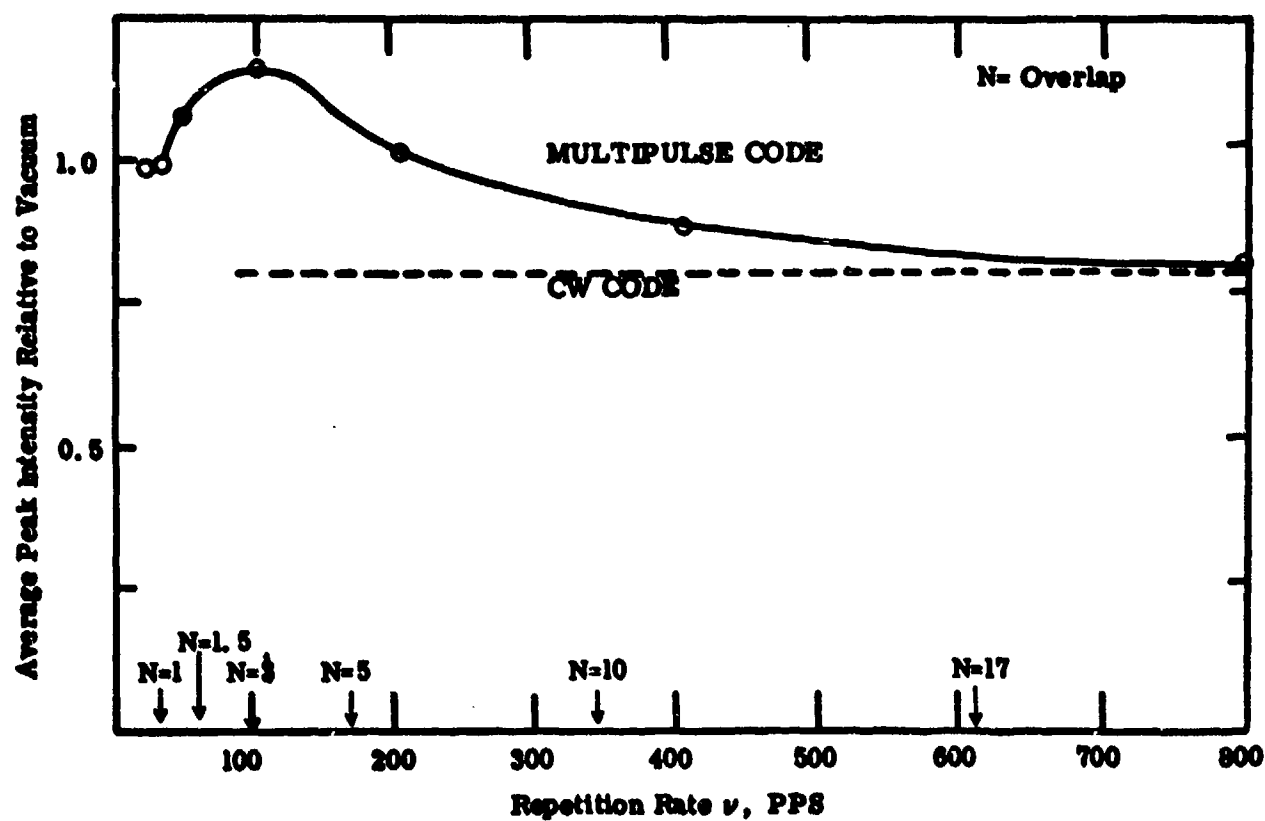


Fig. 12—Normalized irradiance of a multiply pulsed laser beam versus repetition rate; the average power of the laser is held fixed, and $\langle P \rangle = E_p \nu$. The corresponding CW limit is approached asymptotically (the dashed line). (Courtesy of Dr. P.B. Ulrich, NRL.)

AN OVERVIEW OF THE LIMITATIONS ON THE TRANSMISSION OF HIGH ENERGY LASER

BEAMS THROUGH THE ATMOSPHERE BY NONLINEAR EFFECTS*

S. Edelberg
 Massachusetts Institute of Technology
 Lincoln Laboratory
 P. O. Box 73
 Lexington, Massachusetts 02173

ABSTRACT

This paper reviews the important nonlinear effects which limit high energy laser propagation through the atmosphere. The two most important effects are thermal blooming (or thermal defocussing) and air breakdown within the beam. A third, less important effect is Stimulated Raman Scattering. The possibility of transmitting laser beams through fogs, clouds or haze by "boring holes" through these atmospheric media with the laser beam is also reviewed.

The laser's waveform in this paper is a train of pulses. It is shown that the waveform design and other important parameters such as range to the focal plane, aperture and focal spot size, pulse intensity, etc., can be chosen to avoid the thermal blooming of individual pulses and air breakdown. The limit on beam propagation is then caused by thermal blooming due to the cumulative heating by the pulses in the train. An added set of parameters then controls this multipulse blooming including beam slew rate, cross-wind velocity, and interpulse spacing. This paper summarizes the parametric tradeoffs required to satisfactorily control thermal blooming and gives quantitative results for several parametric choices.

1. INTRODUCTION

The propagation of high energy laser beams in the atmosphere can be limited by linear effects such as absorption and scattering, and by nonlinear effects. When the laser waveform is continuous wave (CW), only one nonlinear effect must be considered, thermal blooming (or thermal defocusing). When the waveform is pulsed, either a single short pulse or a train of pulses, then in addition to thermal blooming it is necessary to take into account air breakdown and possibly Stimulated Raman Scattering. When this is done it becomes possible to determine the set of laser parameters and atmospheric conditions which will permit laser beam propagation to a focal plane.

It is also possible to use a nonlinear effect, the evaporation of water droplets by the laser beam, to "bore holes" through haze, fog, or clouds in order to improve propagation through these media. The laser energy required to perform this task is, within factors of about two or three, the energy required to evaporate the water in the beam. However, thermal blooming in the "bored hole" may be large, under some conditions.

2. SINGLE PULSE THERMAL BLOOMING

When a single laser pulse of length τ_p is transmitted in the atmosphere, the laser heating of the air within the beam will generate a transverse density gradient which will be time varying. The characteristic time of this phenomenon is the hydrodynamic time, τ_H , which is the time required for a sound wave to cross the beam (τ_H is the ratio of the beam radius and the sound speed). When $(\tau_p/\tau_H) \ll 1$ the air density changes do not have time to develop completely and thermal blooming will be small. However the pulse length cannot be made too small while maintaining a large pulse energy because the power density will then increase and the atmospheric breakdown limit may be exceeded.

It was stated above that blooming will decrease as (τ_p/τ_H) is decreased. The hydrodynamic time, however is proportional to beam radius. Thus thermal blooming should increase as the beam radius is decreased, i.e., unlike the continuous wave (CW) case, beam blooming is much greater near the focus than near the laser transmitter aperture. Furthermore there is another equally important reason for the blooming being near the focus. It is that the contributions of different parts of the beam to the thermal blooming of the focal spot can be qualitatively described by the transverse gradient of the index of refraction multiplied by the distance to the focus which is acting as a lever arm. The change in the index of refraction is proportional to a^{-4} for the short time limits of the hydrodynamic equations, where a is the beam radius. Thus the regions near the focus will contribute more to focal spot blooming. It follows therefore that when a laser beam is pointed from the ground at high elevation angles so that the regions near the focus are in volumes of the atmosphere which have decreased absorption coefficients, then single pulse thermal blooming will be low.

The level of single pulse thermal blooming will depend on other parameters in addition to (τ_p/τ_H) . This can be seen in Fig. 28-1 (Ulrich, P. B. and Wallace, J., 1973) where normalized intensity versus normalized radius from the beam center (r/a) is shown. The range is the same for each of the two sets of curves shown in the figure. Each set contains curves for five different pulse lengths, τ_p . However, other important parameters such as absorption coefficient and pulse energy are different. It can be seen that the distortion from Gaussian of the transverse intensity due to blooming, is much greater for a given (τ_p/τ_H) in the top set of curves in Fig. 28-1 than in the bottom set.

This can be stated in quantitative and general terms if the intent is to avoid single pulse blooming. For thermal blooming in the short time hydrodynamic regime, i.e., in the t^3 approximation, the critical time for the onset of blooming is (Lencioni, D. E., 1974):

* This work is supported by the Advanced Research Projects Agency of the Department of Defense.

$$\tau_c = 1.74 \times 10^{-3} \left(\frac{J \cdot \text{sec}^2}{\text{cm}^5} \right)^{1/2} \cdot \left[\frac{a_o^2 a_t^4}{\alpha a^{-\alpha} R E_p R^2} \right]^{1/2} \quad (28-1)$$

where a_o (cm) is the e^{-1} beam radius at the transmitter with a transverse gaussian energy distribution truncated at e^{-2} , a_t (cm) is the e^{-1} beam radius at the focal plane, α (cm^{-1}) is the atmospheric absorption coefficient, R (cm) is the range to the focal plane, and E_p (J) is the pulse energy.

It can be seen from Equation 28-1 that the dependence of τ_c on α is quite weak, but the dependence on focal spot radius is very strong, as would be expected from the above discussion. For a given pulse intensity in the focal plane, I_p (W/cm^2), the maximum focal plane energy fluence before the onset of thermal blooming is obtained from Equation 28-1:

$$\epsilon_c = 9.88 \times 10^{-3} \left(\frac{J \cdot \text{sec}^2}{\text{cm}^5} \right)^{1/3} \cdot \left[\frac{a_o^2 a_t^2}{\alpha R^2} \right]^{1/3} \cdot I_p^{2/3} \quad (28-2)$$

where

$$\epsilon_c = \frac{e^{-\alpha R} E_p}{\pi a_t^2} \quad (28-2a)$$

$$= I_p \tau_c \quad (28-2b)$$

3. BREAKDOWN AND STIMULATED RAMAN SCATTERING

The limitation on the transmission of laser energy through the atmosphere due to breakdown is discussed in detail in this volume (Lencioni, D. E., 1975). When the intensity in the laser beam is greater than a threshold, some of the large atmospheric aerosol will generate breakdowns which will limit transmission. This threshold is approximately $5 \times 10^6 \text{ W}/\text{cm}^2$ at a wavelength of $10.6 \mu\text{m}$ and $4 \times 10^7 \text{ W}/\text{cm}^2$ at a wavelength of $3.8 \mu\text{m}$. Very approximately this threshold varies as λ^{-2} , where λ is the wavelength.

For typical intensities and aerosol size distributions and at $10.6 \mu\text{m}$, the maximum energy fluence that can be transmitted through a beam in the presence of aerosol induced breakdown is:

$$\epsilon_{bd} = 3.6 \times 10^{15} \left(\frac{J^5}{\text{sec}^3 \cdot \text{cm}^9} \right)^{1/2} \left(\frac{a_o}{a_t R} \right)^{1/2} \cdot I_p^{-3/2} \quad (28-3)$$

The form of Equation 28-3 is shown in Fig. 28-2 along with the breakdown thresholds at $10.6 \mu\text{m}$, $3.8 \mu\text{m}$, and $1.06 \mu\text{m}$. The form of Equation 28-2, the maximum fluence, ϵ_c , before the onset of thermal blooming is also indicated in Fig. 28-2. In order to avoid single pulse thermal blooming it is necessary to remain below this dashed curve, marked ϵ_c . In order to avoid loss of transmission due to aerosol-generated breakdown or to transmit significant energy in the presence of this breakdown, it is necessary to keep to the left of the solid curves marked ϵ_{bd} . At $10.6 \mu\text{m}$, the shaded region indicates the "atmospheric window" where useful single pulse beam propagation occurs. It can be seen that the "window" is enlarged as the wavelength is decreased (since the thermal blooming curve, ϵ_c , need not vary significantly with decreasing wavelength).

The breakdown thresholds shown in Fig. 28-2 are appropriate for typical aerosol-laden atmospheres at ground level. If all aerosol were to be removed, then the "clean air" threshold is $3 \times 10^9 \text{ W}/\text{cm}^2$ at $10.6 \mu\text{m}$.

The $10.6 \mu\text{m}$ thresholds noted above are the so-called long-pulse thresholds, appropriate for pulses longer than about 50 - 100 nsec. The short-pulse thresholds are energy fluence limited rather than intensity limited. The $10.6 \mu\text{m}$ short-pulse threshold is approximately $10 \text{ J}/\text{cm}^2$.

The clean air threshold varies as λ^{-2} so that for the long-pulse it is $2 \times 10^{10} \text{ W}/\text{cm}^2$ at $3.8 \mu\text{m}$. At the latter wavelength, Stimulated Raman Scattering (SRS) is a more dominant effect than clean air breakdown. At sufficiently high intensities in the laser beam, some of the incident radiation will be scattered and frequency-shifted relative to the frequency of the incident radiation. This type of scattering, called Stimulated Raman Scattering, generates frequency-shifted components called the Stokes and anti-Stokes components which lie on either side of the unshifted radiation. These components are scattered out of the main beam and generate beam filamenting and breakup, leading to focal spot enlargement and distortion.

The intensity at which appreciable Raman conversion takes place is above the clean air breakdown threshold for $10.6 \mu\text{m}$. However for $3.8 \mu\text{m}$ radiation, the threshold for conversion of approximately $2 \times 10^9 \text{ W}/\text{cm}^2$, as shown in Fig. 28-2 is a factor of 10 below the clean air threshold. Hence Stimulated Raman Scattering is a

* All intensities are defined as the power in the focal plane divided by the area containing 63% of the power.

more dominant effect than breakdown in clean air at 3.8 μm . However in most practical applications aerosol breakdown thresholds are of greatest importance.

4. MULTIPULSE THERMAL BLOOMING

The multipulse waveform consists of a finite train of short pulses. For this waveform, thermal blooming contains two components: single pulse blooming (discussed above) and blooming caused by the cumulative heating of previous pulses. Three types of multipulse waveforms should be noted from a blooming point of view. In the first type, the interpulse spacing as well as the pulse length are shorter than a hydrodynamic time. The total train, containing many pulses, is less than a hydrodynamic time in length. It has been found (Herrmann, J., 1973) that for this multipulse train, the blooming level is equal to that which would occur for a single pulse of length equal to the train length and containing the same energy as that in the total train. Thus, in order to minimize blooming the train length should be much less than a hydrodynamic time.

In the second type of waveform, the interpulse spacing is somewhat larger than the hydrodynamic time. In this waveform the mitigating circumstances such as noted in the first type, above, are absent. Hydrodynamics permits refractive index distortions to develop and remain within the laser beam on the time scale of the train length and thermal blooming can be quite large. A simple example of this waveform and the resulting thermal blooming is seen in Fig. 28-3 (Herrmann, J., 1973). In this figure, the first pulse of energy, E_p , heats the air in the beam, causing index of refraction changes which occur on a time scale, τ_H . The second pulse then passes through this perturbed medium and is bloomed or defocused (single pulse blooming is small). The normalized irradiance, in the focal plane, of the second pulse is shown in Fig. 28-3. The blooming caused by the large values of E_p are quite evident.

In the third type of multipulse waveform, the interpulse spacing is large enough for the cross wind (wind component perpendicular to the laser beam axis) to "clean out" the heated air between pulses. That is, a pulse is transmitted along the beam axis to the focal plane, heating the air as it moves along and generating refractive index changes. The pulses which follow will then be bloomed unless the heated air is removed and new, cool air enters the beam. A measure of "removal efficiency" is the pulse overlap number, N_o :

$$N_o = \frac{2 a_o v}{V} \quad (28-4)$$

where v is the pulse repetition rate (sec^{-1}) and V is the cross wind velocity (cm/sec). Equation 28-4 indicates that for an overlap number of unity, the cross wind will permit the presence of approximately one pulse in the beam at a given time. If the repetition rate or the aperture diameter becomes very large, or the cross wind velocity becomes very small, then N_o becomes very large thereby increasing thermal blooming.

There are other important numbers which control multipulse thermal blooming. The first is the energy distortion number, E^* :

$$E^* = \frac{\alpha E_p R k}{a_o^2} \quad (28-5)$$

$$k = \frac{2\pi}{\lambda \beta}$$

where β is the quality of the laser beam, i.e., the beamwidth in units of diffraction limited width. E^* is a measure of the energy per pulse absorbed in the beam. The Fresnel number, N_F , is a measure of the degree of beam focus:

$$N_F = \frac{a_o^2 k}{R} \quad (28-6)$$

P^* , the power distortion number, is a measure of the absorbed average power in the beam:

$$P^* = \frac{1}{2} E^* N_o \quad (28-7)$$

The distortion numbers have been used (Lencioni, D. E., 1974) to obtain a normalized set of thermal blooming curves based on the output of a series of computer runs which include the effects of diffraction (Bradley, L. C. and Herrmann, J., 1973). The normalized curves which are shown in Fig. 28-4, can be used to compute the thermal defocusing of a stationary (no-beam slewing) laser beam in the focal plane. In this figure, the ordinate is proportional to A_o/A_B , where A_o is the unbloomed focal spot area containing 63% of the power and A_B is the bloomed spot area containing 63% of the power.

Four normalized blooming curves are presented, each representing a different set of parameters (E^* , N_F , α R). The straight line is the unbloomed case. The abscissa, P^* , for a given curve, represents N_o , the overlap number. It is seen that when N_o increases above unity thermal blooming begins. Each curve reaches a peak $P^* A_o/A_B$ where delivered average intensity to the focal plane is a maximum, I_{max} , and then decreases. This maximum delivered intensity is:

$$I_{\text{max}} = \frac{E_p e^{-\alpha R}}{\pi a_t^2} \cdot v_m \cdot \left(\frac{A_o}{A_B} \right)_m \quad (28-8)$$

The pulse repetition rate, representing \bar{I}_{\max} is v_m :

$$v_m = \frac{v}{2 a_0} \left[0.82 + \frac{6.24 \times 10^3 \left(\frac{J}{\text{cm}^2} \right)}{\alpha E R k / a_0^2} \left(1.6 + \frac{\omega R}{v} \right) \right] \quad (28-9)$$

Equation 28-9 includes the effects of laser beam slewing where ω is the beam slew rate (rad/sec). Also at maximum average intensity:

$$\left(\frac{A_0}{A_B} \right)_m = \frac{2}{3} \left[1 + \left(\frac{0.41}{v_m} \right) \left(\frac{v}{2 a_0} \right) \right] \quad (28-10)$$

When E^* is very large, from Equation 28-9:

$$v_m \approx \frac{v}{2 a_0} \quad (28-11)$$

implying a single pulse overlap, and when E^* is very small, the pulse overlap is large:

$$v_m \approx \frac{a_0 v}{\alpha E R k} \left[1.6 + \frac{\omega R}{v} \right] \quad (28-12)$$

This case approaches a continuous wave (CW) waveform.

The beam spot radius in Equation 28-8, a_t , is controlled by diffraction:

$$a_{tD} = \sqrt{2} \frac{R}{k a_0} \quad (28-13)$$

or by turbulence:

$$a_{tT} = 3 \lambda^{-1/5} \cdot R^{8/5} \cdot (C_N^2)^{3/5} \quad (28-14)$$

where C_N^2 is the strength of turbulence ($\text{m}^{-2/3}$), or by single pulse blooming and breakdown. If I_p is below the breakdown limit, then the single pulse blooming-limited spot size, a_{tB} , is controlled by Equation 28-1 and:

$$E_p = I_p \tau_c \quad (28-15)$$

The pulse length τ_p is made equal to τ_c and:

$$a_{tB} = 3.68 \left(\frac{\text{cm}^5}{J \cdot \text{sec}^2} \right)^{1/8} \cdot \left[\alpha (a^{-\alpha} R_E)^3 \cdot \left(\frac{R}{a_0 I_p} \right)^2 \right]^{1/8} \quad (28-16)$$

The appropriate a_t to be chosen is the largest of the above three radii, a_{tD} , or a_{tT} , or a_{tB} .

Returning to Equations 28-9, 28-11, and 28-12, it is seen that beam slewing does not control \bar{I}_m very strongly when E^* is very large. This is so because there are very few pulse overlaps for this case, and for a strongly focussed case ($N_F \gg 1$) especially, these overlaps occur near the aperture (where the beam diameter is greatest). However when a beam is slewed the resulting effective transverse wind velocity (ωR) is greatest near the focus and is very small near the aperture. Thus the overlap number cannot be greatly affected. However when E^* is small and there are many overlaps, beam slewing can significantly affect \bar{I}_m .

Very frequently, operation does not occur at maximum intensity. Equation 28-8 then applies without the subscripts (m, max). In such cases, it is appropriate to set a maximum limit on the level of thermal blooming. In this paper, examples of such cases are given for three different wavelengths: 10.6 μm , 3.8 μm , and 1.06 μm . The same level of maximum thermal blooming is chosen for the three examples:

$$\frac{A_0}{A_B} = 0.43 \quad (28-17a)$$

representing a blooming loss of 3.7 db. This level was obtained by choosing the curve in Fig. 28-4 with the following set of parameters:

$$E^* = 20 \frac{\text{KJ}}{\text{cm}^2}$$

$$N_F = 7 \quad (28-17b)$$

$$\alpha R = 0.2$$

and the following value of P^* :

$$P^* = 2 \times 10^4 \frac{J}{cm^3} \quad (28-17c)$$

which implies a choice of the overlap number:

$$N_o = 2 \quad (28-17d)$$

Also the beam slew velocity is zero. The aperture size is chosen to be:

$$2 a_o = 15.4 \text{ cm} \quad (28-17e)$$

so that with the above choice of Fresnel Number, N_F , and for a diffraction limited beam, i.e., a_t is not limited by turbulence or single pulse blooming and β is unity, then:

$$2 a_t = 3.1 \text{ cm} \quad (28-17f)$$

Then, for each wavelength λ the range R is obtained from Equation 28-6 or Equation 28-13. A low cross wind velocity is chosen:

$$V = 1 \text{ m/sec} \quad (28-17g)$$

Then, from Equation 28-4, the pulse repetition rate is:

$$\nu = 13 \frac{\text{pulses}}{\text{sec}} \quad (28-17h)$$

The energy per pulse, E_p , is obtained for each wavelength from E^* . The laser transmitter average power is:

$$P_T = E_p \nu \quad (28-18)$$

As noted after Equation 28-17f, the range is available. The absorption coefficient is then computed from Equation 28-17b. The diameter of the thermally bloomed spot $2 a_B$ in the focal plane is obtained from Equations 28-17a and 28-17f:

$$2 a_B = 4.8 \text{ cm} \quad (28-19)$$

from which the average intensity in the focal plane, \bar{I} , is obtained (see Equation 28-8).

Calculations have been made for the three wavelengths noted above, using the approach just described which yield ranges to the focal plane (R), pulse energy (E_p), average transmitter power (P_T), absorption coefficient (α), and average focal plane intensity (\bar{I}). These results are summarized in Table 28-I.

Table 28-I: Delivered Average Intensity in the Presence of Thermal Blooming

λ (μm)	R (Km)	E_p (J)	P_t (KW)	α (cm^{-1})	\bar{I} ($\frac{W}{\text{cm}^2}$)
10.6	0.5	1,000	13	4×10^{-6}	600
3.8	1.4	360	4.7	1.4×10^{-6}	214
1.06	5	100	1.3	4×10^{-7}	60

In order to avoid single pulse blooming, the pulse length, τ_p , should be less than or equal to τ_c , in Equation 28-1. It can be seen from this equation that:

$$\tau_c \propto \frac{1}{\sqrt{E_p R}} \quad (28-20)$$

Thus for each of the three wavelengths:

$$\tau_{\max} = 12 \mu\text{sec}$$

(28-20a)

in order to avoid single pulse blooming. However, as noted in Section 3, care must be taken to avoid breakdown by remaining in the shaded region of Fig. 28-2. The pulse length can be decreased, while maintaining constant pulse energy, E_p , until the breakdown threshold is reached. Either the long pulse threshold or the short pulse threshold (Section 3) is chosen, whichever is most appropriate. When these thresholds are used at the three wavelengths then the maximum pulse lengths (single pulse blooming) and minimum pulse lengths (breakdown) are those given in Table 28-II.

Table 28-II: Range of Pulse Lengths

λ (μm)	τ_{\max} (μsec)	τ_{\min} (μsec)
10.6	12	9
3.8	12	0.4
1.06	12	0.009

When a laser beam with circular symmetry propagates in the presence of a cross wind and thermal blooming occurs, the beam shape is distorted and a portion of it becomes crescent or kidney-shaped. The beam is also deflected into the wind so that the focal spot is not aligned with the beam axis. This can be seen in the set of contour plots which are shown in Fig. 28-5, appropriate to the 10.6 μm case described above. In each figure of Fig. 28-5, the average intensity distribution in the focal plane (obtained by computer calculations) is represented by a set of constant average intensity isophote or contour lines.

Fig. 28-5a, the case of no atmospheric absorption and therefore no thermal blooming, is shown first for comparison purposes. Within the limitation set by the mesh size of the computer program, the circular symmetry of the beam is evident. Each contour line is labelled with a number which equals $\log_{10} (\bar{I}/\tau_p v)$. Fig. 28-5b represents the thermal blooming case when the beam slew velocity, ω , is zero, i.e., the 10.6 μm case is discussed in detail above. In this figure the cross wind direction is from left to right. A comparison with Fig. 28-5a indicates that the focal spot has moved towards the left, into the wind, and that the spot has enlarged with the formation of a crescent.

The beam is then slewed with increasing velocity, in such a direction that the effective wind across the beam generated by slewing is in the same direction (left to right) as the natural wind in the atmosphere. This avoids stagnation zones (Hayes, J., 1975). The trends can be seen by comparing Fig. 28-5b through Fig. 28-5g where the beam slew velocity, ω , is increased from 0 to 20 mrad/sec. It can be seen that blooming decreases as ω increases, until at 20 mrad/sec, blooming has almost disappeared. Thus even for a relatively small overlap number, N_0 , of 2 (which was used in these calculations), beam slewing decreases thermal blooming.

The thermal blooming results for stationary and slewed beams at the three wavelengths chosen in this paper are summarized in Table 28-III. The change in the position of the focal spot (into the wind) due to thermal blooming is represented by:

$$\bar{x} = \frac{\int x \bar{I}(x,y) dx dy}{\int \bar{I}(x,y) dx dy} \quad (28-21)$$

where x is the abscissa and y is the ordinate in Fig. 28-5, and $\bar{I}(x,y)$ is the average intensity distribution in the focal plane. \bar{x} , whose unit is cm, represents the "center of mass" of the focal plane distribution.

Table 28-III: Thermal Blooming Results for Stationary and Slewed Beams

λ (μm)	A_0/A_B			\bar{I} (W/cm^2)			\bar{x} (cm)		
	$\omega = 0 \frac{\text{mrad}}{\text{sec}}$	$\omega = 2 \frac{\text{mrad}}{\text{sec}}$	$\omega = 5 \frac{\text{mrad}}{\text{sec}}$	$\omega = 0 \frac{\text{mrad}}{\text{sec}}$	$\omega = 2 \frac{\text{mrad}}{\text{sec}}$	$\omega = 5 \frac{\text{mrad}}{\text{sec}}$	$\omega = 0 \frac{\text{mrad}}{\text{sec}}$	$\omega = 2 \frac{\text{mrad}}{\text{sec}}$	$\omega = 5 \frac{\text{mrad}}{\text{sec}}$
10.6	0.43	0.75	0.92	600	1040	1270	1.73	0.98	0.60
3.8	0.43	0.91	0.98	214	450	484	1.73	0.63	0.29
1.06	0.43	0.98	0.99	60	137	138	1.73	0.22	0.09

5. FOG HOLE BORING

Fogs consist of air saturated or supersaturated with water vapor and containing a suspension of water droplets. The number density of drops varies between about $10/\text{cm}^3$ in a light fog to about $1000/\text{cm}^3$ in a heavy fog. The radii vary from below $1\text{ }\mu\text{m}$ to about $25\text{ }\mu\text{m}$, with the peak of the distribution of radii being in the range of a few micrometers. A heavy fog may contain a liquid water content of about 500 mg/m^3 . For such a heavy fog the e-folding transmission distance is only about 13 m at a wavelength of $10.6\text{ }\mu\text{m}$, while for a light fog of density equal to 4 mg/m^3 , the distance is 2.4 km .

In order to efficiently bore a path through a fog it is necessary to vaporize water droplets and therefore to maximize the energy absorbed by the drop. In Fig. 28-6, it is seen that at a wavelength of $10.6\text{ }\mu\text{m}$ (the ordinate is crosssection per unit droplet volume) absorption dominates scatter for droplet radii $\leq 8\text{ }\mu\text{m}$, the peak region in the fog droplet radius distribution. It can be seen from Fig. 28-7, however, that at $3.5\text{ }\mu\text{m}$ and at $0.6\text{ }\mu\text{m}$ (where absorption is too small to plot on the scale of the figure) scattering clearly dominates over absorption. The $10.6\text{ }\mu\text{m}$ wavelength is therefore optimum for fog hole boring.

At a wavelength of $10.6\text{ }\mu\text{m}$, the absorption coefficient of water is approximately 10^3 cm^{-1} , so that the e-folding distance for absorption is $10\text{ }\mu\text{m}$. Therefore when water droplets with radii greater than approximately $20\text{ }\mu\text{m}$ are irradiated surface heating will dominate. However for drops smaller than about $10\text{ }\mu\text{m}$, volume heating will dominate.

Experiments (Kafalas, P. and Herrmann, J., 1973) have shown that when a pulse whose wavelength is $10.6\text{ }\mu\text{m}$ irradiates water droplets in the radius range $5 - 25\text{ }\mu\text{m}$, explosive vaporization occurs. A Mach 1 spherical shock wave is generated which quickly dissipates. This wave is followed by a sphere of hot vapor increasing in size more slowly. This hot vapor sphere will have an index of refraction which is different from that of the cooler ambient air. The ensemble of these vapor spheres will cause laser beam spreading. A quantitative analysis of this spreading or defocussing has not been made as yet. However, a quantitative analysis of the energy required for beam transmission has been made (Glickler, S. L., 1971) and is used below. This analysis has been verified experimentally in the laboratory (Lowder, J. E., Kleiman, H., and O'Neil, R. W., 1974).

In the presence of fog hole boring, the energy transmitted through a fog is:

$$E_t = E_o + \left(\frac{A}{C_1}\right) \ln \{ e^{-\tau_o} + [1 - e^{-\tau_o}] e^{- (C_1 E_o / A)} \} \quad (28-22)$$

where E_t is the transmitted energy, E_o is the incident energy, and A is the area of the collimated beam. The constants C_1 and τ_o are dependent on the properties of the fog:

$$C_1 = \frac{3 Q_a^o}{4 \rho h_v a_o} \quad (28-22a)$$

$$\tau_o = C_1 h_v \frac{Q_a^o}{Q_e^o} \cdot \delta L \quad (28-22b)$$

where δ is the water droplet mass density per unit volume of gas (g/m^3), L is the beam length (Km), Q_a^o and Q_e^o are the absorption and extinction efficiencies respectively at the mean droplet radius \bar{a}_o of the original fog distribution, ρ is the density of water and h_v is the energy required for vaporization, i.e., 2600 J/g which includes the energy required to heat the water from 20°C to 100°C .

The transmission properties of the bored hole are shown in Fig. 28-8, where the ordinate is the fraction of intensity transmitted and the abscissa is either input energy density or time to hole-bore for two different input intensities. Three curves are given, each for a different value of δL with an assumed constant drop radius of $3\text{ }\mu\text{m}$. In Fig. 28-8 is also shown the energy density ($E_\delta L$) or fluence obtained by assuming that all of the absorbed laser power completely vaporizes the droplets:

$$\bar{E}_\delta L = \delta L h_v \left(\frac{Q_e^o}{Q_a^o} \right) \quad (28-23c)$$

It can be seen from this figure that within a factor which is not much greater than two or three, approximately all of the input laser energy is useful in boring a hole in a fog, resulting in very good transmission properties. For example, for a (δL) of $0.05\text{ (g/m}^3 \cdot \text{Km)}$

$$\bar{E}_{0.05} = 17 \frac{\text{J}}{\text{cm}^2} \quad (28-23d)$$

and the fluence required for 100% transmission is approximately 33 J/cm^2 .

A cross wind continually brings new droplets into the beam which must be vaporized during the pulse time, τ_p . If the radius of the collimated beam is a_b so that A , the beam area is πa_b^2 , then to first order the required increase in hole boring energy due to the cross wind of velocity V is

$$\Delta E_v = 1 + \frac{2 V \tau_p}{\pi a_b} \quad (28-24)$$

If, for example, the cross wind velocity is 10 m/sec, the pulse length is 15 msec, and the beam radius is 5 cm, then to first order an increase of a factor of three is required in hole boring energy in order to overcome the influx of new droplets brought into the beam by the wind.

ACKNOWLEDGEMENTS

I would like to acknowledge the excellent technical work by L. C. Bradley, D. E. Lencioni, and M. G. Cheifetz, and stimulating discussions with them, which contributed very significantly to this paper.

REFERENCES

- Bradley, L. C. and Herrmann, J., 1973, private communication.
- Chu, T. S. and Hogg, D. C., 1968, "Effects of Precipitation on Propagation at 0.63, 3.5, and 10.6 Microns", The Bell System Technical Journal, p. 723.
- Glickler, S. L., 1971, "Propagation of a 10.6 μ m Laser Through a Cloud Including Droplet Vaporization", Applied Optics, Vol. 10, p. 644.
- Hayes, J., 1975, this volume.
- Herrmann, J., 1973, private communication.
- Kafalas, P. and Herrmann, J., 1973, "Dynamics and Energetics of the Explosive Vaporization of Fog Droplets by a 10.6 μ m Laser Pulse", Applied Optics, Vol. 12, p. 772.
- Lencioni, D. E., 1974, private communication.
- Lencioni, D. E., 1975, this volume.
- Lowder, J. E., Kleiman, H. and O'Neil, R. W., 1974, "High Energy Laser Pulse Transmission Through Fog", Journal of Applied Physics, Vol. 45, p. 221.
- Ulrich, P. B. and Wallace, J., 1973, "Propagation Characteristics of Collimated Pulsed Laser Beams Through an Absorbing Atmosphere", Journal Optical Society of America. Vol. 63, p. 8.
- Zel'manovich, I. L. and Shiirin, K. S., 1968, "Tables of Light Scattering, Vol. III, Coefficients of Extinction, Scattering, and Radiation Pressure", Hydrometeorological Press, Leningrad.

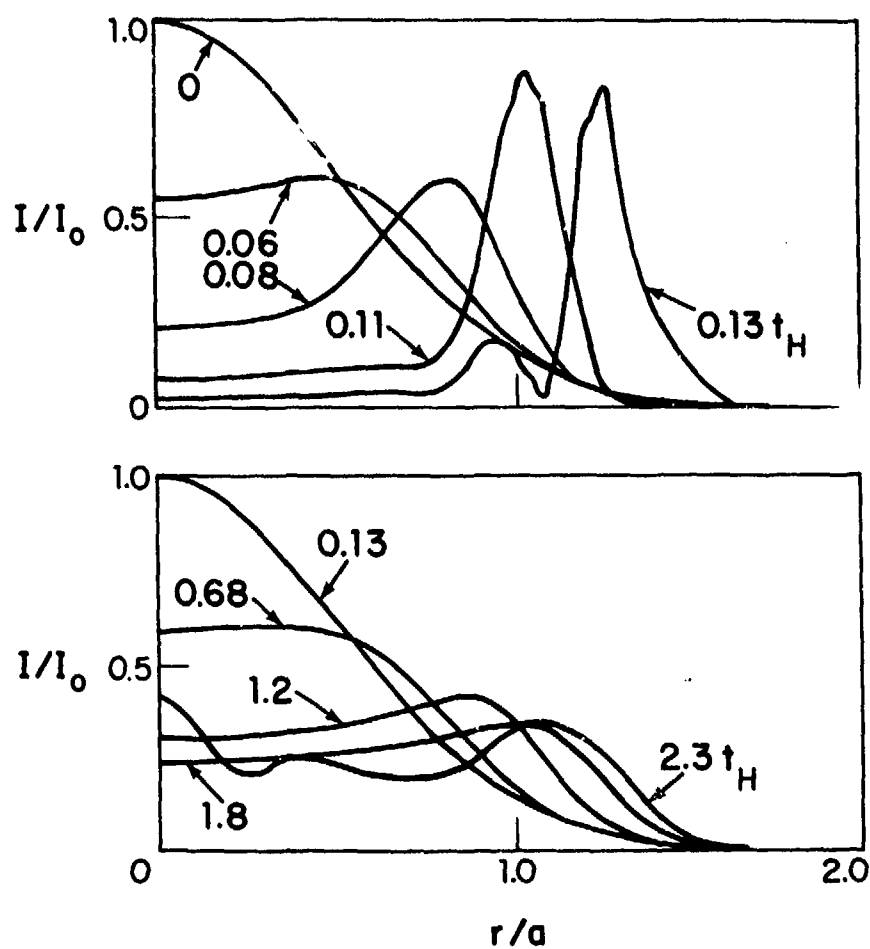


Fig.1 Comparison of Intensity Distributions at the Same Range but Other Parameters Being Different

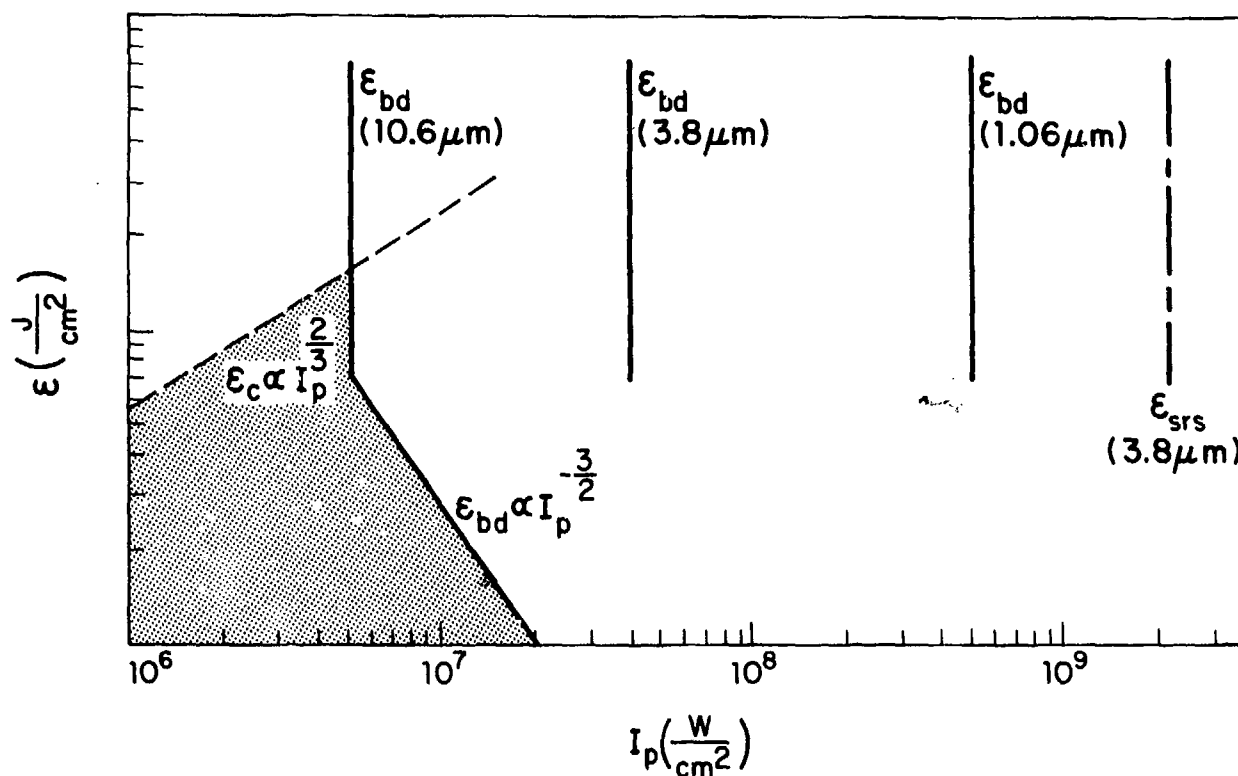


Fig.2 Breakdown, Thermal Blooming, and Stimulated Raman Scattering Limits

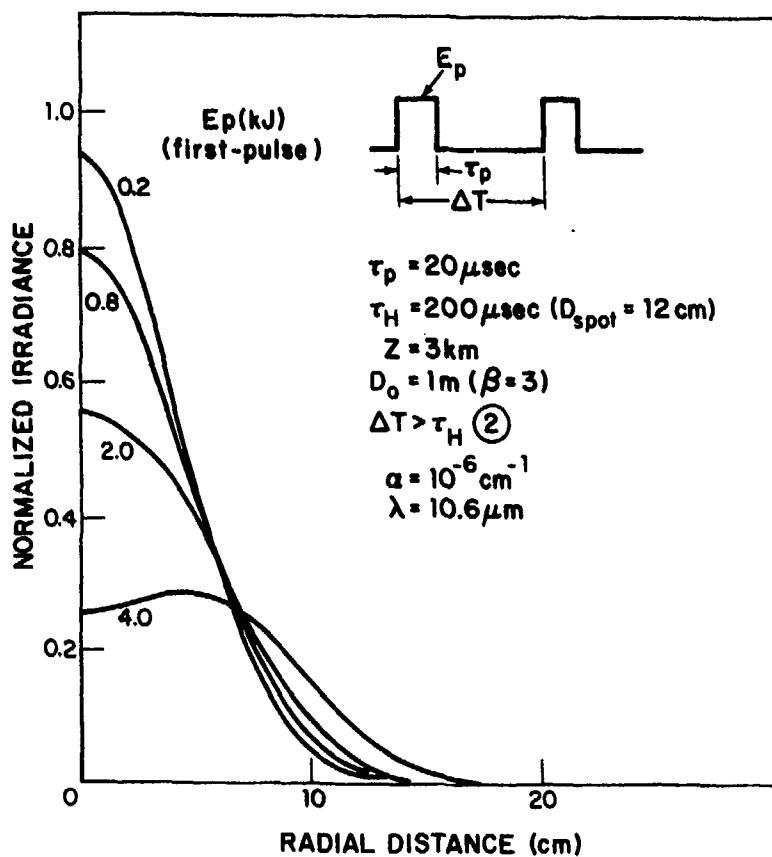


Fig.3 Thermal Blooming of a Second Pulse Caused by Heating of the First Pulse ($\Delta T > \tau_H$)

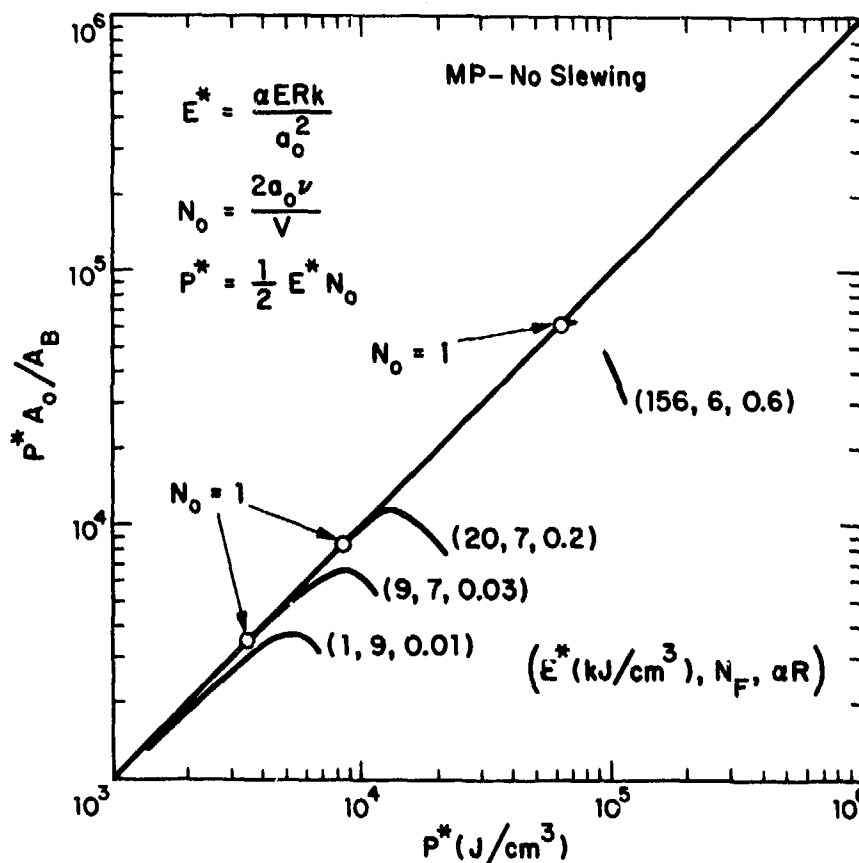


Fig.4 Normalized Multipulse Thermal Blooming Characteristics

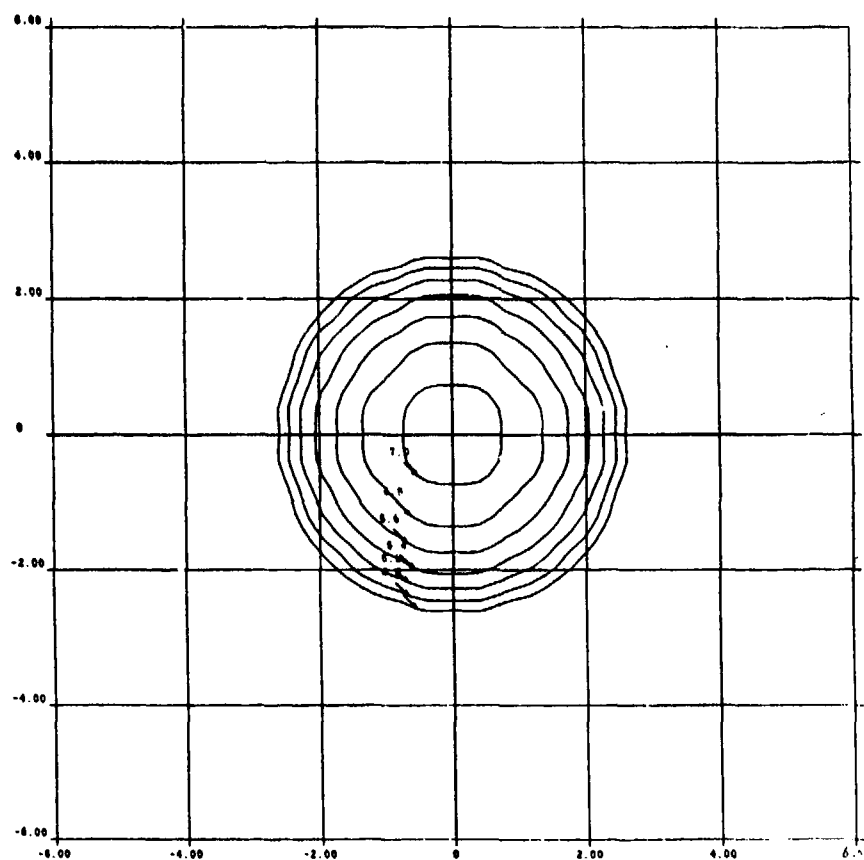


Fig.5a Thermal Blooming Contours at 10.6 μm for Stationary and Slew Beams: no Blooming; $\alpha = 0$

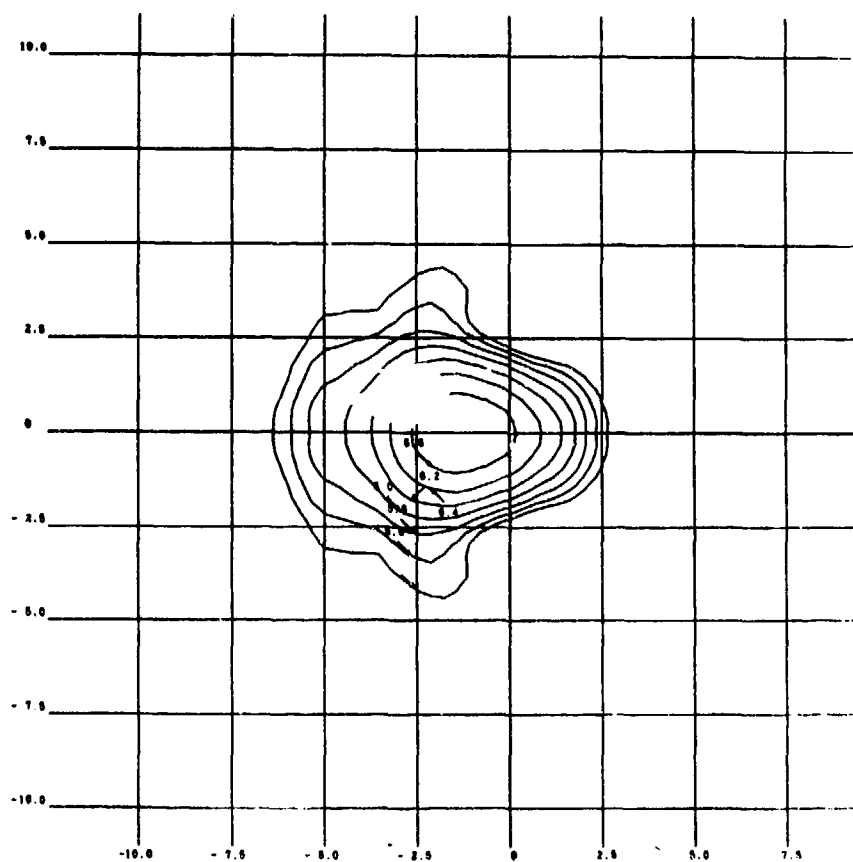


Fig.5b Thermal Blooming Contours at 10.6 μm for Stationary and Slew Beams: no Slewing

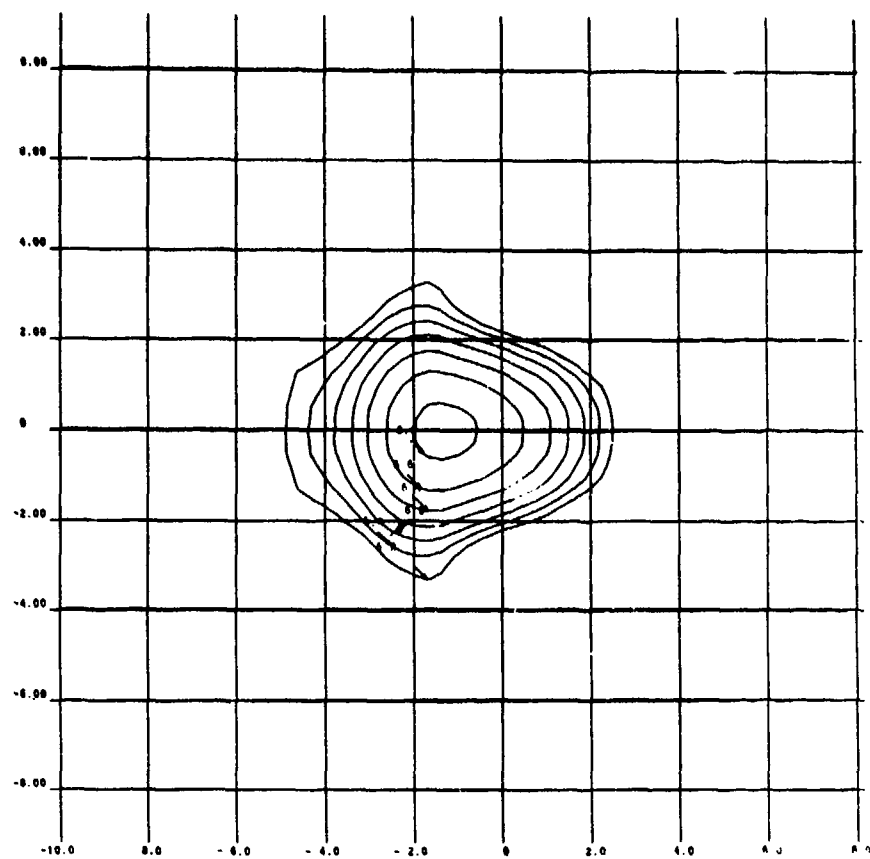


Fig.5c Thermal Blooming Contours at 10.6 μm for Stationary and Slew'd Beams: $\omega = 1$ mrad/sec

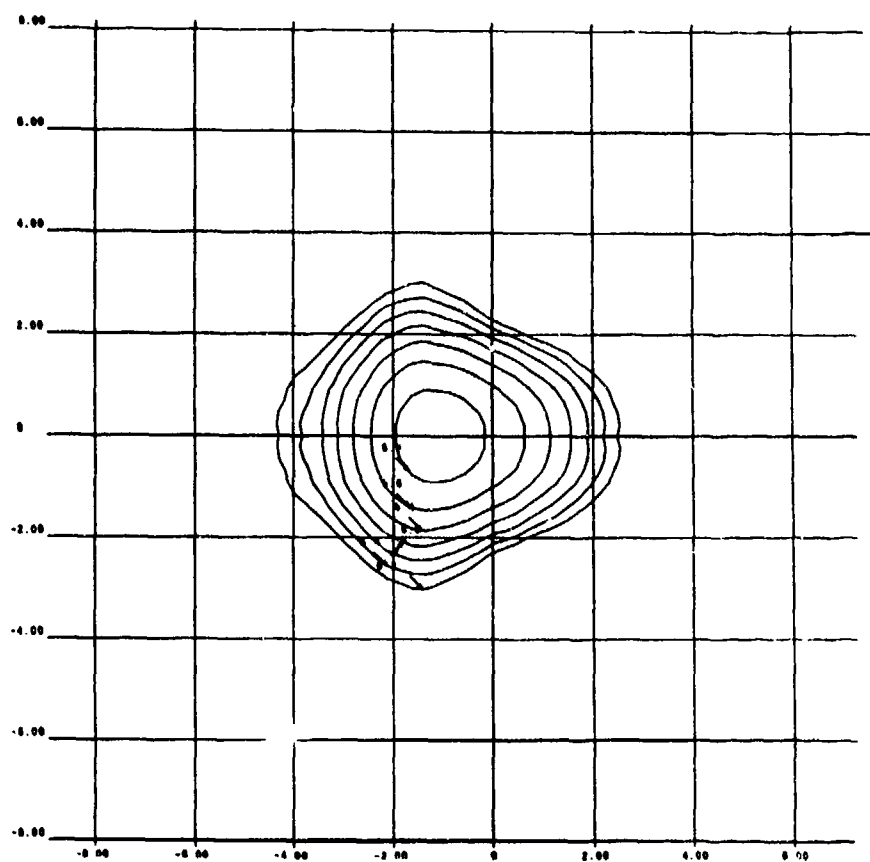


Fig.5d Thermal Blooming Contours at 10.6 μm for Stationary and Slew'd Beams: $\omega = 2$ mrad/sec

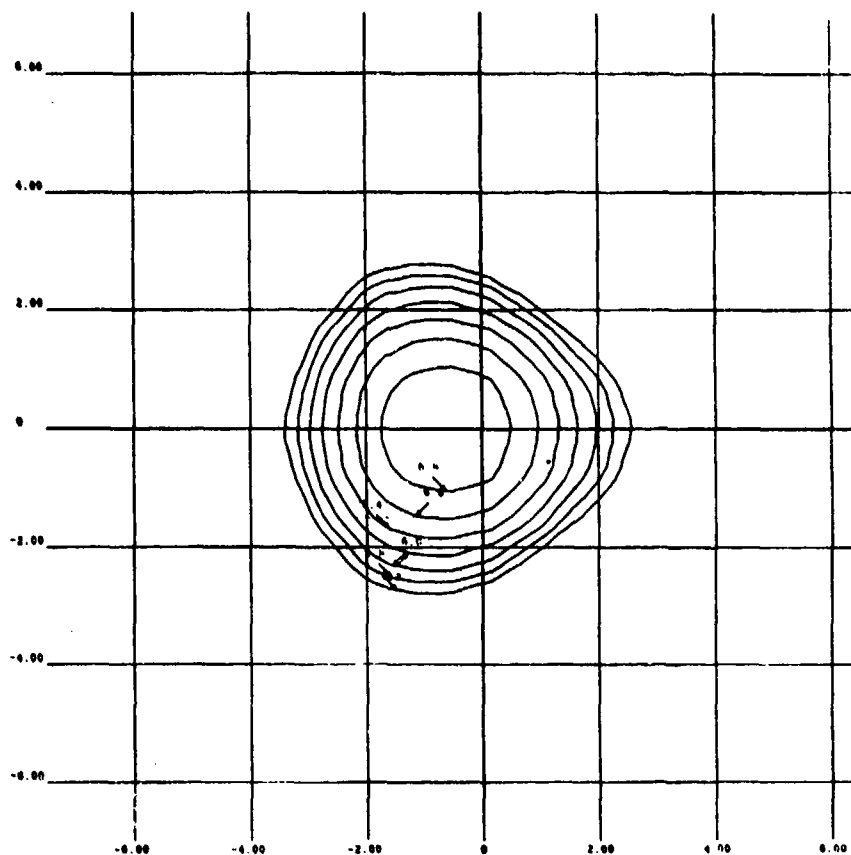


Fig.5e Thermal Blooming Contours at 10.6 μm for Stationary and Slew'd Beams: $\omega = 5$ mrad/sec

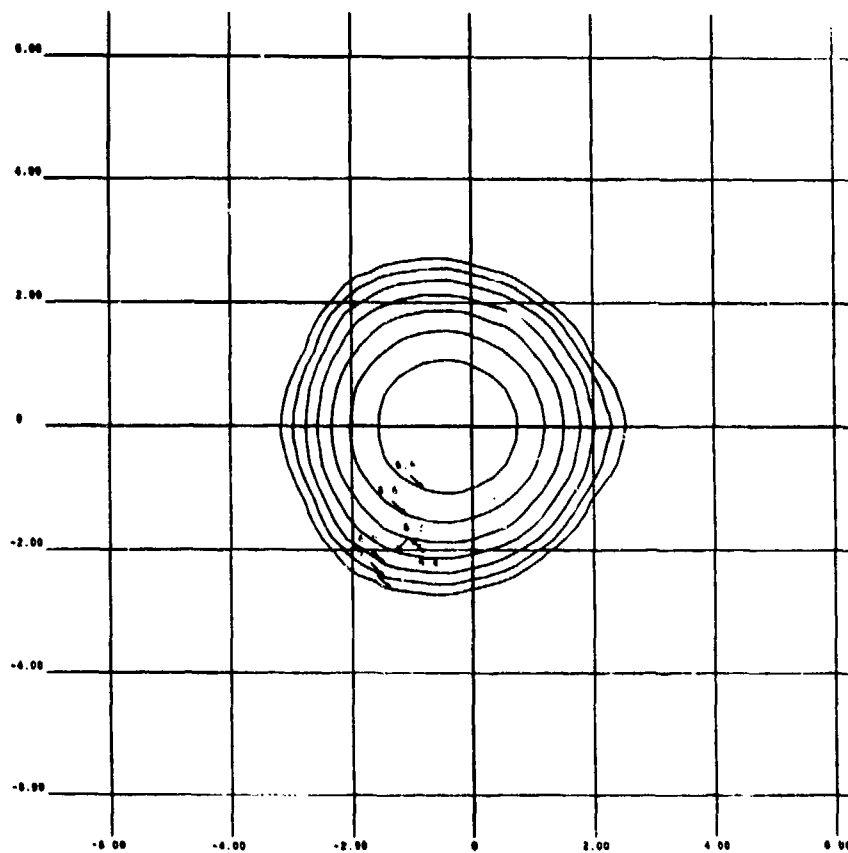


Fig.5f Thermal Blooming Contours at 10.6 μm for Stationary and Slew'd Beams: $\omega = 10$ mrad/sec

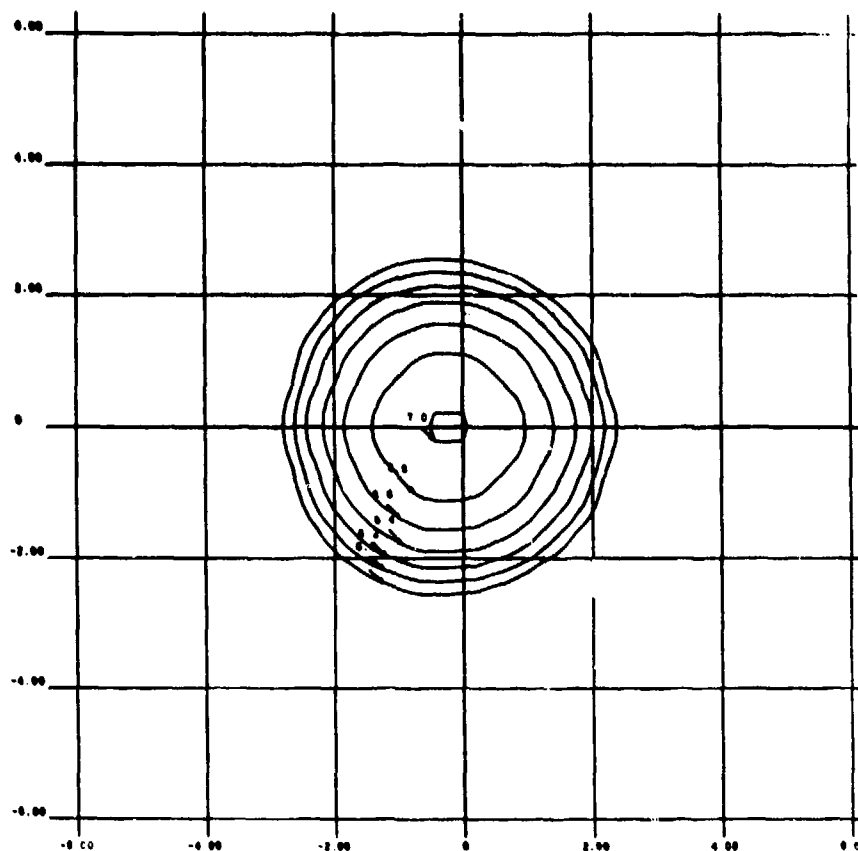


Fig.5g Thermal Blooming Contours at 10.6 μm for Stationary and Slew Beams: $\omega = 20$ mrad/sec

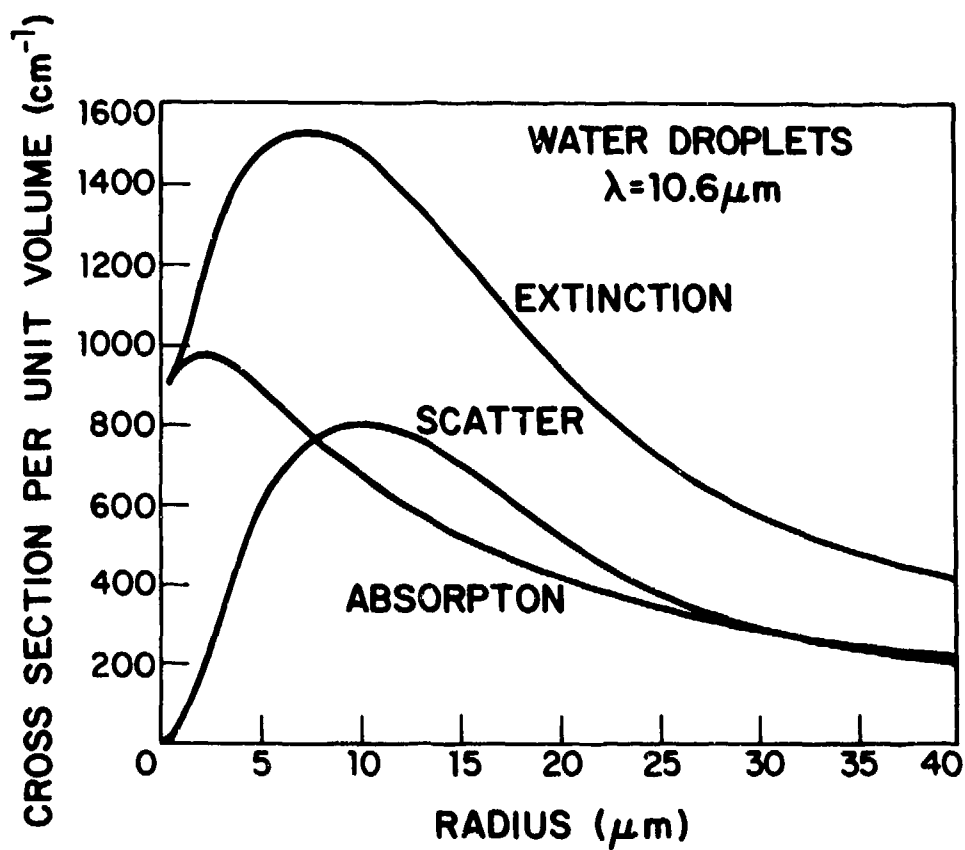


Fig.6 Extinction, Scattering and Absorbing Crosssections Per Unit Volume for Water Droplets at 10.6 μm Wavelength

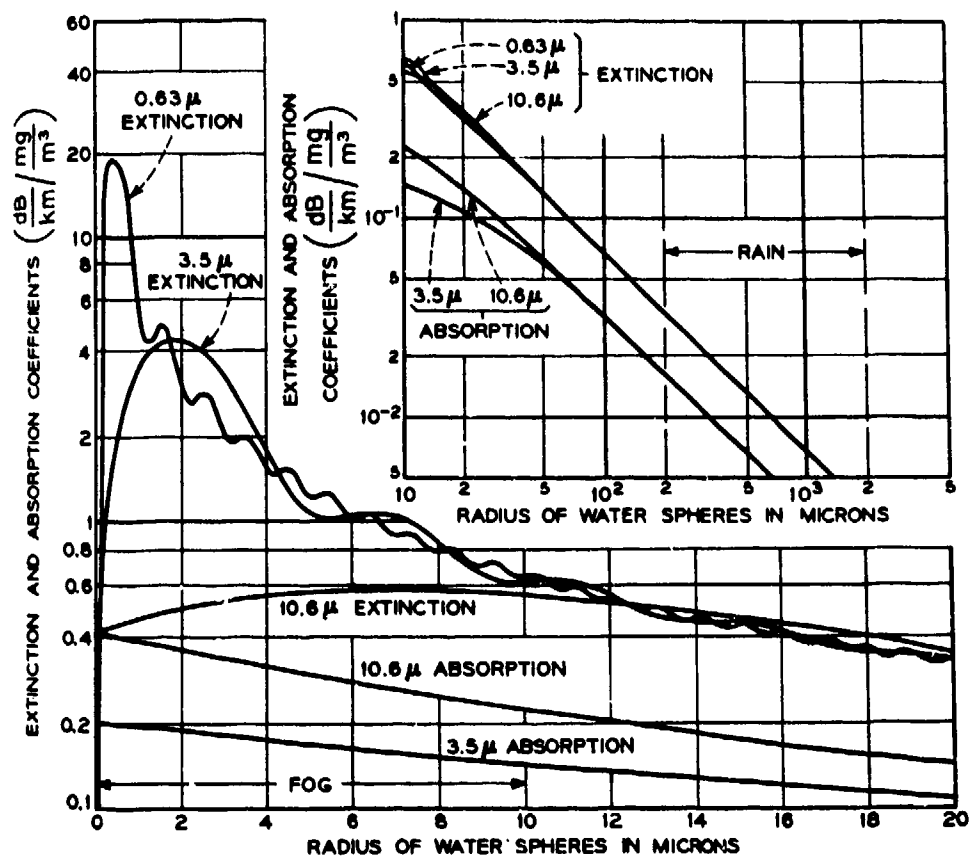


Fig.7 Extinction and Absorption Coefficients of Precipitation with Monodisperse Drop Size Distribution

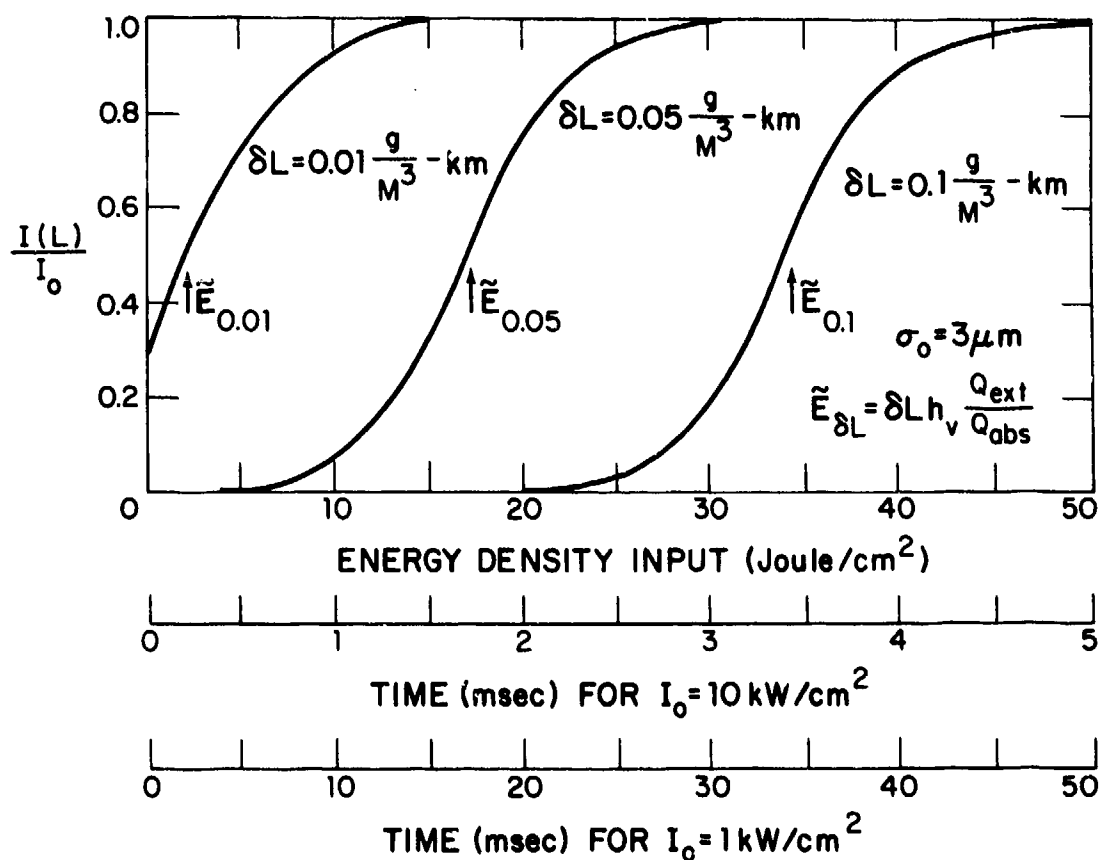


Fig.8 The Fraction of Intensity Transmitted Through Fog Versus Input Energy Density

NUMERICAL METHODS IN HIGH POWER LASER PROPAGATION

Peter B. Ulrich
Optical Sciences Division
Naval Research Laboratory
Washington, D. C. 20375
U.S.A.

Numerical solutions to the complex nonlinear problems of the interaction of high energy lasers with the atmosphere have played an important role in the understanding and development of this important and interesting field. This paper summarizes the relevant partial differential equations that apply, the kinds of numerical algorithms employed in their solution and representative results of a variety of cases of interest. Comparison with experiment is made wherever possible. Other effects which impact the thermal blooming phenomena are also addressed.

I. INTRODUCTION

The last week of October 1975 is of special significance in the history of the development of numerical techniques in high power laser propagation. For it was ten years ago, almost to the day, that a numerical algorithm of the type to be discussed in this paper was successfully applied to a problem in nonlinear optics. The paper (KELLY, P.L., 1965) entitled "Self Focusing of Optical Beams," was submitted to the Physical Review Letters on October 21, 1965. The author, Paul Kelley of MIT Lincoln Laboratory, numerically integrated the scalar wave equation for the electric field in a medium with a susceptibility which depended on the square of the field.

Since the late 60's, when the successful operation of high power lasers was first realized, the use of numerical analysis in nonlinear optics has increased in scope and sophistication. It is the purpose of this paper to survey the developments in this interesting and complex field.

Section II is a brief outline of the physics of the interaction of intense light with an absorbing fluid (liquid or gas) included here both to make the paper self-contained and as background for the discussions of specific applications of the computer codes to problems of interest in atmospheric propagation. In section III a discussion is given of the application of numerical methods to the problems at hand. An important element in the development of accurate and efficient algorithms was the implementation of coordinate system changes and phase changes of the dependent variable designed to better follow the scale and focal properties of the distorting beam. This topic is treated in section IV. Seven general space-time regimes of high power laser propagation are identified in section V and representative results are presented for each together with comparison with experiments where appropriate. Although the main thrust of the development of these computer codes has been a study of the nonlinear interaction of beam and absorber, other effects have been incorporated in order to make the simulation as close to reality as possible. These phenomena, which include turbulence, aerosol scattering (and heating—a nonlinear process), mirror deformation (truncation, obscuration, jitter) multiwavelength laser effects and the interaction of all these, are the subjects of section VI.

II. LIGHT ABSORPTION IN A GAS OR LIQUID

A. Scalar Wave Equation for the Laser Beam

This subject has been developed by parallel efforts at a number of laboratories. Discussion of the physics of the interaction of high power beams with gases can be found in the following papers and references: (WALLACE, J. and CAMAC, M., 1970), (GEBHARDT, F.G. and SMITH, D.C., 1971), (LIVINGSTON, P.M., 1971), (AITKEN, A.H., HAYES, J.N., and ULRICH, P.B., 1971), (HERRMANN, J., and BRADLEY, L.C., 1971), (RANGNEKAR, S.S., 1971), (GEBHARDT, F.G. and SMITH, D.C., 1972), (HAYES, J.N., ULRICH, P.B., and AITKEN, A.H., 1972), (HAYES, J.N., 1972), (AVIZONIS, P.V., HOGGE, C.B., BUTTS, R.R., and KENEMUTH, J.R., 1972), (AITKEN, A.H., HAYES, J.N., and ULRICH, P.B., 1973), (BISSONNETTE, L.R., 1973), (FRIED, D.L., 1974), (BREAUX, H., 1974).

The analysis begins with Maxwell's equations for the propagation of harmonically varying electric field, E

$$\nabla^2 E + k^2 \epsilon E = 0 \quad (1)$$

where $k = \omega/c$, ϵ is the dielectric constant and the depolarization of the field due to gradients of ϵ in distances on the order of a wavelength is ignored. Thus a single linearly polarized amplitude will be studied. Further, the rapidly varying optical phase, $\exp(ik\sqrt{\epsilon_0}z)$ is removed where ϵ_0 is the undisturbed dielectric constant. The equation for the remaining slowly-varying-in-range component, φ , is

$$2ik\partial\varphi/\partial z + \nabla_{\perp}^2 \varphi + k^2(n^2 - 1)\varphi = 0, \quad (2)$$

where the "paraxial approximation,"

$$|k\partial\varphi/\partial z| \gg |\partial^2\varphi/\partial z^2|$$

has been made, where $\nabla_{\perp}^2 \equiv \partial^2/\partial x^2 + \partial^2/\partial y^2$ and where $n^2 = \epsilon$ and $\epsilon_0 = 1$. In the absence of absorption $n^2 = 1$ throughout the path of the light beam and the solution to Eq. (2) is the familiar Fresnel integral

$$\varphi(x, y, z) = (-ik/2\pi z) \iint dx_0 dy_0 \varphi(x_0, y_0, 0) \exp\left\{ik\left[(x-x_0)^2 + (y-y_0)^2\right]/2z\right\}. \quad (3)$$

B. Absorbing Medium Equations

In the presence of absorption the equations describing the medium being heated by the laser beam are added to Eq. (2). These are:

$$\text{conservation of mass,} \quad \partial \rho / \partial t + (\mathbf{v} \cdot \nabla) \rho + \rho (\nabla \cdot \mathbf{v}) = 0 \quad (4)$$

$$\text{conservation of momentum,} \quad \rho [\partial \mathbf{v} / \partial t + (\mathbf{v} \cdot \nabla) \mathbf{v}] + \nabla p = 0 \quad (5)$$

$$\text{conservation of energy,} \quad \partial p / \partial t + (\mathbf{v} \cdot \nabla) p - \gamma p (\nabla \cdot \mathbf{v}) = (\gamma - 1) \alpha I \quad (6)$$

where ρ, p, \mathbf{v} are the density, pressure and velocity of the fluid, $\gamma = \text{ratio of specific heats, } c_p/c_v$, α is the absorption coefficient per unit length, and $I(x, y, z)$ is the laser beam irradiance, power per unit area. Although there are some situations where linearization of these equations is not appropriate due to large temperature changes in the medium (this can occur in absorbing cell experiments in the laboratory (ULRICH, P.B., HAYES, J.N., AITKEN, A.H., 1972)), or due to fluid motion relative to the beam at about the speed of sound (HAYES, J.N., 1974), most cases of interest in atmospheric propagation are quite accurately treated by linearized hydrodynamics. Recently, this hypothesis has been confirmed by solving Eq. (2) and the full nonlinear set Eqs. (4-6) in the case of short laser pulses. (FLECK, J.A., JR., MORRIS, J.R. and FEIT, M.J., 1975). This paper will be confined to a discussion of fluid disturbances which obey the linearized version of Eqs. (4-6). These are:

conservation of mass, (linearized)

$$\partial \rho_1 / \partial t + \rho_0 \nabla \cdot \mathbf{v}_1 + (\mathbf{v}_0 \cdot \nabla) \rho_1 = 0 \quad (7)$$

conservation of momentum, (linearized)

$$\rho_0 [\partial \mathbf{v}_1 / \partial t + (\mathbf{v}_0 \cdot \nabla) \mathbf{v}_1] + \nabla p_1 = 0 \quad (8)$$

conservation of energy, (linearized)

$$\partial p_1 / \partial t + (\mathbf{v}_0 \cdot \nabla) p_1 - \gamma p_0 (\nabla \cdot \mathbf{v}_1) = (\gamma - 1) \alpha I. \quad (9)$$

Where $\rho = \rho_0 + \rho_1$, etc., $\rho_0, \mathbf{v}_0, p_0$ are assumed uniform and constant, and squares of first order quantities are ignored. Depending on the space-time regime, the set of Eqs. (7-9) is solved directly by an appropriate numerical algorithm or the equations are solved for the density change up to a quadrature.

C. Equation Coupling Beam and Absorber

At optical frequencies and for a gas or transparent liquid the relation between index of refraction and medium density is given by the Lorentz-Lorenz equation (JACKSON, J.D., 1962),

$$(n^2 - 1)/(n^2 + 2) = N \rho \quad (10)$$

where N , the molecular refractivity, is independent of wavelength to a good approximation in the visible and near IR and has the value .154 cm³/gram. (WOLFE, W.L., 1965).

Thus the solution to the problem of laser propagation in the atmosphere is obtained by simultaneous solution of Eqs. (2), (7-10). The next section discusses methods for designing stable algorithms to achieve accurate solutions efficiently.

III. NUMERICAL TECHNIQUES

Equation (2) can be rewritten in the form

$$\partial \varphi / \partial z = F(\varphi) \quad (11)$$

where F represents a functional which includes, in general, the operations of transverse differentiation and integration of φ and perhaps also explicit dependence on x, y , and z . In addition, one needs initial conditions at $z = 0$

$$\varphi(x, y, 0) = \varphi_0(x, y) \quad (12)$$

and boundary conditions for $z > 0$

$$\varphi(\pm\infty, \pm\infty, z) = \nabla_{\perp} \varphi(\pm\infty, \pm\infty, z) = 0. \quad (13)$$

Equations (11-13) represent a well-posed problem and so a unique solution can be found in principle at some plane $z > 0$. (COURANT, R., 1962).

A selection of references which deal with algorithms employed to solve partial differential equations and which various investigators have found useful in the thermal blooming problem is given here: (FORSYTHE, G.E. and WASOW, W.R., 1967), (RICHTMYER, R.D.

and MORTON, K.W., 1967), (GODUNOV, S.K. and RYABENKI, V.S., 1964), (ORTEGA, J.M., 1972), (DOUGLAS, J., JR., and DUPONT, T., 1971), (GREVILLE, T.N.E., 1969), (VARGA, R.S., 1961).

The numerical techniques which will be discussed, whether integral or differential will be based on a "marching" technique of the general form

$$\varphi_n = \sum_{i=1}^N \alpha_i \varphi_{n-i} + G \left(\sum_{i=0}^M \beta_i \varphi_{n-i} \right) \Delta z \quad (14)$$

where $\varphi_n = \varphi(x, y, n\Delta z)$. If $\beta_0 = 0$ the algorithm is termed *explicit* and the solution is obtained simply by evaluating the expression on the right-hand side of Eq. (14). Otherwise the algorithm is termed *implicit*. Explicit algorithms, while generally faster per range step, are usually limited by stability criteria to a maximum Δz and therefore require many steps to reach the solution plane. Implicit algorithms are generally stable for all choices of Δz and only consideration of accuracy dictates the size of each step. The implicit algorithm tends to take longer to calculate than the explicit algorithm since a matrix inversion is required to solve a set of simultaneous difference equations.

Another approach which is widely used is to Fourier transform Eq. (11) in the transverse variables, x and y . (BREAUX, H.J., 1974), (WALLACE, J., JR., and LILLY, J.Q., 1974). By suitable coordinate system and dependent variable transformations, which will be exhibited below, the ordinary differential equation that is obtained in transform space can be solved exactly to get the transformed amplitude at the new range step. The use of the Fast Fourier Transform (FFT) algorithm (see e.g., COCHRAN, W.T., et al, 1967) makes this method efficient enough to compete with the other methods.

Yet another method for dealing with Eq. (11) numerically is to write its formal solution as

$$\varphi(x, y, z) = -\frac{1}{4\pi} \iint_{-\infty}^{\infty} dx_0 dy_0 G(x, y, z; x_0, y_0, 0) \varphi(x_0, y_0) \quad (15)$$

where G is the Green's function for the problem. (LYNCH, P.J., and BULLOCK, D.L., 1974).

In practice, an approximation to G is required and one is led thereby to a restriction on the size of the range difference. Thus, Eq. (15) is applied sequentially for a number of steps to the solution plane and, therefore, has many of the features of the direct differential approach. A variant of this integral solution approach (LUTOMIRSKI, R., 1974) is to solve Eq. (15) at the solution plane using the free space Green's function. The resultant amplitude is then used to alter the Green's function and the integration is repeated. This process is reiterated until the amplitude at some step changes negligibly from the amplitude at the previous step.

Examples of these techniques applied specifically to Eq. (2) will now be given.

1. Explicit Algorithm:

This is the algorithm mentioned in the introduction which was used by Kelley. As pointed out by Harmuth (HARMUTH, H.F., 1957) in his study of the Schrödinger equation by numerical means, equations of the type of which Eq. (2) is a sample are stable when a symmetric difference is used to represent the z -derivative. Using the notation

$$\varphi_{k,\ell}^m \equiv \varphi(k\Delta x, \ell\Delta y, m\Delta z) \quad (16)$$

and defining the central difference operator

$$\delta_x^2 \varphi_{k,\ell}^m \equiv (\varphi_{k-1,\ell}^m - 2\varphi_{k,\ell}^m + \varphi_{k+1,\ell}^m) / (\Delta x)^2$$

(similarly for δ_y^2) one has

$$\varphi_{k,\ell}^{m+1} = \varphi_{k,\ell}^{m-1} + (\Delta z / ik) (\delta_x^2 + \delta_y^2) \varphi_{k,\ell}^m + f[\varphi_{k,\ell}^m] \varphi_{k,\ell}^m \quad (17)$$

where

$$f = k^2 [n^2 (|\varphi|^2) - 1] \quad (18)$$

A schematic diagram of the flow of the algorithm is given in Fig. 1, where the dots indicate computational nodes from which data are taken to contribute to the solution at the node $(k, \ell, m+1)$ indicated by the open circle. The y - or l -dimension has been suppressed.

2. Implicit Algorithm:

An example of a popular algorithm which is successfully applied to heat conduction problems is the following (CRANK, J. and NICOLSON, P., 1947):

$$\varphi_{k,\ell}^{m+1} = \varphi_{k,\ell}^m + (\Delta z / 2ik) (\delta_x^2 + \delta_y^2) (\varphi_{k,\ell}^{m+1} + \varphi_{k,\ell}^m) / 2 + f[\varphi_{k,\ell}^m] \varphi_{k,\ell}^m \quad (19)$$

Figure 2 shows a schematic representation of this algorithm. The method is stable for all choices of $\Delta z / (\Delta x)^2$ and $\Delta z / (\Delta y)^2$. Solutions are achieved only after lengthy matrix inversion to completely specify φ at the plane $z = (m+1)\Delta z$. This method has not been actually employed in thermal blooming problems due to the existence of a much more efficient stable algorithm which is discussed next.

3. Combined Implicit and Explicit:

A novel two step procedure which alternates the nature of the algorithm from explicit to implicit for the x -direction and vice-versa for the y -direction provides an efficient stable algorithm (PEACEMAN, D.W. and RACHFORD, H.H., 1955), (DOUGLAS, J., 1955), (DOUGLAS, J. and RACHFORD, H.H., 1956).

At the first step the algorithm is explicit in x , implicit in y :

$$\varphi_{k,l}^{m+1} = \varphi_{k,l}^m + (\Delta x/2ik) [\delta_x^2 \varphi_{k,l}^m + \delta_y^2 \varphi_{k,l}^{m+1}] + f[\varphi_{k,l}^m] \varphi_{k,l}^m. \quad (20)$$

At the next step the algorithm is implicit in x , explicit in y :

$$\varphi_{k,l}^{m+2} = \varphi_{k,l}^{m+1} + (\Delta x/2ik) [\delta_x^2 \varphi_{k,l}^{m+2} + \delta_y^2 \varphi_{k,l}^{m+1}] + f[\varphi_{k,l}^{m+1}] \varphi_{k,l}^{m+1}. \quad (21)$$

The method is unconditionally stable for the two-step process as a whole and at each sub-step the solution requires only the inversion of a tri-diagonal matrix which is rapidly accomplished by Gaussian elimination (FORSYTHE, G.E. and WASOW, W.R., 1967). Figure 3 shows a schematic representation of the algorithm. This method is called the Alternating Direction Implicit, or ADI, method and it has proved extremely useful for studying nonlinear propagation problems.

4. Fast-Fourier Transform Solutions:

As will be shown in the next section, it is possible to transform the amplitude of the laser beam at each step so that the nonlinear term does not appear in the partial differential Eq. (2) but is incorporated, instead, in the phase of a new dependent variable ψ , which satisfies the equation

$$2ik \partial \psi / \partial z + \nabla^2 \psi = 0 \quad (22)$$

i.e., free space propagation. A finite Fourier transform is performed on Eq. (22) by writing

$$\psi(x, y, z) = \sum_{m=1}^{N_x} \sum_{n=1}^{N_y} C_{mn}(z) \exp [ip_m x + iq_n y]. \quad (23)$$

Then

$$2ik \partial C_{mn} / \partial z = -(p_m^2 + q_n^2) C_{mn}. \quad (24)$$

Assume C_{mn} is known at z . Its values at $z + \Delta z$ are given by

$$C_{mn}(z + \Delta z) = C_{mn}(z) \exp [-i\Delta z(p_m^2 + q_n^2) 2k]. \quad (25)$$

The amplitude $\psi(x, y, z + \Delta z)$ is obtained by inverse Fourier transformation of the C_{mn} . (BREAUX, H.J., 1974), (WALLACE, J. and LILLY, J.Q., 1974). The true field is then reconstructed by reintroduction of the nonlinear phase as will be discussed in the next section.

Note that the propagation of the fields is *exact* for all frequencies up to the Nyquist sampling frequency, $1/\Delta x$ or $1/\Delta y$ where Δx , Δy , are the mesh spacings. This means that laser intensity distributions with rapid transverse variation (e.g., truncated or obscured beams) can be well treated by the FFT algorithm without apodization (FLECK, J.A., MORRIS, J.R. and FEIT, M.J., 1975). As an example of the accuracy with which a complicated diffraction pattern can be calculated, Fig. 4 shows a comparison between experiment and calculated patterns for a rectangular aperture. (CORDRAY, D.M., 1975.) The location of the zeros and maxima are accurately calculated. The values of the maxima are given in the table and compared with the theoretical values. When one considers that these maxima are in some cases almost two orders of magnitude below the central peak intensity, the agreement is seen to be extremely good.

A large contributing factor to the accuracy of the calculation of the rectangular aperture problem is the use of a square mesh oriented parallel to the aperture. The patterns calculated with circular or other shaped apertures are not quite as accurately done. Figure 5 shows the comparison for a uniformly illuminated circular aperture (CORDRAY, D.M., 1975). Some of the structure seen in the computer result is due to the interpolations inherent in the contour plotting routine.

5. Integral Methods:

The formal solution of Eq. (2) is given in Eq. (15). In order to exploit this solution an approximation is made to represent the Green's function as

$$G_0(x, y, z; x_1, y_1, z_1) \approx G_0(x, y, z; x_1, y_1, z_1) \exp \left\{ \frac{i}{2k} \int_{z_1}^z dz' f(x_s(z'), y_s(z'), z') \right\} \quad (26)$$

where x_s and y_s are transverse variables which follow the focusing or defocusing of the beam and G_0 is the free space propagator. In order to neglect an amplitude correction which must also be applied to G_0 , in general, a restriction is placed on the step size. Thus an iterative procedure for the complete solution is required as was the case for the differential approach.

IV. IMPROVEMENT OF COMPUTATIONAL EFFICIENCY

There are a number of ways in which the accuracy and speed of the computation can be improved by judicious choice of coordinate system and by appropriate changes in the dependent variable. These changes can be applied *a priori* to the basic equations. These are called nonadaptive coordinate systems. In the most sophisticated approach, transformations are applied as the problem is iterated towards a solution, automatically adjusting the coordinate system to the changes in the beam phase fronts. Such alterations are known as adaptive coordinate and phase changes.

Nonadaptive Coordinate Systems

An example of a collection of nonadaptive changes to the basic equations which has proven useful in thermal blooming calculations will be given here. (ULRICH, P.B., 1971.) Slightly different coordinate systems have been employed by other workers, (HERRMANN, J., and BRADLEY, L.C., 1971), (BREAUX, H.J., 1974), (HOGGE, C.B., 1971) but all systems are essentially equivalent in their ability to enhance the efficiency (speed plus accuracy) of the computation.

The idea here is to utilize a coordinate system in which a fundamental solution to Eq. (2) with $n^2 = 1$ (no blooming) is (1) pure real and (2) constant in range, z . The fundamental mode selected as the TE_{00} gaussian beam with geometrical focus at $z = f$ (KOGELNIK, H., and LI, T., 1966). At $z = 0$ this mode has the form

$$\varphi_0(x, y) = \left(1/\sqrt{\pi a^2}\right) \exp [-(x^2 + y^2)/2a^2 - ik(x^2 + y^2)/2f] \quad (27)$$

where a is a transverse scale length which is a measure of the initial size of the beam. With this mode at the initial plane, the solution for range is given by performing the integrations in Eq. (3) and is,

$$\varphi(x, y, z) = \left(1/\sqrt{\pi a^2 D}\right) \exp \left\{ i \frac{(x^2 + y^2)}{2a^2} d \ln D^{1/2}/d\xi + i \tan^{-1}(\xi/(1 - \xi/f)) - \frac{(x^2 + y^2)}{2a^2} D \right\} \quad (28)$$

where $\xi = z/ka^2$, $f = f/ka^2$, $D(\xi) = \xi^2 + (1 - \xi/f)^2$. The presence of the quadratic terms in the imaginary part of the exponential gives rise to high frequency oscillations in the amplitude for $x > a$, $y > a$. These can exceed the sampling frequency of the computational mesh. Thus, a phase change is made to remove these terms. Additionally, the amplitude is seen to grow in range as $z \rightarrow f$ due to the presence of the term $(\pi a^2 D)^{-1/2}$. Thus, it is desirable to remove this factor as well. As the beam focuses and becomes smaller the mathematical mesh should shrink at the same rate to accurately model the transverse distribution. These considerations lead to the following set of transformations:

- (1) Removal of the quadratic phase and amplitude, leaving a pure real Gaussian amplitude in vacuum.
- (2) Scaling of the transverse coordinates with beam size, $\tilde{x} \equiv x/a\sqrt{D}$, $\tilde{y} \equiv y/a\sqrt{D}$.
- (3) Alteration of step size Δz to automatically take smaller steps in the region of high beam intensity, $dZ/d\xi = 1/D$. Equation (2) then takes the form

$$2i\partial\psi/\partial Z + \nabla_{\tilde{x}\tilde{y}}^2\psi + (2 - \tilde{x}^2 - \tilde{y}^2)\psi + Dk^2a^2(n^2 - 1)\psi = 0. \quad (29)$$

Note that, for $n^2 = 1$, $\psi = \exp [-(\tilde{x}^2 + \tilde{y}^2)/2]$ and $\partial\psi/\partial Z = 0$ as desired. The presence of the last term on the left-hand side of Eq. (29) gives rise to contributions to the imaginary part of ψ . As the blooming becomes severe these contributions become difficult to compute. The surfaces of constant phase of the distorted amplitude become quite different from the coordinate surfaces. The beam grows in one direction and compresses in another—leading to conflicting sampling requirements in x and y . For these cases, a method for adapting the tilt and radius of curvature of the coordinate surface independently in the two transverse directions to match, on the average, the corresponding quantities for the distorted wave front is needed to efficiently calculate the propagation in the presence of strong thermal blooming. A technique for doing this is discussed next.

Removal of the Nonlinear Phase

By removal of the nonlinear contribution to the phase at each step it is possible to derive an equation which looks like the free-space propagation equation. (HERRMANN, J., and BRADLEY, L.C., 1971.)

The alterations are made to Eq. (29).

Define

$$g(\tilde{x}, \tilde{y}, Z) = \tilde{x}^2 + \tilde{y}^2 - 2 - k^2a^2D(Z)(n^2 - 1)$$

and let

$$\psi(\tilde{x}, \tilde{y}, Z) = \Phi(\tilde{x}, \tilde{y}, Z) \exp \left[-\frac{i}{2} \int_{Z_0}^Z g(\tilde{x}, \tilde{y}, Z') dZ' \right] \quad (30)$$

where Z_0 is a constant to be specified.

Let

$$\Gamma(\tilde{x}, \tilde{y}, Z) = \frac{1}{2} \int_{Z_0}^Z g(\tilde{x}, \tilde{y}, Z') dZ'.$$

Then Eq. (29) becomes

$$2i\partial\Phi/\partial Z + H(Z)\Phi = 0 \quad (31)$$

where the operator H is defined to be

$$H(Z) = e^{i\Gamma}\nabla^2 e^{-i\Gamma}.$$

The specification of $H(z)$ for numerical work is now required. $H(z)$ is chosen to operate midway between the computational planes at z and $z + \Delta z$. In addition the lower limit, z_0 , in Γ is chosen to be at $z + \Delta z/2$ as well. Thus $H(z)$ becomes $H(z) = \nabla^2$ so that Eq. (31) is now much simplified and looks like a free space propagation equation

$$2i\partial\Phi/\partial Z + \nabla^2\Phi = 0. \quad (32)$$

The operations taken to propagate one step in range are (1) removal of nonlinear phase at z by Eq. (30), (2) propagation of the new amplitude by Eq. (32), and (3) replacement of phase at the new plane $z + \Delta z$ by the inverse to Eq. (30).

The solution to Eq. (32) is obtained by a variety of means, explicit, (ULRICH, P.B., HAYES, J.N., HANCOCK, J.H., and ULRICH, J.T., 1974), implicit with central differences (ULRICH, P.B., 1974) or with a Galerkin method and splines (HERRMANN, J. and BRADLEY, L.C., 1971), (ULRICH, P.B., 1974), or the fast Fourier Transform. (BREAUX, H.J., 1974), (WALLACE, J. and LILLY, J.Q., 1974.)

Adaptive Coordinate Systems

The nonadaptive changes leading to Eq. (29) can be generalized to allow their application without *a priori* knowledge of the phase front tilt and curvature as a function of range. (BRADLEY, L.C. and HERRMANN, J. 1974.) At each range step the amplitude x is altered by removing the average tilt, curvature and scale of the phase front. At some plane z the phase of the wave amplitude measured with respect to the equiphase surface of the local coordinate system is

$$\varphi(x, y) = \varphi_0 + \nabla\varphi \cdot dr$$

where r lies in the coordinate equiphase surface. Now, a tilt and refocusing is performed on the amplitude to minimize this phase gradient.

Before the correction the amplitude is of the form

$$\psi = A \exp(-i\varphi).$$

Correction is applied to give

$$\psi_c = A \exp(-i\varphi + \alpha_x x^2 + \alpha_y y^2 + \beta_x x + \beta_y y) \equiv A \exp(-i\varphi') \quad (33)$$

where $\alpha_x, \alpha_y, \beta_x, \beta_y$, are determined by minimizing $\nabla\varphi'$ on the average over the computational plane. The minimization is weighted by the beam intensity so that the curvative and tilt at the position of the beam contribute most strongly. The condition

$$\iint dx dy |\psi|^2 (\nabla\varphi')^2 = \text{minimum} \quad (34)$$

is satisfied by taking partial derivatives with respect to the α 's and β 's to get four equations for the four unknowns. These are then used in Eq. (33) to reduce the linear and quadratic phase. In addition coordinate changes in scale and a shift of the center of the coordinate system are also applied to preserve the form invariance of the basic partial differential equation. This permits the algorithm to remain unchanged throughout the calculation. Equation (29) is now generalized to

$$2i \frac{\partial \psi_c}{\partial Z} + \frac{1}{D_x} \frac{\partial^2 \psi_c}{\partial x'^2} + \frac{1}{D_y} \frac{\partial^2 \psi_c}{\partial y'^2} + [2(\gamma_x + \gamma_y) - f_x(x' - y_0)^2 - f_y(y' - y_0)^2] \psi_c + \sqrt{D_x D_y} k^2 a^2 (n^2 - 1) \psi_c = 0 \quad (35)$$

where D_x, D_y are now calculated from α_x, α_y at each step as are $\gamma_x, \gamma_y, f_x, f_y$. This algorithm, while requiring more calculation per step, actually is not much more expensive of computer time for a given problem than the nonadaptive system. This is because a coarser sampling both in the transverse plane and in range is allowed since the coordinate surfaces better follow the phase surfaces of the distorting beam.

V. APPLICATION TO THERMAL BLOOMING PROBLEMS

Because of the wide range of time scales representing the variety of phenomena in Thermal blooming, no one all-inclusive algorithm will solve the simultaneous set of Eqs. (2) and (7) to (10). Instead, the problems are categorized by their time scales and separately solved. This section is devoted to a discussion of seven such thermal blooming time regimes. Let c_s be the speed of sound, v_w be the wind-plus slew velocity, $v_w = v_0 + \Omega z$, v_B be the buoyant velocity, d be a characteristic beam diameter. Let τ be the pulse length. Then the time regimes are:

	Dimensions
(1) Short pulse: $t < d/c_s$	r, z, t
(2) Long pulse: $d/c_s < t \ll d/v_w$	r, z, t
(3) Transient: $\tau \approx d/v_w$ (includes $\tau_B \approx d/v_w$)	x, y, z, t
(4) CW: $\tau \gg d/v_w$	x, y, z
(5) Multipulse Transient – a series of short pulses – $t \ll d/c_s$ – studied in time $\approx d/v_w$	x, y, z, t
(6) Multipulse Steady State – a series of short pulses – $t \ll d/c_s$ – studied at time $\gg d/v_w$	x, y, z
(7) Sonic flow problems, $v_w \approx C_s$	x, y, z, t

Short Pulse Regime (ULRICH, P.B., 1971), (ULRICH, P.B. and WALLACE, J. JR., 1973)

In the short pulse regime, if the initial distribution is symmetric it will remain so since external nonsymmetrical influences such as forced convection (wind) or gravity are too slow to alter the symmetry. The problem is then soluble in cylindrical coordinates and is reduced, thereby, to three dimensions, r, z, t . The set of Eqs. (7) to (9) can be solved numerically as written or a single equation involving only the density can be derived

$$(\partial^2/\partial t^2 - C_s^2 \nabla^2)(\partial \rho/\partial t) = (\gamma - 1)\alpha \nabla^2 I. \quad (36)$$

Both approaches have been employed.

This regime is amenable to analytic study as well (AITKEN, A.H., HAYES, J.N., and ULRICH, P.B., 1973) in both geometrical optics (HAYES, J.N., 1972) and wave optics (ULRICH, P.B., 1972). Comparison of analytic and computer results is made in Fig. 6. The agreement is seen to be excellent and one can rely confidently on the analytic theories for calculating in this time regime. It is always important whenever possible to check computer code results against experiments and this has been accomplished for this time regime (O'NEIL, R.W., KLEIMAN, H., and LOWDER, J.E., 1974). Figure 7 shows the experimental results for the drop in peak power through a slit aperture as a function of time. Plotted as a solid line is the theoretical prediction.

Long Pulse Regime

The computer code which calculates the short pulse regime works here as well since characteristic times are still less than wind transit times and the problem remains symmetric. Thus, Fig. 6 applies in this case as well. Analytic theory is reliable in this time regime only if the distortion of the pulse in the times up to the sound transit time is so small that the beam is still described by its initial distribution. Experimental confirmation of the theory in the long pulse regime has been made as well. (KENEMUTH, J.R., HOGGE, C.B., and AVIZONIS, P.V., 1970), (HAYES, J.N., 1972), (BUSER, R.G. and ROHDE, R.S., 1975). It is just for those cases where appreciable distortion occurs during the whole time regime up to when asymmetries set in that the self consistent computer code is needed. In addition, the analytic results have been carried out for simple beam shapes (e.g., infinite gaussians). More complicated (realistic) shapes are best studied with the computer codes.

Transient Regime

When the externally derived convection distorts the symmetry of the beam and in addition the beam is evolving in time a full four-dimensional computer code must be employed. These conditions occur when a CW beam is propagated and before the steady state has set in. It occurs also when the CW beam is time varying at the source and, hence, is not truly CW. An important phenomenon which falls into this category is propagation through a region of still air caused by wind shear or by the cancellation of net relative air motion by slewing. These "stagnation zones" can have a profound effect on beam quality.

The four dimensional algorithm uses the hydrodynamic Eqs. (7-9) in the isobaric approximation for which the density changes satisfy

$$\partial \rho_1 / \partial t + (\mathbf{v}_0 + \Omega \mathbf{z}) \cdot \nabla_1 \rho_1 = -(\gamma - 1)\alpha I(r, z, t)/c_s \quad (37)$$

where Ω is the slewing rate of the laser beam. The solution to Eq. (37) is

$$\rho_1(r, z, t) = -\frac{(\gamma - 1)\alpha}{c_s^2} \int_0^t I(r - (\mathbf{v}_0 + \Omega \mathbf{z})(t - t'), z, t') dt'. \quad (38)$$

Four dimensional codes have been written which solve Eq. (37) directly by an appropriate algorithm (FLECK, J.A., JR., MORRIS, J.R., and FEIT, M.J., 1975) and which solve Eq. (38) by numerical integration (ULRICH, P.B. and ULRICH, J.T., 1975).

These codes have been experimentally confirmed in a laboratory absorbing cell. The results are shown in Fig. 8. (BROWN, R.T., BERGER, P.J., GEBHARDT, F.G., and SMITH, D.C., 1974), (BERGER, P.J., GEBHARDT, F.G., and SMITH, D.C., 1974), (BERGER, P.J., GEBHARDT, F.G., ULRICH, J.T., and ULRICH, P.B., 1975.) The cell was pivoted to create a stagnation zone at various points along the beam path. Beam size and power were such that natural convection occurred on a time scale like the characteristic intensity drop-off time. Thus, in order to confirm the computer code, inclusion of an intensity dependent buoyancy velocity was made necessary. (ULRICH, P.B. and ULRICH, J.T., 1975.) Instead of Eq. (38) the following equations for the density changes and induced velocity were solved,

$$\rho_1(x, y, t) = -\frac{(\gamma-1)\alpha}{c_s^2} \int_0^t I(x - \Omega z(t-t'), y - v_B(t-t'), z, t') dt' \quad (39)$$

$$v_B(x, y, t) = \frac{g\rho_1}{\rho_0} t + g \frac{(\gamma-1)\alpha}{\rho_0 c_s^2} \int_0^t t' I(x - \Omega z(t-t'), y - v_B(t-t'), z, t') dt'. \quad (40)$$

This additional complexity markedly increases the running time of an already lengthy code. Happily, the characteristic times for buoyancy effects in the atmosphere are usually much longer than all other characteristic times and this additional complexity can usually be dispensed with.

CW Regime

In the limit that the time elapsed since the initiation of the beam greatly exceeds the transit time of the wind across any portion of the beam a steady state condition is reached. Cool air is constantly added to replace the heated air which is driven from the beam region by the wind. Equation (38) is then converted into a relationship independent of time. Let $t \rightarrow \infty$, define $x' = x - (v_0 + \Omega z)(t - t')$. Then Eq. (38) becomes

$$\rho_1(x, y, z) = -\frac{(\gamma-1)\alpha}{(v_0 + \Omega z)c_s^2} \int_{-\infty}^x I(x', y, z) dx'. \quad (41)$$

Which states that the density change of an air parcel is proportional to the integral of the energy absorbed all along the path it followed through the beam.

This density change is normally calculated by some simple numerical integration procedure. The CW code results have also been compared with laboratory experiments and the results are shown in Fig. 9 (ULRICH, P.B., HAYES, J.N., and AITKEN, A.H., 1972).

Multipulse Transient Regime

If one assumes that the laser irradiance which appears in Eq. (38) is made up of a series of pulses: so short that the blooming during the pulse is negligible, then on the time scale of wind transit times the irradiance can be written as,

$$I(x, y, z, t) = \sum_{n=1}^N E_n(x, y, z) \delta(t - t_n) \quad (42)$$

where E_n is the energy of the n th pulse in the train. (WALLACE, J., JR., and LILLY, J.Q., 1974.) Although E_n does not depend explicitly on t due to the assumption of short pulses, the energy distribution changes from pulse to pulse due to the energy deposited by previous pulses. If Eq. (42) is substituted in Eq. (38) one has

$$\rho_1(r, z, t_N) = -\frac{(\gamma-1)\alpha}{c_s^2} \sum_{n=1}^{N-1} E_n(r - (v_0 + \Omega z)(t_N - t_n), z). \quad (43)$$

Thus the density change at any point is given by the sum of changes due to earlier pulses which have arrived at that point at time $t = t_N$.

Multiple pulse propagation has some novel features. If the time between pulses is such that approximately one-half of each beam passes through heated air while the other half passes through cool air on the up-wind side then an enhancement of peak irradiance over the vacuum value is seen. This is due to refraction up-wind by the down-wind half of the beam which adds to the undistorted up-wind portion of the beam. This phenomenon, first predicted by J. Wallace, Jr., has been confirmed by computer runs, see Fig. 10, and also by experiment (BUSER, R., ROHDE, R., GEBHARDT, F.G., BERGER, P.J., and SMITH, D.C., 1975).

It is not always possible to choose parameters such that there is no self-blooming during the individual pulses. Correction for self-blooming can be incorporated in the multiple pulse code in an approximate way which has been confirmed by more detailed calculations (FLECK, J.A., JR., MORRIS, J.R., and FEIT, M.J., 1975).

Multiple Pulse Steady State

After the pulse train has been on for a time longer than the wind transit time, a steady state evolves for the same reasons as given in the discussion of CW propagation above. In this case, E_n in Eq. (43) becomes independent of the subscript n except through its argument.

$$\rho_1(r, z) = -\frac{(\gamma-1)\alpha}{c_s^2} \sum_{n=1}^{\infty} E(r - (v_0 + \Omega z)n\Delta t, z). \quad (44)$$

Thus, the density change in this case is given by the wind-translated density changes due to a series of identically distorted beams. This steady state is rapidly calculated since the actual propagation from z to $z + \Delta z$ need only be done once for the wind-shifted sum to be performed. Run times are about the same as CW code run times. Comparison with transient multiple pulse code runs in the limit of many more pulses than the number per wind transit time confirm that Eq. (44) correctly calculates the asymptotic state of the time dependent problem.

Sonic Flow Problems

The sonic point where $v \approx c_s$ is a singular point for the linearized hydrodynamic equations, but due to the motion of a weak shock up-wind from the source, the sound speed in the heated medium is raised above that of the undisturbed medium and so Mach 1 conditions are not reached. (HAYES, J.N., 1974.) The steady state density calculations can nonetheless be obtained by applying the linearized hydrodynamic equation with the correct upstream sound speed. This suggests that one may obtain information about propagation under transonic conditions by solving the linearized hydrodynamic equations along the entire propagation path (BRADLEY, L.C., 1974). The amount of blooming seen due to transonic regions is a function of where the sonic point occurs along the path but is insignificant except possibly for sonic translation, where the whole beam path moves with $v \approx c_s$. (WALLACE, J. and PASCIAK, J., 1975), (FLECK, J.A., JR., MORRIS, J.R., and FEIT, M.J., 1975.)

VI. OTHER PROPAGATION PHENOMENA

A number of other effects have been incorporated in the thermal blooming codes. Some are linear, others nonlinear. All have the potential for altering the thermal blooming because all affect the beam intensity upon which blooming depends so strongly.

Turbulence

A phase shift of the form

$$\Gamma_{\text{TURB}}(x, y) = k \int_{z_n}^{z_n + \Delta z} \delta n(x, y, z) dz \quad (45)$$

is added to the phase shift created by the laser heating of the atmosphere. $\Gamma_{\text{TURB}}(x, y)$ is calculated by a Monte Carlo technique which simulates the statistical nature of δn in a turbulent atmosphere. (BRADLEY, L.C., HERRMANN, J., 1974), (BRADLEY, L.C., 1975), (BROWN, W.P., JR., 1975), (FLECK, J.A., MORRIS, J.R., and FEIT, M.J., 1975.) These phase functions can be either stationary or made to move with the wind. The results have been determined to be independent, on the average, of the motion of the phase functions (BROWN, W.P., JR., 1974).

Aerosols

Simple aerosol scattering can be treated as a loss mechanism to be added to the absorption coefficient of the laser beam. For high power propagation, however, the aerosol will be heated and conduct heat to the atmosphere as well as vaporize, especially in the case of hydrosols. The rate of conduction and evaporation is a function of the size of the particle so that aerosol distribution information is required for an accurate representation of these phenomena. The computer codes can most easily take into account the effects of the heating of aerosols by means of an intensity-dependent absorption coefficient. Since the absorption coefficient will now be a function of the transverse coordinates the form of the partial differential equation will be altered and new algorithms will have to be employed for its solution. This work is presently under active study.

Multiwavelength Effects

Chemical lasers typically emit on a number of lines of different wavelength. The power in each line is generally different and the atmospheric absorption at each wavelength can be very different. Ideally, one needs a computer code capable of calculating the propagation of each line and coupling the beams via their mutual heating of the intervening atmosphere. Such a computer code has been created (BILOW, H., 1975), but it is costly to run. First results are not forthcoming at this writing. Other attempts have been made to model multiwavelength propagation. One is to average over many lines of nearly equal absorption (ULRICH, P.B., HANCOCK, J.H., 1974). Another uses an integral technique which alters each amplitude by a phase shift proportional to the sum of the contributions of each line (BULLOCK, D.L., 1974). When the initial distribution of each line is identical only one line need be propagated. The heating is derived from a sum of intensities derived from this line and made proportional to the power of each line reduced by the appropriate absorption coefficient. (HOGGE, C.B., 1975.)

Mirror Induced Degradations

These alterations of the beam are both static and time dependent.

Static Effects

Mirror heating, poor machining and spillover of the beam lead to nondiffraction limited propagation. These effects are often crudely accounted for by a change in wavelength which enlarges the computed focal spot. Wavelength appears in the nonlinear portion of the propagation equation, however, so that this technique alters the physics of the thermal blooming as well. (PHILLIPS, E.A., 1975.) A more satisfying way to account for nondiffraction limited behavior is to actually impart the beam with random phase at the input plane. The choice of scale and correction of the phase changes is determined by the desired intensity drop at focus through the Strehl relation (HOGGE, C.B., and BURLAKOFF, M., 1973).

The effect of mirror spillover can be modeled by sharply truncating the beam at the desired transverse mesh node. This result gives excellent results in the focal plane (see section III, above, and Figs. 4 and 5). However, as the plane of observation moves back towards the aperture the agreement is less good. A measure of this agreement is the ability of the computer codes to calculate the on-axis intensity. Figure 11 indicates how the code converges to the correct answer near the focus in spite of its inability to calculate well at all nearer the input plane. This must have repercussions on the ability of the codes to calculate thermal blooming with truncated beams since the heating is not being calculated with the correctly shaped beam in the near field. This question remains unresolved.

Dynamic Effects

An effect which is currently under study is the phenomenon of mirror jitter. The motion of the mirror, while absolutely small, can impart sizable beam motions at long ranges which could effect thermal blooming since the air particles are heated less than full time as the beam moves about.

Medium inhomogeneities in the laser cavity or the evolution of a cascade of lasing lines in a chemical laser impart a complicated time dependence to the output of the laser. The effects of these phenomena have not been studied theoretically. The full four-dimensional computer code will be used for these studies.

VII. CONCLUSION

This paper has presented a review of the numerical approaches taken to solve a variety of nonlinear problems in atmospheric propagation. The field is a young one but has enjoyed a rapid maturity. Very sophisticated techniques have been brought to bear on these complex problems and many successes have been realized. The techniques developed in the numerical solution of the thermal blooming problem will no doubt have application in other areas of nonlinear optics. Furthermore, extension can be made to other problems such as sound propagation and electromagnetic propagation at other wavelengths.

REFERENCES

- AITKEN, A.H., HAYES, J.N., and ULRICH, P.B., 1971, "Propagation of 10.6μ Laser Beams in a Non-turbulent Atmosphere," *J. Opt. Soc. Am.* **61**, 674 (1971).
- AITKEN, A.H., HAYES, J.N., and ULRICH, P.B., 1973, "Thermal Blooming of Pulsed Focussed Gaussian Laser Beams," *Appl. Opt.* **12**, 193 (1973).
- AVIZONIS, P.V., HOGGE, C.B., BUTTS, R.R. and KENEMUTH, J.R., 1972, "Geometric Optics of Thermal Blooming in Gases, Part I," *Appl. Opt.* **11**, 554 (1972).
- BERGER, P.J., GEBHARDT, F.G., and SMITH, D.C., 1974, "Thermal Blooming due to a Stagnation Zone in a Slew Beam," United Aircraft Research Laboratories Report N921724-12, October 15, 1974.
- BERGER, P.J., GEBHARDT, F.G., ULRICH, J.T., and ULRICH, P.B., 1975, "Transient Blooming of a Slew Beam Containing a Stagnation Zone," to be published.
- BILLOW, H., 1975, Naval Surface Weapons Center, Silver Spring, Maryland 20910, Private Communication.
- BISSONNETTE, L.R., 1973, "Thermally Induced Nonlinear Propagation of a Laser Beam in an Absorbing Fluid Medium," *Appl. Opt.* **12**, 719 (1973).
- BRADLEY, L.C., and HERRMANN, J., 1971, "Numerical Calculation of Light Propagation in a Nonlinear Medium," *J. Opt. Soc. Am.* **61**, 668 (1971).
- BRADLEY, L.C., 1974, "Thermal Blooming in the Transonic Regime," MIT Lincoln Laboratory Report LTP-24, 30 January, 1974.
- BRADLEY, L.C., and HERRMANN, J., 1974, "Notes on the Lincoln Laboratory CW Propagation Code," unpublished.
- BRADLEY, L.C., 1975, "Simulation of Atmospheric Index Fluctuations," to be published.
- BREAUX, H.J., 1974, "An Analysis of Mathematical Transformations and a Comparison of Numerical Techniques for Computation of High Energy CW Laser Propagation in an Inhomogeneous Medium," Army Ballistic Research Laboratories Report 1723, June 1974.
- BROWN, R.T., BERGER, P.J., GEBHARDT, F.G., and SMITH, D.C., 1974, "Influence of Dead Zones and Transonic Slewing on Thermal Blooming," United Aircraft Research Laboratories Report N921724-7, February, 1974.
- BROWN, W.P., JR., 1975, "High Energy Laser Propagation," Hughes Research Laboratories Report, February 1975.
- BULLOCK, D.L., 1974, TRW Systems Group, One Space Park, Redondo Beach, California 90278, Private Communication.
- BUSER, R.G., and ROHDE, R.S., 1975, "Transient Thermal Blooming of Long Laser Pulses," *Appl. Opt.* **14**, 50 (1975).
- BUSER, R.G., ROHDE, R.S., GEBHARDT, F.G., BERGER, P.J., and SMITH, D.C., 1975, "Experimental Study of Thermal Blooming of a Repetitively Pulsed Laser," to be published.
- COCHRAN, W.T., et al., 1967, "What is the Fast Fourier Transform?" G-AE Subcommittee on Measurement Concepts IEEE Transactions on Audio and Electroacoustics Vol AU-15, # 2, June 1967, p. 45.
- CORDRAY, D.M., 1975, Optical Sciences Division, Naval Research Laboratory, Washington, D.C. 20375, Private Communication.
- COURANT, R., and HILBERT, D., 1962, "Methods of Mathematical Physics; Vol II, Partial Differential Equations," Interscience Publishers, New York, London, 1962.
- CRANK, J., and NICOLSON, P., 1947, "A Practical Method for Numerical Evaluation of Solutions of Partial Differential Equations of the Heat-Conduction Type," *Camb. Phil. Soc. Proc.* **43**, 50 (1947).
- DOUGLAS, J., JR., 1955, "On the Numerical Integration of $\partial^2 u / \partial x^2 + \partial^2 u / \partial y^2 = \partial u / \partial t$ by Implicit Methods," *J. Soc. Indust. Appl. Math.* **3**, 42 (1955).
- DOUGLAS, J., JR., and RACHFORD, H.H., JR., 1956, "On the Numerical Solution of Heat Conduction Problems in Two and Three Space Variables," *Trans. Amer. Math. Soc.* **82**, 421 (1956).
- DOUGLAS, J., JR., and DUPONT, T., 1971, "Alternating Direction Galerkin Methods on Rectangles," Symposium on Numerical Solution of Partial Differential Equations, Ed. B. Hubbard, Academic Press, N.Y., 1971.
- FLECK, J.A., JR., MORRIS, J.R., and FEIT, M.J., 1975, "Time-Dependent Propagation of High Energy Laser Beams Through the Atmosphere," Lawrence Livermore Laboratory Report UCRL-51826 (Draft), May 20, 1975.

- FORSYTHE, G.E., and WASOW, W.R., 1967, "Finite-Difference Methods for Partial Differential Equations," John Wiley and Sons, New York, London, Sydney.
- FRIED, D.L., 1974, "Absence of Thermal Blooming for a Uniformly Illuminated Square-Aperture High Power Laser Transmitter," *Appl. Opt.* 13, 989 (1974).
- GEBHARDT, F.G., and SMITH, D.C., 1971, "Self-Induced Thermal Distortion in the Near Field for a Laser Beam in a Moving Medium," *IEEE J. Quantum Electronics* QE-7, 63 (1971).
- GEBHARDT, F.G., and SMITH, D.C., 1972, "Effects of Diffraction on the Self-Induced Thermal Distortion of a Laser Beam in a Crosswind," *Appl. Opt.* 11, 244 (1972).
- GODUNOV, S.K., and RYABENKI, V.S., 1964, "Theory of Difference Schemes," North-Holland Publishing Company, Amsterdam.
- GREVILLE, T.N.E., 1969, "Theory and Applications of Spline Functions," Academic Press, New York and London, 1969.
- HARMUTH, H.F., 1957, "On the Solution of the Schroedinger and the Klein-Gordon Equations by Digital Computers," *J. of Math. and Phys.* 36, 269 (1957).
- HAYES, J.N., 1972, "Thermal Blooming of Laser Beams in Fluids," *Appl. Opt.* 11, 455 (1972).
- HAYES, J.N., ULRICH, P.B., and AITKEN, A.H., 1972, "Effects of the Atmosphere on the Propagation of 10.6 μ Laser Beams," *Appl. Opt.* 11, 257 (1972).
- HAYES, J.N., 1974, "Thermal Blooming of Rapidly Slew Laser Beams," *Appl. Opt.* 13, 2072 (1974).
- HERRMANN, J., and BRADLEY, L.C., 1971, "Numerical Calculation of Light Propagation," MIT Lincoln Laboratory Report LTP-10, 12 July 1971.
- HOGGE, C.B., 1971, Air Force Weapons Lab., Kirtland AFB, Albuquerque, N.M., Private Communication.
- HOGGE, C.B., 1975, "A Comparison of Several High Energy Laser Systems with Emphasis on the Propagation Aspects," Air Force Weapons Laboratory Report AFWL-TR-75-140, p. 46, May 1975.
- HOGGE, C.B., and BURLAKOFF, M., 1973, "Thermal Blooming of Nondiffraction Limited Beams," Air Force Weapons Laboratory Report AFWL-TR-73-77.
- HOGGE, C.B., BUTTS, R.R. and BURLAKOFF, M., 1974, "Characteristics of Phase - Aberrated Nondiffraction-Limited Laser Beams", *Appl. Opt.* 13, 1065 (1974)
- JACKSON, J.D., 1962, "Classical Electrodynamics," John Wiley and Sons, N.Y., London.
- KELLEY, P.L., 1965, "Self Focusing of Optical Beams," *Phys. Rev. Letters* 15, 1095, (1965).
- KENEMUTH, J.R., HOGGE, C.B., and BUTTS, R.R., 1970, "Thermal Blooming of a 10.6 μ Laser Beam in CO₂," *Appl. Phys. Lett.* 17, 220 (1970).
- KOGELNIK, H., and LI, T., 1966, "Laser Beams and Resonators," *Proc. IEEE* 54, 1312 (1966).
- LIVINGSTON, P.M., 1971, "Thermally Induced Modifications of a High Power CW Laser Beam," *Appl. Opt.* 10, 426 (1971).
- LUTOMIRSKI, R., 1974, Pacific-Sierra Research Corporation, 1456 Cloverfield Blvd., Santa Monica, California 90404, Private Communication.
- LYNCH, P.J., and BULLOCK, D.L., 1974, "An Integral-Equation Formulation of Thermal Blooming," to be published.
- O'NEIL, R.W., KLEIMAN, H., and LOWDER, J.E., 1974, "Observation of Hydrodynamic Effects on Thermal Blooming," *Appl. Phys. Lett.* 24, 118 (1974).
- ORTEGA, J.M., 1972, "Numerical Analysis," Academic Press, New York and London.
- PEACEMAN, D.W., and ROCHFORD, H.H., JR., 1955, "The Numerical Solution of Parabolic and Elliptic Differential Equations," *J. Soc. Indust. Appl. Math.* 3, 28 (1955).
- PHILLIPS, E.A., 1975, Avco-Everett Research Laboratory, Everett, Massachusetts 02149, Private Communication.
- RANGNEKAR, S.S., 1971, "Hydrodynamic Effects on the Laser Beam Propagation Through Gases," *Canad. J. of Phys.* 49, 1994 (1971).
- RICHTMYER, R.D., and MORTON, K.W., 1967, "Difference Methods for Initial-Value Problems," 2nd Edition, Interscience Publishers, New York, London, Sydney.
- ULRICH, P.B., 1971, "A Numerical Calculation of Thermal Blooming of Pulsed, Focused Laser Beams," Naval Research Laboratory Report 7382, December 30, 1971.
- ULRICH, P.B., 1972, "A Wave Optics Calculation of Pulsed Laser Propagation in Gases," Naval Research Laboratory Report 7413, June 7, 1972.
- ULRICH, P.B., HAYES, J.N., and AITKEN, A.H., 1972, "Comparison of a Wave-Optics Computer Model with Nonlinear Laser-Propagation Experiments," *J. Opt. Soc. Am.* 62, 298 (1972).
- ULRICH, P.B., and WALLACE, J., JR., 1973, "Propagation Characteristics of Collimated Pulsed Laser Beams Through an Absorbing Atmosphere," *J. Opt. Soc. Amer.* 63, 8 (1973).
- ULRICH, P.B., 1974, "PROP-I: An Efficient Implicit Algorithm for Calculating Nonlinear Scalar Wave Propagation in the Fresnel Approximation," Naval Research Laboratory Report 7706, May 29, 1974.
- ULRICH, P.B., HANCOCK, J.H., and HAYES, J.N., 1974, "Simultaneous Two-Wavelength CW Laser Propagation," *J. Opt. Soc. Amer.* 64, 549 (1974).
- ULRICH, P.B., HAYES, J.N., HANCOCK, J.H., and ULRICH, J.T., 1974, "Documentation of Prop-E, a Computer Program for the Propagation of High Power Laser Beams Through Absorbing Media," Naval Research Laboratory Report 7681, May 29, 1974.
- ULRICH, P.B., and ULRICH, J.T., 1975, "Computer Study of Thermal Blooming with Free and Forced Convection," to be published.
- VARGA, R.S., 1961, "On Higher Order Stable Implicit Methods for Solving Parabolic Partial Differential Equations," *J. of Math. and Phys.* 40, 220 (1961).

WALLACE, J., and CAMAC, M., 1970, "Effects of Absorption at 10.6μ on Laser Beam Transmission," *J. Opt. Soc. Am.* 60, 1587 (1970).

WALLACE, J., JR., and LILLY, J.Q., 1974, "Thermal Blooming of Repetitively Pulsed Laser Beams," *J. Opt. Soc. Am.* 64, 1651 (1974).

WALLACE, J., and PASCIAK, J., 1975, "Thermal Blooming of a Rapidly Moving Laser Beam," to be published.

WOLFE, W.L., 1965, "Handbook of Military Infrared Technology," U.S. Government Printing Office, Washington, D.C. 20402.

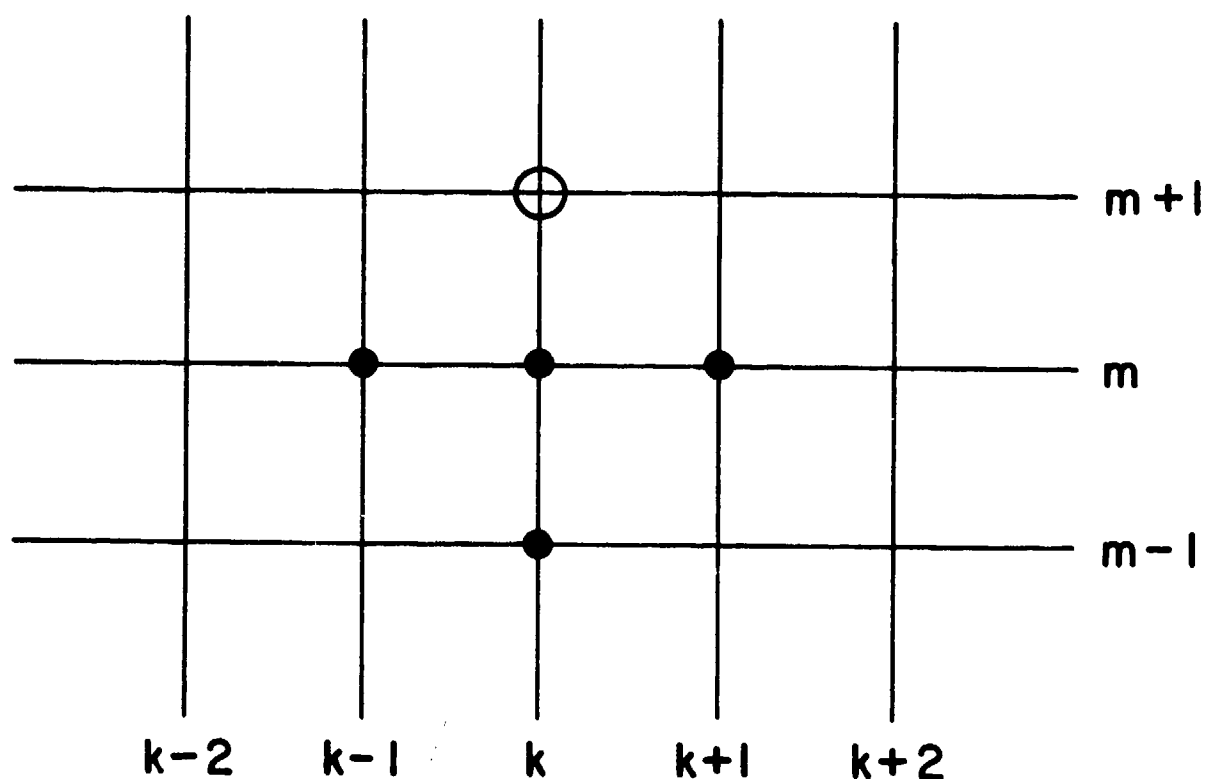


Fig. 1—A schematic representation of the computational mesh. The intersections are called nodes and are represented by a triple of numbers (k, ℓ, m) . The y - or ℓ -dimension is not shown in the figure for ease of presentation. This figure shows an explicit algorithm (cf. Eq. (17)) which has data at nodes on z -planes at m and $m-1$ contributing to the solution at the plane $m+1$. The contribution from nodes adjacent to (k, ℓ, m) is due to the use of a central-difference approximation to the second derivative in x . The y -dimension counterpart is similar.

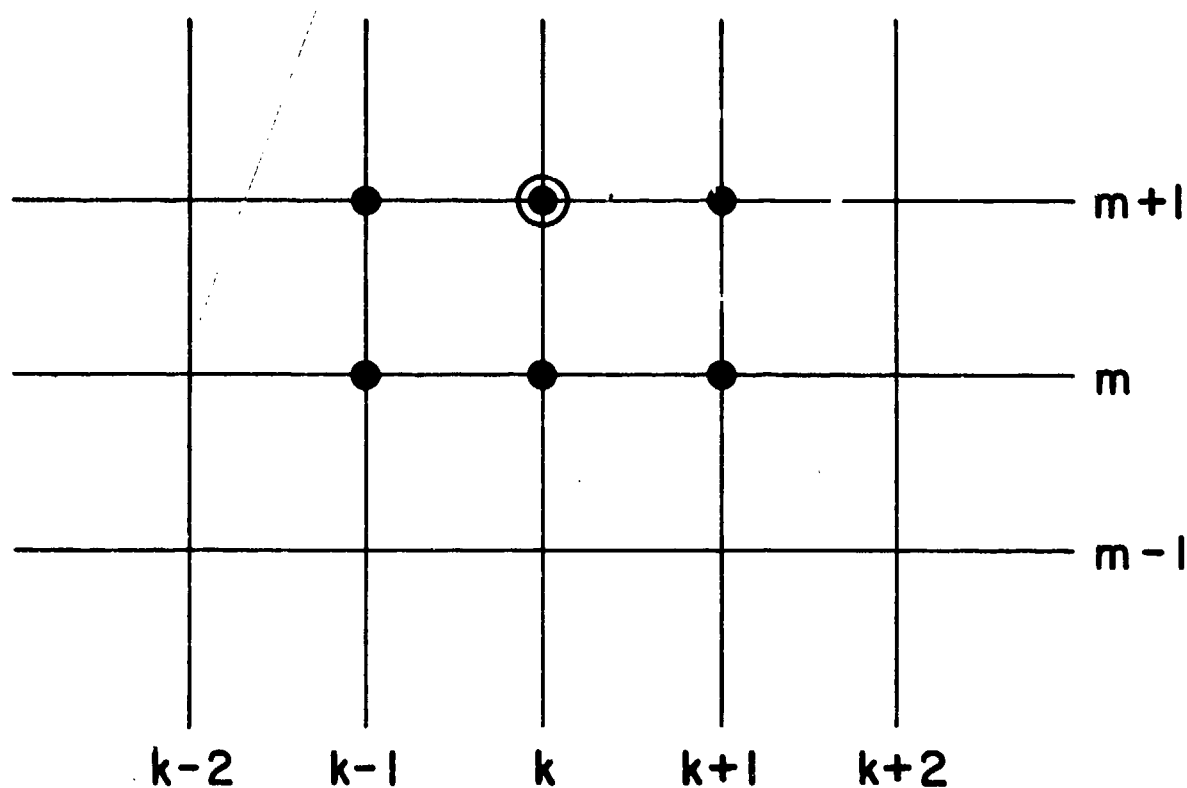


Fig. 2—Similar to Fig. 1 except that this represents schematically the Crank-Nicolson stable implicit method (cf. Eq. (19)). It requires knowledge of the dependent variable at the plane to which the solution is proceeding. Thus,

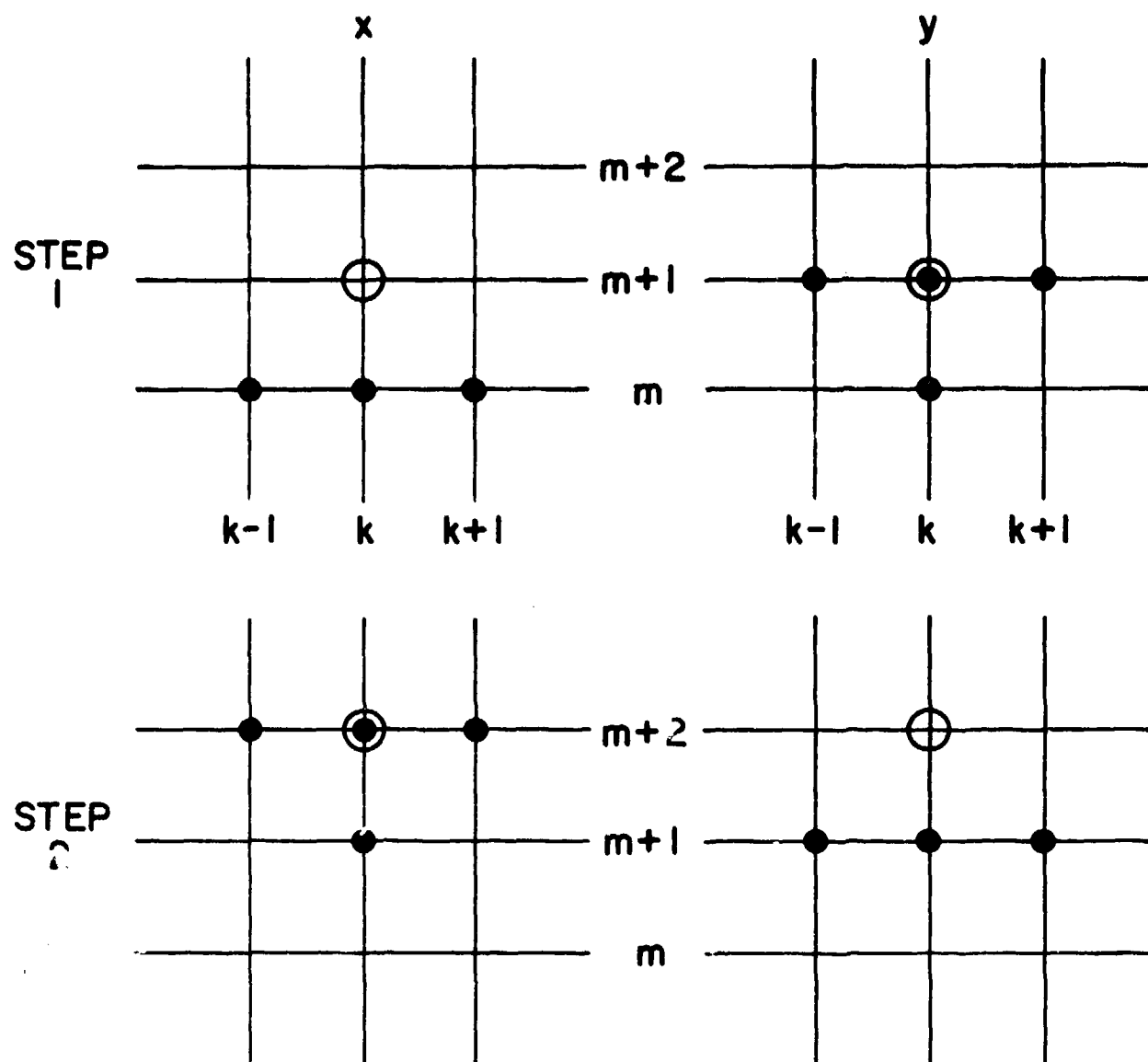
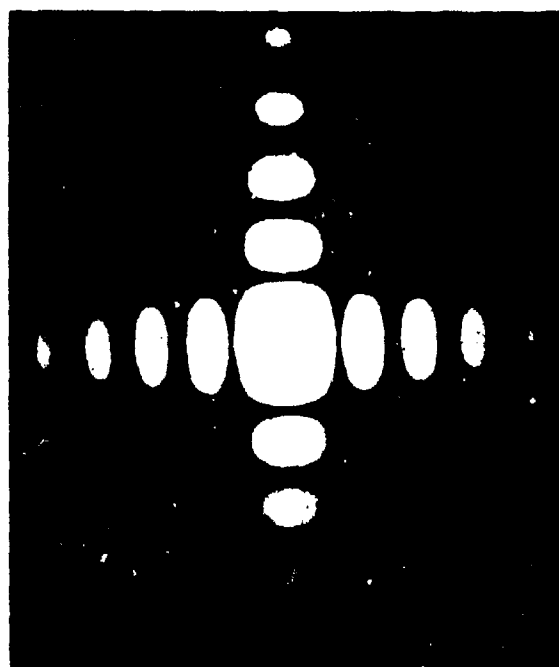
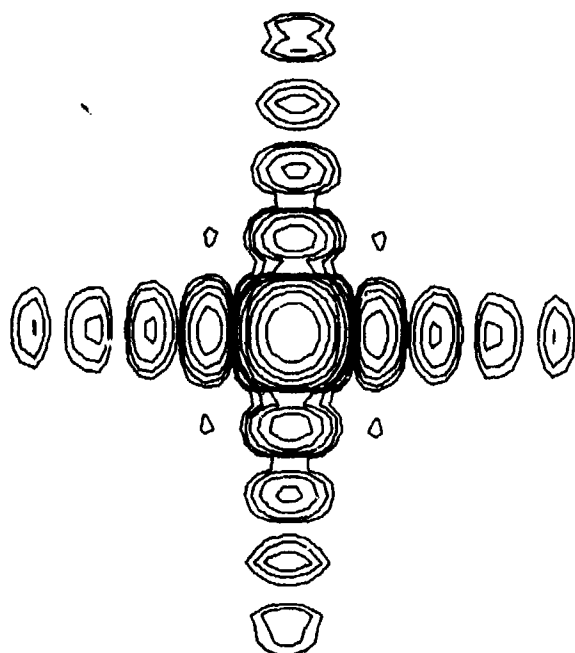
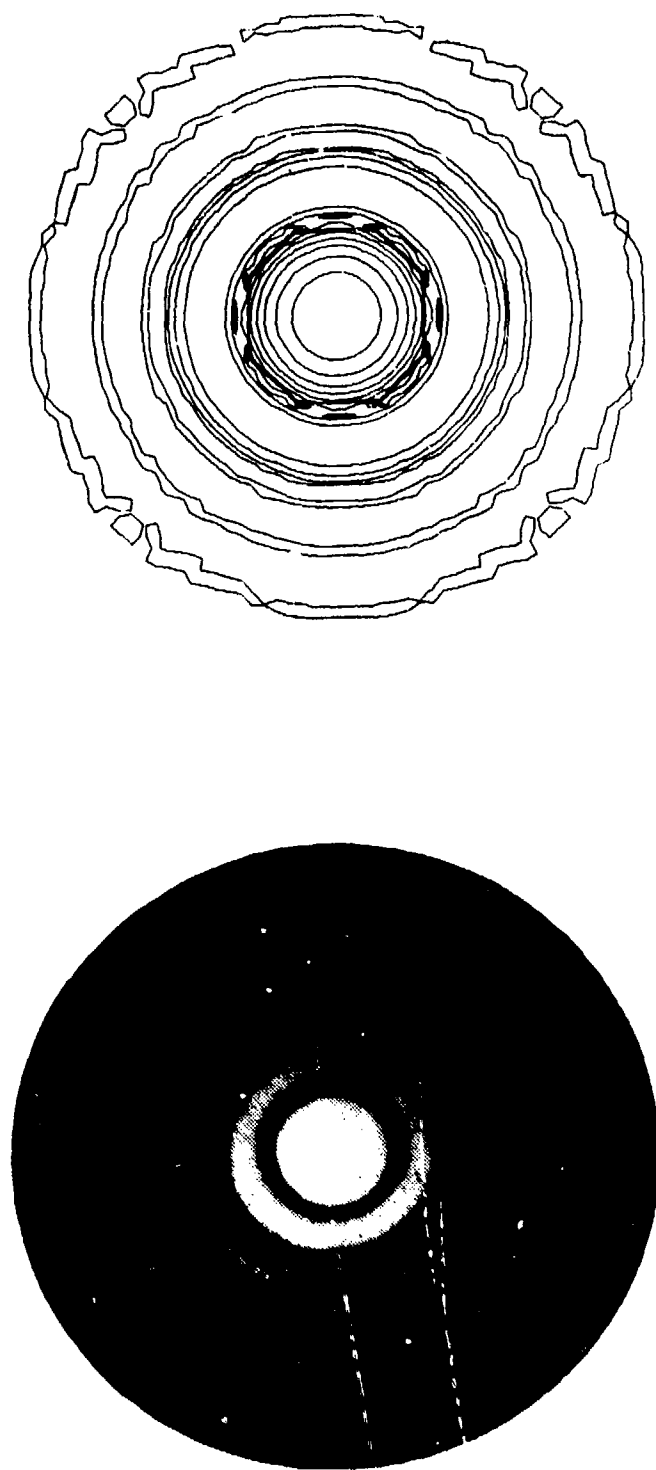


Fig. 3—Schematic of the alternating direction implicit method (ADI). The coordinate directions, x and y , alternate playing host to an implicit algorithm (cf. Eqs. (20) and (21)).



I/I_0	THEORY	COMPUTER
Center	1	1
1 st MAX.	.0496	.0491
2 nd MAX.	.0168	.0169
3 rd MAX.	.0083	.0091
4 th MAX.	.0050	.0073

Fig. 4—A computer calculation of the focal plane diffraction pattern of a uniformly illuminated rectangular aperture compared with an experimental photograph from "Principles of Optics" by M. Born and E. Wolf, Pergamon Press, 1970 (with kind permission of the publisher)



I/I_0	THEORY	COMPUTER
Center	1	1
1st MAX.	.0175	.0159
2nd MAX.	.0042	.0028
3rd MAX.	.0016	.0008

Fig. 5—A computer calculation of the focal plane diffraction pattern of an uniformly illuminated circular aperture compared with an experimental photograph from "Principles of Optics" by M. Born and E. Wolf, Pergamon Press, 1970 (with kind permission of the publisher)

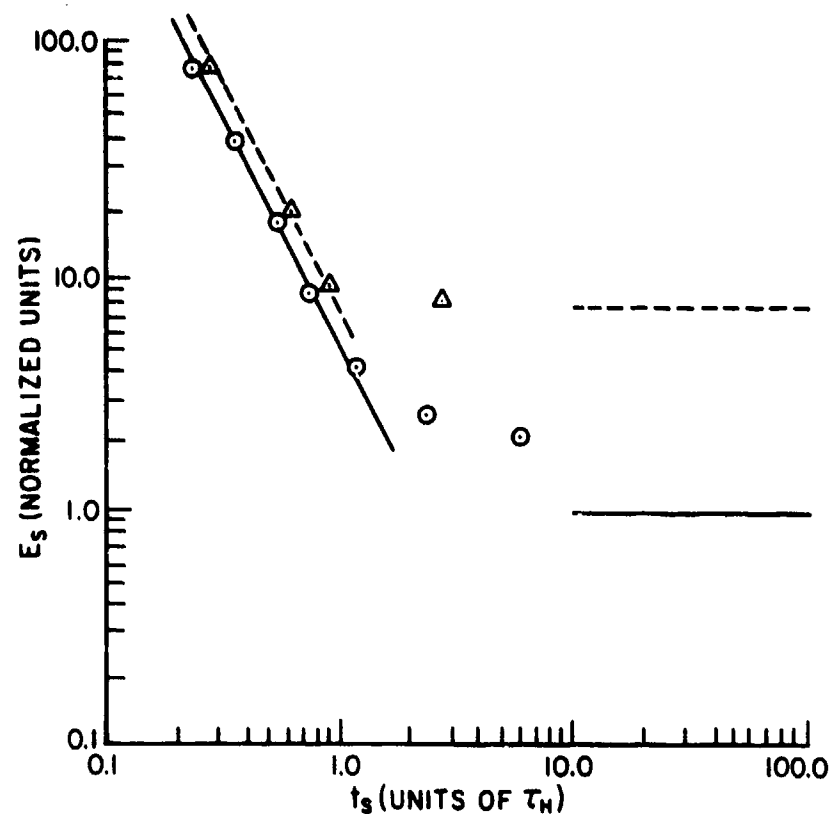


Fig. 6—Plot of pulse fluence vs t_s where t_s is the time for the central intensity of the beam to drop to zero due to thermal blooming. The solid black lines are an analytic calculation for CO₂ laser, the dashed lines are an analytic calculation for a DF laser. The circle and triangles are the corresponding cases calculated by full nonlinear computer codes. Both short pulse regime ($t_s < t_H, E_s \propto t_s^{-2}$) and long time regime ($t_s > t_H, E_s \propto t_s^0$) are shown.

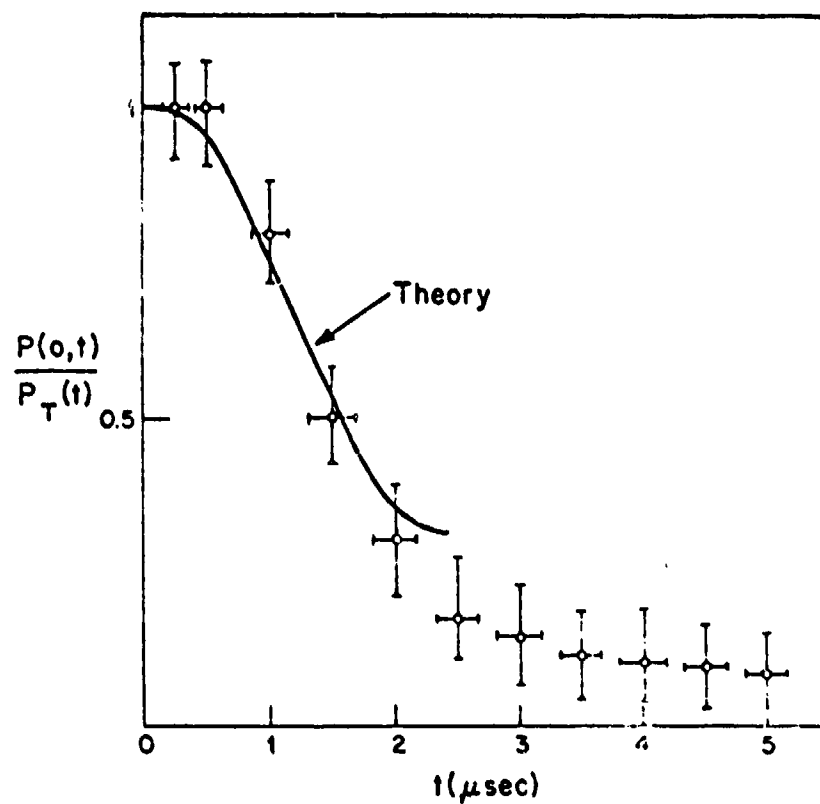


Fig. 7—The drop in power through a slit aperture due to blooming. The aperture was located over the peak of the focal distribution. The theoretical prediction for this case has been plotted for $t < 0.5t_H$.

STAGNATION ZONE STUDY

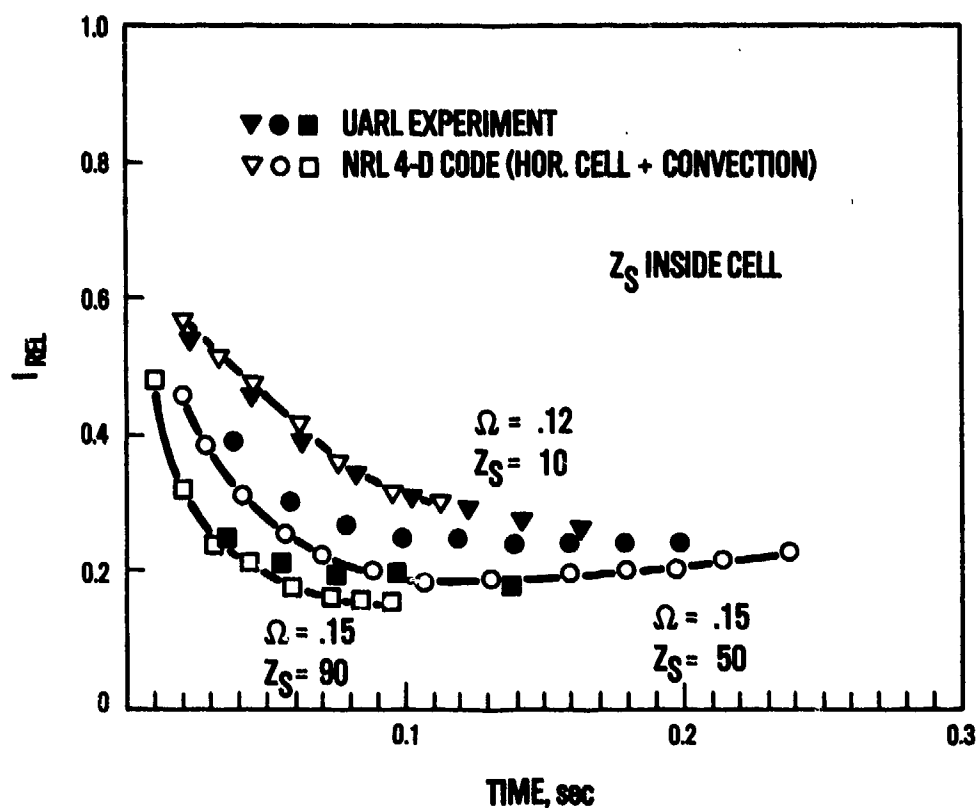


Fig. 8—Comparison of theory and experiment for CW propagation with a stagnation zone at position Z_s , between aperture and focal plane. The irradiance relative to the initial value is plotted vs time for three different combinations of slow rate and Z_s . The convection was included in the code work to achieve closer agreement with the experiment.

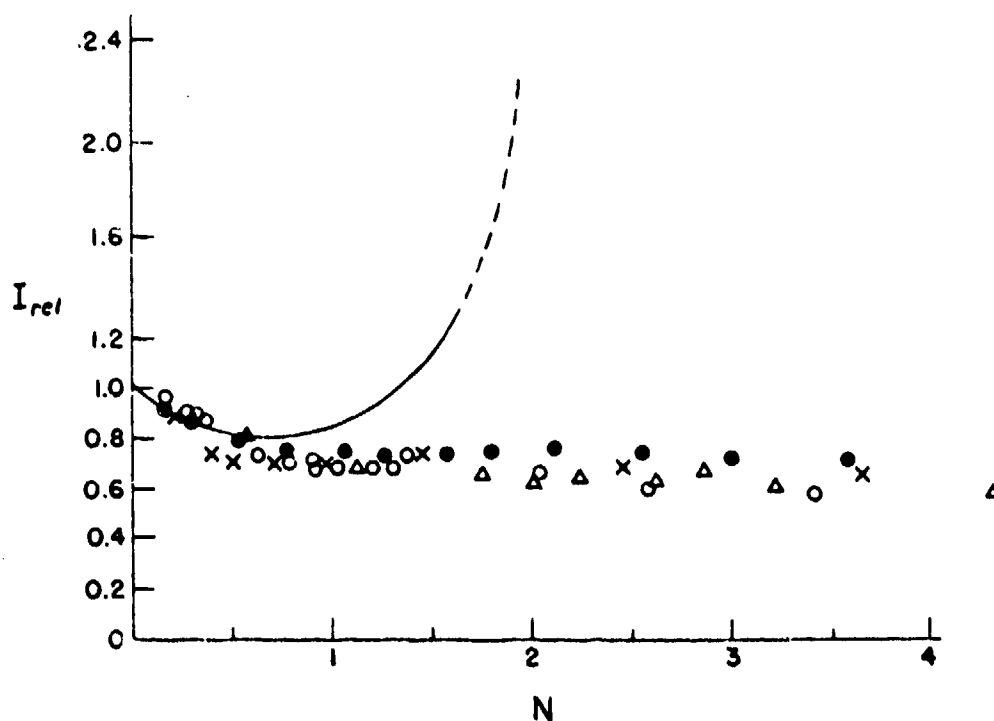


Fig. 9—Comparison of theory and experiment for a CW beam propagating in a steady wind. The irradiance relative to the vacuum value is plotted vs a distortion number which is proportional to beam power. The open circles, triangles and crosses are three different experiments. The black circles are the computer results. The solid line is a geometrical optics calculation.

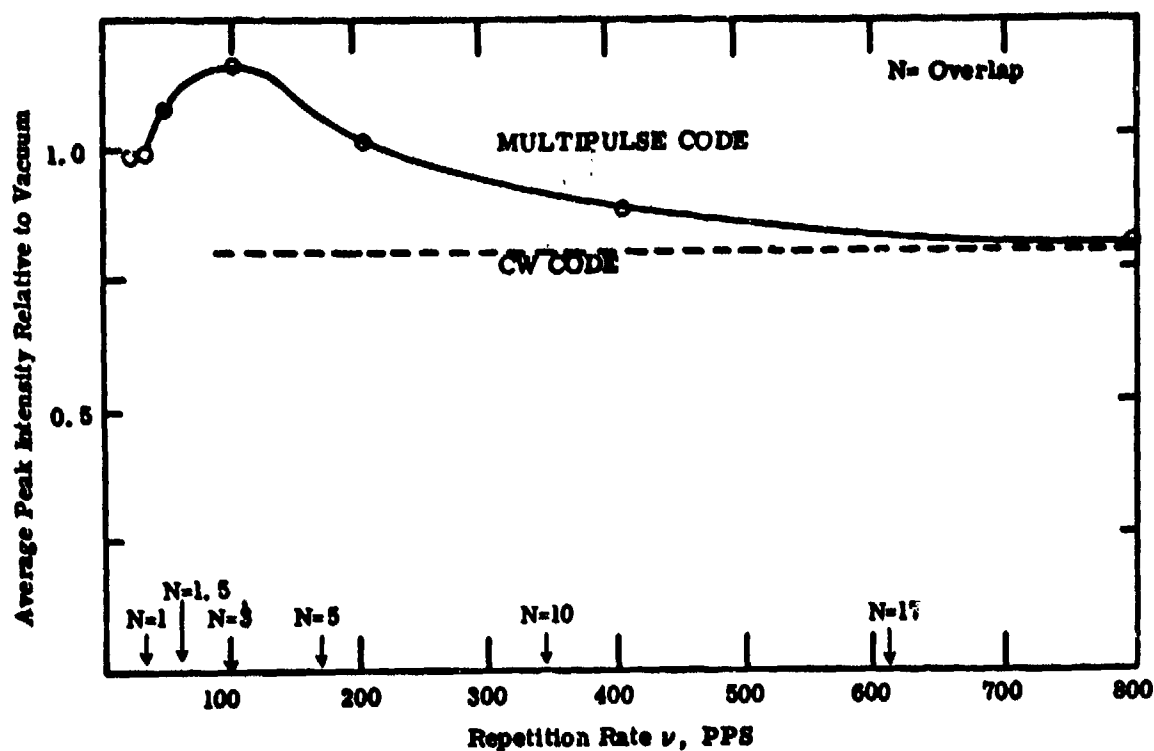


Fig. 10—Plot of average peak intensity relative to vacuum vs the repetition rate of a multiple pulse laser. At low PRF the beams are decoupled and vacuum propagation obtains. At high PRF the value approaches the CW result. At intermediate values the phenomenon of enhancement is seen as discussed in the text.

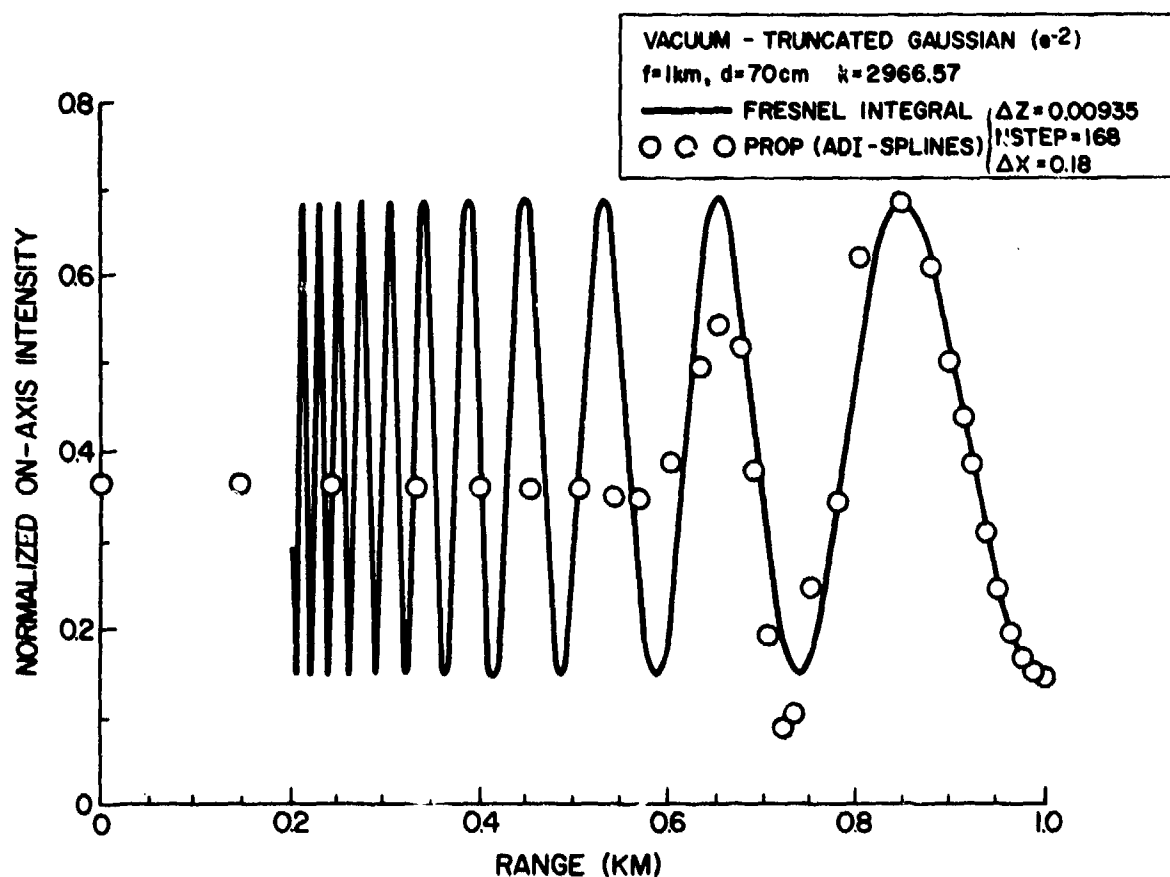


Fig. 11—Normalized on-axis intensity vs range for a truncated Gaussian beam. The solid line is the exact Fresnel integral result. The circles are values computed with an ADI algorithm using a Galerkin method with linear splines for the transverse discretization. Agreement is seen to grow poorer as one moves back towards the laser aperture from the focal plane.

THE LIMITATIONS IMPOSED BY ATMOSPHERIC BREAKDOWN ON THE
PROPAGATION OF HIGH POWER LASER BEAMS*

D. E. Lencioni
Massachusetts Institute of Technology
Lincoln Laboratory
P. O. Box 73
Lexington, Massachusetts 02173

ABSTRACT

This paper presents the results of a series of experiments on laser induced air breakdown at 10.6 and 1.06 μm . Threshold intensities for breakdown were determined for clean air, aerosols, and single particles. The clean air threshold was found to be in good agreement with microwave breakdown theory. The presence of aerosol particles was found to lower the threshold by an amount which depended mainly on particle size and laser pulse length. Only a slight material dependence was found with the one exception of water particles which had the least effect on threshold. The particle induced thresholds were found to scale as λ^{-2} for 100 nsec pulse lengths. The dynamics of the particle initiated thresholds were studied. For intensities slightly above threshold the plasma grew within the beam as an axisymmetric volume surrounding the particle. At higher intensities the plasma formed as a highly absorbing thin disk which grew radially and propagated back towards the laser.

1. INTRODUCTION

It has been established experimentally (Lencioni, D. E., et. al., 1971; Marquet, L. C., et. al., 1972; Lencioni, D. E., 1973; Lowder, J. E., and Kleiman, H., 1973; Schlier, R. E., et. al., 1973; Lencioni, D. E., and Lowder, J. E., 1974; Lencioni, D. E., 1974; Smith, D. C., and Brown, R. T., 1975; Boni, A. A., and Meskan, D. A., 1975) that the threshold for laser induced breakdown in air can be lowered substantially by the presence of microscopic dust particles. This fact has been used (Lencioni, D. E., 1973; Canavan, G. H. and Nielsen, P. E., 1973; Bunkin, F. V., and Savranskii, V. V., 1974) to explain discrepancies between theoretical predictions (Canavan, G. H., et. al., 1972; Kroll, N., and Watson, W. A., 1972) and early experimental results, (Smith, D. C., 1971) such as the observation that the threshold continues to decrease with increasing laser spot size even when electron diffusion is negligible. This paper describes the experimental work done at Lincoln Laboratory over the past several years which was directed towards understanding atmospheric breakdown and in particular, the effects of dust particles on the breakdown process.

2. AEROSOL AND CLEAN AIR EXPERIMENTS

An example of the phenomenon to be discussed is shown in Fig. 1. This is an open shutter photograph of breakdown in air containing a large concentration of carbon dust. The laser beam is incident from the left and brought to a focus just above the lens mount. As can be seen, several discrete breakdowns have occurred in the region of focus. Note also that particles within the beam have been heated to incandescence but did not trigger breakdowns. At higher intensities than in the case shown here, a string of discrete breakdowns is formed from near the focus and extends back towards the laser. These breakdowns are initiated by particles at intensities well below the clean air breakdown threshold. The same effects can occur under normal laboratory dust conditions especially for large beam sizes.

Detailed measurements were made of the breakdown threshold as a function focal spot size (Lencioni, D. E., 1973) in a chamber which provided a variable atmosphere from dusty to highly filtered clean air. The density and size distributions of aerosol particles were monitored with a light scattering particle counter (Royco Model 225) and a 256-channel pulse height analyzer (Northern Model NS-633). Particle diameters in the range 1 - 12 μm could be measured in this way.

Different focal spot sizes were obtained by using different focal length optics. Prior to each threshold measurement the beam profile was measured at focus. The laser power was monitored on each spot. The thresholds quoted here correspond to the peak intensity at focus for which breakdown occurred on 50% of the shots. The pulse lengths are the full width at half maximum. For highly filtered clean air (essentially no particles larger than 0.1 μm) the threshold was found to approach an asymptotic value at large spot sizes. The data for 10.6 μm , 125 nsec laser pulses are shown by the squares in Fig. 2. The solid curve in the figure is from the microwave breakdown theory of Kroll & Watson. The data agree quite well with the theory and show the effect of electron diffusion at small spot sizes.

When dust particles were present in the chamber, the threshold continued to decrease with increasing spot size to values well below the theoretical minimum for clean air. These data are also shown in Fig. 2. It was found that the threshold for any given spot size or aerosol condition was determined by the size of the largest particle present in the focal volume. The largest particle for each condition was determined from the measured particle distribution and focal volume. Three such measurements are indicated in Fig. 2.

The decrease in threshold with increasing spot size can be accounted for (Lencioni, D. E., 1973; Canavan, G. H., and Nielsen, P. E., 1973; Lencioni, D. E., 1974) from the fact that statistically the size of the largest particle in the focal volume is increased by either increasing the focal volume or dust

* This work is supported by the Advanced Research Projects Agency of the Department of Defense.

concentration. This hypothesis was verified by single particle experiments, which will be described below, in which one particle of known size was placed in the focal volume of the beam. It was found that, for a given particle size, the threshold was independent of spot size and depended only on particle size.

Thresholds were obtained for a variety of dust particle materials and sizes. These data are summarized in Fig. 3 for 10.6 μm - 125 nsec laser pulses. It can be seen that particles with diameters less than $\approx .5 \mu\text{m}$ did not significantly lower the threshold below the clean air value ($3 \times 10^9 \text{ W/cm}^2$). Also, with the exception of H_2O particles, there is only a slight material dependence if any. Note that these data include materials which are optically thin at 10.6 μm (NaCl , Ge).

Similar measurements were made with 1.06 μm , 100 nsec laser pulses (Lencioni, D. E., 1974). The threshold in clean air was found to scale very closely as λ^{-2} with an asymptotic value at large spots $\approx 3 \times 10^{14} \text{ W/cm}^2$. This indicates that cascade ionization is a dominant breakdown mechanism, even at 1.06 μm . The thresholds for particle initiated breakdowns were measured as in the 10.6 μm case. Here also it was found that the threshold lowering was greater for larger size particles. These data are shown in Fig. 4 for a carbon aerosol. The data points show the threshold for three particle sizes. The dashed curve shows 10^2 times the corresponding 10.6 μm results. A comparison of the 1.06 and 10.6 μm data give an approximate λ^{-2} scaling for particle initiated breakdowns for pulse lengths 100 - 125 nsec.

The thresholds for particle initiated breakdowns were also found to depend on laser pulse length (Lowder, J. E., Kleiman, H., 1973; Lencioni, D. E., 1972; Schlier, R. E., et. al., 1973). Data taken with 10.6 μm lasers having different pulse lengths are summarized in Fig. 5. This figure shows the threshold for 10.6 μm laser beams in air as a function of pulse length and particle size. The curves are an empirical correlation of the data according to particle size. As was mentioned above the thresholds are fairly insensitive to particle material with the exception of distilled H_2O for which the correlation shown in this figure would not apply. The solid circles are for glass fibers, (Lencioni, D. E., 1973; Lowder, J. E., and Kleiman, H., 1973) which behave as very large particles. As can be seen, for long pulse lengths and large particles the threshold can be reduced to $\approx 10^{-3}$, the clean air value.

It is not clear whether a similar correlation can be made for the 1.06 μm data. The measurements at 100 nsec do scale approximately as λ^{-2} ; however, the wavelength scaling at longer pulse lengths has not yet been determined.

3. SINGLE PARTICLE EXPERIMENTS

The details of the laser particle interaction were investigated (Lencioni, D. E., Pettingill, L. C., 1972) using the experimental setup shown in Fig. 6. The beam from a 5J per pulse Febertson CO_2 laser was focused with spherical mirrors. Three focal spot sizes were used with e^{-1} diameters: 4, 1 and 0.55 mm. A 50 μm carbon particle was dropped into the focal volume from an activated dispenser through a hypodermic needle. When the particle was at a preselected position in the beam, HeNe laser light was scattered through the microscope system into a photomultiplier tube and initiated the experimental triggering sequence. The position of the particle was observed from a back lighted micrograph obtained by firing the nanolight. With this technique particles could be positioned consistently to within $\pm 25 \mu\text{m}$.

An image converter camera, with exposure times down to 10 nsec, was used to obtain time resolved information on the growth of the breakdown in the beam. The transmitted beam was re-imaged and magnified at a pair of photon drag detectors to obtain the radial and temporal dependence of the transmitted beam.

Figure 7 shows a back lighted micrograph of a 50 μm carbon particle taken 6 μsec after being hit by the laser beam incident from the left. This shows what happens to a particle at below threshold intensity. The laser beam heats one side of the particle to incandescence. The resulting vaporization causes the particle to jet (Lencioni, D. E., and Lowder, J. E., 1974). From the measured velocity it was determined that the particle motion during the pulse was $\approx 1 \mu\text{m}$ which had negligible effect on the threshold measurements. The breakdown threshold was determined at three spot sizes for a given size particle in the beam. The results are shown in Fig. 8 for 50 μm carbon particles and 10.6 μm , 150 nsec laser pulses. As can be seen the threshold is independent of spot size.

The breakdown was observed to start at the position of the particle and grow to fill the beam at a finite rate. Figure 9 shows a series of image converter frames which illustrate the growth of a breakdown at near threshold intensity. The two intensities listed at the top of the figure denote the average and peak intensities during the frame sequence. The dashed white lines mark the e^{-1} diameter of the beam which was 1 mm. The laser is incident from the left. The four frames were taken on separate shots at the indicated exposure times relative to the start of the pulse. The breakdown initiates at near the peak laser intensity and grows radially and axially as a volume absorbing plasma. Measurements of the transmitted intensity indicated an absorption depth of $\approx .5 \text{ mm}$.

At higher laser intensities the character of the breakdown growth changed abruptly. This is shown in Fig. 10 where the intensity was a factor of ~ 5 above threshold. In these frames the white dot indicates the position of the particle. Note that at this higher intensity the breakdown develops as a thin absorbing disk which propagates back towards the laser and grows radially. This is a characteristic of the laser supported detonation (LSD) wave described by Raizer (Raizer, Y. P., 1965). The measurements of transmission for this case showed that no radiation was transmitted through the thin plasma disk.

The radial and axial velocities obtained from data of this type are shown in Fig. 11 as a function of intensity. At lower intensities the velocities increase rapidly with intensity. At higher intensities the axial velocity varies roughly as $I^{1/3}$ in agreement with planar LSD wave theory.

4. CONCLUSIONS

The primary conclusions to be drawn from this work are:

1. Laser induced breakdown thresholds in clean air are in good agreement with microwave breakdown theory for wavelengths down to $\approx 1 \mu\text{m}$.
2. Dust particles within the beam can lower the threshold substantially below the clean air value.
3. The threshold lowering is fairly insensitive to the particle materials studied with the exception of distilled H_2O which has the least effect.
4. The threshold decreases with increasing particle size.
5. For $10.6 \mu\text{m}$ the threshold decreases with increasing pulse length for large particles.
6. For pulse lengths $\approx 100 \text{ nsec}$ the particle induced threshold scales as λ^{-2} . The scaling for longer pulse lengths has not been established.
7. At near threshold intensities the plasma grows within the beam as an axisymmetric volume surrounding the particle and at higher intensities it grows as a radially expanding LSD wave.

The implications of these results for atmospheric propagation of high power laser beams are two-fold. First, normal atmospheric dust conditions can reduce the threshold to well below the clean air limit. The exact reduction will depend primarily on the distribution of particle sizes within the beam and the laser pulse length. Secondly, the finite radial growth rate of the particle initiated breakdowns allows the propagation of energy up to some cutoff time. It is easy to show that the beam attenuation is dominated by breakdowns within the depth of focus. The cutoff time is then

$$\tau_c = [L N(I) \pi v_r^2 (I)]^{-1/2} \quad (30-1)$$

where L is the depth of focus, n is the density of particles which ignite breakdowns at intensity I and v_r is the radial growth rate at intensity I . As an example consider the propagation of a $10.6 \mu\text{m}$ beam with a 10 m depth of focus at intensity 10^8 W/cm^2 . From Figs. 5 and 11 particles larger than $6 \mu\text{m}$ will ignite breakdowns at this intensity which grow at $4 \times 10^5 \text{ cm/sec}$. If the distribution of aerosol particles is taken to be $dn/dD = 10^{-11} D^{-4} (\text{cm}^{-4})$ then $\tau_c = 360 \text{ nsec}$. For pulse lengths much shorter than this there will be little effect on the transmitted energy because the breakdowns have not had time to grow.

ACKNOWLEDGMENTS

The author would like to thank Dr. Seymour Edelberg for his interest and helpful suggestions throughout the period this work was done and L. C. Pettingill, and D. P. DeGloria for their technical assistance.

REFERENCES

- Boni, A. A., Maskan, D. A., 1975, "Effect of Impurities on Laser-Induced Air Breakdown at $1.06 \mu\text{m}$ ", Opt. Commun., Vol. 14, p. 115.
- Bunkin, F. V., Savranskii, V. V., 1974, "Optical Breakdown of Gases Induced by the Thermal Explosion of Suspended Microscopic Particles", Sov. Phys. JETP, Vol. 38, p. 1091.
- Canavan, G. H., Nielsen, P. E., 1973, "Focal Spot Size Dependence of Gas Breakdown Induced by Particulate Ionization", Appl. Phys. Lett. 22, p. 409.
- Canavan, G. H., Proctor, W. A., Nielsen, P. E., Rockwood, S. D., 1972, " CO_2 Laser Air Breakdown Calculations", IEEE J. Quantum Electron, QE-8, p. 564.
- Kroll, N., Watson, K. M., 1972, "Theoretical Studies of Ionization of Air by Intense Laser Pulses", Phys. Rev. A5, p. 1883.
- Lencioni, D. E., 1973, "The Effect of Dust on $10.6 \mu\text{m}$ Laser-Induced Air Breakdown", 1973, Appl. Phys. Lett., Vol. 23, p. 12.
- Lencioni, D. E., 1974, "Laser-Induced Air Breakdown for $1.06 \mu\text{m}$ Radiation", Appl. Phys. Lett., Vol. 25, p. 15.
- Lencioni, D. E., 1972, "Characterization of Breakdown Data", Lincoln Laboratory, Optics Research Report, No. 2.
- Lencioni, D. E., Hull, R., Marquet, L., 1971, " CO_2 Laser Induced Air Breakdown", Bull. Am. Phys. Soc. 16, p. 1292.
- Lencioni, D. E., Lowder, J. E., 1974, "Aerosol Clearing with a $10.6 \mu\text{m}$ Precursor Pulse", IEEE J. Quantum Electron., Vol. QE-10.
- Lencioni, D. E., Pettingill, L. C., 1974, 1973, "The Dynamics of Particle Induced Air Breakdown", Bull. Am. Phys. Soc. 19, p. 163, also in Lincoln Laboratory, Optics Research Report, No. 2.
- Lowder, J. E., Kleiman, H., 1973, "Long-Pulse Breakdown with $10.6 \mu\text{m}$ Laser Radiation", J. Appl. Physics, p. 44.
- Marquet, L. C., Hull, R. J., Lencioni, D. E., June 1972, "Studies of Breakdown in Air Induced by a Pulsed CO_2 Laser", IEEE J. Quantum Electron (Dig. Tech. Papers, 1972 Int. Quantum Electron Conf.), Vol. QE-8, p. 564.
- Schlier, R. E., Pirri, A. N., Raily, D. J., 1973, AVCO/Everett Research Lab., unpublished studies.
- Smith, D. C., 1971, "Gas-Breakdown Dependence on Beam Size and Pulse Duration with $10.6 \mu\text{m}$ wavelength Radiation", Appl. Phys. Lett., Vol. 19, p. 405.
- Smith, D. C., Brown, R. T., 1975, "Aerosol-Induced Air Breakdown with CO_2 Laser Radiation", J. Appl. Phys., Vol. 46, p. 1146.
- Raizer, Y. P., 1965, "Heating of a Gas by a Powerful Light Pulse", Sov. Phys. - JETP, Vol. 21, p. 1909.

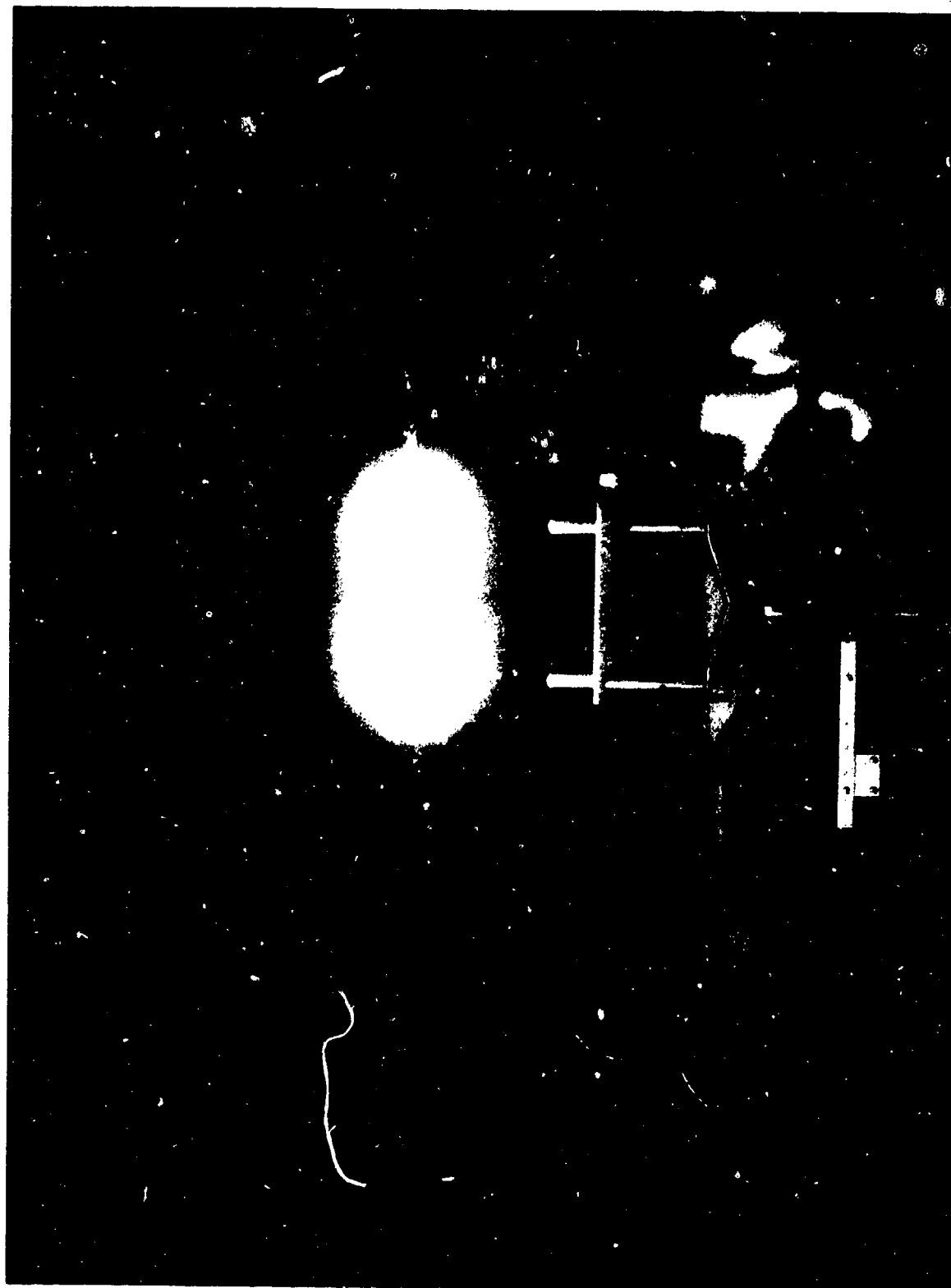


Fig.1 Example of laser induced breakdown in carbon aerosol for $10.6\ \mu\text{m}$, 125 nsec pulse. Several breakdowns are triggered by particles within the focal volume at intensities well below the clean air value

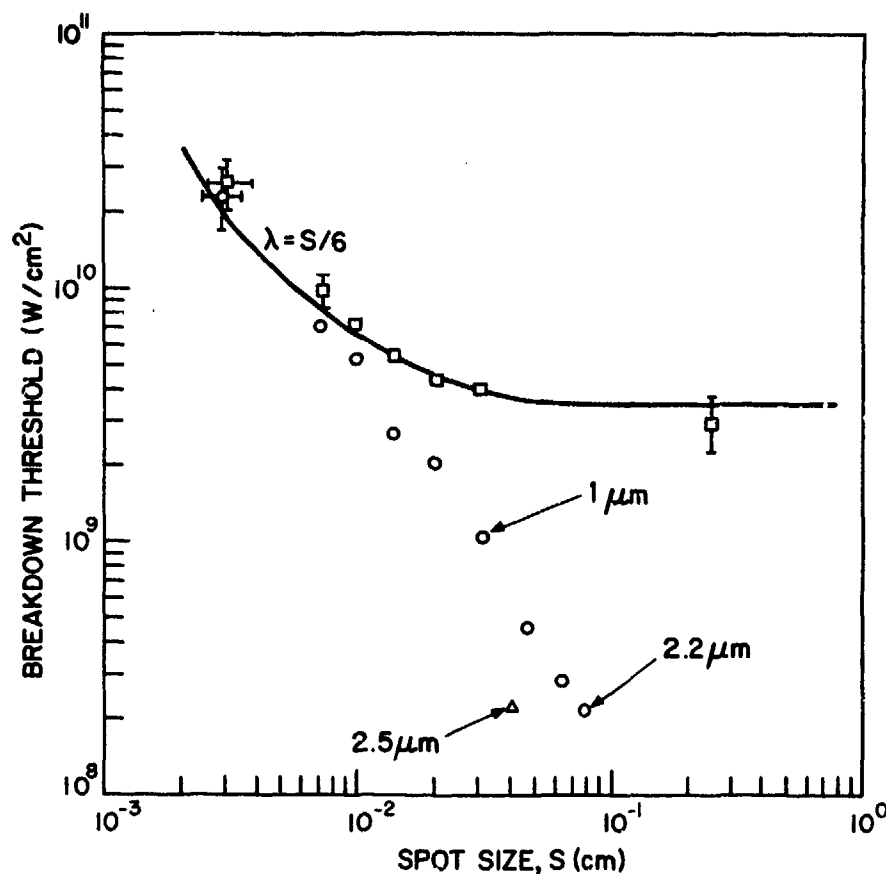


Fig.2 Breakdown threshold versus spot size for 10.6 μm , 125 nsec laser pulses in clean air (squares) and two conditions of carbon dust (circles and triangles). The largest particle present in the focal volume is indicated for three points. The solid theory curve is from Kroll and Watson

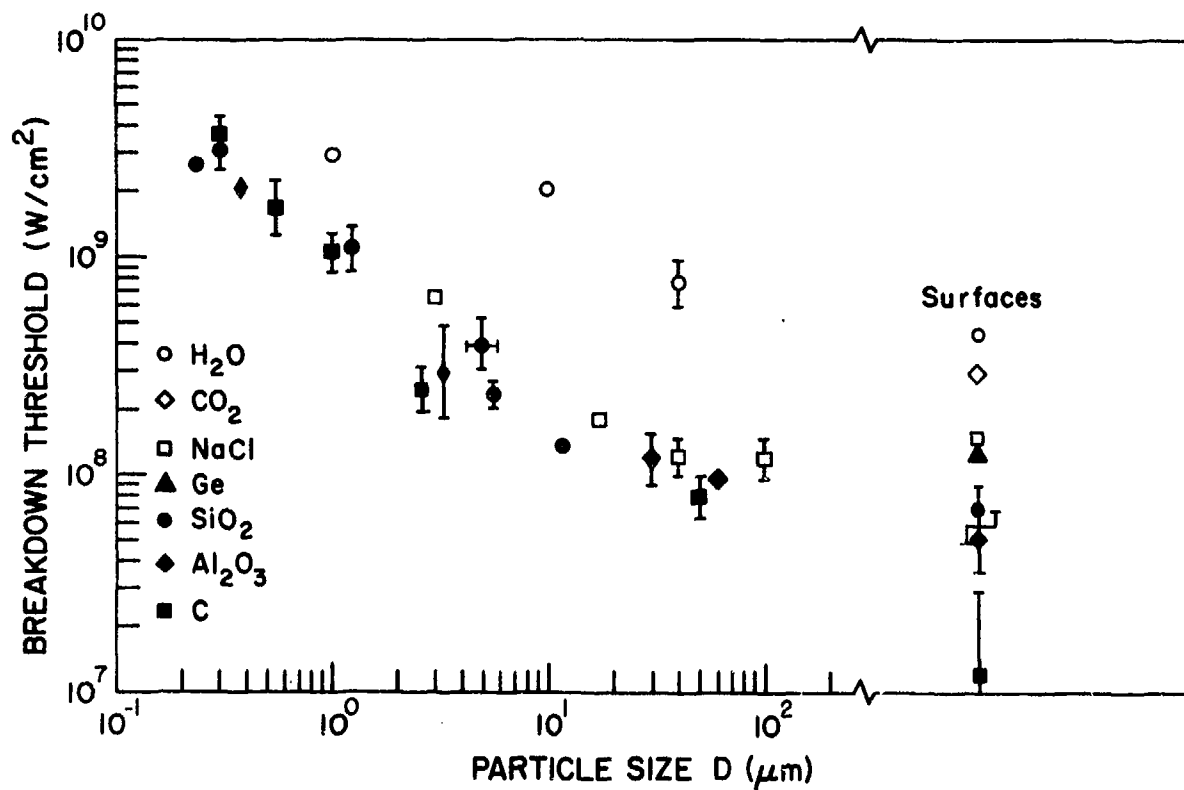


Fig.3 Breakdown thresholds versus particle size for various materials with 10.6 μm , 125 nsec pulses

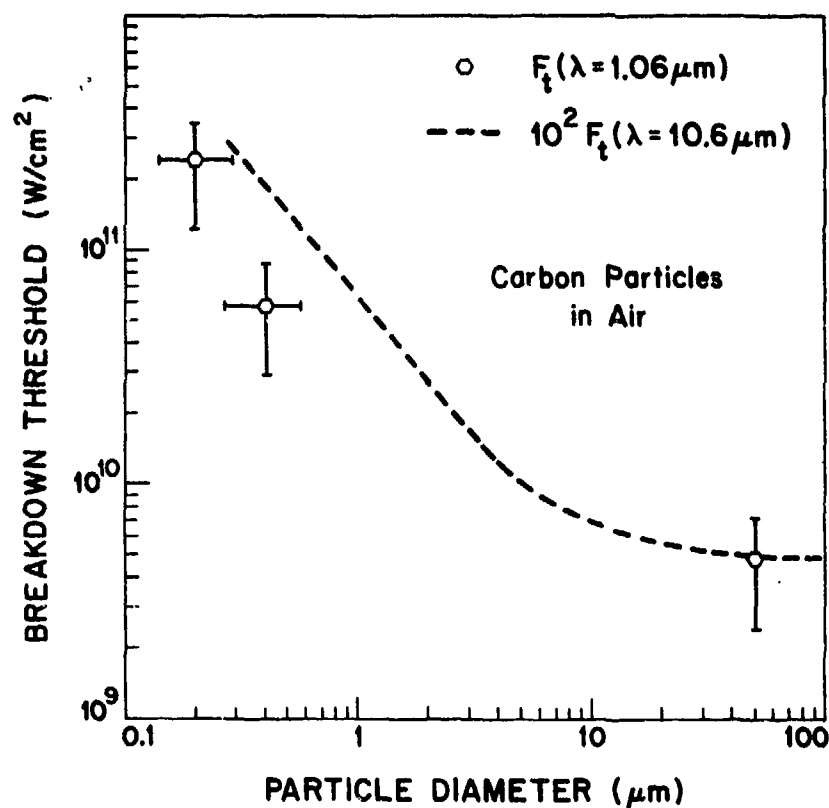


Fig.4 Threshold in carbon aerosol as a function of particle size for 1.06 μm , 100 nsec laser pulses. Dashed curve is 10^2 times threshold for 10.6 μm lasers

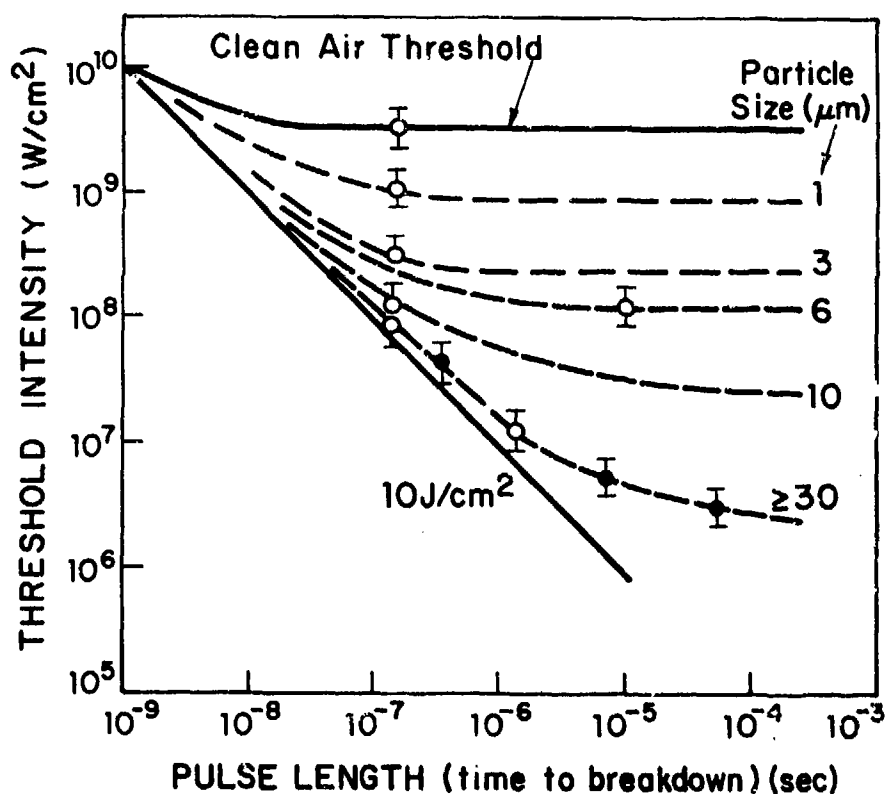


Fig.5 Particle induced breakdown thresholds for 10.6 μm laser pulses in air as a function of pulse time and particle size. The curves are an empirical correlation of the data according to particle size. The experimental thresholds are fairly insensitive to particle material with the exception of distilled H_2O which was found to have a higher threshold. Solid circles are for glass fibers

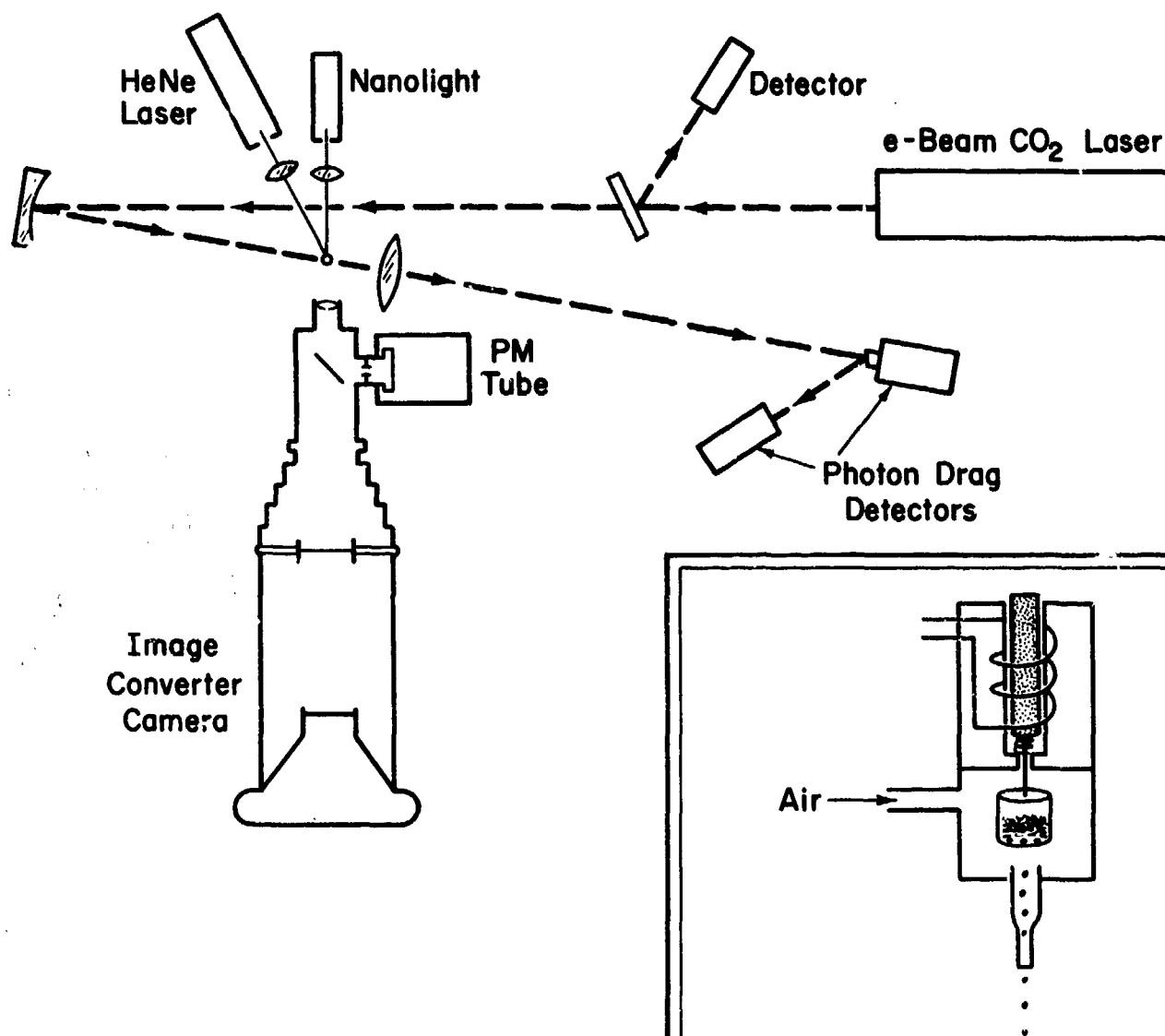


Fig.6 Experimental apparatus used to study breakdown dynamics. Time resolved information on the growth dynamics was obtained with the image converter camera. Particles were placed at a spot in the focal volume with the activated particle dropper shown in the insert



Fig.7 Back lighted micrograph of a $50\text{ }\mu\text{m}$ carbon particle taken $6\text{ }\mu\text{sec}$ after being hit by a laser pulse incident from the left

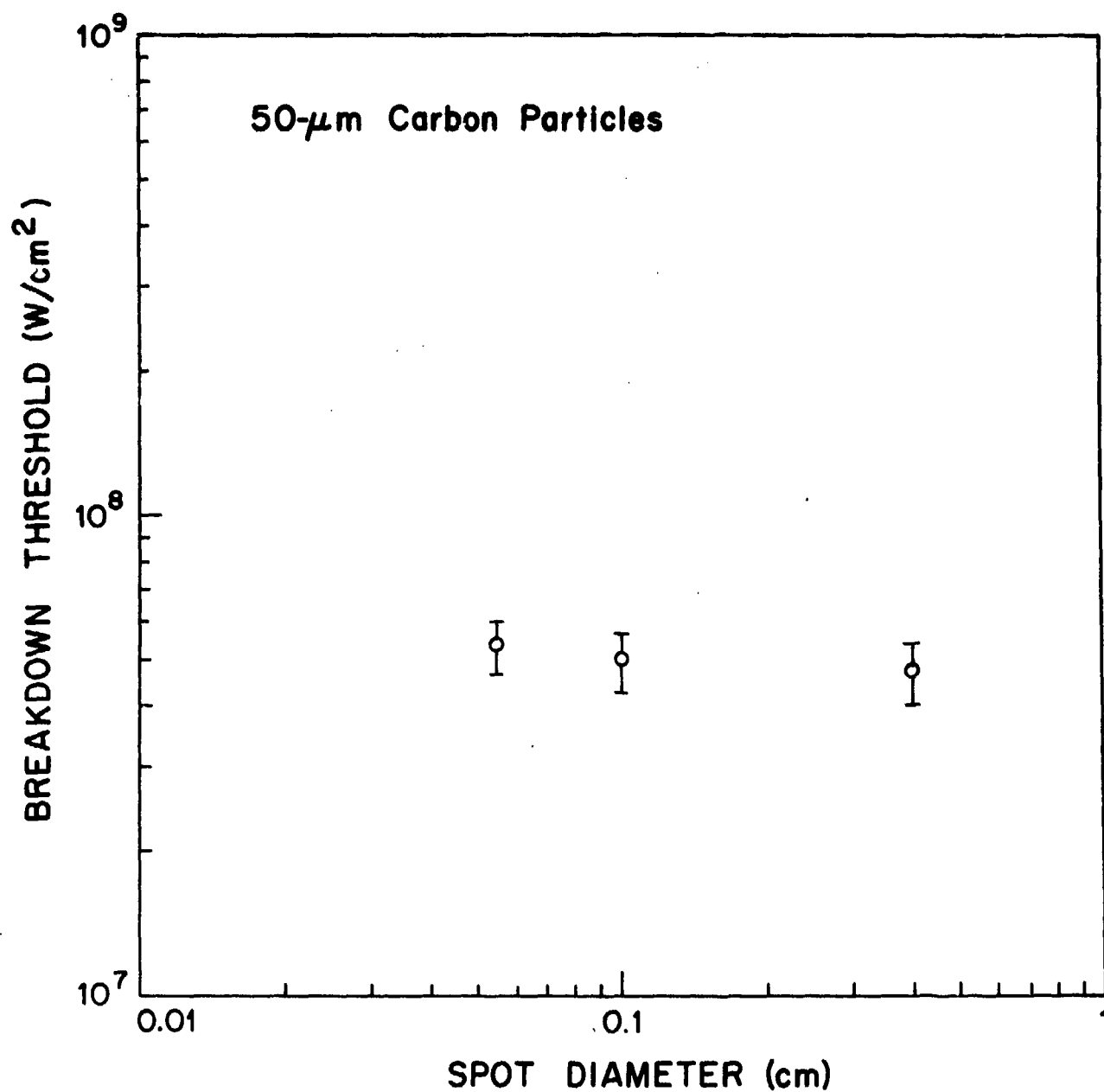


Fig.8 Breakdown threshold for 50 μ m carbon particles as a function of laser spot size for 10.6 μ m, 150 nsec laser pulses

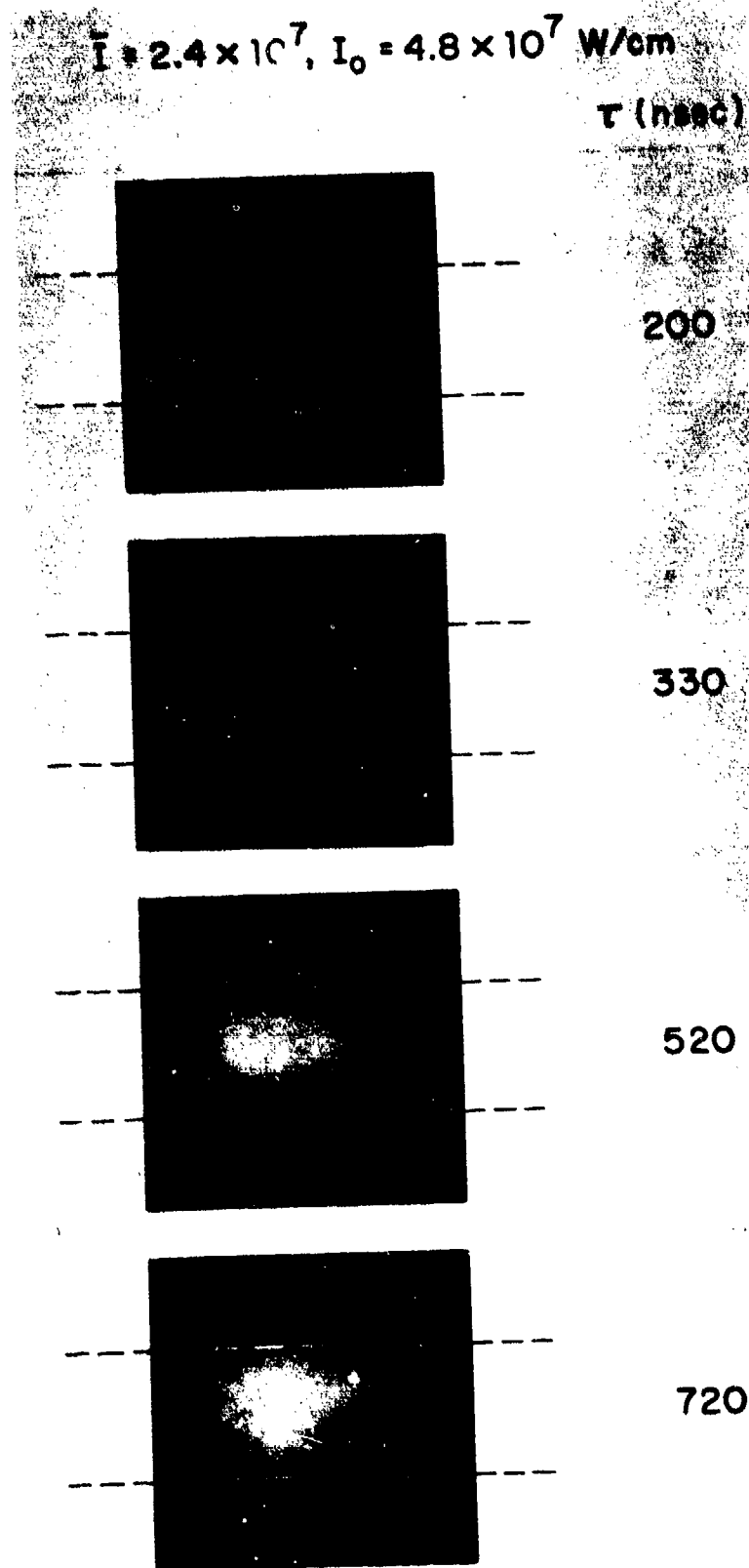


Fig.9 Series of image converter frames illustrating breakdown growth at near-threshold intensity. Dashed lines show e^{-1} diameter of the laser beam which was incident from the left

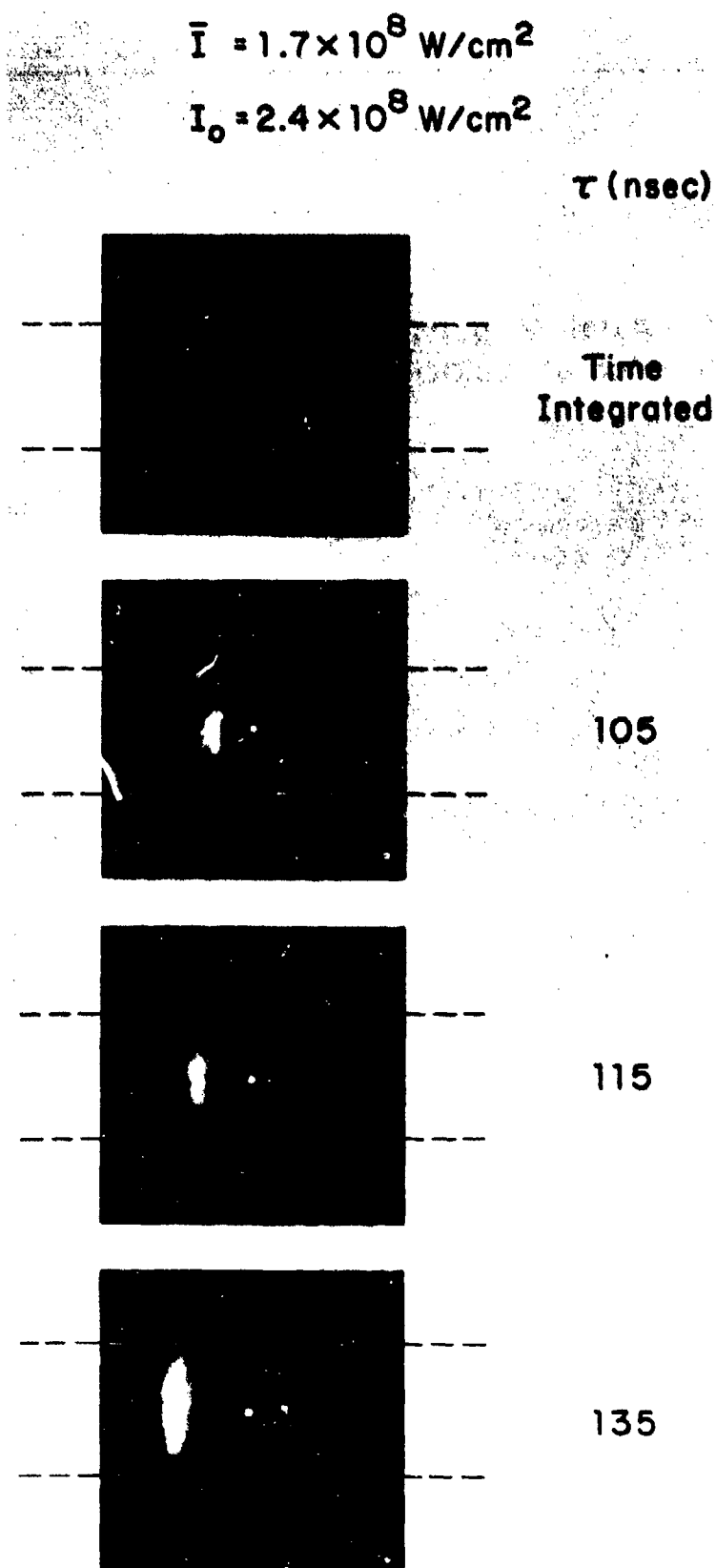


Fig.10 Breakdown dynamics at five times threshold intensity

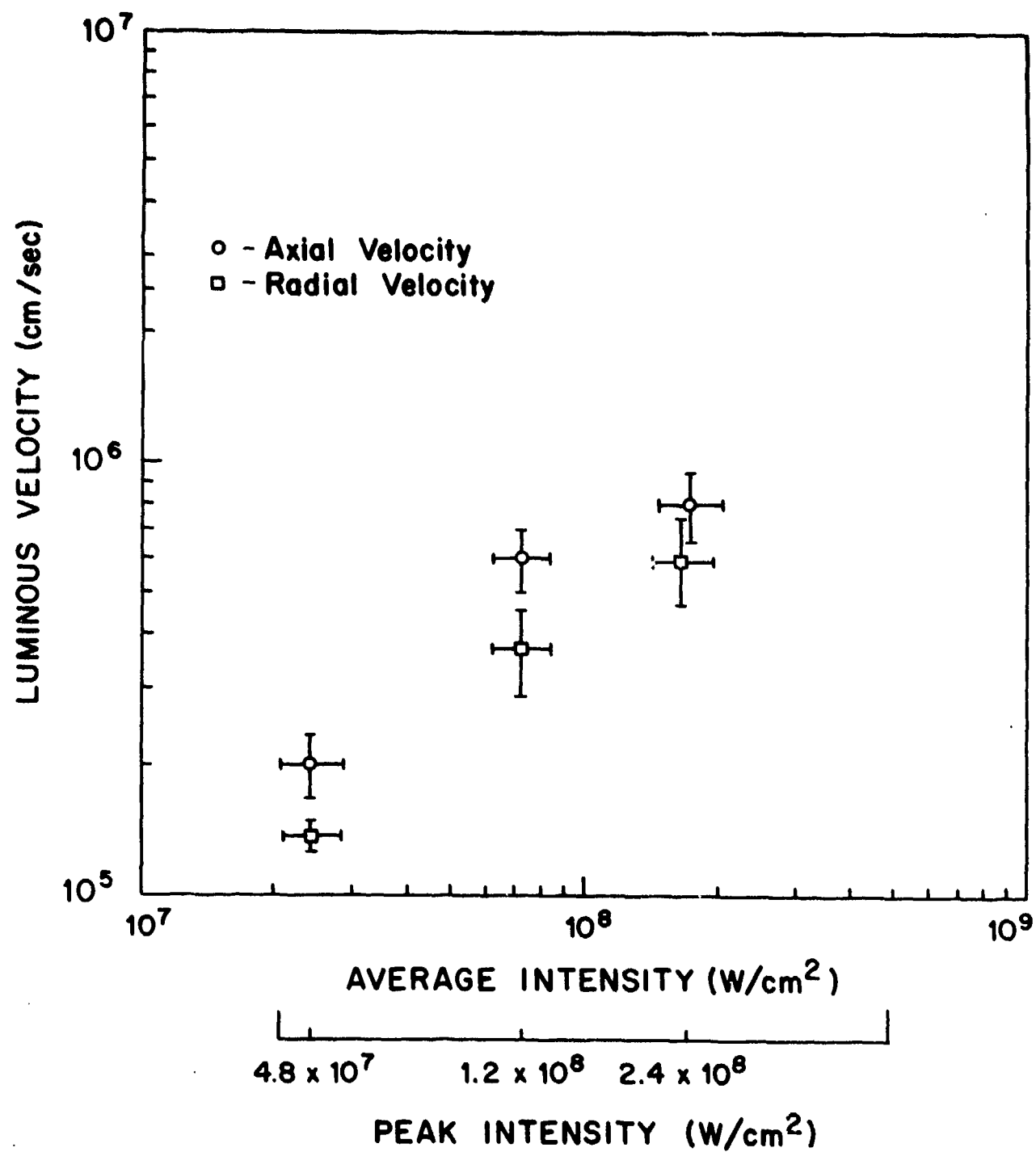


Fig.11 Axial and radial velocities of particle initiated breakdown within the beam

EXPERIMENTAL DETERMINATION OF SINGLE AND MULTIPLE PULSE PROPAGATION*

By

R. W. O'Neil, H. Kleiman, and H. R. Zwicker
Massachusetts Institute of Technology
Lincoln Laboratory
P. O. Box 73
Lexington, Massachusetts 02173

ABSTRACT

In this paper thermal blooming of focused single and multiple pulse lasers is considered. Experimental procedures are described to characterize the reduction in far field irradiance observed for pulses whose duration is comparable to and shorter than τ_H , an acoustic transit time across a focal radius. Experimental measurements of short pulse blooming ($t < \tau_H$) are compared with a scalar wave theoretical computer model embodying the medium hydrodynamics. Agreement with the short pulse theory is generally good. An experiment was designed to test the quantitative predictive capability of a steady state multiple pulse computer code. Blooming of a multiple pulse beam was measured as a function of absorbed energy and spatial overlap of successive pulses. With no adjustable parameters agreement between the actual measurements and those predicted by theory is very good.

1. INTRODUCTION

In this paper we consider laboratory scale propagation of high peak power pulsed lasers through an absorptive atmosphere. Thermal blooming - the reduction of irradiance in the far field resulting from the refractive effects in the laser heated medium - is the limiting mechanism being addressed. As indicated in the preceding paper, breakdown is the other primary limitation to pulse propagation.

Experimental procedures are described to characterize the far field irradiance or energy density distribution of pulsed lasers with and without an intervening absorptive atmosphere. Experimental data are compared with appropriate theoretical models to demonstrate present understanding of pulse blooming. Three series of experiments will be described. Summaries of the first two with appropriate references have been published (Kleiman, H., and O'Neil, R. W., 1973; O'Neil, R. W., Kleiman, H., and Lowder, J. E., 1974); only material illustrative of the development of our understanding of efficient pulse propagation and its measurement will be presented from these sources.

The first experiment, performed at 1.06 μ m, explored thermal blooming of pulses whose duration spanned the time required to reach pressure equilibrium across the laser beam. A many times diffraction limited Nd - glass laser beam was used to obtain data to compare with geometric eikonal models for propagation. In the limits before pressure equilibrium is established along the propagation path (short pulse regime) and after pressure equilibration is substantially complete (long pulse regime) the primary parametric dependencies were verified. To test our theoretical understanding of short pulse blooming a high energy 10.6 μ m laser was propagated in a geometry designed to produce significant blooming in times short compared a hydrodynamic time τ_H , the acoustic transit time across the smallest beam dimension. When the observed behavior was compared with theoretical predictions of a computer model embodying the hydrodynamics of the medium, the agreement was quite good.

In the most recent experimental study we considered a train of identical short 10.6 μ m pulses propagating through an absorbing medium in a controllable crosswind. The experimental geometry was designed using the short pulse theory to eliminate significant single pulse blooming. Multiple pulse blooming results when successive pulses overlap spatially. In the steady state limit the measured blooming was in excellent agreement with quantitative predictions of a multiple pulse computer code constructed for this regime of multiple pulse propagation.

2. TEMPORAL REGIMES OF PULSED BLOOMING

Early in the 1970's large scale CO₂/N₂ electric discharge lasers (EDL) operating at 10.6 μ m demonstrated high pulse energies (> 1KJ) and good beam quality (Daugherty, J. D., Pugh, E. R., and Douglas-Hamilton, D. H., 1972; Fenstermacher, C. A., Nutter, M. J., Leland, W. T., and Boyer, K., 1972). Prior to that time, the lasers with highest available pulse energy were the large solid state oscillator amplifier chains operating at 1.06 μ m (Young, C. G., Kantorski, J. W., and Dixon, E. O., 1966). The first blooming experiments designed to examine pulse phenomenology were performed at 1.06 μ m with such a system. A temporarily smooth variable pulse length (3-100 μ sec), variable pulse energy (20-100 J), many times diffraction limited (~50X) laser was focused through one meter absorption cell containing 6 atmospheres of gaseous ammonia, a convenient absorber at 1.06 μ m. Thermal blooming was observed over a range of pulse lengths that spanned pressure equilibration time across the laser beam. For times larger, than τ_H , geometric (eikonal) models for blooming predict a growth of the focal spot that depends linearly on the absorbed energy as indicated in Equation 1. When the pulse length $t_p < \tau_H$ the growth is reduced by $(t_p/\tau_H)^2$ as indicated in Equation 2.

$$\frac{\Delta S}{S_0} = \frac{(n-1) \alpha P t^2}{3 \pi r_c^2 \tau_a^2 S^2}, \quad t > \tau_H \quad (31-1)$$

*

This work is supported by the Advanced Research Projects Agency of the Department of Defense.

$$\frac{\Delta S}{S_0} = \frac{2(n-1)C^2 \alpha P t^3 Z^2}{15 \pi \rho c T a^4 s^4}, \quad t < \tau_H \approx \frac{s}{C} \quad (31-2)$$

Here ΔS is the growth in focal radius, S_0 , n is the index of refraction of the blooming medium, α , the linear absorption coefficient (cm^{-1}), P , the laser power at time t , Z , the propagation distance, ρ , the medium density, c_p , the specific heat at mean temperature T , a , the aperture radius, and C , the sound velocity. Figure 1 is a plot of the peak on axis irradiance as a function of normalized pulse time for four constant energy pulses having four different pulse times, 0.3, 1, 2, and 10 τ_H . The basic prediction for long pulses ($t_p > \tau_H$) is verified in that the final irradiance is the same for the same absorbed energy. As the pulse time approaches τ_H the magnitude of the integrated on-axis energy deposited at the end of the pulse increases. At $t_p < \tau_H$ the final irradiance is significantly higher which is consistent with the $(\tau_p/\tau_H)^2$ dependency expressed in Equation 2. This abrupt transition results from the inertia of the medium that causes a time lag in the development of the pressure equilibrated index of refraction.

To measure the thermal blooming of a focused pulse simultaneous measurements should be made of the bloomed and unbloomed irradiance distributions. In the microsecond and shorter time regimes discrete detectors feeding parallel input data channels are usually required for adequate temporal resolution. If the focal distribution falls smoothly and monotonically from a central peak, is spatially invariant shot-to-shot and the redistribution in focal irradiance is symmetric, spatial resolution requirements on the detector array can be relaxed.

Since these conditions applied in this experiment, a carefully registered 10 element photodiode array with five elements in e^{-1} focal diameter was adequate for the desired measurements. Location of the array along the x or y axis was facilitated using photography. Bloomed and unbloomed distributions at each energy and pulse time could be obtained on separate firings, the unbloomed distribution being obtained with non-absorbing gas in the cell. Data in Figure 1 is a synthesis of a set of peak on axis irradiance measurements.

3. BEAM DIAGNOSTICS FOR 10.6 μm BLOOMING EXPERIMENTS

Performing an experiment at 1.06 μm was relatively straightforward. Unfortunately, very little of the well developed high irradiance diagnostic technology or equipment could be used at the longer CO_2 wavelengths. A 10 μm laser diagnostic approach was developed using coarse transmission gratings for high irradiance beam splitters and attenuators (O'Neil, R. W., Kleiman, H., Marquet, L. C., Kilcline, C. W., and Northam, D., 1974). Figure 2 is a typical diagnostic configuration now commonly used with high energy pulsed 10.6 μm lasers. In this illustration a high geometric transmittance ($T_G = 90$ percent) linear grating is used to sample a high energy pulse. The peak irradiance of the primary beam (zero order) is attenuated to 81 percent ($[T_G]^2$) of the unsampled incident beam, but is otherwise unperturbed. Energy, power, and focal distribution diagnostics are performed in several of the numerous low irradiance diffraction orders. With proper sampling, many of the monochromatic paraxial orders have a spatial distribution directly comparable to that of the unsampled beam.

Using this basic diagnostic approach, it was found that a large scale (1KJ) EDL's were capable of near diffraction limited performance when they were operated with high out-coupled unstable resonator cavities. In contrast to the many times ($\sim 50\times$) diffraction limited glass laser mentioned above, with its smooth Gaussian distributed focal distribution, the near diffraction limited EDL focal distribution is noticeably structured, typically non-symmetric and has significant energy in the side lobes of the diffraction pattern. To avoid laser breakdown in the laboratory air, a highly probable occurrence at 10.6 μm when the power is above 10^7 W/cm^2 and the pulse length is $> 1 \mu\text{sec}$, long propagation paths (typically $> 25\text{m}$) are necessary to bring these lasers to focus. In early technology lasers, little concern was given to stable platforms. Consequently, the location of the focal distribution tended to move several millimeters between shots and the focal distribution could change measurably during a set of measurements. To take these unavoidable background factors into account, a single shot measurement approach was adopted that virtually eliminates beam jitter in one direction and reduces it to \pm a half resolution element in the other. A series of slit apertures are placed in a number of grating orders so that they are effectively contiguous across an appropriately normalized composite focal distribution. At small sacrifice of useful spatial information this technique virtually eliminates beam jitter effects and the parallel input provides a complete beam measurement for each laser firing.

Figure 3 is a schematic representation of this approach applied to a low resolution measurement of $E(x)$, the one-dimensional energy distribution in the unbloomed focal spot of 1 KJ EDL developed by AVCO Everett Research Laboratory, Everett, Massachusetts, USA, (AERL). Linear apertures ($2 \times 0.2 \text{ cm}$) were placed in the negative grating orders using a visible laser alignment technique. Placement uncertainty was $< \pm 0.05 \text{ cm}$. Total energy in the scan format in each order was measured in the symmetric positive orders with 2 cm square aperture pulse calorimeters. After corrections are applied for grating geometry effects the fractions of the total energy in each order passing through its respective scanning aperture are discrete points of the one dimensional energy distribution. Figure 4 is a plot of the normalized fractional energies measured on 5 consecutive firings of the AERL laser. The solid curves are calculated slit scans of a diffraction limited focal spot ($\beta=1$) and one whose linear dimension has been scaled upward a factor of 2 ($\beta=2$). Generally, the beam quality is better than 1.5 using this criterion.

4. COMPARISON OF THEORY AND EXPERIMENT: SHORT PULSE BLOOMING ($t_p < \tau_H$)

Several investigators have developed theoretical models for short pulse blooming (Hayes, J. N., 1972; Maher, W. E., 1972; Aitken, A. H., Hayes, J. N., and Ulrich, P. B., 1973; and Bradley, L. C., and Herrmann, J., 1973). To determine the predictive capability of the computer model developed by Bradley and Herrmann of Lincoln Laboratory, an experiment was designed to measure blooming for $t_p < \tau_H$. The measurement techniques described above were used with the Lincoln Laboratory 500 J EDL as illustrated in Figure 5. An unbloomed focal distribution is obtained using a linear sampling grating that separates the diagnostic side

orders from the main beam before any blooming occurs. Here an energy distribution measurement is adequate in the absence of blooming. Measurement of the bloomed beam cannot be made directly because the power density is too high. The bloomed focal distribution was imaged through a non-absorbing optical path and sampled with a second grating located appropriately in the re-imaging path. Measurement of the instantaneous power distribution was accomplished with parallel slit scan geometry similar to that described above (5×0.1 cm apertures). Time resolved measurements were made with photon drag detectors modified for 5 cm aperture operation.

Figure 6 illustrates a typical measurement of the peak power density of a bloomed pulse as a function of time. The theoretically predicted power density measurements are plotted as a solid line for $t_p < 0.5 \tau_H$. Included in the error bars are the effects of alignment uncertainty. It can be seen that the theoretical model embodying the short pulse hydrodynamics describes the observed phenomena quite well. In this experiment designed to produce a large amount of blooming it can be seen that the far field irradiance falls very rapidly once it begins. This is a general characteristic of short pulse blooming. Exactly when the blooming begins is primarily a function of beam geometry as it relates to the hydrodynamic time. To achieve short pulse blooming on a laboratory scale, the focal spot diameter was as small as possible (~ 0.3 cm) and the peak focal irradiance was increased to very near the clean air breakdown limit ($\sim 10^9$ W/cm²). (Propagation at irradiance levels greater than $\sim 10^7$ W/cm² was made possible by removing all particulates > 0.3 μ m from the gaseous medium.) When the beneficial effects of medium inertia are used to advantage, i.e., a beam geometry is chosen to maximize τ_H , single energetic pulses can be propagated with very little irradiance loss.

5. COMPARISON OF EXPERIMENT WITH THEORY: MULTIPLE PULSE BLOOMING

Given the theoretical understanding of single pulse blooming a next logical step is to examine the propagation of a train of non-blooming pulses. Several investigators have developed theoretical models for multiple pulse (Wallace, J., and Lilly, J. Q., 1974; Bradley, L. C. and Herrmann, J., 1974; Ulrich, P. B., 1974). Wallace and Lilly have described a computer model that treats each pulse individually and should be generally valid for long and short pulses. For reasons of economy, other investigators have developed similar but more restricted codes that yield substantially the same results in the steady state limit. In this section an experiment is described that was designed to test the limits and accuracy of the steady state code of Bradley and Herrmann of Lincoln Laboratory.

The steady state multiple pulse code considers a train of identical laser pulses propagating through an atmosphere with specified absorption properties. The redistribution of irradiance in the n th pulse in any plane along the path is calculated by propagating a non-blooming pulse through the index of refraction distribution left behind by the preceding pulses that overlap its path. Steady state is defined when independent calculations of the phase disturbance and beam irradiance along the beam become self-consistent. The maximum value of the phase distortion is proportional to

$$\frac{4\pi(n-1)\alpha E_p Z}{\rho c T a_x^2 \lambda} : \frac{2a_x v}{V_x} \equiv N_p \cdot N_o \quad (31-3)$$

Here E_p is the pulse energy, λ , is the wavelength, a_x , is the dimension of the beam aperture in the wind direction, v , is the laser repetition rate, V_x , is the transverse beam velocity, and other symbols are defined as in Equations 1 and 2. N_o is called the overlap number since $N_o = 5$ indicates five laser pulses occur within one flow time across the laser aperture. N_p is a measure of the strength of medium distortion caused by a single pulse. The experiment has been designed to vary α , E_p and N_o , independently at constant Z . Each of these parameters have been varied in the computer code to define an experimental parameter space. Short pulse calculations were performed to insure that peak energy losses due to single pulse blooming were less than 5 percent. Because each pulse does not bloom during its own pulse time, time resolved measurements are not needed and the blooming can be characterized by an energy distribution measurement. Each pulse in the train is measured since the number of pulses required to reach steady state is not explicit in the code calculations. In practice steady state is reached 2 to 3 pulses after the nominal overlap number. The following conditions were established in the experiment:

1. Negligible single pulse blooming
2. Uniform crosswind
3. Maximum peak irradiance $I_o(z) < 10^7$ W/cm², $\alpha > 0$.
4. Negligible convection or conduction
5. Broadband absorption
6. Negligible cell effects (acoustics, turbulence)
7. Low Fresnel Number, ($N_F < 10$)
8. Characterization of blooming by energy redistribution in a focal plane beyond absorption cell.

The last item requires some explanation. To avoid prohibitive single pulse blooming with a laboratory scale laser it was necessary to remove the depth of focus from the absorbing medium. Measurements were made in the focal plane and compared to calculations of the exact experimental conditions.

Figure 7 is a schematic of the multipulse thermal blooming experiment. The 10.6 μ m multiple pulse laser used in the experiments is a 1.6 liter EDL developed by AERL. For these experiments the laser was adjusted to have a pulse length of ~ 5 μ sec (to prevent single pulse blooming), providing a pulse energy of 5 - 10 J in a nominal 2×4 cm aperture. A summary of its characteristics is presented in Table I.

TABLE I
MEASURED PARAMETERS: AERL MULTIPER PULSE EDL

1. Energy/Pulse, E_p	$\leq 7 \text{ J}$
2. Pulse to Pulse Energy Variation ΔE_p	$\sim \pm 10 \text{ percent}$
3. Laser Repetition Rate, ν Variation in ν	1 - 200 Hz $\sim 1 \text{ percent}$
4. Pulse Length, t_p	$\sim 6 \text{ } \mu\text{sec}$
5. Beam Quality, β	≤ 1.2
6. Pulse to Pulse Variation in β	$\leq 10 \text{ percent}$
7. Aperture $D_x \times D_y$	1.65 x 3.4 cm
8. Pointing Stability	
1) Translation	$\leq \pm 3 \text{ mm}$
2) Angular	$\sim 150 \text{ } \mu\text{rad}$

Pulse repetition rates were adjustable from 1 to > 200 pulses per second. The laser aperture was generated by a novel off-axis unstable resonator developed by AERL to provide a good quality, reasonably uniform output irradiance distribution without the central obscuration of the more familiar on-axis unstable resonator (Phillips, E. A., and Reilly, J. P., 1974). The beam leaving the laser was immediately passed through a 2:1 focusing beam expander to bring a converging beam to the entrance of the cell comparable in size to that leaving the laser. Beam scrapers were placed after the beam expander to define a rectangular beam with well-defined truncation. At the relatively low average power level of this laser, a salt beam-splitter could be used to sample the laser beam before it enters the absorption cell. The absorption medium is confined in an evacuable 458 cm long cell 50 cm in diameter closed by 25 cm aperture fast acting mechanical shutters (FAV). The beam focuses 638 cm after entering the cell in a second section filled with particulate free nitrogen - a non-absorbing gas at 10.6 microns. This feature prevents single pulse blooming in the depth of focus and reduces the probability of dirty air breakdown to a negligible level when peak irradiance levels exceed 10^7 W/cm^2 . Well mixed nitrogen and < 2 percent propane are used in the absorbing section as a convenient nonsaturable absorbing medium. Mixed in nitrogen commercially obtained propane has a 10.6 micron absorption of about $10^{-4} \text{ cm}^{-1} \text{ torr}^{-1}$. The exact cell transmittance is measured directly during the experiment.

To examine the propagation characteristics of a train of focused, partially overlapping, laser pulses as a function of overlap, a uniform reproducible wind or beam motion across the cell, was required. To maintain precise control over the effective wind velocity, the laser beam was moved through a stationary gas by translating a precision corner reflector at constant velocity. As is illustrated schematically in Figure 8, the incident beam and corner reflector position are appropriate to the first in a train of short ($\sim 5 \text{ } \mu\text{sec}$) pulses. During an interpulse time (10-25 ms) the reflector moving at velocity V_x , has moved to a new position where the next pulse in the train is depicted by dashed lines. The overlapping volume is illustrated by the cross-hatched region. If there is no spatial overlap of consecutive pulses there is no blooming. The extent of blooming increases with N_0 , the number of pulses overlapping at the cell entrance. Typical N_0 's in the experiment ranged between 1 and 10. To prevent convection from influencing the measurements N_0/ν was $< 0.2 \text{ sec}$. Typical ν 's varied between 20 and 100 Hz, and beam velocities were adjustable from 5 to 75 cm/sec.

To measure the focal distribution of each pulse in the moving multiple pulse beam, the basic re-imaging described above was used in a moving mirror imaging system designed to remove the effect of beam motion in the measurement plane. The unit magnification image position of a moving focal point is spatially invariant if the imaging mirror moves in the direction of travel at exactly half the beam velocity. Since a moving corner reflector translates a beam twice its own velocity, spatial invariance of the bloomed focal distribution is achieved by driving both corner reflector and imaging mirror at exactly the same velocity. Beam motion due to the optical train external to the laser was less than $\pm 0.1 \text{ cm}$ ($\pm 80 \text{ } \mu\text{rad}$) at the detector plane.

Bloomed beam diagnostics were performed in the diffraction orders of a 90 percent linear grating. Five diagnostic orders are used to measure the energy transmitted through the cell, gross energy redistribution and beam motion via burn patterns, power as a function of time, and the x and y one-dimensional energy distribution in the bloomed focal spot. The latter measurement is made with a multipulse pyro-electric calorimeter array with 64, $0.1 \times 1.5 \text{ cm}$ elements. Figure 9 is a schematic of the unbloomed focal distribution super-imposed on the array geometry. The array is capable of 1 KHz operation. A 32 element array of identical design measures the unbloomed focal distribution of each pulse using the reflection from the salt

wedge. Input energy and burn patterns are also measured in the input beam to provide cell transmittance and beam motion data. In separate array measurements the irradiance distribution was measured at the cell entrance. All data were available for real time observation and were tape recorded for computer processing.

To compare experimental data with computer code calculations the beam geometry and input aperture distribution must be properly represented in the calculations. In Figure 10 the dotted line is the one-dimensional array scan of the input beam distribution at the cell entrance, in the wind direction. Generally, this distribution was reproducible pulse-to-pulse and run-to-run. The solid line is a truncated Gaussian distribution fitted to the measured beam half width. Truncation in X and Y was determined from the measured zero's of the unbloomed far field diffraction pattern (x_0, y_0). The dotted line in Figure 11 is a plot of $E(x)$ measured at focus by the 64 element array [$E(x) = \sum E_n(x) \approx \int_{-0.75 \text{ cm}}^{0.75 \text{ cm}} E(x,y) dy$]. The solid curve is the code prediction using the Gaussian approximation assuming diffraction limited propagation. Use of a more detailed amplitude distribution produced results not measurably different from the approximate distribution used for theory - experiment comparisons. In Figures 12a and 12b, the calculated (solid) and measured (dotted) one-dimensional energy distributions, have been plotted for a single pulse after steady state for $N_0 =$ (a) 2.41 and (b) 4.88 when $N_p = 45$. Typically, the differences between theory and experiment are comparable to experimental uncertainty in a single measurement.

To address a comprehensive comparison of experiment with theory, measurements were made of the energy redistribution over a range of absorption coefficients corresponding to cell transmittances of 83 to 47 percent, pulse energies of 6 to 7 joules, and overlap conditions of $N_0 = 2.35, 4.75$, and 9.5 pulses per aperture-clearing-time. Complete bloomed and unbloomed focal distributions were measured for each pulse. To characterize the blooming with a single number the peak energy on a single 1x15 mm array element was chosen. To reduce experimental scatter resulting from variations in pulse energy and/or beam quality the peak focal energy measured in the bloomed pulse was normalized to the peak measured in the unbloomed beam. Overall system response was determined from empty cell conditions. To define blooming for a given condition, typically 3 pulses in each train were measured after steady state and averaged. At least two experiments under the same conditions were always performed. Using this procedure successive measurements differed by less than 5 percent.

During the data reduction process a source of beam motion originating at the laser was identified that modified the nominal overlap number during the measurement period. This motion superimposed a small (~ 3 cm/sec) velocity perturbation on the otherwise constant velocity crosswind during the measurement time. If we take this beam jitter effect into account in presenting data, the theoretical predictions appear as bands indicative of a range in overlap numbers. In Figure 13 the peak energy normalized to unbloomed conditions, F_{pk}/F_0 has been plotted as a function of N_p . Experimental points are plotted with maximum absolute error bars on the measured quantities. Although beam jitter effects are significant at high overlap numbers in this small scale experiment, the blooming measured is generally in good quantitative agreement with the theoretical predictions.

6. CONCLUSIONS

In the three experiments described above a logical progression is illustrated in the understanding of thermal blooming limitations on pulsed laser propagation. As pulsed laser devices were developed appropriate propagation models were constructed. Experiments were designed to test these models on a laboratory scale. In the earliest glass laser experiments gross parametric dependencies were verified: in the most recent multiple pulse experiments the quantitative predictive accuracy of a well developed computer code was determined. This paper demonstrates good understanding of pulsed thermal blooming phenomenology in several key areas.

ACKNOWLEDGMENTS

In the most recent multiple pulse propagation experiments we must acknowledge the contributions of D. H. Dickey, and L. C. Pettingill, of Lincoln Laboratory, to the success of the experimental hardware, of L. Corey, and M. G. Cheifetz, of Aeronutronic Ford for their excellent programming, and of S. Lowder of AERL for his outstanding help during the experiments. We also thank D. E. Lencioni, J. E. Lowder, L. C. Bradley, and J. Herrmann for their many suggestions and especially thank S. Edelberg for his direction of the pulsed laser measurements program at Lincoln Laboratory. This work is supported by the Advanced Research Projects Agency of the Department of Defense.

REFERENCES

- Aitken, A. H., Hayes, J. N., and Ulrich, P. B., 1973, "Thermal Blooming of Pulsed Focused Gaussian Laser Beams", Applied Optics, USA.
- Bradley, L. C., and Herrmann, J., 1973, "Short Pulse Computer Code - JSL-1", Private Communication MIT, Lincoln Laboratory, Lexington, Massachusetts, USA.
- Bradley, L. C., and Herrmann, J., 1974, "Steady State Multiple Pulse Computer Code - JSL-5", Private Communication, MIT, Lincoln Laboratory, Lexington, Massachusetts, USA.
- Daugherty, J. D., Pugh, E. R., Douglas-Hamilton, D. H., 1972, "A Stable Scalable High Pressure Gas Discharge as Applied to the CO₂ Laser", Bulletin of the American Physical Society, USA.
- Fenstermacher, C. A., Nutter, M. J., Leland, W. T., Boyer, K., 1972, "Electron Beam Controlled Electrical Discharge as a Method of Pumping Large Volumes of CO₂ Laser Media at High Pressure", Applied Physics Letter, USA.
- Hayes, J. N., 1972, "Thermal Blooming of Laser Beams in Fluids", Applied Optics, USA.
- Kleiman, H., and O'Neil, R. W., 1973, "Thermal Blooming of Pulsed Laser Radiation", Applied Physics Letters, USA.
- Maher, W. E., 1972, "Laser Beam Propagation Model with Hydrodynamic Treatment of the Transmission Medium", Applied Optics, USA.
- O'Neil, R. W., Kleiman, H., and Lowder, J. E., 1974, "Observation of Hydrodynamic Effects on Thermal

Blooming", Applied Physics Letters, USA.

O'Neil, R. W., Kleiman, H., Marquet, L. C., Kilcline, C. W., and Northam, D. B., 1974, "Beam Diagnostics for High Energy Pulsed CO₂ Lasers", Applied Optics, USA.

Phillips, E. A., and Reilly, J. P., Northam, D. B., "Off-Axis Resonators", 1974, Private Communication, AVCO Everett Research Laboratory, Everett, Massachusetts, USA.

Ulrich, P. B., 1974, "Multiple Pulse Computer Code", Private Communication, U. S. Naval Research Laboratory, Washington, D. C., USA.

Wallace, J., and Lilly, J. Q., 1974, "Thermal Blooming of Repetitively Pulsed Laser Beams", Journal of the Optical Society of America, USA.

Young, C. G., Kantorski, J. W., and Dixon, E. O., 1966, "Optical Avalanche Laser", Journal of Applied Optics", USA.

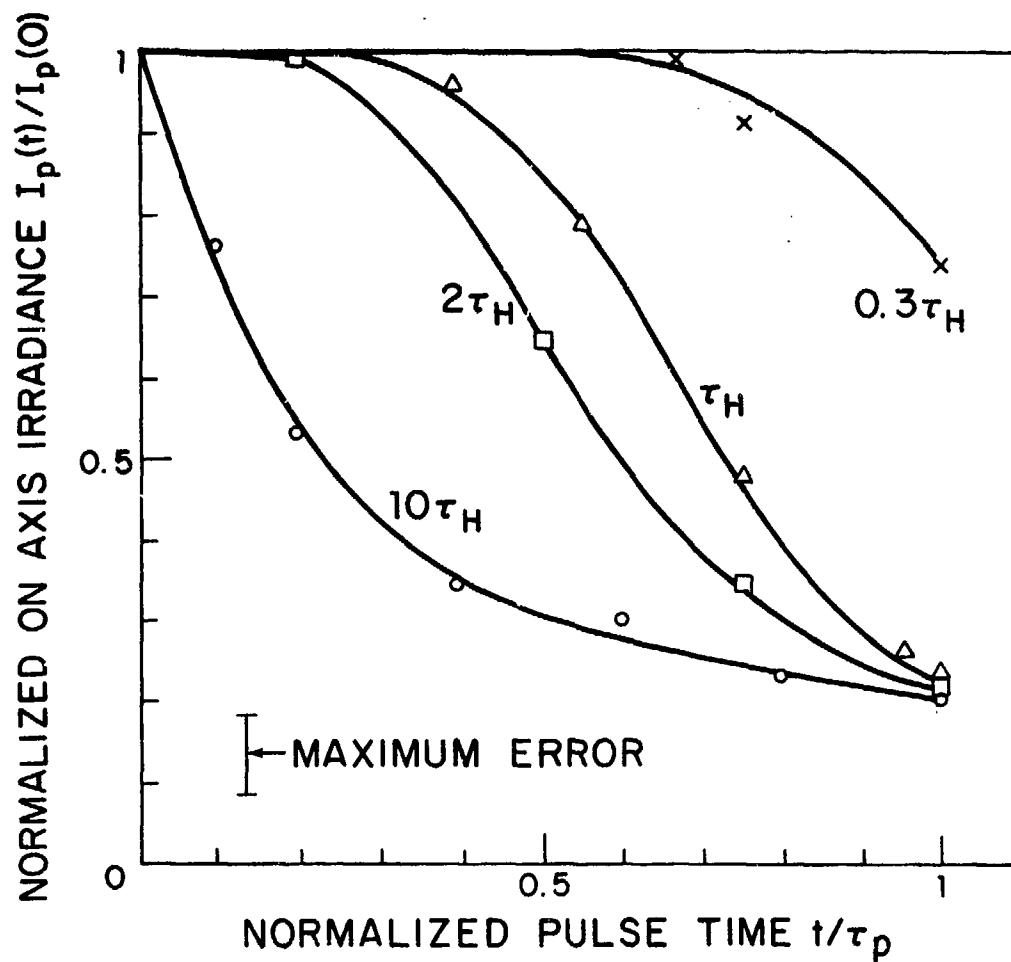


Fig.1 Plot of the normalized on-axis irradiance plotted as a function of normalized pulse time for 4 constant energy pulses with durations of 0.3, 1, 2, and 10 τ_H .

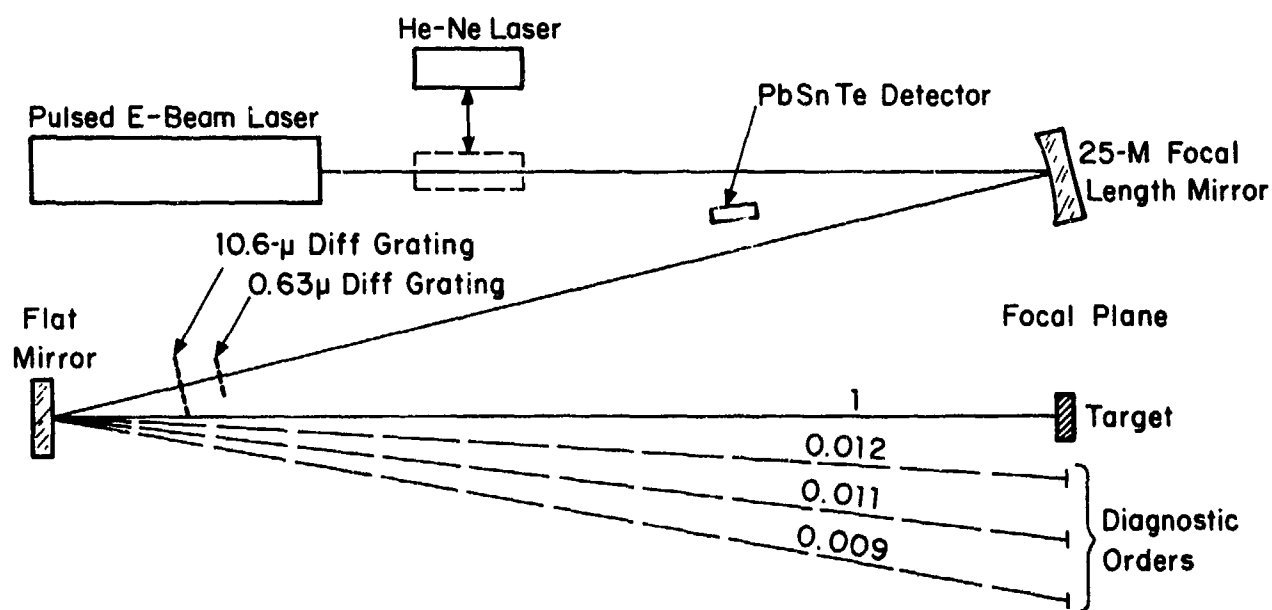


Fig.2 Experimental arrangement for pulsed 10 μm laser diagnostics.

ENERGY SAMPLING WITH LINEAR DIFFRACTION GRATING

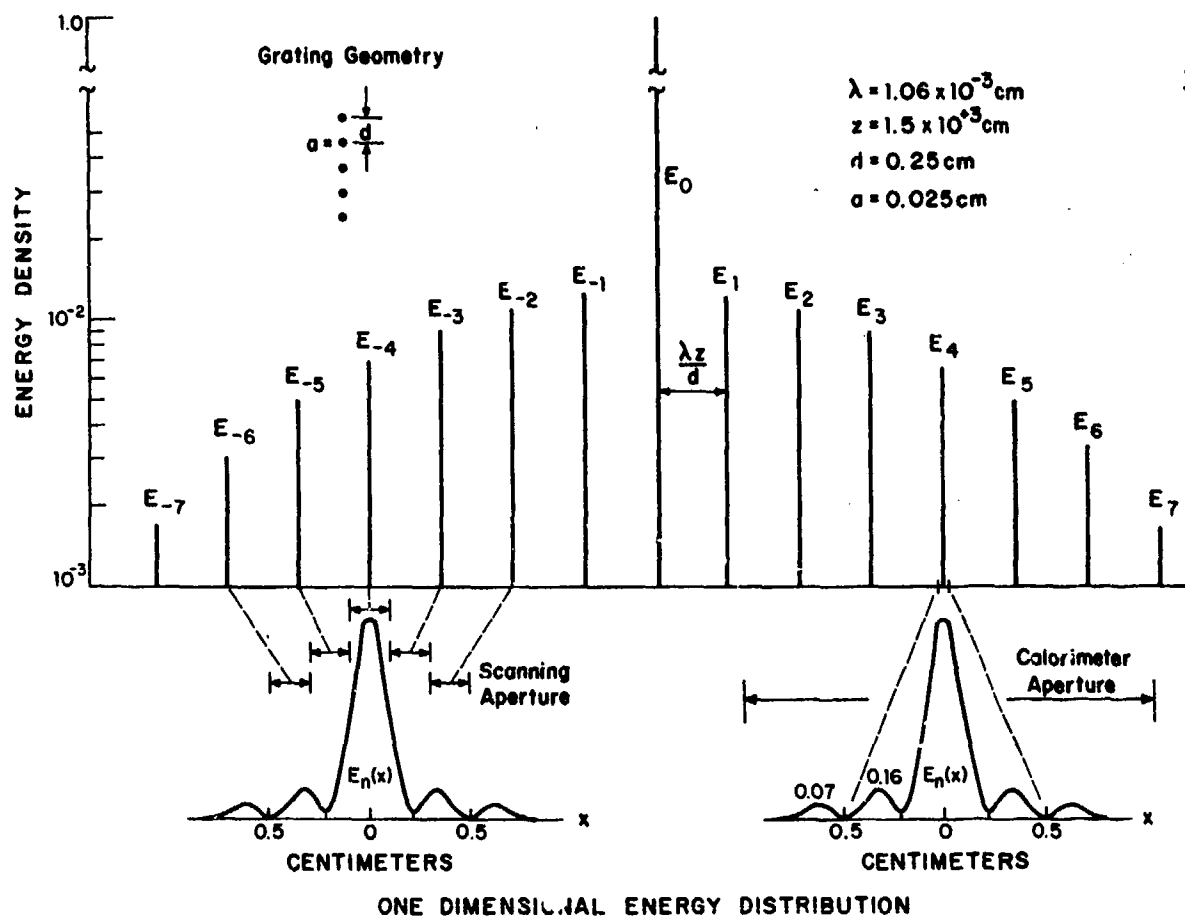


Fig.3 Schematic illustration of focal energy distribution using multiple diffraction orders from a linear transmittance grating.

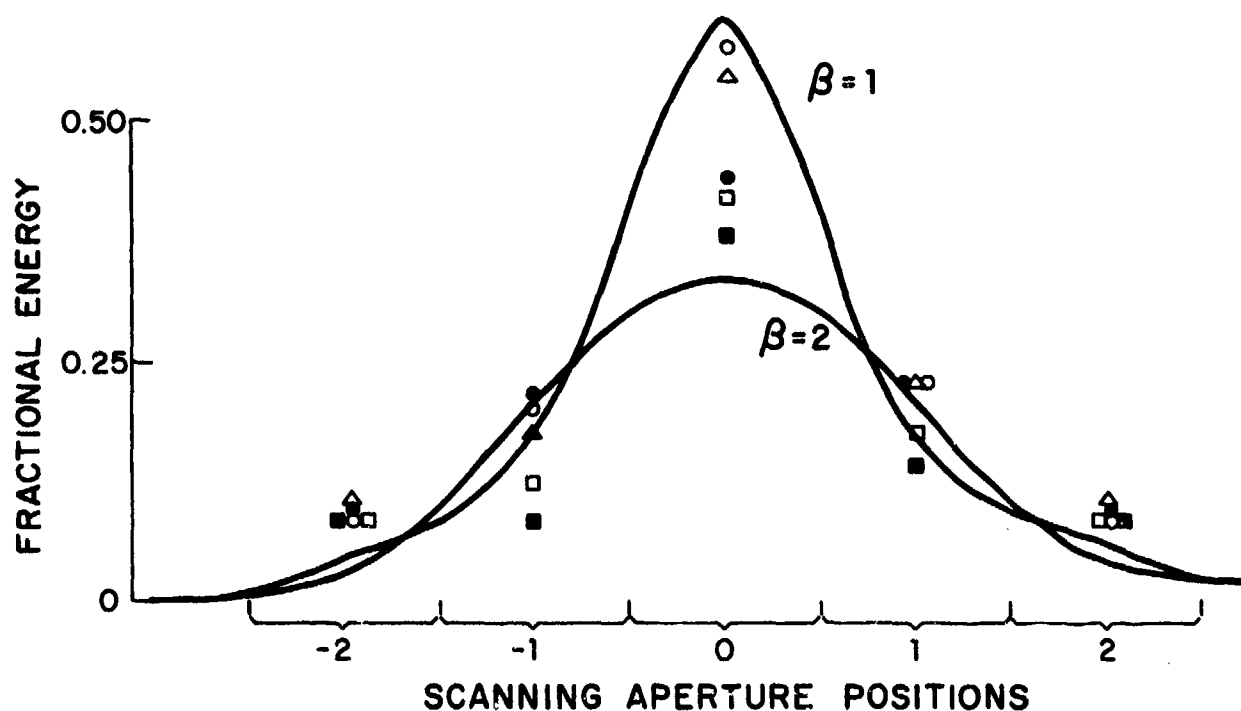


Fig.4 Low resolution scan of the focal energy distribution using slit apertures in multiple grating orders.

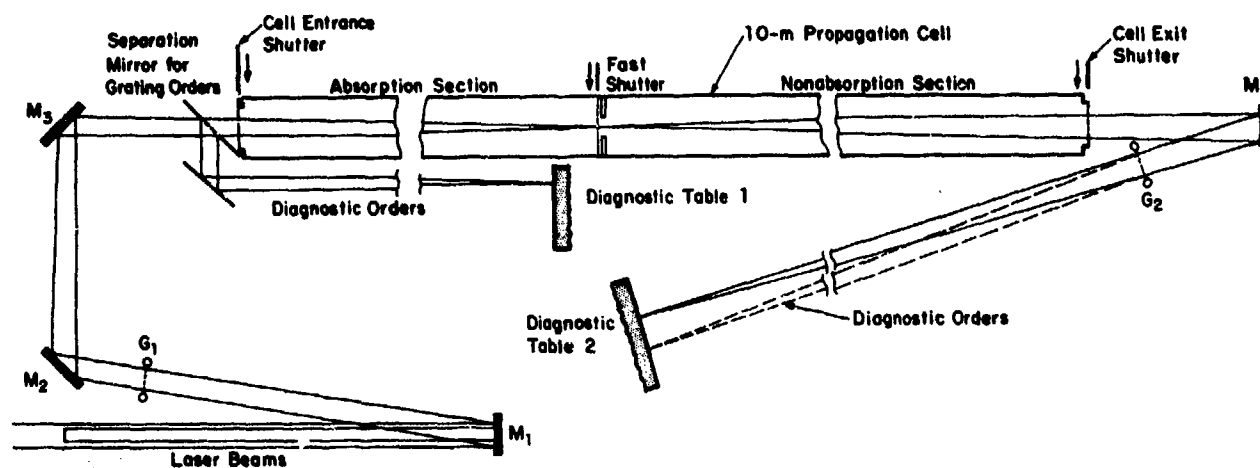


Fig.5 Experiment arrangement for measurement of pulsed thermal blooming.

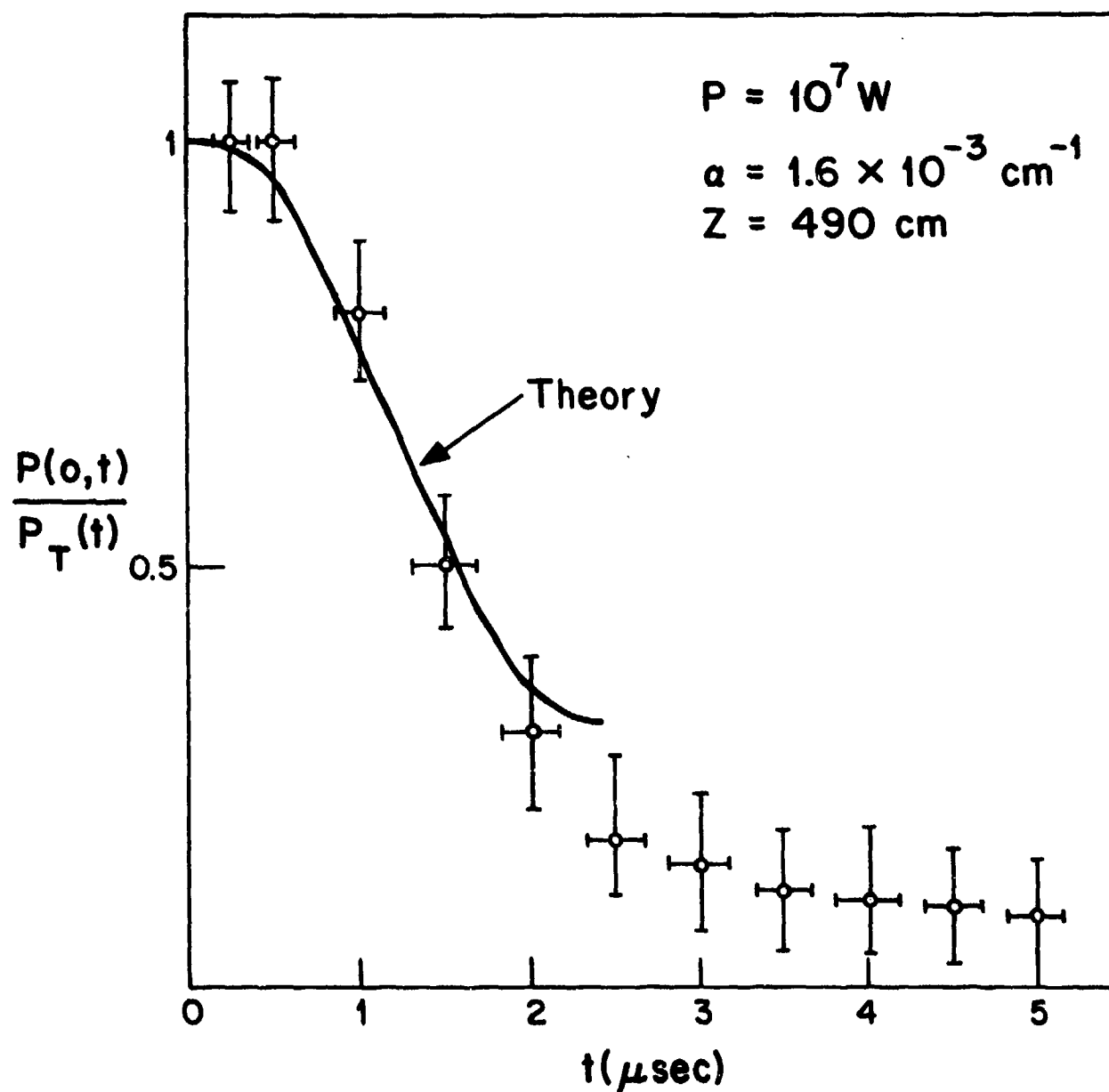


Fig.6 Comparison of the measured drop in peak power density with the theoretically predicted measurement of thermal blooming.

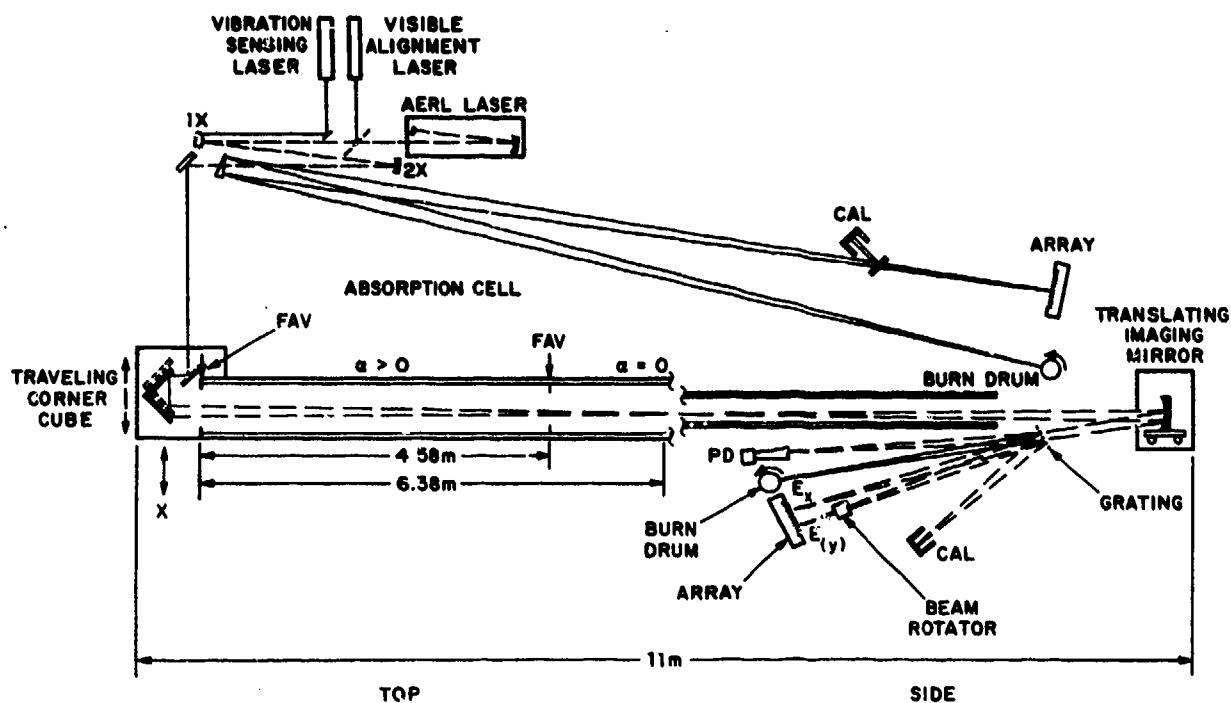


Fig.7 Schematic of multiple pulse blooming experiment.

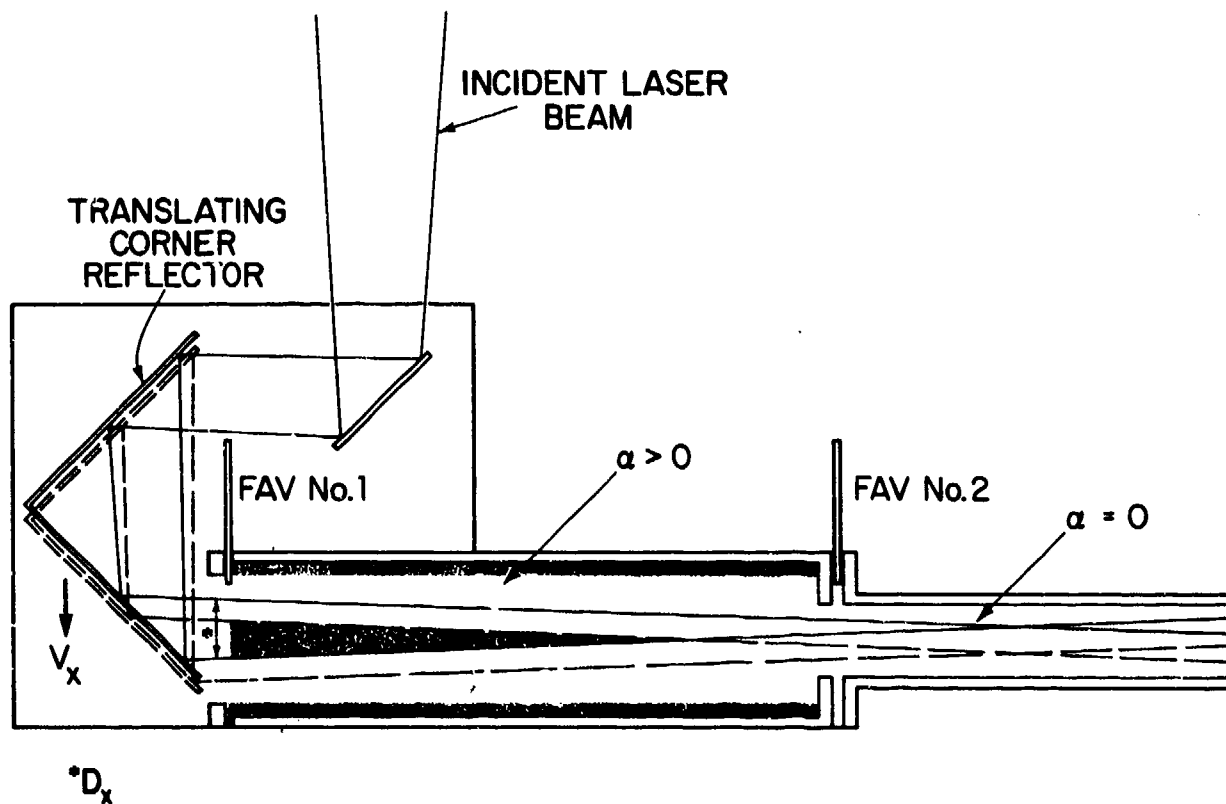
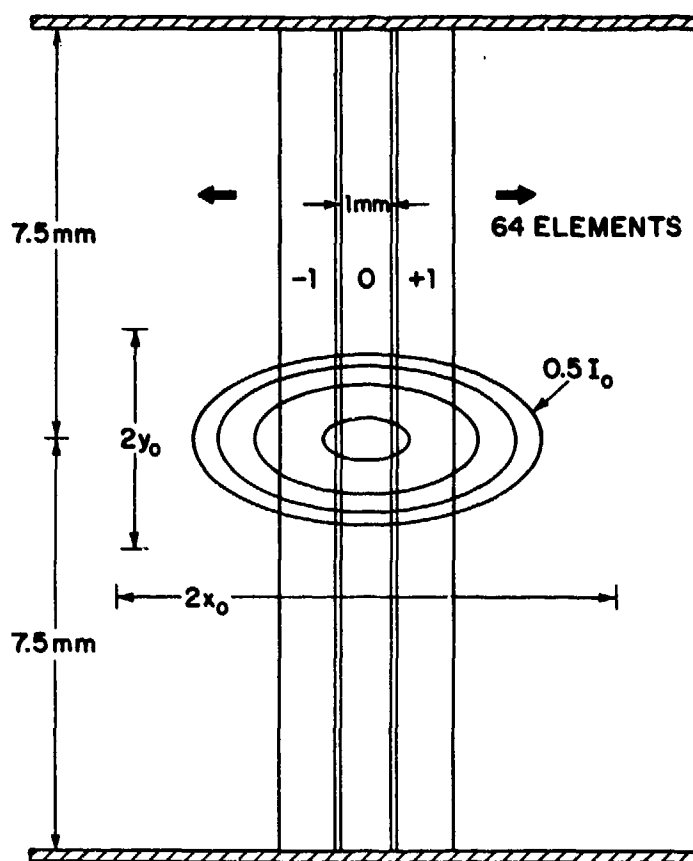
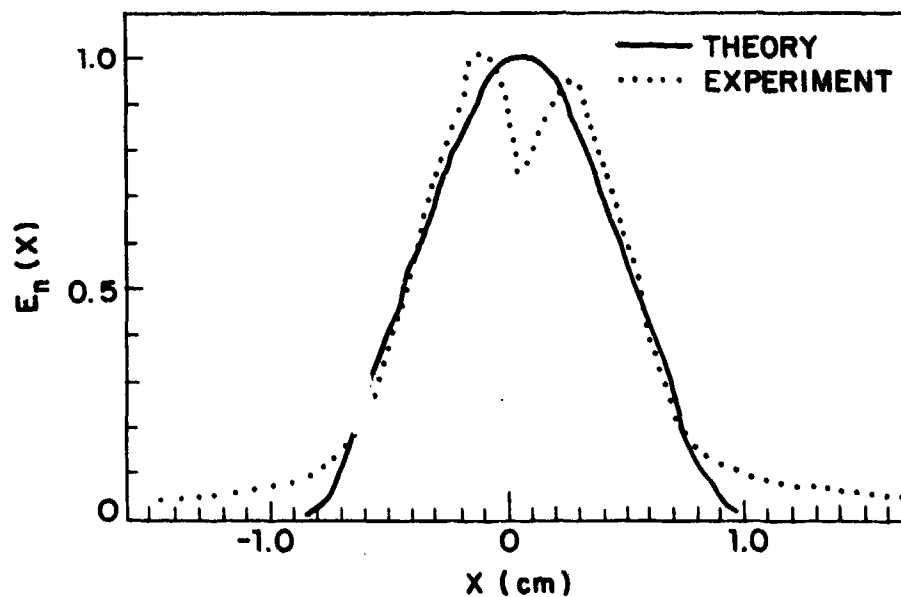


Fig.8 Illustration of moving corner reflector technique used to generate constant velocity beam motion.



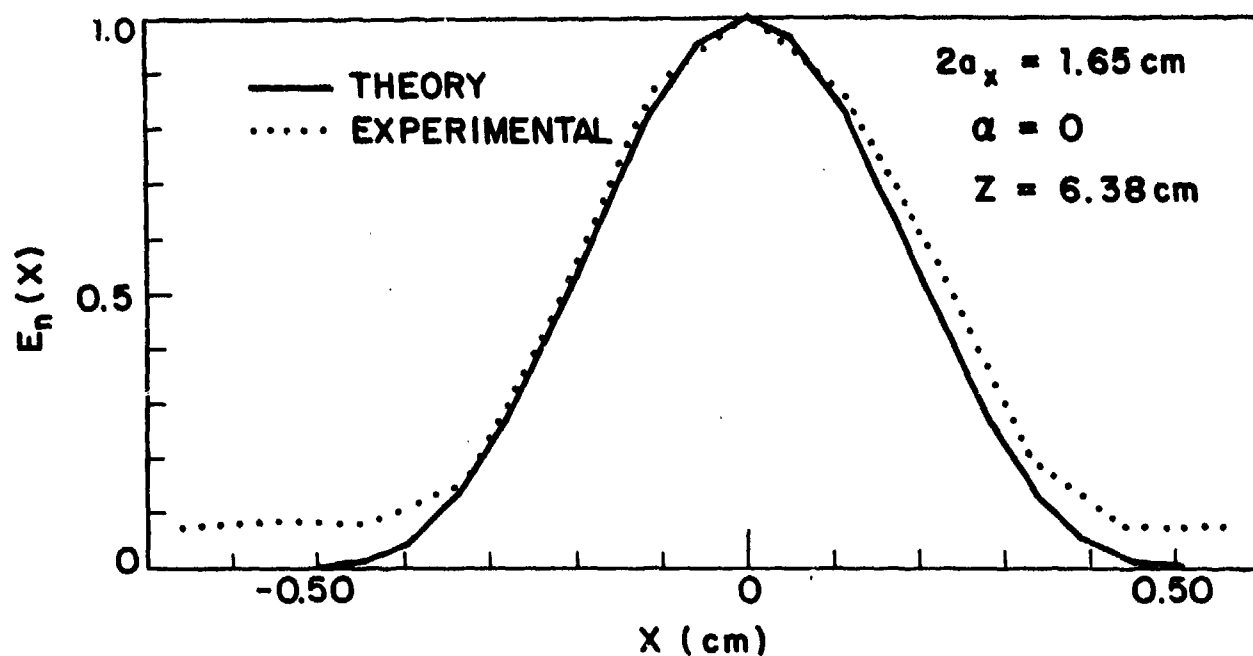
ARRAY MEASUREMENT GEOMETRY

Fig.9 Illustration of the calorimeter array scanning an unbloomed focal spot with diffraction zeroes at x_0, y_0 .



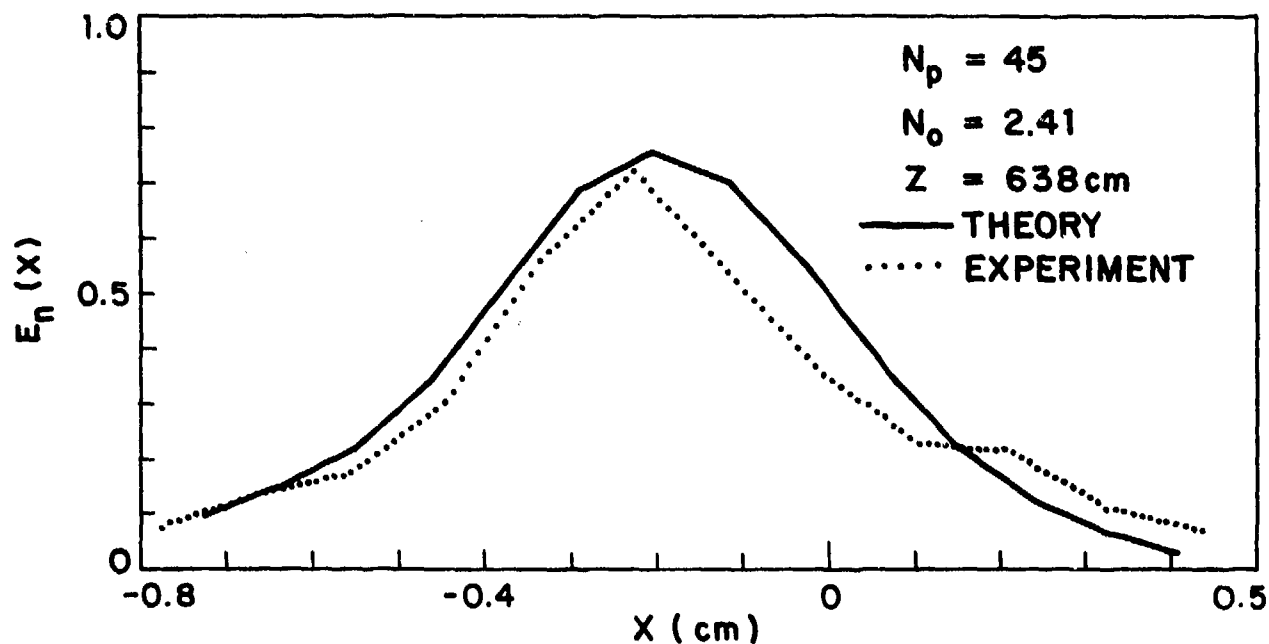
APERTURE DISTRIBUTION

Fig.10 Plot of the measured laser aperture energy distribution in the wind direction (Dotted Curve). The solid curve is a plot of the analytic distribution used to approximate the input aperture distribution in code calculations.



ONE DIMENSION FOCAL ENERGY DISTRIBUTION

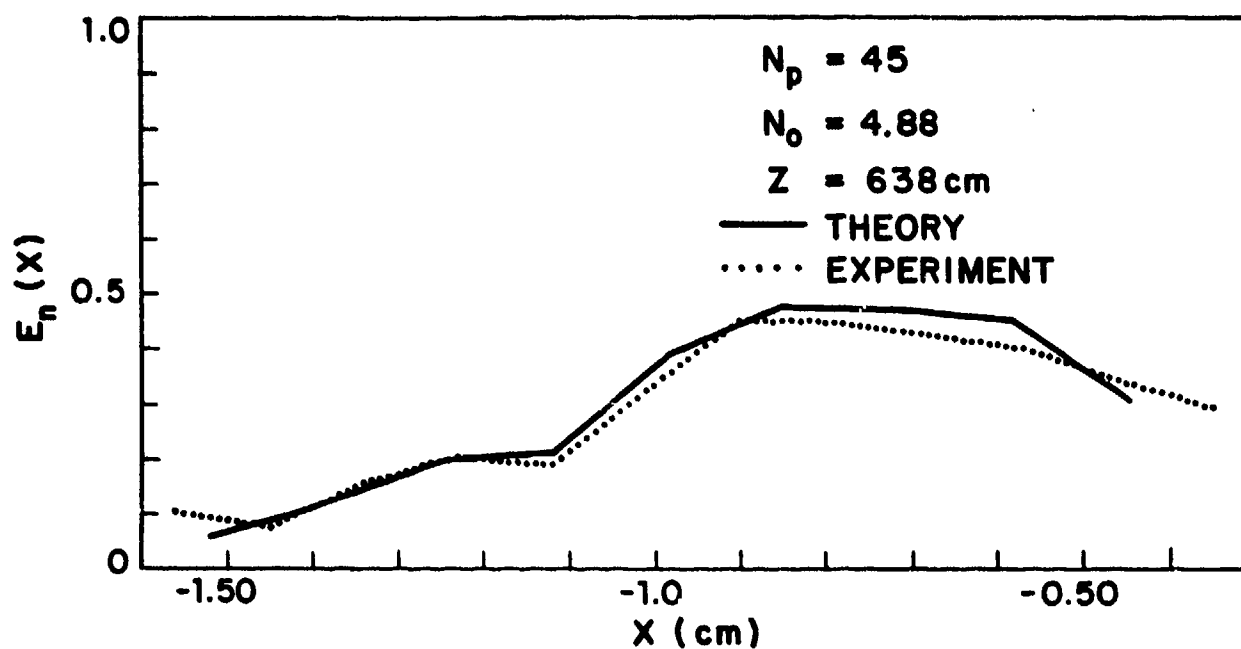
Fig.11 The measured focal energy distribution using the calorimeter array is plotted with a dotted line. The solid line illustrates the theoretically predicted measurement if the analytic approximation in Figure 10 is propagated to a diffraction-limited focus.



(A)

BLOOMED FOCAL ENERGY DISTRIBUTION

Fig.12 Comparison of the measured (dotted line) and calculated energy distributions (solid line) for (a) $N_0 = 2.41$; (b) $N_0 = 4.88$ when $N_p = 45$.



(B)

BLOOMED FOCAL ENERGY DISTRIBUTION

Fig.12 (Concluded)

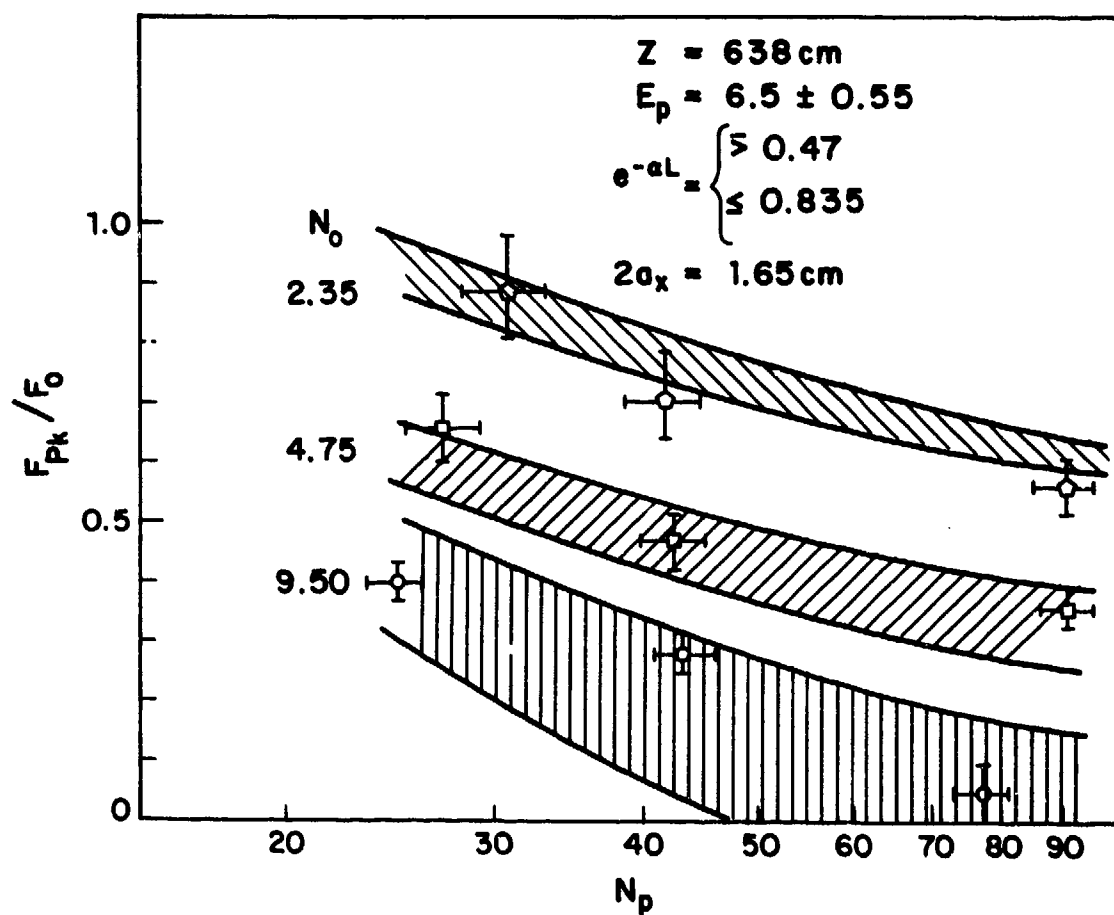


Fig.13 Plot of the peak normalized energy density as a function of N_p for nominal N_0 's of 2.35, 4.75, and 9.5. Effects of laser beam velocity perturbations are reflected in the width of the theory bands.

QUESTIONS AND COMMENTS
ON SESSION IV

EXPERIMENTAL DETERMINATION OF SINGLE AND MULTIPLE PULSE PROPAGATION

- Dr. Peter Ulrich: Your experiments have confirmed the theory and computer calculations for single pulse blooming and multiple pulse blooming separately. Have you seen single pulse blooming in your multiple pulse trains and do you plan to design experiments in the future which combine these effects?
- Dr. Richard O'Neil: In the experiment discussed here, a condition was examined in which a single pulse was decreased in measured energy density by ~ 20 percent. In this regime the blooming was effectively saturated. We plan no experiments to address specifically this condition since single pulse blooming occurs so rapidly once it begins to be significant that such a condition is judged to be a nonpractical option. If evidence is found that single pulse blooming aggravates the multiple pulse propagation this judgement would have to be re-examined.
- Dr. H. T. Yura: Please comment on the threshold sensitivity of rain, clouds and fog in relation to that of distilled water?
- Dr. R. W. O'Neil: Fog, rain, and clouds would tend to be contaminated with atmospheric dust and/or chemicals. I expect the behavior to be comparable to other atmospheric aerosols.

Summary of Session IV
NON-LINEAR PROPAGATION

by

Dr. J. N. Hayes, Chairman

The fourth session of this conference, devoted to the propagation of high energy laser beams through the atmosphere, was the first of its kind for an AGARD Meeting. Because most of the attendees were unfamiliar with this area of propagation research, the first presentation, by Dr. John N. Hayes, was a survey paper designed to acquaint the audience with the types of high power propagation problems, with emphasis on the so called thermal blooming phenomenon. The various aspects of thermal blooming for continuous wave, single pulse and multiple pulse blooming were described, while air breakdown as an impediment to pulsed propagation was introduced. Experiment and theory were shown to be in good agreement with no free parameters to vary. The discussion concluded with a description of the effect of atmospheric phenomena, such as turbulence and the presence of aerosols on beam propagation, and observations on the current status of research in these areas.

A more detailed development of multiple pulse propagation was the subject of the second presentation, made by Dr. Seymour Edelberg, of this session. Empirical development, through the use of computer solutions of the basic theoretical equation, of "scaling laws" to describe the propagation of multiple pulse beams in terms of a set of fundamental dimensionless parameters was given along with illustrative examples. The so-called scaling law was developed for a fixed waveform and the component single pulses were chosen to avoid air breakdown. The potential for boring a hole through a fog with a high power multiple pulse beam was also analyzed; energy requirements for droplet evaporation were deduced and experimental observations described.

Dr. Peter Ulrich's paper was devoted to a survey and analysis of the many varieties of numerical methods that have been developed to calculate the properties of high power beams as they propagate through absorbing media. The advantages and disadvantages of the different methods were discussed and comparisons made. In addition to the analysis of differing algorithms, Dr. Ulrich classified the kinds of codes required according to the physical propagation problem to be solved. Methods for improving any algorithm by the introduction of the so-called "adaptive coordinates systems" were presented. Comparisons between analytical results, and computational results and observational data showed that our understanding of the many thermal blooming phenomena is quite good.

Air breakdown studies were discussed in a paper by D. Lencioni and presented by R. O'Neil; the discussion was devoted to a survey of results on the threshold levels for air breakdown in 10.6 μ and 1.06 μ laser beams. It was shown that the breakdown threshold data for aerosol free air follows the theory of Watson and Kroll quite accurately, but that the presence of dry aerosols or wet nucleated water droplets lowers the threshold. The threshold levels were shown to be generally material independent (with the exception of pure H₂O droplets), but that they are affected by pulse length and by aerosol size. Experimental arrangements by which the data were obtained were described and time lapsed photographs of the growth and evolution of the breakdown plasma were shown. Evidence that aerosol induced breakdown plasma were shown. Evidence that aerosol induced breakdown thresholds are proportional to λ^{-1} was shown, and data taken at other laboratories and at differing wavelengths confirm this result.

The final paper of this session, presented by Mr. Richard O'Neil, discussed in detail the early and recent work performed at Lincoln Laboratory on single pulse and multiple pulse propagation. The experimental arrangements covering both the laser apparatus and beam diagnostics were discussed; the experimental results were compared with a computer simulation (with no free parameters) of the tests. Both the single and multiple pulse theory and experiments were demonstrated to be in excellent agreement. It should be noted that the single pulse propagation experiment was designed to avoid air breakdown while the multiple pulse case avoided breakdown and single pulse blooming as well.

The papers presented in these proceedings and at the conference demonstrated that a good quantitative understanding of the important impedances offered by the atmosphere to high power propagation is available. In contrast to propagation in the real atmosphere, the theories and experiments were clearly oversimplified, but work on the more complex phenomena of turbulence, aerosols, beam jitter, multiple wavelength propagation and high power adaptive apertures has been underway, is continuing and promises to show conclusive results in the near future. It is to be hoped that at the next AGARD conference on optical propagation through the atmosphere, papers in these areas will be presented.

COMPENSATED IMAGING

James W. Justice
Defense Advanced Research Projects Agency
1400 Wilson Blvd, Arlington, Virginia, U.S. 22209

Raymond P. Urtz, Jr.
Rome Air Development Center
Griffiss AFB, New York, U.S. 13441

SUMMARY

The presence of the atmosphere degrades the imaging performance of large telescopes. Optical phase distortion imposed by atmospheric turbulence causes a loss in resolution capability of from 10 to 30 times a system's theoretical performance. Over the past several years, a number of approaches to overcoming image degradation have been proposed. We have developed an approach called Compensated Imaging. Compensated Imaging is an approach which allows the retrieval of low contrast information by active adaptation of the telescope system to atmospheric conditions. This is accomplished through the use of real time wavefront sensing coupled with fast response deformable optics. In practice, the wavefront entering the telescope is measured to determine its wavefront deformation (optical path length differences across the aperture) and a mirror is then deformed to the conjugate of the deformations, producing a near diffraction limited image on a sensor. Analysis of the wavefront correction capabilities has been completed and two approaches to wavefront sensing are being investigated.

1. INTRODUCTION

The prime limiting factor to resolution capabilities of large aperture telescopes is the presence of the atmosphere. Spatial and temporal variations in the index of refraction of the atmosphere introduce distortions in the light from a source as it travels to the telescope. Phase distortions are the dominant effect and result in a reduction of resolution many times a systems theoretical limit. As an example, the operational seeing limit of 60 inch diameter telescopes are typically in the range of 1 to 2 arc seconds as opposed to a theoretical limit of 0.1 arc seconds. At these operational resolutions many astronomical objects are unresolved.

Over the past several years significant effort has been applied to developing imaging approaches which overcome or circumvent the distorting effects of atmospheric turbulence. Before we discuss these approaches, however, some fundamental understanding of the structure of atmospheric turbulence as applied to optical propagation is required.

The turbulent structure of the atmosphere fluctuates in a statistically defined but random manner. A single atmospheric turbulence descriptor is needed in the study of optical propagation through the atmosphere; the three dimensional refractive index spatial power spectrum $\phi_n(\kappa)$.⁽⁸⁾ This function expresses the strength and spatial distribution of the turbulent refractive index fluctuations and has the form

$$\phi_n(\kappa) = 0.033 C_n^2 (\kappa^2 + \kappa_0^2)^{-11/6} \exp[-\kappa/\kappa_m]^2 \quad (1)$$

where C_n^2 = refractive index structure parameter,

L_0 = outer scale

κ_m = inner scale wavenumber, $5.92/\lambda_0$,

and λ_0 = inner scale.

In reality, C_n^2 , L_0 and κ_m are functions of position z along the path, so that $\phi_n(\kappa) = \phi_n(\kappa, z)$. C_n^2 may be considered to represent turbulence strength, whereas L_0^{-1} and κ_m defined the range of applicability of the Kolmogorov spectrum

$$\phi_n(\kappa) = 0.033 C_n^2 \kappa^{-11/3}, \quad L_0^{-1} \ll \kappa \ll \kappa_m. \quad (2)$$

The empirical model for $\phi_n(\kappa)$ in Eq. (1) has been based solely on ground level measurements of the temperature structure function. In fact, for visible and infrared wavelengths, temperature turbulence almost totally governs refractive index fluctuations. Next in order of importance would be humidity fluctuations which are about 10% or less of the total, unless you are propagating near the surface of the water.⁽⁵⁾ Of no direct consequence is wind velocity turbulence, since temperature, humidity and pressure are all that appear in the refractive-index equation.

Implicit in Eq. (1) are the assumptions of isotropy and local homogeneity. Smooth variations in C_n^2 , L_0 and κ_m are allowed, (the behavior of $C_n^2(z)$ in the earth's boundary layer is treated by Wyngaard et. al.⁽¹⁾). The height dependence of L_0 and κ_m are not so well known. Typically $L_0(z)$ is taken as z , \sqrt{z} or $\frac{1}{2}z$; and κ_m is generally assumed to be a constant somewhere between 1 mm and 1 cm. Fortunately, accurate values of κ_m and L_0 are usually not needed. In realistic optics calculations, measurement apertures usually dominate the effect of inner and outer scales. Most measurements involve a large aperture of diameter D-1 to 2 m and a small subaperture of diameter $d > 1$ cm.

When we come to describing phase statistics, we rely heavily on the Rytov method of smooth perturbations, which is a perturbation solution for the wave equation.⁽¹⁾ A single statistical descriptor, the spatial phase structure function, is fundamental to most of the propagation calculations which are affected by phase rather than amplitude variations. The phase structure function D_ϕ is defined in terms of phase at a point $\phi(x)$ as

$$D_\phi(r) = \langle (\phi(x_1) - \phi(x_2))^2 \rangle \quad (3)$$

where $r = |x_1 - x_2|$ indicates an assumption of isotropy as well as homogeneity. Tatarskii⁽¹⁰⁾ has solved the wave equation via the Rytov procedure and provided a relation between the statistics of refractive-index and the desired statistics of phase for a plane wave:

$$D_\phi(r) = 8\pi^2 k^2 \int_0^\infty (1 - J_0(\kappa r)) \kappa \int_0^L \phi_n(\kappa, z) dz d\kappa \quad \begin{matrix} 1 & r \gg \sqrt{\lambda} L \\ \frac{1}{2} & r \gg \sqrt{\lambda} L \end{matrix} \quad (4)$$

where $k = 2\pi/\lambda$ is the wavenumber,
 λ = wavelength,
 and L = path length.

Fried⁽⁴⁾ has solved Eq. (4) to give us

$$D_\phi(r) = 6.88(r/r_0)^{5/3} \quad \begin{matrix} 1 & r \gg \sqrt{\lambda} L \\ \frac{1}{2} & r \gg \sqrt{\lambda} L \end{matrix} \quad (5)$$

$$\text{where } r_0^{5/3} = 0.423k^2 \int_0^L C_n^2(z) dz \quad \frac{1}{2} \quad r \gg \sqrt{\lambda} L \quad (6)$$

Fried's coherence length, r_0 , is the single most dominant parameter used to describe phase degradation in optical propagation.

The effect of r_0 on imaging can easily be demonstrated. Fig. 1 is a simulation showing the short exposure image of a point source for a 60 inch telescope as a function of different values of r_0 . The bar at the top of each frame represents 1 arc sec. As r_0 decreases (turbulence becomes stronger) the point spread function becomes wider. A Strehl ratio (SR) is also given for each image, quantifying the degradation.

Astronomers have attempted to use the random nature of atmospheric turbulence to overcome poor seeing. The classical approach to obtaining high resolution images using ground based telescopes is to take a multitude of short exposure images and hope to obtain a few frames of data when seeing is best. As Fried points out in a companion paper⁽³⁾ the probability of obtaining a high resolution image using this approach is extremely low. His results show that the probability of obtaining a good short exposure image is

$$\text{Prob} = 5.6 \exp[-0.1557(D/r_0)^2], \quad (\text{for } D/r_0 \geq 3.5), \quad (7)$$

where D is the aperture diameter. A good image is defined as one for which the rms wavefront distortion over the aperture is one radian or less. Using this relationship the probability of getting a good image is about 2.5×10^{-3} when $D/r_0 = 7$, it is only 1×10^{-6} when $D/r_0 = 10$ and 3.5×10^{-15} when $D/r_0 = 15$. The message then becomes that if we are to avoid unreasonably long waiting times the telescope aperture must be matched to the atmospheric conditions. For example, in the case above for a probability of 2.5×10^{-3} , (taking a typical value of $r_0 = 10$ cm) the telescope diameter can be no larger than 70 cm.

Even if one were willing to pay the penalty of waiting the prescribed time and use of modest size apertures, this random technique is severely limited to high brightness objects. The exposure times must be shorter than the atmospheric time constant (approximately 1 to 10 millisecc). For low brightness objects the exposure time must be increased in order to produce a recordable image. Since the atmosphere is behaving in a random manner, severe blurring occurs at times longer than a time constant. For astronomical applications where exposure times of many seconds or

minutes may be required, atmospheric averaging always limits resolution even for the smallest aperture telescopes.

A number of approaches to overcoming the limitations of the atmosphere have been described in the literature.^(1,6,9) Most have involved the use of interferometric detection where the output is unfortunately only the autocorrelation function rather than a standard image. While these approaches have shown excellent results for point sources they are severely limited for extended objects. We have developed an approach called Compensated Imaging which will overcome the atmospheric limitations and the drawbacks associated with interferometric detection.

2. COMPENSATED IMAGING

Compensated Imaging is an approach which allows the retrieval of low contrast information by active adaptation of the telescope system to atmospheric conditions. This is accomplished through the use of real time wavefront sensing coupled with rapid response deformable optics. In practice, the wavefront entering the telescope is measured to determine its wavefront deformation (optical path length differences across the aperture) and a mirror is then deformed to the conjugate of the deformations, producing a near diffraction limited image on a sensor.

2.1 General Description.

The basic elements of the system are shown in Fig. 2. The light entering the telescope is first collimated and reflected off a deformable optic and then reimaged onto a wavefront sensor. The optical path length changes are sensed by the detector system and computations performed to reconstruct the wavefront distortions. Signals are fed to a deformable mirror in order to produce the conjugate deformations. Since the deformable optic is the first element in the system the wavefront sensor measures errors in the deformable mirror as well as the entering wavefront and the system operates in a closed loop fashion. Part of the beam is split off and sent to an imaging sensor. Wavefront sensing and correction are accomplished within an atmospheric time constant. The changes in the wavefront are corrected as they occur, allowing long exposure, high resolution images to be obtained.

The basic concept of wavefront correction is illustrated in Fig. 3. A wavefront (a) distorted by atmospheric turbulence enters an aperture of diameter D . The wavefront may have a gross tilt (as indicated by the dashed line) as well as fine scale deformations. The aperture may then be divided into subapertures of diameter d . If a piston like correction is made for each subaperture in order to normalize the wavefront to some mean level (as indicated by the solid line), a correction results as shown in (b). The wavefront still contains significant errors due to the fact that each subaperture may be tilted with respect to the aperture plane. If x and y tilt corrections are made for each subaperture, a final compensated wavefront is produced as shown in (c). This example refers to separate piston and tilt corrections, in reality by using a continuous deformable mirror the two corrections are achieved simultaneously. The concept of piston and tilt however lends itself to analysis as indicated in later discussions.

Certain advantages can be accrued in terms of dynamic range requirements if the gross tilt of the overall wavefront is removed first before piston and tilt correction are attempted. The gross tilt can represent several radians of phase difference from edge to edge but it changes relatively slowly. Removal of the gross tilt can therefore ease the dynamic range requirement of the deformable mirror.

2.1.1 Analysis of Piston and Tilt Requirements.

The requirements for subaperture size and piston and tilt correction range can be determined from a consideration of the spatial and temporal statistics of a propagated wavefront.

Based on the previously presented atmospheric analysis we can obtain the temporal phase statistics from the spatial by making the assumption of frozen flow, or Taylor's hypothesis, which says that in a differential section of the atmosphere transverse to the path

$$\phi(x, t + \tau) = \phi(x - v\tau, t) \quad (8)$$

where v is the transverse wind velocity.

The most important statistical quantity which describes spatial and temporal behavior simultaneously is the phase-difference power spectrum $W_{\delta\phi}(r, f)$. The phase-difference spectrum is the temporal Fourier transform of the spatiotemporal phase structure function $D_{\delta\phi}(r, \tau)$, where $D_{\delta\phi}$ is defined as

$$D_{\delta\phi}(r, \tau) = \langle (\phi(x, t) - \phi(x+r, t)) (\phi(x, t+\tau) - \phi(x+r, t+\tau)) \rangle. \quad (9)$$

After expanding Eq. (9) into four terms, using the definition of D_{ϕ} and the assumption of frozen flow we have

$$D_{\delta\phi}(r, \tau) = -D_{\phi}(v\tau) + \frac{1}{2}D_{\phi}(r+v\tau) + \frac{1}{2}D_{\phi}(r-v\tau). \quad (10)$$

After the temporal Fourier transform is done, we have

$$W_{\delta\phi}(r, f) = 0.1305 r^{-8/3} k^2 \int_0^L dz C_n^2(z) \tau(z)^{5/3} \sin^2 \frac{\pi r f}{v(z)} \quad (11)$$

where we have assumed $f \ll v/\sqrt{\lambda L}$ and r parallel to v .

Although D_ϕ and $W_{\delta\phi}$ are sufficient in themselves to describe the spatio-temporal aspects of a plane wave propagated in turbulence, they are not normally used to describe system performance as they stand. Invariably they undergo some spatial integration since the receiver or imaging optics are of finite extent. The particular case of interest to us is the calculation of power spectral densities which describe the motion of elements in a predetection compensation system. We are treating a segmented system, where the aperture plane is subdivided into an array of circular segments, each adjustable to match the mean and slope of the wavefront. This model is a close approximation to the much more difficult problem of a deformable, continuous mirror.

The general form⁽⁷⁾ for the power spectra of the mean phase and tilt on individual segments is

$$F(f) = -\frac{1}{2} \int W_{\delta\phi}(r, f) T(r) dr, \quad (12)$$

where $T(r)$ is a generalized transfer function, dependent on segment diameter d and segment location r_1 within the telescope of diameter D . We have considered the option of removing overall tilt and have found this removal reduces drive distances significantly, although it does not affect overall bandwidth requirements. In addition, $T(r)$ takes on different forms depending on whether we are considering mean phase ("piston") or tilt; and the behavior of tilt is a function of the orientation of the tilt oscillation axis with respect to r_1 .

A detailed description of the transfer function and the individual power spectra obtained from $T(r)$ is not appropriate here. Rather we shall review the salient results. To establish the size of a piston, or piston with tilt capability, to be used, we evaluated the rms values of residual phase error as a function of piston size:

$$\begin{aligned} \sigma_\phi(d) &= 1.037(d/r_0)^{5/6} && \text{(piston only)} \\ \sigma_\phi(d) &= 0.376(d/r_0)^{5/6} && \text{(piston with tilt)} \end{aligned} \quad (13)$$

(Actually σ_ϕ is also a function of position within the segment itself, and the values in Eq. (13) represent properly weighted averages over that position variable.) For example, if we have a system complete with piston and tilt correctors, then for a goal of $\sigma_\phi \leq 2\pi/10$, the segment diameter is $d \leq 1.85r_0$.

Equation (13) may also be used to evaluate expected excursion distances over the whole aperture, if we let $d \rightarrow D$. The piston condition now becomes the case of overall tilt left in, whereas piston/tilt now refers to overall tilt removed. For example, if we take the average $r_0 = 0.11$ m reported by Fried and Mevers⁽²⁾ and a telescope of diameter $D = 1.6$ m, then $\sigma_\phi(D) = 1.54(2\pi)$ rad for overall tilt left in, and $\sigma_\phi(D) = 0.557(2\pi)$ rad for overall tilt removed.

A similar equation is found for tilt of a segment, in that

$$\sigma_\alpha(d) = 0.429(d/r_0)^{5/6}(\lambda/d), \quad d \gg \lambda_0. \quad (14)$$

For example, if $d/r_0 = 1.85$, we find $\sigma_\alpha d/\lambda = 0.716$. The quantity $\sigma_\alpha d/\lambda$ is the displacement of one edge of a segment with respect to the other side in terms of number of wavelengths.

Equation (14) also applies to the overall tilt corrector, if we simply replace d with D . If we again use $r_0 = 0.11$ m and $D = 1.6$ m, we find $\sigma_\alpha(D)D/\lambda = 4.00$. Obviously, the amount of overall tilt greatly exceeds both local tilt (which was 0.716 waves) and piston for overall tilt removed (which was 0.557 waves).

A system designer should consult the exact forms of the power spectra before deciding upon what type servo should be employed. However, we can make some general statements as to what bandwidths will be needed. For piston drives, the cutoff frequency is typically $v/(\pi d)$, where v represents the highest value of transverse velocity within regions of significant turbulence. For tilt on a segment, the cutoff is roughly v/d ; whereas overall tilt must respond up to v/D .

2.1.2 Simulation Results.

A pictorial representation of the effect of piston and tilt correction as a function of the number of subapertures is shown in a computer simulation furnished by B. McGlamery of the Visibility Laboratory of Scripps Institute.

Fig. 4 is a computer generated phase map representing a 60 inch square aperture. The phase change is equal to 2π radians as represented by the change from light to dark in the phase map. The effect of this phase map on the image of a point source is shown in Fig. 5. The bar represents one arc sec. Since the phase over the entire aperture has been removed in Fig. 5 (as well as in Figs. 6 and 7), the zero value of phase now corresponds to the interface between black and white in the phase map. Two series of simulations were performed. The first series represents piston correction only, as a function of the number of segments (Fig. 6). The aperture was divided into 4, 9, 16, 25 and 49 segments and piston corrections made and images generated. In the second series of simulations (Fig. 7) the aperture was divided as before but both piston and tilt corrections made. It is immediately apparent that the piston and tilt correction provides a sharper image with less segments than piston only. By the time 49 segments are reached the image degradation is almost totally corrected as seen by the uniformity of the phase map and the sharpness of the image.

2.2 Wavefront Sensing and Correction Techniques.

Conceptually, Compensated Imaging is an approach which can completely overcome the degrading effects of atmospheric turbulence. In practice, however, the degree of success depends entirely on the ability to sense optical path length differences in the wavefront and compute and execute conjugate deformations in an adaptive optic.

2.2.1 Deformable Optics.

Over the past several years a high degree of success has been achieved in implementing deformable mirrors. The standard approach has been to use piezoelectric drivers attached to the rear surface of a solid mirror. Fig. 8 shows a diagram of a typical configuration. As voltage differences are applied between the addressing electrodes and the common electrode, the piezoelectric ceramic expands causing deformations in the mirror surface. Fig. 9 is a mirror based on this configuration which was built by Itek Corp. The mirror has a 2 inch active surface with 21 addressing electrodes.

The response of this 21 electrode mirror to various voltages and voltage combinations across the mirror is shown in Fig. 10, through the use of interferograms. Fig. 10a is a steady state condition with no voltage applied. Fig. 10b, c, and d show the results of applying various voltage combinations across the mirror.

Mirrors have been demonstrated with bandwidth capabilities in the range of hundreds of Hertz and surface deformation capabilities of \pm several waves. These capabilities are more than adequate for use in a Compensated Imaging System for astronomical observations.

2.2.2 Wavefront Sensing.

The most critical aspect of Compensated Imaging is the ability to sense the wavefront deformations. This is particularly true when using objects of low brightness where limited photons are available. The requirements for a wavefront sensor are: high optical efficiency, response times faster than the atmospheric time constant (on the order of 10 millisecc) and sensitivity to wavefront changes of finer than $1/10$ wavelength. Of all of the approaches investigated, there are two techniques which appear to possess the necessary capabilities: Interferometric detection and Hartmann sensing.

2.2.2.1 Interferometric Detection

The wavefront sensing techniques which has been investigated the furthest is the white light shearing interferometer. As illustrated in Fig. 11, the incoming wavefront is focused on a phase grating such that the light is diffracted into the \pm 1st order, a lens, then recollimates the light and causes the two orders to overlap. A fringe pattern is generated within the area of overlap of these sheared wavefronts. An array of detectors is placed within the overlap region and the changes in fringe pattern detected as they occur. In practice two shears are detected separately (x and y) in order to reconstruct the two dimensional deformations occurring across the wavefront.

The radial phase gratings in the identical x and y channels are of low spatial frequency and form two overlapping first-order sidebands. Only the first-order sidebands are present due to the use of a grating which has a sinusoidal amplitude transmission with a zero bias level; this ensures high fringe modulation.

The shear distance is proportional to the angular separation of the first-order sidebands which is controlled by the grating frequency. Using a radial grating, the shear is continuously adjustable by moving the center of rotation relative to the optical axis. The interferometer is inherently achromatic due to the use of symmetrical diffraction orders.

The lateral shear interference pattern produced by the overlapping sidebands falls on the detector array which is placed at an image plane of the wavefront corrector. Each detector element corresponds to a sub-aperture of the incoming wavefront over which the wavefront tilt is measured. Rotation of the grating produces intensity modulation

of each element of the interference pattern. The phase of the alternating current signal picked up by each element of the x or y detector array is then proportional to the average tilt of the wavefront (i.e. optical path difference divided by shear distance) in the x or y direction over the corresponding subaperture of the incoming wavefront, using a fixed phase reference obtained directly from the grating. These output tilt measurements are generated simultaneously over the whole aperture, each detector element having its own hard wired output. The optical path length changes are then fed to the deformable mirror for correction of the wavefront.

2.2.2.2 Hartmann Sensing.

The Hartmann sensing approach is analogous to the standard Hartmann test. Fig. 12 illustrates the approach. The incoming wavefront is divided into a series of subapertures by an array of lenslets. Each lenslet focuses the light onto the surface of a centroid detector. Each subaperture is small enough that the portion of the wavefront it senses appears to be undistorted except that its angle of arrival (tilt) with respect to the subaperture is changing as a function of time. By sensing the direction and magnitude of change, by using some form of centroid tracker for each subaperture, the wavefront deformations for the whole aperture can be reconstructed.

High sensitivity can be achieved in this approach by using photon counting detectors. Each detector outputs x and y coordinates. The output of each detector is fed to a computer which then reconstructs the entire wavefront and sends commands to the deformable mirror.

3. SUMMARY AND CONCLUSIONS

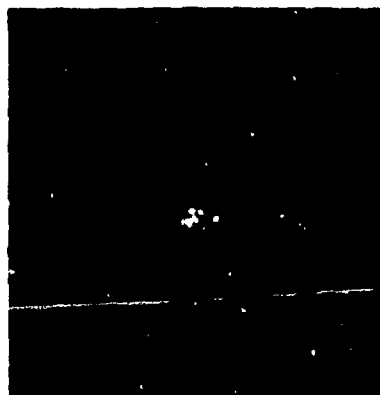
For a Compensated Imaging System the degree of complexity is dependent on the structure of atmospheric turbulence. The number of detectors in the wavefront sensor must be sufficient to adequately sample the deformations and the number of corrector elements must likewise be sufficient to provide adequate spatial correction. The dynamic range of the corrector and the required frequency response is also tied to the statistics of turbulence. The importance of understanding atmospheric effects is obvious. Significant emphasis has already been placed on experimental and theoretical investigations of the structure of turbulence and the statistics of optical phase fluctuations. In summary, the atmospheric constraints for astronomical applications are mirror excursion capabilities of 3-4 wavelengths rms with a bandwidth of approximately 100 Hz (for an $r_0 = 10$ cm).

Efforts are now progressing to thoroughly analyze and experimentally verify the operation of interferometric and Hartmann sensing techniques. Emphasis is being placed on defining the S/N limitations and sensitivities of these techniques in order to define the optimum approach.

The advantages of an adaptive system for removing the degrading effects of atmospheric turbulence are obvious. Efforts have progressed to define the requirements of such a system and to determine the optimum configuration. Mirror technology is adequate to support the development of a large aperture compensated imaging system and wavefront sensing approaches are being thoroughly investigated. It remains now to implement and operate a full scale system. This occurrence will surely be a major breakthrough in astronomical imaging.

- (1) Dainty, J. C., February 1973, "Diffraction-Limited Imaging of Stellar Objects Using Telescopes of Low Optical Quality", Optics Communications, Vol. 7 No. 2, 129-134.
- (2) Fried, D. L. and G. E. Mevers, 1974, Appl. Opt., 13, 2620.
- (3) Fried, D. L., October 1975, "How Many Pictures Do You Have to Take to Get a Good One", Technical Meeting of the AGARD Electromagnetic Wave Propagation Panel on Optical Propagation in the Atmosphere.
- (4) Fried, D. L., 1967, Proc. IEEE, 55, 57.
- (5) Frieke, C. A. and J. C. LaRue, July 1974, Digest, Topical Meeting on Optical Propagation Through Turbulence, O.S.A., paper WB2.
- (6) Gezari, D. Y., A. Labeyrie and R. V. Stachnik, April 1972, "Speckle Interferometry: Diffraction-Limited Measurements of Nine Stars with the 200-Inch Telescope", The Astrophysical Journal, 173, L1-L5.
- (7) Greenwood, D. P. and D. L. Fried, July 1974, Digest Topical Meeting on Optical Propagation Through Turbulence, O.S.A., paper Th B3.
- (8) Greenwood, D. P. and D. O. Tarazano, Feb 1974, A Proposed Form for the Atmospheric Micro-Temperature Spatial Spectrum in the Input Range, Rome Air Development Center, Griffiss AFB NY, RADC-TR-74-19.
- (9) Korff, D., G. Dryden and M. Miller, June 1972, "Information Retrieval from Atmospheric Induced Speckle Patterns", Optics Communications, Vol. 5, No. 3, 187-192.
- (10) Tatarskii, V. I., 1971, The Effects of the Turbulent Atmosphere on Wave Propagation, U.S. Dept. of Commerce, Washington, DC, NTIS #T68-50464.
- (11) Wyngaard, J. C., Y. Izumi and S. A. Collins, Jr., J. Opt. Soc. Am, 61, 1646.

$r_0 = .2 \text{ m}$
 $SR = .064$



$r_0 = .1 \text{ m}$
 $SR = .024$



$r_0 = .05 \text{ m}$
 $SR = .010$



Fig.1 Effect of variations in r_0 on instantaneous point source images

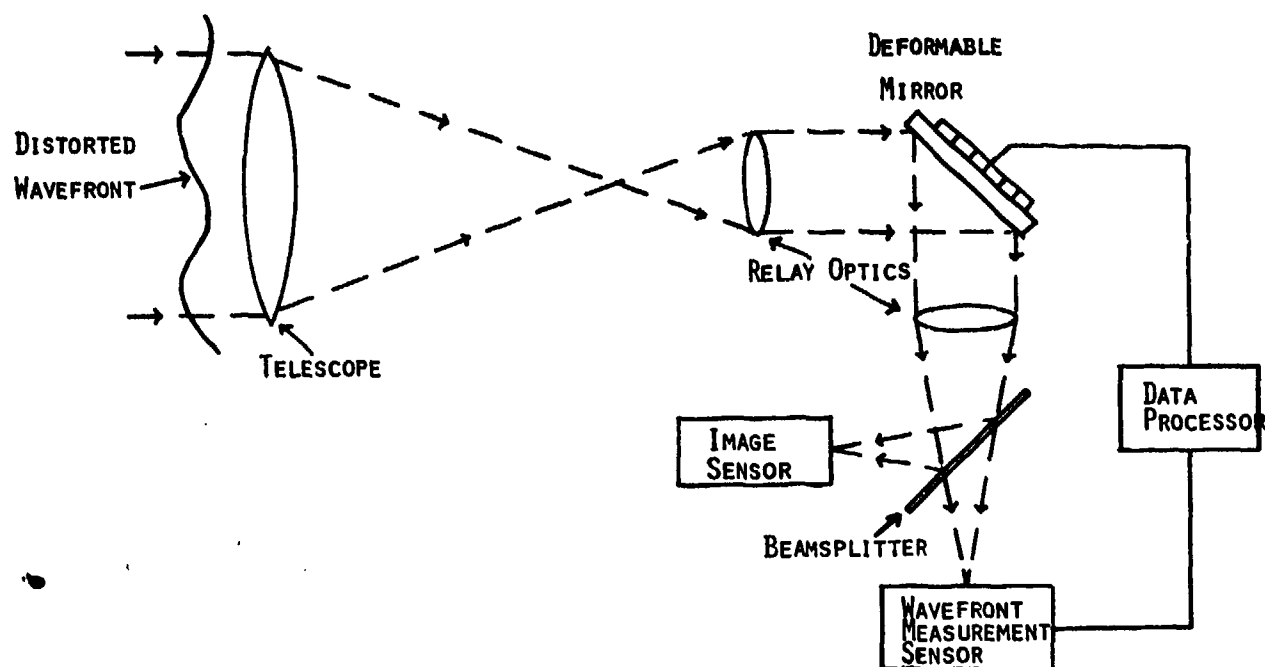


Fig.2 Compensated imaging system block diagram

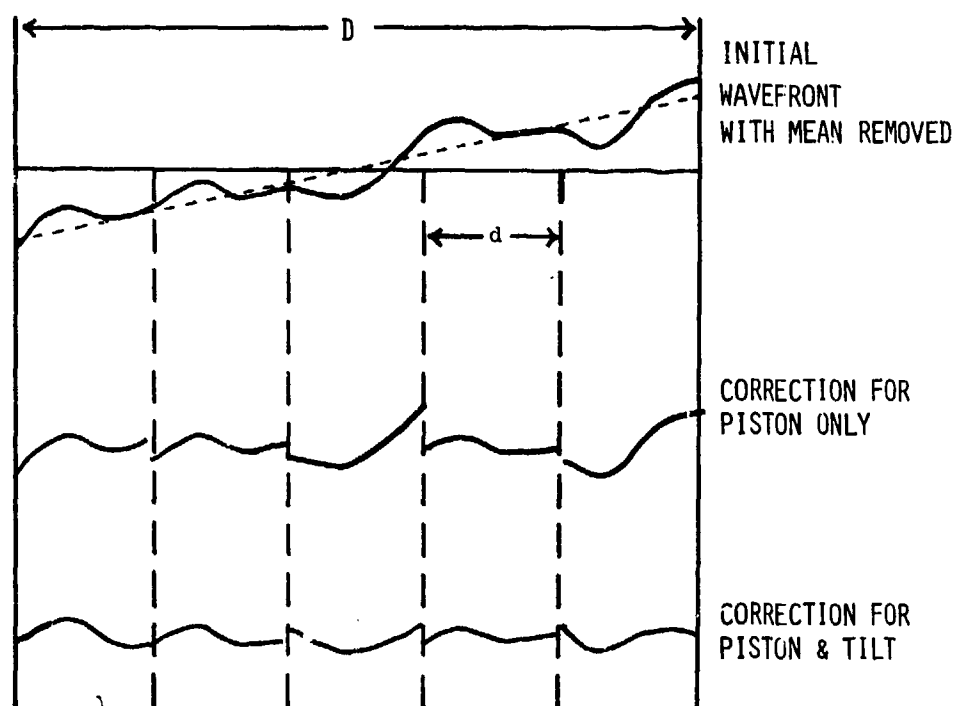


Fig.3 Wavefront compensation

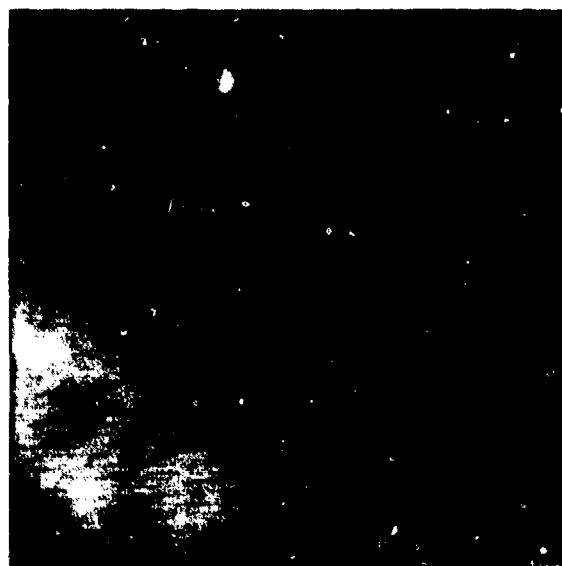


Fig.4 Computer generated phase map

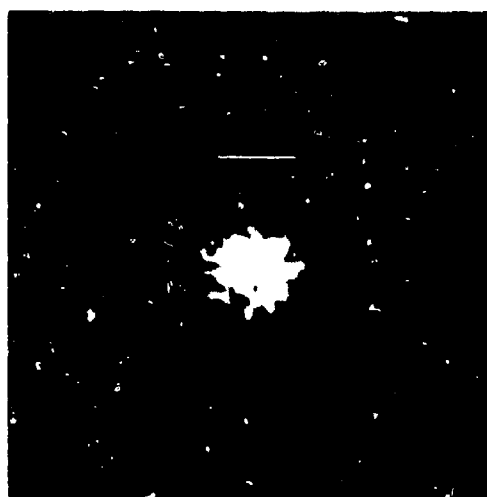
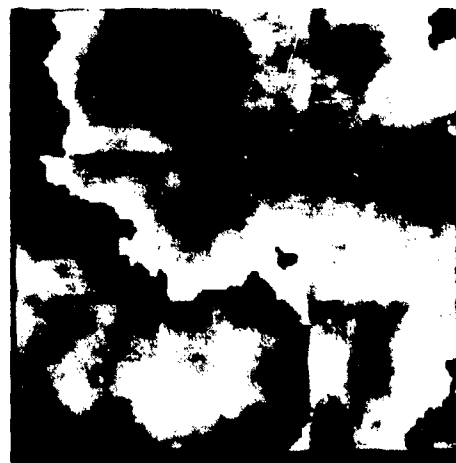
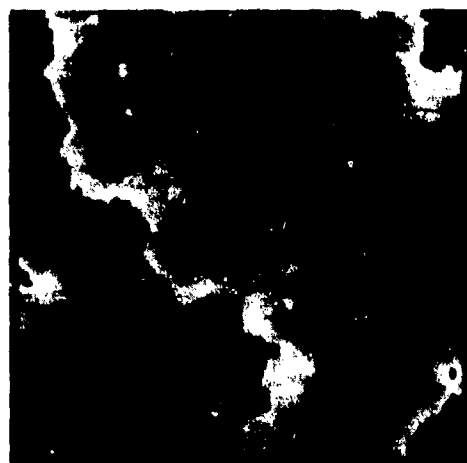


Fig.5 Phase map with resulting point source image



4

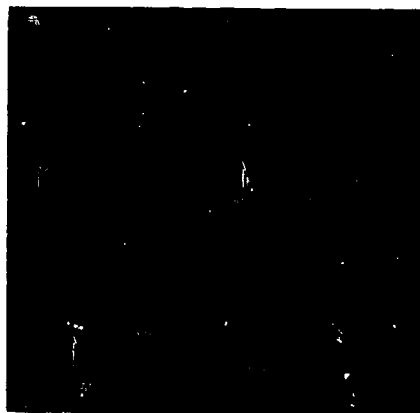
9



Fig.6(a) Simulation - piston correction only



16



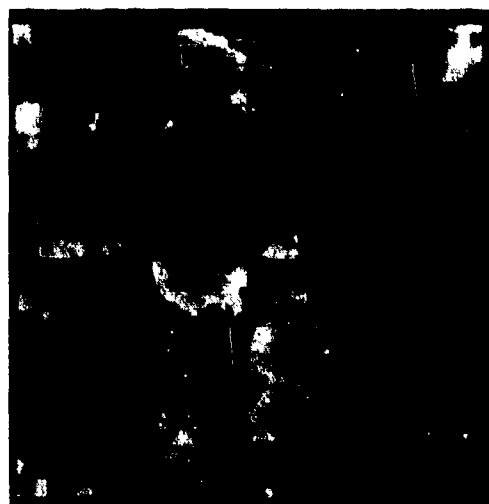
25



49



Fig.6(b) Simulation - piston correction only



4



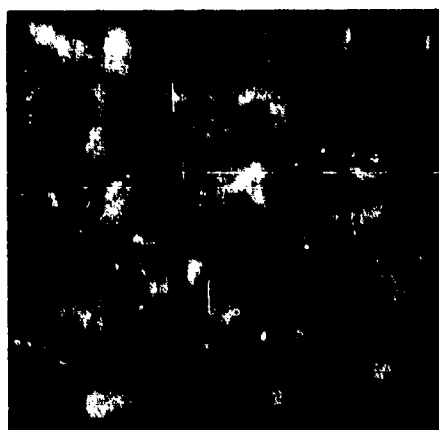
9



Fig.7(a) Simulation - piston and tilt correction



49



25



16



Fig.7(b) Simulation - piston and tilt correction

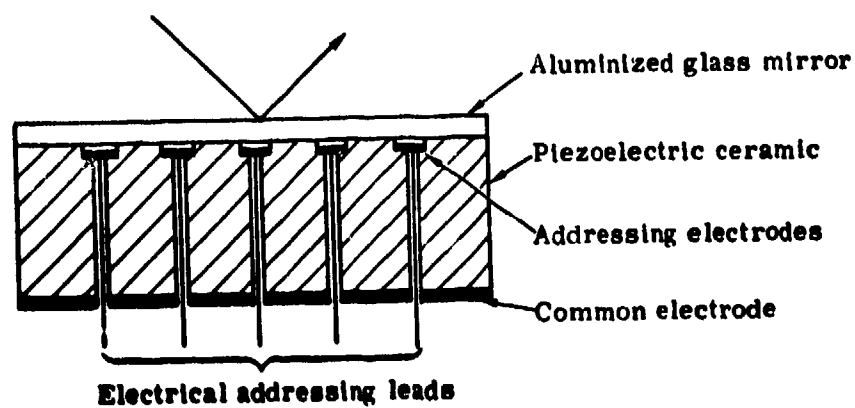


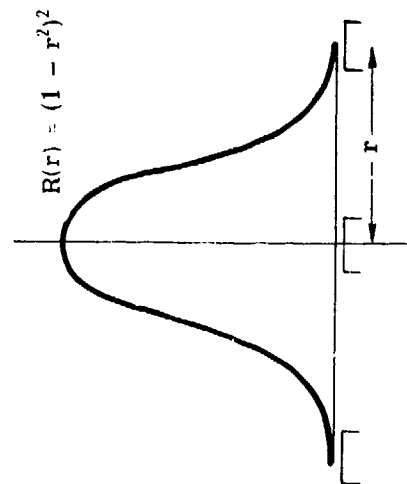
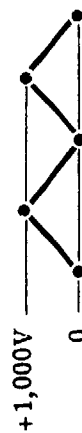
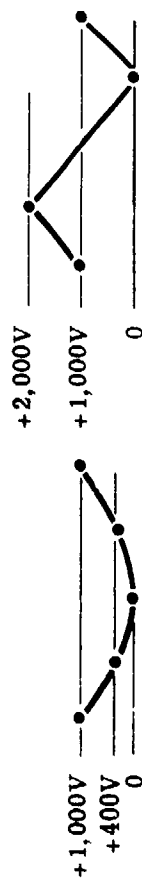
Fig.8 Layout - piezoelectric driven mirror



Fig.9 Monolithic piezoelectric mirror (MPM)



Zero volts



Response function sensitivity:
9.6 micrometer per kilovolt

Fig.10 Response of 21 element MPM to voltage gradients

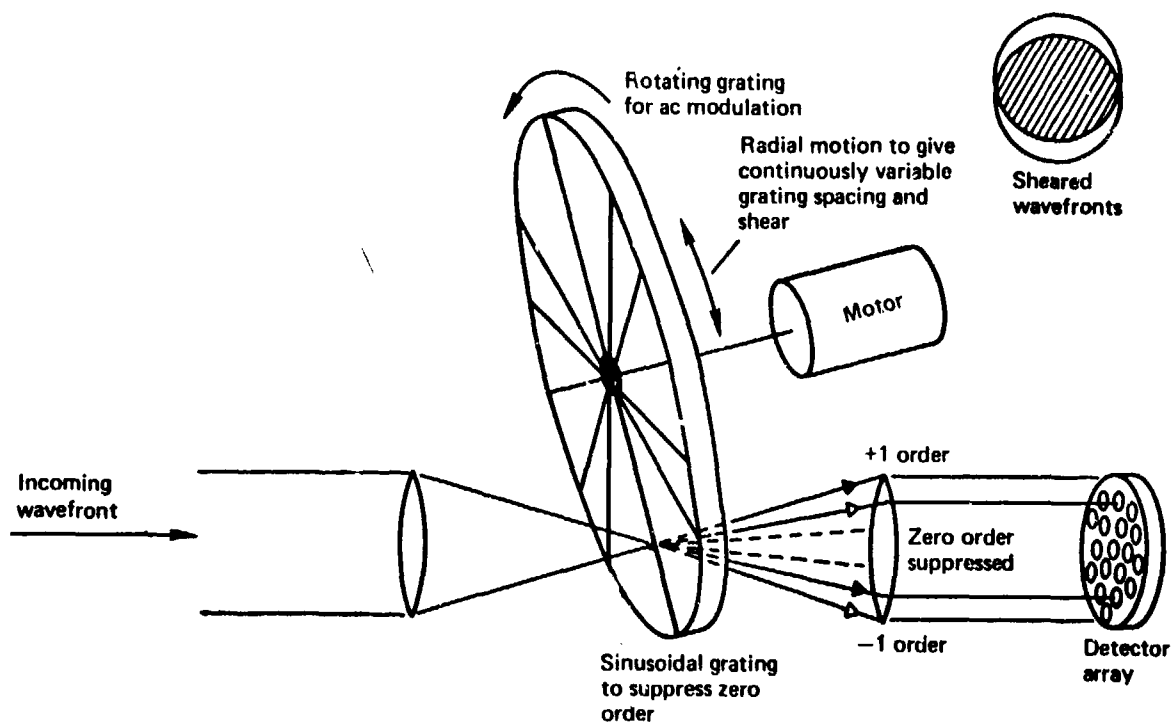


Fig.11 Interferometric sensor

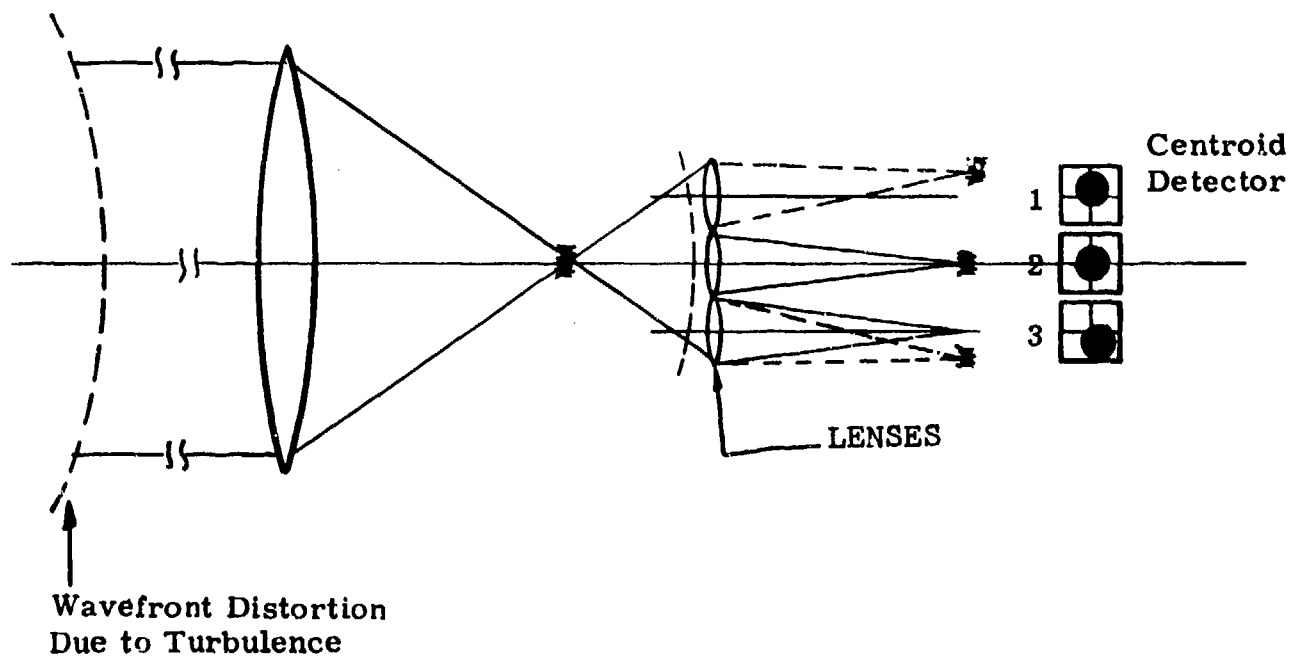


Fig.12 Hartmann sensor

DETERMINATION OF SLANT VISUAL RANGE FROM LIDAR SIGNATURES,
ANALYSIS OF SIMULATED SIGNATURES

Mario Gazzi and Vittorio Vicentini

C.N.R. Istituto di Fisica dell'Atmosfera, sez. Microfisica,
 Via de' Castagnoli 1, Bologna, Italy

Luca Pantani, Bruno Radicati and Leopoldo Stefanutti

C.N.R. Istituto di Ricerca sulle Onde Elettromagnetiche,
 Via Panciatichi 64, Firenze, Italy

Christian Werner

D.F.V.L.R. Institut für Physik der Atmosphäre
 Oberrpfaenhofen, Obb., Federal Republic of Germany

SUMMARY

The measurement of the slant visual-range by means of lidars involves two main problems: the extraction of the atmospheric extinction-coefficient from the lidar signature and the calculation of the slant visual-range from the extinction coefficient. The authors tried to solve these problems in the particular situation of a landing in low visibility conditions. An equation was obtained which allows the computation of the visual range from the extinction coefficient in every hour of the day both for extended and point sources. In order to compare the different methods for the extraction of the extinction coefficient from the lidar signatures some atmospheric situations were simulated on a computer and the lidar equation was calculated. The simulated signatures were then processed by different methods and the result were collated. At the end of the paper a new procedure for the processing of lidar signatures is introduced.

1. INTRODUCTION

A careful measurement of slant visibility becomes every day more important for safe and regular aircraft landing operations. Lidars are particularly suitable for slant visibility measurements since from their signatures information on each point of the atmosphere may be obtained. The problem of slant-visibility measurements by means of lidars can be divided in two steps:

- 1) The extraction of the atmospheric extinction-coefficient σ from the lidar signature.
 - 2) The calculation of the actual slant visual-range from σ and other atmospheric data.
- Step 1 involves only physical problems while step 2 involves also physiological problems.

Up to now attention was preferably given to the σ extraction and the visibility was then computed by means of simple and not always valid equations. Different methods were suggested for σ extraction from lidar signatures, unfortunately they sometimes give different results when they are applied to the same lidar signature (Herrmann H. et al. 1974). The authors considered therefore advisable from one side to investigate for a more actual relation between σ and the visual range, on the other side to simulate different atmospheric situations and to verify on such models the validity of the different methods of σ extraction.

2. VISIBILITY IN LANDING OPERATIONS

In our opinion a general equation connecting σ and the actual visual-range is very difficult to obtain but the problem can be solved in the restricted situation of a landing in low visibility conditions.

When the visibility is low, the ILS is used. This device gives an electromagnetic glide-path which is instrumentally followed by the plane. Nevertheless there is always a point of the glide path below which the inaccuracy of the ILS is too high and the landing has to be carried on by means of visual references which indicate to the pilot the position and direction of the runway. For a safe and regular landing the pilot has to see the visual references before the plane will reach the critical point of the landing class. Since the distance between the references and the critical point is

in the range of hundreds of metres the radiation attenuation is completely due to the scattering by fog. A high luminance light is visible in a fog bank at a distance higher than any other reflecting or luminous target (Olivier J., 1955); the pilot references will be than the airport lights (Fig.1) and not the runway or any signal painted on it. A safe landing does not require the vision of all the airport lights, but the first light-bar of the approach path, at least, has to be clearly seen from the critical point. In practice it is necessary to measure the visual range of the bar in all the directions between BC and the horizontal one (Fig.2) in order to determine the point of the glide path from which the light bar becomes visible.

Since the target is an high-luminance light and the fog bank has a relevant luminance in the observation direction, also at night because of the airport lights, the presence of the land background can be neglected in every hour of the day. The problem is then reduced to the determination of the luminance contrast between the target and the fog background, whose luminance may be assumed to be equal to that of the sky at the horizon in the same direction (Konovalov Yu.G. and Ratsimor M.Ya, 1972). The luminance contrast has to be compared with the threshold ϵ below which the eye does not discern the target from the background:

$$\epsilon = \frac{L_t - L_H}{L_H} \quad (1)$$

where L_t is the threshold luminance and L_H the background luminance *. Both point and extended sources have to be taken into account because of the physical size of high-luminance lights and the relatively small visual-ranges involved. In this situation neither Kosmieder's nor Allard's equation (Middleton W.E.K., 1955) can be assumed since the first one takes into account a black object and the second one a point source and a black background. The equation:

$$\frac{I \exp(-\sigma V)}{V^2} = L_H \omega \epsilon \quad (2)$$

was obtained (Gazzi M. et al., 1975) where I is the light intensity, σ the extinction coefficient in the observation direction, V the light visual range, L_H the sky luminance on the horizon in the observation direction and ω the solid angle under which the observer sees the light at a distance V . Equation (2) is valid by day and by night and takes into account both point and extended sources because it contains the Riccò's law (Riccò A., 1877).

When the source is a point one and there is no air-light ($L_H \sim 0$) equation (2) becomes the Allard's equation:

$$\frac{I \exp(-\sigma V)}{V^2} = E_t \quad (3)$$

where $E_t = \omega L_t$ is the threshold illumination of the pupil.

When the source is an extended one ω and I can be expressed as a function of the area A and of the luminance L of the source:

$$\omega = \frac{A}{V^2} \quad (4)$$

$$I = LA$$

equation (2) becomes the well known equation (Olivier J., 1955)

$$\frac{L}{L_H} \exp(-\sigma V) = \epsilon \quad (5)$$

which gives the visual range of an extended light-source.

* The luminance contrast-threshold may be obtained from the experimental graphs of Fig.3 (Blakwell H.R., 1946) where it is plotted as a function of the source angular diameter and the background luminance.

In the previous equations the light parameters, I , A and L may be assumed known and L_H can be independently measured by means of a photometer but the two remaining parameters, σ and ϵ , are functions of V . In fact σ is the average value of the diffusion coefficient over the range $0-V$ in the observation direction:

$$\sigma = \frac{1}{V} \int_0^V \sigma(r) dr \quad (6)$$

and ϵ is an experimental function of m and therefore through equation (5) of V . In this situation a trial-and-error procedure has to be adopted for the computation of V . An approximated analytical expression of the experimental graphs of Fig.3 is necessary for a practical trial-and-error procedure and this is one of our main goals at this moment.

3. SIMULATED LIDAR SIGNATURES FOR THE ANALYSIS OF σ EXTRACTION METHODS

Four models of atmosphere were considered as it is shown on Fig.4 where σ is plotted as a function of the height h . The first three graphs were obtained with the same assumptions: Only Rayleigh scattering was present over $h = 4.5$ km and the visibility at ground was measured by a nephelometer which uses the Kosmieder equation. The following visibilities 40, 20, 10, 7.5, 5.1 Km were considered. The first graph shows a normal atmosphere and the second one a temperature inversion level at, $h = 700$ m. Below the inversion the following equation for σ has been used (Werner Ch., 1972):

$$\frac{\sigma(U_1)}{\sigma(U_2)} = \left(\frac{1 - U_2}{1 - U_1} \right)^{0.34} \quad (7)$$

where U is the relative humidity which was assumed to be 40% and 80% respectively at ground level and at the inversion level. The third graph simulates a cloud between $h = 500$ m and $h = 800$ m with visibilities of 500 m and 100 m inside the cloud. The last graph represents a fog bank which reaches a height of 500 m with visibilities of 1000, 500, and 200 m inside the bank.

When the σ graphs were obtained the backscattering coefficient β was calculated by means the relation:

$$\beta = K_1 \sigma^{1.5} \text{ or } \beta = \frac{0.43}{4\pi} \sigma \quad (8)$$

and an hypothetical ruby lidar was supposed to fire at elevation angles of 90° , 60° , 45° , 30° , 15° . The lidar equation:

$$P(R) = \frac{k\beta(h)}{R^2} \left\{ \exp \left[-2 \int_0^R \sigma(h) dr \right] \right\} = \frac{k\beta(h)}{R^2} \tau^2(R) \quad (9)$$

where R is the range from the lidar, was calculated every 25 m up to 1000 m. The Raman-Lidar equation for N_2 :

$$P_R(R) = \frac{k'\beta_R(h)}{R^2} \exp \left\{ - \int_0^R \sigma(h) dr - \int_R^0 \sigma_R(h) dr \right\} \quad (10)$$

was also calculated with the assumption that the N_2 concentration in the atmosphere depends only on the height h and β_R is given by:

$$\beta_R = 4.94 \times 10^{-7} \left(\frac{5145}{\lambda_{RN_2}} \right)^4 10^{-0.064h} \text{ part/Km.Sr} \quad (11)$$

where λ_{RN_2} is the wavelength at the Raman frequency for N_2 at which the extinction coefficient is σ_R .

The extinction coefficient was finally computed by different methods from the simulated lidar signatures (9) and (10). Four methods were applied:

- The "slope method" (Collin R.T. et alii, 1970)
 - The "Raman slope-method" (Herrmann H. et alii, 1974)
 - The integral solution of the lidar equation (Vieze W. et alii, 1973)
 - The "aerosol-Raman ratio method" (Herrmann et alii, 1974)
- and the following quantities were respectively computed:

$$\sigma_s = - \frac{\lambda \ln B_u(R)}{2\Delta R} \quad (12)$$

for the slope method, with $B_u(R) = P(R)R^2$,

$$\sigma_{Rs} = - \frac{\lambda \ln B_{uR}(R)}{2\Delta R} \quad (13)$$

for the Raman-slope method, with $B_{uR}(R) = P_R(R)R^2$,

$$\sigma_i = \exp aS(R) \left\{ \frac{1}{\sigma_o} - b \int_{R_o}^R \exp [aS(r)] dr \right\}^{-1} \quad (14)$$

for the integral solution, with $S(R) = 10 \log [B_u(R)/B_u(R_o)]$, R_o a fixed value of R , $\sigma_o = \sigma(R_o)$ and $a = 0.15$ and $b = 1.3$ or $a = 0.23$ and $b = 2.0$ depending from which of the (8) was assumed, and

$$\sigma_{aR} = \frac{4\pi P_R K' P(R)}{0.43 K P_R(R)} \quad (15)$$

for the aerosol-Raman ratio.

4. DISCUSSION OF THE DATA EXTRACTED FROM THE SIMULATED SIGNATURES

The results of the simulation procedures were both printed and plotted; for the plotter the function $\Delta\sigma$:

$$\Delta\sigma = \frac{\sigma_v - \sigma_c}{\sigma_c} \cdot 100 \quad (16)$$

where σ_c is the calculated value of σ and σ_v the initial one, was used in order to point out the difference between the different methods (Fig.5 to 13).

The following results were obtained:

In normal atmosphere and high visibility at the ground both the integral solution and the aerosol-Raman ratio method give good results, while the slope method and the Raman slope-method give values of σ higher than the assigned ones. In order to better understand this fact equation (12) may be rewritten as follows:

$$\sigma_s = \frac{\ln \left[\frac{P(R + \Delta R)}{P(R)} \right] - 2\sigma(R)\Delta R}{2\Delta R} \quad (17)$$

When σ is large, the linear term in equation (17) grows much more rapidly than the logarithmic one which can be omitted; the same happens in the slope-Raman equation. Both slope methods become valid where σ is large, this means at low visibility-levels. Under the same conditions the integral method tends to fail giving solutions which tend to diverge. This divergence is not due to limitations of the mathematical solution but to a systematic error introduced in the computation of the integral; in fact when the sampling interval was reduced to 12.5 m and then to 6.25 m the error reduced to about 1/2 and 1/4 respectively. In actual measurements however the sampling interval can not be arbitrary reduced because of the bandwidth of the sampling unit.

Similar considerations can be done for the temperature-inversion results. In

this situation the slope method gives negative solutions for large elevation angles since the logarithmic term is larger than $-\sigma(R) \cdot AR$. The slope method can not be applied in these situations while it tends to give more reasonable results when the visibility and the elevation decrease.

The cloud and the fog bank seem to be more complex situations. The integral solution seems to give bad results in the presence of a sharp discontinuity; the error becomes smaller but still significant also when the sampling interval is strongly reduced. The two slope methods presents the same behaviour as in the previous models.

A method which always gives good results is the aerosol-Raman ratio method. This fact is analytically evident since equation (15) becomes an identity when the analytical expressions (9) and (10) are substituted to $P(R)$ and $P_R(R)$ under the assumption of $\sigma(6943 \text{ \AA}) \sim \sigma(8280 \text{ \AA})$. It can be underlined, however, that this is the only method which can in a first approximation (Herrmann H. et alii, 1974) take into account the multiple scattering. The aerosol-Raman ratio method seems to be the best for σ measurements but it is a quite complicated one in practice because of the low level of Raman signals.

5. AN APPROXIMATED METHOD FOR THE CALCULATION OF THE SLANT VISIBILITY

In addition to what has been pointed out up to now some words may be spent on a new method for the calculation of the slant visibility from lidar signatures. When a lidar is fired into the atmosphere the light is backscattered into the receiver from every point of the propagation path. Since the received light decreases with the range there is always a range R_m beyond which the signal can not be distinguished from the noise:

$$P(R_m) = A \quad (18)$$

where A is the average noise power. From the lidar equation and equation (18) one can obtain:

$$R_m^2 = \frac{K}{A} \beta(R_m) \tau^2(R_m) \quad (19)$$

With the assumption of $\beta = \text{constant}$, which is the same approximation done in the "slope method", equation (19) can be written:

$$R_m^2 = C \tau^2(R_m) \quad (20)$$

where:

$$C = \frac{K}{A} \beta(R_m) \quad (21)$$

and finally:

$$\sigma = \frac{1}{2R_m} \ln \left[\frac{C}{R_m^2} \right] \quad (22)$$

In order to make a rapid first-approximation test of the method the visibility was then computed through the Koshmieder equation:

$$V_N = \frac{7.814 R_m}{\ln \left[\frac{C}{R_m^2} \right]} \quad (23)$$

In Fig.14 V_N versus R_m is plotted with K corresponding to the system constant of the lidar DFVLR V. In the first graph a A was considered constant and equal to the Rayleigh backscattered signal at a height of 1000m; in the second one an average value of $\beta = 5 \cdot 10^{-6} \text{ m}^{-1}$ was considered. The spreading of the curves is small in both cases and the method should give good results at least for low visibility levels.

We carried out a first experiment on September 23rd, 1975 with the lidar firing at an elevation angle of 30° (Fig. 15). The corresponding data of an integrating nephelo-

meter, an infrared radiometer and a sodar are shown on Fig. 16. It can be noticed that the obtained values of visibility are very close to those given at ground level by the integrating nephelometer.

Since R_n is the only data which has to be extracted from the lidar signature the knowledge of the near field signal is not necessary. This is an interesting advantage of this method which can be employed also for the processing of the data of non-monostatic lidars where the near field signal is absent because of the non overlapping between the laser beam and the telescope field of view.

6. CONCLUSIONS

An equation was introduced for the calculation of the actual visual range in low-visibility landing operations. This equation requires the knowledge of the atmospheric extinction coefficient which may be deduced from lidar signatures.

The processing by different methods of simulated lidar-signatures has shown that: the "slope method" and the "Raman slope method" may be employed when the visibility is low while the "integral solution method" may be employed when the visibility is not too low. The "aerosol-Raman-ratio method" gives always good results. Unfortunately this method requires the analysis of low-level Raman-signals and therefore is not a very practical one but may be a good one for test procedures. The method introduced in the last section is an approximated but very simple one and seems to be very useful especially from the point of view of measurement automatization.

Two main problems were not solved and are our main goal for the future. The first one is the analytical approximation of the curves of Fig. 3 and the second one is the influence of multiple scattering on the lidar signal.

7. REFERENCES

- Collis R.T., Viezee W., Uthe E.E., Oblanas J., 1970, "Visibility Measurement for Aircraft Landing Operations", final Report FAA N. DOTFA70WAI-178, Stanford Research Institute, Menlo Park, Cal.
- Gazzi M., Vicentini V., Vittori C., 1975, "Runway Visual Range Evaluation During the 24hr Day", Riv.It. di Geofisica, 2, 3.
- Herrmann H., Pantani L., Stefanutti L., Werner Ch., 1974, "Lidar Measurements of Atmospheric Visibility", Alta Frequenza, 43, 732.
- Konovalov Yu.G., Ratsimor M.Ya., 1972, "Analysis of Visibility Conditions for Aircraft Landing in Radiative Fogs", USSR Gidrometeorologicheskii Nauchno-Issledovatel'skiy Tsentr, Leningrad, Trudy, n.95, 3.
- Middleton W.E.K., 1955, "Vision through the Atmosphere", University of Toronto Press, Toronto
- Olivier J., 1955, "La Visibilité des Sources Lumineuses dans le Brouillard", Bull. Soc.Francaise des Electriciens. 7, 5,56: p.538.
- Ricco' A., 1877, "Relazione tra il minimo angolo visuale e l'intensità luminosa", Modena, Soc. Tipografica Soliani.
- Viezee W., Oblanas J., Collis R.T.H., 1973, "Lidar Evaluation of Fog Dissipation Techniques", AFRL-TR-73-0052, Stanford Research Institute, Menlo Park, Cal.
- Werner Ch., 1972, "Lidar Measurement of Atmospheric Aerosol as a Function of Relative Humidity", Opto-electronics, 4, 125.

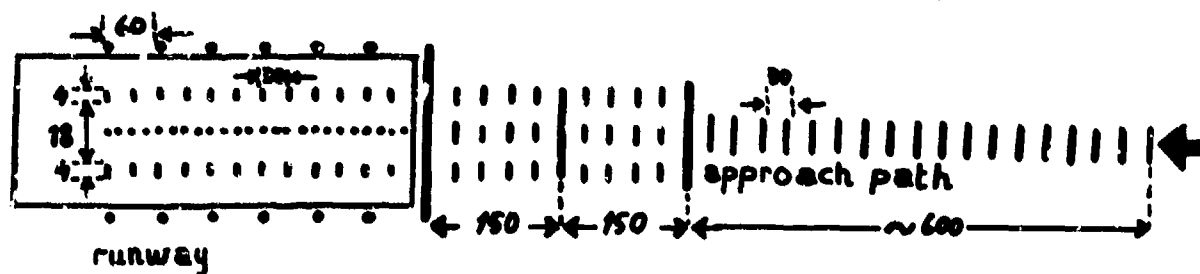


Fig. 1 Example of airport lights. Distances in metres.

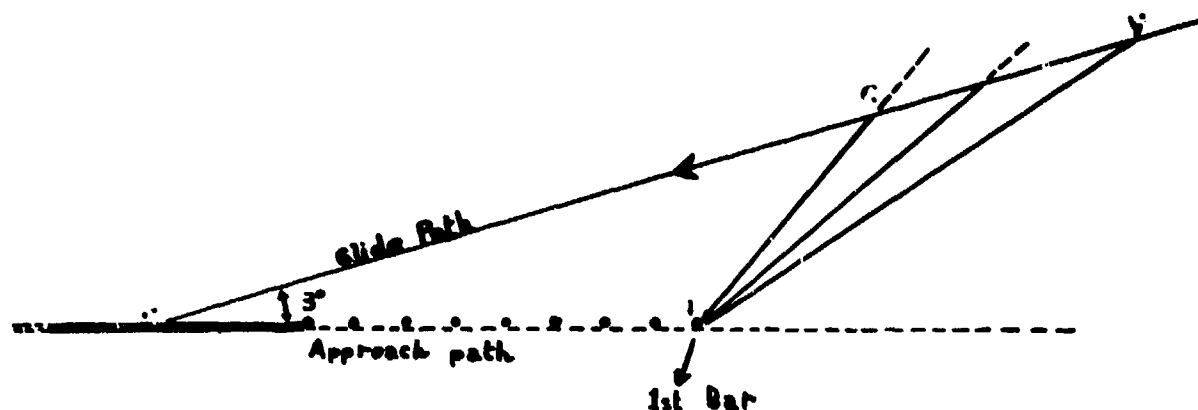


Fig. 2 Vertical section of the landing path. A) contact point. B) First light bar. C) critical point. V) Point of the glide path from which the first bar is visible.

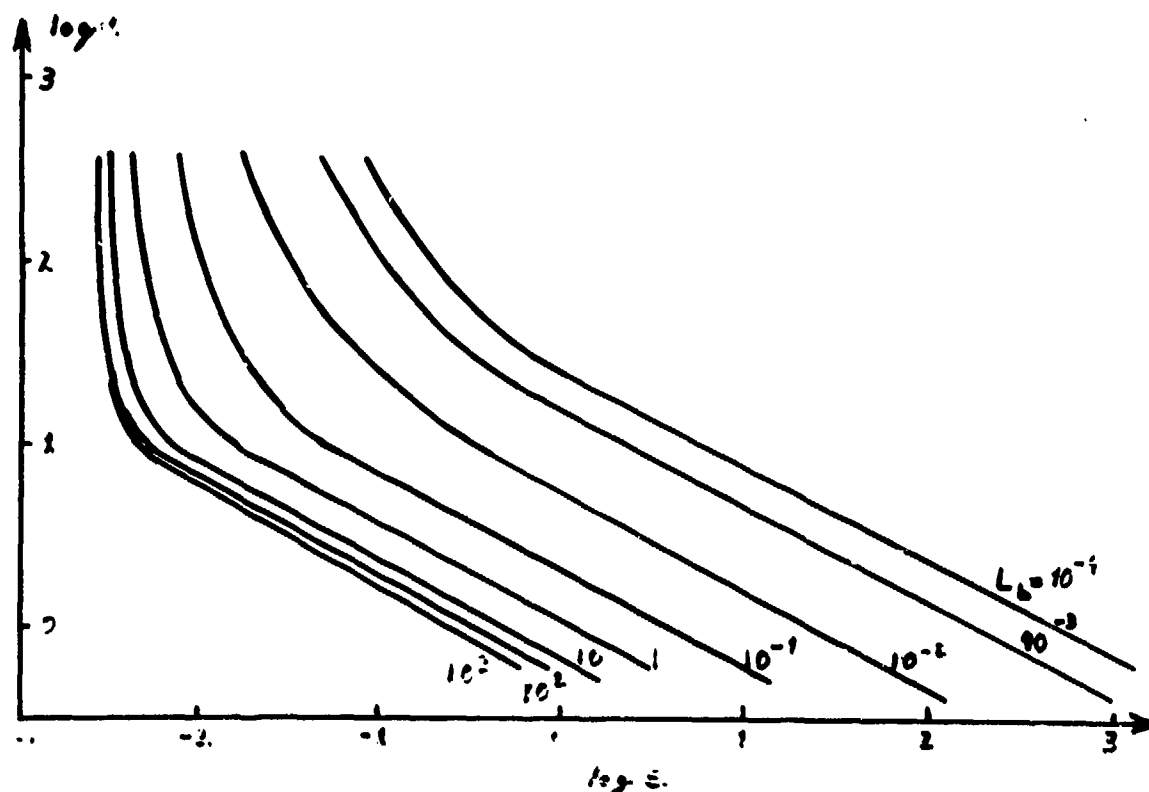


Fig. 3 Contrast threshold (ϵ) as a function of the source angular extension (α) and background luminance L_b .

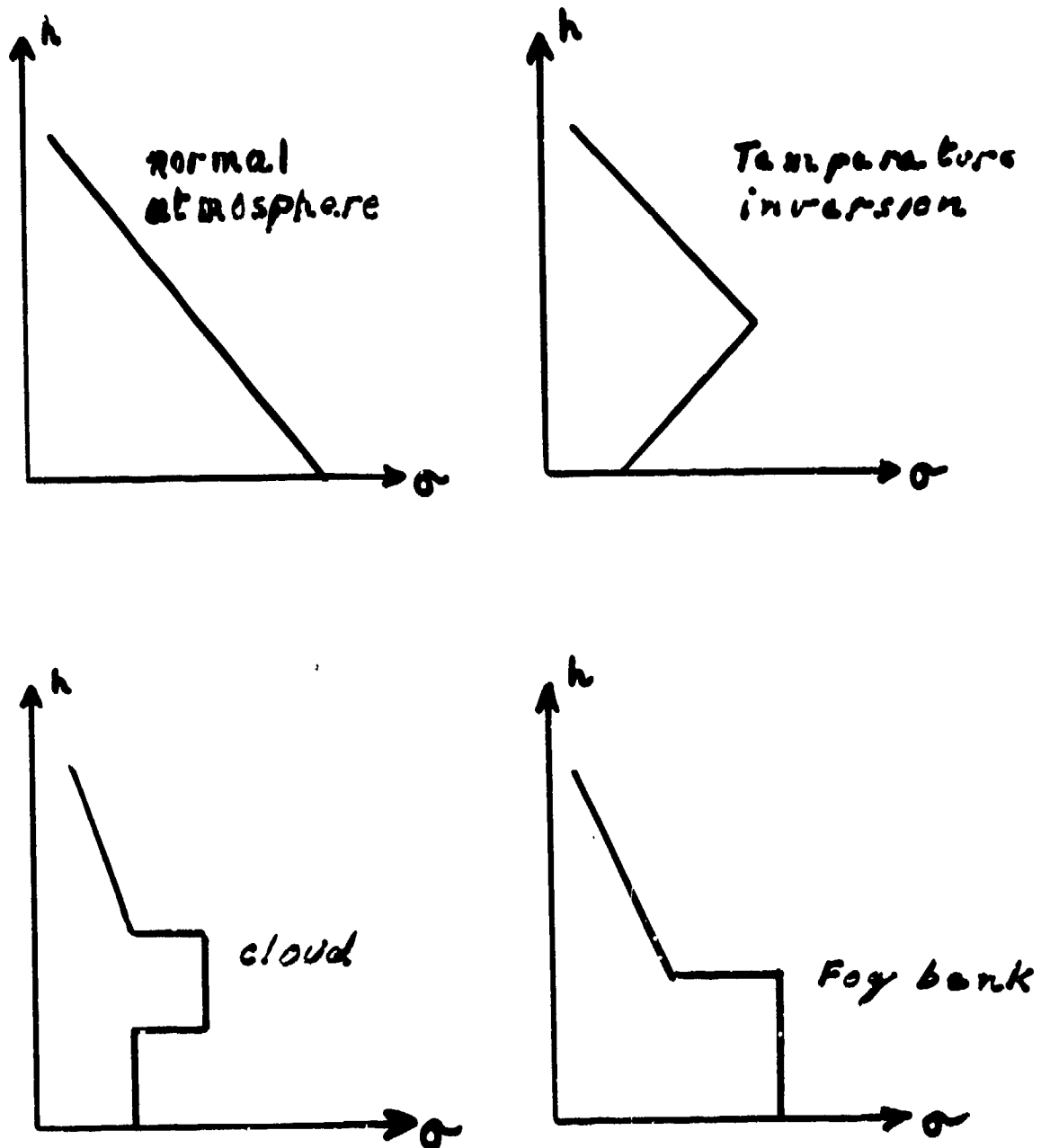


Fig. 4 The four atmospheric situations which were simulated.

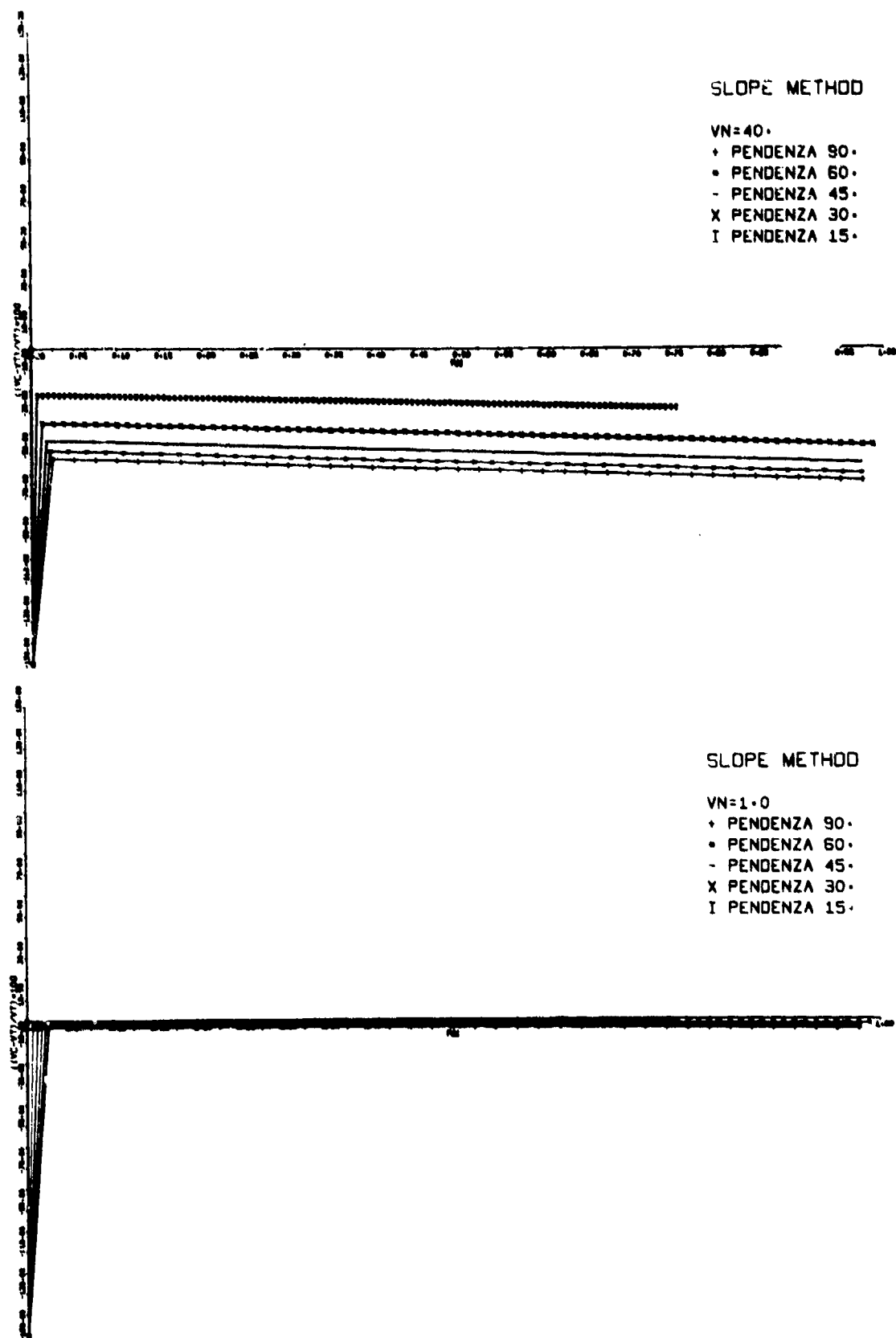


Fig. 5 Processing of normal-atmosphere data by means of the slope method. Visibility at ground: 40 km (top) and 1 km (bottom).

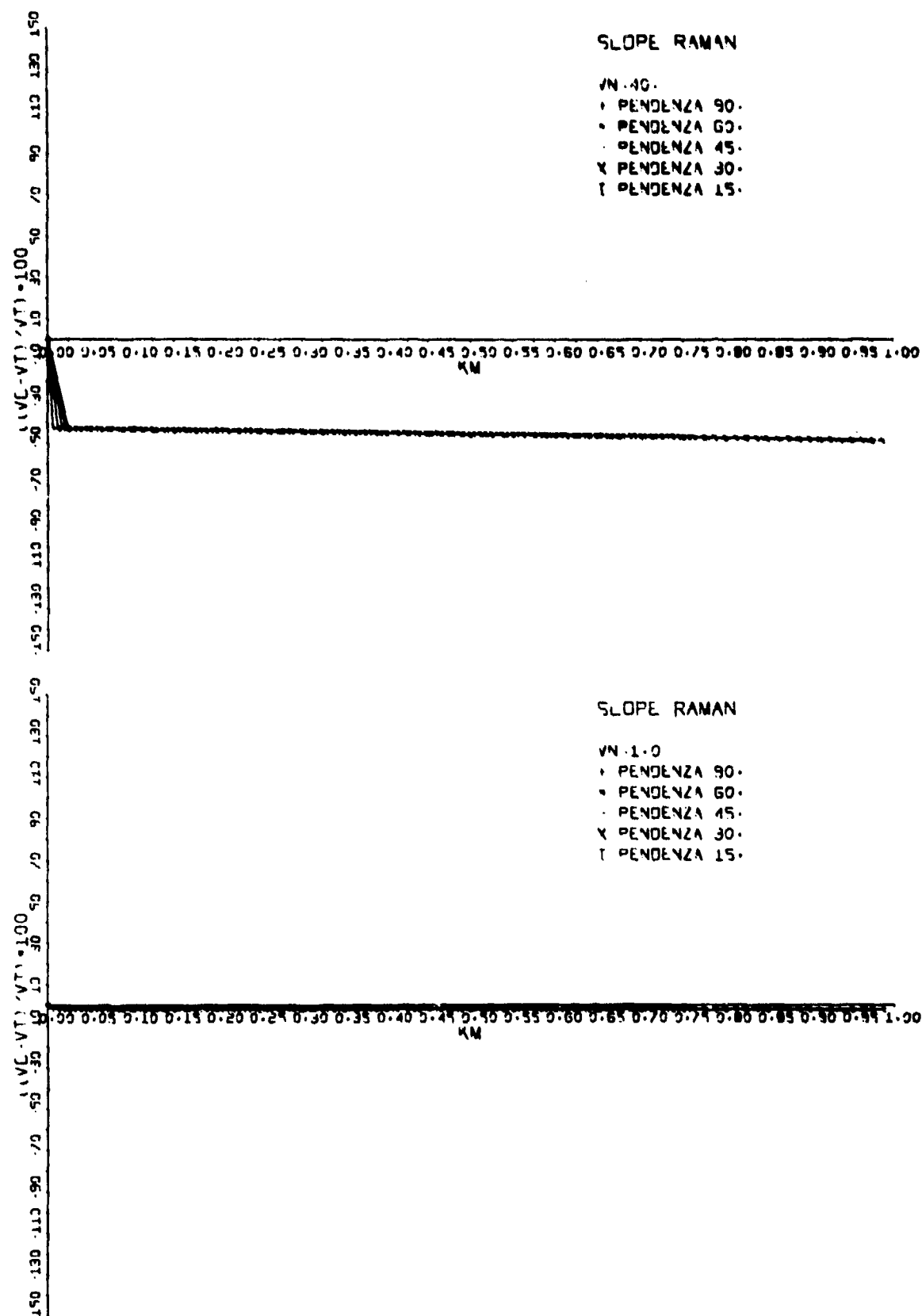


Fig. 6 Processing of normal-atmosphere data by means of the slope Raman method. Visibility at ground: 40 km (top) and 1 km (bottom).

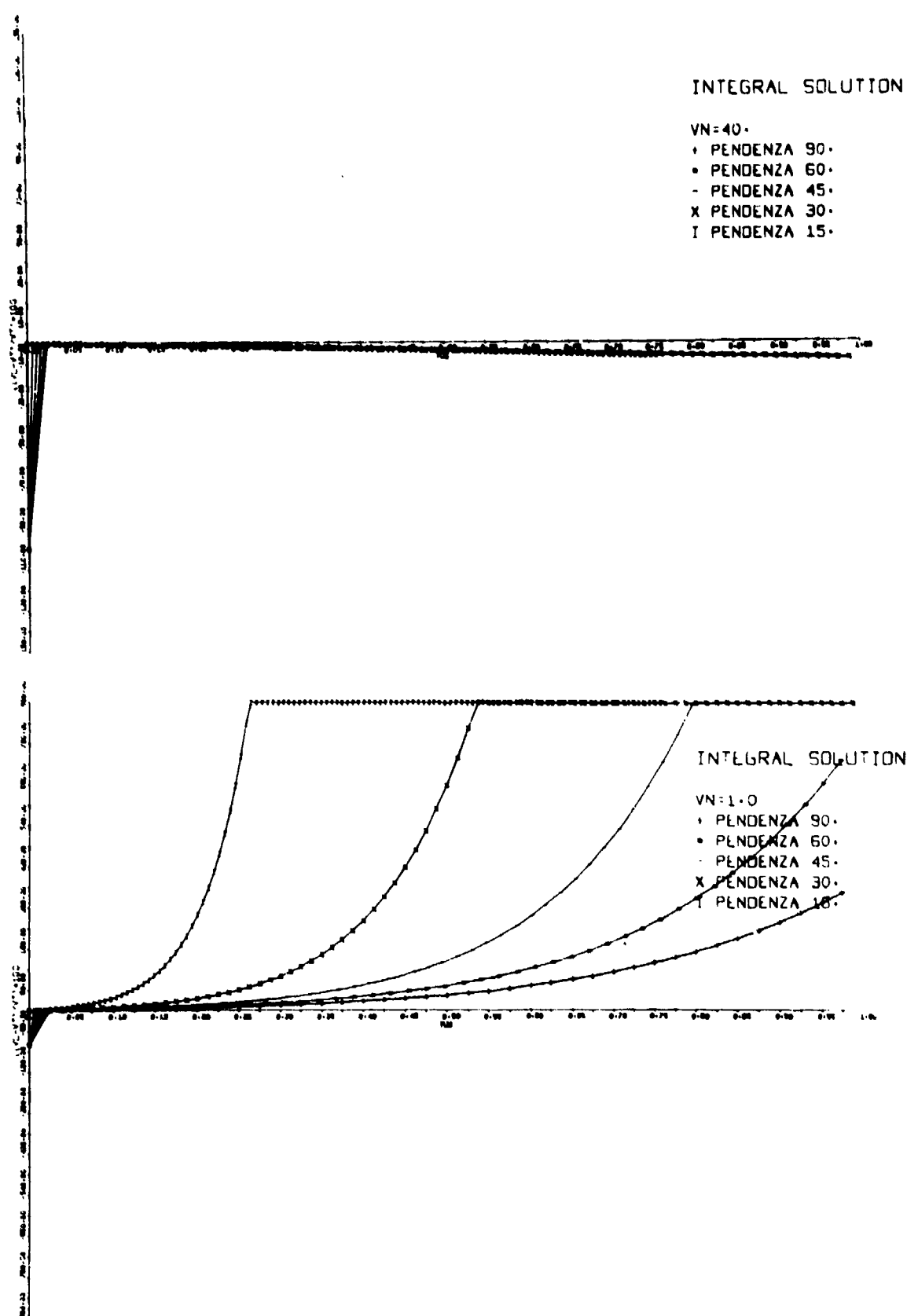


Fig. 7 Processing of normal-atmosphere data by means of the integral-solution method. Visibility at ground: 40 km (top) and 1 km (bottom).

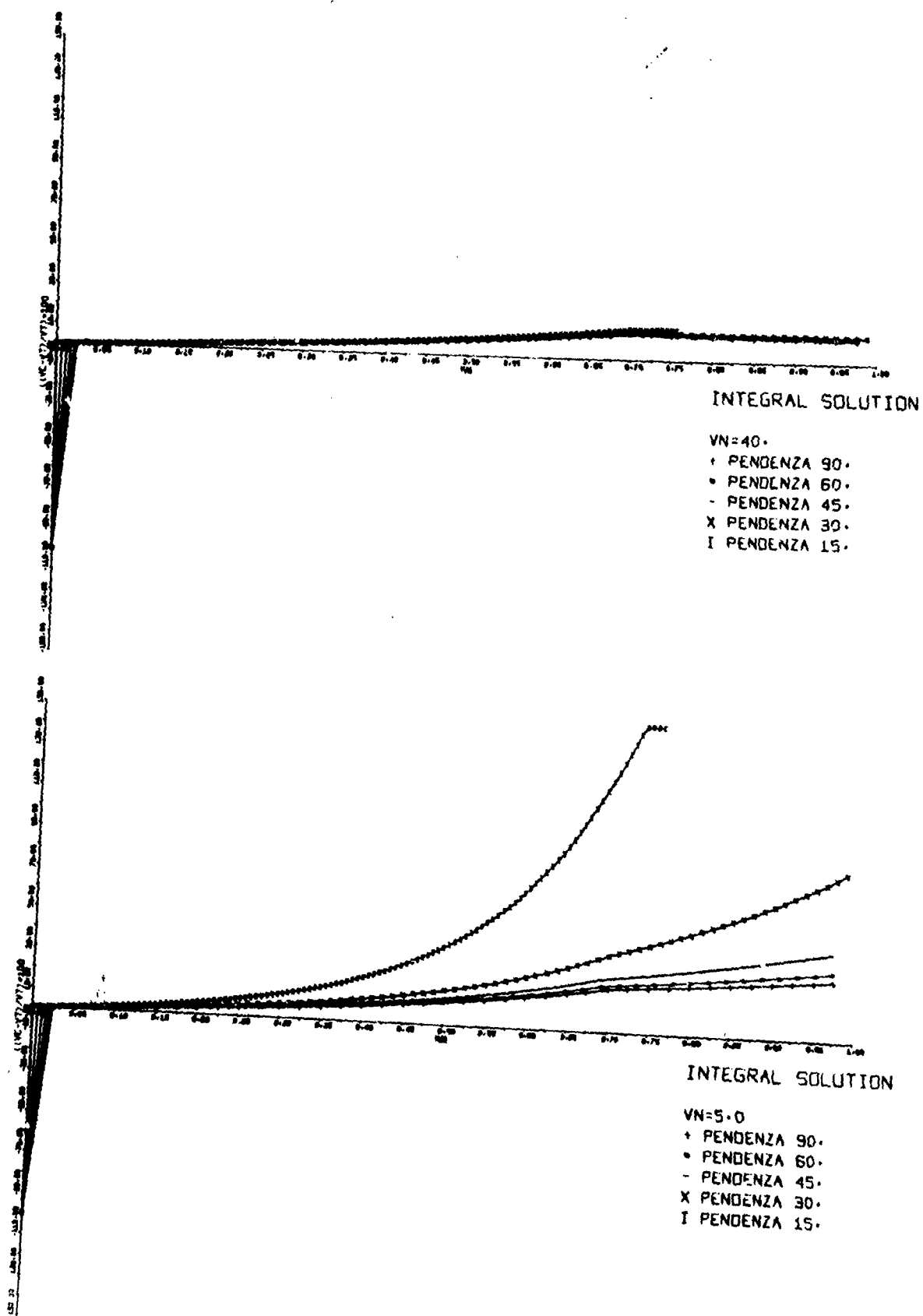


Fig. 8 Processing of temperature-inversion data by means of the slope method. Visibility at ground: 40 km (top) and 5 km (bottom).

TEMPERATURE INVERSION

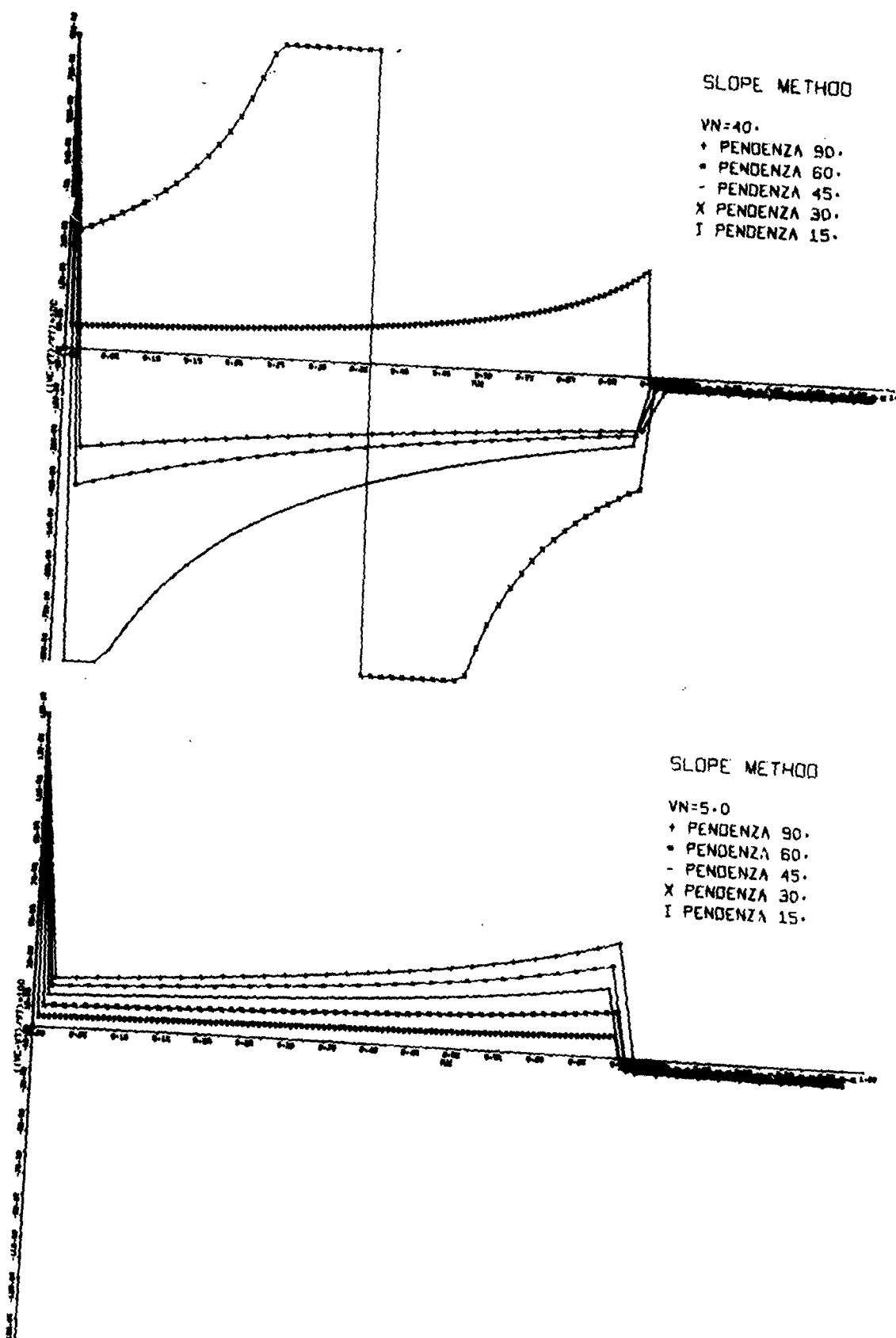


Fig. 9 Processing of temperature-inversion data by means of the integral-solution method. Visibility at ground: 40 km (top) and 5 km (bottom).

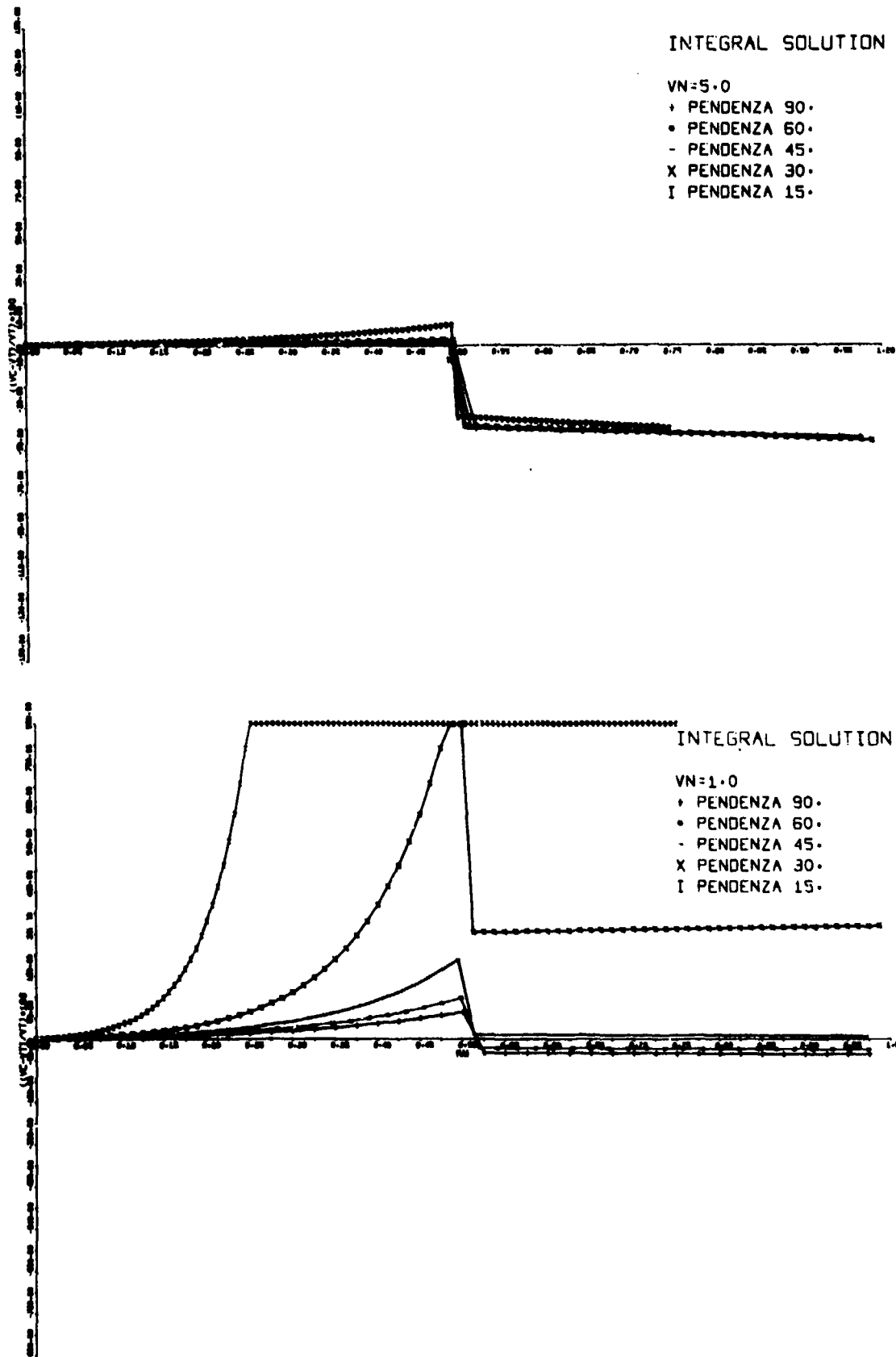
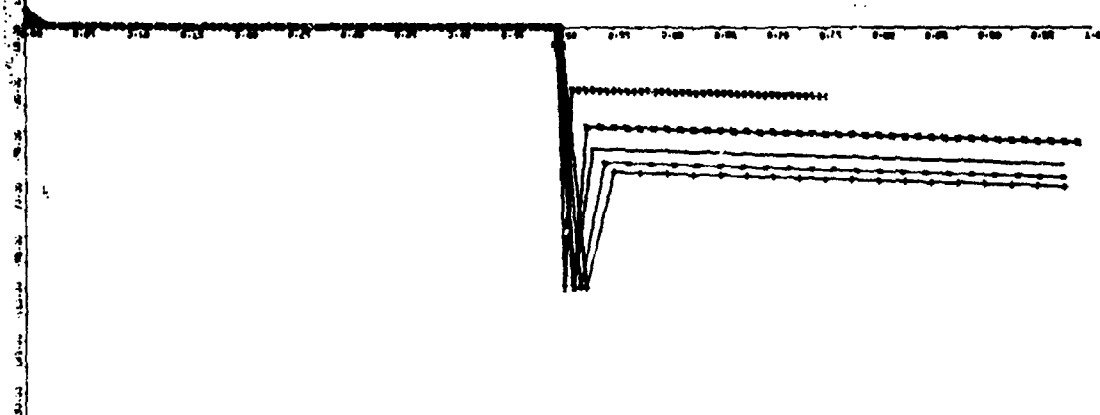


Fig. 10 Processing of fog-bank data by means of the slope method. Visibility in the bank: 5 km (top) and 1 km (bottom).

SLOPE METHOD

VN:5.0
 + PENDENZA 90.
 • PENDENZA 60.
 - PENDENZA 45.
 x PENDENZA 30.
 I PENDENZA 15.



SLOPE METHOD

VN:1.0
 + PENDENZA 50.
 • PENDENZA 60.
 - PENDENZA 45.
 x PENDENZA 30.
 I PENDENZA 15.

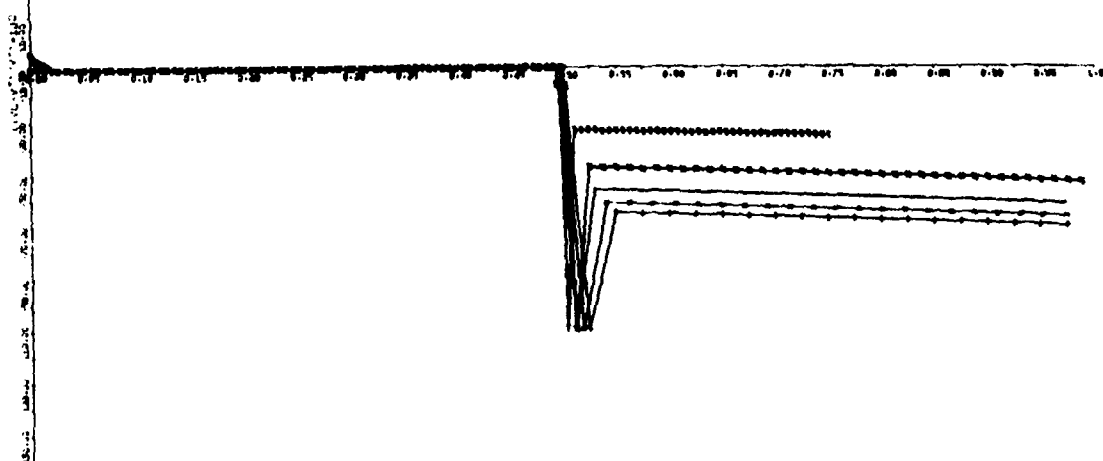


Fig. 11 Processing of fog-bank data by means of the integral-solution method. Visibility in the bank: 5 km (top) and 1 km (bottom).

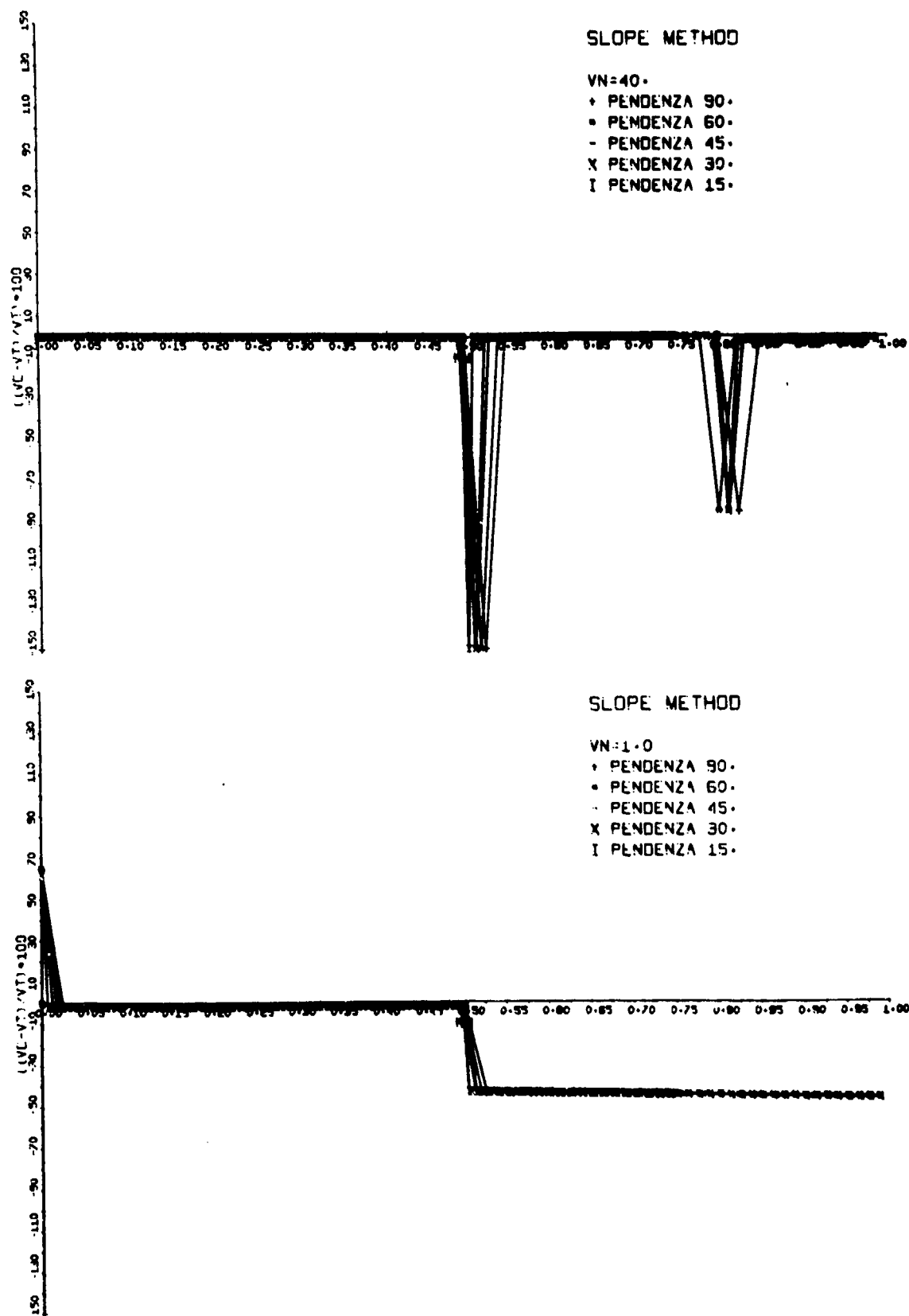


Fig. 12 Processing of cloud data by means of the slope method. Visibility at ground: 40 km (top) and 1 km (bottom).

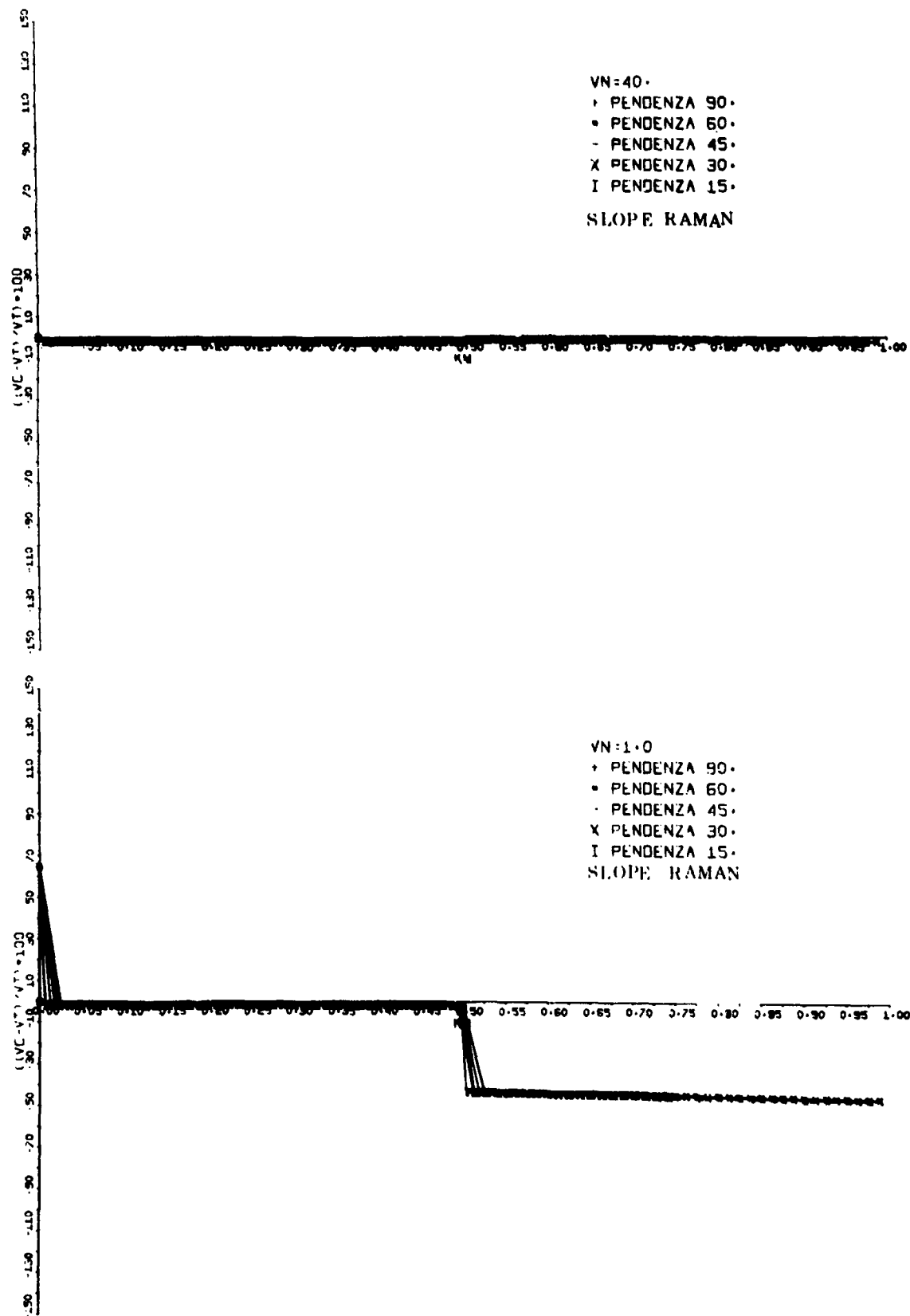


Fig. 13 Processing of cloud data by means of the slope-Raman method. Visibility at ground: 40 km (top) and 1 km (bottom).

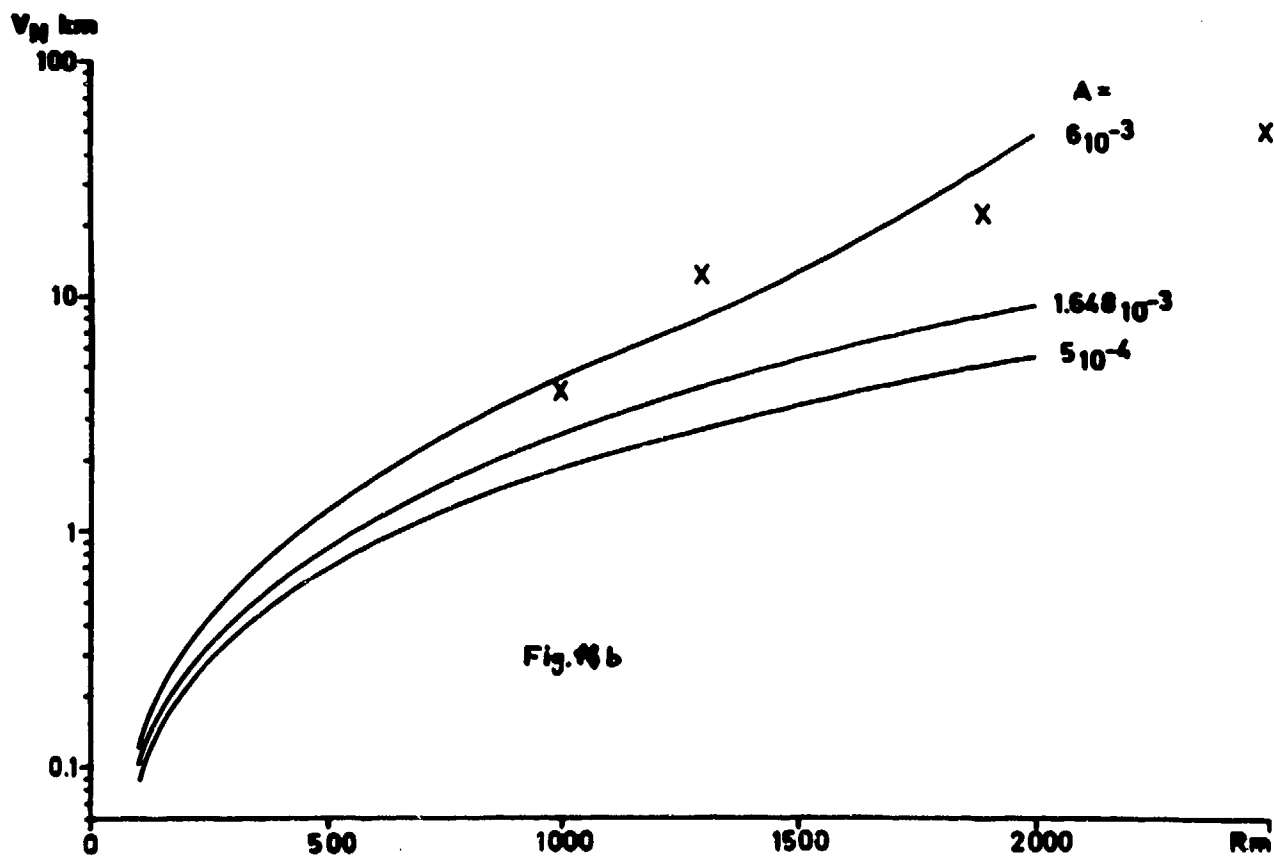
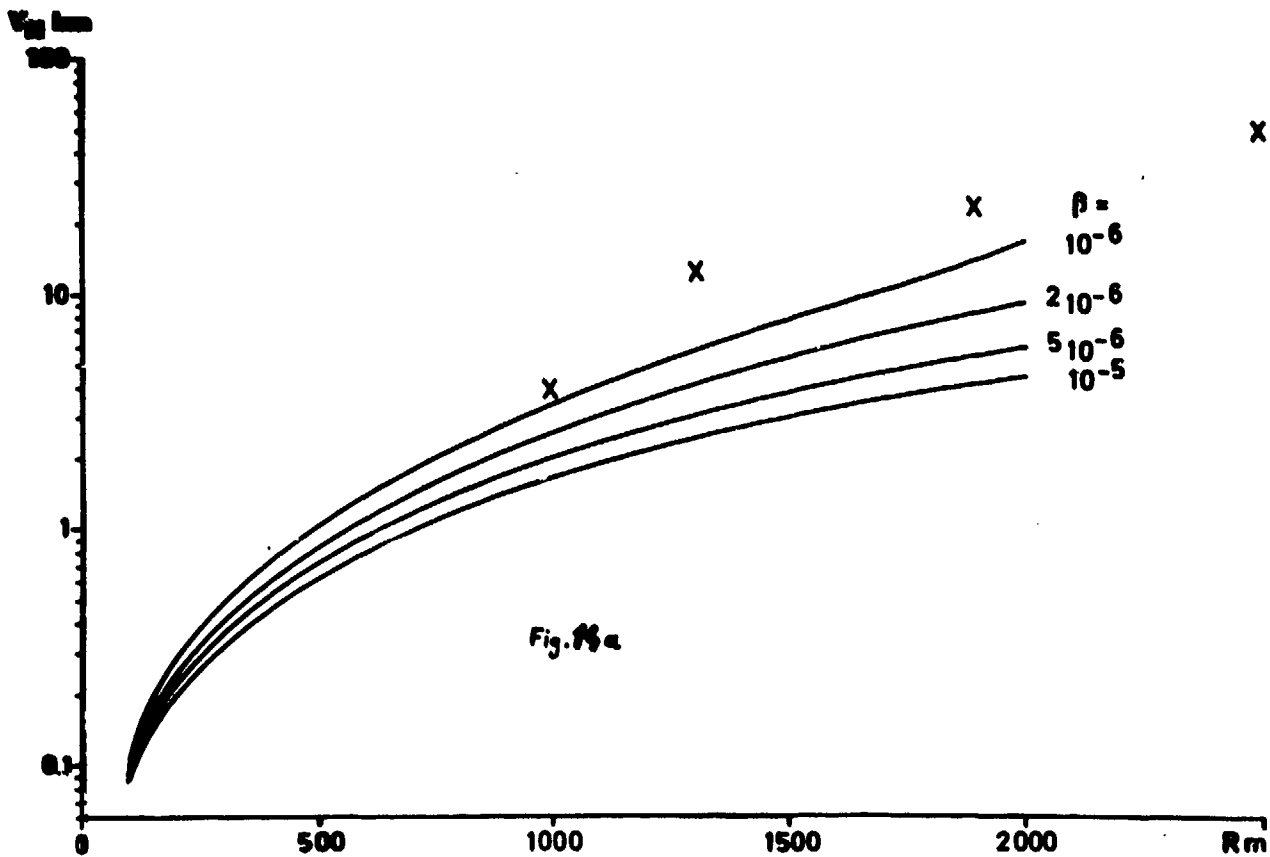


Fig. 14 Plot of equation (23) as a function of R_m . The X indicate the points corresponding to the experiments of the following figure. a) $A = \text{constant}$, b) $B = \text{constant}$.

23.9.1975

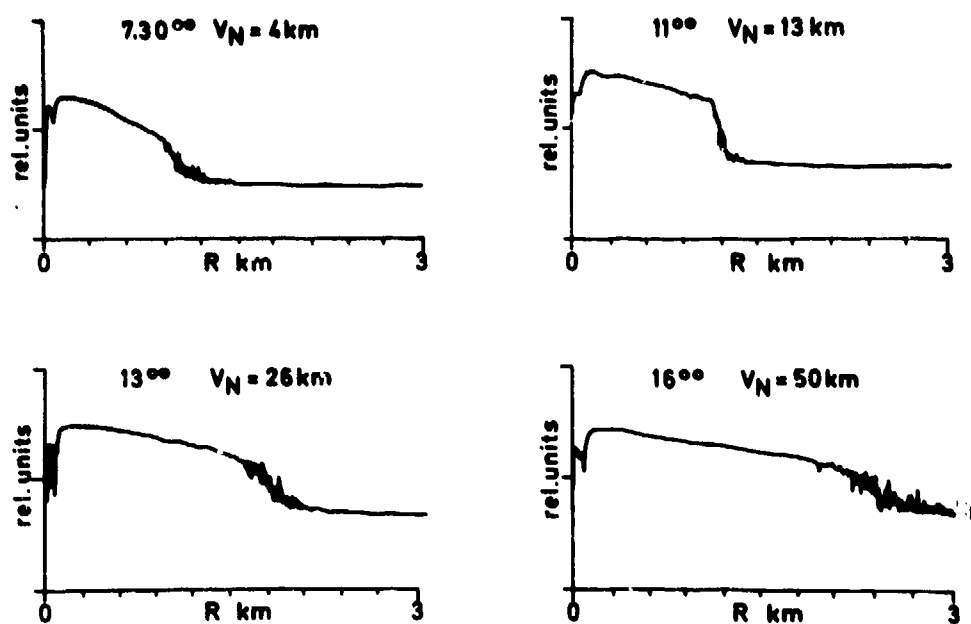


Fig. 15 Four lidar signatures from the experiments done on September 23rd, 1975. V_N is the visibility indicated by the local nephelometer.

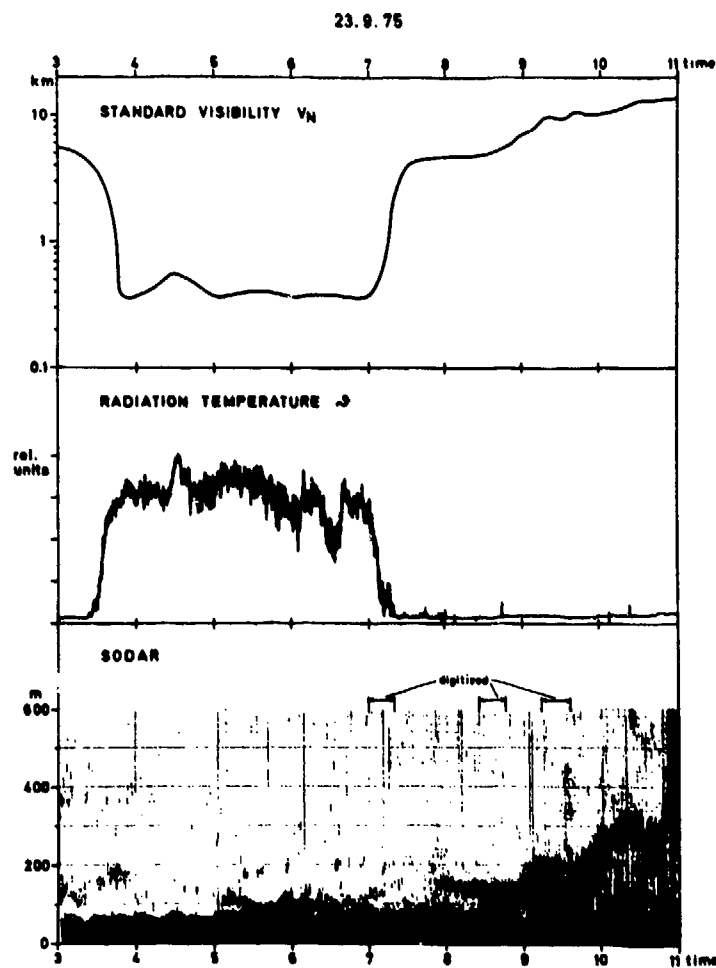


Fig. 16 Measurements given on September 23rd, 1975 by: a local nephelometer (top),

COMPUTER SIMULATION OF ATMOSPHERIC TURBULENCE AND COMPENSATED IMAGING SYSTEMS

B. L. McGlamery
Visibility Laboratory
Scripps Institution of Oceanography
University of California
San Diego, California 92093

SUMMARY

The earth's turbulent atmosphere severely limits the resolution of conventional ground based telescopes. Methods of reducing this limitation for ground based telescopes include post detection processing in which the blurred recorded image is processed to extract information not discernable to the human visual system, and pre detection compensation in which the wavefront deformations are dynamically corrected in the optical system before the image is recorded. This paper presents computer simulations of both of these methods. The simulations demonstrate that the post detection processing method produces only moderate improvement in resolution due to signal to noise limitations while the pre detection method gives very significant improvements. As a part of the simulations, techniques of generating instantaneous realizations of wavefronts deformed by atmospheric turbulence and their corresponding point spread functions are presented.

1. INTRODUCTION

The random spatial and temporal variations of index of refraction of the earth's atmosphere severely limits the resolution of large diameter ground based telescopes. For example the diffraction limit of a perfect 1.5 meter lens in the absence of the atmosphere is on the order of .1 arc seconds (radius of the Airy disk) at $\lambda = 550$ nanometers. With the earth's atmosphere present star images very seldom reach this limit. Instead star images on the order of one arc second are typically observed. Removal of this resolution-limiting degradation is a subject of great interest to the various disciplines concerned with photographing celestial objects. Ideally one would eliminate the atmosphere by placing the telescope above the earth's turbulent atmosphere. While this approach is being actively pursued with the National Aeronautics and Space Administration's Large Space Telescope the need for ground based telescopes will continue for a variety of reasons, and the need to remove the degrading effects of the atmosphere will continue.

Several approaches exist. One approach is post detection processing in which the image is recorded in degraded form, then scanned, digitized, and processed in a digital computer to enhance information extraction from the image. This approach has been under investigation for many years but, as will be demonstrated here, is of limited value because the signal to noise ratio in the degraded image does not permit a significant improvement in resolution.

A more promising approach currently under development in several laboratories is pre detection compensation using an active optical system which, in real time, senses the wavefront deformations introduced by the atmosphere, and corrects these deformations by means of a deformable mirror so that the recorded image is largely free from degradation.

In both post and pre detection compensation the ultimate goal is to increase the amount of information which can be extracted from an object. In some cases it is difficult to formulate an image quality parameter which can measure the increase in image information extraction based on the optical system alone. This is because the improvement in image quality depends on the nature of the object itself and on the kind of information that is to be extracted from the image.

An approach to the problem of analyzing compensated imaging systems performance is by computer simulation of the final image that would be formed by the system. Assessment of image quality improvement can then be made on the basis of analyzing this image in terms of the particular kind of information that is desired from it. In addition the simulation approach is useful for verifying results of analysis and for optimizing system design in those cases where tractable analytical models cannot be formulated.

This paper will present the procedures used in simulating both pre and post compensated images recorded through the turbulent atmosphere and will show examples of these procedures.

This work was sponsored by the Defense Advanced Research Projects Agency and the Air Force Systems Command, Rome Air Development Center.

2. WAVEFRONT MODELING

Simulation of the wavefront entering the optical system is a key element of the overall simulation approach. Given the wavefront or wavefronts, the response to the wavefront by the optical system can then be computed.

Consider a point source at a great distance from the earth so that a wave entering the atmosphere can be considered to be a plane wave. After traversing through the atmosphere the wave will no longer be plane but will have an amplitude and phase distribution across the lens. In this paper we will consider only phase distribution since the phase variations across the wavefront are the dominant image degrading component.

2.1 Generation of Wavefronts.

One way of describing the phase statistically is by means of its power spectrum. For atmospheric turbulence a spatial power spectrum, Φ , commonly used is the Kolmogorov spectrum which has the form of

$$\Phi(f) = C f^{-11/3} \quad (1)$$

where

f = spatial frequency, cycles/meter.

C = is a constant dependent upon turbulence strength and wavelength.

The method of generating an instantaneous phase map using the above power spectrum is based on the following assumptions:

- 1) The modulus of the Fourier transform of the phase map is a random variable. At any given frequency the modulus is a Rayleigh random variable with zero mean over an ensemble average and with a variance, over an ensemble average, equal to the value of the Kolmogorov power spectrum.
- 2) The phases of the Fourier transform of the phase map are independent with frequency, uniformly randomly distributed in the $-\pi$ to $+\pi$ interval.

Based on these assumptions the following procedure is used to generate the phase map.

1. A complex array of Gaussian random numbers is generated. The array represents the spatial frequency domain for the phase map.
2. The array is multiplied by the square root of the power spectrum, $f^{-11/6}$ (since we are at this point working with amplitudes rather than power).
3. This array is subjected to a discrete Fourier transform.
4. The resulting complex array is separated into its real and imaginary components. Each of these arrays represent an independent instantaneous phase map realization.

The left-hand pictures in Figure 1 shows the result of the above process for three separate realizations. Note the cloud like appearance of the phase maps.

Another statistical parameter associated with the phase map is its structure function, defined as

$$D_{\phi}(r) = \langle [\phi(r') - \phi(r' + r)]^2 \rangle. \quad (2)$$

The structure function is the ensemble variance of the phase difference between two points on the wavefront separated by the vector r . In a medium with uniformly varying refractive index structure constant, C_n^2 , the Kolmogorov spectrum can be shown to have a phase structure function of (Tatarski, V.I., 1961)

$$D_{\phi}(r) = 2.91 k^2 r^{5/3} \int_0^H C_n^2(z) dz \quad (\text{radians}^2). \quad (3)$$

The conditions of validity of this equation are $r \gg \sqrt{\lambda H}$ and $\sqrt{\lambda H} \gg l_0$ where l_0 is the inner scale of the turbulence.

The structure function can be written as

$$D_{\phi}(r) = 6.88 \left(\frac{r}{r_0} \right)^{5/3} \quad (4)$$

[...] 3/5

The parameter r_0 is a length frequently used to characterize the strength of atmospheric turbulence with respect to the performance of optical systems. A median value of r_0 for night time seeing has been computed to be on the order of .1 meters (Fried, D. L., 1974).*

The structure function $D_\phi(r)$ and the covariance function $C_\phi(r)$ of a phase map can easily be shown to be related by

$$D_\phi(r) = 2 [C_\phi(0) - C_\phi(r)], \quad (5)$$

where the covariance is defined as

$$C_\phi(r) = \langle \phi(r') \phi(r' + r) \rangle. \quad (6)$$

The covariance function is also the Fourier transform of the power spectrum of the phase map. Thus by applying the discrete Fourier transform to the phase power spectrum, the phase structure function can be computed by use of Eq. (5). The results of doing this, using the $f^{-11/3}$ power spectrum is shown in Figure 2 as a function of r/L where L is the interval used in the spatial domain of the Fourier transform. Here it can be seen that the calculated structure function deviates significantly from the theoretical slope of 5/3 for large r/L . This is due to the fact that the Kolmogorov spectrum assumes an infinite outer scale while the method of generating the phase maps imposes an artificial outer scale of L , since no frequencies lower than $1/L$ exist in the Fourier transform.

The outer scale of L imposed by the discrete Fourier transform method can be shown to cause errors mainly in the average and tilt components of phase across the phase map. This is illustrated in Figure 3 which shows phase variance as a function of distance from the center of a circular pupil with the piston (average) and piston and tilt components of phase subtracted. Compared in this figure are the results of a computer simulation in which the diameter D of the pupil was $L/4$, and analytic results based on the Kolmogorov spectrum with piston and tilt removed. With both piston and tilt components removed from the initial wavefronts the results are very nearly equal apart from a scaling error of approximately 15%. The piston component of phase is of no interest and the tilt component for short time exposures affects only position of the image formed by the telescope. Thus, while the phase simulation technique does presently exhibit limitations, it is entirely adequate for the simulation of short time exposure images. In addition, this limitation is only temporary as there are several methods under development by which the lower spatial frequencies can be added to the phase map to restore the proper shape to the structure function.

2.2 Generation of Point Spread Functions.

The point spread function is the irradiance distribution in the image plane of the telescope using a point source at infinity as an object. It is useful in simulating the image of an extended object in that if the object is incoherently illuminated and the point spread function is invariant over the angular field of view of the object, then the image can be simulated by convolving the point spread function with the radiance distribution of the object.

Let the (u, v) be the pupil plane coordinates and (x, y) the image plane coordinates. Given the instantaneous phase map at a wavelength of λ , $\phi(u, v, \lambda)$, we can compute the path length difference map, $\ell(u, v)$, from

$$\ell(u, v) = \frac{\phi(u, v) \lambda}{2\pi}. \quad (7)$$

The coherent point spread function, $s(x, y, \lambda)$ at any wavelength can then be computed from

$$s(x, y, \lambda) = F \left\{ p(u, v) e^{i \frac{2\pi \ell(u, v)}{\lambda}} \right\}, \quad (8)$$

where F is the Fourier transform operation and $p(u, v)$ is the pupil function of the telescope. This step is based on the fact that under appropriate conditions (i. e. small angle conditions) there is a Fourier transform relationship for coherent light between the pupil plane and the image plane except for a quadratic phase factor (Goodman, J. L., 1968). The quadratic phase factor is of no concern here since it is lost when the intensity point spread function $S(x, y)$, is computed from

$$S(x, y, \lambda) = |s(x, y, \lambda)|^2. \quad (9)$$

The point spread function for all wavelengths is then given by

$$S(x, y) = k_2 \sum_{\lambda} F(\lambda) S(x, y, \lambda). \quad (10)$$

* Dr. Darryl P. Greenwood, Rome Air Development Center, private communication.

where $F(\lambda)$ is a weighting function which is a product of the spectral distribution of the source power, the atmospheric transmittance and the image sensor sensitivity, and k_2 is a normalizing factor which makes the average value of $S(x, y)$ unity over the array. An additional factor not shown in Eq. (10) which must be considered in simulating the polychromatic point spread function is that the angular scale associated with $S(x, y, \lambda)$, as computed from Eqs. (8) and (9) using a discrete Fourier transform, changes with λ . Thus in Eq. (10) the $S(x, y, \lambda)$ arrays must be spatially magnified proportional to λ before the summation is performed.

Point spread functions for monochromatic light for three phase maps are shown in Figure 1. The generation of a polychromatic point spread function is demonstrated in Figure 4.

3. SIMULATION OF DEGRADED IMAGES

As mentioned in Section 2.2 the degraded image which would be present in the image plane can be simulated by convolving the intensity point spread function with the radiance map of the undegraded object, subject to the conditions that the point spread function is invariant over the object and that the object is illuminated by incoherent light. Whether the first condition is satisfied depends on the relative size of the object and the isoplanatic region, the latter being a non rigorous term for the region over which the point spread function is nearly constant. The size of the isoplanatic region depends both on the vertical distribution of the turbulence and the entrance pupil diameter. For turbulence at the entrance pupil the isoplanatic region is unlimited. For turbulence at high altitudes (> 10 kilometers) and a 1.5 meter entrance pupil diameter the isoplanatic region is on the order of ten arc seconds or less. The second condition of incoherent illumination is satisfied for sun illuminated objects.

The convolution process is mathematically described by Eq. (11) where $H(x, y)$ is the image plane irradiance in the absence of turbulence and diffraction and $H_D(x, y)$ is the degraded image.

$$H_D(x, y) = \iint H(x, y) S(x-x', y-y') dx' dy' \quad (11)$$

In practice the convolution process is more easily done in the Fourier transform domain:

$$H_D(x, y) = F^{-1} \{ F[H(x, y)] \cdot F[S(x, y)] \} \quad (12)$$

where F and F^{-1} are the Fourier transform and inverse transform operators.

In addition to the turbulence and telescope, the sensor also degrades the image. Ideally the sensor imposes only quantum noise on the recorded image. In practice the sensor sometimes additionally blurs the image and adds noise not directly related to the light field. However, by suitable selection of the sensor these effects can be minimized. Here we assume that the sensor is ideal so that the recorded image, $H_R(x, y)$, can be expressed as

$$H_R(x, y) = H_D(x, y) + N(x, y)$$

where $N(x, y)$ describes a noise array. For the ideal sensor $N(x, y)$ is a sample from a Poisson noise distribution which at any given (x, y) coordinate has a mean and variance proportional to $H_D(x, y)$.

Figure 5 illustrates the simulation of the degraded image. The object chosen for the simulation is a section of the moon's surface photographed from the Apollo 17 command module. The bar represents the distance subtended by a one arc second angle from the earth. Also shown is the appearance of the image due to diffraction of the telescope alone, the polychromatic point spread function (which includes telescope pupil effects) and the convolution of the undegraded image and the point spread function, which results in the degraded image. Finally the recorded image with sensor noise is shown. The noise has Poisson characteristics based on the mean number of photoelectrons per resolution element for: solar irradiance, a spectral atmospheric transmittance corresponding to one air mass, a telescope transmittance of .75, a sensor sensitivity corresponding to an S20 photocathode, an exposure time of 1/1000 second, and a 1.5 meter diameter telescope. In the picture the noise is easily not discernable. However the noise is present and will manifest itself when image restoration techniques are applied.

4. POST DETECTION PROCESSING

Post detection processing refers to processing done on an image after it has been recorded. The basic steps when digital computer processing is used consists of digitizing the image, applying the appropriate processing algorithms, and displaying the final result or data in some suitable form. Many possible approaches can be taken (Harris, Sr., J. L. 1964, 1966) but the one to be used here is the deconvolution approach in which the goal of the processing is to make the final image visually look like the object (McGlamery, B. L., 1967). Simply stated, given the degraded image and the point spread function, determine the undegraded image. This approach assumes that the instantaneous point spread function is known. While in practice it may be difficult to know the instantaneous point spread function, we will assume that it is known. The limitation to this approach, and in fact all approaches, is the quantum noise in the recorded image. This noise limits the extent to which the image can be deconvolved.

As an example, the degraded image of Figure 5 has been subjected to a least squares processing algorithm (Helstrom, C. W., 1967) modified to account for lack of knowledge of the spatial power spectrum of the undegraded image. The processed image, $H_p(x, y)$, is obtained from

$$H_p(x, y) = F^{-1} \left\{ \frac{F[H_D(x, y)]}{F[S(x, y)] \left[1 + \frac{\sigma^2}{|F[S(x, y)]|^2 G} \right]} \right\}$$

where σ^2 is the spatial noise power spectrum and G is a function which approximates the power spectrum of the undegraded image. Figure 6 shows the result of the processing. The processed image is improved over the degraded image but falls far short of the diffraction limited image. Also shown are the degraded and processed images for exposure times of 1/100 and 1/10 seconds. In each case the atmosphere is assumed to be frozen. In actuality the turbulence changes rapidly so that the 1/100 and 1/10 second exposures would contain time averaging of the image. Time averaging increases the degradation of the image. Thus the increase in image signal to noise ratio is offset by the increase in image degradation. This illustrates a fundamental limitation of post detection processing as applied to turbulence degraded, sun illuminated objects.

5. PRE DETECTION COMPENSATION SYSTEMS

An alternate approach to the problem of eliminating turbulent effects is to correct the wavefront prior to recording the image. This technique was suggested over twenty years ago (Babcock, H. W., 1953) but has received serious attention only recently. Theoretical analyses (Dyson, F. J., 1975) and computer simulations demonstrating concepts (Muller, R. A., and Buffington, A., 1974) have been published. The contribution of this paper is to present simulations based on typical imagery and actual flux levels that will be encountered with sun illuminated objects.

5.1 System Description.

Figure 7 shows the essential components of a pre detection compensation system. Light from the telescope objective is recollimated and reflected off a deformable corrector mirror. Part of this light is reflected into a wavefront sensor which detects the wavefront deformations introduced by the atmosphere. The output from the wavefront sensor is processed by a data processor which determines the necessary signals to be fed to the deformable mirror to cancel out the wavefront deformations. Thus the system is a closed loop servo system. The remaining flux is directed to the image sensor to form the final image.

The wavefront sensor can be implemented in a variety of ways. Most approaches measure the slope of the wavefront over an array of sample points. The data processor then converts the slopes into the required phase corrections. The shearing interferometer and the quadrant detector appear to be two of the more promising wavefront sensors. The shearing interferometer (Wyant, J. C., 1974) has two channels, one for u and the other for v , in which the wavefront is sheared and allowed to interfere with itself. An array of detectors measures the intensity of the interference field. The phase of the sheared wave is temporally modulated so that an alternating signal is obtained from each detector. The phase of this signal is proportional to the slope of the wavefront over the shear distance. The phase at each detector in both channels is measured, thus providing the necessary input to the data processor. The quadrant detector approach uses an array of small sub apertures at an image of the pupil plane (or at some point outside the telescope). Each sub aperture has a lens which images onto a quadrant detector. The image is essentially a sub aperture-diffraction limited image of the object, shifted by the slope of the wavefront across the sub aperture. The quadrant detector outputs allow this shift to be measured in both u and v directions, thereby providing an estimate of the wavefront slope at that point.

The data processor can take several forms. For the purpose of the simulations here, it will consist of a device which makes a simple least squares estimate of the wavefront path length differences based on the slope measurements.

The wavefront corrector can be a segmented mirror or a deformable mirror. In the case of a segmented mirror each segment can be moved in a piston motion, thus requiring one actuator per segment, or can be moved in piston and tilt, thus requiring 3 actuators per segment. In a deformable mirror the mirror is continuous but is actuated by piston type actuators. The continuous mirror provides an interpolation function which smooths out the inputs to the actuators. The shape of this interpolating function, called the mirror function, can be adjusted by design of the mirror, the actuator shape and spacing.

The effect of compensating a wavefront using a segmented mirror with piston drive is illustrated in Figure 8. In this simulation it was assumed that the average phase over each piston element was known exactly and was subtracted from the original wavefront. The residual errors in the compensated wavefront are then due to the variations of the original wavefront about the mean value within each piston.

5.2 Number of Elements.

A critical parameter in a compensated imaging system is the number of sample points and actuators required on the wavefront sensor and corrector. From the standpoint of being able to measure and correct the deformations of the wavefront with sufficient resolution, a large number of elements is desirable. To determine the number of elements required for good compensation, a computer simulation experiment was performed in which the Strehl ratio of the compensated point spread function was computed as a function of the number of degrees of freedom, which is the number of actuators required on the mirror. The Strehl ratio is the ratio of the peak value of the compensated point spread function to the peak value of the diffraction limited point spread function. A value of unity would correspond to perfect compensation. A value well below .1 is usually encountered in uncompensated point spread functions. The experiment was performed for three levels of turbulence corresponding to r_0 values of .043, .086, and .172 meters. For the segmented mirror with piston correction the average phase over each segment was subtracted from the original wavefront. For the segmented mirror with piston and tilt correction a least squares fit of a plane was made to the phase within each segment and this plane was subtracted from the original wavefront over each segment. For the deformable mirror the average phase over a square equal to the actuator spacing was used as the correcting phase for the actuator, and the correction process was iterated four times to converge on the required correction. In all cases 8 different wavefront realizations were used to obtain a statistically significant result.

The results of the simulation are shown in Figures 9, 10 and 11 for piston, piston and tilt, and deformable mirror corrections respectively. Assuming that a Strehl ratio of .7 is desired for good imagery and taking the value of r_0 of .086 meters as being close to typical, the required number of degrees of freedom are:

Piston	~	900 degrees of freedom
Piston and Tilt	~	300 degrees of freedom
Deformable Mirror	~	200 degrees of freedom

These results show that a deformable mirror with a Gaussian mirror function requires the fewest number of elements for a given level of performance and that the number of elements required is on the order of several hundred.

The curves just described are related to the ability of the system to spatially resolve the wavefront deformations. They do not include measurement error of the wavefront sensor due to quantum noise. The output of a single detector in the wavefront sensor contains a signal proportional to wavefront slope and noise due to the shot effect of the photoelectrons. As the number of elements increases, the flux available for a single detector decreases. The signal to noise ratio at each detector then decreases as the number of elements increases. Thus these are two opposing trends: increasing the number of elements improves the ability to resolve the wavefront deformations but at the same time increases wavefront measurement error. Analysis has shown that for a given set of target and system conditions there is an optimum number of elements for which the error in the compensated wavefront is a minimum. The number of elements is in the range of 200 to 400 for typical sun illuminated objects.

5.3 Simulation.

In order to demonstrate its effectiveness, a pre detection compensated imaging system has been computer simulated. The simulation used a shearing interferometer as wavefront sensor and a deformable mirror with a $(1-r^2)^2$ mirror function. The simulator consisted of the following steps:

1. Shifting and differencing the wavefront in u and v and sampling the result to obtain an u and v array of shear values.
2. Computing the actuator drives from the shear values by use of an iterative relaxation algorithm which computes phase values from the shear values.
3. Convoluting the actuator drives with the mirror function to give the mirror correction.
4. Subtracting the mirror correction from the original wavefront to give the corrected wavefront.
5. Using the corrected wavefront as an input to step 1 and repeating the steps 1 through 4 for 4 iterations. This procedure is necessary to get the system initially converged.
6. Adding noise to the converged wavefront slopes by an amount obtained from a signal to noise equation. The noise is a function of the number of photoelectrons generated at the detector in a measurement period and the mutual coherence function associated with the object. The noisy shear values were then used as the input to step 2 and steps 2, 3 and 4 were repeated.
7. The corrected wavefront from step 4 was then used to compute the compensated point spread function.
8. The compensated point spread function was convolved with the undegraded image.

9. Poisson shot noise was added to the final image in proportion to the amount of flux directed towards the sensor by the beam divider.

Parameters used in the simulation are as follows. Object: sun illuminated Lunar surface with the photometric parameters adjusted to give an albedo (reflectance) of approximately 10% on the planes and 30% on the crater edges; atmospheric transmittance associated with one air mass; telescope transmittance of .75, optical efficiency of wavefront sensor of 50% (25% into each channel); quantum efficiency of detectors of 10%; and a 50/50 beam divider.

The results of the simulation are shown in Figure 12 for exposure times of 1/1000, 1/100, and 1/10 of a second assuming a frozen atmosphere. As in the case of post detection processing, caution must be used in interpreting the results for 1/100 and 1/10 second since the atmosphere may change in this time period. Comparison to the post detection processing results in Figure 6 demonstrates that pre detection compensation produces a much better image for the equivalent exposure time.

The problem of isoplanatism has not been discussed with respect to pre detection compensation. The isoplanatic region for pre detection compensation may be much smaller than for post detection compensation. The manner in which the limited isoplanatic region can be extended is unresolved at the present and is a subject for consideration in the design of a pre compensated system.

6. CONCLUSIONS

Computer simulation is a useful technique for analysis of turbulence degraded wavefronts and their effect on the images formed by optical systems. The simulations shown here demonstrate the potential advantage of pre compensating the wavefront prior to recording the image as opposed to post detection correction of the image itself. Since the same amount of flux is available in both cases, the result implies that useful information is irretrievably lost in the recording process. Presumably this lost information is associated with the electromagnetic phase of the atmosphere which is not captured in the recorded image.

Acknowledgment

The author is indebted to Dr. Donald Silva for providing the pre compensated wavefronts used in the simulation of the pre compensated system.

REFERENCES

1. Babcock, H. W., 1953, "The Possibility of Compensating Astronomical Seeing", Astronomical Society of the Pacific, Vol. 65, No. 386, Oct. 1953.
2. Dyson, F. J., 1975, "Theory of Optical Image Improvement", Stanford Research Institute, Technical report JSR-73-11.
3. Fried, D. L., 1974, Evaluation of r_0 for Propagation Down Through the Atmosphere, Applied Optics, 13, 2620.
4. Goodman, J. W., 1968, "Introduction to Fourier Optics", p 85, McGraw Hill Company, San Francisco.
5. Harris, Sr., J. L., 1964, "Resolving Power and Decision Theory", J. Opt. Soc. Am. 54, 606.
6. Harris, Sr., J. L., 1966, "Image Evaluation and Restoration", J. Opt. Soc. Am. 56, 569.
7. Helstrom, C. W., 1967, "Image Restoration by the Method of Least Squares", J. Opt. Soc. Am. 57, 297.
8. McGlamery, B. L., 1967, "Restoration of Turbulence Degraded Images", J. Opt. Soc. Am. 57, 293.
9. Muller, R. A., and Buffington, A., 1974, J. Opt. Soc. Am. 64, 1200.
10. Tatarski, V. I., 1961, "Wave Propagation in a Turbulent Medium", p 170, Dover Publications, Inc., New York.
11. Wyant, J. C., 1974, Appl. Opt. 13, 200.

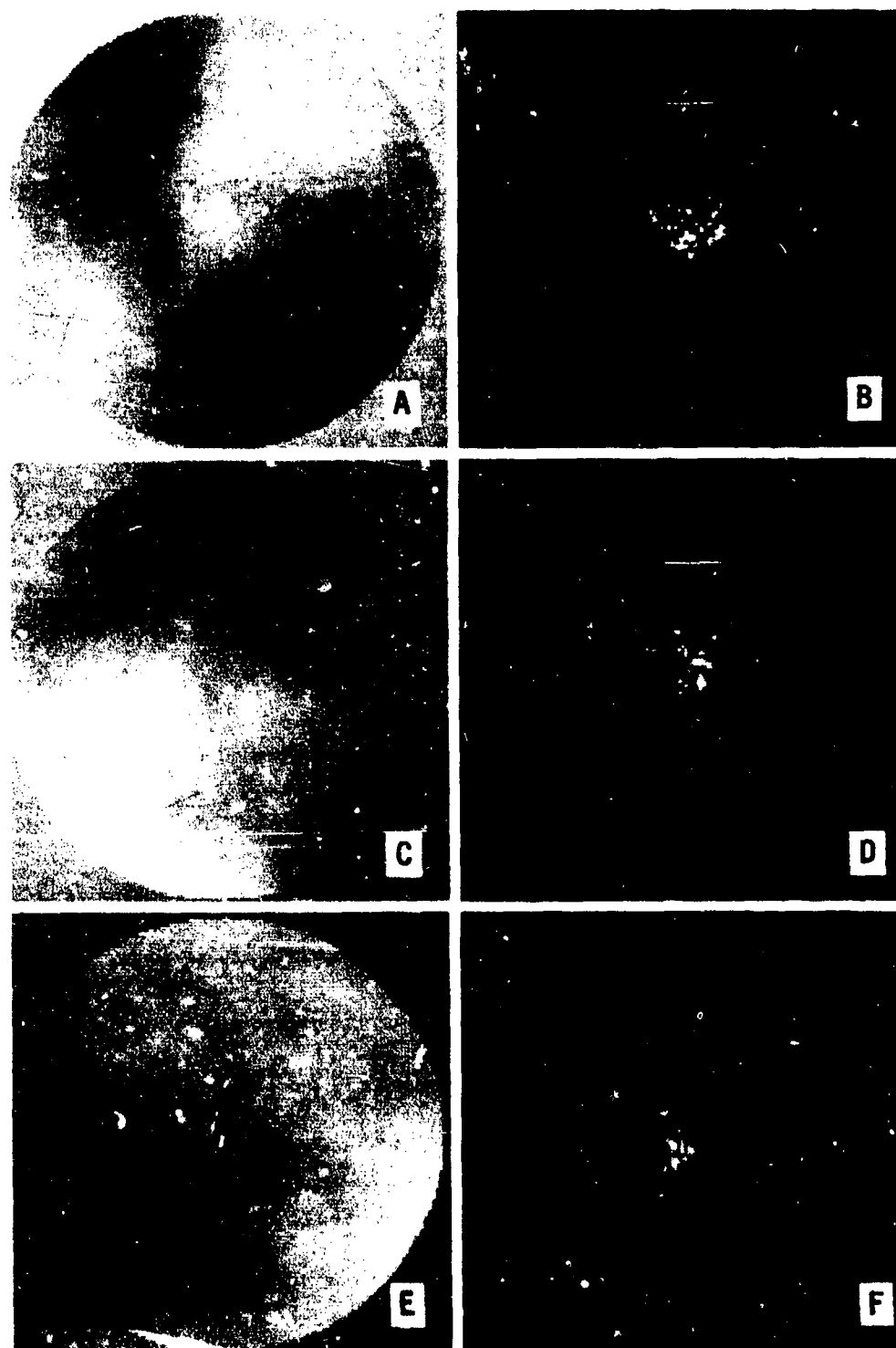


Figure 1. Computer simulated phase maps and their point spread functions. Top row: three instantaneous realizations of the phase map at an entrance pupil due to turbulence with $f^{-11/3}$ power spectrum. Background brightness outside aperture represents zero phase, lighter represents positive phase, darker represents negative phase. Bottom row: point spread functions associated with the phase maps. S. length parameter, $r_0 = .1$ meters, at $\lambda = 550$ nanometers. Pupil diameter = 1.5 meters. Bar indicates one arc second. Strehl ratios = .018, .032, .024. 128 x 128 array.

PHASE STRUCTURE FUNCTION COMPUTED BY FFT METHOD

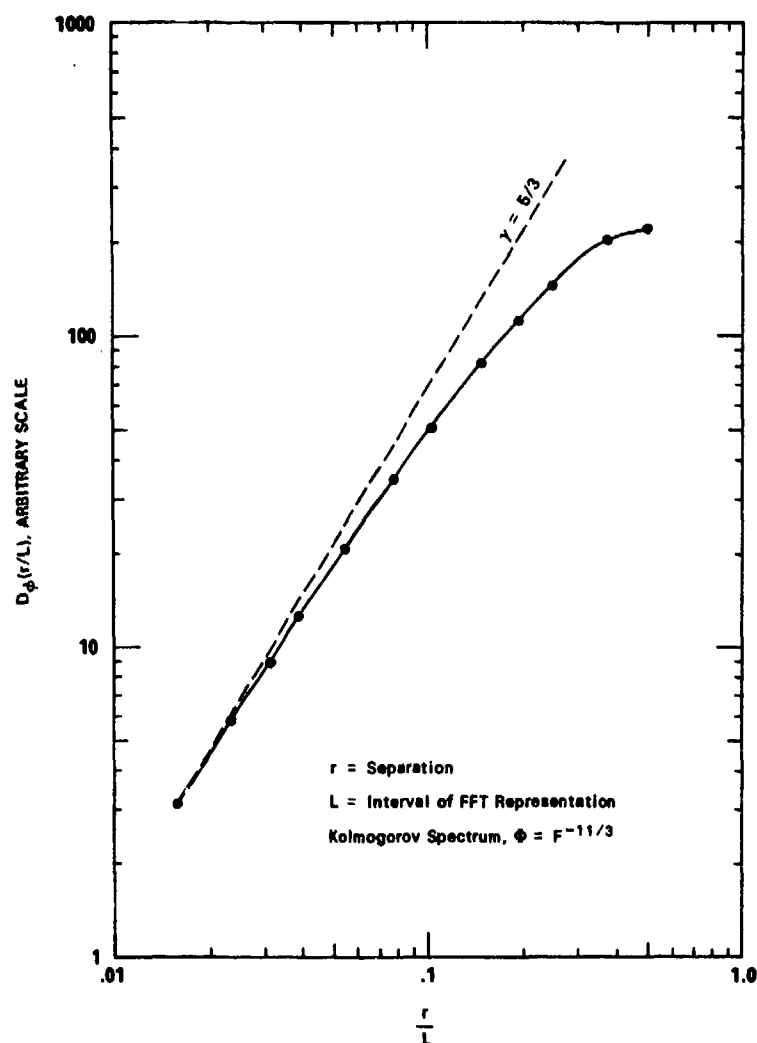


Figure 2. Structure function of simulated phase maps.

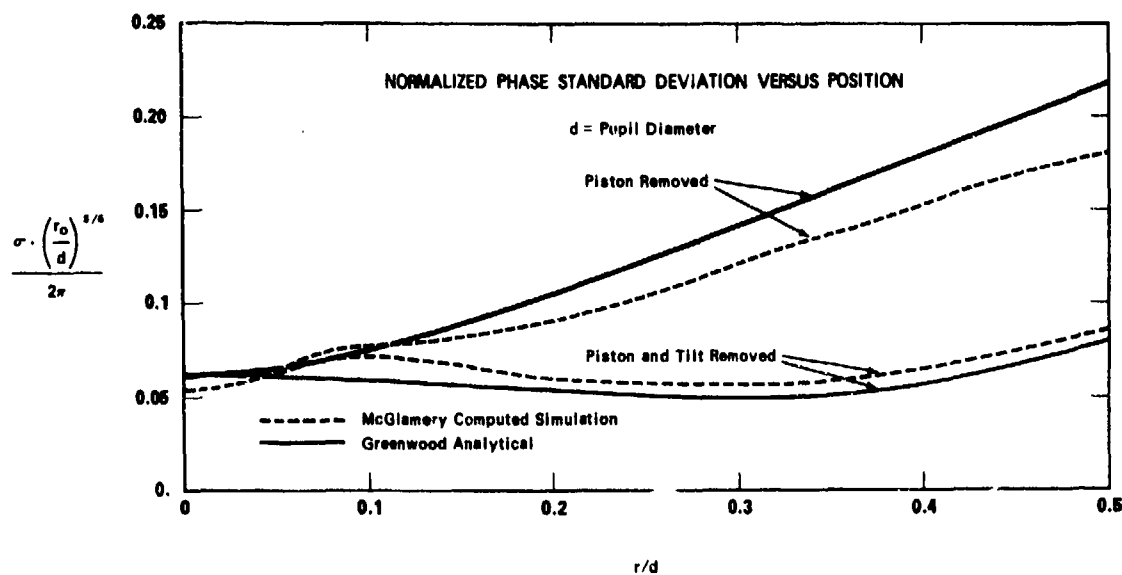


Figure 3. Standard deviation of phase versus distance from center of lens for phase maps with piston and piston and tilt components subtracted.

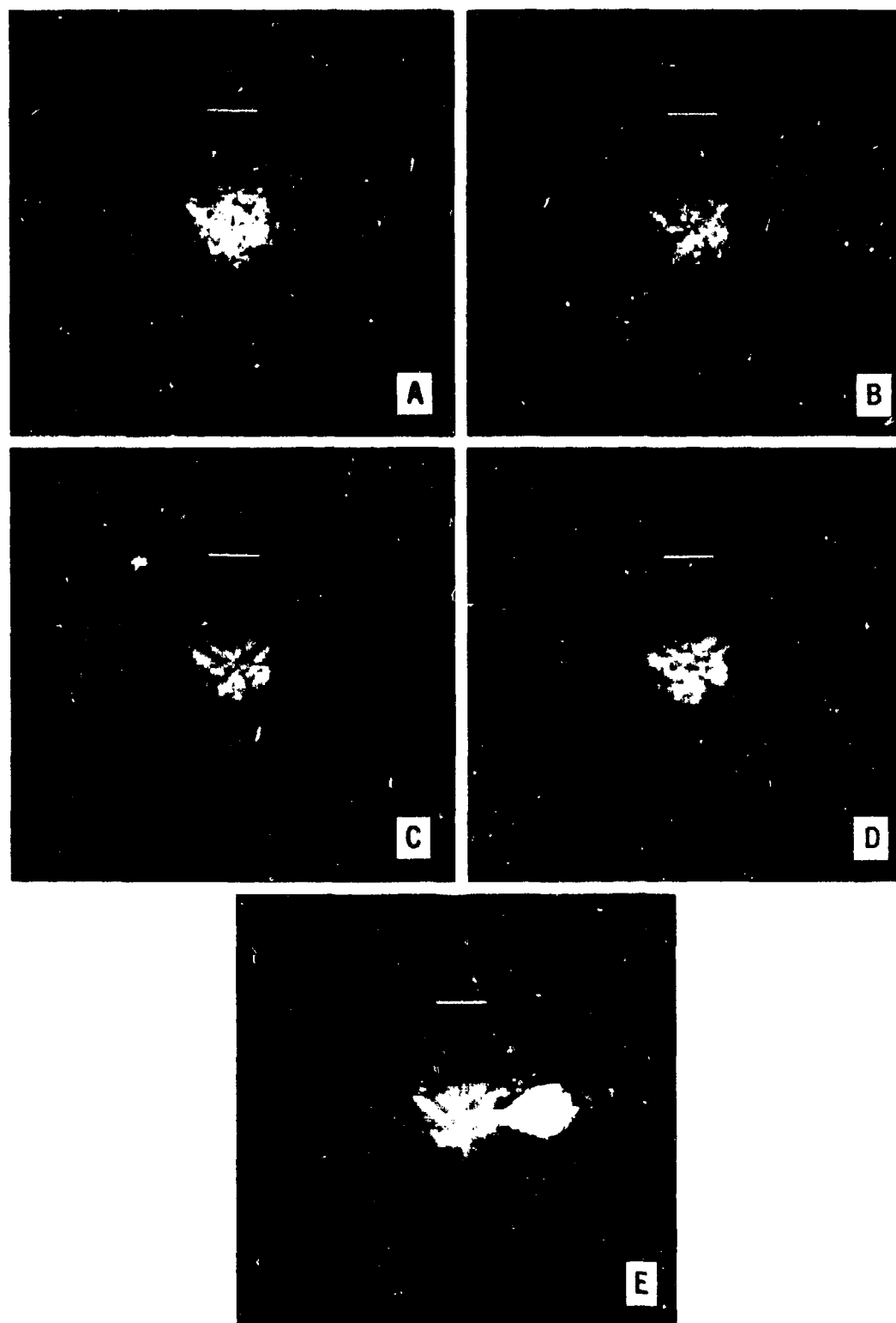


Figure 4. Computer simulation of a polychromatic point spread function using the phase map of Figure 1a. $r_0 = .1$ meter at 550 nanometers. Bar indicates one arc second. 128×128 array.

- a) Monochromatic point spread function, $\lambda = 400$ nm
- b) Monochromatic point spread function, $\lambda = 500$ nm
- c) Monochromatic point spread function, $\lambda = 600$ nm
- d) Monochromatic point spread function, $\lambda = 700$ nm
- e) The polychromatic point spread function formed from a spectrally weighted sum of seven monochromatic point spread functions in the range of 400 to 700 nanometers.

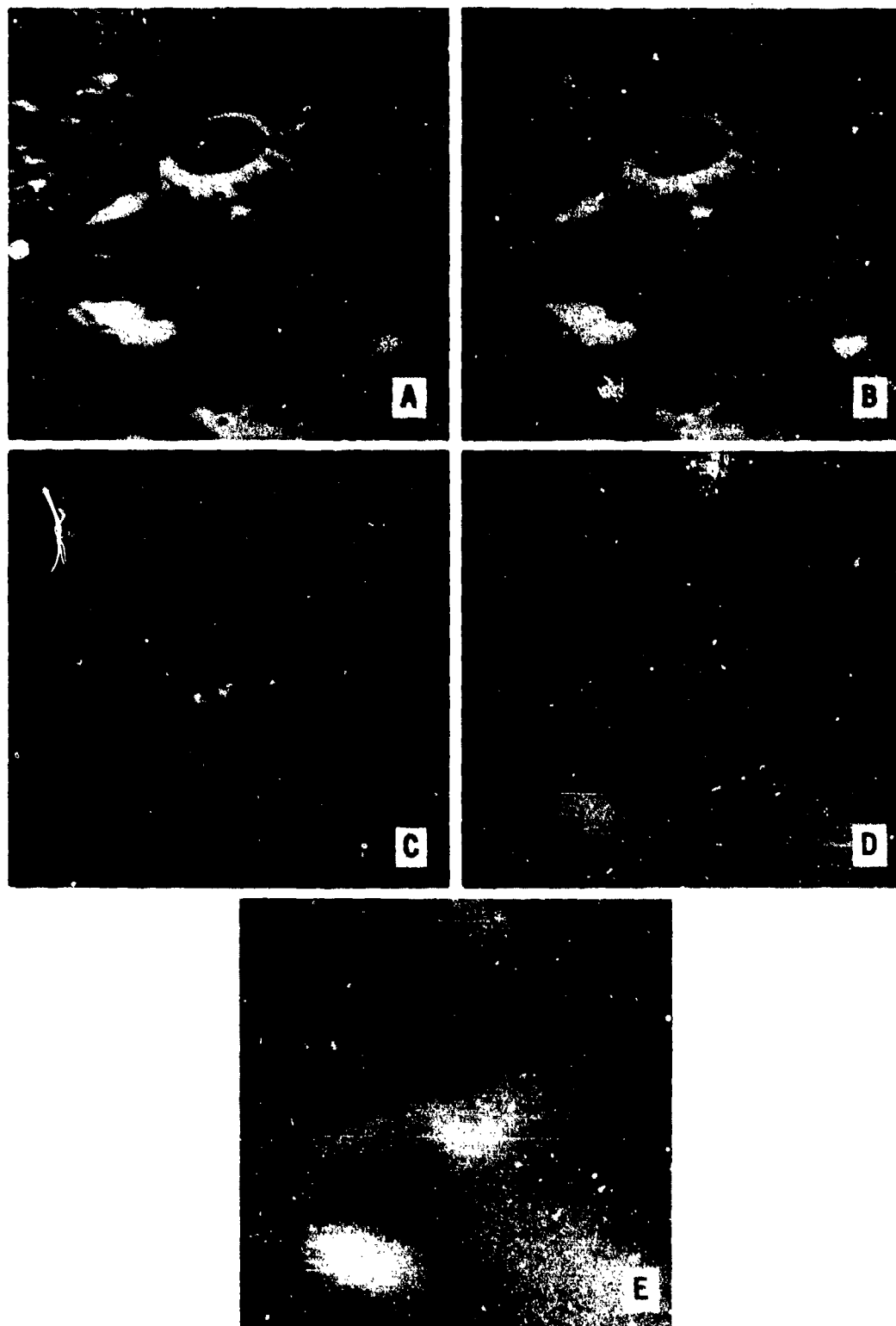


Figure 5. Computer simulation of an atmospherically degraded image. Bar indicates one arc second. 256 x 256 array.

- a) A portion of the Moon's surface from Apollo 17 photography.
- b) Simulated diffraction limited image from Earth-based telescope of 1.5 meter diameter, $\lambda = 550$ nanometers.
- c) Simulated polychromatic atmospheric point spread function.
- d) Degraded image formed by convolution of a) and c).
- e) Poisson noise added to d) for S(20) photocathode, 1/1000 second exposure.



Figure 6. Post detection processed images, using modified least squares filter and full knowledge of point spread function. Frozen atmosphere assumed.

- a) 1/1000 second exposure image processed.
- b) 1/100 second exposure image processed.
- c) 1/10 second exposure image processed.

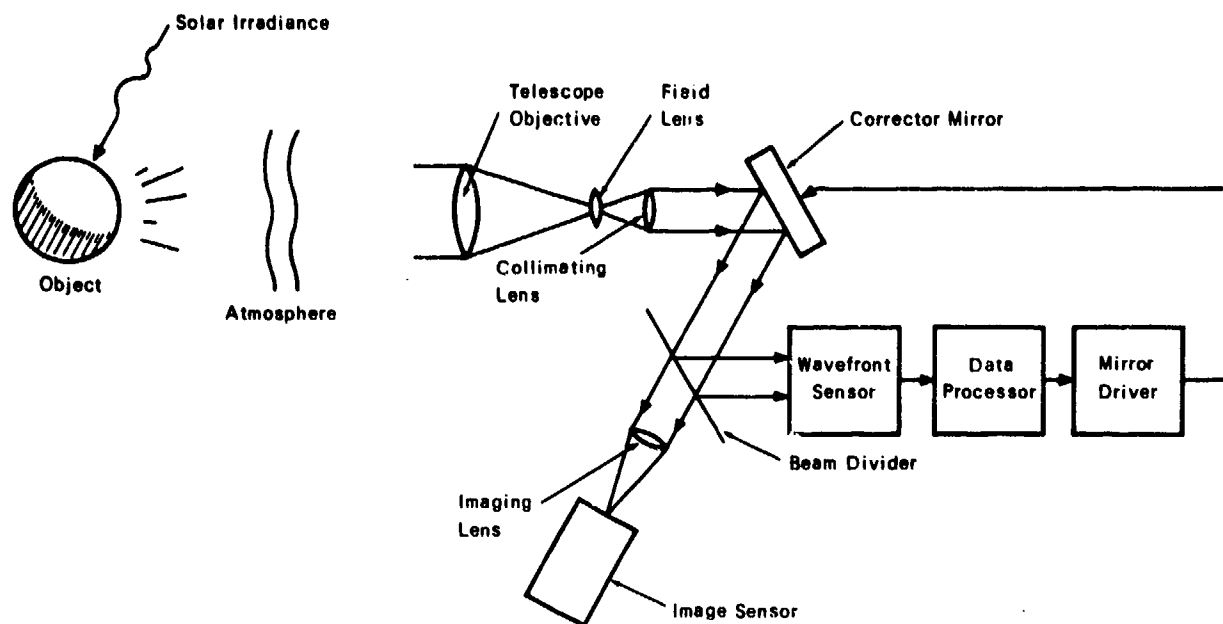


Figure 7. Components of a pre detection compensated imaging system.

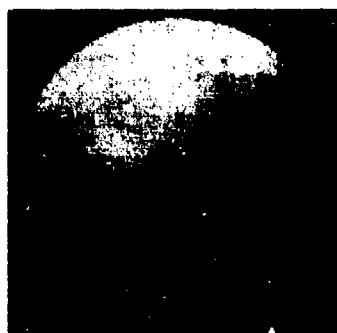


Figure 8. Example of wavefront compensation using a segmented mirror.

- a) Phase map.
- b) Phase map represented by piston displacements.
- c) Residual wavefront, difference between a) and b).

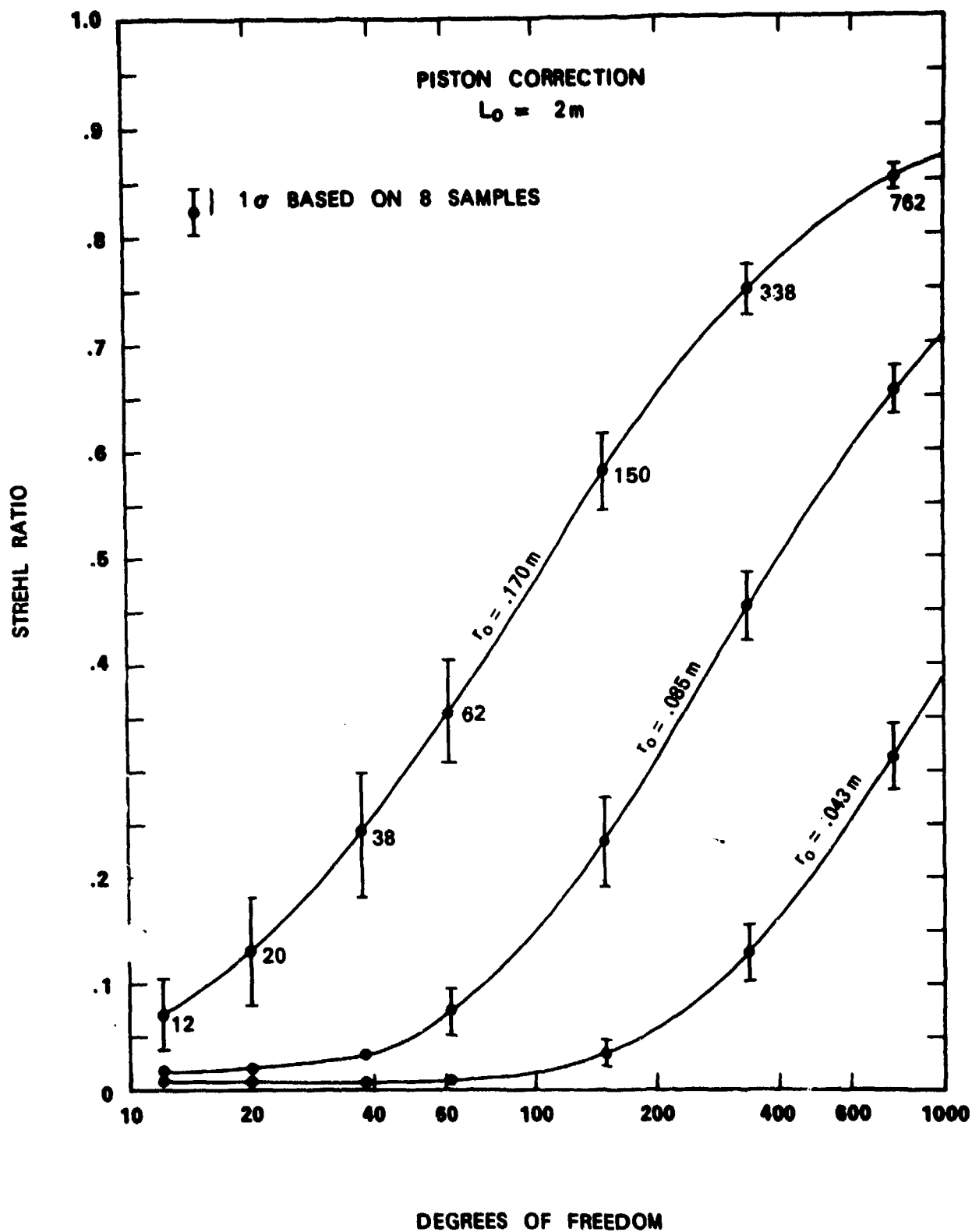


Figure 9. Strehl ratio versus degrees of freedom for a segmented mirror with piston correction.

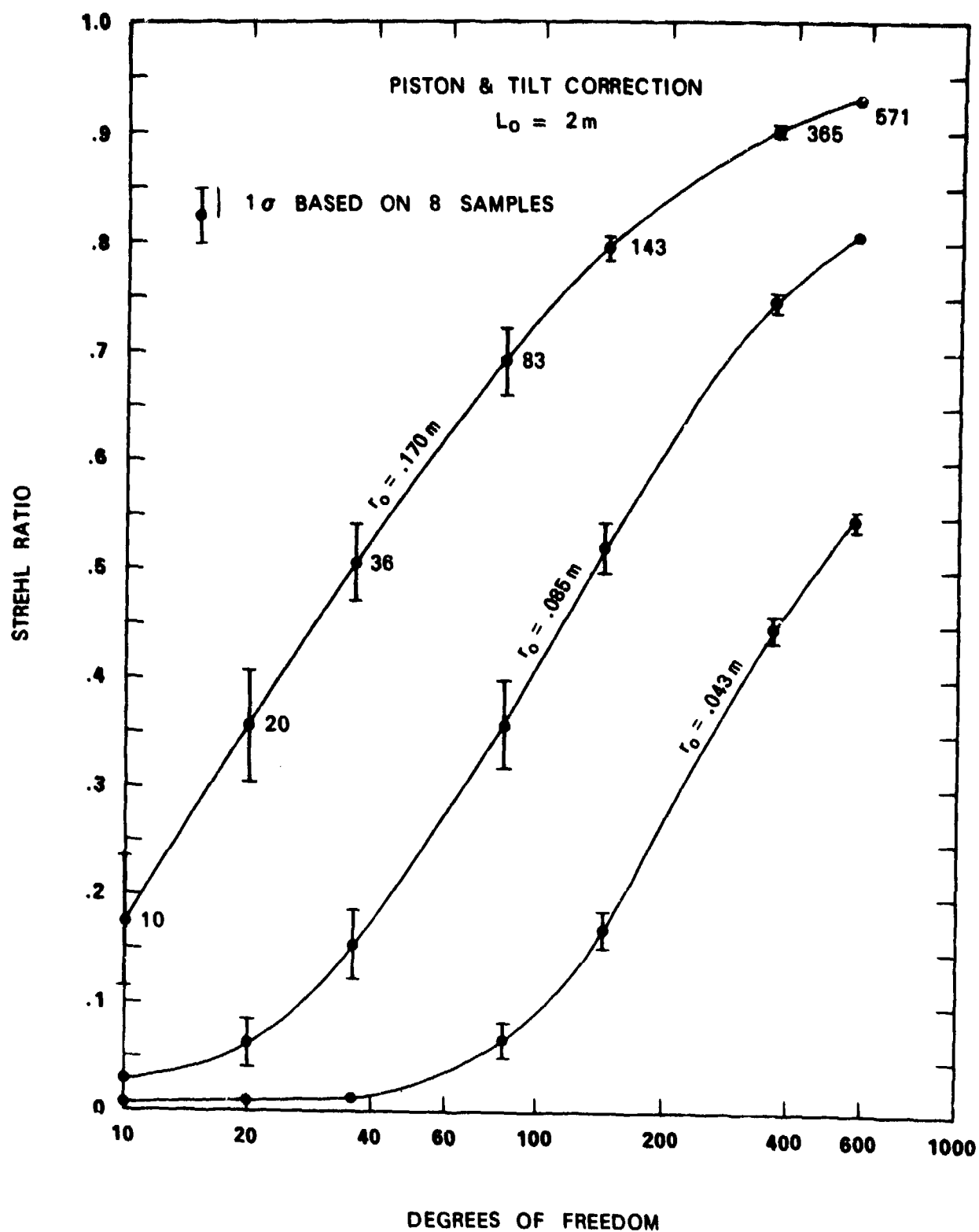


Figure 10. Strehl ratio versus degrees of freedom for a segmented mirror with piston and tilt correction.

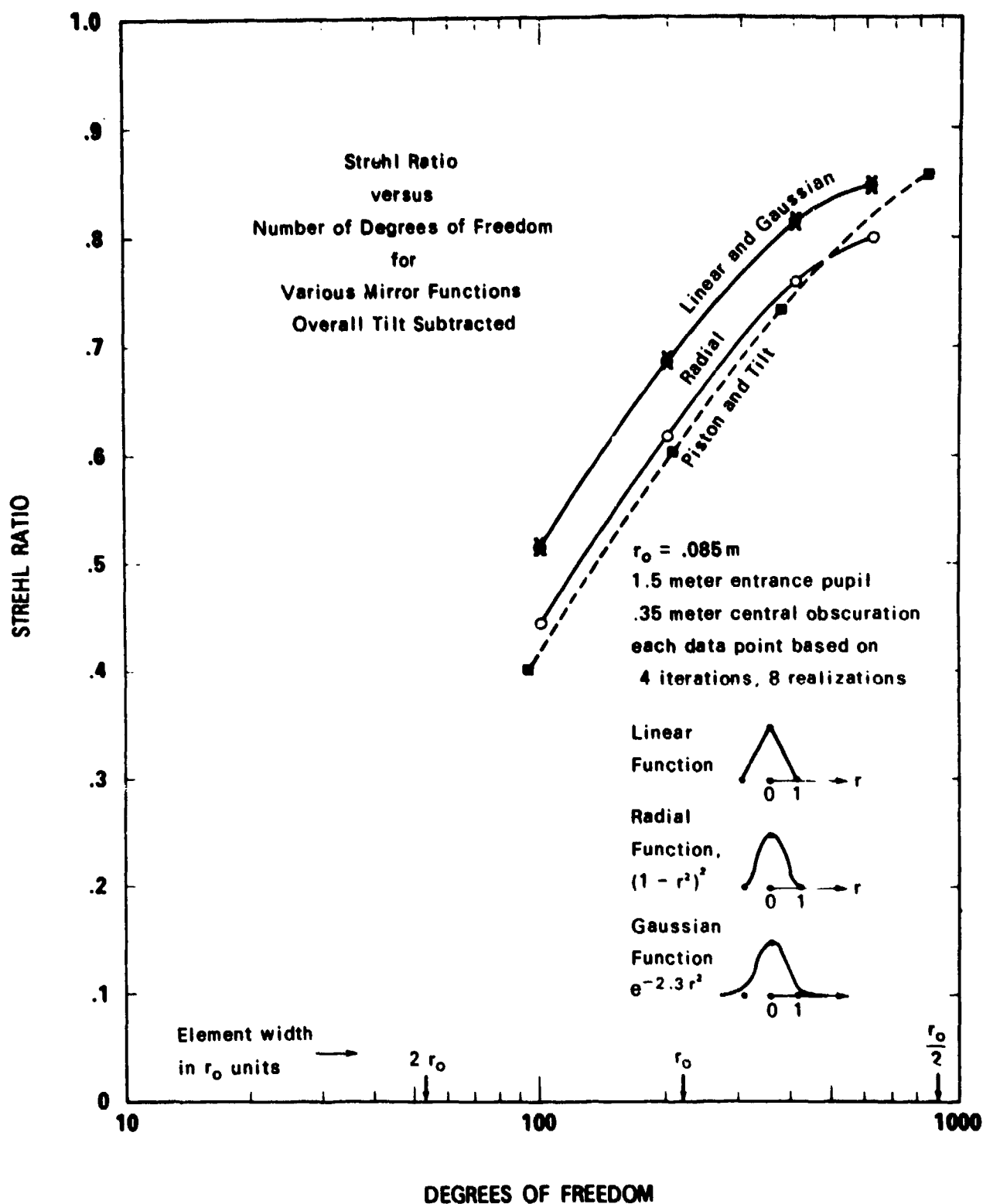


Figure 11. Strehl ratio versus degrees of freedom for a deformable mirror with various mirror functions.



Figure 12. Pre detection compensated images. Number of elements in 1.5 meter diameter clear aperture = 304. $r_0 = .1$ meter. Shearing interferometer used for wavefront sensor, deformable mirror with radial mirror function used for corrector. Frozen atmosphere assumed. 256x256 array.

- a) 1/1000 second exposure.
- b) 1/100 second exposure.
- b) 1/10 second exposure.

HOW MANY PICTURES DO YOU HAVE TO TAKE TO GET A GOOD ONE?*

David L. Fried
Optical Science Consultants
P.O. Box 388, Yorba Linda, CA 92686

SUMMARY

In short exposure imaging through turbulence, there is some probability that the image will be nearly diffraction-limited because the instantaneous wavefront distortion over the aperture was negligible. A number of years ago in a paper of almost the same title as this one, Hufnagel [1966] argued heuristically that the probability of getting a good image would decrease exponentially with aperture area. This paper undertakes a rigorous quantitative analysis of the probability.

We find that the probability of obtaining a good short-exposure image is

$$\text{Prob} \approx 5.6 \exp [-0.1557 (D/r_0)^2] , \quad (\text{for } D/r_0 \geq 3.5) ,$$

where D is the aperture diameter and r_0 is the coherence length of the distorted wavefront, as defined by Fried [1967]. A good image is one for which the squared wavefront distortion over the aperture is one radian² or less.

The analysis is based on the decomposition of the distorted wavefront over the aperture, in an orthonormal series with randomly independent coefficients. The orthonormal functions used are the eigenfunctions of a Karhunen-Loève integral equation. The integral equation is solved using a separation of variables into radial and azimuthal dependence. The azimuthal dependence was solved analytically and the radial numerically. The first 569 radial eigenfunctions and eigenvalues were obtained.

The probability of obtaining a good short-exposure image corresponds to a hyperspace integral in which the spatial dimensions are the independent random coefficients in the orthonormal series expansion. It is equal to the probability that a randomly chosen point in the hyperspace will lie within a hypersphere of unit radius, the points in the hyperspace being randomly chosen in accordance with the product of independent gaussian probability distributions — one distribution for each dimension. The variance of these distributions are directly proportional to the eigenvalues of the Karhunen-Loève equation. This hyperspace integral (involving up to several hundred dimensions) has been evaluated using Monte Carlo techniques.

1. INTRODUCTION

Atmospheric turbulence distorts a wave passing through it so that an image of an object seen through such turbulence may be degraded significantly below the diffraction limit of the imaging system's aperture. The length, r_0 , which is determined by the strength of turbulence over the propagation path, the path length, and the wavelength sets the achievable resolution. Whereas the diffraction-limited resolution might be considered to be λ/D , the turbulence-limited resolution is equal to λ/r_0 . No matter how large the aperture is, the average resolution achieved on imaging through turbulence will not exceed the λ/r_0 limit. This characterizes what is often referred to as the long-exposure image resolution. [For very short exposures, somewhat better average resolution, $\lambda/(3.4 r_0)$, is possible.]

This turbulence limit is a limit on the average performance. It is significant to note that at each instant of time a randomly distorted wavefront is received by the imaging system aperture, and the randomly distorted and spread image is formed. The average resolution, λ/r_0 , refers to the average effect of this distortion and spreading. At some instant of time, the instantaneous distortion of the wavefront may be very severe, i.e., there will be a great deal of "corrugation" of the wavefront. At other moments, the wavefront distortion may be relatively slight. There is a finite probability that at some particular instant of time, the wavefront distortion will be almost negligible. A short-exposure image formed at that time will appear to be almost diffraction-limited. The question we address in this paper is what is the probability that at a particular instant of time the wavefront distortion over the imaging system aperture will, in fact, be almost negligible. The inverse of this probability is the average number of short-exposure pictures we have to take to get a good one.

A number of years ago, this question was briefly addressed by R. E. Hufnagel [1966]. He utilized rather heuristic arguments, considering speckle in the focal plane, the average spread, image size, and the Rayleigh distribution of speckle, and based on these considerations argued that the probability of getting a good image ought to vary as an exponential function of the aperture diameter. Because the arguments were heuristic, he was not able to provide meaningful constants for this relationship. We shall show in this paper that the probability of getting a good image, i.e., the probability that at some instant the wavefront distortion over the imaging system aperture is essentially negligible, is an exponential function of aperture diameter over r_0 , for aperture diameters larger than about $3.5 r_0$. [Here r_0 is the turbulence-limited coherence diameter, as defined by Fried (1967).] We shall show that the probability of getting a good image is adequately represented by the expression

* Acknowledgment: This work sponsored by the Air Force Systems Command's Rome Air Development Center, Griffiss AFB, NY.

$$\text{Prob} \approx 5.6 \exp[-0.1557 (D/\lambda_0)^2]$$

In the next section, we shall outline our approach to a rigorous analysis of this problem. The sections after that will then present the various phases of the analysis and numerical computations.

2. ANALYTIC APPROACH

The basis of our treatment of the problem of calculating the probability of getting a good short-exposure image is through a decomposition of the random wavefront into an orthonormal series of independent components. By developing the statistics of this series representation, we are then able to calculate the probability that a particular sample of the wavefront distortion will correspond to essentially no significant distortion. This is because of the fact that a sample in which the wavefront distortion is essentially negligible has a series representation in which the coefficients are all very small. It is thus simply a matter of calculating the probability that all of the coefficients of the orthonormal series at some instant of time will be very small.

To carry out the detailed analysis required, we start with a functional representation of a sample of a randomly distorted wavefront over the imaging system aperture. Because wavefront tilt, as distinguished from the higher order forms of wavefront distortion, i. e., from wavefront corrugation, does not degrade the resolution of the image of a point source (in a short-exposure), but merely shifts it, we calculate the average wavefront tilt of this random sample and subtract it from the random wavefront distortion. The difference is the effective wavefront distortion, whose statistics we are concerned with.

Having established the functional representation for the effective wavefront distortion, we then wish to decompose this tilt-free randomly distorted wavefront sample over the aperture in terms of some orthonormal series. There are many possible orthonormal series which can be defined for uniform weighting over the aperture. The expression for the decomposition of the tilt-free wavefront distortion is essentially the same no matter which series we use. The basic expression that calculates the coefficients for the series representation of the tilt-free wavefront is a weighted integral of the random tilt-free wavefront distortion function. As a consequence of the fact that the tilt-free wavefront distortion is a gaussian random function, the coefficients of the series are gaussian random variables, since the integral expression is a linear function of the distortion function.

We select which of the infinity of possible orthonormal series is to be used in this decomposition by imposing the requirement that the random coefficients should be statistically independent of each other. Through appropriate manipulations, we are able to show that this requirement gives rise to a definition of the functions in the orthonormal series in terms of the Karhunen-Loève integral equation. The kernel of the integral equation is expressible as a function of the statistics of wavefront distortion. The Karhunen-Loève integral equation is homogeneous and gives rise to a set of eigenvalues, one for each of the eigenfunction solutions. The eigenfunctions are the functions that make up the orthonormal set. The eigenvalues are proportional to the mean square value of the random coefficients in the orthonormal series decomposition of the tilt-free random wavefront distortion.

The evaluation of the eigenvalues, and thus of the mean square random coefficients, is the key to the evaluation of the probability of getting a good short-exposure image. The random coefficients, as we noted before, are gaussian random variables. Their mean values are zero, and thus their mean square values, which are calculated from the eigenvalues, are their variances — which completely define the distribution of expected values of these random coefficients.

The significant point will be established that the mean square wavefront distortion averaged over the aperture for a particular sample of the randomly distorted wavefront is directly proportional to the sum of the squares of the random coefficients for that wavefront sample. Thus, the probability of getting a good short-exposure image is reduced to the calculation of the probability that all of the random coefficients will at some instant have small enough magnitude. We take as our criteria for small enough wavefront distortion the requirement that the tilt-free wavefront distortion squared, averaged over the aperture, will be less than or equal to one radian squared. This leads directly to a constraint on the sum of the squares of the random coefficients. Since we know the probability distribution for all of the random coefficients, it is a straightforward matter to then calculate the probability that their values squared and summed will be appropriately bounded.

In the following work, we rely on analytic techniques to develop the Karhunen-Loève integral equation and the basic expression defining its kernel, and similarly rely on analytic techniques for the formulation of the probability integral we wish to evaluate. The solutions of the Karhunen-Loève integral equation to obtain the eigenvalues (and the eigenfunctions) and the evaluation of the probability integral are of necessity carried out numerically. In the next section, we start the analysis treating the formulation leading up to the expression of the Karhunen-Loève equation.

3. DEVELOPMENT OF THE KARHUNEN LOÈVE EQUATION

We shall let $\phi(\vec{r})$ denote the random phase at a point \vec{r} associated with the random wavefront distortion at the aperture of the imaging system. Here \vec{r} is a two-dimensional variable denoting position in the plane of the imaging system aperture. We use the function $W(\vec{r}, D)$ where

$$W(\vec{r}, D) = \begin{cases} 1 & \text{if } |\vec{r}| \leq \frac{1}{2} D \\ 0 & \text{if } |\vec{r}| > \frac{1}{2} D \end{cases} \quad (1)$$

to define a circular aperture centered at the origin and having a diameter D . Drawing on our previously published results, Fried [1965], we can write for the corresponding average phase over the aperture, $\bar{\phi}$,

$$\bar{\phi} = (\frac{1}{4} \pi D^2)^{-1} \int d\vec{r} W(\vec{r}, D) \phi(\vec{r}) \quad (2)$$

and for the average tilt over the aperture is, $\bar{\alpha}$

$$\bar{\alpha} = (\frac{1}{4} \pi D^2)^{-1} \int d\vec{r} W(\vec{r}, D) \vec{r} \phi(\vec{r}) \quad (3)$$

The effective wavefront distortion as far as the quality of the image is concerned is the random wavefront distortion $\phi(\vec{r})$, less the average phase and a linear function, $\bar{\alpha} \cdot \vec{r}$, corresponding to the average tilt. This effective wavefront distortion, $\varphi(\vec{r}; D)$ is given by

$$\varphi(\vec{r}; D) = \phi(\vec{r}) - \bar{\phi} - \bar{\alpha} \cdot \vec{r} \quad (4)$$

(We note that since $\bar{\phi}$ and $\bar{\alpha}$ are functions of D , it is appropriate to show φ as having a D -dependence.)

The statistics of the random wavefront distortion $\phi(\vec{r})$ is adequately described for our purposes in terms of the phase structure function, \mathcal{B} , where

$$\mathcal{B}(|\vec{r} - \vec{r}'|) = \langle |\phi(\vec{r}) - \phi(\vec{r}')|^2 \rangle \quad (5)$$

For our calculations, all relevant theory concerning propagation through turbulence is adequately represented by taking note of the five-thirds power dependence established by Tatarski [1961] for the phase structure function. This is conveniently represented by the expression given by Fried [1967]

$$\mathcal{B}(|\vec{r} - \vec{r}'|) = 6.88 (|\vec{r} - \vec{r}'| / r_0)^{5/3} \quad (6)$$

The mean square difference of random phase is seen to vary as the five-thirds power of the separations of the points at which the phase is measured. The quantity r_0 , which as we noted earlier, is determined by propagation conditions, is given by the expression

$$r_0 = \left\{ 0.423 k^2 \int_{\text{path}} ds C_N^2 (s/L)^{5/3} \right\}^{-3/5} \quad (7)$$

where C_N^2 is the refractive-index structure constant (a measure of the optical strength of turbulence along the propagation path), L is the total propagation path length, and s runs from zero at the (point) source to L at the aperture plane, where r_0 is measured. r_0 determines the actual "magnitude" of the wavefront distortion.

What we are ultimately going to be concerned with is the covariance function for the effective wavefront distortion, $\varphi(\vec{r}; D)$. This covariance function is given by the expression

$$C_\varphi(|\vec{r} - \vec{r}'|; D) = \langle \varphi^*(\vec{r}; D) \varphi(\vec{r}'; D) \rangle \quad (8)$$

It can be evaluated in terms of the structure function, \mathcal{B} , by making use of Eq.'s (2), (3), (4), and (5). We shall return later to the evaluation of the evaluation of the covariance function, C_φ .

We consider an orthonormal series $\{f_n(\vec{r}; D)\}$, where f_n is the n^{th} -term in the orthonormal series. Because the terms are orthonormal with uniform weighting over the aperture area, it follows that

$$\int d\vec{r} W(\vec{r}, D) f_n^*(\vec{r}; D) f_{n'}(\vec{r}; D) = \begin{cases} 1 & \text{if } n = n' \\ 0 & \text{if } n \neq n' \end{cases} \quad (9)$$

Since the orthonormal series is by definition complete, we can represent the effective wavefront distortion φ in terms of a series based on $\{f_n\}$. Thus we write

$$\varphi(\vec{r}; D) = \sum_n \beta_n f_n(\vec{r}; D)$$

Inasmuch as the effective wavefront distortion φ is a random function, we expect the coefficients of the series β_n to be random variables. If we multiply both sides of Eq. (10) by $f_n^*(\vec{r}; D)$ and integrate over the aperture, then making use of Eq. (9), we obtain the result

$$\beta_n = \int d\vec{r} W(\vec{r}; D) f_n^*(\vec{r}; D) \varphi(\vec{r}; D) \quad (11)$$

This is the standard expression for the coefficients in any type of orthonormal series decomposition.

We note that since the coefficient β_n is a linear function of the effective wavefront distortion, $\varphi(\vec{r}; D)$, and since the effective wavefront distortion is a gaussian random function, it follows that β_n is a gaussian random variable. (Note: Propagation theory, cf. Tatarski [1961], tells us that the wavefront distortion ϕ is a gaussian random function. From Eq.'s (2) and (3), it follows that $\bar{\phi}$ and $\vec{\alpha}$, which are linear functions of ϕ , are gaussian random variables. Since the linear combination of gaussian random functions and gaussian random variables gives rise to a gaussian random function, it follows from Eq. (4) that φ is a gaussian random function.)

At this point, we are ready to introduce the requirement that the random variables β_n be statistically independent. We write this as

$$\langle \beta_n^* \beta_{n'} \rangle = \begin{cases} B_n^2(D) & \text{if } n = n' \\ 0 & \text{if } n \neq n' \end{cases} \quad (12)$$

where $B_n^2(D)$ is the variance associated with the random variable β_n . We show B_n^2 as a function of D , since, as will be seen, the magnitude of the random variable β_n is dependent on the aperture diameter.

Eq. (12) provides the basis for developing equations which define the orthonormal series $\{f_n(\vec{r}; D)\}$. To do this, we define the quantity δ in accordance with the equation

$$\delta = \langle \int d\vec{r}' W(\vec{r}', D) \varphi^*(\vec{r}'; D) \varphi(\vec{r}; D) f_n(\vec{r}'; D) \rangle \quad (13)$$

By the simple procedure of interchanging the order of integration and ensemble averaging, and making use of Eq. (8), we can recast Eq. (13) in the form

$$\delta = \int d\vec{r}' W(\vec{r}', D) C_\varphi(|\vec{r} - \vec{r}'|; D) f_n(\vec{r}'; D) \quad (14)$$

Starting from Eq. (13), and making use of Eq. (10) to allow replacement of $\varphi^*(\vec{r}'; D)$, we obtain

$$\delta = \langle \int d\vec{r}' W(\vec{r}'; D) \varphi(\vec{r}; D) \sum_n \beta_n^* f_n^*(\vec{r}'; D) f_n(\vec{r}'; D) \rangle \quad (15)$$

By the expedient of interchanging the order of summation and integration, and then making use of the orthonormal property expressed in Eq. (9) to allow the integral to be evaluated, and then of the independence property indicated by Eq. (12) so as to allow the n' -summation to be performed, we can cast Eq. (15) in the form

$$\begin{aligned} \delta &= \langle \varphi(\vec{r}; D) \sum_n \beta_n^* \int d\vec{r}' W(\vec{r}', D) f_n^*(\vec{r}'; D) f_n(\vec{r}'; D) \rangle \\ &= \langle \varphi(\vec{r}; D) \beta_n^* \rangle \end{aligned} \quad (16)$$

Now if we again make use of Eq. (10) to replace φ by its series representation, and then interchange the order of summation and ensemble averaging, and finally make use of Eq. (12) to facilitate performance of the n' -summation, we obtain

$$\begin{aligned} \delta &= \langle \sum_n \beta_n f_n(\vec{r}; D) \beta_n^* \rangle \\ &= \sum_n f_n(\vec{r}; D) \langle \beta_n^* \beta_n \rangle \\ &= B_n^2(D) f_n(\vec{r}; D) \end{aligned} \quad (17)$$

Equating the right-hand-side of Eq.'s (14) and (17), we obtain the Karhunen-Loève homogeneous integral equation

$$\int d\vec{r}' W(\vec{r}', D) C_\varphi(|\vec{r} - \vec{r}'|; D) f_n(\vec{r}'; D) = B_n^2(D) f_n(\vec{r}; D) \quad (18)$$

Our problem at this point is to solve the integral equation for the eigen functions $f_n(\vec{r}; D)$, and the corresponding eigenvalues $B_n^2(D)$.

4. REDUCTION AND SOLUTION OF THE KARHUNEN-LOÈVE INTEGRAL EQUATION

The kernel of the Karhunen-Loève integral equation, Eq. (18), can be written in the form

$$\begin{aligned} C_{\phi}(|\vec{r} - \vec{r}'|; D) &= \langle [\phi(\vec{r}) - \bar{\phi} - \vec{\alpha} \cdot \vec{r}]^* [\phi(\vec{r}') - \bar{\phi} - \vec{\alpha} \cdot \vec{r}'] \rangle \\ &= \langle \phi^*(\vec{r}') \rangle - \langle \phi^*(\vec{r}) \bar{\phi} \rangle - \langle \phi(\vec{r}') \bar{\phi} \rangle + \langle \bar{\phi}^* \bar{\phi} \rangle \\ &\quad - \langle \phi^*(\vec{r}) \vec{\alpha} \cdot \vec{r}' \rangle - \langle \phi(\vec{r}') \vec{\alpha} \cdot \vec{\alpha}^* \cdot \vec{r} \rangle + \langle \bar{\phi}^* \vec{\alpha} \cdot \vec{r}' \rangle \\ &\quad + \langle \bar{\phi} \vec{\alpha}^* \cdot \vec{r} \rangle + \langle \vec{\alpha}^* \cdot \vec{r} \vec{\alpha} \cdot \vec{r}' \rangle \end{aligned} \quad (19)$$

If we make the change of variables

$$\vec{x} = \vec{r}/D \quad (20a)$$

$$\vec{x}' = \vec{r}'/D \quad (20b)$$

we find that the D and r_0 -dependence of the kernel can be extracted, and we can write

$$C_{\phi}(|\vec{r} - \vec{r}'|; D) = (D/r_0)^{5/3} \mathfrak{C}(|\vec{x} - \vec{x}'|) \quad (21)$$

If we further write

$$f_{\phi}(\vec{r}; D) \equiv \mathfrak{F}_{\phi}(\vec{x}) \quad (22)$$

$$B_{\phi}^2(D) = D^3 (D/r_0)^{5/3} \mathfrak{B}_{\phi}^2 \quad (23)$$

$$W(\vec{r}; D) = \mathfrak{W}(\vec{x}) = \begin{cases} 1 & \text{if } |\vec{x}| \leq \frac{1}{2} \\ 0 & \text{if } |\vec{x}| > \frac{1}{2} \end{cases} \quad (24)$$

then we can recast Eq. (18) in the form

$$\int d\vec{x}' \mathfrak{W}(\vec{x}') \mathfrak{C}(|\vec{x} - \vec{x}'|) \mathfrak{F}_{\phi}(\vec{x}') = \mathfrak{B}_{\phi}^2 \mathfrak{F}_{\phi}(\vec{x}) \quad (25)$$

The key to this extraction of the D and r_0 -dependence from the Karhunen-Loève integral equation is our ability to extract a $(D/r_0)^{5/3}$ dependence from C_{ϕ} , as expressed in Eq. (21). After considerable algebraic manipulations, starting from Eq. (1), and making use of Eq. (6), as appropriate, we find that we can write C_{ϕ} in the form

$$\begin{aligned} C_{\phi}(|\vec{r} - \vec{r}'|; D) &= (D/r_0)^{5/3} \{ -\mathfrak{G}_0(|\vec{r}/D - \vec{r}'/D|) + \mathfrak{G}_1(r/D) + \mathfrak{G}_1(r'/D) - \mathfrak{G}_2 \\ &\quad + (r'/D) \cos \theta' \mathfrak{G}_3(r/D) + (r/D) \cos \theta' \mathfrak{G}_3(r'/D) - (r/D)(r'/D) \\ &\quad \times \cos \theta' \mathfrak{G}_4 \} \end{aligned} \quad (26)$$

where

$$\mathfrak{G}_0(x) = 3.44 x^{5/3} \quad (27a)$$

$$\mathfrak{G}_1(x) = 3.44 \left(\frac{1}{2}\pi\right)^{-1} \int_0^{1/2} dx'' x'' \int_0^{2\pi} d\theta'' (x^2 + x''^2 - 2xx'' \cos \theta'')^{5/3} \quad (27b)$$

$$\mathfrak{G}_2(x) = 8 \int_0^{1/2} dx'' x'' \mathfrak{G}_1(x'') \quad (27c)$$

$$\mathfrak{G}_3(x) = 3.44 \left(\frac{1}{2}\pi\right)^{-1} \int_0^{1/2} dx'' x''^2 \int_0^{2\pi} d\theta'' \cos \theta'' (x^2 + x''^2 - 2xx'' \cos \theta'')^{5/3} \quad (27d)$$

$$\mathfrak{G}_4(x) = 64 \int_0^{1/2} dx'' x''^2 \mathfrak{G}_3(x'') \quad (27e)$$

This constitutes the basis for writing C_{ϕ} in the form shown on the right-hand-side of Eq. (21).

Gathering all these results together, we would write \mathfrak{C} for use in Eq. (25) in the form

$$\begin{aligned} \mathfrak{C}(|\vec{x} - \vec{x}'|) &= \mathfrak{G}_0(|\vec{x} - \vec{x}'|) + \mathfrak{G}_1(x) + \mathfrak{G}_1(x') - \mathfrak{G}_2 + x' \cos \theta' \mathfrak{G}_3(x) \\ &\quad + x \cos \theta' \mathfrak{G}_3(x') - xx' \cos \theta' \mathfrak{G}_4 \end{aligned} \quad (28)$$

The quantity θ' appearing in Eq.'s (26) and (28) represents the angle between the vectors \vec{r} and \vec{r}' , and also between the vectors \vec{x} and \vec{x}' .

Eq. (25) is now essentially ready for us to start work on developing its solutions. Examination of the kernel and cognizance of the awkward powers involved (i.e., the 5/3-power and the 5/6-power) makes it clear that an analytic solution is not likely, and that numerical techniques will be necessary. The fact that the integral equation involves a two-dimensional integral makes the task an exceedingly difficult one for a digital computer. However, it is not strictly necessary to work with the two-dimensional integral equation, and in fact, we can cast our job in terms of obtaining a solution to a one-dimensional integral equation. To do this, we make use of the fact that working in (x, θ) -polar coordinates where

$$\vec{x} = (x, \theta) \quad (29)$$

we can show that a separation of variables is possible according to which $\mathcal{Y}_n(\vec{x})$ can be expressed as a product of a function of x and a function of θ . Moreover, we can show that the function of θ is an exponential. We write

$$\mathcal{Y}_n(\vec{x}) \equiv \mathcal{R}_{p,q}(x) \exp(iq\theta) \quad (30)$$

We shall see that it is a member of an orthonormal set defined by a Karhunen-Loève one-dimensional integral equation, where $\mathcal{R}_{p,q}(x)$ is a radial function to be determined.

Where previously n was an ordinal number arranging the eigenfunctions and eigenvalues, we now replace it with the ordinal number pair (p, q)

$$n = (p, q) \quad (31)$$

where q is the ordinal number for the azimuthal dependence. There is a different set of radial functions for each azimuthal dependence — hence the q associated with $\mathcal{R}_{p,q}(x)$. p is the ordinal number for the various radial functions in a given set associated with a particular q .

To show that Eq. (30) is valid, it is merely necessary to substitute it into the left-hand-side of Eq. (25) and show that the results can be cast in a form which is consistent with the right-hand-side of Eq. (25), as interpreted in terms of Eq. (30), i.e., we show consistency in our assumption. (Because the functions $\mathcal{R}_{p,q}(x)$ and $\exp(iq\theta)$ define complete sets, this is a necessary and sufficient proof.) To proceed, we define the modified kernel

$$\mathcal{K}_q(x, x') = x' \int_0^{2\pi} d\theta' \mathcal{G}(x, x', \theta') \exp(iq\theta') \quad (32)$$

and the alternate notation for the eigenvalue

$$\mathcal{R}_{n,q}^2 \equiv \mathcal{R}_{p,q}^2 \quad (33)$$

Now, substituting Eq. (30) into the left-hand-side of Eq. (25), we get

$$\begin{aligned} \int d\vec{x}' \mathcal{G}(\vec{x}) \mathcal{G}(|\vec{x} - \vec{x}'|) \mathcal{Y}_n(\vec{x}') &= \int_0^{1/2} dx' x' \int_0^{2\pi} d\theta' \mathcal{G}(x, x', \theta' - \theta) \mathcal{R}_{p,q}(x') \exp(iq\theta') \\ &= \exp(iq\theta) \int_0^{1/2} dx' \mathcal{K}_q(x, x') \mathcal{R}_{p,q}(x') \\ &= \mathcal{R}_{p,q}^2 \mathcal{R}_{p,q}(x) \exp(iq\theta) \end{aligned} \quad (34)$$

We note that in the last form presented in Eq. (34), the result interpreted in terms of Eq. (30) is consistent with the right-hand-side of Eq. (25). This proves the validity of the separation of variables expressed by Eq. (30). In developing the final result in Eq. (34), we have made use of the fact that the final dx' -integral is simply a function of x .

The function, $\mathcal{R}_{p,q}$, which is the radial dependence of \mathcal{Y}_n as indicated in Eq. (30), is defined by the requirement that it satisfy the one-dimensional homogeneous integral equation

$$\int_0^{1/2} dx' \mathcal{K}_q(x, x') \mathcal{R}_{p,q}(x') = \mathcal{R}_{p,q}^2 \mathcal{R}_{p,q}(x) \quad (35)$$

The key point here is, of course, our freedom to choose $\mathcal{R}_{p,q}$ to satisfy this equation and use the functions so defined in Eq. (30).

We note that the kernel of this one-dimensional homogeneous integral equation can be written in terms of the functions defined in Eq. (27a). If we substitute Eq. (28) into Eq. (32) and perform what simplifications are possible, we obtain

$$\mathcal{K}_0(x, x') = -x' \int_0^{2\pi} d\theta' \mathcal{G}_0([x^2 + x'^2 - 2xx' \cos \theta']^{1/2}) 2\pi x' [\mathcal{G}_1(x) + \mathcal{G}_1(x') - \mathcal{G}_2] \quad (36a)$$

$$R_{\pm 1}(x, x') = -x' \int_0^{2\pi} d\theta' Q_0 ([x^2 + x'^2 - 2xx' \cos \theta']^{1/2}) \exp(i\theta) + \pi x' [x' Q_3(x) + Q_3(x') - xx' Q_4] \quad (36b)$$

$$R_q(x, x') = -x' \int_0^{2\pi} Q_0 ([x^2 + x'^2 - 2xx' \cos \theta']^{1/2}) \exp(iq\theta) , \quad q = \pm 2, \pm 3, \pm 4, \dots \quad (36c)$$

Our problem now is the solution of the one-dimensional homogeneous integral equation presented by Eq. (35), with the kernel defined by Eq. 's (36a, b, or c).

For our numerical analysis, we have carried out this solution for the first 42 values of q , i.e., $q = 0$ to $q = 41$, using a 20-point radial space in the interval 0 to $\frac{1}{2}$. Sorting the eigenvalues in accordance with their magnitude, we find that we have obtained at least the first 569 of the eigenvalues. (Though more than 569 eigenvalues were actually calculated, we have no assurance that the $p = 1$, $q = \pm 42$ eigenvalue which we did not obtain does not rank above the 570th of the eigenvalues that we did obtain. We are, however, sure that it is smaller than the 569th eigenvalue which is for $p = 1$, $q = 41$. Hence our termination of the list at that point.) As a check on the accuracy of our calculations and the completeness of our list, we have been able to separately show, making use of earlier work, Fried [1965], quite distinct from this Karhunen-Loève decomposition, that the infinite sum of eigenvalues must have the value of

$$\sum_{n=1}^{\infty} \lambda_n = 0.1056 \quad (37a)$$

We note that

$$\sum_{n=1}^{569} \lambda_n = 0.1047 = .9915 \sum_{n=1}^{\infty} \lambda_n \quad (37b)$$

which gives us fairly strong assurance that our list is essentially complete and our computations reasonably accurate. In Table 1, we list these eigenvalues and their cumulative sum for the first 100 eigenvalues. We note that because the integral equation and kernel are symmetric between q and $-q$, it is not necessary for us to solve with negative values of q . The eigenvalues obtained for all values of q other than $q = 0$ are doubly degenerate since they correspond to both $+q$ and $-q$. Accordingly, in Table 1 we have counted twice those eigenvalues for which q is not equal to zero, though they are listed only once, and the cumulative sum as shown corresponds to the double addition of those eigenvalues.

TABLE 1

Eigenvalue Listing, $\lambda_n^2 = \lambda_{p,q}^2$

Eigenvalues are ranked by magnitude, with ordinal number n assigned according to rank. Where the eigenvalue is degenerate, (i.e., $q \neq 0$), two values of n are assigned. This is indicated in the (p,q)-numbering by listing both a positive and a negative value for q . The p-values shown for each eigenvalue represent an ordinal ranking by magnitude for each value of the azimuthal number, q . The eigenvalues are listed along with the cumulative sum of the eigenvalues. Whenever the eigenvalue is degenerate, the corresponding cumulative sum represents the addition of the eigenvalue twice.

n	Eigenvalue λ_n^2	Cumulative Sum $\sum_{i=1}^n \lambda_i^2$	p q	n	Eigenvalue λ_n^2	Cumulative Sum $\sum_{i=1}^n \lambda_i^2$	p q
1, 2	.018765000	.037530000	1 2, -2	51, 52	.000091963	.099660738	1, 11, -11
3	.018733000	.056263000	1 0	53, 54	.000089079	.099838896	4 3, -3
4, 5	.005215500	.066694000	1 3, -3	55, 56	.000085452	.100009800	2 8, -8
6, 7	.005180000	.077054000	1 1, -1	57, 58	.000084808	.100179416	4 1, -1
8, 9	.002153400	.081360800	1 4, -4	59, 60	.000069736	.100318888	3 6, -6
10, 11	.001645600	.084652000	2 2, -2	61, 62	.000069646	.100458180	1 12, -12
12	.001632200	.086284200	2 0	63, 64	.000063398	.100584976	2 9, -9
13, 14	.001084800	.088453800	1 5, -5	65, 66	.000062420	.100709816	4 4, -4
15, 16	.000773650	.090011100	2 3, -3	67, 68	.000058784	.100927384	5 2, -2
17, 18	.000757140	.091515380	2 1, -1	69	.000057899	.100885283	5 0
19, 20	.000617730	.092750840	1 6, -6	70, 71	.000053855	.100992993	1 13, -13
21, 22	.000428150	.093607140	2 4, -4	72, 73	.000051459	.101095911	3 7, -7
23, 24	.000382540	.094372220	1 7, -7	74, 75	.000048271	.101192453	2 10, -10
25, 26	.000382130	.095136480	3 2, -2	76, 77	.000045524	.101283501	4 5, -5
27	.000373790	.095510270	3 0	78, 79	.000042494	.101368489	5 3, -3
28, 29	.000262110	.096034490	2 5, -5	80, 81	.000042428	.101453345	1 14, -14
30, 31	.000251910	.096538310	1 8, -8	82, 83	.000041356	.101536057	5 1, -1
32, 33	.000224370	.096987050	3 3, -3	84, 85	.000039058	.101614173	3 8, -8
34, 35	.000215100	.097417250	3 1, -1	86, 87	.000037553	.101689279	2 11, -11

(Continued on next page)

short-exposure image

$$\text{Prob (Good Short-Exposure Image)} = \text{Prob} \left(\sum_n S_n^2 \leq 1 \text{ rad}^2 \right) \quad (45)$$

can be written in terms of the gaussian distributions for each of the variables

$$\text{Prob (Good Short-Exposure Image)} = \prod_{n=1}^{\infty} \int_{\text{limits}} dS_n (2\pi\sigma_n^2)^{-1/2} \exp(-\frac{1}{2} S_n^2/\sigma_n^2), \quad (46)$$

where the limits correspond to a hypersphere in the multidimensional S_n -space, the sphere being of unit radius.

This calculation, though it bears some resemblance to the ordinary Chi-squared integral, because of the dependence of σ_n^2 on n , can not be performed in closed form. We have therefore made use of Monte Carlo techniques for evaluation of this probability. The results obtained are shown in Table 2.

TABLE 2

Probability of Obtaining a Good Short-Exposure Image

D/r_0	Probability
2	0.986 ± 0.006
3	0.765 ± 0.005
4	0.334 ± 0.014
5	$(9.38 \pm 0.33) \times 10^{-2}$
6	$(1.915 \pm 0.084) \times 10^{-2}$
7	$(2.87 \pm 0.57) \times 10^{-3}$
10	$(1.07 \pm 0.48) \times 10^{-6}$
15	$(3.40 \pm 0.59) \times 10^{-15}$

In Fig. 1, we have plotted this probability in a form which makes manifest an exponential dependence on $(D/r_0)^2$. As can be seen, the results are very strongly suggestive of this type of dependence, and we have fitted the equation

$$\text{Prob} \approx 5.6 \exp[-0.1557 (D/r_0)^2] \quad , \quad (\text{if } D/r_0 \geq 3.5) \quad (47)$$

to this data. It is quite obvious that the probability is a strong function of D/r_0 , and that if we intend to have a reasonable probability of obtaining a good short-exposure image, we must be careful not to push the aperture diameter beyond some reasonable multiple of r_0 . Exactly how large this multiple can be depends on how many short-exposure images we are willing to take or how long we are willing to wait before we get a good image.

6. DISCUSSION OF RESULTS

The results presented in Table 2 and Fig. 1 are fairly self-explanatory. They are certainly in good agreement with Hufnagel's [1966] conjecture that the probability ought to be a negative exponential function of aperture area. The quantitative results tell us that if we want a probability of the order of 1×10^{-3} of obtaining a good short-exposure image, the aperture diameter should not be significantly larger than $7 r_0$ or $8 r_0$. If we are willing to accept a probability of 1×10^{-6} , only a minor increase in diameter up to $10 r_0$ is allowed. Working with diameters any larger than this leads to what are almost certainly unacceptable probabilities.

It is particularly interesting to note the operationally high probabilities that apply for diameters of about $7 r_0$ or a bit less. This suggests that for many imagery purposes significantly better than ordinary turbulence-limited resolution can be achieved if we carefully choose our aperture diameter and take several hundred short-exposures and select from these the best. This, of course, calls for not merely an adjustable aperture on our imaging system, but some method of measuring r_0 so that we know what aperture diameter to use.

It is appropriate to note that the probability we have calculated applies independently to separate isoplanatic patches on the image. This means that in any one image, rather than its being entirely good or entirely poor resolution, there will be distributed over the image field-of-view a set of rather small

TABLE 1 (Continued)

n	Eigenvalue β_n^2	Cumulative Sum $\sum_{i=1}^n \beta_i^2$	p	q	n	Eigenvalue β_n^2	Cumulative Sum $\sum_{i=1}^n \beta_i^2$	p	q
36, 37	.000173860	.097764970	1	9, -9	88, 89	.000034265	.101757809	4	6, -6
38, 39	.000172040	.098109050	2	6, -6	90, 91	.000033936	.101825681	1	15, -15
40, 41	.000143750	.098396550	3	4, -4	92, 93	.000031680	.101889041	5	4, -4
42, 43	.000133880	.098664310	4	2, -2	94	.000030739	.101919780	6	0
44	.000129880	.098794190	4	0	95, 96	.000030339	.101980458	3	9, -9
45, 46	.000124560	.099043310	1	10, -10	97, 98	.000029757	.102039972	2	12, -12
47, 48	.000118870	.099281050	2	7, -7	99, 100	.000029734	.102099440	6	2, -2
49, 50	.000097881	.099476812	3	5, -5					

With the eigenvalues thus tabulated, we are ready to turn our attention to the formulation and evaluation of the probabilistic integral determining the probability that at any instant the random wavefront distortion will yield a good short-exposure image.

5. PROBABILITY FORMULATION AND EVALUATION

The square of the effective wavefront distortion, $\phi(\vec{r}; D)$ averaged over the aperture can be written as

$$\Delta^2 = (\frac{1}{2} \pi D^2)^{-1} \int d\vec{r} W(\vec{r}, D) |\phi(\vec{r}; D)|^2 \quad (38)$$

If we use Eq. (10) to replace ϕ in Eq. (38), and then interchange the order of summation and integration, we get

$$\Delta^2 = (\frac{1}{2} \pi D^2)^{-1} \sum_{n, n'} \beta_n^* \beta_{n'} \int d\vec{r} W(\vec{r}, D) f_n^*(\vec{r}) f_{n'}(\vec{r}) \quad (39)$$

Making use of the orthonormality condition expressed in Eq. (9), Eq. (39) can be reduced to the form

$$\begin{aligned} \Delta^2 &= (\frac{1}{2} \pi D^2)^{-1} \sum_{n, n'} \beta_n^* \beta_{n'} \\ &= \sum_n S_n^2 \end{aligned} \quad (40)$$

where S_n is defined in terms of β_n as

$$S_n = [(\frac{1}{2} \pi D^2)^{-1} \beta_n^* \beta_n]^{1/2} \quad (41)$$

Since β_n is a gaussian random variable, so is S_n . Moreover, since β_n has a zero mean value, so does S_n . Its variance is

$$\sigma_n^2 = \langle S_n^2 \rangle \quad (42)$$

Substituting Eq. (41) into Eq. (42), and making use of Eq. (12), we obtain

$$\sigma_n^2 = (\frac{1}{2} \pi D^2)^{-1} \langle \beta_n^* \beta_n \rangle = (\frac{1}{2} \pi D^2)^{-1} B_n^2(D) \quad (43)$$

Now if we make use of Eq. (23), we can cast Eq. (43) in the form

$$\sigma_n^2 = \frac{4}{\pi} (D/r_0)^{2\alpha} \beta_n^2 \quad (44)$$

At this point, we see that the aperture averaged, squared wavefront distortion, Δ^2 , as given in Eq. (40), is equal to the sum of the square of a set of gaussian random variables, S_n , each with mean value zero, and with a variance, σ_n^2 given by Eq. (44). The value of σ_n^2 is given in terms of the eigenvalues we have just solved for and which are listed in Table 1. The dependence of the aperture-averaged wavefront distortion squared on aperture diameter, D , and on the wavefront distortion coherence length, r_0 , is contained in the $(D/r_0)^{2\alpha}$ dependence shown in Eq. (44).

Our problem now is to figure out the probability that the random variables, S_n , squared and summed, as in the right-hand-side of Eq. (40), will have a value less than some amount. We define a good image as one that is formed when the wavefront distortion over the aperture is less than one radian rms, i.e., when Δ^2 is less than one radian-squared. The probability of obtaining such a good

short-exposure image

$$\text{Prob (Good Short-Exposure Image)} = \text{Prob} \left(\sum_i S_i^2 \leq 1 \text{ rad}^2 \right) \quad (45)$$

can be written in terms of the gaussian distributions for each of the variables

$$\text{Prob (Good Short-Exposure Image)} = \prod_{i=1}^n \int_{L_i} dS_i (2\pi\sigma_i^2)^{-1/2} \exp(-\frac{1}{2} S_i^2/\sigma_i^2), \quad (46)$$

where the limits correspond to a hypersphere in the multidimensional S_i -space, the sphere being of unit radius.

This calculation, though it bears some resemblance to the ordinary Chi-squared integral, because of the dependence of σ_i^2 on n , can not be performed in closed form. We have therefore made use of Monte Carlo techniques for evaluation of this probability. The results obtained are shown in Table 2.

TABLE 2

Probability of Obtaining a Good Short-Exposure Image

D/r_0	Probability
2	0.986 ± 0.006
3	0.765 ± 0.005
4	0.334 ± 0.014
5	$(9.38 \pm 0.33) \times 10^{-2}$
6	$(1.915 \pm 0.084) \times 10^{-2}$
7	$(2.87 \pm 0.57) \times 10^{-3}$
10	$(1.07 \pm 0.48) \times 10^{-6}$
15	$(3.40 \pm 0.59) \times 10^{-15}$

In Fig. 1, we have plotted this probability in a form which makes manifest an exponential dependence on $(D/r_0)^2$. As can be seen, the results are very strongly suggestive of this type of dependence, and we have fitted the equation

$$\text{Prob} \approx 5.6 \exp[-0.1557 (D/r_0)^2] \quad , \quad (\text{if } D/r_0 \geq 3.5) \quad (47)$$

to this data. It is quite obvious that the probability is a strong function of D/r_0 , and that if we intend to have a reasonable probability of obtaining a good short-exposure image, we must be careful not to push the aperture diameter beyond some reasonable multiple of r_0 . Exactly how large this multiple can be depends on how many short-exposure images we are willing to take or how long we are willing to wait before we get a good image.

6. DISCUSSION OF RESULTS

The results presented in Table 2 and Fig. 1 are fairly self-explanatory. They are certainly in good agreement with Hufnagel's [1966] conjecture that the probability ought to be a negative exponential function of aperture area. The quantitative results tell us that if we want a probability of the order of 1×10^{-3} of obtaining a good short-exposure image, the aperture diameter should not be significantly larger than $7 r_0$ or $8 r_0$. If we are willing to accept a probability of 1×10^{-6} , only a minor increase in diameter up to $10 r_0$ is allowed. Working with diameters any larger than this leads to what are almost certainly unacceptable probabilities.

It is particularly interesting to note the operationally high probabilities that apply for diameters of about $7 r_0$ or a bit less. This suggests that for many imagery purposes significantly better than ordinary turbulence-limited resolution can be achieved if we carefully choose our aperture diameter and take several hundred short-exposures and select from these the best. This, of course, calls for not merely an adjustable aperture on our imaging system, but some method of measuring r_0 so that we know what aperture diameter to use.

It is appropriate to note that the probability we have calculated applies independently to separate isoplanatic patches on the image. This means that in any one image, rather than its being entirely good or entirely poor resolution, there will be distributed over the image field-of-view a set of rather small

regions, isoplanatic patches, in which the resolution is good. The rest of the image area will have much poorer resolution. To image a large object and determine all of the fine details of that object, it would be necessary to piece together the image from a set of short-exposures, selecting the high resolution regions in each of the images, to put together one high resolution image.

As a word of caution, it is appropriate to recollect here that we have assumed that the statistics of turbulence and the value of r_0 remain constant over the period of the "experiment." What we have calculated is the probability that a sample drawn from the ensemble of wavefront distortions will be a sample with almost no distortion. Our ensemble is restricted to samples from the same value of r_0 , i. e., there is no change in the strength of turbulence over the propagation path. There is, however, a larger ensemble associated with different values of r_0 . r_0 changes with changing turbulence conditions, and this larger ensemble includes cases for which r_0 may sometimes, though infrequently, be significantly larger than the typical value. Average probabilities over this grand ensemble might be expected to yield significantly higher probabilities of a good short-exposure image for large aperture diameters. However, obtaining an average over this grand ensemble corresponds in the physical world to waiting over periods of hours, perhaps days, for the variety of turbulence conditions that can exist over the propagation path. This may not be practical. The ensemble average for which we have evaluated the probability of obtaining a good short-exposure image in this paper corresponds to taking a set of images in rapid succession over a short period of time during which we do not expect or require the nature of the turbulence in the propagation path to change. We believe this case corresponds to a variety of nominal practical limitations. Our results show that in this type of situation, a judicious choice of aperture diameter and careful selection of the images to be utilized can yield results which have significantly better image resolution than the typical atmospheric turbulence limit.

REFERENCES

- Fried, D. L., "Statistics of a Geometric Representation of Wavefront Distortion," J. Opt. Soc. Am. 55, 1427 (1965)
- Fried, D. L., "Optical Heterodyne Detection of an Atmospherically Distorted Signal Wavefront," Proc. IEEE 55, 57 (1967)
- Hufnagel, R. E., in "Restoration of Atmospherically Degraded Images," National Academy of Sciences, Washington, D. C., 1966; Vol. 3, Appendix 2, p. 11
- Tatarski, V. I., "Wave Propagation in a Turbulent Medium," McGraw-Hill, New York 1961.

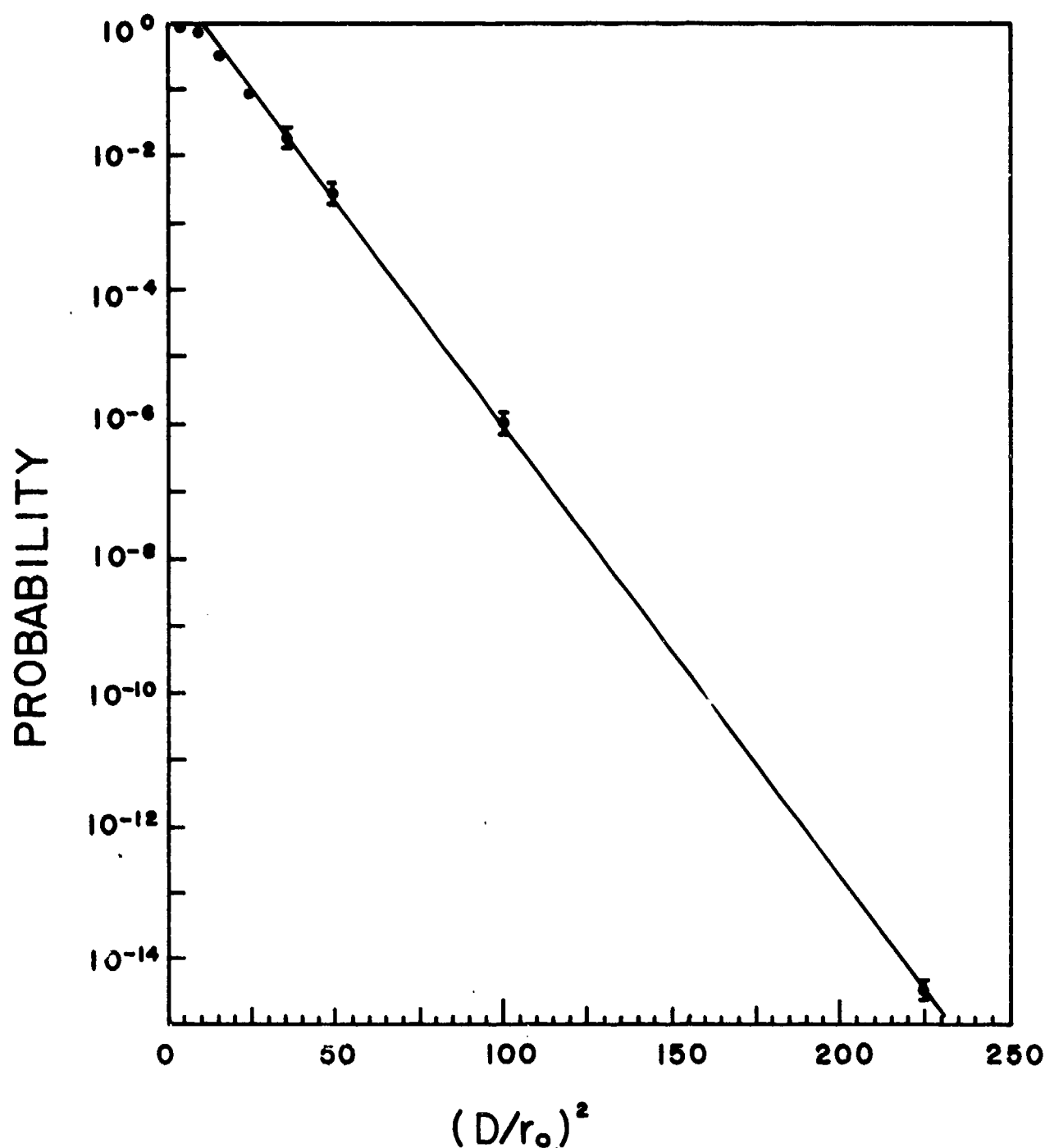


Figure 1. Probability of Obtaining a Good Short-Exposure Image.

The probability is plotted on a logarithmic scale against the aperture diameter divided by r_0 ratio-squared. A straight line on this graph shows an exponential dependence of the probability on the aperture area. The data plotted corresponds to the values in Table 2, with the spread due to the fact that Monte Carlo integral evaluation was used. The straight line fit to the data matches Eq. (47).

REMOTE PROBING OF WINDS AND REFRACTIVE TURBULENCE USING OPTICAL TECHNIQUES

S. F. Clifford
National Oceanic and Atmospheric Administration
Environmental Research Laboratories
Wave Propagation Laboratory
Boulder, Colorado 80302

SUMMARY

At the Wave Propagation Laboratory (WPL) of the National Oceanic and Atmospheric Administration (NOAA), we have considerable experience in the development of techniques of measuring wind and refractive turbulence C^2 using both active and passive optical sources. From the initial development of our path-average laser wind sensor, we have further developed systems for measuring horizontal profiles of wind and C^2 . Recently, we have constructed a passive wind sensor that requires no active light source; it responds to fluctuations of light reflected from a target to determine the path-averaged crosswind. Finally, we have made recent progress in the application of the horizontal-path techniques to the problems of remotely sensing wind and C^2 profiles aloft from observations of stellar scintillations. In this paper, we analyze the principles of operation of these devices and compare their performance with more conventional meteorological instruments.

1. INTRODUCTION

In recent years, many authors (LAWRENCE, R. S. et al., 1972; LEE, R. W., 1974; WANG, T-i, et al., 1974; SHEN, L., 1970; ISHIMARU, A., 1972; MANDICS, P.A., et al., 1973; HARP, J. C., 1971; MANDICS, P. A., 1971; and KJELAAS, A. G. and G. R. OCHS, 1974) have considered the possibility of remote probing of winds over optical, microwave, and acoustic paths. At the Wave Propagation Laboratory of NOAA, we have demonstrated (LAWRENCE, R. S. et al., 1972) the feasibility of using a line-of-sight laser link to measure the path-averaged crosswind. From the initial development of our path-average laser wind sensor, we have further developed techniques for measuring horizontal profiles of crosswind and refractive turbulence (WANG, T-i, et al., 1974). More recently, we have constructed a passive wind sensor that measures wind without the need of a light source (CLIFFORD, S. F. et al., 1974). This system responds to the fluctuations of light from a naturally occurring scene such as the horizon or a hillside.

We at NOAA (OCHS, G. R., et al., 1974) and others (VERNIN, J. and F. RODDIER, 1973) have measured winds aloft from observations of stellar scintillations and we are currently testing a device to measure vertical profiles of refractive turbulence. The vertical distribution of refractive turbulence is important to know since it is refractive turbulence that limits our ability to resolve objects in orbit and produces enhanced error rates in optical communication systems. We will review progress in each of the above areas with emphasis on techniques to remotely sense meteorological information relevant to the design of optical systems.

2. THEORY OF OPERATION

Each of the techniques mentioned is an outgrowth of our path-average laser system and, because of this fact, they have quite similar principles of operation. Figure 1 shows the general configuration of our laser sensor. A laser beam, diverged to approximate a point light source, illuminates two detectors. The temperature irregularities along the optical path produce irradiance fluctuations at each of the detectors. As the wind advects these irregularities across the laser beam, the irradiance fluctuations that they produce propagate from one detector to the other in a time of the order of ρ/v_{\perp} where ρ is the sensor spacing and v_{\perp} is the transverse wind speed. If we time-lag correlate the signals observed by the two detectors, we obtain the normalized covariance function shown in Figure 2. The wind speed information is contained in both the time lag to the peak of the covariance function and the slope at zero time lag. We compute the slope at zero time lag to determine the wind speed rather than the peak delay because the former is a linear function of windspeed and the latter is non-linear (LAWRENCE, R. S., et al., 1974). Also, the slope technique is much less sensitive to random temporal fluctuations in the spatial scintillation pattern than the peak delay technique (LAWRENCE, R. S., et al., 1974).

Figure 3 shows a typical sample of a laser wind sensor record compared with the more conventional anemometer measurements. The top record is the reading of the optically derived wind speed transverse to a 300 m laser beam. The lower record is the average wind speed measured by six propeller anemometers spaced uniformly along the optical path. The agreement between the two curves is excellent showing that the laser wind sensor can be effectively employed to measure winds wherever a spatially-averaged value is desirable, as in determining crosswinds along airport runways, measuring the flow of pollutants down a valley, or by using a triangular array of such sensors to measure a spatially averaged divergence of the wind field.

3. THE PASSIVE WIND SENSOR

In certain applications where a two-ended system is impossible or impractical; as when one end of the optical path is inaccessible, the laser wind sensor cannot operate. To overcome this limitation we have developed a modification of our optical wind sensor (CLIFFORD, S. F., et al., 1974) that measures the path-averaged crosswind by observing the fluctuations in irradiance of a naturally illuminated scene such as a sunlit hillside, a forest, or a variety of other natural targets. Figure 4

illustrates the geometry of the passive wind sensor. Two detectors having a two-dimensional sensitivity spectrum H^2 are separated by a distance ρ and observe the fluctuations in irradiance from ambient light reflected off the target. As before, we compute the time-lagged covariance of the two detectors and determine the wind from the slope at zero delay. This technique is more complicated than the laser system because we now must specify the spectral density of the scene Q^2 to determine the weighting function for the measured wind. For example, Figure 5 illustrates the wind weighting function for the case of a trailer observed by two detectors arranged in the configuration shown in the lower left corner. The detectors are narrowband spatial filters of wavelength $2.5/\lambda L$, where λ is the mean frequency of the reflected light and L is the distance to the target. The tendency of the passive sensor to emphasize the winds near the receiver is characteristic of the device and applies to nearly all scene spectra. In the upper right corner of Figure 5, we show the behavior of the passive sensor compared with the average of 10 anemometers spaced uniformly along the optical path. The agreement is quite satisfactory. Finally, Figure 6 shows a similar comparison for the same target. We have plotted the reading of the passive wind sensor and the average of the five anemometers closest to the receiver. The optical system gain (upper trace) was increased to displace the curves for convenient comparison. The agreement in detail is quite remarkable.

4. WIND AND REFRACTIVE TURBULENCE PROFILING

In some applications, it may be desirable to obtain profiles of wind and refractive-turbulence intensity C^2 . We accomplish this by crossing two laser beams (see Figure 7) so that their common volume is located at the path position that we wish to probe. (The two beams must be offset in the horizontal direction to measure wind.) If we again calculate the time-lagged covariance function of two horizontally separated sensors each looking independently at one of the beams (we accomplished this by polarization coding of the two beams--the upper detectors in Figure 7 would see only the horizontally polarized light from the lower laser and the lower detectors only the vertically polarized light from the upper laser), the resultant signal will depend only on the effects of the turbulence within the common volume of the two beams.

In Figure 8, we have plotted the theoretical path-weighting function for C^2 (solid curve) along with experimental data points (crosses) obtained with fine wire temperature probes. We calculate C^2 from C_T^2 , the temperature structure parameter, by using the equation (LAWRENCE, R. S., et al., 1970)

$$C_n^2 = [(79p/T^2)10^{-6}]^2 C_T^2 \quad (1)$$

where p is the background pressure in millibars and T is the temperature in Kelvin. The fine wire probes measure the small fluctuations in temperature at two different points. The probe responses are then subtracted, squared, and averaged to obtain C_T^2 , i.e.,

$$C_T^2 = \langle [T(x) - T(x+r)]^2 \rangle / r^2 \quad (2)$$

where r is the separation of the two temperature sensors and the angle brackets indicate an ensemble average. (C_T^2 may be considered the mean square difference in temperature of two thermometers separated a unit distance.) The data points in Figure 8 are determined by having a computer take the five measured values of C^2 and multiply them by appropriate weights to maximize the correlation between the optical covariance measurement (a function of $C^2(z)$) and this weighted sum of C^2 values. So, the resulting curve depicts the relative importance of refractive turbulence at each path position for producing our optical measurement. We may increase our path resolution, i.e., narrow the weighting function, by simultaneously increasing the vertical separation of the transmitters and receivers. We change path positions by independently increasing or decreasing the transmitter's or receiver's vertical separation. We obtained the midpath crossover and the resolution shown in Figure 8 by separating the transmitters and receivers by 1.8 Fresnel zones $\sqrt{\lambda L}$, where λ is the wavelength of the radiation and L is the optical pathlength.

Similarly, we may measure transverse windspeed in the common volume of the two beams (provided they are offset slightly in the horizontal direction) by measuring the slope of the time lag covariance function at zero delay. Figure 9 illustrates the type of weighting function expected (solid line) and the experimental points derived from the measurements of five anemometers. We obtained the crossover at midpath and the path resolution shown by vertically separating the transmitters and receivers by 1.8 Fresnel zones $\sqrt{\lambda L}$ and using a horizontal beam offset of 0.3 Fresnel zones. Again, if we increase the vertical separation the peak will narrow. For further discussion and a more complete description of the systems advantages and limitations see WANG et al. 1974.

5. MEASUREMENTS OF WINDS AND C^2 ALOFT

There are extremely interesting applications of the above-mentioned techniques for measuring winds and C^2 aloft from observations of stellar scintillations. Vertical profiles of wind, remotely sensed at, say, 10 levels, provide invaluable data for weather forecasting. Remotely sensed profiles of C^2 provide the necessary information to determine the performance degrading effects of atmospheric turbulence on such optical systems as telescopes and optical communication links. In a recent report (OCHS, G. R., et al., 1974), we analyzed several techniques for remotely measuring wind and C^2 aloft.

Figure 10 is a photograph of an instrument that we designed to measure horizontal winds aloft. The system consists of four photomultipliers arranged orthogonally in pairs as shown in Figure 11. One pair (1-2) measures the slope of the time-lag covariance function at zero delay while a servo system rotates the mount so that this quantity is maintained at zero. When this pair of detectors registers zero wind speed parallel to their separation, the other two detectors (3-4) are oriented parallel to the horizontal wind. We then compute the wind speed by measuring the delay to the peak of the covariance function of the observed stellar scintillations and dividing this number into

the detector separation. From the mount orientation and the delay to the peak, we can then determine the wind speed and direction.

Figure 12 shows the optically measured wind velocities compared with those determined by a rawinsonde launched 55 km away during 3 days in March 1972. From the geometry of our system, and the use of 5-cm apertures separated a distance of 6.5 cm, we expected the wind reading to be largely determined by winds near the tropopause. We then, somewhat arbitrarily, compared our velocity measurements with the average of the rawinsonde data above the tropopause. In Figure 12 there is good agreement in direction and poorer agreement in wind speed, but the overall correlation between the two sets of data is quite good considering the more than 50 km separation between the optical instrument and the rawinsonde launching site.

To measure profiles of wind or C^2 , we must have much better height resolution than that afforded by the simple two circular aperture system. We have undertaken a theoretical study of our ability to measure profiles using narrow band spatial filtering of stellar scintillation (OCHS, G. P. et al., 1974). From the diffraction theory of the production of scintillation, we expect that at each height range one eddy size of refractive turbulence, the one that is a Fresnel zone for the rest of the optical path to the ground, will be the most important contributor to scintillation from that given height. If we adjust our spatial filter to select only that wavelength disturbance in the received scintillation pattern, then we should be observing scintillation produced by refractive turbulence primarily at that height. Of course, spatial filters have side lobes and the theory shows that other heights will contribute to the observation at a given spatial wavelength, but we would expect the weighting function to have some sort of emphasis in the desired height range. We are trying to discover how well we can determine a height profile of wind and C^2 , i.e., how many levels and with what height averaging, by constructing a weighted sum of measurements of many different spatial wavelength detectors. By adding and subtracting these data, we can synthesize an optimum weighting function. Preliminary evidence indicates that we are able to obtain C^2 profiles averaged over six height ranges using observations of a single star. The height averaging interval ranges from about 2 km for the lowest altitude to 5 km for the highest altitude data.

The technique of looking at a single star can be modified in the same way as we did for our horizontal path work. For example, we could look at binary stars (ROCCA, A., et al., 1974), or two points on the limb of the sun or moon and obtain weighting functions quite analogous to our laser technique (OCHS, G. R. et al., 1974). Many modifications of the horizontal techniques have potential for vertical profile work.

6. DISCUSSION

We have discussed recent progress at NOAA in the remote sensing of winds and refractive turbulence using optical techniques. The ability to remotely sense these quantities has impact on such varied fields as weather forecasting, astronomical and satellite imaging with telescopes, ballistics and optical communication systems. Remote sensing, as opposed to in-situ measurements, provides the only hope of acquiring sufficient quality and quantity of data to understand fully and to compensate for the performance degrading effects of atmospheric turbulence on optical systems.

7. REFERENCES

- CLIFFORD, S. F., G. R. OCHS, and T-i WANG, 1974, "Theoretical Analysis and Experimental Evaluation of a Prototype Passive Sensor to Measure Crosswinds", NOAA Tech. Rept. ERL312-WPL35, Supt. of Doc., U. S. Gov't Printing Office, Washington, D. C. 20402.
- HARP, J. C., 1971, Ph.D. Thesis, AFCRL-71-0451, SV-SEL-71-042, Scientific Report 1.
- ISHIMARU, A., 1972, "Temporal Frequency Spectra of Multifrequency Waves in Turbulent Atmosphere", IEEE Trans. Antennas Propag. AP-20, 10.
- KJELAAS, A. G. and G. R. OCHS, 1974, "Study of Divergence in the Boundary Layer Using Optical Propagation Techniques", J. Appl. Meteorol. 13, 242-248.
- LAWRENCE, R. S., G. R. OCHS, and S. F. CLIFFORD, 1972, "The Use of Scintillations to Measure Average Wind Across a Light Beam", Appl. Opt. 11, No. 2, 239-243.
- LEE, R. W., 1974, "Remote Probing Using Spatially Filtered Apertures", J. Opt. Soc. Am. 64, No. 10, 1295-1303.
- MANDICS, P. A., 1971, "Line-of-Sight Acoustical Probing of Atmospheric Turbulence", Ph.D. Dissertation, Stanford, Univ., Stanford, Calif.
- MANDICS, P. A., R. W. LEE, and A. T. WATERMAN, Jr., 1973, "Spectra of Short-term Fluctuations of Line-of-Sight Signals--Electromagnetic and Acoustic", Radio Sci. 8, 185.
- OCHS, G. R., S. F. CLIFFORD, R. S. LAWRENCE, and T-i WANG, 1974, "Development of a Ground-Based Optical Method for Measuring Atmospheric Turbulence Aloft", NOAA Tech. Rept. ERL297-WPL30, Supt. of Doc., U. S. Gov't Printing Office, Washington, D. C. 20402.
- ROCCA, A., F. RODDIER, and J. VERNIN, 1974, "Detection of Atmospheric Turbulent Layers by Spatiotemporal and Spatioangular Correlation Measurements of Stellar-Light Scintillation", J. Opt. Soc. Am. 64, No. 7, 1000-1004.
- SHEN, L., 1970, "Remote Probing of Atmosphere and Wind Velocity by Millimeter Waves", IEEE Trans. Antennas Propag. AP-18, 493.

VERNIN, J., and F. RODDIER, 1973, "Experimental Determination of Two-Dimensional Spatiotemporal Power Spectra of Stellar Light Scintillation. Evidence for a Multilayer Structure of the Air Turbulence in the Upper Troposphere", J. Opt. Soc. Am. 63, No. 3, 270-273.

WANG, T-i, S. F. CLIFFORD, and G. R. OCHS, 1974, "Wind and Refractive-Turbulence Sensing Using Crossed Laser Beams", App. Opt. 13, No. 11, 2602-2608.

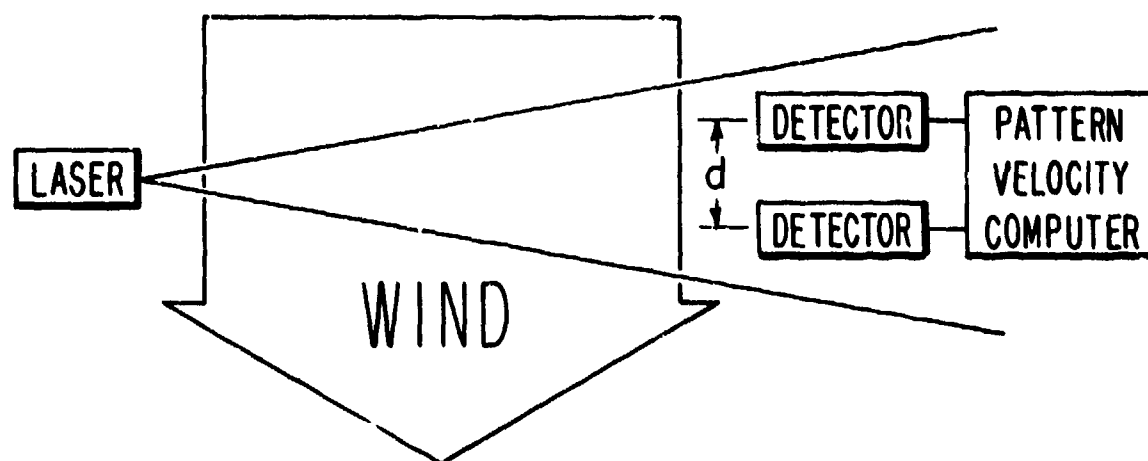


Fig. 1. The general arrangement used to measure the average component of the wind across a laser beam, parallel to the spacing of two detectors.

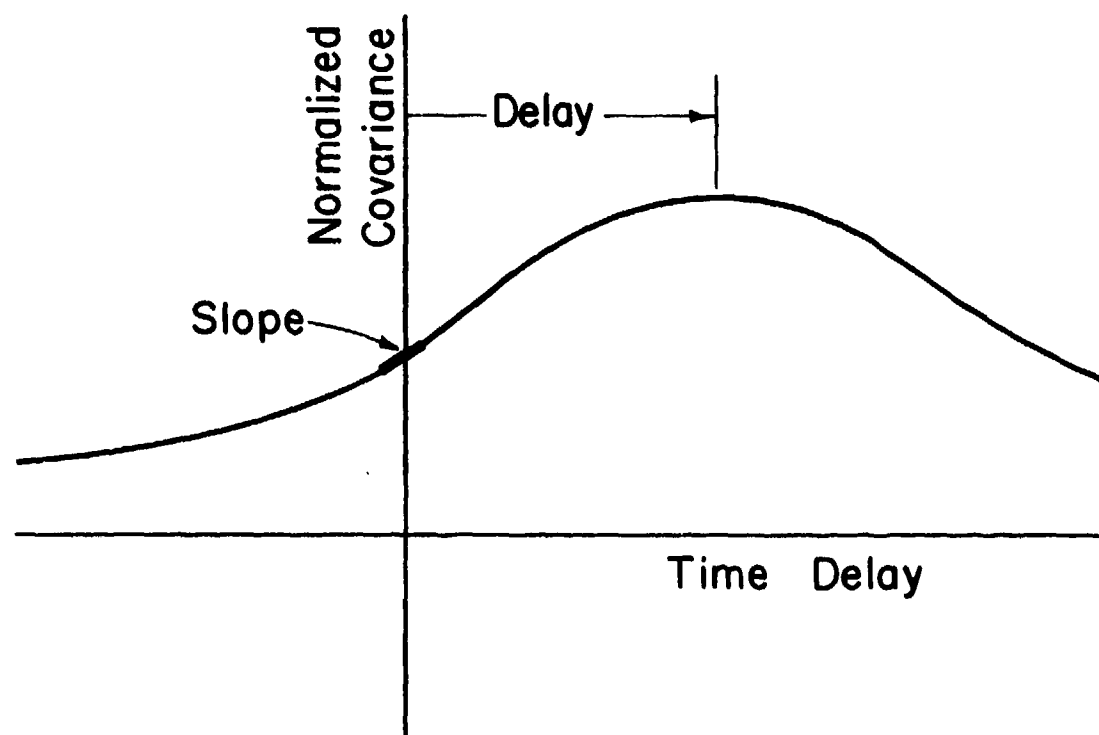


Fig. 2. A schematic of the normalized covariance function, showing the delay to the peak and the slope at zero time lag.

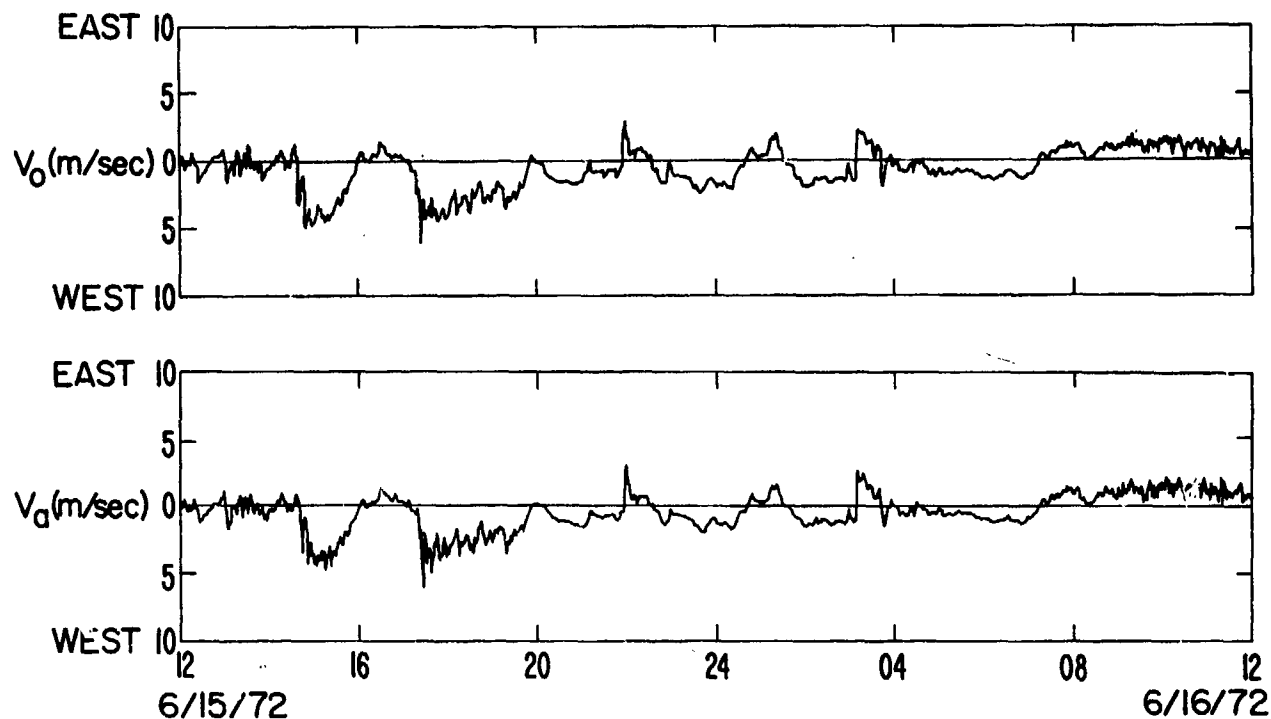


Fig. 3. A 24 hr comparison between the optically measured wind V_o and the mean of six propeller-type anemometers spaced evenly along the 300 m test path.

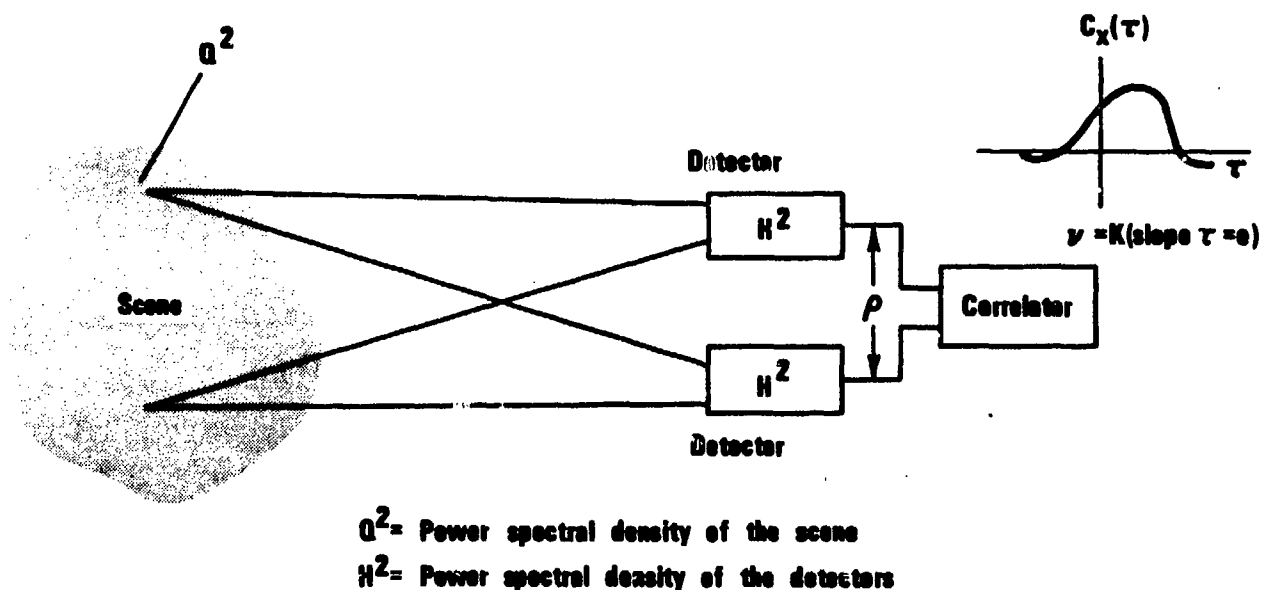


Fig. 4. Schematic of the operation of our passive optical wind sensor showing the covariance function output of the two detectors observing a random scene.

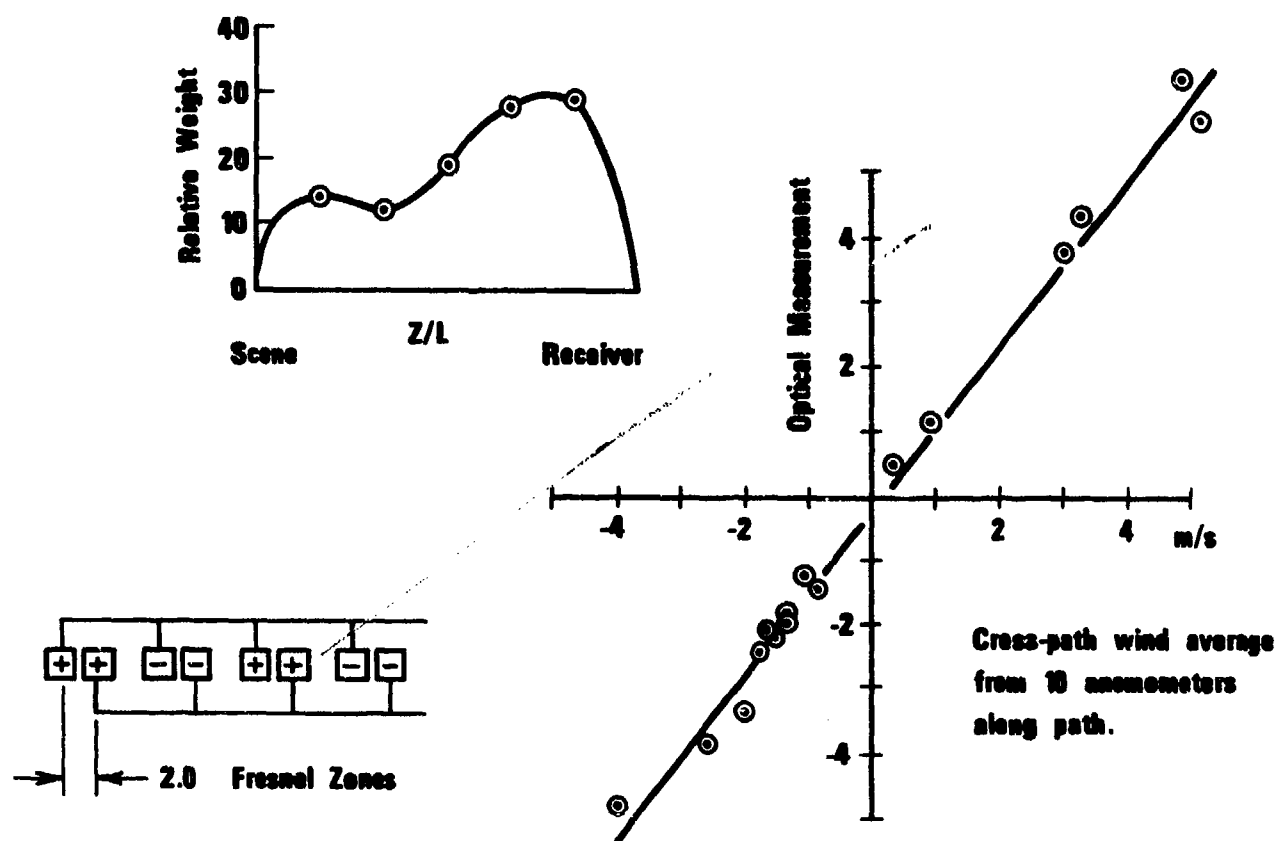


Fig. 5. Comparison of the passive wind sensor reading with the average of 10 anemometers spaced uniformly along a 500 m test path. Also shown are the detector configuration and the path weighting function.

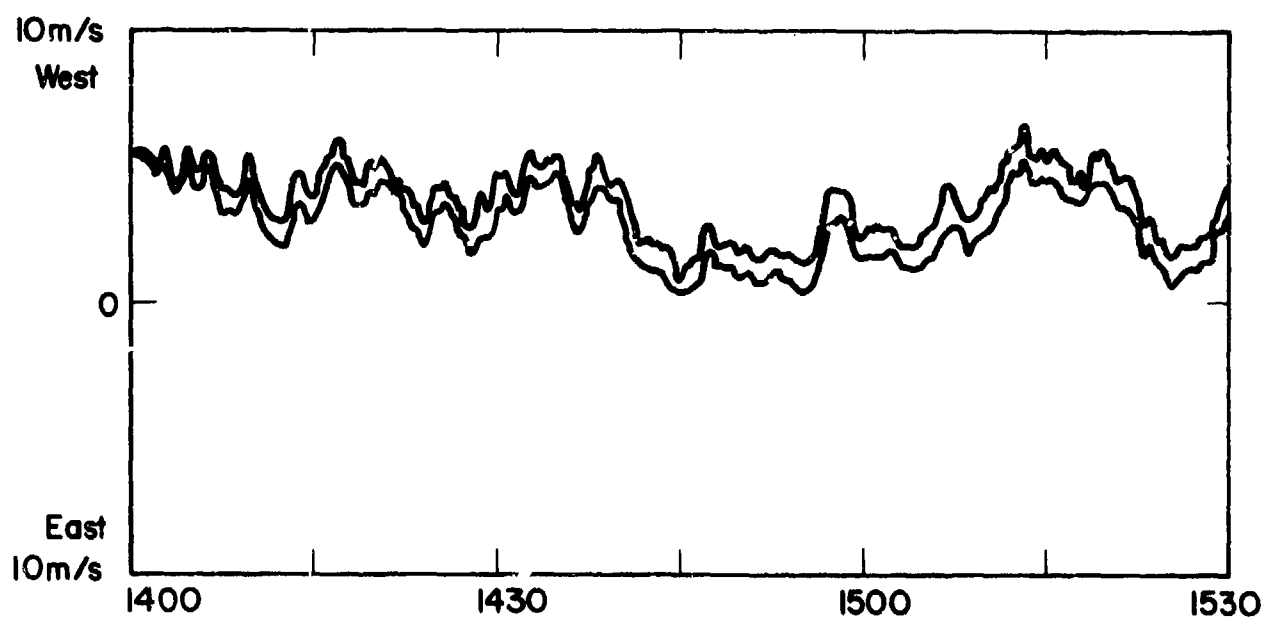


Fig. 6. Comparisons of the transverse wind speed measured by the passive optical system with the average of wind speeds measured by five anemometers equally spaced on the half of the 500 m path nearest the instrument.

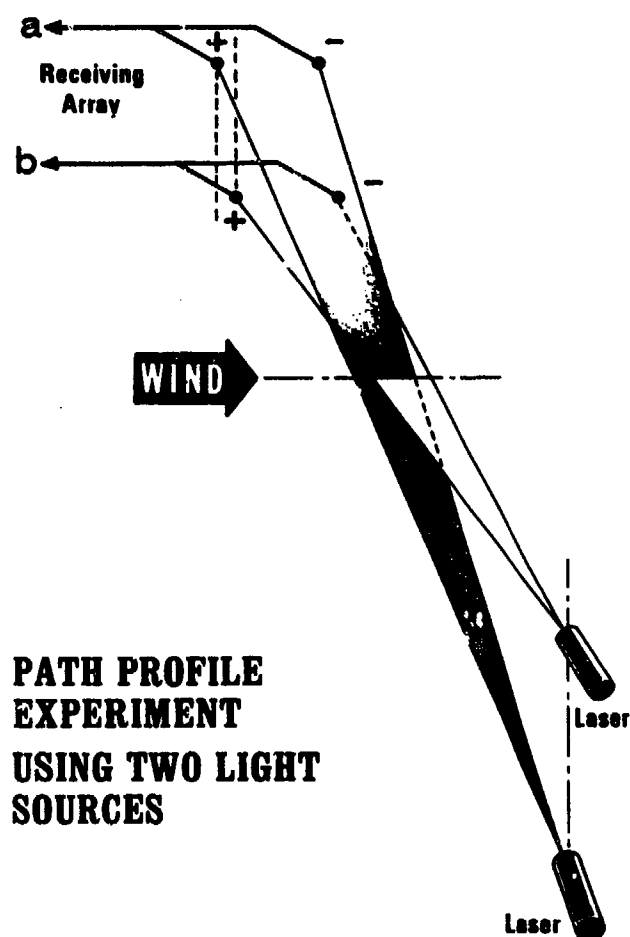


Fig. 7. Diagram of our wind profiling instrument showing two vertically separated lasers and two sets of sensor pairs separated vertically and offset slightly in the horizontal direction.

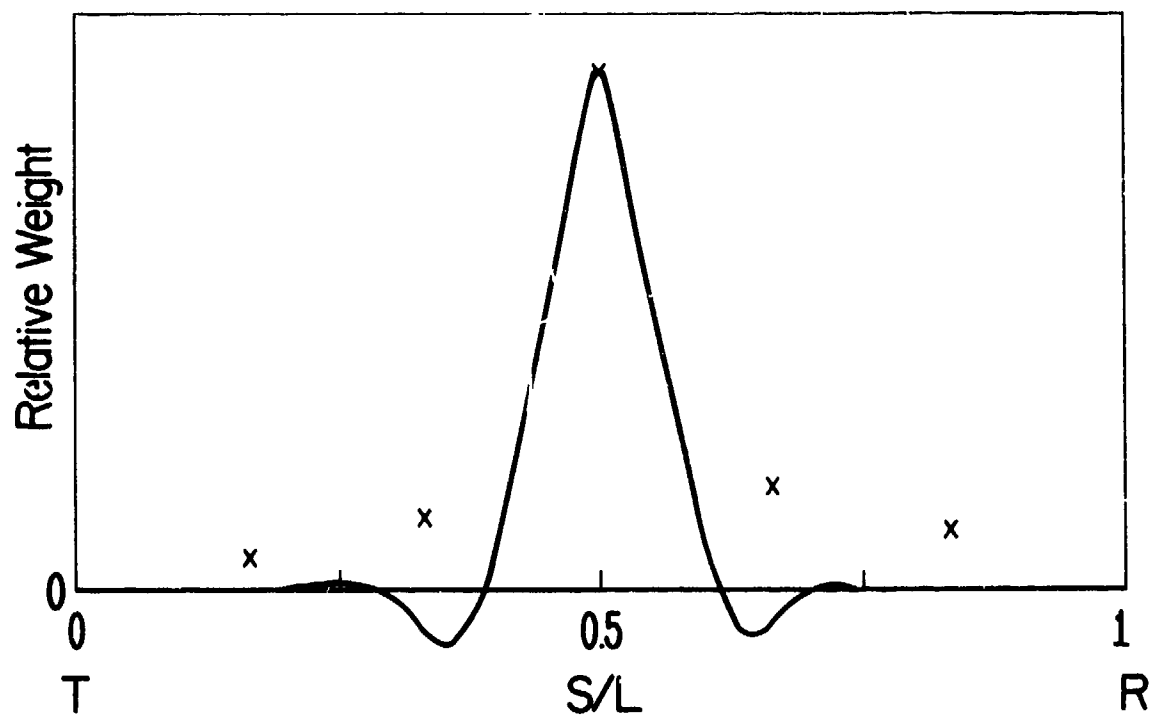


Fig. 8. Theoretical weighting function for C^2 (solid curve) with five experimental weights (crosses) determined by high-speed temperatureⁿ sensors.

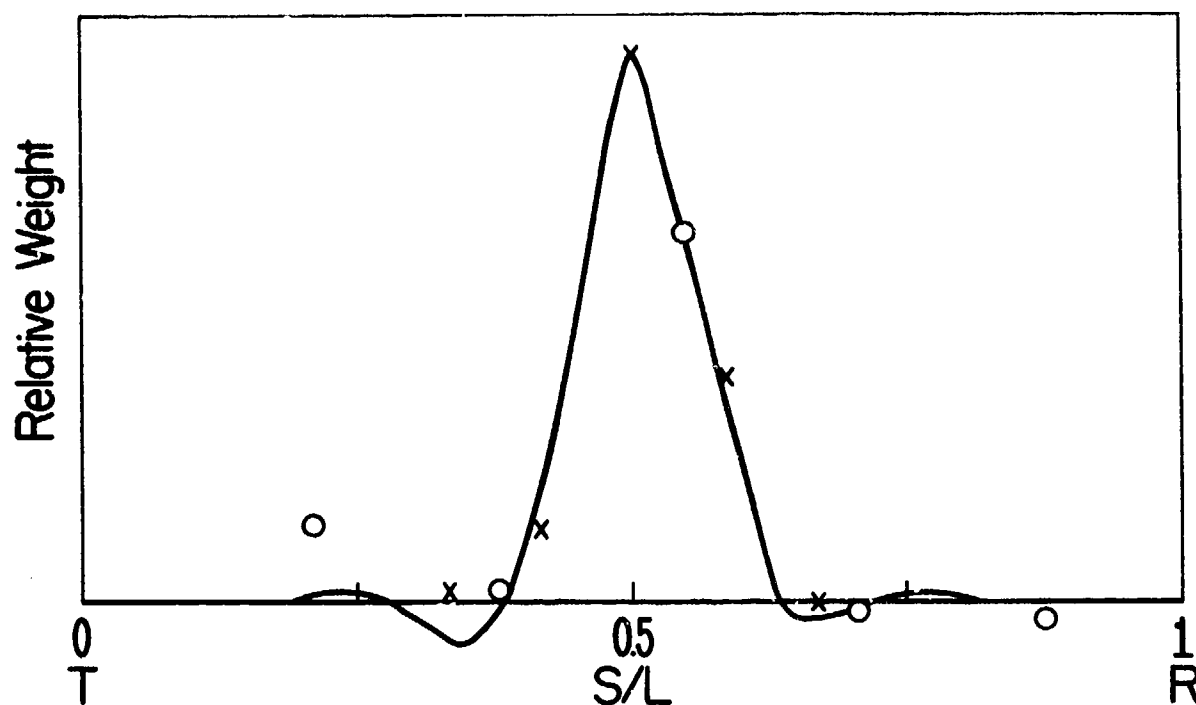


Fig. 9. Theoretical weighting function for transverse wind (solid curve) with crosses and circles representing experimental weights determined from propellor-type anemometer measurements of crosswind.



Fig. 10. Optical system for measurement of high altitude winds.

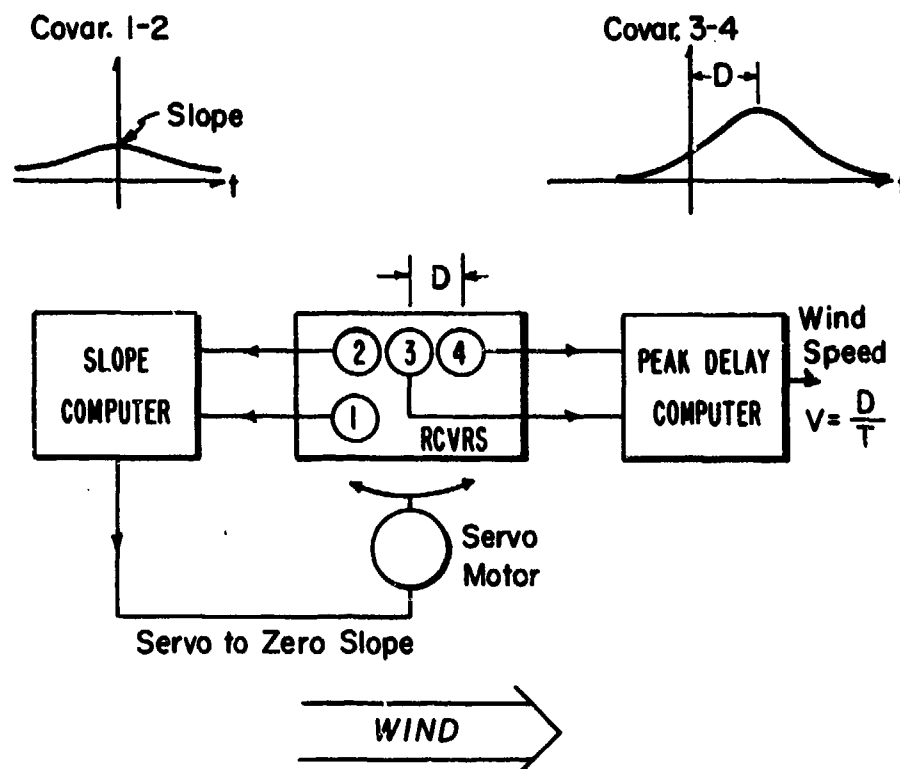


Fig. 11. Block diagram of high-altitude wind measurement system.

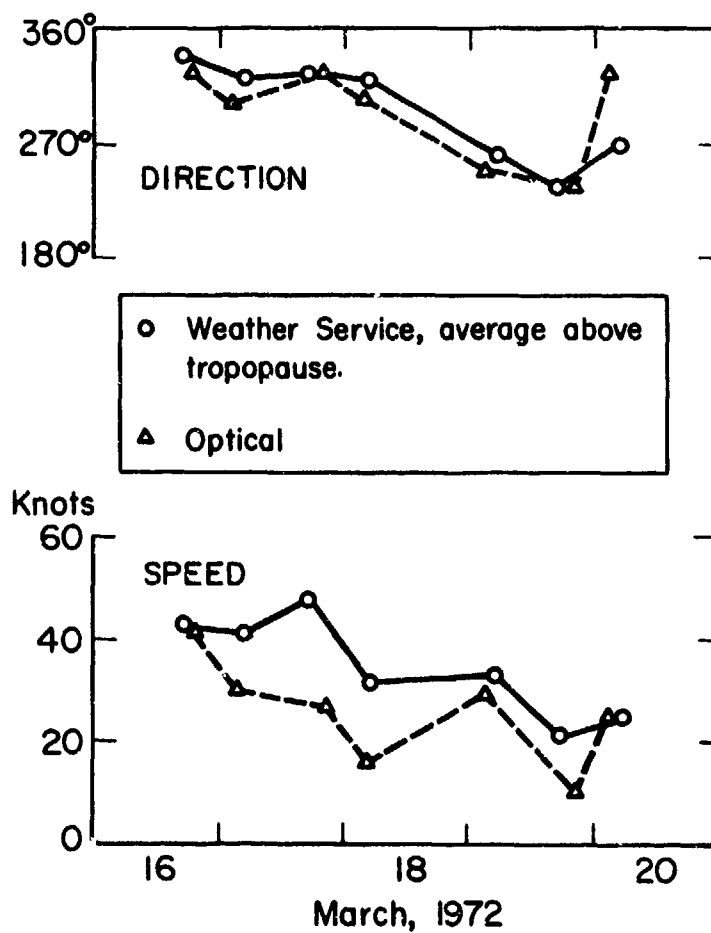


Fig. 12. Comparison of optical wind measurements and rawinsonde data during March 1972.

MEASURED VISIBLE SPECTRUM PROPERTIES

OF REAL ATMOSPHERES

Dr. S. Q. Duntley
Professor and Director
of the Visibility Laboratory
University of California, San Diego
La Jolla, California 92037

SUMMARY

Measurements of the visible spectrum properties of the atmosphere which govern the apparent contrast of objects have been made by the author and his colleagues from aircraft, spacecraft, and ground stations in various parts of the world throughout the past thirty years. Samples of these data are presented in this paper. The techniques of measurement that were used are described. Examples are given to illustrate how the data can be used to predict the limiting range of detection, recognition, classification, and identification of any specific object by airborne, spaceborne, and ground based observers or imaging devices.

1. INTRODUCTION

Thirty-five years ago I became responsible for finding the maximum distances at which specific objects could be sighted and recognized from aircraft. I knew from previous flight experience that the lower atmosphere is usually non-uniform, both horizontally and vertically. I believed that reliable measurement of the optical nature of the atmosphere was a necessary prelude to mathematical modeling. Thirty-five years ago this month I began a continuing series of flights with hand held photometers. Soon I evolved mathematical models based upon the data I obtained. Those here today to whom the terms *sky-ground ratio* and *optical equilibrium in the path of sight* are familiar are using models which had their origin in my writings in that early period. Today I shall talk only about the capability of looking through long paths of sight at objects on the ground, as illustrated by Figure 1. The object is lighted by the sun (or moon) as well as by the sky and is observed by someone who is either on the ground or is airborne. The object is viewed against some background which appears to be immediately adjacent to the edges of the object.

2. GENERAL INFORMATION

Figure 1 also contains a stylized representation of various components which form the total system. Both the object and its background are illuminated by some source of light, which can be the sun, moon, and sky or it can be a man-made lighting device such as a flare, a searchlight, or a laser. Information about the object is encoded on the light through the process of reflection. Decoding is accomplished by forming an image of the object. Decision and action occur after image information enters man through his visual channel and is processed by his brain. All image-forming light must traverse a path of lighted atmosphere before reaching the observer. Some of it is lost in this transit and the remainder is diluted by non-image forming ambient light that is scattered toward the observer all along the path of sight. At some limiting range the image-forming light becomes too small a portion of the total to activate the human visual system sufficiently to enable the required degree of object discrimination to be achieved. Every limiting range depends upon the object and its background as well as upon many physical factors, which always include the lighting, the optical state of the atmosphere and, of course, sensor system properties. Visual aids, such as telescopes, electro-optical devices, or photographic systems may also be part of the image transmitting chain; their transfer characteristics must, therefore, be properly allowed for.

Once within the human system, the image information goes through an intricate signal processing network before it is displayed within the brain. There its information content is combined with a priori knowledge and compared with stored memory in the process of perception, decision, and action by man.

Complex though the total system may be, enough is known about every part of it to enable predictions to be made in advance about its limiting capabilities for virtually any real-world visual task.

In a previous NATO Seminar on "Detection, Recognition and Identification of Line of Sight Targets," that was held at The Hague six years ago I gave a paper entitled, "Prediction of Visual Recognition Range," which treated that part of the problem which concerns the eye, the brain, the role of a priori knowledge, the function of memory, and the way these factors combine to produce decision and action. It illustrates a technique that was evolved in my laboratory for reliably predicting the limiting range at which the human visual system can make a correct decision and initiate an action. My paper is contained in the Proceedings of that NATO Seminar. I feel free, therefore, to concentrate my remarks here today on atmospheric effects which reduce the apparent contrast of distant objects. The inflight measurements I began 35 years ago have continued with almost no interruptions up to the present. For nearly twenty years most of this work has been performed under research contracts with the Air Force Cambridge Research Laboratory of the United States Air Force but some of it was done for NASA in support of the Gemini and Apollo Programs. In fact, I am very glad that the altitudes visited by our photometers have included orbital ones. Dr. Robert Fenn, who mentors our work for the U.S. Air Force, is here today. He gave the second speech on the program of this meeting.

The present series of inflight optical measurements for the AFGL makes use of a C-130 aircraft that has long been dedicated to this work. Before describing the C-130 program, let me show some interesting measurements that were made during the 1940's and 1950's.

The best data secured during the 1940's were obtained with an airborne photographic spectro-radiometer, called the spectrogeograph. Figure 2 shows that instrument installed in the camera pit (radio room) of a B-17 aircraft. In addition to recording spectra from objects on the ground it could map the spectral radiance of the sky above the aircraft through a periscope which may be seen protruding through the open upper hatch.

Figure 3 shows an interior view of the spectrogeograph and a schematic of its optical system. It could measure spectral radiance throughout any octave between 430 and 900 nanometers with a spectral resolution of 7 nanometers and a spatial resolution of 3.2×10^{-6} steradians.

Figure 4 is a typical picture from the identification camera of the spectrogeograph showing the position of the slit at the moment the spectrogram was made. The spectra of the white and black ground panels show prominently in the spectrogram, as does the dark shadow of the parked aircraft.

One early result from the spectrogeograph was a comparison between the reflectance spectrum of a single leaf with that of the tree from which it came. This is shown in Figure 5.

The spectrogeograph could be used both airborne and at ground level to explore atmospheric effects. Figure 6 compares reflectance spectra over shallow ocean bottoms measured at an altitude of 1310 meters with corresponding spectra as measured from a glass-bottomed boat. The differences between the sets of spectra are due to the effect of 1310 meters of atmosphere as well as to reflection of the sky by the surface of the sea.

Spectra of ground panels, like those in Figure 4, obtained at various altitudes aided and confirmed the early theoretical developments. I shall skip over the extensive experiments we made during the late 1940's, the 1950's, and the 1960's, partly because they are described in literature references, except to note that optical conditions at altitudes beyond 50,000 feet were measured from a Navy F2H twin jet fighter carrying instruments we designed, and that our instruments flew in orbit on Gemini 5 and 7 with coordinated C-130 documentation of the lower atmosphere.

Since 1970 there has been a steadily increasing flow of high quality atmospheric optical data measured from the C-130 aircraft in Europe and America. Most of these data banks are more completely presented than their predecessors, but thus far only in the form of unclassified contract reports. Even so, not all of the usable new flight data are in printed form ready for general use. In our experience, many applications of the in-flight optical data are for such specific locations, seasons, times of day, and weather conditions that special readouts from our data banks stored on magnetic tape seem to be the only satisfactory procedure. In fact, computer interpolations between measured data are often necessary.

It is impossible in the time available for presenting this paper to undertake an in-depth treatment of our present theoretical structure or the airborne instrumentation, but the quoted references will fill that gap. In the remainder of this talk I will describe our customary data-taking procedure, including the flight patterns we are using and the kinds of measurements we make. I will then describe our data reduction philosophy and practice by means of flow charts, and finally discuss the data outputs we achieve and illustrate them with a sample.

The C-130 has made two sets of experiments in Germany; the first, in 1972, used a flight track between the towns of Mengen and Mindelheim which lie a short distance west of Munich, as shown in Figure 11. Ten flights were completed on that flight track. In 1974 the C-130 operated on a track centered on Oldenburg not far from the Netherlands border in northern Germany as shown in Figure 12. Eighteen flights were completed on that track. The C-130 has also obtained data on tracks located in northern Spain, in the western Mediterranean and in northern Morocco, as shown in Figure 13.

In the United States, our bank of C-130 data includes flights over southern California, central New Mexico, southern Illinois, southern New Hampshire, northern Michigan and western Washington as well as data taken over the ocean off California and off western Florida. Figure 14 is a tabular summary of available recent data of high quality.

At this meeting are single copies of two of the reports that summarize some of our data banks in graphical and tabular form. They describe diagrams like Figure 15 which shows the computer data processing sequences. More important perhaps are the scientific flow charts like that illustrated by Figure 16, which illustrates that the design of the experiment is such that most of the end-product results can be calculated from more than one set of data input channels; that is to say, two or more different kinds of experiments are made simultaneously throughout the flights and the given end-product atmospheric property can be calculated from these independently measured inputs. If they agree, the credibility of the data is enhanced. This experimental design did not occur by accident, but was achieved as a result of a great deal of theoretical and experimental work over the years. We consider it to be a cornerstone of our program.

Time will not permit me to show more than a sample of data. Figure 17 is a semi-logarithmic plot showing altitude on its vertical scale and total volume scattering coefficient, in reciprocal meters on its horizontal scale. Clear air, evidenced by small scattering coefficient, is at the left and hazy air, having a larger scattering coefficient, is on the right. The results from six flights on different days over the Mengen track near Munich are shown. At ground level the scattering coefficients cluster close together, and at altitudes between two and five kilometers they are tightly clustered to about the same extent. Between the ground and two kilometers, however, major dissimilarities were found. Consider the data represented by the triangular points. Note how scattering coefficient increases with altitude

beginning at ground level. There is a layer of haze more than a kilometer thick in which the scattering coefficient is nearly twice that at ground level. Above the haze layer the air becomes clearer until above two kilometers the points approximate a straight line that denotes an exponential atmosphere. The data represented by the crosses represent a very different atmospheric structure. In the first 1.25 kilometers above the ground the air becomes clearer, almost exponentially. From 1.25 to 1.90 kilometers is a weak haze layer within which the scattering coefficient becomes smaller exponentially with altitude. Between 2.2 and 4.6 kilometers is very clear air in which the scattering coefficient did not change with altitude. Above that is a very weak haze layer.

Optical circumstances of the type illustrated by Figure 17 are commonplace. The bottom of the clear atmosphere usually contains a convectively mixed layer having many optical complexities. It often terminates at a temperature inversion that caps the convective process. Above are exponential layers of clearer air that are often separated by weak haze layers. Optical correlations with air temperature structure are poor, but correlation with dew point temperature (or the partial pressure of water vapor) can be excellent, as shown by Figure 18 (DUNTLEY, S.Q., 1957), which represents B-29 data from 1956.

Duntley, S.Q., 1957: Image Transmission by the Troposphere. J. Opt. Soc. Am. 47, 499-506, Fig. 10, p. 506.

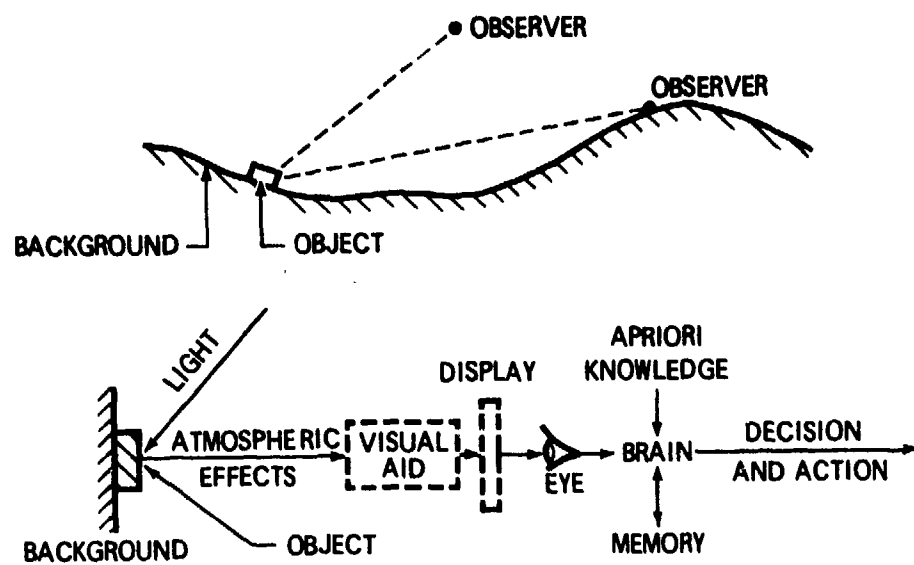


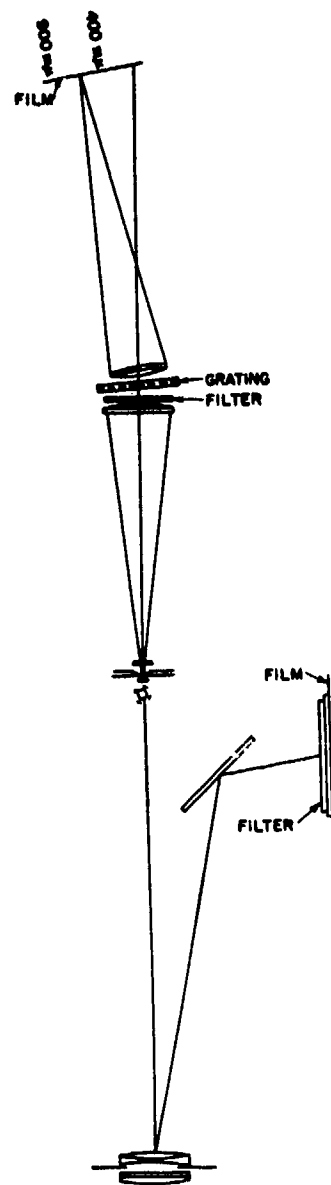
Figure 1



Figure 2



Figure 3



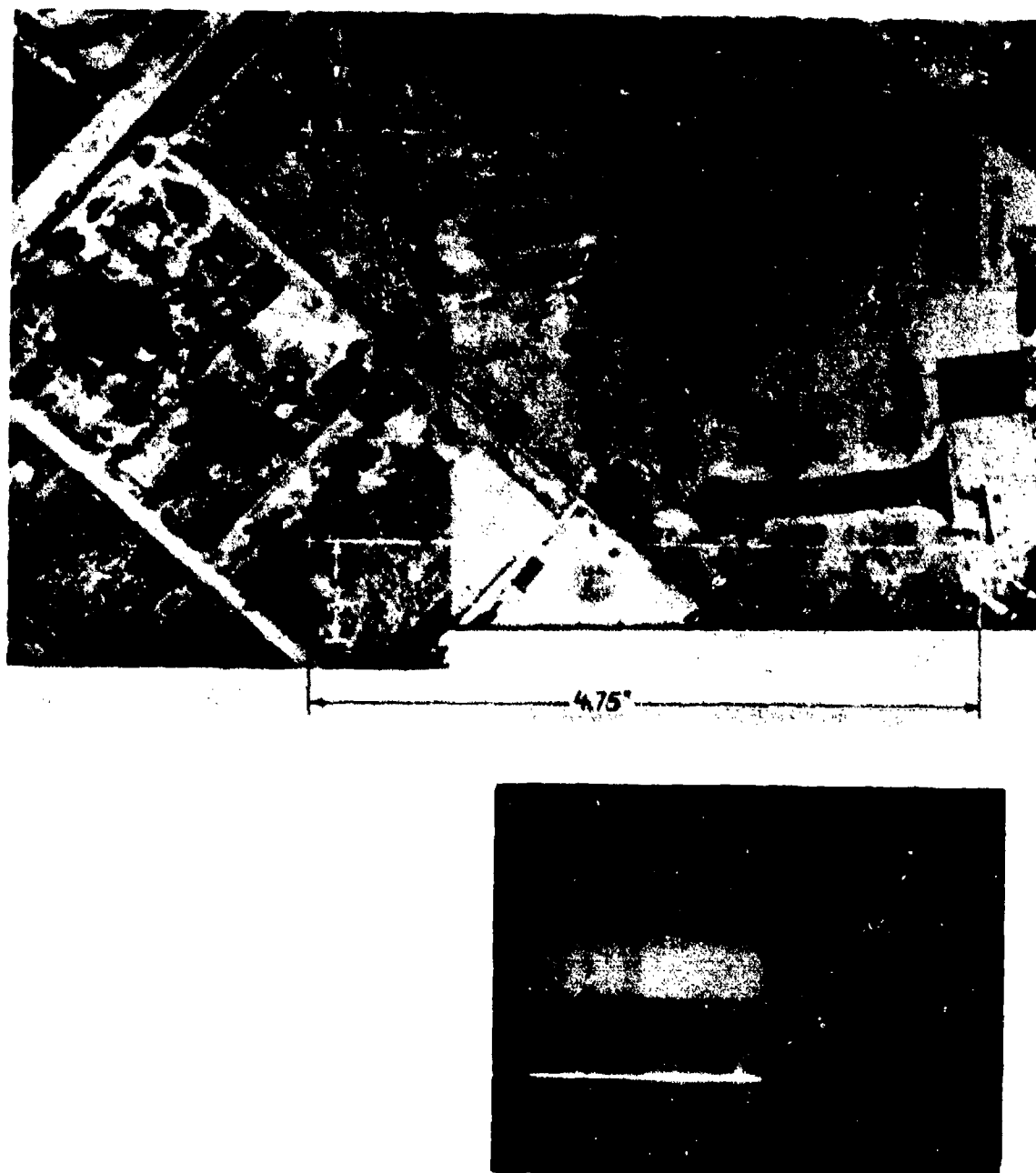


Figure 4

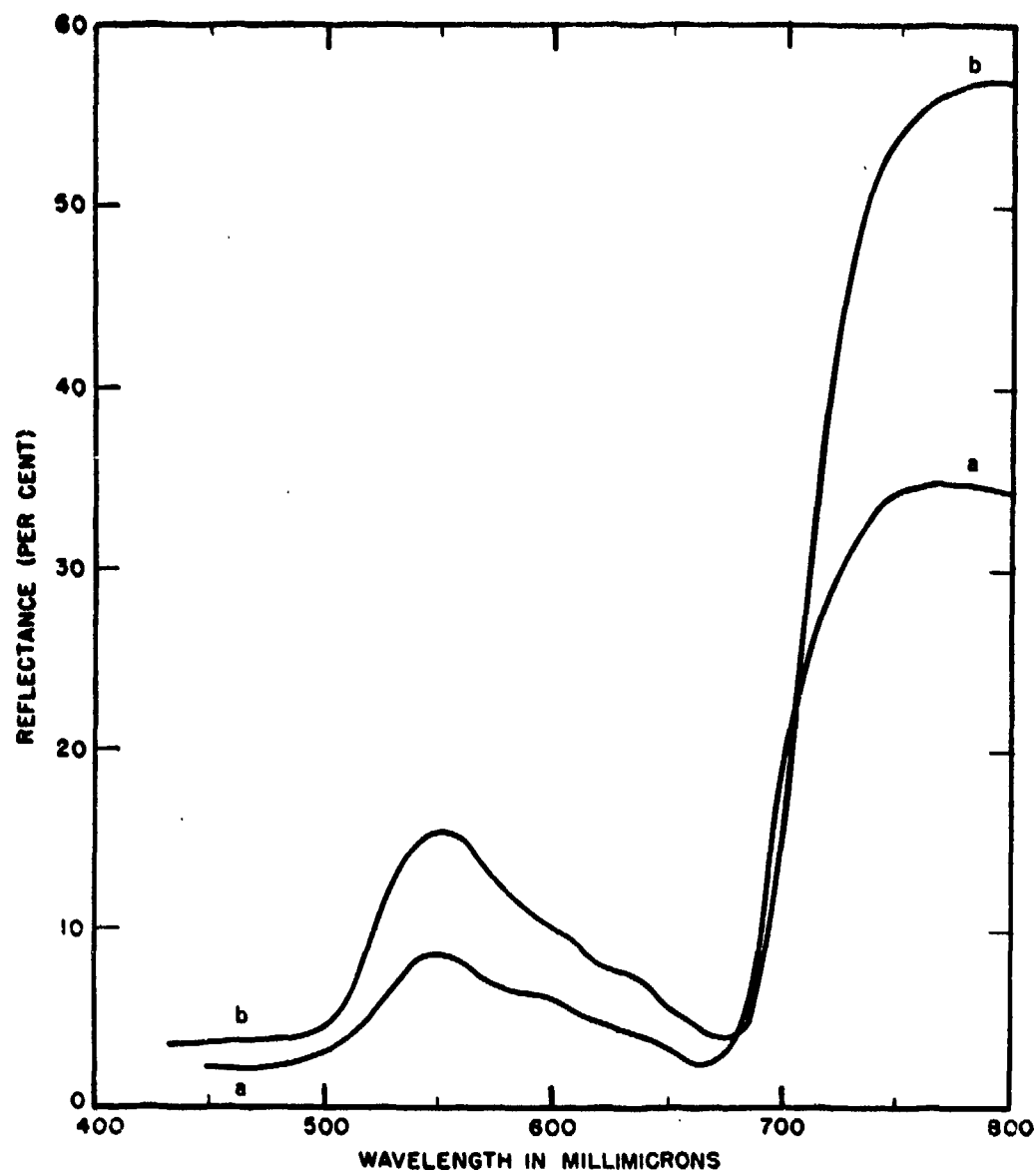


Figure 5

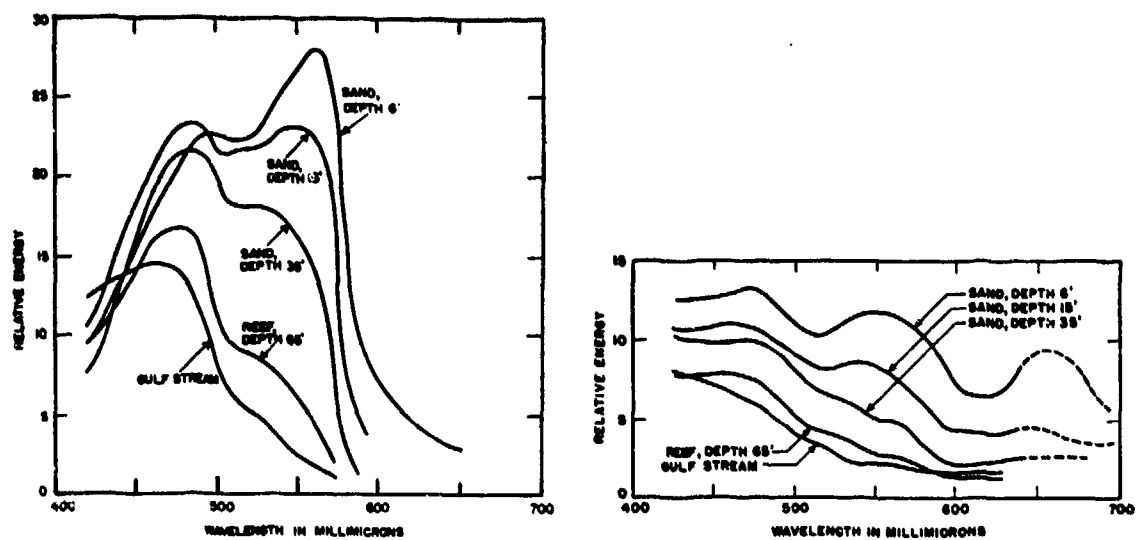


Figure 6

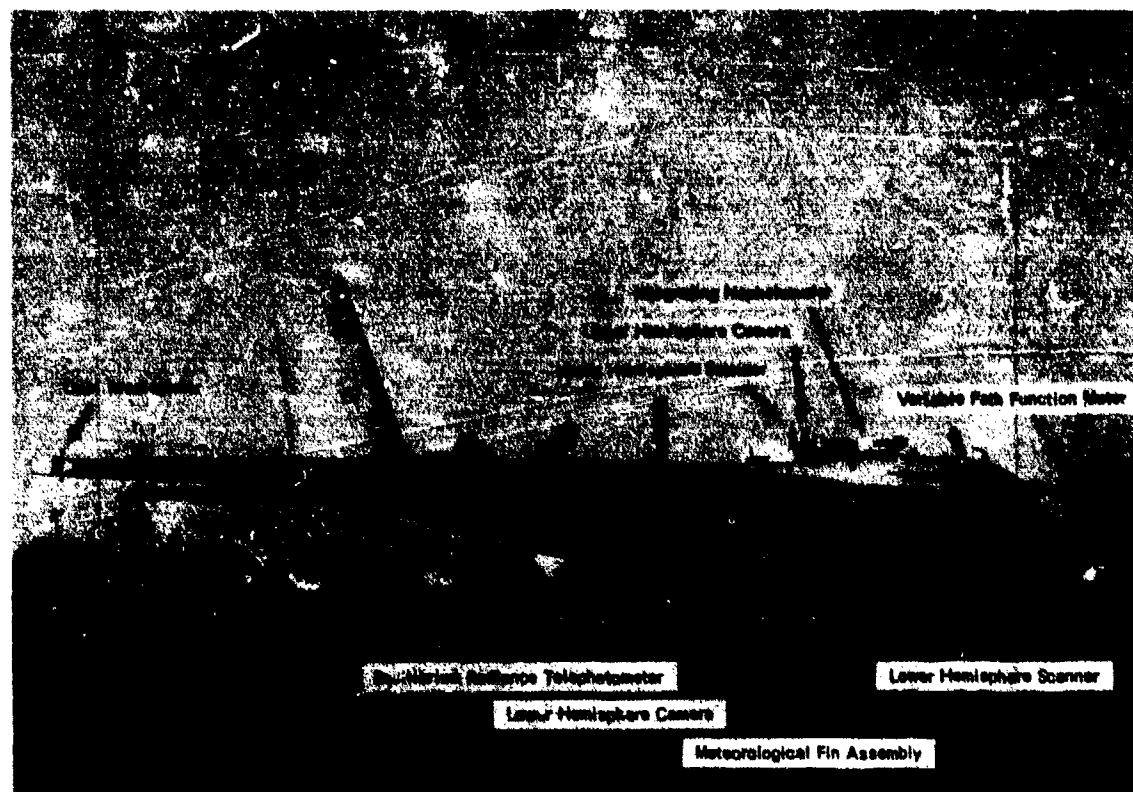


Figure 7

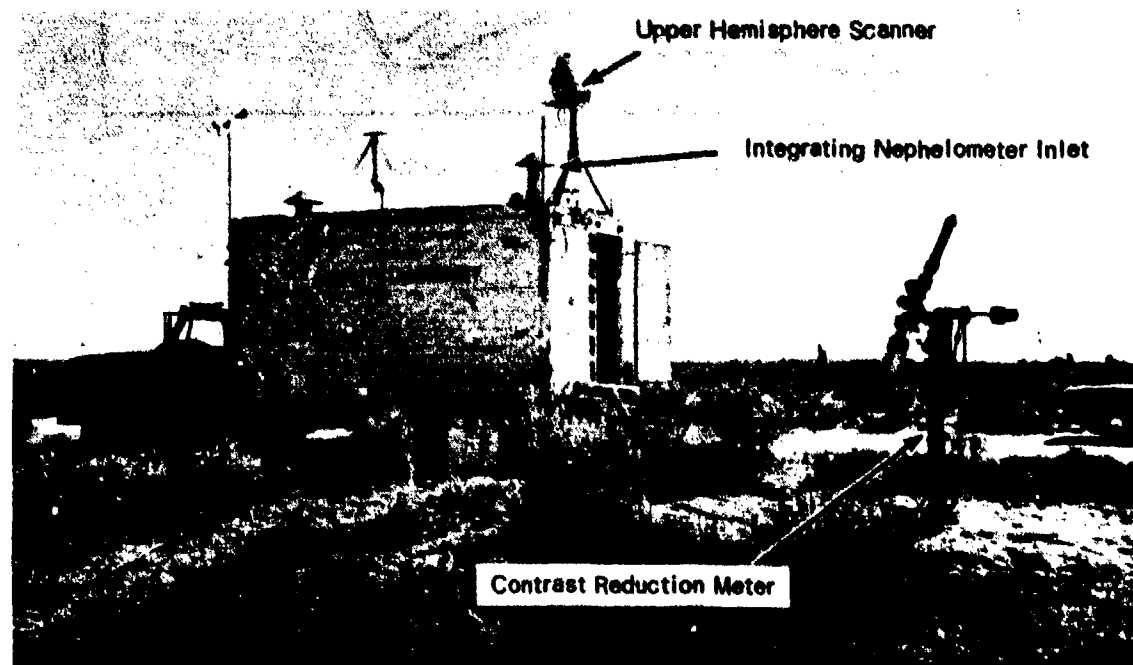


Figure 8

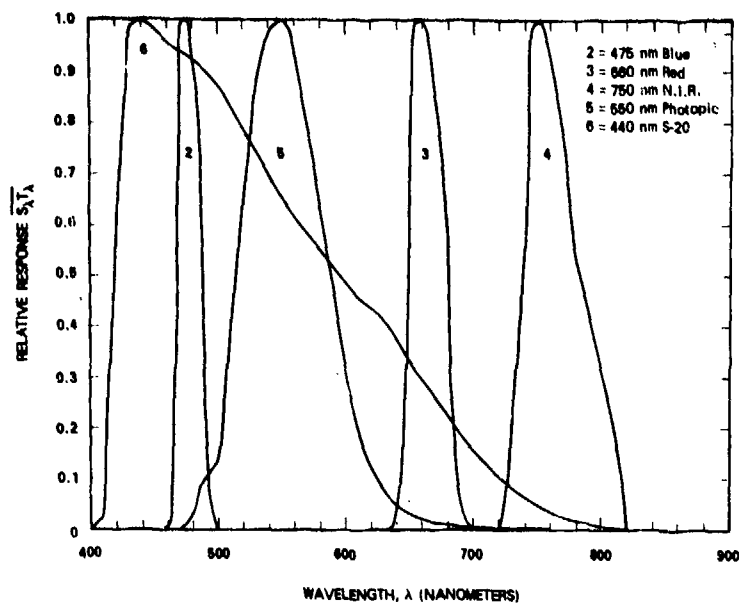


Figure 9

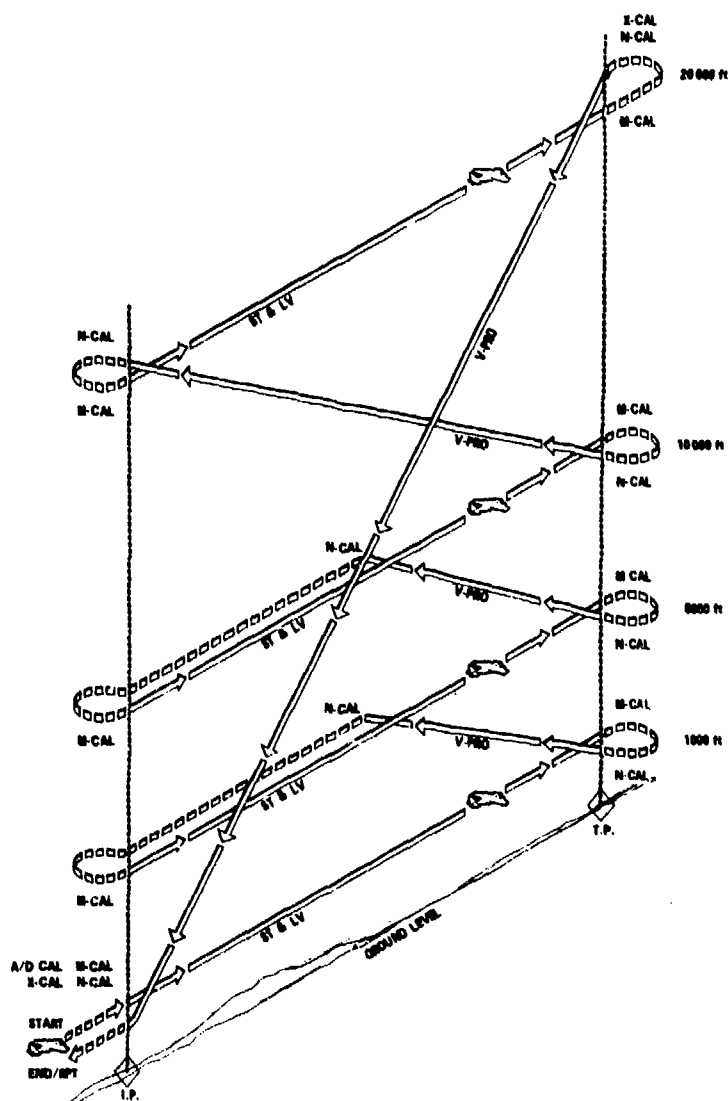


Figure 10

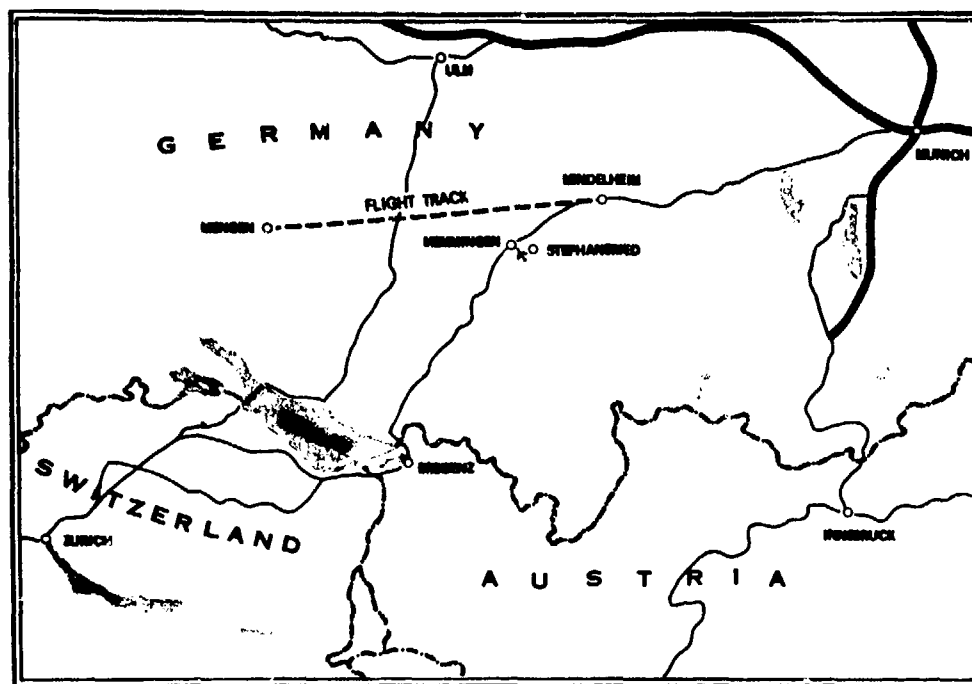


Figure 11

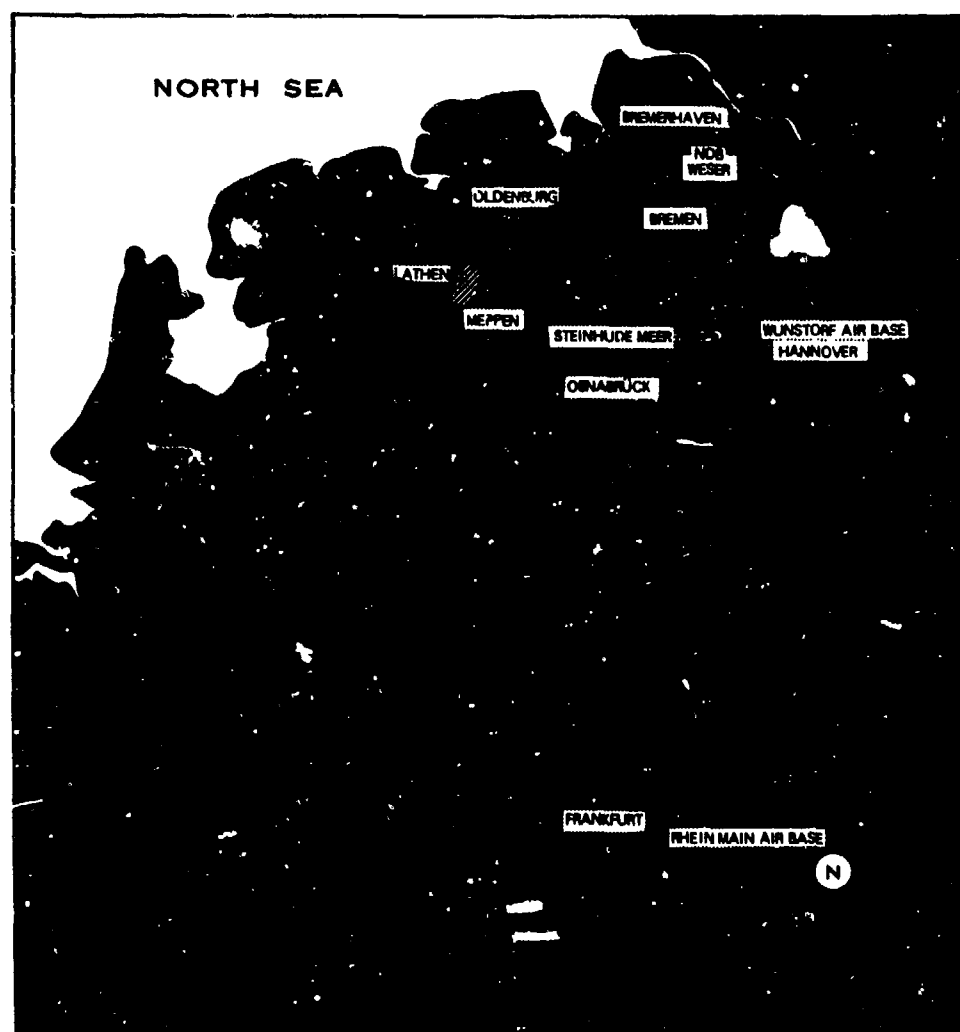


Figure 12

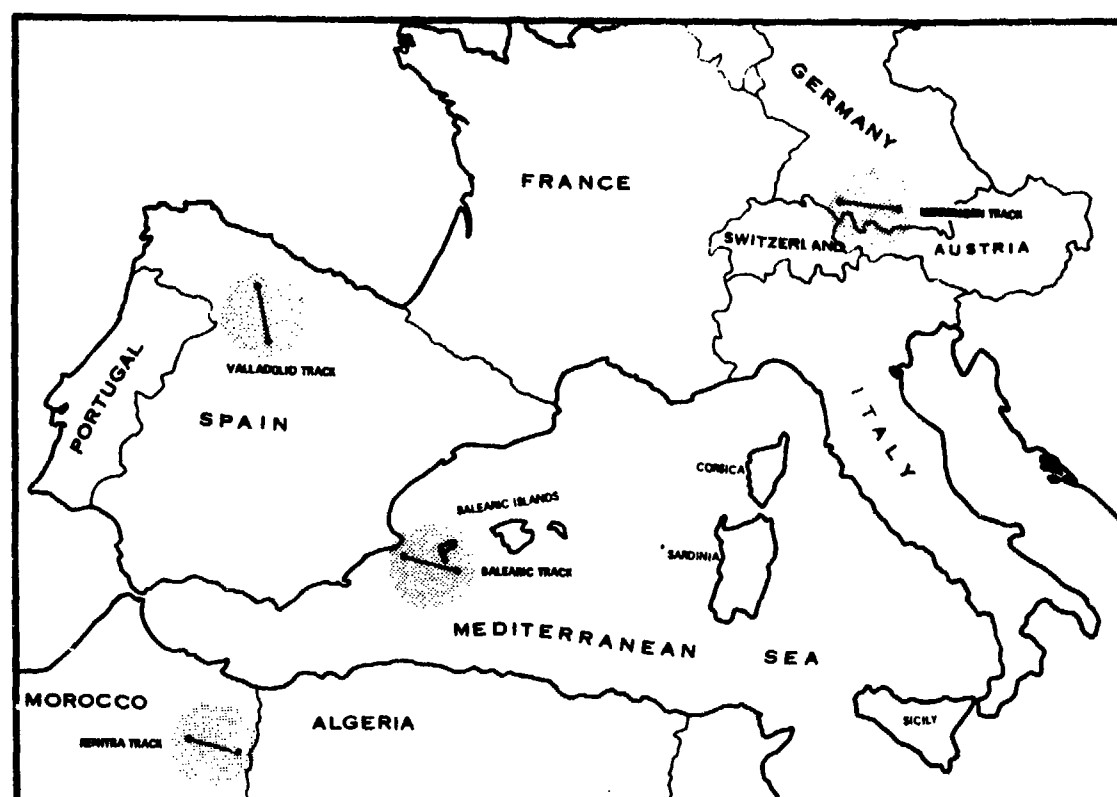


Figure 13

Available Data Bank of Daytime Data

Latitude	Season	Terrain	Field Trip	Geographical Location	No. Complete Flights
53° N	May, Jun	Green pasture	HAVEN VIEW II	Northern Germany	18
48° N	May, Jun	Green pasture	HAVEN VIEW I	Southern Germany	10
46.8° N	Jul	Brown prairie	SEEKVAL	Western Washington	10
45.5° N	Mar.	Snow, ice	SNOWBIRD	Northern Michigan	4
43.3° N	Apr	Rolling hills, wooded	SENTRY	New Hampshire	8
41.5° N	Apr, May	Dry range	HAVEN VIEW I	Northern Spain	2
38.5° N	Apr	Oce.	HAVEN VIEW I	Western Mediterranean	4
38.5° N	Aug	Cultivated farm	METRO	Southern Illinois	14
28.5° N	Jan	Cultivated farm	GATEWAY	Southern Illinois	6
35.0° N	Jan	Desert	LOCAL III	Southern California	3
33.5° N	May	High desert	HAVEN VIEW I	Eastern Morocco	3
33.3° N	Oct, Nov	High desert	ATOM	Central New Mexico	7
33.2° N	Mar.	Low desert	LOCAL I	Southern California	2
33.2° N	Oct	Low desert	LOCAL II	Southern California	1
33.2° N	Jan, Feb	Low desert	LOCAL III	Southern California	2
32.7° N	Mar., Apr	Ocean	LOCAL I	Southern California	2
-	Oct	Ocean	LOCAL II	Southern California	1
-	Feb	Ocean	LOCAL III	Southern California	1
29.9° N	Jan, Feb	Ocean	SEMINOLE	Western Florida	9

Figure 14

COMPUTATIONS FROM BASIC AIRBORNE DATA

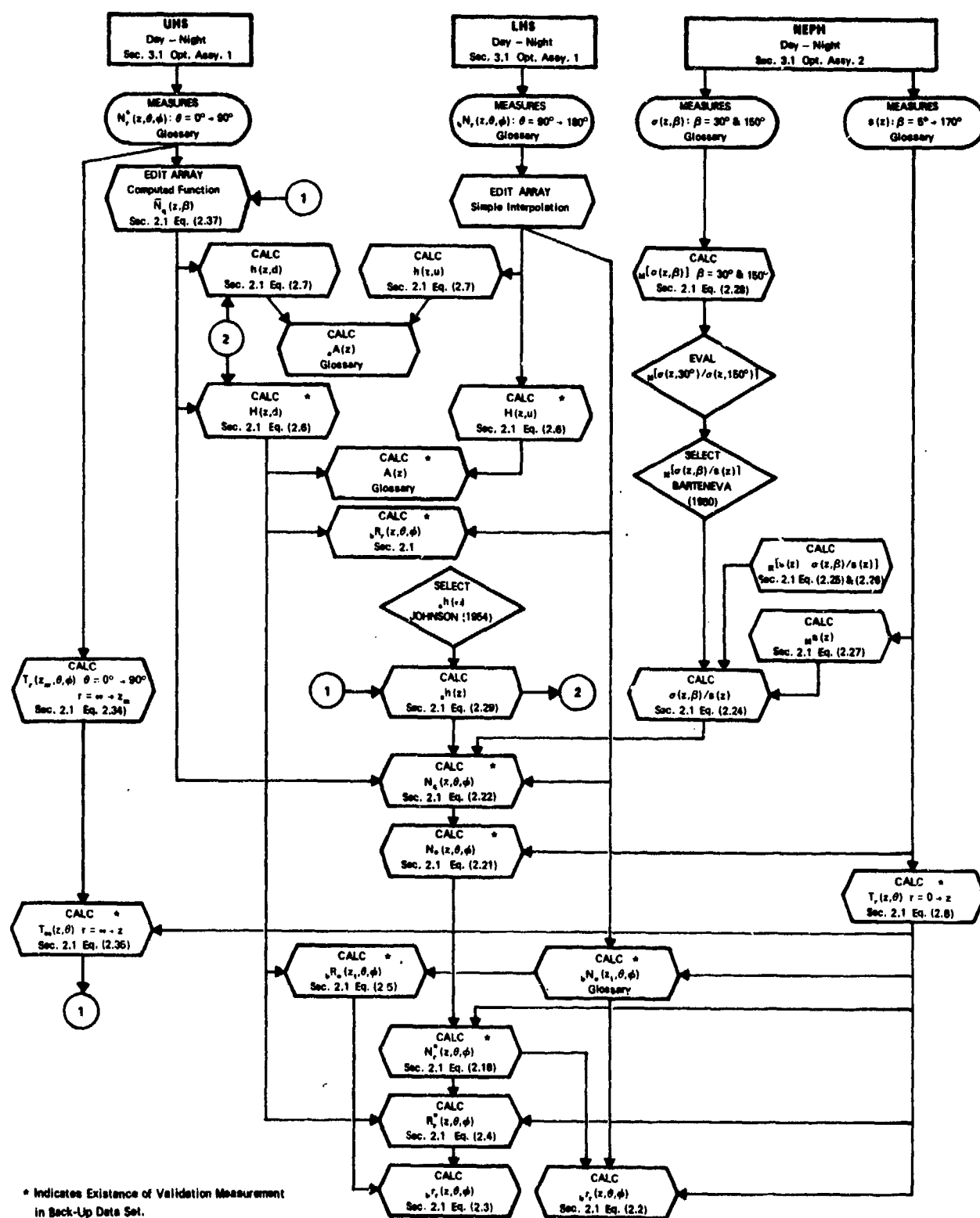


Figure 16

SCATTERING FOR HAVENVIEW FLIGHTS FILTER 5 PSEUDO-PHOTOPIC MEMMINGEN TRACK

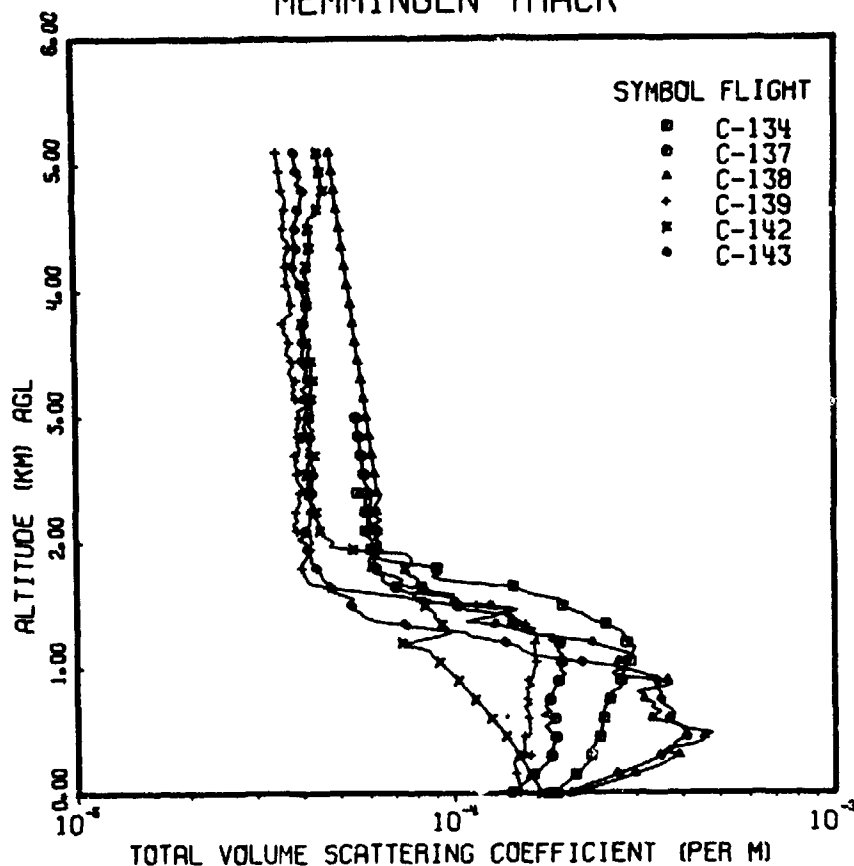
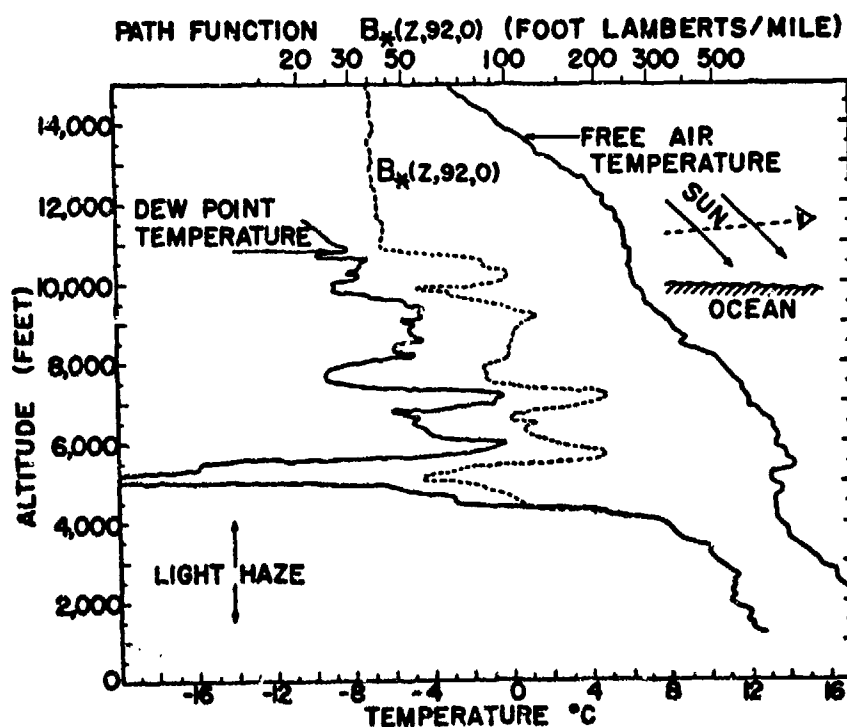


Figure 17



PASSIVE AND ACTIVE ATMOSPHERIC VISION

D.H.Höhn
Forschungsinstitut für Optik
74 Tübingen 1, Schl.Kressbach
F.R.Germany

SUMMARY

The main features of an unique theory of atmospheric passive and active vision for $0.35 \mu\text{m} \leq \lambda \leq 14 \mu\text{m}$ will be presented and discussed. The signal-to-noise ratio $\Delta Q/\sigma_{\Delta}$ corresponding to the detection of the vision signal, i.e. the apparent radiance difference at the observation site, is used as the basic physically limiting magnitude. It establishes a general vision formula. Different noise limitations (detector, device radiation, signal photon noise) are used to derive in special, more applicable equations. Koschmieder's theory for human vision follows as a special case. The theoretical results are applied numerically to passive thermal vision. The optimization of optoelectronic vision systems is considered by approaching signal-limited photon noise (SLIP) conditions in contradiction to BLIP-conditions, and using reduced wavelength bands for atmospheric vision. Finally the problem of defining and measuring characteristic lengths comparable to the Visual Range V will be touched and a proposal is presented.

1. INTRODUCTION

Atmospheric conditions together with target, background and imaging device characteristics are limiting the performance of optoelectronic and other observation systems, with what e.g. the human eye or a photographic camera is used as imaging device. Based on ambient and/or self-emitted radiation "passive" systems can be realized at least within the wavelength range from about $0.35 \mu\text{m}$ to $14 \mu\text{m}$ beside of the application of longer wavelengths for imaging, e.g. that of mm-waves. "Active" systems, including a controlled radiation source, e.g. a laser, beneath the atmospheric ozone layer might be applicable already for wavelengths larger than about $0.25 \mu\text{m}$. They will be considered in this context up to about $14 \mu\text{m}$ beside of the formal applicability of the theory to longer wavelengths covering at least the overlapping area between ir-systems and radar-systems.

Different types of observation principles can be combined into multi-observation systems, which are using simultaneously or alternatively different spectral bands, passive and active modes, including range gating, different spatial and time resolutions, 1- and 2-dimensional scanning etc. They are of very high interest regarding observation tasks like detection, recognition and identification, if they should be performed with one instrument, especially under conditions of limited atmospheric observability. An unique analytical description of atmospheric vision including basic target, background and device parameters is necessary to evaluate and compare different imaging methods and systems. Having in mind mostly 2-dimensional systems in the following often the terms "vision" and "imaging" will be used in a general sense instead of observation and beside of the fact that the 1-dimensional aspect is fully included.

The main features of such a theory will be presented and discussed. Especially regarding the influence of different noise limitations. Its application to passive thermal vision is illustrated by numerical examples. Optimization and the problem of defining and measuring characteristic lengths comparable to the Visual Range V are touched finally.

For $\lambda \leq 3 \mu\text{m}$, especially within the visual band atmospheric limitations can be described by Koschmieder's well-known theory (Koschmieder, H., 1924; elaborated on and applied by Duntley, S.Q., 1948, Middleton, W.E., 1952 and 1957, and others). Using the contrast $K = (L_1 - L_2)/L_2$, where L_1 = apparent radiance at the observation site, as an empirically found limiting figure for human vision (e.g. Schober, H., 1970, or Grand, Y.le, 1968) this theory results in range equations and a characteristic length, the Visual Range V . More recently it was often

used with the contrast definition $C = (L_1 - L_2) / (L_1 + L_2)$. V is the maximum distance at what during daylight conditions a large "black", i.e. non-radiating object can be observed by the human eye against the horizon under simplifying, but usually applicable conditions. The corresponding contrast threshold is $K_{\min} = 0.02 \approx 2 C_{\min}$. It is equivalent to an atmospheric transmission of $\tau = 0.02$ along V . For human twilight and night vision higher, empirically determined values of K_{\min} have to be used.

For $\lambda \geq 3 \mu\text{m}$ the 3 to 5 μm and 8 to 14 μm atmospheric window regions offer the possibility of thermal vision.

An unique theory of passive vision for $0.35 \mu\text{m} < \lambda < 14 \mu\text{m}$, from what Koschmieder's theory follows as a special case, was presented recently (Hahn, D.H., 1975). Active, especially gated viewing could be incorporated afterwards based on an analysis of the performance of gated viewing systems, presented earlier (Buchamann, W. and D.H.Hahn, 1973). The following is devoted to a short review including the active aspects, and the results of recent detail analysis and applications of the theory to thermal vision, as mentioned above.

2. MAIN FEATURES OF AN UNIQUE THEORY OF ATMOSPHERIC VISION

2.1 Vision Signal

Observation is equivalent to discriminating the apparent radiance difference, including the special case of a luminance difference, $\Delta L = L_1 - L_2$, between the object of observation and its surrounding or between different resolution areas at an object in the cases of recognition and identification. The observed ensemble of L_1 will be called scene in the following. The observation has to be performed at a certain distance R from the scene within a certain time Δt corresponding to a bandwidth of $\Delta f \approx 1/\Delta t$. At the detector or amplifier output it results in a mean vision signal \bar{S} related to ΔL , and the corresponding noise N . The physical limitation is given by the signal-to-noise ratio $\bar{S}/N \geq p$ with p being a threshold value dependent on the signal processing and final detection method used with the system. In the following $p = 1$ will be used as a significant order of magnitude. For the evaluation of a special imaging system the appropriate value p has to be determined, maybe based on other figures of merit, e.g. the contrast at a display including an additional time integration due to human vision as final perception process behind the display. So even values $p < 1$ are possible.

If L_1^T is the mean initial radiance of a resolution area in the scene at R , τ the atmospheric transmission, and L^A the atmospheric path radiance along R , the apparent radiance L_1 at the observation site can be described by

$$L_1 = L_{1,p} + L_{1,a} \quad (1)$$

$$= (\tau_p L_{1,p}^T + \tau_a L_{1,a}^T) + (L_p^A + L_a^A) \quad (2)$$

$$= \tau L_1^T + L^A \text{ for } \tau_p = \tau_a \text{ or pure passive vision.} \quad (3)$$

p is standing for passive, a for active contributions. From these equations it results the apparent radiance difference:

$$\Delta L = \tau_p \Delta L_p^T + \tau_a \Delta L_a^T \quad (4)$$

$$= \tau \Delta L^T \leq \Delta L^T \text{ with } \tau \leq 1, \quad (5)$$

for $\tau_p = \tau_a$ or pure passive vision.

Certainly all magnitudes have to be weighted for source, atmospheric, target, background and device spectral characteristics, if necessary regarding the spectral band used. The index i no longer is used in this context, e.g. Equ.(4) and (5). Contributions from other scene elements onto the two elements under consideration, i.e. the aspect of optical transfer function OTF, is not incorporated into this theoretical attempt therefore up to now. The same is true concerning the effects of atmospheric turbulence on imaging resulting in an atmospheric OTF. For slant path vision models are necessary to calculate τ and L^A .

With passive vision the initial radiances of the scene elements, L_i^T , are either due to ambient irradiation and coded by different reflectivities, or to self-emitted radiation coded by temperature and/or emissivity. $\lambda \lesssim 3 \mu\text{m}$, often used in this context, defines the corresponding wavelength regions roughly. With active vision L_i^T is due to the irradiation of the scene by the additional source. It is dependent on its radiant intensity, the relevant atmospheric transmission τ_a , and the reflectivities in the scene. Reflection coding is the dominant process establishing the image beside of the possible change of scene temperatures by high power laser irradiation.

The path radiance L^A is due to atmospheric scattering and atmospheric emission being the dominant effects with passive vision for $\lambda < 3 \mu\text{m}$ and $\lambda > 3 \mu\text{m}$ resp. Contributing to the apparent radiance, Equ.(1) to (3), as an additive term L^A is not affecting the mean vision signal ΔL directly. But it is the reason for an increase of the noise N of \bar{S} resulting in a decreasing observability using signal-photon noise limited systems. In addition to this it is the reason for a decrease of the contrast K or C being essential for purely contrast limited systems like the human eye under daylight conditions. Different imaging methods result in different expressions for the path radiance L^A , and will be summarized shortly in the following.

In the visual band, and in the following atmospheric window regions up to about $3 \mu\text{m}$ L^A can be presented as

$$L^A = L^H (1 - \exp(-\sigma R)) = (L'^A / \sigma) (1 - \exp(-\sigma R)), \quad (6)$$

where $\tau = \exp(-\sigma R)$ = atmospheric transmission with σ = extinction coefficient, R = distance, L^H = horizon radiance and L'^A = differential path radiance [$\text{Wm}^{-2}\text{sr}^{-1}/\text{m}$] or luminance, often called path function offering the treatment of slant path vision.

Concerning thermal vision, usually dominant for $\lambda > 3 \mu\text{m}$, the assumption of small thermal signals, i.e. of similar temperatures of the scene elements and the atmosphere (T_0) results in a comparable presentation:

$$L^A = \epsilon L_0 = L_0 (1 - \tau), \quad (7)$$

with $L_1^T - L_2^T = \Delta L^T \ll L_1^T$, $L_2^T \sim L_0(T_0)$ = black-body radiance for ambient temperature T_0 , ($\epsilon \approx 1 - \tau$) = emissivity.

The transmission τ , if not monochromatic radiation is considered, usually cannot be presented as an exponential for Ir-bands. Again it is possible to think of L_0 as thermal horizon radiance because $\tau \rightarrow 0$ if $R \rightarrow \infty$ in a plane atmosphere already assumed with Equ.(6). For the apparent radiance L_i , Equ.(3), with Equ.(7) it holds the approximation $L_i \sim L_0(T_0)$ too, if not ΔL has to be calculated.

In general, both Equ.(6) and (7) have to be applied, especially around $3 \mu\text{m}$. Beside of their range gating capability the interesting feature of gated viewing systems is the reduction of the path radiance L^A . The passive contributions in Equ.(1) to (3) are reduced by the duty cycle of the gated imaging device and the spectral filtering possible with small band sources like lasers. L_a^A is mostly due to radiation scattered backwards out of the transmitter cone into the receiver cone in the effective gated area $\Delta R_{\text{eff}} \leq \Delta R$ dependent on the transparency and the position of the object within the gated range ΔR defined by the source pulse duration and the detector gating time. ΔR is lying around R that is defined by the delay between back radiation reflected at other scene elements, but mostly in the neighborhood of the resolution elements under observation, and scattered forward into the receiver cone within the time limitations of gating, results in a higher, lower contribution to L_a^A , affecting the actual OTF of the system. Detail analysis showed (Büchtemann, W. and D.H.Höhn, 1973) that with usual gated viewing systems not the remaining path radiance $L_p^A + L_a^A$ is limiting its performance but the signal induced photon noise, i.e. the lack of photons with decreasing atmospheric transmission τ_a and source intensity.

2.2 General Vision Formula

To derive in a general vision formula the ultimate noise limitation, i.e. photon noise, has to be considered together with other noise sources. Using the relevant device figures, the geometrical parameter

$$g = F^T \sigma^R \xi \sim (\sigma^D)^2 D_0^2 \xi, \quad (8)$$

and the photon parameter

$$\gamma = \eta \lambda_{\text{eff}} / \Delta f h c, \quad (9)$$

the average photon number ΔQ corresponding to ΔL , and its noise σ_{Δ} can be calculated. The following notation was used with Equ. (8) and (9): F^T = resolution area in the scene, Ω^R = solid angle subtended by the collecting optics as seen from the scene, ξ = transmission of the device, θ^D = resolution angle of the device, D_0 = diameter of the collecting optics; η = quantum efficiency, λ_{eff} = effective wavelength, Δf = bandwidth $\sim 1/\Delta t$, h = Planck's constant, c = speed of radiation.

The relevant noise is due to three effects: (1) Signal induced photon noise: $\sqrt{\tau Q_1^T + Q^A}$, (2) photon noise of additional radiation Q^D that does not carry useful image information, like thermal emission in the device: $\sqrt{Q^D}$, and (3) pure detector noise: $\sqrt{Q^N}$. The latter is represented for convenience by the hypothetical photon number Q^N , which would result in the same photon noise but which actually is not entering the detector. If the same bandwidth Δf is governing this noise component, it can be represented by

$$Q^N = \gamma^2 \text{NEP}_{\text{eff}}^2. \quad (10)$$

The signal-to-noise ratio $\Delta Q / \sigma_{\Delta}$ establishes the general vision formula:

$$\frac{\bar{S}}{N} = \frac{\Delta Q}{\sigma_{\Delta}} = \frac{Q_1 - Q_2}{\sqrt{Q_1 + Q_2 + 2Q^N}} \quad (11)$$

$$= \frac{\tau \Delta Q^T}{\sqrt{\tau(Q_1^T + Q_2^T) + 2(Q^A + Q^D + Q^N)}} \geq p \approx 1. \quad (12)$$

ΔQ is the mean quantum number related to ΔL of Equ. (4) and (5), σ_{Δ} is the noise present including photon noise $(Q_1 + Q_2)$, and detector noise (Q^N) . $(Q_1 + Q_2)$ consists of the apparent vision signal $(\tau(Q_1^T + Q_2^T) + 2Q^A)$ and the photon flux (Q^D) not carrying useful vision information, that can be made very small with properly designed imaging devices. It is representing the background noise limitation in the meaning of a BLIP-condition. With the notation used in Equ. (10) this noise should not be incorporated in NEP_{eff} . BLIP-values would be represented by $Q^D + Q^N$. $Q^D = 0$ with $Q^N \ll Q_1 + Q_2$ corresponds to no background and no essential detector noise limitations. The device is working under signal limited photon noise (SLIP)-conditions in this case. $p \approx 1$ is an order of magnitude only as mentioned already earlier.

3. DISCUSSION

In the context of this discussion the thermal imagers defined in Table 1 will be considered as examples for passive thermal vision systems. There other relevant figures for $T_0 = 300$ K and $\Delta T = 1$ K are compiled too.

3.1 Detector/Device Noise Limited Systems

$$2(Q^N + Q^D) \gg \tau(Q_1^T + Q_2^T) + 2Q^A, \quad (13)$$

$$\gg 2Q_0 \text{ for small thermal signals,}$$

defines systems limited by detector (Q^N) and/or device radiation (Q^D) noise. Unequ. (13) holds for the imagers described in Table 1. The NEP'_{eff} - values given there contains Q^N and Q^D contributions corresponding nearly to a 2π - BLIP condition.

wavelength band $\Delta\lambda$ eff. wavelength λ_{eff} used	3 to 5 4	8 to 13 10.5	μm μm
collecting optics diam. D_0 resolution angle θ^D device transmission ξ quantum efficiency η bandwidth Δf NEP'_{eff} geom. parameter g photon parameter γ	10 1 0.8 0.8 100 6×10^{-11} 8×10^{-9} 1.6×10^{14}		cm mrad KHz W $\text{m}^2 \text{sr}$ W^{-1}
bl.-body radiance + diff.bl.-body rad. + diff.bl.-body contrast C + noise number $Q^N + Q^D$ initial photon number Q_0 + initial diff. " " ΔQ^T +	1.46 5.8×10^{-2} 2×10^{-2} 9.2×10^7 1.9×10^6 7.4×10^4	50 7.5×10^{-1} 0.8×10^{-2} 2.8×10^{10} 1.7×10^8 2.5×10^6	$\text{Wm}^{-2} \text{sr}^{-1}$ $\text{Wm}^{-2} \text{sr}^{-1} \text{K}^{-1}$ K^{-1} K^{-1}
device lim.min.transm. τ_{min} + photon " " " τ_{min} +	0.18 0.03	0.09 0.007	K^{-1} K^{-1}

Table 1: Thermal imaging device and scene parameters, and limiting atmospheric transmission τ_{min} for passive vision of small thermal signals around ambient temperature.

The figures marked with + are calculated for $T_0 = 300 \text{ K}$. With this example rectangular bands $\Delta\lambda$ are assumed, the center wavelength is used as λ_{eff} . The bandwidth Δf determines the photon counting period (Equ.(9)), and the NEP' -values presented (Equ.(9) and (10)). With detail analysis of a special device the actual scanning method has to be taken into account. The latter may result in different Δf - values characterizing the photon collecting period and the detector noise.

The general vision formula Equ.(12) with condition (13) reduces to

$$\tau_{\text{min}}(R_{\text{max}}) = \frac{\sqrt{2(Q^N + Q^D)}}{\Delta Q^T} = \sqrt{2} \text{NEP}'_{\text{eff}} / g \Delta L^T \quad (14)$$

$$= 0.18 \text{ K}^{-1} \text{ and } 0.09 \text{ K}^{-1} \text{ resp. (see Table 1).}$$

The maximum range R_{max} , implicitly given by Equ.(14), under these conditions concerning the atmosphere is only dependent on transmission, but not on path radiance. The contrast C is no essential assessment figure. The critical scene figure ΔL^T often is called "thermal contrast" in contradiction to the "relative thermal contrast" C and K resp.

The numerical results presented beneath Equ.(14) for the thermal imagers defined in Table 1 for the 3 to 5 μm and 8 to 13 μm band are calculated for small thermal signals (see Chapter 2.1) with $\Delta T = 1 \text{ K}$. For $\Delta T = 0.1 \text{ K}$ it would follow $\tau_{\text{min}} = 1.8$ or 0.9 resp., indicating that with the 3 to 5 μm imager $\Delta T = 0.1 \text{ K}$ cannot be detected with the given values g and γ . $\tau = 1$ would result in 0.18 K as a limiting temperature difference in

agreement with typical values realized by commercial imagers of this type.

3.2 Signal-Photon Noise Limited Systems

The corresponding SLIP-condition is given by

$$2(Q^N + Q^D) \ll \tau(Q_1^T + Q_2^T) + 2Q^A, \quad (14)$$

$$\ll 2Q_0 \text{ for small thermal signals.}$$

Cooled apertures and spectral filtering should allow a reduction of Q^D by factors around 10^2 approaching the condition (14), see Table 1, and therefore resulting in almost optimized imaging devices even in the thermal range. In the visual range and the very near ir they can be realized usually. The general vision formula, Equ.(12), with condition (14) and introducing the contrast $C = (Q_1 - Q_2)/(Q_1 + Q_2)$ reduces to

$$\sqrt{C} \sqrt{\tau \Delta Q^T} \geq 1, \quad (15)$$

indicating that the contrast C can be used as a meaningful assessment figure in this case, equivalent to the fact that concerning the atmosphere transmission and path radiance are limiting the observation. τ in general cannot be separated as in Equ.(13) resulting in a $\tau_{\min}(R_{\max})$ -relation.

Koschmieder's theory for human daylight vision follows with $C_{\min} \approx K_{\min}/2 = 0.01$. For twilight and night vision higher C_{\min} -values dependent on the actual adaption luminance have to be used.

With small thermal signals around ambient temperature (see Equ.(7)) it would follow for thermal SLIP-systems

$$C = \frac{\tau \Delta Q^T}{2Q_0} = \tau C_0 \geq C_{\min} = \frac{1}{\tau \Delta Q^T} \quad (16)$$

or

$$\tau_{\min}(R_{\max}) = \frac{\sqrt{2Q_0}}{\Delta Q^T} = \frac{\sqrt{2L_0/g\gamma}}{\Delta L^T} \quad (17)$$

$$= 0.03 \text{ K}^{-1} \text{ and } 0.007 \text{ K}^{-1} \text{ resp.}$$

for the imagers defined in Table 1 but optimized according to condition (14). Formally this situation is comparable to the observation of a grey object against the horizon using the contrast C instead of K as by Koschmieder.

With $\tau_{\min} = 0.3$ and 0.07 resp. for $\Delta T = 0.1 \text{ K}$ under SLIP-conditions the imagers defined in Table 1 would be ready to observe it but only at the 8 to $13 \mu\text{m}$ band with a spatial resolution of 0.1 mrad equivalent to $g = 8 \times 10^{-11} \text{ m}^2/\text{sr}$.

3.3 Optimized Atmospheric Spectral Bands

In addition to the optimization based on the reduction of Q^N and Q^D , i.e. approaching SLIP-conditions for the device, an optimization is possible to some extent regarding the atmospheric spectral band used with the observation. This has to be equivalent to a decrease of the signal-photon noise itself represented by $\tau(Q_1^T + Q_2^T) + 2Q^A$. Time gating as example is resulting in this type of optimization by reducing the atmospheric path radiance with another method.

A limitation of the spectral band to regions of high atmospheric transmission is reducing the path radiance L^A , as shown by Equ.(6), but usually even the vision signal ΔQ corresponding to $\Delta L = \tau \Delta L^T$. For small thermal signals around ambient temperature Equ.(14) and (17) can be used to discuss this effect qualitatively. They show that systems with different noise limitations are influenced in a different way. With detector-noise (Q^N) limited systems the reduction of ΔQ^T would have to be balanced by the increase of τ , so that basically a linear relation has to

hold between $\tau(\Delta\lambda)$ and $\tau(b\Delta\lambda)$ around a λ_{eff} with the reduction factor $b < 1$, so that

$$b \tau(b\Delta\lambda) > \tau(\Delta\lambda), \quad (18)$$

corresponding to an increase of R_{max} . Usually this condition cannot be fulfilled. Therefore with detector-noise limited systems R_{max} is increasing with $b > 1$, i.e. with a broadening of the spectral band, equivalent to the fact that they are not limited by atmospheric path radiance but only by atmospheric transmission.

With SLIP-devices only a square-root relation has to be fulfilled basically:

$$\sqrt{b} \tau(b\Delta\lambda) > \tau(\Delta\lambda) \quad (19)$$

results in a higher R_{max} . Numerical calculations based on spectral atmospheric transmission has to be used to determine the actual factor in Equ.(19) because this relation is only a zero order approximation. The same is necessary if the system is limited by device radiation Q^D . It can be reduced too with $b < 1$ so that factors between b and \sqrt{b} are effective in this practical case.

4. CHARACTERISTIC LENGTHS

In the visible region the Visual Range V with $\tau(V) = 0.02$ corresponds to the observability of a special scene (black, i.e. non-radiating object against the horizon during day) using the human eye as observation device, see Chapter 1. Beside of this interpretation following from Koschmieder's theory and the assumptions used with it this magnitude is a purely atmospheric figure. Often instead of V , weighted for photopic vision and therefore dependent on the spectral distribution of the source, the Meteorological Range (Normsichtweite) V_N with $\tau(0.55 \mu\text{m}, V_N) = 0.02$ and $V_N \sim V$ is used. At other wavelengths or wavelength bands, i.e. usually connected with the analysis of optoelectronic imaging devices, it does not exist an exceptional imaging device comparable to the human eye. So often the above mentioned definition of V_N is applied extrapolated to other wavelengths or wavelength bands as proposed by G. Ruppenberg, DFVLR, and others resulting in a purely atmospheric figure:

$$\tau(\lambda, \Delta\lambda, V_{\lambda, \Delta\lambda}) = 0.02. \quad (20)$$

$V_{\lambda, \Delta\lambda}$ can be called Atmospheric Range. Its direct measurement would imply a variation of range used with a transmissometer, therefore being not applicable in general. If the exponential extinction law, resulting as wellknown in $V = 3.912/b$, does not hold, atmospheric spectral transmission models like LOWTRAN have to be used to calculate the Atmospheric Range $V_{\lambda, \Delta\lambda}$ from transmission measurements at shorter ranges using the same or other wavelength bands, or from meteorological quantities only. To derive in standard measurement methods of thermal Atmospheric Ranges, that can be used for synoptic analysis too, definitions of wavelength bands and source temperatures for this purpose are necessary.

To compare different imaging devices or principles a standard scene has to be assumed. For $\lambda < 3 \mu\text{m}$ the above mentioned black, i.e. non-radiating object against the horizon can be accepted. For $\lambda > 3 \mu\text{m}$ a standard thermal scene has to be defined. $(T_0, T_0 + \Delta T)$ with T_0 = ambient temperature and $\Delta T = 1\text{K}$ seems to be meaningful. For each device it would result a Standard Maximum Range V_S , implicitly presented above for the imagers defined in Table 1 as $\tau_{\text{min}}(R_{\text{max}})$ for $\Delta T = 1\text{K}$, Equ.(14) and (17). Regarding human daylight vision $V_S(\text{eye}) = V \sim V_N$ per definition. For other devices $V_S = V_S(\tau'_{\text{min}}, V_{\lambda, \Delta\lambda})$ with τ'_{min} calculated for the standard scene.

For a special scene it follows an Actual Maximum Range R_{max} with usually $R_{\text{max}} \neq V_S$. $R_{\text{max}} \leq V_S$ for $\lambda < 3 \mu\text{m}$ because the standard scene, as described above, corresponds to maximum initial negative contrast $C = -1 \leq C$. A realistic thermal scene, as proposed above with $\Delta T = 1\text{K}$, allows for $R_{\text{max}} \leq V_S$.

REFERENCES

Büchtemann, W., and D.H.Hahn, 1973, Performance of Gated Viewing Systems, Report FFO 1973/63, Tübingen, and NATO Laser Seminar Report, Ottawa, Sept.1973.

Duntley, S.Q., 1948, The Reduction of Apparent Contrast by the Atmosphere, J.Opt.Soc.Am., Vol.38, 179 - 191, and The Visibility of Distant Objects, J.Opt.Soc.Am., Vol.38, 237 - 249.

Grand, Y.le, 1968, Light, Colour and Vision, Chapman & Hall, London.

Hahn, D.H., 1975, Atmospheric Vision $0.35 \mu\text{m} \leq \lambda \leq 14 \mu\text{m}$, Appl.Optics, Vol.14, 404 - 412.

Koschmieder, H., 1924, Theorie der horizontalen Sichtweite, Beitr.Phys.fr.Atmos., Vol. 12, 33 - 53, and 171 - 181.

Middleton, W.E., 1952, Vision Through the Atmosphere, Univ.Toronto Press, and 1957 in Handbuch der Physik, Vol.48, Springer, Berlin.

Schober, H., 1970, Das Sehen, Fachbuchverlag Leipzig.

DECREASE OF CONTRAST IN THE ATMOSPHERE: STATISTICAL PRESENTATION OF THE
RESULTS OF DAYTIME AND NIGHT-TIME MEASUREMENTS.

J.VAN SCHIE
Physics Laboratory TMO. P.O.Box 2864
The Hague. The Netherlands.

J.ROGGE
Royal Military Academy, Kasteelplein 10
Breda. The Netherlands.

Summary. An outline is given of the model in which the decrease of contrast in the atmosphere in the visible region is described with two parameters: the extinction coefficient α and the luminance of the atmosphere B_a ; also the distance s_1 over which the initial contrast is halved, is introduced.

The results of a number of measurements of these parameters, both at day and at night, that were carried out during the last few years on different locations, are presented in the form of several histograms. In the short discussion some comments concerning the results of the various measurements are given.

A. Introduction.

The use of vision equipment is strongly influenced by the atmosphere between the target and the Observer: absorption, scattering and turbulence are the most important effects. When considering the use of image intensifiers, with a spectral sensitivity mainly in the visible part of the spectrum, the decrease of contrast in the atmosphere, caused by scattering, is important, because

- * there is no optical or electronic way to enhance the contrasts in the display of the device.
- * the contrasts in military scenes usually are small. Therefore any decrease of that contrast quickly makes the targets undetectable.

There exists the well-known Koschmieder model (MIDDLETON, W.E. 1952; HÖHN, D.H. 1975) with which the contrast-alteration in the atmosphere can be described. We will use this model for a horizontal viewing direction at ground level.

B. Description of the model.

The luminance $B(o)$ of a diffuse reflecting flat object perpendicular to the line of sight with reflectance r is given by

$$B(o) = \frac{rE}{\pi} \quad (1)$$

where E is the illuminance on that object. If one looks at this object from a distance s , the luminance seems to be changed, due to two effects:

- a. on a part ds of the line of sight, some of the light, coming from the object, is scattered out of the viewing direction, so the apparent luminance decreases:

$$dB = -\alpha B ds \quad (2)$$

- b. light, coming from other sources (sun, moon, etc) is scattered into the viewing direction, so the apparent luminance increases:

$$dB = g ds \quad (3)$$

A combination of equations (2) and (3) yields:

$$dB = -\alpha B ds + g ds \quad (4)$$

and the solution is found by integrating from 0 until s , assuming constant α and g :

$$B(s) = B(o) e^{-\alpha s} + \frac{g}{\alpha} (1 - e^{-\alpha s}) \quad (5)$$

When α and g vary in the same way along the viewing direction until infinity (including the case that both are constant) they can be written (MIDDLETON, W.E. 1952):

$$\alpha(s) = \alpha_0 f(s)$$

$$g(s) = g_0 f(s)$$

This situation can occur when the density of scattering elements is not constant along the line of sight and the other conditions, including the particle size distribution, remain constant. In that case g/α is constant and equal to the apparent luminance of the horizon B_h ($s = \infty$):

$$B(s) = B(o) e^{-\alpha_0 x} + B_h (1 - e^{-\alpha_0 x}) \quad (6)$$

when $x = \int_0^s f(s) ds$.

Defining an average scattering coefficient $\bar{\alpha} = \alpha_0 x/s$ gives, instead of (6):

$$B(s) = B(o) e^{-\bar{\alpha} s} + B_h (1 - e^{-\bar{\alpha} s}) \quad (7)$$

In case of an inhomogeneous cloud cover, the situation is more complex: g_o varies along the viewing direction and g/α is no longer constant. In that case the quantity $B_a = g/\alpha$ is sometimes introduced, assuming that over the measuring path the quantities α and g are constant, but not necessarily until the horizon (VAN SCHIE, J. 1969).

With (1) we can introduce the apparent reflectance $r(s)$ of an object at a distance s from the observer:

$$r(s) = r(o)e^{-\alpha s} + b_a (1 - e^{-\alpha s}) \quad (8)$$

where b_a , the reduced luminance of the atmosphere (the "reflectance" of the horizon) follows from

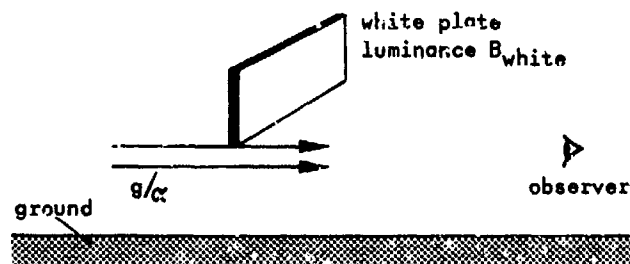
$$B_a = \frac{b_a E}{\pi} \quad (9)$$

and this quantity is an important parameter in the contrast-loss model that is described here; therefore we will give some attention to the calculation of b_a . Combining equations (5) and (9) gives

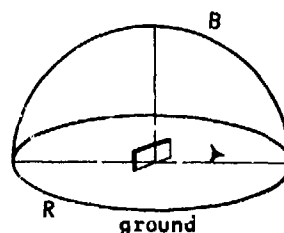
$$b_a = \frac{g/\alpha}{\frac{1}{\pi} E} \quad (10)$$

where, with (1), $\frac{E}{\pi}$ is the luminance of a vertical, diffuse reflecting, white plate ($r = 1$)

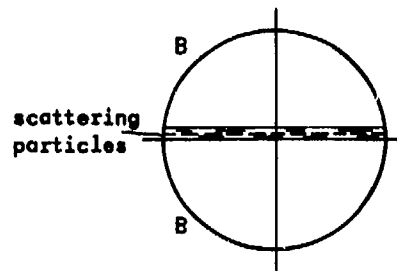
$$b_a = \frac{g/\alpha}{B_{\text{white}}} \quad (11)$$



Suppose now that the scattering atmosphere around the observer is illuminated by a sphere of uniform luminance B :



and that a thin layer of scattering particles is situated above the ground. If the reflectance R of the ground is equal to 1 (or, which is the same, the presence of the ground is ignored)



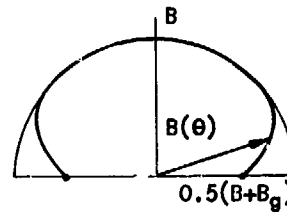
then each scattering particle is illuminated by a sphere with homogeneous luminance B . If we neglect absorption, the luminance of all particles (and therefore of the layer) will be the same as the luminance B of the sphere; so $g/\alpha = B$.

As the vertical white plate will have this luminance too, the reduced luminance of the atmosphere b_a equals 1 in this case.

If, next, we suppose a black ground (reflectance $R = 0$), the vertical white plate only receives half the amount of light as in the previous case and thus has a luminance $\frac{1}{2}B$. Also the light scattered in the layer reduces with a factor 2, so $g/\alpha = \frac{1}{2}B$ and therefore again the reduced luminance of the atmosphere b_a equals 1.

More general: if the ground has a reflectance R , resulting in a luminance of the ground equal to B_g , then g/α , that is the luminance of the layer of scattering particles, consists of two parts: a contribution $\frac{1}{2}B$ from the upper hemisphere and a contribution $\frac{1}{2}Bg$ from the ground; thus $g/\alpha = \frac{1}{2}(B + Bg)$. The same applies for the vertical white plate: $B_{\text{white}} = \frac{1}{2}(B + Bg)$ and therefore $b_a = 1$.

It is clear that the above standing discussion is only correct when the layer of scattering particles is so thin that all scattering elements are illuminated in the same way; in other words: the transmission T through the layer equals 1 in all directions, except in the direction of the horizon, where $T = 0$. Under this condition the apparent luminance of the sky, looking in horizontal direction, is $\frac{1}{2}(B + Bg)$ and of the rest of the sky is B . In a polar diagram:

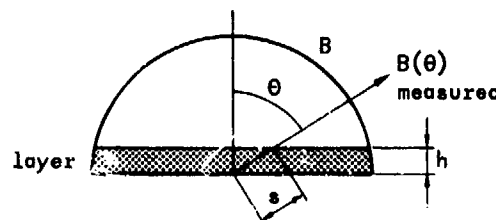


In the calculation of the luminance of the vertical white plate and of g/α at the place of the observer, the decrease of the apparent luminance of sky to the horizon has not been taken into account.

If the observer looks to the sky around him, or measures the luminance of the sky, he finds with equation (5):

$$B_{\text{measured}}(\theta) = B e^{-\alpha s} + \frac{g}{\alpha} (1 - e^{-\alpha s})$$

where B is the luminance of the sphere around the observer, α is the scattering coefficient in the layer of scattering particles and $s = s(\theta)$ is the thickness of the layer in the viewing direction:



and, as $s = h/\cos \theta$ (except for $\theta \rightarrow \pi/2$):

$$B(\theta) = B_e^{-\alpha h/\cos \theta} + \frac{1}{2} (B + B_g) (1 - e^{-\alpha h/\cos \theta}) \quad (12)$$

where it is assumed that g/α is independent of the viewing angle θ is almost $\pi/2$. For smaller values of θ the transmission through the layer $T \approx 1$, so the actual value of g/α is of no importance.

Thus for horizontal observation ($\theta = \frac{\pi}{2}$) the transmission T of light through the layer is zero, therefore $B(\text{horizon}) = \frac{1}{2} (B + B_g)$; near the horizon the exact form of $B(\theta)$ depends on the thickness of the layer and the scattering coefficient; and further above the horizon $B_{\text{measured}} = B$ (because $T = 1$); see the polar diagram above.

As has been shown in the foregoing model, for an observer looking in a horizontal direction, the reduced luminance of the horizon b_a equals one, independent of the luminance of the ground.

The situation is different when there are bright parts in the sky, either in front of the observer or behind him.

For example, when the sky is brighter in front of the observer, according to (10) b_a becomes greater than one (the luminance of the white plate remains unchanged, whereas the amount of light scattered towards the observer, increases).

When the sky is brighter behind the observer, the luminance of the white plate increases, whereas (dependant on the scattering function) the amount of light towards the observer (mostly back-scatter) increases a little. In most cases therefore under this circumstances b_a will be smaller than one.

Using some simple formulae, all statements given in the foregoing text, can be illustrated mathematically.

Referring to fig 1 and equation (1) the amount of light that is scattered per unit of length towards the observer, can be expressed as (BAL, A.J.B.C. 1974):

$$g = \iint \beta [\underline{\epsilon}, \underline{\epsilon}^*] \alpha B^* d\omega^* \quad (13)$$

and the luminance of the white plate as

$$B_{\text{white}} = \frac{-1}{\pi} \iint [\underline{\epsilon}, \underline{\epsilon}^*] B^* d\omega^* \quad (14)$$

To these formulae the following explanation can be given: from the radiation $B^* = B^*(\theta, \phi)$ that arrives in P, an amount αB^* will be scattered in all directions; a fraction

$\beta [\underline{\epsilon}, \underline{\epsilon}^*] = \beta(\cos \gamma)$ of this will be scattered in the direction towards the observer, determined by the angle γ . The volume scattering function $\beta(\cos \gamma)$ must obey the relation

$$\iint \beta(\cos \gamma) d\omega^* = 1 \quad (15)$$

Remembering that $d\omega^* = \sin \theta d\theta d\phi$ and $\cos \gamma = \sin \theta \cos \phi$ we get

$$b_a = \frac{\int_{\theta=0}^{\pi} \int_{\phi=0}^{2\pi} \beta(\cos \gamma) B^*(\theta, \phi) \sin \theta d\phi d\theta}{\frac{1}{\pi} \int_{\theta=0}^{\pi} \int_{\phi=0}^{2\pi} B^*(\theta, \phi) \cos \phi \sin^2 \theta d\phi d\theta} \quad (16)$$

Making the same assumption on the thickness of the layer of scattering particles as in the previous discussion, $B^*(\theta, \phi)$ is (except for $\theta = \frac{1}{2}\pi$) the luminance of the sky. The apparent luminance of the horizon ($\theta = \frac{1}{2}\pi$) is g/α , the numerator of equation (16).

Now b_a can be calculated if some assumptions are made concerning the volume scattering function $\beta(\cos \gamma)$ and the distribution of the luminance around the scattering element. Let us write first

$$B^*(\theta, \phi) = B_o + f(\theta) \quad (17)$$

then

$$b_a = \frac{B_o + \int_{\theta=0}^{\pi} \int_{\phi=0}^{2\pi} f(\theta) \beta(\cos \gamma) \sin \theta d\phi d\theta}{B_o + 2\pi \int_{\theta=0}^{\pi} f(\theta) \sin^2 \theta d\theta} \quad (18)$$

In the foregoing discussion on b_a it was assumed that $B^*(\theta, \phi) = B$, so $f(\theta) = 0$; $f(\theta)$ was added in this case to introduce more flexibility. From (18) it follows that for $f(\theta) = 0$, independent of the volume scattering function, $b_a = 1$, as was argued earlier.

Now let us assume that the ground has a luminance B_g and that $f(\theta) = B_1 \cos \theta$, so $B^* = B_o + B_1 \cos \theta$. Therefore:

$$B^*(\theta, \phi) = B_o + B_1 \cos \theta \quad 0 < \theta < \frac{\pi}{2}$$

$$= B_g \quad \frac{\pi}{2} < \theta < \pi$$

This gives for the luminance of the white plate (the denominator of (18)):

$$B_{\text{white}} = \frac{1}{2} (B_o + B_g) + \frac{2}{3\pi} B_1 \quad (19)$$

and the earlier discussed situation ($B_1 = 0$) gives indeed $B_{\text{white}} = \frac{1}{2} (B_o + B_g)$.

The numerator of (18) cannot be calculated before an assumption has been made concerning $\beta(\cos \gamma)$. It is reasonable to assume that the volume scattering function is an even function of γ , so we write.

$$\beta(\cos \gamma) = \sum_{n=0}^{\infty} k_n \cos^n \gamma = \sum k_n \sin^n \theta \cos^n \phi \quad (20)$$

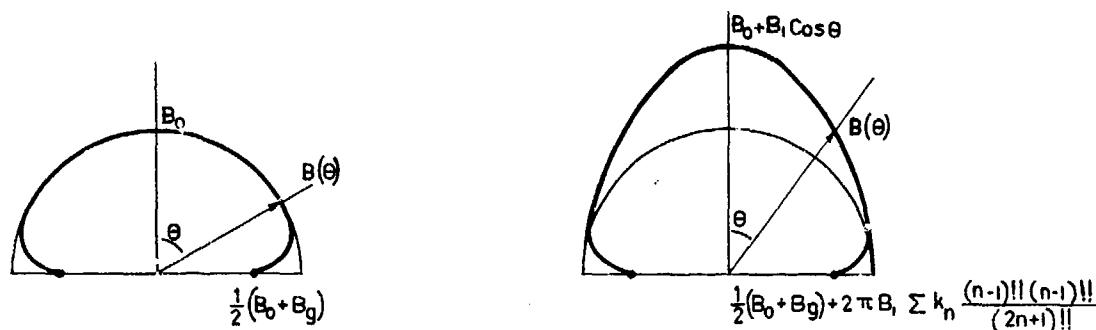
From (15):

$$\sum k_n \frac{1}{n+1} = \frac{1}{4\pi} \text{ for even values of } n$$

Equation (18) then gives (n even) :

$$b_a = \frac{\frac{1}{2} (B_o + B_g) + 2\pi B_1 \sum k_n \frac{(n-1)!! (n-1)!!}{(2n+1)!!}}{\frac{1}{2} (B_o + B_g) + \frac{2}{3\pi} B_1} \quad (21)$$

and the apparent luminance of the sky is given in the following polar diagrams:



Conclusion:

a) For $B_1 = 0$ (thus $B^* = B$ for $0 < \theta < \frac{\pi}{2}$ and $B^* = B_g$ for $\frac{\pi}{2} < \theta < \pi$) is $b_a = 1$, in agreement with what we found earlier. The apparent luminance of the horizon is $\frac{1}{2} (B_o + B_g)$, the numerator of (21).

b) For $B_1 \neq 0$ the exact value of b_a depends on the volume scattering function. Let us take as an example

$$\beta(\cos \gamma) = k (\cos^2 \gamma + \cos \gamma + 0.35)$$

in which $k = 3/8\pi$, according to (15).

In fig 2 this scattering function is shown, together with the scattering functions belonging to clear air and industrial haze (MIDDLETON, W.E. 1952); then

$$b_a = \frac{\frac{1}{2} (B_o + B_g) + 0.3 B_1}{\frac{1}{2} (B_o + B_g) + 0.2 B_1} \approx 1$$

so we conclude that when the luminance around the observer is rotationally symmetric, in most cases $b_a \approx 1$.

We finally consider the case that the distribution of B^* also is a function of ϕ (fig 1). Suppose

$$B^*(\theta, \phi) = B_o + B_1 \cos \theta + B_2(\phi) \quad \text{for } 0 < \theta < \frac{\pi}{2} \\ = B_g \quad \frac{\pi}{2} < \theta < \pi$$

The luminance of the white plate becomes:

$$B_{\text{white}} = \frac{1}{2} (B_o + B_g) + \frac{2}{3\pi} B_1 + \frac{1}{4} \int_{-\frac{\pi}{2}}^{\frac{\pi}{2}} B_2(\phi) \cos \phi d\phi$$

So both the numerator and denominator of (16) cannot be calculated before an assumption concerning $B_2(\phi)$ has been made; as an example we introduce

$$B_2(\phi) = B_2 \text{ for } \phi_1 < \phi < \phi_2$$

$$= 0 \text{ for } -\frac{\pi}{2} < \phi < \phi_1 \text{ and } \phi_2 < \phi < \frac{\pi}{2}.$$

It makes a difference whether the lighter parts of the sky are in front of the observer (ϕ_1 and ϕ_2 are greater than $\frac{\pi}{2}$) in which case B_{white} is the same as in (19) or behind the observer (ϕ_1 and ϕ_2 are between $-\pi/2$ and $\pi/2$) in which case.

$$B_{\text{white}} = \frac{1}{2} (B_o + B_g) + \frac{2}{3\pi} B_1 + \frac{B_2}{4} (\sin \phi_2 - \sin \phi_1)$$

So we can distinguish two situations:

a) the sky is brighter (between ϕ_1 and ϕ_2) in front of the observer; then (n even)

$$b_a = \frac{\frac{1}{2} (B_o + B_g) + 2\pi B_1 \sum k_n \frac{(n-1)!! (n-1)!!}{(2n+1)!!} + B_2 \sum k_n \frac{n!!}{(n+1)!!} \int_{\phi_1}^{\phi_2} \cos^n \phi d\phi}{\frac{1}{2} (B_o + B_g) + \frac{2}{3\pi} B_1}$$

Therefore it is reasonable to expect in this situation $b_a > 1$

b) the sky is brighter behind the observer; then (n even)

$$b_a = \frac{\frac{1}{2} (B_o + B_g) + 2\pi B_1 \sum k_n \frac{(n-1)!! (n-1)!!}{(2n+1)!!} + B_2 \sum k_n \frac{n!!}{(n+1)!!} \int_{\phi_1}^{\phi_2} \cos^n \phi d\phi}{\frac{1}{2} (B_o + B_g) + \frac{2}{3\pi} B_1 + \frac{B_2}{4} (\sin \phi_2 - \sin \phi_1)}$$

When forward scattering is dominant, the extra term in the numerator can be neglected with respect to the extra term in the denominator and therefore we expect here $b_a < 1$.

Now let us return to our model, describing the decrease of contrast in the atmosphere.

The contrast between an object with reflectance $r_o(o)$ and its surroundings with reflectance $r_s(o)$

$$C(s) = \frac{r_o(s) - r_s(s)}{r_o(s) + r_s(s)} = \frac{C(o)}{1 + \frac{F}{b_a} (e^{\alpha s} - 1)} \quad (22)$$

where $F = \frac{1}{2} \{r_o(o) + r_s(s)\}$

Remark: more and more the contrast defined in this way is called the modulation of the luminance.

The distance at which the apparent contrast between the object and its neighbourhood equals $C(o)/n$ is

$$s_{1/n} = \frac{R}{3} \ln \left\{ 1 + (n-1) \frac{F}{b_a} \right\} \quad (23)$$

where $R = \frac{3}{\alpha}$, the meteorological range ($e^{-\alpha R} = 0.05$).

The significance of equation (23) can be illustrated by defining the "viewing distance" V as the distance over which the contrast $C(o)$ is reduced to the threshold contrast $C_{th} = 2.5\%$; then

$$V = \frac{R}{3} \ln \left\{ 1 + \left(\frac{C(o)}{C_{th}} - 1 \right) \frac{F}{b_a} \right\}$$

In a paper by EKLOF, T.H. (1969), results are given of experiments in which the detection range (detection: the object can be discerned as a discrete object separated from its background) and the recognition range (recognition: the object can be seen as belonging to a certain class of objects as differentiated from another class of objects) of large objects (target diameter 30 m) were determined under various meteorological and brightness conditions; some of the results for $C(o) = 10\%$ are given in the next table:

$R = 33-40$ km	full daylight	overcast sky	twilight
detection range (km)	11	10	8.3
recognition range (km)	9.2	8.3	6.5

These data can be compared with equation (24) which gives $V = 7-8.5$ km for $b_a = 1$ and $F = 0.3$. In

applying this equation (24) to real military situations it must be remembered that b_a usually equals not one; with $C(o) = 20\%$ (EKLOF, T.H. 1969 and ROGGE, J. 1971) fig 3 gives the viewing distance as a function of the meteorological range with b_a as a parameter.

As a measure of the decrease of contrast in the atmosphere we will use the distance s_1 over which the initial contrast is halved. Starting again with $C(o)=20\%$ gives $C(s=s_1)=10\%$ after which the viewing device (e.g. image intensifier) reduces this contrast further until for the final contrast in the display $C < C_{th}$ detection is no longer possible.

Conclusion: we feel s_1 is a useful measure of the decrease of contrast in the atmosphere. It depends both on the extinction coefficient α and the distribution of light sources around the observer, illustrated in b_a . The purpose of our measurements was to get statistical information on α , b_a and s_1 , both by day^a and by night.

C. Description of the measurements

The parameters α and b_a can be determined by placing black and white targets with reflectance $r_b(o)$ and $r_w(o)$ at several s_1 distances from the measuring point where the apparent reflectances $r_b(s)$ and $r_w(s)$ have to be measured. From the foregoing theory the following equations can be written down:

$$\begin{aligned} r_w(s) &= r_w(o) e^{-\alpha s} + b_a (1 - e^{-\alpha s}) \\ r_b(s) &= r_b(o) e^{-\alpha s} + b_a (1 - e^{-\alpha s}) \\ r_w(s) - r_b(s) &= \{r_w(o) - r_b(o)\} e^{-\alpha s} \end{aligned} \quad (25)$$

$$r_w(s) = r_b(s) \frac{b_a - r_w(o)}{b_a - r_b(o)} + b_a \frac{r_w(o) - r_b(o)}{b_a - r_b(o)} \quad (26)$$

Equation (25) is a straight line in a single logarithmic graph and equation (26) is a straight line in a linear graph $r_w(s)$ vs $r_b(s)$. Substituting $r_w(s) = r_b(s)$ in the last equation gives $r_w = r_b = b_a$, so from the graphs, illustrated in fig 4, in which the measured values of $r_w(s)$ and $r_b(s)$ are plotted, α and b_a can be calculated easily.

The measurement of the apparent reflectance has been done in two ways:

- * with a telephotometer (photoelectric)
- * with photographic equipment.

The calibration of the telephotometer has been performed with a built-in light source and the calibration of the photographic method with a number of grey plates of different reflectances that are placed directly in front of the camera and recorded on each picture.

During the last few years we measured at different sites:

- C1. daytime measurements at Woensdrecht
- C2. daytime measurements at the Hague
- C3. night-time measurements at Meppen
- C4. night-time measurements at Woensdrecht.

The location of these sites is indicated in fig 5.

C1. Daytime measurements (ROGGE, J and DIRKSEN, H.J. 1972)

carried out at Woensdrecht from September 1970 until July 1971 on one day every week, 4 times a day (11.00, 12.00, 13.00 and 14.00 o'clock MET).

- Number of black and white targets : 11
- measuring range : 2 km
- measuring direction: West → East
- measuring method : photographic

The results of the total measuring period are given in fig 6.

C2. Daytime measurements (VAN MEETEREN, A.A. and VAN SCHIE, J)

carried out at the Hague from March 1971 until September 1974, every day, maximum 8 times a day (every two hours on the even hours).

- Number of targets : 2
- measuring range : 610 m
- measuring direction : 42° East of true North
- measuring method : photoelectric

During these measurements simultaneously the value of other parameters has been recorded.

Contrary to the other measurements, where the height of the measuring path is about 1.50 m., in this experiment the sensor and the target were placed on the roof of the laboratory and a tower respectively (height ± 15 m).

The results of the total measuring period are given in fig 6 and the results for the different seasons in fig 7.

- C3. Night-time measurements (VAN SCHIE, J. 1969) carried out at Meppen from October 1967 until October 1968, every week three nights, 2 or 3 times a night.

Number of targets : 3 (at 100, 300 and 600 m).
 measuring range : 600 m
 measuring direction : West → East
 measuring method : photoelectric

The results of the total measuring period are given in fig 6.

- C4. Night-time measurements (ROGGE, J. 1974) carried out at Woensdrecht during 1973, one night every week, 10 times a night (20.00, 21.00, ..., 05.00 o'clock MET).

Number of targets : 11
 measuring range : 1000 m
 measuring direction : West - East
 measuring method : photographic, both using fast film and with the aid of an image intensifier.

The results of the total measuring period are given in fig 6 and the results of the measurements in the different seasons (using fast film) are given in fig 8.

D. Discussion of the results

a. Night-time measurements.

In Woensdrecht the luminance of the sky is not the same in different directions (fig 9), in the direction backwards relative to the measuring range, the sky is brighter, due to the lights of small towns and this results in b_a being mostly smaller than 1. In Meppen are no cities in the direct neighbourhood of the measuring site and in that circumstances b_a varies around 1, the actual value depending on the place of the moon.

As a smaller b_a results in less contrast-loss it can be expected that the measurements in Woensdrecht give a larger value of s_1 .

To investigate the consequence on the decrease of contrast of the use of a yellow filter in combination with an image intensifier, a filter with a cut-off wavelength $\lambda = 0.5 \mu\text{m}$ has been used.

In fig 10 a comparison is given between the results of the measurements using the image intensifier in front of the camera, with and without the filter. It can be seen that the use of the filter gives no improvement as far as the contrast-loss in the atmosphere is concerned.

b. Daytime measurements.

In Woensdrecht during the day (contrary to the night-time) b_a varies around 1 (measuring path West-East); whilst in the Hague b_a mostly is smaller than one (measuring path 42° East of true North).

The difference in R_a can be attributed to the difference in location, length of the measuring period, height of the measuring path and the year of the measurements.

We assume that the differences in s_2 can be explained by a combination of these factors.

- c. With regard to a comparison between the three day-time measurements and the two night-time measurements, it is not possible to draw firm conclusions from our measurements because of the above mentioned factors. As these difficulties are not encountered in the project OPAQUE, it is hoped that after that project on better understanding can be obtained.

- d. Under the conditions, described in section B, the reduced atmospheric luminance b_a is equal to the reduced luminance of the horizon b_h . In fig 11 both quantities are compared; for a night-time from measurements at Meppen, for day-time from measurements at Woensdrecht and the Hague, the last sub-divided for unclouded and clouded sky.

References.

- BAL, A.J.B.C. 1974. Private communication.
 EKLOF, T.H. 1969. Visual reconnaissance in tactical air operations. USAF Tactical Air Reconnaissance Center.
 HÖHN, D.H. 1975. Atmospheric Vision $0.35 \mu\text{m} < \lambda < 14 \mu\text{m}$. Applied Optics Vol 14 No 2 (Febr 1975) pp 404-412.
 MIDDLETON, W.E. 1952. Vision through the atmosphere. University of Toronto Press.
 ROGGE, J. 1971. The apparent reflectance of some military vehicles and their contrast with two backgrounds. Royal Military Academy; the Netherlands.
 ROGGE, J. and DIRKSEN, H.J. 1972. Daytime measurements of the decrease of contrast in the atmosphere. Royal Military Academy, The Netherlands.
 ROGGE, J. 1974. Night-time measurements of the decrease of contrast in the atmosphere. Royal Military Academy, the Netherlands.
 VAN MEETEREN, A.A. and VAN SCHIE, J. SOLUMAT, a program for measuring the influence of the atmosphere on contrast transfer. Report in preparation.
 VAN SCHIE, J. 1969. Nocturnal illumination and decrease of contrast in the atmosphere. Report PhL 1969-4. Physics Laboratory TNO, the Hague.

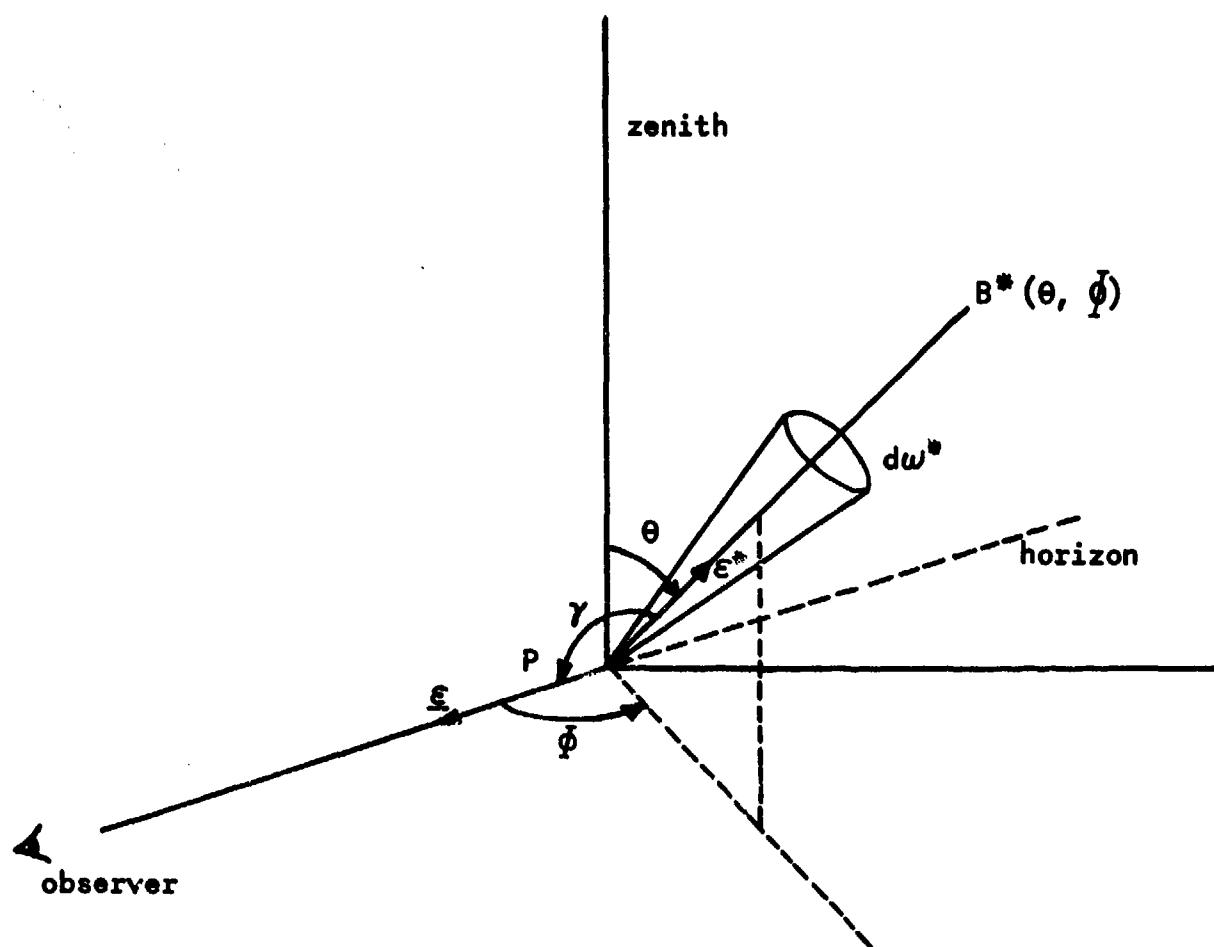
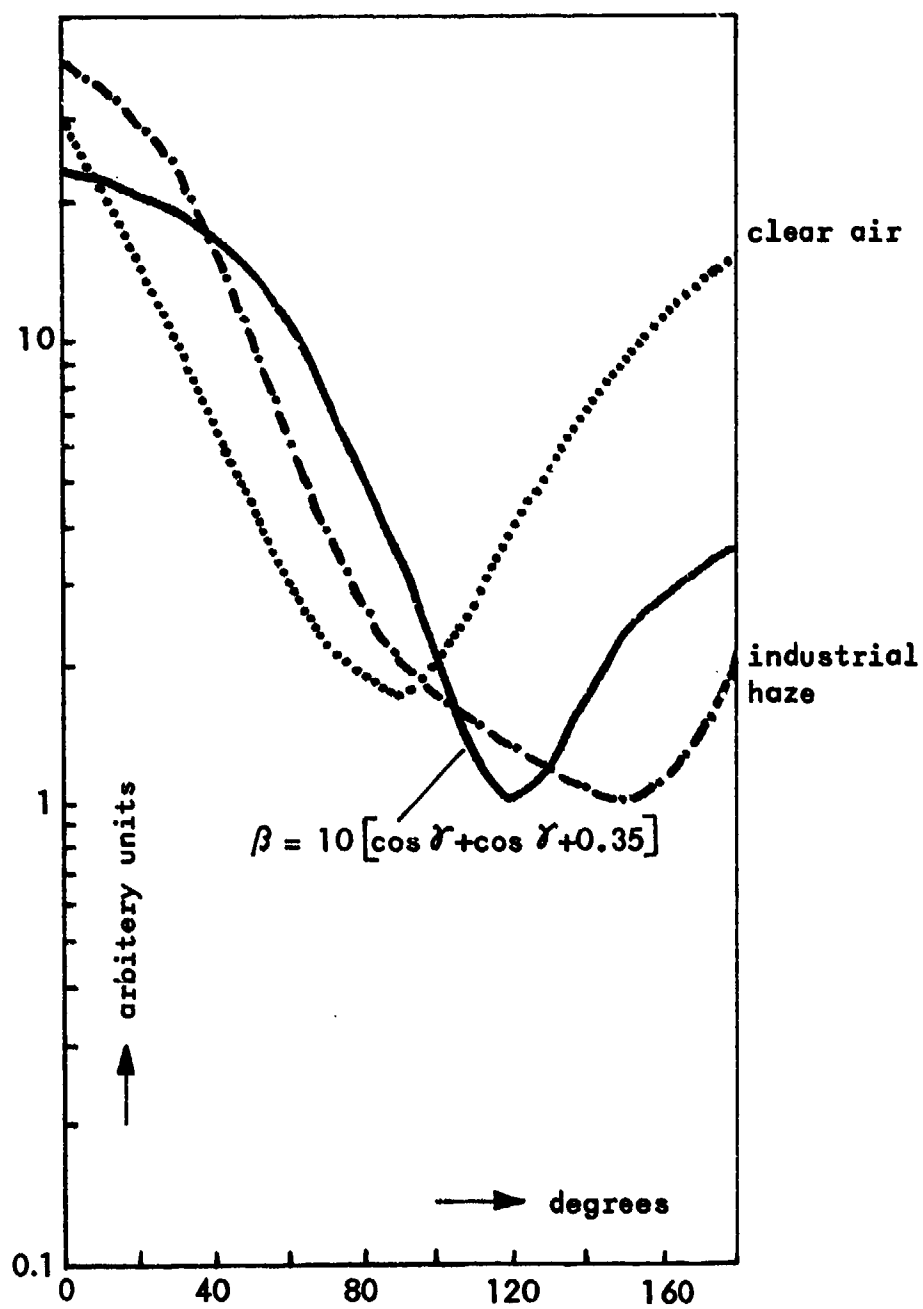
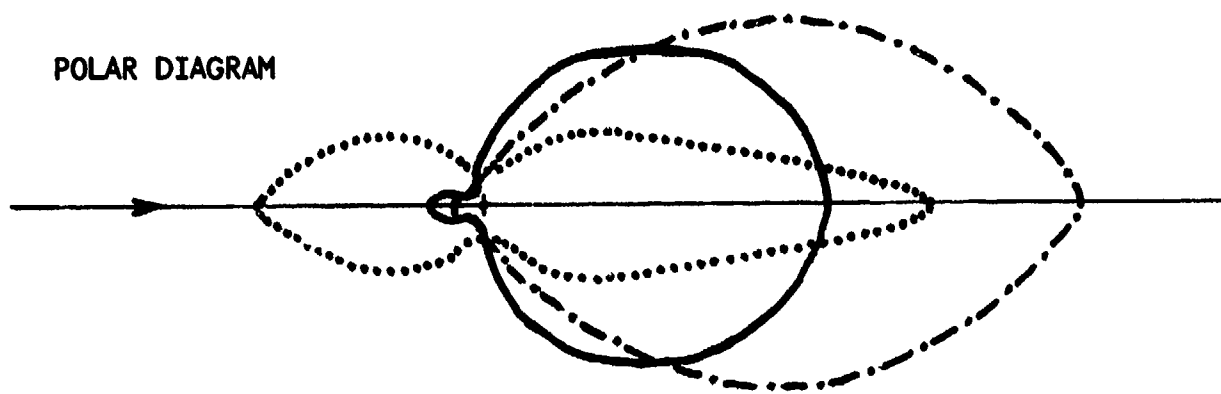


Fig.1 Geometry used in the description of the volume scattering function

POLAR DIAGRAM

Fig.2 Examples of scattering functions normalized $\int \beta' \omega = \alpha$

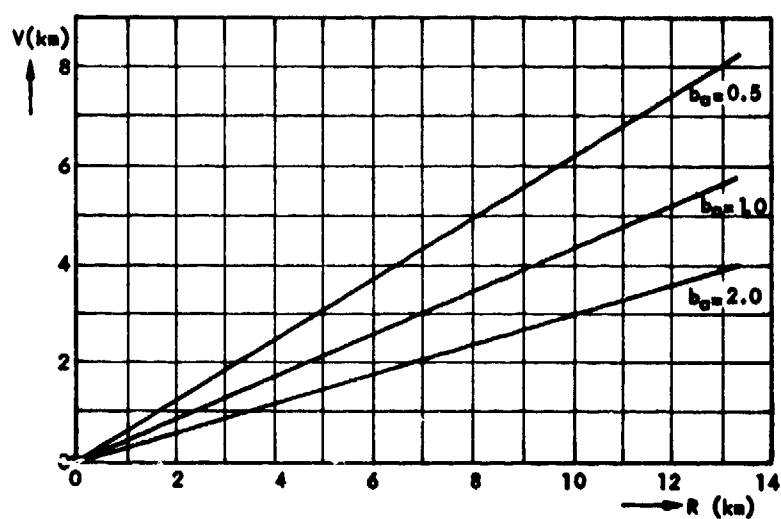


Fig.3 Viewing distance as a function of meteorological range

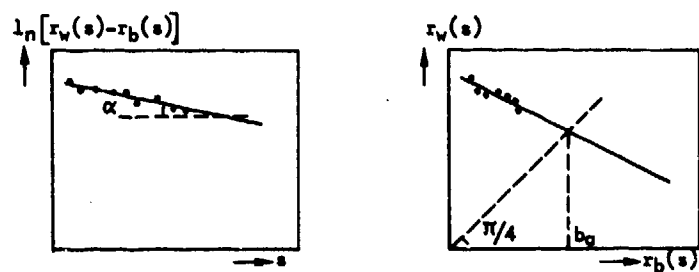
Fig.4 Determination of α and b_0 

Fig.5 Location of the measuring sites

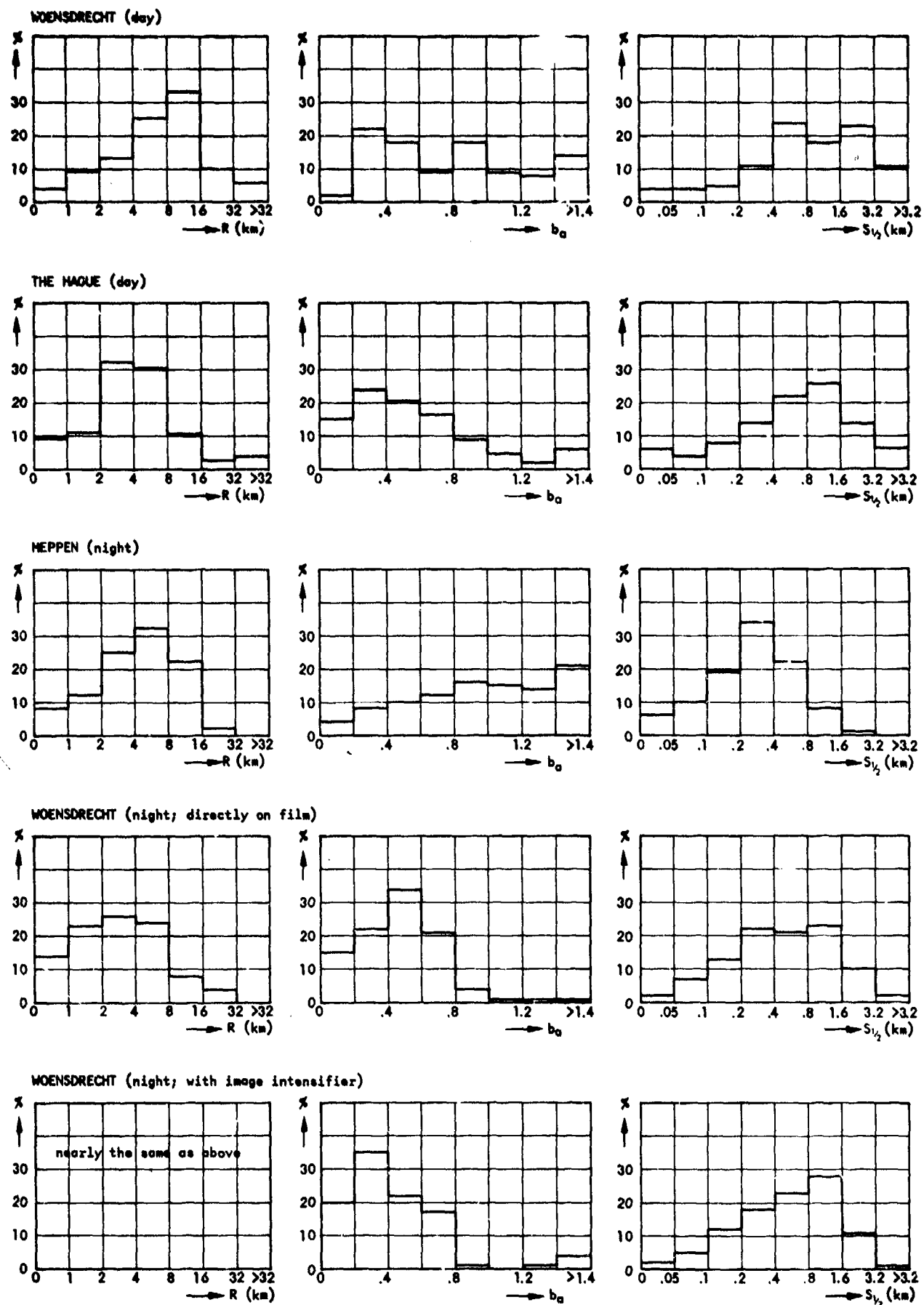


Fig.6 Histograms of R , b_a and $S_{1/2}$, covering the total measuring period for each site

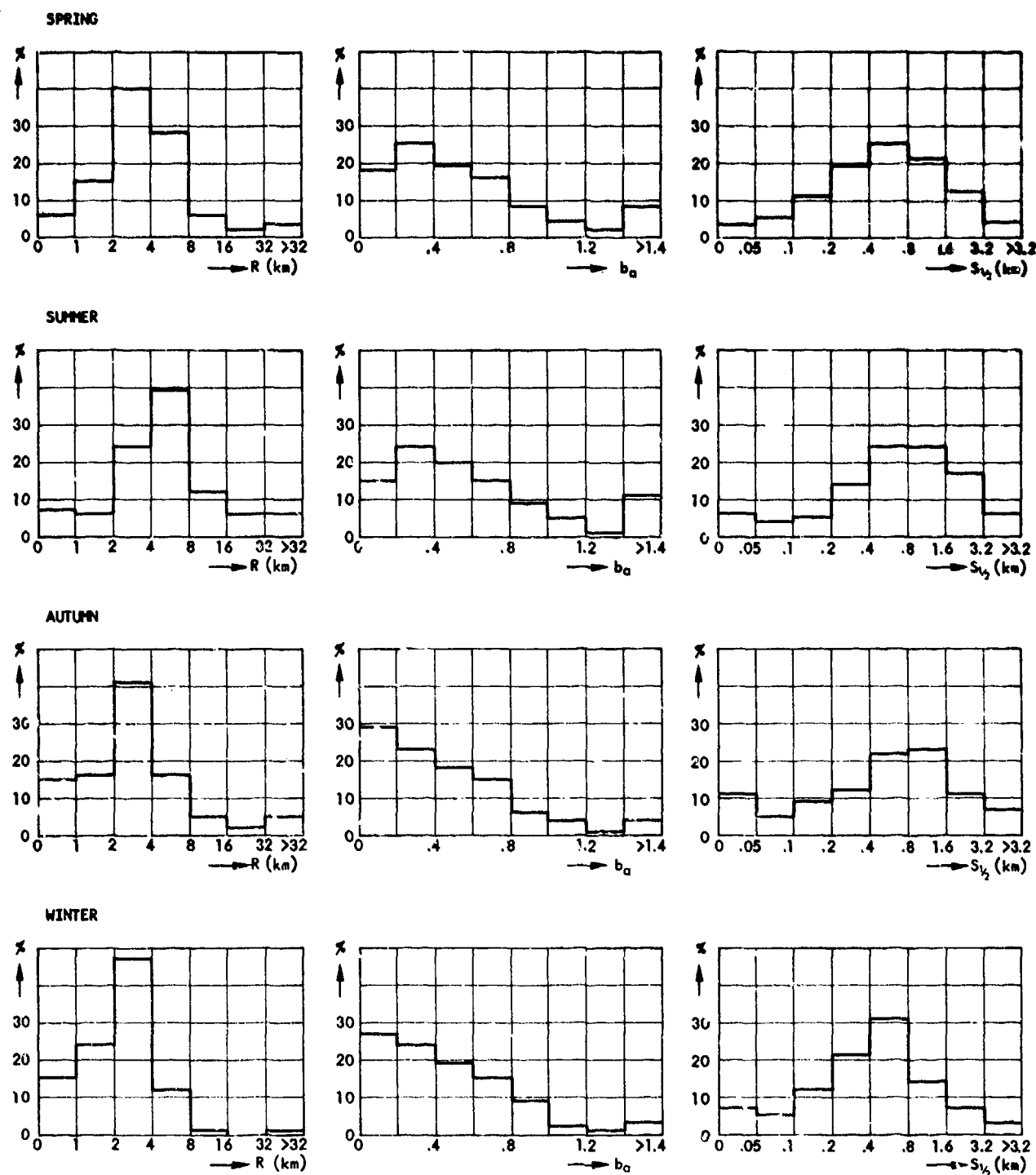


Fig.7 Results of daytime measurements in the Hague for different seasons

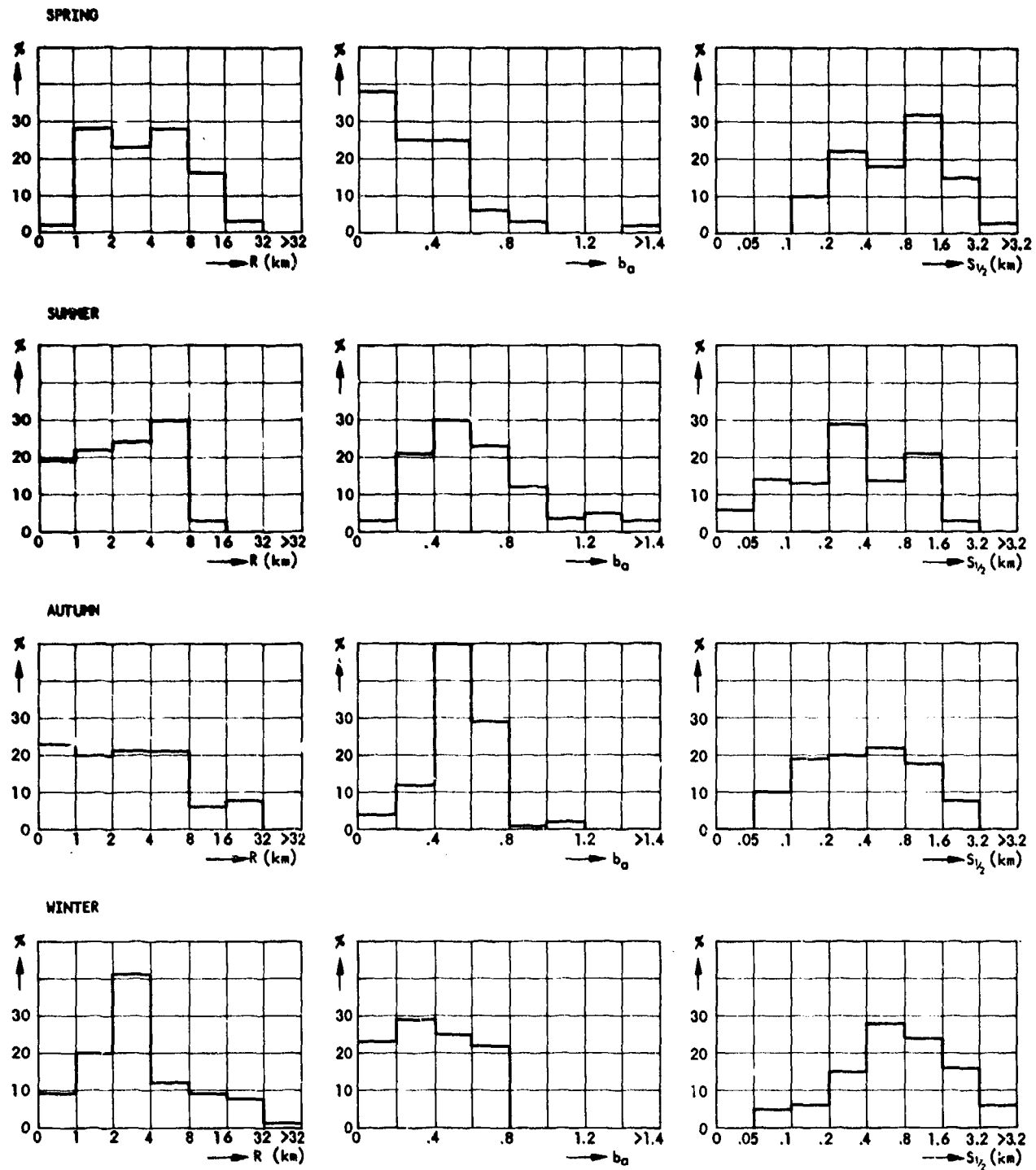


Fig.8 Results of night-time measurements (film) in Woensdrecht for different seasons

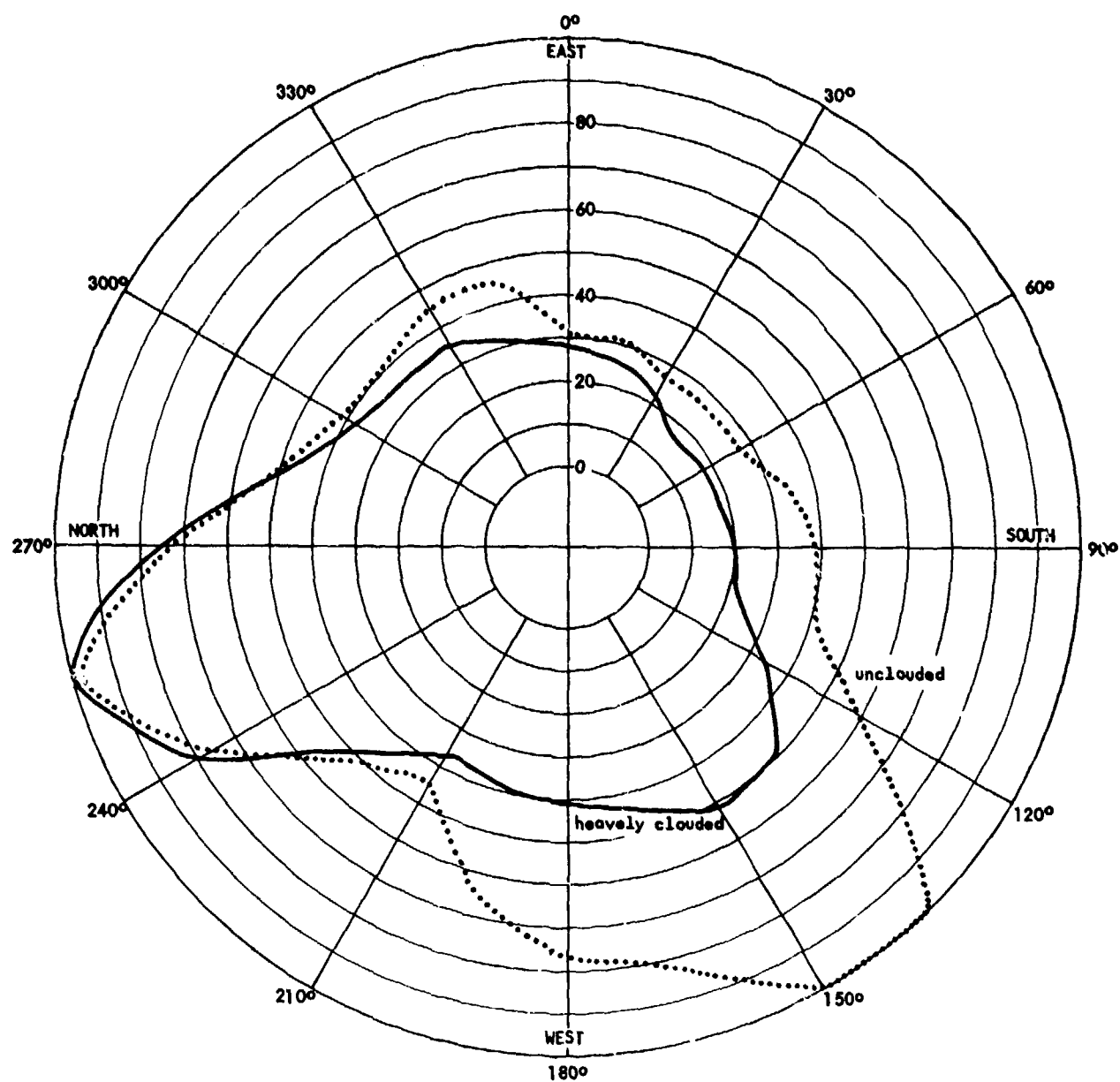
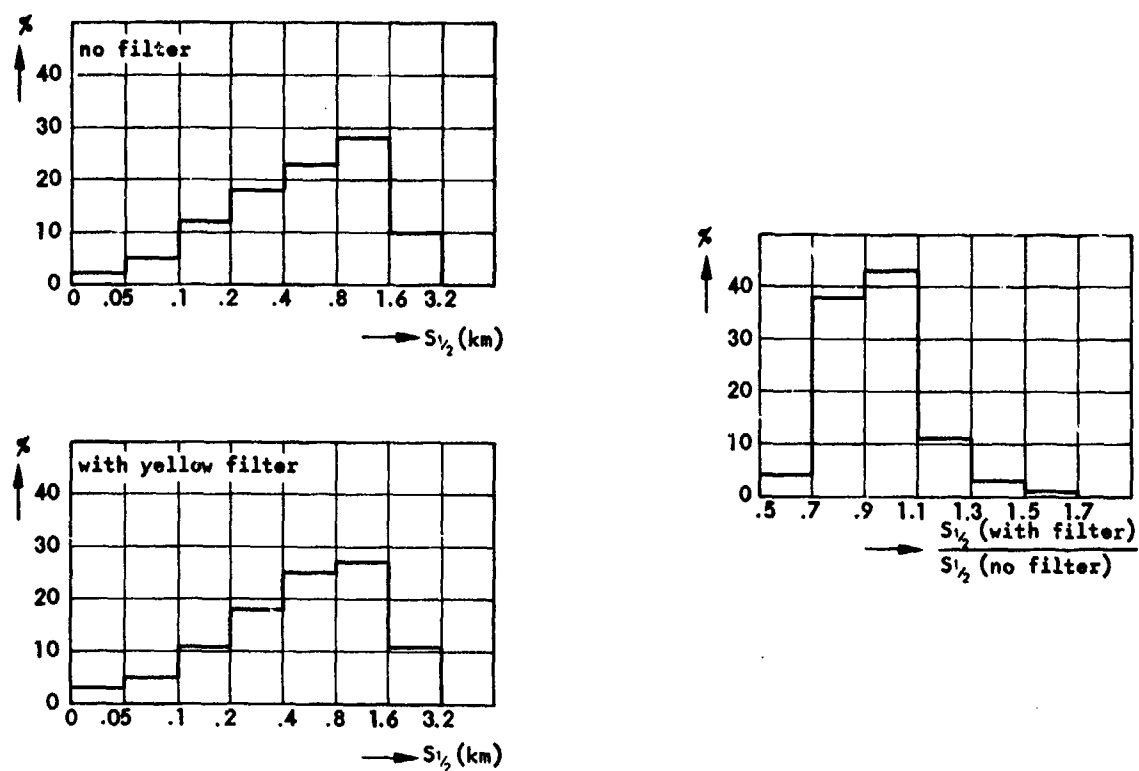
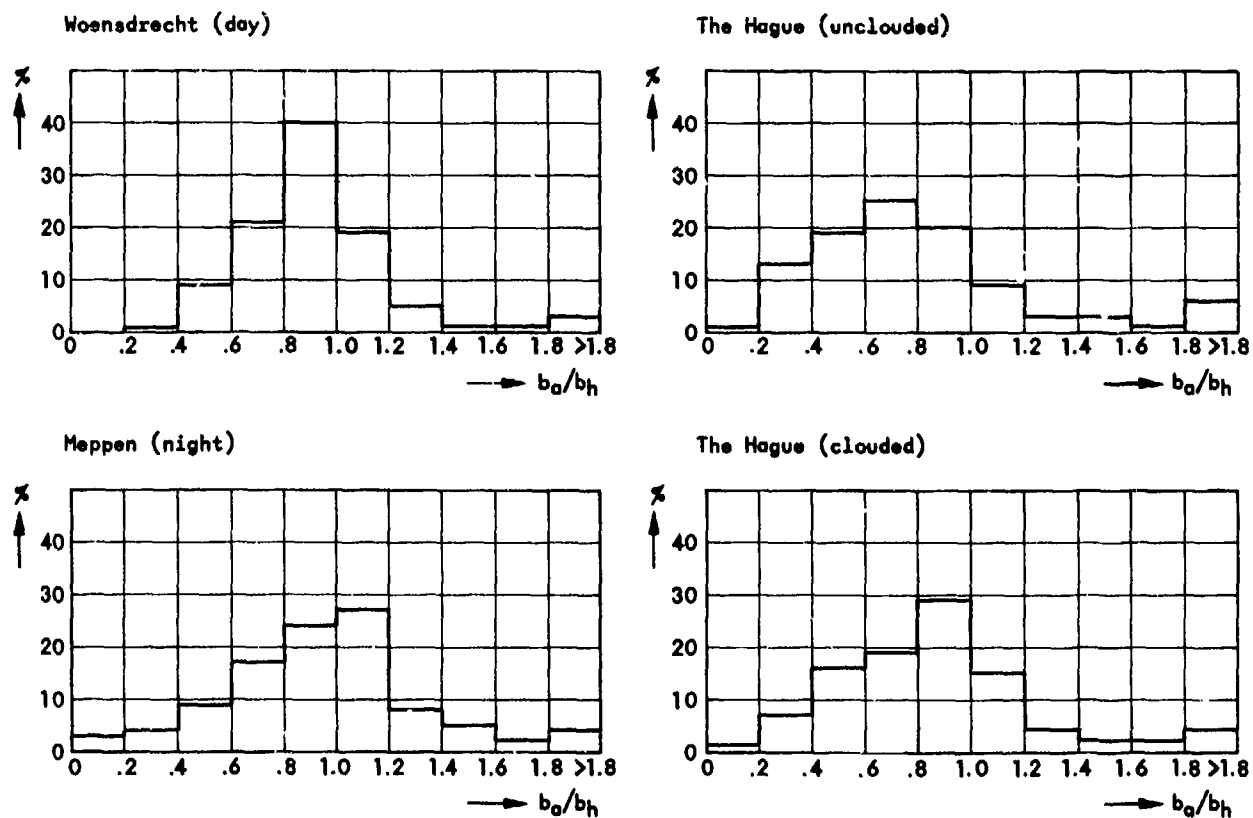


Fig.9 Typical luminance of the sky just above the horizon at Woensdrecht during the night

Fig.10 Influence of a yellow filter on $S_{1/2}$ Fig.11 Histogram of b_a/b_h

BENDING OF RAYS OF LIGHT ABOVE THE SEA SURFACE

P.A. Stokseth
A Nordbryhn
Norwegian Defence Research Establishment
P.O. Box 25, N-2007 Kjeller
Norway

SUMMARY

A temperature difference between the sea and the air above it, sets up a stable vertical air temperature gradient in the first few metres above the sea surface. This temperature inhomogeneity causes a similar refractive index gradient. Rays of light passing through this optical inhomogeneous medium are bent, and imaging of objects through this medium may be subject to strong distortion. Such image distortion has been investigated, theoretically and experimentally. The main experimental results were obtained by taking pictures of a suitable test object with a photographic camera and a telephoto lens at 6.2 km range just above the sea surface. A large number of pictures were taken during varying conditions. From these pictures typical forms and magnitudes of the distortion were found. A mathematical model tracing rays of light through a vertically varying optical medium was used to predict image distortions. The theoretical results have been compared with the experimental results, and good similarity has been found. Comparison between calculated and experimental image distortions is suggested as a method to find the air temperature profile just above the sea surface.

1. INTRODUCTION

Sea-faring men have often noticed that under certain meteorological conditions islands and ships appear to float in the air. This well-known phenomenon is due to the curvature of rays of light because of vertical gradients in the refractive index of the air near the sea. These gradients are caused by temperature gradients in the atmosphere above the sea. A rarer and more extreme example of the same effect is the genuine fata morgana. This can give the illusion of seeing for example non-existing towns with walls, towers and spires (MINNAERT, M., 1959). An example of the first mentioned phenomenon is given in Figure 1.1. A ship is photographed at short range (Figure 1.1, upper). During certain atmospheric conditions the ship may be strongly distorted when imaged at long ranges. The two lower parts of Figure 1.1 depict the ship photographed with a telephoto lens at 5 km and 8 km range, respectively.

Such distortion is most often observed within an angle of $\pm 2-3$ mrad in elevation about the tangential plane of the earth. It is only observed at ranges exceeding 3-4 km between observer and target, when both are located less than 5-10 meters above the sea surface.

In this paper measuring results are presented primarily in the form of photographs showing how an object may be distorted in different ways due to ray bending. The main purpose of the measurements has been to investigate to what extent ray bending may reduce the range and efficiency of optical and electro-optical instruments with high resolution or small field of view when used across an expanse of water. We also discuss how imaging of a suitable object may be used for determining a vertical temperature profile in the atmosphere above the sea. The described method may be well suited for studying the heat balance near the sea/air interface.

The frequency of the ray bending phenomenon can not be determined from the relatively small number of measurements made. However, both the sign and the absolute value of the temperature difference between sea and air determines the shape and size of the distortion. In this paper, therefore, we have included data from the Norwegian Meteorological Institute, showing the frequency distribution of the mentioned temperature difference from some selected places along the Norwegian coast.

Different authors have measured the vertical temperature distribution by direct (ROLL, H.V., 1952 and FLEAGLE, R.G., 1956) and indirect methods (BROCKS, K., 1954). Brocks has shown that averaged temperature profiles may be very accurately determined by measuring the effect of ray bending. He has performed such measurements with the aid of a theodolite (BROCKS, K., 1955). The measured temperature profiles have mainly been used to derive a better understanding of the heat exchange between air and sea. Very few seem to have explored thoroughly how objects are distorted and their images lowered in quality due to ray bending when observed over long ranges.

In the next section the two main types of ray bending which can occur are described. A description of the photographic equipment used follows in section 3. A presentation of the measuring results is then given. A mathematical model of the phenomenon is presented and discussed in section 5, and the model results are compared with the measuring results.

2. DESCRIPTION OF PHENOMENON WITH EXAMPLES

Bending of rays of light above the sea is caused by a variation in the air refractive index with height. One differentiates between randomly oriented rapid fluctuations in the refractive index caused by turbulence, and vertical refractive index gradients which are stable during long periods. This paper is mainly concerned with the long duration stable gradients. The influence by turbulence will be briefly treated in section 4.

For optical frequencies the refractive index n is implicitly given by the following approximative equation

$$N = (n-1) \cdot 10^{-6} = \frac{77.6 P}{T} + 0.584 \frac{P}{T \lambda^2} \quad (2.1)$$

where N is called the refractive modulus, P is the atmospheric pressure in mbar, T is the temperature in Kelvin and λ the wavelength in μm . The refractive index above the sea will often vary in the vertical direction, while being relatively constant in the horizontal direction. For optical frequencies this is caused by a vertical temperature gradient above the sea. n is influenced relatively little by pressure and water vapour content at optical frequency (OWENS, J.C., 1967). An approximate expression for a variation in the refractive index, Δn , is given by

$$\Delta N = 10^6 \Delta n = -\Delta T \quad (2.2)$$

This expression is derived if $P = 1000$ mbar, $\lambda = 0.55 \mu\text{m}$ and $T = 281$ K are inserted into Equation (2.1).

Below, the imaging of three different types of temperature profiles near the sea will be described qualitatively. It is assumed that the temperature, and consequently also n , only depends on height, and also that the height dependence is invariant from one place to another.

In the first case the temperature (and refractive index) is constant with height (Figure 2.1d). All rays of light will in this case follow straight lines (Figure 2.1e), and the image of an object will not be distorted (Figure 2.1f). This image will serve as a reference, and will be compared with the imaging obtained when the air temperature increases or decreases with height.

In the next case the air temperature increases with height, as shown in Figure 2.1a. The temperature increase is strongest near the sea surface. As the refractive index decreases with height, all rays are bent towards the sea. The bending is stronger the nearer one comes to the sea surface (Figure 2.1b). The object will seem to be displaced upwards (Figure 2.1c). At the same time the object appears to be compressed. The compression is stronger near the sea surface.

In the last example the air temperature decreases with height. The gradient is again strongest near the sea surface. Temperature and refractive index may vary as shown in Figure 2.1g. The rays are curved, in a direction away from the sea (Figure 2.1h). The curvature is stronger for rays near the sea. It will be noticed that for long ranges, some rays may cross each other. This means that the same object may be seen in two different directions. The object will be displaced downwards at the same time as it is elongated vertically (Figure 2.1i). The lower part of the image is a mirage of part of the object. The lower part of the object has disappeared below a virtual horizon. The observed reflection does not occur in the sea surface, but in the atmosphere near to the sea surface. A more detailed discussion of the magnitude of the compression, elongation and reflection is given in section 5.

In these three cases we have assumed different temperature profiles above the sea surface, and discussed how the corresponding refractive index variations distort an object. There will be a close connection between the particular temperature profile and the temperature difference $\Delta T(h) = T_{\text{air}}(h) - T_{\text{sea}}$, when the air temperature is measured at an appropriate height h . The temperature near the sea surface usually decreases monotonically as a function of the height when $\Delta T(h) < 0$, and increases monotonically when $\Delta T(h) > 0$. This relationship becomes more probable the larger the absolute value of the temperature difference is.

3. INSTRUMENTATION

A Nikon F camera body and a Questar telephoto lens have been used for the investigation. The objective lens has an effective aperture diameter of 83.5 mm, the focal length is 4900 mm and the f -number is 59. The film size is 24 x 36 mm, giving a field of view of 4.9 mrad x 7.4 mrad. The diffraction limited resolution of this type of system, according to the Rayleigh criterion is given by the angle

$$\theta = \frac{1.22 \lambda}{D} \quad (3.1)$$

where λ is the wavelength of light and D the aperture diameter of the objective lens. With $D = 0.55 \mu\text{m}$ and $D = 83.5$ mm one obtains $\theta = 8 \mu\text{rad}$, which means that points 0.8 mm apart may be resolved at 100 m range. In practice, it is possible to resolve on the developed prints black/white line pairs which span an angle of 8-10 μrad . It may therefore be concluded that the complete system including the photographic process, is near diffraction limited (STOKSETH, P.A., 1973).

The camera with telescope is mounted on a platform which is bolted to a heavy iron n-profile base (Figure 3.1). To obtain the mentioned resolution a movable mirror in the camera body has to be made fast during exposure. The iron profile has three supports, of which one is variable in height. A horizontal spirit level is mounted on the platform. This is calibrated against a theodolite, so that the camera's optical axis may be oriented parallel to the tangential plane of the earth.

Different film types have been used for the measurements, in the majority of cases Ilford FP4 (200 ASA). For specially short exposures Kodak TRI-X (700 ASA) or Kodak 2475 (3000 ASA) was used.

4. MEASURING RESULTS

Most of the measurements have been made across the Oslo fjord at Horten, a distance of 6.2 km. The measuring object in most cases consisted of a vertical measuring rod, two letters and a house. In Figure 4.1 they have been photographed at 6.2 km range. In the vertical direction, the whole picture format has been reproduced in the figure, i.e. the vertical angular extent of the picture is 4.9 mrad. The resolution in this picture is about twice the diffraction limited resolution of the instrument and is the best obtained during measurements at 6.2 km range.

The first series of photographs (Figure 4.2) displays some results from five different expeditions. Figures 4.2c and 4.2d were taken on the same expedition, at an interval of a quarter of an hour. The camera was in all cases mounted 1.0 meters \pm 0.1 meter above sea level. (The tidal difference is small in the Oslo fjord.) The optical axis of the camera is parallel to the earth's tangential plane at the observation site. A plane parallel to the tangential plane, and containing the optical axis, intersects the film plane in a horizontal line in the centre of the photograph. This line, which corresponds to zero elevation angle, is marked at the edge of every picture. Figures 4.2a - 4.2f are arranged according to decreasing elevation angle to the apparent air/sea interface. The measured temperature difference between the air 4 meters above sea and the sea temperature, $\Delta T(4\text{ m}) = T_{\text{air}}(4\text{ m}) - T_{\text{sea}}$, is shown on each photograph. The air temperature was measured over land at the camera site. The measured value of $\Delta T(4\text{ m})$ may therefore deviate from the average $\Delta T(4\text{ m})$ along the entire range.

It can be seen that when the pictures are arranged sequentially in this way, the measured temperature difference also decreases from Figure 4.2a to 4.2f. This indicates that the temperature difference between air at a certain level and sea also determines the air temperature profile below that level. The qualitative exploration given in section 2 on ray bending agrees well with these observations.

A strong correlation is observed between displacement upwards and compression of the object, as well as between displacement downwards and elongation. Compression and elongation is greater for the parts of the object nearer the sea. Consequently the temperature and refractive index change are greater near the sea surface.

In Figure 4.2c, 4.2d, 4.2e and 4.2f parts of the object are inverted and reflected in a horizontal plane. This plane intersects the vertical object plane in a line which we call the reflection line. The apparent vertical angle between this reflection line and the air/sea intersection line changes from picture to picture. In Figure 4.2c and 4.2d displacement and reflection allow the entire letters to be seen. Large portions of the letters have disappeared in Figures 4.2e and 4.2f. In the angular span between the reflection line and the sea, only a mirage of parts of the object can be seen. This may cause strong shape distortions in the imaging of an object, for example as seen in Figure 4.2e. Due to the ray bending the image of the letters V and S looks like a rectangle and an ellipse respectively. It should be pointed out that the image distortion due to ray bending, unlike most other types of image impairments, may give a sharp, good-quality image. The shape of the observed object can, however, be quite wrong.

When the sea temperature is the higher, and the difference between sea and air temperature increases, an increasing part of the object seems to disappear in the sea. The reason for this is that rays that almost strike the sea are so strongly deflected that they hit the object at great height. (The rays of light do not, of course, strike the object - they come from the object. We feel however that the argumentation is somewhat simpler to follow if one regards the rays as originating in the camera and hitting the object.)

The largest difference in displacement is found by comparing Figures 4.2a and 4.2f, the difference being about 1.5 mrad. The angle between the apparent sea/air interface and the reflection line equals the extension of the inverted object. This angle is largest (0.5 mrad) in Figure 4.2e.

In the second image series (Figure 4.3) all the pictures were taken during a short time interval with approximately constant temperature conditions. They were taken with the camera at different heights. The height is shown on each picture, and varies from 1.9 m to 0.4 m. The range between object and camera was 4.7 km. The height of the object was 1.3 m, its lower edge being 0.6 m above sea level. The sea temperature was measured and found to be 0.1°C lower than the air temperature. However, the pictures indicate that the average air temperature decreased with increasing height.

In this series the optical axis is not known. The object displacement can not therefore be calculated. The figure illustrates the importance of the observation height for the resulting image. As the camera is moved down from the upper height of 1.9 meters, the lower part of the letters becomes elongated. Further downward movement of the camera causes the lower part of the object to disappear and the remaining part to be elongated. At a camera height of 0.5 m the letters V and S are seen as a square and a circle.

Only in a few cases have we investigated how quickly the image quality can change. In one single case the image of the letters changed considerably during a period of 15 minutes. This means that also the average temperature profile may vary considerably during relatively short time intervals.

As mentioned in section 2, the atmospheric turbulence will cause rapid fluctuating inhomogeneities in the refractive index. The image distortion due to turbulence varies greatly with differing meteorological conditions. Figure 4.1 shows how sharp an image may be when the influence of turbulence and ray bending is small. The series of photographs in Figure 4.4 were taken in rapid succession during conditions of strong turbulence. During a short exposure time (1/500 s) the atmosphere will be "frozen", and a snapshot will be obtained of the influence of turbulence. The shape of the object may be distorted, but the image be relatively sharp. At longer exposures (0.5 s) temporal fluctuations will be averaged. The shape of the object will be reproduced better, but the image will be indistinct.

5. DISCUSSION

Based on each of the pictures in Figure 4.2 a curve has been drawn depicting the relationship of apparent angle versus real angle to different points on the object. These curves are presented in Figure 5.1. The sketch at the bottom of the figure illustrates what is meant by apparent and real angle. The apparent angle is found by measuring directly from the picture. The real angle is the angle at which the object would be seen under conditions where the rays of light would follow straight lines. The curves will be called displacement curves, since they depict how much the different points on the object have been displaced due to ray bending. The absolute accuracy of the curves is about 0.1 mrad, but the relative error between points on one curve is less.

The lower terminal of each curve indicates that for small apparent angles the ray meets the sea. A straight line through origo and at 45 degrees to the coordinate axes represents the "displacement curve" obtained when the refractive index is completely homogeneous. For curves above and below this reference line the displacement is respectively upwards and downwards in the field of view. If the curve is parallel to the reference, the displacement is constant over the whole picture. Deviations from such a parallel results in compression if the curve bends upwards, and elongation if the curve bends downwards. Some of the curves reach a minimum value for the real angle at a certain apparent angle. For lower apparent angles the real angle increases. Thus, in a given angular range there are two apparent angles for each real angle. This indicates reflection. By studying the displacement curves one may readily come to the same conclusions concerning displacement, elongation/compression and reflection as discussed in section 4.

Theoretical calculations have also been made in order to find the form of such displacement curves for a number of given vertical refractive index profiles. By means of numerical solution of the differential equations for a number of rays of light in a given refractive index field a theoretical displacement curve can be derived (HEIER, H.). For each refractive index profile one displacement curve is obtained. In principle there is also only one profile for each displacement curve. It is therefore possible to find the average temperature profile during the conditions when a distortion is measured, by selecting the theoretical displacement curve which most closely matches the experimental displacement curve. In practice, however, the accuracy with which a profile can be determined depends on the accuracy of the experimental curve and the suitability of the refractive index model.

In order to obtain the best possible basis for choosing refractive index profiles for the calculations a search was made in the literature for measured temperature profiles over the sea. A number of such measurements were found (ROLL, H.V., 1952, FLEAGLE, R.G., 1956, BRUCH, H., 1940 and WUST, G., 1937). The measured profiles vary strongly for different cases. Sometimes the temperature was found to be a linear function of height, but most often an almost logarithmic dependence of the height on temperature had been found.

A simple expression for the refractive index, which covers both the linear and logarithmic case is:

$$n(h) = n_0 + K_p \cdot \Delta T(4 \text{ m}) h^{\frac{1}{p}} \quad (5.1)$$

Here $\Delta T(4 \text{ m})$ is, as usual, the difference between the air temperature 4 meters above sea level and the sea temperature. The constant K_p is given by the equation (2.2) and a requirement that the refractive indices at 0 m and 4 m are to be the same for all values of p . p determines the shape of the profile between 0 m and 4 m. The linear profile corresponds to $p = 1$, while the dependence is nearly logarithmic when p is large.

The minimum apparent angle $\theta_t(\min)$ indicates where in the image field the interface between sea and air is located. This angle may be found from the following approximate equations:

$$\theta_t(\min) \approx -\left(2 \left(\frac{\Delta n}{n_0} + \frac{hc}{R}\right)\right)^{\frac{1}{2}} \quad (5.2)$$

where n_0 is the refractive index for $h = 0$, Δn is the difference in refractive index between camera height h_c and the sea, and R is the radius of the earth.

Displacement curves have been calculated for two sets of refractive index profiles. An observation height of 1 m has been assumed, and a distance to the object of 6.2 km. For one of the sets of curves the coefficient p is in all cases equal to 3 (such that $n - n_0 = h^{1/3}$), while the temperature difference is varied. The displacement curves (Figure 5.2, left-hand side) are located above the 45° reference curve when the air temperature is highest, and below when the sea is warmest. The displacement of the object increases with decreasing apparent angle and increasing value of the temperature difference. The curves show that when $n - n_0 = h^{1/3}$ a part of the object will always be reflected if the sea is warmer than the air. In the second set of refractive index profiles the value of the temperature difference is in all cases equal to 1°C, while the coefficient p is varied. The displacement curves (Figure 5.2, right-hand side) show that the whole object is displaced but not distorted when $p = 1$, i.e. when $n - n_0 = h$. When $p > 1$ the displacement increases with decreasing apparent angle. Compression or especially elongation of the object will occur over a large angle. With increasing values of p , an increasing part of the object will be reflected.

Comparing Figure 5.1 and 5.2, it can be seen that the refractive index must have varied approximately linearly with height under the conditions when Figure 4.2f was taken. For the conditions which gave Figures 4.2c, 4.2d and 4.2e the refractive index must have varied more strongly with height for small elevations. In order to obtain perfect curve fitting, it is necessary to utilize a more general form for the refractive index than used earlier.

The matching technique mentioned here may serve as a basis for a long duration investigation of the mean temperature profile. As a suitable measuring object a 10 - 20 m long rod could be set up with one end in the sea. The rod should be in a plane perpendicular to the direction to the observer, but be inclined 45° to the horizontal. It should be painted white and have electric light bulbs or tubes along the entire length. A camera with a telephoto lens should be sited some kilometers away from the target. The optical axis of the camera must be parallel to the horizontal plane at the site. Automatic devices should enable the film

to be exposed and advanced as often as desired. The picture of the rod will then directly describe the displacement curve, which we earlier had to calculate. One may then assume a general form of $n(h)$ and thus also of $T(h)$. By means of suitable optimization one may find the coefficients in the general expression so that theoretical and measured displacement curves become fairly equal. It seems to us that a good approximation to the refractive index often may be derived by using the form

$$n(h) = n_0 + k(h+a)^{\frac{1}{p}} \quad (5.3)$$

where a and p are coefficients describing the shape of the profile. k depends on the temperature difference between sea and air.

As we have seen in Figures 1.1, 4.2 and 4.3, it is especially distortion through elongation and reflection which makes identification of objects difficult. We have seen that elongation and reflection occur when the sea temperature is higher than the air temperature. It is therefore desirable to know the distribution of ΔT in the region of the sea in which one is interested. The Norwegian Meteorological Institute has kindly provided such distributions from their measuring data for selected places along the Norwegian coast. They are presented in Figure 5.3 as cumulative distributions of the temperature difference $T_{\text{air}}(h) - T_{\text{sea}}$ for three stations along the coast and one station in the North Sea. The air temperature has been measured in different heights h at the different stations. The results include measuring data for periods of at least 10 years and are presented separately for the summer and winter half year. The measured temperature difference when the pictures in Figures 4.2e and 4.2f were taken was -0.5°C and -0.7°C respectively. In these cases there is a significant image distortion. Assuming that the distortion always is significant when the temperature difference is at least -1°C , the curves in Figure 5.3 show that the probability for distortion at all the measuring stations during winter is at least 50%.

6. CONCLUSIONS

This paper describes the type and degree of image distortion observed above the sea. The distortion is caused by stable, vertical refractive index gradients near the sea bending the rays of light. The refractive index gradients are caused by temperature gradients. An important difference between this type of distortion and most other types is that the picture may be sharp, but the shape of the object entirely wrong.

Measuring results are presented in the form of pictures showing how an object is displaced and distorted by different amounts of ray bending. One has found that the sign of the difference between the sea and air temperature determines the type of image distortion observed. When the sea temperature is the higher, the object is elongated and reflected. This distortion is far more serious than the compression of the object which is observed if the air is warmer than the sea. The probability of a temperature profile causing a strong distortion through elongation and reflection is found to be at least 50% during winter at most places along the Norwegian coast.

The displacement and distortion of an object is usually observed within a narrow angular range of $\pm 2-3$ mrad in elevation about the earth's tangential plane. The object as well as the observer have to be near the sea surface, and the distance between them at least a few kilometers. The effect of ray bending above the sea may limit the usefulness of optical and electro-optical instruments with small field of view and good resolution. The least serious effect of ray bending is a pure displacement of the object. The displacement may vary more than 1 mrad. The measurements performed show that image distortion increases when the observation height decreases. Optical instruments in ships should therefore be used from the highest possible position.

If it is assumed that the refractive index above the sea is only a function of height, there will exist an unambiguous relation between a recorded distorted image and the refractive index gradient causing the distortion. As a refractive index change is proportional to a temperature change, there will be only one temperature profile corresponding to a given picture. In this paper we have suggested a simple measuring method making it possible to find the average temperature profile above the sea. The method may prove valuable for studies of the heat exchange between sea and air.

REFERENCES

- BROCKS, K., 1954, "Eine räumlich integrierende optische methode für die Messung vertikaler Temperatur- und Wasserdampfgradienten in der untersten Atmosphäre", Archiv f. Meteor., Serie A, 6, 370-402.
- BROCKS, K., 1955, "Atmosphärische Temperaturschichtung und Austauschprobleme über dem Meer", Berichte des Deutschen Wetterdienstes, 22, 10-15.
- BRUCH, H., 1940, "Die Vertikale Verteilung von Windgeschwindigkeit unter Temperatur in den untersten Metern über der Wasseroberfläche", Veröff. Inst. Meeresk. Berlin, A38, Berlin.
- FLEAGLE, R.G., 1956, "The Temperature Distribution near a Cold Surface", J. Meteorol. 13, 160-5.
- HEIER, H., The numerical solution is performed by computer. The programme is developed by H. Heier, NDRE, and is available in concept form.
- MINNAERT, M., 1959, "Light and Colour in the Open Air", G. Bell and Sons Ltd, London.
- OWENS, J.C., 1967, "Optical Refractive Index of Air: Dependence on Pressure, Temperature and Composition", Appl. Opt. 6, 51-9.

ROLL, H.V., 1952, "Temperaturmessungen nahe der Wasseroberfläche", Deutsche Hydrograph Zeitschr. 2, 2/3, 141-3.

STOKSETH, P.A., 1973, "Description of the Questar/Nikon F Photographical Equipment", Teknisk notat E-552, Norwegian Defence Research Establishment.

WÜST, G., 1937, "Temperatur- und Dampfdruckgefälle in den untersten Metern über der Meeresoberfläche", Meteor. Z. 54, 4.

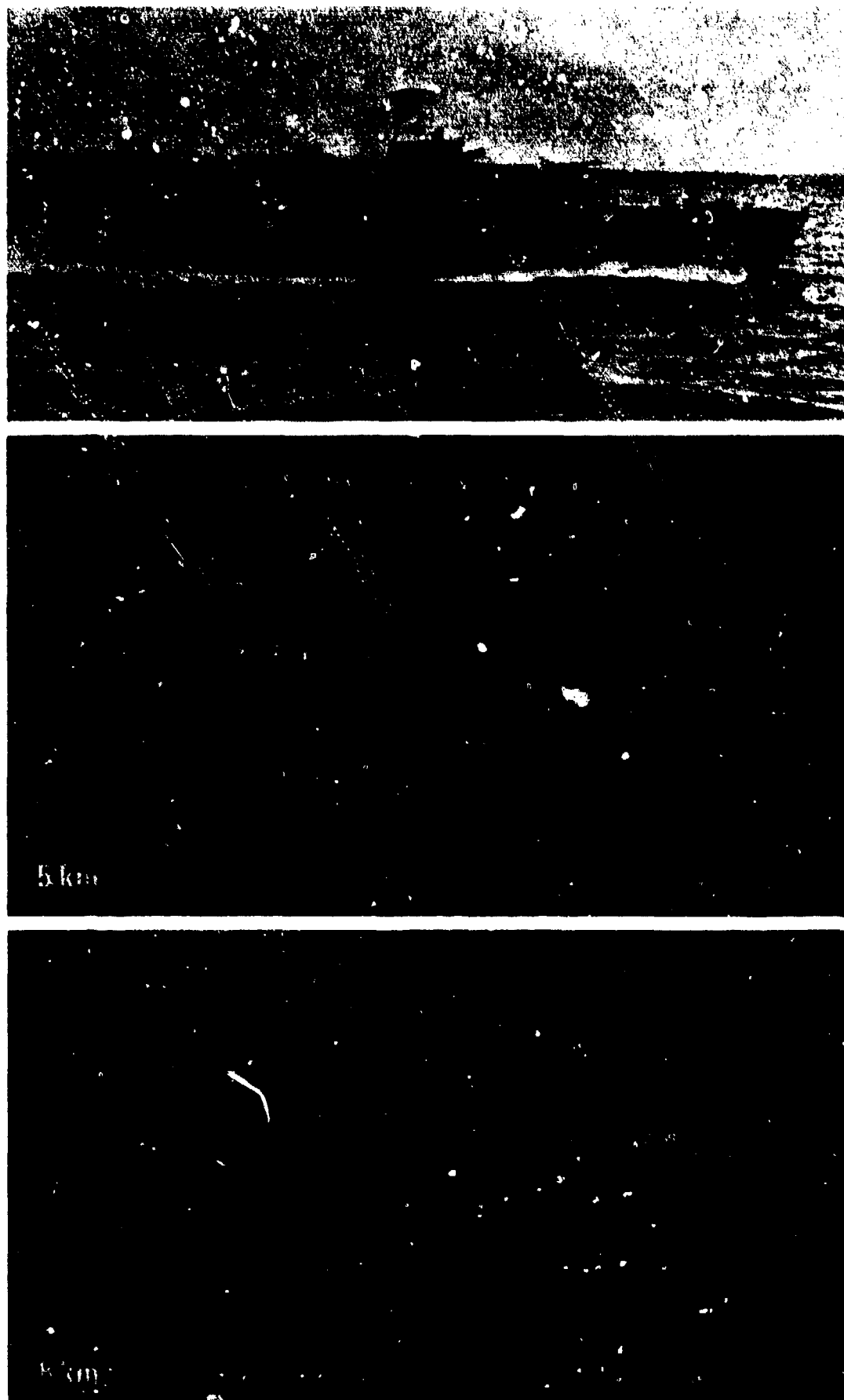


Figure 1.1 Image distortion due to ray bending.
A ship is photographed at short range (upper). The same ship is photographed with a telephoto lens from a site 3 meters above sea level at a 5 km and 8 km range. The sea temperature was 3°C higher than the air temperature.

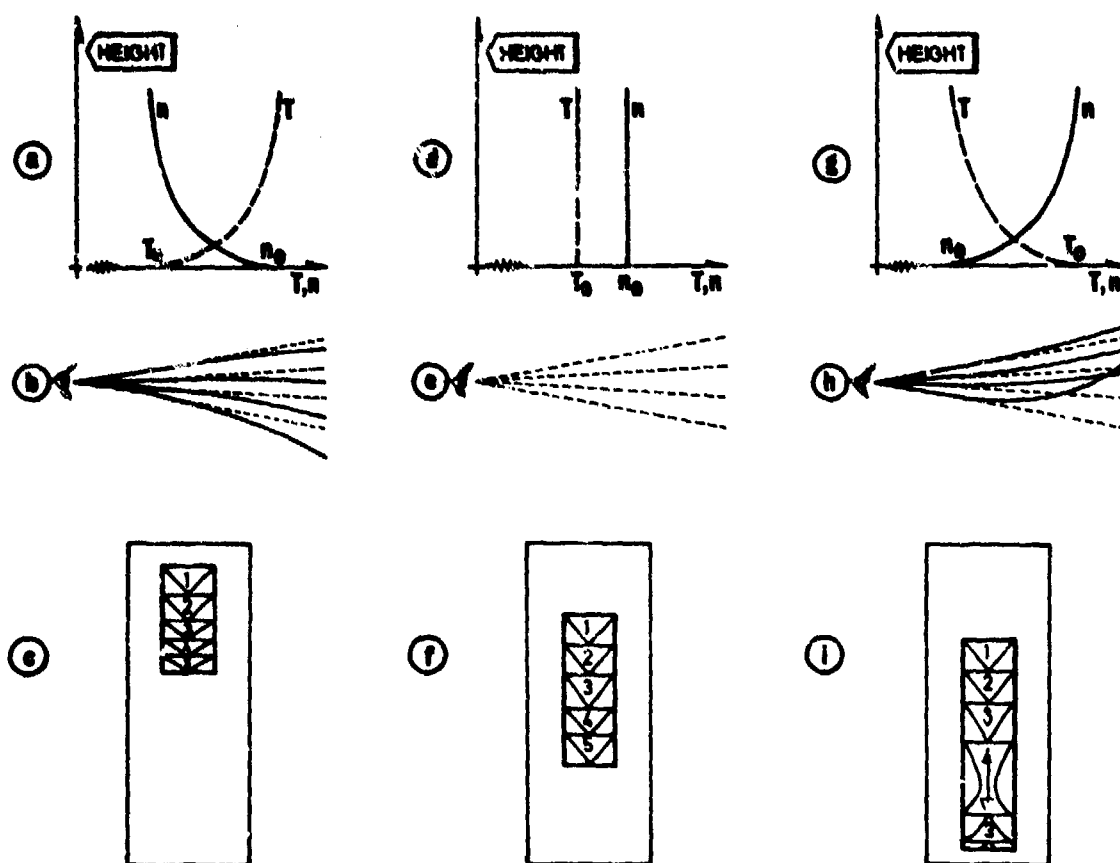


Figure 2.1 Imaging of object for three different temperature profiles. When the air temperature is homogeneous (d), the rays of light are straight lines (e) and the image of an object is not distorted (f). When the air temperature increases with increasing height (a), the rays of light are bent towards the sea (b). The object is compressed and displaced upwards in the field of view (c). When the temperature decreases with increasing height (g), the rays of light are bent away from the sea (h), and the object is displaced downwards in the field of view (i). The object is stretched and parts of it is reflected, while other parts disappear.

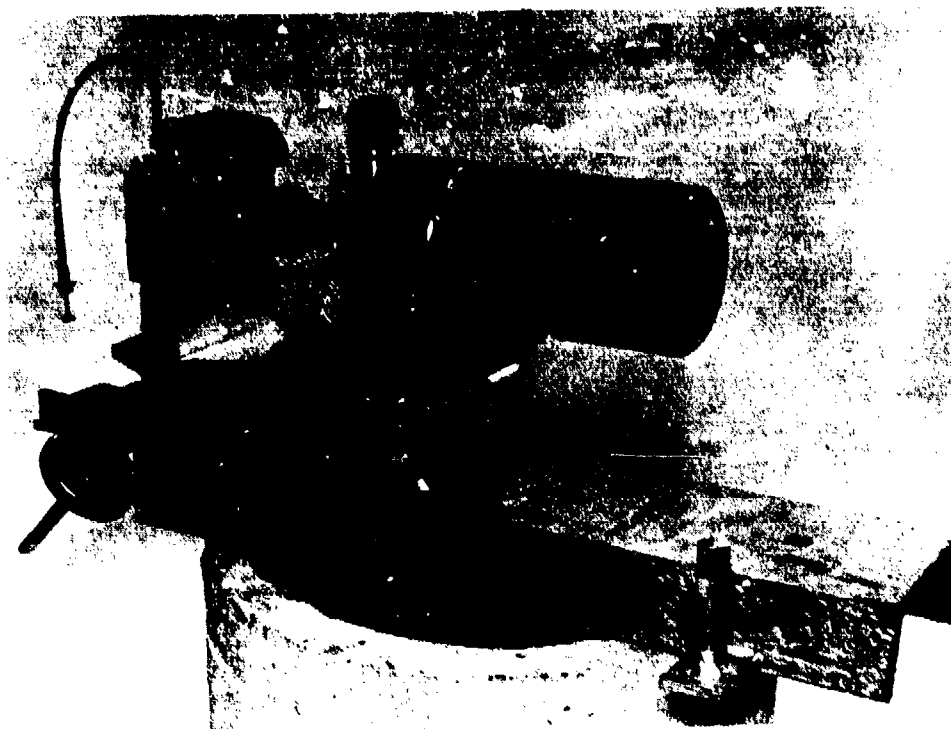


Figure 3.1 The camera.

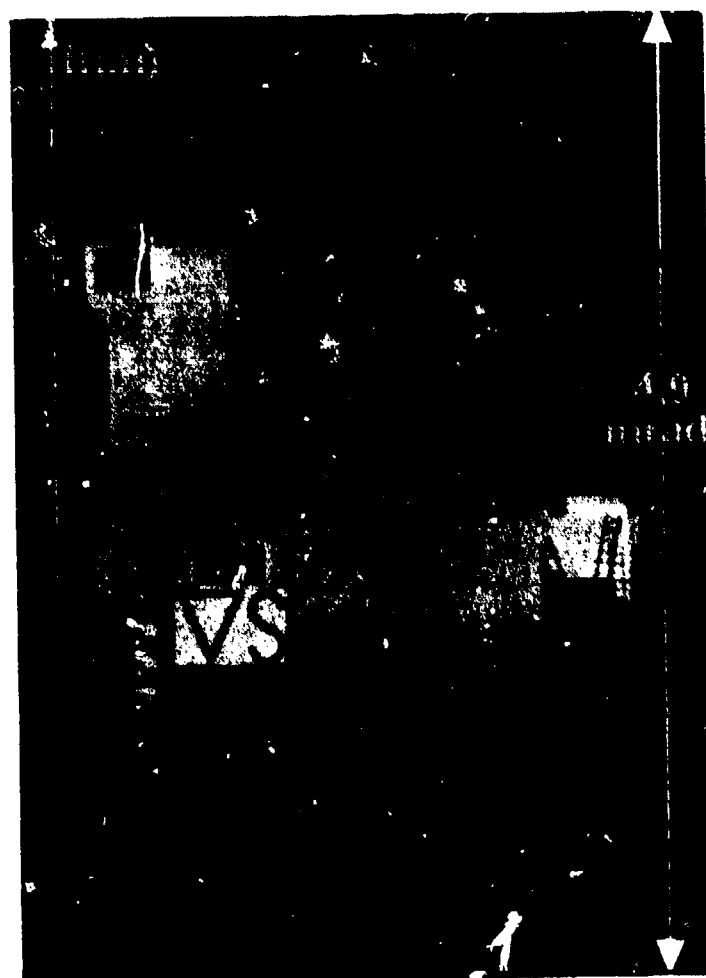


Figure 4.1 The measuring object taken at 6.2 km range.

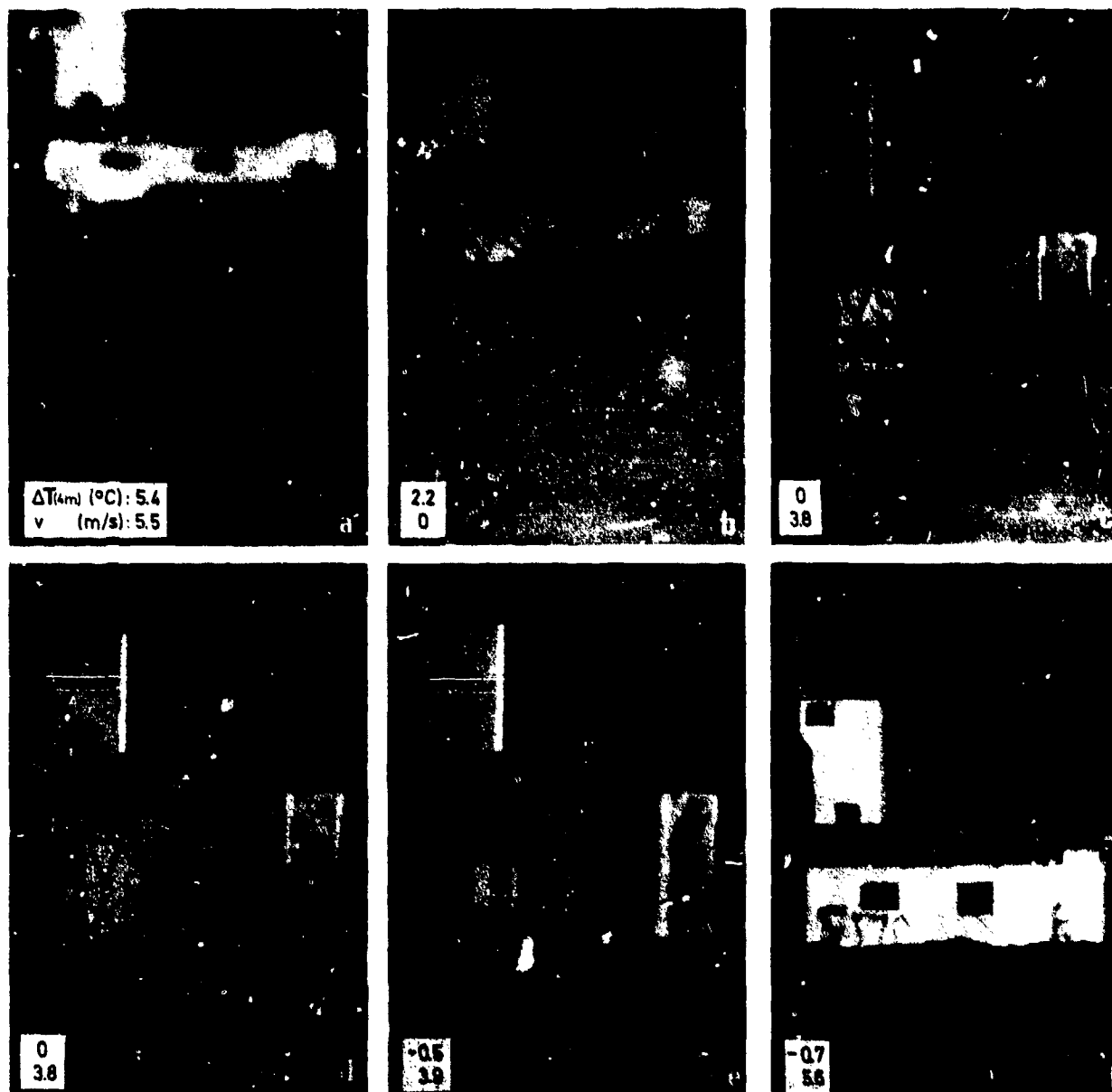


Figure 4.2 Results from five different expeditions. The pictures in c and d are taken on the same day, at an interval of fifteen minutes. The camera height is 1 meter above sea level and the distance to the object is 6.2 km. The measured temperature difference $\Delta T(4\text{ m})$ between the air temperature at 4 meters height on camera site and the sea temperature is noted on the pictures. v is the measured wind speed. The exposure times range from $1/4$ s to 1 s.

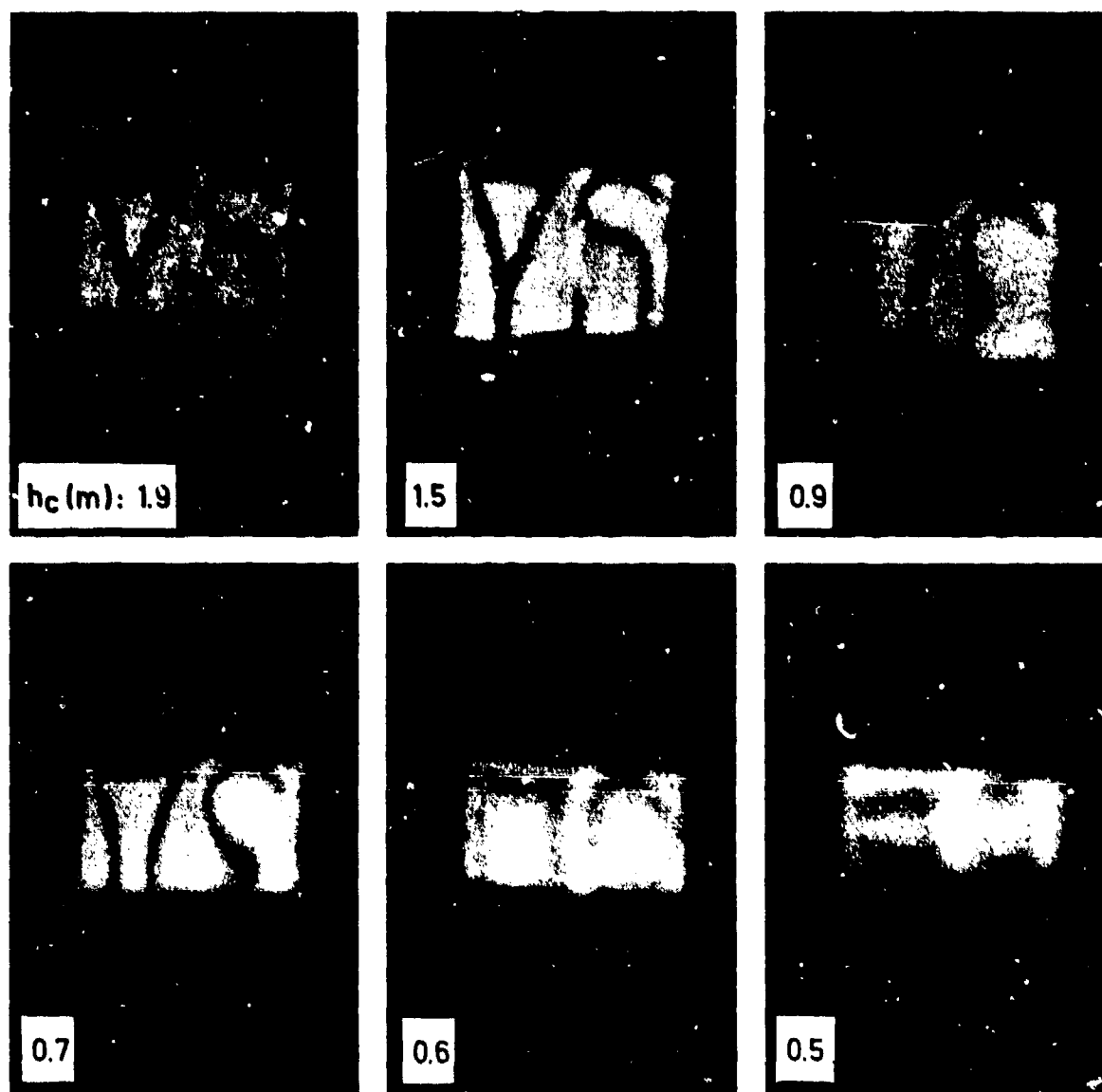


Figure 4.3 Results of measurements from varying camera heights h_c , during a period with stable conditions. The distance from camera to object was 4.7 km. The temperature difference between air and sea was $+0.1^\circ\text{C}$. The wind speed was less than 1 m/s. The exposure times range from $1/4$ s to 1 s.

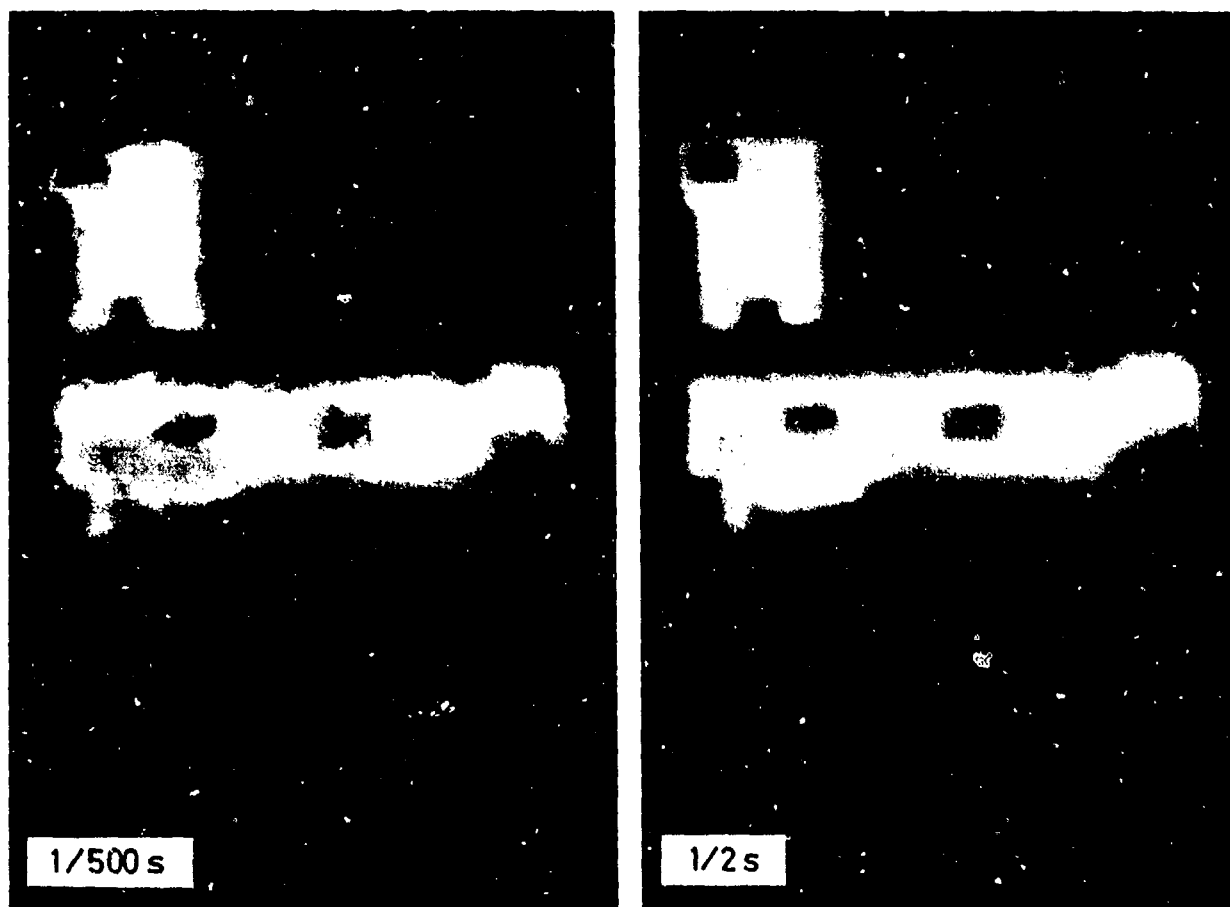


Figure 4.4 Influence of the exposure time on the imaging during conditions with strong turbulence. The range to the object was 6.2 km, the camera was situated 5 m above sea level, the sea/air temperature difference was +5.4°C and the wind speed was 5.5 m/s.

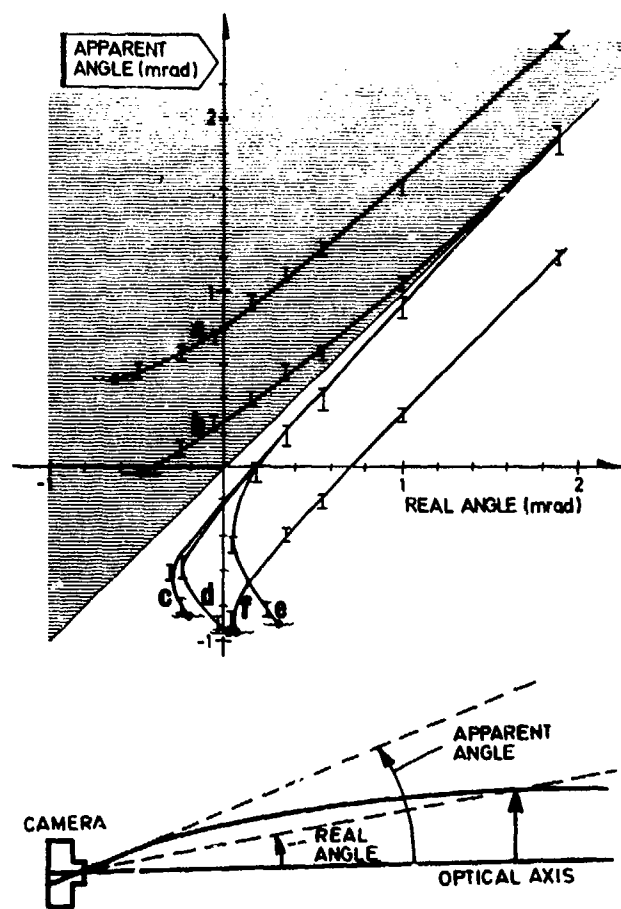


Figure 5.1 Displacement curves calculated from the pictures in Figure 4.2. The displacement curves indicate the connection between apparent angle and real angle for different object points. The lower sketch defines the terms "apparent angle" and "real angle".

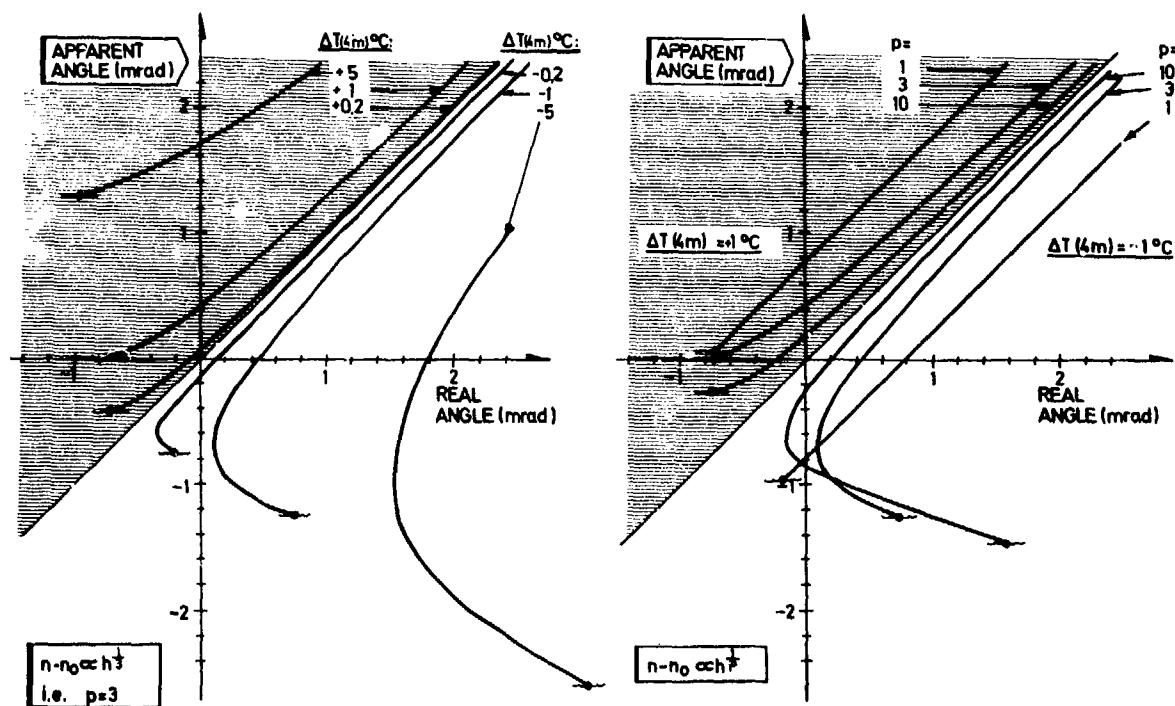


Figure 5.2 Theoretical displacement curves, calculated from refractive index profiles given by equation (5.1). The temperature difference $\Delta T(4m)$ and the constant p is noted on the figures.

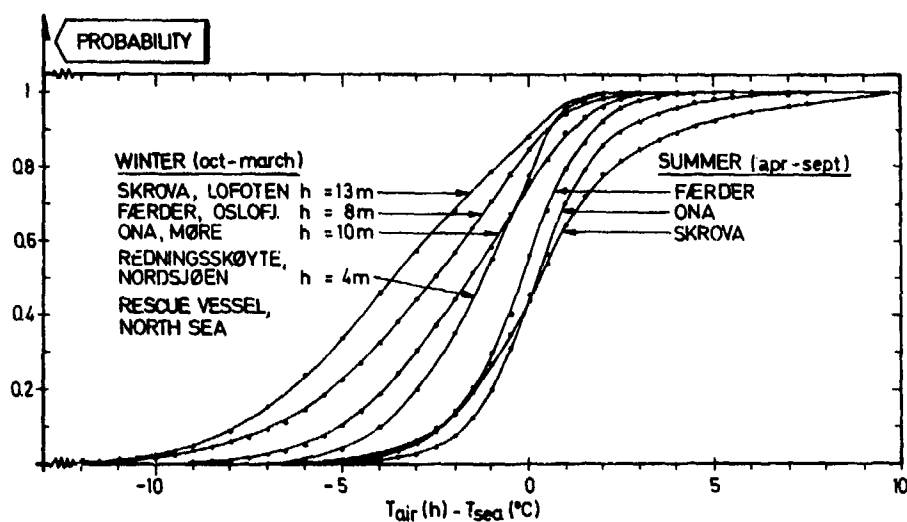


Figure 5.3 Cumulative distribution of the temperature difference $\Delta T(h)$ between the air at a height h above sea level and the sea, from four meteorological stations. The temperatures are read every day at 1.00 pm (every 3 hours for the rescue vessel). The measurements are taken during the following time intervals; Skrova 1957-69, Ona and Færder 1951-66, rescue vessel 1959-69. (Data from the Norwegian Meteorological Institute.)

ATMOSPHERIC LIMITATIONS OF ACTIVE AND PASSIVE

NIGHT VISION SYSTEMS

E.G.D. Youngs
Marconi-Elliott Avionic Systems Limited
Electro-Optical Systems Division
Christopher Martin Road
Basildon
Essex
England

SUMMARY

The paper begins with a brief review of the types of night vision systems which have emerged from the decades following the second world war. The fundamental limits of all such devices (including the human eye) are set by photon noise.

The ways in which the earth's atmosphere affect the image quality of night vision devices are next discussed and of particular interest here is the effect on apparent contrast.

The second part of the paper considers the atmospheric problems associated with the use of supplementary illumination. Continuously emitting searchlights are briefly considered but the paper concentrates on the techniques associated with pulsed illuminators. A summary is given of a basic mathematical model of such a system.

The paper concludes with a short list of some of the more urgent problems which remain.

1. INTRODUCTION

Throughout the decades since the second world war there has been a steadily increasing amount of scientific effort devoted to the development of night vision sensors. Most of the stimulus for this work has arisen out of the war and the future needs of military systems, although there are many peaceful applications as well. The principal military interest in night vision is the detection, recognition and identification of enemy vehicles and personnel under conditions of poor illumination but a broader aim is to be able to conduct all night-time operations with near-daylight efficiency. Many types of equipment have been developed for these purposes but they can be roughly classified under four main headings.

Firstly, there are the purely optical devices such as night telescopes and binoculars. As is well known these do not increase the apparent luminance of the scene (no ordinary optical system can ever do that) but, by providing angular magnification they contrive to offset the reduced resolution of the human eye at low light levels. An essential feature of design is that the exit pupil of the system should be at least as large as the dark-adapted pupil of the eye.

The second category of night vision devices, the image intensifier, takes us into the field of electro-optics. The basic intensifier consists essentially of an evacuated cylinder containing a photocathode at one end and an electro-luminescent phosphor at the other. Photoelectrons emitted by the photocathode are accelerated by an applied electric field and focused to form an image on the phosphor. Owing to the increased energy of the accelerated electrons, more photons are emitted by the phosphor image than were originally incident on the photocathode and so a light amplification is effected. The luminous gain of such a device is typically about 50. By cascading several such intensifiers it is possible to achieve considerably higher gains. For example, a three-stage system may have a gain of about 30,000.

Television equipments form the third category of this brief survey. Most low light television (LLTV) systems use an image intensifier of the type we have just described, as a first stage of light amplification. This is then coupled to one of the many forms of TV pick-up tube such as the SEC vidicon, the SIT vidicon and the image isocon. It is beyond the scope of this paper to discuss the relative merits of these various types. Suffice it to say that they all contain additional stages of gain in addition to a storage mechanism. Three obvious advantages of LLTV over the first two categories of night vision sensor are:

- (a) that the display can be remote from the optical sensor
- (b) that the size of the display can be chosen independently of the rest of the system
- (c) that the human eye can be used in its normal light-adapted state to view a bright display.

A fourth category of sensor is perhaps not properly included with the rest since its operation depends mainly on radiation emitted by the elements of the scene by virtue of their temperatures, rather than by reflected incident light. This group includes of course, the various types of infra-red sensors and has only been included for the sake of completeness.

2. FUNDAMENTAL LIMITS

It is natural first to examine the performance of the human eye since, were it not for limitations of this, we would probably not consider other types of sensor at all. At the highest light levels which occur naturally (say a scene illumination of 10^5 lux, corresponding to direct sunlight) the human eye provides its possessor with a full-colour, high-definition impression of some 5 steradians or so of the external world. This statement is a broad generalisation. In fact the perception of colour and fine detail falls off considerably towards the periphery of the field of view but this is largely offset by the rapidity with which the eye can be directed toward the point of interest. As the light level falls, a complicated system of psychological and physiological controls ensures that the system maintains most of

its efficiency over a considerable range of scene illuminations. However, around the twilight levels (of the order of 1 lux) it becomes noticeable that both resolving power and colour perception begin to decrease, and this tendency continues as the light level falls still further.

The lowest naturally occurring level under the open sky is about 10^{-4} lux (corresponding to an overcast, moonless night) but there are situations of military importance where it can be even lower, for example in a dense forest. Under these conditions, the human eye seems to lose all of its sense of colour and very nearly all of its resolution of fine detail. Furthermore, the mere detection of light, to which the observer is reduced under these circumstances, is now performed by the periphery of the retina, rather than the centre (the technique of averted vision).

In a classic paper Albert Rose analysed the performance of an 'ideal picture pick-up device', namely one that is limited only by random fluctuations in the primary process of conversion of photons to electrons (Rose A 1948). His basic result, converted into modern units is:

$$B \left(\frac{C}{1+C} \right)^2 \cdot \alpha^2 = 2.3 \times 10^{-5} \cdot \frac{k^2}{D^2 t \theta} \dots\dots\dots (1)$$

where B = scene luminance in lm/m²/sr

C = Contrast between target and background defined as $(T_1 - B_1)/(T_1 + B_1)$ where T_1 and B_1 are the target and background luminances.

α = target subtense in milliradians

k = threshold S/N ratio

D = objective lens diameter in cm

t = integration time of device

θ = quantum yield

Rose goes on to compare this result with actual data on the performance of the eye and shows that, within certain limits of the variables, the eye may be matched to an ideal device with a quantum yield of 0.05 at low light levels and 0.005 at high light levels. It is known that the system of control of the eye includes this variation of quantum yield (θ). Other factors in the control system are dilation of the pupil (D), variation of integration time (t), integrating the signal over larger areas on the retina by effectively paralleling the outputs from several elementary receptors, lowering of sensitivity thresholds etc.

The fundamental limit examined by Rose is a limit which applies to all night vision devices, since randomness is a characteristic of any primary photo-process i.e. one in which incident photons cause the release of photo-electrons which become the 'signal'. This source of noise remains after all others have been eliminated. Apart from light level, its magnitude will depend on

- (a) the elementary image area over which integration may be considered to occur (this obviously relates to resolving power)
- (b) the integration time of the system, usually, but not always, that of the human eye.

3. ATMOSPHERIC LIMITATIONS

So far we have only considered the limits imposed on a night vision system arising from the quantities of light available. There is another, and in some cases more serious, limitation. In the basic military task of detecting the presence of an enemy, we are frequently concerned with ranges of the order of several kilometres. In modern war, the early detection and recognition of an enemy vehicle at the greatest possible range, may make all the difference between the success and failure of a given mission. At such ranges however, the earth's atmosphere will play a major role in determining the quality of the image presented to an observer.

As a broad generalisation, we can say that the presence of the atmosphere will influence image quality in three distinct ways:

- (a) Light reflected by the target and its background and travelling towards the electro-optical sensor will be absorbed by molecules of the atmospheric gases, scattered out of the direct path both by molecules and by suspended particles (chiefly water droplets) and finally, refracted by density gradients arising mainly from temperature inhomogeneities. The net result will be a loss of light which would otherwise have contributed to the optical image. We will group together the above effects under the general heading of attenuation.
- (b) The detection of a target against its background amounts fundamentally to detecting a radiance (or luminance) difference between the two. If this difference is zero, detection is clearly impossible by any of the devices we are considering here. (This statement is, of course, a gross simplification. In a real situation we must consider the spectral distribution of the light from target and background and its relation to the spectral responsivity of the primary photocathode of the sensor. A true luminance difference of zero may still give rise to a finite difference of signal current in a sensor which has a different spectral responsivity from that of the eye).

The ease with which the difference is detected is a function of the radiance levels themselves, a given difference being less significant at higher levels. This is usually expressed by referring to the contrast between target and background. The definition used throughout this paper has already been given in connection with the result of Rose above.

so increase the apparent radiances of both target and background. Clearly this will decrease the apparent contrast and so make the detection task more difficult. The effect of attenuation in (a) above also worsens this contrast reduction since it reduces the useful light as a proportion of the scattered light. A well-known simple result for uniform atmospheres, which includes effects (a) and (b) is:

$$N_R = N_O e^{-\sigma R} + N_H (1 - e^{-\sigma R}) \quad \dots\dots\dots (2)$$

where N_R = apparent radiance of object at range R

N_O = intrinsic radiance of object

N_H = radiance of horizon sky

R = range

σ = atmospheric extinction coefficient

- (c) The third atmospheric effect on image quality is a dynamic one, namely the optical aberrations arising from refractive index fluctuations over the optical path. The result of these fluctuations is a random variation of the geometry of image details, resulting in a loss of resolution and contrast. The effects (usually referred to as shimmer and scintillation) are extremely difficult to quantify and will not be considered further in this paper. The reader is referred to (Lawrence R.S. and Strohbehn J.W. 1970) (for example) for a summary of theoretical work in this field.

In the case of television sensor systems there are various techniques available which go some way towards compensating for the contrast losses caused by atmospheric scattering and attenuation. These techniques make use of non-linear (or even discontinuous) transfer characteristics during the stages of electronic signal amplification and in some cases, can be applied to selected portions of the picture only (Clark W.J.R., 1975).

Simple contrast expansion can be achieved by over or under-compensating at the 'gamma correction' stage. If the original optical image contains the whole tone range from black to white this technique is only of limited application.

A more effective method is the 'Auto-black' technique in which the least bright part of the scene (regardless of its actual brightness) is reproduced as black in the display, whilst the brightest part of the scene is reproduced as peak white. The contrast expansion is therefore greatest when the total scene contrast is least.

Other more sophisticated methods are described in the paper by W.J.R. Clark.

4. SYSTEMS USING SUPPLEMENTARY ILLUMINATION

The fundamental photon limit which applies to all night vision devices at a sufficiently low light level, can be avoided by supplying more photons artificially i.e. by the use of a searchlight. Whether this searchlight supplies radiation within the visible spectrum or not, in military terms it constitutes an 'active' system. This has certain tactical implications which will not be discussed here. The rest of this paper will be devoted to examining the ways in which such supplementary illumination can be used to help us towards solutions of the low light problem in a scattering atmosphere.

In most applications it is desirable that any artificial light source which is employed be situated close to the imaging sensor so that the whole equipment (illuminator + sensor) can be conveniently controlled by a single operator. In considering ranges of several kilometres it will be clear that we must concentrate on illuminating only a small area of the scene in order to conserve efficiency. Thus the illuminating beam will, in general, be of narrow angle and fairly well defined. The field of view of the sensor could be similarly restricted but as it may be required to operate without an illuminator at high light levels, a wide field of view may be more appropriate. This choice will depend on the particular operational requirement.

An atmospheric problem arises immediately we attempt to use a searchlight in this manner, namely backscatter from the atmospheric aerosol in the path of the beam. Close proximity of source and sensor implies that a great deal of the beam will lie across the line of sight of the sensor and backscatter from this region will reduce the target contrast against its background. For reasons which will be self-evident, backscatter will increase as atmospheric attenuation increases so that we would expect the whole situation to become rapidly worse as the atmospheric extinction coefficient increases.

It would appear that there are two basic techniques for combating this problem and we will now examine each of these in turn.

Figure 1 shows the relation between backscattered radiance and range, for three different atmospheric conditions. The ordinates are the apparent radiances of a 1 metre thick lamina of atmosphere when irradiated by a source of radiant intensity 1 W/sr at the stated ranges. This diagram has been included to emphasize the sensitivity of backscatter to range. A useful rough rule is readily apparent from the figure, namely that an order of magnitude decrease in range results in two orders of magnitude increase in back-scattered radiance.

Thus by far the most dominant part of the radiance comes from short ranges. It will be clear that, by laterally separating source and sensor, we can make use of the geometry of the situation to ensure that the parts of the atmosphere close to the sensor are not illuminated by the beam and do not contribute to the

total backscatter. This technique is sometimes referred to as 'spatial gating'. It is very limited in its application since, if source and sensor are to be regarded as a single unit, equipment size will restrict the available separation distance.

It can be shown that the apparent radiance due to backscatter in this situation is given approximately by the expression:

$$N = \frac{JG}{4\pi S} \int_{-\phi_0}^{+\phi_0} \exp \left[-\frac{GS}{\tan \frac{1}{2}(\theta - \phi)} \right] d\phi \quad \text{.....} \quad (3)$$

where J = source intensity in W/sr
 σ = extinction coefficient
 G = relative scattering function for the case of backscatter
 S = source-sensor separation
 θ = convergence angle between illuminator beam and optical axis of sensor
 ϕ = half illuminator beam angle

The second technique for eliminating much of the close backscatter is usually called 'time gating'. By providing the additional illumination in the form of short pulses and using some form of time gating in the sensor equipment, it is possible to differentiate on a time basis between radiation scattered or reflected from different ranges. In particular, by arranging that light reflected from the object of interest reaches the sensor during the open period of the gate, the effect of backscattered light from other ranges can be largely eliminated (Adlington R.E., 1975).

Figure 2 is a simple diagram which helps to clarify the basic principle and is useful for determining the limits of certain integrals which occur in the analysis. The diagram is largely self-explanatory, but the reader should note one or two points. The gradient of all sloping lines is equal to $\pm c$, where c is the velocity of light. A little consideration will show that only objects and atmospheric particles within the space-time limits shown shaded will scatter light which will be perceived by the sensor since, for all other ranges, the time of arrival of light at the sensor will occur during the closed period of the gate. Clearly, by narrowing both the illuminator pulse and the gating pulse we can reduce this range of backscatter and so improve the object to background contrast.

An analysis which considers primary scattering only leads to the following results (Youngs E.G.D., 1975).

The light reflected by the target itself will give it an apparent radiance given by:

$$N_1 = \text{PRF} \left(\frac{\rho}{\pi \omega} \right) \cdot \frac{e^{-2bL}}{L^2} \int_0^T g \left(t + \frac{2L}{c} \right) \cdot p(t) \cdot dt \quad \text{.....} \quad (4)$$

where PRF = pulse repetition frequency
 ρ = target reflectance
 ω = solid angle of illuminator beam
 b = atmospheric scattering coefficient
 L = target range
 T = time for a complete illuminator cycle $\left(\frac{1}{\text{PRF}} \right)$

The functions $g(t)$ and $p(t)$ represent the form of the gating and illuminator pulses respectively.

A useful simplification of this result can be obtained by assuming a rectangular gate profile of length equal to the output pulse. In this case $g(t + 2L/c) = 1$ for the range of the integral for which $p(t) \neq 0$ and since the mean illuminator power $W = \text{PRF} \int_0^T p(t) \cdot dt$ we have

$$N_1 = \frac{\rho}{\pi \omega} \cdot \frac{e^{-2bL}}{L^2} \cdot W \quad \text{.....} \quad (5)$$

Note that this expression does not include light which is backscattered from the atmosphere lying in front of the target. This light will be included in the target radiance as perceived by the system. To calculate the contrast of the target against its background we must now state the equations for backscatter. In this context the term 'background' will generally be used to mean 'atmospheric background', that is the background radiance will be considered to arise from light scattered from haze particles etc. The problem of a solid background such as rock or vegetation can be treated as for the target.

(Youngs E.G.D. 1975) derives the following expression for the effective perceived radiance of a particular space-time region of the scattering atmosphere:

$$N_2 = \frac{bG}{4\pi} \cdot \frac{\text{PRF}}{\omega} \int_{t_A}^{t_B} \int_{r_A}^{r_B} \frac{e^{-2br}}{r^2} p(t) \cdot g \left(t + \frac{2r}{c} \right) dr \cdot dt \quad \text{.....} \quad (6)$$

The limits of the integrals have been left in a general form as these have to be chosen according to the particular case which is to be calculated. Note that the time limits are within one cycle. It will be clear that it is now necessary to integrate over range as well as time since the scattering atmosphere extends in depth.

By making the simplifying assumption that the gate profile is rectangular we can separate the integrals and write:

$$N_2' = \frac{bQ PRF}{4\pi\omega} \int_{t_A}^{t_B} P(t) \left[\frac{E_2(x_A)}{x_A} - \frac{E_2(x_B)}{x_B} \right] dt \dots\dots\dots (7)$$

where E_2 is the usual notation for an exponential integral of order 2, and $x_A = 2br_A$, $x_B = 2br_B$.

By using appropriate time and space limits in this expression we can calculate:

- (a) the entire atmospheric backscattered radiance which is perceived by the sensor as 'background'
- (b) the backscattered radiance which contributes to the apparent radiance of the target and hence
- (c) the target to background contrast

This theoretical treatment has been used to compute the way in which the apparent contrast of an object varies with its position in the 'range gate' (the shaded region in Figure 2). In general the position of maximum positive contrast is found, as might be anticipated, somewhere near the centre of the range gate, but for high values of scattering coefficient this position shifts towards shorter ranges.

One interesting and, by now, well known result of this technique occurs when the target is wholly in front of the shaded space time region so that it will appear to have zero radiance. The background will consist of the complete backscatter from the shaded region so that the object will appear as a dark silhouette of contrast -1. If the range now increases, the object will disappear momentarily from view as it enters the tip of the shaded region since its contrast will pass through zero. Behind the range gate the object will, of course, be invisible.

If the time delay between the illuminator pulse and gate is increased so that the range gate follows a receding object, it can be shown that the apparent contrast will slowly increase to a maximum at infinite range. The value of this maximum will depend upon object reflectance, scattering coefficient and the gating condition.

Contrast under natural illumination alone almost invariably decreases with increasing range and scattering coefficient. Thus there will always be some range at which the pulsed illuminator system can improve contrast. Unfortunately, contrast is only one of the parameters which determine the usefulness of the displayed image of an electro-optical sensor. As range and/or atmospheric attenuation increase, the absolute values of the effective radiances decrease drastically as can be seen from equations 4 and 6. Thus the actual signal levels obtainable from the sensor will also decrease and the problem will eventually revert back to the question of photon noise.

5. OUTSTANDING PROBLEMS

Although the techniques mentioned have already achieved some success in overcoming the difficulties of night vision imposed by the properties of the atmosphere, many problems remain. Indeed, in some cases new problems have arisen out of the techniques themselves.

In the case of pulsed illuminators, it will be appreciated that in many cases high-power lasers are employed for this work. But this brings with it the dangerous possibility of severe eye damage for any person irradiated by such a beam at short range. Whether this is acceptable in war is perhaps debatable but it constitutes a serious drawback perhaps for peaceful application or in a 'cold war' situation.

The spectral content of an artificial illuminator would normally be chosen to match the response of the photocathode of the sensor, although it must be remembered that scene parameters also have an influence on this choice. For example, the reflectivities of many man-made objects are similar to that of natural vegetation over most of the visible spectrum but in the near infra-red the reflectivity of vegetation rises considerably and provides a good contrast with man-made objects. Unfortunately, beyond 1μ there are at present no suitable photocathodes of high sensitivity. Considerable interest is being shown in new photocathode materials based on gallium arsenide. These are likely to have improved infra-red responses which would enable more efficient use to be made of natural night radiation, in addition to the possibility of a Nd-YAG laser (1.06μ) as an illuminator.

6. ACKNOWLEDGEMENTS

The author wishes to thank the Directors of Marconi-Elliott Avionic Systems Limited for permission to publish this paper.

7. REFERENCES

- Rose, A., 1948, 'The sensitivity performance of the human eye on an absolute scale' J.O.S.A. Vol. 38 No. 2
- Lawrence, R.S. and Strohbehn, J.W., 1970, 'A survey of clear-air propagation effects relevant to optical communications'. Proc. I.E.E.E. Vol. 58 No. 10.
- Clark, W.J.R., 1975, 'Some aspects of signal processing for LLTV systems'. I.E.E. International Conference on Low Light and Thermal Imaging Systems.

Youngs, E.G.D., 1975, 'The theory of pulsed-illuminator-aided viewing'. I.E.E. International Conference on Low Light and Thermal Imaging Systems.

Adlington, R.E., 1975, 'Laser Aided Viewing Systems'. I.E.E. International Conference on Low Light and Thermal Imaging Systems.

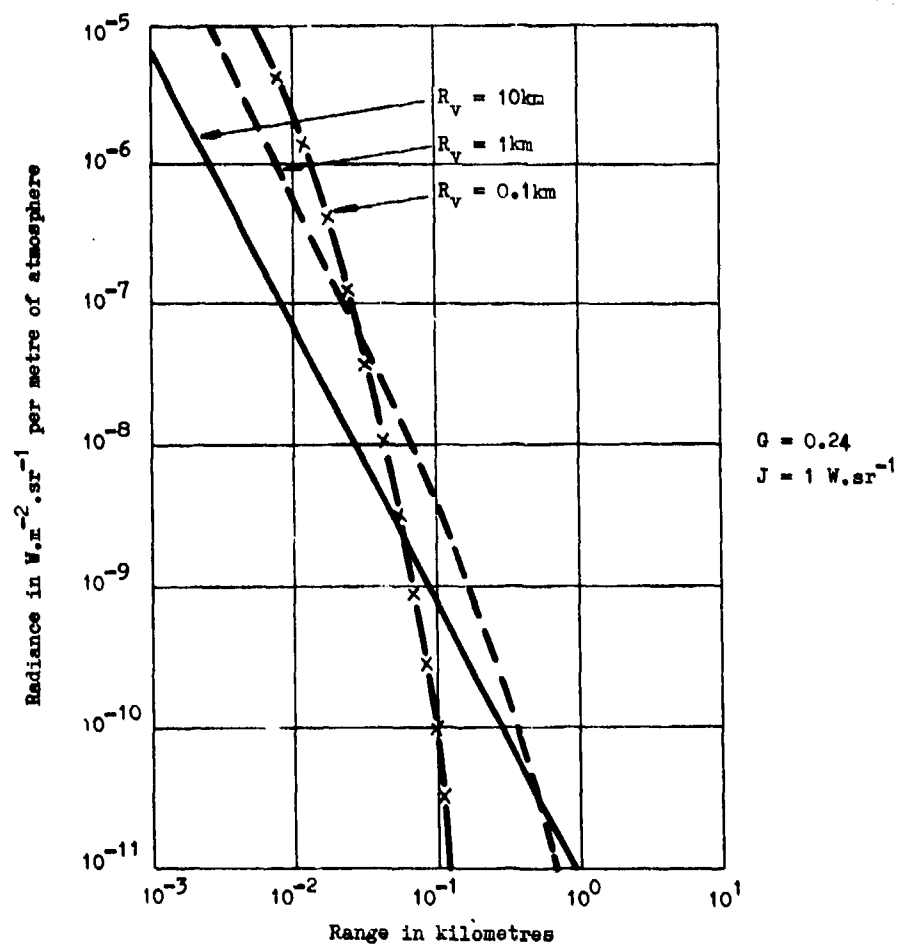


FIGURE 1 RELATION BETWEEN BACKSCATTERED RADIANCE AND RANGE

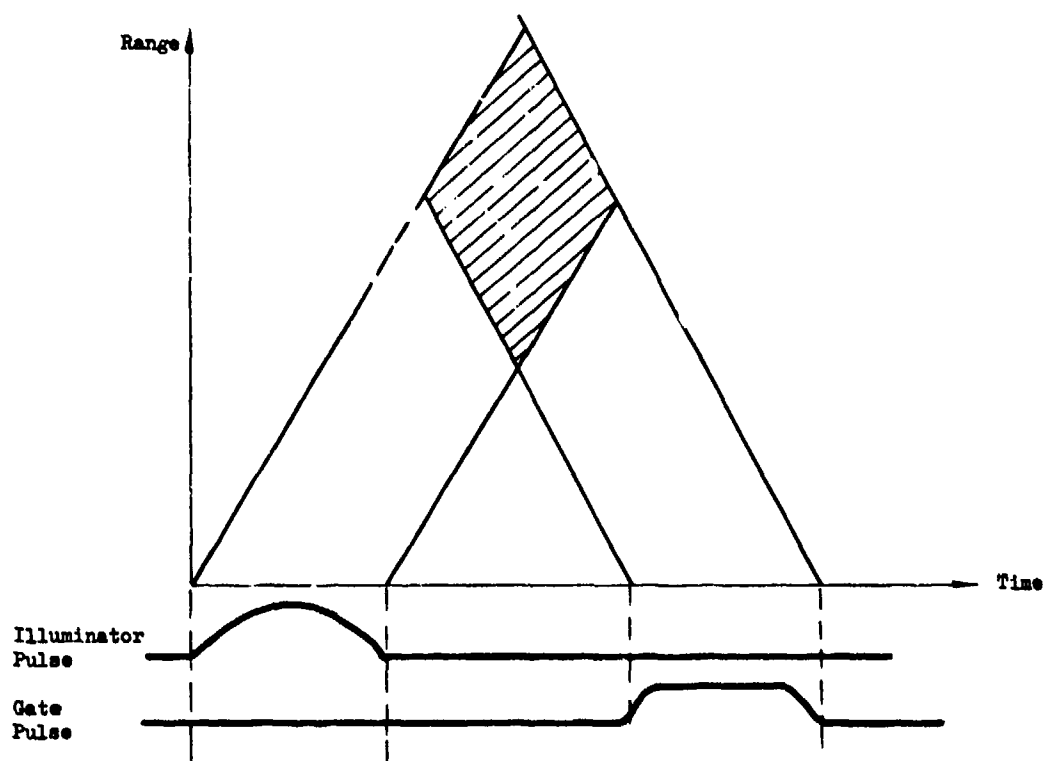


FIGURE 2 RANGE - TIME DIAGRAM

USING LIDAR FOR MEASURING VISIBILITY

Dr. James F. Ruger
ELTRO GMBH
6900 Heidelberg / BRD

SUMMARY

The performance of a slant visibility equipment and the data processing techniques used are described herein. Special attention is given to the correlation data which compares the accuracy of the slant visibility system to that of a recognized transmissiometer.

Approximately 800 slant visibility readings were compared with the transmissiometer-visibility data at three different airports in order to obtain the correlation function.

The results show that the slant visibility readings although consistently higher than the transmissiometer-visibility readings the factor is always approximately two. Therefore the correlation factor is a constant and the visibility data plots of the two systems lie exactly parallel one another. Considering this parallel shift it can readily be said that the two systems show very good agreement in visibility data.

The use of the LIDAR technique in a SVR (Slant Visual Range) system which would supplement the RVR (Runway Visual Range) systems at airports may very well become a near future application especially when reliable eye-safe lasers are available at a reasonable price.

1. INTRODUCTION

The visibility at various heights as well as along a slant path is of special interest for meteorologists and flight-safety personnel. For aircraft landing operations the visibility along the "Landing Glide Path" is of special importance.

Research and development in the pulse-laser field has shown that a laser-radar method called lidar probes the atmosphere such that the back scatter signal is characterized by the aerosol particles along the laser beam path and is referred to as the lidar signature.

If the atmosphere along the beam path is assumed to be homogeneous - or at least consisting of homogeneous intervals - the backscatter coefficient remains constant within these intervals and the descending curve of the lidar signature is caused by the product of extinction and reciprocal squared distance. Since the visibility is inversely proportional to the extinction coefficient, the former can be obtained via a careful analysis of the lidar signature.

The lidar principle has a significant feature in that it is a single ended system and can be aimed in any slant direction. Thus the system is often referred to as a "Slant Visibility Measurement System".

The purpose of our investigation was to find an automatic processing and display method which had a high data evaluation accuracy for determining the visibility in a homogeneous atmosphere which could be expanded for evaluation of an inhomogeneous atmosphere. Such a system was analysed and built as an experimental model.

Although this model utilizes a ruby laser and can possibly be a hazard to the eye /7/ further developments in the field of eye-safe-lasers /5/ show that an erbium glass laser having the same power and pulse width of our ruby laser is completely eye safe.

2. Theoretical Principles

The theory of visibility measurement using lidar has been dealt with by various authors /1/, /2/, /4/. As a matter of information the most important equations are listed below:

The common lidar equation is given as:

$$P_r(R) = \frac{P_t \cdot K_1 \cdot B'(R)}{8\pi R^2} \cdot e^{-2 \int_0^R \sigma(R) \cdot dR} \quad (1)$$

$P_r(R)$ = received power (watt)

P_t = transmitted power

K_1 = constant incorporating optical parameters, light velocity, pulse width etc.

$B'(R)$ = volume backscatter coefficient at a distance R (m^{-1})
 R = one way penetration of the atmosphere
 $\sigma(R)$ = extinction coefficient at the distance R (m^{-1})

If a homogeneous aerosol distribution is considered then the extinction coefficient is independent of distance such that

$$B'(R) = \text{constant} = K_2 \quad (2)$$

and $\sigma(R)$ is inversely proportional to the meteorological visibility in accordance to the equation

$$\sigma = \frac{3.912}{V_m} \quad (3)$$

V_m = meteorological visibility

If equation (2) and (3) are substituted into equation (1) the following results:

$$P_r(R) \cdot R^2 = \frac{P_t \cdot K_1 \cdot K_2}{8\pi} \cdot e^{-\frac{7.824}{V_m} \cdot R} \quad (4)$$

In order to solve equation (4) for V_m the logarithm of both sides is taken:

$$\ln [P_r(R) \cdot R^2] = \ln \left[\frac{P_t \cdot K_1 \cdot K_2}{8\pi} \right] - \frac{7.824}{V_m} \cdot R \quad (5)$$

and equation (5) is differentiated in respect to r yielding

$$\frac{d}{dr} [\ln P_r(R) \cdot R^2] = -\frac{7.824}{V_m} \quad (6)$$

As can be seen in equation (6) the visibility solution is independent of system parameters and transmitter power providing that the lidar signature is large enough to be analysed.

As mentioned previously a homogeneous atmosphere had been assumed so that the visibility along the measurement path is constant. This means that the left side of equation (6) depicts a line of constant slope. Therefore ΔR can be substituted for dr in the above equation and solving for V_m yields:

$$V_m = -7.824 \cdot \frac{\Delta R}{\Delta [\ln P_r(R) \cdot R^2]} \quad (7)$$

If the term in the brackets of the denominator of equation (7) is plotted as a function of the penetration k then a straight line of negative slope is obtained. The product of this slope value with -7.824 gives the visibility.

This theoretical approach is valid for a homogeneous atmosphere. However, the degree of inhomogeneity which is to be encountered along landing glide paths can be averaged by applying a least-means-square-fit to the term in brackets in equation (7) thus obtaining an average visibility value. This approach can be applied with success for landing glide paths since the approach angle is only in the order of 3 to 5 degrees.

3. Slant Visibility Equipment

The slant visibility equipment (see Fig. 1) consists of two main units

- a) transmitter/receiver
- b) processing electronics with program logic

The transmitter/receiver unit houses the laser, the receiver optics, photomultiplier with spectral filter and preamp. (see Fig. 2).

The processing electronics/program logic unit (see Fig. 3) incorporates the log amplifier, A/D convertor, memory, clock pulse generator, program logic, tape puncher with interface.

3.1 Transmitter/Receiver

The ruby laser with Galilei telescope has a divergence of 0.5 mrad and a pulse repetition of 6 per minute. A Cassegrain objective system having an F.O.V. of 0.9 mrad comprises the receiver optics. By means of a lens of focal length being 100 mm the light rays are directed to the cathode of the photomultiplier. A spectral filter of 9 Å bandwidth restricts the detector to light within the ruby wavelength.

3.2 Processing Electronics

A block diagram of the processing electronics and program logic is shown in Fig. 3. Since laser beam propagates with the velocity of light the time interval between the A-trigger and each instant time of the backscatter signal is directly proportional to the penetration distance. Therefore the 100 ns interval used for A/D conversion correspond to 15 meter penetration steps. The backscatter signal for a penetration depth maximum of 2055 meters is stored. The memory has a capacity for storing 8 lidar signatures before it is automatically read out with the tape puncher.

In order to calculate the visibility from the backscatter signals the tape is fed into a computer having a prestored program. In addition to calculating the visibility the function

$$\ln [P_r(R) \cdot R^2] \quad \text{versus } R$$

is automatically plotted at the terminal. If the slope is continuous and approximates a straight line it is certain that the atmosphere was homogeneous.

Deviations from a straight line are caused by inhomogeneous aerosol distributions.

In order to obtain the average visibility in the latter case a least-means-square-fit /3/ is applied as in equation (8).

$$\hat{S} = \frac{n \cdot \sum_{i=1}^n x_i y_i - \sum_{i=1}^n y_i \cdot \sum_{i=1}^n x_i}{n \cdot \sum_{i=1}^n x_i^2 - \left(\sum_{i=1}^n x_i \right)^2} \quad (8)$$

\hat{S} = matched slope

x_i = instantaneous penetration distance

y_i = corresponding instantaneous value for $\ln P_r(R) \cdot R^2$

n = number of values used

After the computer calculates equation (8) it goes on to equation (9)

$$V_m = - \frac{7.824}{\hat{S}} \quad (9)$$

to determine visibility.

4. Results and Analysis

Fig. 4 shows a typical plot of the function $\log P_r(R) \cdot R^2$ versus R as obtained at the computer terminal. The y-axis which gives the amplitude of the function starts at an origin value of 13 and continues in increments of .05. The x-axis is scaled in meters. The y-axis was expanded in order to make amplitude deviations from that of a straight line more noticable. In order to determine the average slope of the curve as in Fig. 4 the computer applies a least-means-square-fit as in equation (8) and calculates the visibility in accordance with equation (9).

Visibility comparison measurements were conducted at three different airports using the Eltro transmissometer type TMM 150 D for comparison. Fig. 5 shows the comparison of this data as plotted at the computer terminal. The visibility data obtained via lidar is plotted along the y-axis as a function of the transmissometer-visibility data of the x-axis.

A straight line is drawn from the origin having identical visibility values for both systems. Should all measured data lie on this line then the correlation of the two systems would be perfect. As can be seen most of the lidar data results in higher visibility values.

Fig. 5 only gives an indication of min and max values obtained with the lidar system for a particular transmissometer value since only one point for a particular value is plotted regardless how many comparisons show this value.

For this reason an average is taken of all the lidar results pertaining to a specific transmissometer value and this is plotted in Fig. 6. As can be seen the lidar values lie a factor 2 higher than the corresponding transmissometer-visibility values and that this correlation factor of 2 remains constant independent of visibility. In consideration of this aspect it can surely be said that the correlation is rather good.

- /1/ Borchhardt, H. / Kössler, J.
Erfahrungen und Überlegungen mit LIDAR am Meteorologischen Observatorium Aachen,
Bericht des Deutschen Wetterdienstes Nr. 125, Offenbach a.M., 1971
- /2/ Collis, R.T.H. / Viezee, W. / Uthe, E.E. / Oblanas, J.
Visibility Measurement for Aircraft Landing Operations
Stanford Research Inst., Menlo Park, California
September 30, 1970
- /3/ Gellert / Dr. Küstner / Dr. Hellwich / Kästner
Kleine Enzyklopädie Mathematik
Pfalz Verlag, Basel, 1967, Seite 637
- /4/ Dr. Lang, M.
Untersuchungen über die Anwendungsmöglichkeiten eines Lasers für Schrägsichtmessungen
Eltro-Bericht, Heidelberg, 30. Juni 1969
- /5/ Lund, D. / Landers, M.E. / Brosnick, G.H. / Powell, J.O. / Chester, J.E. / Carver, C.
Ocular Hazards of the Q-Switched Erbium Laser
Frankford Arsenal, Philadelphia, Pa., March 20, 1970
- /6/ Viezee, W. / Oblanas, J. / Collis, R.T.H.
Evaluation of the Lidar Technique of Determining Slant Range Visibility for
Aircraft Landing Operations
Stanford Research Inst., Menlo Park, California
November 1973
- /7/ Wyman, P.W.
Laser Radar Eye Hazard Considerations
Applied Optics, Vol. 8, No. 2, Pg. 383-392, February 1969

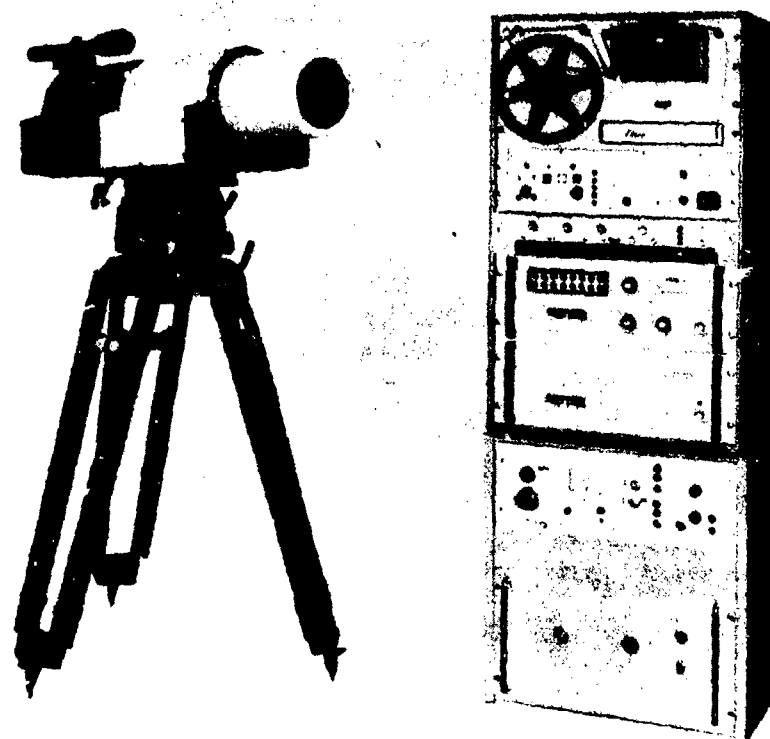


Fig.1 Slant visibility equipment

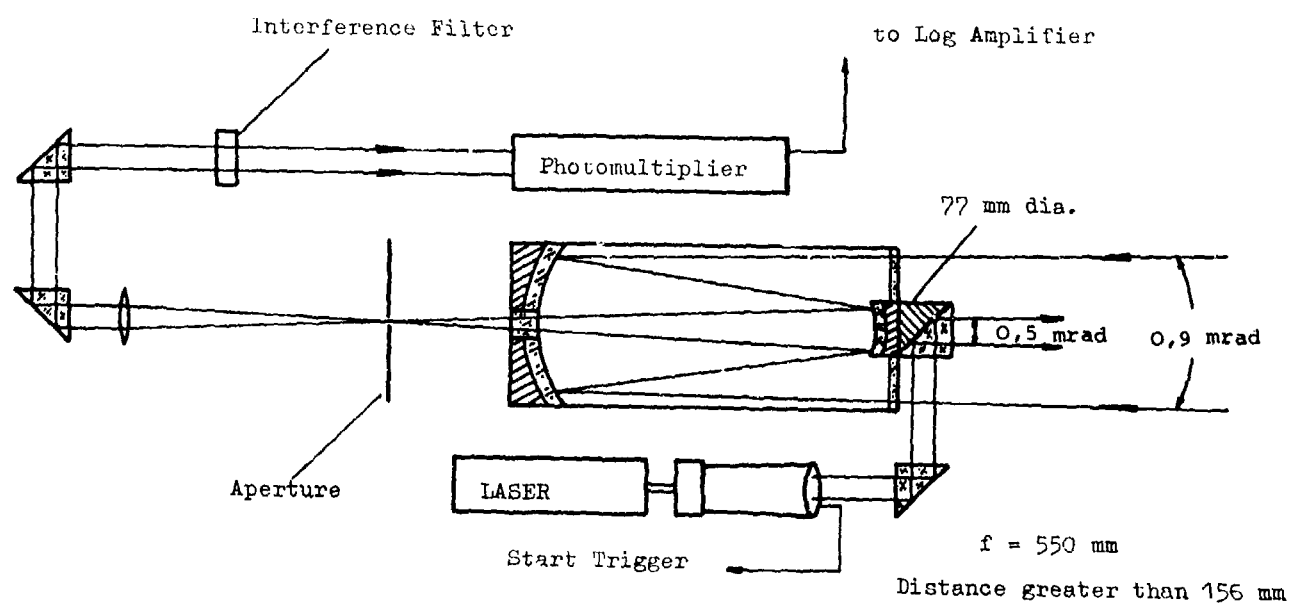


Fig.2 Transmitter/receiver

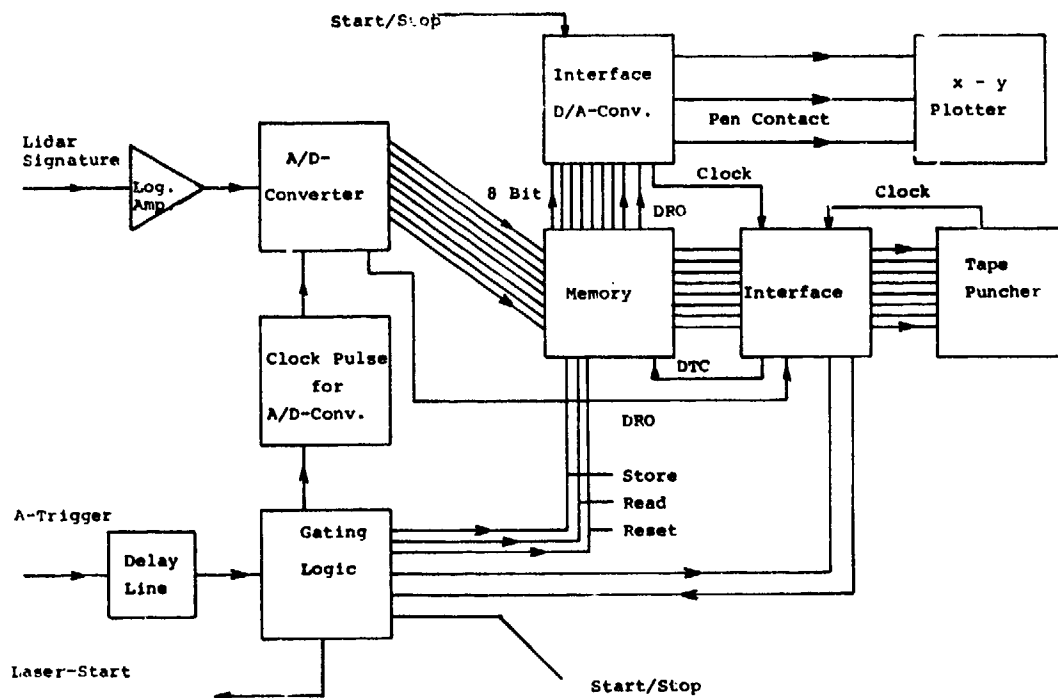


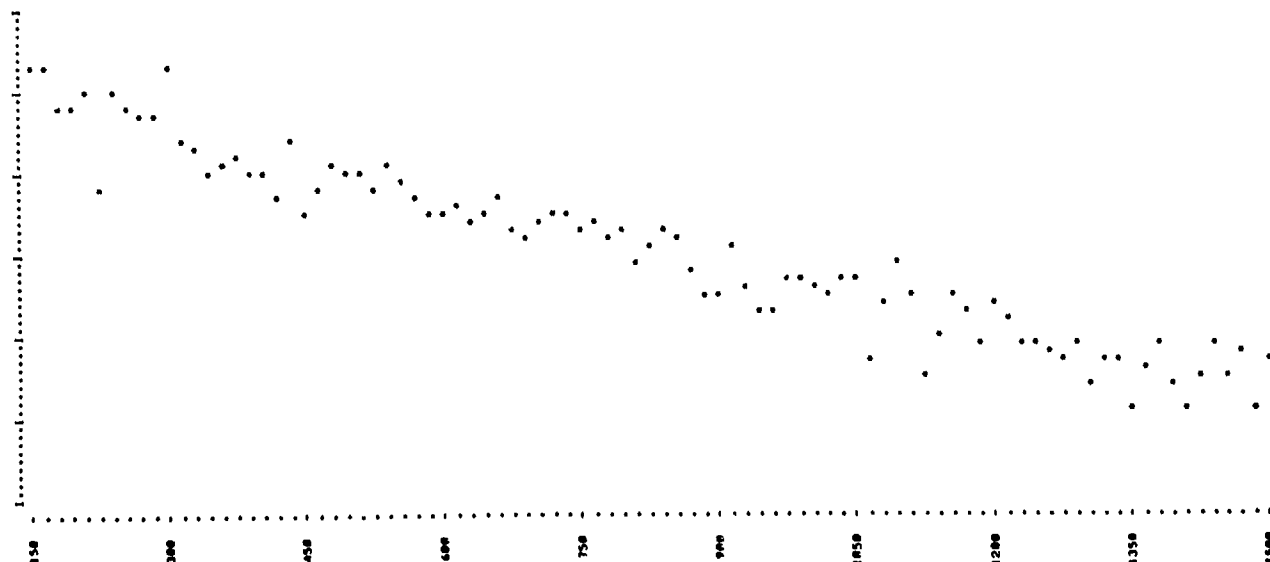
Fig.3 Processing electronics/program logic

Comparison Interval: 180 to 660 meters

Transmissometer Visibility Value: 2400 meters

Lidar Visibility Value: 4140 meters

y-coordinate: $\log P(R) \cdot R^2$.05 intervals origin = 13
 x-coordinate: R in meters

Fig.4 $\log P(R) \cdot R^2$ versus R

The curve shows the visibility values obtained from the Lidar system and compared to those obtained from the Transmissometer system for a penetration of 150 to 450 meters.

y-coordinate: Lidar Visibility Values
x-coordinate: Transmissometer Visibility Values

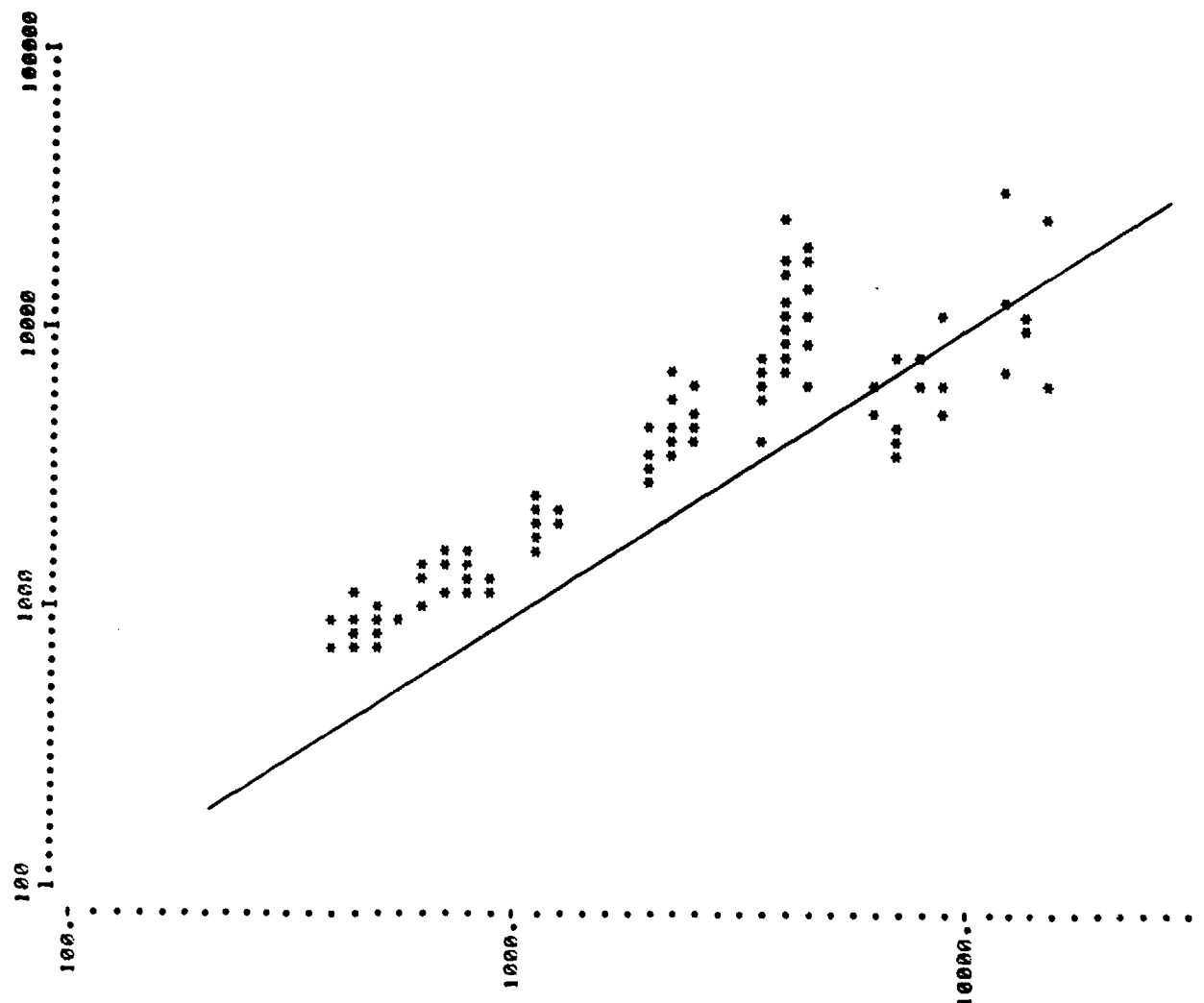


Fig.5 Comparison transmissometer/lidar

The curve shows the visibility values obtained from the Lidar system and compared to those obtained from the Transmissometer system for a penetration of 150 to 450 meters.

y-coordinate: Lidar Visibility Values

x-coordinate: Transmissometer Visibility Values

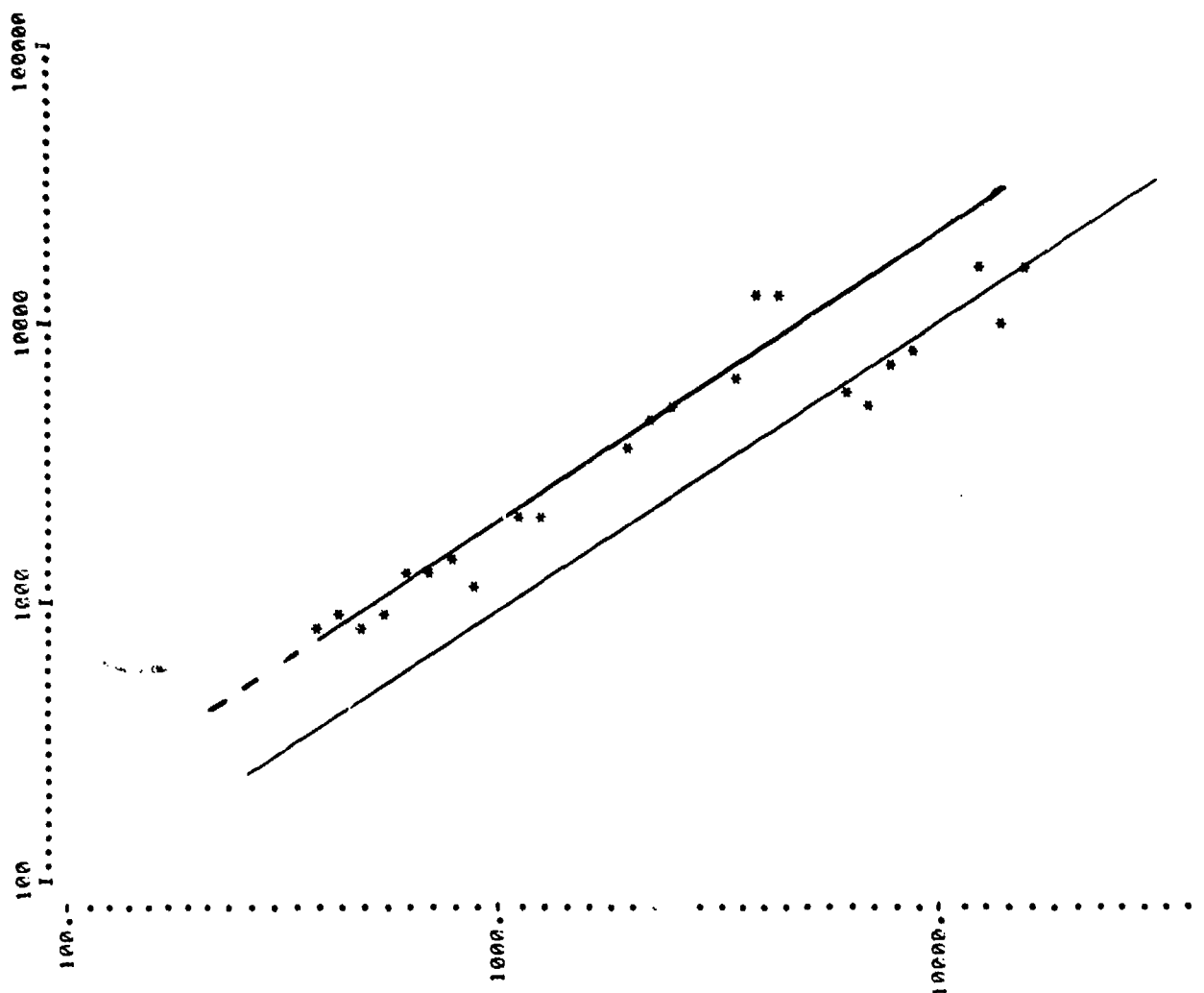


Fig.6 Average value comparison transmissometer/lidar

THE INFLUENCE OF THE ATMOSPHERE BETWEEN HELICOPTERS AND GROUND-
TARGETS ON THE DOWNWARD AND UPWARD VISIBILITY

H.-E. Hoffmann
DEUTSCHE FORSCHUNGS- UND VERSUCHSANSTALT FÜR LUFT- UND RAUMFAHRT E. V.
DFVLR - Institut für Physik der Atmosphäre
8031 Oberpfaffenhofen / Germany

SUMMARY

During some preliminary tests about the visibility air-to-ground and ground-to-air in autumn 1974, the maximum detection range and the maximum recognition range were determined. A tank Leopard, a 1,5 t military truck and a special test board were observed from air to ground. The aircraft were a Bell UH 1D helicopter and a Dornier Do 27. The experiments took place only at standard visibilities between 36 and 57 km. - The maximum detection range ground-to-air was between 6 and 12 km larger than the maximum detection range air-to-ground. For the maximum detection range ground-to-air values between 9 and 16 km were reached and for the maximum detection range air-to-ground they were between 2 and 4 km. The maximum recognition range air-to-ground was up to 2 km smaller than the maximum detection range. The maximum detection range for observations of a special test board - which in about corresponded with Nato test boards - was smaller than that for observations of the 1,5 t military truck. The maximum recognition ranges, however, determined at observations of the test board and of the 1,5 t military truck did not differentiate significantly from each other.

1. INTRODUCTION

During a rather big program of experiments in autumn 1974 in Northern Germany some preliminary tests were conducted in order to answer the question:

Who can see whom first, the observer in the helicopter the tank or the observer in the tank the helicopter?

As the time available for these preliminary tests was very short, the experiment took place under mainly idealized conditions for observations air-to-ground and ground-to-air in order to get some concrete answers. Idealized means that aircraft and ground vehicle did not conduct in a military-tactically correct manner and that the meteorological conditions for experiments were favorable. In detail this means:

- (a) The observer was familiar with the direction and time of the approaching aircraft
- (b) Altitude and direction of the aircraft remained constant during an approach
- (c) The altitude of the approaching aircraft was between 200 and 300 m
- (d) The helicopter (a Bell UH 1D) resp. the airplane (a Dornier Do 27) approached from distances between 15 and 40 km
- (e) The helicopter resp. the airplane approached in front of sky background
- (f) The tank (a Leopard) resp. the 1,5 t military truck were standing on a meadow without any camouflage
- (g) The observers in the helicopter resp. in the airplane were familiar with the position of the ground targets and this remained unchanged during the whole test series subsequently discussed
- (h) The tests were only conducted at daylight brightness

- (i) For the horizontal standard visibility values between 36 and 57 km were obtained

It never rained during the tests and the air temperature was between +5 and +20° Celsius.

In order to find an answer to the above mentioned question, who can see whom first resp. how is the difference between the visibility ground-to-air and the visibility air-to-ground, the maximum detection range and the maximum recognition range were used. The maximum detection range is the distance in which the observer in the approaching helicopter is just able to perceive the ground object resp. in which the ground observer is just able to perceive the approaching aircraft. In a distance corresponding to the maximum detection range, an observer can only determine that something is located there. He cannot yet specify the observed object i.e. he cannot yet recognize or identify it. In a distance, however, which at least equals the maximum recognition range, details about the observed object can be differentiated.

To contrast the maximum detection ranges air-to-ground with ground-to-air, observation results of only one approach or one test period were compared with each other. This guaranteed that the observation results used for comparing were determined at almost the same test conditions.

Due to little changes of the horizontal standard visibility (about 20 km) during each test period, quite unexpected no information from the below shown test results have been got, how the maximum detection range and the maximum recognition range air-to-ground resp. ground-to-air change in dependence on the horizontal standard visibility. The same is of course valid for the differences between the maximum detection ranges air-to-ground and ground-to-air.

Detailed informations about the maximum detection range at observations of aircraft from the ground can be taken from the reports (SEYB, E.K. 1966 and 1967; HOFFMANN, H.-E. 1966 and 1974; HOFFMANN, H.-E., BUELL, R.H. 1974).

Following, also some results are shown concerning the maximum recognition range which, however, only could be determined during observations air-to-ground. Likewise at observations air-to-ground the maximum detection range and the maximum recognition range were determined using a special test board.

2. TEST DESCRIPTION

2.1 The observed aircraft

For determination of the maximum detection range ground-to-air an airplane of the type Dornier Do 27 and a helicopter of the type Bell UH 1D were available (see Fig. 1 and 2). Both aircraft were dark-green so that their contrast against the sky background was negative.

$$C = \frac{L_o - L_s}{L_o}$$

C = Contrast
L_o = Luminance of object
L_s = Luminance of sky

The inherent contrast was approximately 0,90. One side door of the helicopter had been removed so that special observers in the helicopter could not be impeded by a too narrow field of view or by the window-glass.

2.2 The observed ground objects

The ground target to be detected resp. recognized from the aircraft were a tank Leopard or a 1,5 t military truck of the Bundeswehr. The longitudinal axis of the tank Leopard showed in the direction from which the aircraft was approaching (see. Fig. 3). The 1,5 t military truck was standing in a manner that either its longitudinal axis had the same direction as the approaching aircraft or that this axis was traverse. For the observers in the aircraft was a meadow the background of the two ground targets. The biggest part of the vehicles visible to the observers had a negative contrast i.e. the vehicles too appeared dark against their background.

In order to find out how the maximum detection range resp. the maximum recognition range at observations of the military vehicle corresponded with those received at observations of a so-called Nato-test, during some approaches two special test boards were observed. The test board for detection was a disk with a diameter of 2,3 m with four grey-white pairs of lines on it (line width = 28,7 cm) (see Fig. 4). The test board for recognition had 7 grey-white pairs of lines (line width = 16,4 cm). The inherent contrast between the grey and the white lines of the test boards for the maximum detection range and the maximum recognition range was about 50%.

2.3 The course of the tests

The area of the ground targets (see Fig. 5) was approached by the aircraft in altitudes between 200 and 300 m from eastern direction in distances in which the objects to be

detected could not be seen any more. It was the task of the observers to advise the moment in which they could just see the targets to be detected (UH 1D, Do 27, tank Leopard, 1,5 t military truck) resp. in which they could just recognize the target (1,5 t military truck). During observation of the test board, the grey-white pairs of lines had to be resolved.

The pilots by means of their instrument panel and their flying direction knew quite exactly the position of the test area, so that the sector they had to search over was very small (about 10°). The special observers in the helicopter, however, had to search within a sector of $30-40^\circ$. During their observations the helicopter was hovering and its axis was traverse to the direction of approach.

2.4 The observers

The observers during these tests were 15 soldiers of an anti-aircraft defence battalion of the Bundeswehr. 7 of them were special observers in the helicopter UH 1D, the others were employed as observers ground-to-air. The soldiers whose observation values were used as well as the pilots of the Do 27 and the helicopter had normal visual acuity.

2.5 Measurement of the distance ground object - aircraft

For determination of the distance ground target-aircraft a mobile 3 cm-radar set was available. During the approaches the slant distance was measured continually and was registered in intervals of one second.

2.6 The determination of the horizontal standard visibility

The horizontal standard visibility was determined by means of an integrating nephelometer and by contrast measurements of natural and artificial targets. To describe the test conditions of the results in the following chapter, values for the horizontal standard visibility have been applied, received by contrast measurements of natural targets (edges of woods) (HOFFMANN, H.-E., 1967 and 1971). In most cases the values thus received for the horizontal standard visibility at ground level were valid too for the slant standard visibility helicopter (resp. airplane)-to-ground target, this due to the fact that approaches took place in low altitudes and that the atmosphere with regard to the degree of its turbidity up to the flying altitude appeared vertically homogeneous.

2.7 The determination of the slant standard visibility

At larger altitudes and (or) vertical inhomogeneities of the atmosphere, the horizontal standard visibility at ground level is no sufficient measurement for the degree of the atmospheric turbidity in slant directions. For fundamental researches being conducted to clarify in which relation is the slant standard visibility - at different elevation angles, at different altitudes, at different meteorological conditions - with the horizontal standard visibility at ground level, it has been tried to get also values for the slant standard visibility. For this purpose the test board was photographed from different distances during several approaches of the helicopter. Tests are made to conclude values for the slant standard visibility by means of the density curve of the used films and by means of a microphotometer.

3. TEST RESULTS

Informations about registration and processing of observation values and measurement values can be taken from the reports (HOFFMANN, H.-E., BUELL, R.H., 1974).

In Figures 8-13 the values for the horizontal standard visibility V_s result from weighted means and cubic interpolation of contrast measurements at different natural targets. The values for the maximum detection ranges D_m and the maximum recognition ranges R_m (showed by lines parallel with the abscissa) are arithmetic mean values of various single values. The hatched region with the mean value symmetrically arranged around indicates the confidence region belonging to this mean value, i.e. here the region in which the mean value, basing on a normal distribution for the single values of observation, can be expected at a probability of 95%. In case, a confidence region is missing, this means, that the single values for the corresponding mean values have been got during a discontinuous approach of the helicopter Bell UH 1D and that all special observers in the helicopter have detected resp. recognized the object at the same traverse position of the helicopter. This means that the confidence region in this case equals zero. The number of single values appears in parentheses above their mean value resp. their confidence region. On top of the parentheses it is shown which object has been observed.

In Figures 8-13 the maximum detection range D_m and the maximum recognition range R_m during observations air-to-ground have been confronted with the maximum detection range D_m during observations ground-to-air. The test results of each Figure have been received only during one day and during one test period i.e. observations took place at the same day and therefore at nearly the same conditions.

During the tests mentioned in the report, the horizontal standard visibility only changed insignificantly. The tests were conducted at horizontal standard visibilities between 36 and 57 km. Figures 6 and 7 show, how the maximum detection range changes in dependence on the horizontal standard visibility; they are taken out of reports by SEYB, E.K., 1966 and HOFFMANN, H.-E., 1974. With regard to the curve "naked eye" in Fig. 7, it should

be remarked that only few values for the maximum detection range at large horizontal standard visibilities were available for the calculation of this curve. Later tests conducted at large horizontal standard visibilities have shown that larger horizontal standard visibilities are to be associated with larger values for the maximum detection range. Therefore at larger horizontal standard visibilities the curve must have a larger distance from the abscissa.

3.1 The maximum detection range air-to-ground and ground-to-air

For the tests, results of which are shown in Figures 8 and 9, a tank Leopard or a 1,5 t military truck were used. The observations air-to-ground were performed by the pilot resp. the co-pilot or the special observers in the helicopter. From the aircraft observations were made with naked eye that means without field glasses or telescope. Observations ground-to-air took place with naked eye or with 10x50 field glasses unsupported used. During all tests in Figures 8 and 9 the horizontal standard visibility only changed insignificantly between 53 and 57 km.

The main results of Figures 8 and 9

(1) The maximum detection range ground-to-air (observations ground-to-air with naked eye or with unsupported 10x50 field glasses) was between 6 and 12 km larger than the maximum detection range air-to-ground (observations air-to-ground only with naked eye).

(2) The maximum detection range air-to-ground at observation of the tank Leopard was 4 km and at observation of the 1,5 t military truck, it was between 2 and 4 km (the horizontal standard visibility was between 39 and 57 km).

(3) The maximum detection range ground-to-air at observation of the Do 27 and the UH 1D was between 9 and 16 km (the horizontal standard visibility was between 53 and 57 km).

(4) No significant differences were got between the maximum detection ranges ground-to-air at observations with naked eye and at observations with unsupported used 10x50 field glasses.

(5) During one single test period the special observers have detected the 1,5 t military truck about 2 km farther out than the pilots resp. co-pilots.

3.2 The maximum detection range resp. the maximum recognition range air-to-ground and the maximum detection range ground-to-air

In Figures 10 and 11 test results are shown in which the maximum detection range and the maximum recognition range air-to-ground was determined by means of a 1,5 t military truck. Criterion for the recognition was the correct statement of the observers in the aircraft, saying in which direction - left hand or right hand versus observation direction - the driver's cabin of the 1,5 t military truck showed.

The main results of Figures 10 and 11

(1) The observations air-to-ground of the pilots resp. co-pilots did not result in any significant differences between the maximum detection range and the maximum recognition range. The observation of the special observers, however, resulted in the fact that the value for the maximum recognition range was 2 km smaller than for the maximum detection range.

(2) The maximum recognition range was about 1 km; the tests had been conducted at horizontal standard visibilities between 39 and 41 km.

3.3 Comparison of the maximum detection range and the maximum recognition range air-to-ground at observation of a tank Leopard and of a test board

In the following Figures 12 and 13 it is shown, how the values for the maximum detection range and for the maximum recognition range at observation of a military object (tank Leopard, 1,5 t military truck) correspond with the values received at observation of a special test board for detection resp. recognition. Details about the test board used can be taken from chapter 2.2.

The main results of Figures 12 and 13

(1) The maximum detection range at observation of the test board was about 3 km smaller than the maximum detection range at observation of the tank Leopard resp. of the 1,5 t military truck.

(2) The maximum recognition range at observation of the test board and the maximum recognition range at observation of the 1,5 t military truck did not show any significant differences.

4. CONCLUSION

Our results are mainly idealized conditions during a rather big program of experiments in autumn 1974. There have also been conducted some preliminary tests in order to answer the

question:

Who can see whom first, the observer in the helicopter the tank or the observer in the tank the helicopter?

"Idealized conditions" means, that the tests took place under most favorable conditions for observing, compared with the conditions of tactically correct behaviour of the air- and ground vehicles:

- (a) The observer was familiar with the direction and time of the approaching aircraft
- (b) Altitude and direction of the aircraft remained constant during an approach
- (c) The altitude of the approaching aircraft was between 200 and 300 m
- (d) The helicopter (a Bell UH 1D) resp. the airplane (a Dornier Do 27) approached from distances between 15 and 40 km
- (e) The helicopter resp. the airplane approached in front of sky background
- (f) The tank (a Leopard) resp. the 1,5 t military truck were standing on a meadow without any camouflage
- (g) The observers in the helicopter resp. in the airplane were familiar with the position of the ground targets and this remained unchanged during the whole test series subsequently discussed
- (h) The tests were only conducted at daylight brightness
- (i) For the horizontal standard visibility values between 36 and 57 km were obtained

To answer the above question the maximum detection range air-to-ground and ground-to-air were determined. The maximum detection range is the distance, in which an observer can just see an object without being able to say what kind of object it is. Some tests for determination of the maximum recognition range air-to-ground - this is the distance in which statements about the kind of the observed object can be made - have also been conducted.

Among other facts the tests resulted in the following:

- (1) The helicopter Bell UH 1D and the airplane Do 27 always were detected farther out from the ground than the tank Leopard and the 1,5 t military truck from the aircraft. The maximum detection range ground-to-air was between 6 and 12 km larger than the maximum detection range air-to-ground. (The horizontal standard visibility during these tests was between 39 and 57 km; observations out of the air were made with naked eye and from the ground they were made with naked eye resp. with unsupported used 10x50 field glasses).
- (2) The maximum detection range air-to-ground at observation of the tank Leopard and of the 1,5 t military truck was between 2 and 4 km, the maximum detection range ground-to-air at observation of the Bell UH 1D resp. of the Do 27, however, was between 9 and 16 km.
- (3) The maximum recognition range air-to-ground at observation of the 1,5 t military truck was 2 km smaller than the maximum detection range air-to-ground respectively did not differ significantly.
- (4) The maximum detection range air-to-ground at observation of a special test board - which about corresponded with Nato test boards - was about 3 km smaller than at observation of the tank Leopard resp. of the 1,5 t military truck.
- (5) The maximum recognition ranges air-to-ground at observation of a special test board and of the 1,5 t military truck did not differ significantly.

REFERENCES

HOFFMANN, H.-E., 1966, "Die maximale Auffaßreichweite bei der optischen Beobachtung tief anfliegender Flugzeuge vom Boden aus", DFL-Bericht Nr. 0344, Braunschweig

HOFFMANN, H.-E., 1967, "Die Bestimmung der horizontalen Normsicht durch Kontrastmessungen an natürlichen Sichtzielen", Deutsche Luft- und Raumfahrt, Forschungsbericht 67-11

HOFFMANN, H.-E., 1971, "Über einige Erfahrungen bei der Bestimmung der horizontalen Normsicht durch Kontrastmessungen an natürlichen Sichtzielen", Deutsche Luft- und Raumfahrt, Forschungsbericht 71-22

HOFFMANN, H.-E., BUELL, R.H., 1974, "Ergebnisse von Versuchen zur Bestimmung der maximalen Auffaßreichweite und der maximalen Erkennbarkeitentfernung bei der Beobachtung von Flugzeugen im Alpenvorland", DFVLR IB 553-74/1, Oberpfaffenhofen

HOFFMANN, H.-E., BUELL, R.H., 1974, "Ergebnisse von Versuchen zur Bestimmung der maximalen Auffaßreichweite bei der Beobachtung von Luftfahrzeugen vom Boden aus in Norddeutschland", DFVLR IB 553-74/4, Oberpfaffenhofen

SEYB, E.K., 1966, "A Study on Ground-to-Air Visual Detection", Professional Paper PP-4, Den Haag, Shape Technical Centre

SEYB, E.K., 1966, "A Mathematical Model for the Calculation of Visual Detection Range", Technical Memorandum TM-152, Den Haag, Shape Technical Centre



Fig.1 Aircraft Dornier Do 27



Fig.2 Helicopter Bell UH 1D



Fig.3 Tank Leopard



Fig.4 Test board used for determination of the maximum detection range



Fig.5 Test area with tank Leopard and test board

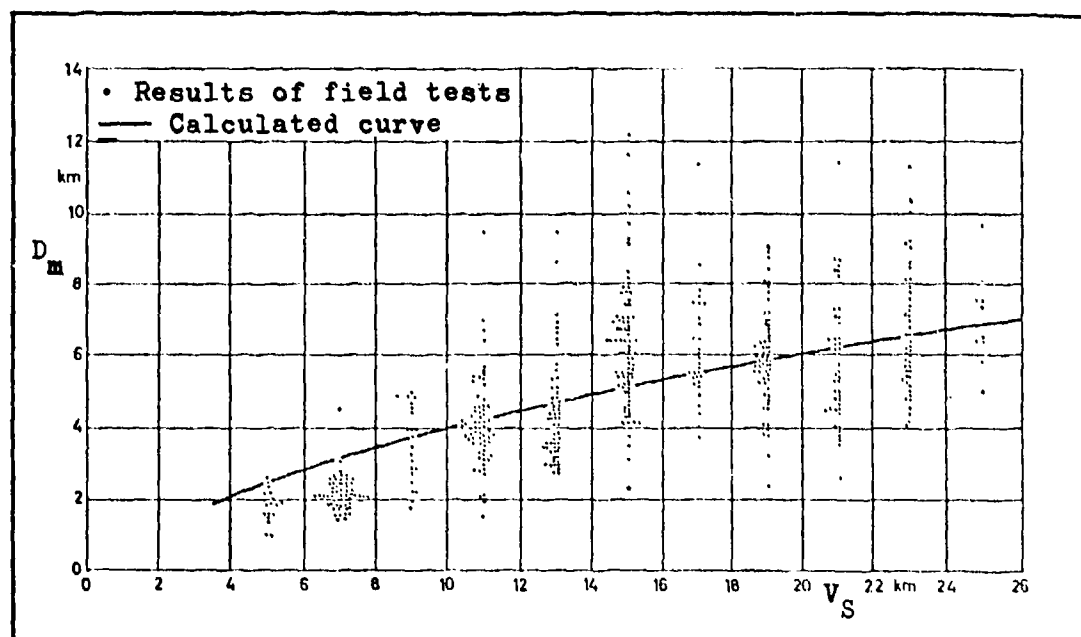


Fig.6 The maximum detection range D_m in dependence on the horizontal standard visibility (by Seyb)

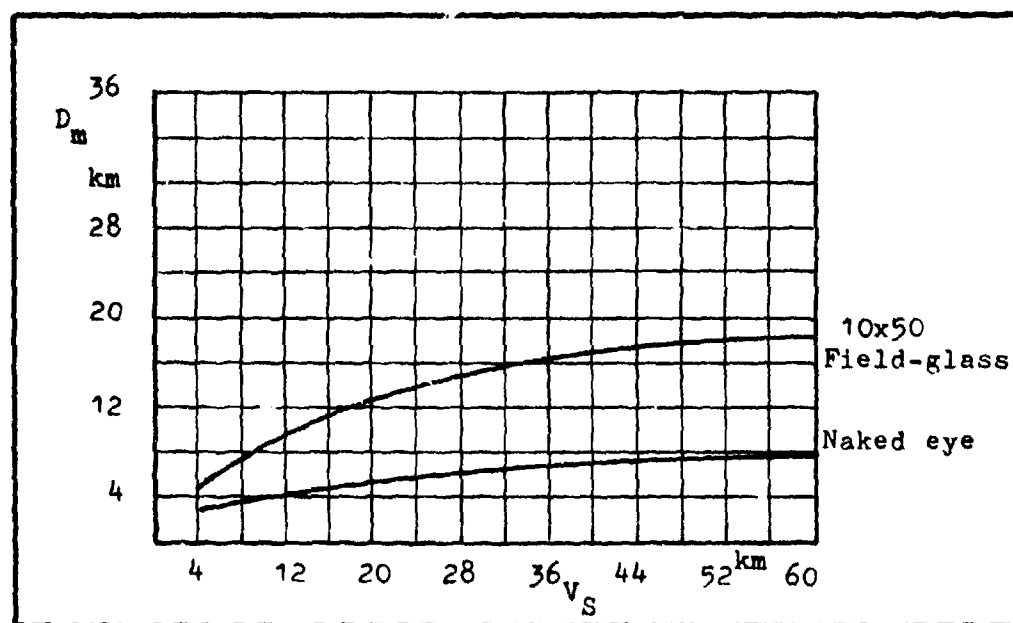


Fig.7 The maximum detection range D_m in dependence on the horizontal standard visibility (results of field tests)

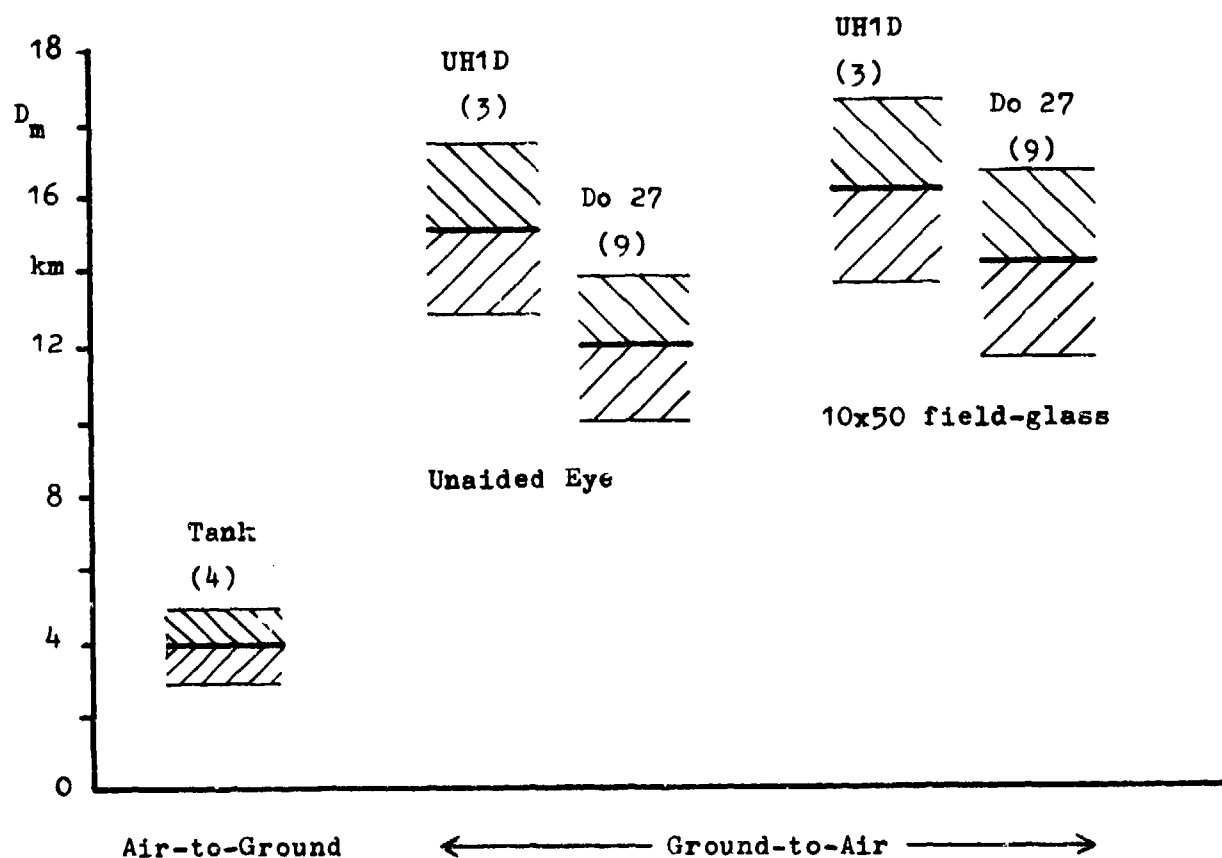


Fig.8 The maximum detection range D_m at observations air-to-ground and ground-to-air

Observers ground-to-air: Naked eye and 10x50 field glasses

Observers air-to-ground (pilot and co-pilot): Naked eye

Altitude of approach: 700 and 900 ft

Horizontal standard visibility: 53-57 km

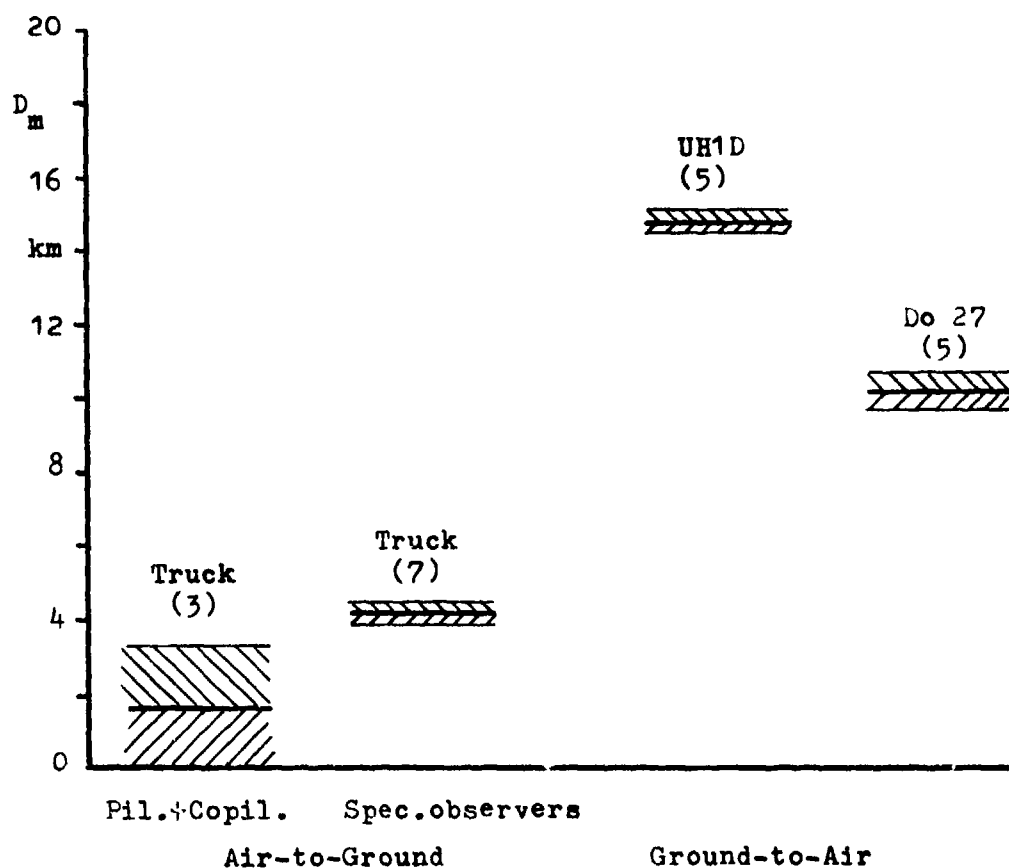


Fig.9 The maximum detection range D_m at observations air-to-ground and ground-to-air

Observers ground-to-air: Naked eye

Observers air-to-ground (pilot and co-pilot resp. special observers): Naked eye

Altitude of approach: 700 and 900 ft

Horizontal standard visibility: 39-42 km

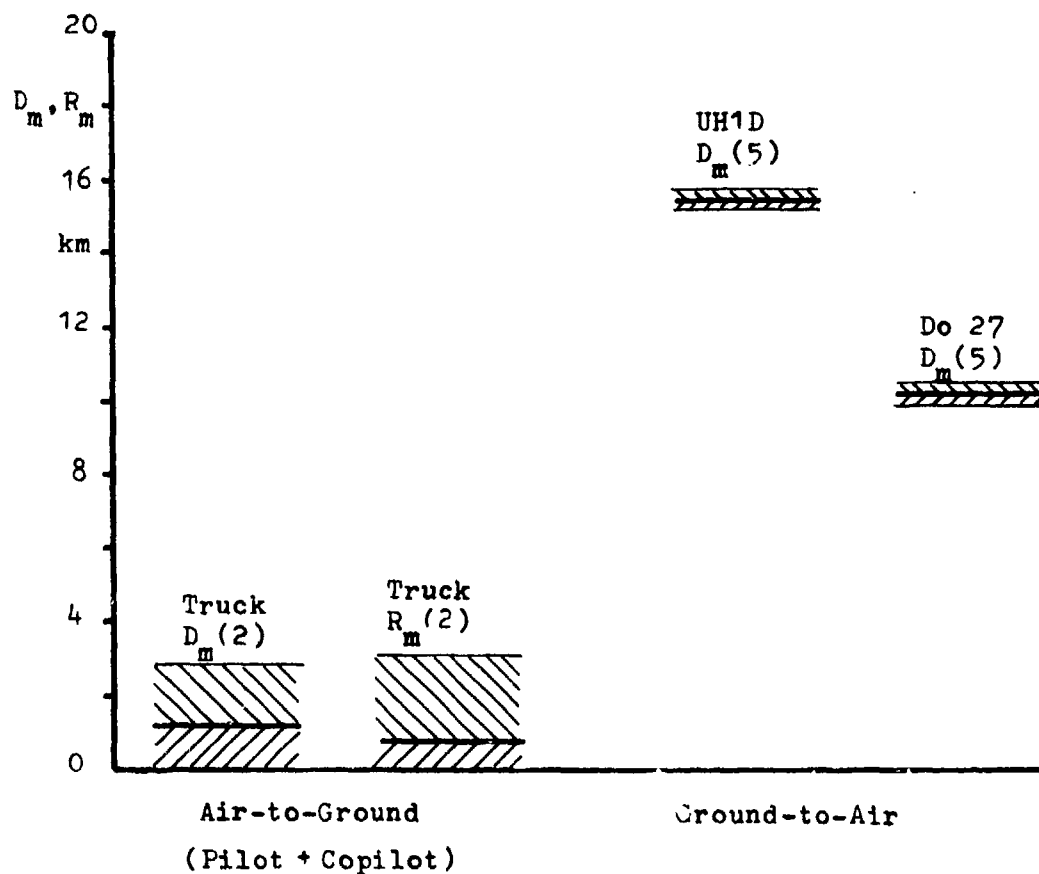


Fig.10 The maximum detection range D_m and the maximum recognition range R_m at observations air-to-ground and the maximum detection range D_m at observations ground-to-air

Observers ground-to-air: Naked eye

Observers air-to-ground: Pilot and co-pilot

Altitude of approach: 700 and 900 ft

Horizontal standard visibility: 39-40 km

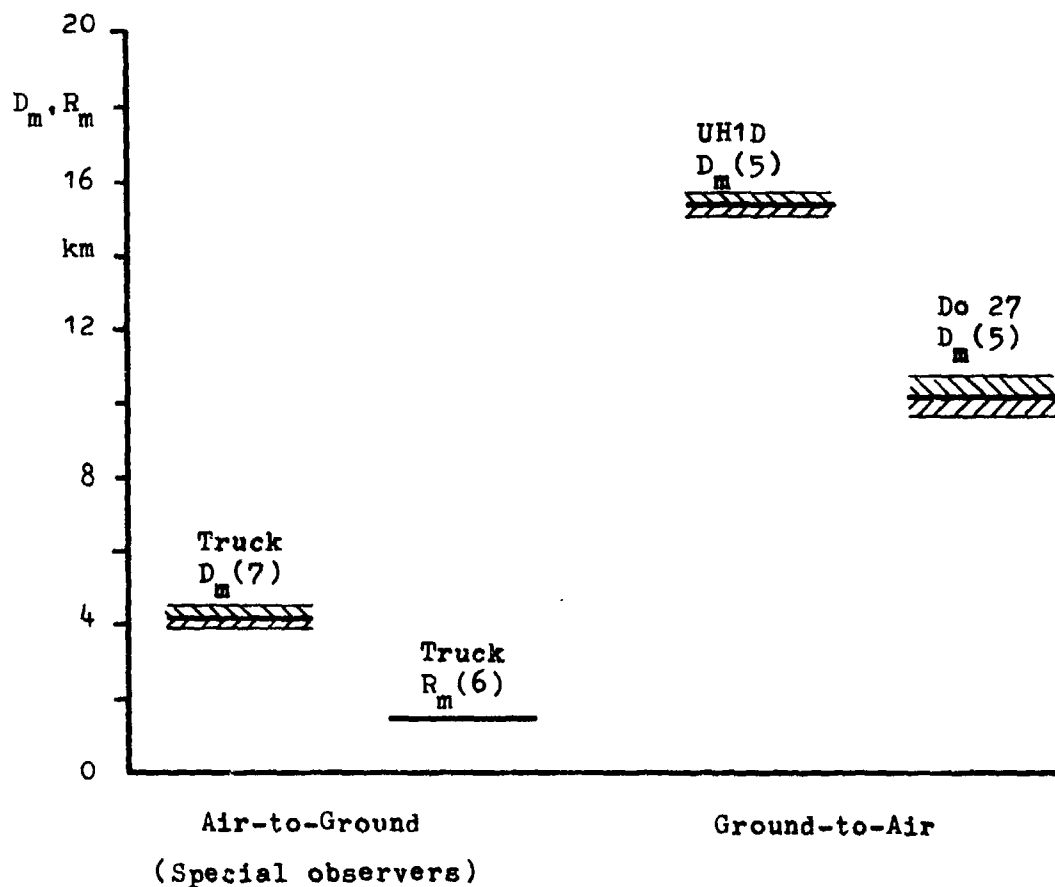


Fig.11 The maximum detection range D_m and the maximum recognition range R_m at observations air-to-ground and the maximum detection range D_m at observations ground-to-air

Observers ground-to-air: Naked eye

Observers air-to-ground (special observers): Naked eye

Altitude of approach: 700 and 900 ft

Horizontal standard visibility: 39-41 km

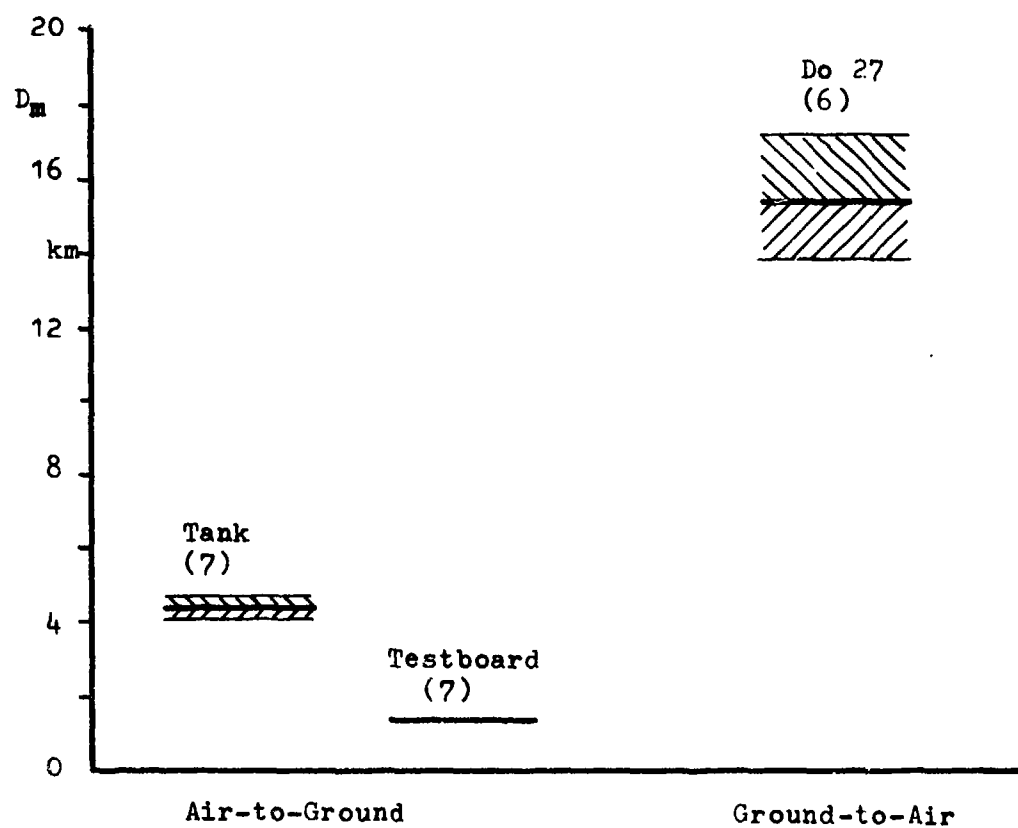


Fig. 12 The maximum detection range D_m at observations air-to-ground and ground-to-air

Observers ground-to-air: Naked eye

Observers air-to-ground (special observers): Naked eye

Altitude of approach: 700 and 900 ft

Horizontal standard visibility: 45-57 km

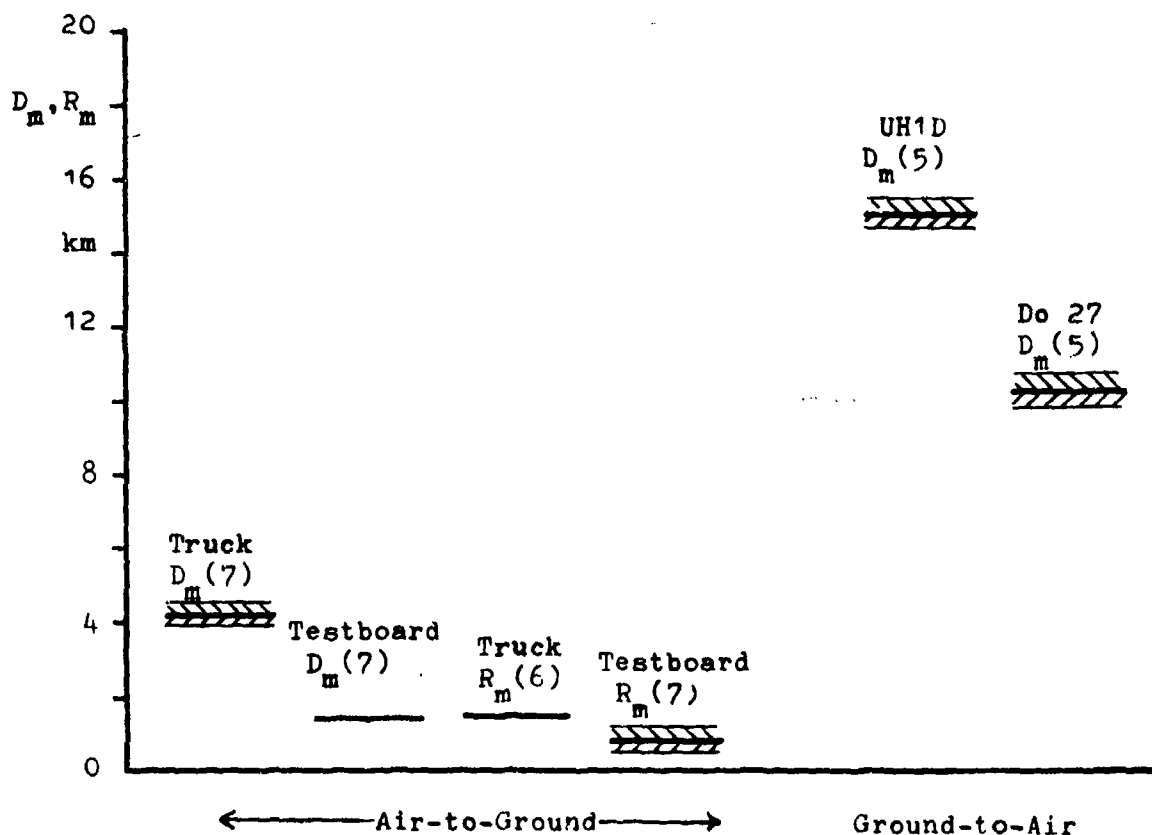


Fig.13 The maximum detection range D_m and the maximum recognition range R_m at observations air-to-ground and the maximum detection range U_m at observations ground-to-air

Observers ground-to-air: Naked eye

Observers air-to-ground (special observers): Naked eye

Altitude of approach: 700 and 900 ft

Horizontal standard visibility: 38-41 km

QUESTIONS AND COMMENTS
ON SESSION V

DECREASE OF CONTRAST IN THE ATMOSPHERE: STATISTICAL PRESENTATION OF THE RESULTS
OF DAYTIME AND NIGHTTIME MEASUREMENTS

Dr. Hoffman: Do you think that you may measure by your system for contrast measurements the inhomogeneity of the atmosphere over the measuring range, for example, the differences of the extinction coefficient between 100 and 200 m, 200 and 300 m and so on?

Dr. J. V. Schie: In principle this is indeed possible. However, the accuracy of every measuring point is comparable with the possible natural differences in the extinction coefficient. Therefore, it is not possible to decide whether or not the spread of the measuring points in Figure 4 is due to natural differences in α or to measuring errors.

Dr. Eckl: Can you please tell me how the histogram of the reflectance of the atmosphere (b_a) goes on for values greater than 1.4, which you integrated in the histogram with one bar?

Dr. J. V. Schie: The measurements indicated that the histogram of b_a for values greater than 1.4 decreases as a rule for every following class.

Summary of Session V

PROPAGATION LIMITATIONS ON SYSTEMS

by

Dr. R. R. Allan

The Chairman had invited Messrs. S. Q. Duntley, D. L. Fried, D. H. Hohn, J. van Schie and R. P. Urtz to form a panel for the round table discussion. In introducing the discussion the Chairman said he had been particularly impressed by the papers on compensated imaging. The theoretical study by McGlammer illustrated the possibilities beautifully, starting from a photograph of part of the moon's surface taken from Apollo 17. This was transformed by computer simulation into the corresponding image seen by an Earth-based telescope after degradation by turbulence, diffraction limiting and Poisson detector noise. The procedure was then reversed both for post-detection processing and also for pre-detection compensated imaging. There followed a discussion on the implications for telescope systems of the future.

Dr. Fried pointed out that the big problem which everyone seemed to be ducking was the measurement of the aerosol size distribution, and the refractive index including the absorptive part, and also the shape of the particles. Dr. Fenn elaborated on the difficulties of making direct measurements of the particle size distribution.

The topic of lidar systems was also related to the Chairman's own interests at R.A.E., Farnborough, England. He wondered whether enough was known about how the backscattering might vary? Dr. van Schie confirmed that the backscatter cross-section showed considerable variations. There was also some discussion of the Raman lidar approach: If there was a significant probability of more than one scattering, one would not know at which scattering the Raman shift had taken place.

ADDITIONAL COMMENTS ON SESSION V

by

Professor S. Q. Duntley and Dr. B. L. McGlammer

A panel composed of Dr. Allan, Professor Duntley, Dr. Fried, and Dr. Consortini summarized their assessment of the present state of knowledge of the effects of atmospheric scattering and turbulence on seeing and imagery. It was the consensus that more than half a century of research on this topic, chiefly at modest levels of funding, has produced much theory and a considerable body of atmospheric optical data but comparatively little in the way of careful experiments designed to test the validity of predictions of atmospheric effects on imagery by means of that theory and optical measurements of the atmosphere. Even less tested have been the connections with conventional meteorology. The panel unanimously endorsed the need for such trials, but recognized that on the basis of existing experience such endeavors tend to be difficult due to adversities of the outdoor working environment and to very high costs.

REPORT DOCUMENTATION PAGE			
1. Recipient's Reference	2. Originator's Reference AGARD-CP-183 ✓	3. Further Reference ISBN 92-835-0164-0	4. Security Classification of Document UNCLASSIFIED
5. Originator	Advisory Group for Aerospace Research and Development North Atlantic Treaty Organization 7 rue Ancelle, 92200 Neuilly sur Seine, France ✓		
6. Title	OPTICAL PROPAGATION IN THE ATMOSPHERE ✓		
7. Presented at	the Electromagnetic Wave Propagation Panel Symposium held in Lyngby, Denmark, 27-31 October 1975		
8. Author(s)	Various		9. Date May 1976
10. Author's Address	Various		11. Pages 646
12. Distribution Statement	This document is distributed in accordance with AGARD policies and regulations, which are outlined on the Outside Back Covers of all AGARD publications.		
13. Keywords/Descriptors Optical equipment Light scattering Weather		Atmospheric scattering Performance	14. UDC 681.7.013:551.59
15. Abstract A majority of military optical systems operate in the atmosphere and their performance is often degraded by weather. For several decades researchers have studied in-depth the performance limitations imposed by the atmosphere and devised techniques to get around these problems. The purpose of this symposium was to bring together and update the understanding of atmospheric optical propagation, present a comprehensive review of the state-of-the-art, and provide interaction among the key researchers in the NATO community.			

<p>AGARD Conference Proceedings No.183 Advisory Group for Aerospace Research and Development, NATO OPTICAL PROPAGATION IN THE ATMOSPHERE Published May 1976 646 pages</p> <p>A majority of military optical systems operate in the atmosphere and their performance is often degraded by weather. For several decades researchers have studied in-depth the performance limitations imposed by the atmosphere and devised techniques to get around these problems. The purpose of this symposium was to bring together and update the understanding of atmospheric optical propagation, present a comprehensive review of the state-of-the-art, and provide interaction among the key researchers in the NATO community.</p> <p>P.T.O.</p>	<p>AGARD-CP-183 681.7.013:551.59</p> <p>Optical equipment Atmospheric scattering Light scattering Performance Weather</p>	<p>AGARD Conference Proceedings No.183 Advisory Group for Aerospace Research and Development, NATO OPTICAL PROPAGATION IN THE ATMOSPHERE Published May 1976 646 pages</p> <p>A majority of military optical systems operate in the atmosphere and their performance is often degraded by weather. For several decades researchers have studied in-depth the performance limitations imposed by the atmosphere and devised techniques to get around these problems. The purpose of this symposium was to bring together and update the understanding of atmospheric optical propagation, present a comprehensive review of the state-of-the-art, and provide interaction among the key researchers in the NATO community.</p> <p>P.T.O.</p>	<p>AGARD-CP-183 681.7.013:551.59</p> <p>Optical equipment Atmospheric scattering Light scattering Performance Weather</p>
<p>AGARD Conference Proceedings No.183 Advisory Group for Aerospace Research and Development, NATO OPTICAL PROPAGATION IN THE ATMOSPHERE Published May 1976 646 pages</p> <p>A majority of military optical systems operate in the atmosphere and their performance is often degraded by weather. For several decades researchers have studied in-depth the performance limitations imposed by the atmosphere and devised techniques to get around these problems. The purpose of this symposium was to bring together and update the understanding of atmospheric optical propagation, present a comprehensive review of the state-of-the-art, and provide interaction among the key researchers in the NATO community.</p> <p>P.T.O.</p>	<p>AGARD-CP-183 681.7.013:551.59</p> <p>Optical equipment Atmospheric scattering Light scattering Performance Weather</p>	<p>AGARD Conference Proceedings No.183 Advisory Group for Aerospace Research and Development, NATO OPTICAL PROPAGATION IN THE ATMOSPHERE Published May 1976 646 pages</p> <p>A majority of military optical systems operate in the atmosphere and their performance is often degraded by weather. For several decades researchers have studied in-depth the performance limitations imposed by the atmosphere and devised techniques to get around these problems. The purpose of this symposium was to bring together and update the understanding of atmospheric optical propagation, present a comprehensive review of the state-of-the-art, and provide interaction among the key researchers in the NATO community.</p> <p>P.T.O.</p>	<p>AGARD-CP-183 681.7.013:551.59</p> <p>Optical equipment Atmospheric scattering Light scattering Performance Weather</p>

<p>Copies of papers presented at the Electromagnetic Wave Propagation Panel Symposium held in Lyngby, Denmark, 27-31 October 1975.</p> <p>ISBN 92-835-0164-0</p>	<p>Copies of papers presented at the Electromagnetic Wave Propagation Panel Symposium held in Lyngby, Denmark, 27-31 October 1975.</p> <p>ISBN 92-835-0164-0</p>
<p>Copies of papers presented at the Electromagnetic Wave Propagation Panel Symposium held in Lyngby, Denmark, 27-31 October 1975.</p> <p>ISBN 92-835-0164-0</p>	<p>Copies of papers presented at the Electromagnetic Wave Propagation Panel Symposium held in Lyngby, Denmark, 27-31 October 1975.</p> <p>ISBN 92-835-0164-0</p>

AGARD

NATO  OTAN

7 RUE ANCELLE · 92200 NEUILLY-SUR-SEINE
FRANCE

Telephone 745.68.10 · Telex 610176

**DISTRIBUTION OF UNCLASSIFIED
AGARD PUBLICATIONS**

AGARD does NOT hold stocks of AGARD publications at the above address for general distribution. Initial distribution of AGARD publications is made to AGARD Member Nations through the following National Distribution Centres. Further copies are sometimes available from these Centres, but if not may be purchased in Microfiche or Photocopy form from the Purchase Agencies listed below.

NATIONAL DISTRIBUTION CENTRES

BELGIUM

Coordonnateur AGARD - VSL
Etat-Major de la Force Aérienne
Caserne Prince Baudouin
Place Dailly, 1030 Bruxelles

CANADA

Science Scientific Information Service
Department of National Defence
Ottawa, Ontario K1A 0Z2

DENMARK

Danish Defence Research Board
Østerbrogades Kaserne
Copenhagen Ø

FRANCE

O.N.E.R.A. (Direction)
29 Avenue de la Division Leclerc
92 Châtillon sous Bagneux

GERMANY

Zentralstelle für Luft- und Raumfahrt-
dokumentation und -information
D-8 München 86
Postfach 860880

GREECE

Hellenic Armed Forces Command
D Branch, Athens

ICELAND

Director of Aviation
c/o Flugrad
Reykjavik

ITALY

Aeronautica Militare
Ufficio del Delegato Nazionale all'AGARD
3, Piazzale Adenauer
Roma/EUR

LUXEMBOURG

See Belgium

NETHERLANDS

Netherlands Delegation to AGARD
National Aerospace Laboratory, NLR
P.O. Box 126
Delft

NORWAY

Norwegian Defence Research Establishment
Main Library
P.O. Box 25
N-2007 Kjeller

PORTUGAL

Direccao do Servico de Material
da Forca Aerea
Rua de Escola Politecnica 42
Lisboa
Attn: AGARD National Delegate

TURKEY

Department of Research and Development (ARGE)
Ministry of National Defence, Ankara

UNITED KINGDOM

Defence Research Information Centre
Station Square House
St. Mary Cray
Orpington, Kent BR5 3RE

UNITED STATES

National Aeronautics and Space Administration (NASA),
Langley Field, Virginia 23365
Attn: Report Distribution and Storage Unit

THE UNITED STATES NATIONAL DISTRIBUTION CENTRE (NASA) DOES NOT HOLD
STOCKS OF AGARD PUBLICATIONS, AND APPLICATIONS FOR COPIES SHOULD BE MADE
DIRECT TO THE NATIONAL TECHNICAL INFORMATION SERVICE (NTIS) AT THE ADDRESS BELOW.

PURCHASE AGENCIES

Microfiche or Photocopy

National Technical
Information Service (NTIS)
5285 Port Royal Road
Springfield
Virginia 22151, USA

Microfiche

Space Documentation Service
European Space Agency
114, Avenue Charles de Gaulle
92200 Neuilly sur Seine, France

Microfiche

Technology Reports
Centre (DTI)
Station Square House
St. Mary Cray
Orpington, Kent BR5 3RF
England

Requests for microfiche or photocopies of AGARD documents should include the AGARD serial number, title, author or editor, and publication date. Requests to NTIS should include the NASA accession report number. Full bibliographical references and abstracts of AGARD publications are given in the following journals:

Scientific and Technical Aerospace Reports (STAR),
published by NASA Scientific and Technical
Information Facility
Post Office Box 8757
Baltimore/Washington International Airport
Maryland 21240, USA

Government Reports Announcements (GRA),
published by the National Technical
Information Services, Springfield
Virginia 22151, USA

